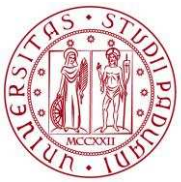

UNIVERSITÀ
DEGLI STUDI
DI PADOVA

Università degli Studi di Padova
Dipartimento di Fisica e Astronomia “Galileo Galilei”

CORSO DI DOTTORATO DI RICERCA IN: FISICA
31° CICLO

PhD THESIS

THE DECAY OF THE ^{46}Ti*: A COMPARATIVE STUDY OF FOUR ENTRANCE CHANNELS

Tesi redatta con il contributo finanziario dell’INFN – Laboratori Nazionali di Legnaro

Coordinatore: Prof. Cinzia Sada
Supervisore: Dott.ssa Fabiana Gramegna

Dottoranda: Magda Cicerchia

Contents

Summary

During the early stages of the reaction, non-equilibrium processes play an important role in the dynamics of heavy-ion collisions; in particular, they contribute to determine the features of the remaining hot thermalized sources. The fast emissions issued by these processes depend both on the entrance channel mass asymmetry and on the beam velocity [45]. In this context, a comparative study of four reactions has been conceived: the idea is to study these systems in two energy regimes. Firstly, at energies close to the onset of the pre-equilibrium process, to evaluate its properties in a quite well-known framework; then, to carry out a following experiment of the same systems at higher bombarding energies, where the pre-equilibrium part is well assessed and may play a major role. In this work, the first measurement is presented. The four reactions studied reactions are: $^{16}O +^{30} Si$, $^{18}O +^{28} Si$ and $^{19}F +^{27} Al$ at 7 MeV/u and $^{16}O +^{30} Si$ at 8 MeV/u. Through central collisions and when the complete fusion occurs, the four studied cases all lead to the same compound nucleus, the excited ^{46}Ti, even if with slightly different excitation energies. Small differences in their de-excitation chain are expected, except for the cases $^{16}O +^{30} Si$ at 8 MeV/u and $^{18}O +^{28} Si$ at 7 MeV/u, which were chosen to populate the compound nucleus at the same excitation energy. On the other hand, the choice of the same beam energy (7 MeV/u) for three of the four reactions should imply that the non-equilibrium processes are compatible, given the same projectile velocity [45]. The main characteristics of the four reactions are shown in Table 1.

The main goal of this experiment is to measure and compare different mass entrance channel reactions with the aim of estimating the pre-equilibrium components. This will be done by analyzing the competition between fast and statistical emissions; by evaluating

Entrance channel beam + target	$E_{beam,lab}$ MeV	η	**CN**	E^* MeV
$^{16}O +^{30} Si$	111	0.30	^{46}Ti	88.0
$^{16}O +^{30} Si$	128	0.30	^{46}Ti	98.4
$^{18}O +^{28} Si$	126	0.22	^{46}Ti	98.5
$^{19}F +^{27} Al$	133	0.17	^{46}Ti	103.5

Table 1: The main charcteristic of the reactions.

exclusive observables through correlation analysis and by comparison with model predictions. Moreover, information about the influence of structure effects, like α-clustering, will be investigated for medium mass systems.

The experiment was performed by the NUCLEX collaboration at the Legnaro National Laboratory (LNL), where the four beams have been provided by the TANDEM acceleration system and have been used respectively onto the different thin (100 $\mu g/cm^2$) targets: ^{30}Si, ^{28}Si and ^{27}Al. The employed energies are close to the lower thresholds for the pre-equilibrium emission process. The GARFIELD plus Ring Counter (RCo) detector fully equipped with digital electronics [51, 52] has been used to detect light charged particles (LCP), light fragments (LF) and evaporation residues (ER).

A very strict selection on experimental data was performed for the subsequent analysis since an evident Oxigen-contamination of the Si and of the Al targets have been observed. In order to define quantitatively the amount of contaminants, a dedicated measurement was performed on the targets with RBS technique [100, 101], at the LNL AN-2000 accelerator: a ratio of about 1:1 was measured for the Oxygen with respect to both ^{30}Si and ^{28}Si targets, while a ratio of 1:2 was present in the ^{27}Al target. The contaminant reactions were simulated using the $GEMINI^{++}$ code and the $HIPSE + SIMON$ codes; such simulations are then compared with the experimental data and analyzed. The experimental high contamination of the target is not separable from the other inclusive data due to the superposition with the deep inelastic collisions products. Therefore, it is not possible to

study this "contaminant" reaction. Fortunately, the reactions of interest are well separable from the "contaminant" reactions and from the other reaction mechanisms. In order to avoid contaminated data, the considered events are those for which the total detected charge is larger than the 70% and the longitudinal momentum is around the unit; to select such specific events a graphical contour has been applied on the plot of correlation between total charge and longitudinal momentum. These graphical cuts were read by the analysis program and applied not only to the experimental data but also to the simulated ones.

As a consequence of this first data selection, the amount of the experimental selected events is around the 10% of the total detected events. A further selection was applied asking for the detection of the light charge particles (detected in the whole apparatus: GARFIELD+RCo) in coincidence with at least one evaporation residue (in forward angles: RCo); such events characterize the central collisions. The combined effects of the two cuts (on Z_{tot} *vs.* q_z/q_{beam} and on Z *vs.* E_{lab}) imposed on the experimental data are analyzed and cross-checked in comparison with the same cuts imposed on the $AMD{+}GEMINI^{++}$ simulation.

In order to select only the event produced by fusion-evaporation reactions, an additional constraint was imposed to the selection of residues: in a "good" event only one fragment with a charge heavier than 6 can exist; in this way, the fission events are excluded from the selection.

To obtain a theoretical feedback, the selected experimental observables have to be compared with the simulations produced with different codes based on theoretical models; in particular, the code $GEMINI^{++}$ by R. Charity [67, 68], was used to describe the statistical decay of the compound nuclei produced in the reactions. In addition, the dynamical codes AMD by A. Ono [77, 78, 79] and $HIPSE$ by D. Lacroix [96], were used to simulate the dynamical part of the reactions. The AMD code is based on a stochastic equation of motion for the Gaussian wave-packets representing the colliding nucleons. It describes the cluster structure of the interacting particles and takes into accounts the particle-particle correlations. The $HIPSE$ code used the sudden approximation and can describe the nuclear collisions in the intermediate energy range. Both codes can describe

the first evolution part of the reactions; after a time, t, the $GEMINI^{++}$ code has been coupled to dynamical model as afterburner to simulate in a statistical environment how the produced primary excited fragments decay, so to simulate the entire secondary particle and fragment production.

A detailed analysis of experimental data in comparison with $GEMINI^{++}$, $HIPSE+GEMINI^{++}$ and $AMD+GEMINI^{++}$ simulations are presented for selected observables. For the $GEMINI^{++}$ code, a specific choice of the level density has been considered, which take into account the angular momentum induced deformation of the $^{46}Ti^{*}$ nucleus, already observed by A. Maj and co-workers. Moreover, in order to take into account the effects of a possible deformation induced by temperature, different values of the parameter w have been considered: this parameter permits to simulate the emission from nuclei with a convolution of barriers going from $r + dr$ to $r - dr$, where $dr = w\sqrt{T}$. In our case, we began by using the default value of $w = 1.0\ fm/\sqrt{T}$, which corresponds to an axes ratio $b : a$ of $2 : 1$; afterwards, values of $w = 0.0\ fm/\sqrt{T}$, which corresponds to a unique barrier of a spherical nucleus, and $w = 1.1\ fm/\sqrt{T}$, which corresponds to a ratio of the nucleus axes of $b : a = 2.2 : 1$ have been considered. The AMD code has been run with the default parameters set. In particular, the cluster correlation degree was fixed to $nnchange_gamma = -1d0$; a screened nucleon collision cross section without any suppression of cluster correlations was imposed ($screened_y = 0.85d0$); the cluster-cluster binding process was considered ($coacc_set(enable = .true.)$). The parameter considered for $HIPSE$ are listed in Table 2. The analysis have been performed for all the four reactions.

Hardness of potential	**Percentage of exchange**	**Percentage of NN collision**
-0.1	0.60	0

Table 2: $HIPSE$ input parameters set optimized for $E_{lab} \sim 10MeV/u$.

Firstly, the analysis of the events for which at least the 70% of the total charge has been collected was performed comparing experimental light charged particle energy spectra,

multiplicities, angular distributions with those simulated with the different models.

A similar analysis has been performed for the complete events studying experimental light charged particle energy spectra, multiplicities, angular distributions. In order to better understand differences and similarities observed between simulations and experimental data and between the four reactions, which differ from each other by small amounts in terms of beam velocities, excitation energies, entrance channel isospin content and mass asymmetry, a deeper study has been carried out for complete events, looking at exclusive decay channels. For each reaction, selected evaporation residues from $Z_{res} = 21$ down to $Z_{res} = 13$ have been studied in coincidence with light charged particles or light fragments and compared to theoretical predictions. For each Z_{res}, all main decay channels have been identified and compared, in such a way to observe relative yields and characteristics and to determine the branching ratios. Moreover, the angular distributions, the multiplicities and the energy spectra of the different coincident particles have been observed and compared to simulations for each selected residue. Both experimental and calculated yields are normalized to the number of their own residues.

A quantitative information on the studied reactions can be derived by the branching ratios calculated for each detected evaporation residue and compared to theoretical predictions. Each specific decay channel has been also analyzed in terms of Q-value and of the characteristics of the emitted particles (energy and angular distributions). In general, a larger dissipation in the experimental data set is observed.

Finally, a more detailed study on the multiple α-channels (1α, 2α and 3α) is presented, where the correlations among the α-particles have been analyzed. In particular, in the 2α decay channel, the origin of the observed major experimental yield with respect to simulations have been looked for, observing particular configurations of relative energies and correlation angles, which were not predicted by models. Even in the three α-particles case the correlations among the $\alpha-\alpha$ relative energies are relevant; from different conceived Dalitz plots some information on the event configuration was deduced, which underlined both similarities to model predictions (configurations with 3α characterized by the same energies) and discrepancies (configurations with 3α with the same relative energies).

As a conclusion of this thesis work we can say that in the four analyzed systems, selecting central fusion-evaporation reactions, we observed both standard characteristics well described by simulation models (especially when referring to odd evaporation residue exit channels) and very peculiar behavior when dealing with exit channels in which the maximum number of α-particles could be emitted. These peculiarities indicate that the role of preformed α-cluster inside a nucleus should not be under-evaluated, since it may drastically change the path towards the final exit channel.

Further study on the analyzed systems will be continued by changing parameters in the dynamical models, but these are out of the present thesis work.

Introduction

The purpose of this thesis is to report on the analysis done on the four reactions: $^{16}O+^{30}Si$, $^{18}O+^{28}Si$ and $^{19}F+^{27}Al$ at 7 MeV/u and $^{16}O+^{30}Si$ at 8 MeV/u, which have been measured at Legnaro National Laboratories [1] with the GARFIELD+RCo detectors array [2, 51, 52] in June 2015, just before the start of the XXXI PhD series.

The idea behind this experiment (*ACLUST2*) is to evaluate the properties of the pre-equilibrium emission process in an energy regime close to the onset of such emission with the future project to carry out a following experiment of the same systems at higher bombarding energies, where the pre-equilibrium component is well assessed and may play a more important role.

This experiment finds employment in the wider framework of an extensive research campaign on pre-equilibrium emission of light charged particles from hot nuclei [46, 47, 48, 49] made by the NUCLEX collaboration [3] in the last decade. The study of pre-equilibrium emitted particles is a useful tool to examine nuclear clustering analyzing the effects of possible cluster structures on the nuclear reactions [9].

The thesis is organized as follows: the theoretical issues behind the described analysis are reported in Chapter 1, which is followed by the description of the main features of the analyzed experiment and of the experimental apparatus in Chapter 2. The link between theory and experiment is made by comparison to simulations produced in our work with three simulation codes; the statistical $GEMINI^{++}$ by R. Charity [67], the dynamical *AMD* by A. Ono [77, 78, 79] and the phenomenological *HIPSE* by D. Lacroix [96]. A simplified description of those codes are presented in Chapter 3. In order to consider the hyper-deformation of the compound nucleus ^{46}Ti, largely described by A. Maj and

collaborators [106, 107, 108] as reported in Chapter 4, the $GEMINI^{++}$ parameters, related to the angular momentum of the compound nucleus, have been discussed and verified.

During the first stage of our analysis, we found a huge contamination of the targets; subsequently a careful selection of data have been carried out to avoid any further trouble in the data analysis. This is reported in Chapter 5, together with the software filtering applied to simulations, taking into account the experimental conditions, in order to be directly compared with experimental data.

The second part of the thesis (in Chapter $6 \div 9$) is devoted to the data analysis:

- Chapter 6: quasi-complete events ($Z_{tot} \geq 18$) analysis;
- Chapter 7: complete events ($Z_{tot} = 22$) analysis;
- Chapter 8: study of selected evaporation residue channels ($Z_{ER} = 13 \div 21$);
- Chapter 9: characterization of specific multiple (1, 2 and 3) α-channels.
- Chapter 10: evaluation of quantitative observables (BR and Q-value) of the major populated channels;

Each analysis Chapter has its own conclusion, while the main conclusions of this work is given at the end, in the Conclusions.

Chapter 1

The Scientific Framework

Reaction dynamics is a very interesting tool, which complements nuclear structure studies to get information and to deepen our knowledge on nuclear matter properties. In particular, in the framework of the heavy-ion nuclei reactions, pre-equilibrium processes are a nice example of nuclear mechanisms, which can correlate reaction dynamics to nuclear structure. In fact, several approaches, which are dedicated to the description of the pre-equilibrium processes, have been proposed in which a particular attention have been devoted to cluster emission: possible effects on the dynamics due to cluster structure in the reaction partners have also been proposed, suggesting the possibility of disentangling the possible pre-formation of clusters from those dynamically formed through the comparison between different reactions.

This chapter is devoted to present a classification of reactions mechanisms (Section 1.1) with particular emphasis on the fusion-evaporation mechanism (Section 1.2) and on the pre-equilibrium emission (Section 1.3); in the last Section (1.4) the influence of clustering in pre-equilibrium models is treated.

1.1 Reaction Mechanisms

Nuclear reactions allow to investigate a large number of nuclear degrees of freedom, both collective and intrinsic, characterized by different typical energies and time scales. The

interaction between nucleons inside two colliding nuclei can be explained via a mean field potential (one-body) and/or, in a complementary way, via a two-body dissipation process, depending on the energy involved in the reaction. In the first case, when a nucleon hits a nucleus, it feels all the nucleons together inside the nucleus, while in the second case the interactions are with the individual nucleons. In the nuclear reactions, the final inclusive yields represent an integrated contribution over the whole time evolution of the reaction and, because of that, the information they bear on specific excitation energy regions of the different nuclei explored during the reaction may be model dependent. In reality, both dynamical aspects and structural properties play an important role in the evolution of the reaction: what is measured is always a convolution of different emitting sources and processes taking place, at different times, in a wide range of excitation energies.

In order to achieve a classification of the reaction mechanisms, the main factors are:

- mass (A_p), charge (Z_p) and structure (J_π of the ground state and excitation spectrum) of the projectile;
- mass (A_T), charge (Z_T) and structure (J_π of the ground state and excitation spectrum) of the target;
- the projectile impinging energy (E_{beam}) in the laboratory frame;
- the impact parameter (b), defined as the distance between the straight-line trajectory of the projectile approaching the nucleus and its parallel crossing the center of the target.

The beam energy allows to evaluate the wavelength of each nucleon in the projectile:

$$\lambda = \frac{h}{m_N v_p} = \frac{h}{\sqrt{\frac{2E_{beam}}{M_p}}} \tag{1.1}$$

where M_p, A_p and v_p are, respectively, the projectile mass, mass number and velocity, m_N is the nucleon mass and h is the Planck constant. Above the Coulomb barrier, the wavelength of each nucleon of the projectile is larger than the nucleon-nucleon distance

in the target and so due to the less effectiveness of the Pauli blocking the two-nucleons collisions become more important; therefore, a collective behavior of nucleons during the reaction is expected and an excited hot system is produced.

Furthermore, the reaction mechanisms can be distinguished by comparison of the impact parameter with the grazing impact parameter, b_{graz}. This latter is defined as the least distance between the projectile trajectory and the center of the target for which the nuclear interaction is negligible and so the cross section corresponds to the Rutherford cross section:

$$\frac{d\sigma}{d\Omega} = \left(\frac{Z_1 Z_2 e^2}{4E_{kin} sin^2 \frac{\theta}{2}} \right)^2 . \tag{1.2}$$

In the case of Coulomb interaction, a good approximation of the grazing impact parameter is given by the conservation of angular momentum:

$$b_\infty p_\infty = R_C p_C \tag{1.3}$$

where:

- b_∞ is the asymptotic impact parameter;
- $R_C = 0.5 + 1.36 \left(A_1^{1/3} + A_2^{1/3} \right)$ is the distance between the centers of the two interacting nuclei at the Coulomb barrier;
- p_∞ and p_C are, respectively, the initial momentum of the projectile with energy $E_{c.m.}$ (in the center of mass frame) at an infinite distance and the momentum of the ion at Coulomb barrier (R_C). Therefore:

  $$b_{graz} = R_C \sqrt{1 - \frac{V_{Coul}}{E_{c.m.}}} \tag{1.4}$$

  where $V_{Coul} = 1.44 \frac{Z_1 Z_2}{R_1 + R_2}$ MeV is the Coulomb barrier height, with Z_1 and Z_2 the projectile and target charge and R_1 and R_2 the projectile and target radii.

Referring to the previous considerations and looking at Fig. 1.1, one can identify different energy-impact parameter regions connected to different reaction mechanisms:

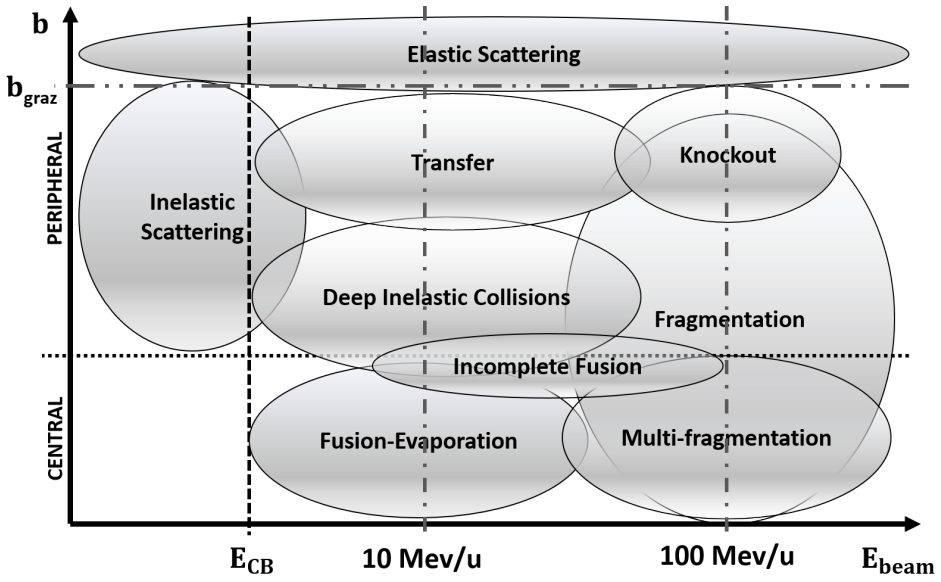

Figure 1.1: Different reaction mechanisms regions as a function of E_{beam} and of b.

- $E_{beam} < 10$ MeV/u:
  - central collisions ($b << b_{graz}$ and $b < b_{graz}$) give rise to complete and incomplete fusion [4] with the creation of a thermalized source, called Compound Nucleus (CN), which is formed by the sum of the projectile and target nucleons, when the fusion is complete;
  - peripheral collisions ($b \leq b_{graz}$) are characterized by a strong interaction between the two nuclei with interchange of nucleons (from few nucleons transfer to highly dissipative processes, in which a large portion of mass, charge, energy and angular momentum are exchanged): in the exit channel, two fragments similar to the entrance partners, the quasi-projectile (QP) and the quasi-target (QT), are produced [5];
  - in the case of $b \sim b_{graz}$, direct (or grazing) reactions arise [6]: the kinematics of the two nuclei is just slightly perturbed with few nucleons transfer between projectile and target.
- in the energy region with $E_{beam} > 100$ MeV/u the nucleon-nucleon interaction is de-

scribed with a mean-field approximation; at such energies, the two-nucleon collisions are also more important:

  - in central collisions ($b << b_{graz}$ and $b < b_{graz}$), the high excitation energy brings from multifragmentation to vaporization of the nucleus;
  - in peripheral collisions ($b \leq b_{graz}$), the interaction is described with the participant-spectator model: only a part of the nucleons of the projectile and the target interact strongly, forming a so called "fire-ball", which may disintegrate either via vaporization or multifragmentation depending on the excitation energy; the other part of nucleons continues their colliding trajectory almost undisturbed.

- the energy region 10 MeV/u $< E_{beam} <$ 100 MeV/u is that of transition from binary reactions to explosive ones and from nuclei described as liquid drop to nuclei described as gases; in particular, for central collisions ($b << b_{graz}$ and $b < b_{graz}$) the main process is the incomplete fusion, where not all the projectile momentum is transfered to the CN. It is in this range of energies that a new mechanism takes place, which is the multifragmentation process, related to the liquid-gas phase transition in nuclei [7].

In all the three-energy range, for $b > b_{graz}$ elastic scattering occurs because the nuclear force is completely negligible with respect to the Coulomb one due to the large distance between projectile and target.

Finally, an important factor which helps in the classification of the reaction mechanisms is the time scale of the process and its relation with the transit time of the projectile nucleons in the target nucleus. It is determined by the number of intranuclear collisions taking place before any nucleon emission occurs. Typical times for direct reactions are of the order of 10^{-22}s, which is compatible with the time needed by the projectile to cross the target nucleus; these are one-step processes with a strong correlation between the initial and final reaction channels. On the other side, CN reactions proceeded through a long series of intranuclear collisions that lead to the energy equilibrium of the fused object; therefore, the time evolution of such process is much slower ($10^{-18} \div 10^{-16}$ s). The

thermalized CN might be excited and, to settle to a stable condition, emits either charged particles or γ-ray in the, so called, particle evaporation (decay) process (see Section 1.2.2).

Between these two extreme possibilities (direct reactions and CN formation-decay) a continuous spectrum of possibilities is expected, which may be classified as a series of pre-equilibrium mechanisms, which are characterized only partial energy and angular momentum dissipation (see Section 1.3). Such a schematic classification of the reactions is also supported by the observation of typical angular distributions. Forward peaked angular distributions are observed in the case of direct reactions: the oscillatory behaviour is characteristic of the structure of the residual nucleus. On the other hand, symmetric angular distributions are associated with CN reactions: for which the Bohr hypothesis [8] states that the thermalization process brings to a complete loss of information about the entrance channel. A sketch of this behavior is shown in Fig. 1.2.

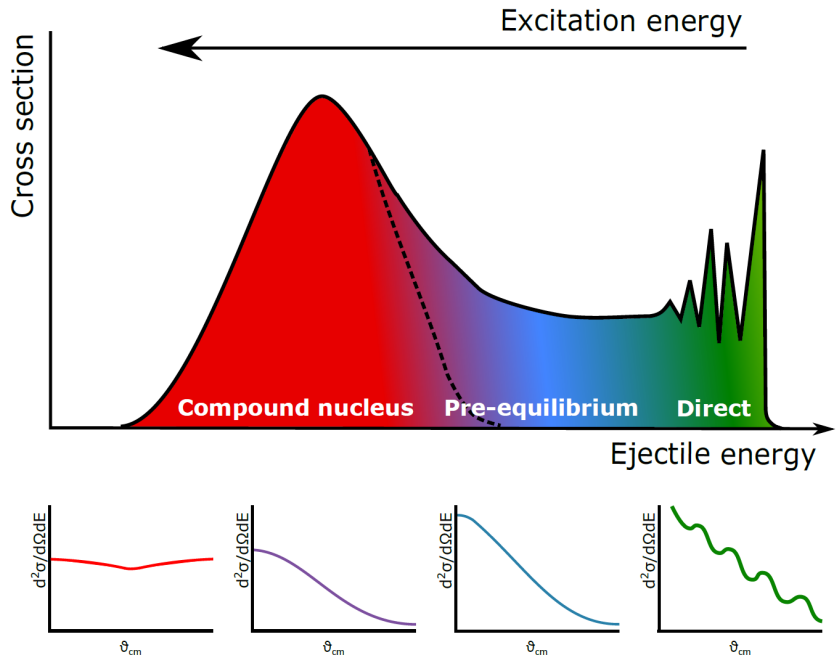

Figure 1.2: "Energy spectrum of a reaction between nuclei $A(a,b)B$ and associated angular distributions, which show a gradual transition from forward peaked oscillatory behavior to isotropy for decreasing energy in the output channel". From [9]

1.2 Fusion-Evaporation Reactions

At beam energy lower than 10 MeV/u and considering central collisions, the interacting partners form a fused system due to a considerable overlap of their density distribution. Such phenomenon can be described as the result of a strong friction between the two participating nuclei which leads to a merging of all their nucleons: through successive nucleon-nucleon collisions, the nucleons from the projectile transfer energy to the nucleons of the target until a complete thermalization is reached, with the equipartition of energy over all the nucleons. The formation of a unique thermalized object is obtained when the interaction time becomes long enough in comparison to the thermalization time and the initial available kinetic energy of the projectile turns into internal energy of the whole system, which becomes excited. The compound nucleus (CN) is formed if the strong attractive force prevails on Coulomb force; it is produced in an excited state and, when the collision is occurring between two heavy nuclei, it is highly rotating, due to the large transferred angular momentum. If the bombarding energy is low (generally $<$ 10 MeV/u) a complete fusion can be reached and therefore the mass and charge of the CN is equal to the sum of the two partners. However, depending on the entrance channels and with the growth of the incident energy, some nucleons or cluster of nucleons may be emitted before full thermalization is reached; such process is defined pre-equilibrium or fast emission (see Section 1.3) and, as a result a CN with a reduced mass and excitation energy is formed. Nucleon and cluster pre-equilibrium emission is a fast process (10^{-22} s) and increases gradually with the increase of the impinging energy.

1.2.1 Complete Fusion

As previously reported, the complete fusion is the process in which projectile and target fuse together to form the CN, which is then characterized by an angular momentum J_{CN} and an excitation energy E^*_{CN}, which depend on the energy and mass asymmetry of the entrance channel. The excitation energy is given by:

$$E^*_{CN} = E_{cm} + Q_{fus} \tag{1.5}$$

where:

- $E_{cm} = E_{beam}\dfrac{A_T}{A_p + A_T}$ is the energy available in center of mass;
- $Q_{fus} = [(m_p + m_T) - m_{CN}]c^2$ is the Q-value associated to the formation of the CN in its ground-state with m_p, m_T and m_{CN} projectile, target and CN mass at their ground-state, respectively.

Complete fusion [10] can be interpreted introducing an effective potential, $V_\ell(r)$ (shown

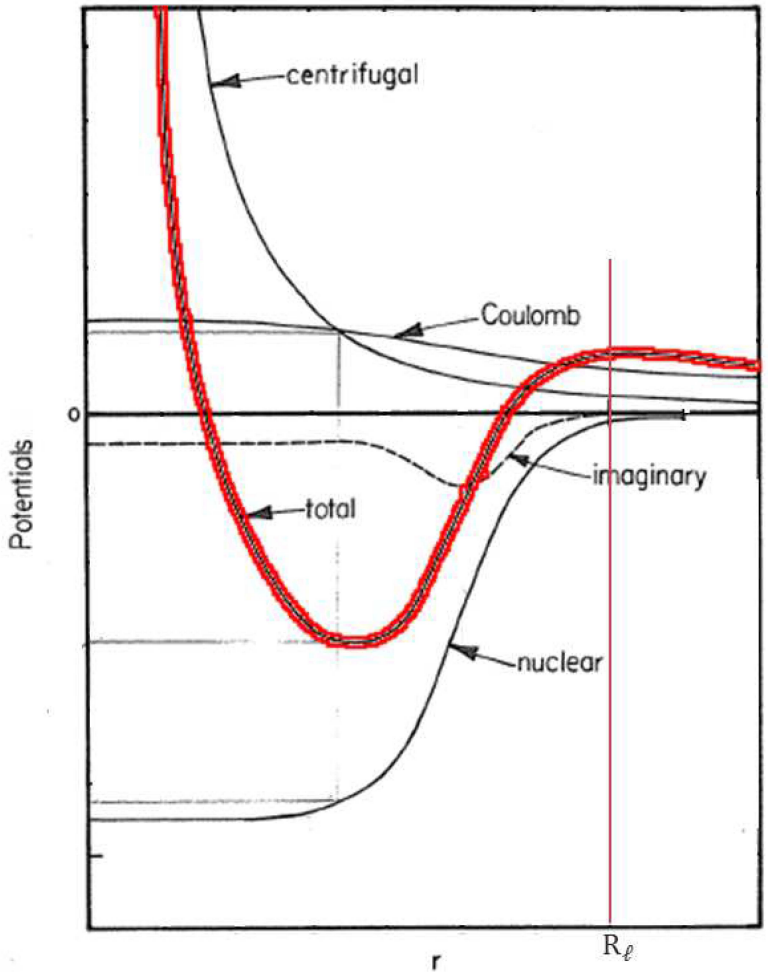

Figure 1.3: Effective barrier (total) is shown as sum of Coulomb, nuclear and centrifugal potentials. Figure adapted from [10]

in red in Fig. 1.3), given by the sum of the Coulomb, nuclear and the centrifugal potentials:

$$V_\ell(r) = V_{Coul}(r) + V_{Nucl}(r) + \frac{\ell(\ell+1)\hbar^2}{2\mu r^2} \tag{1.6}$$

In such potential a well occurs for $\ell < \ell_{crit}$: the maximum, achieved for $\ell = \ell_{crit}$, represents the fusion barrier, $V_\ell(R_\ell)$. Classically, if the relative kinetic energy (ε) is greater than the fusion barrier there is a high probability that the system is trapped in the well; moreover, if the angular momentum is dissipated bringing to a reduced centrifugal barrier, this may enhance fusion probability.

From the theory on nuclear reactions, the fusion cross section can be expressed, in a semi-classical approach, as the product of geometrical cross section and transmission coefficient, T_ℓ:

$$\sigma_{reac} = \sum_\ell \sigma_{reac}(\ell) = \frac{\pi}{k^2}\sum_0^\infty (2\ell+1)T_\ell. \tag{1.7}$$

The transmission coefficients define the probability of creating the CN in a specific state characterized by an energy E^*_{CN} and an angular momentum J_{CN} and depend on impinging energy and angular momentum.

When $\varepsilon \simeq V_\ell(R_\ell)$, the transmission coefficients can be approximated as the barrier penetration probability for a parabolic barrier with a curvature $\hbar\omega_\ell$ [11]:

$$T_\ell(\varepsilon) = \frac{1}{1 + exp\left\{2\pi\frac{V(r)-\varepsilon}{\hbar\omega_\ell}\right\}} \tag{1.8}$$

where ω_ℓ is the curvature of the barrier at its maximum. This equation is usually compared to the results of optical model fits to elastic scattering data in order to extract realistic values of the potential $V(r)$ and the curvature ω_ℓ. In the optical potential model [12] the projectile-target interaction is represented by a combination of a real and a complex potential. The real potential represents the elastic scattering, while the imaginary part provides a simple way of treating a loss of elastic flux, that is the nuclear absorption.

1.2.2 Compound nucleus decay

Complete and incomplete fusion bring to an excited thermalized source, the CN, which, being formed in an excited state in equilibrium, decays after a time longer than the transient time, through statistical processes, in which γ-rays and/or particles are emitted or eventually the fission process occurs, generally for heavy nuclei and high angular momentum. The decay may be treated in terms of nuclear thermodynamics, in particular using statistical models, which, as previously reported, are essentially based on Bohr's CN picture [8]: when the CN is formed, as a consequence of the thermalization, the specific memory of the entrance channel is lost and the subsequent CN evolution and decay depend only on conserved quantities. Therefore, the cross section associated with the total reaction results:

$$\sigma_{\alpha\beta}(E,J) = \sigma_\alpha P_\beta = \sigma_\alpha \frac{\Gamma_\beta}{\sum_i \Gamma_i} \tag{1.9}$$

where σ_α is the CN formation cross-section as a function of energy E and angular momentum J and P_β is the decay probability for a specific exit channel $b + B$.

In the evaporation process every emitted particle remove a part of energy and angular

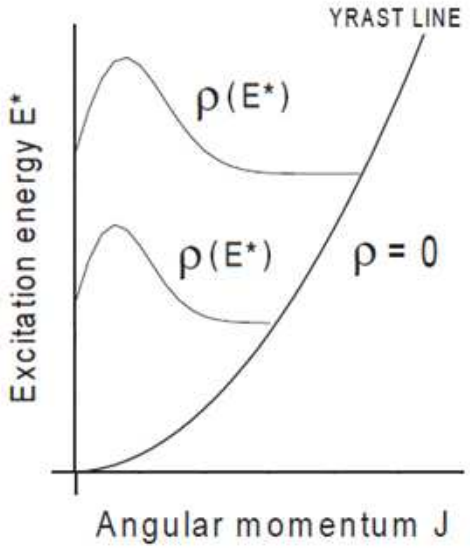

Figure 1.4: E^*-J plane and yrast line. Figure adapted from [13].

momentum from CN. The de-excitation of CN can be represented in the E^*-J plane, as shown in Fig.1.4. In this plane the yrast line, $E^*(J_Y)$, determines the maximum angular momentum for a given excitation energy E^* and represents the nuclear states for which all excitation energies are rotational:

$$E_{ROT} = E^* = \frac{J_Y(J_Y+1)\hbar^2}{2I}. \tag{1.10}$$

Particles emission is possible only if the excitation energy is above the yrast line.

Evaporation

The evaporation of light particles from a CN can be described by the Statistical Model [8, 14, 15, 16, 17, 18, 19, 20, 21]. This model attemps to predict the energy spectra and the angular distribution of evaporated particles, assuming as a base statement, the principle of detailed balance, which correlates the transition probability from the initial state α to the final state β to the reverse transition probability from the final state β to the initial state α. For a system in statistical equilibrium, the rates of forward and reverse reactions are the same:

$$g_\alpha \rho_\alpha W_{\alpha\beta} = g_\beta \rho_\beta W^*_{\alpha,\beta} \tag{1.11}$$

where ρ_α and ρ_β are the level densities of systems α and β, g_α and g_β are the statistical weighting factors account for the $2s_{\alpha,\beta}+1$ degenerate states of each level due to the spins $s_{\alpha,\beta}$ of the system, $W_{\alpha\beta}$ and $W^*_{\alpha\beta}$ are transition probability from α to β and the reverse transition probability, respectively.

The emission of particles from CN is approximated to classical statistical evaporation of molecules from a hot rotating fluid as it is described in Weisskopf theory [14, 15]. In this theory, the transition probability per unit time for emitted particle with kinetic energies ε_b, can be seen as:

$$W_\beta \propto \int \varepsilon_b \sigma_{bB} \rho_B(E^*_B) d\varepsilon_b \tag{1.12}$$

where σ_{bB} is the cross-section for the inverse reaction $b+B \rightarrow CN$, which can be identified with the fusion cross section and $\rho_B(E^*_B)$ is the level density in the excited nucleus B with energy $E^*_B = E_{bB} - \varepsilon_b$.

In the approximation of the evaporation model, the nuclear temperature is considered constant and the Fermi gas model represents a valid theoretical framework to calculate the residue level density, which is given by the Bethe formula [16]:

$$\rho\left(E_B^*\right) = \frac{1}{4\sqrt{3}E_B^*} e^{2\sqrt{aE_B^*}} \tag{1.13}$$

where a is the level density parameter related to the excitation energy via $E_B^* = aT^2$.

A more complete description is given in the Hauser-Feshbach Model, where the evaporation of nucleons is studied according to a quantum mechanical treatment of angular momentum [17, 18]. In principle, it is very similar to Weisskopf theory, but the major modification is to replace the Bohr hypothesis (Eq.1.9) by assuming that the independence applies to cross-sections corresponding to given values of the total angular momentum and parity. Assuming that the total angular momentum J is conserved, the integrated cross-section is obtained as a sum of orbital angular momentum contributions for entrance and exit channels:

$$\sigma_{\alpha\beta}\left(J, S'\right) = \frac{\pi}{k_\alpha^2} \sum_{\ell,j} (2\ell+1) g_\alpha T_\ell(\varepsilon_\alpha) \frac{\sum_{\ell',j'} T_{\ell'}(\varepsilon_\beta) \rho_B\left(E_B^*, S'\right)}{\sum_{\gamma,\ell'',j''} T_{\ell'',\gamma} \rho_G\left(E_G^*\right)} \tag{1.14}$$

where, $g_\alpha = \frac{2j+1}{(2s+1)(2S+1)} \frac{2J+1}{(2j+1)(2\ell+1)}$ is the statistical factor, in which $j = s + S$ is the spin for j-th channel, formed from projectile of spin s and target of spin S, and $\ell = J + j$.

The transition probability [19] per unit time for emitted particle with kinetic energies ε_b, and orbital angular momentum ℓ at an angle ϕ with respect to the spin J_{CN} of a parent nucleus of total excitation energy E_{CN}^* is:

$$W_\beta \propto \int\int \widetilde{\ell} T_\ell \rho_B\left(E_B^*, J_B\right) d\varepsilon_b d\phi \tag{1.15}$$

where $\widetilde{\ell} = 2\ell + 1$ and $\rho_B\left(E_B^*, J_B\right)$ is the nuclear level density, given by Fermi gas model combined with the independent particle model to take into account the angular momentum dependence:

$$\rho\left(E_B^*, J_B\right) \propto e^{2\sqrt{aU}} \tag{1.16}$$

where U is the thermal energy: $U = E_B^* - E_{ROT} \cong aT^2$. Here, T is the nuclear temperature and E_{ROT} is the rotational energy given by: $E_{ROT} = \frac{J_B(J_B+1)\hbar^2}{2I_B}$ with I_B is the moment

of inertia. The level density parameter can be described as:

$$a = \frac{\pi^2}{6}\omega(\epsilon_F) \tag{1.17}$$

where $\omega(\epsilon_F) = \omega(\epsilon) + \sum_k \delta(\epsilon - \epsilon_k)$ is the zero-temperature single-particle level density with ϵ_F is the Fermi energy; the sum $\sum_k$ is performed over all individual states of the system irrespective of their energies. Note that the single-particle level density counts the number of single particle levels per unit energy, while the nuclear level density counts the number of accessible states as a function of the total energy of the nucleus. In the calculation of the nuclear level density, likewise in that of the level density parameter, the Fermi energy ϵ_F plays an important role due to the fact that at low temperature the first levels which can be emptied are the least bound ones, which are close to the Fermi energy. Elementary excitations, promoting nucleons lying just below the Fermi level to above it, become dominant.

To reproduce the experimental value of a, calculations involving realistic mean-field are not sufficient; it is necessary to take also into account effects beyond the mean-field to reproduce the data [21].

1.3 Pre-equilibrium Emission

Several theoretical approaches have been developed to describe pre-equilibrium yields of light particles in nuclear reactions. An understandable picture of these processes is given by classifying the pre-equilibrium particles as those deriving from an intermediate step between the direct reactions and the reactions related to the CN decay. However, both projectile and target have a complex structure which plays a role in the pre-equilibrium emission; to take into account the importance of the structure, classical treatments of phenomena related to the pre-equilibrium emission, like incomplete fusion and massive transfer have been used. They formulate the decay into the continuum of a system characterized by an initial partition of the projectile energy between relatively few (intrinsic) degrees of freedom; the process continues progressing through more complicated configurations until an equilibrium distribution of energy is attained.

A quite simplified picture to describe the pre-equilibrium processes was proposed by J. J. Griffin with the Exciton Model [22, 23]: this model describes the formation of a compound system and the subsequent decay. A schematic representation is shown in Fig. 1.5. The compound system still presents a weak two-body residual interaction, which produces transitions among the eigenstates of an Hamiltonian based on independent particles: these eigenstates were lying in a region of energy dE near the compound nucleus excitation energy E.

In the exciton model, the nucleus is characterized by an excitation energy E, a number $n_0 = p + h$ of excited quasi-particles (excitons with p excited particles and h excited holes) and a level density:

$$\omega_n(E) = \omega_{ph}(E). \tag{1.18}$$

The level density, $\omega_{ph}(E)$ is proportional to the number of possible states accommodating p particles and h holes on the single particle level because, using the detailed balance principle, it enters directly in the calculation of the partial decay rates for particle emission, where the excitation of the nucleus is shared between the number of excitons, $n = p+h$. The only allowed transition are those which conserve the energy, namely those which change the number of excitons by 0 or ± 2. All transitions are assumed to proceed by binary processes. Every time a nucleus undergoes a transition to an independent-particle state, in which one exciton has the energy E_0 in the continuum, and the remaining excitons will share the energy $U = E - (E_0 + B)$, with B the binding energy of the emitted particle, the emission of the exciton to the continuum occurs in a very short time producing an outgoing particle of energy E_0 and a residual nucleus of energy U. The decay is predicted to occur in this way in the case of nucleon induced reaction on an even-even target, while for more complex configurations the residual interaction is expected to cause successive transitions to 3, 5, 7-exciton states [22]. Such decays are pre-compound decays and can describe the high energy tail in the particle energy spectra.

Close to the Fermi energy, ϵ_F, the density $\omega_{ph}(E)$ is strongly dependent on the single-particle level density and it has an almost linear dependence on the single particle energy, ϵ. When the excitation energy increases, also the partial contribution increase to $\omega_n(E)$ of

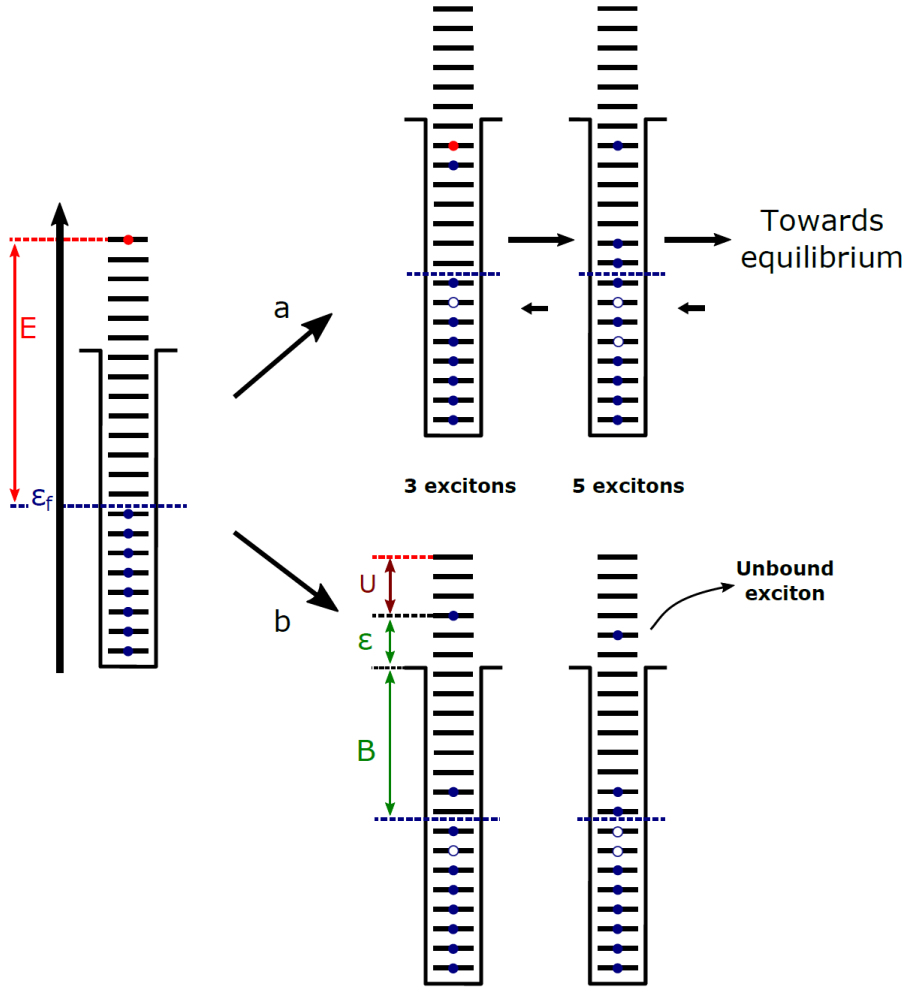

Figure 1.5: "Schematic representation of the first few stages of a reaction in the pre-equilibrium model. Particles are shown as solid circles, holes as empty circles and horizontal lines are the equally spaced levels in a potential well. The blue dashed line indicates the Fermi Energy of the system and the incoming nucleon is indicated by the red dot. In case (a), the thermalization process proceeds through the formation of exciton-hole couples following the big arrows. A small probability of returning to the previous exciton-hole configuration is shown by the small arrows. In case (b), the exciton is unbound and can be emitted as pre-equilibrium particle". From [9]

highly excited single particle states and, in some cases, some excitons can even be located in the continuum. This have to be taken into account considering the decrease of $g(\epsilon)$ with ϵ when high energy is involved.

At the end, after a certain number of two body interactions, the equilibrium is reached; hence, the normal decay from an thermalized source can be taken into account, from a nucleus with a residual excitation energy U. Testing the exciton model simulations by comparison with experimental data, the main prediction is that the same initial configuration, characterized by the initial exciton parameter n_0, for whatever target in the collision depends on the projectile structure; the only uncertain source is due to pairing effects.

After this first simplified model by J.J. Griffin, many other considerations have been made in order to give a reasonable description of the pre-equilibrium emission. Among the others it is worth mentioning the following models:

- The model developed by Harp, Miller and Berne in 1968 [24] describes the statistical evolution of different systems evolving from an initial state far from statistical equilibrium to an equilibrium state through a sequence of two-body interactions and emitting unbound particles to the continuum; it is based on a Boltzmann Master Equation (BME) approach, which is a nuclear transport model based on nucleon-nucleon collision processes in the nuclear potential.

- The Hybrid model by M. Blann [25] is based on the simplified exciton model and on the BME approach: as the first, the calculation of the excited particle populations during thermalization phase is performed starting from the partial state densities; while, like in the case of the master equation formalism, the intranuclear transition rates of the excited particles were determined by the calculations of the mean free paths of the nucleons in nuclear matter.

- The Geometry-Dependent Hybrid (GDH) model [26] is an improved version of the hybrid model, in which the importance of the nuclear density distribution on pre-equilibrium decay is evaluated taking into account the effects of interactions in the diffuse nuclear surface.

Lately, the Milano group have generalized the GDH model [27, 28, 29]: the time evolution of the energy distribution of the nucleons, in heavy-ion induced reactions, can be evaluated as a result from the two-body nucleon-nucleon interactions and from the emission of particles in the continuum [30]. The BME approach is used, still fulfilling some initial conditions, like low variation of the states of bound nucleons in a potential well during the time evolution of the dinuclear system in the case of in-compressible nuclear matter and volume-conserving deformations. Unifying the description of nucleon induced and heavy ion induced reactions, the BME theory may reproduce successfully the hardest part of the angle integrated inclusive spectra of nucleons, photons, light clusters and intermediate mass-fragments emitted in heavy ion collisions up to incident energies of few tens of MeV/u.

In order to have a comparison with exclusive experimental results of coincidence among particles a Monte Carlo calculation [31], where the differential multiplicities were interpreted as the probability of emission of the considered particle in the considered time interval, have been developed. The Monte Carlo cascade samples the emission of a particle from the integrated multiplicity distribution, along all the time intervals, at each step. If an emission occurs, the energy and the direction of the particle is chosen randomly and accepted or rejected through a comparison with the corresponding double differential multiplicity, properly normalized with a random number. The energy and emission angle of the particle are calculated in the center of mass system of the initial composite system and then transformed in the laboratory system, together with the evaluation of the momenta of the recoiling nucleus, always in the laboratory system. The fast emission is stopped when the ejection of fast particles become negligible, which normally happen after about $50 \div 100$ fm/c after the two nuclei come in contact. At this time the equilibrium is reached and the subsequent evolution follows a statistical decay: particle type, kinetic energy, angle of emission, together with excitation energy, recoil angle, recoil velocity for the residual nucleus are registered event by event. Such simulations are reasonably in agreement with experimental data. The main trouble, however, for calculating the pre-equilibrium emission in heavy ion collisions, is the determination of the initial configuration of excitons,

which has to be performed, essentially, by evaluating the overlap of the colliding nuclei in their momentum space [32].

A further upgrading of such formulation is related to the introduction of the probability of break-up of the projectile.

Of course, a simple description of the initial condition, like the one used with nucleon induced reactions, may cause differences in simulation of complex systems, like the heavy ions, respect to experimental data: influence from either target or projectile structure, possible Coulomb interaction between projectiles and targets, coupling of angular momenta etc. can complicate the scenario.

1.4 Pre-equilibrium models considering α-clustering

In order to study of the emission of particles other than nucleons as due to pre-equilibrium decay, different approaches have been developed. Due to the complex mechanisms related to the clusters formation, some difficulties arise to involve the formalism needed to describe formation probabilities and numbers of level densities per MeV for clusters (e.g. α, d, t, ^3He), together with transition probabilities.

The main important approaches are:

- In the nucleus a preformed cluster (formed by p_x of the total p excited particles) may interact with the same kinematics of nucleons; it is treated as an exciton in the exciton model formulation, replacing the exciton number of the residual nucleus $(p-1,\, h)$ with $(p-p_x,\, h)$.

- The cluster is formed during the partition phase: some fraction of all the energy partitions is assumed to have the right number of nucleons and associated momenta to permit a cluster emission.

- A quasi-free scattering approach is used for complex particles (like cluster) in the exit and entrance channels (elastic scattering angular distribution, Pauli exclusion principle etc.).

Pre-equilibrium theories, incorporating one of the above approaches, bring to the possibility to describe heavy-ion reactions where even emission of fast clusters is possible.

Many nuclear reactions involve the emission or capture of clusters of nucleons of different nature: from the strongly bound α-particles to the weakly bound deuterons and even to higher mass fragments. The study of cluster is very important since it gives information both in nuclear structure and in nuclear reaction mechanisms, providing important contributions to the knowledge on the single particle states and on the multiparticle nature of states. A cluster is a well defined spatially located sub-system, which is composed by strongly correlated nucleons: its intrinsic binding energy is stronger than its external binding.

The idea that cluster of nucleons could be preformed in nuclei is one of the oldest idea

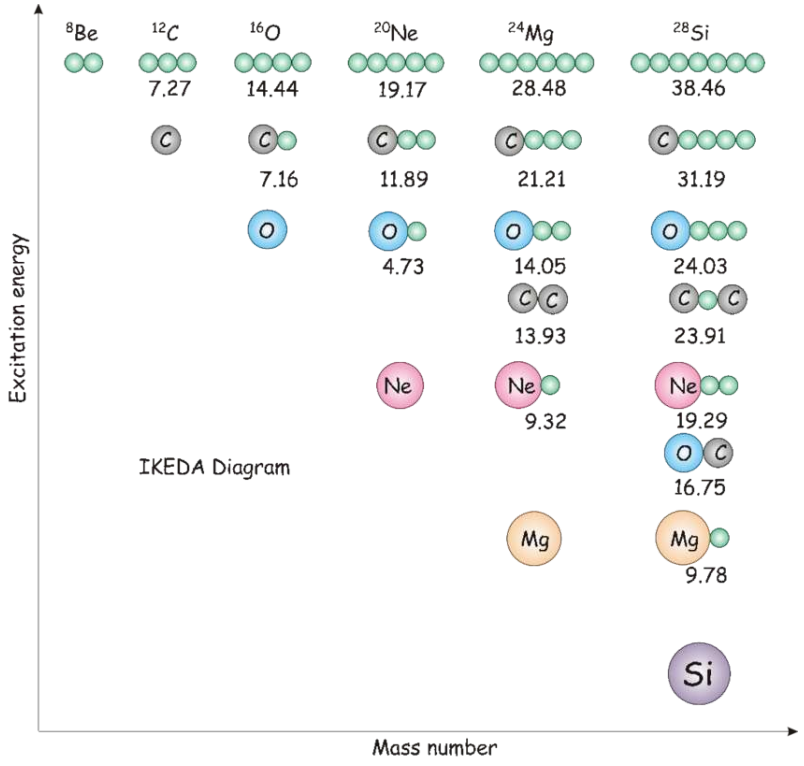

Figure 1.6: The Ikeda threshold diagram for nuclei with α-clustering. It shows how the cluster degree of freedom evolves as the excitation energy increases; the energies needed for the decomposition of the normal nucleus into the cluster structures are indicated in MeV.

proposed to describe nuclear structure since the α-cluster model was developed even before the discovery of the neutron; such idea was proposed by Hastaf and Teller in 1938 [33]. Examining the binding energy per nucleon of the α-conjugate light nuclei as a function of the mass number, a systematic trend has been found, well described by the liquid drop model: the α-conjugate light nuclei are particularly stable and cluster structures are typically observed as excited states close to the decay threshold into clusters. This concept has been summarized, in the late sixties, in the Ikeda diagram [34], which links the energy required to release the cluster constituents to the excitation energy at which the cluster structure prevails in the host nucleus; such diagrams are shown in Fig. 1.6. Afterwards, this concept has been extended to non α-conjugated nuclei, described in the extended Ikeda diagram [35], which are shown in Fig. 1.7; in neutron-rich systems, neutrons may

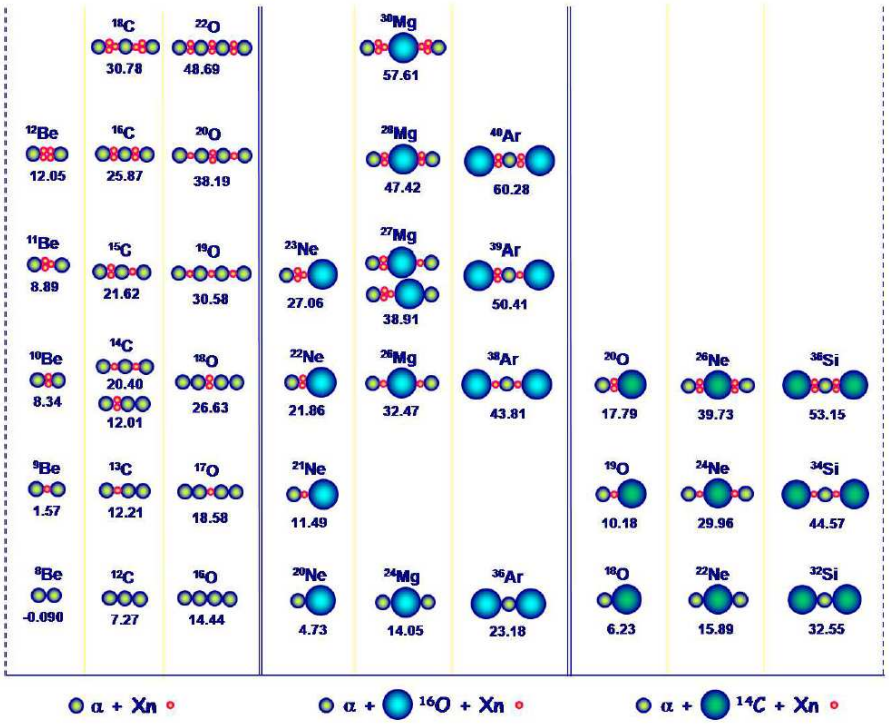

Figure 1.7: "Extended threshold diagram for states in nuclei. Some molecular structures with clusters and covalent valence neutrons are shown. Only α-particles and ^{16}O-nuclei are used. The schematic shapes are given with the threshold energies for the decomposition into the constituents". From [35]

act as valence particles and can be exchanged between the α-particle cores, in a similar way, electrons are exchanged in atomic molecules. These covalent neutrons stabilize the unstable multi-cluster states, giving rise to nuclear structure which can be described by molecular concepts, well reproduced in model independent approaches like the Fermionic Molecular Dynamics (FMD) [36, 37] or the Antisymmetrized Molecular Dynamics (AMD) with effective N-N forces [84, 38, 39].

The link between pre-equilibrium phenomena and cluster structure is considered very strong due to common hypotesis, verified by many observations, that nucleons in nuclei spend part of their time in a cluster structure, especially when close to the nuclear surface. Accordingly, during the years a lot of efforts have been devoted to the description of cluster emission in fast processes.

Normally a nucleus is described as composed of an ensample of nucleons, characterized by a quantum number; each of them occupies a well defined shell-model orbital. Sometime, some of those nucleons can condense and produce a cluster. The strongest cluster, in terms of binding energy is the α-particle, which is formed by two neutrons and two protons.

If a transient cluster is close to the surface and its kinetic energy is enough to overcome the binding energy, it can escape from the nucleus, producing the so-called cluster decay. Several mechanisms can be at the bases of cluster excitation, decay, transfer: as an example the escape of a cluster can be provocated by the knock-out reaction induced by an incoming nucleon. If the constituents of a cluster are present in the nucleus, since they are surrounded by other nucleons they cannot have the same properties as if they were in a free state. Moreover, if the conditions of the nucleus change, condensation of nucleons in cluster is possible. Typically for density variation, this is supposed to happen when the density reach about one third of the normal nuclear density. Such a phenomenon has been evidenced in highly damped collisions at intermediate energies, where, for example, clusters could be emitted from the neck in semi-peripheral collisions [40, 41].

In pre-equilibrium reactions formalism, the clusters emission is mainly described based on two diametrically opposed models:

- pre-formation of α-particles, which is a very strongly coupled object; the limitation of

such approch is that it can describe only α-cluster and it usually fails for all different kind of cluster;

- formation of a cluster during the reaction in a dynamical way, described with coalescence models, like that of C.K. Cline [42].

The two pictures are quite different in the sense that, while in the first case the α-particle is considered so compact to be described as an exciton state, on the other case nucleons are all equal and the creation of a cluster by nuclear coalescence is a specific process, which can bring to different kind of clusters, from weakly bound to strongly coupled ones (d,t ^3He, α-particles and heavier fragments etc.).

Among the coalescence models, it is worthy to mention:

- Iwamoto-Harada coalescence model [43] is a spin-dependent model suitable for different kind of emitted clusters; its basic idea is that not only the excited nucleons can group together to form clusters, but both the excited and those from unexcited levels (lower than the Fermi level) can contribute, with a particular form of pick-up reaction.

- Bislinghoff generalized coalescence model [44] takes into account that not all the nucleons are available for cluster formation, but only those close to the Fermi energy, determining a kind of availability band on the bases of the binding energies of nucleons within the cluster. As a consequence, the results become close to the pre-formed models, in the sense that strongly bound entities like α-particles have a large available space for pick up in this approach, while the pick-up possibility for loosely coupled objects like the deuterons becomes very small, but nevertheless they are considered. In this approach, as in evaporation theory, the coalescence of nucleons to form the cluster (their momentum correlation, angular momentum coupling, etc.) enters only as far as it places constraints on the residual level density accessible.

Further update of the model was performed in order to keep the consistency between the compound nucleus (Weisskopf-Ewing) formula and the Exciton model not only for

nucleons, but also for the cluster emission [45, 42]. In this formulation the full expression for the cluster emission rate is

$$\lambda_x^C(n, E, \epsilon_x) = \frac{2s_x+1}{\pi^2\hbar^3}\mu_x\epsilon_x\sigma_{INV}^* \frac{\omega(p-p_x, h, U)}{\omega(p, h, E)} \frac{\omega(p_x, 0, \epsilon_x + B_x)}{g_x} R_x(p)\gamma_x \qquad (1.19)$$

where:

- μ_x and s_x are the ejectile reduced mass and spin;
- σ^{INV} is the inverse cross-section (optical model cross section able to capture a projectile x by a nucleus in the ground state);
- $U = E - B_x - \epsilon_x$ is the energy of the residual nucleus, which is produced in an exciton $(n - p_x)$ (cluster) state;
- g_x is the single cluster level density;
- R_x is the charge factor, which takes into account the charge composition of the exciton/cluster (i.e. accounts for the proton-neutron distinguishability);
- γ_x is the cluster formation probability; nucleon emission is a special case of the cluster one, with $\gamma_x = 1$. Often it is considered a parameter $\gamma_x \leq 1$ that is obtained from the fit to the data; it depends on the energy and decrease when the number of mass of the composite system increases.

These models, either if based on the exciton quite simple description or on the complete more sophisticated BME formalism, are somehow the link between the description of a dynamical process and the underlying structure. A typical example of this link derives, for example, on the interest for super-deformed and/or hyper-deformed nuclear shapes coming from structure community, which are predicted to exist for masses $A \leq 40$.

Chapter 2

The Experiment

As previously mentioned, this thesis is dedicated to the study of four reactions leading, for central collisions and when complete fusion occurs, to the formation of the same compound nucleus; in particular, we are interested in both fast and thermalized emission of light charged particles from the hot source.

In fact, during the early stages of the reaction, non-equilibrium processes play an important role in the dynamics of heavy-ion reactions; in particular, they contribute to determine the features of the remaining hot thermalized sources. Fast emissions, issued in these processes, depend both on the entrance channel mass asymmetry and on the beam velocity [45]. When nucleons as well as clusters of nucleons (like d, t, ^3He and α-particles) are emitted or captured in a nuclear reaction, a strong correlation between nuclear structure and reaction dynamics arises. It is, in fact, important to study both the pre-formation of the α-clusters, which may be preferential in α-conjugate nuclei, and the dynamical condensation of clusters during nuclear reactions. Within the NUCL-EX collaboration, we have performed some experimental campaigns of exclusive measurements: on one side fusion-evaporation reactions have been studied when two light nuclei were colliding to form systems in the mass region $A \sim 20$; on the other side a campaign of measurements are being performed on central collisions induced by light projectiles, the structure of which can induce important effects on the dynamics and, finally, on the decay of the excited system [46, 47, 48, 49]. Special importance is given by α-cluster structure of

such projectiles; in fact clustering is particularly important at the drip–line, where weakly bound systems prevail [50] and the nuclear density distribution is more diffuse; actually, it might be the preferred structural mode for the exotic light nuclei. However, a strong interest, addressed to the study of the pre-formation of α-clusters in α-conjugate nuclei or the condensation of clusters during nuclear reactions, has been also evidenced using stable beams, where upgraded and dedicated instruments can perform an almost complete reconstruction of the events. Moreover, the search for the α-clustering effects through the observation of fast emission processes is promising and allows to gain complementary information with respect to nuclear structure studies on the nuclear clustering process.

In this context, the comparative study of three reactions has been conceived: the idea is to study these systems in two energy regimes. Firstly, at energies close to the onset for the pre-equilibrium emission process, to evaluate its properties in a framework, where the thermalization process is quite well known; then, to carry out a further experiment studying the same systems at higher bombarding energies, where the pre-equilibrium part plays a major role.

In the present work, the measurement related to the low energy part is presented; it involves four reactions: $^{16}O+^{30}Si$, $^{18}O+^{28}Si$ and $^{19}F+^{27}Al$ at 7 MeV/u and $^{16}O+^{30}Si$ at 8 MeV/u. For central collisions and when the complete fusion occurs, all the four studied cases lead to the same compound nucleus, the excited ^{46}Ti, even if with slightly different excitation energies; therefore, small differences in their de-excitation chain are expected. In particular, the cases $^{16}O+^{30}Si$ at 8 MeV/u and $^{18}O+^{28}Si$ at 7 MeV/u have been chosen to populate the compound nucleus at the same excitation energy. On the other hand, the choice of the same beam energy (7 MeV/u) for three of the four reactions have been made since the non-equilibrium processes should be almost the same [45]. For more peripheral collisions, a study of special correlations to underline the cluster structure of the projectile, among which $^{12}C+\alpha$ for the ^{16}O, $^{14}C+\alpha$ for the ^{18}O and $^{15}N+\alpha$ in the case of ^{19}F, will be carried out. Such study is, however, outside of the scope of this thesis. The main characteristics of the four reactions are shown in Table 2.1.

The goal of this experiment has been to measure and compare different mass entrance

Entrance channel	$E_{beam,lab}$	θ_{graz}	**CN**	η	σ_{fus}	E^*	**Lab. Vel.**	$\theta_{lab,E.R.}$
beam+target	MeV	deg			mb	MeV	cm/ns	deg
$^{16}O + ^{30}Si$	128	8,8	^{46}Ti	0,30	1070	98,4	1,37	0-30
$^{16}O + ^{30}Si$	111	10,1	^{46}Ti	0,30	1081	88,0	1,28	0-30
$^{18}O + ^{28}Si$	126	9,0	^{46}Ti	0,22	1110	98,5	1,44	0-28
$^{19}F + ^{27}Al$	133	8,9	^{46}Ti	0,17	1100	103,5	1,52	0-28

Table 2.1: The main characteristic of the reactions

channel reactions with small differences in terms of neutrons and protons contents in the colliding partners by analyzing the four reactions through correlation studies and comparison with model predictions and by emphasizing the differences which may be signatures of structure effects. In particular, observing discrepancies in the emission yields of specific α-decaying channels, a trace back to α-cluster structure might be suggested.

The experiment was performed by NUCL-EX collaboration at the Legnaro National Laboratory (LNL), where the four beams have been provided by the TANDEM XTU accelerator and have been used respectively onto three different thin (100 $\mu g/cm^2$) targets: ^{30}Si, ^{28}Si and ^{27}Al. Moreover, specific runs on 200 $\mu g/cm^2$ Gold target have been carried out for calibration purpose. The employed energies, that were the maximum available with TANDEM alone, were close to the onset thresholds for the pre-equilibrium emission process.

The GARFIELD plus Ring Counter (RCo) detector fully equipped with digital electronics [52] has been used to detect LCP, light fragments (LF) and evaporation residues (ER). This experimental setup is discussed in the first part of this chapter (Section 2.1); the second part of the chapter is devoted to the discussion of the data calibration and physical event reconstruction (Section 2.2).

2.1 The Experimental Setup

The GARFIELD apparatus [51] (a General ARray for Fragment Identification and for Emitted Light particles in Dissipative collisions) is a multi-detector based on the $\Delta E - E$ technique for fragment and light charged particle identification; it was designed in the 1990s to study complex nuclear events produced in the medium-low energy range (5-20 MeV/u) heavy ions induced reaction. Since 2010, it was coupled with the ancillary Ring Counter (RCo) placed at forward angles ($5^o - 17^o$); they were fully equipped with digital electronics [52]. A sketch of a transverse section of the two Garfield drift chambers and of the three stage RCo annular telescopes is shown in Figure 2.1.

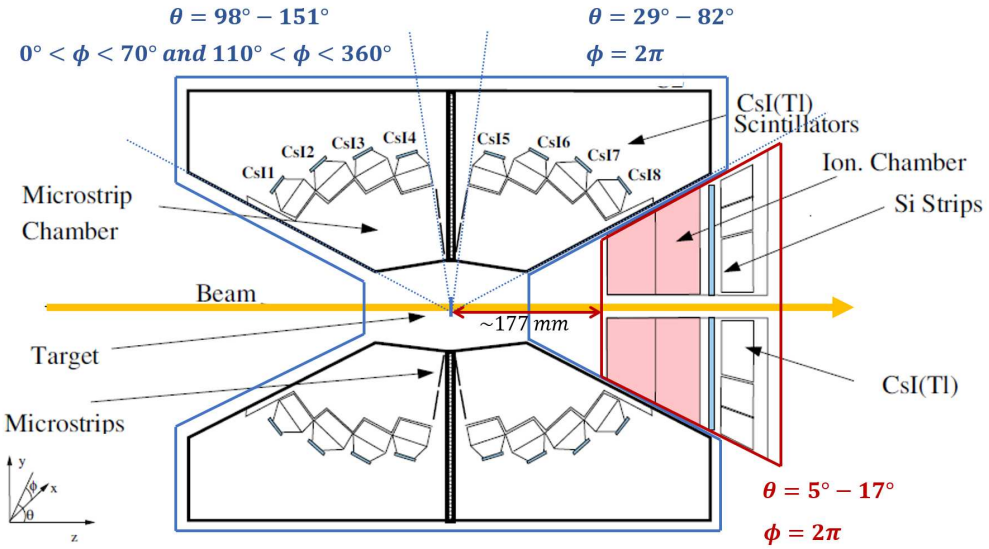

Figure 2.1: Sketch of the experimental array: the two GARFIELD drift chambers coupled with the RCo three element annular telescope. See text for details.

2.1.1 GARFIELD

The GARFIELD's main components are two independent large-volume drift chambers, having cylindrical symmetry and placed back to back with respect to the target (see Fig. 2.1). The forward chamber covers the polar angular range $29^o < \theta < 82^o$ and the complete azimuthal angle, which is divided into 24 sectors. Instead, to permit the allocation of

different ancillary detectors, the backward chamber has a reduced total coverage in the azimuthal angle with a side opening of $\Delta\phi \sim 45^o$ (three missing sectors) and it covers the polar region $98^o < \theta < 151^o$. Each sector of both chambers contains four CsI(Tl) crystals and a trapezoidal micro-strip pad, which is divided in four collection region to obtain a larger granularity. Each detection cell covers, therefore, an angular region of $\Delta\phi = 7.5^o$ and $\Delta\theta = 13^o$.

The chosen gas filling the drift chamber is CF_4 (carbon tetrafluoride): it is a stable gas with high density (0.19 mg/cm^3 at a pressure of 50 mbar and a temperature of 20^{o}C); its high stopping power (five times larger than CH_4 and 17 % more than isobutane) together with a low working pressure ($\sim$ 50 mbar in the standard condition) establish an optimal compromise to permit the detection of heavy ion, together with low intensity particles (like protons). The high drift velocity of the primary electrons (10 $cm/\mu s$ at 1 $V/(cm \times mbar)$ and the average ionizing potential (16 eV) allow to optimize the count rate of the gas chamber and to minimize the pile-up on the micro-strips. A semi-automatic recycling gas system, forcing CF_4 to flow in a continuous cycle, has been mounted to reduce contamination and impurity and to avoid problems connected to possible decrease of the gas quality.

The GARFIELD apparatus layout has been designed to apply the $\Delta E - E$ technique, since it is organized in telescopes, which exploit energy measurements in two distinct stages of the detector to obtain charge identification and accurate energy measurements of the reaction products, with very low energy threshold. The energy loss signal (ΔE) is given by the Micro-Strip Gas Chamber (MSGC) while the residual energy (E) is obtained from the signals of CsI(Tl) crystals with a photodiode readout. In this experiment, due to the kinematics only light particles can reach the backward angles ($\theta > 90^o$); these particles can be effectively identified and measured with the CsI(Tl) scintillators via Pulse Shape Analysis (PSA). Therefore, the gas stage of the backward chamber has not been used to collect data. Nevertheless, the backward chamber was kept in gas flow at low pressure ($\sim$ 20 mbar) without increasing too much the dead layer in front of the scintillators in order to provide a sufficient cooling of the CsI(Tl) photodiode preamplifiers that are mounted

within the gas volume.

Micro Strip Gas Chambers

The MSGC, initially designed to satisfy the needs of high energy physics (good position resolution, high gain and high counting rate), are also used in low energy regime [53, 54]; *i.e.* in GARFIELD array. The drift chamber operating mechanism is relatively simple and schematically illustrated for a single GARFIELD sector in Figure 2.2: the particles produced in the projectile-target interaction enter into the drift chambers, passing through the 6 μm thick ($0.78 mg/cm^2$) mylar entrance window and ionize the gas. The produced electron-ion (primary ionization) formed along the trajectory of the particles are forced to drift: in particular the electrons are directed toward the microstrip pads (see Figure 2.2) due to a transverse electrical field generated by a drift cathode ($\sim$ -1000 V) and a Frisch grid ($\sim$ -60 V). Since the drift cathode and the Frisch grid are not parallel, a series of additional electrodes are placed on the whole internal surface of the chambers to make the electric field as uniform as possible and they are kept at the proper voltages via resistive dividers, which take into account the irregular shape of the chamber.

The Frisch grid prevents the induction of signals on the microstrips when charge carriers drift in the active gas volume and it eliminates the positive ions contribution to the signals; it is placed close to the microstrip plane (at distance of 3.7 mm) to delimit the region close to the microstrips, where the electric field reaches a much greater intensity ($\sim 10^7\ V/m$) sufficient to generates electrons avalanche phenomenon of multiplication of the primary electrons (secondary ionization) [55].

The microstrip pads are placed on the basis of the two cylindrical chambers almost perpendicular to the beam axis. Each pad (Figure 2.3) has a trapezoidal shape and is divided into four charge collection zones to provide the ΔE values to be used for $\Delta E - E$ correlations. The microstrip are made with photo-lithographic techniques depositing a thin layer of metal tracks, alternately anodize and cathodic, on an insulating glass substrate; the very small distance (50 μm) between the anodize (width $\sim$ 10 μm) and cathodic (width $\sim 85\ \mu m \div 190\ \mu m$) tracks permits a fast collection of electrons and of positive ions formed

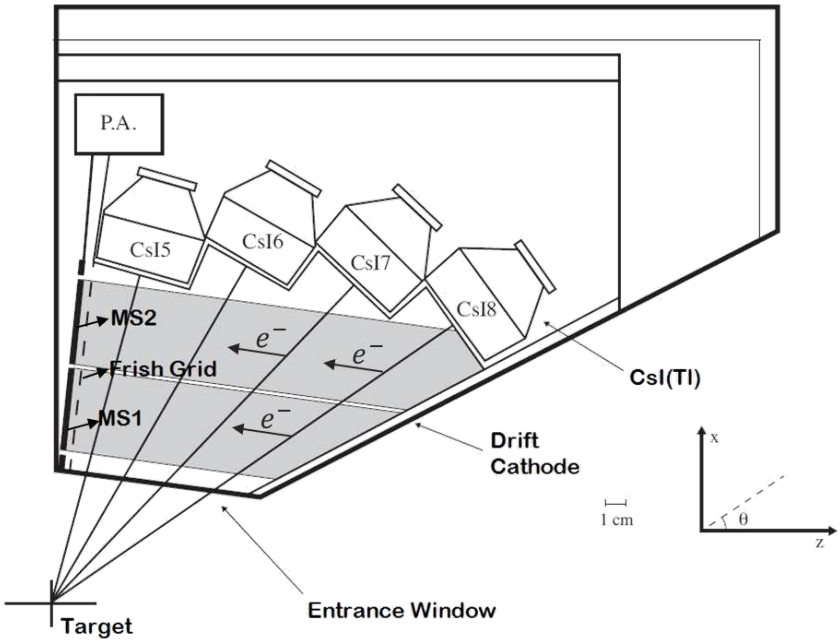

Figure 2.2: Scheme of a GARFIELD sector. Here, the drift chamber operating mechanism is shown: the electrons, produced by the charged particles penetrating the gas, drift towards the micro-strip pad allowing to measure the energy loss; the residual energy of the charged particle is measured by the CsI(Tl). P.A. represents the mother-board carrying eight preamplifiers.

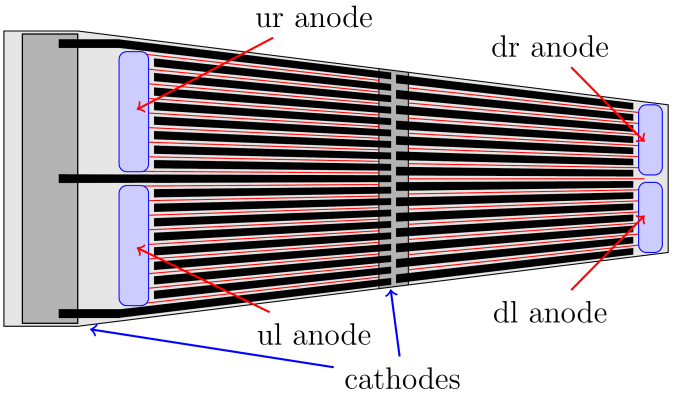

Figure 2.3: Schematic view of a GARFIELD micro-strip pad.

close to the microstrips plane.

Whereas the anodes (MSGC) are connected to a fixed bias voltage (+420 V), the drift cathodes are generally grounded allowing the device to operate in a proportional mode; therefore, the number of collected electrons and the output signal are proportional to the particle total kinetic energy deposited in the gas, ΔE.

Due to the large dynamical range and to the signal-to-noise ratio for the low ionizing ions, the main advantage of using MSGC is the simultaneous identification of both light charged particles and heavy ions ($Z \sim 1 \div 18$) with low energy thresholds (identification threshold $\sim 0.8 \div 1$ MeV/A and detection threshold $\sim 10 \div 20$ keV/A). Typical gains, which can be obtained with CF_4 at 50 mbar, are of the order of $\sim 30 \div 50$.

CsI(Tl) scintillators

In GARFIELD, CsI(Tl) crystals are used as second stage of the telescope, in which the particle with sufficient kinetic energy to cross the gas stage (ΔE) is stopped and loses its remaining energy (E_r).

Thallium doped Cesium Iodide (CsI(Tl)) scintillators are commonly used as last-stage detectors in a telescope due to their characteristics [56]: high stopping power, sufficiently good energy resolution, low hygroscopic level and small sensitivity to the radiation damage; their lower resolution than a Silicon detector is balanced by their moderate cost and by the fact that they can be grown in thick blocks able to stop high energy particles.

In each sector of GARFIELD, four CsI(Tl) are mounted (96 in the forward chamber and 84 in the backward chamber); their shapes are different as a function of their angle position to maximize the geometric efficiency of the apparatus (see Fig. 2.4 and Table 2.2). Each crystal covers a polar angular range of $\Delta\theta \sim 15^o$ and an azimuthal angular range of $\Delta\phi \sim 15^o$ and it has a thickness of 4 cm to stop protons and α-particles with energies up to ~ 100 MeV/u. Their allocations are designed to place their front face always perpendicular to the radial trajectory of the particle emitted from the target. Each of them has been laterally wrapped in a white diffusive paper to maximize the light collection and it has been protected in the front face with an aluminized mylar foil to avoid light penetration

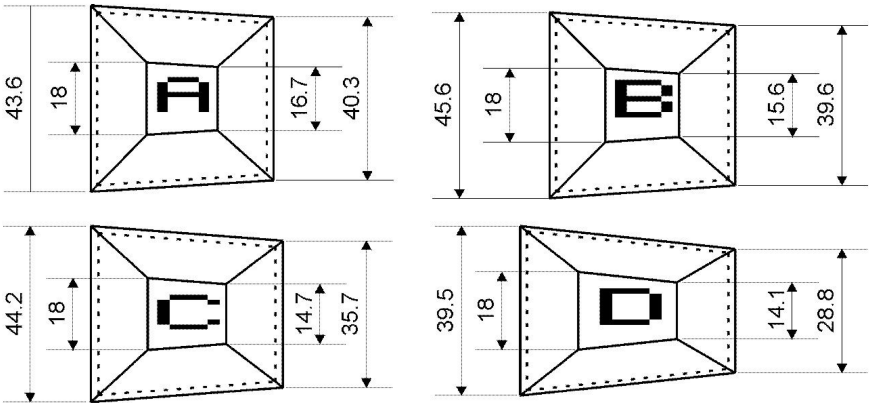

Figure 2.4: Drawing of the four different shape of GARFIELD CsI(Tl). The "A" corresponds to the shape of the CsI(Tl) closer to the micro-strip plane; therefore, it has the larger angle respect to the beam.

		θ_{min}	θ_{max}	θ_c	**distance (mm)**
	CsI 1	139.9^o	150.4^o	145.2^o	216
GARFIELD	**CsI 2**	127.5^o	138.5^o	133.0^o	194
Backward	**CsI 3**	113.5^o	126.5^o	120.0^o	172
	CsI 4	97.5^o	112.0^o	104.8^o	150
	CsI 5	68.0^o	82.5^o	75.3^o	150
GARFIELD	**CsI 6**	53.0^o	66.0^o	60.0^o	172
Forward	**CsI 7**	41.0^o	52.0^o	47.0^o	194
	CsI 8	29.5^o	40.0^o	34.9^o	216

Table 2.2: Angular region ($\theta_{min} \div \theta_{max}$) covered by each Garfield CsI(Tl) crystal and its distance from the target; the "central" angle (θ_c) indicates the position at which a particle coming from the target impinges perpendicularly to the crystal face.

from outside. Their rear part has been tapered to behave as a light guide to optimize the optical coupling with the photodiode S3204-05 manufactured by Hamamatsu [58]. The choice of photodiodes instead of photomultiplier tubes was due to their greater stability,

low power dissipation, much smaller size and to their low bias voltage ($\sim$ 100 V) which makes it possible to be operated inside the GARFIELD low pressure gas chamber.

The resolution and light output results, obtained from measurements performed with α- and γ-sources, provide an indication on the crystal properties and on the gluing to the photodiode; in particular, detecting 5.5 MeV α-particles emitted by ^{241}Am source, the energy resolution (FWHM) is $\sim 3\% - 4\%$.

2.1.2 The Ring Counter

The Ring Counter (RCo) is an annular three-stage telescope with a truncated cone shape, designed to be centered at 0^o with respect to the beam direction; it covers the polar angular range $5.5^o < \theta < 17.4^o$ corresponding to 30% of the forward cone not covered by Garfield (0^o to 29.5^o) [54]. It is mounted on a sliding plate that allows to move it forward and backward with a remote control; during the measurement, the RCo is inserted just in the forward cone of the GARFIELD metallic cage and its entrance window is placed 177 mm far from the target.

A picture of the whole RCo apparatus is shown in Figure 2.5. The first stage is an ionization chamber (IC) filled with CF_4 and divided in eight azimuthal sectors, perfectly matching the eight Si-pads placed behind, which are further segmented into eight independent annular strips on the front surface; the last stage is composed by 48 CsI(Tl) scintillators, six in each sector to increase the global granularity of the detector. On the same sliding plate of the RCo, placed in metallic boxes and cooled by a water recirculating system, the preamplifiers are mounted inside the scattering chamber to minimize the noise contribution due to the length and the capacitance of the cables.

To protect the silicon detectors, which can suffer rapid radiation damage by elastically scattered beams at the angles subtended by the RCo, during beam focusing or during calibration run, an automatized collimator system has been built-up, able to operate under vacuum and to position different screens in front of the RCo. In the present experiment, due to the high counting rate of elastic scattering, the smallest angles were shielded through an appropriate collimation system; therefore, the evaporation residues have been collected

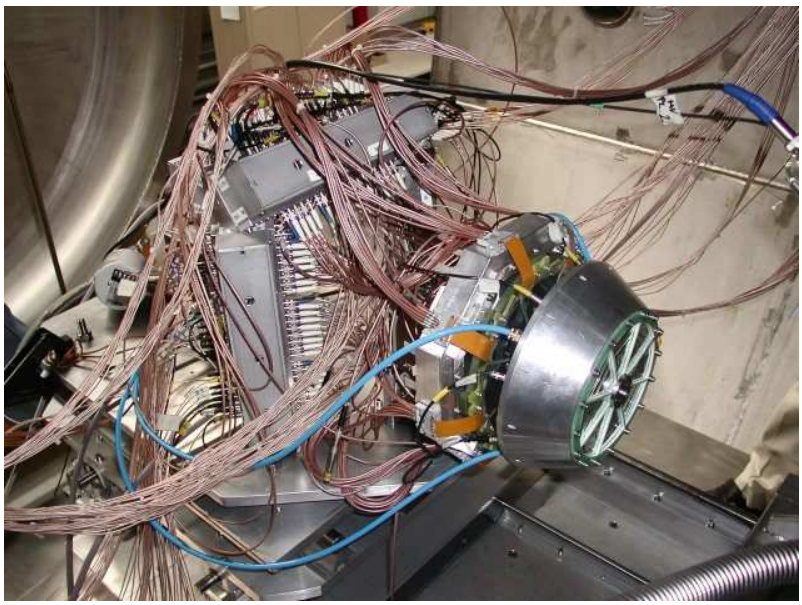

Figure 2.5: A picture of the complete RCo array. From right to left: the ionization chamber divided in eight sector; the silicon pads; the CsI(Tl). Behind the metallic boxes where the preamplifiers are mounted.

in an angular range $8.6^o < \theta < 17.0^o$, just beyond the grazing angles (see Table 2.1).

The Ionization Chamber

The IC, with an active gas region depth of 6 cm, is of the axial type with electric field parallel to the ion tracks in the gas; this field is generated by three aluminized mylar electrodes (3 μm): two input-output electrodes, metallized only on the internal face, are the grounded cathodes and act also as gas windows; the anode, a foil with metal deposition on both faces, is placed between the two cathodes. The cathodes are azimuthally divided into eight parts to follow the 8-sector partition of the RCo.

As in GARFIELD, the filling (CF_4) gas is continuously flowing in the chamber; the typical working conditions are a pressure of 50 mbar and a temperature of 20^oC. Under these conditions, the IC has an active thickness of 1.1 mg/cm^2 and its signal resolution results of $\sim 7\%$ for the energy loss of a ^{32}S beam at 550 MeV scattered on Au target [59]. Nevertheless, in the present experiment, the pressure has been set to 25 mbar in order to

get a higher evaporation residue signal in the Silicon detectors.

The Silicon strip detectors

Behind each IC sector a trapezoidal 300 μm thick Silicon (nTD) pad, segmented into eight strips, is placed (see Fig. 2.6) [54, 61].

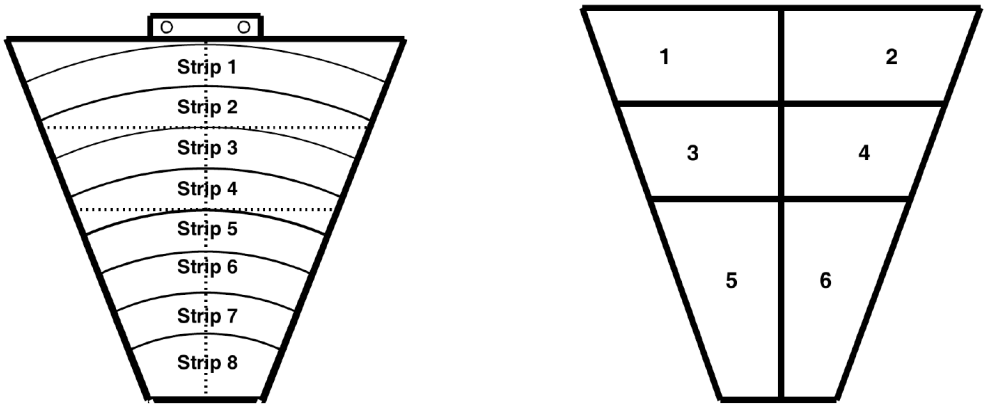

Figure 2.6: A sketch of a silicon strip pad (left) and of the CsI(Tl) scintillators (right) for one of the eight sectors of the RCo.

	θ_{min}	θ_{max}	*Int.Radius* **(mm)**	*Ext.Radius* **(mm)**
strip 1	16.0^o	17.4^o	77.9	85.0
strip 2	14.6^o	16.0^o	70.8	77.8
strip 3	13.2^o	14.6^o	63.7	70.7
strip 4	11.8^o	13.2^o	56.6	63.6
strip 5	10.3^o	11.7^o	49.4	56.4
strip 6	8.8^o	10.3^o	42.3	49.3
strip 7	7.4^o	8.8^o	35.2	42.2
strip 8	5.5^o	7.3^o	26.2	35.1

Table 2.3: Polar angular region ($\theta_{min} \div \theta_{max}$) cover by each silicon strip of the RCo.

The covered solid angles are around 2-6 msr, corresponding to the polar angle intervals and radii, shown in Table 2.3. The angular resolution of each strip is up to $\Delta\theta \sim \pm 0.7^o - 0.9^o$ and the geometrical coverage of the Si detector is about 90%. The remaining inactive area is due to the interstrip regions (about 220 μm wide), containing the guard rings, which must be properly biased to minimize the effects due to the field distortion in the inter-strip region. This strongly reduces the charge split and the cross-talk between contiguous strips.

The silicon detectors are built from neutron transmutation doped (nTD) material to have a high doping uniformity; the front surface (junction side) of each silicon detector is segmented into eight strips, while the rear surface (ohmic side) consists of an unique electrode. They are reverse mounted, namely with the ohmic side oriented to the impinging particles, to enhance the particle identification by means of the pulse shape discrimination method. Each strip has a bonding contact to a track in a Kapton ribbon ending with a multiple connector, allowing the connection to the preamplifiers.

The energy thresholds for particles punching through the detectors are of ~ 6 MeV/u for protons and α-particles and 7-11 MeV/u for light fragments, with a resolution of 0.3% for elastic scattered ions in both ^{32}S beam at 550 MeV and ^{12}C beam at 95 MeV [62] on Au targets.

The CsI(Tl) scintillation detectors

The CsI(Tl) crystals are very similar to those employed in GARFIELD, but being grown up more recently they are characterized by a more uniform doping, with a higher percentage of thallium (1500 $\div$ 2000 ppm instead of 1200 ppm), which enhance their light output and result in a better scintillation response. The geometrical shapes of the CsI crystals have been designed to cover the cone subtended by the IC. For each sector, there are 6 CsI(Tl) crystals [54]: two behind the four internal strips and four behind the four external strips. The designed overlap between Silicon pads and CsI(Tl) crystals is illustrated in Figure 2.6 and it can be seen that at least two Silicon strips correspond to each crystal.

The crystals are wrapped with polyvinylidene fluoride (PVDF) and Teflon tape to avoid the noise due to the external light and to maximize the reflections on the detectors wall in order to optimize the light collection in the photodiode. The energy resolution of the CsI(Tl) resulted about $3 \div 4\%$ [56, 62].

2.1.3 The Electronics

As already said, the fully digitized treatment of GARFIELD and RCo signals have been applied, of which the main features will be described hereinafter: the signals, coming from the preamplifiers, are directly fed into a digital card, containing a 125 MHz, 12 bit ADC (Analog-to-Digital Converter) and a DSP (Digital Signal Processor). The DSP is a programmable processor capable to read sample data, store them in its internal data memory and perform advanced on-line data reduction; it substitutes the charge amplifier and the peak sensing ADC that were present in the "old analogic" chain. Instead of sending all the digitized samples to acquisition, the DSP elaborates the data and reduces them applying some algorithms (mainly filtering and shaping). During the experiment, for each sampled waveform validated by a trigger, the DSP program makes the pulse analysis and outputs the requested data; the signal is convoluted with a semi-gaussian shaper to extract the signal amplitude. For instance, the DSP associated to a CsI(Tl) crystal implements a function that extracts the shaped signal of both slow and fast components; both shapers, used for signal amplitude calculation, are semi-gaussian filter: the fast shaper has a shorter peaking time respect to the slow one. These two different integrations of the signal allow to exploit Pulse Shape Analysis. A complete description of digitized treatment of the signals and of the DSP implemented algorithms is provided in Ref. [60, 61, 63, 64].

The DSP sends the data to acquisition only when a validation signal arrives and the acquisition threshold is exceeded; the validation is generated by the triggerbox, which is a VME standard electronic board, featuring a field-programmable logic array (FPGA), specifically programmed to perform coincidence and trigger handling tasks. The triggerbox collects all the local triggers and performs some logical operations to decide whether to send a validation signal. In particular, it queries a user defined table of possible com-

binations of local triggers inside specific time windows. The logical conditions on triggers and the time windows are editable by the user during the measurement. Inside the trigger-box, up to eight different trigger combinations can be programmed. The used trigger bits, "name" and reduction with a brief description are reported in Table 2.4. Depending on the specific run, different triggers have been used: during a silicon strip pulser run, only trigger 2 was selected with a reduction factor of 1; while during the main physics measurement, the adopted triggers are reported in the Table 2.4. To note that, during the running of the reaction $^{16}O+^{30}Si$ at 111 MeV, a high counting rate of the strip 6 occurred due to the larger grazing angle; therefore, to monitor it separately, the trigger 2, "RCo strip 1-6", was splitted into two triggers: "RCo strip 1-5" with bit 2 and "RCo strip 6" replacing the unused trigger "RCo IC" with bit 1.

bit	trigger	reduction	description
0	RCo CsI(Tl)	8	OR among all RCo scintillators
1	RCo IC (*)	-	OR among all RCo IC sectors
2	RCo Stip 1-6 (*)	1	OR among RCo the strips 1÷6 of all sectors
3	GARF & RCo Stip 1-6	1	AND between the OR among GARFIELD scintillators and trigger 2
4	GARF & RCo IC	1	AND between the OR among GARFIELD scintillators and trigger 1
5	RCo strip 8	-	OR among RCo silicon strip 8 of all sectors
6	RCo strip 1-6 & RCo IC	-	AND between trigger 2 and 1
7	Plastic	200	Plastic scintillator

Table 2.4: Synthesis of the experimental trigger-box. (*) During the running of the reaction $^{16}O+^{30}Si$ at 111 MeV, an high counting rate of the strip 6 occured; therefore, to monitor it separately, the trigger 2, "RCo strip 1-6", was splitted into two triggers: "RCo strip 1-5" with bit 2 and "RCo strip 6" replacing the unused trigger "RCo IC" with bit 1.

2.2 Data Calibration and Physical Event Reconstruction

The physical event reconstruction is needed before any further analysis can be performed: it consists in the transformation of the so called "raw data" in an event file in which physical quantitatives are listed, characterizing the reaction products. Raw data are normally organized in a list mode, where the number of channel and of the ADC/TDC or digital converter is written before the recorded values, which define specific acquisition data parameters. A configuration file is then needed in order to translate from such a list mode to a series of quantities, which are related to a specific detector and signal. An intermediate data file is then constructed which, as a function of the event number, list an identification number of each hit detector or telescope, followed by the parameter which characterize that detector/telescope (*i.e.* for CsI(Tl) the "slow", "fast", "time", "baseline", etc.) The final step is to translate those parameters in physical quantities after the calibration procedure, which is divided in identification and in energy calibration.

The used detectors are in general not position sensitive and the angular resolution is in fact given by the detector granularity; therefore, the positions of the particles (i.e. their emission angles) correspond to the angles of the hit detector. In particular, in the analysis, the position of a particle is randomly extracted on the active area of the hit detector.

Our collaboration developed, in the last years, a complex framework, able to reconstruct and calibrate the experimental data: the package is called "ODIE" and consists of several routines used to elaborate raw data and a database containing the calibration parameters and the identification matrices; its output is a root-tree containing the calibrated physical data.

2.2.1 The Particle Identification Phase

Each single signal registered by GARFIELD and RCo is re-organized to reconstruct the needed correlations, which permit to identify the reaction products; different particle identification (PID) procedures and techniques have been used and they are hereafter described. Several identification methods can be used in experimental heavy-ion physics; in particular, in our set-up the $\Delta E - E$ technique and the pulse shape analysis (PSA) are

used. For each kind of correlation, the charge and mass (where possible) were extracted by applying graphical cuts and/or by interpolating between lines clicked over the ridges corresponding to different atomic species.

Due to the non-linearity and dependence of the energy calibration from the charge (Z) and possibly mass (A) of the particle, the PID was needed before energy calibration for the CsI(Tl) crystals. Since the procedure which permits to calculate the energy loss in the detectors dead layer, which is necessary to evaluate the initial particle energy starting from the particle measured energy, needs the knowledge of Z (and possibly A) of the particle, we decided to perform previously the PID even for the gas and the silicon detectors.

$\Delta E - E$ technique

Due to their multi-layer structure, both GARFIELD and RCo allow to perform the identification in charge Z of the detected particles through $\Delta E - E$ technique. Moreover, in the case of the $\Delta E - E$ correlation between the energy loss in silicon pads and the residual energy in the CsI(Tl) of RCo, also A can be determined because of the very good energy resolution of Silicon detectors. This identification technique requires that the incident particle punches through at least the first detection layer.

The specific energy loss (dE/dx) for charged particles in a given absorber, with density ρ, charge Z_T and mass A_T, is described by the Bethe-Bloch formula [55]:

$$-\frac{dE}{dx} = 4\pi N_A r_e^2 \rho m_e c^2 \frac{Z_T}{A_T} \left(\frac{Z}{\beta}\right)^2 \left[ln\left(\frac{2m_e c^2 \beta^2}{I\left(1-\beta^2\right)}\right) - \beta^2\right] \tag{2.1}$$

where $r_e = \frac{e^2}{4\pi\epsilon_0 m_e c^2}$ is the classical electron radii and m_e the electron rest mass; I represents the average excitation and ionization potential of the absorber; Z and β are the charge state and velocity of the incident ion, respectively. Eq. (2.1) takes into account interactions between the incident ion and the electrons of the absorber, neglecting the interactions with the nuclei of the absorber, which are significant just at the end of the particle's track. It is generally valid for different types of charged particles provided their velocity remains large compared with the velocity of the orbital electrons in the absorbing atoms. In non-relativistic limit ($\beta \to 0$) and for a fixed absorber, the main dependencies of the Eq. (2.1)

are:

$$-\frac{dE}{dx} \propto \frac{Z^2 A}{E} \tag{2.2}$$

The energy loss inside a material strongly increases with the impinging particle charge and slightly with its mass, while it decreases with energy. Therefore, it is possible to identify particles by putting two different detectors one behind the other: the particle cross the first detector and then stops in the second layer.

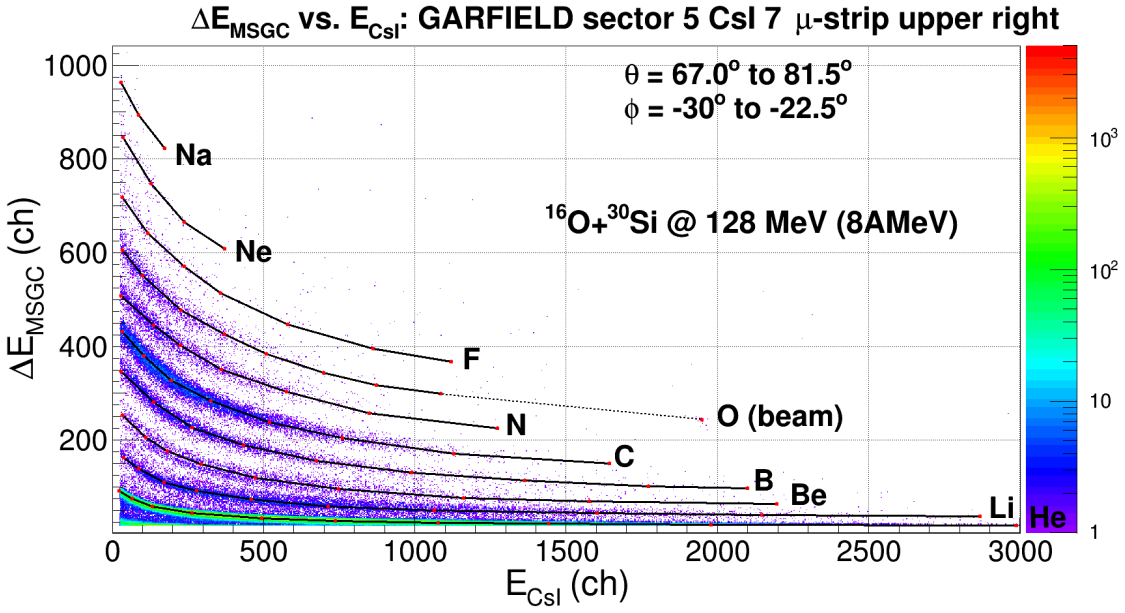

Figure 2.7: The $\Delta E - E$ correlations between MSGC and CsI(Tl) in GARFIELD for the reaction $^{16}O +^{30} Si$ at $128 MeV$ $(8 MeV/u)$.

In the GARFIELD+RCo array different $\Delta E - E$ correlations have been used. In particular, in the GARFIELD detection system the ΔE signal is provided by the microstrip pads and the residual energy signal E is obtained by the CsI(Tl) light output. In this case, as it is shown in Fig. 2.7, the charge identification is obtained by recognizing the different hyperboles derived by the $\Delta E - E$ correlations. Typically, the ΔE energy resolution is $5 \div 6\%$, which has allowed reaching an identification power of $Z/\Delta Z = 34$ at $Z = 16$. The energy threshold for identification is around $0.8 \div 1$ MeV/u, depending on Z.

For what concerns the RCo, again a first $\Delta E - E$ correlation is provided betweeen the

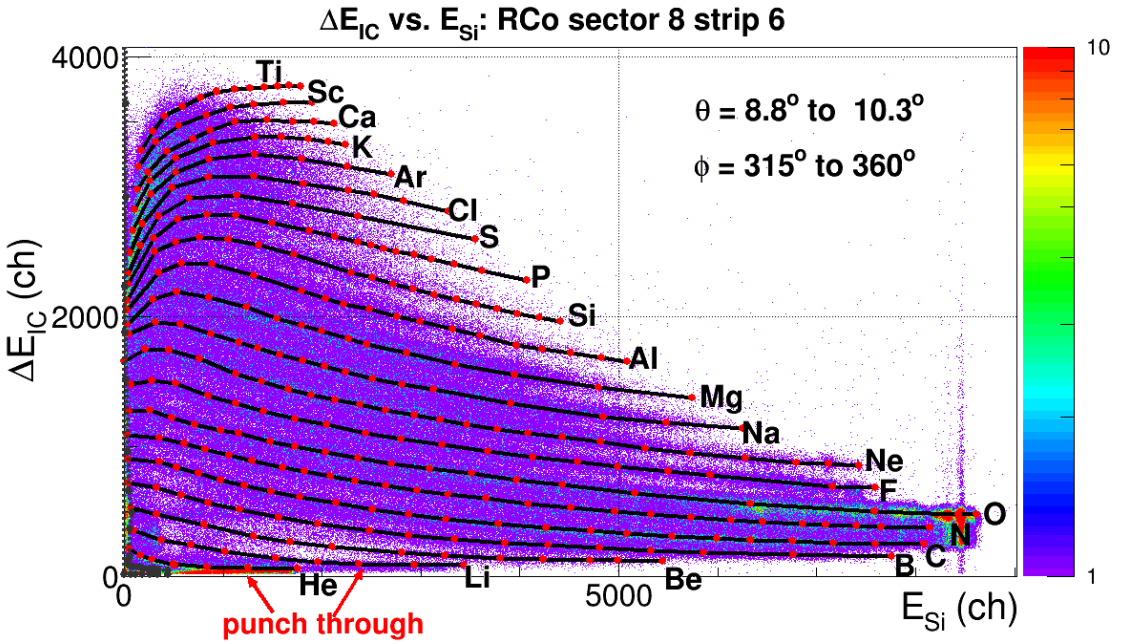

Figure 2.8: The $\Delta E - E$ correlations between ionization chamber and silicon pads in RCo for the reaction $^{16}O +^{30} Si$ at $128MeV$ $(8MeV/u)$.

gas stage (Ion Chamber) and the Silicon strip detector, for particles which stops in the second element. Particles which punch through the Silicon have to be recognized in the further detector. In this case a typical $\Delta E - E$ spectrum is shown in Fig. 2.8, where the region of heavier products, corresponding mainly to evaporation residues can be observed at high energy loss in the gas, together with lighter ions down to α-particles. Again an energy resolution of $5 \div 6\%$ is obtained for the IC signal, and a similar energy threshold for identification as previously defined GARFIELD, can be reached. In this case a $Z/\Delta Z \sim 40$ at $Z = 20$ has been reached as charge resolution. Furthermore, a second $\Delta E - E$ correlation in the RCo is the one between the energy loss in the silicon pads and the residual energy in the CsI(Tl) (see Fig. 2.9). A mass separation at least up to $Z \sim 12$ can be reached in this case because of the excellent energy resolution of the silicon pads ($\sim 0.05\%$).

For all these correlation plots the identification of particle and fragments has been performed by clicking lines on the hyperbolic ridges and assigning each line a code respectively related to Z and A (where possible). A dedicated procedure then assigns the Z and A,

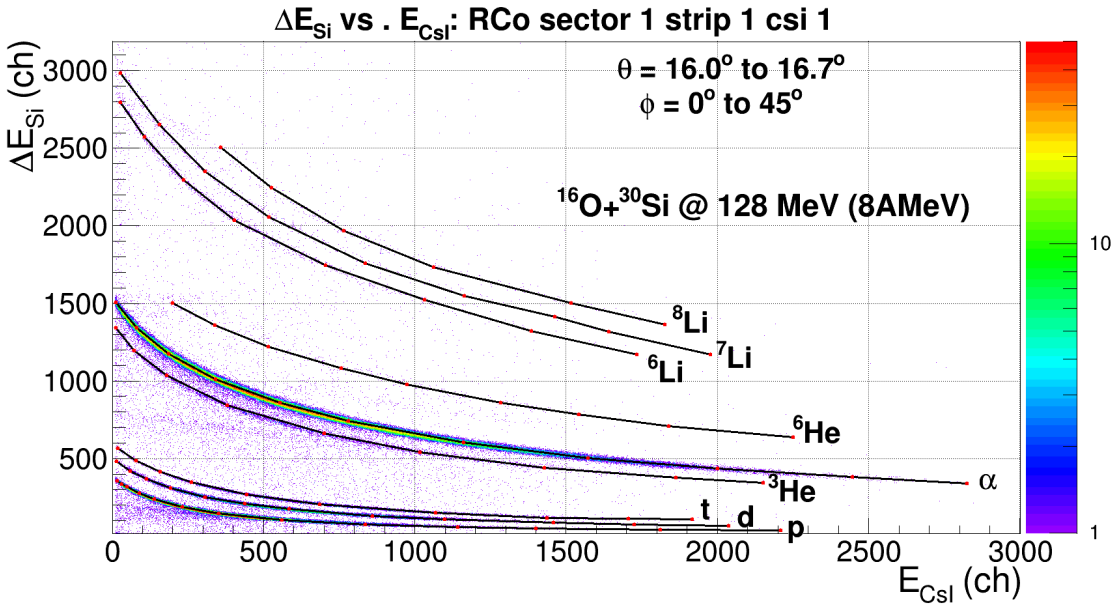

Figure 2.9: The $\Delta E - E$ correlations between the silicon pads and the CsI(Tl) in RCo for the reaction $^{16}O + ^{30}Si$ at $128MeV$ $(8MeV/u)$.

based on a defined and minimum distance from the line. In the case of IC-Si correlations, for the low energy region of high Z, contours have been used to better separate neighboring elements.

In the present analysis only element up to $Z = 3$ could reach the CsI(Tl) in the RCo due to low energy of the studied reactions. Therefore, to get some more information on the elements stopped in the Silicon detector a further technique was used as described in the following paragraph.

PSA technique in Silicon detector

Another important particle identification technique is the pulse shape analysis (PSA), especially useful for those particles which stops in the Silicon detector, when they are mounted, like in our case, in reverse mode.

The application of the PSA technique to the signals coming from the Si detectors of the RCo gives the possibility of identifying the reaction products both in charge and mass.

It consists in the correlations between the energy signal and the rise time, which is defined as the time interval needed by the signal to go (in our case) from 20% to 80% of its full amplitude. For a fixed energy of the impinging particles, heavier ions tend to create more electron-hole couples and to form a plasma region in which the electric field is weaker; therefore, the longer charge collecting process, the longer correspondingly charge signal risetime.

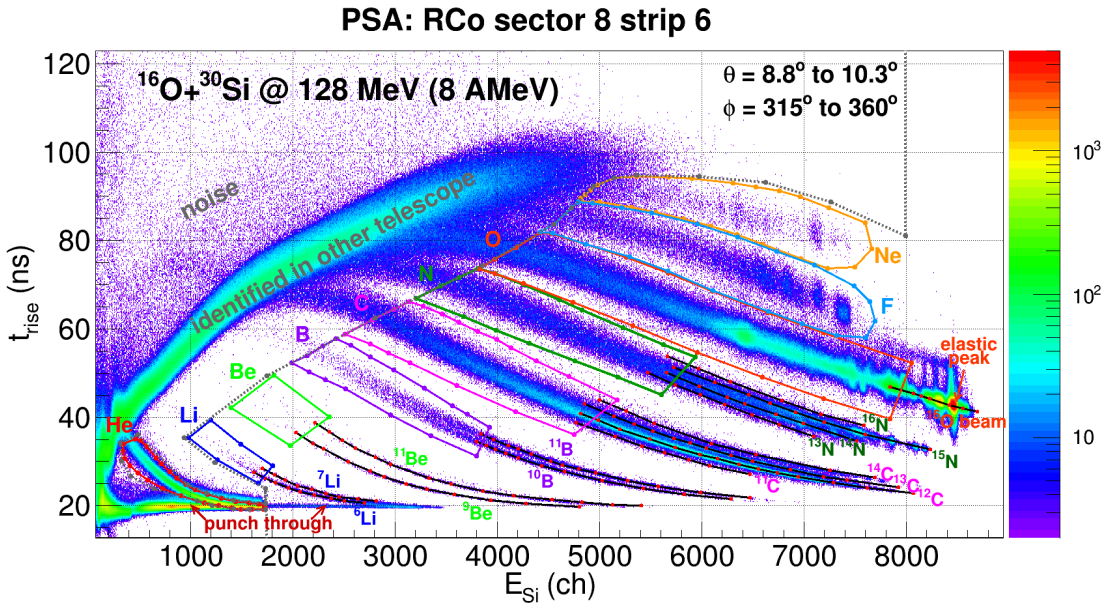

Figure 2.10: The silicon PSA, correlation between energy vs. rise time, for the reaction $^{16}O +^{30} Si$ at $128MeV$ ($8MeV/u$): the particles from $Z = 2$ up to $Z = 10$ are well identified in charge while mass identification is obtained in the specific case, for $3 \leq Z \leq 8$ and with an energy threshold, defined in the plot by the contours.

A plot of this kind is shown in Fig. 2.10 for chosen Si strip; the charge identification could be achieved for products from $Z = 2$ up to $Z = 10$, with a threshold corresponding approximately to the energy needed by the fragment to pass through the first $\sim 30\mu m$ of the detector ($\sim 2,5$ MeV/u); moreover, also the mass identification is possible via pulse shape on Si signals for fragments with charge from $Z = 3$ up to $Z = 8$. An energy threshold, defined in the plot by the contours is however applied in the present case.

PSA technique in scintillator

For particles detected in GARFIELD and for particles punching through the $300\mu m$ of RCo silicon detectors, the identification can be achieved by applying the pulse shape analysis technique on the CsI(Tl) signals, exploiting the correlation between the fast and slow components of the light output.

When an incident radiation (*i.e.* a charged particle) is detected by a CsI(Tl) crystal, a light output signal is produced, which can be described as the sum of two exponentials with different time constants:

$$L(t) = L_1 exp\left[\frac{-t}{\tau_f}\right] + L_2 exp\left[\frac{-t}{\tau_s}\right] \tag{2.3}$$

where:

- $L(t)$ is the light pulse amplitude at time t;
- L_1, L_2 are the light amplitude for the fast and slow components;
- τ_f, τ_s denote the decay time constant of the fast and slow components of the light pulse, respectively. For CsI(Tl) the typical value are $\sim 700ns$ and $\sim 2\mu s$ respectively [61].

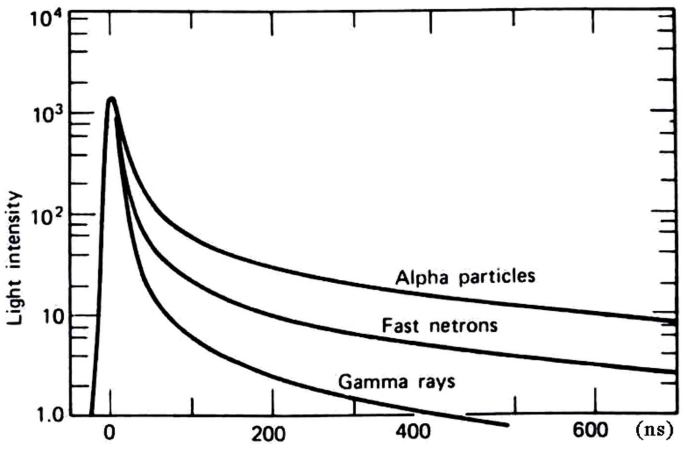

Figure 2.11: Pulse shape of charged particles in CsI(Tl).

Consequently, the whole collected charge at a fixed time is the sum of the short and long components of scintillation. Particle identification capability comes from the dependence on charge and mass of the incident particle of short and long components; in general, once fixed the same total collected charge, the short component is larger for increasing Z (Fig.2.11) [55]. By means of two shapers with different shaping constants it is possible to determine the intensity of the two components and to perform PSA. In GARFIELD+RCo array these different shaping operations have been implemented directly on the DSP purposely designed for such setup [60, 62].

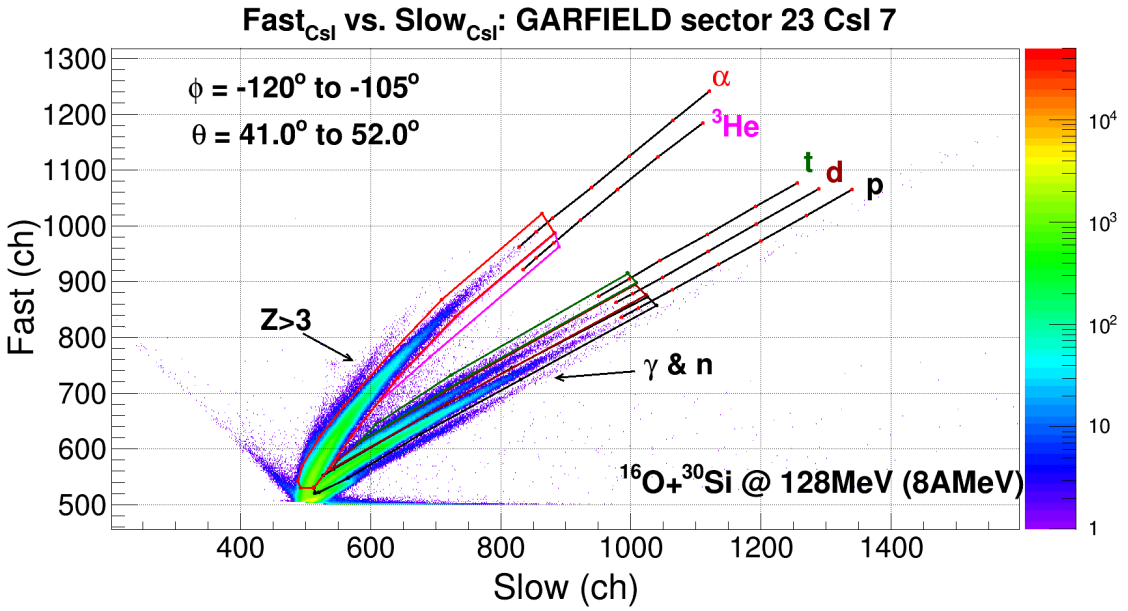

Figure 2.12: GARFIELD forward Fast vs. slow CsI(Tl) components correlation for the reaction ^{16}O +^{30} Si at $128MeV$ $(8MeV/u)$; in backward GARFIELD and in RCo similar correlations are present.

The identification scatter plot is then achieved by plotting the fast *versus* the slow component as shown in Fig. 2.12; isotope ridges are clearly visible in the plots for $Z = 1$ and $Z = 2$.

A summary of the whole GARFIELD+RCo identification capability is reported in the Table 2.5.

detector	ID technique	Z	A
MSGC vs. CsI(Tl) GARFIELD	$\Delta E - E$	$2 \div 11$	–
CsI(Tl) GARFIELD	PSA	1 & 2	$1 \div 4$
IC vs. Si RCo	$\Delta E - E$	$2 \div 22$	–
Si RCo	PSA	2	–
		$3 \div 8$	$6 \div 18$
		9 & 10	–
Si vs. CsI(Tl) RCo	$\Delta E - E$	$1 \div 3$	$1 \div 7$
Cs(Tl) RCo	PSA	1 & 2	$1 \div 4$

Table 2.5: Summary of GARFIELD+RCo identification capabilities in the present work.

2.2.2 Energy Calibration

For nearly linear detectors such as the Garfield microstrips, the Ring Counter ionization chamber and the Silicon detectors, the energy calibration is relatively easy; for this kind of detectors, in principle, the energy calibration can be done by associating the peak position of the energy spectrum with the known deposited energy for specific particles in specific events (typically elastic scattering reactions). For this purpose, during the experiment, some calibration runs with a ^{197}Au target were performed. On the contrary, more complex calibration techniques are needed for CsI(Tl). In fact, the light output (LO) of CsI(Tl) scintillators is not proportional to the released energy and the literature reports on many different attempts to obtain an analytical form to convert the LO to deposited energy [65]. Our collaboration adopted a semi-empirical expression, deduced from experiments devoted to GARFIELD CsI calibrations carried out in LNL [66]:

$$LO\left(Z_{eff}, E\right) = \left(d_1 + d_2 e^{-d_3 Z_{eff}}\right)\left(1 + d_4 Z_{eff}\right) E^{d_5 - d_6 e^{-d_7 Z_{eff}}} \tag{2.4}$$

The parameters were fixed by a fitting procedure on elastic scattering particles and fragments and different energies for which the various LO peak positions were associated to the calculated deposited energy. To better take into account the charge and mass dependence

of the light output [66, 62], the use of $Z_{eff} = (AZ^2)^{1/3}$ is required. This formula provides the energy dependence of the acquired CsI(Tl) signal apart from an overall normalization factor depending on the electronic gain. For each CsI, in every new experiment one or more elastic scattering peak energies is then registered. The ratio between the L.O. value so far obtained by Equation 2.4 and the experimental value in channel, the specific gain factor of each experiment is obtained.

The Equation 2.4 was specifically obtained for the GARFIELD CsI(Tl) crystals and it is not a priori guaranteed to work properly for other crystals with different Tl doping rates and different shapes, wrapping materials and photodiodes. We verified that it is working fine also for the RCo CsI(Tl).

Chapter 3

The simulation codes

In order to obtain a theoretical feedback, the experimental data (Chapter 2) have to be compared with simulations (Chapters 5÷6) produced with different codes based on theoretical models; in particular, the statistical code $GEMINI^{++}$ by R. Charity [67, 68], described in Section 3.1, can be used in this energy range to describe the statistical decay of the compound nuclei produced in the reactions under study; furthermore, the dynamical codes *AMD* by A. Ono [77, 78, 79, 82, 83, 84, 85] and *HIPSE* by D. Lacroix [96, 97, 98], described in Sections 3.2 and 3.3 respectively, were used to take into account any possible influence of the dynamics on the reaction evolution and, therefore, on the subsequent decay of the excited fragments and, consequently, on the final reaction products. In the following sections a brief description of the simulation codes will be given, together with the motivation for the specific code parameters chosen. In particular, the statistical $GEMINI^{++}$ code has been used either stand alone or as afterburner of the two dynamical codes.

3.1 The $GEMINI^{++}$ Code

$GEMINI^{++}$ is an improved version of GEMINI statistical decay model, developed by R. J. Charity in 1986 [69] with the goal of describing complex-fragment emission following CN formation by fusion reactions. It implements the decay of a CN through a sequence

of binary decays, generated by a Monte Carlo code which follows the de-excitation of a series of excited nuclei, from the excited CN to the last daughter nucleus, until a further decay is forbidden due to energy conservation or it is improbable due to the competition of γ-ray emission. Since CN created in fusion reactions are typically characterized by large intrinsic angular momentum, the GEMINI and $GEMINI^{++}$ models explicitly consider the influence of spin and angular momentum on particle emission. Moreover, these statistical codes do not restrict binary-decay modes to nucleon and light-nucleus evaporation, which are the dominant decay channels, but allow the decaying nucleus to emit a fragment of any mass. The introduction of a generic binary-decay mode is necessary for the description of complex-fragment formation and it is one of the features that set GEMINI and $GEMINI^{++}$ apart from most of the other de-excitation models.

The original version was written in Fortran77 and subsequently changed to Fortran90; on the contrary, $GEMINI^{++}$ is written in the C++ language and, in this work, we have used the most updated version of this code [70].

$GEMINI^{++}$ is based on a statistical approach which simulates the mechanisms of light-particle evaporation and/or of fission from the CN; the light-particle evaporation is treated with the Hauser-Feshbach formalism [71], which explicitly treats and conserves angular momentum. The fission is based on Bohr-Wheeler one-dimensional transition state formalism [72] generalized with Moretto formalism [73] in conjugation with Sierk finite range calculations [74] to consider asymmetric fission.

Evaporation Formalism in $GEMINI^{++}$

The Hauser-Feshbach formalism permits to treat the CN with high spins taking explicitly into account the spin degrees of freedom; the partial decay width of a CN with excitation energy E^*_{CN} and spin J_{CN} for the evaporation of particle b is

$$\Gamma_b\left(E^*_{CN}, J_{CN}\right) = \frac{1}{2\pi\rho_{CN}\left(E^*_{CN}, J_{CN}\right)} \int d\varepsilon_b \sum_{J_B=0}^{\infty} \sum_{J=|J_{CN}-J_B|}^{J_{CN}+J_B} \sum_{\ell=|J-S|}^{J+S} T_\ell\left(\varepsilon_b\right) \rho_B\left(E^*_B, J_B\right) \tag{3.1}$$

where:

- J_B and $E_B^* = E_{CN}^* - E_S - \varepsilon_b$ are the spin and the energy of the residue;
- ε_b and E_S are the kinetic and the separation energies of the evaporated particle; S, J and ℓ are its spin, total angular momentum and orbital angular momentum;
- T_ℓ is the transmission coefficient;
- ρ_B and ρ_{CN} are the level densities of the residue and CN, respectively;

The sum includes all angular momentum couplings between the initial and final states.

The nuclear level densities, $\rho_B\left(E_B^*, J_B\right)$, are calculated with the Fermi gas formula:

$$\rho\left(E^*, J\right) \sim exp\left(2\sqrt{a(U)U}\right) \tag{3.2}$$

where E^* is the total excitation energy, J is the spin and U is the thermal excitation energy after the pairing, rotational and deformation energies are removed; $a(U)$ is the level density parameter, which should be considered as an effective value, since no collective enhancement factors are used in the level density formula (3.2).

To systematically describe evaporation spectra from CN over a large range of excitation energies, in agreement with Hauser-Feshbach formalism, it is necessary to consider three ingredients of the model:

- the transmission coefficients, which define the slope in the Coulomb barrier region;
- the level density parameter, which defines the slope of the exponential tail of the evaporation spectrum the inverse of which is correlated to the nuclear temperature of the emitting source;
- the angular momentum dependence of $E_{Yrast}(J)$, which is very important in light nuclei, where the moments of inertia are small and thus $E_{Yrast}(J)$ rises rapidly with spins. In particular, E_{Yrast} has a strong influence on the heavier clusters, such as α-particles, which can remove large amounts of spin. For these particles, the functional form of $E_{Yrast}(J)$ can make significant modifications to the predicted shape of the evaporation spectrum in the exponential tail and even in the Coulomb barrier region.

The evaporation formalism is justified by the condition of detailed balance; therefore, the transmission coefficients for charged particle emission are obtained from the inverse reaction using optical model parameters computed from global optical model fits to elastic scattering data. Such transmission coefficients contain the effects of transparency which is not appropriate in evaporation. Instead, the real optical model potentials should be used, but to ensure full absorption, the IWBC (Incoming Wave Boundary Condition) model are used to calculate T_ℓ. However also these transmission coefficients are not associated with the true inverse reaction of evaporation, which is an absorption of the particle by a hot, rotating target nucleus, impossible to measure experimentally. So also IWBC transmission coefficients fail to reproduce the shape of the low-energy or "sub-barrier" region of the spectra of α and other heavier particles. In order to reproduce the shape of experimental heavy LCP spectra, a distribution of Coulomb barriers is required. This distribution may originate by contributions from CN thermal shape fluctuations and/or fluctuation in the diffuseness of the nuclear surface or nuclear size. It could arise also from a static nuclear deformation if evaporation is averaged over the nuclear surface.

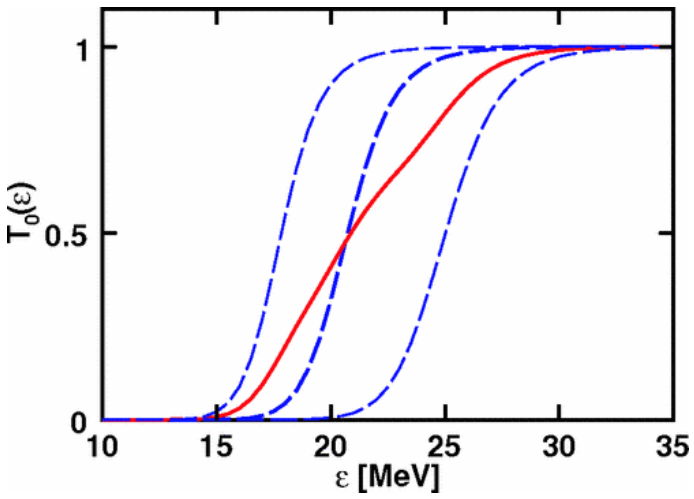

Figure 3.1: Transmission coefficients at $\ell = 0$ as a function of energy. The dashed curves show three transmission coefficients of different nuclear radii which are averaged in Eq.3.3 and the solid curve is the average result. From Ref. [67]

In $GEMINI^{++}$, a simple scheme was implemented to incorporate the effects of barrier

distributions. The transmission coefficients are calculated as the average of three IWBC transmission coefficients (Fig.3.1) calculated with three different radius parameters of the nuclear potential. It is assumed that:

$$T_\ell(\varepsilon_b) = \frac{T_\ell(\varepsilon_b)^{R_0-\delta r} + T_\ell(\varepsilon_b)^{R_0} + T_\ell(\varepsilon_b)^{R_0+\delta r}}{3} \tag{3.3}$$

The radius parameter of the nuclear potential is given by:

$$\delta r = w\sqrt{T} \tag{3.4}$$

where T is the nuclear temperature of the residue and w is a parameter.

This average value is a way to take into account the effect of the source deformation due to the thermally induced shape fluctuations. The effects of the barrier distributions is to increase the width of the kinetic-energy window around the barrier where the transmission coefficients change significantly. The transmission coefficients are sensitive to the charge and mass distributions and define the shape in the Coulomb barrier region; in particular, a change in w produces a change in the rising slope of the average IWBC transmission coefficient with kinetic energy and, as consequence, a change is produced also in the barrier.

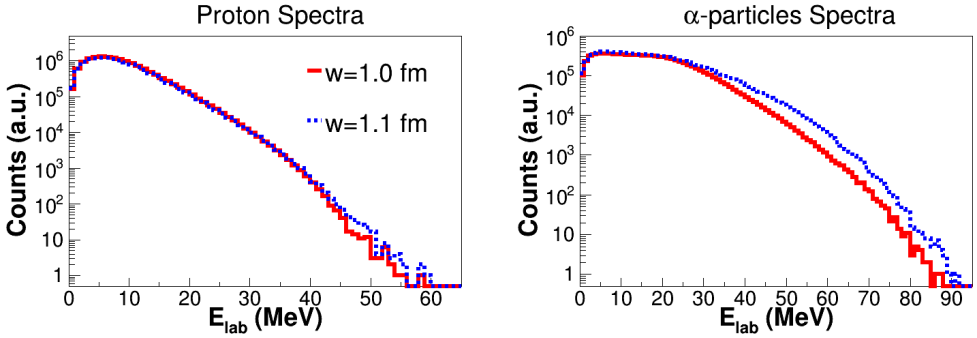

Figure 3.2: Protons and α-particles spectra simulated with two different w-parameter: $w = 1.0\ fm/\sqrt{T}$ and $w = 1.1\ fm/\sqrt{T}$ for the reaction $^{16}O +^{30} Si$ at 128 Mev.

The slope of the exponential tail of the kinetic-energy spectrum gives sensitivity to the nuclear temperature, which depends on the rate of change of the level density, but not its absolute value (see Fig. 3.2). The level density parameter $a(U)$ is excitation energy dependent. In $GEMINI^{++}$, the Fermi gas level density is refined by including the pairing

interaction in the definition of the thermal excitation energy: $U = E_B^* - E_{Yrast}(J) + \delta P$ and the level density parameter, having a strong fluctuations owing to shell effects, is parametrized as:

$$a(U) = \tilde{a}_{eff}(U)\left[1 - h\left(\frac{U}{\eta}\frac{J}{J_\eta}\right)\frac{\delta W}{U}\right] \tag{3.5}$$

where:

- $\tilde{a}_{eff}(U)$ is an effective level density parameter;
- δW is the shell correction to the liquid drop mass;
- $\eta = 19MeV$ and $J_\eta = 50\hbar$ are the obtained best fit to the experimental data through the formula $h(x) = tanh(x)$.

The separation energies, the nuclear masses, the shell δW, and the pairing corrections δP are obtained from the tabulations of Möller et al. [75]. The effective level density parameter is enhanced above the single particle estimate of level density parameter and decreases with excitation energy owing to the fadeout of long-range correlations.

These correlations modify the Fermi gas level density in two ways: collective enhancement, such as collective rotations of each single-particle configuration of a deformed nucleus, and collective vibrational motions for both spherical and deformed nuclei. The shell-smoothed level-density parameter was assumed to have the form:

$$\tilde{a}_{eff} = \frac{A}{k_\infty - (k_\infty - k_0)\, e^{-\frac{\kappa}{k_\infty - k_0}\frac{U}{A}}} \tag{3.6}$$

which varies from $\frac{A}{k_0}$ at low excitation energies to $\frac{A}{k_\infty}$ at high values; here, $k_0 = 7.3$ MeV, consistent with neutron-resonance counting data at excitation energies near the neutron separation energy, and $k_\infty =$ is set to 12 MeV.

The parameter κ defines how fast the long-range correlations wash out with excitation energy; it is essentially zero for light nuclei and increases roughly exponentially with A for heavier nuclei: $\kappa(A) = 0.00517e^{0.0345A}$

The excitation dependence is very strong for the heaviest compound nuclei, but for $A < 100$, there is very weak dependence. The strong excitation-energy dependence of

$\tilde{a}_{eff}$ for heavy nuclei leads to increased nuclear temperatures, which enhance very weak decay channels. For very fissile systems, these weak decay channels include p, n and α evaporation and thus $GEMINI^{++}$ calculations predict enhanced evaporation-residue production consistent with some experimental data.

The level density parameters are sensitive to the magnitude of long-range correlations associated with collective excitations and defines the slope of the exponential tail of the evaporation spectrum. In particular, k_0 is the most important parameter to monitor the variation of the level density parameter a; it is sensitive to the magnitude of long-range correlations and it takes into account the temperature of the residue. Furthermore, when k_0 increases as an effect, also the slope of the exponential tail in the energy spectra increases. At fixed U, when k_0 increases $a_{eff}(U)$ decreases. The decrease of $a_{eff}(U)$ reflects in an increase of the nuclear temperature of the residues.

The level density and the Coulomb barrier distribution are important to correctly predict particles multiplicities, and, in particular, α particles multiplicities are quite sensitive their prescriptions, being, on the contrary, the protons multiplicities somewhat less sensitive to these ingredients.

The exponential-like dependence of $\kappa(A)$ on mass is not enough in the case of lighter nuclei, as it was discussed in literature [76]; this component can cause quite pronounced effects on the simulated spectra of α-particles, which can remove appreciable angular momentum from the decaying system. This is due to the quite strong spin dependence of E_{Yrast} in light nuclei.

The standard values of E_{Yrast}, based on Sierk or the Rotating Liquid Drop Model (RLDM) are incapable of reproducing α-particle spectra emitted by hot light systems with large angular momentum; but, good fits could be obtained using a modified Yrast energy, where the Sierk calculations ($E_{Sierk}(J)$) is used out to an angular momentum J_* and subsequently it allows $E_{Yrast}(J)$ to increase linearly for higher spins, given by:

$$E_{Yrast}(J) = \left\{ \begin{array}{c} E_{Sierk}(J), if J < J_* \\ E_{Sierk}(J) = E_{Sierk}\left(J_*\right) + \left(J - J_*\right) E'_{Sierk}\left(J_*\right), if J > J_* \end{array} \right\} \tag{3.7}$$

If J_* is made larger than the input CN spin distribution, it has no effect. Thus, if J_*

increase with A, it allows a smooth transition to a heavier nucleus where Sierk's values can reproduce experimental data. In Fig. 3.3, the value of J_* obtained in Ref. [67] from fits to the data from different CN are plotted against the A of the daughter system. The data points can fit with the linear function: $J_* = 0.319A$ shown by the solid line.

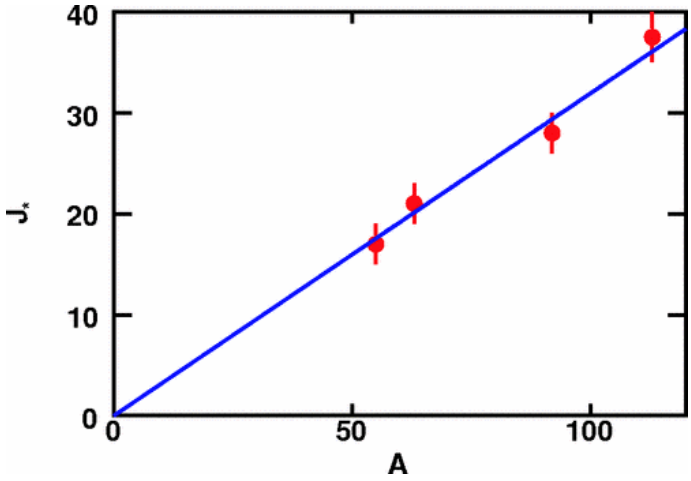

Figure 3.3: "Values of J_*, the angular momentum for which the Sierk yrast line energy is modified, are plotted again the mass of the first α-daughter nucleus. The line shows a fit to these values which is used in $GEMINI^{++}$ calculations." From Ref. [67].

3.2 The AMD Code

Microscopic simulations of heavy ion reactions are an important tool necessary for the understanding of different reaction mechanisms and of the transitions among them. They can give back a unified theoretical framework for the description of heavy ion reactions. Among these approaches it is interesting the development of the AMD (Antisymmetrized Molecular Dynamics) code, developed by A. Ono [77, 78, 79, 82, 83, 84, 85, 86, 87, 88], which is based on a stochastic equation of motion for the Gaussian wave-packets representing the colliding nucleons; AMD is the antisymmetrized version of the molecular dynamics combined with the frictional cooling method [89] and it is very powerful to study nuclear structure, being this method free from model assumptions like the axial symmetry and the clustering structure. The model treats the time development of the wave function and,

therefore, it can describe quantum mechanical features such as shell effects and clustering effects if any. Moreover, in AMD even the Pauli blocking in two-nucleon collisions is formulated: nucleons are prohibited from entering into the Pauli forbidden region. The ground states of colliding nuclei, that is the initial states of simulation are supplied as wave functions calculated with the frictional cooling method and describe the observed spectroscopic properties well. Therefore, shell and clustering effects, if any, are present in the initial configuration. The capability of AMD to treat shell effects can positively influence the description of the dynamical fragment formation process. Two initial nuclei prepared with the frictional cooling method are boosted toward each other on the Coulomb trajectory.

The AMD describes the nuclear many body system by a Slater determinant of Gaussian wave packets as

$$\Phi(Z) = det\left[exp\left\{-\nu\left(\mathbf{r}_j - \frac{\mathbf{Z}_i}{\sqrt{\nu}}\right)^2 + \frac{1}{2}\mathbf{Z}_i^2\right\}\chi_{\alpha_i}(j)\right] \tag{3.8}$$

where:

- the complex variables $Z \equiv \{\mathbf{Z}_1, \mathbf{Z}_2, ..., \mathbf{Z}_N\}$ are the centers of the wave packets;
- ν is a parameter corresponding to the width of the wave packets (usually $\nu = 0.16fm^{-2}$);
- $\chi_{\alpha_i}(j) = p\uparrow, p\downarrow, n\uparrow, n\downarrow$ are the spin isospin states.

The time evolution of Z, determined by the time-dependent variational principle and by the two-nucleon collision process, which is indispensable to describe heavy ion nuclear reactions, is given by:

$$i\hbar\sum_{j\tau} C_{i\sigma,j\tau}\frac{dZ_{j\tau}}{dt} = \frac{\partial\mathcal{H}}{\partial Z^*_{i\sigma}} \tag{3.9}$$

with the Hermitian matrix $C_{i\sigma,j\tau}$ $(\sigma,\tau = x,y,z)$ and the expectation value of the Hamiltonian, after the subtraction of the spurious kinetic energy of the zero-point oscillation of the center of masses of the fragments, $\mathcal{H} = \langle H\rangle - \frac{3\hbar^2\nu}{2M}A + T_0\,(A - N_F)$ where:

- N_F is the fragment number;
- T_0 is, in principle, equal to $\frac{3\hbar^2\nu}{2M}$ but it is used as a free parameter to adjust the binding energies of nuclei;
- $H = \sum_{i=1}^{A} \frac{\mathbf{p}_i^2}{2M} + \sum_{i<j} v_{ij}$ is the quantum Hamiltonian, which includes an effective two-body interaction; in the present work all calculations are performed using the Skyrme SLy4 force [80, 81] as an effective interaction with the spin-orbit term omitted.

Due to the antisymmetrization effects, the centers of Gaussian wave packets, Z, do not always represent the positions and momenta of nucleons. It is, therefore, needed to transform the Z coordinates into the new coordinates $W = \{\mathbf{W}_1, \mathbf{W}_2, ..., \mathbf{W}_A\}$, which can be interpreted as the centers of incoherent Gaussian wave packets:

$$\mathbf{W}_i = \sum_{j=1}^{A} \left(\sqrt{Q}\right)_{ij} \mathbf{Z}_j = \sqrt{\nu}\mathbf{R}_i + i\frac{\mathbf{P}_i}{2\hbar\sqrt{\nu}} \tag{3.10}$$

where:

- $Q_{ij} = \frac{\partial ln \langle \Phi(Z) \mid \Phi(Z) \rangle}{\partial (\mathbf{Z}_i^* \cdot \mathbf{Z}_j)}$;
- $\mathbf{R}_i$ and $\mathbf{P}_i$ are, respectively, the real and the imaginary parts. They can be treated as physical positions and momenta of nucleons in the two-nucleon collision processes.

Since a AMD Slater determinant represents the wave function of A-body system, the fermionic nature of nucleons is treated exactly. Hence, the model fully incorporates Pauli principle in the wave function. Such physical coordinates are used to reproduce the two-nucleons collision processes: the positions $\mathbf{R}_i$ and $\mathbf{R}_j$ are not changed by the collision, while the momenta $\mathbf{P}_i$ and $\mathbf{P}_j$ are changed stochastically into $\mathbf{P}_i^{'} = \frac{1}{2}\mathbf{P}_{cm} + p_{rel}^{'}\hat{\mathbf{n}}$ and $\mathbf{P}_j^{'} = \frac{1}{2}\mathbf{P}_{cm} - p_{rel}^{'}\hat{\mathbf{n}}$, where:

- $\mathbf{P}_{cm} = \mathbf{P}_i + \mathbf{P}_j$;
- $\hat{\mathbf{n}}$ is an unit vector randomly chosen;

- p_{rel} is the relative momentum of final state. At the beginning, it is set equal to the initial relative momentum $\frac{\mid \mathbf{P}_i - \mathbf{P}_j \mid}{2}$. Finally, it has been modified with some correction steps to reach the final relative momentum p_{rel}, which follows both the antisymmetrization and the energy conservation rules. Normally, if energy conservation is not achieved after 4 correction steps, the collision is considered as not taking place.

This basic approach of the original version of AMD has been improved by taking into account the formation of correlated clusters in the final states of every two-nucleon collision. In fact, AMD has been updated incorporating all the advantages of the mean field models such as the time-dependent Hartree–Fock (TDHF) theory and the Vlasov–Uehling–Uhlenbeck (VUU) equation [90, 91]. These models are good for a precise description of the single-particle dynamics in the mean field, while they cannot normally describe the fragment formation. In fact, generally, microscopic transport models, including the standard version of AMD, have not been able to describe the formation of clusters and fragments in a consistent way. Often, nucleon multiplicity is strongly overestimated. This conceptual difficulty has been solved in AMD, which has been improved by incorporating the quantum branching into channels (Fig. 3.4). In other words, the AMD has been developed so that the single-particle dynamics is as precise as in mean field models while the single-particle wave functions can localize to produce many-body correlations for fragment formation. It was, therefore, defined that cluster correlations should be more explicitly considered in the dynamics of heavy-ion collisions.

In the used version of AMD, a two-nucleon collision is treated as a stochastic transition from an initial state $\mid \Psi_i\rangle$ to one of the possible final states $\mid \Psi_f\rangle$, which is assumed to occur instantaneously and it conserves the energy expectation value $\langle\Psi_i \mid H \mid \Psi_i\rangle = \langle\Psi_f \mid H \mid \Psi_f\rangle$. The transition probabilities are evaluated assuming that different clustering configuration are induced by a residual interaction V between the two colliding nucleons and taking into account the Pauli blocking for the scattered nucleons. In the collision process $N_1 + N_2 + B_1 + B_2 \rightarrow C_1 + C_2$, each of the scattered nucleons N_j(j = 1,2) may form a cluster C_j with the spectator particle B_j. The special case $C_j = N_j$ with empty B_j

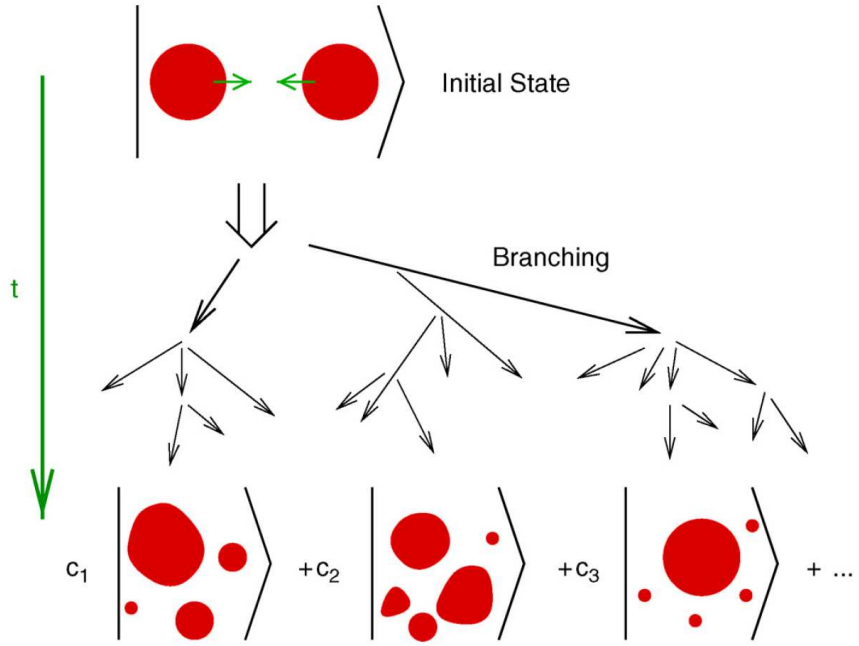

Figure 3.4: A schematic picture of the quantum branching processes for multichannel reactions. From Ref. [82].

tales into account the collisions without cluster formation. The partial differential cross section for the collision of the two nucleons N_1 and N_2 with the initial relative velocity, v_{NN}, is given by:

$$\frac{d\sigma}{d\Omega} = \frac{2\pi}{\hbar}|\langle\varphi_1^{'}|\varphi_1^{\mathbf{q}}\rangle|^2|\langle\varphi_2^{'}|\varphi_2^{-\mathbf{q}}\rangle|^2|\mathbf{M}|^2\delta\left(E_f - E_i\right)\frac{p_{rel}^2 dp_{rel}}{(2\pi\hbar)}v_{NN} \tag{3.11}$$

where:

- **M** is the two-nucleon scattering matrix element;
- p_{rel} and Ω are, relatively, the relative momentum and the scattering solid angle in the two-nucleon center-of-mass system;
- $\langle\varphi_j^{'}|\varphi_j^{\pm\mathbf{q}}\rangle$ with (j=1,2) are the overlap matrices between $|\varphi_j^{\pm\mathbf{q}}\rangle = e^{\pm i\mathbf{q}\cdot\mathbf{r}_j}|\varphi_j\rangle$ and $|\varphi_j^{'}\rangle$; $|\varphi_j\rangle$ and $|\varphi_j^{'}\rangle$ are, respectively, the initial and final states of the $N_j + B_j$ systems and the operators $e^{\pm i\mathbf{q}\cdot\mathbf{r}}$ give the momentum transfer to nucleons N_j. When a cluster is formed, the corresponding wave packets are placed at the same phase-space

point; i.e., the cluster internal state is represented by the harmonic-oscillator $(0s)^n$ configuration.

In a two-nucleon collision, there are many possible ways of forming a cluster for each N of the scattered nucleons N_1 and N_2. A scattered nucleon N may form a cluster with one of the spectator nucleons $\{B_1, B_2, ...\}$, which has the same spin-isospin state. This spin-isospin state has to be studied. Firstly, it is randomly decided: the cluster-formed state, $|\Phi_f\rangle$, is obtained changing the state to $|\Phi^{\pm\mathbf{q}}\rangle$ by the momentum transfer $\pm\mathbf{q}$ to N. Then, it is changed again moving the two wave packets of N and $\{B_k\}$ to the same phase-space point without changing their center of mass. Since the different final states are not orthogonal, $\mathcal{N}_{kl} = \langle\Phi_k^{'}|\Phi_l^{'}\rangle \neq \delta_{kl}$, the probability that N forms a cluster with one of B_k should be calculated as

$$P = \sum_{kl}\langle\Phi^{\mathbf{q}}|\Phi_k^{'}\rangle\mathcal{N}_{kl}^{-1}\langle\Phi_l^{'}|\Phi^{\mathbf{q}}\rangle = \sum_{l}\mathcal{N}_{kl}^{-\frac{1}{2}}\langle\Phi_l^{'}|\Phi^{\mathbf{q}}\rangle = \sum_{k}|v_k|^2, \tag{3.12}$$

This probability is calculated with an approximation that the many-body state is a direct product of wave packets centered at the physical coordinates. With the calculated probability P, a cluster will be formed with one of $\{B_k\}$. It is somewhat arbitrary which one of $\{B_k\}$ should be chosen with what probability. With the rest of the probability $(1-P)$, N does not form a cluster with a nucleon of this spin-isospin state. The procedure is repeated for other spin-isospin states for $\{B_k\}$. The particle N should be regarded as a cluster, instead of a scattered nucleon, if a (sub)-cluster has been already formed in previous steps of the repetition. Thus the formation of light clusters is considered up to an α-particle. This procedure determines the probability $P_{C_1C_2}(p_{rel}, \Omega)$ for the combination of final clusters (C_1,C_2) as a function of the momentum transfer $\mathbf{q}$ or (p_{rel},Ω). Since the probability satisfies the normalization $\sum_{C_1C_2} P_{C_1C_2}(p_{rel}, \Omega) = 1$, the factor $|\langle\varphi_1^{'}|\varphi_1^{\mathbf{q}}\rangle|^2|\langle\varphi_2^{'}|\varphi_2^{-\mathbf{q}}\rangle|^2|\mathbf{M}|^2$ in Eq. (3.2) should be replaced by $P_{C_1C_2}(p_{rel}, \Omega)$. Even when the cluster formation is introduced, the many body state is always represented by an AMD wave function which is a Slater determinant of nucleon wave packets. The time evolution of the many-body state is solved just as usual without depending on whether some of the wave packets form clusters due to collisions in the past.

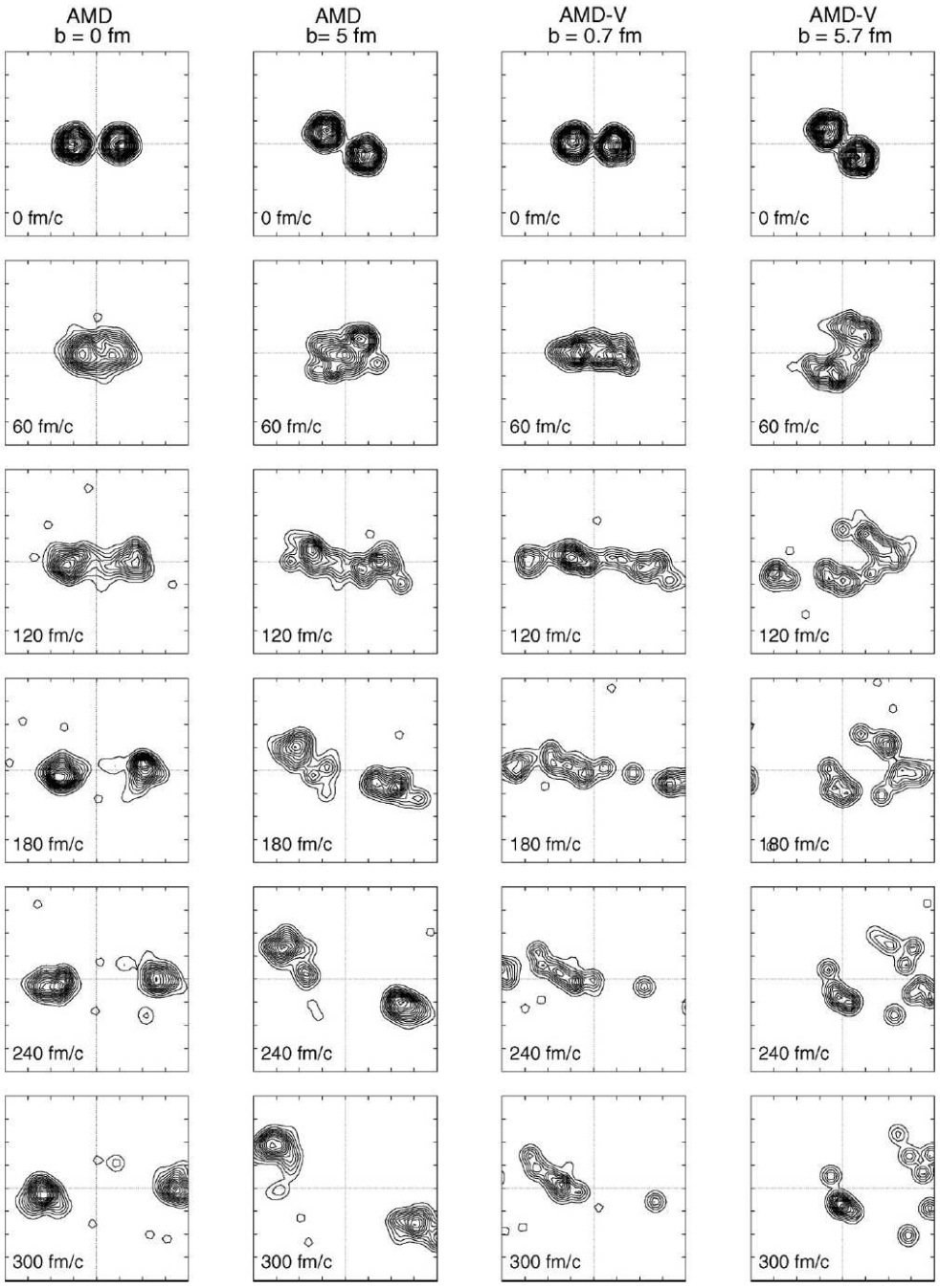

Figure 3.5: Time evolution of the density projected onto the reaction plane from $t = 0$ fm/c to $t = 300$ fm/c for $^{40}Ca + ^{40}Ca$ at 35 MeV/u. Calculated results with AMD and with AMD-V for impact parameters $b \sim 0$ fm and $b \sim 5$ fm. From Ref. [82].

A typical example of AMD simulation is shown in Fig. 3.5, where the density plots in the coordinate space as a function of collision time are shown.

The AMD code has been used to simulate our data. The code has been run up to 500 fm/c and then the produced excited fragments have been given as an input to $GEMINI^{++}$ used as afterburner to follow their statistical decay. The results from secondary decay have been compared to experimental data after a proper filtering procedure through a software replica of the apparatus.

3.3 The HIPSE Code

The HIPSE (Heavy-Ion Phase-Space Exploration) code, developed by D. Lacroix, A. Van Lauwe and D. Durand [96], is a phenomenological event generator allowing a detailed comparison with experimental data and accounting for both dynamical and statistical effects, related to the two extreme approaches: the microscopic approach, based on the transport theory, and the statistical approach, based on the reduction of the reaction to a few important parameters. It is based on the sudden approximation (approaching phase) and can describe the nuclear collisions in the intermediate energy range.

This code consists in three main steps. The first, namely *approaching phase* of the collisions, ends when the two partners of the reactions are at maximum overlap: such phase is evaluated solving the classical equation of motion of the partners in their mutual interaction potential. Using the sudden approximation, the two interacting nuclei are described as a collection of nucleons with momentum and space distributions corresponding to their ground state boosted by the relative momentum and distance associated with the maximum overlap between the two incoming nuclei. The latter, namely *partition formation phase*, corresponds to the rearrangement of the nucleons into clusters and light particles according to the impact parameter of the reaction. This partition is built following coalescence rules in momentum and position spaces. The main consequence of this approximation is a strong memory of the entrance channel in the observables of the produced particles. In the last, namely *exit channel and after-burner phase* the partition is propagated taking into account explicitly re-aggregations among the various species of

the partition until the "freeze-out" is reached; afterwards s secondary in-flight decay took place.

3.3.1 The approaching phase

During the approaching phase, a classical two-body dynamics is assumed: the evolution of the system is described by the Hamiltonian

$$E_0 = \frac{p^2}{2\mu} + V_{A_T A_p}(r) \tag{3.13}$$

where:

- $E_0 = \frac{A_T}{A_T + A_p} E_b$ is the available energy in the center of mass with E_B is the beam energy;
- **p** is the relative momentum;
- $\mu = \frac{m_T m_p}{m_t + m_p}$ is the reduced mass with m_T and m_p the target and projectile mass, respectively;
- $V_{A_T A_p}(r =\mid \overline{r}_T - \overline{r}_p \mid)$ is the interaction potential between the target and the projectile.

The interaction potential is described by the proximity potential when the two nuclei are well separated; but, the proximity potential is not well suited for small relative distance $r \leq R_T + R_p$ (where R_T and R_p are target and projectile radii, respectively). In this case, another description of nuclear potential between the two strongly overlapping nuclei is needed; such a potential is to a large extent unknown and should normally depend on different parameters describing the configurations of the system. Such potential is expected to be not unique; moreover, as the beam energy increases, the internal degrees of freedom have less time to reorganize and the potential is expected to be sharper. In the HIPSE code, the energy dependence of the potential is included in a phenomenological way, with a simple approximation for the construction of the potential: $V_{A_T A_p}(r)$ is assumed to depend on r uniquely even for small distances; then, to obtain the potential for $r < R_T + R_p$, the

potential between $r = 0$ and $r = R_T + R_p$ is interpolated using a third-order polynomial and assuming continuity of the derivative of the potential at each point. At minimum distance of approach, the two partners of the reaction overlap more or less according to the impact parameter and to a parameter α_a, fixed by comparison with experimental data. At this point the two nuclei are at maximum overlap and the potential value is expressed as:

$$V(r = 0) = \alpha_a V^{Froz}_{A_T A_p}(r = 0) \tag{3.14}$$

where $V^{Froz}_{A_T A_p}(r = 0)$ is the energy of the system evaluate with the frozen density approximation; such approximation assumes that the reactions is fast compared to the time scale of the reorganization of nucleonic single-particle degrees of freedom. For this reason, the spatial and momentum distributions of the (A_T, Z_T) and (A_p, Z_p) nucleons constituting the target and the projectile are not expected to differ significantly from the ones they do have in the initial ground state of the two partners.

3.3.2 The partition-formation phase

The frozen approximation samples the positions and momenta of the nucleons in the center of mass of each partner of the reaction. In order to have realistic density ground state distributions, a semi-classical approximation, based on the Seyler-Blanchard parametrization of the force [99] and on Metropolis algorithm to sample nucleons roughly considering the Pauli principle for each nucleus, is used. This procedure ensures a uniform arrangement of the nucleons in each nucleus. A final (small) correction is applied to the position and momentum of the nucleons in order to keep the position and momentum of the center of mass constant.

The description of nucleons outside the overlap region, namely quasi-projectile (QP) and quasi-target (QT) fragments, is based on geometrical hypotheses; such simplified approach does not take into account that, in the realistic case, QP and/or QT fragments have kinetic energies slightly reduced with respect to the initial projectile and target due to the particles exchange between the two partners during the reaction. Such effect is introduced "by hand" in HIPSE code assuming a number of transferred nucleons, depending on the

initial energy, coming initially from the target (projectile) and belonging to the overlap region is transferred to the projectile (target).

Considering the nucleons located inside the overlap region, at beam energies above the Fermi energy, another contribution sets in corresponding to the pre-equilibrium emission of light particles with large transverse momenta; these particles are generally assigned to promptly emitted particles induced by hard nucleon-nucleon collisions. In HIPSE code, the description of fragments built from nucleons that have suffered no collisions is separated from that of fragments produced with collided nucleons. The first case aggregates the nucleons to form the fragments using a coalescence algorithm. The last takes into account the increase of the effect of the nucleon-nucleon collisions, which distort more or less the initial Fermi distribution of the nucleons and lead to a slight modification of the promptly emitted particles and light clusters.

The formation of fragments from the nucleons that have experienced no hard collisions is described following coalescence algorithm: a nucleon, "*1*", (with mass number $A_1 = 1$, position R_1 and momentum P_1) is randomly chosen and it constitutes a coalescence point from which a fragment is built; another, randomly chosen, nucleon, "i", in the overlap region, can be captured by the cluster "*1*" according to the existence condition, which is a test of the composite nucleus existence checking its presence in an experimental mass table, and to the position and momentum condition, for which only nucleons that are close enough in phase space to the considered fragment can be absorbed. This latter condition can be formulated as:

$$\frac{p_i^2}{2m} + \frac{V_{cut}}{1 + exp\left\{\dfrac{r_i - d_f}{a}\right\}} < 0 \tag{3.15}$$

where:

- r_i and p_i are the position and momentum of the nucleon with respect to the fragment; m is its mass;
- d_f ia a direct cut off in coordinate space: $d_f = R_f + r_{cut}$, where R_f is the equivalent sharp radius of the fragment while r_{cut} is a parameter kept constant;

- V_{cut} is a cut off in momentum space of the considered nucleus: $V_{cut} = -\frac{p_{cm}^2}{2m}$.

If the two preceding conditions are fulfilled, the nucleon is absorbed by the fragment and the position and momentum of the cluster of mass $A_1 = 2$ is recalculated according to the positions and momenta of its constituents. If one of the conditions is not met, the nucleon serves as a new coalescence point. A new nucleon is then chosen from the remaining nucleons and the procedure is iterated. The aggregation procedure stops when all available nucleons have been considered.

An increase of the effect of nucleon-nucleon collisions is expected when the beam energy increases. Such collisions tend to wash out the memory of the entrance channel and may eventually lead to the formation of a compound nuclear state. A simplified procedure to treat the nucleon-nucleon collisions is used: during two-body collision, the two particles exchange momentum, while in r-space, a complete loss of the memory of the positions before collisions is explicitly assumed. The new positions of the two particles are supposed to be randomly distributed inside a sphere of radius

$$R_{coll} = 1.2A_{over}^{1/3} + r_{coll} \tag{3.16}$$

where:

- A_{over} is the number of nucleons in the overlap region;

- r_{coll} is a parameter taken sufficiently large to enable the particles to escape rapidly the dense matter ($r_{coll} = 4fm$).

Due to the Pauli exclusion principle, not all the sphere of radius R_{coll} is accessible.

At the end of these different steps, a set of fragments (including the QP and QT) with mass number, position, momentum, and angular momentum (A_f, $\mathbf{R}_f$, $\mathbf{P}_f$, $\mathbf{L}_f$), by considering the characteristics of the nucleons belonging to each fragment, are produced. At that point, a "clock" is started corresponding to $t = 0$ fm/c for the forthcoming dynamics.

3.3.3 Exit channel and afterburner phase

During times comparable to the reaction time ($\sim$ 10 fm/c), the fragments, produced in the partition-formation phase, can overlap; for this reason, it is needed to propagate the partition before the freeze-out is reached. This is first achieved during a time of 50 fm/c according to the Hamiltonian

$$H = \sum_i \frac{P_i^2}{2mA_i} + \sum_{i>j} V_{A_iA_j}(\mid \mathbf{R}_i - \mathbf{R}_j \mid) \tag{3.17}$$

For the sake of continuity and consistency, the same interaction potentials as for the entrance channel part of the reaction are used. However, for protons or neutrons interacting with nuclei, we used standard Woods-Saxon potential for the nuclear part of the interaction. At that time an important reorganization in spatial and momentum configuration may have occurred. It leads generally to less compact configurations. It however may happen that two fragments cannot separate because their relative energy is lower than the fission barrier. In that case, the two nuclei fuse and the properties of the fused system are calculated accordingly. At very low incident energy, most of the fragments produced in highly fragmented partition will fuse possibly producing a single composite system.

After this first propagation at high density and the reaggregation phase, the interaction between the fragments is purely Coulombic. However, it is expected that the fragments emerge from the reaction with a sizable excitation energy. It is then assumed that the thermalization of the nucleons inside each fragment occurs on a time scale of the order of a few tens of fm/c after the reaggregation. Further decay of such excited fragments is described by means of a statistical evaporation code. Since the thermalization is not described at the microscopic level, the estimation of the excitation energy can only be obtained with help of a global energy balance of the reaction, that in center of mass frame reads:

$$E_0 = Q + E_k + E_{pot} + E^* + E_{rot} \tag{3.18}$$

where:

- E_k and E_{pot} are, respectively, the sum of the kinetic and potential energies of the fragments;

- E_{rot} is the sum of their rotational energies, estimated assuming rigid sphere for fragments;
- Q is the mass energy balance between the entrance channel and the considered partition;
- E^* corresponds to the total excitation energy. If the quantity E^* is negative, the partition is rejected since it then corresponds to unaccessible phase space according to the initial available energy. The total excitation energy must be shared among fragments.

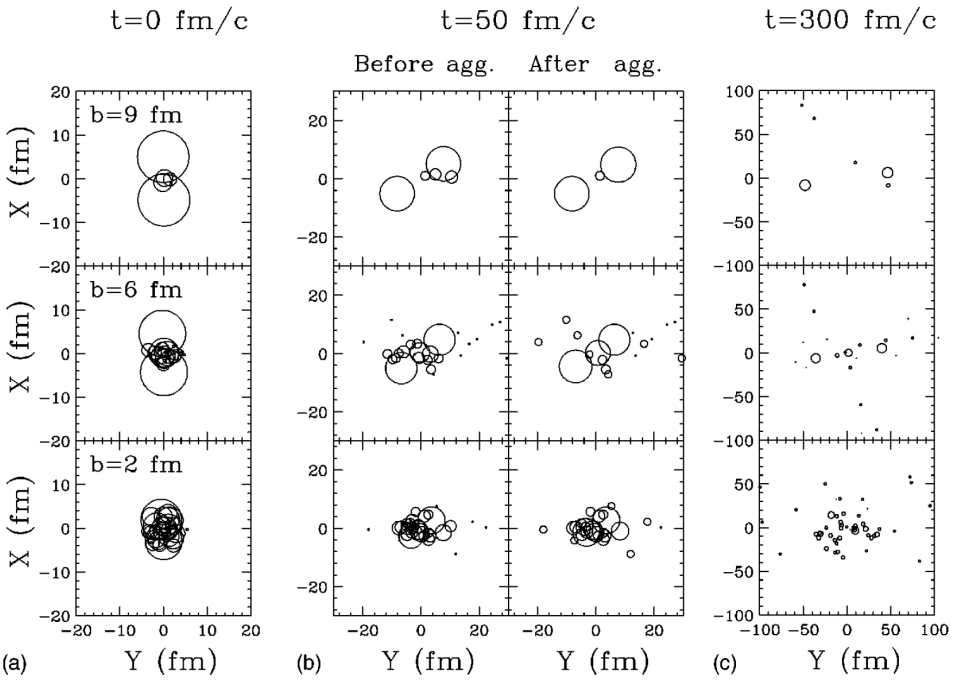

Figure 3.6: "Example of nuclear dynamics for the reaction $^{129}Xe+^{120}Sn$ at $E = 50$ MeV/u. From top to bottom, the initial impact parameters $b = 9$ fm, $b = 6$ fm and $b = 2$ fm are presented. In each case, from left to right figures correspond to the initial cluster configuration ($t = 0$ fm/c), the configuration before and after the reaggregation ($t = 50$ fm/c) and during the deexcitation ($t = 300$ fm/c)." From Ref. [96].

An example of the application of the HIPSE code is reported in Fig. 3.6. Here,

partitions in space configuration for different impact parameters and time of the reaction from peripheral to central collisions are shown: in the left panels, the approaching phase is illustrated; in the middle panels, the nuclei partitions before and after the reaggregation are presented, this figure testifies that a large fraction of light nuclei is issued from the very first instant of the collision in the overlap region and it is also clear that final state interactions play a significant role; finally, in the right side, an intermediate stage during the deexcitation is shown, illustrating the possible in-flight statistical emissions of different species.

Chapter 4

The deformed ^{46}Ti*

The ^{46}Ti is one of the five stable isotopes of the natural Titanium; its ground state is characterized by a 0^+-state of spin-parity and it has a binding energy $BE/A = 8.656$ MeV/u. As reported in the papers of A. Maj and collaborators works (Refs. from [104] to [115]) the nucleus ^{46}Ti becomes a quasi-superdeformed nucleus (see Section 4.1) when it is excited and its deformation depends on the spin. In our analysis we take into account this deformation by modifying the Yrast line in the statistical decay code $GEMINI^{++}$ as reported in Sections 4.2.

4.1 The ^{46}Ti a Quasi-Superdeformed Nucleus

In many light- and medium-mass nuclei, a change of equilibrium nuclear shape from an oblate ellipsoid, non-collectively rotating around its symmetry axis, via triaxial shape up to an elongated prolate, collectively rotating around the shortest axis, has been predicted to appear with the increase of the angular momenta up to the fission limit [104, 105]. This phenomenon is known as Jacobi phase transition and is studied using classical or semi-classical models, as for example the Lublin-Strasbourg Drop (LSD) model [105, 106] (see Fig. 4.1).

The LSD model is a realistic version of the nuclear Liquid Drop Model; it introduces some extra degrees of freedom associated with the *curvature* of the nuclear surface. The

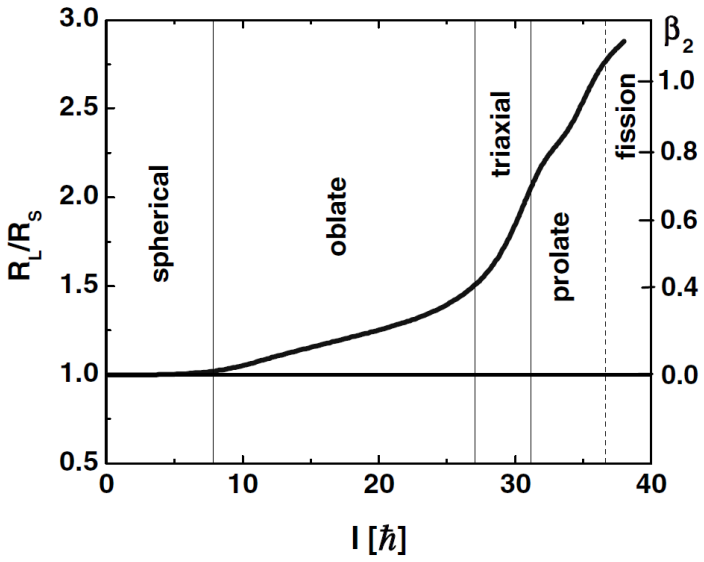

Figure 4.1: "Long-to-short axis ratio and β_2 parameter for the equilibrium deformation as a function of spin, obtained from the LSD model calculations for ^{46}Ti." From Ref. [106]

macroscopic nuclear Liquid Drop Model energy in its LSD form is formulated as a function of the number of neutrons (N) and protons (Z), of the nuclear collective angular momentum (J) and of a parameter (α) representing an abbreviation of all the deformation parameters. It can be expressed as the sum of different terms:

$$E_{total}(N,Z;\alpha;J) = E(N,Z)+E_{Coul.}(N,Z;\alpha)+E_{surf.}(N,Z;\alpha)+E_{curv.}(N,Z;\alpha)+E_{rot.}(N,Z;\alpha;J) \tag{4.1}$$

where:

- $E(N,Z)$ denotes the deformation independent term related to the atomic mass;
- $E_{Coul.}(N,Z;\alpha)$ represents the deformation depending on the Coulomb electrostatic energy term;
- $E_{surf.}(N,Z;\alpha)$ depends on the surface energy term;
- $E_{curv.}(N,Z;\alpha)$ related to the curvature energy term; this is a characteristic term of the LSD model;

- $E_{rot.}(N, Z; \alpha; J)$ depends on the rotational energy and, therefore, on the spin.

In particular, in the case of the excited ^{46}Ti, the tri-axial Jacobi shape transition was demonstrated in Ref. [107] describing the nuclear surface in terms of a basis set of functions such as spherical harmonics, $Y_{\lambda,\mu}$ and of the relative deformation coefficients α_{λ_μ}, which are considered up to a value of maximum multipolarity λ_{max} which define the basis cut off parameter. A study of the stability properties of the basis cut off as been performed by examining the spins of the Jacobi phase transitions, besides the usual axially symmetric deformation.

In Fig. 4.2, the results, obtained in Ref. [107], corresponding to the usual $\{\beta, \gamma\}$-plane representation, in which β and γ are the leading (quadrupole) deformation parameters for the two nuclei ^{46}Ti (left panels) and ^{142}Ba (right panels).

These energy maps are meant to define the energy scale within which the basis cut-off instability tests have been analyzed; the potential energies of Fig. 4.2 have been labeled E_{22} despite the fact that minimization over several axially-symmetric deformations is performed. A cross-check on the impact of the triaxial deformations α_{42} and α_{62} has been performed by the authors, who claim that the effect of the higher-order triaxial deformations α_{42} and α_{62} are negligible for the Jacobi shape transition in the studied nuclei.

The LSD model calculations predict that the excited ^{46}Ti nucleus is nearly spherical at low angular momenta, it increases its oblate deformation up to $J \sim 26\hbar$ with an elongation parameter $\beta \sim 0.3$. For higher spins, the Jacobi shape transition sets in: the nucleus becomes triaxial with an elongation parameter increasing up to $\beta \geq 1$ for $J \sim 38\hbar$; finally, fission takes place at $J \sim 40\hbar$. See right panel of Fig. 4.3 and refer to [108, 109] for major details.

In the work of M. Brekiesz *et al.* Ref. [108, 113], the excited ^{46}Ti was populated through the fusion-evaporation process, induced by the reaction $^{27}Al + ^{19}F$ at bombarding energy of 144 MeV. Similar results, relatively to ^{46}Ti deformation are reported in [109], where the entrance channel was $^{18}O + ^{28}Si$ at 105 MeV: the CACARIZO code was again used to simulate the statistical decay of the compound nucleus. In the CACARIZO code,

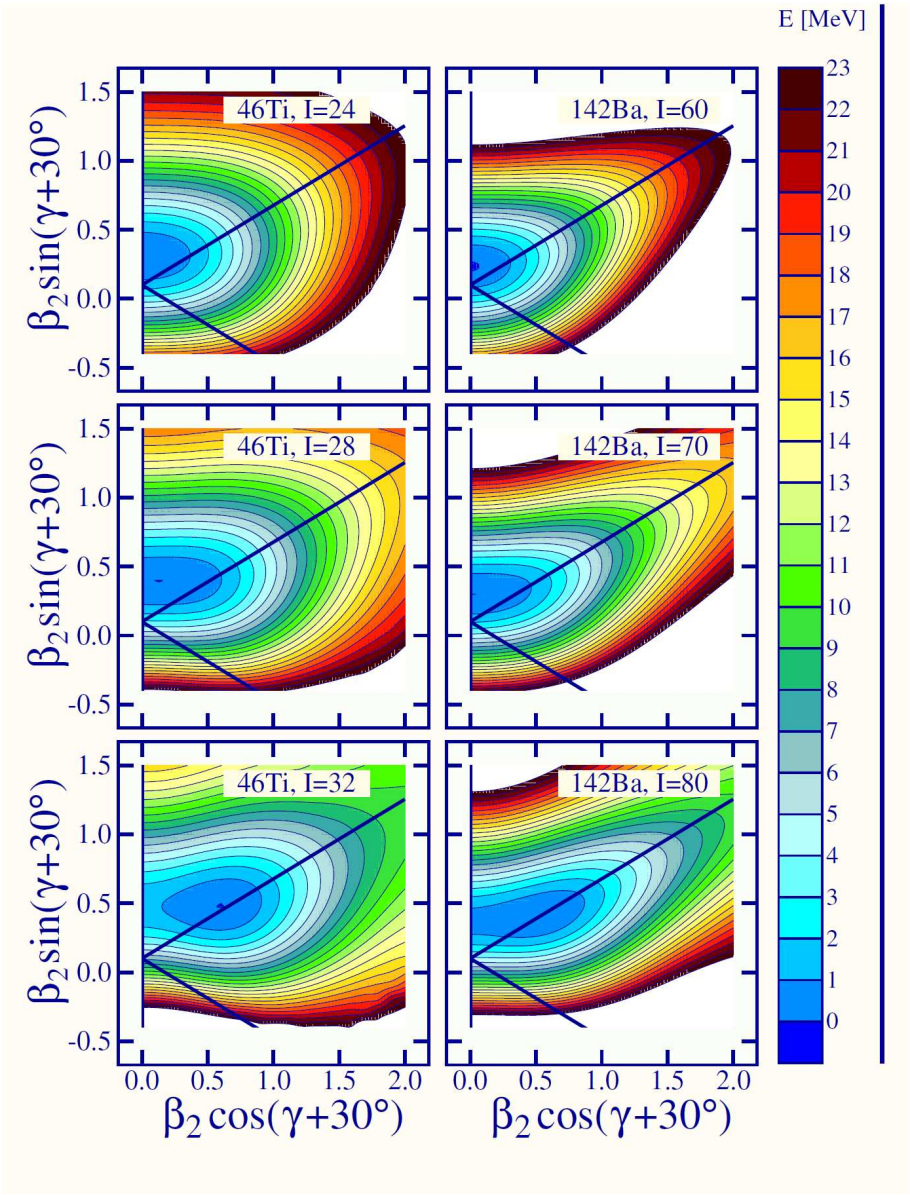

Figure 4.2: "Total energy $\{\beta, \gamma\}$-plane projections for the nuclei indicated at spins along the Jacobi transitions. At each $\{\beta, \gamma\}$-point the energy was minimized over the even-λ deformations α_{λ_0} for $\lambda \leq 16$." From Ref. [107].

the Yrast line is parametrized with deformability parameters δ_1 and δ_2:

$$E_J = \frac{\hbar^2 J\,(J+1)}{2\Im_{eff}} \tag{4.2}$$

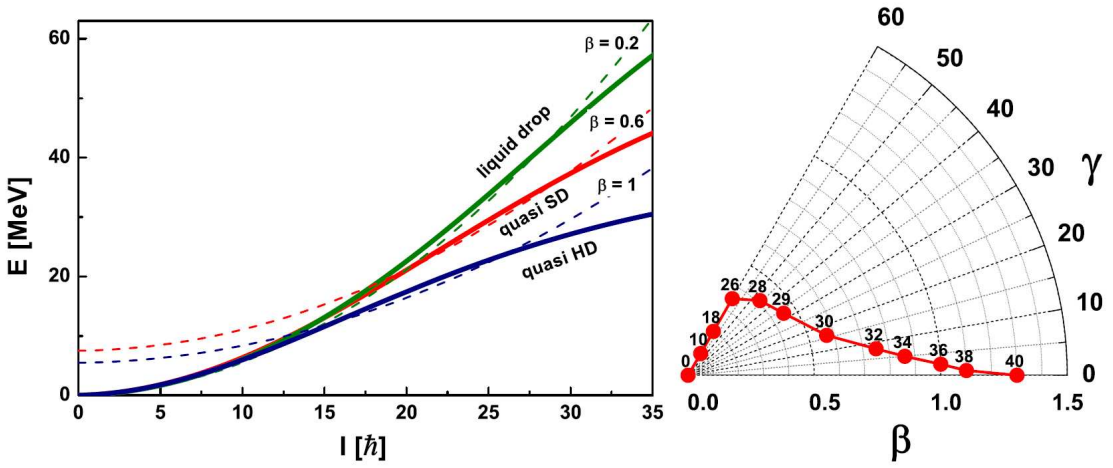

Figure 4.3: "Left: the yrast line used in the calculations(solid line) and the rigid body yrast line with different deformation parameters (dotted lines). Right: the evolution of the equilibrium shape of the ^{46}Ti as a function of spin predicted by LSD mpdel." From Ref. [108]

with the effective moment of inertia: $\Im_{eff} = \Im_{sphere}\left(1 + \delta_1 J^2 + \delta_2 J^4\right)$, where $\Im_{sphere} = \frac{2}{5}A^{\frac{5}{3}}r_0^2$ is the rigid body moment of inertia of the spherical nucleus and r_0 is the radius parameter (set $r_0 = 1.3$ fm).

The left panel of the Fig. 4.3 taken from the work of M. Brekiesz *et al.* [108] shows the Yrast lines obtained as a result of calculations performed using the statistical decay code CACARIZO. The green solid line (labeled "liquid drop") represents the standard RLDM (rotating liquid drop model) Yrast line generate by CACARIZO code and can be approximated by the rigid body Yrast line with small deformation parameter ($\beta = 0.2$), this parametrization does not reproduce well the α-particle spectra and angular correlations. The red solid line (labeled "quasi-SD" - quasi-superdeformed) represents the Yrast line obtained with the deformability parameters: $\delta_1 = 4,7 \times 10^{-4}$ and $\delta_2 = 1,0 \times 10^{-7}$. This Yrast line corresponds to the spin region $J = 15 \div 30\ \hbar$ for the Yrast line of the rigid body with deformation parameter $\beta = 0.6$; in the referred work, the calculations with this parametrization reasonably reproduce the experimental spectra for $Z = 18$ and $Z = 19$, while the spectra associated with $Z = 20$, related to the emission of a single α-particle, still deviate significatively from the model results. The blue solid line (labeled "quasi-HD"

- quasi-hyperdeformed) represents the Yrast line for the rigid body with a deformation parameter $\beta = 1$ fo spin $J = 15 \div 30\ \hbar$ and it is generated with CACARIZO deformability parameters: $\delta_1 = 1,1 \times 10^{-3}$ and $\delta_2 = 1,0 \times 10^{-7}$; the simulated α-particle energy spectra with this last parametrization permit to better reproduce the $Z = 20$ α-spectra and angular correlations. More details are reported in Refs. [108, 113, 109]. In particular, in Ref. [108] a possible explanation, related to the time scale of the evaporation process, is given: when many particles are evaporated, the time needed for this process is long enough to permit a change of residual nucleus shape to smaller deformation, thereby the effective level density of final states can be described by the "quasi-superdeformed" Yrast line; in contrast, when only one α-particle is emitted (like in the case of Z = 20), it is possible that the residual

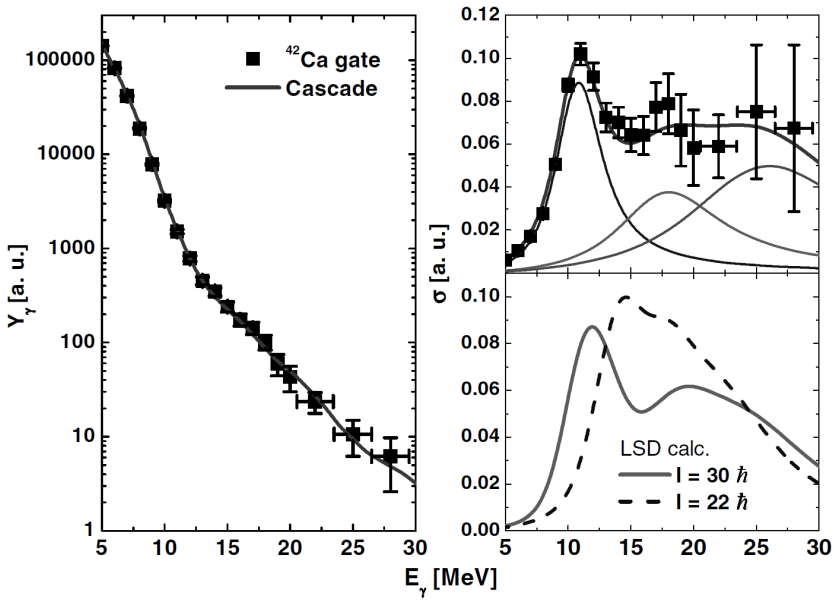

Figure 4.4: "Left: Energy spectrum of the γ-rays from the decay of the GDR built on hot ^{46}Ti compound nucleus in coincidence with the discrete transitions on the residual ^{42}Ca nucleus, together with the CASCADE calculations, which were performed assuming 3-Lorentzian GDR strength functions with E_{GDR} = 10.8, 18, 26 MeV. Upper right: experimentally obtained GDR absorption cross-section and the GDR strength function used in CASCADE calculations. Bottom right: thermal shape fluctuation predictions based on potential energies from the LSD model calculations for $I = 22\hbar$ and for $I = 30\hbar$." From Ref. [106]

nucleus is still in the process of changing shape and the Yrast line can be a halfway between a "quasi-hyperdeformed" and a "quasi-superdeformed" Yrast line. Such an effect can be understood as an existence of a "dynamical hyperdeformation".

Experimentally, the Jacobi shapes of nuclei should manifest by influencing and modifying the observables in which the moment of inertia is involved: γ-decay of the giant dipole resonance (GDR) [106, 108, 109, 110, 111, 112], as reported in Fig. 4.4; giant back-bending of the E2 γ-transition energies [104, 114, 115]; angular distribution of the emitted particles [108, 113]. The signature for Jacobi shapes in ^{46}Ti would be a pronounced high energy bump at $E_\gamma = 25MeV$ in the strength function of the GDR together with a rather large anisotropy of the γ-rays de-exciting the GDR.

The energy spectrum of the γ-rays emitted from the decay of the GDR built on hot ^{46}Ti compound nucleus is reported in Fig. 4.4, when a selection is performed on discrete transitions of the residual ^{42}Ca nucleus. Experimental data have been compared to CASCADE simulations assuming 3-Lorentzian GDR strength functions with E_{GDR} = 10.8, 18., 26. MeV respectively. The energy spectrum shape is reasonably in agreement with experimental data and with the predicted energy spectrum shape obtained by LSD model calculation in which thermal shape fluctuation are considered.

4.2 The $GEMINI^{++}$ deformation parameter selection

In order to reproduce the correct Yrast line for the quasi-superdeformed ^{46}Ti in the present thesis work, the $GEMINI^{++}$ parameter related to the deformation dependent on the angular momentum J_* (Section 3.1) has been modified and the produced simulated data have been analyzed.

In $GEMINI^{++}$, the Yrast line is described using the Sierk calculations (Eq. (3.7)) as reported in Section 3.1; but, it is also possible describing the Yrast line with the RLDM. The best agreement between the Yrast line produced by $GEMINI^{++}$ and the *quasi-superdeformed* Yrast line by A. Maj and collaborators is reached imposing the Sierk calculation for the Yrast line, as shown in Fig. 4.5. In this figure the rotational-plus-deformation energies *vs.* nuclear angular momentum for the excited ^{46}Ti are presented: the red line

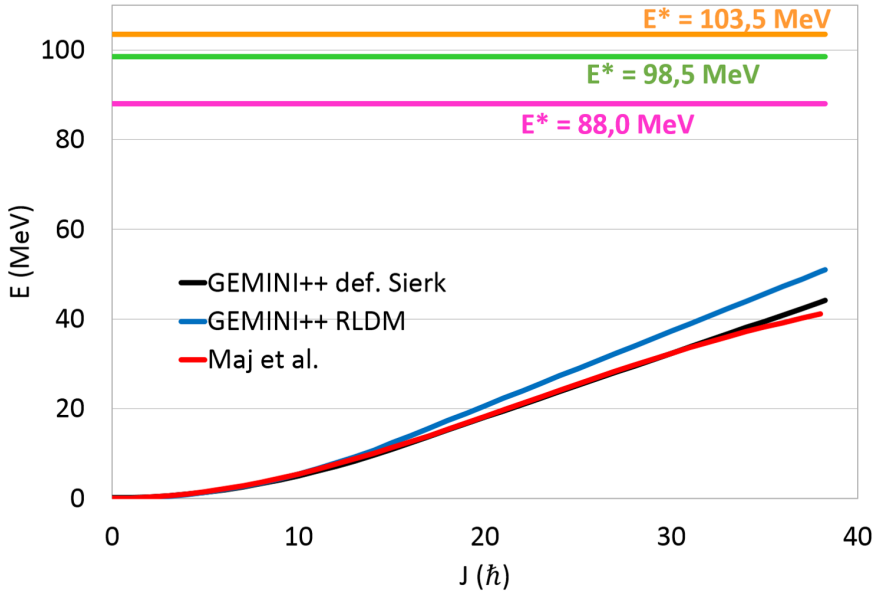

Figure 4.5: Rotational-plus-deformation energies *vs.* nuclear angular momentum for the ^{46}Ti. The red line is the "quasi-superdeformed" Yrast line from Refs. [104] ÷ [115]; the black is the Yrast line produced by $GEMINI^{++}$ with Sierk calculations and imposing the deformation; finally, the blue line is the $GEMINI^{++}$ RLDM Yrast line imposing the deformation. The upper line are the excitation energies of the ^{46}Ti compound nuclei formed by the different reactions. See text for more details.

is the *quasi-superdeformed* Yrast line from Refs. [104] ÷ [115]; the black is the Yrast line produced by $GEMINI^{++}$ with Sierk calculations and imposing the deformation; finally, the blue line is the $GEMINI^{++}$ RLDM Yrast line imposing the deformation. The upper lines are the excitation energies of the ^{46}Ti compound nuclei formed by the different reactions: $^{16}O +^{30} Si$ at 111 MeV forms a compound nucleus at $E^* = 88,0$ MeV (pink line); $^{16}O +^{30} Si$ at 128 MeV forms a compound nucleus at $E^* = 98,4$ MeV and $^{18}O +^{28} Si$ at 126 MeV forms a compound nucleus at $E^* = 98,5$ MeV, the two line are superimposed in only one (green line); $^{19}F +^{27} Al$ at 133 MeV forms a compound nucleus at $E^* = 103,5$ MeV (orange line). The excitation energy of the compound nucleus is given by the formula:

$$E^*_{CN} = U + E_{rot} \tag{4.3}$$

where $U = aT^2$ is the internal thermal energy and E_{rot} is the rotational energy.

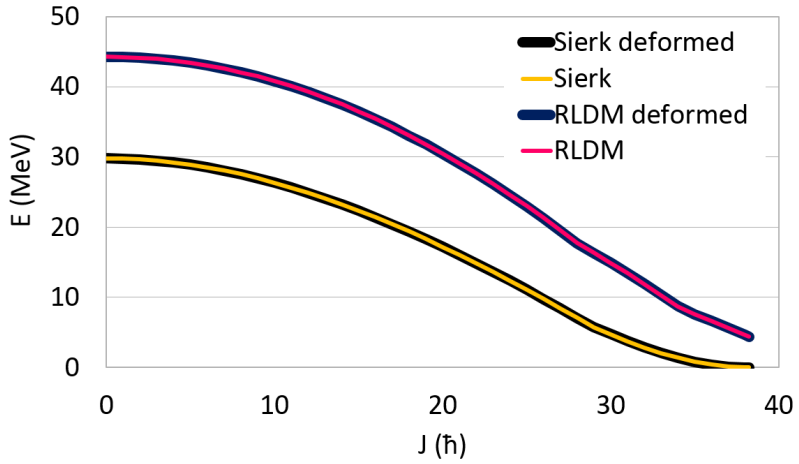

Figure 4.6: Fission barrier as a function of angular momentum: the fission barrier simulated by $GEMINI^{++}$ with Sierk calculations with (blue) and without (orange) deformation; the fission barrier produced with $GEMINI^{++}$ with RLDM with (black) and without (pink) deformation.

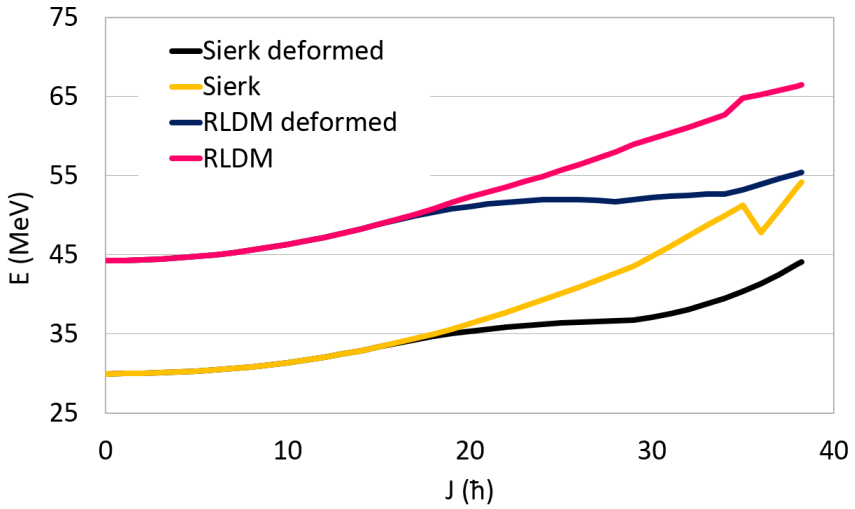

Figure 4.7: Saddle point energy for symmetric fission as a function of angular momentum: for $GEMINI^{++}$ simulations with Sierk calculations with (blue) and without (orange) deformation; for $GEMINI^{++}$ simulations with RLDM with (black) and without (pink) deformation. $E_{saddle} = E_{rot} + E_{F.B.}$.

As an example, in the following figures some of the observables related to the fission competition are reported for the two used parametrization (either RLDM or Sierk), especially in relation to the introduced deformation parameter, which influence the Yrast lines. In Fig. 4.6, the $GEMINI^{++}$ simulated fission barriers as a function of angular momentum are illustrated for the calculations based on the RLDM and on the Sierk model. Essentially no differences are observed for fission barrier whether it is used a deformed or not deformed Yrast line, as shown in the figure, while the two recipes are quite different from each other.

In Fig. 4.7, the saddle point energies for symmetric fission, as a function of angular momentum, are reported, simulated using $GEMINI^{++}$ respectively with RLDM with and without deformation and with the Sierk parametrization with and without deformation. In this case it is quite evident the difference in the saddle energy at a certain angular momentum, depending on the deformation and parametrization used for the Yrast line.

Chapter 5

The Data Selection

Besides the energy, mass, charge and angular resolution, a further feature to be taken into account when dealing with experimental apparatus is the efficiency. In particular, when a complex apparatus is used, the overall efficiency has to be considered, which connects all the involved combination of detectors working together.

In the case of neutral particles or gamma radiation, the detection efficiency is strongly related to the probability that an interaction takes place and the energy deposition is also determined in a probabilistic way according to the different involved interaction processes [55]. For light charged particles and fragments, on the contrary, what determines a loss in the efficiency is related to the energy threshold, which is the minimum energy that a particle should have in order to pass through dead layers of materials before reaching the active detector area and produce a signal distinguishable from the noise [55].

Moreover, a common feature that limit the overall efficiency for all kind of radiation is the limitation in the angular coverage: this also has to be appropriately taken into account when comparing experimental results to simulations made by codes based on theoretical models.

The efficiency of the experimental apparatus, related to the detectors energy thresholds and to the geometrical acceptance (angular range), is reflected in the so called global variables (E_{tot}, Z_{tot}, A_{tot} etc.) and in the distributions of other variables, which may result distorted by the lack of detection in specific angular regions. For example, a basic

global variable is the event charged particle multiplicity ($Molt$), which represents the number of charged particles emitted in each event. From the experimental point of view, this variable may be affected by the efficiency, which can distort its distribution especially due to the lack in angular coverage. Another example is the charge distribution of the reaction products (Z), which, unless any selection on the collected data is performed, is an inclusive variable and therefore gives only a qualitative information on the processes underlying the studied reactions. A good method to control the efficiency of the apparatus, and therefore, the quality of the collected data is building up global variables like the total collected charge in each event (Z_{tot}) or the total momentum (q_{tot}) and to use these variables to select different classes of more or less complete events. Since the Z_{tot} in each event is related to the initial charge involved in the system, that is $Z_{projectile} + Z_{target}$, only events in which the total amount of collected charge is $Z_{tot} = Z_{projectile} + Z_{target}$ can be classified as complete events. All the other events can be studied taking into account, when possible, the missing mass/charge to recover the initial partition.

As previously reported, another important example of global variable, that can be built, is the total momentum along the axis (q_z). Since it is correlated to the impact parameter, it can give information on the centrality of the collision: in the central collisions, q_z has values around the velocity of the center of mass of the system, while, in peripheral collisions, it is approximately close the velocity of the beam.

In order to compare all these variables and to draw any consideration on the collected experimental data, it is worth to compare them with models, which contain the physics underlying the processes. In fact, in the experimental data analysis, the simulation codes can be very powerful tools; in the comparison between experimental data and theoretical models, it is very important to define those experimental observables which may be significant in addressing the choice between different theoretical approaches. Divergences between experimental and simulated data may be evidenced and critically studied. To obtain simulations comparable with experimental data, a software replica of the set-up is prepared, which emulate the experimental detection conditions. This is needed to filter the simulated data in the same way of the experimental ones. The effects of such filtering

phase, in the case of the present analysis, are reported in Section 5.1. Moreover, some further selections on the experimental data (and therefore also on the simulated one) are required in order to clean up the final set of events which will be finally analyzed, as it will be explained in Section 5.2.

5.1 A software replica of the GARFIELD+RCo setup

A software replica ("Classe_GEO") of the GARFIELD+RCo experimental array is used to filter $GEMINI^{++}$, $AMD + GEMINI^{++}$ and $HIPSE + GEMINI^{++}$ simulations. This tool reproduces the experimental detection conditions starting from the features of the experimental array, such as the geometry, the solid angle, the energy thresholds and energy resolution for each detector of GARFIELD+RCo and the gas pressure set in the ionization chambers. The energy thresholds and resolutions imposed into the geometry code, are those evaluated from calibration and energy loss calculations, taking into account the real geometry of the set-up, considering all the crossing steps in the different stadium of the telescopes; in the case of the ionization and drift chambers, any change of pressure is obviously taken into account. Moreover, specific experimental circumstances can be included, such as malfunctioning, and therefore switching off of single detectors.

It is useful to present the comparisons between filtered and unfiltered simulations to keep under control the information on the specific cuts that the geometry introduces, in order to avoid erroneous conclusions and interpretations on experimental distributions, which might be due to fictitious distortions determined by incomplete geometries.

5.1.1 Effects of the Apparatus Filter on the Simulations

The effects of the geometrical filter applied on simulations are hereafter shown. In particular in Fig. 5.1 the comparison between experimental data and $GEMINI^{++}$ simulation is shown for the reaction ^{16}O+^{30}Si at 111 MeV, where the geometrical coverage of the apparatus is shown in the polar plot of particles identified both in the whole apparatus (GARFIELD +RCo) and zooming only the RCo. As it can be observed from an inclusive point of view, the filtering of the simulated data is working properly. Similar plots are

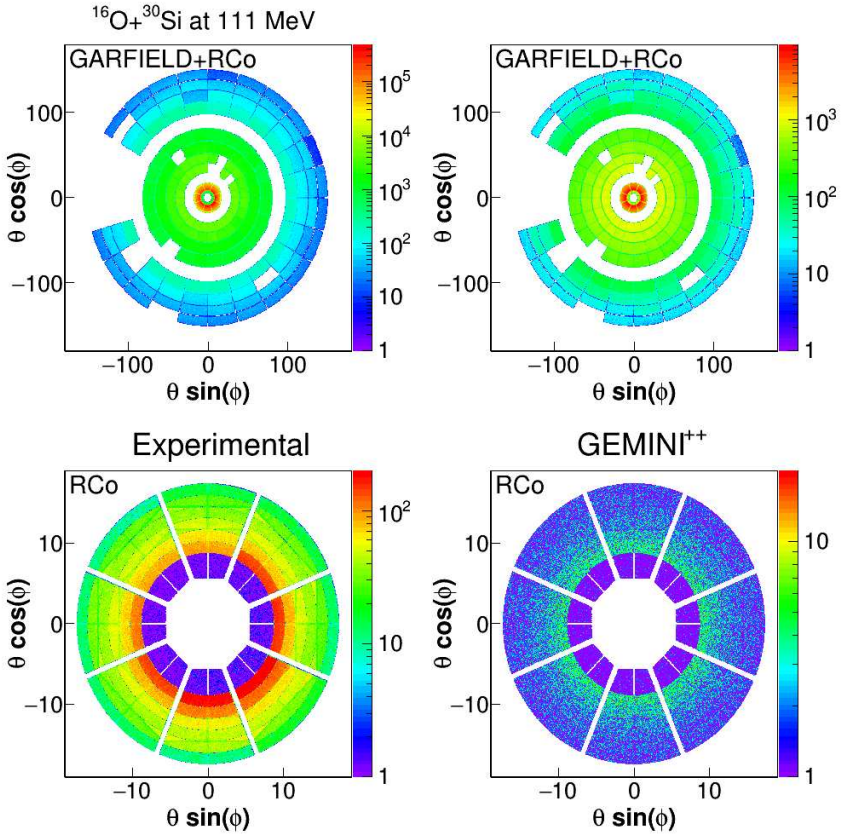

Figure 5.1: Polar plot of particles identified in the whole apparatus (upper panels) and only in the RCo (lower panels) for the experimental data (left panels) and for $GEMINI^{++}$ (right panels) for the reaction $^{16}O+^{30}Si$ at 111 MeV.

obtained for all the other studied reactions and for all the other simulation codes.

In Fig. 5.2, the Z-distribution simulated by $GEMINI^{++}$ for the same reaction is presented, as an example: the distribution drawn with the continuous red line represents the filtered simulated data while the continuous blue line represents the original distribution, without any filter; it is obvious that the setup filter produces a decrease in the detected yields, even though almost no visible distortion is present in the spectrum. It has to be noted that, of course, what are completely missing are neutrons ($Z = 0$ in the codes), which are present in the blue distribution, but not detected in our experimental apparatus. The U-shape of Z-distributions is due to the evaporation-decay of the compound nucleus, in

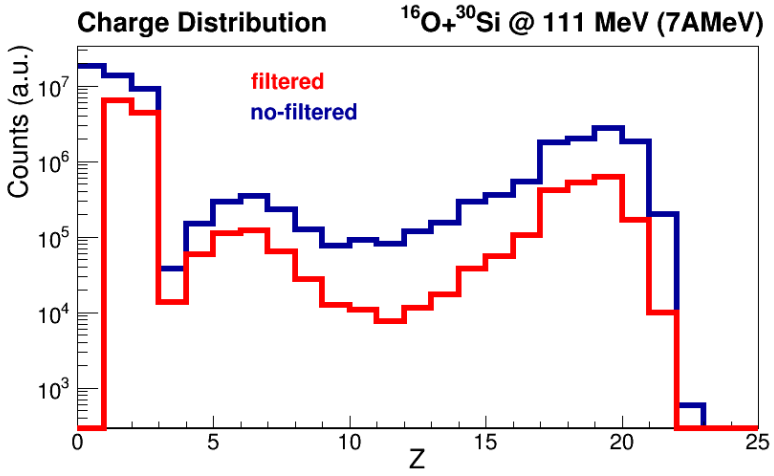

Figure 5.2: Effects on the simulated Z-distribution of the geometrical filter, emulating the GARFIELD+RCo setup experimental conditions, applied on the predictions of $GEMINI^{++}$ code for the reaction $^{16}O+^{30}Si$ at 111 MeV; in blue the 4π simulation and in red the filtered one.

which light evaporated particles with small Z ($1 \div 3$) and the corresponding residue with large Z ($14 \div 22$) are produced; while, the bump in the charge region $Z = 4 \div 8$, related to the tail of the residues bump ($12 \div 14$), is the consequences of the fusion-fission process. The simulated Z-distributions of the other reactions have a similar behavior. The inclusive experimental distribution is quite different from the $GEMINI^{++}$ simulated results, since experimentally we are dealing with different reaction mechanisms concurring to the total yield. Therefore, only after a careful selection of the central collisions a comparison will be meaningful.

Again, as an example, the effect of the experimental conditions on the residue distribution simulated by $GEMINI^{++}$ is shown for the four reactions: in Fig. 5.3 the scatter plots of the laboratory energy of the residues *versus* their laboratory emission angle are shown for the four studied reactions. In the Figure, on the left panels, the original distributions are plotted, while, in the right panels, the distribution detected in the RCo are displayed (from top to bottom panels): $^{16}O+^{30}Si$ at 111 MeV, $^{16}O+^{30}Si$ at 128 MeV, $^{18}O+^{28}Si$ at 126 MeV and $^{19}F+^{27}Al$ at 133 MeV. When the $GEMINI^{++}$ simulated events are filtered,

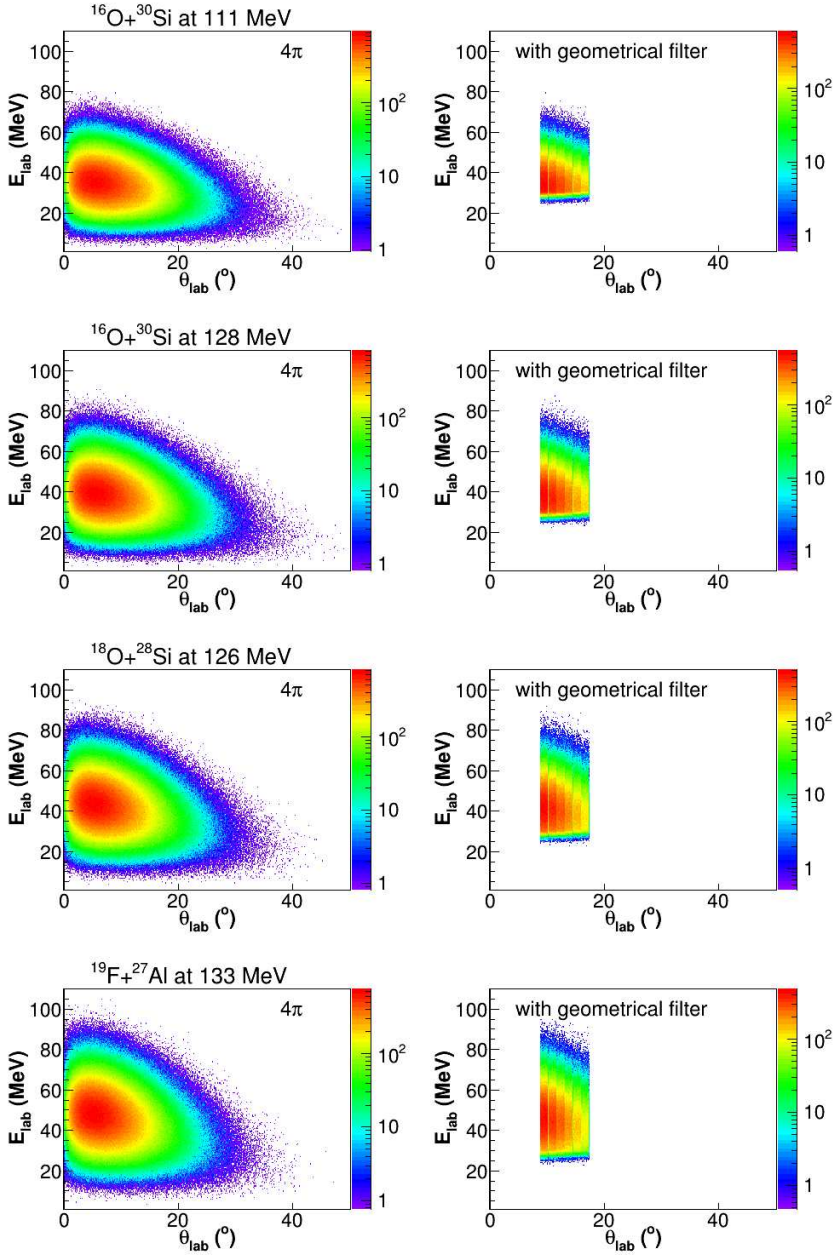

Figure 5.3: Two-dimensional plots of residues laboratory energy *vs.* their laboratory emission angle as predicted by $GEMINI^{++}$ code with (right panels) and without (left panels) geometrical filter. From top to bottom panels, the four reactions $^{16}O+^{30}Si$ at 111 MeV, $^{16}O+^{30}Si$ at 128 MeV, $^{18}O+^{28}Si$ at 126 MeV and $^{19}F+^{27}Al$ at 133 MeV.

the residues angular distributions are limited in the angular range covered by the RCo ($5^o \div 17.4^o$), while the energy threshold for residue is $E_t^{res} \sim 25$ MeV (that is $\sim 0.6 \div 0.8$ MeV/u) due to the fact that to be identified the residues have to cross the ionization chamber and arrive at least in Silicon detector. It is however clear that, even though the geometrical cut is large, the peak of the cross section is within the detection region (red part in the plot) especially for what concerns the energy distribution. Even though the RCo could have been used at forward angles (down to 5^o), it was decided to allow the detection only beyond the grazing angles to avoid the high counting rate deriving from elastic scattering, which would have affected all the measurements (as previously described).

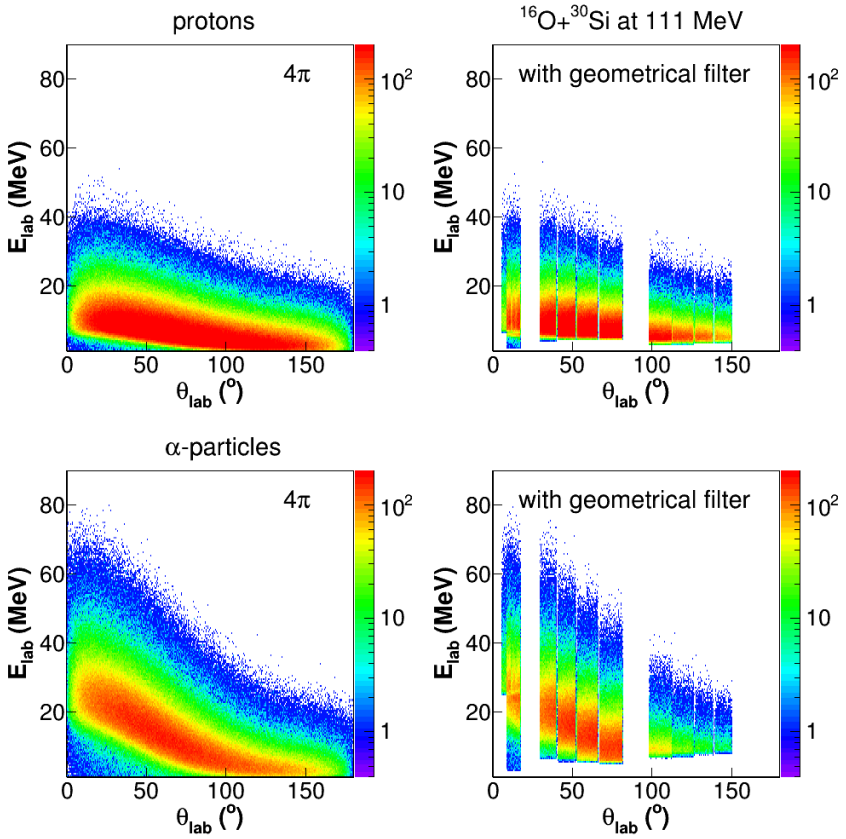

Figure 5.4: Two-dimensional plots of protons (upper panels) and α-particles (lower panels) laboratory energy *vs.* their laboratory emission angle as predicted by $GEMINI^{++}$ code with (right panels) and without (left panels) geometrical filter for the reaction $^{16}O+^{30}Si$ at 111 MeV.

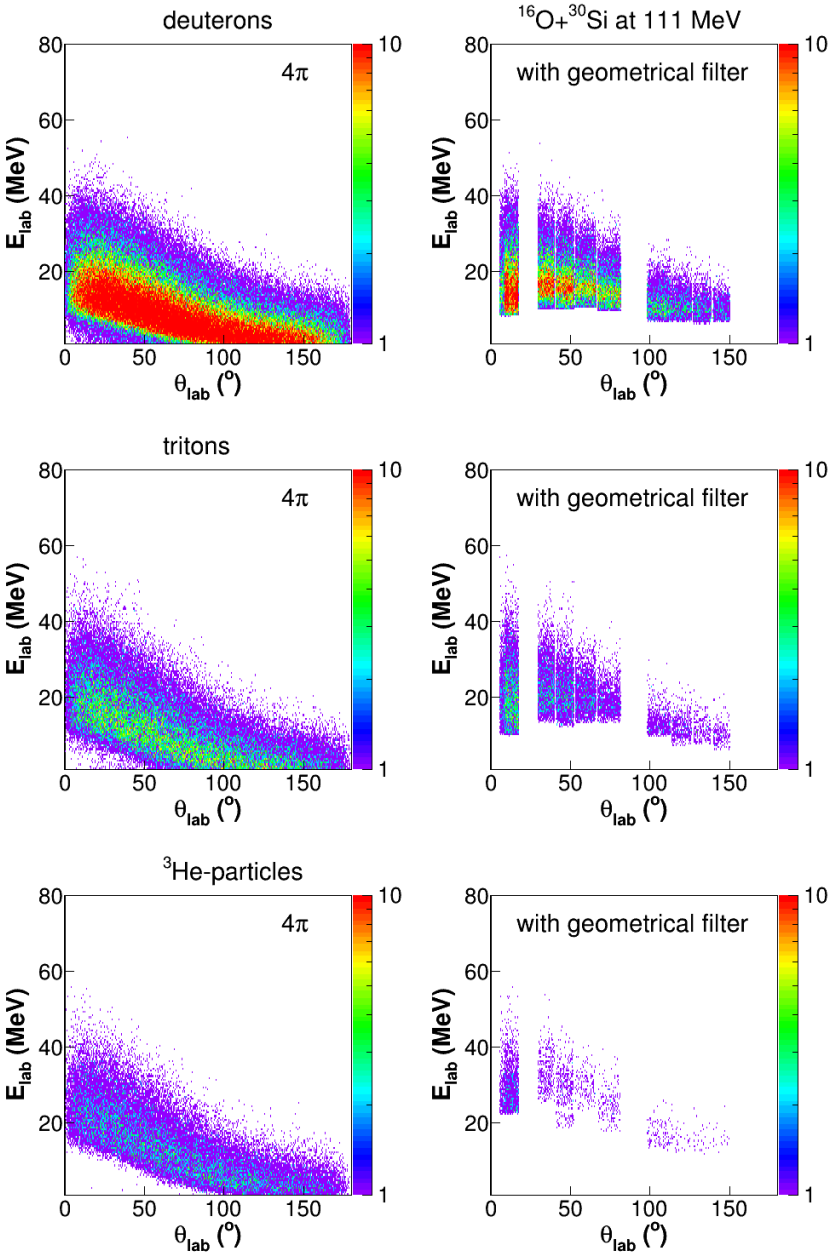

Figure 5.5: Two-dimensional plots of deuteron (upper panels), triton (medium panels) and ^3He (lower panels) laboratory energy *vs.* their laboratory emission angle as predicted by $GEMINI^{++}$ code with (right panels) and without (left panels) geometrical filter for the reaction $^{16}O+^{30}Si$ at 111 MeV.

In Figs. 5.4 and 5.5, the two-dimensional plots of light charged particles laboratory energy *versus* their laboratory emission angle as predicted by $GEMINI^{++}$ code are shown for the reaction $^{16}O+^{30}Si$ at 111 MeV: protons (upper panels) and α-particles (lower panels) are presented in Fig. 5.4, while deuterons (upper panels), tritons (medium panels) and ^{3}He-particles (lower panels) in Fig. 5.5: for both figures, the left panels show the 4π-simulation and the right panels the filtered simulation. The evaporated light charged particles are detected both in GARFIELD and in the RCo arrays: almost no cut in the energy distribution is observed for light charged particles detected in the RCo, while the filter start having a role in the GARFIELD array especially in the backward detector. The main losses of their yields are due to the angular dead zone in the detection arrays, namely the areas not covered by detectors ($\theta < 5.0^{o}; 17.4^{o} \div 29.5^{o}; 82.5^{o} \div 97.5^{o}; > 150.4^{o}$). As expected, for all light particles, the maximum of the distribution is shifted towards forward angles due to the center of mass motion.

As one can see, the detection thresholds for deuterons, tritons and ^{3}He are much higher than for α-particles and protons. This is due to the fact that, experimentally, only over these thresholds they are undoubtedly identified. See for major details the paragraph 2.2 on calibration procedure.

Due to the previously shown cuts in the energy and angular distributions of both residues and light charged particles, it is obvious to observe that also particle multiplicities are affected by the filtering and their distributions may be distorted somehow. Geometrical filter effects on the multiplicities are illustrated in Fig. 5.6 for the different particles produced in the reaction $^{16}O+^{30}Si$ at 111 MeV: (a) evaporation residues; (b) protons; (c) α-particles; (d) deuterons; (e) tritons; (f) ^{3}He-particles. The blue lines represent the 4π-simulations produced by $GEMINI^{++}$ and the red lines represent the $GEMINI^{++}$ predictions filtered by the software replica of the experimental array. Of course, in the filtered case, the multiplicity plots are affected by incompleteness of the detected event, which lowers the total yields. Moreover, we can somehow have a control on the simulated filtered events on how and how many mixed-up events may contribute to the selected yields (typically in the $GEMINI^{++}$ case fission and evaporation events might not be

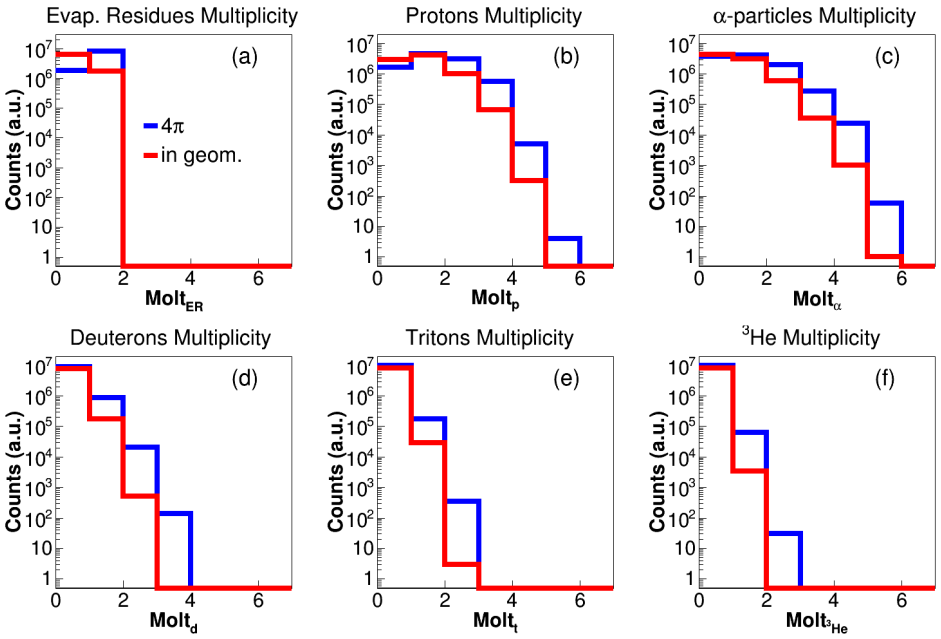

Figure 5.6: Comparison of filtered (red line) and no-filtered (blue line) simulated multiplicity for residues (a) and light charged particles (b÷f) for the reaction $^{16}O+^{30}Si$ at 111 MeV generated by $GEMINI^{++}$. No normalization is introduced: relative yields differences are coming only by the filtering process.

disentangled, when only one fragment is detected): this can help to analyze and clean up, when possible, experimental data where no tag is present on the different de-excitation mechanisms. This fact may be even more effective when using the dynamical codes $HIPSE$ and AMD, which simulate, in a similar way than experimentally, and mix up even events deriving from peripheral and semi-peripheral collisions to the selected events. This will be discussed more in detail in the following chapters on the specific analysis of the selected data.

All these comparisons of filtered and non-filtered simulated events underline the importance of the detailed controls of the experimental conditions which must be monitored during the experimental runs and stress how essential is the role played by the filter. Moreover, as it will be shown in the following, going to more exclusive data, filtering may be even more effective in determining either variation or distortion of the final distributions.

Therefore, it is undoubted necessary to take all this into account every time we discuss the comparisons with experimental data. In fact, for this reason we applied all the constraints applied to our data to the simulated data: due to the high reduction of simulated data due to filtering, simulations had to be run on a huge number of initial events, which reflected in very long cpu time especially for the dynamical models.

5.2 Events Selection

The experimental detected particles and fragments are produced by different reaction mechanisms: in the case of peripheral and semi-peripheral collisions, elastic and quasi-elastic scattering or deep inelastic collisions occur; instead, in the case of central collisions, the formation of a complete or incomplete compound nucleus are the main open channels, with different excitation energies and angular momenta of the produced excited sources. After the formation of the compound nucleus, it decays through the competition between two modes: either the evaporation of light particles or the fission, as previously described in the scientific introduction. In general, the final open channels can be characterized by analyzing and studying some specific correlations between the detected particle observables.

In Fig. 5.7, the inclusive experimental correlation plots between the charge (Z) and the laboratory energy (E_{lab}) of the detected particles (left panels) and between the total charge (Z_{tot}) and the longitudinal momentum (q_z/q_{beam}) of each event (right panels) are shown for the four reactions ^{16}O+^{30}Si at 111 MeV, ^{16}O+^{30}Si at 128 MeV, ^{18}O+^{28}Si at 126 MeV and ^{19}F+^{27}Al at 133 MeV. In those plots the different reaction mechanisms can be distinguished by comparison with similar plots produced via simulation codes: as an example, in Fig. 5.8, the Z *vs.* E_{lab} plot (left panels) and the Z_{tot} *vs.* q_z/q_{beam} plot (right panels) are displayed for one of the four reactions (^{16}O+^{30}Si at 111 MeV), simulated by different codes: $GEMINI^{++}$ (upper panels), $AMD + GEMINI^{++}$ (central panels) and $HIPSE + GEMINI^{++}$ (lower panels). Since results for the other three reactions are very similar, we do not think it is worth to show them here.

The elastic scattering, which can be only simulated by $AMD + GEMINI^{++}$ (middle panels in Fig. 5.8), is clearly evident in both inclusive experimental plots of Fig. 5.7 for the

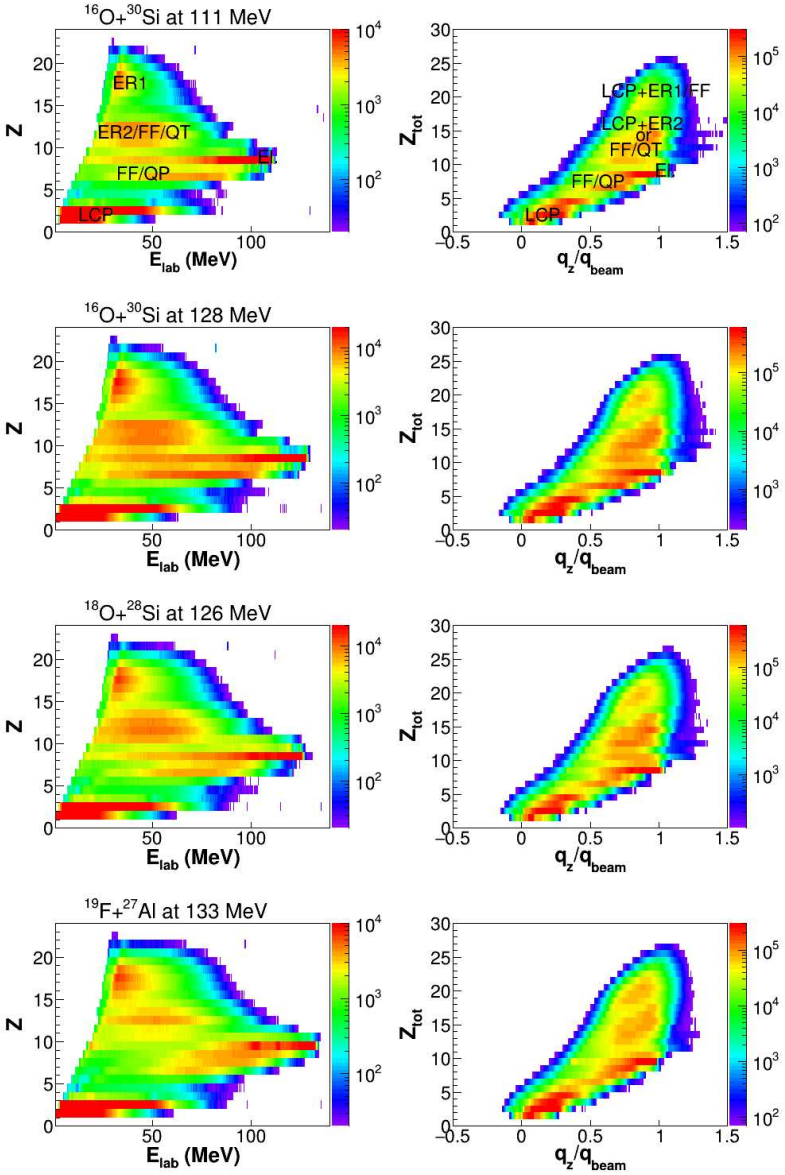

Figure 5.7: Two-dimensional inclusive experimental plots for correlation between charge (Z) and laboratory energy (E_{lab}) of the detected particles (left panel) and between total charge (Z_{tot}) and relative longitudinal momentum (q_z/q_{beam}) of each event (right panel) for the four reactions $^{16}O+^{30}Si$ at 111 MeV, $^{16}O+^{30}Si$ at 128 MeV, $^{18}O+^{28}Si$ at 126 MeV and $^{19}F+^{27}Al$ at 133 MeV. See text for details.

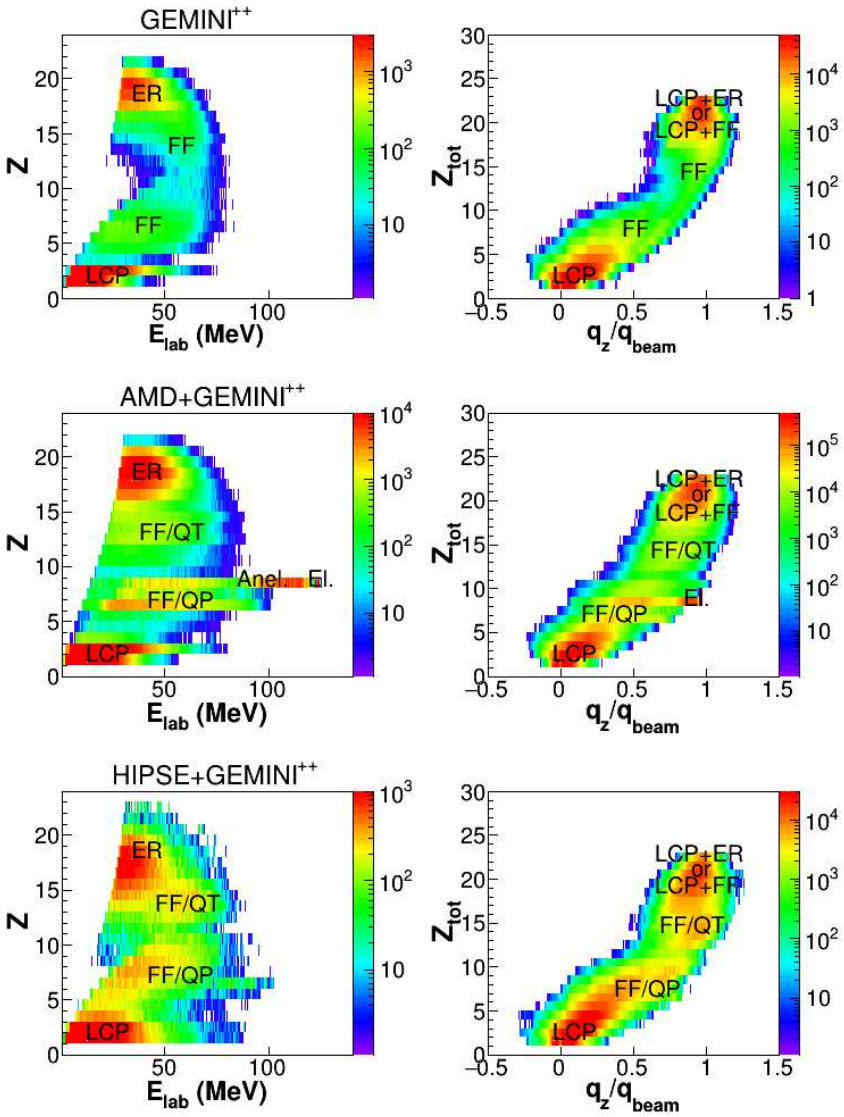

Figure 5.8: Two-dimensional simulated inclusive plots: Z *vs.* E_{lab} (left panels) and Z_{tot} *vs.* q_z/q_{beam} (right panel) for the reaction ^{16}O+^{30}Si at 111 MeV. The simulations are generated by: $GEMINI^{++}$ (upper panels), AMD+$GEMINI^{++}$ (medium panels) and HIPSE+SIMON (lower panels).

three O-beam induced reactions at $Z = 8$ (in left panels) and at $Z_{tot} = 8$ (in right panels), while obviously, for the reaction induced by ^{19}F at $Z = 9$ and at $Z_{tot} = 9$. Z_{tot} is obviously equal to the Z_{proj} in case of elastic and inelastic scattering, since in fact, coincident target nuclei are not detected due to their very low energy.

The compound nucleus formation-decay channel (*e.g.* $^{16}O +^{30} Si \rightarrow^{46} Ti^*$) generates light charged particles (visible in charge-region $Z = 1 \div 3$ in the Z *vs.* E_{lab} plots of the Fig. 5.7 and labeled "LCP") in coincidence with evaporation residues ($Z = 14 \div 22$), labeled "ER1", or in coincidence with fission fragments ($Z = 4 \div 18$); in the total charge *versus* longitudinal momentum plots (right panels), this channel fills the Z_{tot}-region between 15 and 25 with a longitudinal momentum around 1 (actually it is slightly less, ~ 0.7, due to the fact that in the total energy/momentum reconstruction the energy/momentum of emitted neutrons, which are not detected, are lost).

The deep inelastic collisions, described by both dynamical codes ($AMD{+}GEMINI^{++}$ and $HIPSE + GEMINI^{++}$), are placed in the charge-region and in total-charge-region immediately around the projectile or target position in the plots. The quasi-projectile (QP) is well visible in both the correlation plots: $Z \sim 6 \div 9$, in the charge-energy correlation plots, and $Z_{tot} \sim 6 \div 9$ with $q_z/q_{beam} \sim 0.5 \div 0.8$, in the Z_{tot} *vs.* q_z/q_{beam} plots depending either if it is detected in coincidence with its partner for less dissipative collisions or alone, when the partner is too low in energy or it has been lost for angular reasons. On the contrary, the quasi-target (QT) is not well distinguishable in the experimental plots, while it has a recognizable bump in the dynamical simulation data, especially evident in the $HIPSE$ results. As it will be explained in the following, this is due to the fact that these events are almost completely hidden in the experimental case: in fact, a large cross section due to the fusion reaction on a huge O-contamination in the target is present in the experimental data. We call these events "ER2" in the plot. These "contaminant" reactions ($^{16}O + O$, $^{18}O + O$ and $^{19}F + O$) fill the charge region $Z = 11 \div 16$ in Z vs. E_{lab} plots and the total charge region $Z_{tot} = 11 \div 17$ with $q_z/q_{beam} \sim 1$ in Z_{tot} vs. q_z/q_{beam} plots. More details about this specific events and how to get rid of them will be given in the following paragraph.

5.2.1 Target Contamination

In order to define quantitatively the amount of contaminants, a dedicated measurement was performed on the targets with RBS technique [100, 101], at the LNL AN-2000 accelerator: a ratio of about 1 was measured for the O with respect to both ^{30}Si and ^{28}Si targets, while a ratio of 0.5 was found in the ^{27}Al target. Strong effects of such contamination in the α-particles emission spectra have been observed, which brought to a preliminary wrong interpretation of the experimental data [102].

At first, in order to check whether the observed anomalous huge yield was coming from the contaminant reaction, they were simulated with $GEMINI^{++}$ to observe where the polluted "ER2" would have been positioned in our plots. This first check was meant to previously analyze the part related to the statistical decay of the excited source.

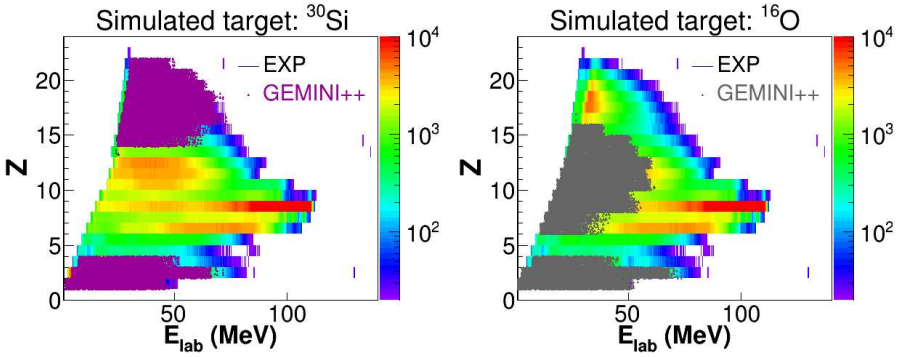

Figure 5.9: Two-dimensional simulated inclusive plots of charge (Z) *vs.* laboratory energy (E_{lab}) correlations superimposed on the analogue experimental plot. The experimental plot is the same in both panels and is the colored one; $GEMINI^{++}$ simulates the reaction $^{16}O+^{30}Si$ (purple dots in left panel) and the reaction $^{16}O+^{16}O$ (gray dots in right panel)

In particular, we show as an example the calculation performed for the 111 MeV ^{16}O case on the two targets ^{30}Si and ^{16}O respectively. The contaminant reactions were simulated in both cases using the $GEMINI^{++}$ code, in only fusion-evaporation mode. In Fig. 5.9, the simulated plots of charge *versus* laboratory energy are separately superimposed on the analogue single experimental plot, in which obviously the effects of the two reactions are mixed. In the left panel, the Z *vs.* E_{lab} of $GEMINI^{++}$ simulation for the

reaction $^{16}O + ^{30}Si$ is presented: the residue bump, located at $Z = 14 \div 22$, well matches the experimental bump "ER1" (so labeled in left upper panel of Fig. 5.7). On the other hand, the "ER2" experimental bump is well overlapped by the $GEMINI^{++}$ simulated ($Z = 6 \div 16$) from the reaction $^{16}O + ^{16}O$, as shown in right panel. Those quite good reproduction of the experimental bumps confirm the previous idea that the "ER1" bump contains the residues produced by the reaction $^{16}O + ^{30}Si$, while, the "ER2" is the effect of the fusion-evaporation of the "contaminant" reaction $^{16}O + ^{16}O$. In both simulations the light charged particles ($Z = 1 \div 3$) are quite well reproduced confirming, however, that a strong effect on the light charged particles energy and yield is present due to contamination. Therefore, a specific and stringent selection has to be performed on the further data analysis, to get rid of this problem.

Furthermore, a second simulation was performed with the dynamical code $HIPSE$ followed by $SIMON$ [103] as afterburner in order to take into account also the other possible contamination deriving from more peripheral collisions. In Fig.5.10, the experimental plots (upper panels) of the correlations Z vs. E_{lab} (left panel) and Z_{tot} vs. q_z/q_{beam} (right panel) are compared with similar plots (lower panels) simulated by $HIPSE + SIMON$ code for the reaction induced by ^{16}O-beam at bombarding energy of 111 MeV on a compound target, composed for the 50% of ^{30}Si and for the 50% of ^{16}O. To reproduce the same condition of the experimental case, the mixed simulated data were treated in the following analysis as if they were produced only by a target of 100% of ^{30}Si. For cpu time reasons only few hundred thousand events were run on each system, with the only purpose of giving an overall view of the situation and to check if the further constraints that have been put on the experimental data could cut out the contamination in a proper way.

Comparing the experimental plots (upper panels) with the $HIPSE + SIMON$ simulated ones (lower panels), it can be observed that $HIPSE + SIMON$ code well reproduce the overall behavior. However, it seem that specifically looking to the relative yield between fusion and deep inelastic a different trend is shown with respect to the experiment. As we already observed previously, $HIPSE$ is not able to describe the elastic and at least partially the inelastic $Z = Z_p$ channels.

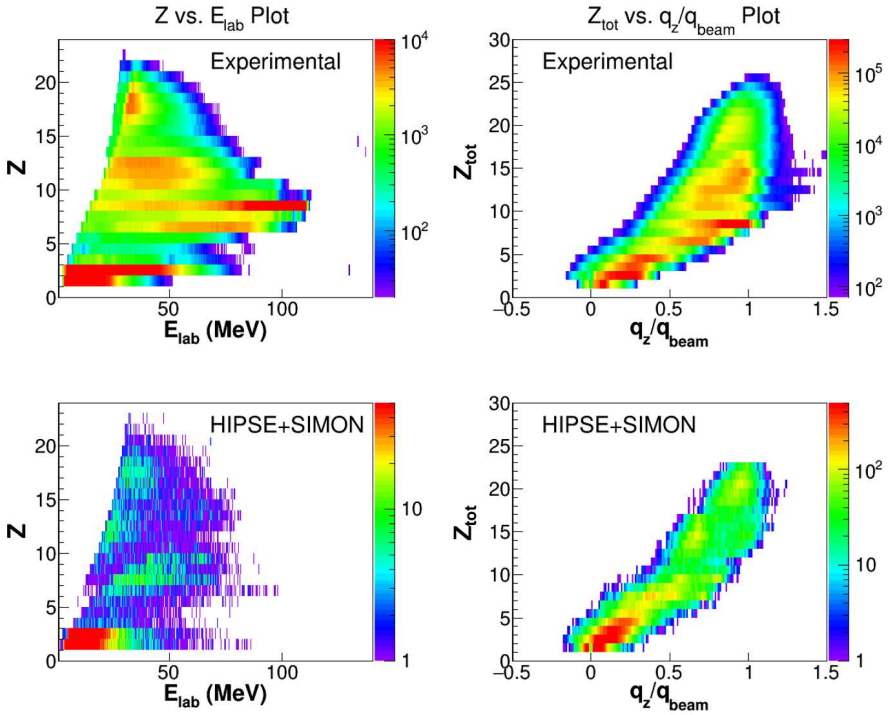

Figure 5.10: Experimental inclusive distributions (upper panels) and simulated with $HIPSE + SIMON$ (lower panels) for the reaction ^{16}O (at 111 MeV) + $(^{30}Si + O)$: on the left the event-by-event correlation between the charge (Z) *versus* the energy in the laboratory system (E_{lab}), on the right the plot of the Z_{tot} *versus* the longitudinal momentum ratio (q_z/q_{beam}).

Focusing on the "contamination" region where both "ER2" and deep inelastic from $^{16}O + ^{30}Si$ reaction are concentrated, (in the left panels: $Z \sim 10 \div 14$; in the right panels: $Z_{tot} \sim 12 \div 16$), it can be evidenced that, in the case of the $HIPSE+SIMON$ simulation, the "ER2" region is better separated from the region populated by deep inelastic collisions; in the experimental case, such regions are merged and a somehow major production of deep inelastic events with respect to simulation appear. The higher experimental yields of deep inelastic collisions can be even better highlighted in the total charge vs. longitudinal momentum plots and, in particular, looking at specific Z_{tot}, as shown in Fig. 5.11, where the experimental and $HIPSE + SIMON$ simulated normalized yields are compared as function of q_z/q_{beam} for $Z_{tot} = 12 \div 17$. In the $HIPSE + SIMON$ case (red line), for

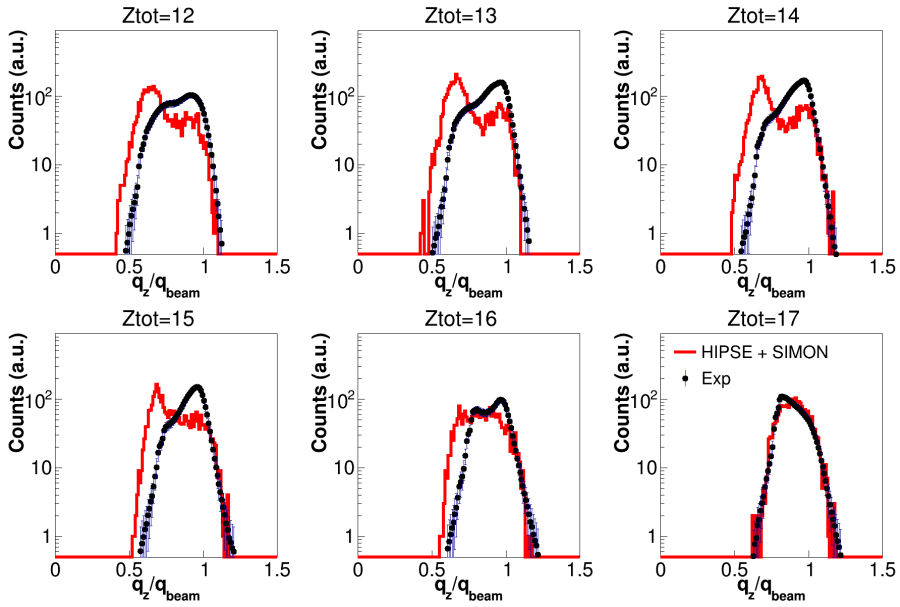

Figure 5.11: Comparison of normalized yields between experimental data (black dots) and HIPSE+SIMON simulation (red line) as function of q_z/q_{beam} for $Z_{tot} = 12 \div 17$ for the reaction ^{16}O (at 111 MeV) + $(^{30}Si + O)$.

$Z_{tot} = 12 \div 14$ the two peaks (the left peak is related to the fusion-evaporation of $^{16}O + O$; the right peak is related to the deep inelastic collision produced from the $^{16}O +^{30} Si$ reaction) are well distinguished; for $Z_{tot} = 16 \div 17$, the two peaks disappear leaving only one, which is only related to the $^{16}O +^{30} Si$ reaction. In the experimental case (black dots), for $Z_{tot} = 12 \div 15$, an opposite situation with respect to the simulation is observed for $Z_{tot} = 12 \div 14$: the right peak (deep inelastic collisions) is higher that the left one (fusion evaporation from $^{16}O + O$); for $Z_{tot} = 16$, the two peaks have a similar yield; finally, for $Z_{tot} = 17$, the same situation of $HIPSE + SIMON$ $Z_{tot} = 16 \div 17$ is found.

In summary, the experimental high contamination of the target is not easily separable from the other inclusive data and a careful selection has to be performed to clean up the desired events to be further analyzed, as it will be explained in the following paragraph. The situation is very similar for all the reactions. On the other hand, due to the superimposition between fusion $(^{16}O + O)$ and deep inelastic $(^{16}O +^{30} Si)$ mechanisms between the two reactions, it is not possible to study this "contaminant" reaction alone, even if it could

have been very interesting.

5.2.2 Complete Events Selection

After the cross-check previously described and performed on the mixing from the contaminants, which is affecting our experimental data, a very strict selection on experimental data was performed in order to select some specific exit channels and namely the central collisions where complete and incomplete fusion are expected. An almost complete event reconstruction has been required, which cut off the unwanted contamination: the considered events are those for which the total detected charge is larger than the 70% of the total charge $Z_p + Z_T$; to select such specific events a graphical contour was applied on the plot of correlation between total charge and longitudinal momentum as shown in Fig.5.12.

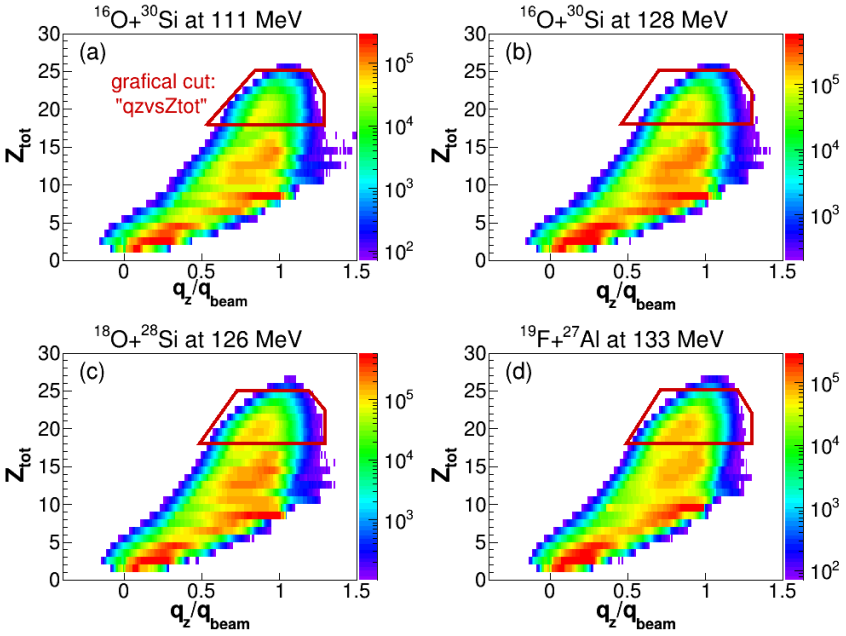

Figure 5.12: Total charge vs. longitudinal momentum plot with graphical cut (red lines) to select central events for the reactions: (a) $^{16}O + ^{30}Si$ at 111 MeV; (b) $^{16}O + ^{30}Si$ at 128 MeV; (c) $^{19}F + ^{27}Al$ at 133 MeV; (d) $^{18}O + ^{28}Si$ at 126 MeV.

The selected events (for all the four reactions) are those for which the total charge is in the range of $Z_{tot} = 18 \div 24$ and the longitudinal momentum is around the source velocity

$q_z/q_{beam} = 0.7$. These graphical cuts were read by the analysis program and applied both to the experimental data and to the simulated ones. At first, we studied the effects of the cuts studying the correlation plot Z vs. E_{lab}. In particular, in Fig. 5.13 the experimental correlation plot is shown for the reaction $^{16}O +^{30} Si$ at 111 MeV (left panel), which is firstly compared to the simulated data performed with $HIPSE + SIMON$ in which we have considered a contaminated target ($^{16}O + (^{30}Si{+}O)$ at 111 MeV). This was done with the purpose of checking if this constraint was sufficient to clean up the data as expected. In fact, the "contaminated" residue bumps disappear for both cases, while the "good" ER remain together with their LPC in coincidence. With such a cut, still some QT and QP elements remain, for those cases in which both fragments are detected in the apparatus, giving as a result a total detected charge $Z_{tot} \geq 0.7$.

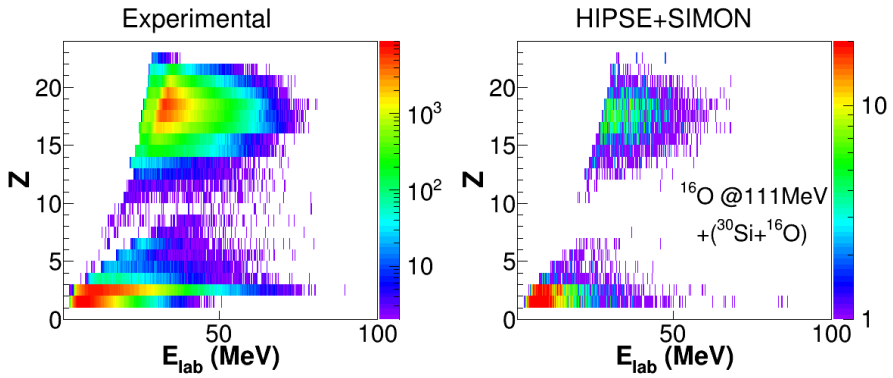

Figure 5.13: Effects of data selection on the charge vs. laboratory energy plot in the experimental case and in the $HIPSE + SIMON$ simulation case for the reaction ^{16}O (at 111 MeV) + $(^{30}Si{+}O)$.

In Fig. 5.14, we report the same correlation plot Z vs. E_{lab} as before (Fig. 5.13), but obtained from the constrained simulation performed with $GEMINI^{++}$ (left panel), $AMD + GEMINI^{++}$ (central panel) and $HIPSE + GEMINI^{++}$ (right panel).

It has to be underlined that this first selection of data reduces the number of events to about 10% of the total collected experimental statistics. However, it is true that the cut is much more effective on peripheral reactions, where often only a partner of the reaction is detected: this means, therefore, that the effective reduction on solely central collision,

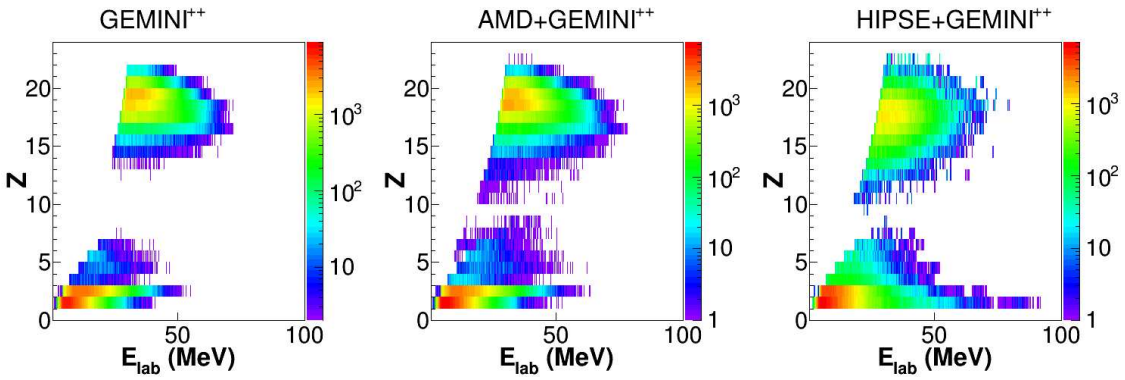

Figure 5.14: Effects of data selection on the simulated Z *vs.* E_{lab} plots for the reaction $^{16}O + ^{30}Si$ at 111 MeV. Left panel: $GEMINI^{++}$; central panel: $AMD + GEMINI^{++}$; right panel: $HIPSE + GEMINI^{++}$.

which we are interested in, is smaller. The percentage of selected data with respect to the initial population, which we can deduce from simulations are:

- $GEMINI^{++}$ 30% (only CN decay);
- $AMD + GEMINI^{++}$ 25%, (Elastic, inelastic, Deep, CN decay);
- $HIPSE + GEMINI^{++}$ 22%. (Deep, CN decay).

A further selection was required asking for the detection of the light charged particles (detected in the whole apparatus: GARFIELD+RCo) in coincidence with at least one evaporation residue (in the forward angles: RCo); such events characterize the central collisions, where fusion-evaporation has occurred. The coincidences with evaporation residues have been set choosing a proper gate in the charge vs. laboratory energy plots, as shown in Fig.5.15, and asking for any coincident particle in the entire apparatus.

The combined effects of the two cuts (on Z_{tot} vs. q_z/q_{beam} and on Z vs. E_{lab}) imposed on the experimental data are analyzed and checked in comparison with the same cuts imposed on all simulations. A more detailed discussion will be here reported on the comparison with $AMD + GEMINI^{++}$ simulation.

In particular, in Fig. 5.16, the charge vs. impact parameter plots are reported for AMD simulated data. The four panels represent: (a) the primary partitions produced by

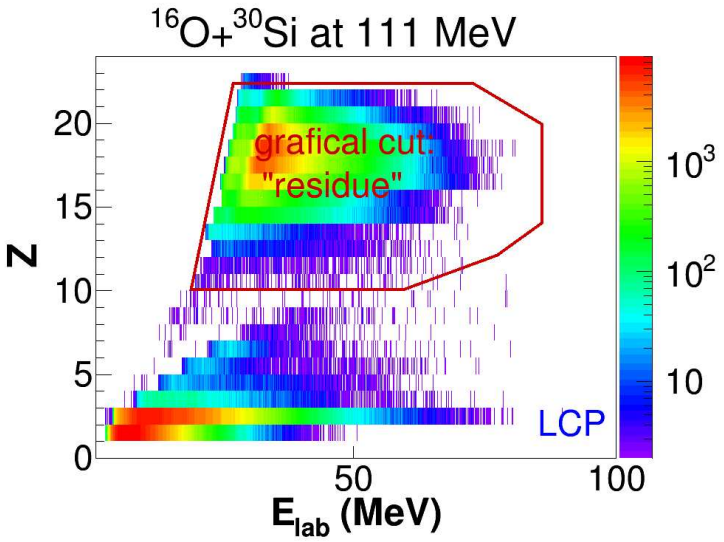

Figure 5.15: Charge vs. laboratory energy plot with graphical cut (red line) to select events in which light charged particles are in coincidence at least with one fragment for the reaction $^{16}O + ^{30}Si$ at 111 MeV.

AMD without any filter, which are taken as an input for the afterburner $GEMINI^{++}$. In the plot, three charge region are clear: in the first, between $Z = 20 \div 22$, excited big fragments are present; the two bumps around $Z = 15$ and $Z = 8$ are related to elastic scattering, inelastic, multi-nucleon transfer or deep inelastic processes; finally, the particles with charge $Z < 3$ are pre-equilibrium emitted particles. (b) The distribution of products as a function of the impact parameter b produced by AMD followed by $GEMINI^{++}$ as afterburner, without any filter. Again here, from the plot clearly three separate regions of charges can be observed: $Z = 15 \div 22$, where the evaporation residues are present; the two bumps around $Z = 15$ and $Z = 8$ are still related to elastic scattering, inelastic, multi-nucleon transfer or deep inelastic processes; here, a major spread of the distributions are related to de-excitation of such of those fragments which were excited in the primary partitions and to the contributions coming from fission fragments. Finally, the lower Z ($Z < 5$) derive by the de-excitation mainly of the ER but also of the fission fragments and deep inelastic fragments. (c) The same distribution of products as a function of the impact parameter b produced by AMD followed by $GEMINI^{++}$ as afterburner, but after

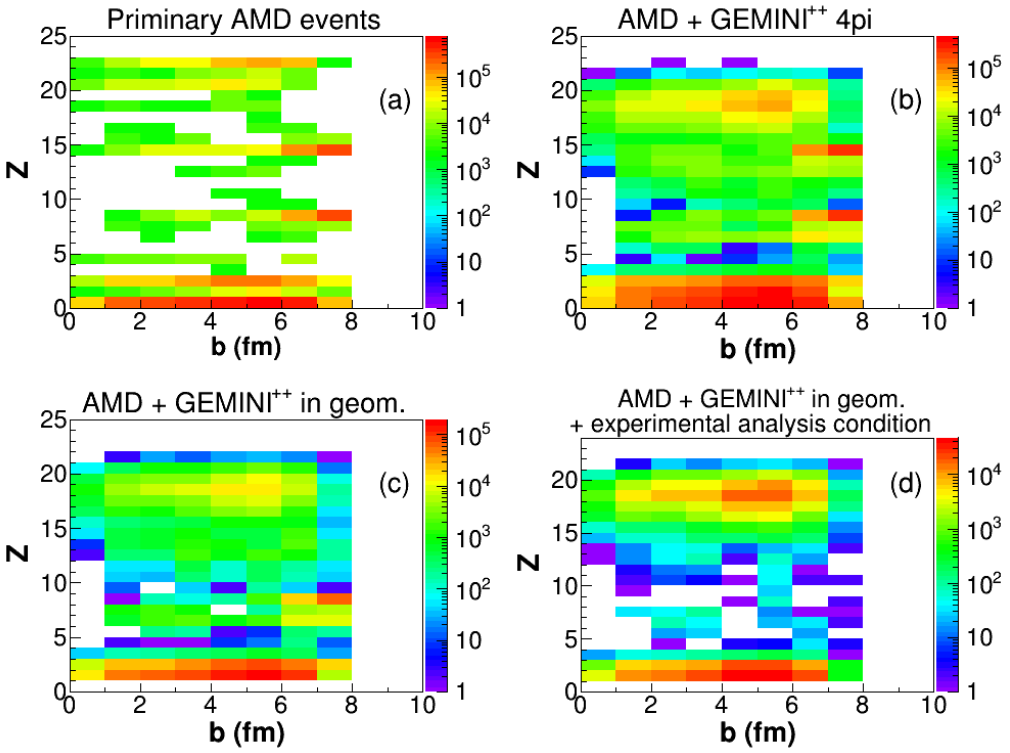

Figure 5.16: Charge *vs.* parameter plots of simulated events generated by: (a) AMD; (b) $AMD + GEMINI^{++}$; (c) $AMD + GEMINI^{++}$ filtered by the software replica of the experimental array; (d) AMD+$GEMINI^{++}$ filtered and selected by cuts previously described.

filtering through the software replica of the apparatus. The region of $Z = 15 \div 22$, where the evaporation residues are present, still remain, even with a reduced yield (see Fig. 5.3 for an example of the ER reduction due to filtering); the bump around $Z = 8$ is still there (again with a reduction in yield), while in the $Z = 15$ region the cut of the elastically scattered target is evident while a part of the strongly dissipated Q_T remains. The lower Z ($Z < 5$) are still there, of course opportunely diminished in yield. (d) Here all previously described cuts are applied. A further filter is also imposed, asking for a coincidence of LCP detected in the whole apparatus with at least one residue in the forward angles. It is evident the cut of almost all the reaction mechanisms except for the CN decay (ER + part of FF).

As already said, when the geometrical filter is applied, some fragments and particles are

lost due to their emission in a region where no detection is provided. Asking for fragment-particle coincidences, this further constraint brings to an extra reduction of the yields and to a selection of more specific exit channels: in the applied selection, the removing of the major part of the events, which were not produced in fusion-evaporation reactions, is obtained. However still some events coming from other mechanisms are present as it can be observed analyzing the correlation between the two largest fragments of each selected event. In particular, in Fig. 5.17 the correlation between the biggest fragment towards the second biggest are shown for the experimental set of data (left panel) and for the $AMD + GEMINI^{++}$ (right panel).

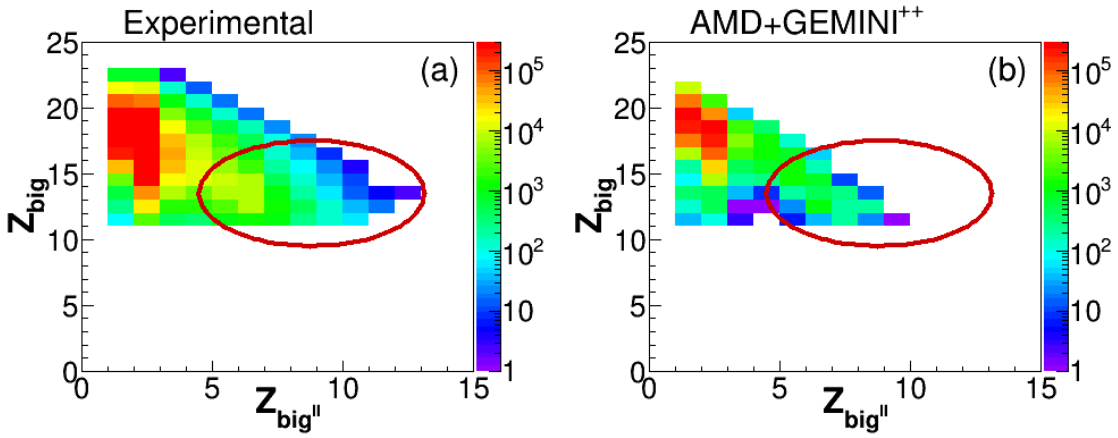

Figure 5.17: Correlation between the heaviest fragment of the reaction and the second heaviest, for the experimental set of data in left panel and for the $AMD + GEMINI^{++}$ in right panel.

Non-fusion-evaporation fragments are those inside the red circles in the figure and they can be related either to deep inelastic fusion-fission events.

Therefore, in order to select only the event produced by fusion-evaporation reaction mechanisms, an additional constraint was imposed to the selection of residues: in a "good" event only one fragment with a charge heavier than 6 can exist; in this way, the fusion-fission/deep inelastic events were cut away. The effects of those selections on the different observables/distributions are illustrated in Figs. 5.18 $\div$ 5.20. In particular, the summed effects of all selections on the experimental charge distribution are presented in Fig. 5.18.

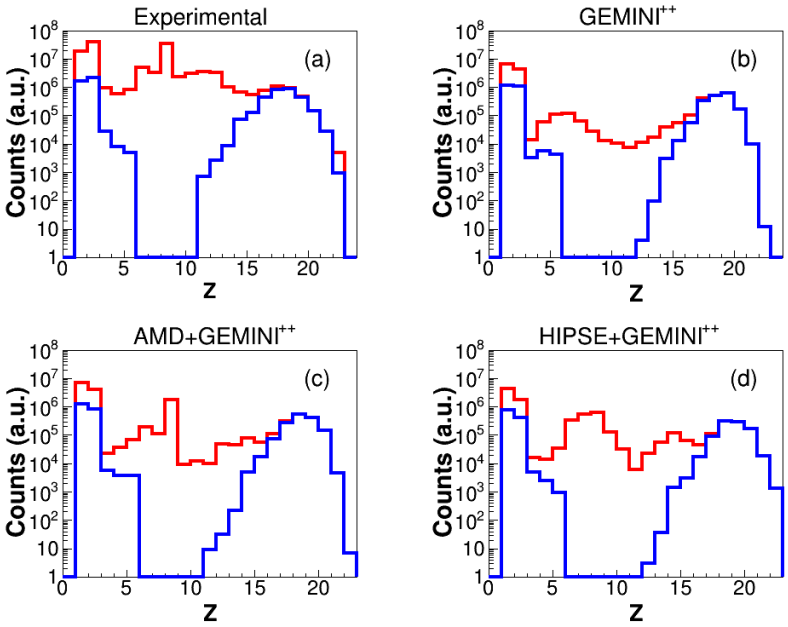

Figure 5.18: Charge distribution: cuts effect on (a) experimental data, (b) $GEMINI^{++}$, (c) $AMD + GEMINI^{++}$ and (d) $HIPSE + GEMINI^{++}$ simulations.

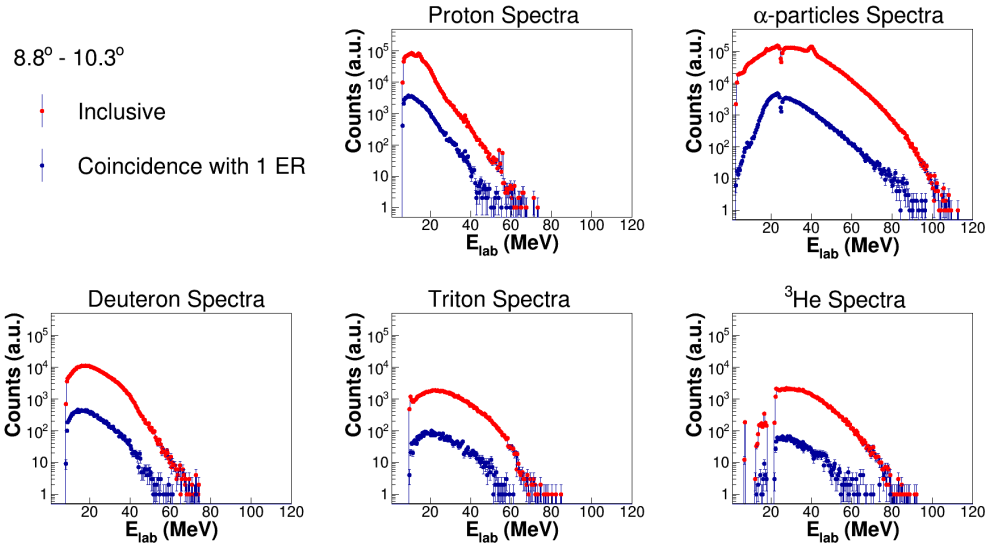

Figure 5.19: Experimental LCP energy spectra: cuts effect.

In Fig. 5.19 and in Fig. 5.20, the effects of the selections on LCP spectra and multiplicity respectively are illustrated.

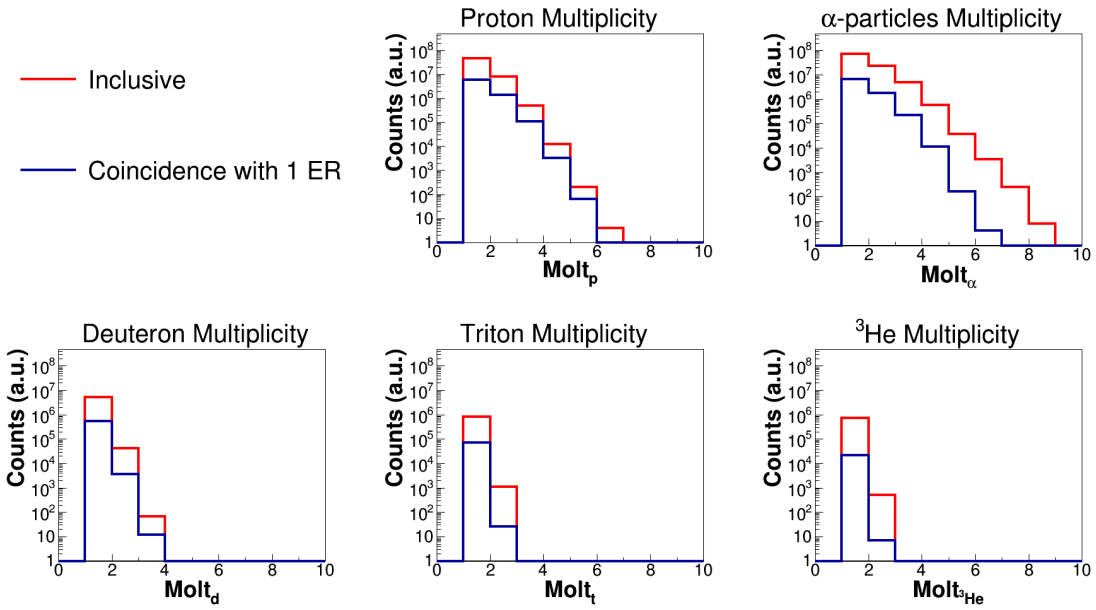

Figure 5.20: Experimental LCP Multiplicity plots: cuts effect.

As a consequence of all the imposed selections, the remaining events to be analyzed are $\sim 8\%$ of the total initial detected experimental events; even though apparently a significant amount of statistics has been rejected, the remaining events are very clean and related to fusion-evaporation processes, so that a very precise analysis can be performed.

Chapter 6

Quasi-complete events analysis: $Z_{tot} \geq 18$

In the Chapter 5, the event selection procedure was explained and the effects that those selections have produced on the original event distributions were also outlined. Besides such selections, in the present Chapter, the analysis of the events, for which at least the 70% of the total charge was collected, has been performed. In particular, the comparison between the experimental data and the simulations performed by $GEMINI^{++}$ and $AMD + GEMINI^{++}$ are presented for selected observables.

For the simulation with $GEMINI^{++}$ code, as it was discussed in the Section 3.1, a specific choice of the level density was considered, which takes into account the angular momentum induced deformation of the $^{46}Ti^{*}$ nucleus, already observed by A. Maj and coworkers (see Chapter 4). Moreover, in order to take into account the effects of a possible deformation induced by temperature, different values of the parameter "w" have been considered. As previously explained, such parameter permits to simulate the emission from deformed nuclei through a convolution of emission barriers, in which the transmission coefficients are calculated with different radii, going from $r+dr$ to $r-dr$ (where $dr = w\sqrt{T}$). In our case, we have used: the default value of $w = 1.0$ fm, corresponding to a ratio of the nucleus axes ($b : a$) of $2 : 1$; a value of $w = 0.0$ fm to describe an unique barrier of a spherical nucleus; and $w = 1.1$ fm, producing a ratio of the nucleus axes of $b : a = 2.2 : 1$.

On the other hand, the *AMD* code (see Section 3.2) has been run with the default parameters set: *nnchange_gamma=-1d0*, which indicate a quite large cluster correlation degree; *screened_y=0.85d0*, imposing a screened nucleon collision cross section without any suppression of cluster correlations; *coacc_set(enable=.true.)*, representing the cluster-cluster binding process. Moreover, it was coupled to $GEMINI^{++}$, used as afternurner to simulate the decay of primary fragments. As a first case, due to CPU time, $GEMINI^{++}$ was run here just with the barrier parameter $w = 1.1$ fm since it was the case which globally better represented the semi-complete data.

The analysis of the quasi-complete events have been performed for all the four reactions, by comparing the experimental light charged particles (LCP) energy spectra, multiplicities and angular distributions with simulations.

For sake of synthesis, in the following Sections we will use some abbreviation for the different models:

- **G00**: $GEMINI^{++}$ with $w = 0.0$ fm;
- **G10**: $GEMINI^{++}$ with $w = 1.0$ fm;
- **G11**: $GEMINI^{++}$ with $w = 1.1$ fm;
- **AMD**: $AMD + GEMINI^{++}$.

All LCP energy spectra shown in this Chapter are normalized to the maximum, for shape comparison purpose only; yields comparisons will be performed in the LCP angular distributions and multiplicity spectra, where a normalization to the detected evaporation residue (after all selection on events for both experimental data and simulations) is performed. We remind that all the results shown in the present Chapter are referred to selected events in which the total detected charge is $Z_{tot} \geq 18$ and in which one and only one fragment has been detected in coincidence with at least one LCP or fragment with $Z < 6$. For sake of clarity, in the case of energy spectra, the words as under(over)-estimation/production are used improperly only related to the shape comparison in the different angular regions.

Each following Section is dedicated to one of the four reactions: $^{16}O+^{30}Si$ at 111 MeV (Section 6.1), $^{16}O+^{30}Si$ at 128 MeV (Section 6.2), $^{18}O+^{28}Si$ at 126 MeV (Section 6.3) and $^{19}F+^{27}Al$ at 133 MeV (Section 6.4).

6.1 $^{16}O+^{30}Si$ at 111 MeV.

The experimental energy spectra for protons detected at different θ_{lab} are shown in comparison with data simulated by $GEMINI^{++}$ and by $AMD + GEMINI^{++}$ in Fig. A.1 (**G00** and **G10**) and in Fig. A.2 (**G11** and **AMD**) of the Appendix A. At a first observation, we can notice that in the case of protons, almost all simulations well describe the overall distributions, a part for very small differences, which can be observed in the case of the **AMD** calculations in the angular range $\theta_{lab} = 29.5^o \div 82.5^o$.

In Fig. A.3 and Fig. A.4 (panel c.), the corresponding experimental deuteron spectra are also shown in comparison with $GEMINI^{++}$ predictions obtained with the three different barrier parameters, as previously described; again in Fig. A.4 (panel d.), the comparisons between experimental deuterons and $AMD + GEMINI^{++}$ predictions are performed. In the case of deuterons, almost all the simulations describe well the experimental spectra in the range between $\theta_{lab} = 29.5^o \div 150.4^o$, while it is clear that a better and comparable description is obtained in the forward region ($\theta_{lab} = 8.8^o \div 17.4^o$) with **G11** and **AMD**.

The experimental triton spectra are compared with the same simulations in Fig. A.5 and Fig. A.6 of the Appendix A. In this case, almost no differences can be observed between the four simulations, which reasonably describe all the spectral shapes.

In Figs. A.7 (a. **G00**; b. **G10**) and A.8 (c. **G11**; d. **AMD**) the same comparison is performed for the experimental ^3He energy spectra. Due to the quite low ^3He production predicted by almost all simulations, the comparison to experimental data are quite qualitative. However, as it will better underlined in the following in a more quantitative way, it seems that, as a general trend, the forward experimental production of ^3He is larger than those predicted by all the simulations.

Finally, in Fig. A.9 and Fig. A.10 (panel c.) the experimental α energy spectra are

presented in comparison with $GEMINI^{++}$ and in Fig. A.10 (panel d.) in comparison with $AMD + GEMINI^{++}$. The overall description of the α-spectra are good for all the simulations in the angular range between $\theta_{lab} = 29.5^o \div 150.4^o$; however, a better agreement is observed for the $29.5^o \div 40.0^o$ angular range in the case of **G11** and **AMD**. In the forward region ($\theta_{lab} = 8.8^o \div 17.4^o$) no simulation is able to well reproduce the α-spectra, even though, again, **G11** and slightly better **AMD** are better describing the forward experimental distributions, a part for the limited simulated data statistics due to cpu time.

To look in a more quantitative way to the relative yield distribution in the angular region, another observable to be globally checked is the LCP angular distribution; it complements the information coming from the energy spectra shape comparison.

In Fig. 6.1 protons, α-particles, deuterons, tritons and ^3He experimental angular distributions are compared with simulations: **G00** (green triangles), **G10** (red triangles),**G11** (blue triangles) and **AMD** (pink triangles); each distribution is normalized to the number of their specific (experimental or simulated) evaporation residues, obtained after the above specified selections. One can observe that: the experimental proton angular distribution is reproduced by $GEMINI^{++}$ in the whole angular range in a very similar way by all the three cases, confirming a small sensitivity of protons to the difference in emission barrier; a small experimental underproduction is, however observed in the central angular region $\theta_{lab} = 29.5^o \div 66.0^o$. $AMD + GEMINI^{++}$ largely overestimates the proton yields in the angular range between $\theta_{lab} = 29.5^o \div 150.4^o$.

For what concern the α-particles angular distribution, it is almost well described in the angular range between $\theta_{lab} = 29.5^o \div 82.5^o$; moreover, only $GEMINI^{++}$ with $w = 1.0$ fm does not reproduce the backward yields ($97.5^o < \theta_{lab} < 150.4^o$). However, no one is able to reproduce the forward production ($8.8^o < \theta_{lab} < 17.4^o$), confirming what was previously observed looking at the energy spectra shape.

A similar experimental overproduction at forward angles is observed also for ^3He, which is strongly also underestimated by all simulations in the backward direction. **AMD** is somehow slightly overestimating the central angular region and it is a little bit closer in

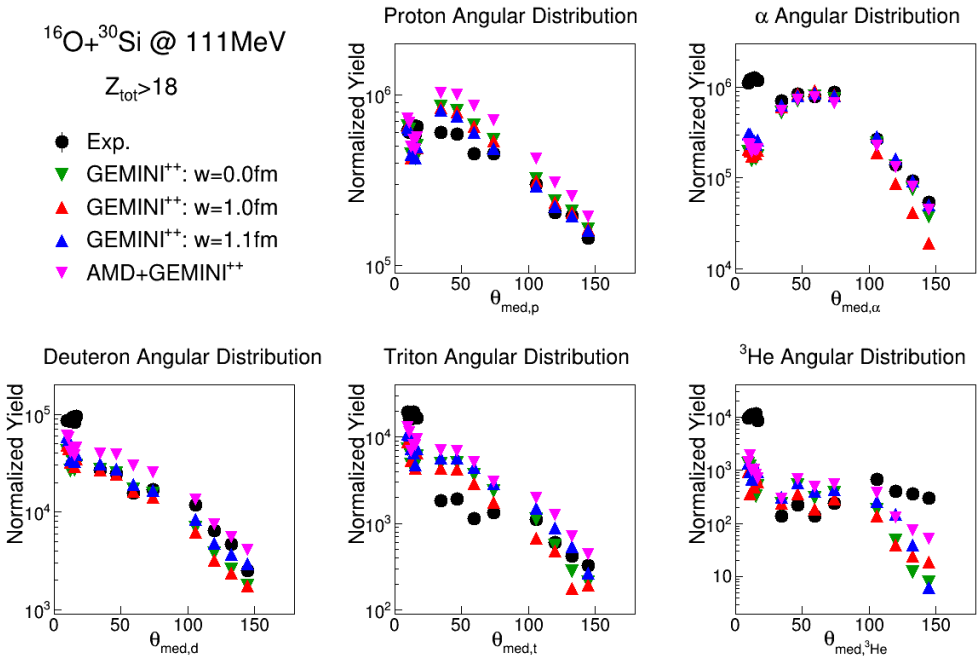

Figure 6.1: Angular distributions of experimental LCP (black dots) emitted in central collisions in the reaction $^{16}O + ^{30}Si$ at 111 MeV. Comparison with $GEMINI^{++}$ simulations with $w = 0.0$ fm (green triangles), $w = 1.0$ fm (red triangles) and $w = 1.1$ fm (blue triangles) and with $AMD + GEMINI^{++}$ simulations ($w = 1.1$ fm - pink triangles). The experimental error bars are inside the points. See text for more details.

the backward part, but still largely underestimating it.

For tritons, the central angular region is largely overestimated by all simulations, in particular by $AMD + GEMINI^{++}$; while the backward region is quite well reproduced by **G11** and **G00**, it is overestimated by **AMD** and it is underestimated by **G10**. In the forward region, a similar but smaller experimental overproduction, like in the case of the α-particles and ^3He is present also for tritons and deuterons with respect to all simulations. In both cases $AMD + GEMINI^{++}$ simulation is closer to the experimental points in the forward part. Experimental deuteron angular distribution is reasonably well reproduced by **AMD** and **G11** in the backward part, even if **AMD** tends to overestimate while **G11** to underestimate the experimental yield. The central part is quite well reproduced by the three $GEMINI^{++}$ alone, while $AMD + GEMINI^{++}$ still overestimates the yield in this

angular region similarly at the case of protons and tritons.

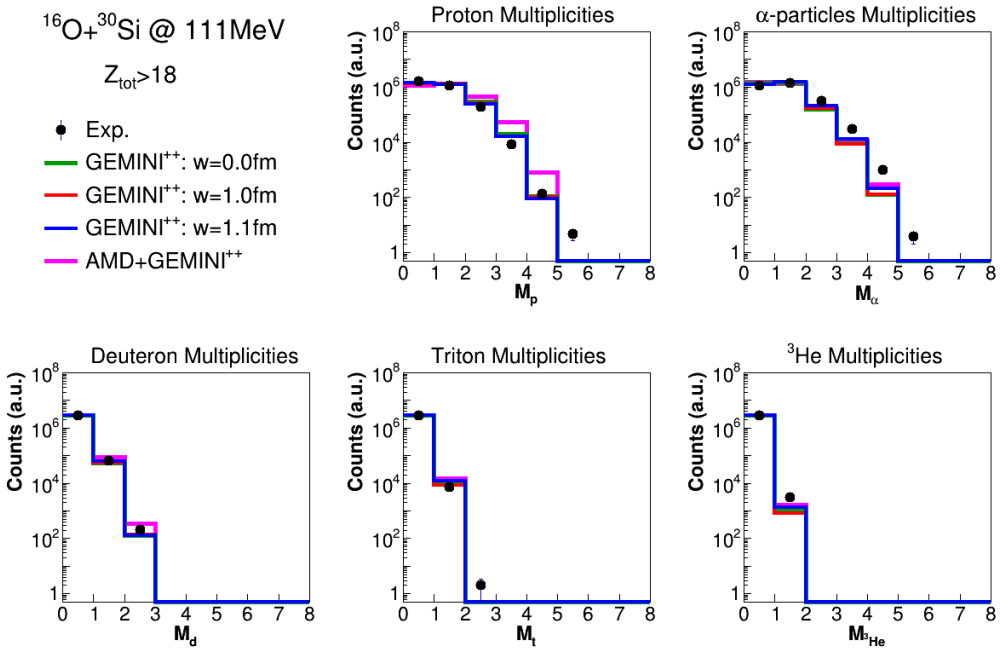

Figure 6.2: Light charge particles multiplicity distributions: experimental particles (black dots) emitted in central collisions in the reaction $^{16}O + ^{30}Si$ at 111 MeV. Comparison with $GEMINI^{++}$ simulations with $w = 0.0$ fm (green lines), $w = 1.0$ (red lines), $w = 1.1$ (blue lines) and $AMD + GEMINI^{++}$ ($w = 1.1$ fm - pink lines). See text for more details.

A further interesting information derives by looking, for the coincidence selected events, at the LCP multiplicity distributions. In Fig. 6.2 the experimental proton, α-particle, deuteron, triton and ^3He multiplicities are shown in comparison to the three $GEMINI^{++}$ cases and to $AMD + GEMINI^{++}$. Again, each distribution is normalized to its specific number of detected residues. A rather good global agreement is observed for all the $GEMINI^{++}$ predictions and all the LCP, even though a slight overproduction of experimental α-particles can be observed at larger multiplicities ($M_\alpha \geq 3$). **AMD** tends to overestimate the proton multiplicities, while underestimates, in the same way of $GEMINI^{++}$ alone, the higher α-particle multiplicities ($M_\alpha \geq 3$). The other particles (d,t,^3He) are relatively well described.

6.2 $^{16}O+^{30}Si$ at 128 MeV.

The reaction $^{16}O+^{30}Si$ at 128 MeV is analyzed; this reaction is the same system as the previous one, but it has a higher projectile velocity with respect to all the other studied reactions. Furthermore, it forms an excited nucleus of $^{46}Ti^{*}$ in case of complete fusion which has an excitation energy about 10 MeV higher than previous one and equal to that of the ^{18}O induced reaction (see Section 7).

In Figs. A.11 and A.12 of the Appendix A, the experimental proton energy spectra detected at different laboratory angles are compared with simulations. Like in the lower energy case, proton spectra do not show any particular sensitiveness to the different calculation hypothesis and are generally well described in the whole angular range.

The Figs. A.13 and A.14 of the Appendix A represent the deuteron energy spectra. Experimental deuterons are well described in the angular range between $\theta_{lab} = 29.5^{o}$ and 150.4^{o} by all models, while in the forward angles an over production of experimental deuterons is foreseen, which is only slightly better taken into account both by **G11** and **AMD** cases. The difference between experimental data and simulations in the forward direction are larger than in the low energy reaction previously discussed.

In Fig. A.15 and in Fig. A.16 of the Appendix A the triton energy spectra are shown. At variance with the lower energy case, tritons are well described in the angular range between $\theta_{lab} = 29.5^{o} \div 150.4^{o}$, while in the most forward direction some discrepancies are visible, especially for **G00** and **G10**.

The ^{3}He energy spectra are shown in Fig. A.17 and Fig. A.18 of the Appendix A. Here the differences with model predictions seem more evident, from the shape point of view especially in the angular range between $\theta_{lab} = 29.5^{o}$ and 82.5^{o}, while it is clear that also a problem of relative yields is particularly present at forward angles, as it will be underlined in the following.

Experimental and simulated α-particle energy spectra are displayed in Fig. A.19 and A.20 of the Appendix A. The α-particle spectra are well reproduced by the **G00**, **G11** and **AMD** cases in the angular range $\theta_{lab} = 29.5^{o} \div 150.4^{o}$, while a small disagreement is appearing with **G10** in the angular range between 29.5^{o} and 82.5^{o}. In the forward angles,

all simulations underestimate the experimental production, but **G11** and **AMD** are closer to the experimental situation for what concern the shape.

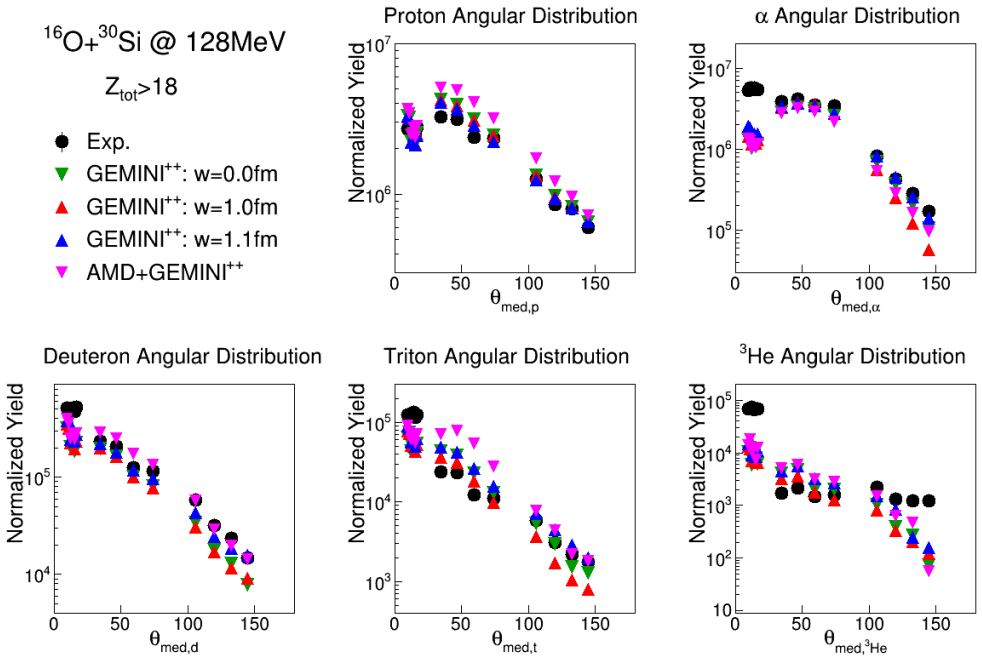

Figure 6.3: Angular distributions of light charged particles emitted in central collisions in the reaction $^{16}O + ^{30}Si$ at 128 MeV. Same as in Fig. 6.1.

Looking to the angular distributions of the LCP, which are shown in Fig. 6.3, the situation is very similar to what was found at lower energy, apart from the relative yields which are growing for every kind of particle, as expected. However, some peculiar observations can be addressed: the differences in the forward angular range (RCo) between simulations and experiment are reduced for deuterons and especially for tritons, even if they are still not completely described. Looking to deuterons a reasonable agreement is observed with $AMD + GEMINI^{++}$, which slightly overestimate deuterons in the angular range $29.5^o \div 82.5^o$, while giving a better reproduction of the yield at the backward angles with respect to $GEMINI^{++}$ alone. For triton, on the contrary, **AMD** is quite good in reproducing the angular distribution in the forward angles and in the backward angles, while it predict an overproduction between $\theta_{lab} = 29.5^o$ and 82.5^o, not present in

the experimental data, like what observed at low energy.

Regarding protons, the three $GEMINI^{++}$ alone, in particular **G11**, reproduces quite well the experimental angular distribution, while $AMD+GEMINI^{++}$, as it was observed at low energy, tends to overestimate the protons in the angular range between 29.5^o and 126.5^o; in this last case, a quite good reproduction is obtained in the forward direction (RCo) and in the GARFIELD detectors covering the $\theta_{lab} = 127.5^o \div 150.4^o$.

For α-particles the trend is similar to the case at lower energy, with an overall good description apart from the very forward angles (RCo) which is strongly underestimated. A very small difference can be observed even at the very backward ($\theta_{lab} = 127.5^o \div 150.4^o$).

The description of ^3He is still not good, even if one can observe a slightly better trend of the $AMD+GEMINI^{++}$ predictions in the forward and backward direction, suggesting some privileged emission of such clusters. In general, ^3He particles show a peak in the forward direction and then a quite flat angular distribution which is not reproduced by any simulation.

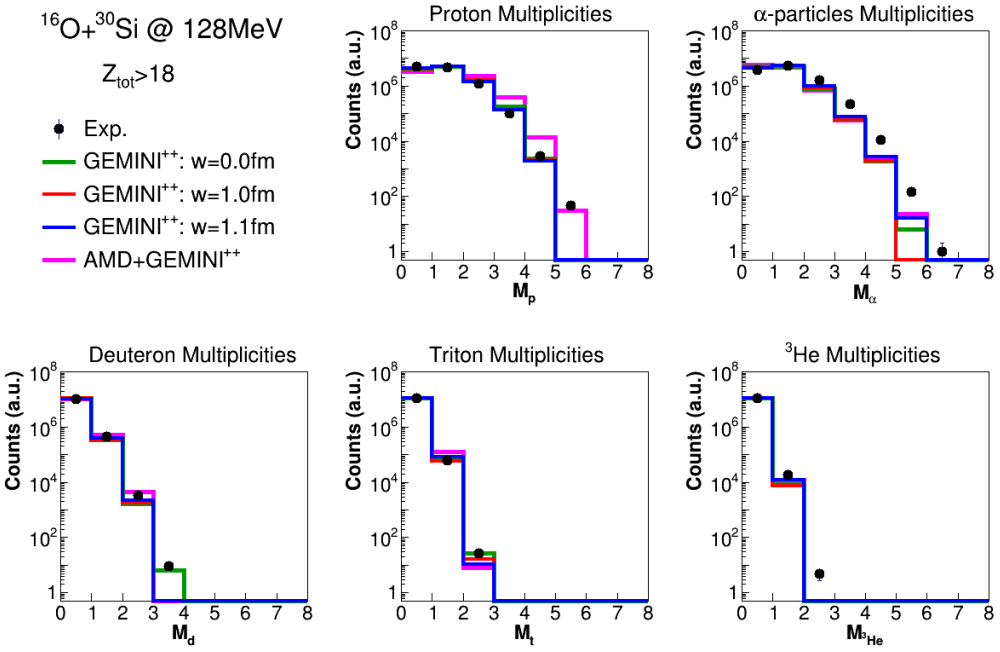

Figure 6.4: Light charge particles multiplicity distributions for the reaction $^{16}O+^{30}Si$ at 128 MeV. Same as in Fig. 6.2.

Experimental LCP multiplicity plots (black dots) are presented in the Fig. 6.4 in comparison with simulations. The overall multiplicity plots for all LCP are again well described by all simulations, even if a slight underestimation of α-particle is observed for high multiplicities ($M_\alpha \geq 3$). For what concerns protons, the multiplicity $M_p = 5$, present in the data, is not produced by the $GEMINI^{++}$ alone; on the contrary, **AMD** reproduces this multiplicity, but it overestimates protons with $M_p = 2 \div 4$.

6.3 ^{18}O+^{28}Si at 126 MeV.

The $^{18}O + ^{28}Si$ at 126 MeV is studied. The comparison of the results obtained in this case with the previous reaction ($^{16}O + ^{30}Si$ at 128 MeV) is very important, since the two reactions are supposed to form, in case of complete fusion, the same compound nucleus at the same excitation energy.

The proton energy spectra are displayed in Fig. A.21 and Fig. A.22 of the Appendix A. Also for this reaction, protons are well reproduced demonstrating almost no sensitivity to the change of simulation parameters and physical constraints.

For what concerns deuterons, which energy spectra are displayed in Fig. A.23 and in Fig. A.24 of the Appendix A, they are better reproduced by all simulations with respect to the previous cases. The best agreement is obtained by using **AMD** and **G11**.

Triton energy spectra are displayed in Figs. A.25 (a. **G00** and b. **G10**) and A.26 (c. **G11** and d. **AMD**) of the Appendix A. Almost no differences can be observed between the four simulations, which reasonably describe all the spectral shapes. Small differences are observed in the forward angles, which are normally better described by **G11**.

In Fig. A.27 and in Fig. A.28 of the Appendix A, the ^3He energy spectra are shown. As in the previous reaction, the difference with model predictions is evident: from the shape point of view, discrepancies are observed in the angular range $\theta_{lab} = 29.5^o \div 82.5^o$, while differences in relative yields are particularly visible at forward angles. However, at least qualitatively discrepancies with the models are slightly reduced, with respect to the ^{16}O-induced reactions, especially for **G11** case.

Experimental and simulated α-particles enrgy spectra are displayed in the Fig. A.29

and in Fig. A.30 of the Appendix A. The α-particle energy spectra are reasonably reproduced by **G00**, apart from a small underestimation in the forward angle region (RCo). They are underestimated in the **G10** case both at forward angles (RCo) and to some extent in the region $\theta_{lab} = 41.0^o \div 82.5^o$. They are almost well reproduced in the forward angle (RCo) and slightly overestimated by **G11** in the angular range $\theta_{lab} = 29.5^o \div 82.5^o$: this was similar in the ^{16}O induced reaction, but the differences were reduced with respect to the present case, as it will be discussed later in complete analysis. The **AMD** is quite well reproducing almost all the spectral shapes.

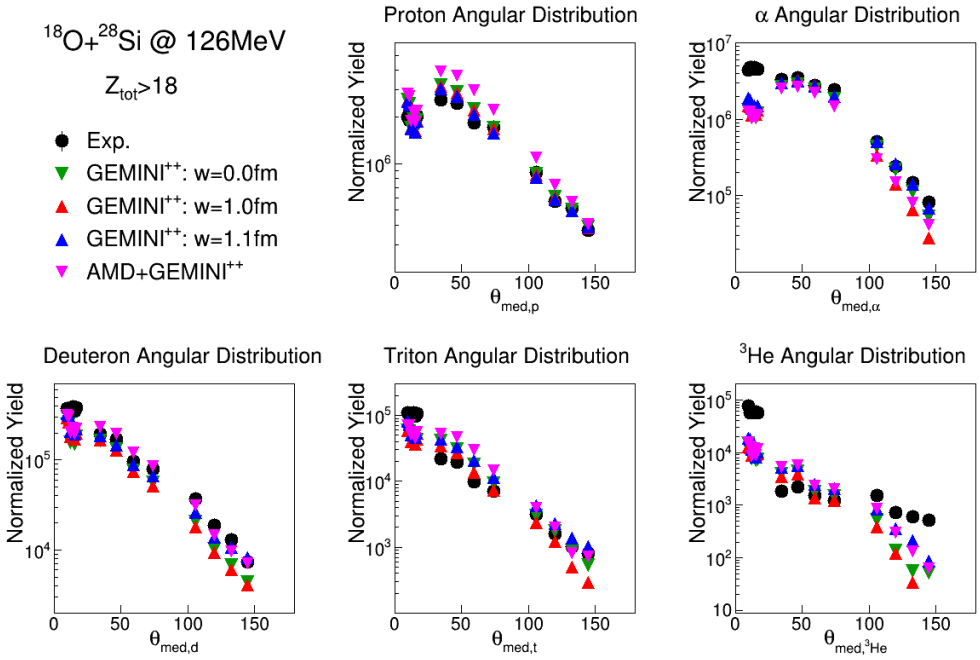

Figure 6.5: Angular distributions of light charged particles emitted in central collisions in the reaction $^{18}O + ^{28}Si$ at 126 MeV. Same as in Fig. 6.1.

Looking at the angular distributions of the LCP, which are shown in Fig. 6.5 we can observe a situation very similar to the previous reaction, both when compared to $GEMINI^{++}$ alone (for every choice of the "w" parameter) and when compared to **AMD**. Even if still **AMD** overestimates triton in the angular region $\theta_{lab} = 29.5^o \div 82.5^o$, it is slightly better than in the ^{16}O induced reaction case.

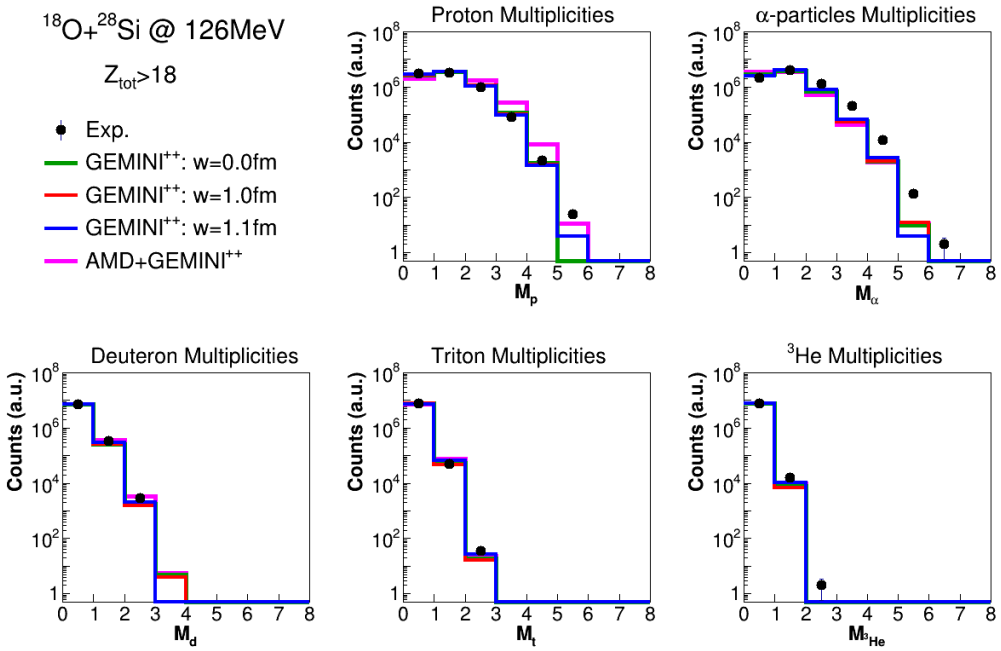

Figure 6.6: Light charge particles multiplicity distributions for reaction $^{18}O + ^{28}Si$ at 126 MeV. Same as in Fig. 6.2.

LCP multiplicity plots are presented in the Fig. 6.6. The overall multiplicity plots are well described by simulations; again, a slight underestimation of α-particle is observed for high multiplicities ($M_\alpha \geq 3$). The proton multiplicity, $M_p = 5$, is reproduced by textbfG10 and **G11**, even if still they underestimate the experimental value. **AMD** overestimates protons with $M_p = 2 \div 4$ and predicts a lower $M_p = 5$ yields.

6.4 $^{19}F+^{27}Al$ at 133 MeV.

The reaction $^{19}F +^{27} Al$ at 133 MeV is also analyzed: this reaction is the one forming the $^{46}Ti^*$ at the highest excitation energy (103.5 MeV) among the four studied reactions. However it has the same projectile velocity as the $^{16}O +^{30} Si$ at 111 MeV and of the $^{18}O +^{28} Si$ at 126 MeV.

The proton energy spectra are shown in Fig. A.31 and in Fig. A.32 of the Appendix A. Once more, protons are well reproduced as in the previous reactions.

The deuterons energy spectra are displayed in Fig. A.33 and in Fig. A.34 of the Appendix A. Even deuterons are reasonably well reproduced by all simulations: the best agreement is obtained by **G11** and **AMD**.

Triton energy spectra are displayed in Fig. A.35 and in Fig. A.36 of the Appendix A. Small differences are observed in the forward angles, when compared to **G00** and **G10**. A quite good description is obtained, instead with **G11**. **AMD** reproduces quite well the GARFIELD angular region ($41.0^o \div 150.4^o$), while some differences are presents in more forward angle ($8.8^o \div 17.4^o$).

In Figs. A.37 and A.38 of the Appendix A, the ^3He energy spectra are shown. Similar differences with model predictions are observed as in the previous reactions. A better agreement can be observed at forward angles (RCo) and at backward angles ($\theta_{lab} > 97.5^o$) with **G11**. **AMD** does not predict ^3He in the $\theta_{lab} = 139.9^o \div 150.4^o$ angular range.

The α-particles energy spectra, displayed in the Fig. A.39 and Fig. A.40 of the Ap-

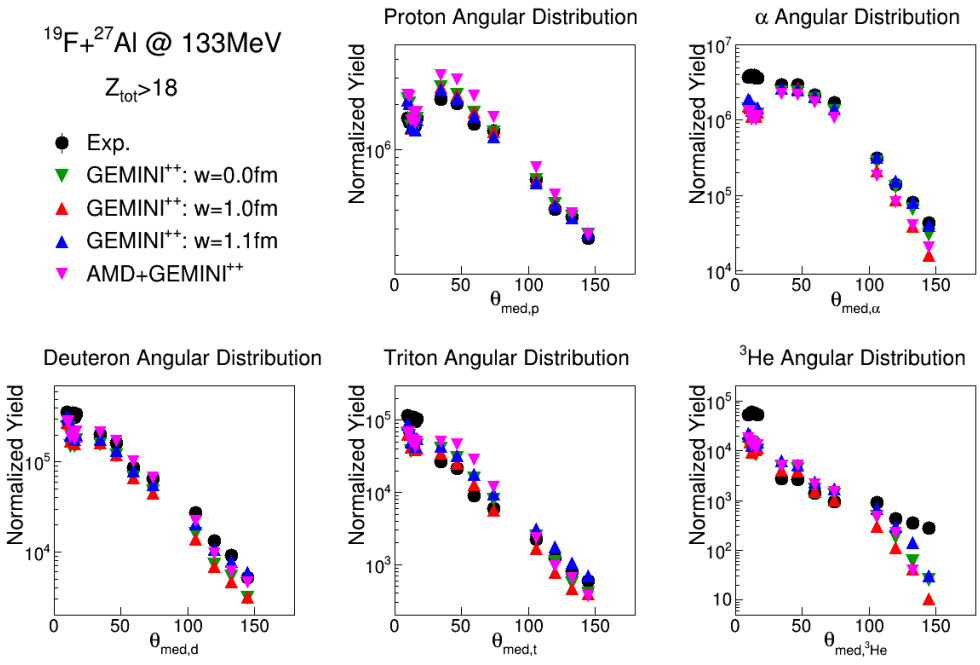

Figure 6.7: Angular distributions of light charged particles emitted in central collisions in the reaction $^{19}F+^{27}Al$ at 133 MeV. Same as in Fig. 6.1.

pendix A, are very well reproduced by the **G00**, are slightly underestimated by the **G10** in the forward angles (RCo) and partially overestimated by the **G11** in the angular range $\theta_{lab} = 29.5^o \div 82.5^o$. **AMD** is well reproducing almost all the spectral shapes.

Looking at the angular distributions of the LCP, showing in Fig. 6.7, $GEMINI^{++}$ alone reproduces the experimental data likewise the previous reactions. **AMD** for this reaction better reproduces the experimental deuterons, tritons and ^3He. A smaller over-production of α-particles, ^3He and triton at forward angles is observed.

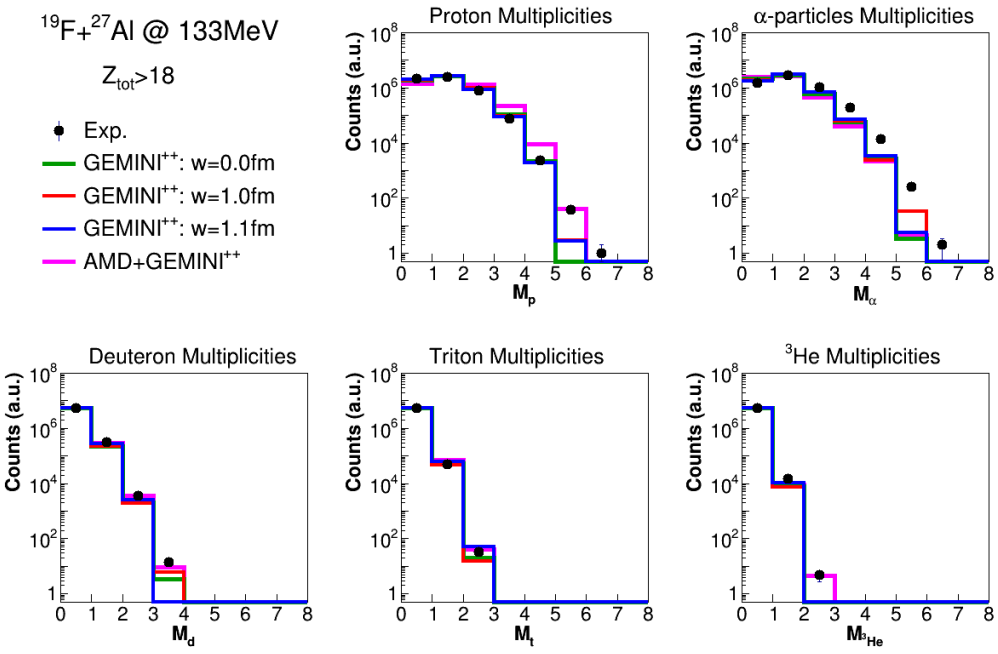

Figure 6.8: Light charge particles multiplicity for the reaction $^{19}F + ^{27}Al$ at 133 MeV. Same as in Fig. 6.2.

LCP multiplicity plots are presented in the Fig. 6.8, where the experimental data are well described by simulations. Again, a slight underestimation of α-particle is observed for high multiplicities ($M_\alpha \geq 3$). The proton multiplicities $M_p = 5$ and $M_p = 6$ are underestimated by $GEMINI^{++}$. **AMD** well reproduces $M_p = 5$ and it is the solely to predict the observed $M_{^3He} = 3$.

6.5 Conclusions

Selected events in which almost complete events have been recorded with a total detected charge larger than 70% of the total charge $Z_{tot} = Z_p + Z_t = 22$ have been analyzed for the four studied reactions. Interesting results have been outlined by comparing the LCP energy spectra, angular distributions and multiplicities, which have been collected for central collisions in coincidence with a large evaporation residues ($Z > 12$). Differences between the reactions have been observed which goes beyond the expected behavior due to the different excitation energies involved. Proton energy spectra are well reproduced for all the four reactions and by all the used simulations, showing that no sensitivity of this exit channel in semi-inclusive variables is present. Quite different is the behavior of the other LCP: deuterons and tritons show a clear dependence on the different used recipes in the simulations; ^3He are the most difficult probes to be described. The α-particles are very sensitive to the different simulations: in particular, a forward peaked production is observed but it is not described by any simulation, which indicates a different decay of the hot formed source depending on the different entrance channels. To be more quantitative, an analysis of complete events ($Z_{tot} = 22$) have been performed and will be described in the following Chapters.

Chapter 7

Complete Events: $Z_{tot} = 22$

Complete events have been selected imposing a total detected charge corresponding to the total entrance channel charge ($Z_p + Z_T = 22$). As described in Chapter 5, the event selection was done by asking the coincidence of at least one light charged particle (LCP) or light fragment ($Z < 6$) with one and only one evaporation residue ($Z_{ER} \gtrsim 12$). For these events the comparison between experimental and simulated energy spectra, multiplicity, angular and charge distributions have been performed as in the case of almost complete events (see Chapter 6; $Ztot > 18$).

In the following pages, for sake of synthesis, the different comparison with models are still recalled in the text with abbreviations (like in Chapter 6):

- **G00**: $GEMINI^{++}$ with $w = 0.0$ fm (drawn in green);
- **G10**: $GEMINI^{++}$ with $w = 1.0$ fm (drawn in red);
- **G11**: $GEMINI^{++}$ with $w = 1.1$ fm (drawn in blue);
- **AMD**: $AMD + GEMINI^{++}$ (drawn in pink);
- **HIPSE**: $HIPSE + GEMINI^{++}$ (drawn in orange).

As in the previous part, each Section of the present Chapter focuses on one of the four studied systems: $^{16}O + ^{30}Si$ at 111 MeV (Section 7.1), $^{16}O + ^{30}Si$ at 128 MeV (Section 7.2), $^{18}O + ^{28}Si$ at 126 MeV (Section 7.3) and $^{19}F + ^{27}Al$ at 133 MeV (Section 7.4).

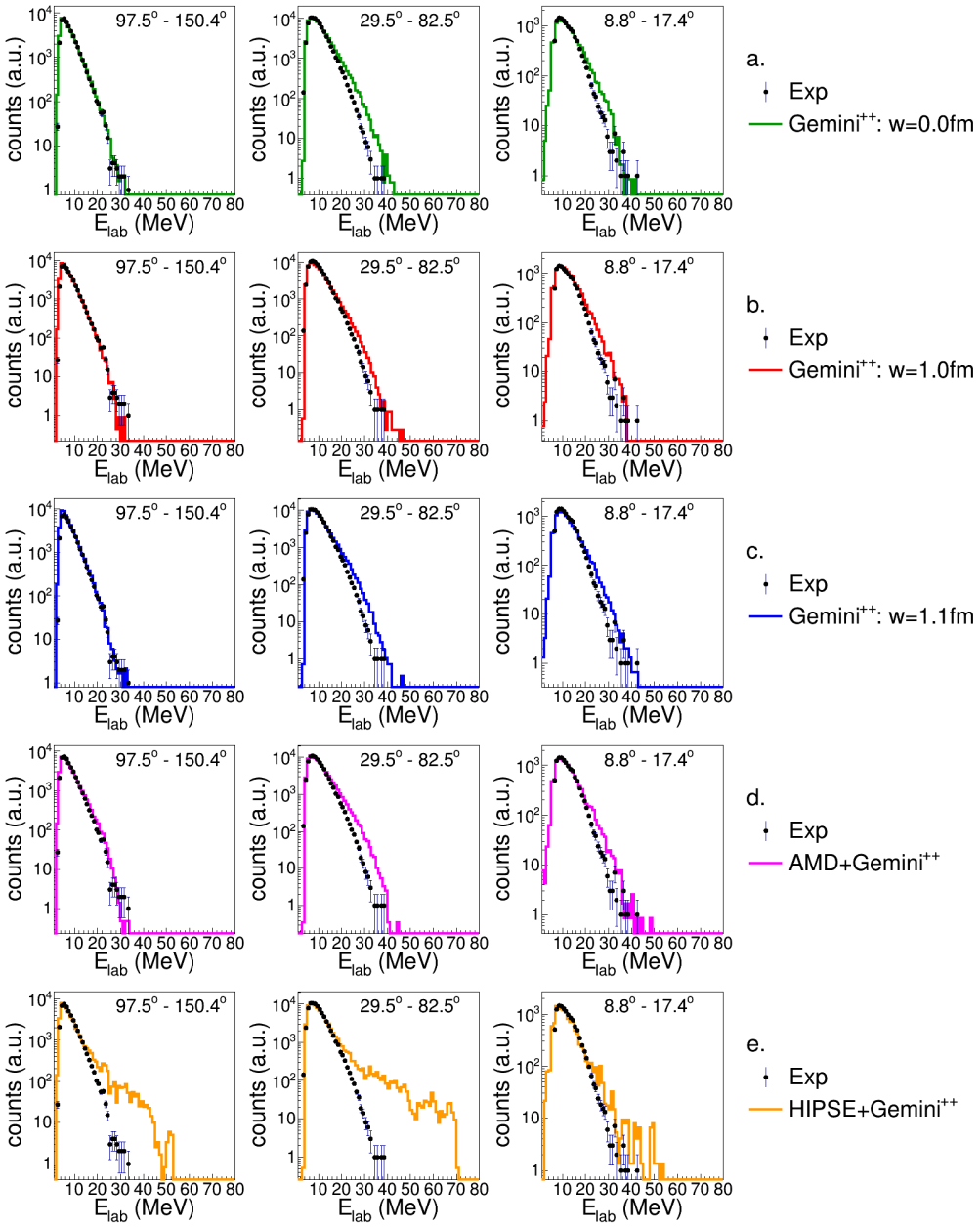

Figure 7.1: Comparison of normalized proton spectra between experimental data (black dots) and simulations made by $GEMINI^{++}$ $w = 0.0$ fm (green line), $w = 1.0$ fm (red line), $w = 1.1$ fm (blue line), by $AMD + GEMINI^{++}$ (pink line) and by $HIPSE + GEMINI^{++}$ (orange line) for the reaction $^{16}O +^{30} Si$ at 111 MeV. The simulated spectra are normalized to the experimental maximum. See text for details.

7.1 $^{16}O+^{30}Si$ at 111 MeV.

Starting from the $^{16}O+^{30}Si$ at 111 MeV, that is the reaction at lower excitation energy, a first surprise can be observed looking to proton energy spectra, which are compared to different model calculations. At variance with the case of almost complete events, in this case we see some discrepancies of the proton spectra when compared to the different simulations as it is shown in Fig. 7.1. Proton energy spectra are, in fact, well reproduced by all calculations (except **HIPSE**) at backward angles ($\theta_{lab} = 97.5^o \div 150.4^o$), while a clear difference is visible in the angular range $\theta_{lab} = 29.5^o \div 82.5^o$: such difference is more

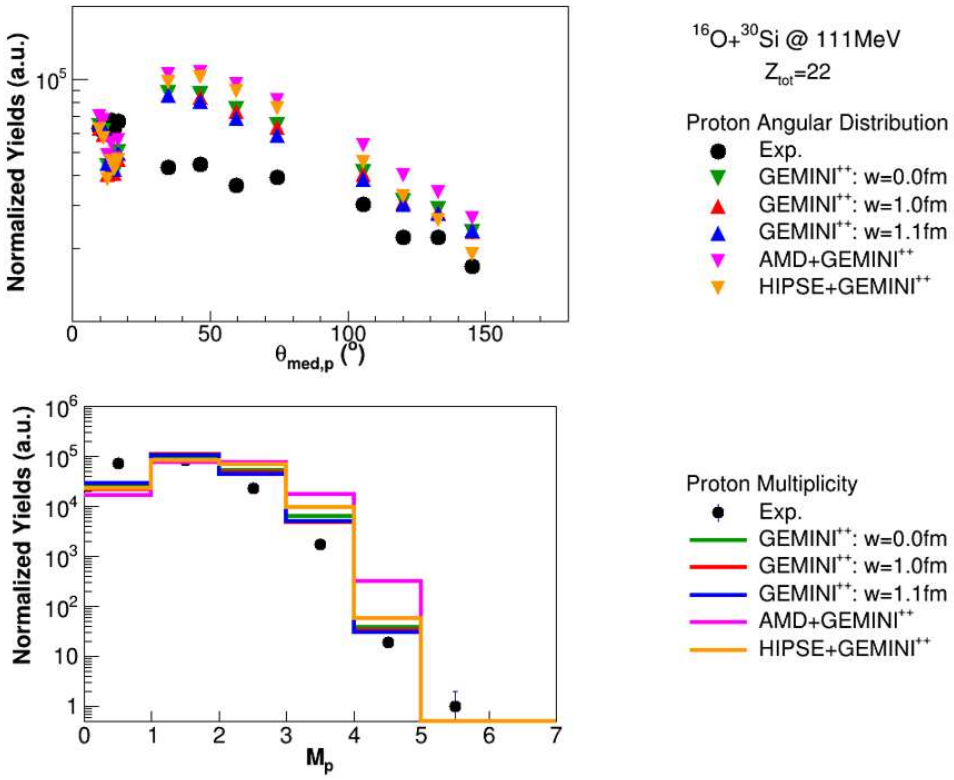

Figure 7.2: Comparison of experimental and simulated ($GEMINI^{++}$ with $w = 0.0$ fm in green, with $w = 1.0$ fm in red), $w = 1.1$ fm in blue; $AMD + GEMINI^{++}$ in pink; $HIPSE + GEMINI^{++}$ in orange) proton angular distribution and multiplicity for the reaction $^{16}O+^{30}Si$ at 111 MeV. The simulations are normalized to the relative number of residues $\left(\frac{\#_{res,exp}}{\#_{res,sim}}\right)$. See text for details.

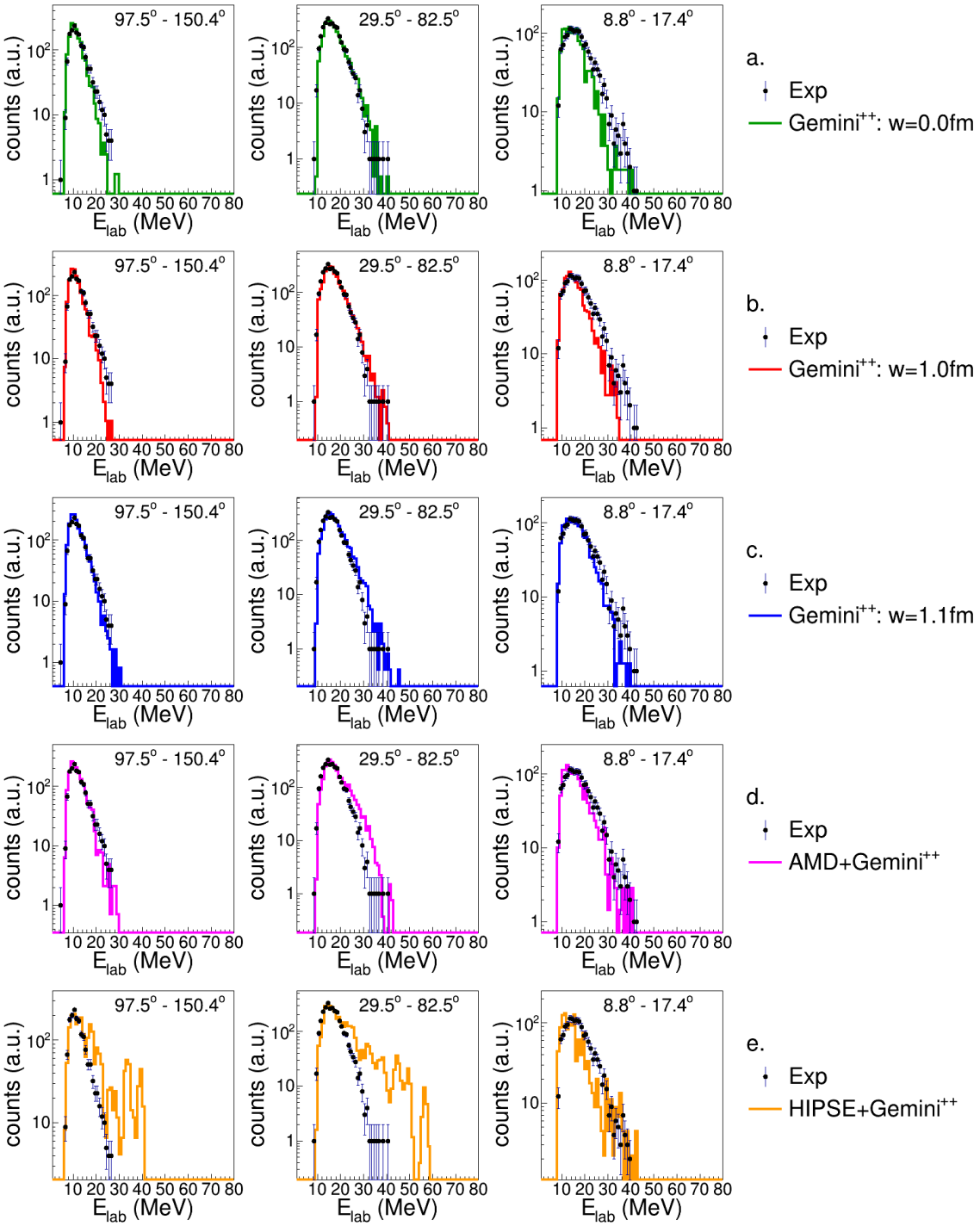

Figure 7.3: Same as in Fig. 7.1 but for deuteron. See text for details.

evident for **G00** and **AMD**, while it is reduced for **G10**. **HIPSE** is a distinct case; for the two above cited angular regions ($\theta_{lab} = 97.5^o \div 150.4^o$ and $\theta_{lab} = 29.5^o \div 82.5^o$), it presents longer and higher tails in proton energy spectra respect to both experimental and other simulations: we have checked in the simulation that these are due to the protons emitted in the primary stages of the reactions, prior to the decay. Even in the forward angles (RCo) all the five simulations shown a harder slope in the distributions. This difference of the emitted protons is also confirmed quantitatively by looking at their angular distribution (upper panel of Fig. 7.2), where the experimental protons are under-produced with respect to simulations in the $\theta_{lab} = 29.5^o \div 150.4^o$ angular range. The same information comes from the multiplicity plots (lower panel of Fig. 7.2) where almost all simulations overestimate events with $M_p \geq 2$. This is more evident in the case of the **AMD** simulation.

Different is the situation of the deuteron spectra (Fig. 7.3): in this case for the

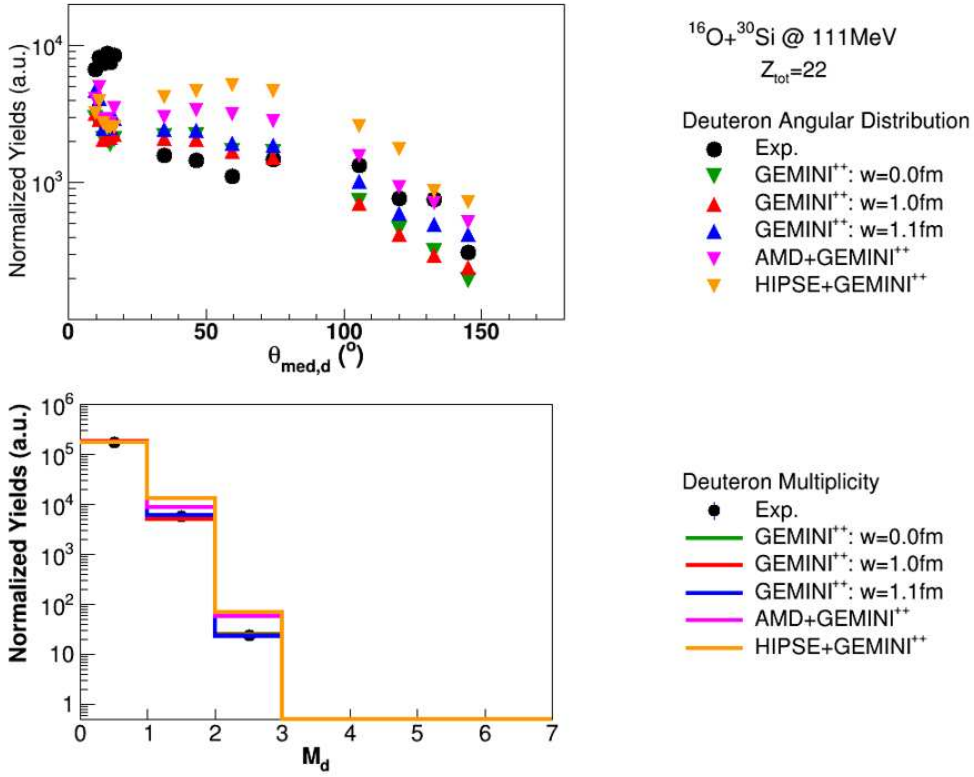

Figure 7.4: Same as in Fig. 7.2 but for deuteron. See text for details.

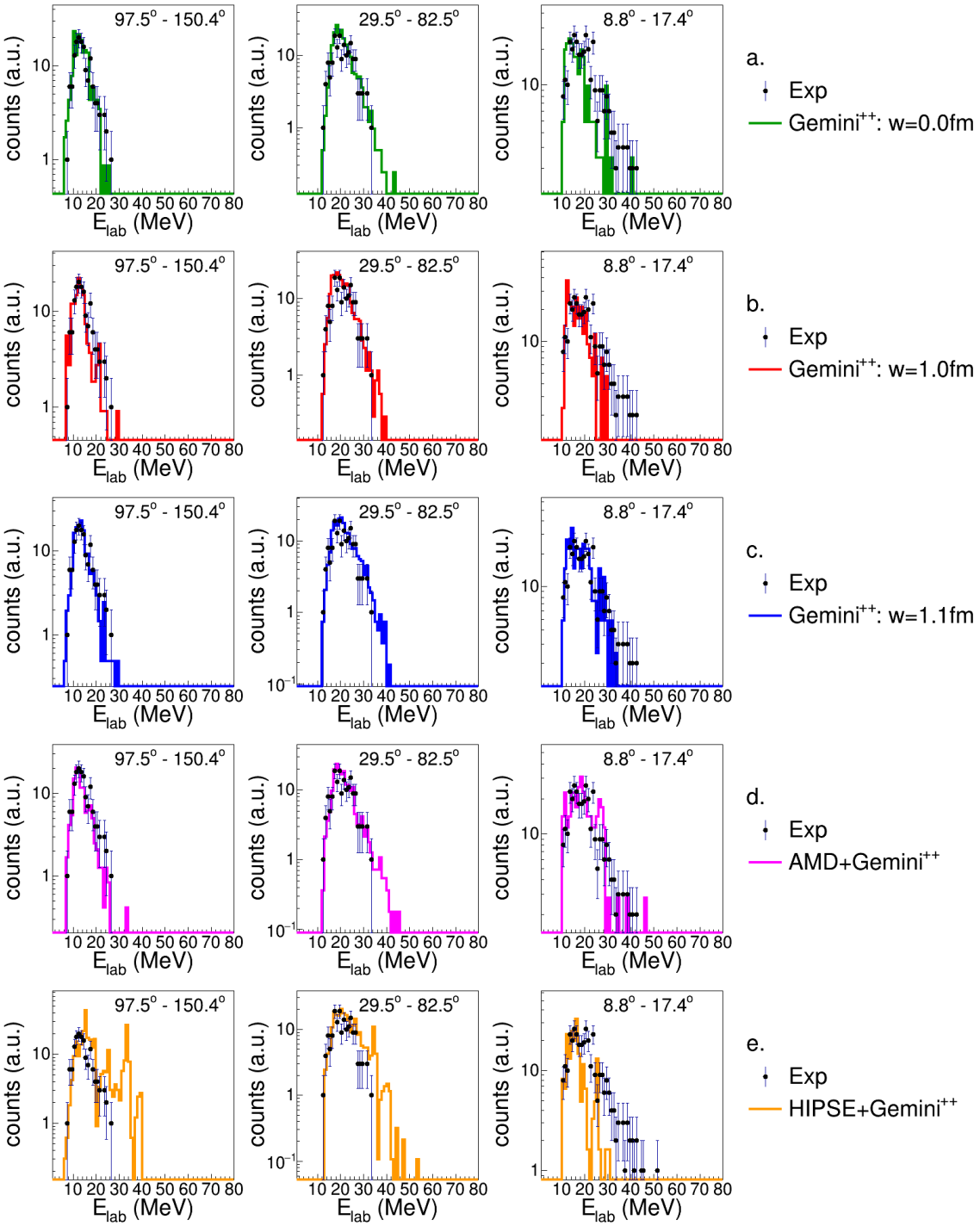

Figure 7.5: Same as in Fig. 7.1 but for tritons. See text for more details.

$GEMINI^{++}$ cases a very good reproduction of the spectra is obtained for $\theta_{lab} = 29.5^o \div 150.4^o$. In the forward direction only the **G11** case is well reproducing the data, while going from **G10** to **G00** the discrepancy is growing. On the contrary, **AMD** is able to reproduce well both the forward and the backward angular region, but discrepancies are observed in the intermediate angular region. Again, **HIPSE** spectra present longer and higher tails in the angular region: $\theta_{lab} = 29.5^o \div 150.4^o$; while, in the forward angles such simulation does not reproduce the experimental data, in a similar way to **G00** and **G10**. Looking at the angular distributions (upper panel of Fig. 7.4), in the forward direction, the experimental data show a peak, not reproduced by any model. In the intermediate angular region the three $GEMINI^{++}$ are close to the data, while the dynamical codes are far overestimating them. On the contrary, in the backward region, **AMD** is the closest. The deuteron multiplicity (lower panel of Fig. 7.4) are well accounted for by all calculations

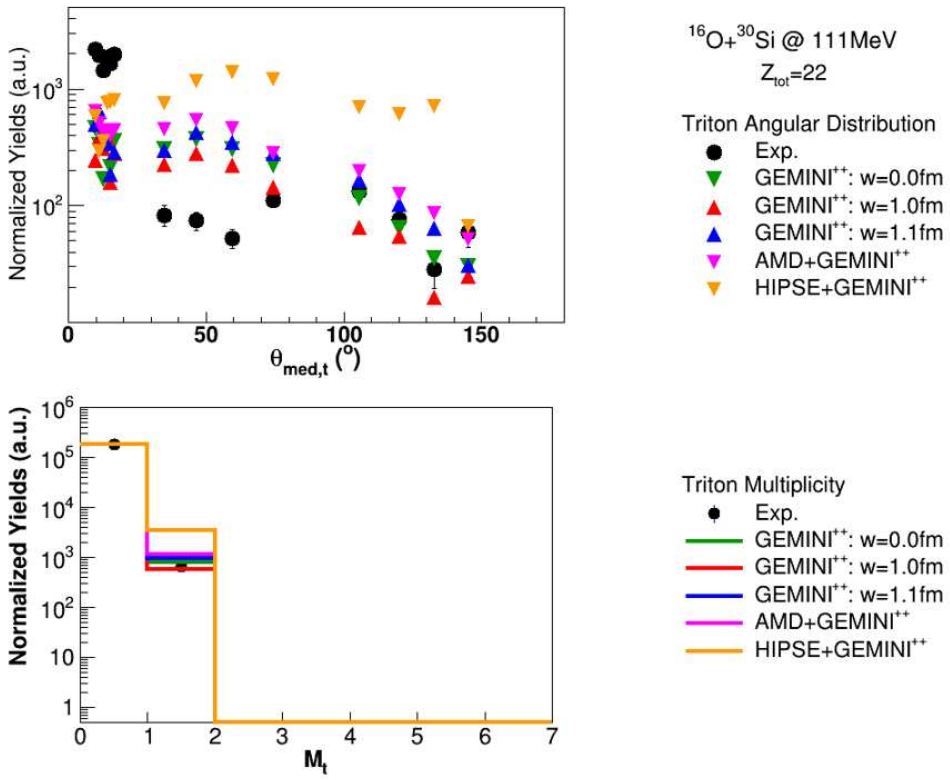

Figure 7.6: Same as in Fig. 7.2 but for tritons. See text for more details.

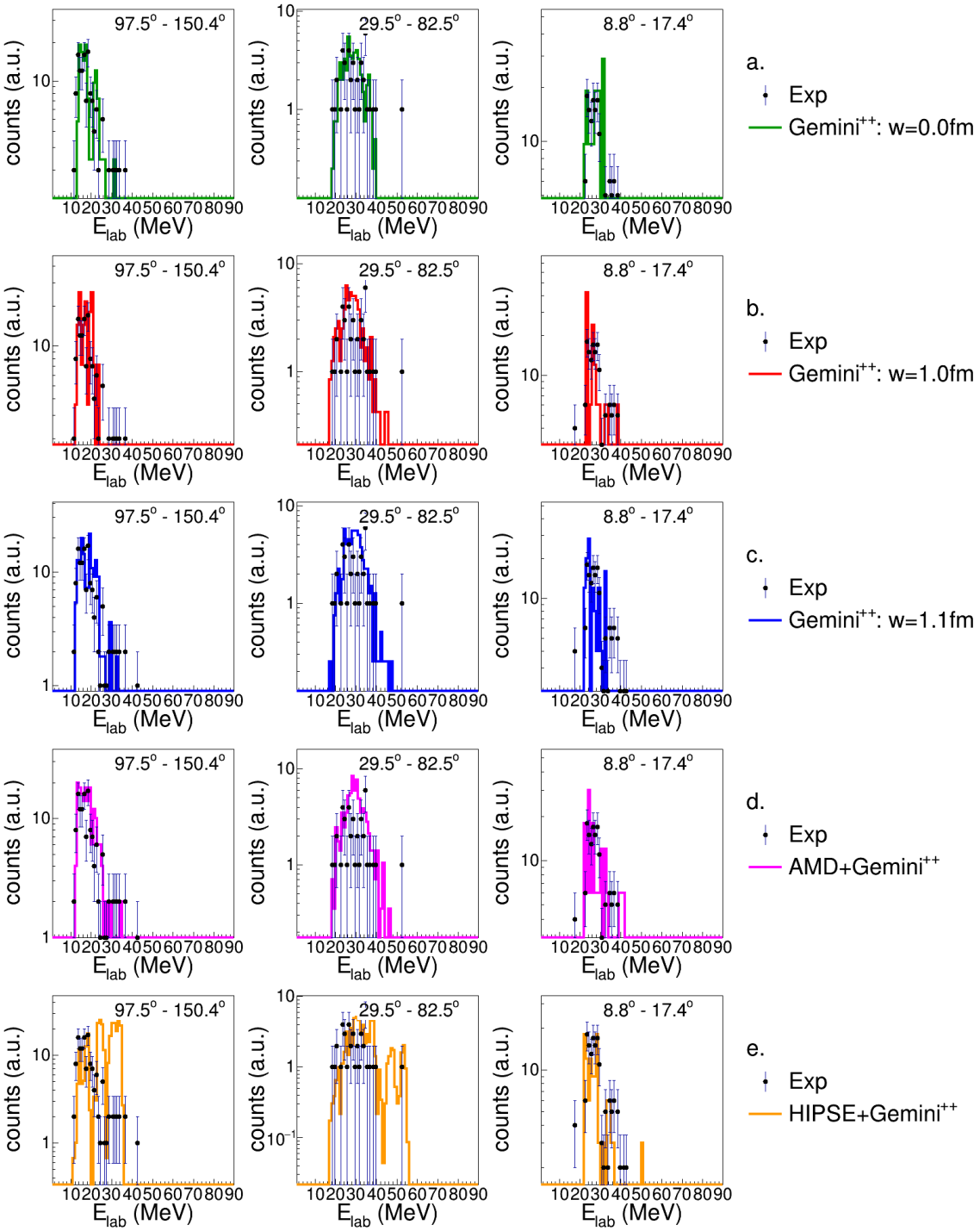

Figure 7.7: Same as Fig. 7.1 but for ^3He. See text for details.

with a slight overestimation of **AMD** and **HIPSE**.

The triton energy spectra shapes (Fig. 7.5) are well reproduced, apart from **HIPSE** and a small discrepancy with **G00** at forward angles. Triton experimental angular distribution (upper panel of Fig. 7.6) shows a privileged emission at forward angles and a flatter shape with respect to models predictions. All $GEMINI^{++}$ and **AMD** simulations reproduce quite well the experimental multiplicity (lower panel of Fig. 7.6), while **HIPSE** overestimates it. The low statistics of ^3He particles (Fig. 7.7) do not permit to draw conclusion on the differences between experiment and simulations. Looking at the angular distributions (upper panel of Fig. 7.8) we observe stronger focused emission of ^3He particles with respect to all simulations. **HIPSE** never reproduces the distribution, while $GEMINI^{++}$ and **AMD**, respectively overestimate the central region and underestimate the backward one. The multiplicity plots (lower panel of Fig. 7.8) are, instead, well

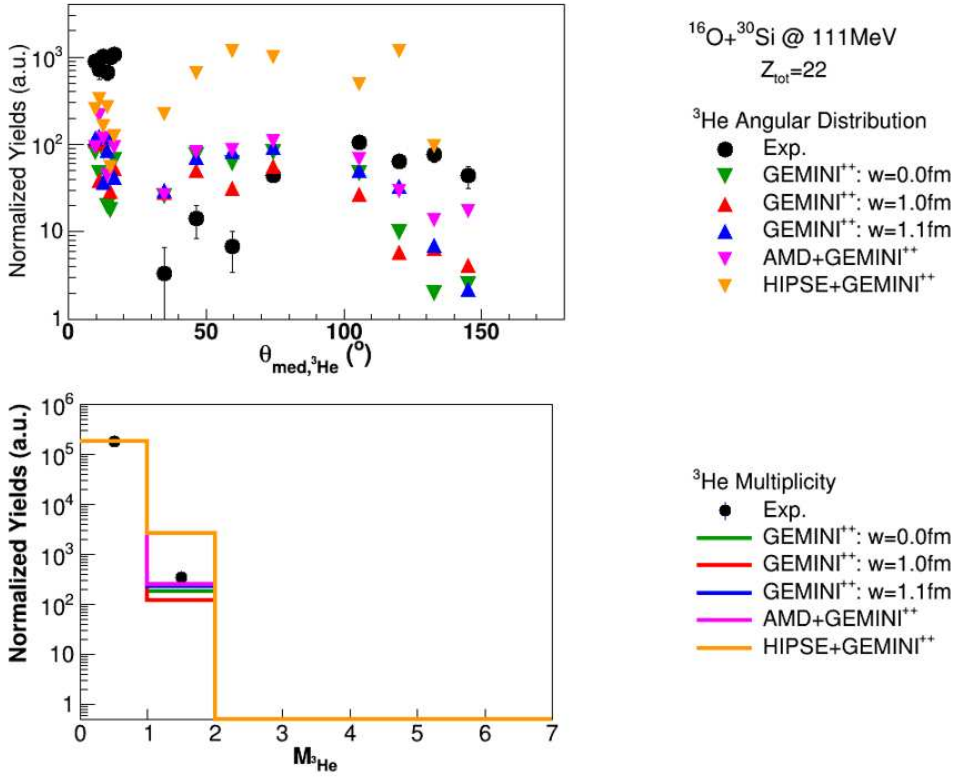

Figure 7.8: Same as Fig. 7.2 but for ^3He. See text for details.

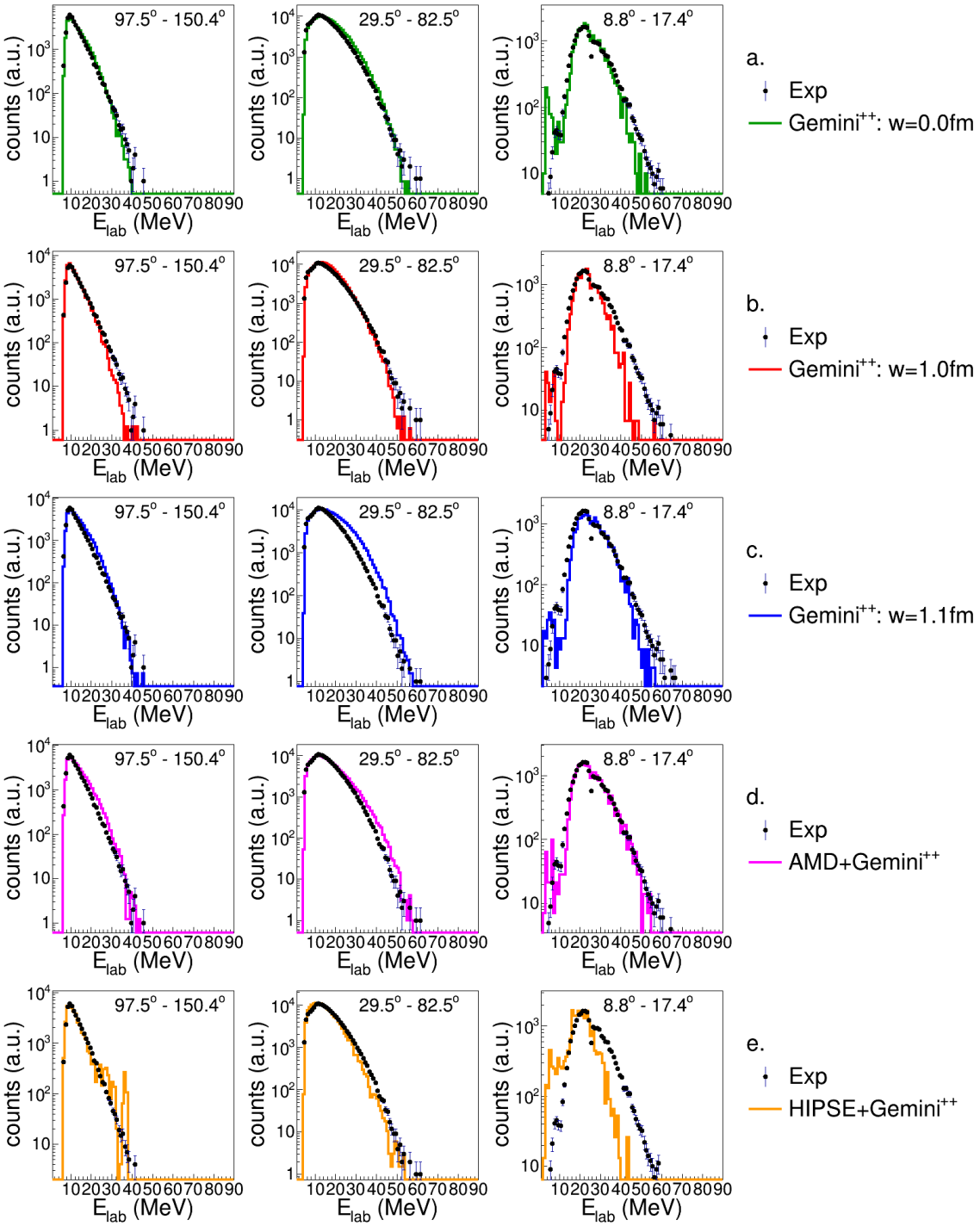

Figure 7.9: Same as in Fig. 7.1 but for the α-particles. See text for details.

accounted for by all simulations, except **HIPSE** which strongly overestimates it.

The α-particle energy spectra give some interesting information (see Fig. 7.9): **G00** well describes the experimental α energy distributions in the GARFIELD detection region and shows only a small difference, less than what observed previously in the $Z_{tot} \geq 18$ selection, in the RCo detection region. **G10** is much worse in the description of both backward ($\theta_{lab} = 97.5^o \div 150.4^o$) and of forward ($\theta_{lab} = 8.8^o \div 17.4^o$) angular regions. **G11** better describes the aforementioned regions, while the shape in the intermediate region is more rounded in the energy region 30 MeV $< E_{lab} <$ 50 MeV. **AMD** is somehow similar to **G11**, but it better reproduces all α energy spectra in the whole angular range. **HIPSE** describes the central angular region and the backward one, except for some peaks in the energy range 25 MeV $< E_{lab} <$ 40 MeV. At forward angles, it is worse than **G10**. The observations are confirmed by the angular distributions (upper panel of Fig. 7.10): **G10**

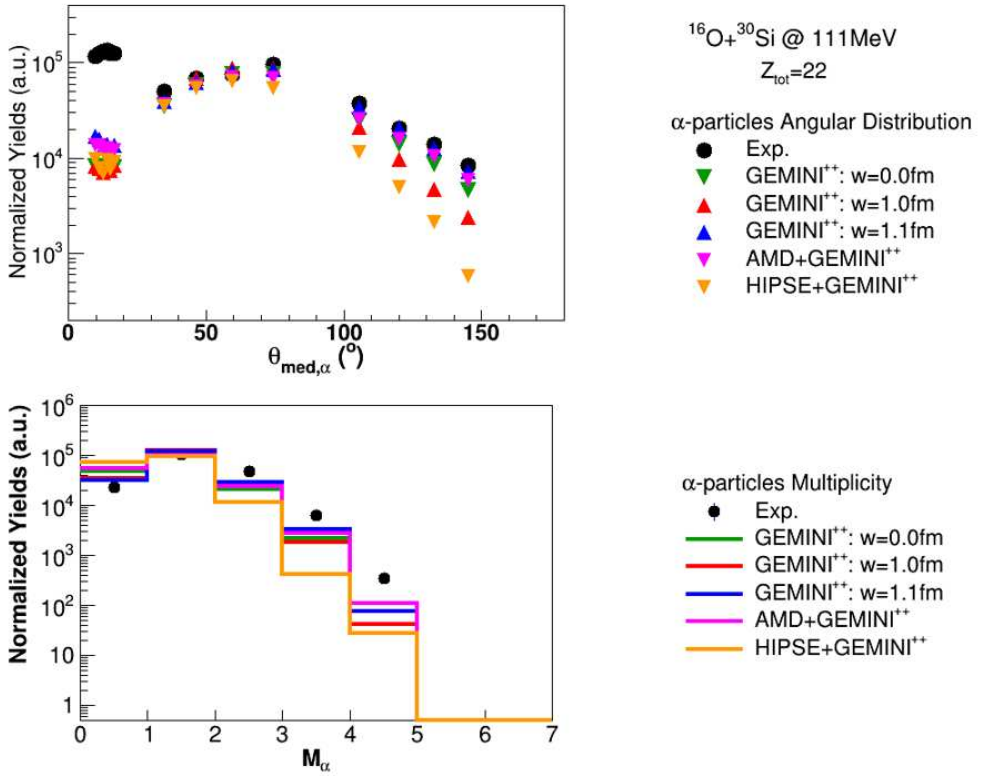

Figure 7.10: Same as in Fig. 7.2 but for the α-particles. See text for details.

and **HIPSE** do not reproduce neither the forward nor the backward directions, while the other three simuations are better describing the total distribution apart from the very forward angular region, totally underestimated. A slight underestimation of large multiplicities ($M_\alpha \geq 2$) is still observed in the multiplicity plot (lower panel of Fig. 7.10).

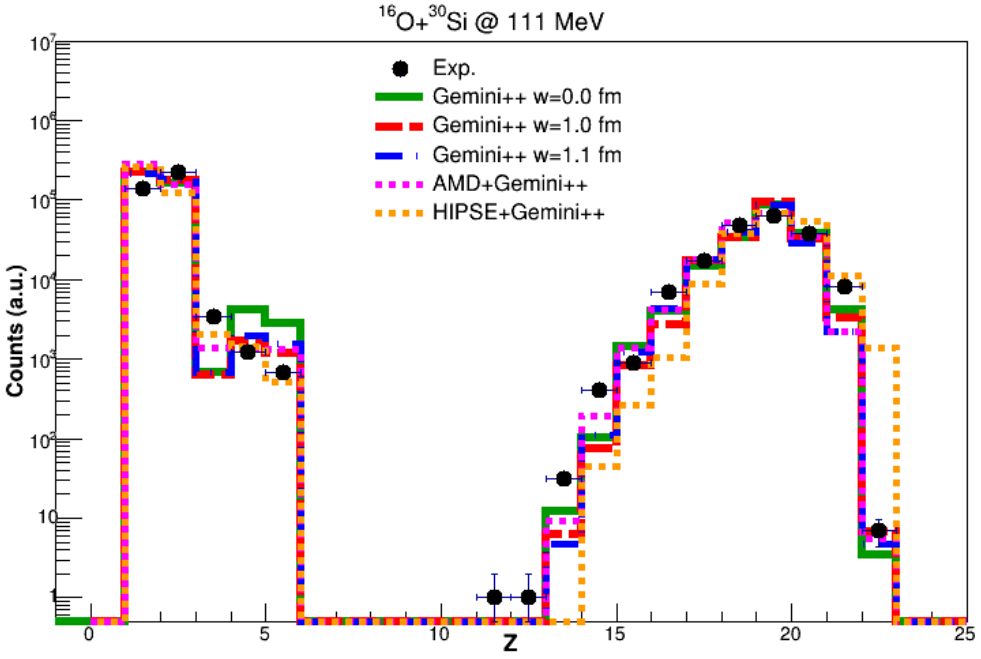

Figure 7.11: Comparison of normalized charge distribution between experimental data (black dots) and simulations with $GEMINI^{++}$ w=0.0 fm (green line), w=1.0 fm (red line), w=1.1 fm (blue line), with $AMD + GEMINI^{++}$ (pink line) and with $HIPSE + GEMINI^{++}$ (orange line) for the reaction $^{16}O +^{30} Si$ at 111 MeV. The simulations are normalized to the relative number of residues $\left(\frac{\#_{res,exp}}{\#_{res,sim}}\right)$. See text for details.

Finally, the charge distribution for the reaction $^{16}O +^{30} Si$ at 111 MeV is shown in Fig. 7.11; here, the experimental data (black dots) are well accounted for by the different simulations with some exceptions: the H-isotopes are slightly overestimated by all simulations; the three $GEMINI^{++}$ simulations largely underestimate the Li-isotopes, while the discrepancies are less important in the **AMD** and **HIPSE** cases; **G00** widely overproduces the Be and B-isotopes; while the Be-isotopes are well reproduced by all other simulations, B-isotopes are still not reproduced. The lower charge evaporation residues ($Z_{ER} < 17$) are

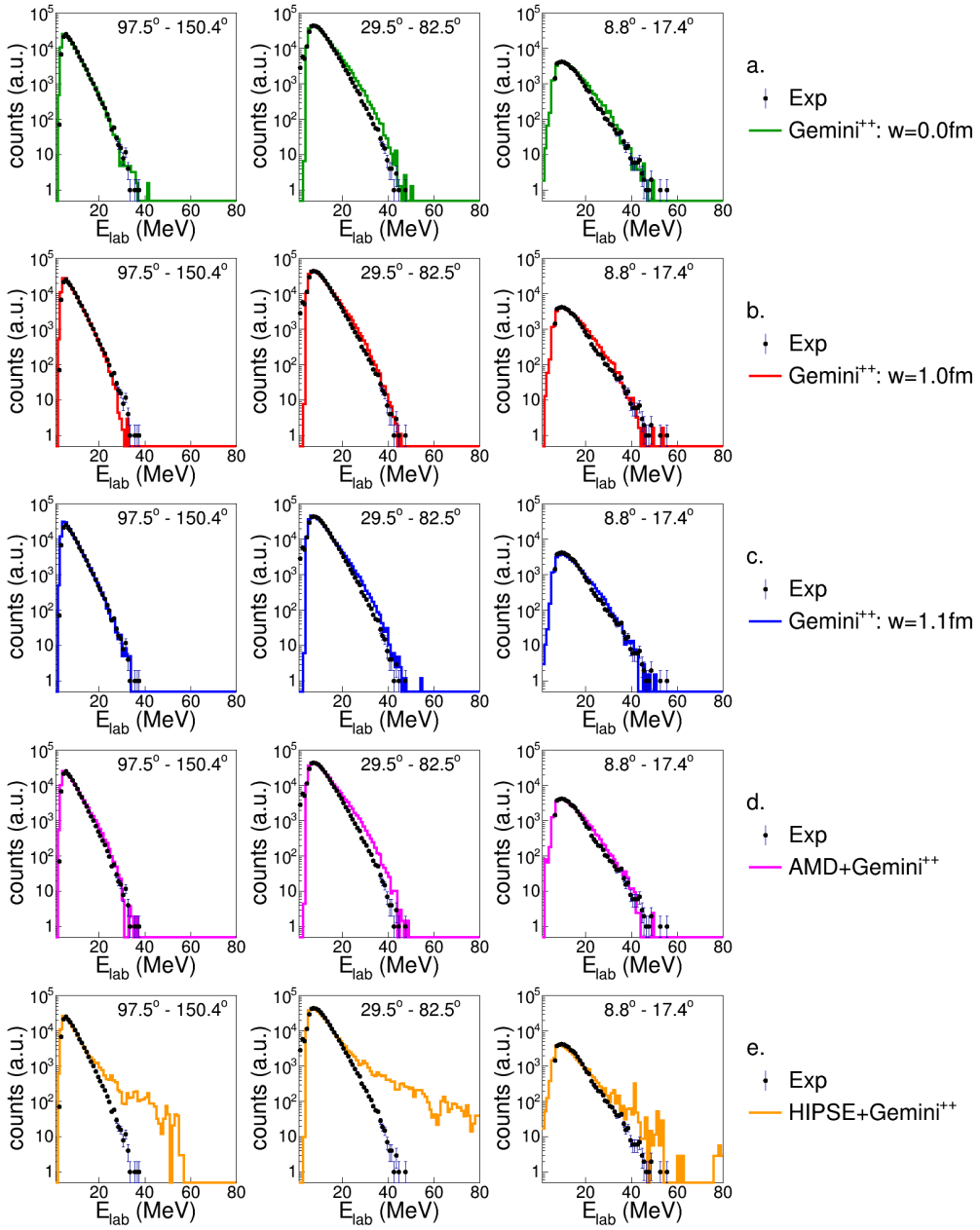

Figure 7.12: Comparison of normalized proton spectra between experimental data (black dots) and simulations made by $GEMINI^{++}$ $w = 0.0$ fm (green line), $w = 1.0$ fm (red line), $w = 1.1$ fm (blue line), by $AMD + GEMINI^{++}$ (pink line) and by $HIPSE + GEMINI^{++}$ (orange line) for the reaction $^{16}O + ^{30}Si$ at 128 MeV. The simulated spectra are normalized to the experimental maximum. See text for details.

underestimated by all the models. This is the case also of the Sc ($Z_{ER} = 21$), apart from **HIPSE**. Ti evaporation residue (Z=22) is strongly over-predicted by **HIPSE**. Anyhow, it will be not further studied, since it is in coincidence only with neutrons, which we do not measure. For sake of clarity, the presence of the Ti in the charge distribution is due to those events in which the only one fragment id detected in the forward direction.

7.2 $^{16}O+^{30}Si$ at 128 MeV.

In Fig. 7.12 the proton energy spectra are shown for the reaction $^{16}O+^{30}Si$ at 128MeV

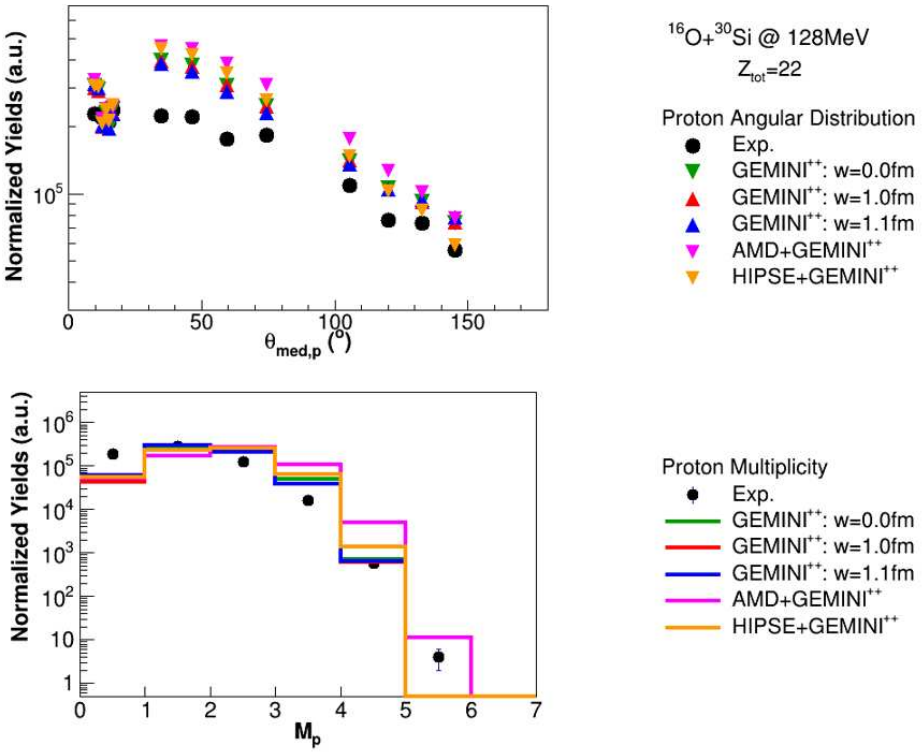

Figure 7.13: Comparison of experimental and simulated ($GEMINI^{++}$ with $w = 0.0$ fm in green, with $w = 1.0$ fm in red), $w = 1.1$ fm in blue; $AMD + GEMINI^{++}$ in pink; $HIPSE + GEMINI^{++}$ in orange) proton angular distribution and multiplicity for the reaction $^{16}O+^{30}Si$ at 128 MeV. The simulations are normalized to the relative number of residues $\left(\frac{\#_{res,exp}}{\#_{res,sim}}\right)$. See text for details.

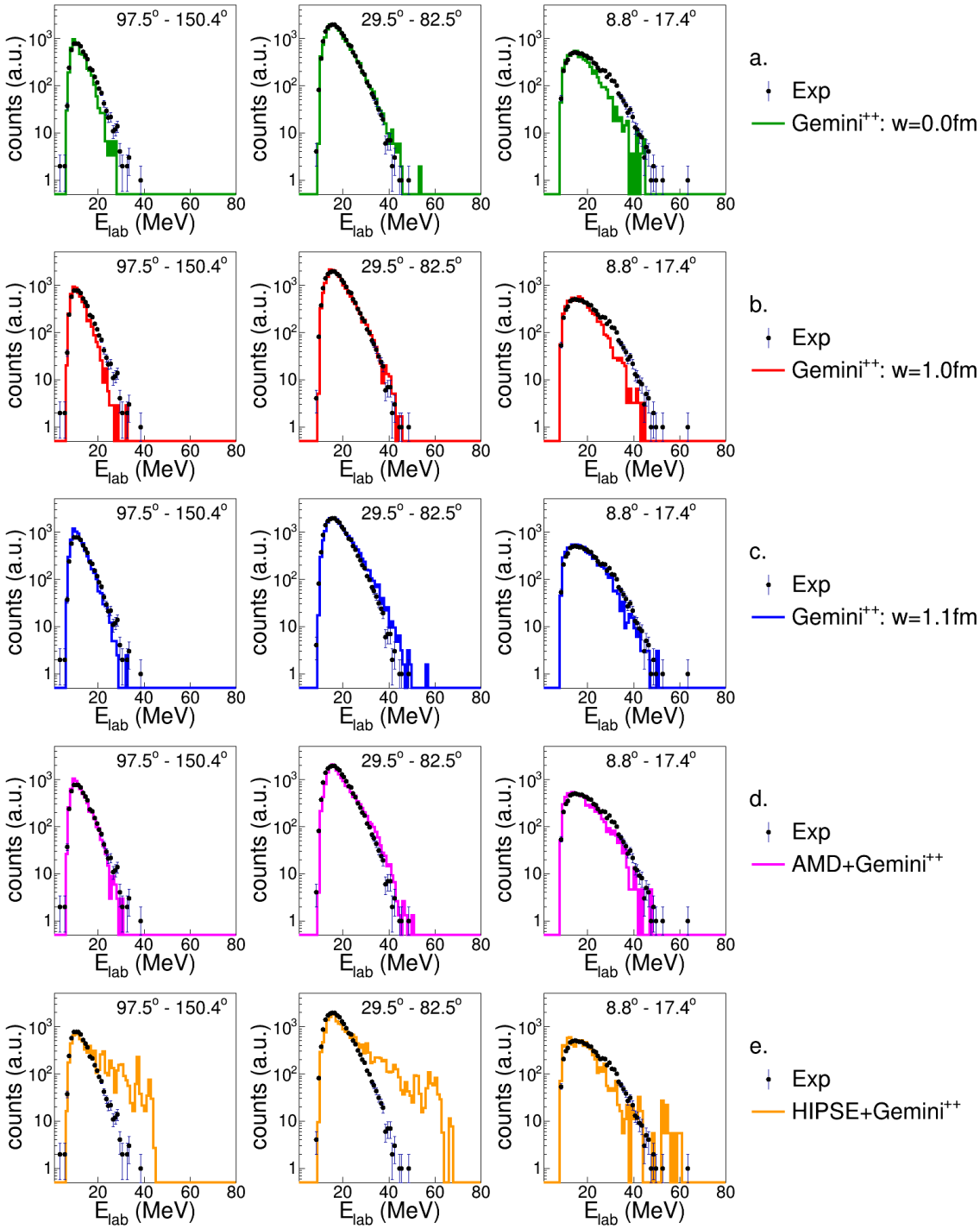

Figure 7.14: Same as in Fig. 7.12 but for deuteron. See text for details.

and compared with simulations, like in the previous case. At variance with the case at 111 MeV, here the protons are almost well described by all simulations, except by **HIPSE** for the same reasons explained above. Apart from **HIPSE** only a small overproduction is observed in the $\theta_{lab} = 29.5^o \div 82.5^o$ case for the **G00** (very feeble) and for the **AMD** cases. However, looking both to angular distributions and multiplicity spectra (Fig. 7.13), some overestimation both of $GEMINI^{++}$, all cases, and of the two dynamical codes appears evident. Only in the forward part of the angular distribution (RCo), experimental data are reasonably reproduced.

Deuterons energy spectra (Fig. 7.14) are, on the contrary, well accounted for by **G11** and **AMD**, while **G10** and **G00** underestimate both the backward angles and the very forward ones; **HIPSE** presents the same behavior mentioned in the protons case. The better reproduction of the experimental situation by **G11** and **AMD** is also shown in the

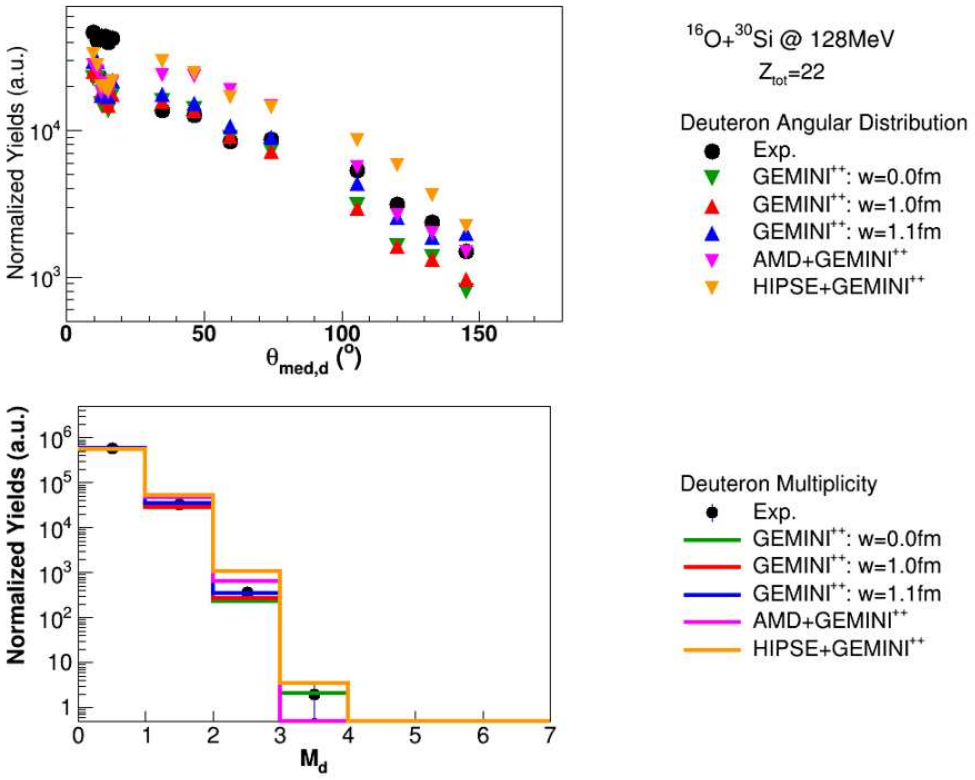

Figure 7.15: Same as in Fig. 7.13 but for deuteron. See text for details.

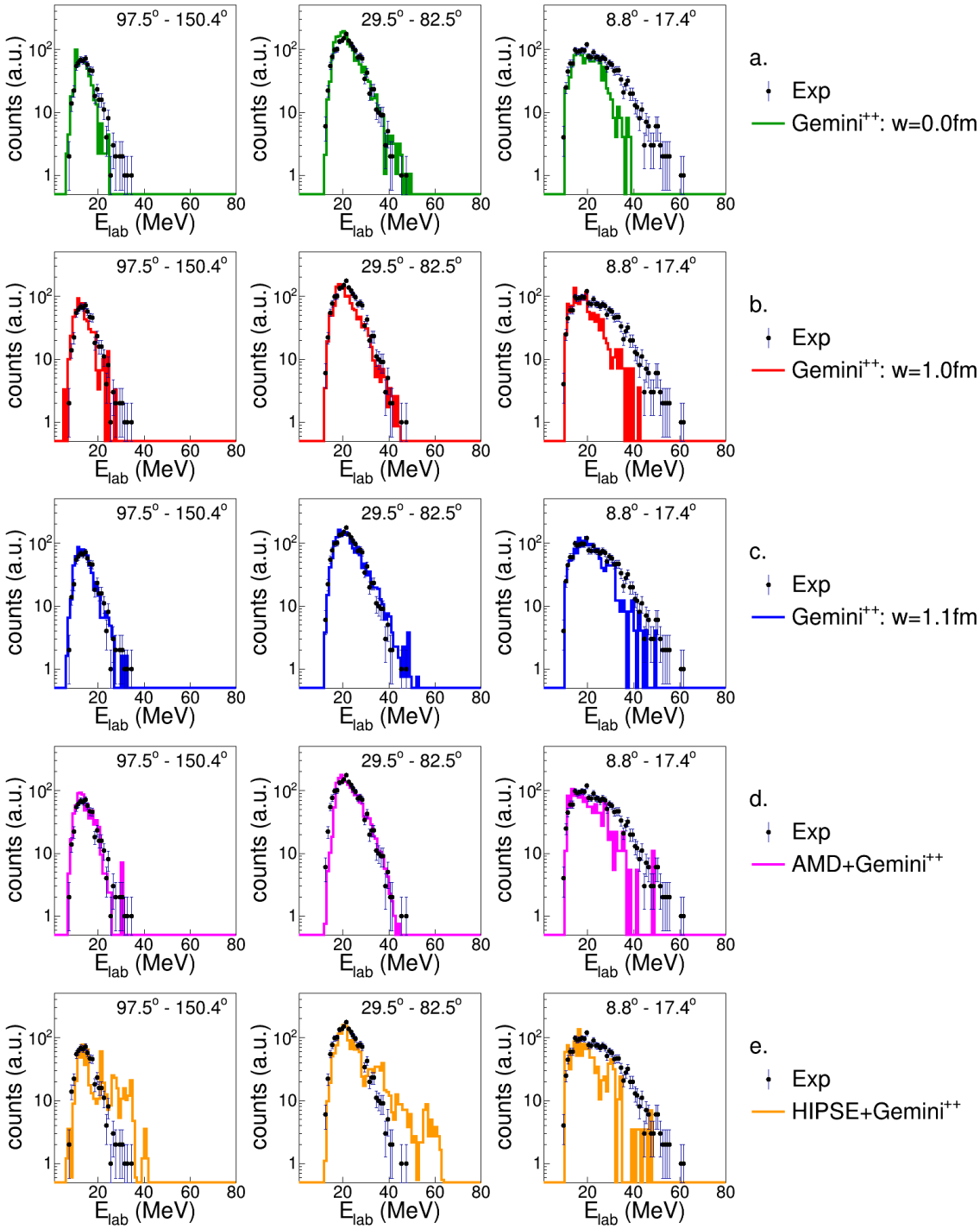

Figure 7.16: Same as in Fig. 7.12 but for triton. See text for details.

angular distribution (upper panel of Fig. 7.15), apart from the very forward angular region (RCo). At variance, even if **HIPSE** and **AMD** tend to follow a peaked distribution at the forward angles, no simulation is able to properly describe the experimental findings. Deuteron multiplicity (lower panel of Fig. 7.15) are well simulated by $GEMINI^{++}$ alone, while the two dynamical codes are less in agreement.

The triton energy spectra (Fig. 7.16) are well described by all the codes in the $\theta_{lab} = 29.5^o \div 150.4^o$, apart from **HIPSE**. The forward angles are not reproduced by any simulation, with **G11** the closest. In the triton angular distribution, as it is shown in the upper panel of the Fig. 7.17, the forward angular region ($\theta_{lab} = 8.8^o \div 17.4^o$) is completely underestimated. The central angular region is largely overestimated by dynamical codes, while by a smaller amount by $GEMINI^{++}$ alone. The better agreement is obtained at backward angles by **G00**. $GEMINI^{++}$ reproduces the multiplicity $M_t = 1$ (lower

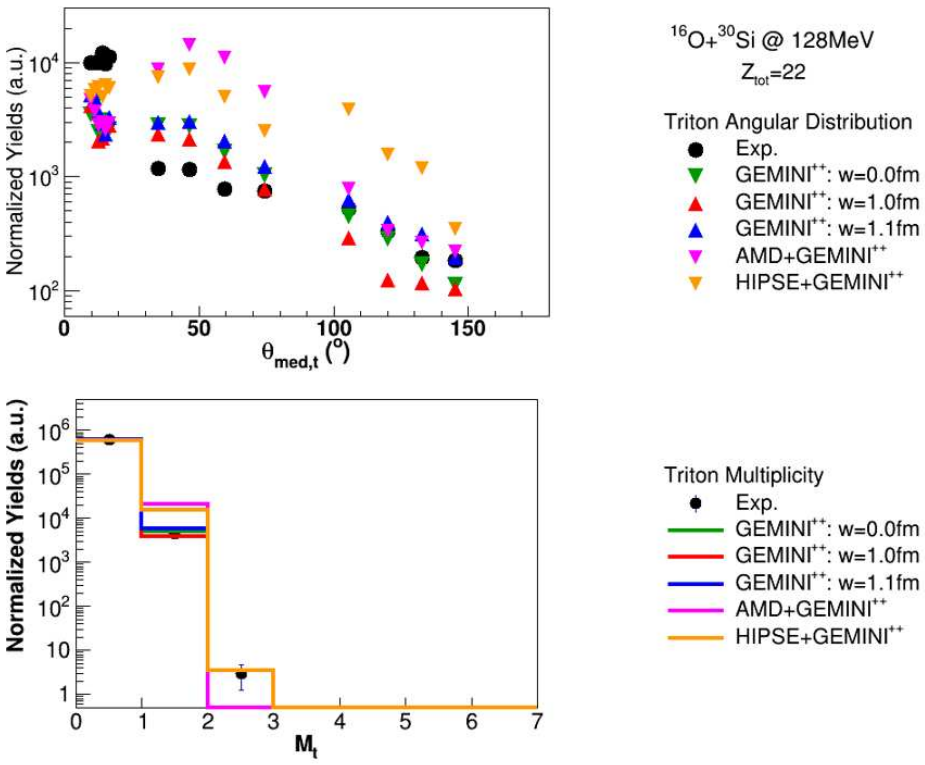

Figure 7.17: Same as in Fig. 7.13 but for triton. See text for details.

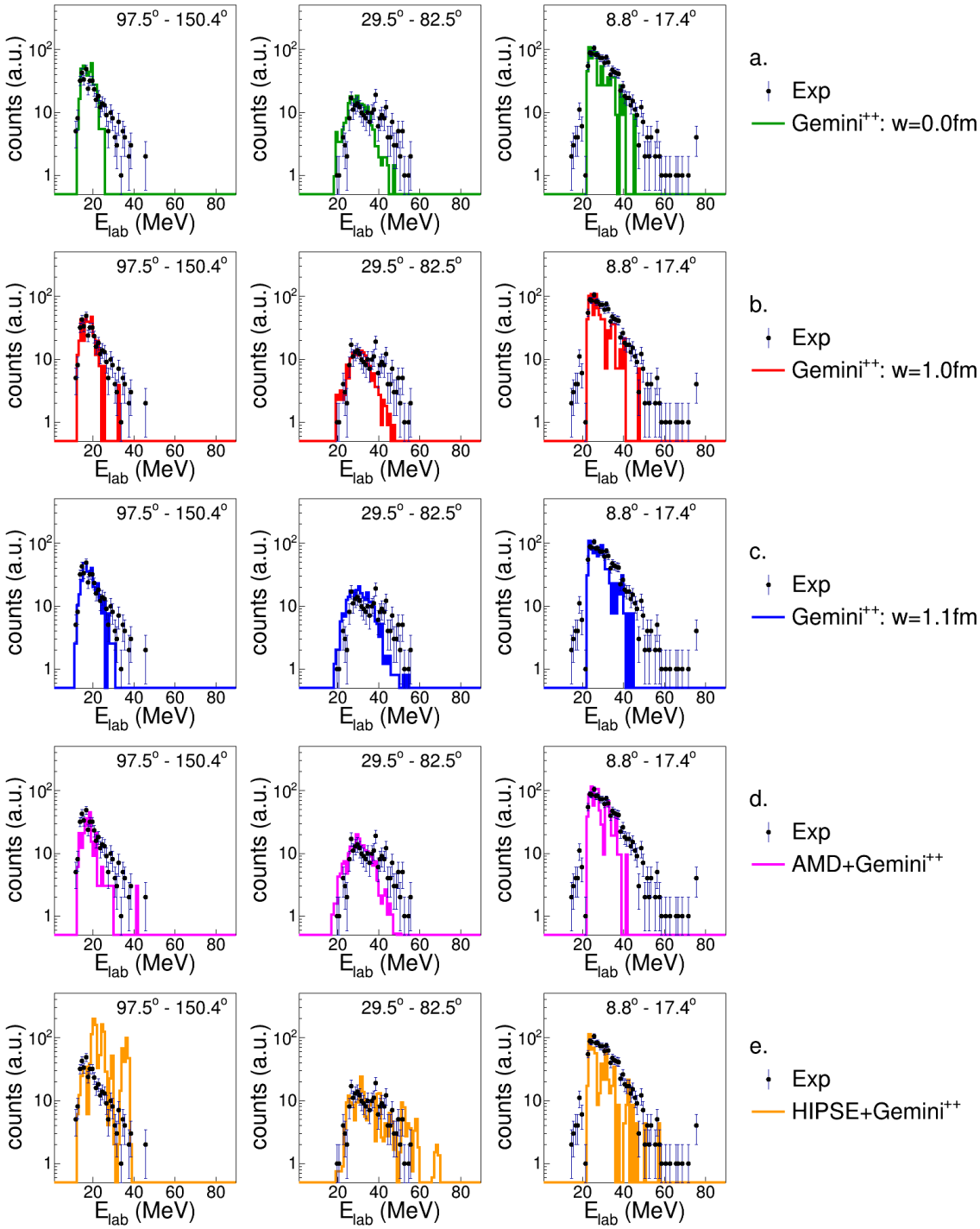

Figure 7.18: Same as in Fig. 7.12 but for ^3He. See text for details.

panel of Fig. 7.17), while $M_t = 2$ is only predicted by **HIPSE**, even though statistic is not really significant.

At this energy the ^3He energy spectra have slightly more statistics, which permits to see differences from simulations: **G00** and **G10** are not well accounting for the central angular region spectral shape, while they are reasonably good in the backward and forward regions. **G11** is the best in all the angular region, while **AMD** seems to underestimate slightly the experimental distributions everywhere. **HIPSE** reproduces quite well the central and forward angular regions, while at backward angles it presents the usual peaked shape. The experimental angular distribution of ^3He (upper panel of Fig. 7.19) shows a somehow strange behavior: while in the very forward region there is the usual overproduction, which may agree with a possible fast emission, the other part of the angular distribution is almost flat, eventually growing slightly going towards the backward angles. This is at variance

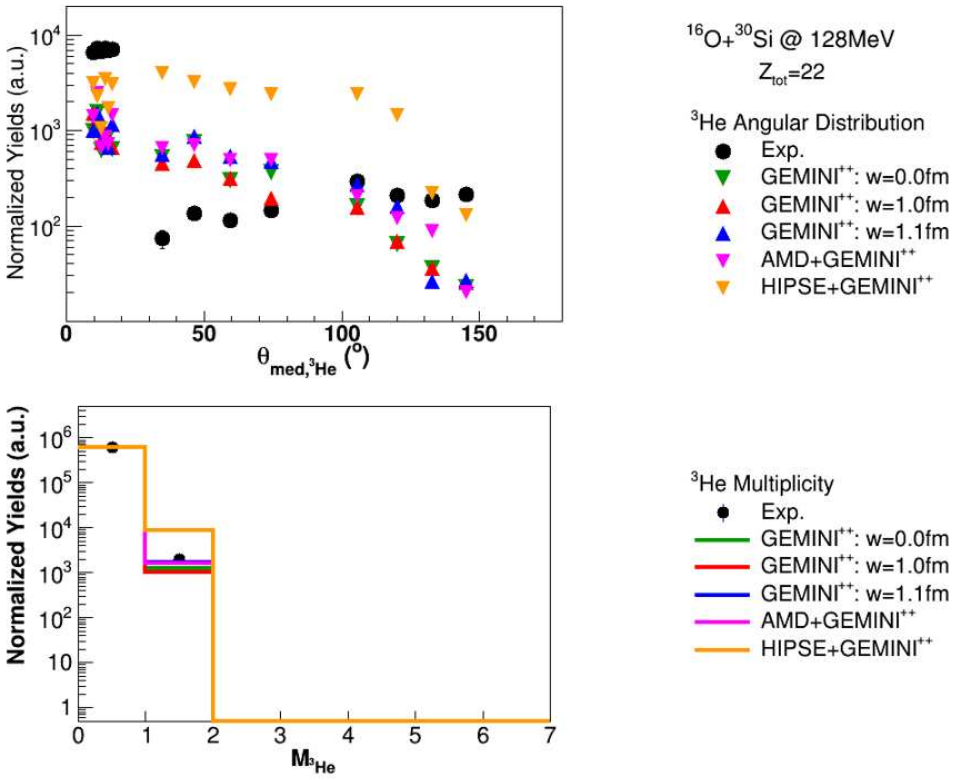

Figure 7.19: Same as in Fig. 7.13 but for ^3He. See text for details.

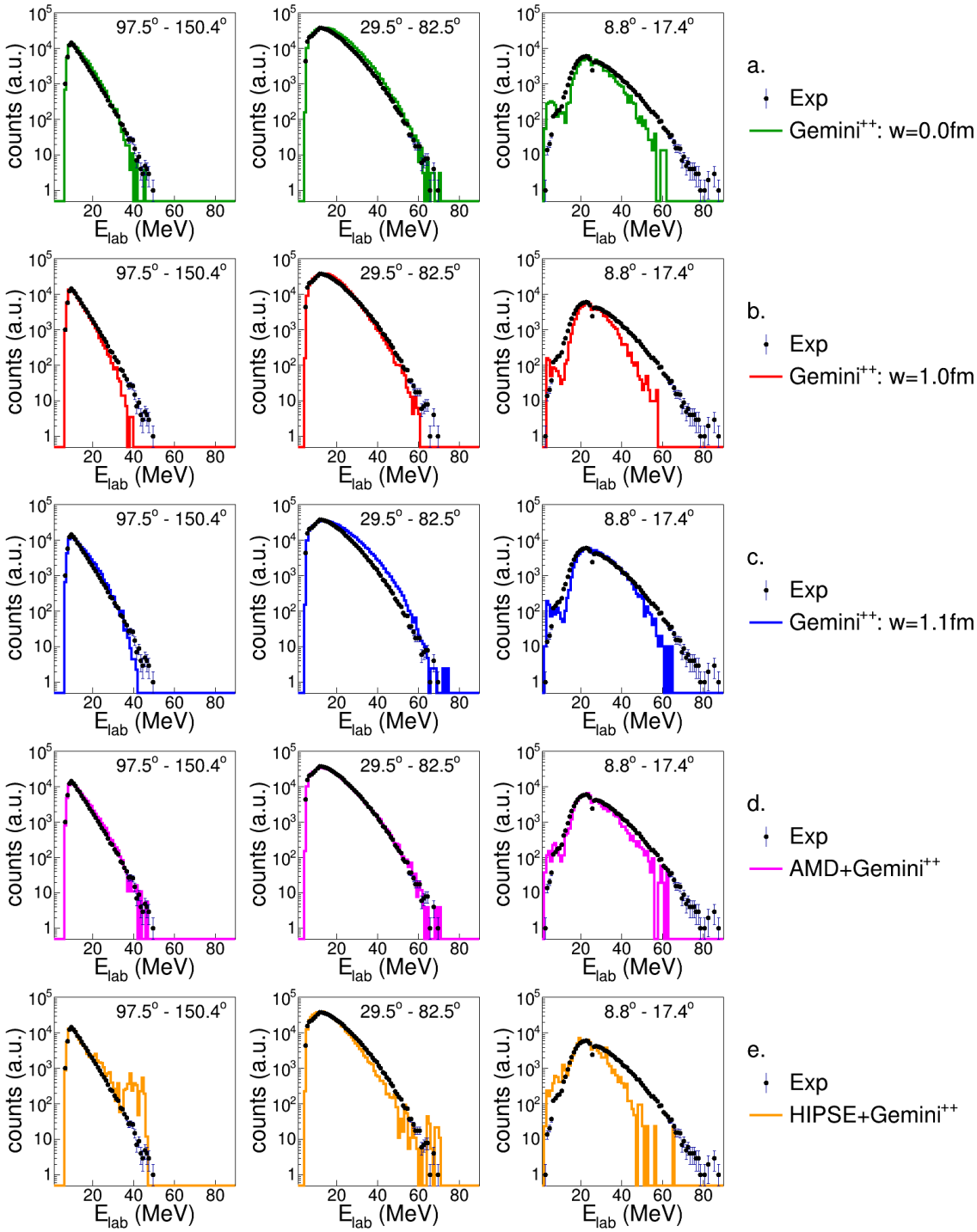

Figure 7.20: Same as in Fig. 7.12 but for α-particles. See text for details.

with what expected by simulations with a growing angular distribution towards the most forward laboratory angles. Multiplicity distribution (lower panel of Fig. 7.19) are well accounted for by all simulations, except by **HIPSE**, which overestimates the $M_{^3He} = 1$.

The α-particles energy spectra are very well accounted for by **AMD** simulated data, where a very small deviation is only observed at very forward angles. On the contrary, $GEMINI^{++}$ alone is never able to account for the spectra in the whole angular region: **G00** is not describing at all the RCo angles ($\theta_{lab} = 8.8^o \div 17.4^o$) and slightly overestimate the central angular region ($\theta_{lab} = 29.5^o \div 82.5^o$); **G10** is not reproducing both very forward angles and backward angles ($\theta_{lab} = 97.5^o \div 150.4^o$); **G11** reproduces no angular region, even if with smaller disagreements in the forward and backward region with respect to the other two $GEMINI^{++}$ simulations. An overproduction in the energy region $E_{lab} = 35 \div 60$ MeV is observed in the intermediate region for the **G11** calculation, as observed at lower

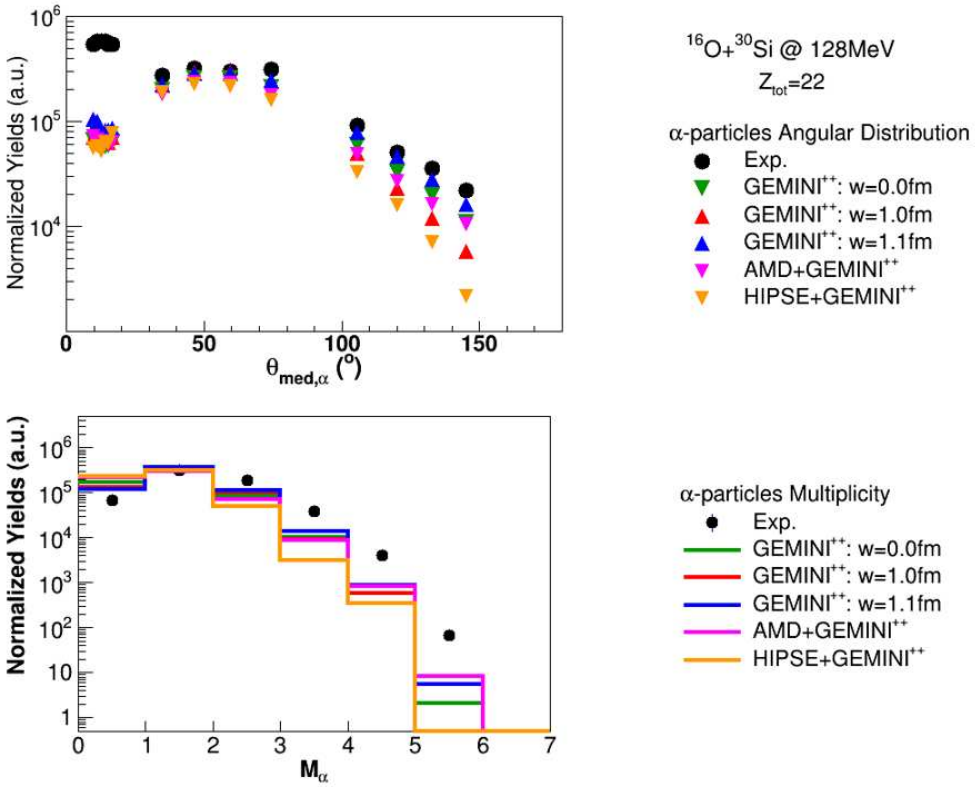

Figure 7.21: Same as in Fig. 7.13 but for α-particles. See text for details.

energy. **HIPSE** underestimates the energy spectra for $\theta_{lab} = 8.8^o \div 82.5^o$ and at backward angles it shows some peaks in the energy region $E_{lab} = 30 \div 50$ MeV. Angular distribution (upper panel of Fig. 7.21) is almost well accounted for in the intermediate angular region, while in the backward region the best reproduction is obtained by **G11**, even if still a little bit lower in yield. All other simulations are visibly underestimating the experimental yields. Moreover, no calculation is able to reproduce the forward peak at small angles. The multiplicity distribution (lower panel of Fig. 7.21) is again not accounted for at $M_\alpha \geq 3$ for all models.

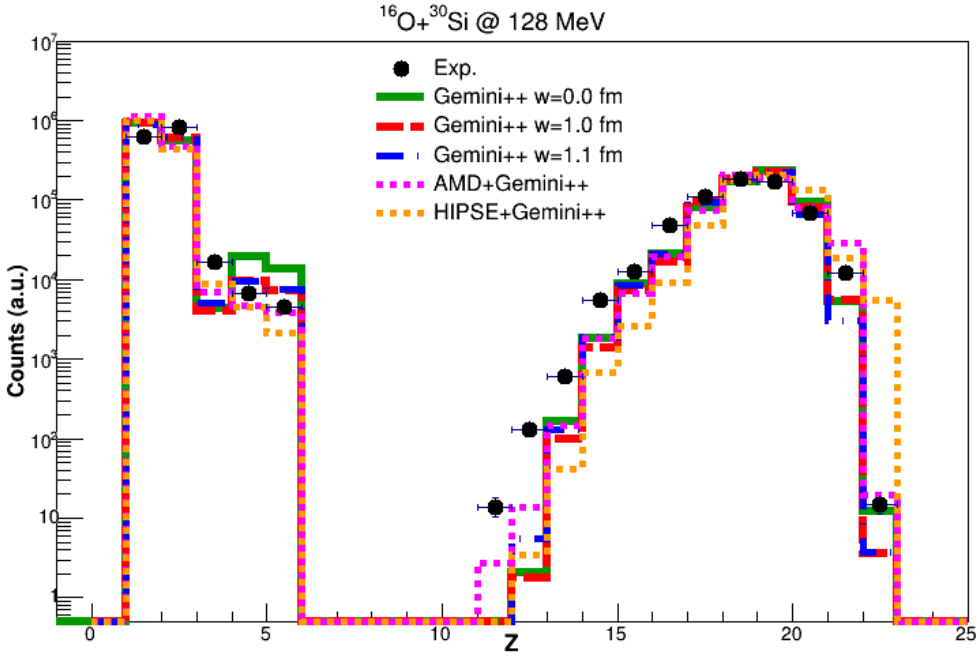

Figure 7.22: Comparison of normalized charge distribution between experimental data (black dots) and simulations made with $GEMINI^{++}$ w=0.0 fm (green line), w=1.0 fm (red line), w=1.1 fm (blue line), with $AMD+GEMINI^{++}$ (pink line) and with $HIPSE+GEMINI^{++}$ (orange line) for the reaction $^{16}O+^{30}Si$ at 128 MeV.

In Fig. 7.22, the charge distribution for the reaction $^{16}O+^{30}Si$ at 128 MeV is shown; the global trend is very similar to the previous case (same reaction participants than in the previous case, but with a higher bombarding energy), but some dissimilarities are also present: the Be-isotopes are not reproduced, while the B-isotopes are well accounted for

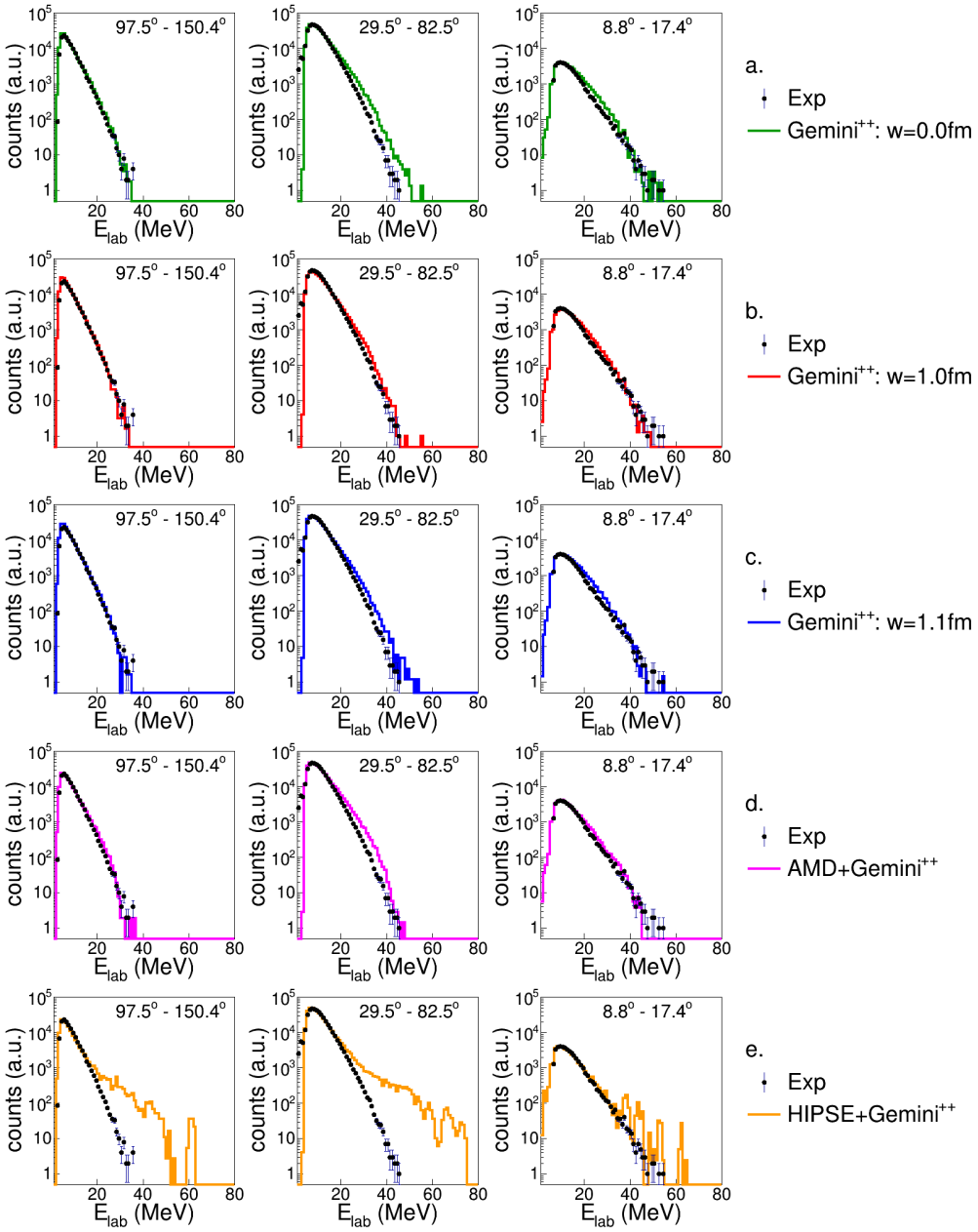

Figure 7.23: Comparison of normalized proton spectra between experimental data (black dots) and simulations made by $GEMINI^{++}$ $w = 0.0$ fm (green line), $w = 1.0$ fm (red line), $w = 1.1$ fm (blue line), by $AMD + GEMINI^{++}$ (pink line) and by $HIPSE + GEMINI^{++}$ (orange line) for the reaction $^{18}O + ^{28}Si$ at 126 MeV. The simulated spectra are normalized to the experimental maximum. See text for details.

by **AMD** and underestimated by **HIPSE**. The ER, with charge lower than 17, are widely underestimated by all simulations. The Sc-residues ($Z = 21$) are overestimated by the two dynamical simulations and underestimated by statistical ones. In the present case, the Ti ($Z = 22$) yield is reproduced only by the **G00** case.

7.3 $^{18}O + ^{28}Si$ at 126 MeV.

In Fig. 7.23 the proton energy spectra are compared with simulations, like in the previous cases. At variance with the previous case, which should be very similar since they

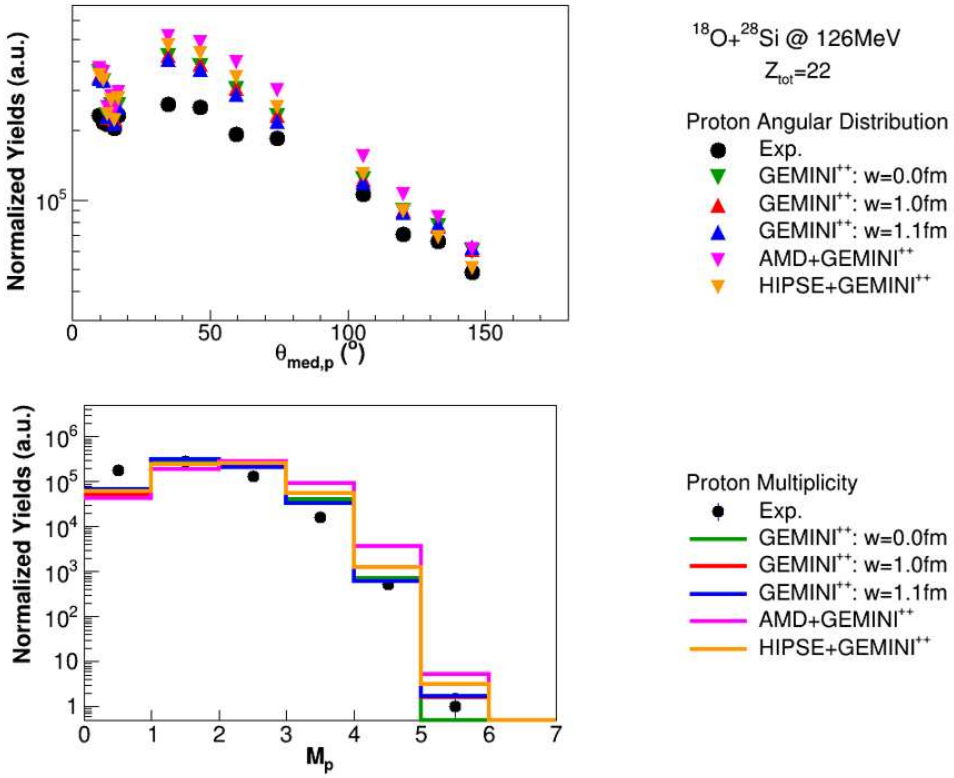

Figure 7.24: Comparison of experimental and simulated ($GEMINI^{++}$ with $w = 0.0$ fm in green, with $w = 1.0$ fm in red), $w = 1.1$ fm in blue; $AMD + GEMINI^{++}$ in pink; $HIPSE + GEMINI^{++}$ in orange) proton angular distribution and multiplicity for the reaction $^{18}O + ^{28}Si$ at 126 MeV. The simulations are normalized to the relative number of residues $\left(\frac{\#_{res,exp}}{\#_{res,sim}}\right)$. See text for details.

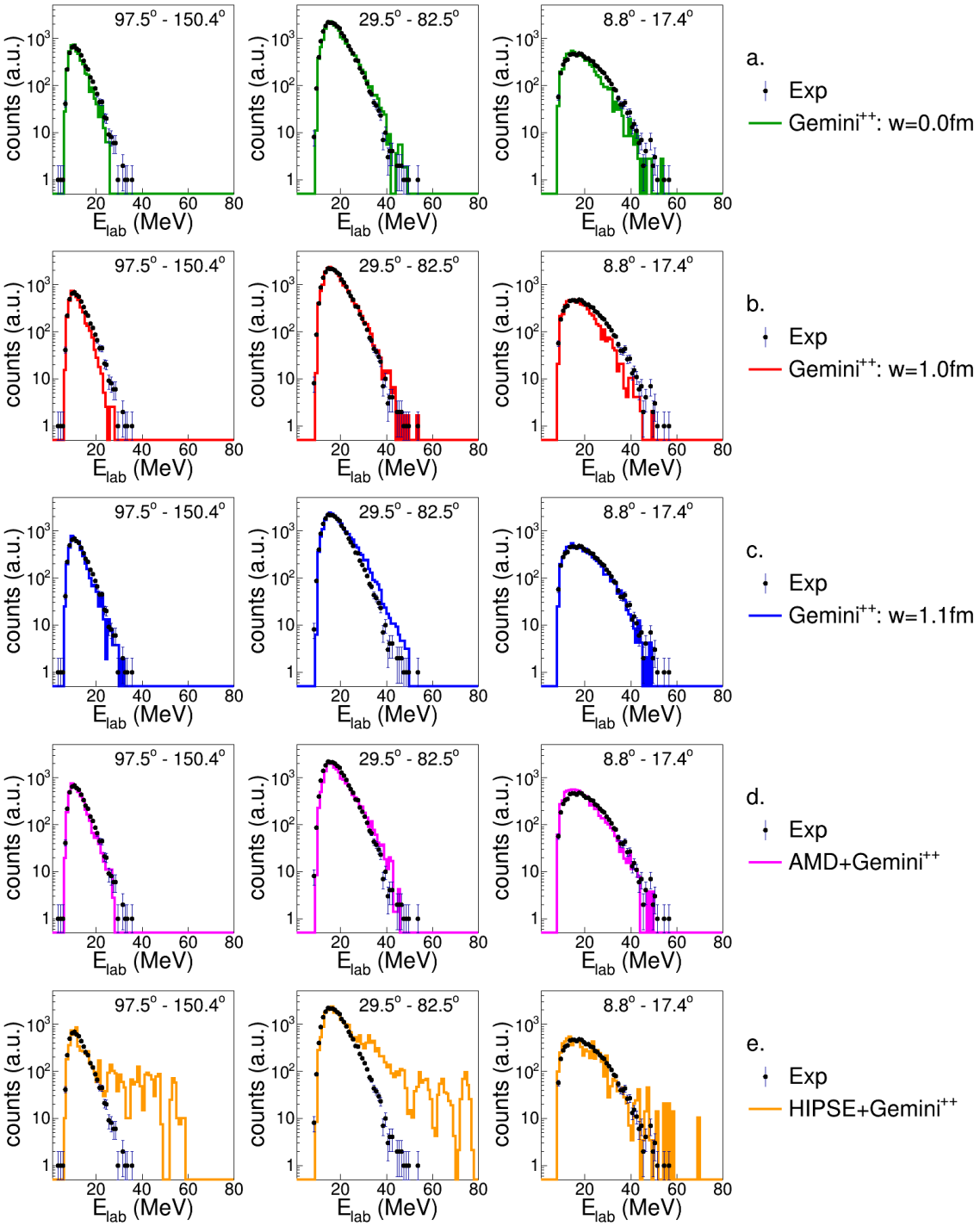

Figure 7.25: Same as in Fig. 7.23 but for deuteron. See text for details.

are the two reactions bringing to same excitation energy in the $^{46}Ti^*$ compound nucleus, in case to same excitation energy in the $^{46}Ti^*$ compound nucleus, in case of complete fusion, here the proton energy spectra are well described by **G10**. On the contrary, they are not described, especially in the region $\theta_{lab} = 29.5^o \div 82.5^o$ by the **G00** case. Only a small overproduction is observed in the $\theta_{lab} = 29.5^o \div 82.5^o$ case for the **G11** (very feeble) and for the **AMD** case. Again, **HIPSE** fails in the description of the experimental data; its energy spectra has longer and higher tails. Like in the previous reaction, looking to angular distributions spectra (Fig. 7.24), some overestimation is clear both when looking to $GEMINI^{++}$ alone and, larger, when compared to the dynamical codes simulations in the central angular region. Both backward and forward regions are better described, differently from the previous reaction. Regarding the multiplicity spectra, they are very similar to the findings of the previous reaction, with an overestimation of proton higher

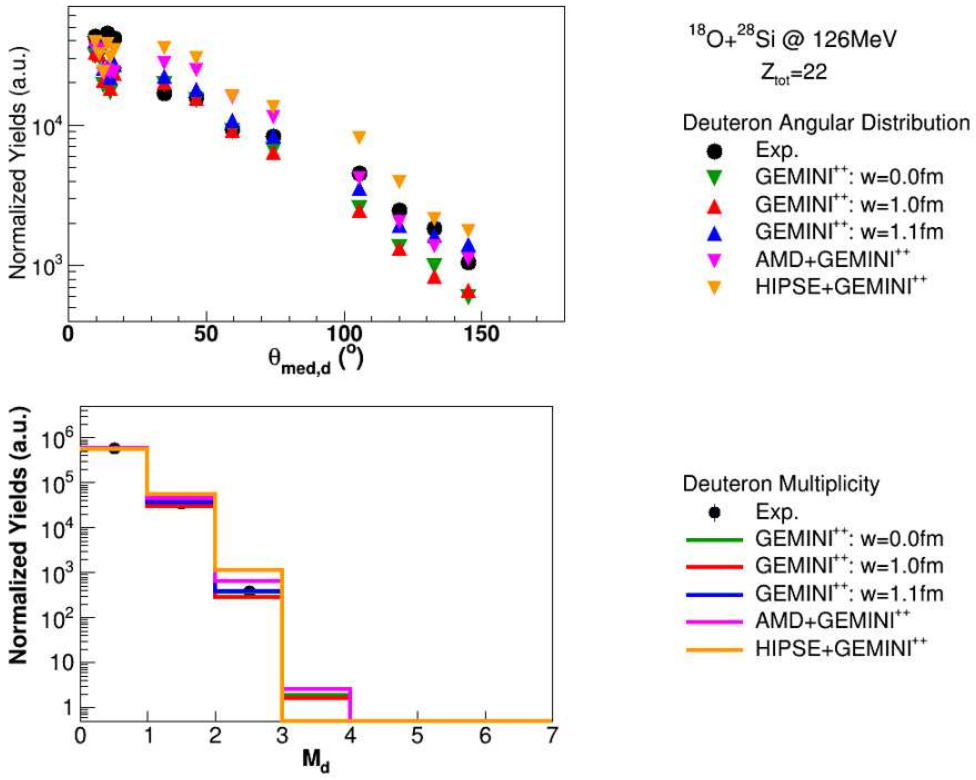

Figure 7.26: Same as in Fig. 7.24 but for deuteron. See text for details.

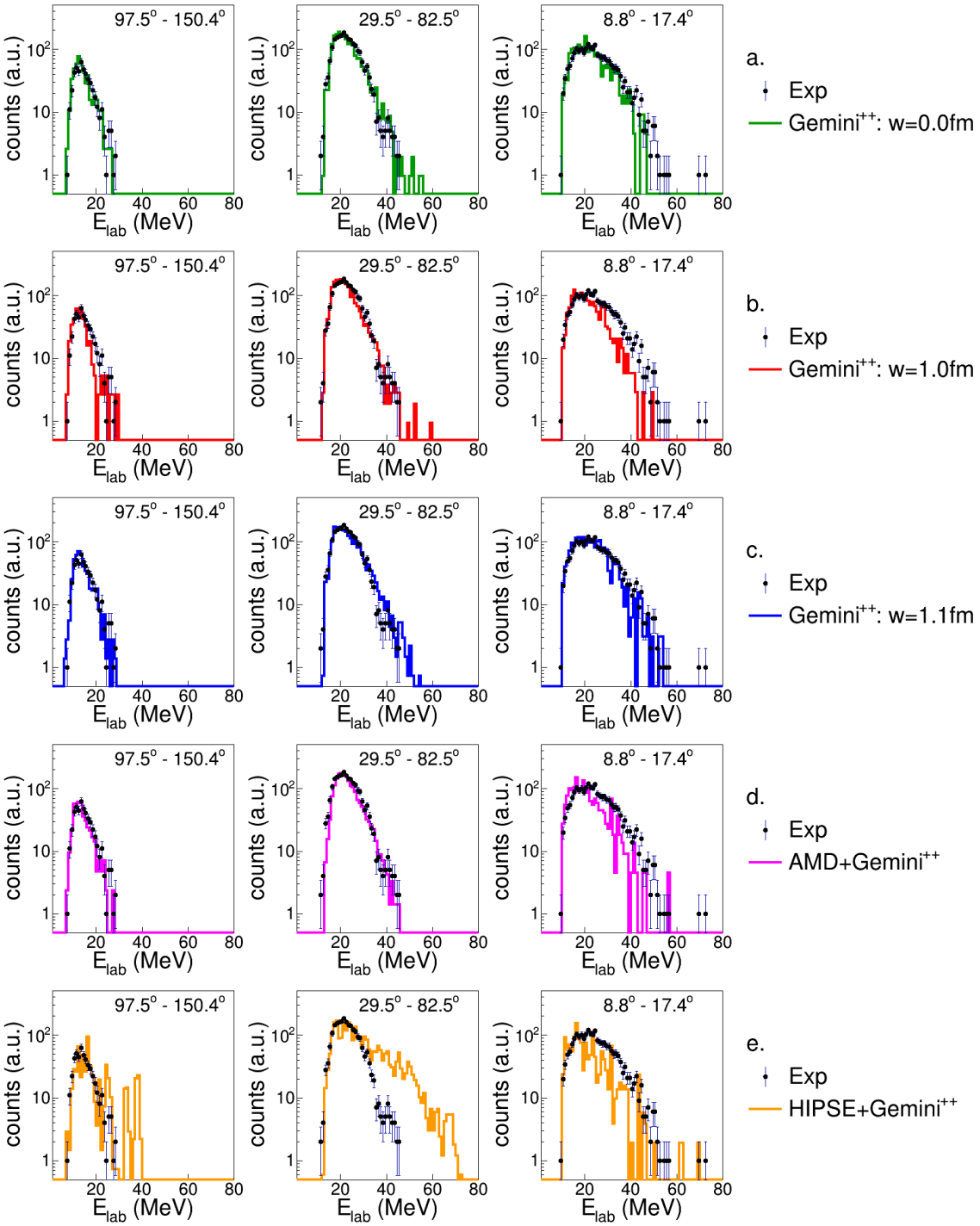

Figure 7.27: Same as in Fig. 7.23 but for triton. See text for details.

multiplicities ($M_p \geq 2$).

Deuterons energy spectra (Fig. 7.25) are, in this reaction, well accounted for by **AMD** and **G00**. **G10** slightly underestimates both the backward angles and the very forward ones, while **G11** slightly overestimates the intermediate angular region $\theta_{lab} = 29.5^o \div 82.5^o$ confirming the findings of the proton energy spectrum. **HIPSE** still reproduces only the barrier, but it fails completely to describe the tails of the energy spectra. Looking at the angular distributions (upper panel of Fig. 7.26) the forward angles are well reproduced by **HIPSE** and the other simulations are close to experimental data. The central angular region is reproduced by $GEMINI^{++}$ alone, while it is largely overestimated by dynamical models. At backward angles, **AMD** gives the best description. Multiplicity (lower panel of Fig. 7.26) are well accounted for by $GEMINI^{++}$. The better reproduction of experimental triton energy spectra is given by **G11**, as in the case of the ^{16}O at 128 MeV induced

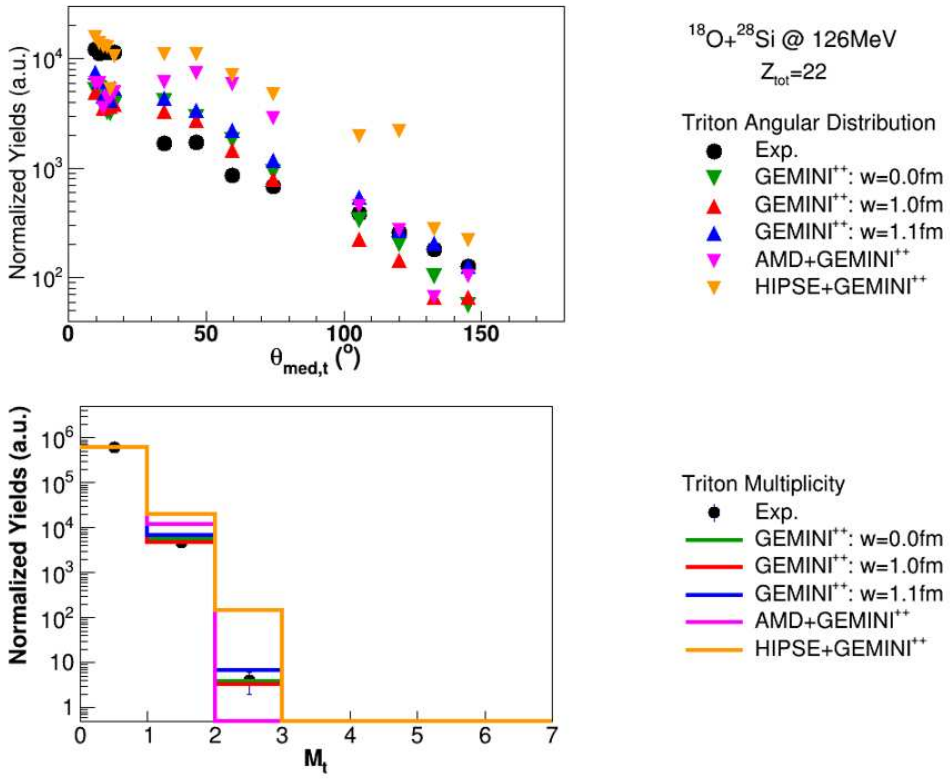

Figure 7.28: Same as in Fig. 7.24 but for triton. See text for details.

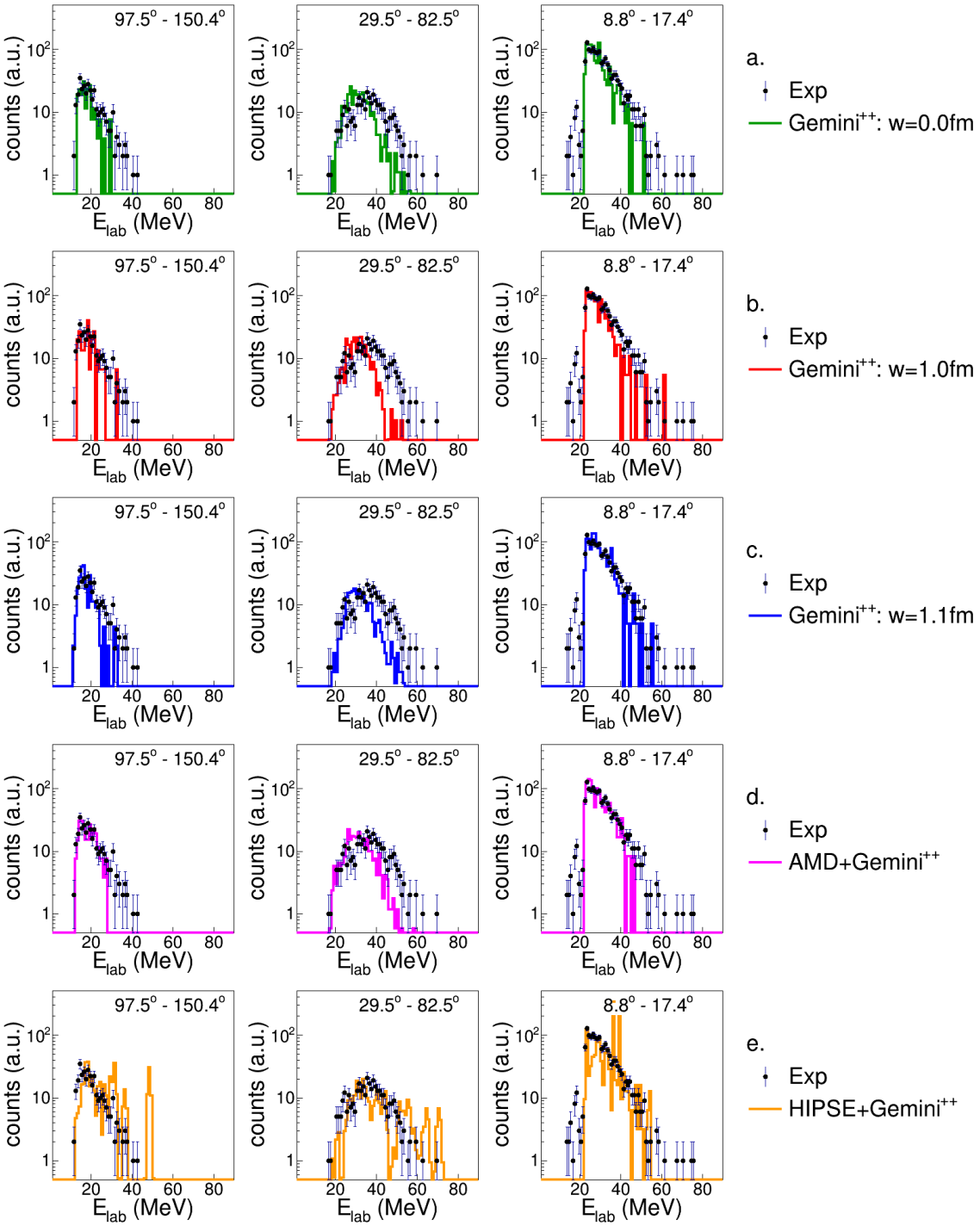

Figure 7.29: Same as in Fig. 7.29 but for ^3He. See text for details.

reaction, and by **G00**; **G10** underestimates the experimental energy spectra, slightly in GARFIELD region ($\theta_{lab} = 29.5^o \div 150.4^o$) and more in the RCo region ($\theta_{lab} = 8.8^o \div 17.4^o$); **AMD** reproduces quite well the backward and intermediate regions but underestimates the forward one. The usual **HIPSE** peaked structures are largely present. The peak in the very forward angular region observed in the experimental triton angular distribution (upper panel of Fig. 7.26, is described only by **HIPSE**. As in the previous reaction, **AMD** and **G11** well reproduce the backward part; while, the intermediate region is overestimated by all simulations, strongly by **AMD** and **HIPSE**. $GEMINI^{++}$ reproduces the multiplicity spectrum (lower panel of Fig. 7.26), at variance of the dynamical models. Even in this case the ^3He energy spectra (Fig.7.29) have slightly more statistics, which permits to see differences from simulations: no simulation, at variance with the previous case, is able to account for the central angular region spectral shape ($\theta_{lab} = 29.5^o \div 82.5^o$),

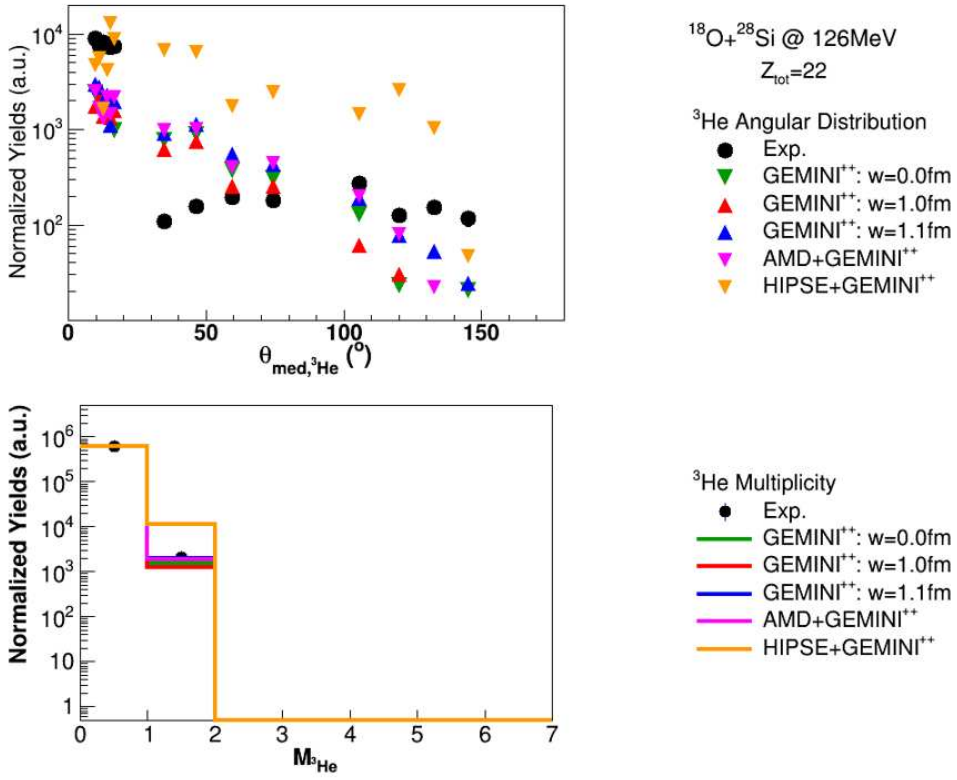

Figure 7.30: Same as in Fig. 7.24 but for ^3He. See text for details.

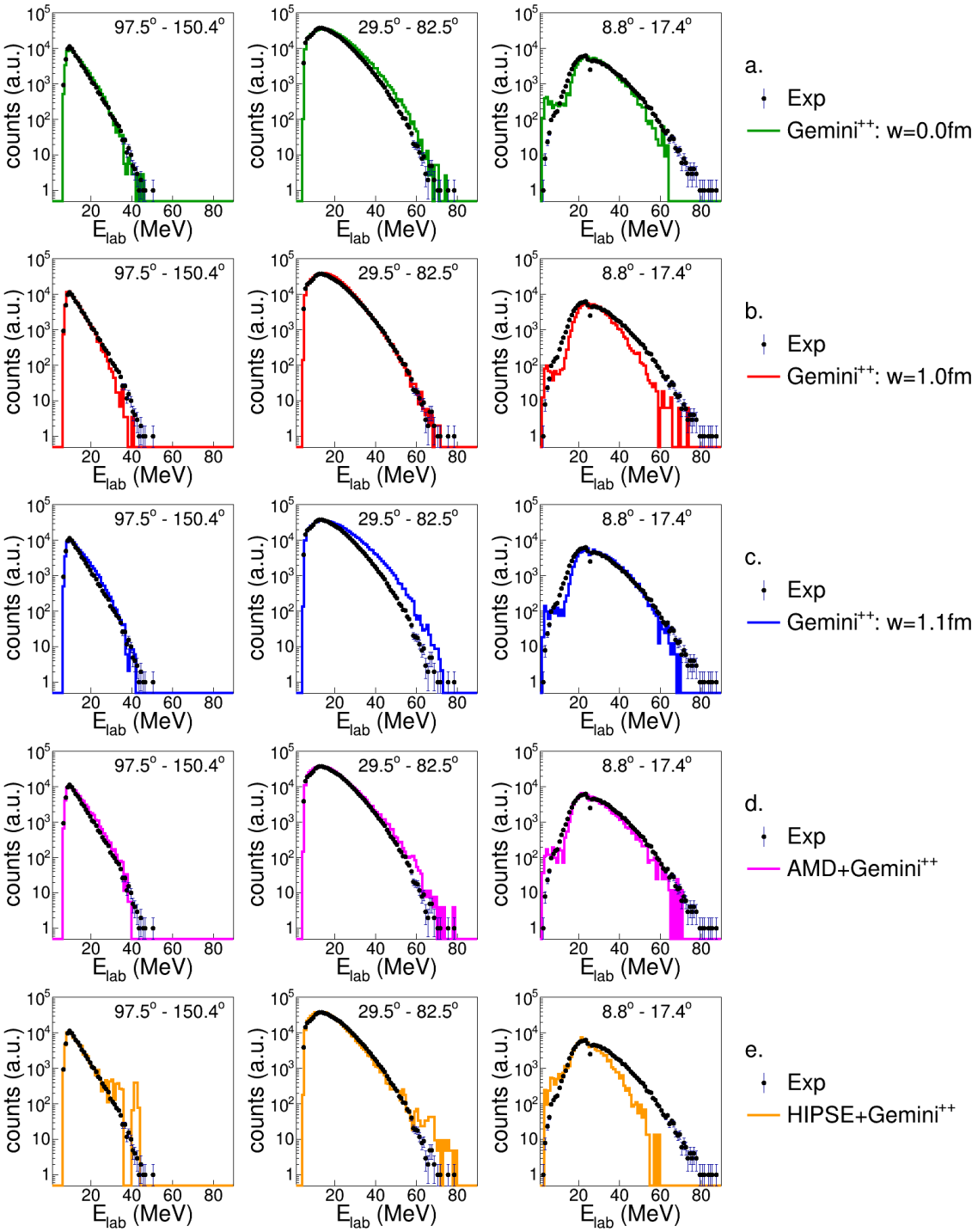

Figure 7.31: Same as in Fig. 7.23 but for α-particles. See text for details.

while they are reasonably good in the backward and forward regions. **G11** and **AMD** are the best and very similar in the forward and backward regions. As usual, **HIPSE** present some peaks in the simulated spectra. Apart from these anomalous peaks, the **HIPSE** predictions are the more similar to the experimental data. The experimental angular distribution of ^3He (upper panel of Fig. 7.30) is very similar to what obtained with the previous reaction, with a peaked distribution for $\theta_{lab} < 8.8^o$ and an almost flat distribution for $\theta_{lab} = 29.5^o \div 150.4^o$. This is again different from simulation expectations. Only **HIPSE** can describes the forward part. On the contrary, multiplicity distribution are well accounted for by all simulations, apart from **HIPSE**, which strongly overestimates the ^3He. The α-particles energy spectra are very well accounted for by **AMD**, as in the reaction induced by ^{16}O at higher energy. On the contrary, $GEMINI^{++}$ alone is never able to reproduce the spectra in the whole angular region, even if the differences are very

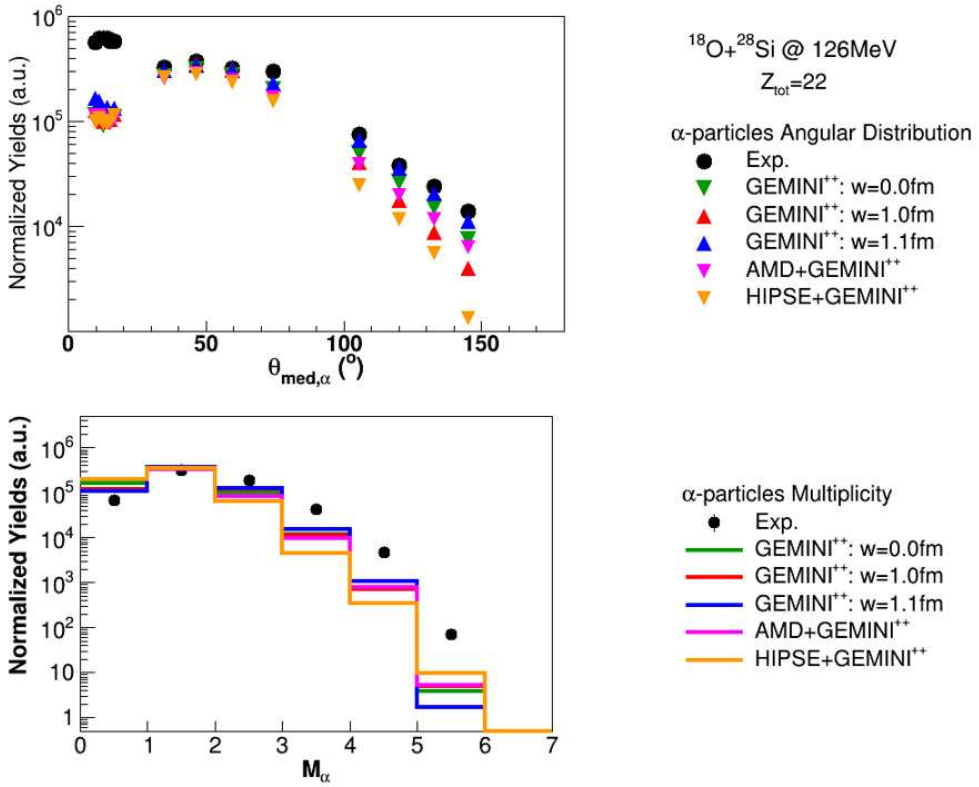

Figure 7.32: Same as in Fig. 7.24 but for α-particles. See text for details.

small: **G00** quite well describes all the angular range, but it is underestimating slightly the forward region ($\theta_{lab} = 8.8^o \div 17.4^o$) and slightly overestimating the intermediate region ($\theta_{lab} = 29.5^o \div 82.5^o$); **G10** is not reproducing both very forward angles and backward angles ($\theta_{lab} = 97.5^o \div 150.4^o$); **G11** is overproducing the alphas in the region $30 \div 80$ MeV in the intermediate angular region. **HIPSE** has some peaks overlapping the energy spectra tails in the angular region $\theta_{lab} = 29.5^o \div 150.4^o$, while, it strongly underestimates the experimental spectrum at very forward angles. A very similar situation with respect to the case of the ^{16}O at 128 MeV induced reaction, for what concerns the angular distribution is found, as it is shown in the upper panel of Fig. 7.32. Again, no calculation can reproduce the forward peak at small angles, the intermediate angular region is reasonably reproduced and the backward region is underestimated (still, here, the closest simulation is **G11**). The multiplicity distribution (lower panel of Fig. 7.32) is again not accounted for at $M_\alpha \geq 3$

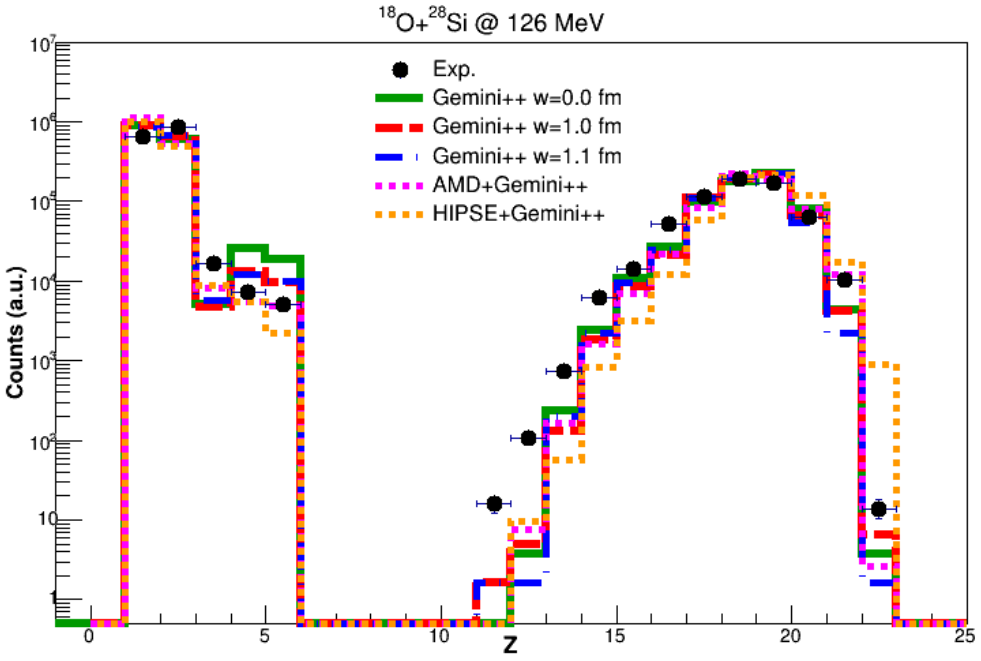

Figure 7.33: Comparison of normalized charge distribution between experimental data (black dots) and simulations made with $GEMINI^{++}$ w=0.0 fm (green line), w=1.0 fm (red line), w=1.1 fm (blue line), with $AMD+GEMINI^{++}$ (pink line) and with $HIPSE+GEMINI^{++}$ (orange line) for the reaction $^{18}O +^{28} Si$ at 126 MeV.

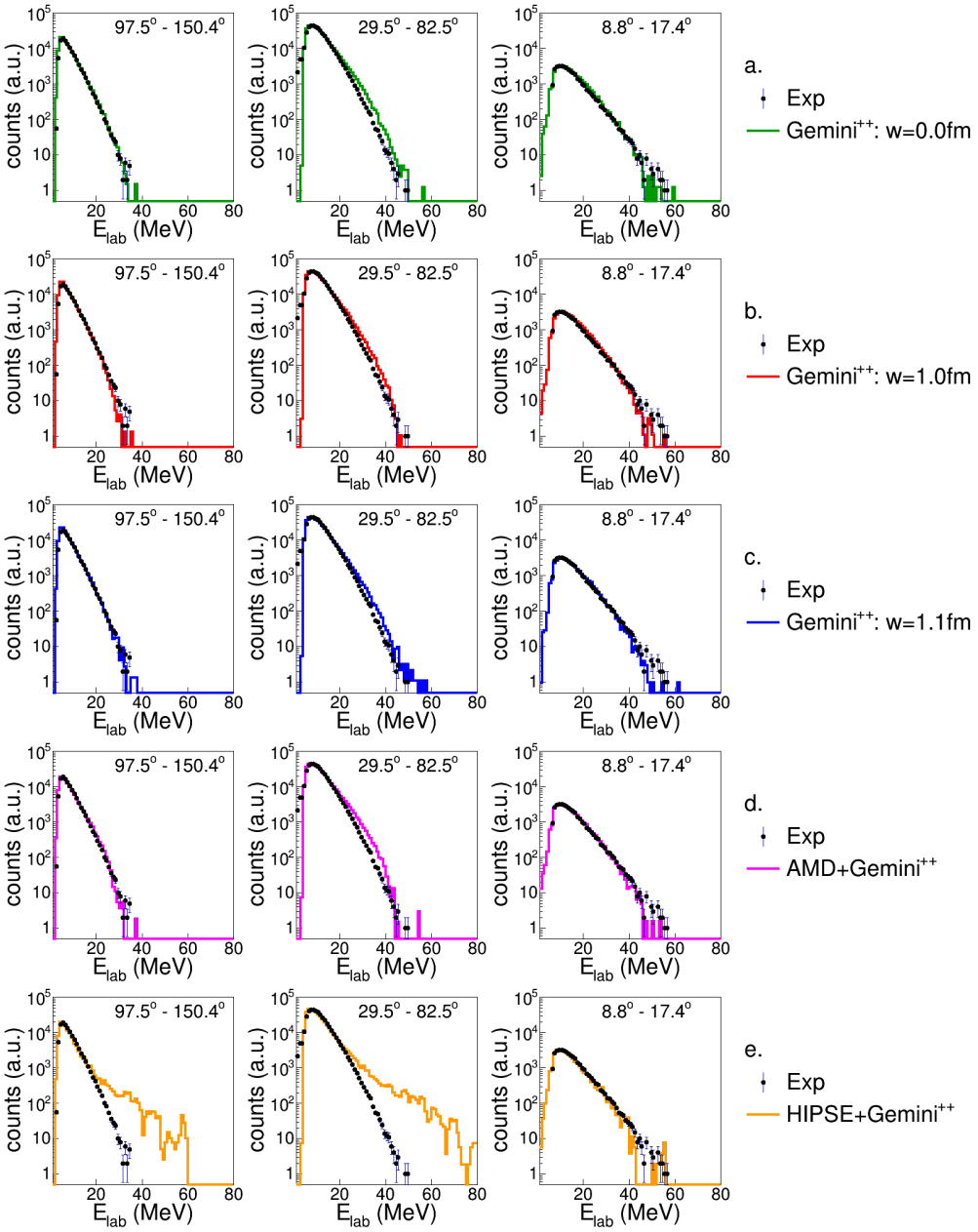

Figure 7.34: Comparison of normalized proton spectra between experimental data (black dots) and simulations made by $GEMINI^{++}$ $w = 0.0$ fm (green line), $w = 1.0$ fm (red line), $w = 1.1$ fm (blue line), by $AMD + GEMINI^{++}$ (pink line) and by $HIPSE + GEMINI^{++}$ (orange line) for the reaction $^{19}F + ^{27}Al$ at 133 MeV. The simulated spectra are normalized to the experimental maximum. See text for details.

for all calculations.

In the Fig. 7.33, the charge experimental distribution for the reaction $^{18}O+^{28}Si$ at 126 MeV is illustrated in comparison with the simulated ones; the LCP and light fragments ($Z = 1 \div 5$) are reproduced by models in a very similar way of the "twin"-reaction ($^{16}O+^{30}Si$ at 128 MeV). For what it concerns the ER some differences, can be noticed, for example, which are not present in the experimental data comparison.

7.4 $^{19}F+^{27}Al$ at 133 MeV.

Finally, we deal with the complete events ($Z_{tot} = 22$) for the reaction $^{19}F+^{27}Al$ at

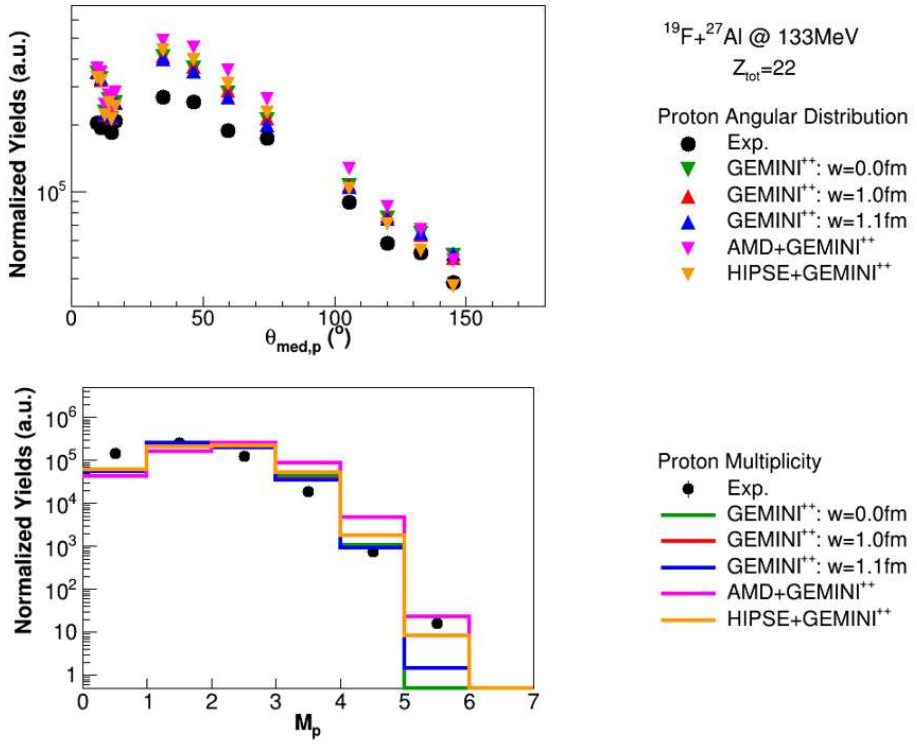

Figure 7.35: Comparison of experimental and simulated ($GEMINI^{++}$ with $w = 0.0$ fm in green, with $w = 1.0$ fm in red), $w = 1.1$ fm in blue; $AMD + GEMINI^{++}$ in pink; $HIPSE + GEMINI^{++}$ in orange) proton angular distribution and multiplicity for the reaction $^{19}F+^{27}Al$ at 133 MeV. The simulations are normalized to the relative number of residues $\left(\frac{\#_{res,exp}}{\#_{res,sim}}\right)$. See text for details.

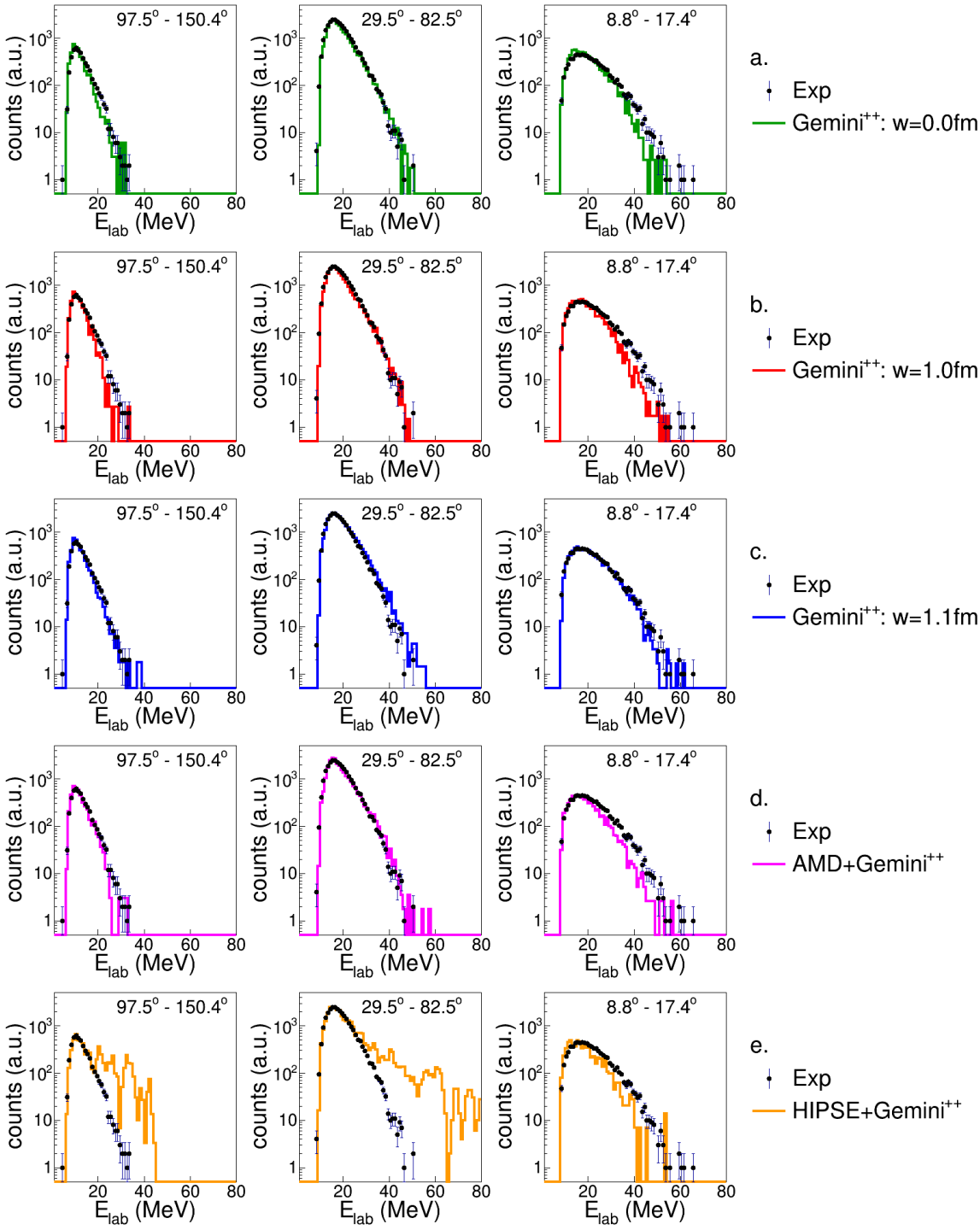

Figure 7.36: Same as in Fig. 7.34 but for deuteron. See text for details.

133 MeV. In Fig. 7.34 still the comparisons of experimental proton energy spectra with simulations are shown. The proton energy spectra are well accounted for by **AMD** and all $GEMINI^{++}$ simulations, even if all $GEMINI^{++}$ cases show a slight difference in the intermediate angular region, even though much smaller than in the previous cases; again, **HIPSE** shows the usual trend (too many fast particles) in GARFIELD angular region ($\theta_{lab} = 29.5^o \div 150.4^o$), while the forward angles are well accounted for. Similarly to previous reactions, all simulations overestimate the proton angular distributions, as one can see in the upper panel of Fig. 7.35. The multiplicity spectra (lower panel of Fig. 7.35) are in general well accounted for by all $GEMINI^{++}$ calculations, apart for $M_p = 5$, which is only predicted by **G11**. **AMD** and **HIPSE** overestimate the $M_p = 2 \div 4$, but they are the closest to $M_p = 5$.

Deuterons energy spectra (Fig. 7.36) are, in this reaction, well accounted for by **G11**.

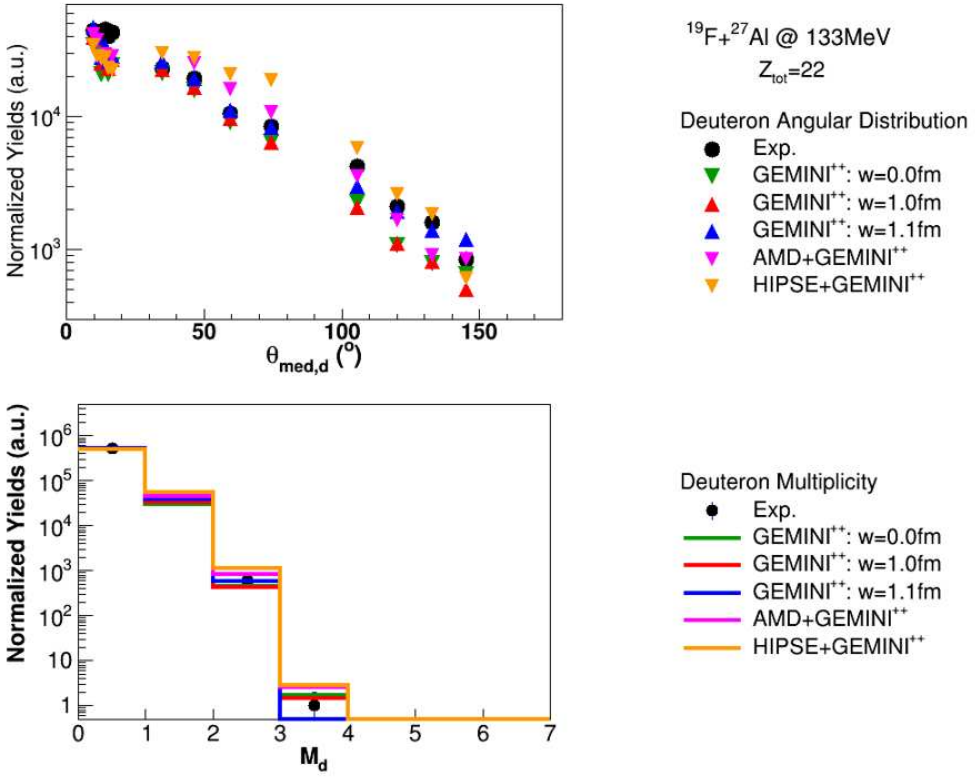

Figure 7.37: Same as in Fig. 7.35 but for deuteron. See text for details.

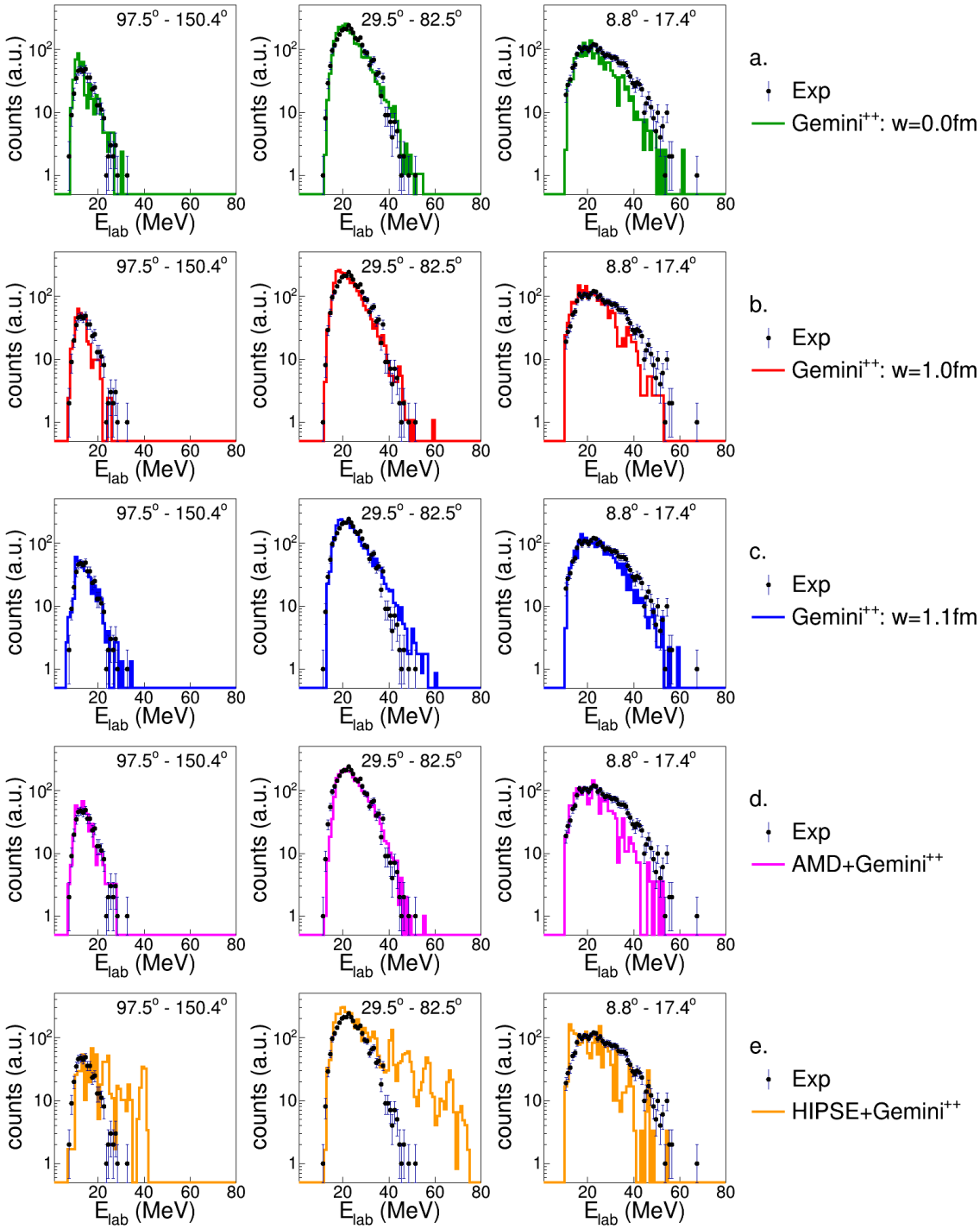

Figure 7.38: Same as in Fig. 7.34 but for triton. See text for details.

G00 and **G10** slightly underestimate both the backward angles and the very forward ones. **AMD** well reproduces the angular region $\theta_{lab} = 29.5^o \div 150.4^o$, but it underestimates the very forward angular region, like also **HIPSE**. Again, **HIPSE** is not able to simulates deuteron spectra in the backward and intermediate angular regions. Looking at the angular distributions (upper panel of Fig. 7.37), the forward angles are closer to all simulations with respect to the previous reaction, but, slightly better represented by **G11** and **AMD**. **G11** reproduces very well the intermediate angular region ($\theta_{lab} = 29.5^o \div 82.5^o$) and is the nearest also in the backward region. The multiplicity spectra (lower panel of Fig. 7.37) are quite well accounted for by all simulations; the case with **G10** and **G00** are the closest to the $M_p = 3$. A slightly overproduction of $M_p = 2$ is present in both dynamical simulations.

The triton energy spectra, displayed in the Fig. 7.38, are differently reproduced by the three $GEMINI^{++}$ simulations: **G00** and **AMD** well reproduce the spectra in the

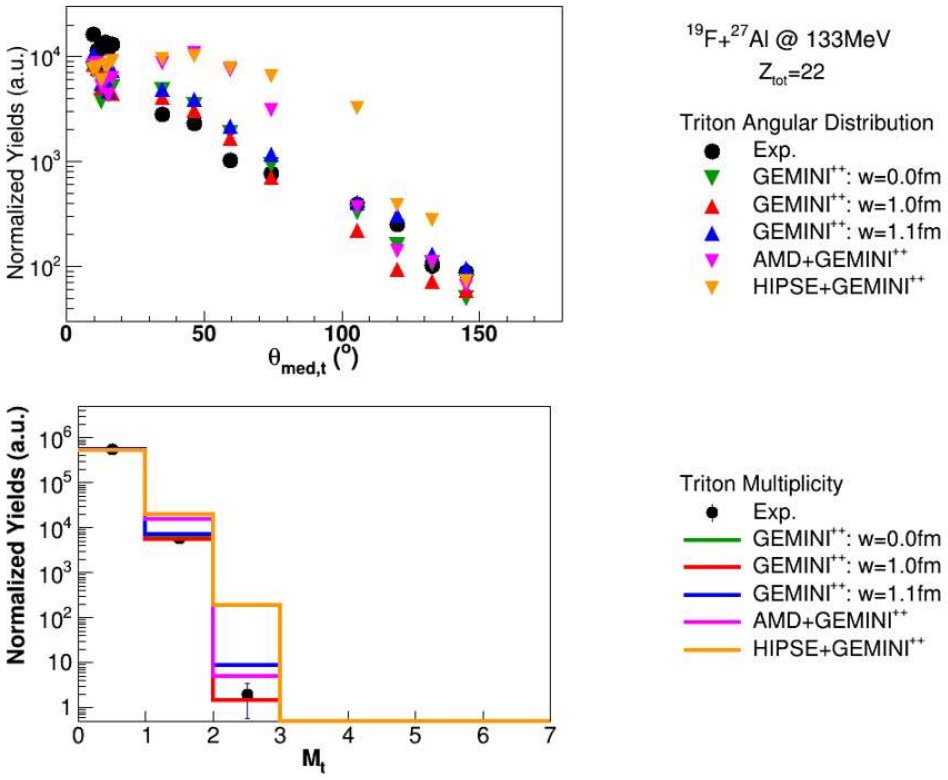

Figure 7.39: Same as in Fig. 7.35 but for triton. See text for details.

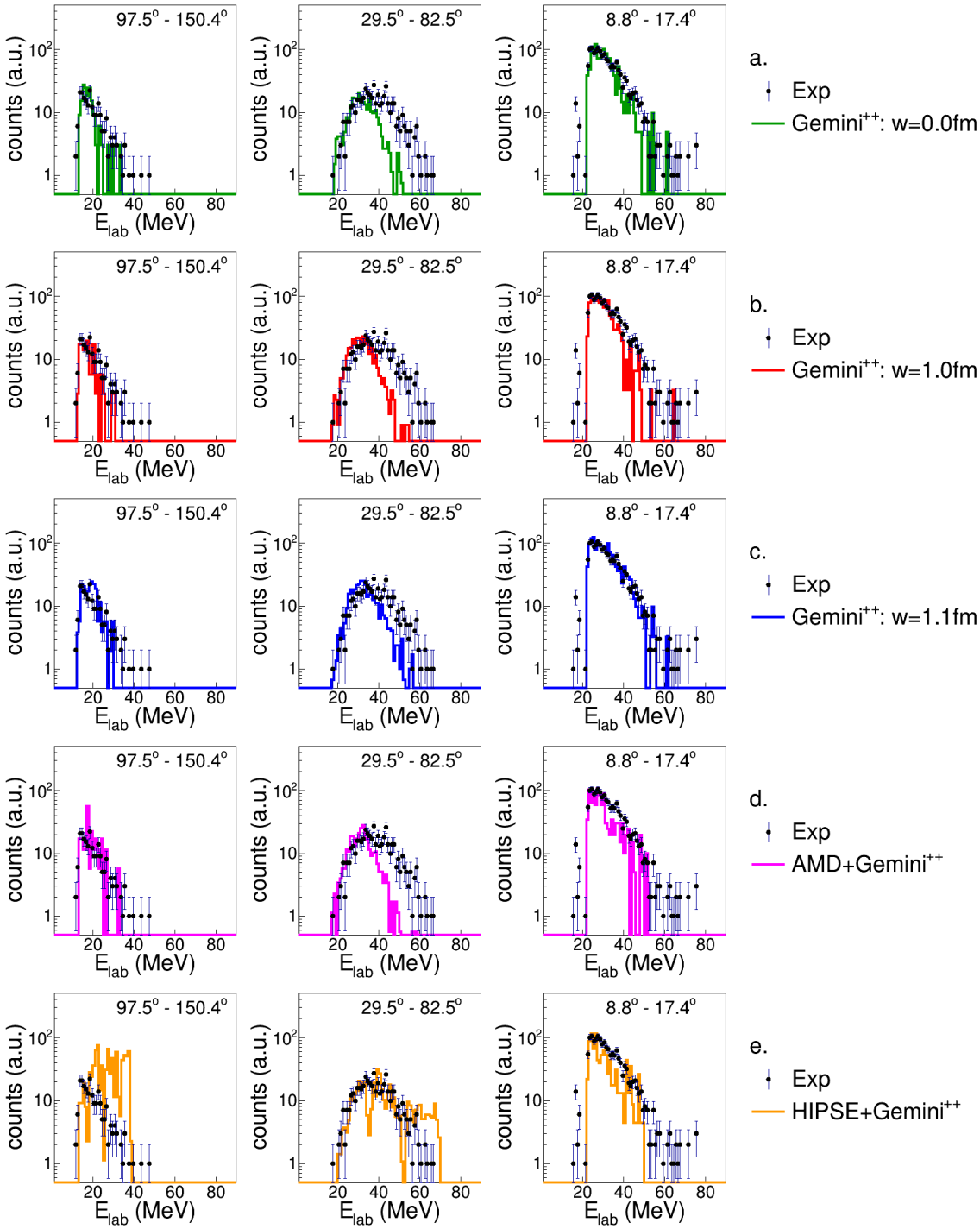

Figure 7.40: Same as in Fig. 7.34 but for ^{3}He. See text for details.

$\theta_{lab} = 29.5^o \div 150.4^o$; **G10** well reproduce the $\theta_{lab} = 29.5^o \div 82.5^o$; **G11** well reproduce the forward and backward regions. Also, here, **HIPSE** presents the usual troubles of extra yield due to the fast emission excess. The angular distribution (upper panel of Fig. 7.39) is almost well accounted for by all $GEMINI^{++}$ simulated data: even in the very forward angular region (RCo) the yields are better reproduced with respect to the previous reactions. The dynamical simulations largely overestimate the central part, while they are closer to the experimental one forward and backward. $GEMINI^{++}$ reproduce the multiplicity spectrum (lower panel of Fig. 7.39). **AMD** and **HIPSE** overestimate the triton multiplicities.

The ^3He energy spectra are shown in Fig. 7.40: again, no simulation is able to describe the central angular region spectral shape ($\theta_{lab} = 29.5^o \div 82.5^o$). The experimental angular distribution (upper panel of Fig. 7.41) of ^3He is very similar to what obtained in the

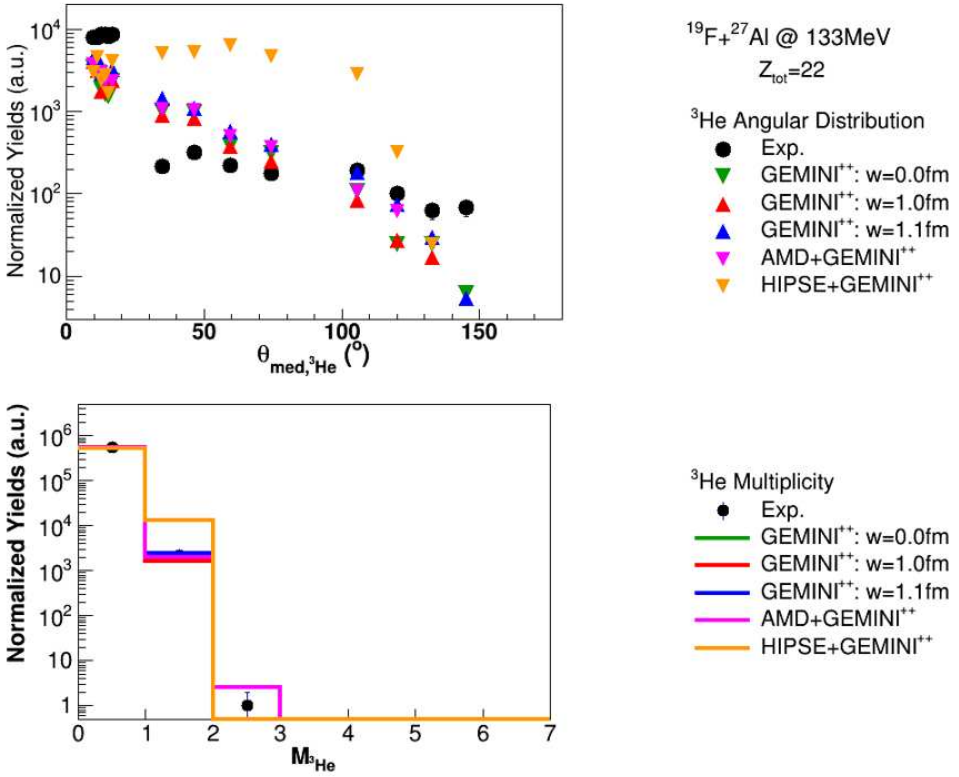

Figure 7.41: Same as in Fig. 7.35 but for ^3He. See text for details.

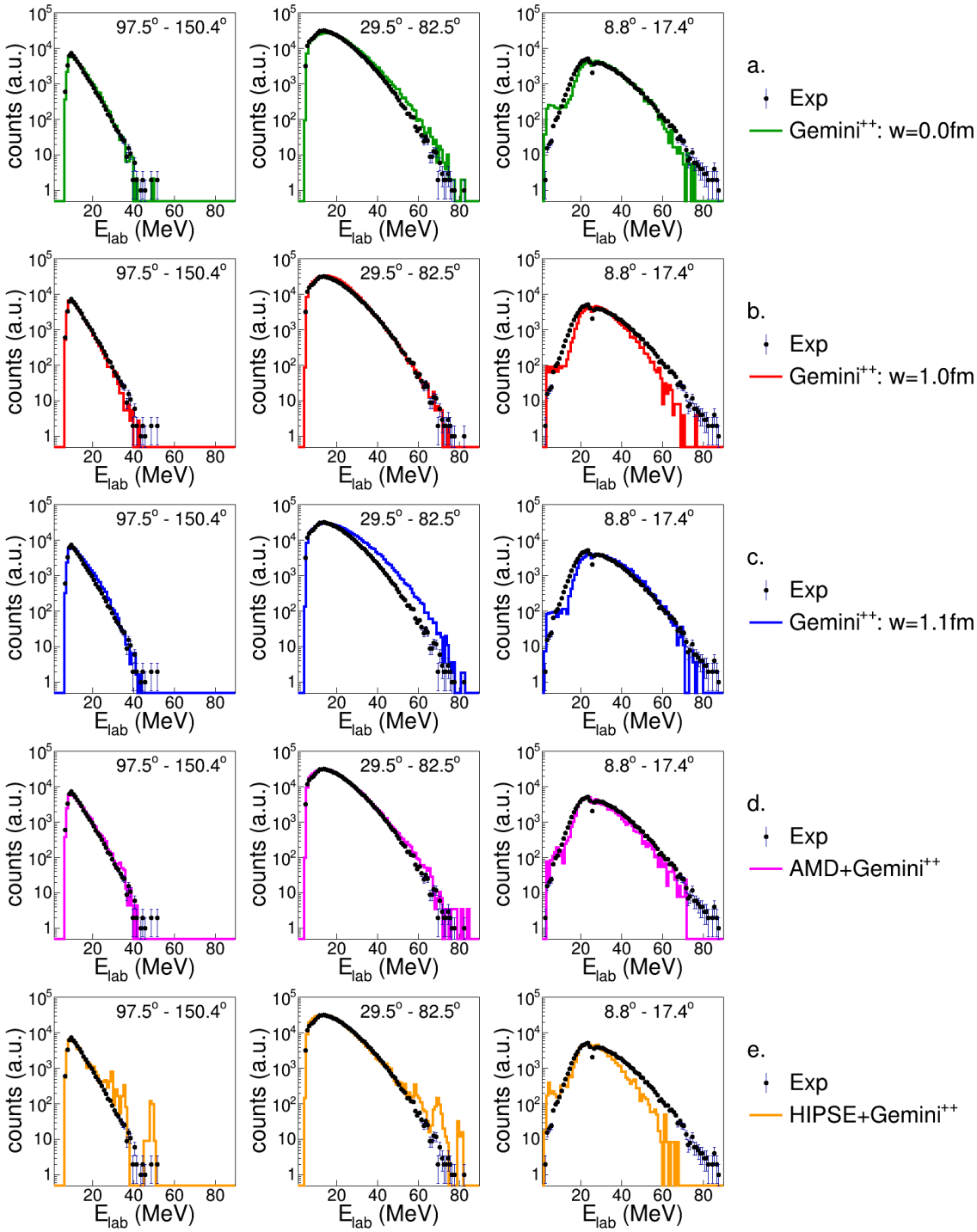

Figure 7.42: Same as in Fig. 7.12 but for α-particles. See text for details.

previous cases with a peaked distribution for $\theta_{lab} < 8.8^o$ and an almost flat distribution for $\theta_{lab} = 29.5^o \div 150.4^o$. Multiplicity distribution (lower panel of Fig. 7.41) are well accounted for by all simulations, apart from **HIPSE**, which overestimates $M_{^3He} = 1$. $M_{^3He} = 2$ is only predicted by **AMD**, which is slightly over-predicting the experimental yield.

The α-particles energy spectra are displayed in the Fig. 7.42 and compared to simulations. **G00** and **AMD** are describing quite well the spectra with a small overproduction in the intermediate angular region and a slight underproduction at forward angles. When using **G10** a well description of the region $\theta_{lab} = 29.5^o \div 150.4^o$ is obtained, while a quite visible lack of agreement is in the forward angles. **G11**, on the contrary well accounts for the energy spectra in the backward and forward direction, while it overestimates the intermediate angular region in the energy range $E_{lab} = 35 \div 70$ MeV, at backward and in-

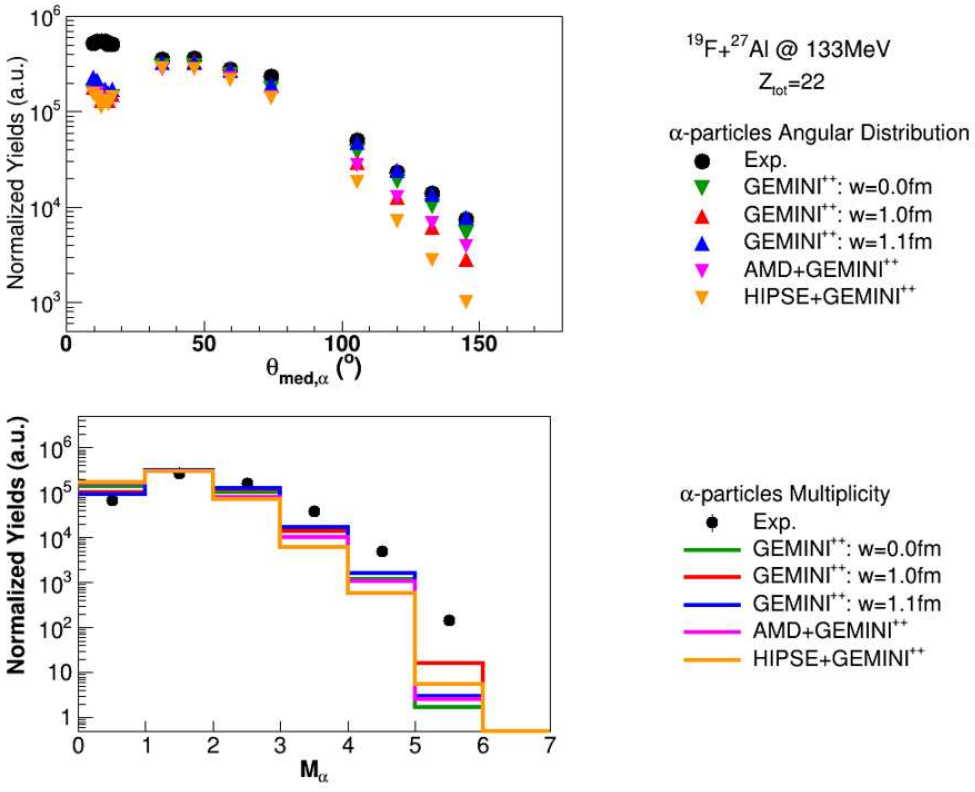

Figure 7.43: Same as in Fig. 7.35 but for α-particles. See text for details.

termediate angular regions apart from the usual peaks, while it underestimates the forward

angles. The α angular distribution (upper panel of Fig. 7.43) is very similar to previous cases. Again, no calculation is able to reproduce the forward peak at small angles and only **G11** can describes the backward angular region. The central region is well accounted for by all the simulations. The multiplicity distribution (lower panel of Fig. 7.43) is not again reproduced for $M_\alpha \geq 3$ by all simulated data.

The charge distribution for the reaction $^{19}F+^{27}Al$ at 133 MeV is shown in Fig. 7.44. The reproduction of LCP and light fragments ($Z = 1 \div 5$) by different simulations is very similar to other reactions, apart from a slight better description of H and Li-isotopes.

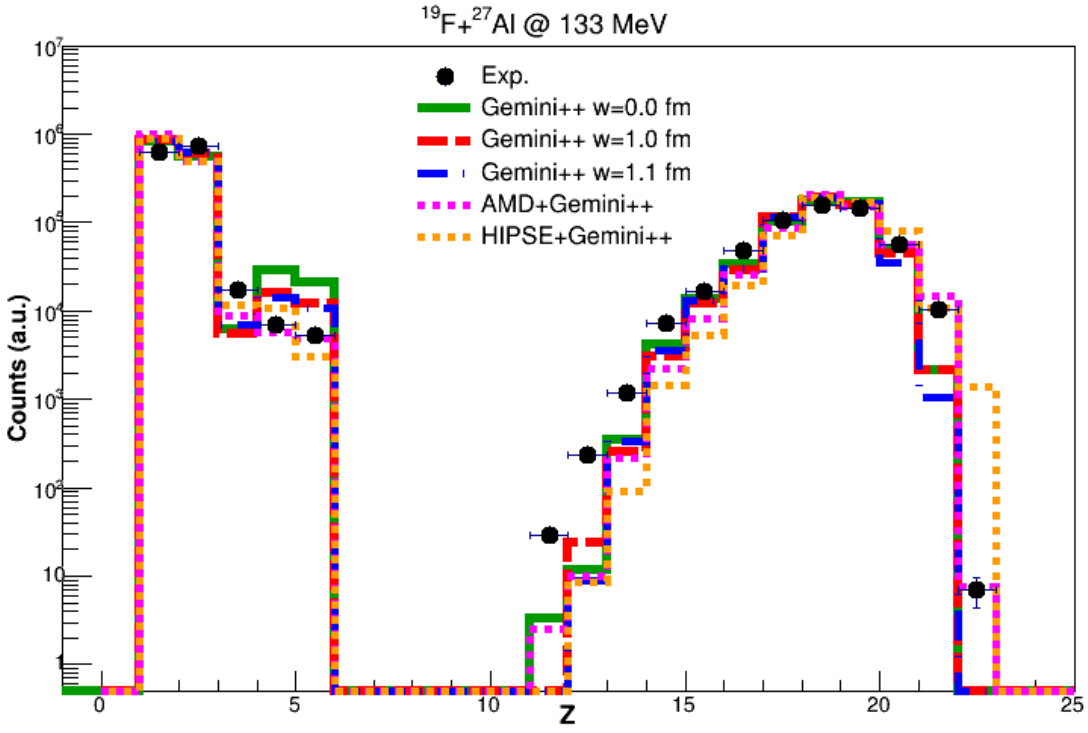

Figure 7.44: Comparison of normalized charge distribution between experimental data (black dots) and simulations made with $GEMINI^{++}$ w=0.0 fm (green line), w=1.0 fm (red line), w=1.1 fm (blue line), with $AMD+GEMINI^{++}$ (pink line) and with $HIPSE+GEMINI^{++}$ (orange line) for the reaction $^{19}F+^{27}Al$ at 133 MeV.

7.5 Conclusions

For a faster comparison, and a summary of the experimental findings the differences between the experimental and the simulated yields for the three angular region: backward, that is $\theta_{lab} = 97.5^o \div 150.4^o$, central, that is $\theta_{lab} = 29.5^o \div 82.5^o$, and forward that is $\theta_{lab} = 8.8^o \div 17.4^o$, are reported in the Figs. 7.45 and 7.46. In particular, in Fig. 7.45 the yield difference is displayed as a function of the parameter $\eta * E^*$, that is the product of the excitation energy and the entrance channel mass asymmetry parameters, while in Fig. 7.46 the same differences are displayed toward the $\frac{\eta}{E^*}$ parameter. In each panel, the plot relative to the two information are just complementary.

The choice to use a composite parameter, instead of just η or E^* alone, derives from the fact that these combinations of the two are something that differently characterize the four reactions and takes into account both effects of different temperature/decay path of the emitting nuclei and effects due to initial colliding partner mass asymmetries.

In Table 7.1 the correspondence between the different reactions and the parameters are listed.

	$^{16}O +^{30} Si$ at 111 MeV	$^{16}O +^{30} Si$ at 128 MeV	$^{18}O +^{28} Si$ at 126 MeV	$^{19}F +^{27} Al$ at 133 MeV
$\frac{\eta}{E_*}$	0,00346	0,00309	0,00221	0,00168
$\eta * E_*$	26,8	29,9	21,4	18,0

Table 7.1: Value of $\eta * E_*$ and $\frac{\eta}{E_*}$ for the four reactions.

It is quite evident from the two figures that a reasonable description of the deuterons, tritons and ^3He is observed at almost all energies and models in the angular range $\theta_{lab} = 29.5^o \div 150.4^o$. To guide the eye a dashed line corresponding to 0 difference is also plotted in the figures. Moreover, an opposite trend is observed for protons and α-particles, that is the more α-particles are under-evaluated by codes the more protons are over-evaluated. The best code seems to be in an overall picture the **G11**. In the forward region a larger

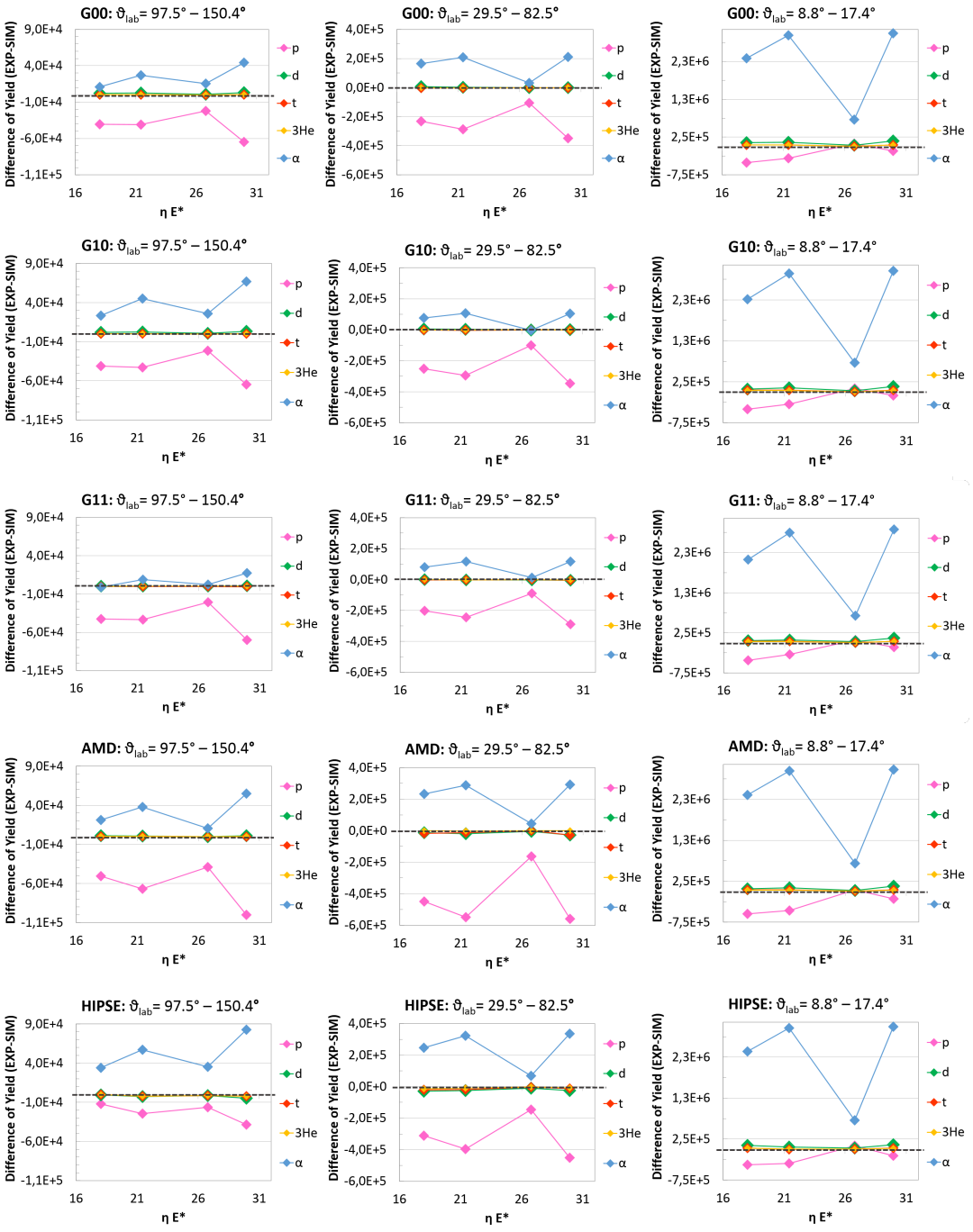

Figure 7.45: Differences between experimental data and simulations of the integrated angular yields as a function of $\eta * E^*$. See text for more details.

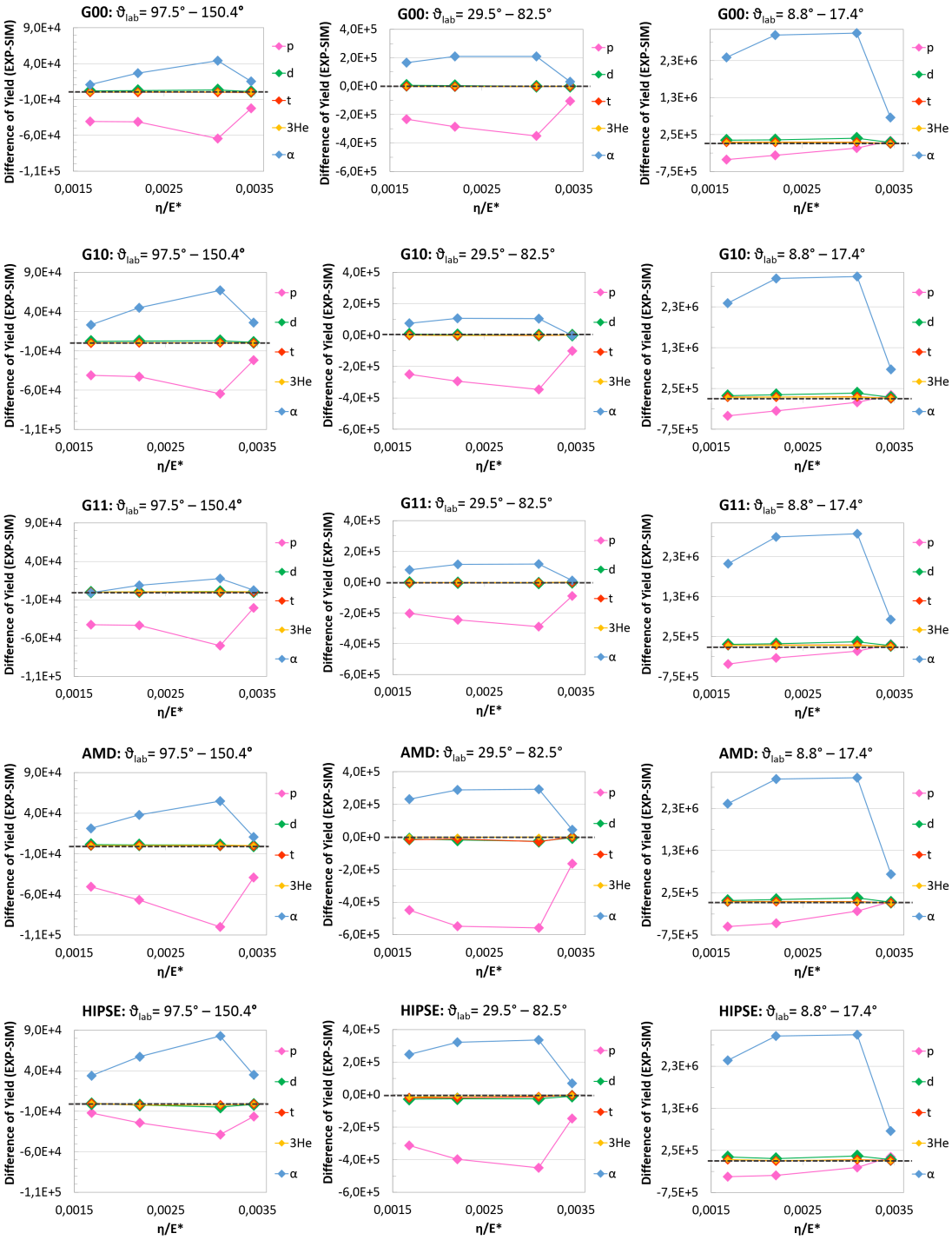

Figure 7.46: Same as Fig. 7.45, but dislayed as a function of the $\frac{\eta}{E^*}$.

discrepancy is observed for α-particles: in fact, at all energies an overproduction in the forward region was observed. On the contrary, protons are better represented, even still not completely.

The reaction with the smallest discrepancies, for what it concerns the experimental angular distribution yields with respect to models, is the ^{16}O at 111 MeV, that is the forth value on the graphs in Fig 7.46, corresponding to $\frac{\eta}{E^*} = 0,0035$, and the third value on the graphs displayed in Fig. 7.45, corresponding to $\eta * E^* = 26.8$.

The ^{16}O at 128 MeV and ^{18}O at 126 MeV reactions show similar trends except in the case of backward angles, where a larger discrepancy is observed for the ^{16}O case with respect to ^{18}O. The ^{19}F at 133 MeV shows an intermediate situation demonstrating that these differences are not scaling only with the excitation energy.

Chapter 8

Exclusive analysis

In order to better understand differences and similarities observed between simulation and experimental data and between the four reactions, which differ from each other by small amounts in terms of beam velocities, excitation energies, entrance channel isospin content and mass asymmetry, a deeper study has been carried out, looking at exclusive decay channels.

To better discuss the following results derived by the comparison between experimental and simulated events some considerations have to be performed: in Table 8.1 we report the total number of events that have been processed during the analysis both for the experimental data and for the different simulations, and how these events are reduced when major constraints are imposed up to the final strict selection discussed in the Chapter 7 ($Z_{tot} = 22$). In particular, the number of both experimental and simulated events for the inclusive case, the quasi-complete events case and the complete events case are presented.

All simulations were run up to 10 M-events; the label "Inclusive Evts N." in Table 8.1 represents the number of inclusive events which remain after the geometrical filter in the simulated cases and the number of detected events in the experimental cases. Of course, while in the $GEMINI^{++}$ cases all 10 M-events are relative to central collision only (CN statistical decay), in the case of both **AMD** and **HIPSE**, they consider collisions from $b = 0 \div 8$ fm and therefore the selection acts more strictly. Running a larger amount of events however was not possible due to CPU time (and the many cases we had to run).

$^{16}O + ^{30}Si$ at 111 MeV	Inclusive Evts # ($\times 10^6$)	$Z_{tot} \geq 18$ # ($\times 10^6$)	Evts N. %	$Z_{tot} = 22$ # ($\times 10^5$)	Evts N. %
Experimental	80.280 ± 0.009	2.967 ± 0.002	3.7	1.831 ± 0.004	0.23
$GEMINI^{++}$ w=0.0 fm	7.653	1.408	18.4	2.656	3.5
$GEMINI^{++}$ w=1.0 fm	8.011	1.721	21.5	3.244	4.0
$GEMINI^{++}$ w=1.1 fm	8.045	1.742	21.7	3.039	3.8
$AMD + GEMINI^{++}$	9.328	1.479	15.9	2.349	2.5
$HIPSE + GEMINI^{++}$	6.199	0.912	14.7	1.730	2.8
$^{16}O + ^{30}Si$ at 128 MeV	Inclusive Evts # ($\times 10^6$)	$Z_{tot} \geq 18$ # ($\times 10^6$)	Evts N. %	$Z_{tot} = 22$ # ($\times 10^5$)	Evts N. %
Experimental	205.800 ± 0.014	11.092 ± 0.003	5.4	6.215 ± 0.008	0.30
$GEMINI^{++}$ w=0.0 fm	8.187	1.698	20.7	2.959	3.6
$GEMINI^{++}$ w=1.0 fm	8.432	1.698	24.7	3.450	4.1
$GEMINI^{++}$ w=1.1 fm	8.491	2.065	24.3	3.330	3.9
$AMD + GEMINI^{++}$	7.766	1.439	18.5	2.210	2.8
$HIPSE + GEMINI^{++}$	6.072	1.005	16.5	1.748	2.9
$^{18}O + ^{28}Si$ at 126 MeV	Inclusive Evts # ($\times 10^6$)	$Z_{tot} \geq 18$ # ($\times 10^6$)	Evts N. %	$Z_{tot} = 22$ # ($\times 10^5$)	Evts N. %
Experimental	163.500 ± 0.013	7.573 ± 0.003	4.6	6.215 ± 0.008	0.38
$GEMINI^{++}$ w=0.0 fm	8.213	1.583	19.3	3.272	4.0
$GEMINI^{++}$ w=1.0 fm	8.450	1.887	22.3	3.810	4.5
$GEMINI^{++}$ w=1.1 fm	8.513	1.945	22.8	3.751	4.4
$AMD + GEMINI^{++}$	7.146	1.349	18.9	2.416	3.4
$HIPSE + GEMINI^{++}$	6.166	0.985	16.0	1.953	3.2
$^{19}F + ^{27}Al$ at 133 MeV	Inclusive Evts # ($\times 10^6$)	$Z_{tot} \geq 18$ # ($\times 10^6$)	Evts N. %	$Z_{tot} = 22$ # ($\times 10^5$)	Evts N. %
Experimental	96.470 ± 0.010	5.650 ± 0.002	5.9	5.528 ± 0.007	0.57
$GEMINI^{++}$ w=0.0 fm	8.421	1.646	19.6	3.278	3.9
$GEMINI^{++}$ w=1.0 fm	8.617	1.926	22.4	3.752	4.4
$GEMINI^{++}$ w=1.1 fm	8.686	2.018	23.2	3.771	4.3
$AMD + GEMINI^{++}$	6.691	1.247	18.6	2.201	3.3
$HIPSE + GEMINI^{++}$	7.293	1.008	13.8	1.974	2.7

Table 8.1: Number of events (Evts N.) in the three cases: inclusive events, quasi-complete events ($Z_{tot} \geq 18$) and complete events ($Z_{tot} = 22$) for the four reactions. In the second column of each selected event raw the percentage with respect to the inclusive number of events are also reported. See text for detail.

In the Table, the columns with $Z_{tot} \geq 18$ and $Z_{tot} = 22$ refer to the selection discussed previously and the reported numbers are also representing the number of collected evaporation residues in semi-complete and complete events, due to the requested coincidence between any LCP or fragments with $Z < 6$ and only one ER.

The same information is given in a graphical way in Fig. 8.1: here, the inclusive charge distribution are compared to those related to the quasi-complete ($Z_{tot} \leq 18$) and complete ($Z_{tot} = 22$) events cases. Such comparison are presented for the experimental and all the simulations case for all the four systems under study.

Another observation to be made is that the experimental inclusive events are the sum of two different reactions (as previously reported) due to the O-contamination in the targets. This is why the reduction on the experimental data already when selecting semi-complete events is much larger, since as previously explained with our selections we are completely cutting the contaminated events (for which the maximum Z_{tot} is 16).

8.1 Major exit channels ($Z_{res} = 13 \div 21$) in complete events ($Z_{tot} = 22$)

For each studied reaction, selected evaporation residues from $Z_{res} = 21$ down to $Z_{res} = 13$ have been studied in coincidence with LCP or light fragments ($Z \leq 5$) and compared to theoretical predictions. For each selected residue (Z_{res}), all main decay channels have been identified and compared, in such a way to observe relative yields and characteristics and to determine the branching ratios, as it will be discussed in the following Section.

As a first step, a plot of the multiplicity versus each identified particle in the event has been built: such plot gives a qualitative idea on the different decay pattern followed by the excited nuclei down to the final partition. For sake of simplicity, the particle identification parameter (P.Id.) has been defined as:

- $P.Id.(Z = 1) = 10 \times Z + A$
- $P.Id.(Z = 2) = 10 \times Z + A - 2$

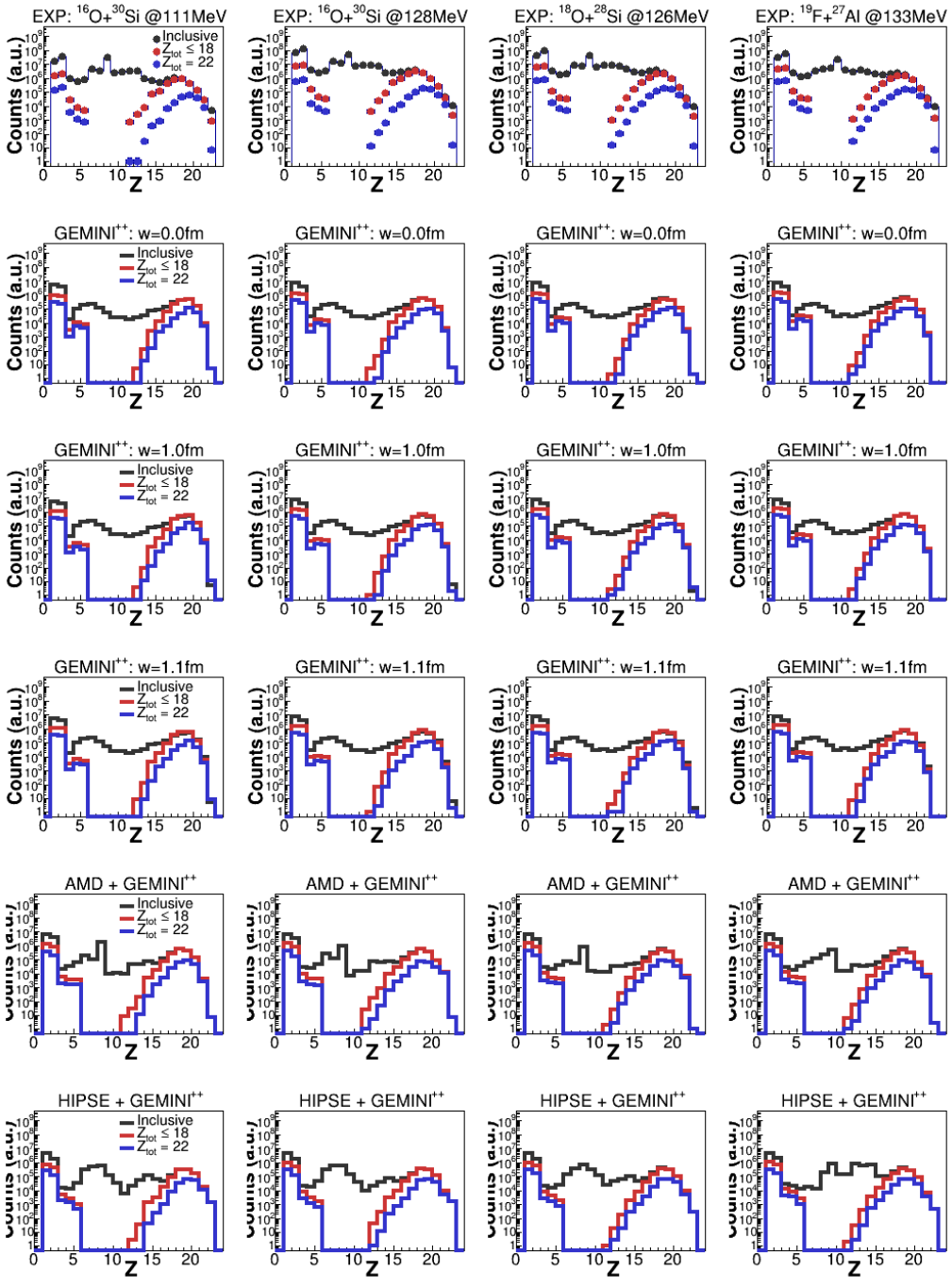

Figure 8.1: Comparison of inclusive, quasi-complete and complete events charge distributions for experimental data and different simulations of the four studied reactions. See text for details.

- $P.Id.(Z = 3) = 10 \times Z + A - 5$
- $P.Id.(Z = 4) = 10 \times Z + A - 6$
- $P.Id.(Z = 5) = 10 \times Z + A - 9$

In Table 8.2 the P.Id. is displayed together with the kind of particle.

particles	p	d	t	^{3}He	^{4}He	^{6}He	^{6}Li	^{7}Li	^{8}Li	^{7}Be	^{9}Be	^{10}Be	^{10}B	^{11}B
P.Id.	11	12	13	21	22	24	31	32	33	41	43	44	51	52

Table 8.2: Particles identification parameter (P.Id.) and relative kind of particles.

Moreover, the angular distributions of the different coincident particles have been also observed and compared to simulations for each selected residue. The calculated yields are normalized to the relative number of residues $\left(\frac{\#_{res,exp}}{\#_{res,"sim"}}\right)$.

8.1.1 The Sc residue: $Z_{res} = 21$

In Table 8.3 the number of Sc-residue and the total branching ratio (BR) of channels with such residue have been reported for experimental and simulated data for the four reactions. The BR is defined as the ratio between the yield of the number of evaporation residues with $Z_{res} = 21$ over the total number of residues, either collected or simulated respectively, which remain after the final selection ($Z_{tot} = 22$). We have already said that absolute numbers of residues are not directly comparable between experiment and simulations since they strongly depend both on the total experimentally collected and simulated inclusive events and on the effects of filtering and constraints, as previously discussed. Differences in the BR, on the contrary, can indicate the differences between experimental and simulated yields on the specific channel. Generally, for the Sc isotopes **HIPSE** seems to better represent the BR for all reactions, while $GEMINI^{++}$ alone tends to underestimate them in all the cases, almost independently by the w parameter used. The BR resulting from **AMD** is, on the contrary, close to the data only in the two cases $^{18}O +^{28} Si$ at 128 MeV and $^{19}F +^{27} Al$ at 133 MeV. For the ^{16}O induced reactions

$AMD + GEMINI^{++}$ strongly underestimates the low energy reaction case and predict approximately twice the BR at the higher energy case.

	$^{16}O +^{30} Si$	111 MeV	$^{16}O +^{30} Si$	128 MeV
	n^o residues	BR(%)	n^o residues	BR(%)
Experimental	7633 ± 87	4.6	11350 ± 107	2.2
$GEMINI^{++}$ $w = 0.0$ fm	6038	2.3	2605	0.9
$GEMINI^{++}$ $w = 1.0$ fm	5930	1.8	3063	0.9
$GEMINI^{++}$ $w = 1.1$ fm	3639	1.2	1648	0.5
$AMD + GEMINI^{++}$	2803	1.2	10480	4.8
$HIPSE + GEMINI^{++}$	7252	5.7	2510	1.8
	$^{18}O +^{28} Si$	126 MeV	$^{19}F +^{27} Al$	133 MeV
	n^o residues	BR(%)	n^o residues	BR(%)
Experimental	9493 ± 97	1.8	9811 ± 99	2.1
$GEMINI^{++}$ $w = 0.0$ fm	2309	0.7	1264	0.4
$GEMINI^{++}$ $w = 1.0$ fm	2580	0.7	1426	0.4
$GEMINI^{++}$ $w = 1.1$ fm	1365	0.4	703	0.2
$AMD + GEMINI^{++}$	4774	2.0	5899	2.8
$HIPSE + GEMINI^{++}$	3609	2.5	2510	1.8

Table 8.3: Number and total branching ratio (BR) of channels with Sc-residue.

$^{16}O +^{30} Si$ at 111 MeV (panel a.), $^{16}O +^{30} Si$ at 128 MeV (panel b.), $^{18}O +^{28} Si$ at 126 MeV (panel c.) and $^{19}F +^{27} Al$ at 133 MeV (panel d.).

The only open channels when selecting a Sc residue are:

- $^{45-xn}Sc + p + xn$;
- $^{44-xn}Sc + d + xn$;
- $^{43-xn}Sc + t + xn$.

The experimental distributions are compared with simulations: the relative yields between the three channels are almost well accounted for by all the simulations, for the $^{16}O +^{30} Si$ at 111 MeV, as it will be quantitatively discussed in the Chapter 10, where branching ratios will be discussed. It is however clear that **AMD** is slightly overestimating the channels

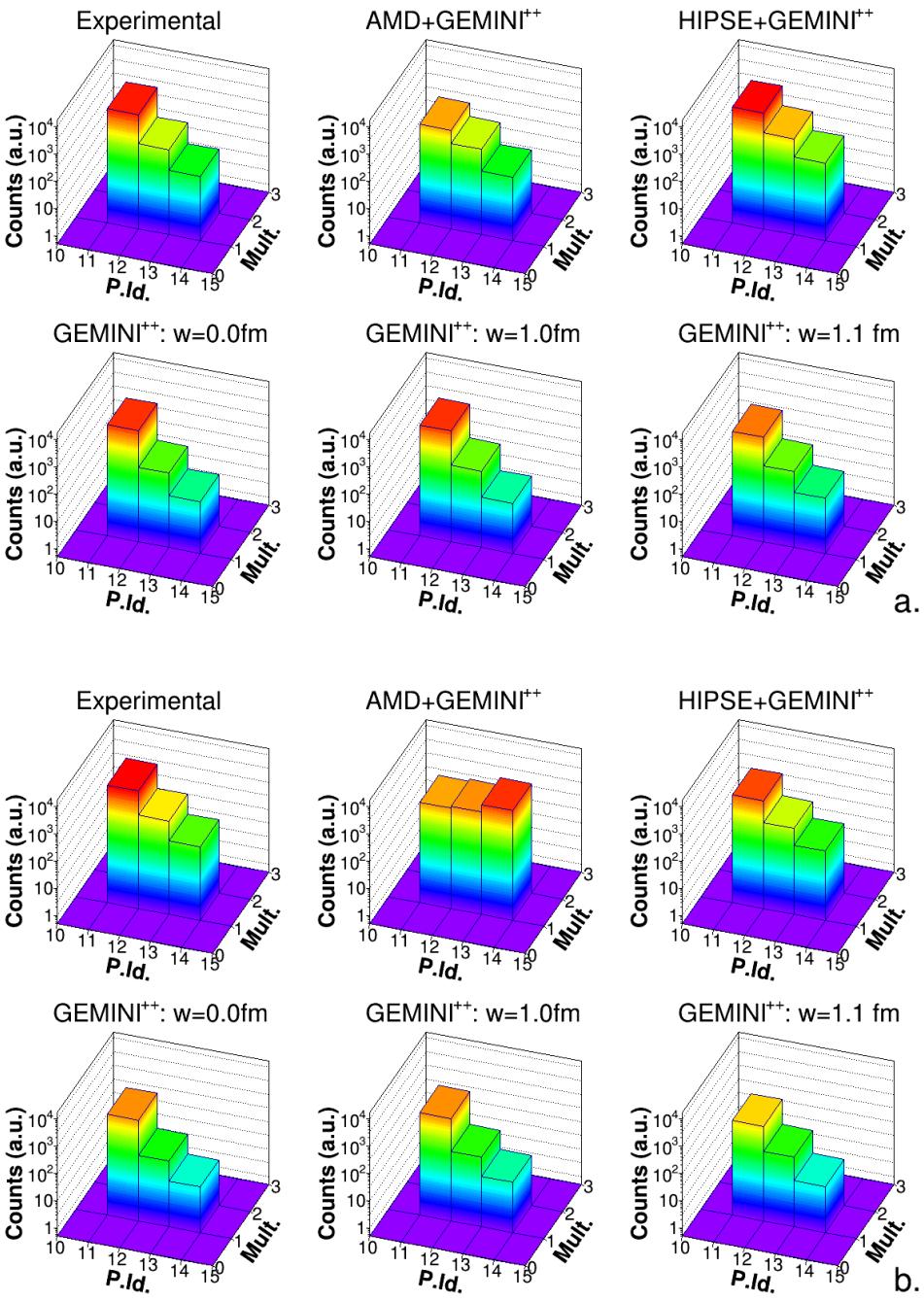

Figure 8.2: Open decay channels: particles in coincidence with a Sc-residue for the reactions $^{16}O + ^{30}Si$ at 111 MeV (panel a.) and $^{16}O + ^{30}Si$ at 128 MeV (panel b.). The Particles Identification is: 11 protons, 12 deuterons, 13 triton. See text for more details.

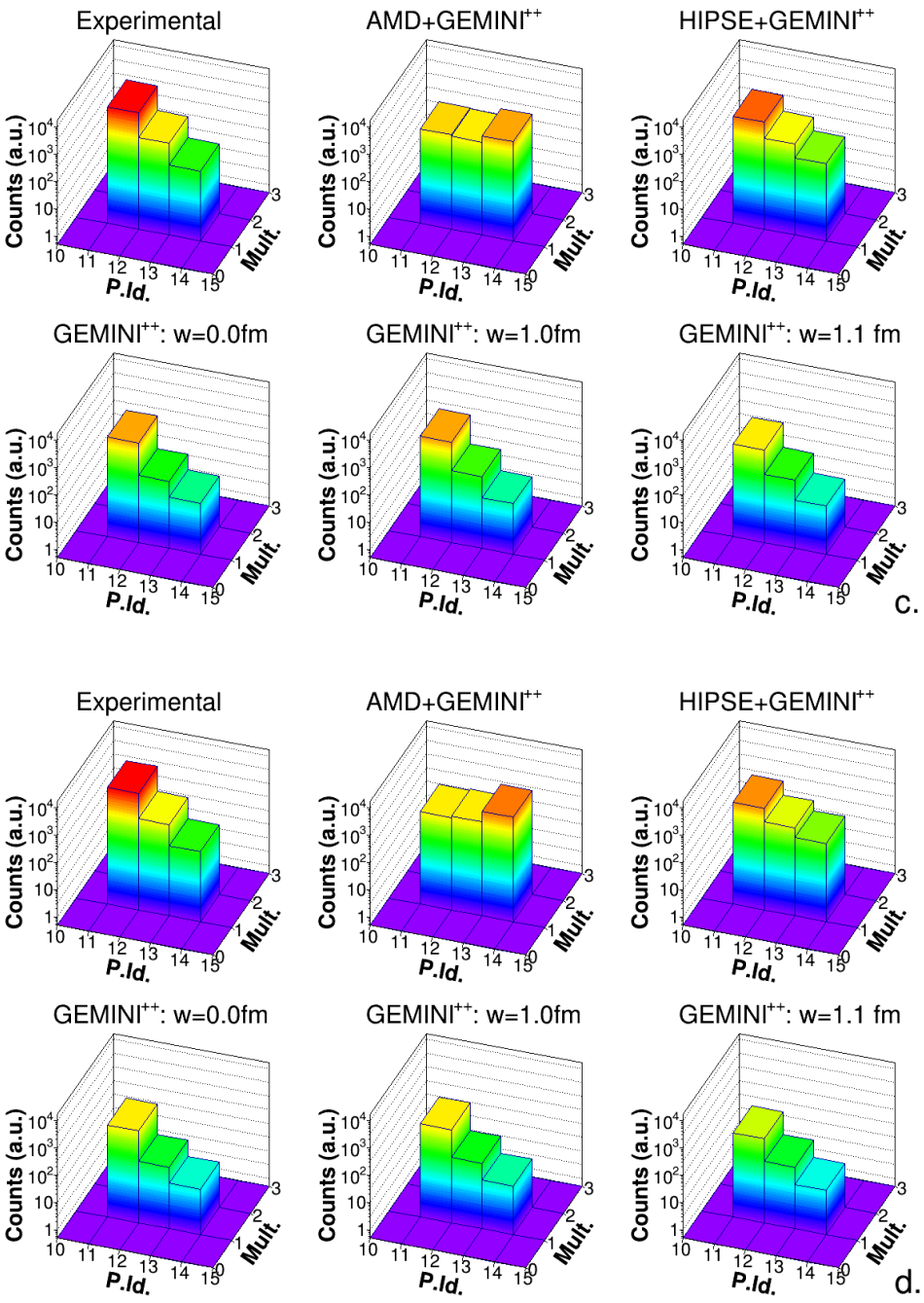

Figure 8.3: Same as in Fig. 8.2 but for the reactions $^{18}O + ^{28}Si$ at 126 MeV (panel c.) and $^{19}F + ^{27}Al$ at 133 MeV (panel d.).

in which either a deuteron or a triton is emitted with respect to the proton channel, but this last is still the one with a larger probability, as observed in the data. On the contrary, for the other three reactions, **AMD** is completely over-predicting the deuteron and, more, triton channels, like if such cluster emissions were privileged; the experimental findings are reasonably represented by **HIPSE**, while at variance with them $GEMINI^{++}$ follows somehow the expected relative ratio between proton, deuteron and triton (this will be seen quantitatively in the following) but a general underproduction is observed which was already underlined by the total BR of Table 8.3.

Since neutron emission is not measured, something can be inferred by looking at the Q-value spectra of the three emission channels in comparison to simulations: in Figs. 8.4 $\div$ 8.7, the Q-value spectra of the channels $^{45-xn}Sc + p + xn$, $^{44-xn}Sc + d + xn$ and $^{43-xn}Sc + t + xn$ are displayed. It has to be pointed out that the shown experimental and "filtered" simulated distributions (green **G00**; red **G10**; blue **G11** fm; pink **AMD**, orange **HIPSE**), which are normalized to their relative evaporation residues (ER) number for a quantitative comparison, are in reality *missing energy Q-values*:

$$Q = \sum_{i=LCP+ER} E_i - E_{beam} \tag{8.1}$$

where, the energy of possible emitted neutrons is not considered since experimentally we do not measure them. On the contrary, the light blue dashed spectrum is the *true Q-value*; it is obtained, for each simulation, from the 4π simulation in which both neutrons and complete charged particles (events), which are also partly lost in the experiments due to dead zone of the experimental apparatus are considered:

$$Q_{true} = \sum_{i=n+LCP+ER} E_i - E_{beam}. \tag{8.2}$$

An opportunely reduced number of 4π-simulated events have been considered just for an easier visual comparison. In the Q-value figures, for the sake of comparison, the lines relative to the different n-emission thresholds are also drawn.

In general, a rather good description is observed between filtered $GEMINI^{++}$ data and the experimental results in the $^{16}O + ^{30}Si$ at 111 MeV (Fig. 8.4), while some discrepancies

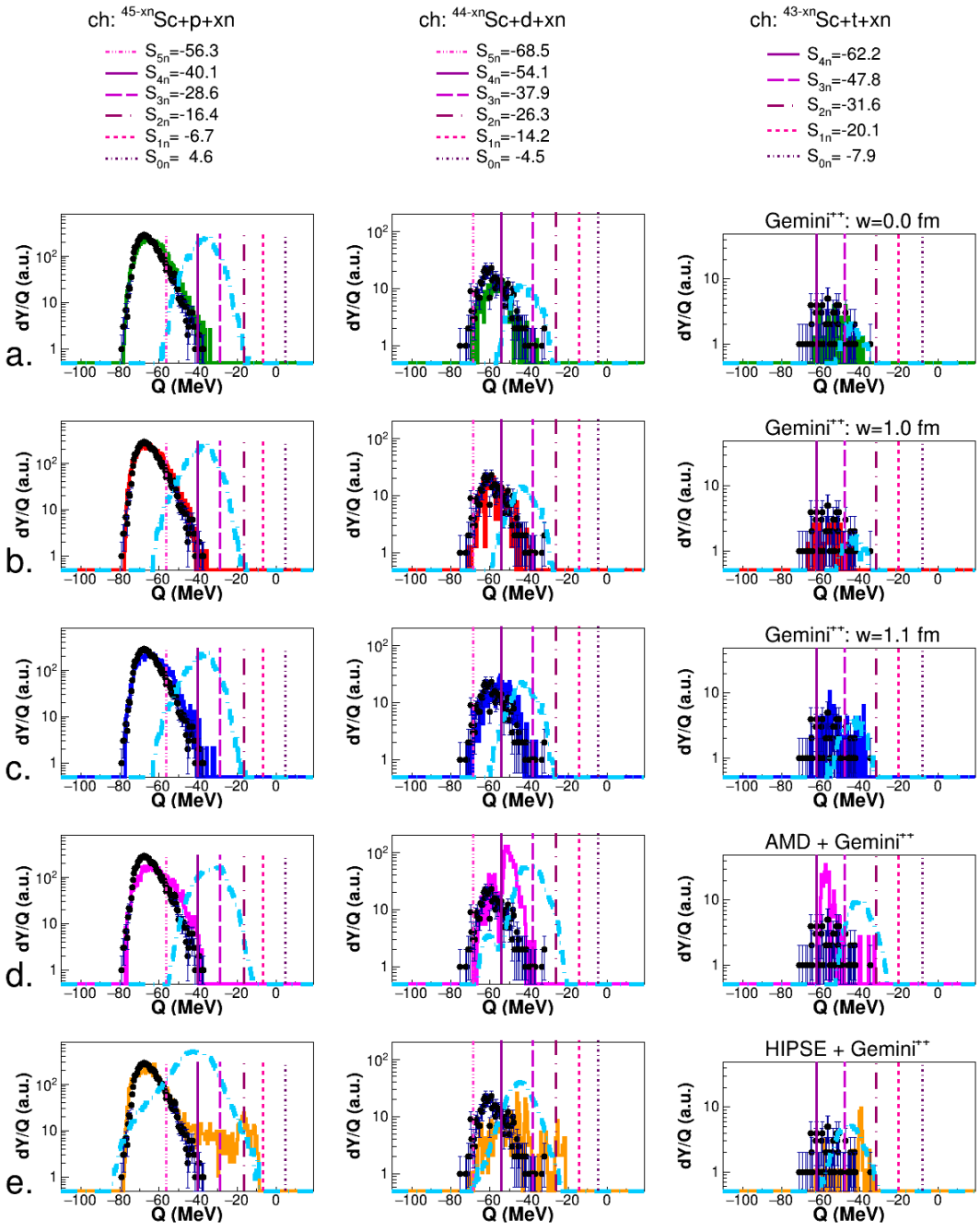

Figure 8.4: Q-value of LCP in coincidence with a *Sc*-residue for the reaction $^{16}O + ^{30}Si$ at 111 MeV. **G00** in green, **G10** in red, **G11** in blue, **AMD** in pink and **HIPSE** in orange.

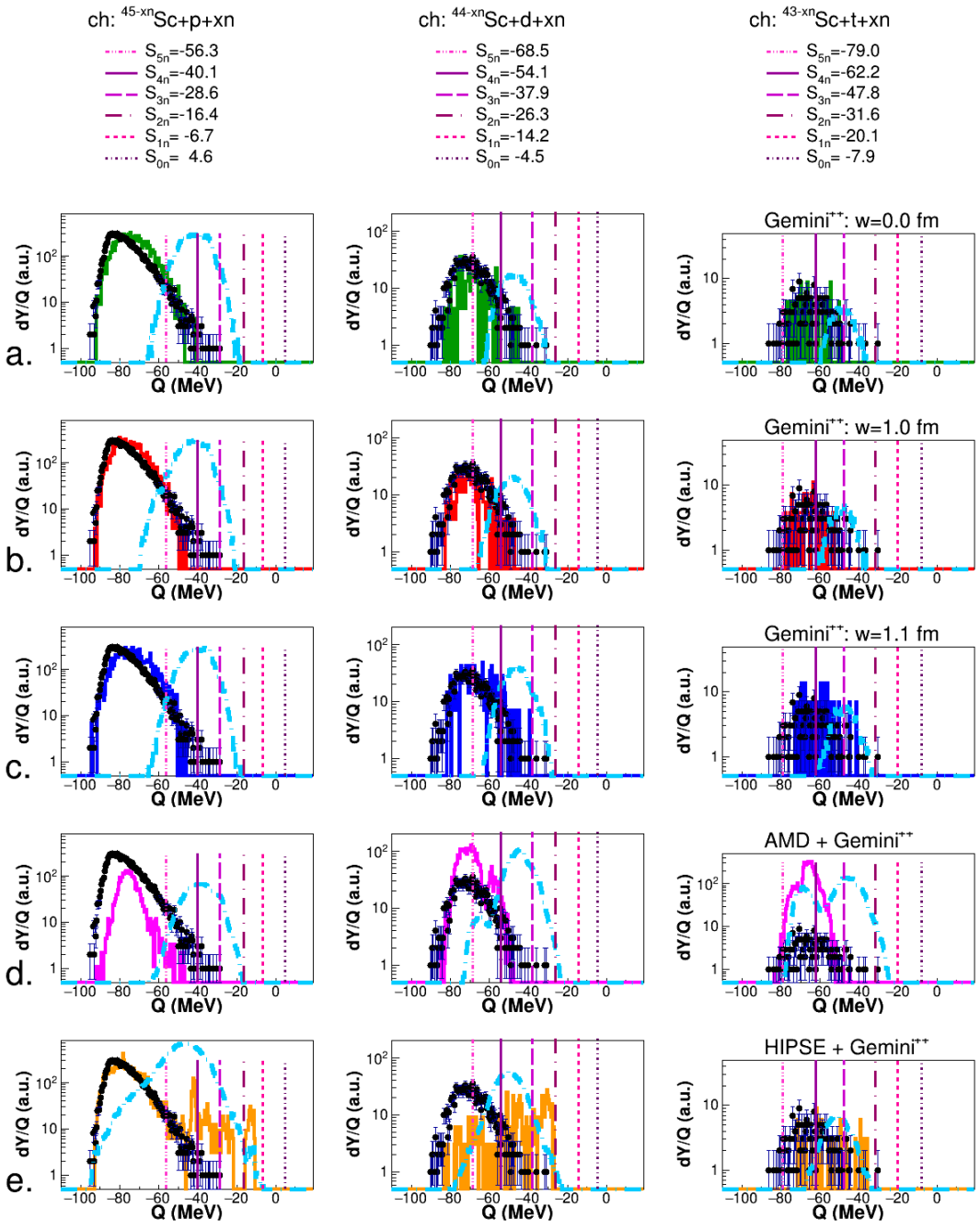

Figure 8.5: Q-value of LCP in coincidence with a *Sc*-residue for the reaction $^{16}O + ^{30}Si$ at 128 MeV.

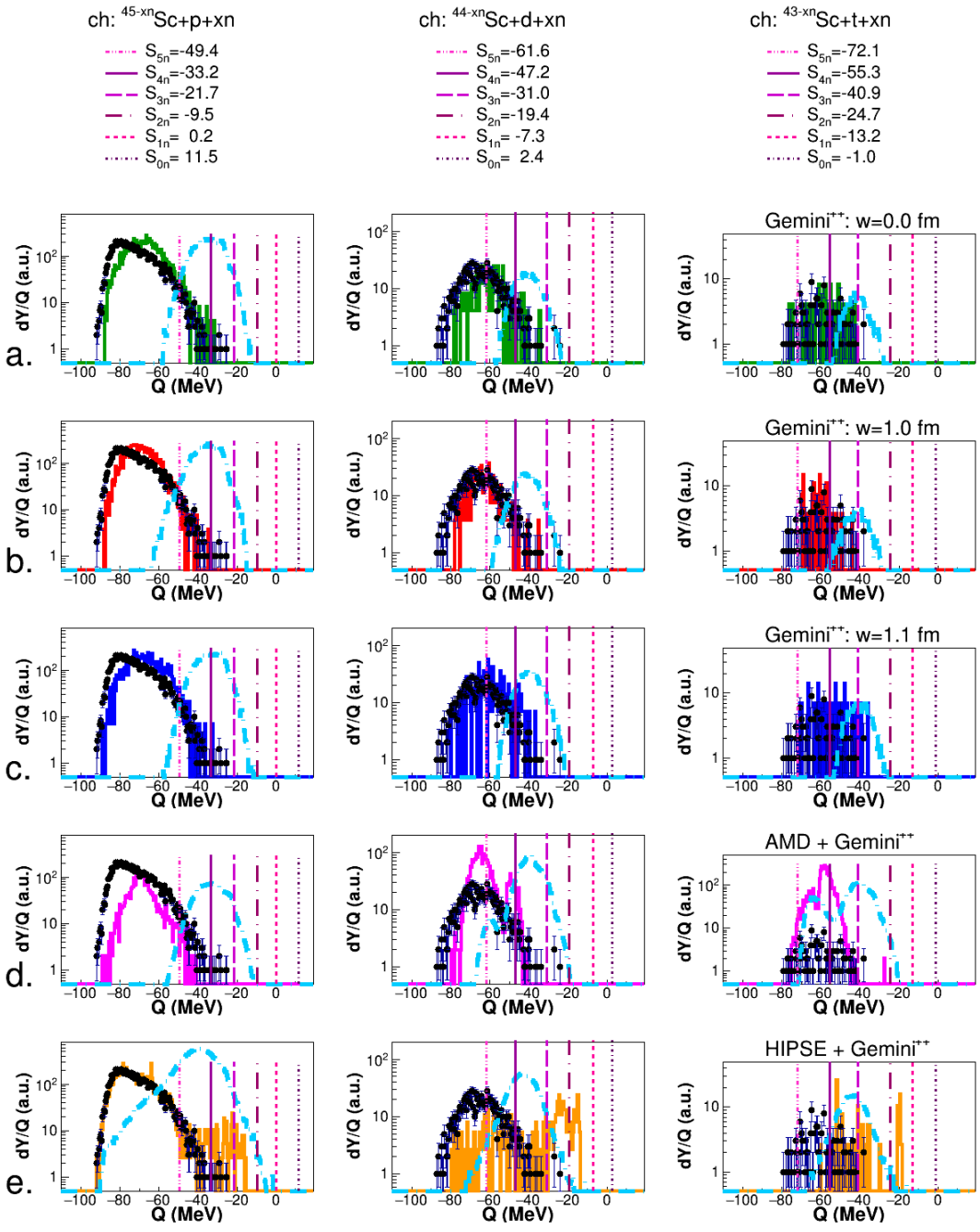

Figure 8.6: Q-value of LCP in coincidence with a *Sc*-residue for the reaction $^{18}O + ^{28}Si$ at 126 MeV.

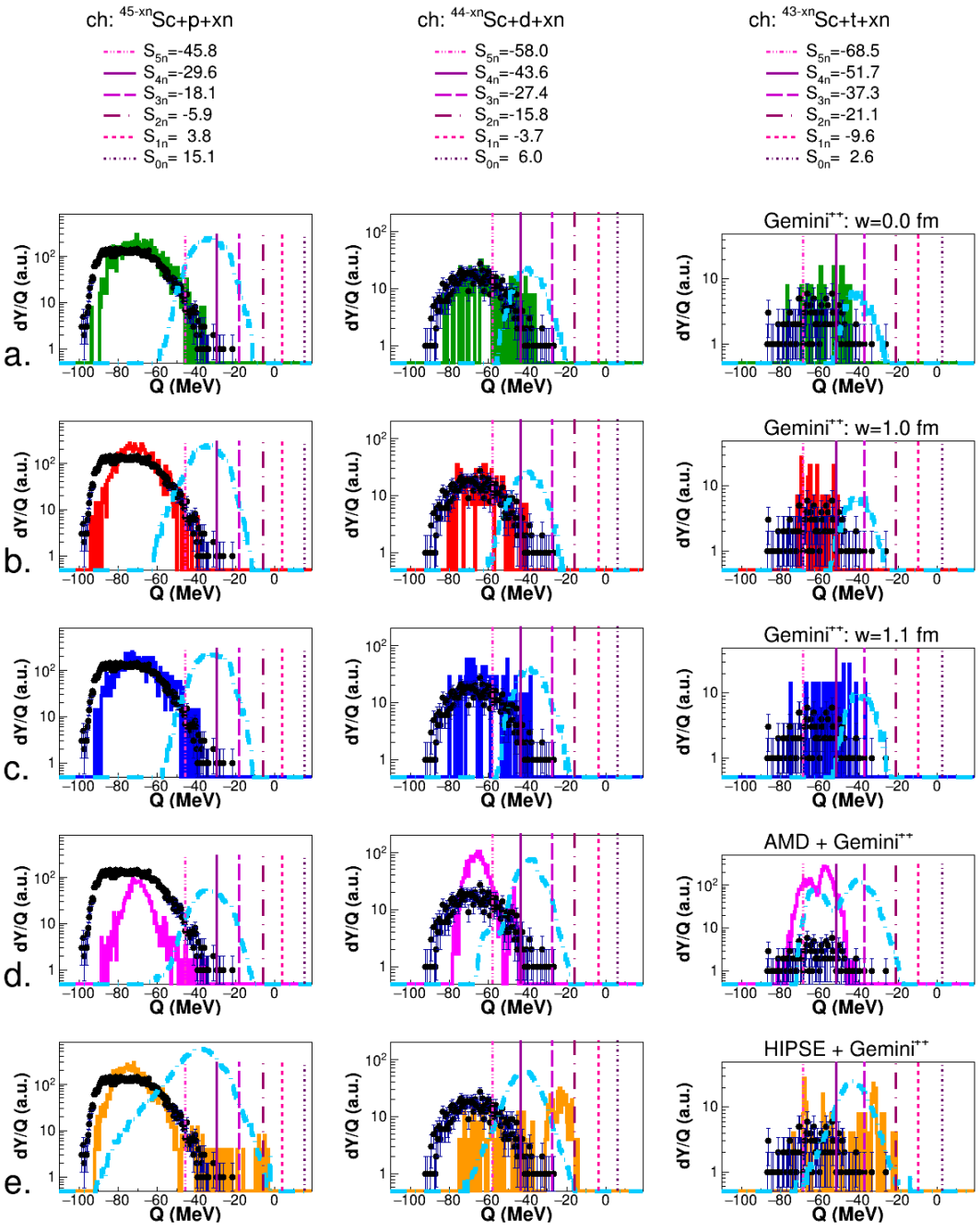

Figure 8.7: Q-value of LCP in coincidence with a *Sc*-residue for the reaction $^{19}F + ^{27}Al$ at 133 MeV.

are observed with **AMD**, especially for deuterons and tritons. In the **HIPSE** case protons are relatively well described, except from the region at low dissipation ($-35 \div -10$ MeV) where it shows some peaks not observed in the data; deuterons and tritons are not well described. Looking therefore to the $GEMINI^{++}$ simulations (the better of which is the **G10** case) and observing its prediction for the true Q-value, one can infer that the most populated channels for each LCP are:

- $^{42}Sc + p + 3n$, followed by $^{43}Sc + p + 2n$ and $^{41}Sc + p + 4n$;
- $^{41}Sc + d + 3n$ followed by $^{42}Sc + d + 2n$;
- $^{41}Sc + t + 2n$.

At higher energy and with the same ^{16}O induced system (Fig. 8.5), the Q-value situation is similar, except for the fact that **AMD** is no more reproducing even the Q-value spectrum relative to protons. A slight difference can be observed even with $GEMINI^{++}$, since at least the in p-channel case experimental distribution seems to be peaked towards a slightly more dissipative region ($\sim$ 10 MeV in average) but the general reproduction is still reasonable. However, still a better description of the main distribution peak is made by **HIPSE**, except for the low dissipative part, which still is not present in the data. In this case, again looking at the 4π reconstructed *true Q-value* in the **G10** case for which the agreement with data is reasonably good, we can infer that the populated channels are: $^{42}Sc + p + 3n$ and $^{41}Sc + p + 4n$ with similar probability followed by $^{43}Sc + p + 2n$ and $^{40}Sc + p + 5n$ with a quite smaller probability. Looking at **HIPSE**, which even better predict the experimental shape at high dissipation, it predicts a slightly larger dissipation with a major probability of feeding the longer n-chain ($> 4n$). For the d-channel the main probability is observed towards the $^{41}Sc+d+3n$ followed by a small amount of $^{42}Sc+d+2n$ and $^{40}Sc+d+4n$ and finally, for the t-channel, a shared distribution between $^{41}Sc+t+2n$ and $^{40}Sc + t + 3n$ is predicted.

The ^{18}O induced reaction should be similar to the previous one since they should bring to the same excitation energy, but a larger discrepancy is observed in the p-channel, with respect to simulations. Moreover, the experimental distribution presents also a slightly

different shape with respect to the ^{16}O case, with a second bump around $Q = -55 \div -60$ MeV, which was not present in the previous case. Again, for the p-channel **HIPSE** is the one which better describe the experimental distribution up to -30 MeV and, again, the 4π-**HIPSE** predicts a larger dissipation with respect to all $GEMINI^{++}$ cases with a major probability of feeding the longer n-chain ($> 4n$). On the contrary, a similar behavior with respect to the ^{16}O induced reaction is observed for the deuterons and tritons channels.

Going up with the CN excitation energy and looking to the ^{19}F induced reaction, the situation is getting more and more different: the p-channel Q-value distributions are larger and with an almost flat top between -65 MeV <Q-value< -90 MeV, which is not reproduced by any simulation; **G00** and **G11** are the closer, but they still do not reproduce the more dissipative part. A similar situation is seen for the deuterons and tritons channels where still **G00** is the best.

As a general trend from the 4π distributions the protons and tritons channels show a tendency to go toward an expected larger dissipation (respectively privileging $4n$ and $3n$ emission), while from the p-channel all simulations predict a higher cross section in the $4n$ channels, with opening of the $5n$ emission: since the experimental Q-value distribution is slightly more dissipative we may expect that $5n$ emission may be even more privileged than predicted.

In Fig. 8.8 and in Fig. 8.9 the experimental angular distribution (black dots) of protons, deuterons and tritons in coincidence with the Sc-residue are compared with those produced by simulations.

Looking to these angular distributions globally, one can observe that proton spectra (panel a. of Fig. 8.8) show an overproduction at forward angles at low energy ($^{16}O + ^{30}Si$ at 111 MeV), which are not reproduces by any of the calculations; in the central angular region is more or less well accounted for by almost all calculations, with small deviations, while they are underestimated at backward angles ($\theta_{lab} = 127.5^o \div 150.4^o$). At higher energy, $^{16}O + ^{30}Si$ at 128 MeV (panel b. of Fig. 8.8), the agreement with the simulation of $GEMINI^{++}$ alone is better in the whole angular range, with a better description by **G00**, followed by **G11**. **HIPSE** is reasonably describing the distribution apart from the

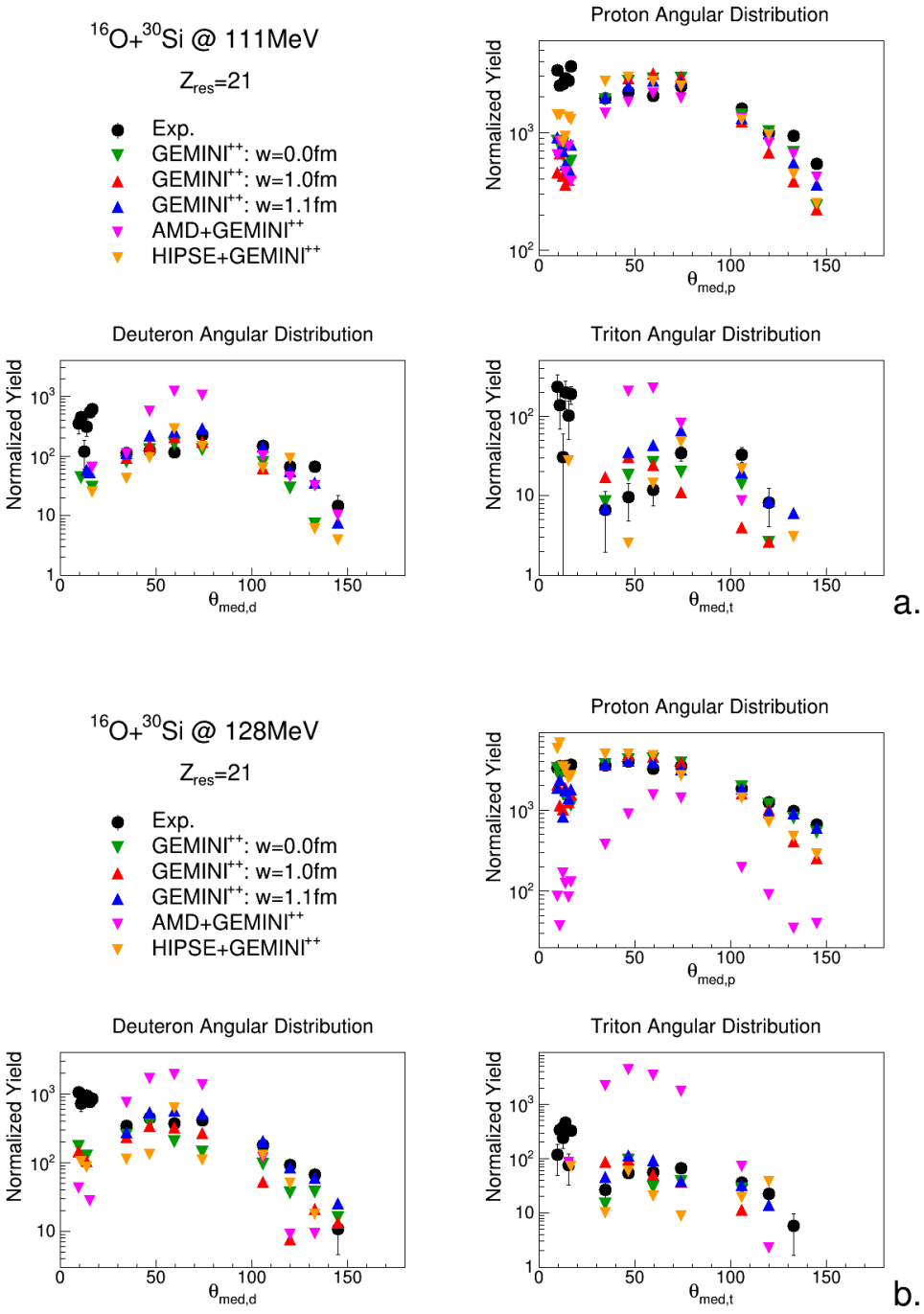

Figure 8.8: Angular distributions of LCP in coincidence with Sc-residue for the reactions $^{16}O + ^{30}Si$ at 111 MeV (panel a.) and $^{16}O + ^{30}Si$ at 128 MeV (panel b.).

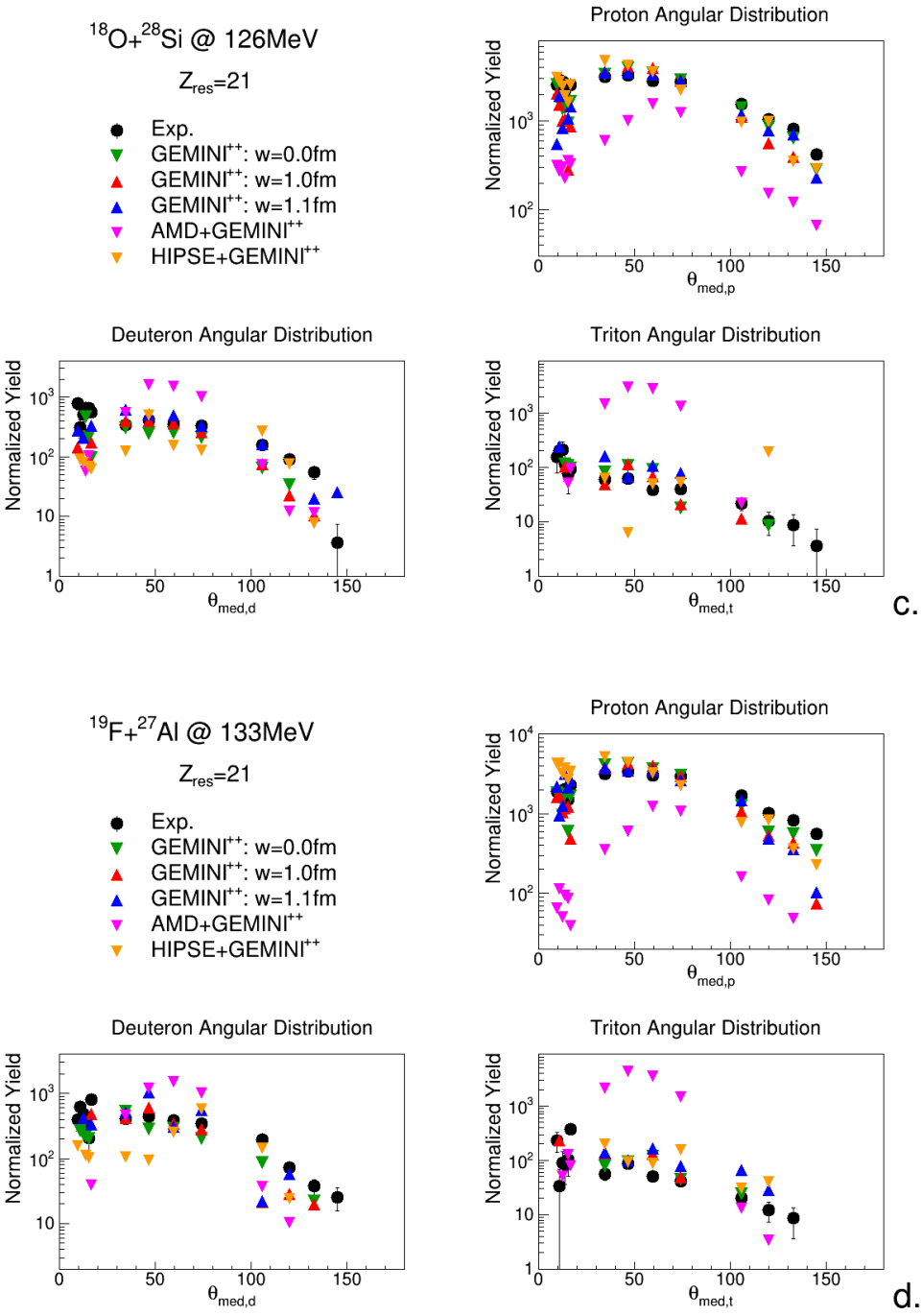

Figure 8.9: Same as in Fig. 8.8 but for the reactions $^{18}O + ^{28}Si$ at 126 MeV (panel c.) and $^{19}F + ^{27}Al$ at 133 MeV (panel d.).

very forward region ($\theta_{lab} = 8.8^o \div 11.7^o$) and the very backward one ($\theta_{lab} = 127^o \div 150.4^o$). **AMD** is, on the contrary, completely underestimating the protons. A similar behavior can be observed for the other two reactions ($^{18}O+^{28}Si$ at 126 MeV and $^{19}F+^{27}Al$ at 133 MeV), shown in Fig. 8.9. In F-induced reaction, a better description of the forward angular region ($\theta_{lab} = 8.8^o \div 17.4^o$) is generally obtained with all $GEMINI^{++}$ cases and with **HIPSE**, while a slight underestimation can be observed at backward angles ($\theta_{lab} = 97.5^o \div 150.4^o$); instead again, **AMD** is not able to describe protons for the two reactions.

Deuterons are reasonably well described in the intermediate angular region ($\theta_{lab} = 29.5^o \div 82.5^o$) by $GEMINI^{++}$ for all reactions, with a slightly better description by the **G11** case. In the two cases with ^{16}O induced reactions, the forward region is not accounted for by any calculation, while the backward region is reasonably described again by **G11** and, in the low energy case, also by **AMD**. For the ^{18}O and ^{19}F reactions the forward region is better described by $GEMINI^{++}$ (especially **G00**), while the backward part is slightly underestimated by all calculations. Again, **AMD** is not able to reproduce the data, showing a peaked distribution for $\theta_{lab} = 29.5^o \div 82.5^o$, where the simulated data strongly over-predict the deuteron yields: this is slightly more evident for the O-induced reactions. **HIPSE** is similar to $GEMINI^{++}$ with ^{16}O at low energy, underestimating the distribution at 128 MeV, while in the case of ^{18}O it is closer to the experiments in the central region ($\theta_{lab} = 41.0^o \div 126.5^o$) but still underestimates both the forward and the backward part. For the F case it reproduces the data only in a more restricted central part ($\theta_{lab} = 53.0^o \div 113.0^o$).

Again, in the triton case, an experimental overproduction is observed at forward angles for the ^{16}O induced reactions, relatively more evident at lower incident energy. In the other part of the angular distribution, an overall agreement can be observed with $GEMINI^{++}$: it is difficult to choose between the different parametrizations at 111 MeV, while it is slightly better the **G11** simulation at 128 MeV. In the case of ^{18}O and ^{19}F, on the contrary, almost no overproduction is observed at forward angles: therefore, a reasonable overall description of the distribution is performed by $GEMINI^{++}$. **AMD** is, on the contrary, overestimating the central angular region in a larger way than for deuterons. **HIPSE** is reasonable in the

case of F for for $\theta_{lab} > 29.5^o$, while do not predict any emission at forward angles; for the ^{16}O induced reactions it reasonably follows the up and down behavior at 111 MeV and the more flat distribution at 128 MeV, while for the ^{18}O reaction it is difficult to draw any conclusion.

The experimental energy spectra (black dots) of protons, deuterons and tritons in coincidence with the Sc-residue, compared with those produced by simulations (green **G00**; **G10** red; **G11** blue; **AMD** pink; **HIPSE** orange), have also been studied. For the sake of simplicity they are displayed in the Appendix B. Normalization to the maximum has been performed for shape comparison: the displayed spectra Fig. B.1 $\div$ B.12 correspond to the forward region ($8.8^o < \theta_{lab} < 17.4^o$), the central region ($29.5^o < \theta_{lab} < 82.5^o$) the backward region ($97.5^o < \theta_{lab} > 150.4^o$).

From the comparison to the different simulations we observe that proton energy spectra are never well accounted for by simulations with $GEMINI^{++}$ and **AMD**. Experimental spectra are normally softer especially in the central angular region. The best description is so far obtained by **G10**. On the contrary, **HIPSE** is well accounting for the shape of the proton spectra in all the angular region, apart from the fact that it also predicts a production of fast particles especially emitted in the central angular region, which are not present in the data. For deuteron the description by $GEMINI^{++}$ is more in agreement at all energies (especially the **G10** case), apart from the fact that these simulations do not predict so many deuterons as experimentally observed in the forward angles. **AMD** and **HIPSE** are instead unable to describe the data. For tritons, due to the very low statistics it is difficult to say something: however still **G10** is probably the one which better describes the central region but every no simulation is able to describe the forward and backward triton production.

Concluding we can say that for what it concerns the Sc exit channel the protons, deuterons and tritons observables are only partially reproduced by the different code: **AMD** completely fails to describe the results obtained with the higher energies reactions; nevertheless, looking at Figs. 8.10 and 8.11, where the difference between the experimental and simulated yield are presented as a function of the detected angles, it is often good,

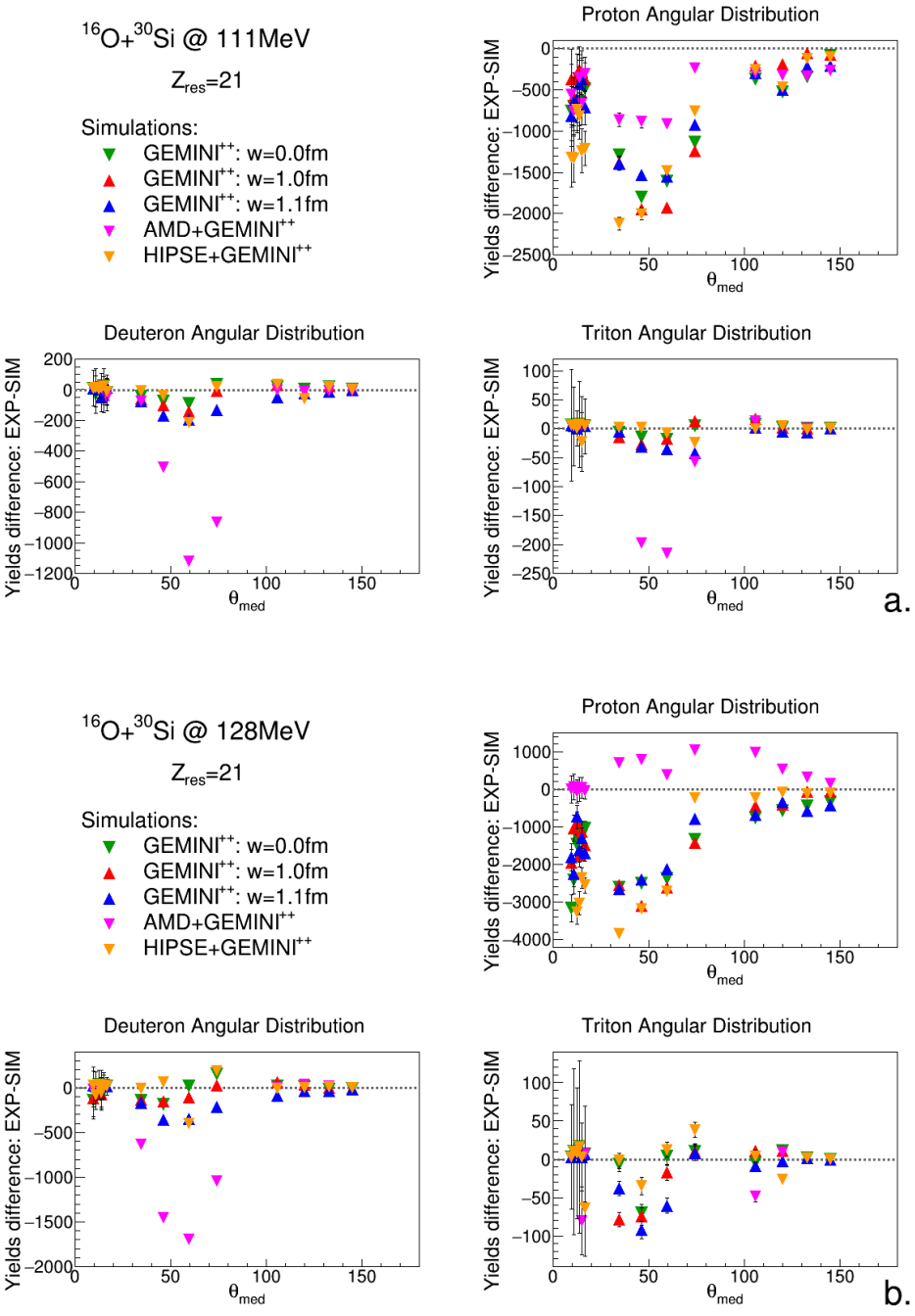

Figure 8.10: Difference of experimental and simulated angular distribution of proton, deuteron and triton in coincidence with the *Sc*-residue for the reactions $^{16}O + ^{30}Si$ at 111 MeV (panel a.) and $^{16}O + ^{30}Si$ at 128 MeV (panel b.).

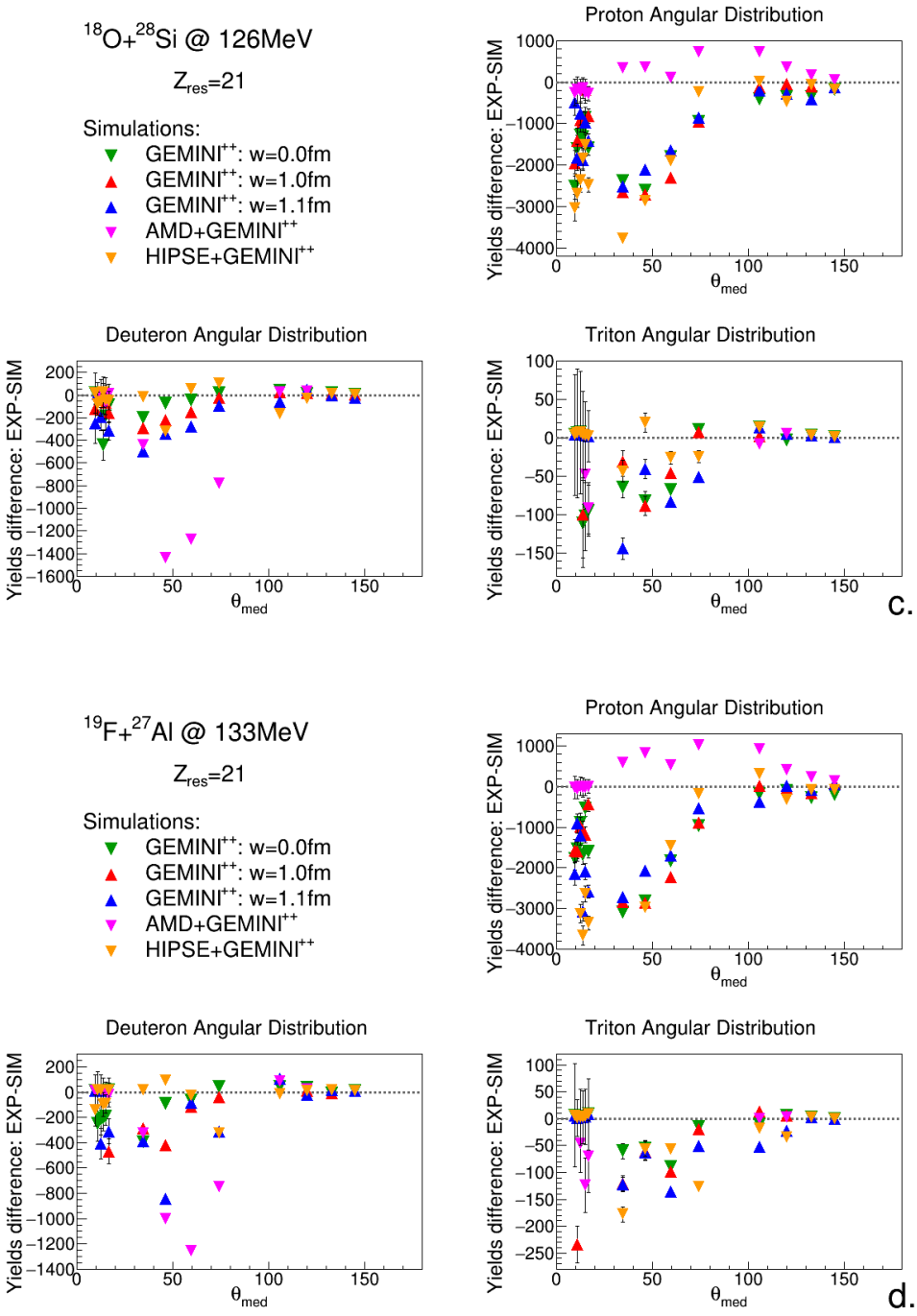

Figure 8.11: Same as in Fig. 8.10 but for the reactions $^{18}O + ^{28}Si$ at 126 MeV (panel c.) and $^{19}F + ^{27}Al$ at 133 MeV (panel d.).

and sometime the best, in reproducing the LCP detected at forward angles for the same reactions. The trend of the differences between experimental and **HIPSE** angular distribution is more similar to those with the statistical codes; it is reasonably able to reproduce deuteron and triton in forward and backward angles, but it does not reproduce (or it reproduces in a worse way, depending on the reaction) the experimental yields in the central angular region.

8.1.2 The Ca residue: $Z_{res} = 20$

In Table 8.4 the number of Ca-residue and the total branching ratio of channels with such residue have been reported for experimental and simulated data for the four reactions. The BR is again defined as the ratio between the number of evaporation residues with

	$^{16}O + ^{30}Si$	111 MeV	$^{16}O + ^{30}Si$	128 MeV
	n^o residues	BR(%)	n^o residues	BR(%)
Experimental	35365 ± 188	21.4	62307 ± 250	11.9
$GEMINI^{++}$ $w = 0.0$ fm	56096	21.1	45908	15.5
$GEMINI^{++}$ $w = 1.0$ fm	57419	17.7	46084	13.4
$GEMINI^{++}$ $w = 1.1$ fm	48813	16.1	35355	10.6
$AMD + GEMINI^{++}$	45004	19.3	28869	13.3
$HIPSE + GEMINI^{++}$	36948	29.2	18541	13.3
	$^{18}O + ^{28}Si$	126 MeV	$^{19}F + ^{27}Al$	133 MeV
	n^o residues	BR(%)	n^o residues	BR(%)
Experimental	58107 ± 241	10.9	51110 ± 226	10.9
$GEMINI^{++}$ $w = 0.0$ fm	41774	12.8	29957	9.1
$GEMINI^{++}$ $w = 1.0$ fm	40827	10.7	29970	8.0
$GEMINI^{++}$ $w = 1.1$ fm	33098	8.8	23593	6.3
$AMD + GEMINI^{++}$	31083	13.1	22124	10.4
$HIPSE + GEMINI^{++}$	26092	18.0	18541	13.3

Table 8.4: Number and total branching ratio (BR) of channels with Ca-residue.

$Z_{res} = 20$ over the total number of residues. At variance with the previous case, in this channel the experimental branching ratios are not too different by the calculated ones and

a quite similar trend is observed as a function of the different reactions.

The total LCP multiplicity (Mult.) in coincidence with a Ca-residue defined for each event is plotted as a function of the Particle Identification (P.Id.) in Figs. 8.12 and 8.13 for the four reactions: $^{16}O + ^{30}Si$ at 111 MeV (panel a.), $^{16}O + ^{30}Si$ at 128 MeV (panel b.), $^{18}O + ^{28}Si$ at 126 MeV (panel c.) and $^{19}F + ^{27}Al$ at 133 MeV (panel d.). In this case either two particles with $Z = 1$ or one with $Z = 2$ are emitted in coincidence with the ^{A-xn}Ca, where A depends on the light isotope masses (p,d,t, ^3He, α) and on the number of emitted neutrons. The experimental distributions show clearly, in all systems a major production of ($Z = 2$)-clusters, especially α-particles, which are not accounted for by any of the calculations. Moreover, a small production of ^6He is also observed and not described by simulations, which is larger in the ^{18}O and ^{19}F induced reactions. At variance with experimental data and other simulations **HIPSE** tends to overestimate the isotopes ^3He, with respect to α-particles, and tritium, with respect to proton and deuteron.

In Fig. 8.14 and in Fig. 8.15 the experimental angular distribution (black dots) of LCP in coincidence with the Ca-residue are compared with those produced by simulations. The angular distributions show for all the reactions a strong overestimation of protons in the whole angular range and a corresponding strong underestimation of α-particles. It has to be reminded that both the simulations are normalized to the relative number of residues $\left(\frac{\#_{res,exp}}{\#_{res,"sim"}}\right)$. Moreover, a forward peaked structure is observed for the experimental α-particles which is more evident for the two ^{16}O induced reactions, it is a little bit reduced for ^{18}O and almost flat, with respect to the central angular region yield, in the case of ^{19}F. The trend simulated by calculations which generally presents a reduction in the forward yields with respect to the central angular region, is not followed by any of the experimental data set, which, on the contrary, show a larger α production at forward angle in all cases, with a larger focusing effect in the O induced reactions. Deuterons are almost well described by all simulations in the F induced reaction. In the ^{18}O case, a small overestimation is visible in the angular region $29.5^o < \theta_{lab} < 66.0^o$; the same overestimation is observed for the ^{16}O at 128 MeV data set, which shows in addition a small underestimation in the forward region ($\theta_{lab} = 8.8^o \div 17.4^o$). At low energy (panel a.) the difference in the central angular

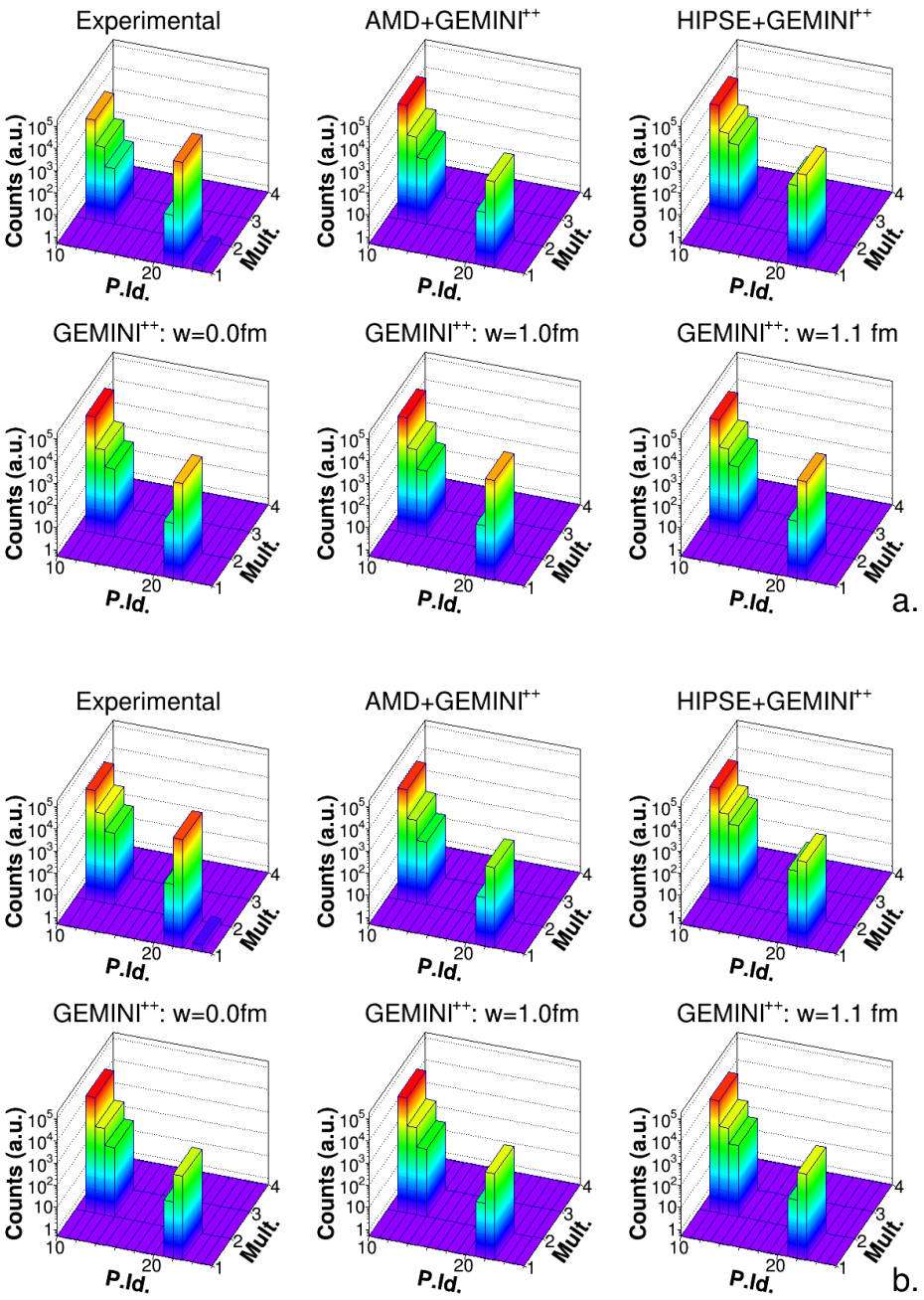

Figure 8.12: Open decay channels: particles in coincidence with a Ca- residue for the reactions $^{16}O +^{30} Si$ at 111 MeV (panel a.) and $^{16}O +^{30} Si$ at 128 MeV (panel b.). The Particles Identification is: 11 protons, 12 deuterons, 13 triton, 21 ^3He and 22 α-particles. See text for more details.

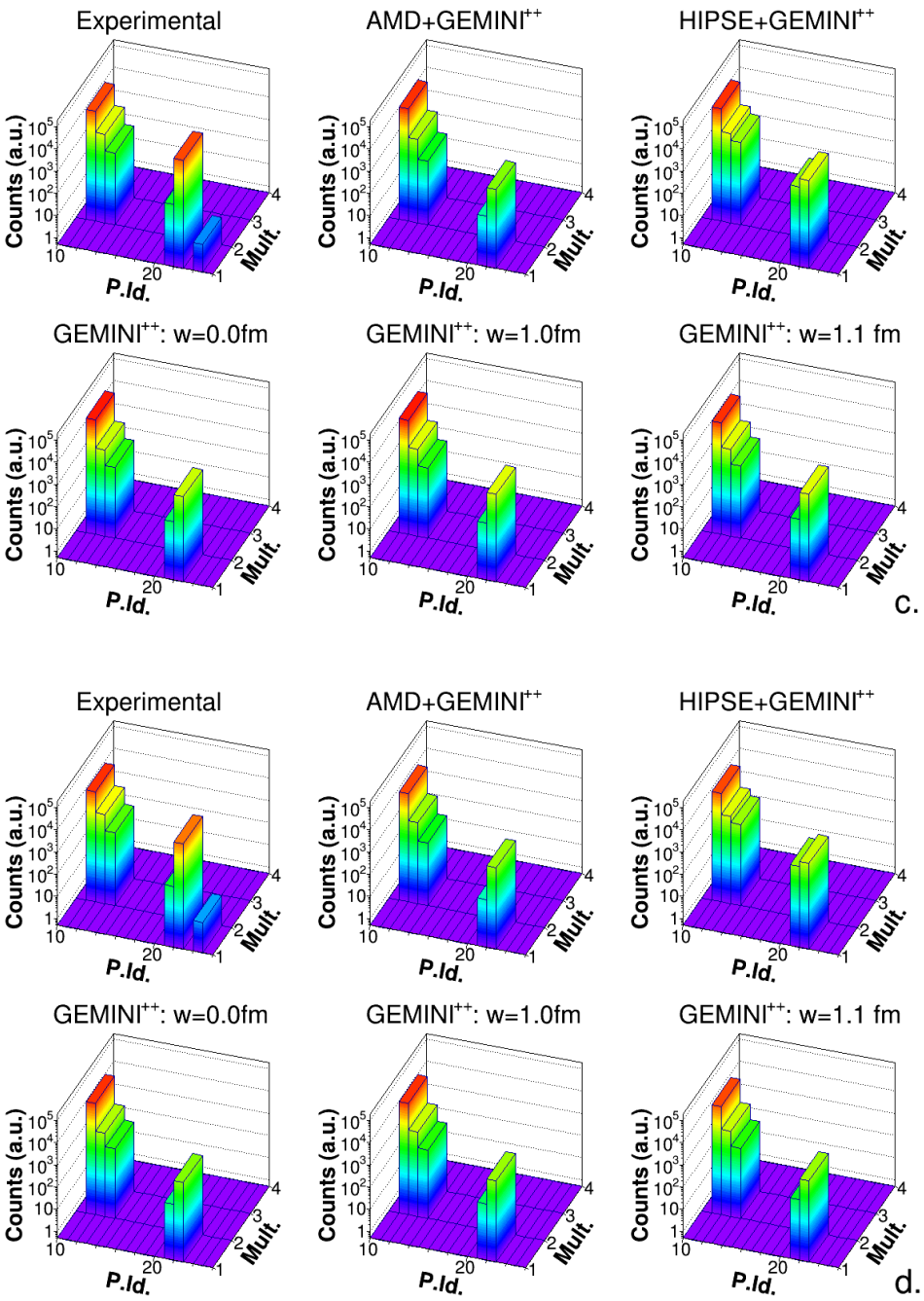

Figure 8.13: Same as in Fig. 8.12 but for the reactions $^{18}O + ^{28}Si$ at 126 MeV (panel c.) and $^{19}F + ^{27}Al$ at 133 MeV (panel d.).

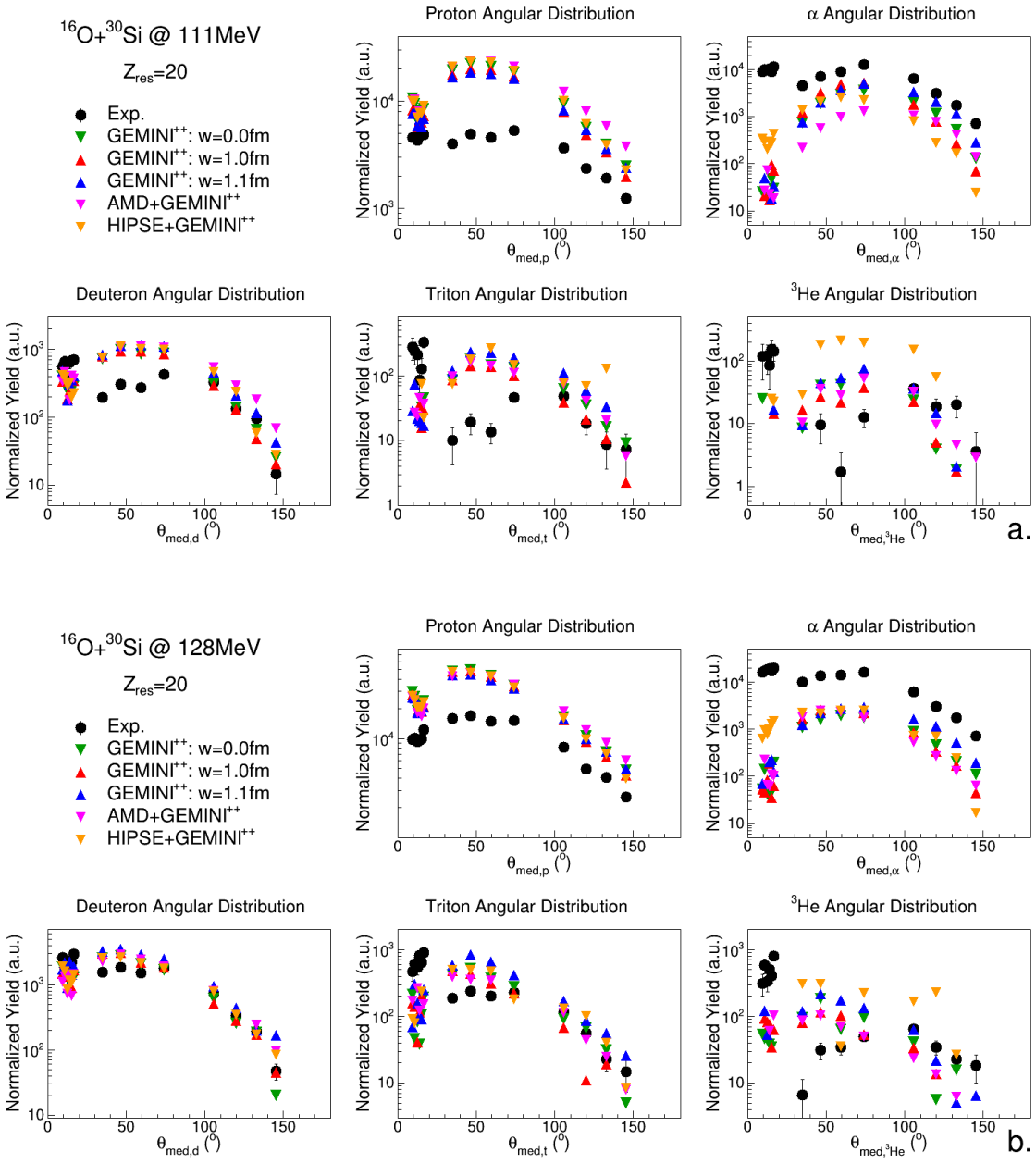

Figure 8.14: Angular distributions of LCP in coincidence with Ca-residue for the reactions $^{16}O + ^{30}Si$ at 111 MeV (panel a.) and $^{16}O + ^{30}Si$ at 128 MeV (panel b.) in comparison with $GEMINI^{++}$ with $w = 0.0$ fm (green triangles), $GEMINI^{++}$ with $w = 1.0$ fm (red triangles), $GEMINI^{++}$ with $w = 1.1$ fm (blue triangles), $AMD + GEMINI^{++}$ (pink triangles) and $HIPSE + GEMINI^{++}$ (orange triangles).

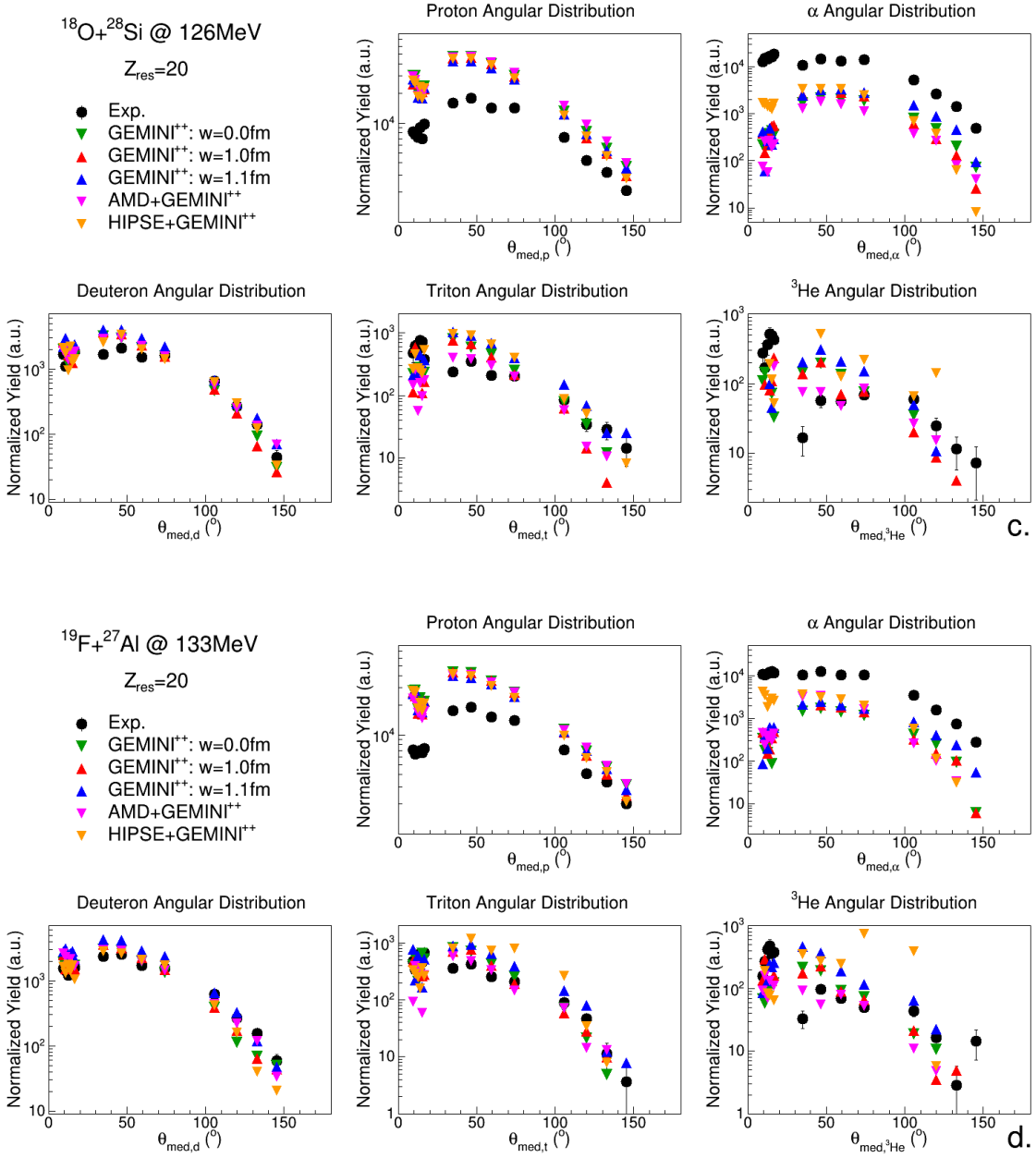

Figure 8.15: Same as in Fig. 8.14 but for the reactions $^{18}O + ^{28}Si$ at 126 MeV (panel c.) and $^{19}F + ^{27}Al$ at 133 MeV (panel d.).

region ($\theta_{lab} = 29.5^o \div 82.5^o$) is even larger, while, in the forward part, a similar behavior of the higher energy ^{16}O induced reaction is observed. A similar behavior is observed for tritons. The ^3He case is more complex: **HIPSE** is strongly over-predicting its production for all other reaction. In the ^{19}F case, the **AMD** is the closest to the experimental data, while in the O-induced reaction cases the general trend of experimental data is not well accounted for by any simulation.

The experimental energy spectra shapes (black dots) of LCP in coincidence with the Ca-residue, compared with those produced by simulations (green **G00**, red **G10**, blue **G11**, pink **AMD** and orange **HIPSE**), are again presented in Appendix B, in the Figs. B.13 $\div$ B.32.

For the low energy ^{16}O induced reaction, proton spectra are well described by $GEMINI^{++}$ even though a harder spectrum is observed in the central angular region ($\theta_{lab} = 29.5^o \div 82.5^o$); this difference is even enhanced if comparing the data with **AMD**. In general, the better description is coming from **HIPSE**, apart from a small overproduction at high energy in the central angular region (same origin as the previous one discussed for the Sc-case). At the higher energy for both ^{16}O and ^{18}O cases, a better description can be observed in the central region for the $GEMINI^{++}$, especially the **G10** case, while a small disagreement start to appear at forward angles $\theta_{lab} = 8.8^o \div 17.4^o$; again, **HIPSE** is more able to describe to whole angular range, taking into account the possible overproduction of fast protons in the forward angles, apart from the central region where the small contribution from fast emission is still visible in the simulation but not in the experimental data. In the F case the situation is similar, but with a smaller disagreement with $GEMINI^{++}$ in the forward angular region, which may indicate a smaller fast proton emission.

A rather good description is obtained for deuteron of the low energy ^{16}O induced reaction by **G00** and **G10**, while in the **G11** case and for **AMD** the shape is not well described in the angular range $29.5^o < \theta_{lab} < 82.5^o$. **HIPSE** well describe the overall shape except for a small peak between 30 and 40 MeV which is not present in the experimental data. At higher energy in the ^{16}O induced reaction all $GEMINI^{++}$ cases and **AMD** well describe the spectral shapes, while **HIPSE** still predicts some extra peaks at high deuteron

energy especially in the central angular range, in disagreement with experimental data. A very similar situation can be observed for the ^{18}O and ^{19}F data sets, with a small difference from experimental data arising in comparison to **G11** in the central angular region while a slightly better description by **HIPSE** (smaller amount of predicted fast deuterons) can be observed.

For tritons, due to the very low statistics it is difficult to say something at low energy, while at higher energies the ^{16}O reaction is well described by all simulations in the GARFIELD angular range ($29.5^o < \theta_{lab} < 150.4^o$); no one is really able to describe the forward emission ($\theta_{lab} = 8.8^o \div 17.4^o$). For the ^{18}O case only **G00** and **G10** well account for the spectra, **G11** predicts a harder spectrum in the central angular region, while **AMD** underestimates the forward region. **HIPSE** shows an overproduction of fast tritons in the central region. In the F-induced reaction triton spectra are almost well reproduced by all simulations, apart from **HIPSE**.

^3He are normally not well described at all energies and they are especially underestimated in the forward region.

The α-particles spectra are also generally not described by simulations; in particular we can see that for ^{16}O at 111 MeV the best reproduction is obtained by **G10** and from **HIPSE** in the angular region $\theta_{lab} = 29.5^o \div 150.4^o$, while in the forward part no simulation is able to describe the experimental data; only **HIPSE** shows a larger production, which still is far from the experimental findings. In the ^{16}O at 128 MeV case, a better reproduction, apart, again, the very forward direction, is still given by **G10**, but in this case also **AMD** seems closer to the data. For the ^{18}O at 126 MeV, only **G10** is able to describe the data, apart from the forward part which is still underestimated. A similar behavior is seen for the ^{19}F induced reaction, but in this case also **AMD** seems closer to the data. Again, however the forward yield and shape is not described.

Concluding we can say that for what it concerns the Ca exit channel, all the simulation codes predict an inversion of the proton and α-particle yields: they largely underestimate the α production in coincidence with the Ca-residue, while they widely overestimate the proton emission. Furthermore, looking to the α-spectra we can assert that more or less

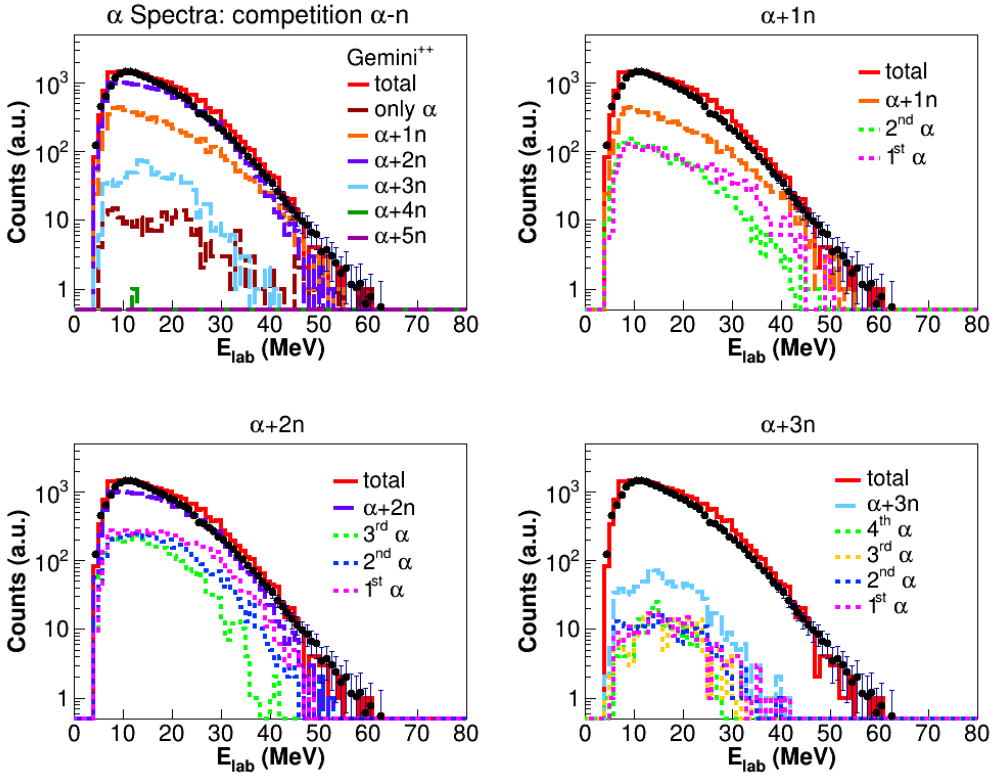

Figure 8.16: Experimental α-particle spectra (black dots) for the reaction $^{16}O + ^{30}Si$ at 111 MeV in comparison to the simulation made by $GEMINI^{++}$ with $w = 1.0$ fm (red line). For the simulated spectra are illustrated the different components associated to the neutron emission in coincidence with the α-particle; the dashed line represents the different xn-channels, the dotted lines, for each xn-channel, the position of α See text for more details.

all models for all the reactions fail to reproduce the spectral shape; this can be explained in terms of competing n-emission in coincidence with the α-particle. In fact, the final α spectrum depends directly both on the number of neutrons emitted in coincidence with the α-particles and on the emission step of the α-particle in the α-xn chain: in Fig. 8.16, the experimental α spectrum (black dots) is compared to the simulation made by $GEMINI^{++}$ with $w = 1.0$ fm (red line). Since our experimental apparatus is not able to detect neutron, we do not know neither the real number of neutrons emitted in coincidence of the α-particle nor the emission step at which the α-particle is emitted. On contrary, the simulation has

memory of the α-xn chain and this is shown in the figure; the dashed lines represent the different α-xn chain (related to the number of emitted neutrons), while the dotted lines represent when the α is emitted in each chain. From the figure it is observed that for $GEMINI^{++}$, it is the $\alpha + 1n$ channel, in particular the stage at which the α is the first emitted particle, which primarily influence the tail of the global spectrum; it is instead the $\alpha + 2n$ channel (mostly when the α is the second or third emitted particle), which mainly influence the shape of the "barrier".

8.1.3 The K residue: $Z_{res} = 19$

The total branching ratio of channels with K as residue and the number of K-residue have been reported for experimental and simulated data in Table 8.5 for the four reactions.

	$^{16}O +^{30} Si$	111 MeV	$^{16}O +^{30} Si$	128 MeV
	n^o residues	BR(%)	n^o residues	BR(%)
Experimental	56872 ± 239	34.4	149060 ± 386	28.4
$GEMINI^{++}$ $w = 0.0$ fm	124241	46.8	111061	37.5
$GEMINI^{++}$ $w = 1.0$ fm	163717	50.5	124406	36.1
$GEMINI^{++}$ $w = 1.1$ fm	147086	48.4	122400	36.8
$AMD + GEMINI^{++}$	88874	38.0	67053	30.9
$HIPSE + GEMINI^{++}$	46735	36.9	42244	30.4
	$^{18}O +^{28} Si$	126 MeV	$^{19}F +^{27} Al$	133 MeV
	n^o residues	BR(%)	n^o residues	BR(%)
Experimental	150719 ± 388	28.2	129999 ± 361	27.7
$GEMINI^{++}$ $w = 0.0$ fm	117653	36.0	100958	30.8
$GEMINI^{++}$ $w = 1.0$ fm	133087	34.9	106089	28.3
$GEMINI^{++}$ $w = 1.1$ fm	133428	35.6	111207	29.5
$AMD + GEMINI^{++}$	72754	30.7	58438	27.4
$HIPSE + GEMINI^{++}$	48180	33.3	42244	30.4

Table 8.5: Number and total branching ratio (BR) of channels with K-residue.

In this case, the BR is defined as the ratio between the number of evaporation residues with $Z_{res} = 19$ over the total number of residues. For all the reactions the BR are quite

well reproduced by **AMD** and **HIPSE**, while are overestimated by $GEMINI^{++}$ for the O induced reactions. On the contrary for the F case almost all simulations are reasonably in agreement with the experimental BR.

The total LCP and light fragment (Z<6) multiplicity (Mult.) in coincidence with a K-residue defined for each event is plotted as a function of the Particle Identification (P.Id.) in Fig. 8.17 and in Fig. 8.18 for the four reactions: $^{16}O + ^{30}Si$ at 111 MeV (panel a.), $^{16}O + ^{30}Si$ at 128 MeV (panel b.), $^{18}O + ^{28}Si$ at 126 MeV (panel c.) and $^{19}F + ^{27}Al$ at 133 MeV (panel d.). For the selected K-isotope, the general trend observed of the multiplicity towards P.Id. are very similar between experiment and simulations, even if some small differences appear for the Li production: experimentally more ^{6}Li are produced with respect to any prediction together with some ^{7}Li and ^{8}Li, which are not seen in the simulations. However, on the contrary to what observed in the previous decay channels, in the present case both the α and protons channels seem to be closely represented, especially by the three $GEMINI^{++}$ alone and **HIPSE**.

In general, simulations tend to overestimate the channel with $Z = 1$ and $Mult = 3$, with respect to those with $Z = 1$ and $Mult = 2$, in which also a $(Z = 2)$-particle is emitted. This is especially visible looking to **AMD**, which visibly over-predicts this channel for the four reactions, while for the other simulations the effect is more limited: in other words, it is clear, as it will be better discussed more quantitatively in the following, that the p (or $Z = 1$) + α (or $Z = 2$) channels seem to be slightly privileged in the experiments with respect to $3p$ (or $Z = 1$), as it will be shown in the following.

In Fig. 8.19 and in Fig. 8.20 the experimental angular distribution (black dots) of LCP in coincidence with the K-residue are compared with those produced by simulations.

The proton spectra (shown in Appendix B) are reasonably well described at low energy by all $GEMINI^{++}$ simulations with a slightly overestimation of $\theta_{lab} = 29.5^o \div 66.0^o$ while they are overestimated, especially in the central angular region ($\theta_{lab} = 29.5^o \div 82.5^o$) by **AMD** and **HIPSE**; but the latter well accounts for the yields at backward angles ($\theta_{lab} = 97.5^o \div 150.4^o$). The overestimation of the central angular region yields become visible even for all the $GEMINI^{++}$ simulations when looking to the higher energy reactions;

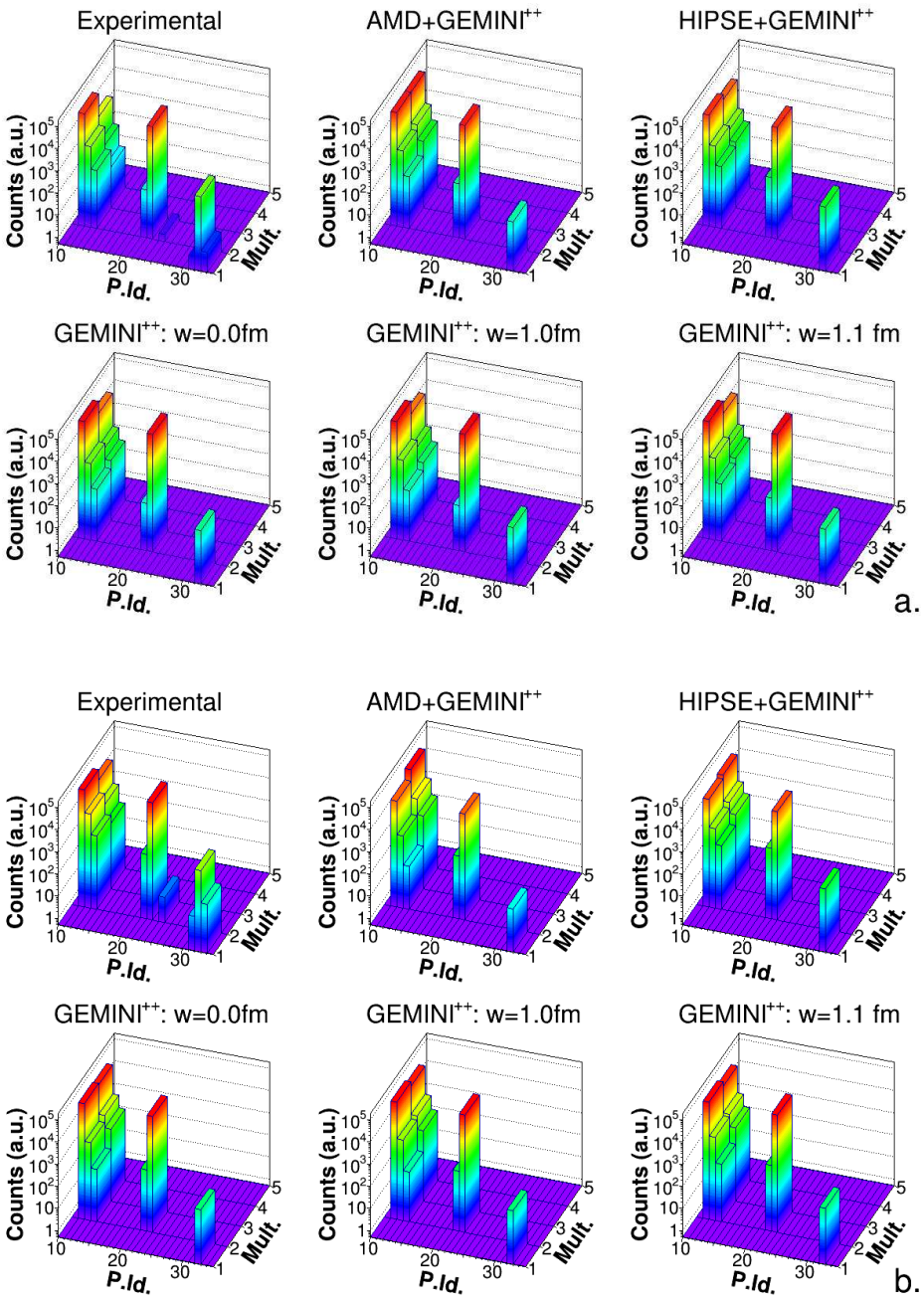

Figure 8.17: Open decay channels: particles in coincidence with a K-residue for the reactions $^{16}O + ^{30}Si$ at 111 MeV (panel a.) and $^{16}O + ^{30}Si$ at 128 MeV (panel b.). The Particles Identification is: 11 protons, 12 deuterons, 13 triton, 21 ^3He, 22 α-particles, 31 ^6Li, 32 ^7Li and 33 ^8Li. See text for more details.

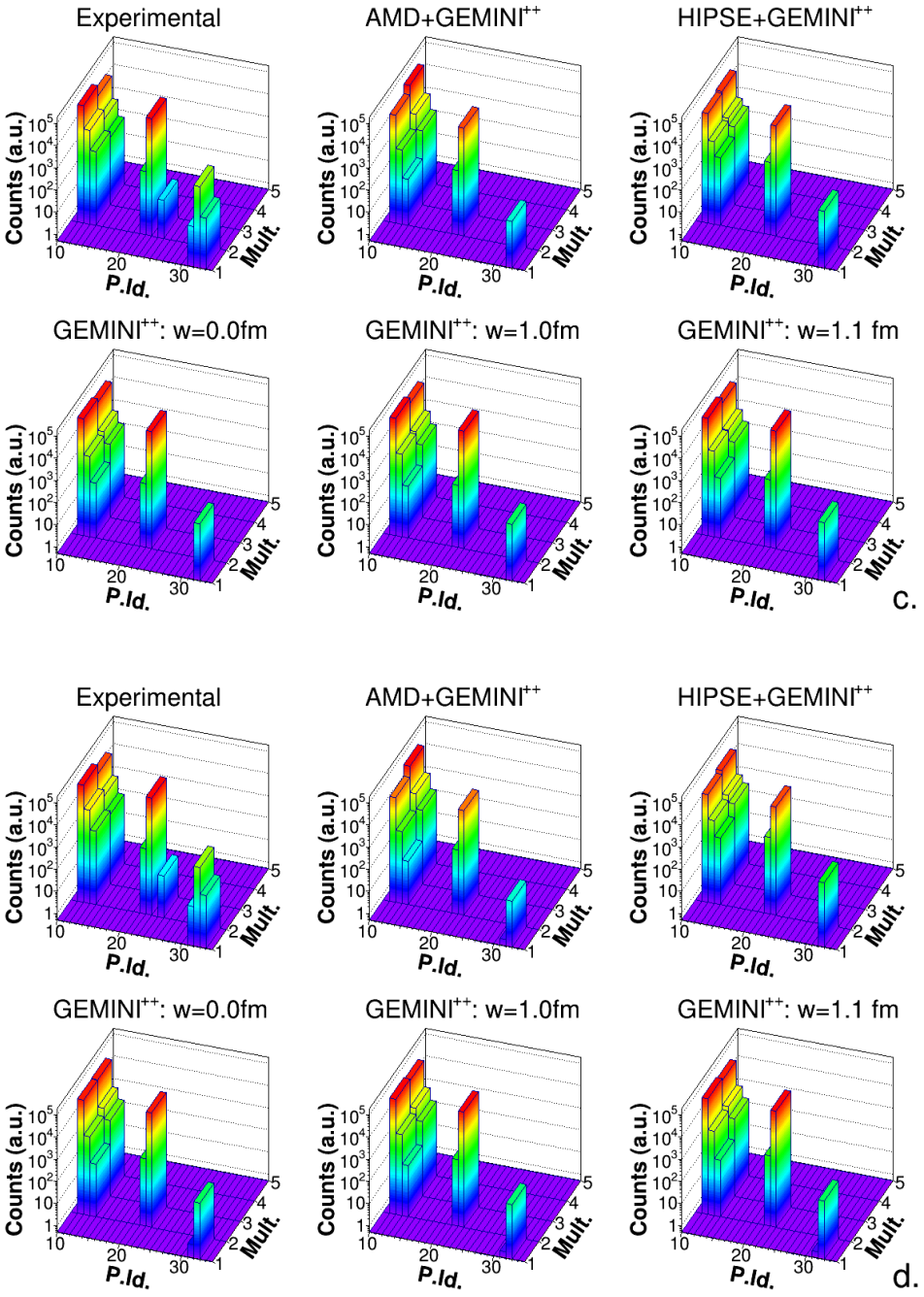

Figure 8.18: Same as in Fig. 8.17 but for the reactions $^{18}O + ^{28}Si$ at 126 MeV (panel c.) and $^{19}F + ^{27}Al$ at 133 MeV (panel d.).

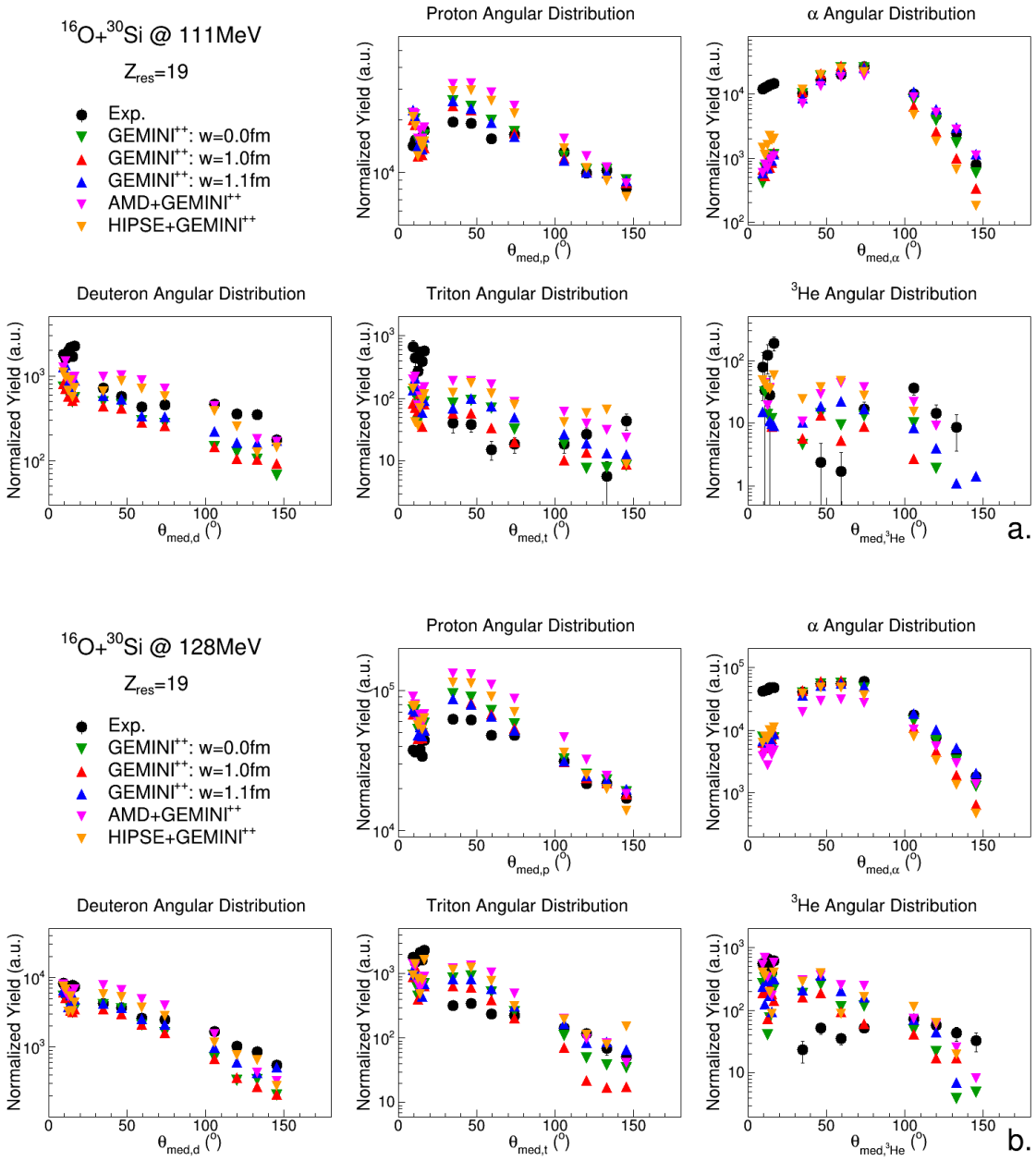

Figure 8.19: Angular distributions of LCP in coincidence with K-residue for the reactions $^{16}O + ^{30}Si$ at 111 MeV (panel a.) and $^{16}O + ^{30}Si$ at 128 MeV (panel b.) in comparison with $GEMINI^{++}$ with $w = 0.0$ fm (green triangles), $GEMINI^{++}$ with $w = 1.0$ fm (red triangles), $GEMINI^{++}$ with $w = 1.1$ fm (blue triangles), $AMD + GEMINI^{++}$ (pink triangles) and $HIPSE + GEMINI^{++}$ (orange triangles).

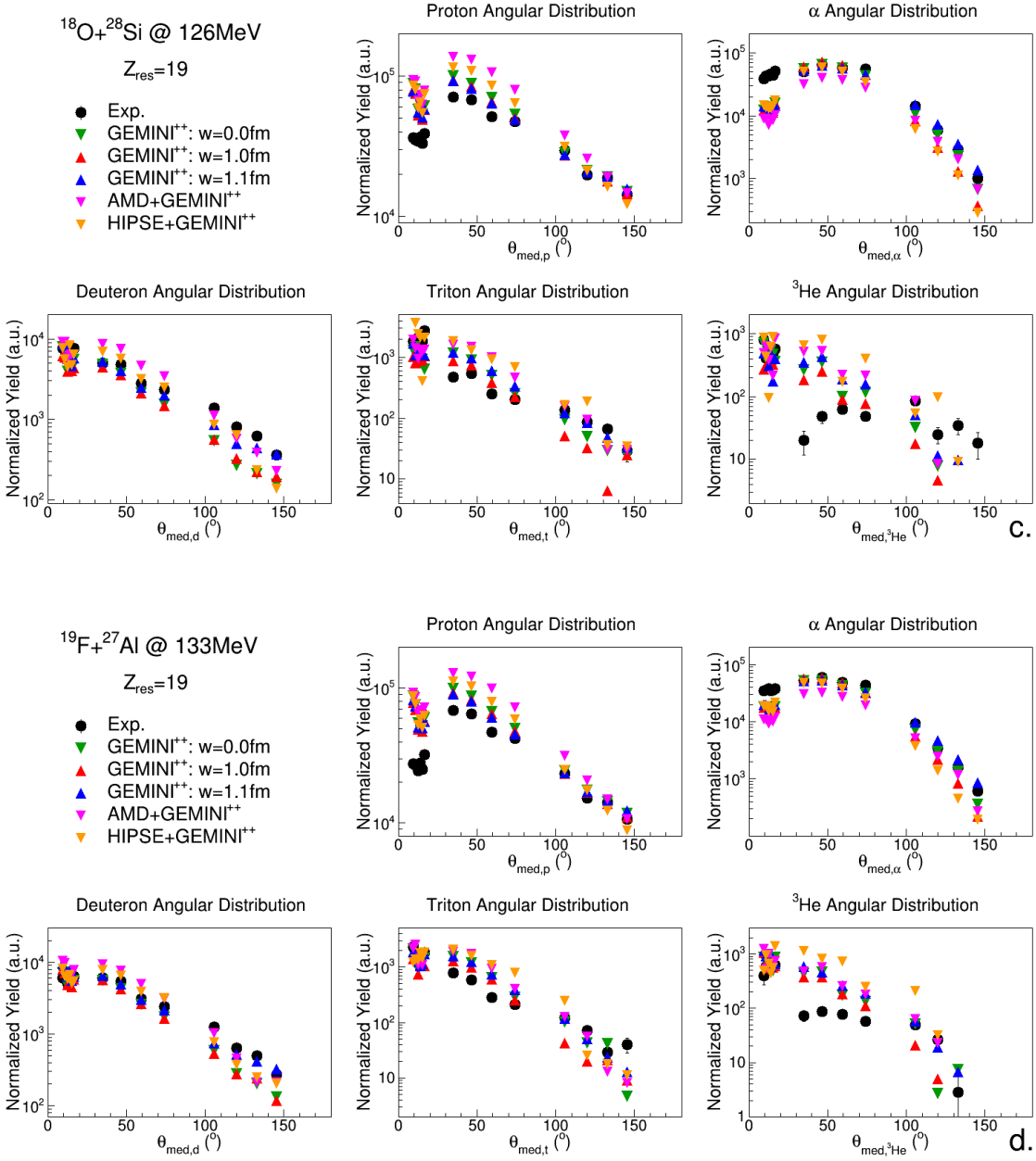

Figure 8.20: Same as in Fig. 8.19 but for the reactions $^{18}O + ^{28}Si$ at 126 MeV (panel c.) and $^{19}F + ^{27}Al$ at 133 MeV (panel d.).

moreover, an underproduction of protons appears evident also in the forward region ($\theta_{lab} = 8.8^o \div 17.4^o$), with a difference with respect to simulation which grows going from ^{16}O to ^{18}O to ^{19}F induced reaction.

On the contrary, for α particles, in the case of ^{16}O at 111 MeV induced reaction, almost all simulations well represent the $\theta_{lab} = 29.5^o \div 150.4^o$ angular region; apart from **G10** and **HIPSE**, which underestimate the data at backward angles. For the other reactions, this is still almost true, apart from **AMD**, which tends to underestimate also the central region ($\theta_{lab} = 29.5^o \div 82.5^o$). Looking at forward angles ($\theta_{lab} = 8.8^o \div 17.4^o$), at variance with the proton case, a better agreement of simulations with experimental α-spectra is observed for the ^{19}F induced reaction, even if with some discrepancies, which grow going from ^{18}O to ^{16}O, with the worst case being the low energy reaction; for all reactions **HIPSE** is the closest to the experimental data.

For sake of clarity, in Figs. 8.21 and 8.22, the differences between experimental and simulated angular distribution are displayed comparing the four studied reactions. One can see that for proton the forward part is reproduced only for the reaction with the lower CN excitation energy; the higher the CN excitation energy the greater the difference. Such behavior of increasing disagreement as a function of excitation energy remains also in the central angular region, with the only difference that in this region even the 111 MeV ^{16}O-induced reactions data set is not reproduced. The situation changes for the backward angles, where the proton are better described. For what concerns the α-particles a similar behavior as a function of excitation energy is observed, with the important difference that in the present case the experimental yields are generally underestimated. In particular, the α are never reproduced at forward angles, while the different parametrizations of statistical code succeeds in approaching the experimental data in the central angular region. Again, the backward angles are better reproduced.

For deuterons, the forward region is not completely described in the ^{16}O at 111 MeV, while it is reproduced by **AMD** and **HIPSE** in the ^{16}O at 128 MeV and from all simulations for the other two reactions. On the contrary, the central angular region is overestimated by **AMD** and quite well reproduced by $GEMINI^{++}$ alone; **HIPSE** overestimates the

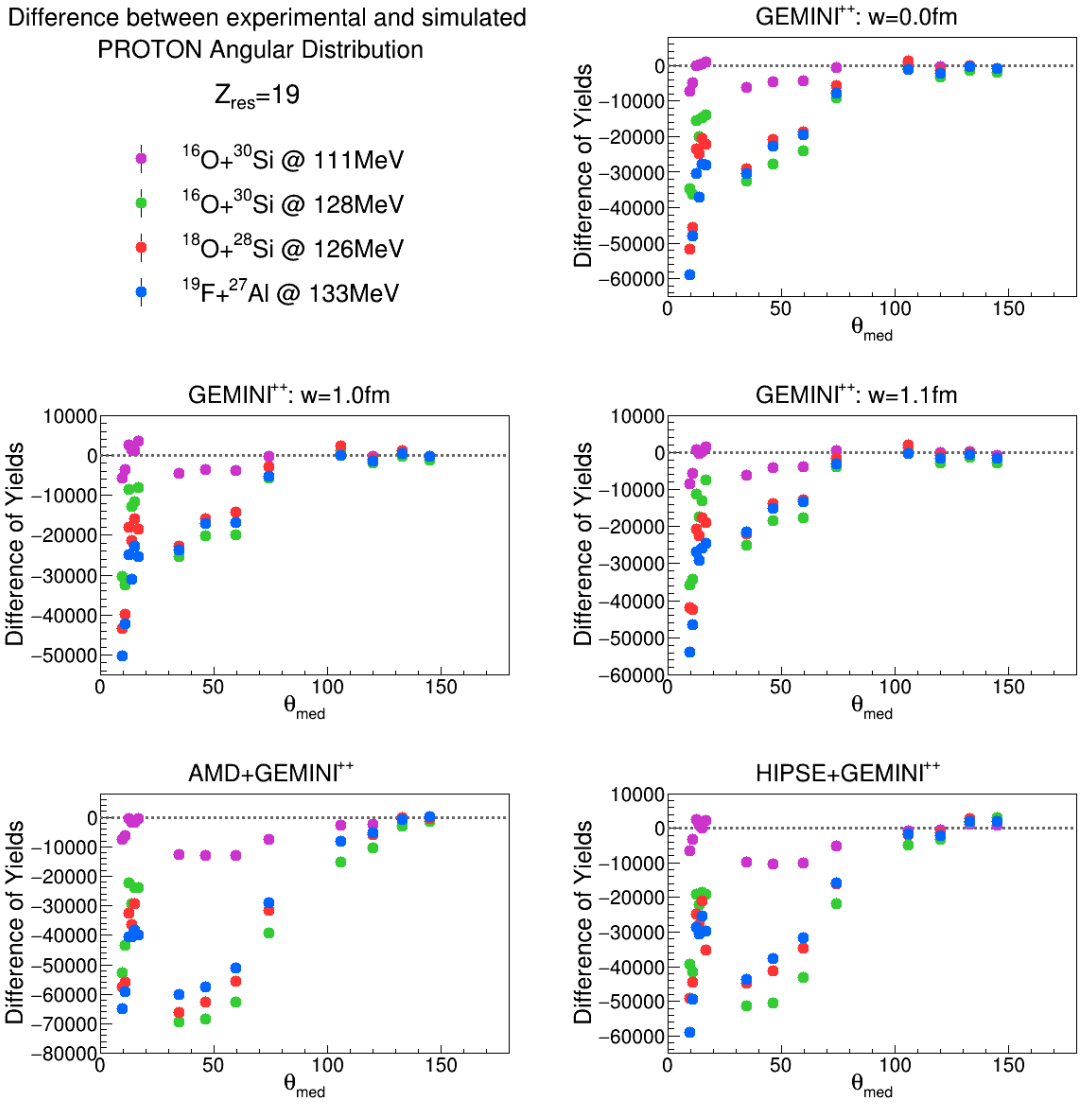

Figure 8.21: Difference between the experimental and the simulated proton angular distribution: comparison of the four reactions: $^{16}O +^{30} Si$ at 111 MeV (magenta), $^{16}O +^{30} Si$ at 128 MeV (green), $^{18}O +^{28} Si$ at 126 MeV (orange) and $^{19}F +^{27} Al$ at 133 MeV (azure).

yields in this angular region at low energy, but it is somehow closer to the data at higher energy. In the backward region ($\theta_{lab} = 97.5^o \div 150.4^o$) all simulations are underestimating the deuterons, with **AMD** and **HIPSE** somehow closer to the data.

Tritons are well described at forward angles only for ^{18}O and ^{19}F induced reactions;

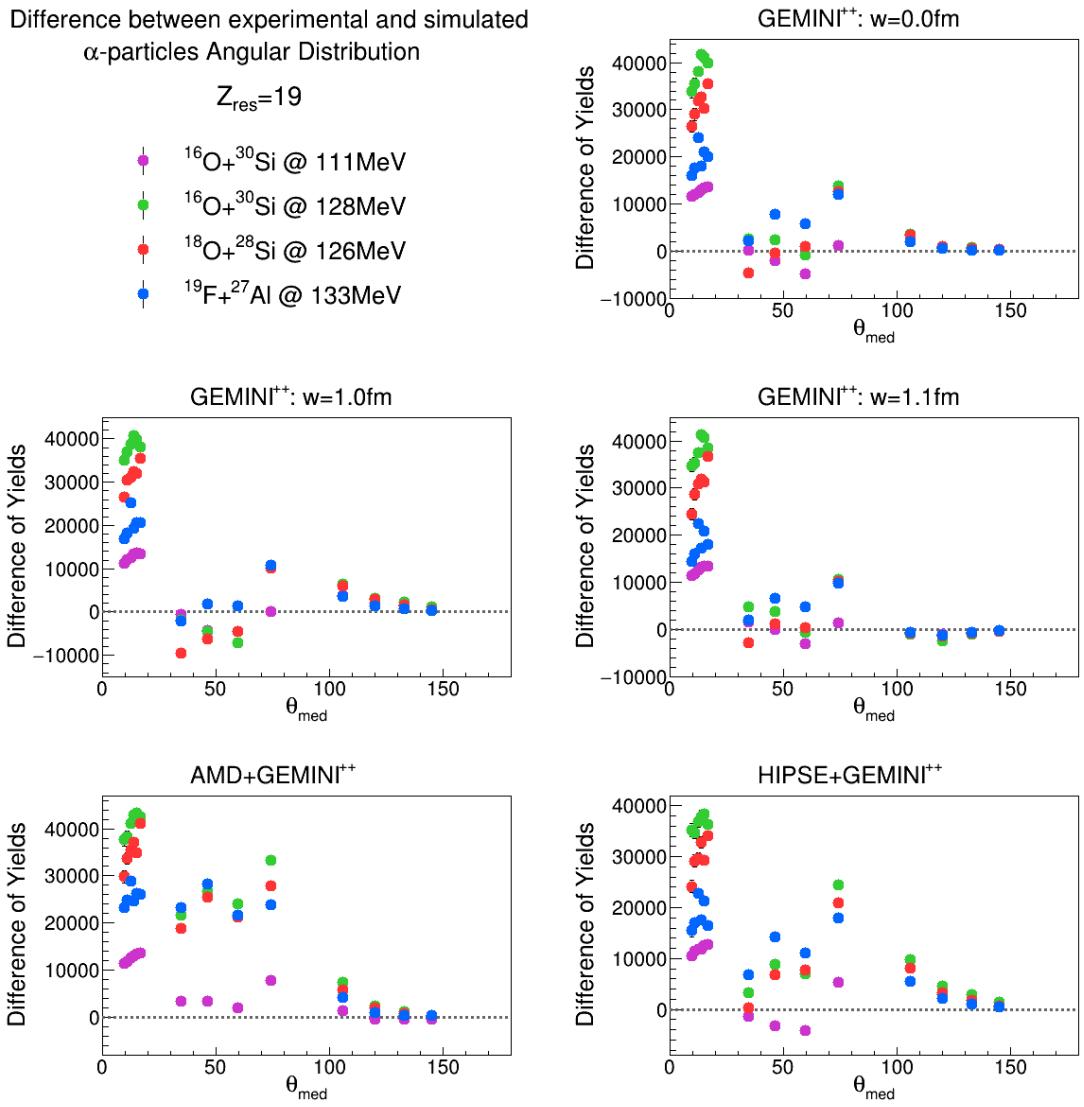

Figure 8.22: Same as in Fig. 8.21 but for α-particles.

for the ^{16}O induced reactions they are completely underestimated at low energy, while **HIPSE** tends to partially represent them at high energy. The central angular region is, generally, overestimated by all simulations, with **G10** the closest to the data and the two dynamical models the worst. In the backward direction, in the case of ^{18}O and ^{19}F beams, the yields are almost well described by all simulations apart from **G10**. In the case of ^{16}O at 128 MeV, **AMD** and, only partially, both **HIPSE** and **G11** are able to describe

the experimental values. At low energy due to low statistics, it is difficult to draw any conclusion.

^3He is well accounted for in the F induced reaction in the forward region, while in the central angular region it is overestimated by all calculations; the backward region is reproduced better by **HIPSE**. For ^{18}O at 126 MeV and ^{16}O at 128 MeV induced reaction only the forward region is well accounted for, while in the other part the experimental distribution is more flat than simulations. For ^{16}O at low energy, it is difficult to say something due to low statistics, except for an overproduction of ^3He at forward angles, only very partially taken into account by **AMD** and **HIPSE**.

The experimental energy spectra (black dots) of protons, deuterons, tritons, ^3He and α-particles in coincidence with the K-residue, compared with those produced by simulations are presented in Appendix B, in the Figs. B.33 $\div$ B.52.

For the low energy ^{16}O induced reaction proton spectra are reasonably described by all simulations, even though slightly harder experimental spectra are observed in the central and in the forward angular region. Looking at the **HIPSE** simulated data still a visible overproduction at high energy is observed, especially pronounced in the central angular region (same origin previously discussed for the Sc and Ca cases). It is however better in describing the energy spectrum shape at forward angles. At the higher energy for all ^{16}O, ^{18}O and ^{19}F cases, a better description can be observed, which is very good for **AMD**. The overall description, with respect to $GEMINI^{++}$, is slightly better in the ^{16}O induced case. Again, **HIPSE** shows a strong contribution of fast proton emission, not present in the experimental data.

For the deuterons a quite good agreement is observed for all simulations in all reactions: the best description can be however observed with respect to **G11**, while the worst is **HIPSE** due to the unexpected peaks in the intermediate and backward angular region. Triton are also well reproduced and again **G11** is the best. It is difficult to draw conclusions on ^3He due to low statistics.

In the α-particle case **G10** and **HIPSE** are able to describe all reactions in the angular region $\theta_{lab} = 29.5^o \div 150.4^o$. For ^{18}O and ^{19}F induced reaction, **G10** is still able to describe

also the forward angles ($\theta_{lab} = 8.8^o \div 17.4^o$), while **HIPSE** is slightly underestimating the shape. In the ^{16}O cases at forward angles a better description is obtained with **G11**. **AMD** is able to reproduce the forward angles for all reactions but **AMD**, as well as **G11**, has a largely different shape in the central angular region, which might be related to a different priority in the decay chain between α-particles and n, as discussed in the previous case.

8.1.4 The Ar residue: $Z_{res} = 18$

Table 8.6 reports the number of Ar-residue and the total branching ratio of channels with such residue for experimental and simulated data for the four reactions. The BR is still calculated as the ratio between the number of evaporation residues with $Z_{res} = 18$ over the total number of residues. At lower energy, the experimental BR is more similar to that one obtained by **AMD** and **HIPSE**, while at higher energies, it is more similar to $GEMINI^{++}$.

	$^{16}O +^{30} Si$	111 MeV	$^{16}O +^{30} Si$	128 MeV
	n^o residues	BR(%)	n^o residues	BR(%)
Experimental	42940 ± 207	25.9	153369 ± 392	29.2
$GEMINI^{++}$ $w = 0.0$ fm	49463	18.6	81162	27.4
$GEMINI^{++}$ $w = 1.0$ fm	60532	18.7	104831	30.4
$GEMINI^{++}$ $w = 1.1$	65494	21.6	104074	31.3
$AMD + GEMINI^{++}$	66544	28.5	73949	34.1
$HIPSE + GEMINI^{++}$	28185	22.2	50622	36.4
	$^{18}O +^{28} Si$	126 MeV	$^{19}F +^{27} Al$	133 MeV
	n^o residues	BR(%)	n^o residues	BR(%)
Experimental	157954 ± 397	29.6	131474 ± 363	28.0
$GEMINI^{++}$ $w = 0.0$ fm	93426	28.6	103508	31.6
$GEMINI^{++}$ $w = 1.0$ fm	118316	31.1	129914	34.6
$GEMINI^{++}$ $w = 1.1$ fm	119073	31.7	130572	34.6
$AMD + GEMINI^{++}$	85546	36.1	80551	37.8
$HIPSE + GEMINI^{++}$	48305	33.4	50622	36.4

Table 8.6: Number and total branching ratio (BR) of channels with Ar-residue.

In Figs. 8.23 and 8.24, the total LCP and light fragment ($Z < 6$) multiplicity (Mult.) in coincidence with a Ar-residue defined for each event is plotted as a function of the Particle Identification (P.Id.) for the four studied reactions. As a first observation, more kind of experimental isotopes, especially related to Li and B light fragments, are seen, which are not produced by calculations. Moreover, experimentally the more populated channel is the one with $Mult = 2$, which is mainly related to the two α-particle decay channel or, more generally, to the two $Z = 2$ particle decay; on the contrary, models tend to privilege the channels with $Mult = 3$, where 1α-2p (1($Z = 2$)-2($Z = 1$)) are emitted.

A more quantitative information on the relative production yields of the competing decay channels will be discussed in the following, since the multiplicity plots just give the indication on the number of single particles and are not indicating the relative channel branchings.

The comparison of experimental and simulated angular distribution (black dots) of LCP in coincidence with the Ar-residue are shown in Fig. 8.25 and in Fig. 8.26. It is well evident that α-particles are not at all accounted for at forward angles ($\theta_{lab} = 8.8^o \div 17.4^o$) for all reactions. For the ^{16}O reaction at low energy an underestimation is present in all the angular distribution, even if at backward angles ($\theta_{lab} = 97.5^o \div 150.4^o$) **G11** and **G00** seem to better account for the produced yields. For the other reactions, instead, the central angular region ($\theta_{lab} = 29.5^o \div 82.5^o$) is well accounted for by all calculations, while the backward part is underestimated, especially by **G10**, **AMD** and **HIPSE**. Protons are, on the contrary, strongly overestimated by calculations, especially for the ^{16}O induced reactions; for ^{18}O and, even more, for F induced reactions calculations tend to be slightly closer to the experimental backward angular distribution.

As in the case of the K-residue case, again here, the difference between the experimental and simulated angular distribution are illustrated in Fig. 8.27 and 8.28 to better visualize how the simulation reproduce the experimental data comparing the four reactions. As previously discussed, it is visible the better reproduction of the data set at the lower excitation energy. Looking to α-particles at forward angles, it is however clear that the observed differences are not related to excitation energy only, but it is probably true that

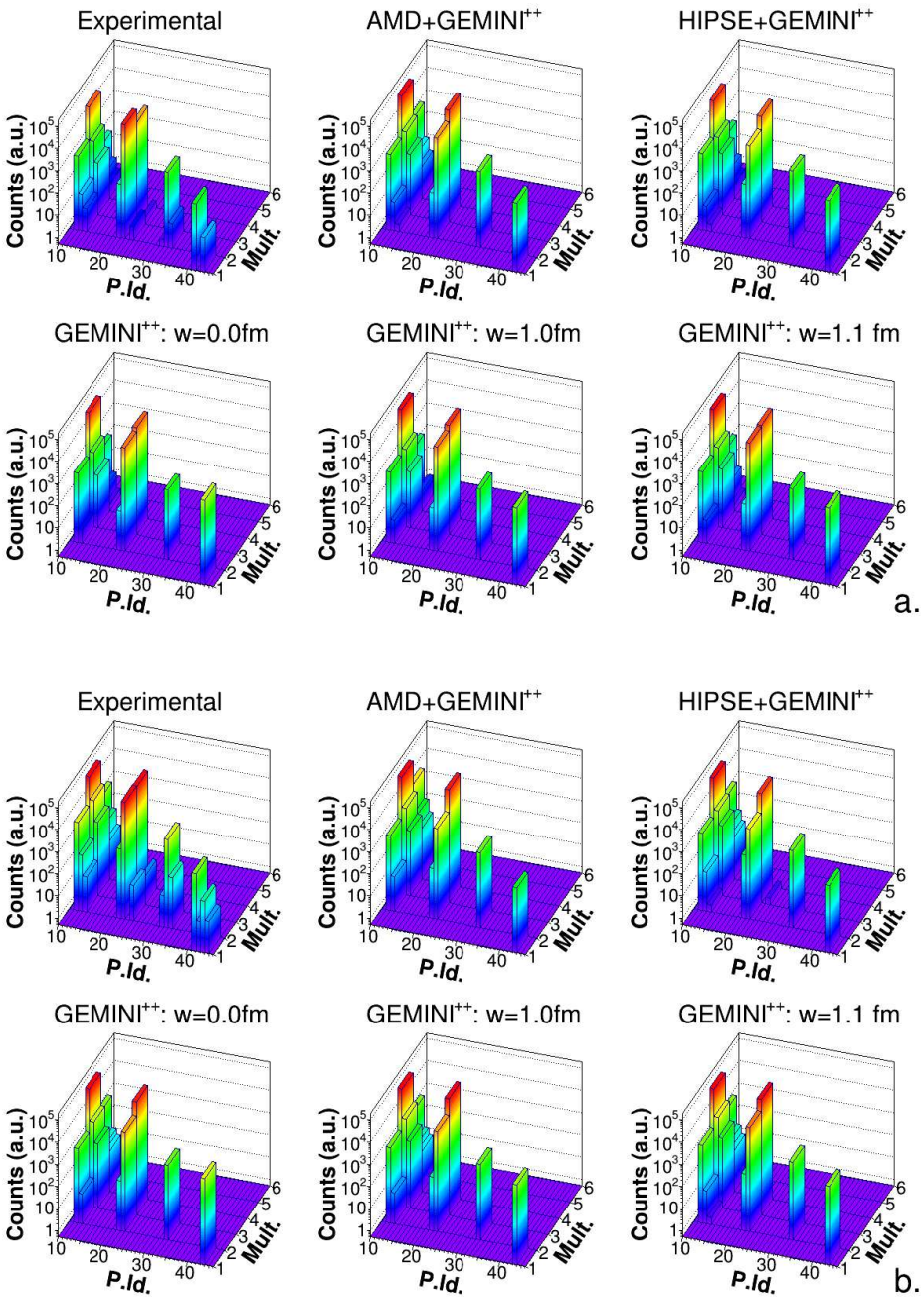

Figure 8.23: Open decay channels: particles in coincidence with a Ar-residue for the reactions $^{16}O + ^{30}Si$ at 111 MeV (panel a.) and $^{16}O + ^{30}Si$ at 128 MeV (panel b.). The Particles Identification is: 11 protons, 12 deuterons, 13 triton, 21 ^3He and 22 α-particles. See text for more details.

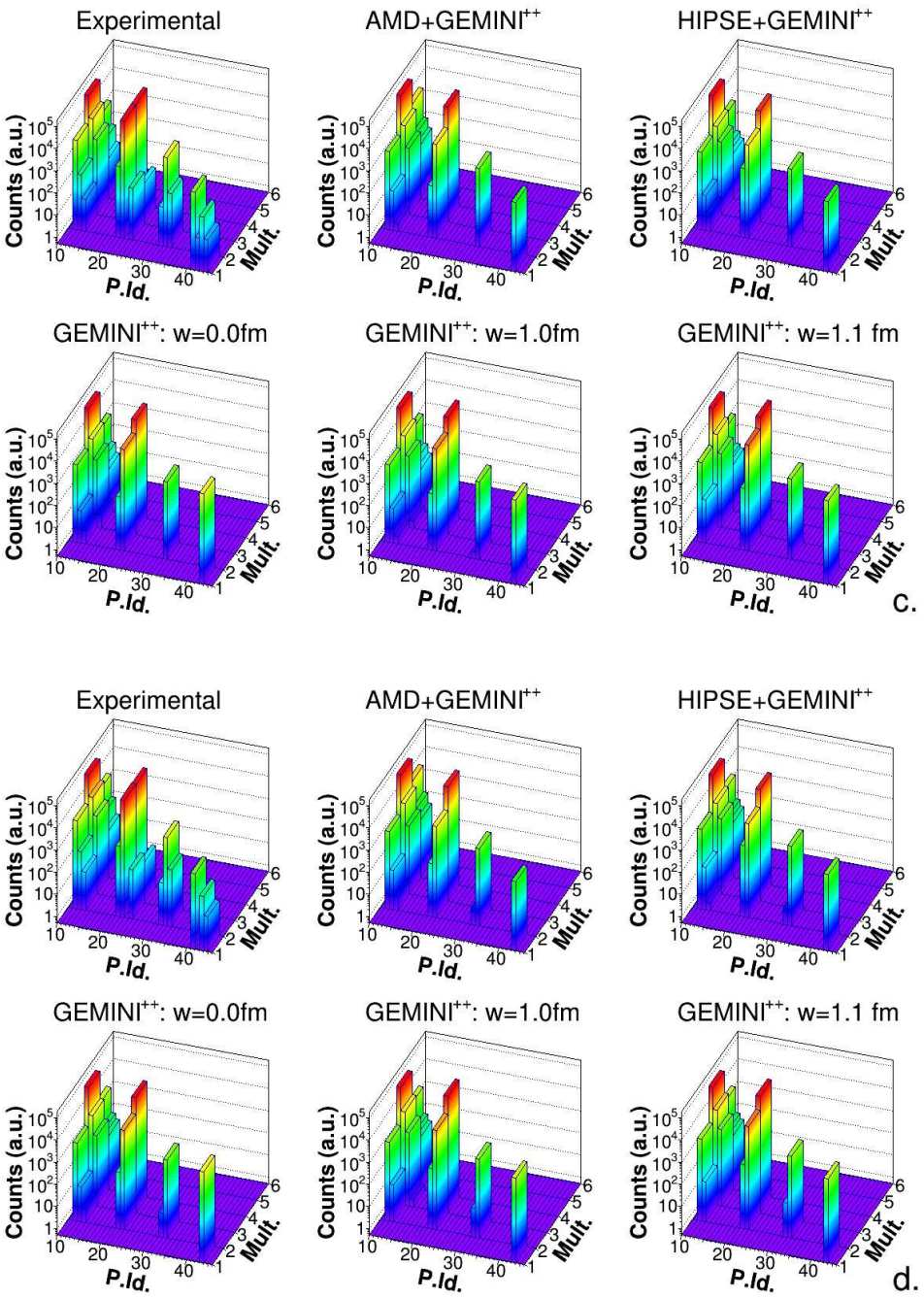

Figure 8.24: Same as in Fig. 8.23 but for the reactions $^{18}O + ^{28}Si$ at 126 MeV (panel c.) and $^{19}F + ^{27}Al$ at 133 MeV (panel d.).

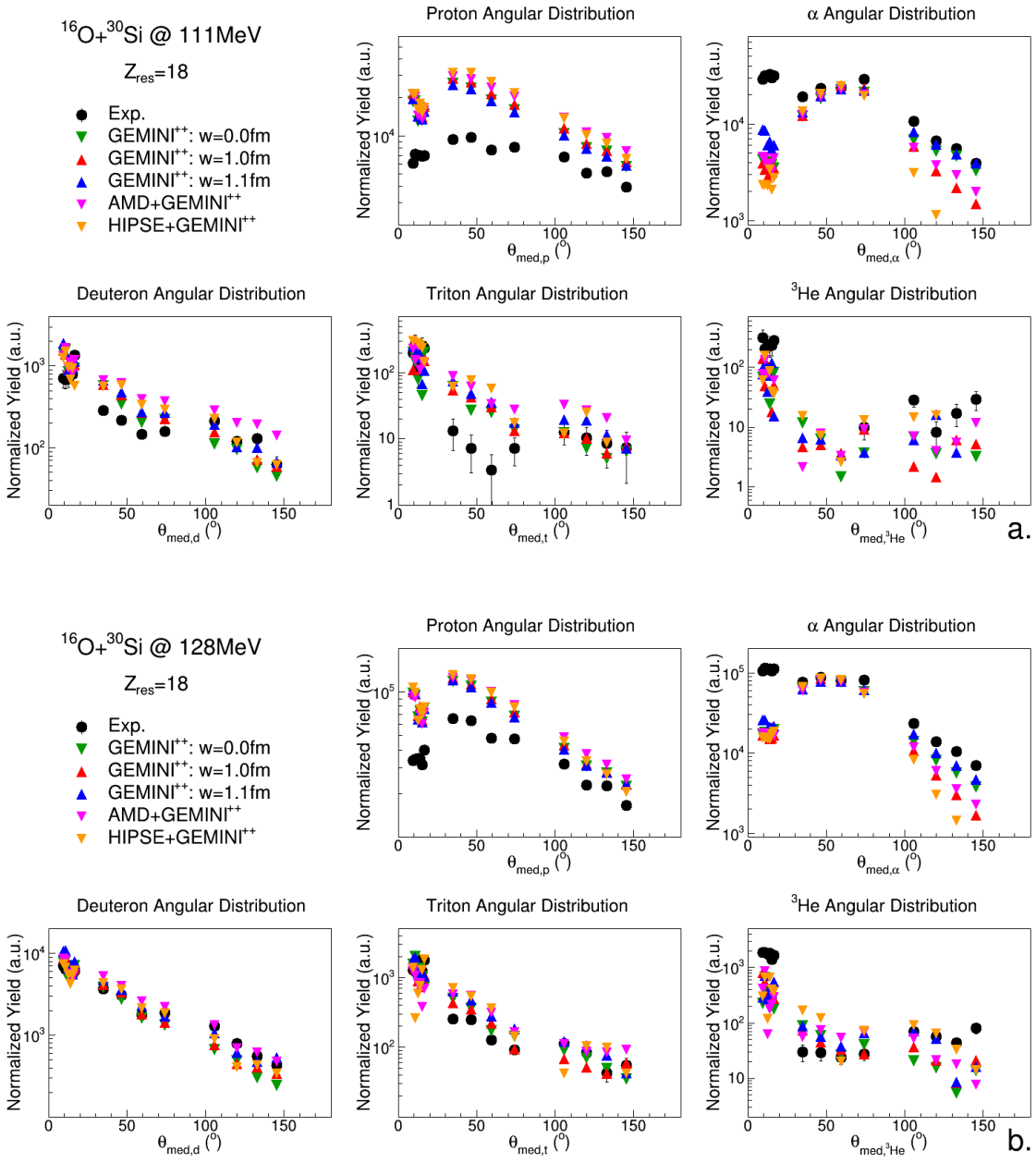

Figure 8.25: Angular distributions of LCP in coincidence with *Ar*-residue for the reactions $^{16}O + ^{30}Si$ at 111 MeV (panel a.) and $^{16}O + ^{30}Si$ at 128 MeV (panel b.) in comparison with $GEMINI^{++}$ with $w = 0.0$ fm (green triangles), $GEMINI^{++}$ with $w = 1.0$ fm (red triangles), $GEMINI^{++}$ with $w = 1.1$ fm (blue triangles), $AMD + GEMINI^{++}$ (pink triangles) and $HIPSE + GEMINI^{++}$ (orange triangles).

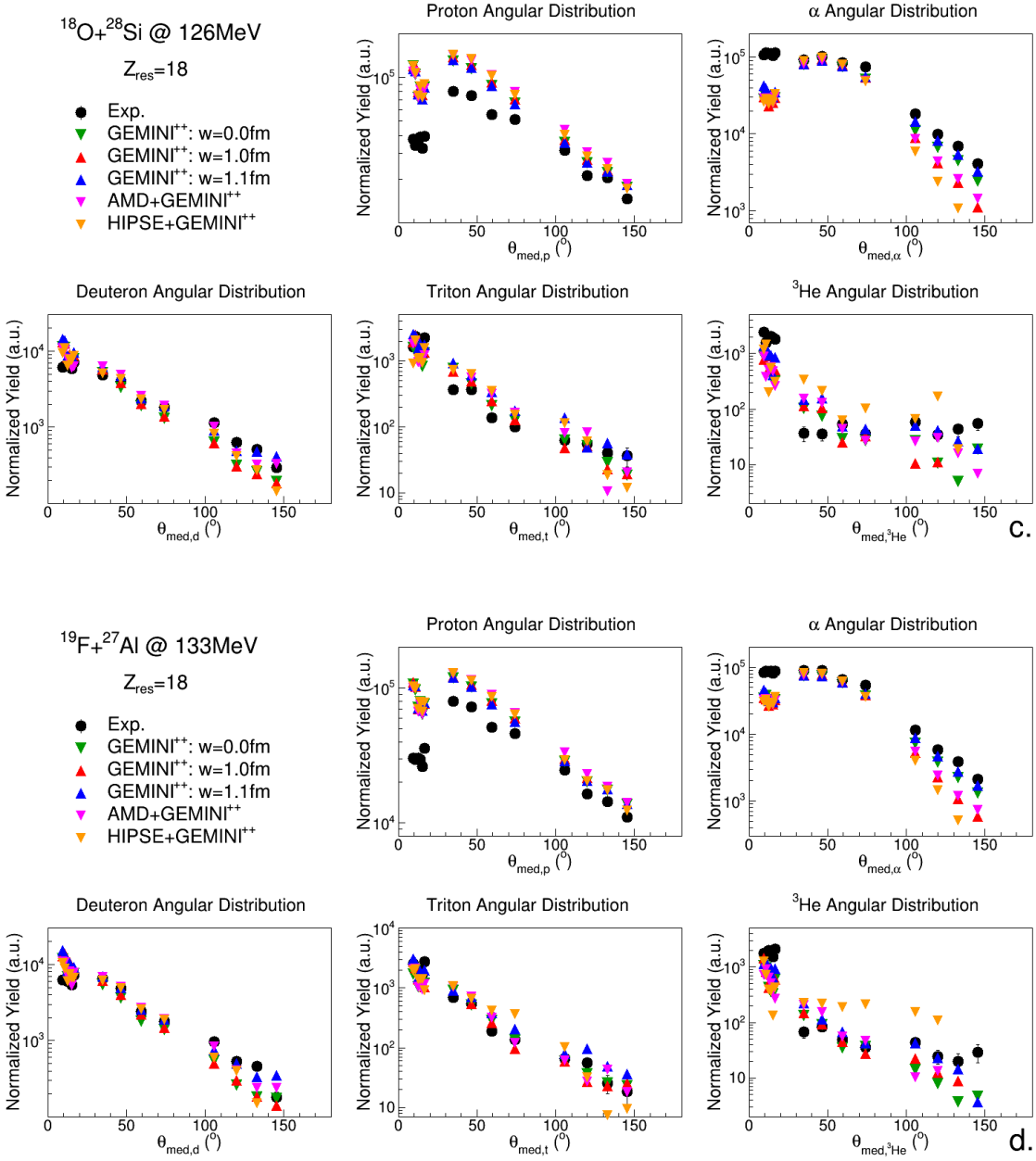

Figure 8.26: Same as in Fig. 8.25 but for the reactions $^{18}O+^{28}Si$ at 126 MeV (panel c.) and $^{19}F+^{27}Al$ at 133 MeV (panel d.).

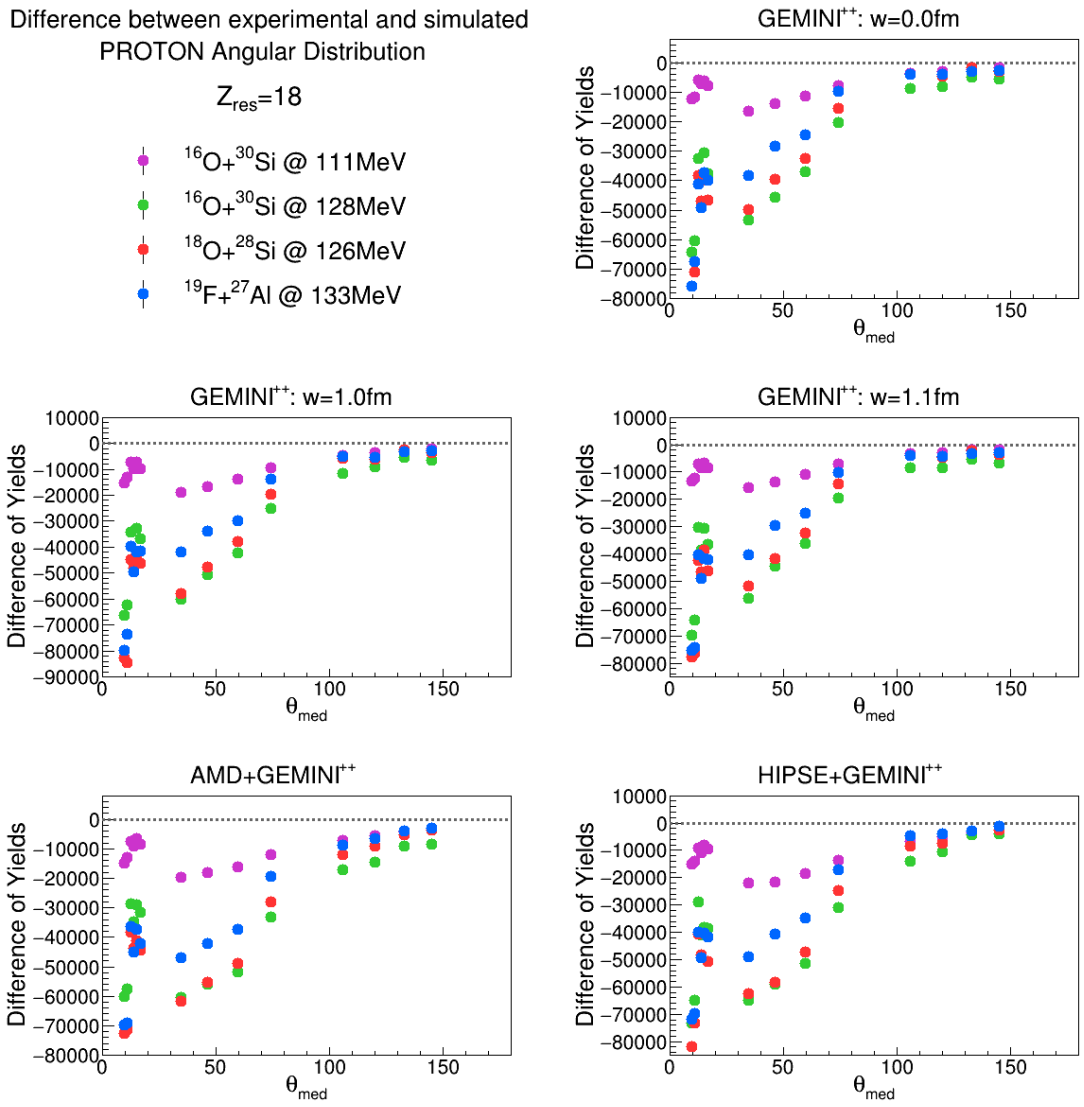

Figure 8.27: Difference between the experimental and the simulated proton angular distribution: comparison of the four reactions: $^{16}O + ^{30}Si$ at 111 MeV (magenta), $^{16}O + ^{30}Si$ at 128 MeV (green), $^{18}O + ^{28}Si$ at 126 MeV (orange) and $^{19}F + ^{27}Al$ at 133 MeV (azure).

the colliding partner structure may have a role.

For deuterons the situation is more similar between simulations and experiments for the ^{16}O at 128 MeV, ^{18}O at 126 MeV and ^{19}F at 133 MeV, where especially **G11** and **AMD** are closer to the data in all the angular region. The situation is slightly different for

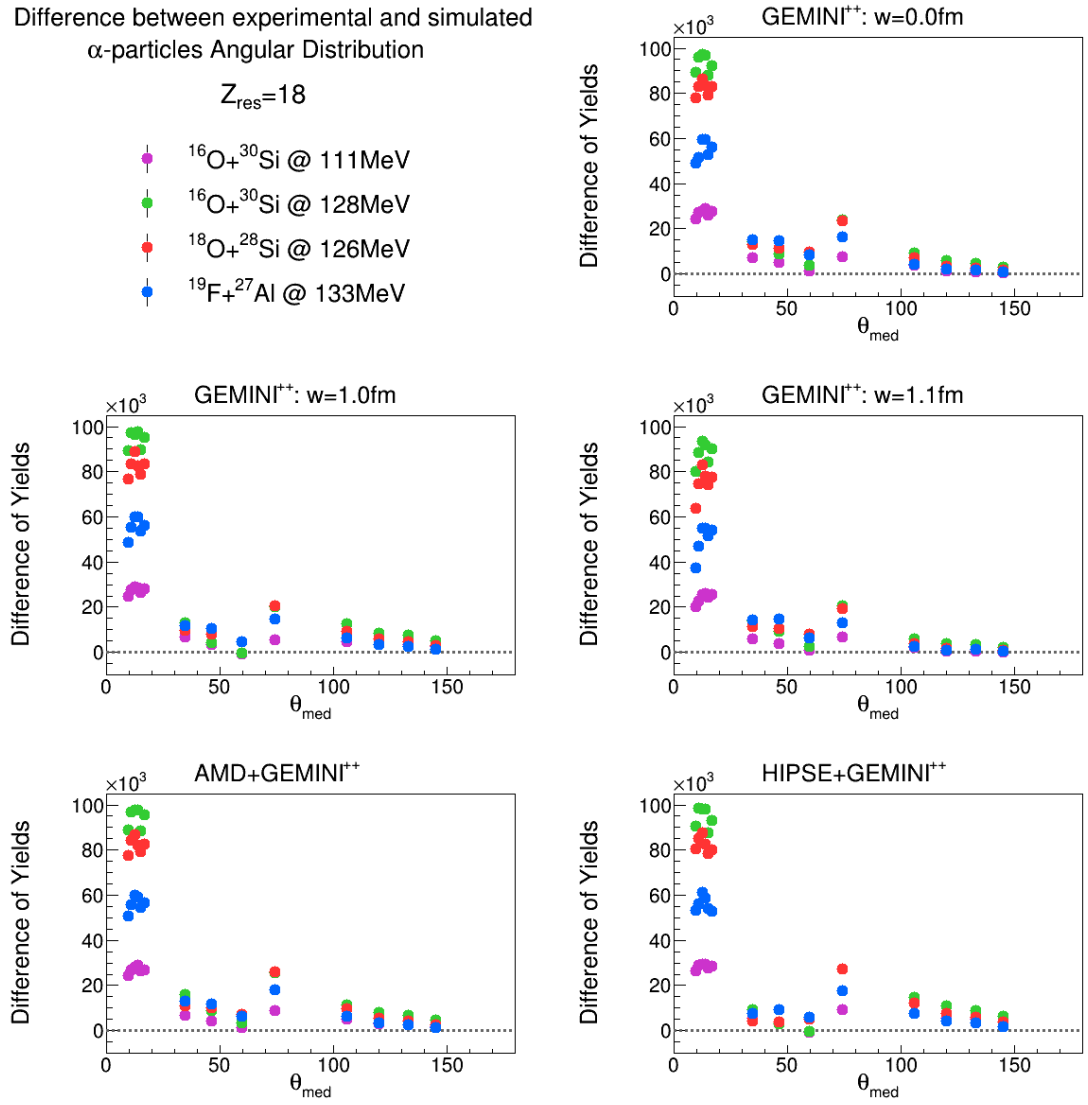

Figure 8.28: Same as Fig. 8.27 but for α-particles.

the low energy ^{16}O induced reaction, where still small discrepancies are present, mainly in the $\theta_{lab} = 29.5^o \div 82.5^o$ angular region. A quite similar trend as in the case of deuterons is observed for tritons, with a slightly larger disagreement in the central angular region especially for the low energy reaction.

Finally, the ^3He distributions: for all reactions an experimental overproduction at small angles is observed ($\theta_{lab} < 17.4^o$), which is not completely taken into account by calculation.

Generally the experimental distribution is quite flat in the other angular regions and this trend is not well reproduced by any of the calculations. Only in some cases **G11** seem to be closer to the data, at variance with **HIPSE** which is completely overestimating them (F-induced reaction).

The comparison of experimental and simulated energy spectra of protons, deuterons, tritons, ^3He and α-particles in coincidence with the Ar-residue are presented in Appendix B: proton spectra, displayed in the Figs. B.53 $\div$ B.56, are well described by all $GEMINI^{++}$ simulations for all experimental cases; **AMD** tends to overestimate of a small quantity the high energy tail in all the angular range at low energy, while only in the intermediate angular range for the other reactions. **HIPSE** is quite good at low energy with ^{16}O and at high energy with ^{19}F, while in the other two cases a small deviation in the intermediate energy range is observed.

Deuterons (Figs. B.57 $\div$ B.60) are well described by all simulations in all cases, except for small discrepancies in the forward region, for some of the simulations.

A similar behavior is observed with tritons (Figs. B.61 $\div$ B.64).

^3He (Figs. B.65 $\div$ B.68) has very low statistics at low energy, while in the other three cases simulations are closer to data, better for the ^{19}F and ^{18}O cases. In all cases, however the spectra in the central angular region show up an experimental yield at higher energy with respect to simulations.

On the contrary, α-particles (Figs. B.69 $\div$ B.72) are not badly described at all excitation energies, with **G11** being the best for the O induced reactions, while for the ^{19}F the better case seems the **G00**. Also **AMD** is good for all the reactions, even though a small underestimation is observed for forward emitted α-particles.

8.1.5 The Cl residue: $Z_{res} = 17$

The number of Cl-residue and the total branching ratio of channels with such residue have been reported in Table 8.7 for experimental and simulated data for the four reactions: again, the BR is defined as the ratio between the number of evaporation residues, in this case, with $Z_{res} = 17$ over the total number of residues. The experimental values are

comparable with simulations, but generally closer to the $GEMINI^{++}$ predictions.

	$^{16}O + ^{30}Si$	111 MeV	$^{16}O + ^{30}Si$	128 MeV
	n^o residues	BR(%)	n^o residues	BR(%)
Experimental	15186 ± 123	9.2	91191 ± 302	17.4
$GEMINI^{++}$ $w = 0.0$ fm	21748	8.2	39548	13.4
$GEMINI^{++}$ $w = 1.0$ fm	30372	9.4	52295	15.2
$GEMINI^{++}$ $w = 1.1$ fm	29416	9.7	52312	15.7
$AMD + GEMINI^{++}$	23190	9.9	26622	12.3
$HIPSE + GEMINI^{++}$	6613	5.2	18732	13.5
	$^{18}O + ^{28}Si$	126 MeV	$^{19}F + ^{27}Al$	133 MeV
	n^o residues	BR(%)	n^o residues	BR(%)
Experimental	95481 ± 309	17.9	85514 ± 292	18.2
$GEMINI^{++}$ $w = 0.0$ fm	50923	15.6	61385	18.7
$GEMINI^{++}$ $w = 1.0$ fm	66739	17.5	77710	20.7
$GEMINI^{++}$ $w = 1.1$ fm	65882	17.6	78541	20.8
$AMD + GEMINI^{++}$	31160	13.2	32415	15.2
$HIPSE + GEMINI^{++}$	14589	10.1	18732	13.5

Table 8.7: Number and total branching ratio (BR) of channels with Cl-residue.

In Figs. 8.29 and 8.30, the total LCP and light fragment ($Z < 6$) multiplicity (Mult.) in coincidence with a Cl-residue defined for each event is plotted as a function of the Particle Identification (P.Id.) for the four systems under study. From a first observation, a major production of isotopes with $Z \geq 3$ in the experimental data with respect to simulations is again observed. However, it seems that the major cross section which goes to $Mult = 3$ for the channel $2\alpha + 1p$ is almost well accounted for by all predictions. **AMD** and **HIPSE** tend to slightly overestimate the 1α-3p decay channel even with respect to $GEMINI^{++}$ alone, especially for the three reaction at higher excitation energy. This will be discussed later more quantitatively.

The experimental angular distribution (black dots) of protons, deuterons, tritons, ^3He and α-particles in coincidence with the Cl-residue, are compared with those produced by simulations, are illustrated in Figs. 8.31 and 8.32.

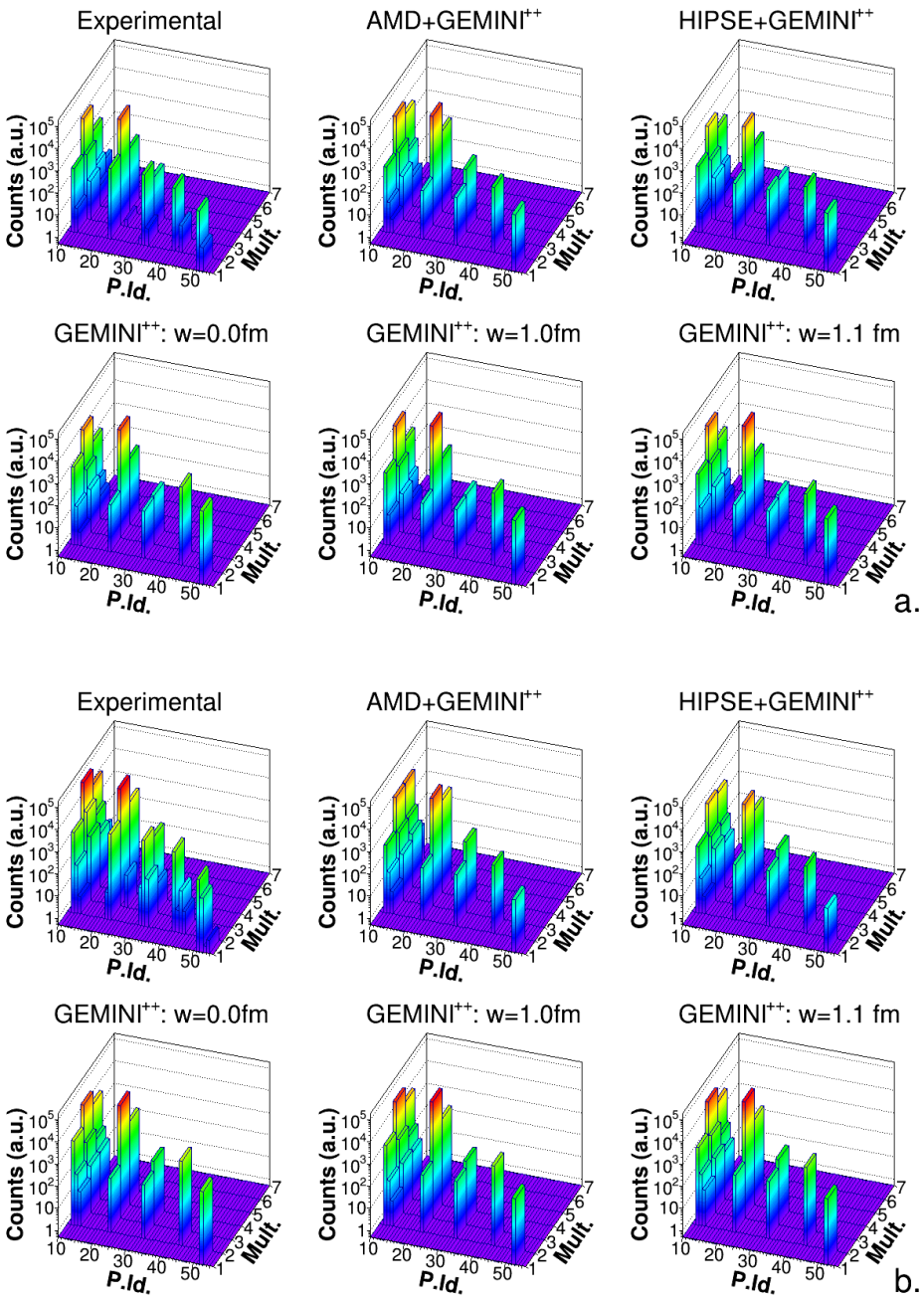

Figure 8.29: Open decay channels: particles in coincidence with a Cl-residue for the reactions $^{16}O + ^{30}Si$ at 111 MeV (panel a.) and $^{16}O + ^{30}Si$ at 128 MeV (panel b.). The Particles Identification is: 11 protons, 12 deuterons, 13 triton, 21 ^{3}He, 22 α-particles, 31 ^{6}Li, 32 ^{7}Li, 33 ^{8}Li, 41 ^{7}Be, 43 ^{9}Be, 51 ^{10}B and 52 ^{11}B. See text for more details.

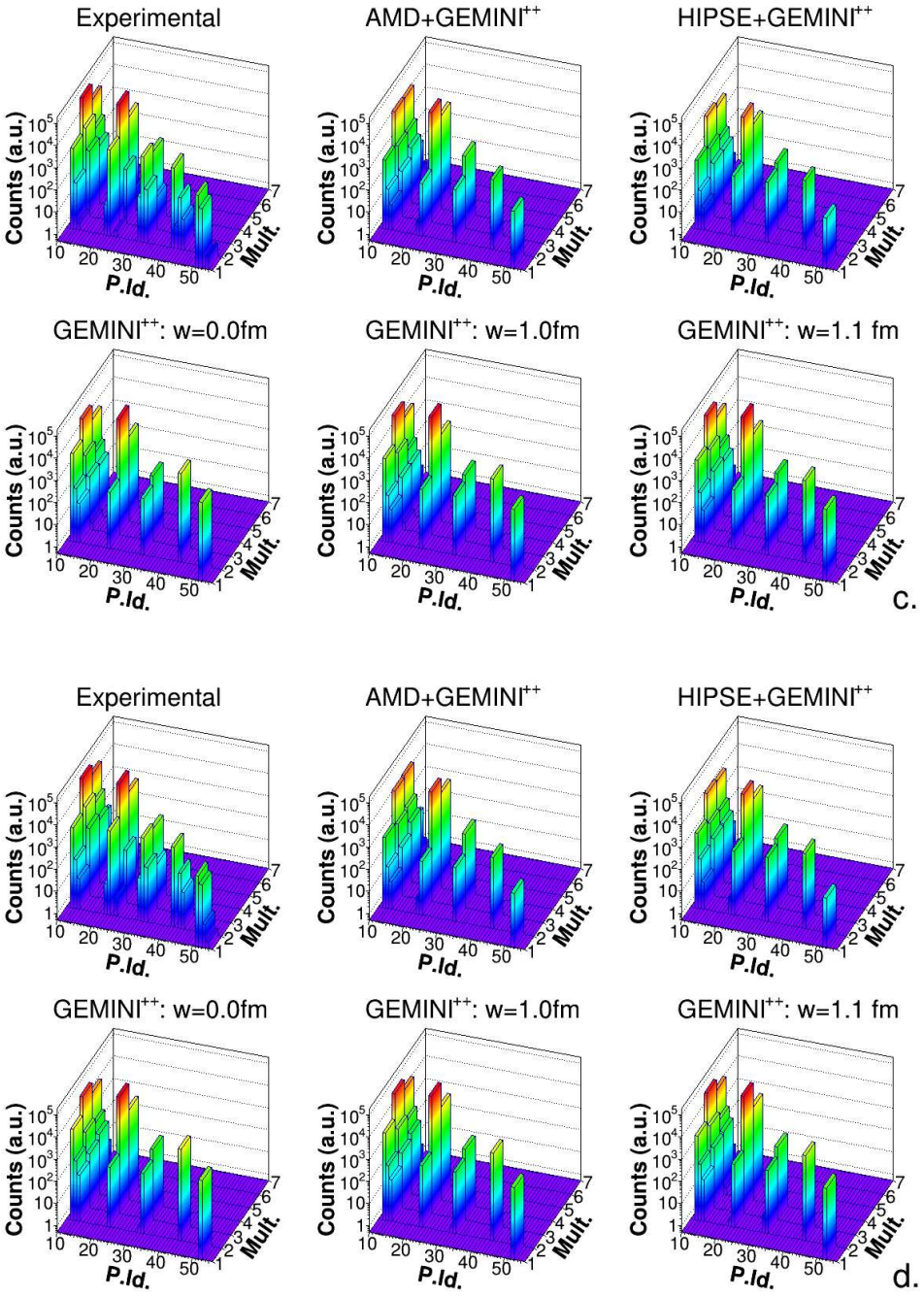

Figure 8.30: Same as in Fig. 8.29 but for the reactions $^{18}O + ^{28}Si$ at 126 MeV (panel c.) and $^{19}F + ^{27}Al$ at 133 MeV (panel d.).

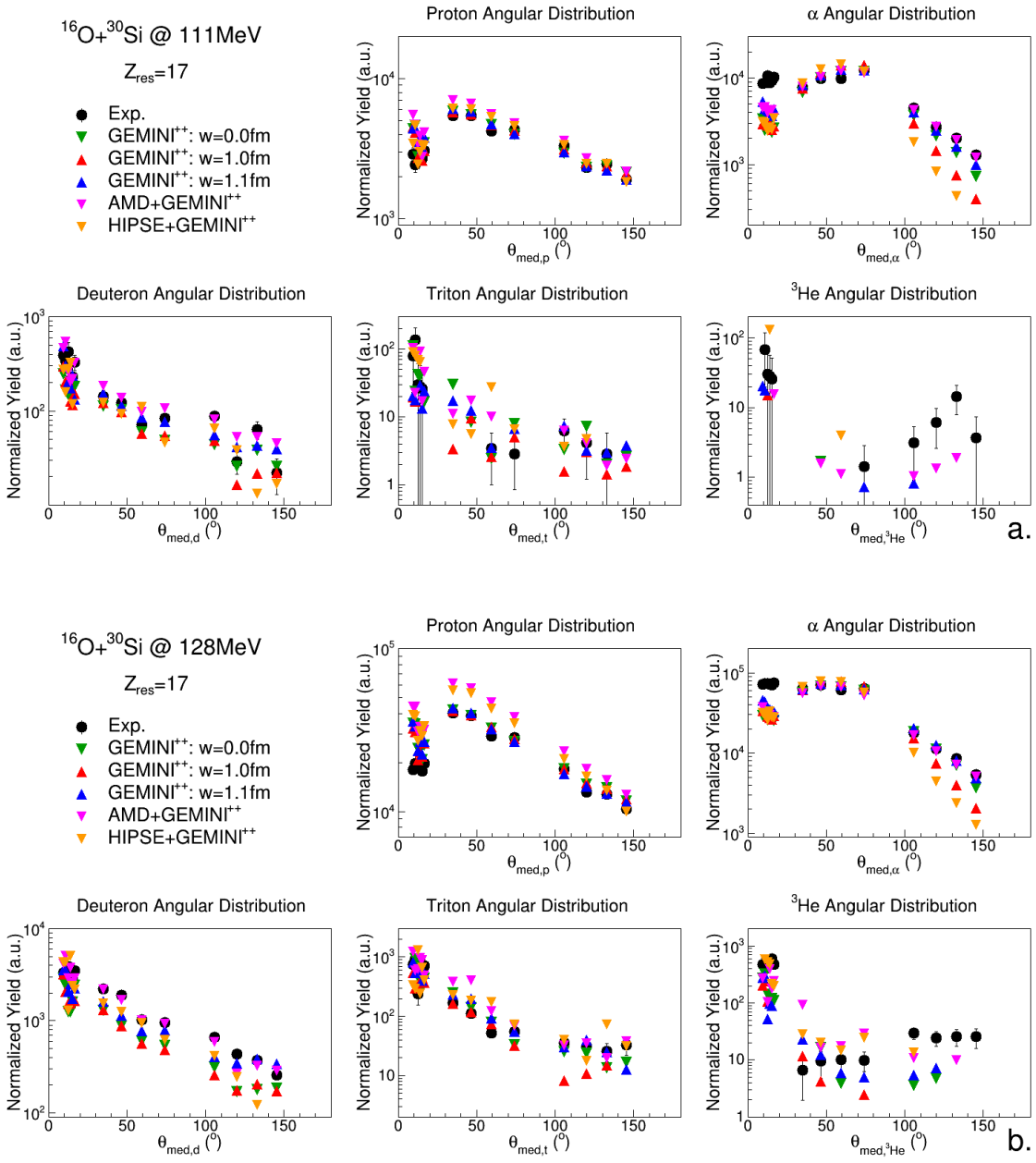

Figure 8.31: Angular distributions of LCP in coincidence with Cl-residue for the reactions $^{16}O + ^{30}Si$ at 111 MeV (panel a.) and $^{16}O + ^{30}Si$ at 128 MeV (panel b.) in comparison with $GEMINI^{++}$ with $w = 0.0$ fm (green triangles), $GEMINI^{++}$ with $w = 1.0$ fm (red triangles), $GEMINI^{++}$ with $w = 1.1$ fm (blue triangles), $AMD + GEMINI^{++}$ (pink triangles) and $HIPSE + GEMINI^{++}$ (orange triangles).

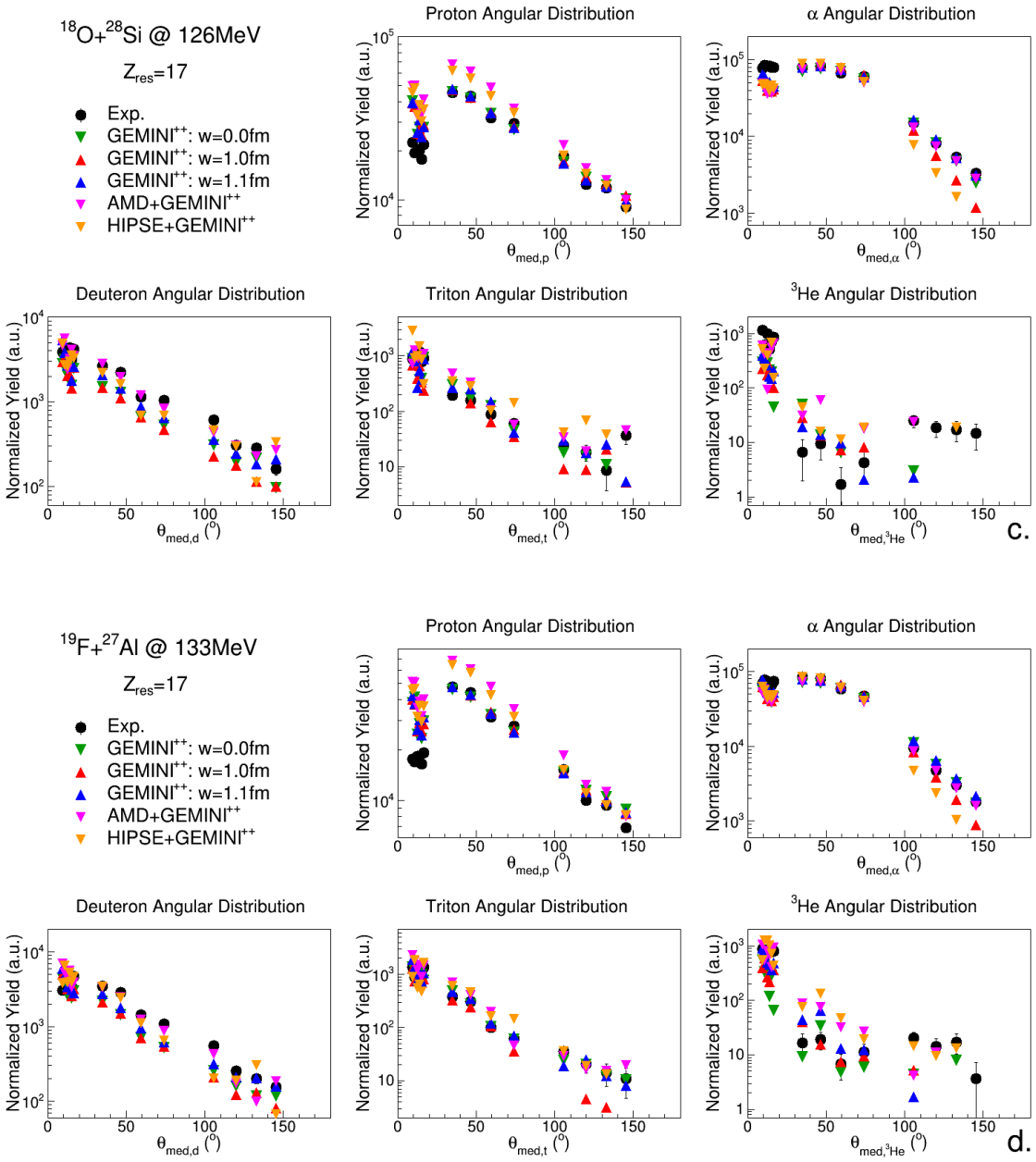

Figure 8.32: Same as in Fig. 8.31 but for the reactions $^{18}O+^{28}Si$ at 126 MeV (panel c.) and $^{19}F+^{27}Al$ at 133 MeV (panel d.).

The α-particle angular distributions are normally well accounted for the ^{16}O induced reactions especially by **AMD**, apart from the overproduction observed at small angles ($\theta_{lab} > 17.4^o$). Generally **G10** strongly underestimate even the backward region ($\theta_{lab} = 97.5^o \div 150.4^o$) together with **HIPSE**. For ^{18}O, the trend is similar, but also the forward part is somehow better represented, and, finally, for the ^{19}F induced reaction it is almost well described especially by **G11**.

On the contrary, protons are well described by almost all calculations for the ^{16}O at 111 MeV in the reaction, with a very slight overestimation by **AMD**. They are well accounted for by $GEMINI^{++}$ alone for the other reactions, apart from the forward region where experimental protons are quite strongly under-produced. They are completely overestimated by **AMD** in the whole angular region, even if with a slightly better reproduction at backward angles. **HIPSE** is also over-predicting the experimental yields in the central angular region ($\theta_{lab} = 29.5^o \div 82.5^o$).

Instead, deuterons are almost well reproduced by **AMD** and **HIPSE** for the three higher energy reactions while slightly underestimated by $GEMINI^{++}$ alone. At lower energy the agreement is reasonably good even if it is difficult to choose the best agreement between simulations. For triton a general good agreement is also obtained.

For ^3He, apart from a probable underestimation of the experimental yields by simulations at low energy, in the other cases taking into account the low statistics, a reasonable general agreement can be observed even with a peaked distribution in the $\theta_{lab} = 8.8^o \div 17.4^o$ region and a quite flat distribution elsewhere, partially reproduced by simulations.

In Appendix B (Figs. B.73 $\div$ B.92), the experimental energy spectra (black dots) of protons, deuterons, tritons, ^3He and α-particles in coincidence with the Cl-residue, compared with those produced by simulations are presented. In particular, the proton spectra are fairly well reproduced by all simulations for all the reactions and the same situation is observed in the case of deuteron energy spectra. For tritons a quite small statistics is observed especially at low energy. Generally, spectra are reasonably described especially by **G11**. Despite the very low statistics also ^3He is reasonably described, even if some differences may be observed in the different angular region between the different

simulations. Even α-particles spectra are well described, especially with **G11** and **AMD** for the ^{16}O induced reactions, and even with **G00** for the ^{18}O reaction. In the ^{19}F case the best description is obtained by **G00**, **AMD** and also **HIPSE**.

We can, therefore, say that the Cl exit channels seem to be all in agreement with simulations, with very small dependence on the different model predictions.

8.1.6 The S residue: $Z_{res} = 16$

In Table 8.8 the number of S-residue and the total branching ratio of channels with such residue have been reported for experimental and simulated data for the four reactions. The BR is the number of evaporation residues with $Z_{res} = 16$ over the total number of residues. In this case the experimental BR are larger than predictions, almost a factor 2 with respect to $GEMINI^{++}$ and **AMD** and close to a factor from 3 to 4 with respect to **HIPSE**.

	$^{16}O +^{30} Si$	111 MeV	$^{16}O +^{30} Si$	128 MeV
	n^o residues	BR(%)	n^o residues	BR(%)
Experimental	6324 ± 80	3.8	40877 ± 202	7.8
$GEMINI^{++}$ $w = 0.0$ fm	5755	2.2	10358	3.5
$GEMINI^{++}$ $w = 1.0$ fm	4794	1.5	9464	2.7
$GEMINI^{++}$ $w = 1.1$ fm	7170	2.4	11468	3.4
$AMD + GEMINI^{++}$	5363	2.3	6904	3.2
$HIPSE + GEMINI^{++}$	760	0.6	4783	3.4
	$^{18}O +^{28} Si$	126 MeV	$^{19}F +^{27} Al$	133 MeV
	n^o residues	BR(%)	n^o residues	BR(%)
Experimental	43410 ± 208	8.1	40010 ± 200	8.5
$GEMINI^{++}$ $w = 0.0$ fm	14113	4.3	19898	6.1
$GEMINI^{++}$ $w = 1.0$ fm	13047	3.4	19505	5.2
$GEMINI^{++}$ $w = 1.1$ fm	14906	4.0	20844	5.5
$AMD + GEMINI^{++}$	8145	3.4	9745	4.6
$HIPSE + GEMINI^{++}$	2923	2.0	4783	3.4

Table 8.8: Number and total branching ratio (BR) of channels with S-residue.

The total LCP and light fragment ($Z < 6$) multiplicity (Mult.) in coincidence with a S-residue defined for each event is plotted as a function of the Particle Identification (P.Id.) in Fig. 8.33 and in Fig. 8.34 for the four reactions: $^{16}O + ^{30}Si$ at 111 MeV (panel a.), $^{16}O + ^{30}Si$ at 128 MeV (panel b.), $^{18}O + ^{28}Si$ at 126 MeV (panel c.) and $^{19}F + ^{27}Al$ at 133 MeV (panel d.). Looking at figure, in a qualitative way, we can say that the experiment privileged the 3α-particle decay channels, while for the simulations a stronger path is the decay through 2α-2p decay (especially evident for **AMD** and **HIPSE**) and also the 1α-1Be, 1p-1B decay channels are more probable in the simulations with respect to experiment. A major and quantitative discussion will be performed in the next chapter.

In Fig. 8.35 and in Fig. 8.36 the experimental angular distribution (black dots) of LCP in coincidence with the S-residue are compared with those produced by simulations. For the 111 MeV ^{16}O induced reaction, α-particles are reasonably described by **AMD** and **G11** except for the forward angles ($\theta_{lab} = 8.8^o \div 17.4^o$). **G00** and **G10** are slightly underestimating data in all angular region and **HIPSE** is the best in reproducing the central angular region($\theta_{lab} = 29.5^o \div 82.5^o$). On the contrary, it largely underestimates both the forward and the backward part ($\theta_{lab} = 97.5^o \div 150.4^o$). Quite similar is the situation of α-particles for the two reactions ^{16}O at 128 MeV and ^{18}O at 126 MeV, with a feeble growing of the differences between experiment and simulations for $\theta_{lab} > 66.0^o$. For the F-induced reaction a slightly better description is observed in all the angular region, where even the forward α-particles peak is better represented by **AMD** and even better by **HIPSE**. In the backward it is **G11** the closest to the data.

For protons, at low energy, simulations overestimate quite strongly the angular distribution apart from **G11**, which describes reasonably the backward and very forward yields, even though it is not completely in agreement in the central region ($\theta_{lab} = 29.5^o \div 82.5^o$). At the higher energies, **G11** is reasonably describing the angular distributions and a slightly better prediction is also observed for **G00** and **G10**. Both **AMD** and **HIPSE** are still over-predicting the yields. Moreover, all the simulations are further and further over-predicting the forward experimental yields distribution going from ^{16}O at 128 MeV, to ^{18}O at 126 MeV up to ^{19}F at 133 MeV.

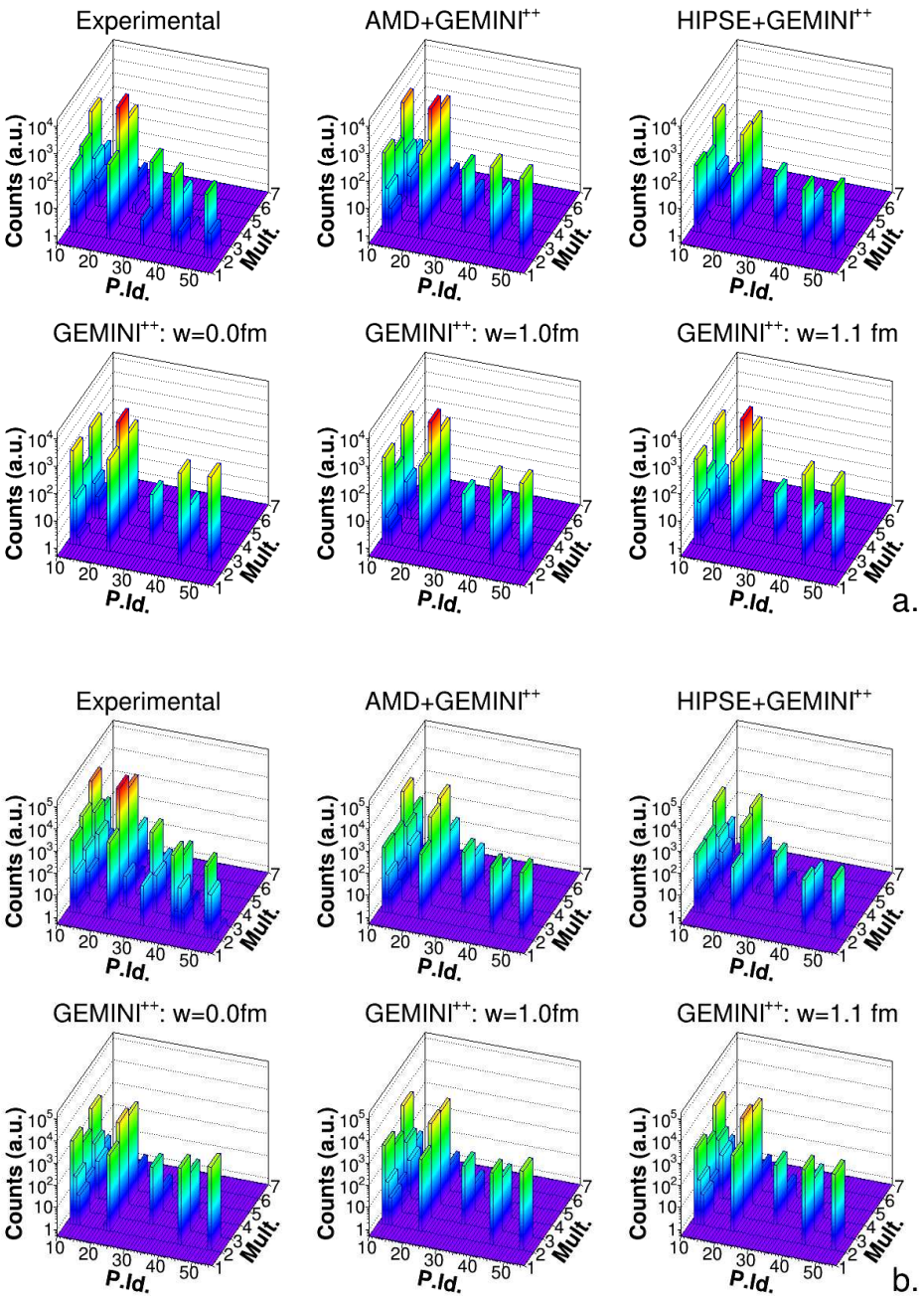

Figure 8.33: Open decay channels: particles in coincidence with a S-residue for the reactions $^{16}O +^{30} Si$ at 111 MeV (panel a.) and $^{16}O +^{30} Si$ at 128 MeV (panel b.). The Particles Identification is: 11 protons, 12 deuterons, 13 triton, 21 ^{3}He, 22 α-particles, 31 ^{6}Li, 32 ^{7}Li, 33 ^{8}Li, 41 ^{7}Be, 43 ^{9}Be, 51 ^{10}B and 52 ^{11}B. See text for more details.

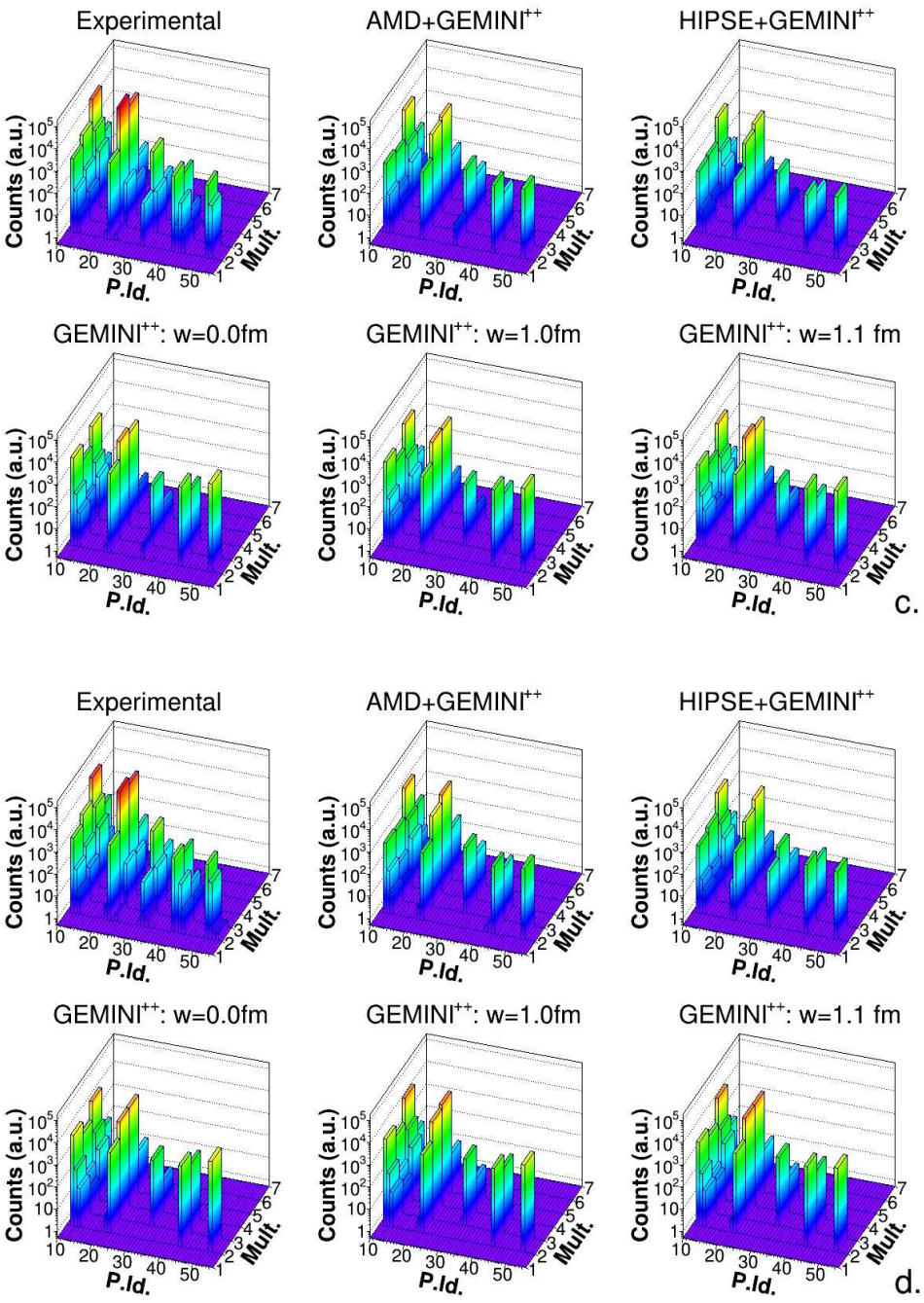

Figure 8.34: Same as in Fig. 8.33 but for the reactions $^{18}O + ^{28}Si$ at 126 MeV (panel c.) and $^{19}F + ^{27}Al$ at 133 MeV (panel d.).

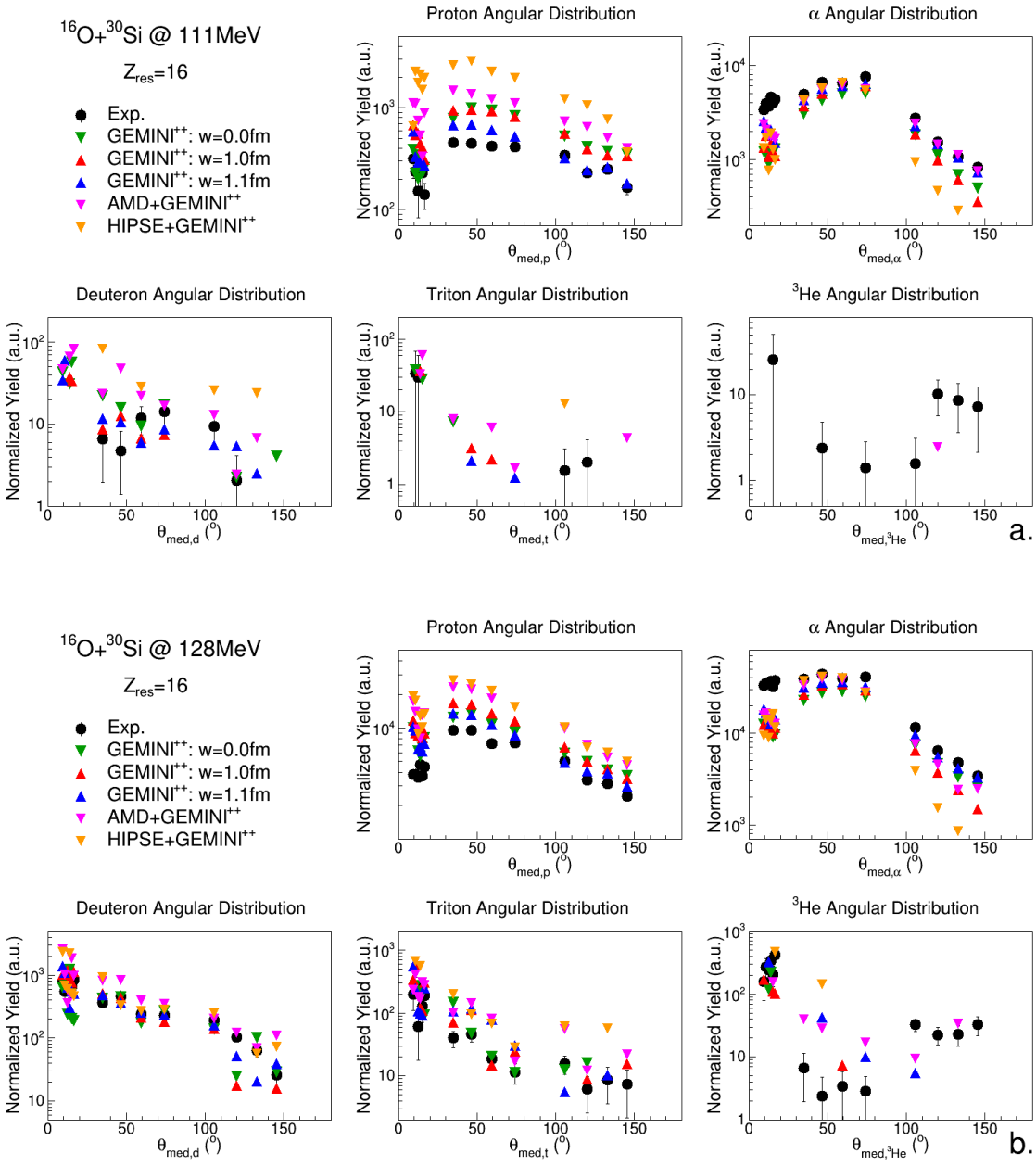

Figure 8.35: Angular distributions of LCP in coincidence with S-residue for the reactions $^{16}O + ^{30}Si$ at 111 MeV (panel a.) and $^{16}O + ^{30}Si$ at 128 MeV (panel b.) in comparison with $GEMINI^{++}$ with $w = 0.0$ fm (green triangles), $GEMINI^{++}$ with $w = 1.0$ fm (red triangles), $GEMINI^{++}$ with $w = 1.1$ fm (blue triangles), $AMD + GEMINI^{++}$ (pink triangles) and $HIPSE + GEMINI^{++}$ (orange triangles).

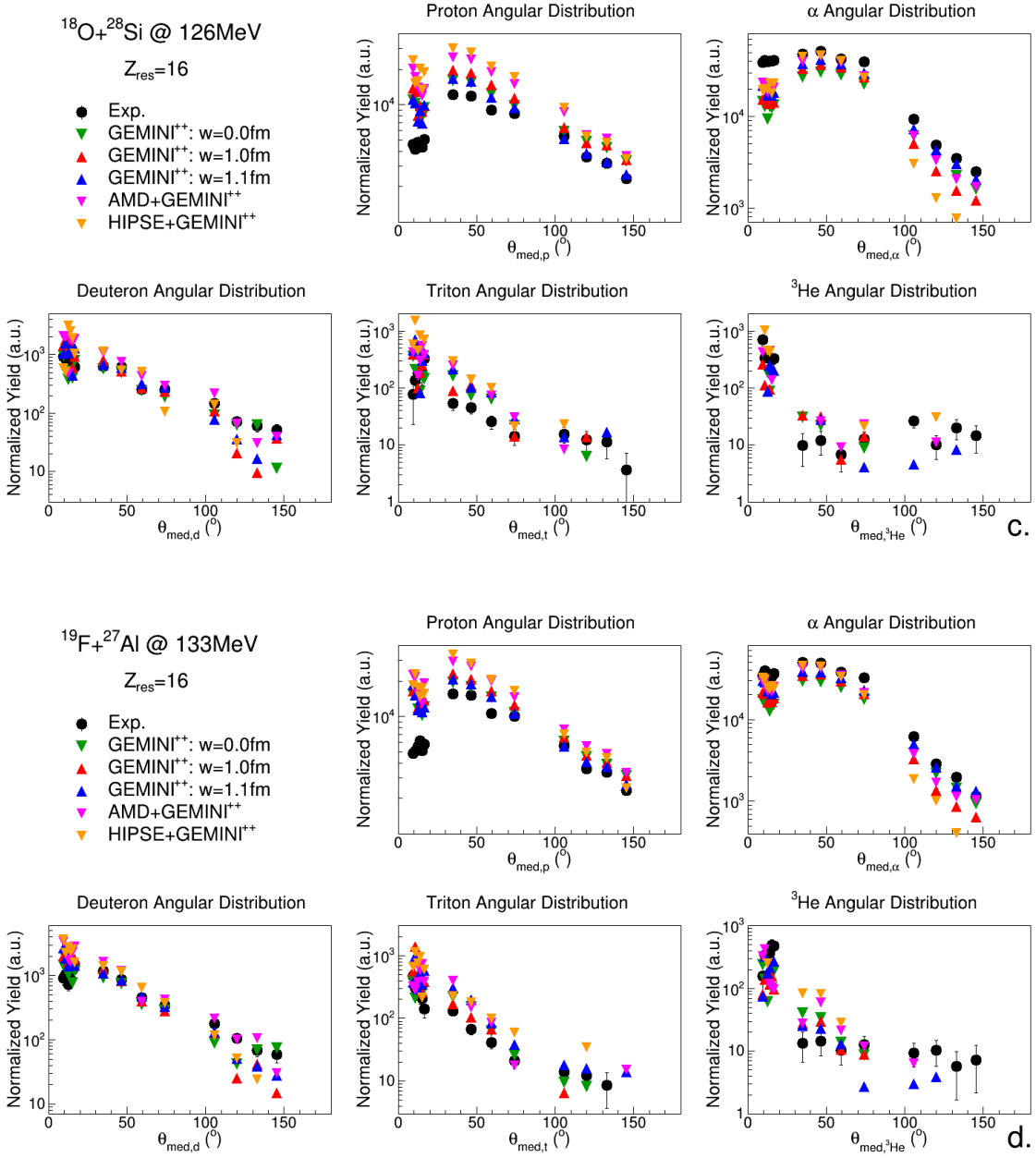

Figure 8.36: Same as in Fig. 8.35 but for the reactions $^{18}O + ^{28}Si$ at 126 MeV (panel c.) and $^{19}F + ^{27}Al$ at 133 MeV (panel d.).

Deuterons and tritons are reasonably described for the high energies reactions, but statistics is too little to draw any conclusion for the 111 MeV ^{16}O induced one.

For ^{3}He, despite the very low statistics it is to be underlined the shape of the experimental distribution which is quite flat in the region $\theta_{lab} = 29.5^{o} \div 150.4^{o}$ or even growing in the backward region for the ^{16}O induced reactions. The peak in the forward region is normally described by simulations which are less in agreement in the remaining angular region. In particular only **AMD** and **G11** are able to predict some ^{3}He in the backward direction. At low energy, despite the low experimental production, no simulation is showing any ^{3}He, apart from 1 point of **AMD**.

Again in Appendix A, the experimental energy spectra of protons, deuterons, tritons, ^{3}He and α-particles in coincidence with the S-residue, compared with those produced by simulations are presented.

Protons, which are shown in Figs. B.93 $\div$ B.96 of the Appendix B, are reasonably well described at all excitation energies from all the models. Almost the same is observed for deuterons, even though, in this case, some small differences can be observed between the different simulations especially in the $\theta_{lab} = 8.8^{o} \div 17.4^{o}$ angular region. A similar behavior is seen for tritons, which have however a quite low statistics to draw any definite conclusion.

For ^{3}He, despite the very poor statistics, it seems that experimental production is in any case somehow larger than expected by simulations especially either in the ^{16}O induced reactions or in specific angular regions for the other two reactions.

Even α-particles are reasonably well described by almost all simulations. A slight disagreement is observed with **HIPSE**. For the ^{19}F case the best agreement is observed with **G11**. As a conclusion it seems that the decay channels bringing to S isotopes are quite well reproduced by calculations from the shape point of view, even if a slight difference in the total yields have been observed from the BR and the angular distributions.

8.1.7 The P residue: $Z_{res} = 15$

The total branching ratio of channels with P-residue and the number of P-residue have been reported for experimental and simulated data for the four reactions in Table 8.9: the BR is the ratio between the number of evaporation residues with $Z_{res} = 15$ over the total number of residues. For the P residue the experimental BR is similar to $GEMINI^{++}$ and **AMD** at lower energy, while it is a little bit larger for the higher excitation energies reactions. The dynamical codes predict a smaller BR, especially the **HIPSE** case.

	$^{16}O + ^{30}Si$	111 MeV	$^{16}O + ^{30}Si$	128 MeV
	n^o residues	BR(%)	n^o residues	BR(%)
Experimental	846 ± 29	0.5	11398 ± 107	2.2
$GEMINI^{++}$ $w = 0.0$ fm	2131	0.8	4300	1.5
$GEMINI^{++}$ $w = 1.0$ fm	1461	0.5	4062	1.2
$GEMINI^{++}$ $w = 1.1$ fm	2072	0.7	4599	1.4
$AMD + GEMINI^{++}$	1742	0.7	2411	1.1
$HIPSE + GEMINI^{++}$	199	0.2	1342	1.0
	$^{18}O + ^{28}Si$	126 MeV	$^{19}F + ^{27}Al$	133 MeV
	n^o residues	BR(%)	n^o residues	BR(%)
Experimental	12690 ± 113	2.4	14625 ± 121	3.1
$GEMINI^{++}$ $w = 0.0$ fm	5564	1.7	8152	2.5
$GEMINI^{++}$ $w = 1.0$ fm	5222	1.4	8304	2.2
$GEMINI^{++}$ $w = 1.1$ fm	5868	1.6	8880	2.4
$AMD + GEMINI^{++}$	2636	1.1	3023	1.4
$HIPSE + GEMINI^{++}$	793	0.5	1342	1.0

Table 8.9: Number and total branching ratio (BR) of channels with P-residue.

The total LCP and light fragment ($Z < 6$) multiplicity (Mult.) in coincidence with a P-residue defined for each event is plotted as a function of the Particle Identification (P.Id.) in Fig. 8.37 and in Fig. 8.38 for the four reactions: $^{16}O + ^{30}Si$ at 111 MeV (panel a.), $^{16}O + ^{30}Si$ at 128 MeV (panel b.), $^{18}O + ^{28}Si$ at 126 MeV (panel c.) and $^{19}F + ^{27}Al$ at 133 MeV (panel d.). Experimentally, at all energies, the most populated channel is the 3α-1p, which is also strongly populated in the simulations. However, it seems that the

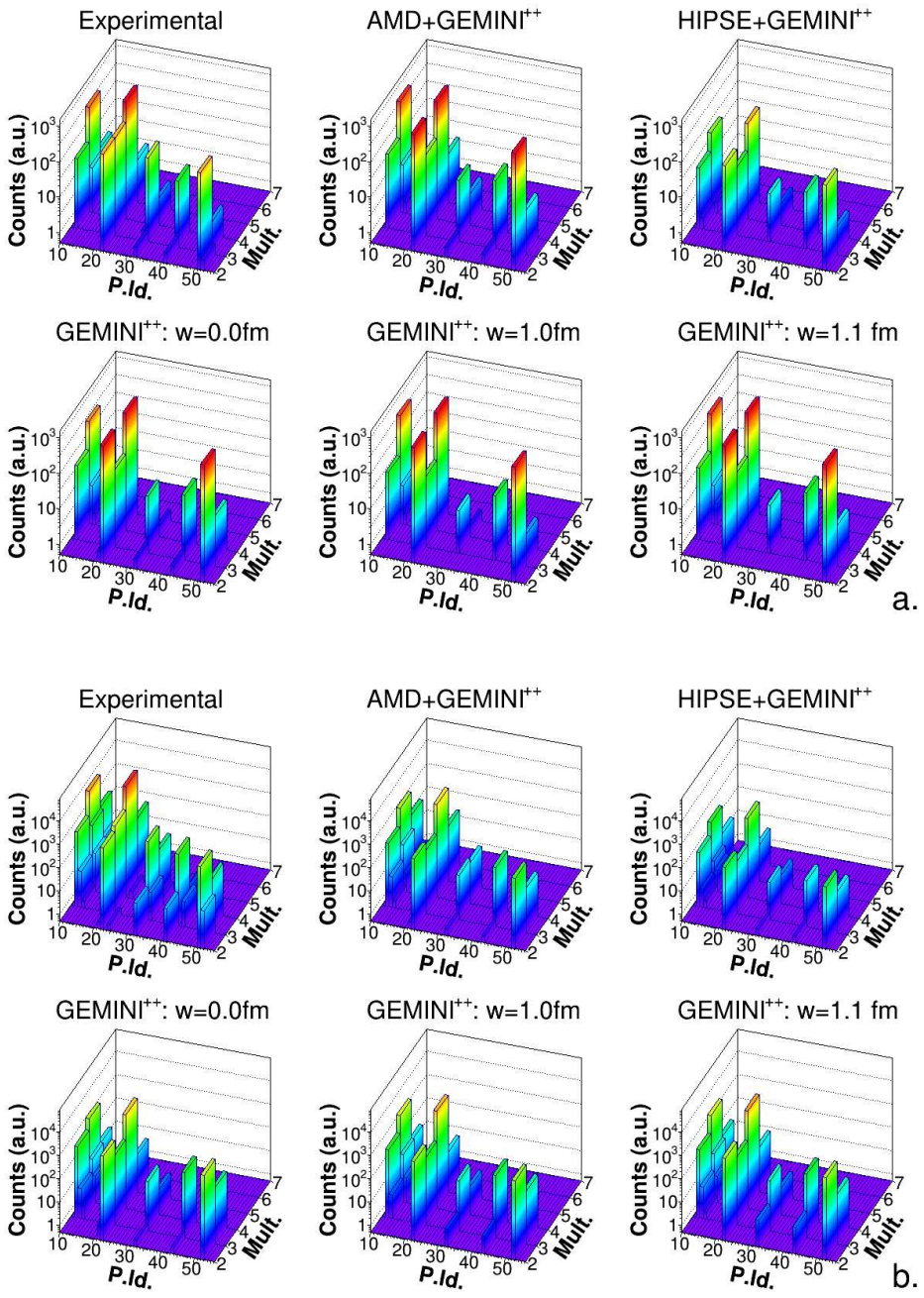

Figure 8.37: Open decay channels: particles in coincidence with a P-residue for the reactions $^{16}O +^{30} Si$ at 111 MeV (panel a.) and $^{16}O +^{30} Si$ at 128 MeV (panel b.). The Particles Identification is: 11 protons, 12 deuterons, 13 triton, 21 ^{3}He, 22 α-particles, 31 ^{6}Li, 32 ^{7}Li, 33 ^{8}Li, 41 ^{7}Be, 43 ^{9}Be, 51 ^{10}B and 52 ^{11}B. See text for more details.

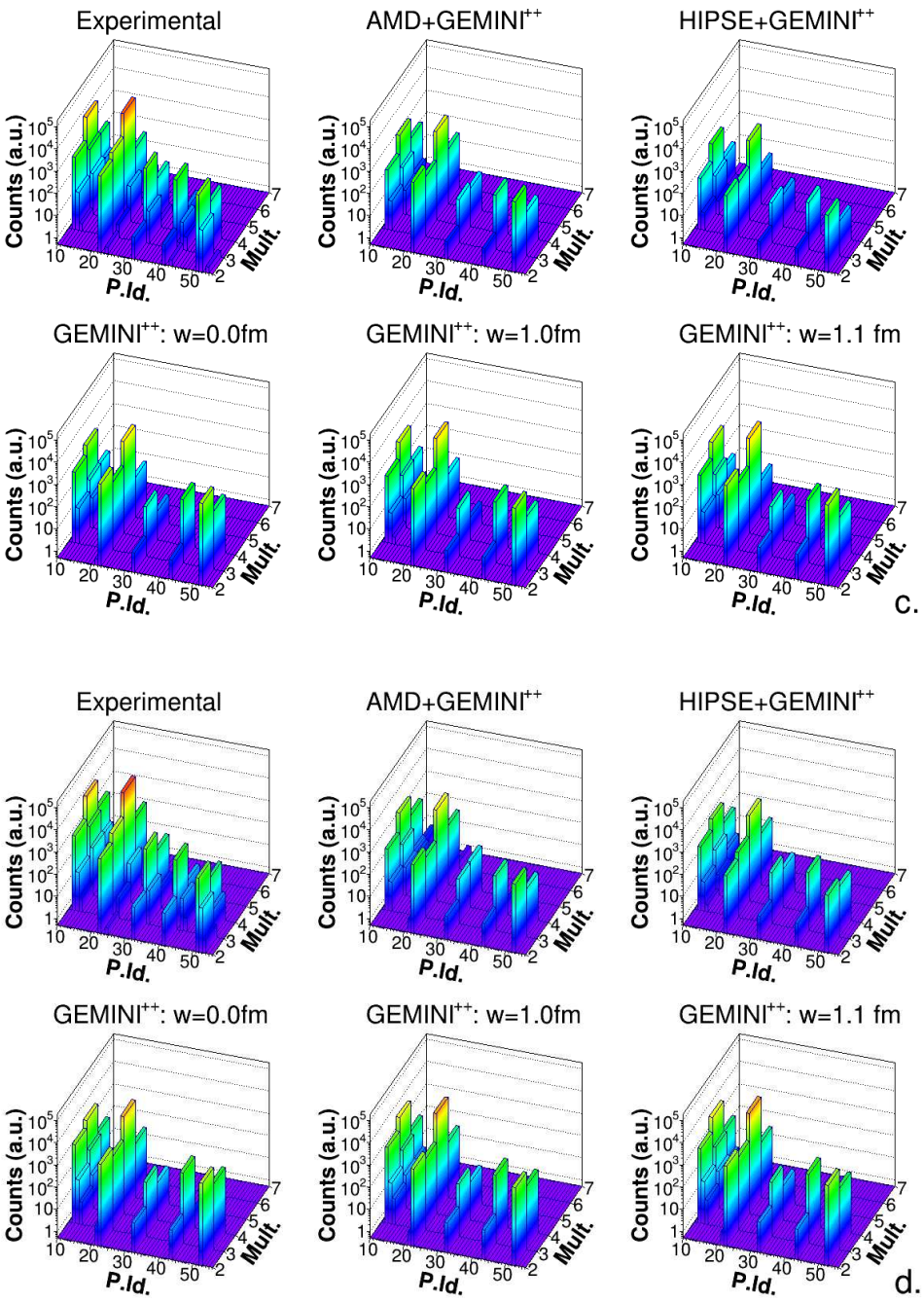

Figure 8.38: Same as in Fig. 8.37 but for the reactions $^{18}O + ^{28}Si$ at 126 MeV (panel c.) and $^{19}F + ^{27}Al$ at 133 MeV (panel d.).

other channel 1α-1B is slightly less strong in experimental data than in simulations. This will be discussed more quantitatively in the next chapter.

In Fig. 8.39 and in Fig. 8.40 the experimental angular distribution (black dots) of LCP in coincidence with the P-residue are compared with those produced by simulations. The α-particle angular distribution spectra are, in the case of coincidence with $Z_{ER} = 15$, well accounted for by **AMD** at low energy, while both **AMD** and **G11** are good at higher energies. At 111 MeV, a small underestimation of the forward peak ($\theta_{lab} = 29.5^o \div 82.5^o$) can be observed, which is, on the contrary well described at higher energies. **HIPSE** at low energy is describing only the central angular region, with almost no α-particles predicted in the forward direction, while at higher energies a better description is obtained with only a small underestimation of the backward angular region ($\theta_{lab} = 97.5^o \div 150.4^o$).

Protons are underestimated by all calculations in the whole angular range at 111 MeV, except by **HIPSE**, which is reasonably taking into account the proton yields. Anyhow, even **AMD** (and also **G10**) are quite closer to the data. With ^{16}O at 128 MeV, a quite good description is obtained with **AMD**, except for the forward angular region where protons are under-produced. $HIPSE{+}GEMINI^{++}$ is reasonably close to the experimental yields in the whole angular range, even if slightly underestimating it in the backward region. A slight underestimation is observed, for the ^{18}O case, by all simulations apart from **HIPSE** in the region $\theta_{lab} > 29.5^o$, while only partially the forward experimental points can be described by some of the simulations. In the ^{19}F case it is **AMD** to better describe the whole distribution for $\theta_{lab} > 29.5^o$, while the forward angles the experimental yields are much lower than predicted.

Deuterons, tritons and ^3He particles can be discussed only relatively between the four reactions: at low energy, only deuterons are observed with very small statistics, while, for the ^{16}O at 128 MeV and for the ^{19}F at 133 MeV, all the three kind of clusters are observed at almost all angles; finally, in the case of ^{18}O at 126 MeV, ^3He seem to be essentially forward focused. However, statistics is too low to draw any further conclusion, apart that deuterons are reasonably described by simulations.

The experimental energy spectra of protons, deuterons and α-particles in coincidence

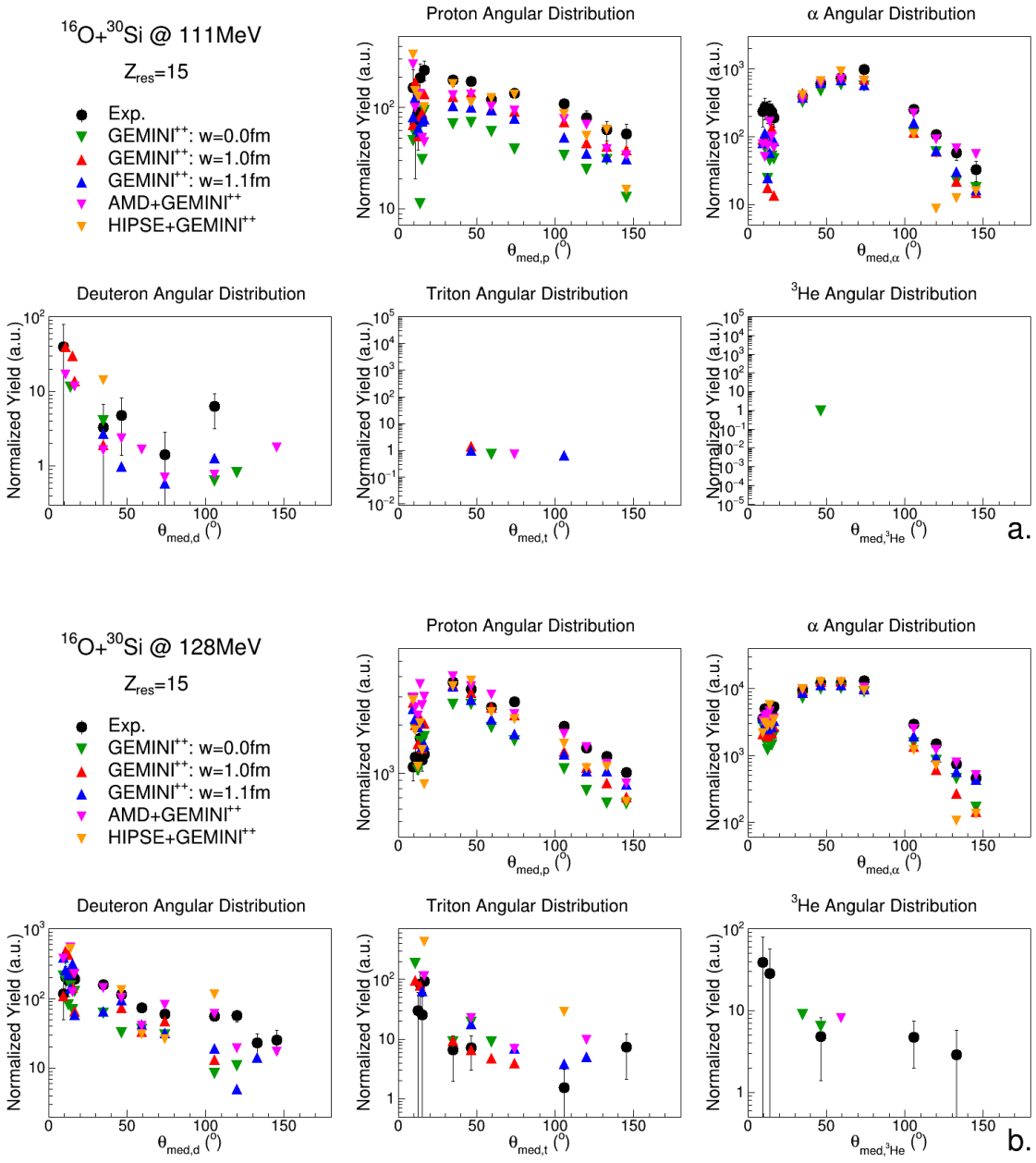

Figure 8.39: Angular distributions of LCP in coincidence with P-residue for the reactions $^{16}O + ^{30}Si$ at 111 MeV (panel a.) and $^{16}O + ^{30}Si$ at 128 MeV (panel b.) in comparison with $GEMINI^{++}$ with $w = 0.0$ fm (green triangles), $GEMINI^{++}$ with $w = 1.0$ fm (red triangles), $GEMINI^{++}$ with $w = 1.1$ fm (blue triangles), $AMD + GEMINI^{++}$ (pink triangles) and $HIPSE + GEMINI^{++}$ (orange triangles).

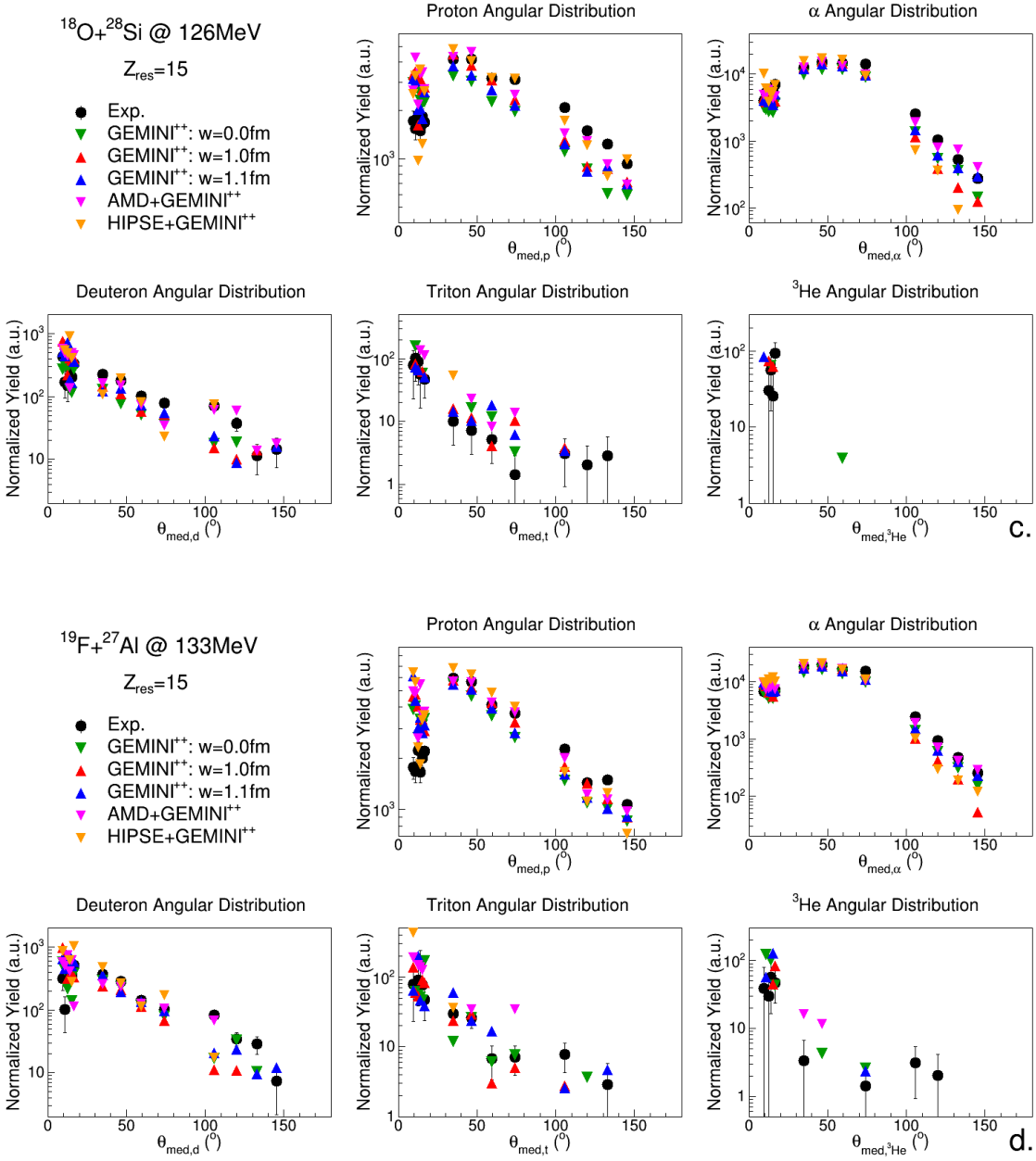

Figure 8.40: Same as in Fig. 8.39 but for the reactions $^{18}O + ^{28}Si$ at 126 MeV (panel c.) and $^{19}F + ^{27}Al$ at 133 MeV (panel d.).

with the P-residue, compared with those produced by simulations are presented in Appendix B (Figs. B.113 $\div$ B.124): the proton energy spectra shapes are quite well reproduced by simulations in the whole angular range, with relatively small differences between them. Deuterons spectra are very poor, especially at low energy. However, one can say that all simulations reasonably describe the shapes, apart from **HIPSE**, mainly because of the very low statistics. Tritons and ^3He have too low statistics to be displayed as energy spectra and they are not reported. The α-particle spectra are very well described at the higher excitation energies by all the simulations. At low energy, some small differences between experimental data and predictions can be noticed in the central angular region, which might also be due to the low statistics. In particular, **HIPSE** is not predicting any α-particle in the forward region, as already observed in the angular distribution.

8.1.8 The Si residue: $Z_{res} = 14$

The total branching ratio (BR) of channels with Si-residue, defined as the number of evaporation residues with $Z_{res} = 14$ over the total number of residues, and the number of Si-residue have been reported for experimental and simulated data for the four reactions in Table 8.10. The experimental values are small, but quite larger than predicted by models at all energies. Their growth with excitation energy is, in any case quite coherent with the relative increase estimated by simulations.

Fig. 8.41 and Fig. 8.42 display the multiplicity (Mult.) of LCP and light fragment (Z<6) in coincidence with a Si-residue have been plotted as a function of the Particle Identification (P.Id.) for the four reactions: $^{16}O + ^{30}Si$ at 111 MeV (panel a.), $^{16}O + ^{30}Si$ at 128 MeV (panel b.), $^{18}O + ^{28}Si$ at 126 MeV (panel c.) and $^{19}F + ^{27}Al$ at 133 MeV (panel d.). In the case of $Z_{ER} = 14$, the observed plots show a quite strong decay channel, which is the 4α long decay chain. However, other decay channels are predicted by simulations quite strongly: the $1B + 1\alpha + 1p$ channel, which is much more feeble experimentally, especially with respect to $GEMINI^{++}$ predictions; at higher energies also the $3\alpha - 2p$ channel is opening up quite evidently and, in this case, the experiment is somehow showing a privileged decay path in this direction with respect to simulations, especially $GEMINI^{++}$.

	$^{16}O+^{30}Si$	111 MeV	$^{16}O+^{30}Si$	128 MeV
	n^o residues	BR(%)	n^o residues	BR(%)
Experimental	367 ± 19	0.2	4951 ± 70	0.9
$GEMINI^{++}$ $w = 0.0$ fm	148	0.06	872	0.3
$GEMINI^{++}$ $w = 1.0$ fm	133	0.04	781	0.2
$GEMINI^{++}$ $w = 1.1$ fm	184	0.06	1024	0.3
$AMD + GEMINI^{++}$	245	0.10	620	0.3
$HIPSE + GEMINI^{++}$	34	0.03	338	0.2
	$^{18}O+^{28}Si$	126 MeV	$^{19}F+^{27}Al$	133 MeV
	n^o residues	BR(%)	n^o residues	BR(%)
Experimental	5587 ± 75	1.0	6200 ± 79	1.3
$GEMINI^{++}$ $w = 0.0$ fm	1279	0.4	2486	0.8
$GEMINI^{++}$ $w = 1.0$ fm	1137	0.3	2108	0.6
$GEMINI^{++}$ $w = 1.1$ fm	1319	0.4	2480	0.7
$AMD + GEMINI^{++}$	612	0.3	826	0.4
$HIPSE + GEMINI^{++}$	186	0.13	338	0.2

Table 8.10: Number and total branching ratio (BR) of channels with Si-residue.

More quantitative details will be given in the following chapter.

The comparison of experimental simulated angular distribution of LCP in coincidence with the Si-residue are illustrated in Fig. 8.43 and in Fig. 8.44. The α-particles are well described by simulations, especially by **AMD** except for an underestimation of the backward angular region ($\theta_{lab} = 97.5^o \div 150.4^o$), which is larger for the O induced reactions. The proton angular distribution shape is reasonably reproduced by simulations, but the yields are overestimated. In the backward angular region, the overestimation is slightly bigger for the O induced reactions.

Considering the low statistics, we can say only that the deuterons and the triton clusters are reproduced in the F case; for the other cases, statistics, either for experiment or for calculations, do not permit any particular conclusion: no data are observed at the lower energy (where the total statistics of events was much lower than for the other three cases).

The experimental energy spectra (black dots) of protons and α-particles in coincidence

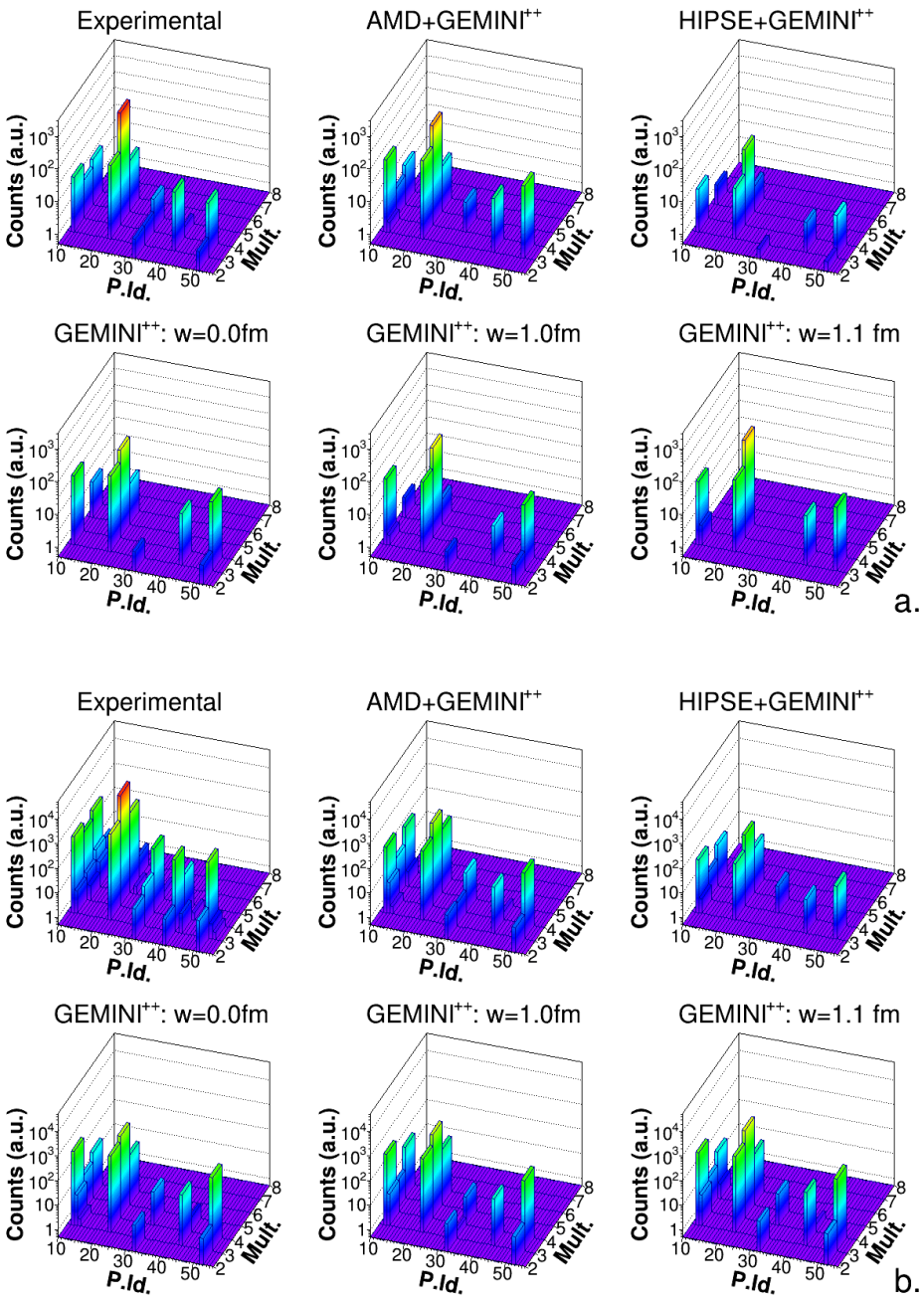

Figure 8.41: Open decay channels: particles in coincidence with a Si-residue for the reactions $^{16}O + ^{30}Si$ at 111 MeV (panel a.) and $^{16}O + ^{30}Si$ at 128 MeV (panel b.). The Particles Identification is: 11 protons, 22 α-particles, 32 ^{7}Li, 43 ^{9}Be and 52 ^{11}B. See text for more details.

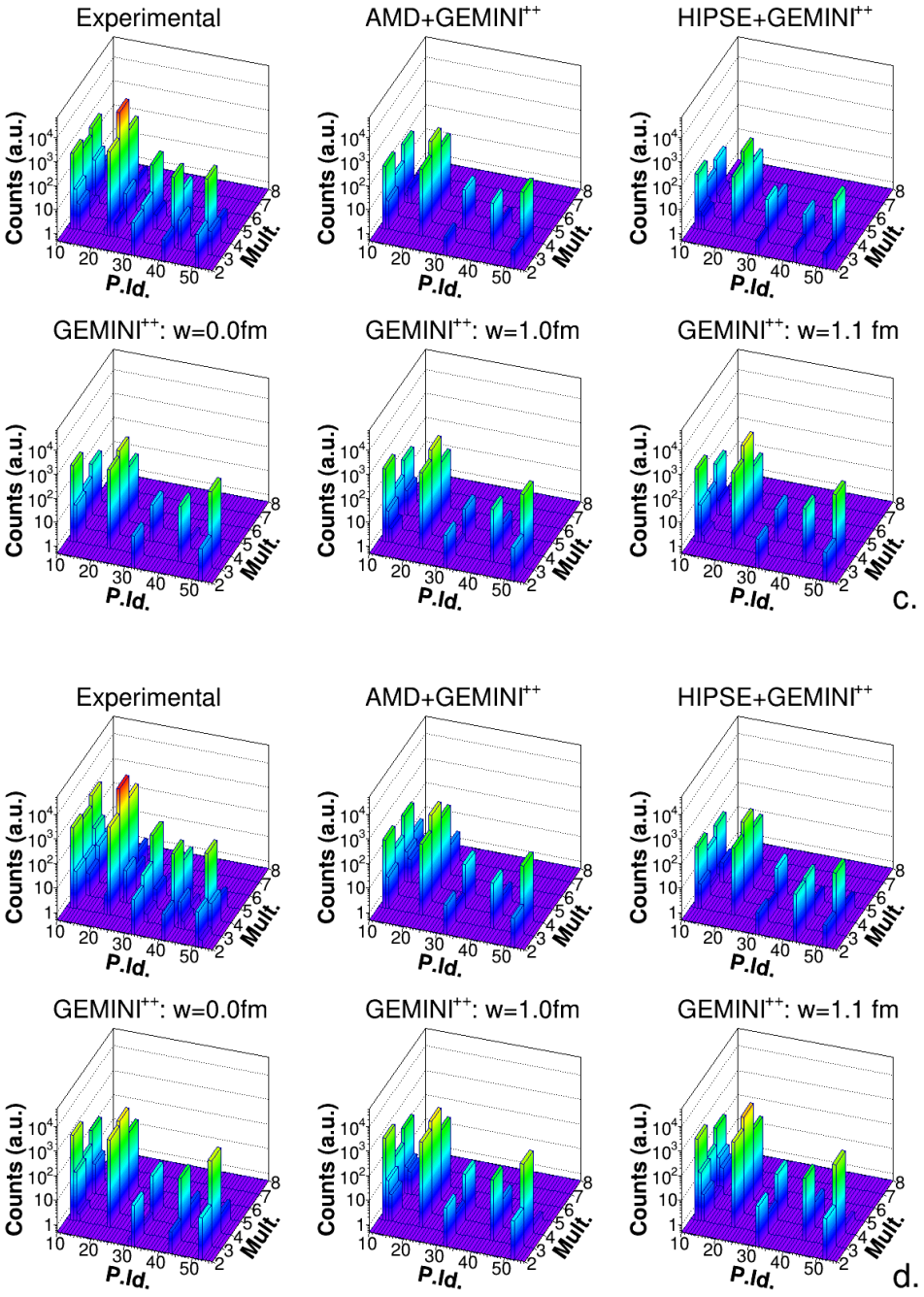

Figure 8.42: Same as in Fig. 8.41 but for the reactions $^{18}O + ^{28}Si$ at 126 MeV (panel c.) and $^{19}F + ^{27}Al$ at 133 MeV (panel d.).

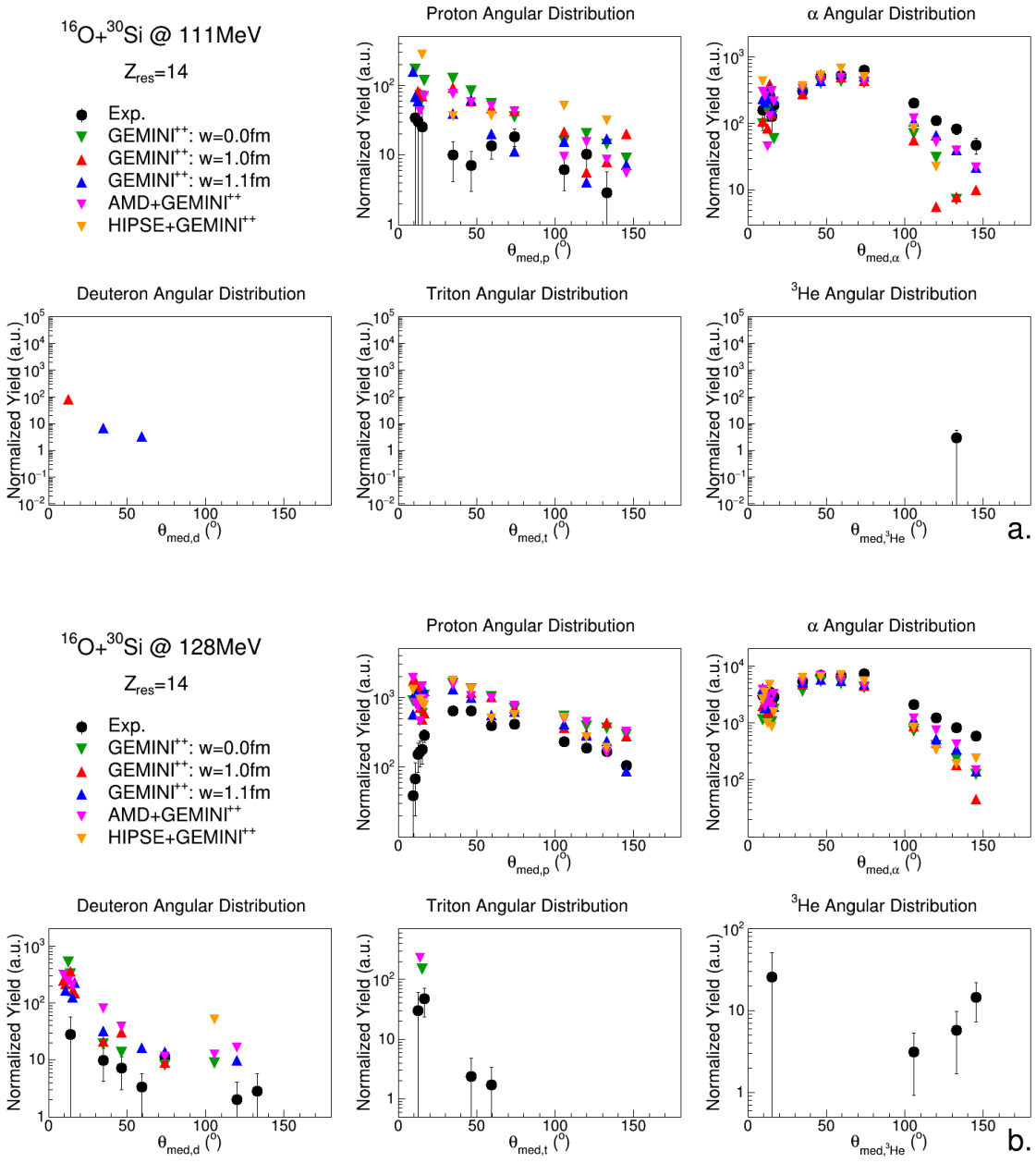

Figure 8.43: Angular distributions of LCP in coincidence with Si-residue for the reactions $^{16}O + ^{30}Si$ at 111 MeV (panel a.) and $^{16}O + ^{30}Si$ at 128 MeV (panel b.) in comparison with $GEMINI^{++}$ with $w = 0.0$ fm (green triangles), $GEMINI^{++}$ with $w = 1.0$ fm (red triangles), $GEMINI^{++}$ with $w = 1.1$ fm (blue triangles), $AMD + GEMINI^{++}$ (pink triangles) and $HIPSE + GEMINI^{++}$ (orange triangles).

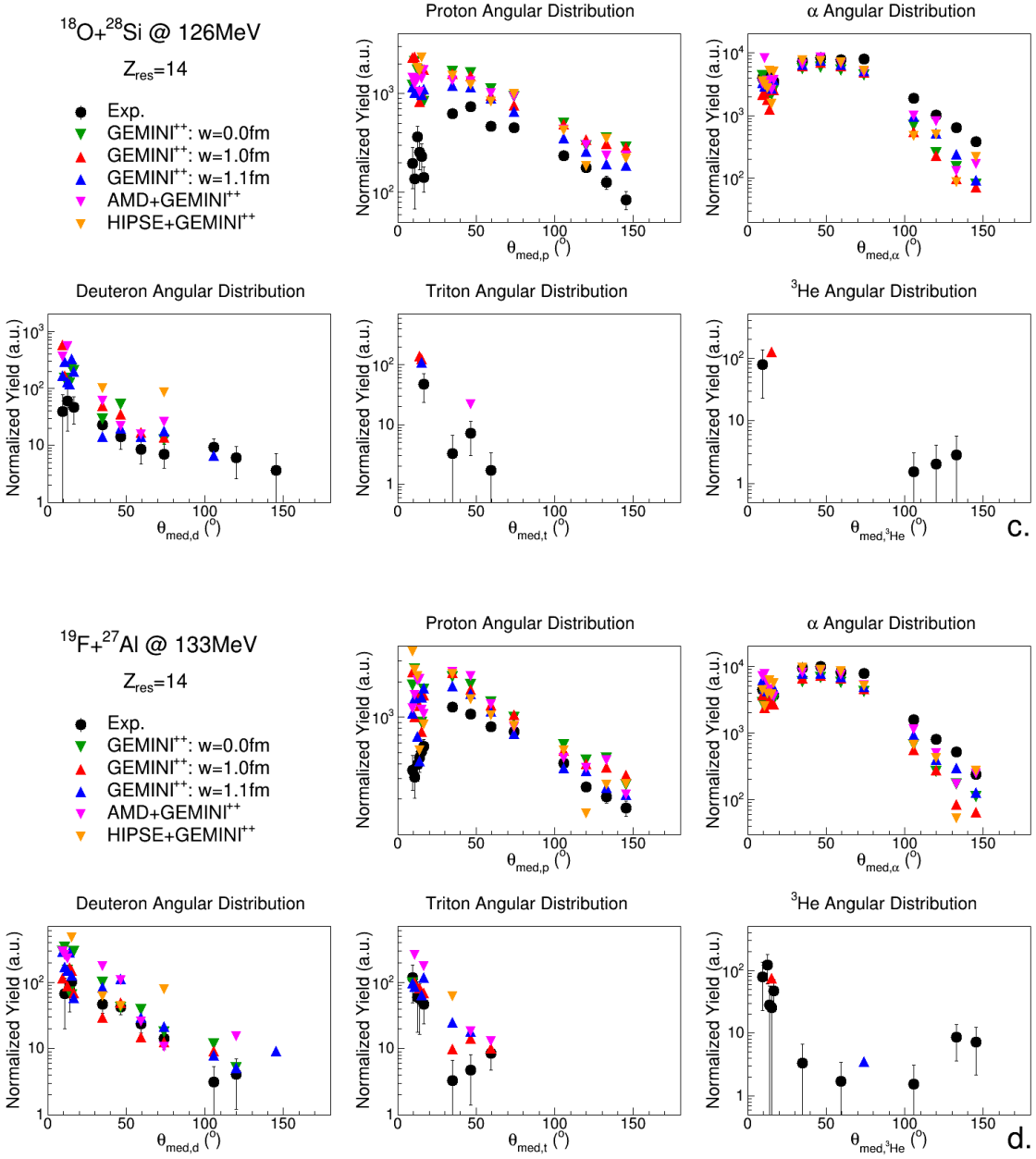

Figure 8.44: Same as in Fig. 8.43 but for the reactions $^{18}O+^{28}Si$ at 126 MeV (panel c.) and $^{19}F+^{27}Al$ at 133 MeV (panel d.).

with the Si-residue, compared with those produced by simulations, are presented in Appendix B. Proton spectra shapes are well reproduced, especially at the higher excitation energies by $GEMINI^{++}$ and **AMD**. **HIPSE** have generally a worse agreement, because of its lower statistics (see relative BR). Even α-particles spactra are reasonably described by all simulations: again, **HIPSE** is showing a lower statistics with a missing yield especially visible at very forward and backward angles.

8.1.9 The Al residue: $Z_{res} = 13$

In Table 8.11 the number of Al-residue and the total branching ratio of channels with such residue have been reported for experimental and simulated data for the four reactions; the BR is the ratio between the number of evaporation residues with $Z_{res} = 13$ over the total number of residues. Again, the experimental values, despite it is very small and, therefore, affected by a large error, is much larger than predicted. Also in this case the trend is coherent with the expected growth as a function of the excitation energies.

The multiplicities (Mult.) of LCP in coincidence with a Al-residue have been plotted as a function of the Particle Identification (P.Id.) in Fig. 8.45 and in Fig. 8.46 for the four reactions: $^{16}O + ^{30}Si$ at 111 MeV (panel a.), $^{16}O + ^{30}Si$ at 128 MeV (panel b.), $^{18}O + ^{28}Si$ at 126 MeV (panel c.) and $^{19}F + ^{27}Al$ at 133 MeV (panel d.). The observation in the experimental data of the 4α+1p channel, is interesting since it show up even at low energy where simulation almost do not predict it. It has to be noted, moreover, that this channel is in absolute much more populated than in the simulations, due to the quite higher experimental BR of the Al-channel.

In Fig. 8.47 the experimental angular distribution (black dots) of protons and α-particles in coincidence with the Al-residue are compared with those produced by simulations. The α-particles are reasonably reproduced for the higher energies, even though in the case of ^{16}O the forward region is slightly overestimated, while for ^{18}O and ^{19}F almost all simulations well describe it, apart from **HIPSE**. In the case of ^{16}O at lower energy the statistic is too low. For protons the situation is more confused and no simulation is really able to describe the angular distribution especially in the forward angular range.

	$^{16}O+^{30}Si$	111 MeV	$^{16}O+^{30}Si$	128 MeV
	n^o residues	BR(%)	n^o residues	BR(%)
Experimental	26 ± 5	0.02	639 ± 24	0.11
$GEMINI^{++}$ $w = 0.0$ fm	18	0.007	80	0.03
$GEMINI^{++}$ $w = 1.0$ fm	11	0.003	56	0.02
$GEMINI^{++}$ $w = 1.1$ fm	8	0.003	72	0.02
$AMD + GEMINI^{++}$	12	0.005	50	0.2
$HIPSE + GEMINI^{++}$	-	-	14	0.010
	$^{18}O+^{28}Si$	126 MeV	$^{19}F+^{27}Al$	133 MeV
	n^o residues	BR(%)	n^o residues	BR(%)
Experimental	639 ± 25	0.12	1002 ± 32	0.2
$GEMINI^{++}$ $w = 0.0$ fm	122	0.04	204	0.06
$GEMINI^{++}$ $w = 1.0$ fm	80	0.02	170	0.05
$GEMINI^{++}$ $w = 1.1$ fm	121	0.03	224	0.06
$AMD + GEMINI^{++}$	62	0.03	82	0.04
$HIPSE + GEMINI^{++}$	11	0.008	14	0.010

Table 8.11: Number and total branching ratio (BR) of channels with Al-residue.

The experimental energy spectra (black dots) of protons and α-particles in coincidence with the Al-residue, compared with those produced by simulations are presented in Appendix B: Figs. B.133 ÷ B.140. No enough statistics for proton is present at lower energy. For the ^{16}O at 128 MeV, ^{18}O at 126 MeV and ^{19}F at 133 MeV, despite the low statistics, we can observe that the forward angular region ($\theta_{lab} = 8.8^o \div 17.4^o$) is generally not described by any calculation; **HIPSE** is not even able to describe the backward region ($\theta_{lab} = 97.5^o \div 150.4^o$), due to a too small production. Only for the ^{19}F case **G11** is close to the experimental data in all the observed range. Even for α-particle too low statistics is present to comment on the energy spectra. At higher energies, again, we can observe a reasonable agreement with all $GEMINI^{++}$ cases; **AMD** is missing some yields in the forward angular region, while **HIPSE** is too low in statistics, so that it cannot reproduce neither the forward nor the backward part of the experimental distribution.

As a conclusion we may say that the Al residue is produced with a larger cross section

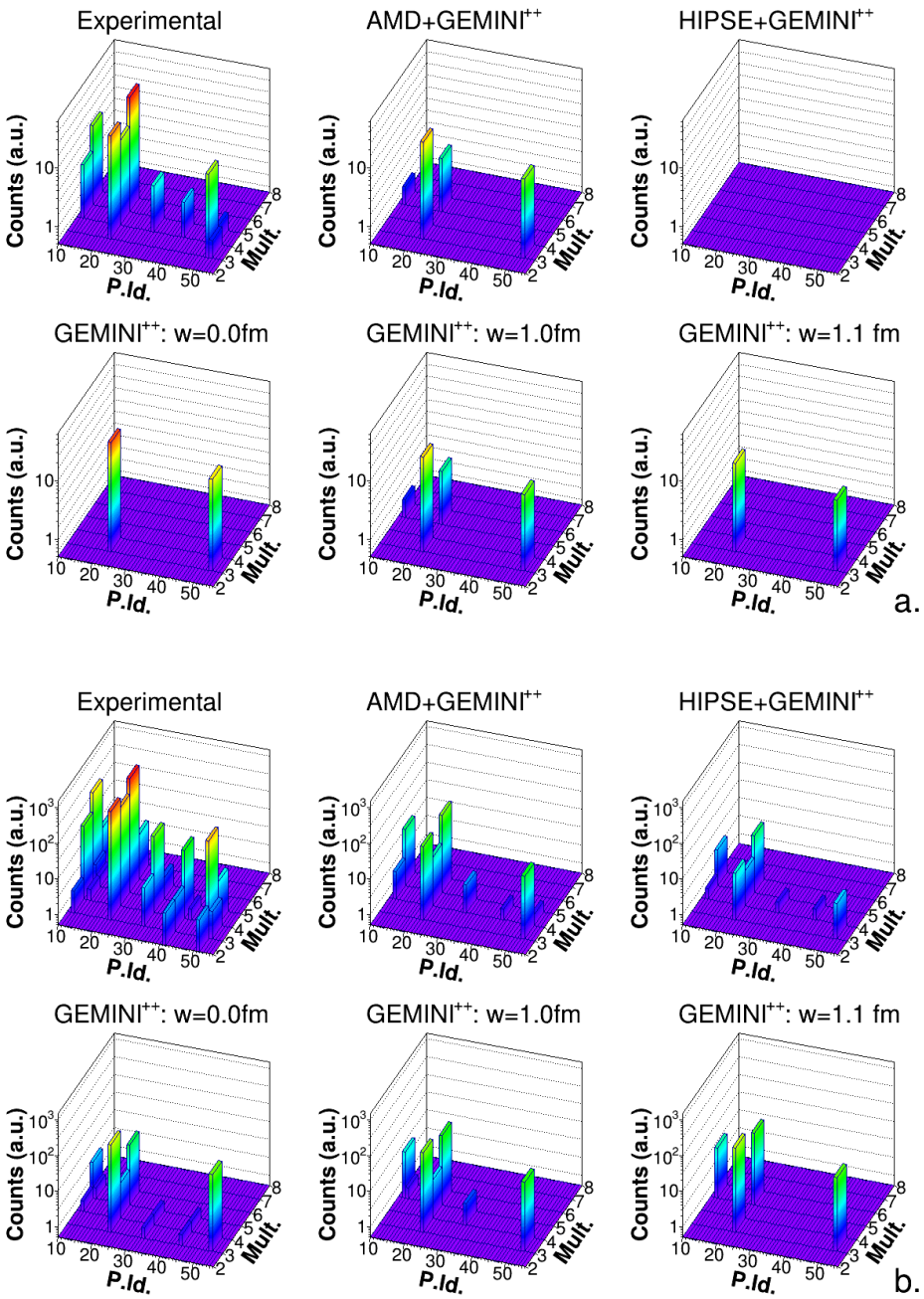

Figure 8.45: Open decay channels: particles in coincidence with a *Al*-residue for the reactions $^{16}O + ^{30}Si$ at 111 MeV (panel a.) and $^{16}O + ^{30}Si$ at 128 MeV (panel b.). The Particles Identification is: 11 protons, 22 α-particles, 32 ^{7}Li, 43 ^{9}Be and 52 ^{11}B. See text for more details.

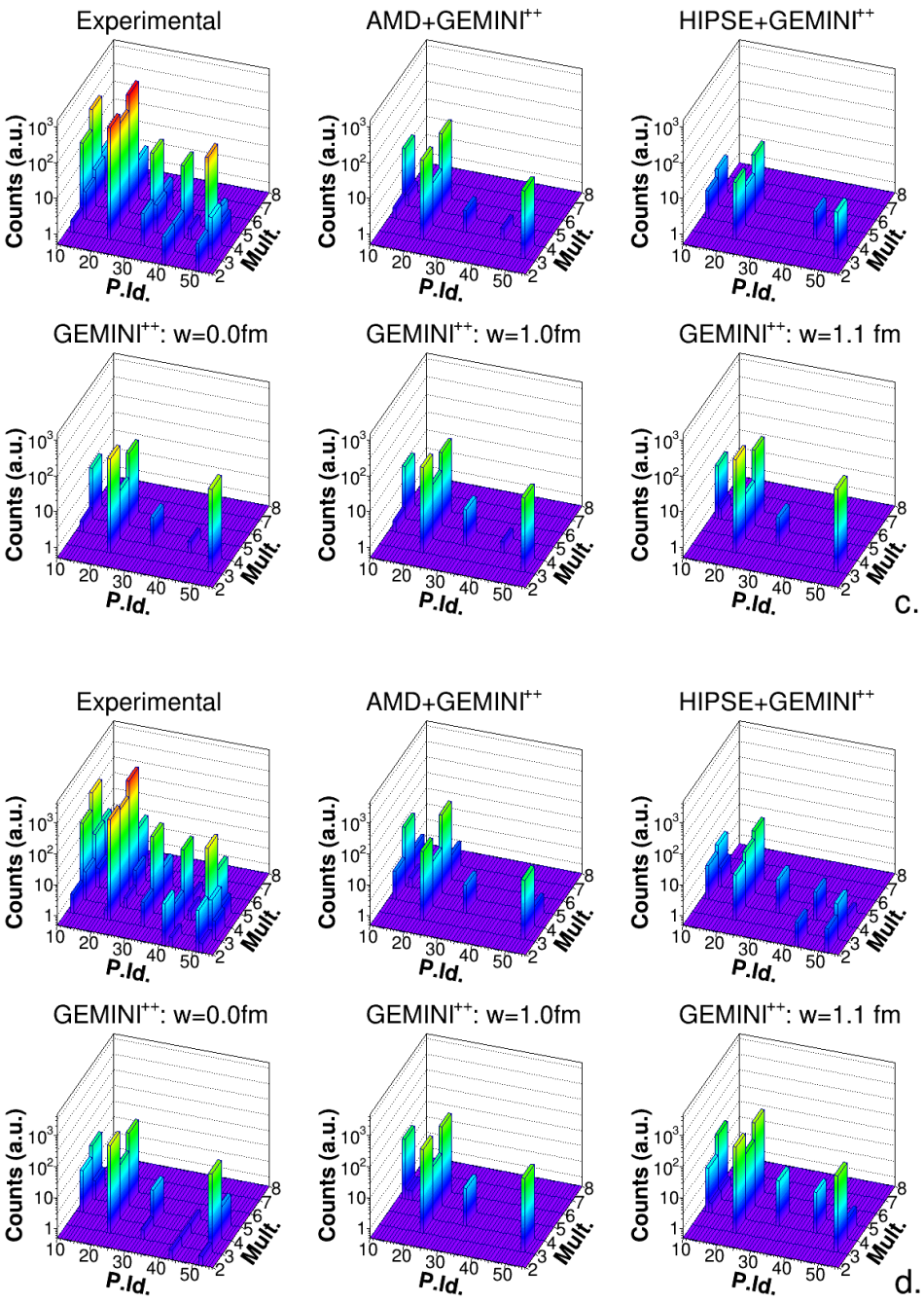

Figure 8.46: Same as in Fig. 8.45 but for the reactions $^{18}O + ^{28}Si$ at 126 MeV (panel c.) and $^{19}F + ^{27}Al$ at 133 MeV (panel d.).

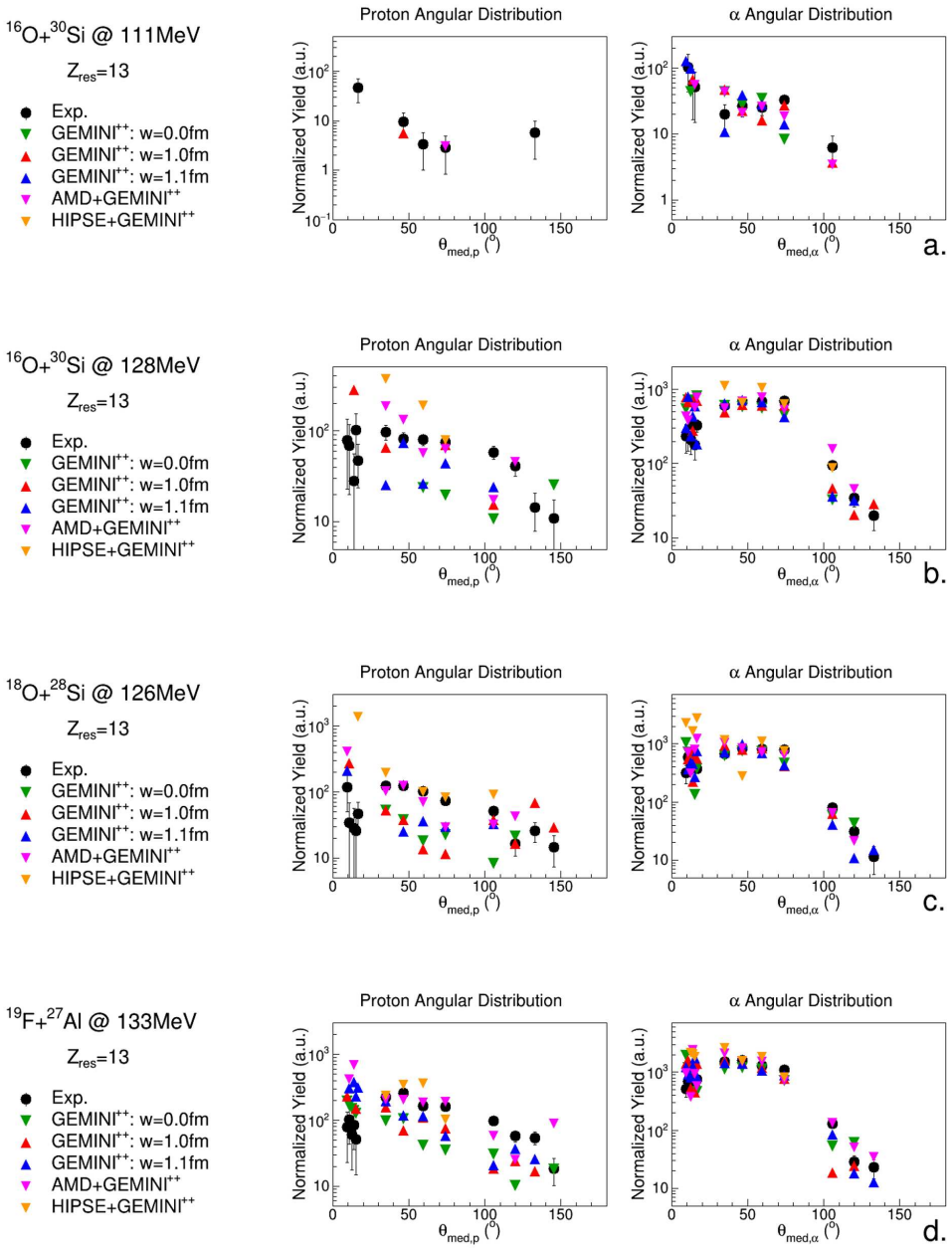

Figure 8.47: Angular distributions of LCP in coincidence with *Al*-residue for the reactions $^{16}O + ^{30}Si$ at 111 MeV (panel a.), $^{16}O + ^{30}Si$ at 128 MeV (panel b.), $^{18}O + ^{28}Si$ at 126 MeV (panel c.) and $^{19}F + ^{27}Al$ at 133 MeV (panel d.) in comparison with $GEMINI^{++}$ **with** $w = 0.0$ **fm G00**(green triangles), **G10** (red triangles), **G11** (blue triangles), **AMD** (pink triangles) and **HIPSE** (orange triangles).

with respect to the expectation, but it is generally quite in agreement with the expected decay path. A more quantitative discussion will be performed in the next chapter.

Chapter 9

Analysis of Multiple-α Channels

9.1 Exclusive observables for 2 α-channel

For specific channels a more detailed analysis can be performed by studying particular correlations between emitted particles: in particular, in the 2α decay channel it is very interesting to study the relative energy and momentum of the two emitted α-particles and to compare them to simulations, to verify the origin of the observed major experimental yield and to evidence if it might be associated to a particular configuration.

In the case of the 2α-particles exit channel: $^{38-xn}Ar + 2\alpha + xn$, the three relative $\alpha - \alpha$ variables:

$$E_{\alpha-\alpha} = \frac{\overrightarrow{k}^2_{\alpha-\alpha}}{2\mu} \tag{9.1}$$

$$cos(\theta_k) = \frac{\overrightarrow{k}_{ER} \cdot \overrightarrow{k}_{\alpha-\alpha}}{\mid \overrightarrow{k}_{ER} \mid\mid \overrightarrow{k}_{\alpha-\alpha} \mid} \tag{9.2}$$

$$\epsilon_{\alpha-\alpha} = \frac{E_{\alpha-\alpha}}{E_{\alpha-\alpha} + E_{ER}} \tag{9.3}$$

can be defined. In particular, the variable $E_{\alpha-\alpha}$ represents the relative α-α-energy; the variable $cos(\theta_k)$ is the cosine of the angle between the Jacobi angular momenta [116, 117];

finally, the $\epsilon_{\alpha-\alpha}$ links the relative α-α-energy to the energy of the evaporation residue ($E_{ER} = \frac{\vec{k}^2_{ER}}{2m_{ER}}$).

These variables have been studied in correlation with the Q-value and the results are reported in the Figs. from 9.1 to 9.20. Each figure is organized as it follows: in the upper left panel, the plots $cos(\theta_k)$ vs. Q-value for the experimental data are displayed; in the upper central panel the corresponding plots for the simulations are reported; in the upper right panel, the comparison of experimental $cos(\theta_k)$ (black dots) and simulated one (colored lines) is shown; in the lower central panel, the plots of $E_{\alpha-\alpha}$ vs. Q-value for the experimental data is presented; in the lower right panel the comparison between experimental (black dots) and simulated (colored lines) $E_{\alpha-\alpha}$ is displayed. All this is repeated for the four studied systems. As in previous chapters the simulations are made with $GEMINI^{++}$ with $w = 0.0$ fm (**G00**, green in figures), $w = 1.0$ fm (**G10**, red), $w = 1.1$ fm (**G11**, blue), $AMD{+}GEMINI^{++}$ (**AMD**, pink) and $HIPSE{+}GEMINI^{++}$ (**HIPSE**, orange).

Moreover, in Fig. 9.21 $\div$ 9.24, the direct correlation between $E_{\alpha-\alpha}$ and $cos(\theta_k)$ are displayed.

Looking at the $E_{\alpha-\alpha}$ *vs.* Q-value correlations of the reaction $^{16}O +^{30} Si$ at 111 MeV, one can observe experimentally two main groups of correlations: the first is a distribution centered at Q-value $= -50$ MeV and $E_{\alpha-\alpha} < 20$ MeV, while the latter starting from about $E_{\alpha-\alpha} = 10$ MeV up to 60 MeV slightly bended. in Q-value ($\sim -60 \div -40$ MeV). These two distributions are more evident when looking to simulated data with **G00**, where both distributions are slightly bended. The first one goes from $Q = -50$ to -25 MeV in a relative energy window $E_{\alpha-\alpha} < 20$ MeV, while the second one is more similar to the data. Moreover, it can be observed that **G00** predicts a larger yield for the less energetic distribution, while in experimental data they are more similar each other, like it can be observed in **G10**, **G11** and **AMD**. Furthermore, a peak is present in the experimental at very small relative energy (~ 5 MeV), which is not reproduced by any of the simulations. This can be better observed in the projection of the relative energy spectra.

If one look to the $cos(\theta_k)$ *vs.* Q-value distributions spectra, one can observe that experi-

mentally the distribution is slightly backward peaked (~ -0.2) and a little bit asymmetric, with two little "horns" at -1 and $+1$, which are not present in the simulated data.

Looking at the $E_{\alpha-\alpha}$ *vs.* $cos(\theta_k)$ correlation reported in Fig. 9.21, one can observe that the events, which contribute to the "horns", come both from the couple of α-particles with higher relative energies (20 MeV $< E_{\alpha-\alpha} <$ 50 MeV) and from the particles with very small relative energies ($E_{\alpha-\alpha} <$ 5 MeV). Particles correlated in this way are not predicted by any simulation. As a conclusion it appears that no simulation is really able to reproduce the $E_{\alpha-\alpha}$ and $cos(\theta_k)$ distributions suggesting that at least a part of the emitted α-particles are behaving differently than expected.

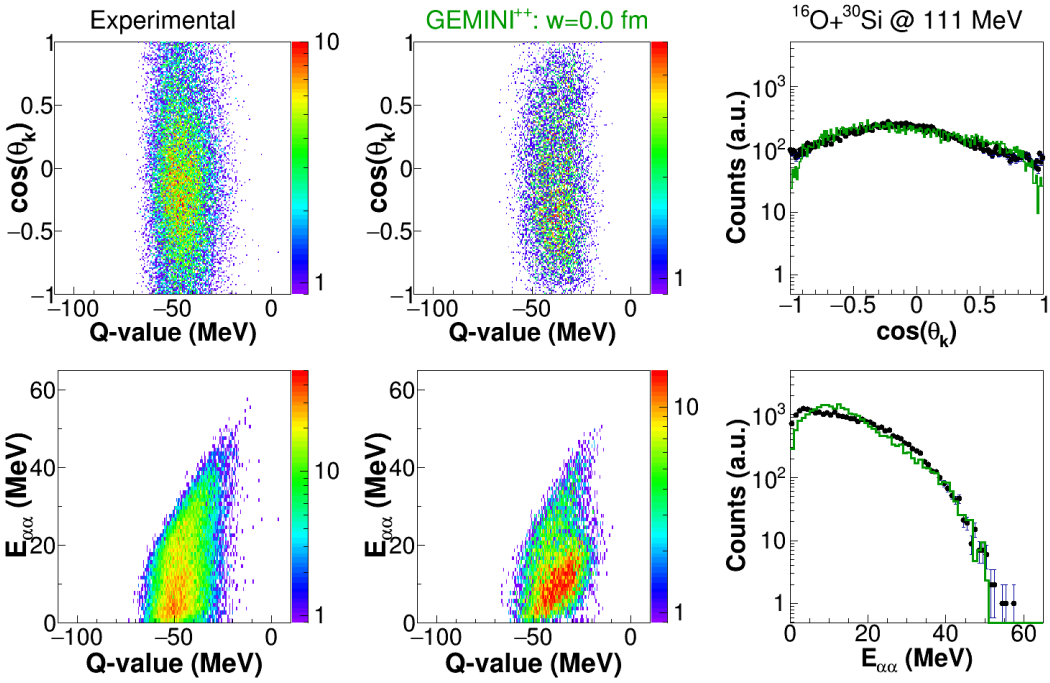

Figure 9.1: UPPER PANELS: Plots of $cos(\theta_k)$ *vs.* Q-value for the experimental (left panel) and simulated (central panel) data. LOWER PANELS: Plots of $E_{\alpha-\alpha}$ vs. Q-value for the experimental data (left panel) and simulation (central panel). In right panels, the experimental (black dots) relative $\alpha - \alpha$ variables are compared with the simulated one (green line); the simulation is made with $GEMINI^{++}$ with $w = 0.0$ fm. For the exit channel $^{38-xn}Ar+2\alpha+xn$ from the reaction $^{16}O +^{30} Si$ at 111 MeV.

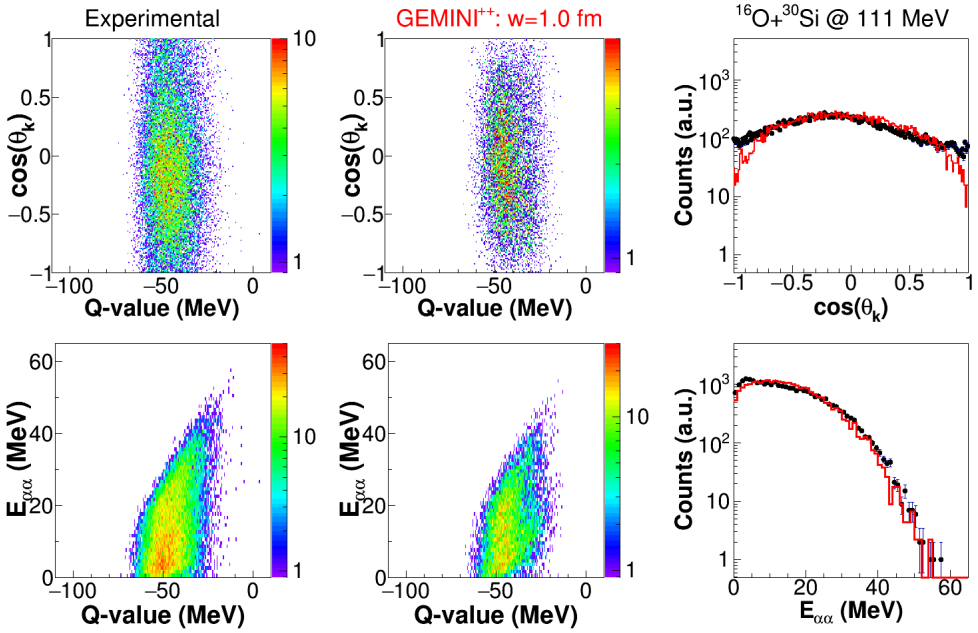

Figure 9.2: Same as in Fig. 9.1 but the simulation is made with **G10**.

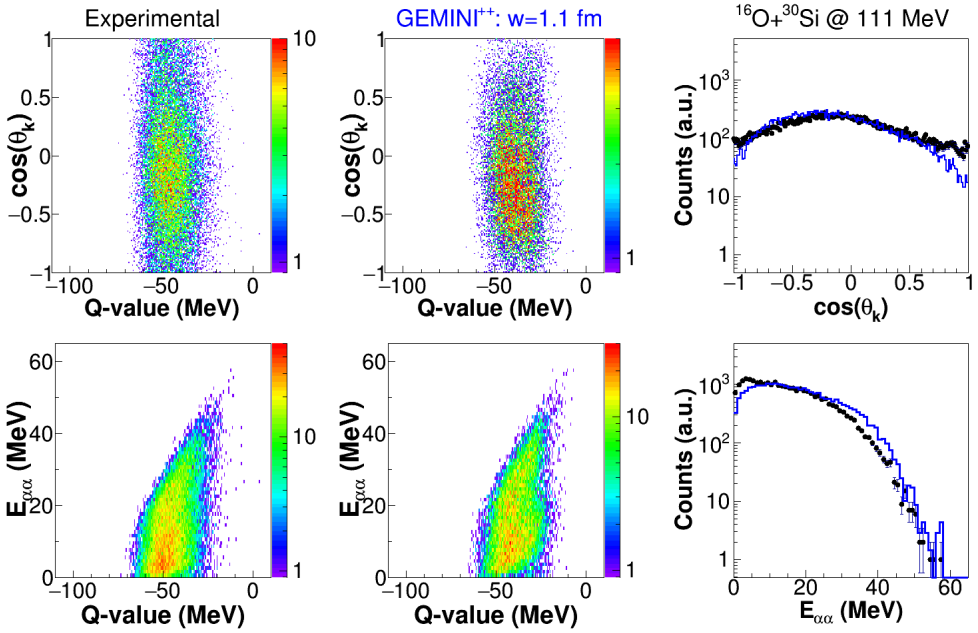

Figure 9.3: Same as in Fig. 9.1 but the simulation is made **G11**.

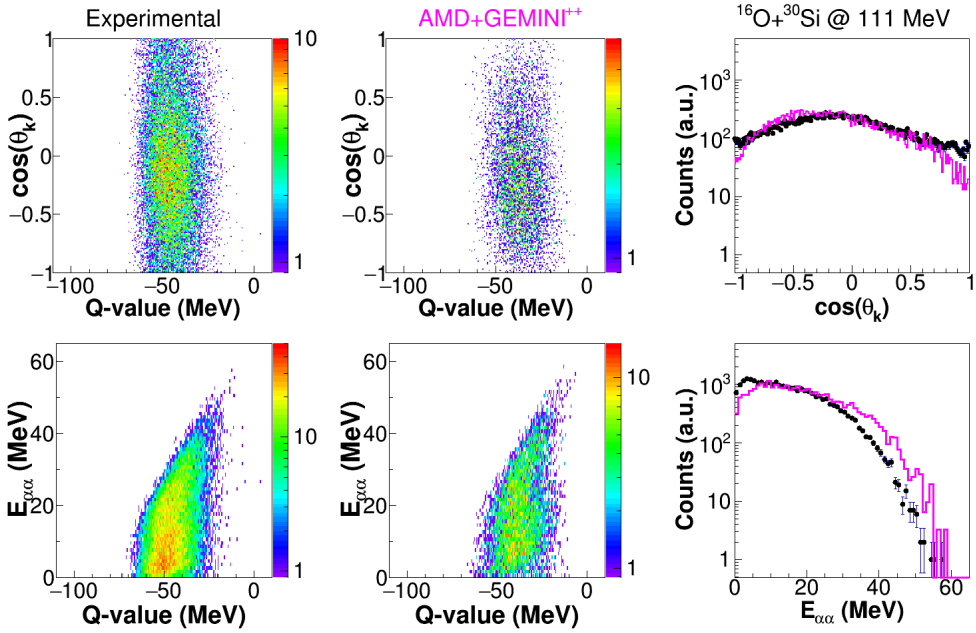

Figure 9.4: Same as in Fig. 9.1 but the simulation is made with **AMD**.

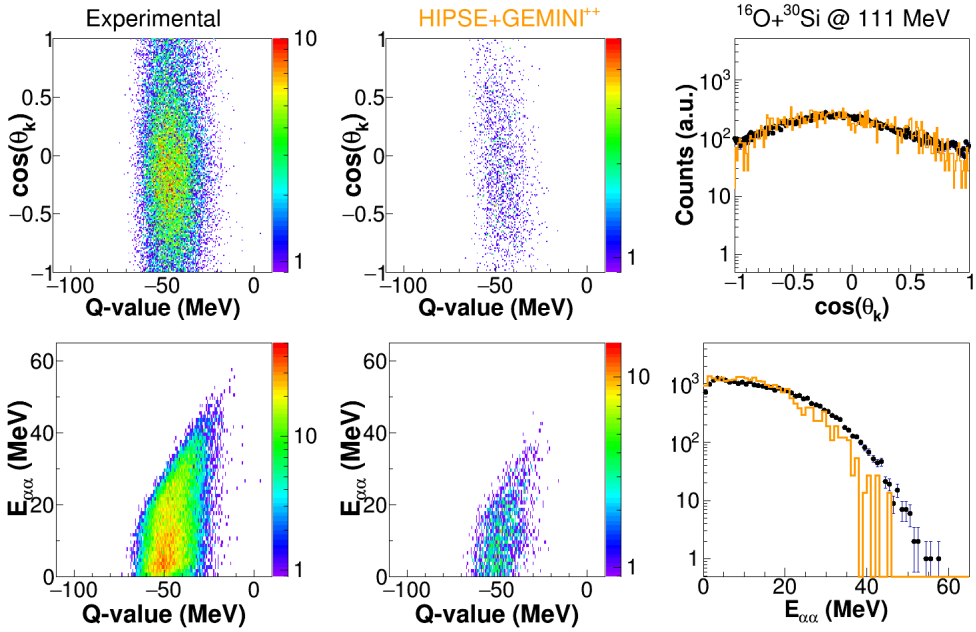

Figure 9.5: Same as in Fig. 9.1 but the simulation is made with **HIPSE**.

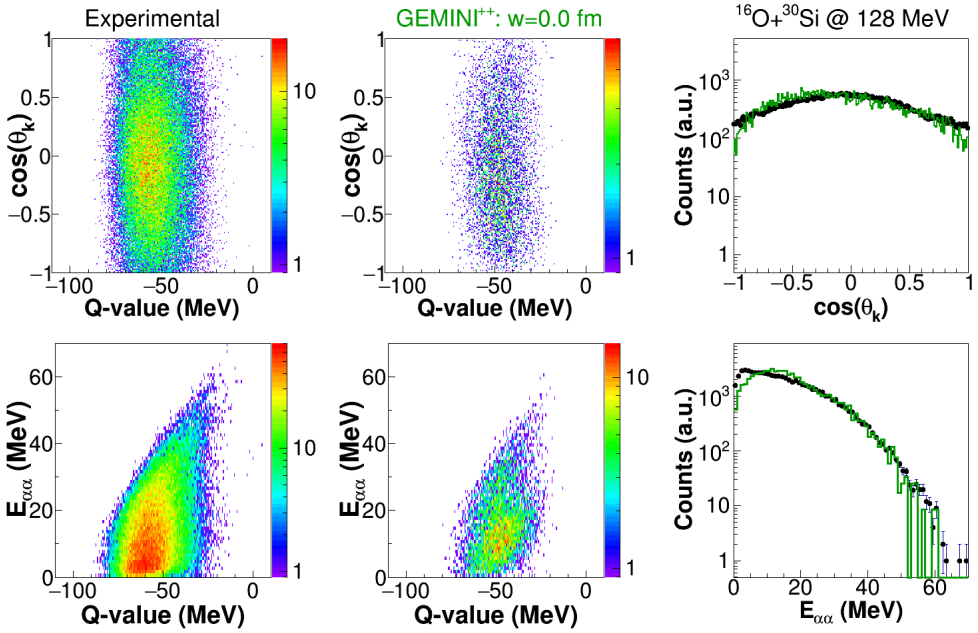

Figure 9.6: Same as in Fig. 9.1 but for the reaction $^{16}O + ^{30}Si$ at 128 MeV.

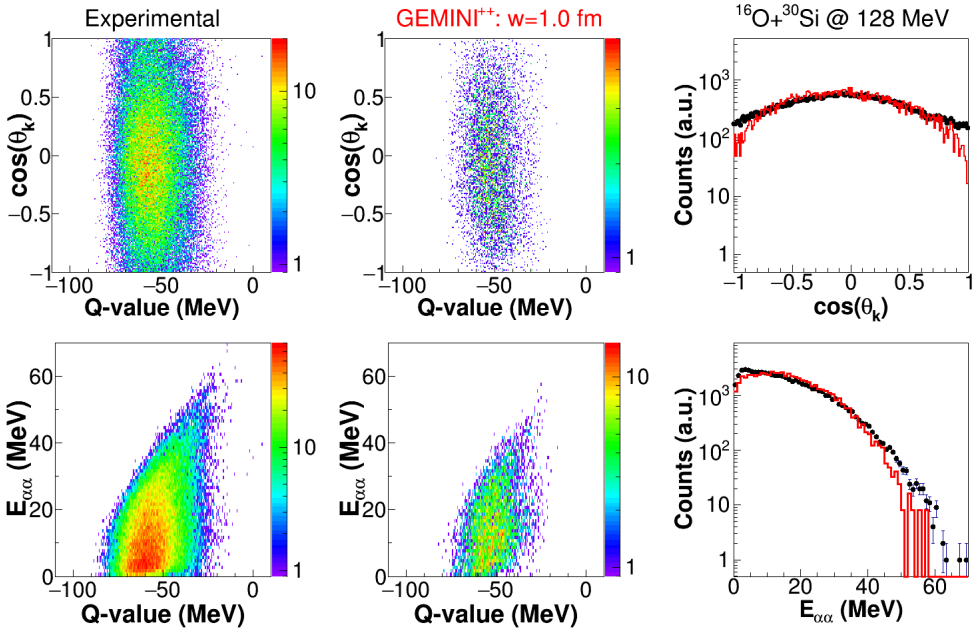

Figure 9.7: Same as in Fig. 9.2 but for the reaction $^{16}O + ^{30}Si$ at 128 MeV.

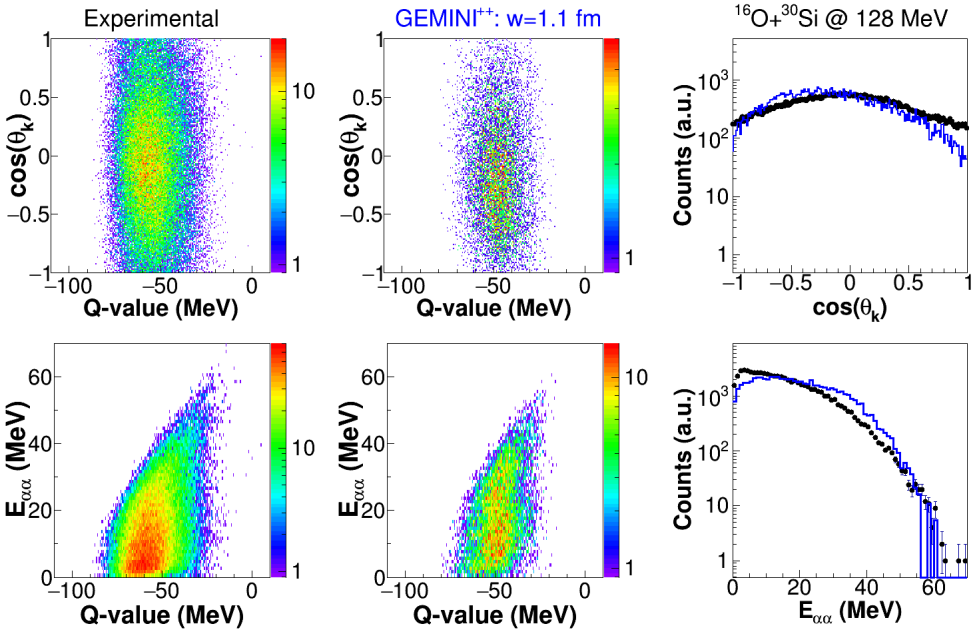

Figure 9.8: Same as in Fig. 9.3 but for the reaction $^{16}O + ^{30}Si$ at 128 MeV.

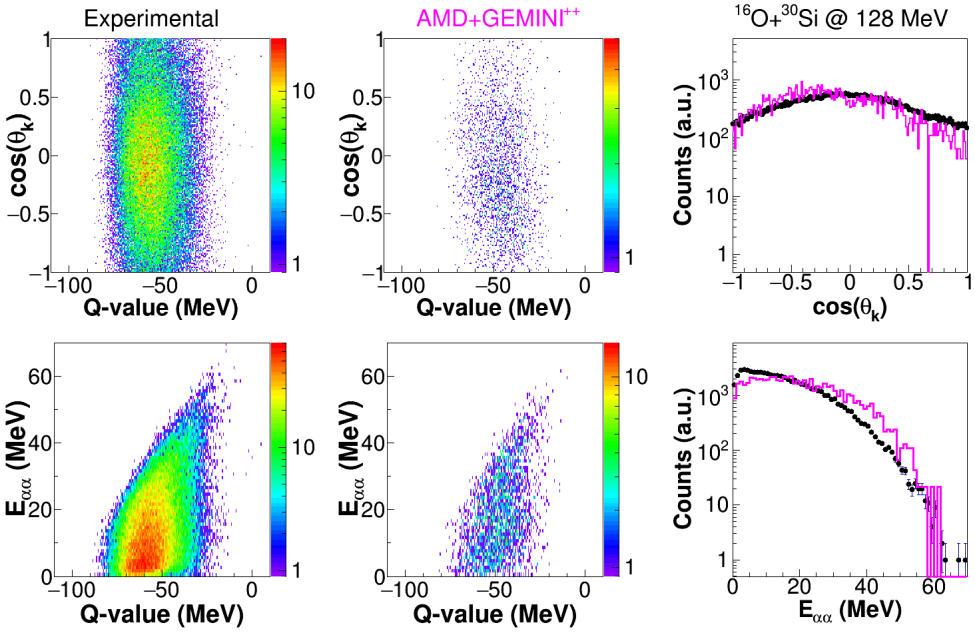

Figure 9.9: Same as in Fig. 9.4 but for the reaction $^{16}O + ^{30}Si$ at 128 MeV.

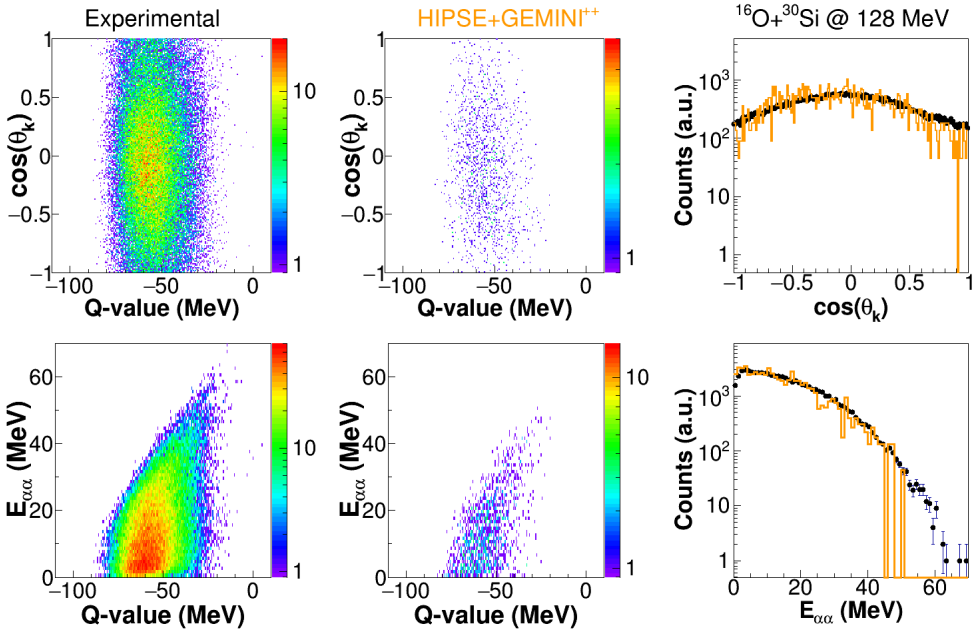

Figure 9.10: Same as in Fig. 9.5 but for the reaction $^{16}O + ^{30}Si$ at 128 MeV.

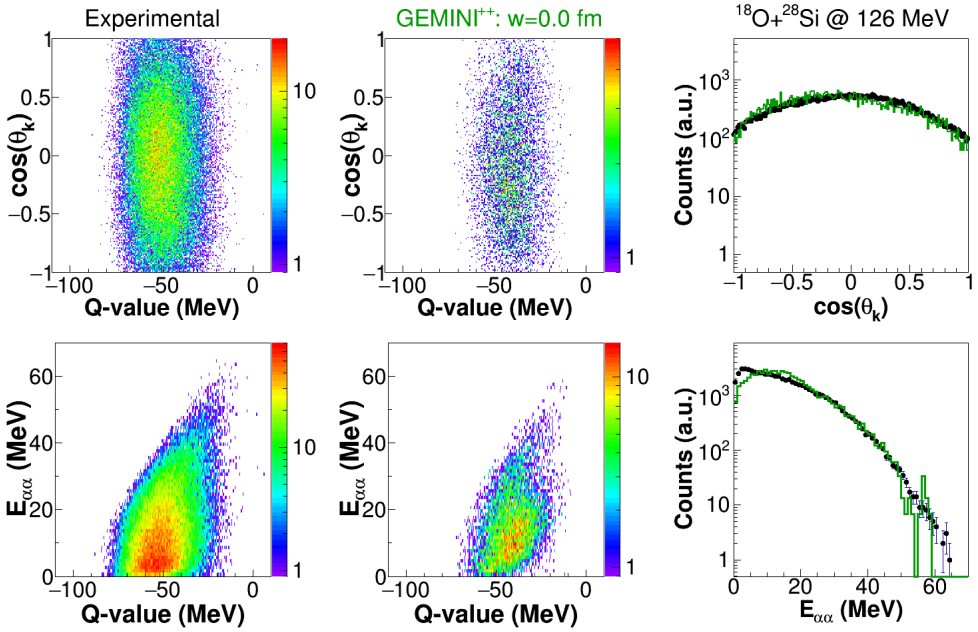

Figure 9.11: Same as in Fig. 9.1 but for the reaction $^{18}O + ^{28}Si$ at 126 MeV.

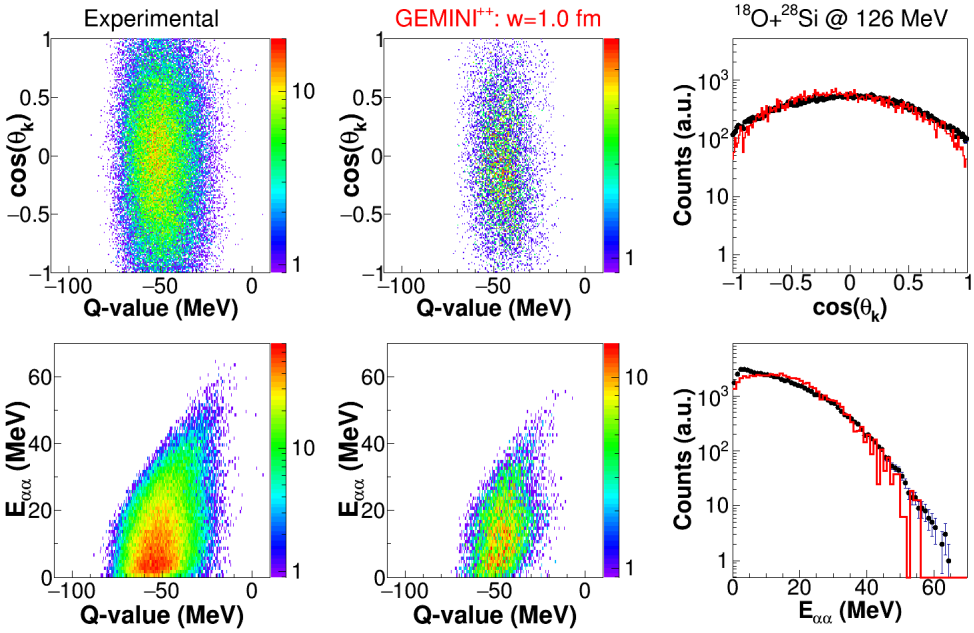

Figure 9.12: Same as in Fig. 9.2 but for the reaction $^{18}O + ^{28}Si$ at 126 MeV.

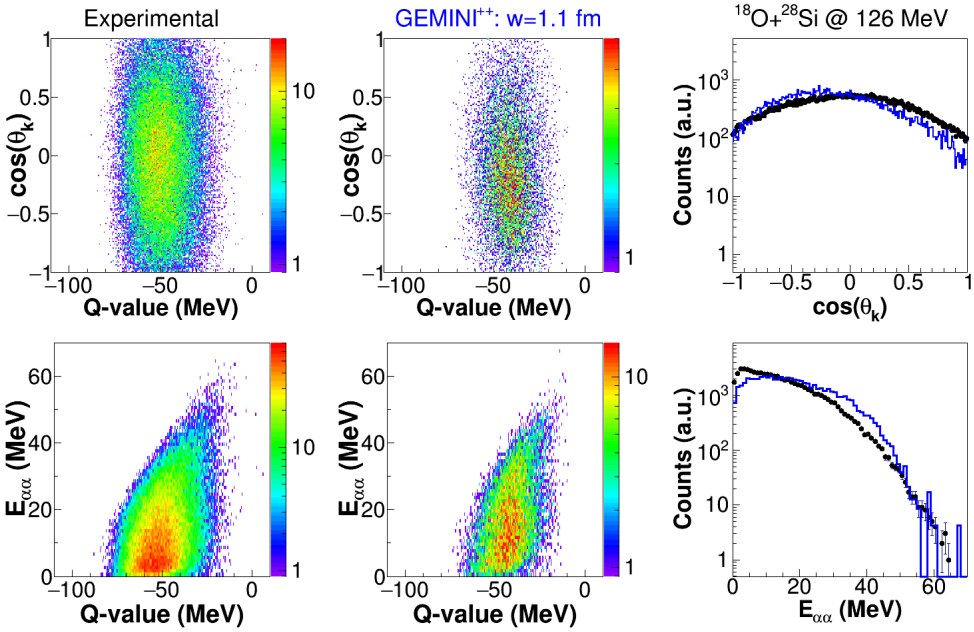

Figure 9.13: Same as in Fig. 9.3 but for the reaction $^{18}O + ^{28}Si$ at 126 MeV.

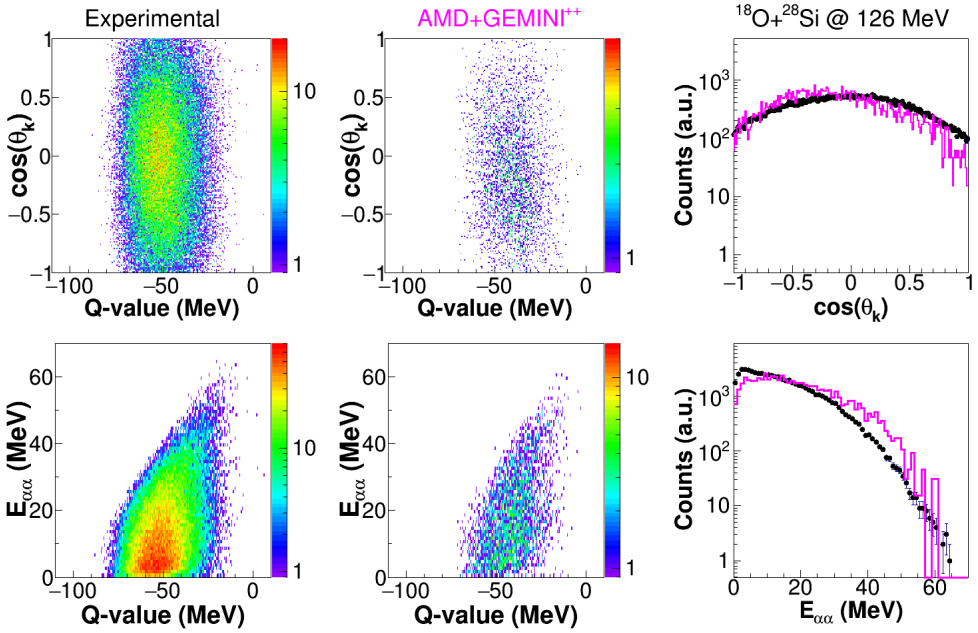

Figure 9.14: Same as in Fig. 9.4 but for the reaction $^{18}O + ^{28}Si$ at 126 MeV.

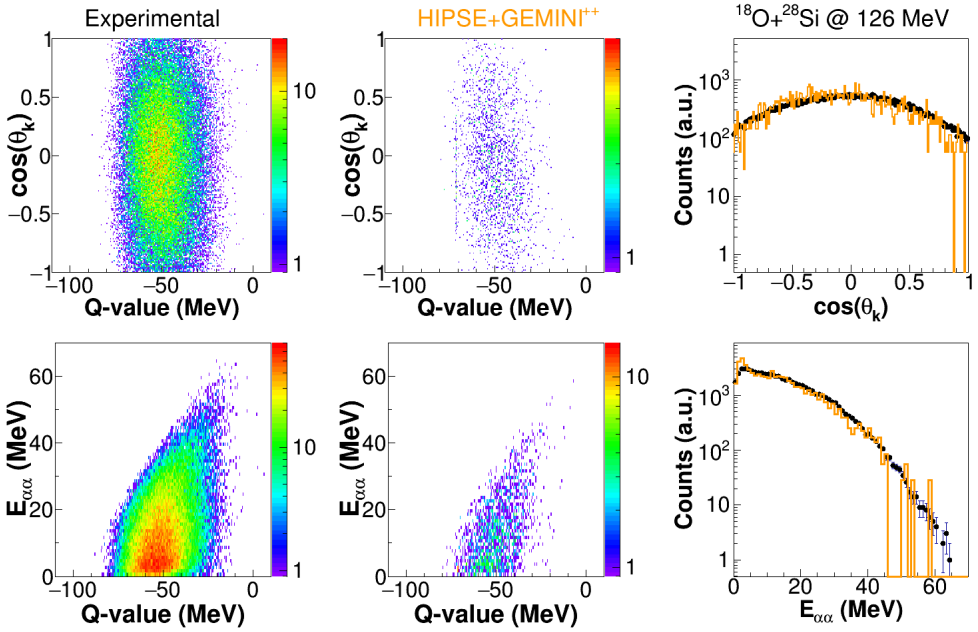

Figure 9.15: Same as in Fig. 9.5 but for the reaction $^{18}O + ^{28}Si$ at 126 MeV.

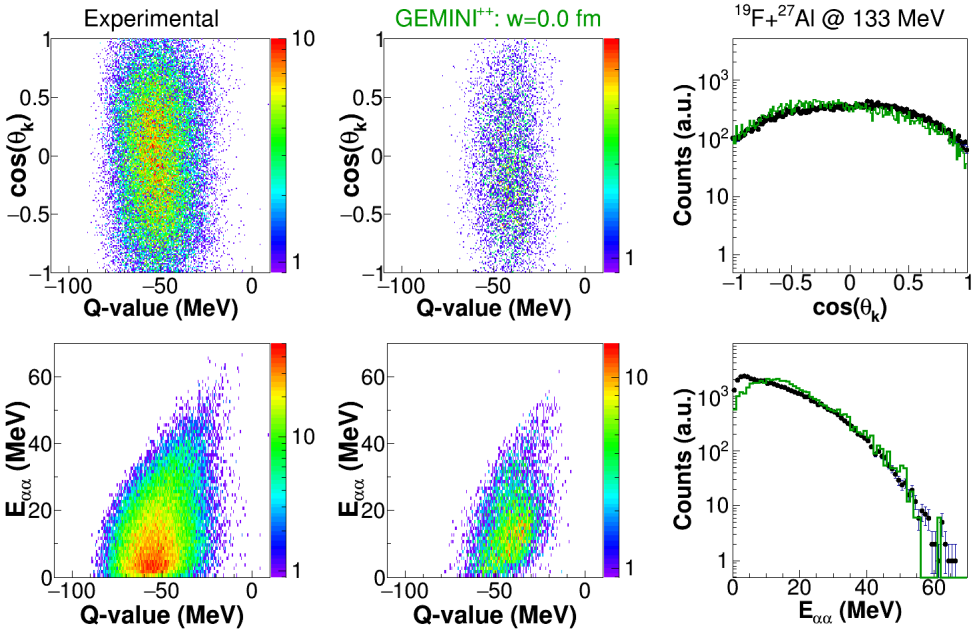

Figure 9.16: Same as in Fig. 9.1 but for the reaction $^{19}F + ^{27}Al$ at 133 MeV.

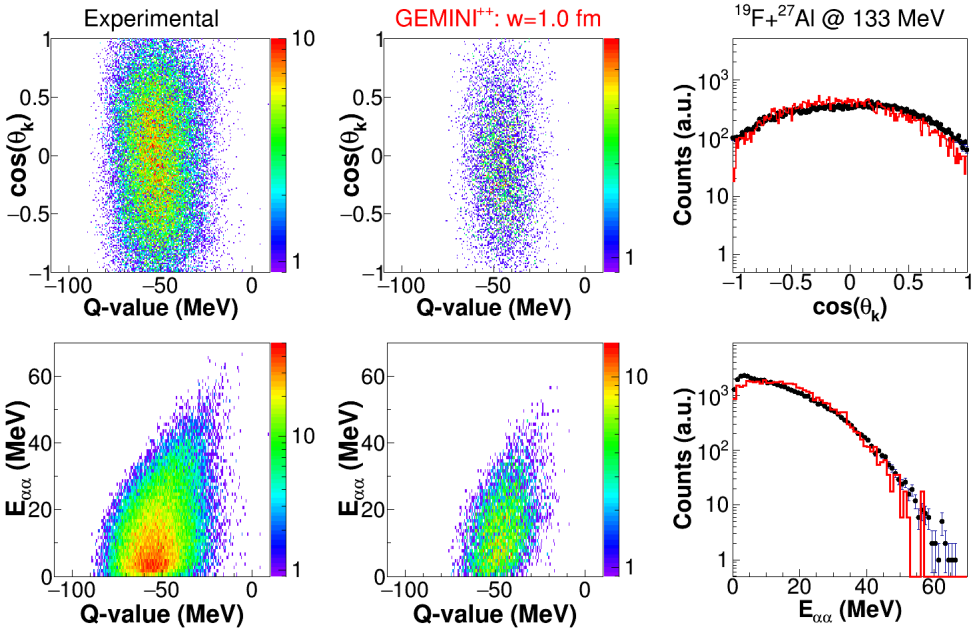

Figure 9.17: Same as in Fig. 9.2 but for the reaction $^{19}F + ^{27}Al$ at 133 MeV.

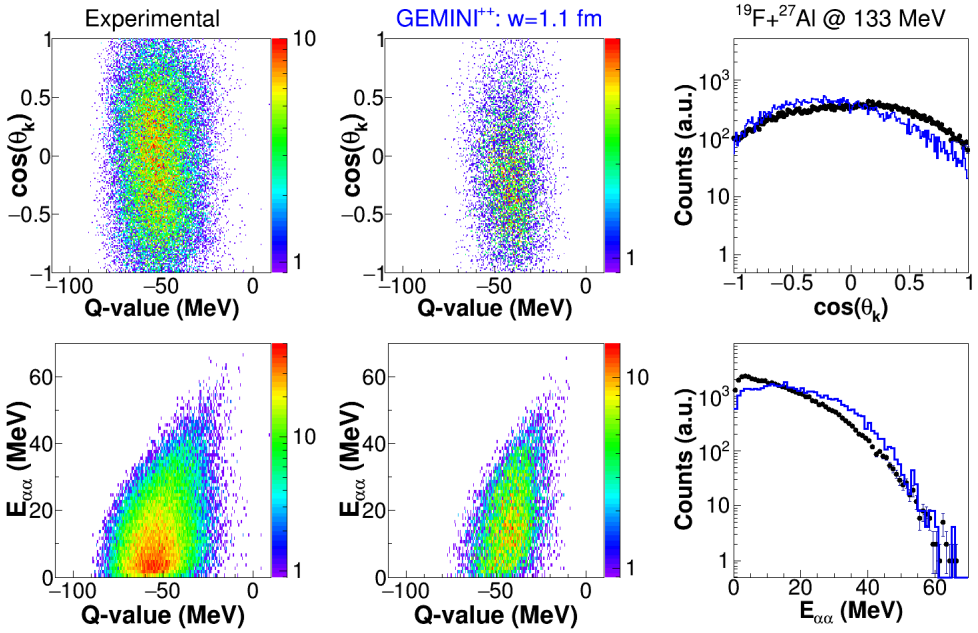

Figure 9.18: Same as in Fig. 9.3 but for the reaction $^{19}F + ^{27}Al$ at 133 MeV.

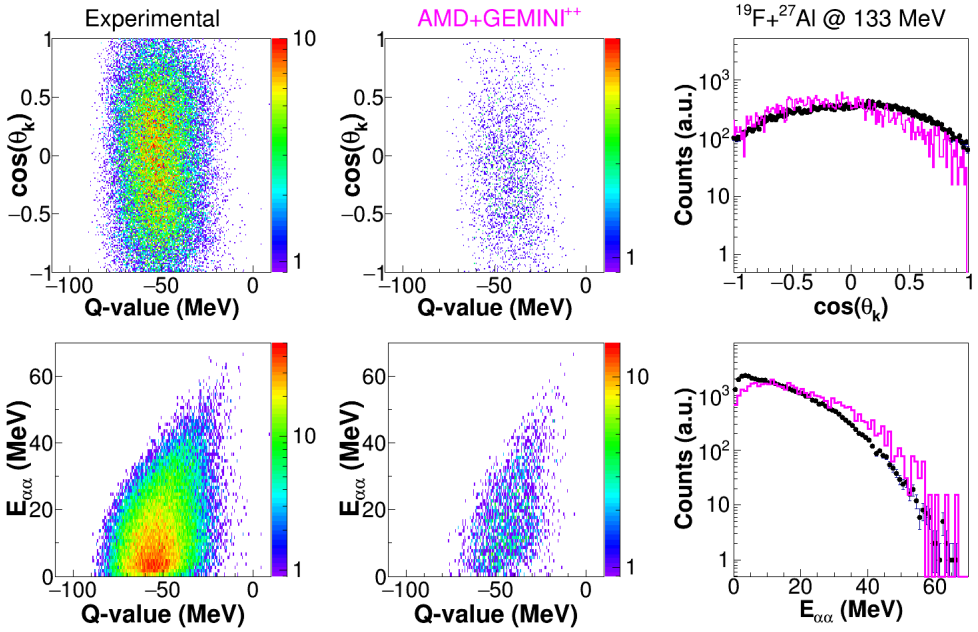

Figure 9.19: Same as in Fig. 9.4 but for the reaction $^{19}F + ^{27}Al$ at 133 MeV.

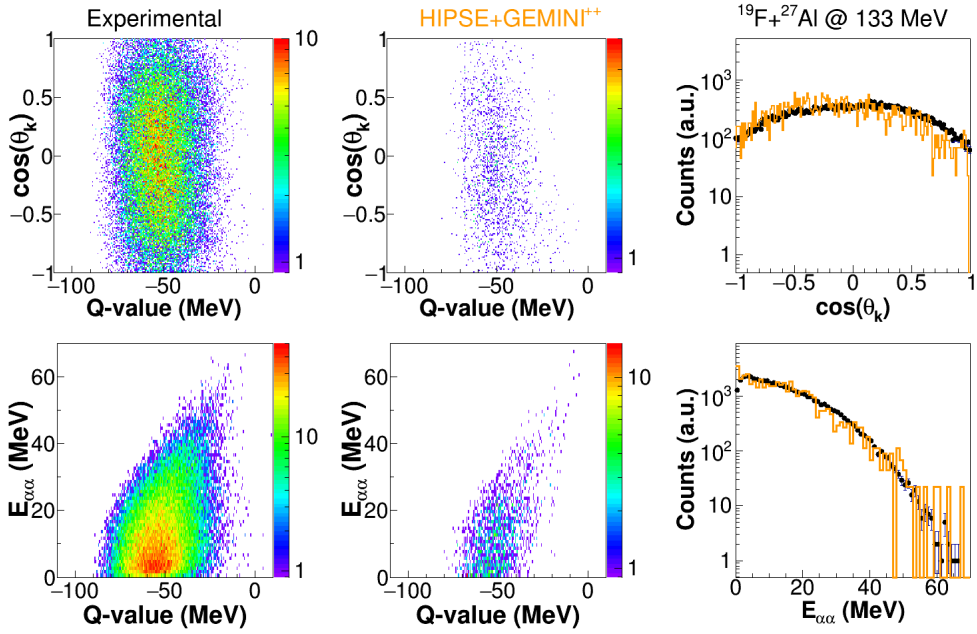

Figure 9.20: Same as in Fig. 9.5 but for the reaction $^{19}F + ^{27}Al$ at 133 MeV.

Going up with the energy and looking to the $^{16}O + ^{30}Si$ at 128 MeV reaction, the $E_{\alpha-\alpha}$ *vs.* Q-value experimental distribution is no more divided in two distinct branches, but they are merged together and peaked around Q-value $= -60 \div -70$ MeV, slightly bending at the higher $E_{\alpha-\alpha}$ towards -50 MeV. This is at variance with models which still show the double structure. Again there is an evident peak at small $E_{\alpha-\alpha}$, which is still not described by models. The $cos(\theta_k)$ experimental distribution is quite symmetric, while models predict generally a more backward peaked distribution and in any case with a larger drop of the yield at $cos(\theta_k) = \pm 1$. Again the major contribution to the experimental yield close to ± 1 is due either to particles with $E_{\alpha-\alpha} \lesssim 5$ MeV or to particles with $E_{\alpha-\alpha} \gtrsim 15$ MeV and this is not observed in simulated data.

The data derived from the reaction $^{18}O + ^{28}Si$ at 126 MeV are similar to the previous one. Experimentally almost a single component of $E_{\alpha-\alpha}$ *vs.* Q-value can be observed, slightly larger in Q-value with respect to the previous case. Again, in simulations the two regions of correlations are visible, generally with a predominance of the bump at low $E_{\alpha-\alpha}$. The $cos(\theta_k)$ experimental distribution is again symmetric, while models still

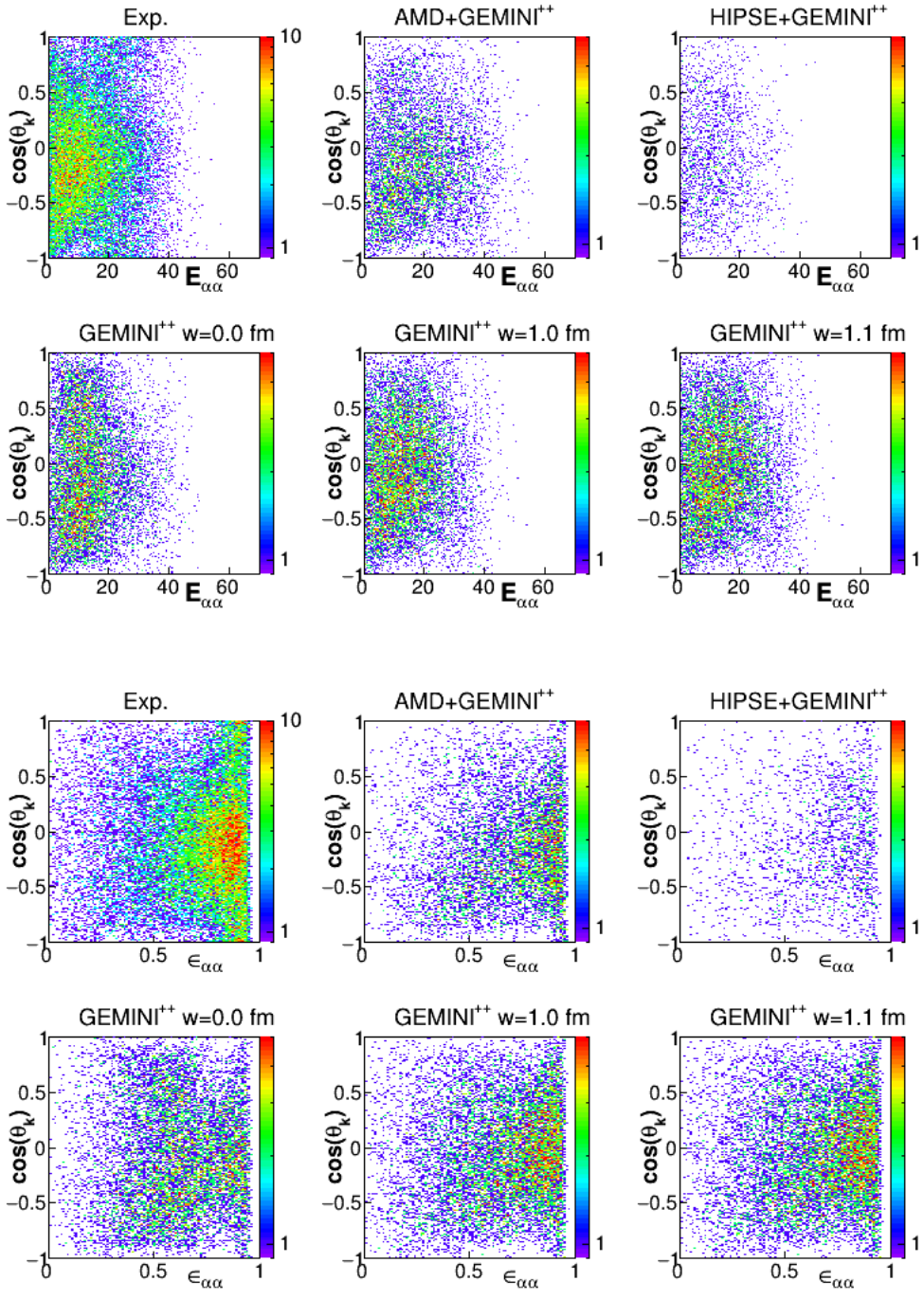

Figure 9.21: Plots of the correlation of $cos(\theta_k)$ with $E_{\alpha-\alpha}$ (upper panel) and with $\epsilon_{\alpha-\alpha}$ the exit channel $^{38-xn}Ar + 2\alpha + xn$ from the reaction $^{16}O + ^{30}Si$ at 111 MeV.

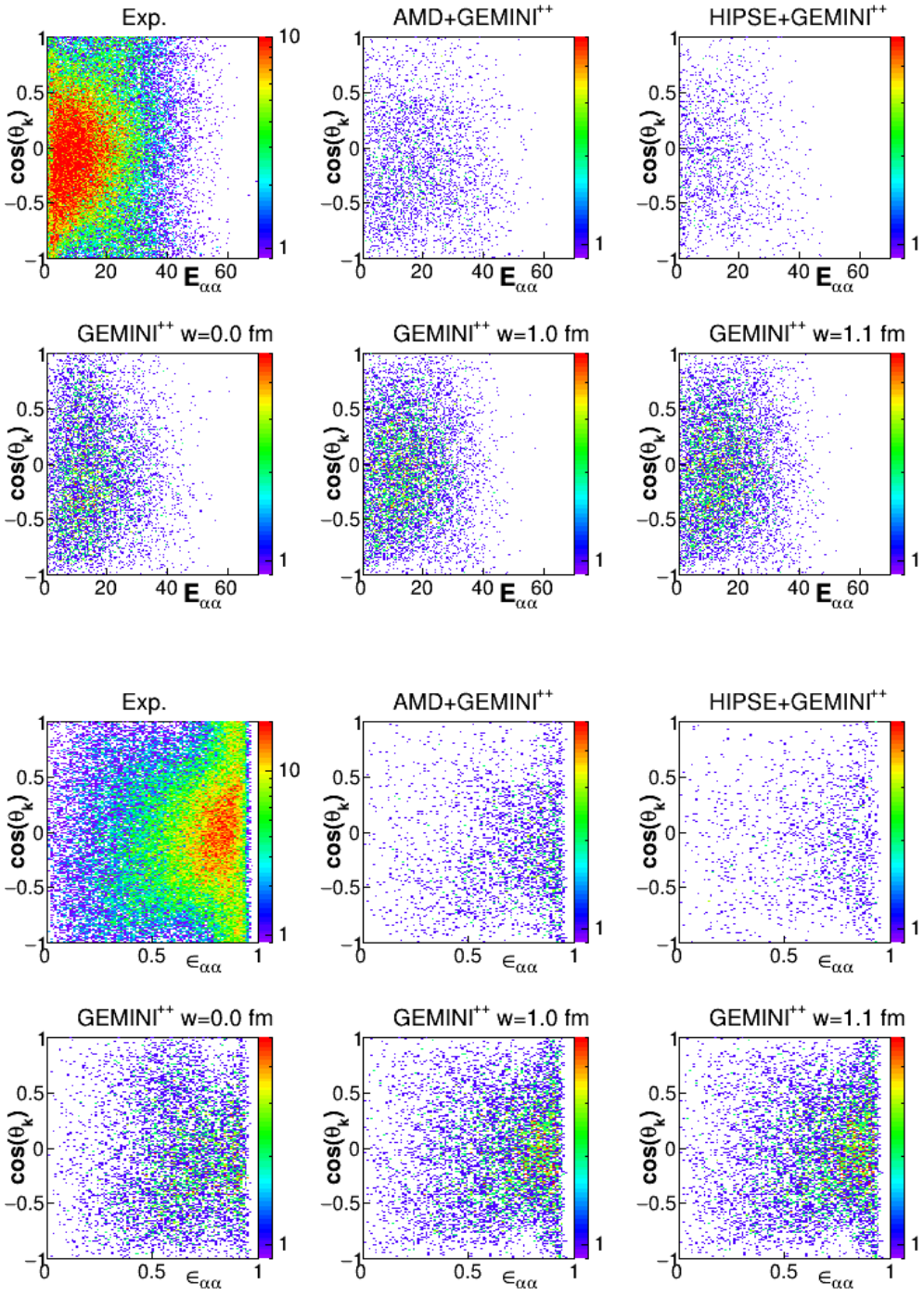

Figure 9.22: Same as in Fig. 9.21 but for the reaction $^{16}O + ^{30}Si$ at 128 MeV.

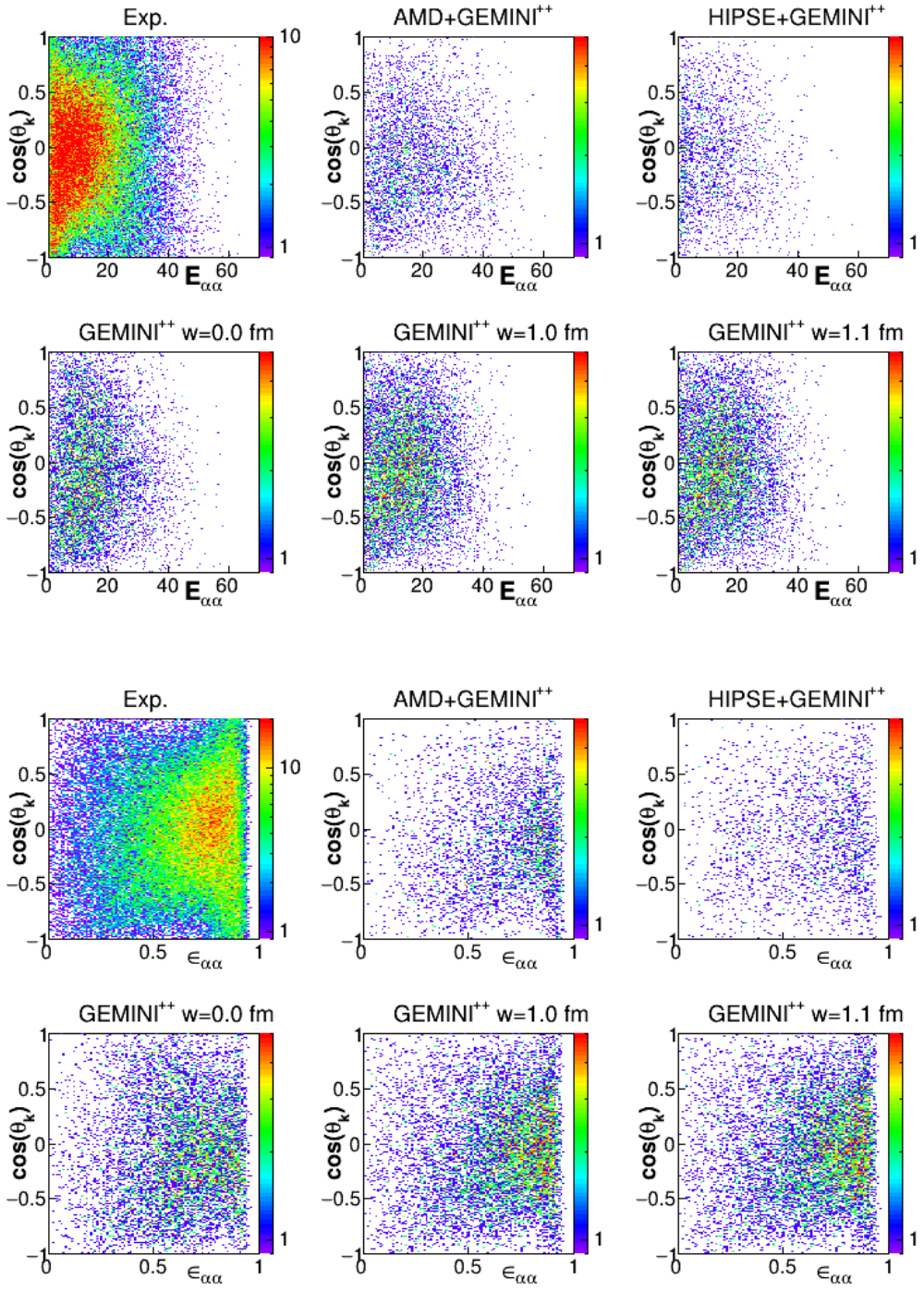

Figure 9.23: Same as in Fig. 9.21 but for the reaction $^{18}O + ^{28}Si$ at 126 MeV.

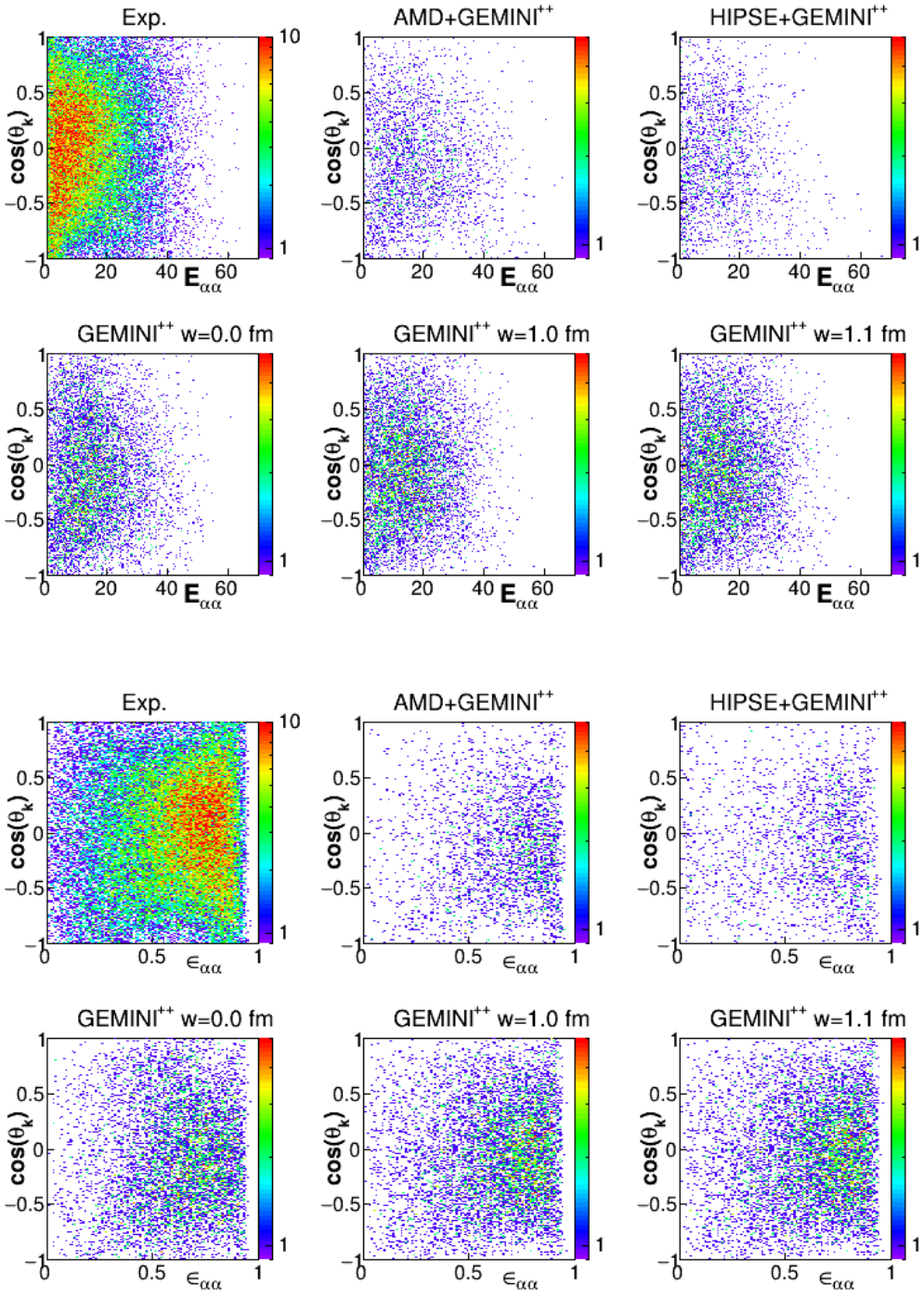

Figure 9.24: Same as in Fig. 9.21 but for the reaction $^{19}F + ^{27}Al$ at 133 MeV.

predict generally a more backward peaked distribution: in this case a larger drop of the simulated yield still is observed at $cos(\theta_k) = 1$, especially for **G11** and **AMD**, while a better description is observed at $cos(\theta_k) = -1$.

The last reaction $^{19}F + ^{27}Al$ at 133 MeV still presents a similar large $E_{\alpha-\alpha}$ *vs.* Q-value distribution centered at larger dissipation than expected by simulations. The $cos(\theta_k)$ experimental distribution is very similar to the previous case, symmetric around $cos(\theta_k) = 0$, and the same comparison to models, which predict a more backward peaked distribution and a larger drop of the yield at $cos(\theta_k) = 1$.

A major detail on the observed differences may be found either looking to other correlations or cutting in slices of Q-values and/or $E_{\alpha-\alpha}$. For example, one can look to the $\epsilon_{\alpha-\alpha}$ *vs.* $cos(\theta_k)$ correlation plot: $\epsilon_{\alpha-\alpha}$ is the relative energy in some way weighted by the energy of the residue and when it is close to 1, it means that E_{ER} is small. These events are those which mainly contribute to the $cos(\theta_k) = \pm 1$ and they are more probable in the reaction induced by the O beam. It has been discussed, in fact, in a previous work that even the different sequential emission can influence the $cos(\theta_k) = 1$ distribution [47] and also the relative velocity of the two α-particles. This is, however, out of the aim of this thesis and it will be afforded in a future work.

9.2 Exclusive observables for 3α-channel

Again, for another specific channel we decided to study correlations: in this case we are dealing with the 3α-decay channel and the correlation between the 3 emitted α-particles will be the subject of this analysis.

From Fig. 9.25 to Fig. 9.28 the comparison of experimental and simulated (**G00** in green, **G10** in red, **G11** in blue, **AMD** in pink and **HIPSE** in orange) relative α-α-energy between faster-medium α-particles (left panels), between faster-slower α-particles (central panels) and medium-slower α-particles (right panels) are shown for the exit channel $^{34-xn}S + 3\alpha + xn$ for the four studied reactions in the laboratory frame.

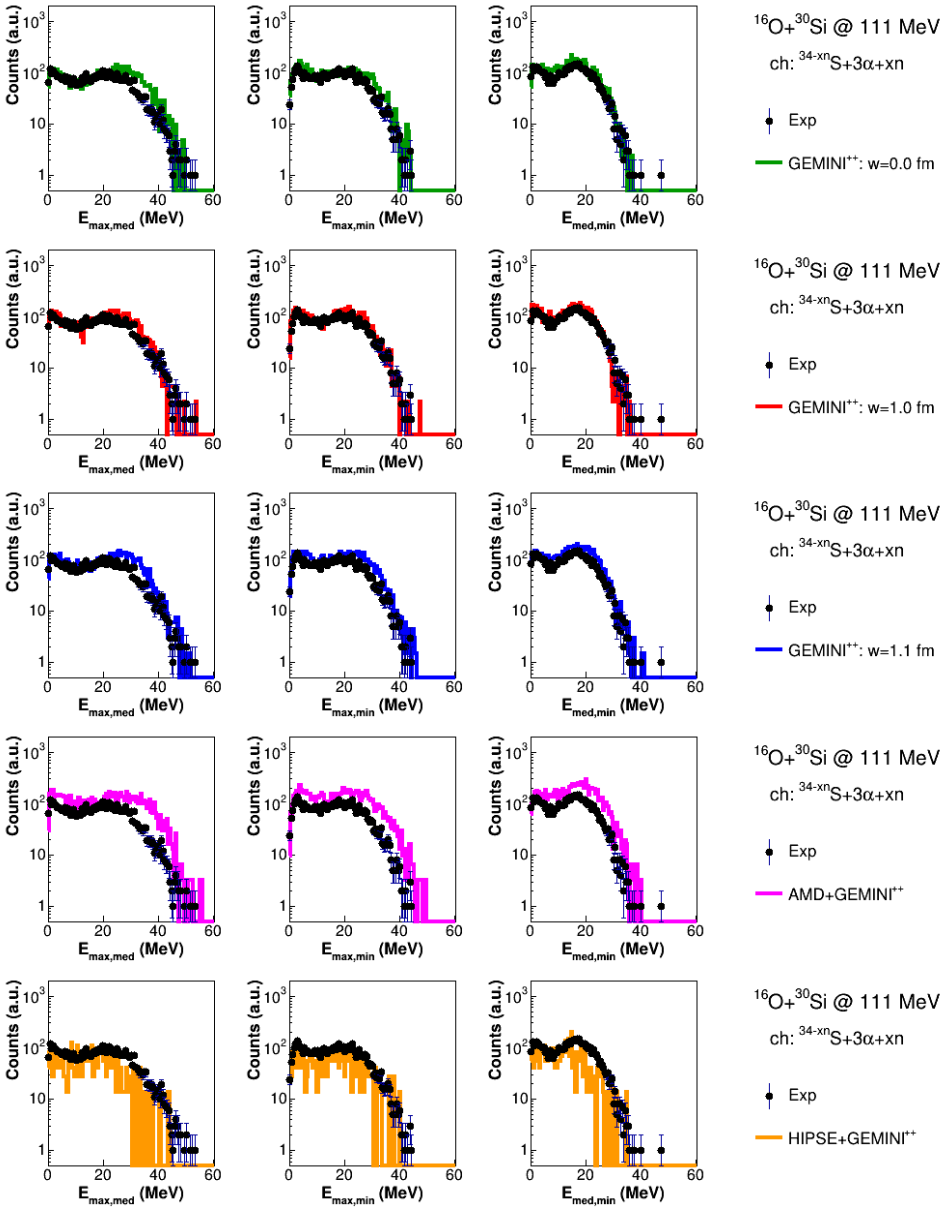

Figure 9.25: Experimental relative α-α-energy between faster-medium α-particles (left panels), between faster-slower α-particles (central panels) and between medium-slower α-particles (right panels) are compared with simulations made by $GEMINI^{++}$ with $w = 0.0$ fm (green), $w = 1.0$ fm (red), $w = 1.1$ fm (blue), $AMD{+}GEMINI^{++}$ (pink) and $HIPSE{+}GEMINI^{++}$ (orange). For the exit channel $^{34-xn}S + 3\alpha + xn$ from the reaction $^{16}O + ^{30}Si$ at 111 MeV.

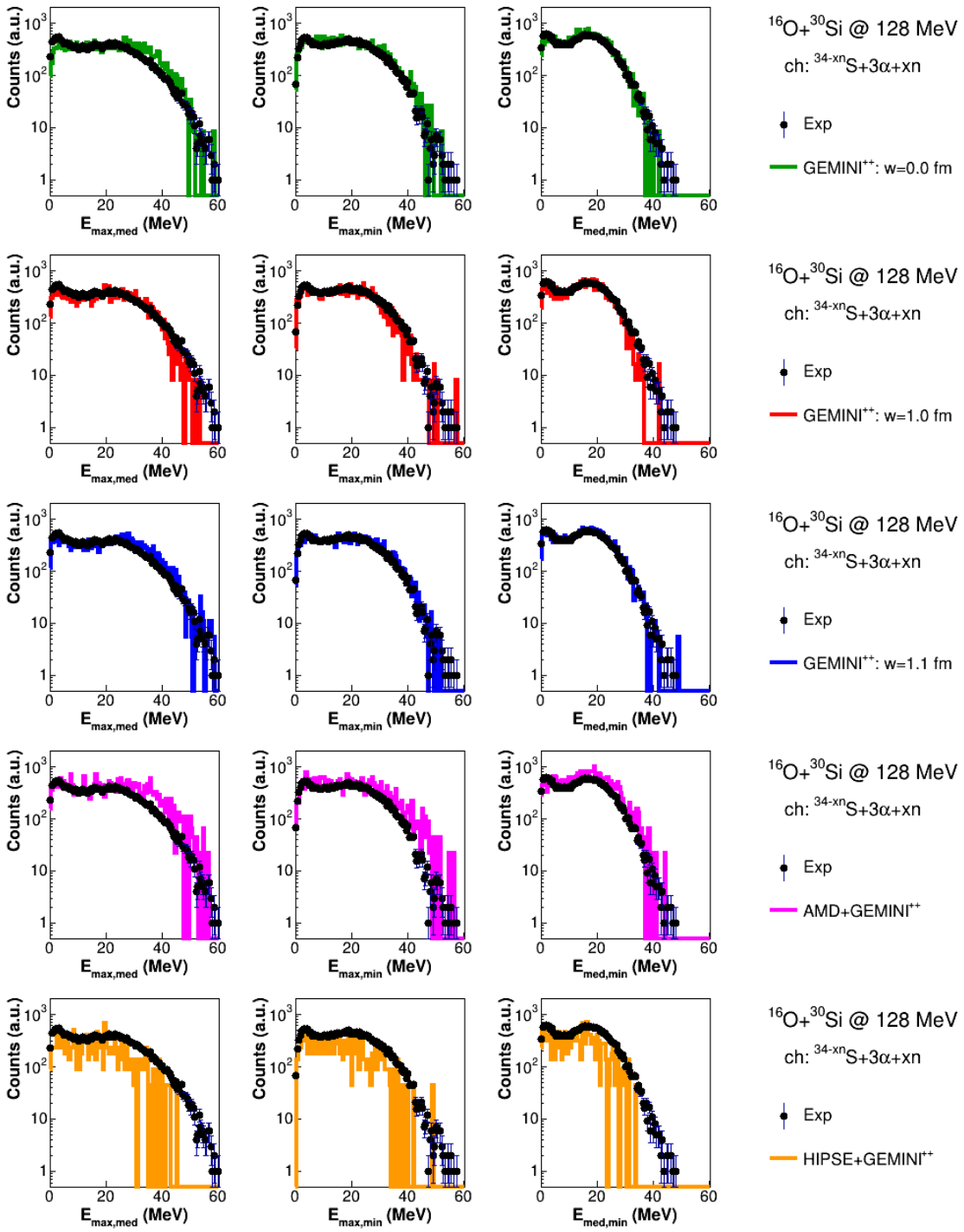

Figure 9.26: Same as in Fig. 9.25 but for the reaction $^{16}O + ^{30}Si$ at 128 MeV.

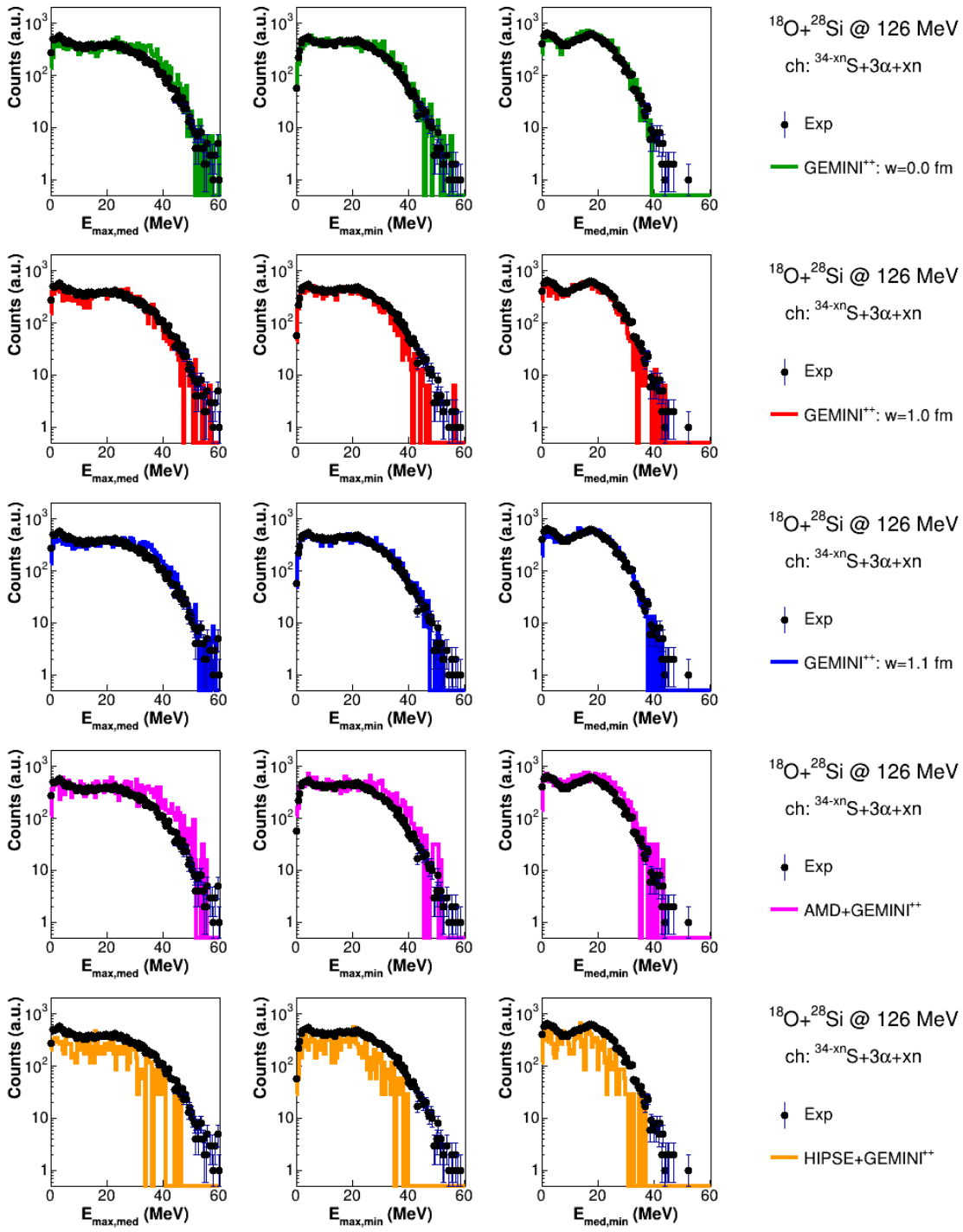

Figure 9.27: Same as in Fig. 9.25 but for the reaction $^{18}O + ^{28}Si$ at 126 MeV.

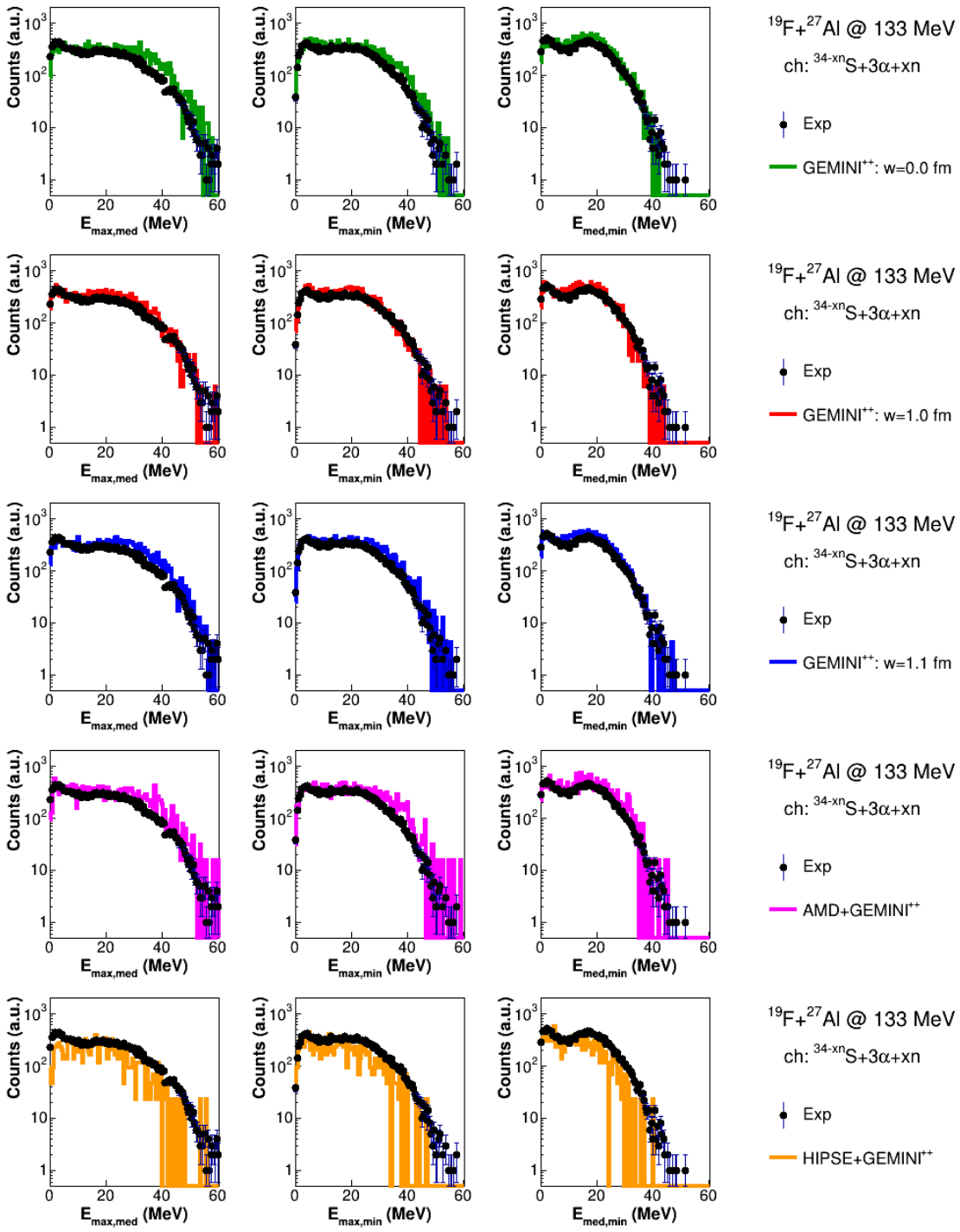

Figure 9.28: Same as in Fig. 9.25 but for the reaction $^{19}F + ^{27}Al$ at 133 MeV.

The relative $\alpha - \alpha$ energies are evaluated as:

$$E_{\alpha-\alpha} = \frac{\overrightarrow{k}^2_{\alpha-\alpha}}{2\mu} \tag{9.4}$$

where $\overrightarrow{k}_{\alpha-\alpha}$ is the relative momentum between two α particles. The simulations are normalized to the ratio between the simulated and experimental number of residue in the channel $^{34-x}S + 3\alpha + xn$. In the Figures one can observe the comparison of the relative energies with the simulated data. The simulations are normalized to the ratio simulated and experimental number of residue in the channel $^{34-xn}S+3\alpha+xn$. It is quite evident that in the experimental spectra a double peak is evident in all the relative energies, which imply that there are in all combinations some α-particles which have a very small relative energy (and therefore relative momentum), which might indicate a decay from ^{8}Be. However, at variance with the 2α decay channel, in this case the low energy bump is well accounted for by almost all simulations.

Looking more into details, it seem that at low energy ($^{16}O+^{30}Si$ 111 MeV) the relative energy spectra are well described by the **G10** simulation. **G00** and **G11** fails partially to reproduce some of the distributions, while **AMD** does not represent correctly the relative energy spectra shape for any of the three correlations. **HIPSE** presents a too small statistics, but, at least qualitatively it seems to better follow the experimental shapes.

For the reaction $^{16}O+^{30}Si$ at 128 MeV, the situation is very similar, with the **G10** well describing the experimental data, while the **G00** and **G11** case are slightly better describing the spectra with respect to the low energy case, with only some small discrepancies visible in the $E_{max,med}$ distribution. **AMD** is still over-predicting high energy relative velocities in the $E_{max,med}$ and $E_{max,min}$ distributions. For **HIPSE** again the very low yield makes it difficult to draw conclusion from the distributions.

Very similar to the last one is the $^{18}O +^{28} Si$ at 126 MeV case. In this case, **AMD** is better reproducing two of the three correlations, while **HIPSE**, despite the poor yield seems to reasonably follow the experimental trend.

In the last reaction, the $^{19}F+^{27}Al$ at 133 MeV, again the **G10** is reasonably describing all the distributions, **G00** and **G11** show very small discrepancies in the $E_{max,med}$ case.

AMD is still over-predicting the energies in the 40 MeV range, especially in the $E_{max,med}$ distribution, and **HIPSE** is still very poor in statistics to draw conclusions.

Using different correlations between the energies of the 3α-particles different Dalitz plots can be built, which can give more clear information on the event configuration. We will show and discuss in this section the different methods.

In Figs. 9.29, 9.30, 9.31 and 9.32 the Dalitz plot, which correlate the three emitted α-particles are shown for the four reaction respectively. In particular, in the upper 6 panels the "D1" Dalitz plot is shown, where the x and y variables have been constructed from an ordered combination of the relative energies as:

$$x_D = \sqrt{3}\frac{E_{max,med} - E_{med,min}}{2} \tag{9.5}$$

$$y_D = \frac{2E_{max,min} - E_{max,med} - E_{med,min}}{2} \tag{9.6}$$

In the lower 6 panels, instead, the "D2" Dalitz plot is shown, where the "x" and "y" variables have been constructed starting from an ordered combination α-particle energies in the laboratory, but using the corresponding center of mass energies (this is why we can have also negative values for x and y) as:

$$x_D = \sqrt{3}\frac{E_3^{cm} - E_2^{cm}}{2} \tag{9.7}$$

$$y_D = \frac{2E_1^{cm} - E_3^{cm} - E_2^{cm}}{2} \tag{9.8}$$

The two different correlations bring similar information on the energy partition between the three α-particles: when both x and y are zero in plot "D1" it means that the relative energies of the three particles are equal, while, in the "D2", it means that the particle energies are equal.

From the figures we can surely see that "D2" experimental plots show a majority of equal energy partition events, which are partially described by $GEMINI^{++}$ calculations at all energies. For ^{18}O and ^{19}F data are more represented by **G11**, while for the ^{16}O

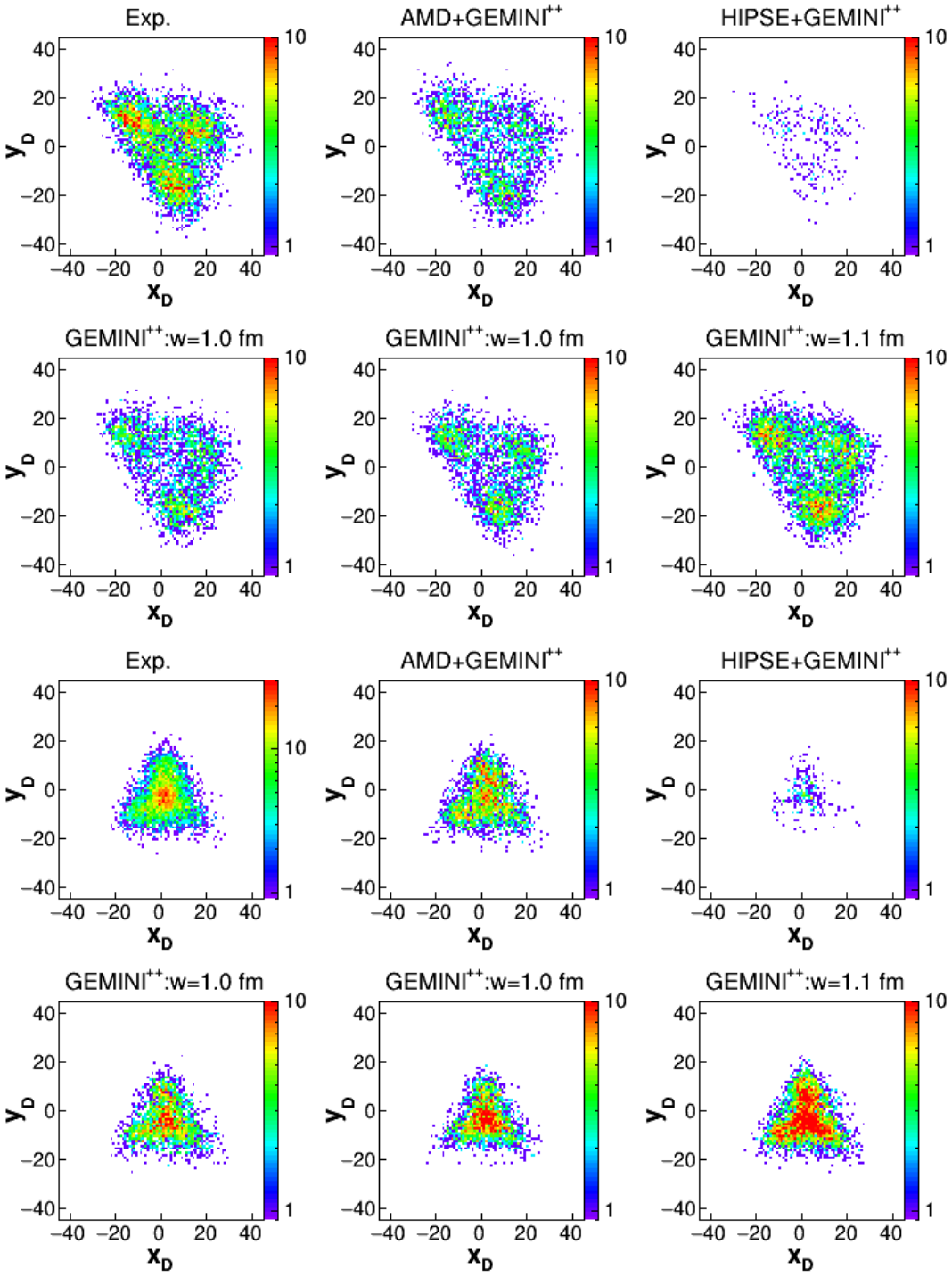

Figure 9.29: Dalitz plots for the reaction $^{16}O + ^{30}Si$ at 111 MeV. See text for more details.

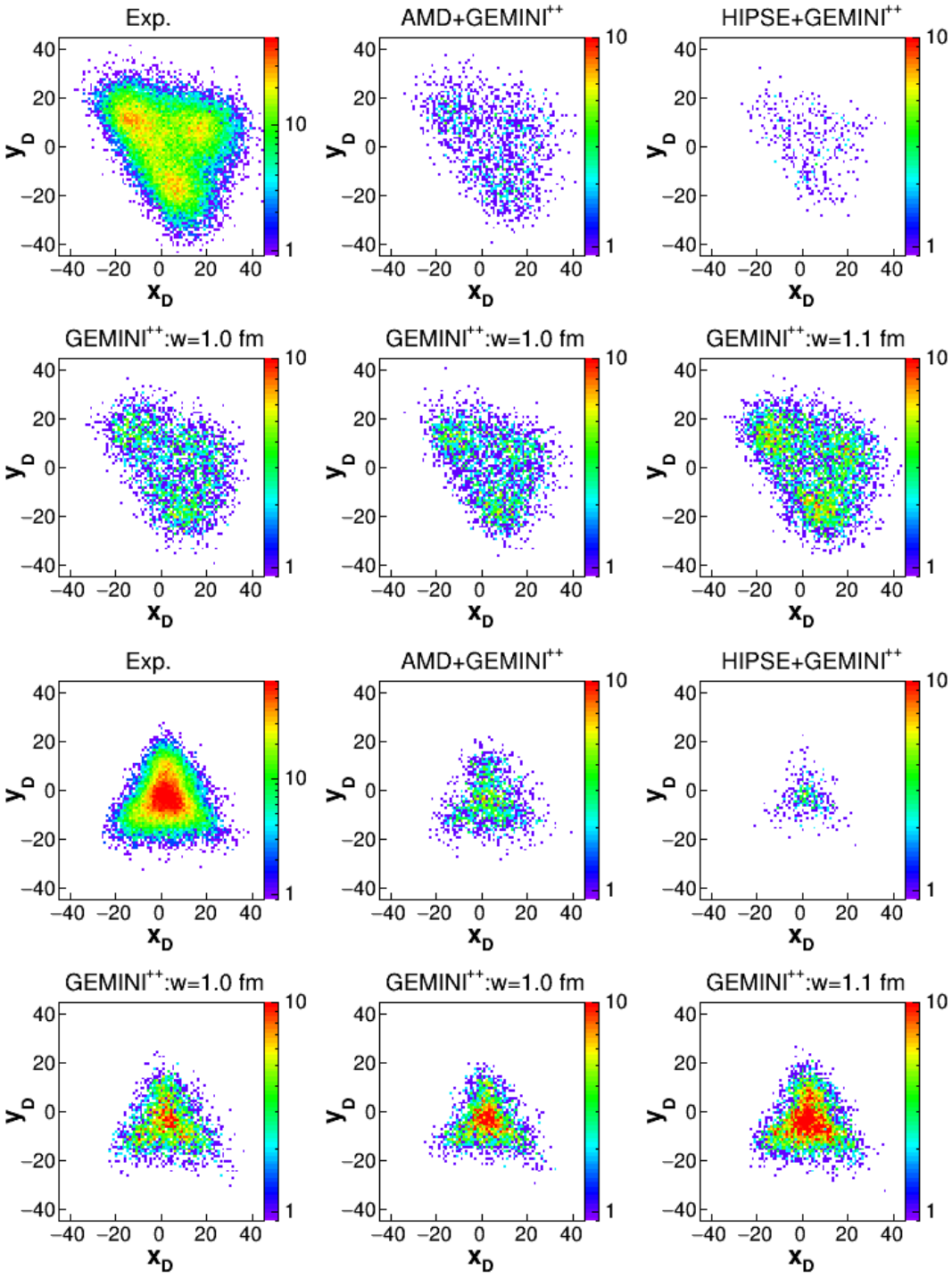

Figure 9.30: Dalitz plots for the reaction $^{16}O + ^{30}Si$ at 128 MeV. See text for more details.

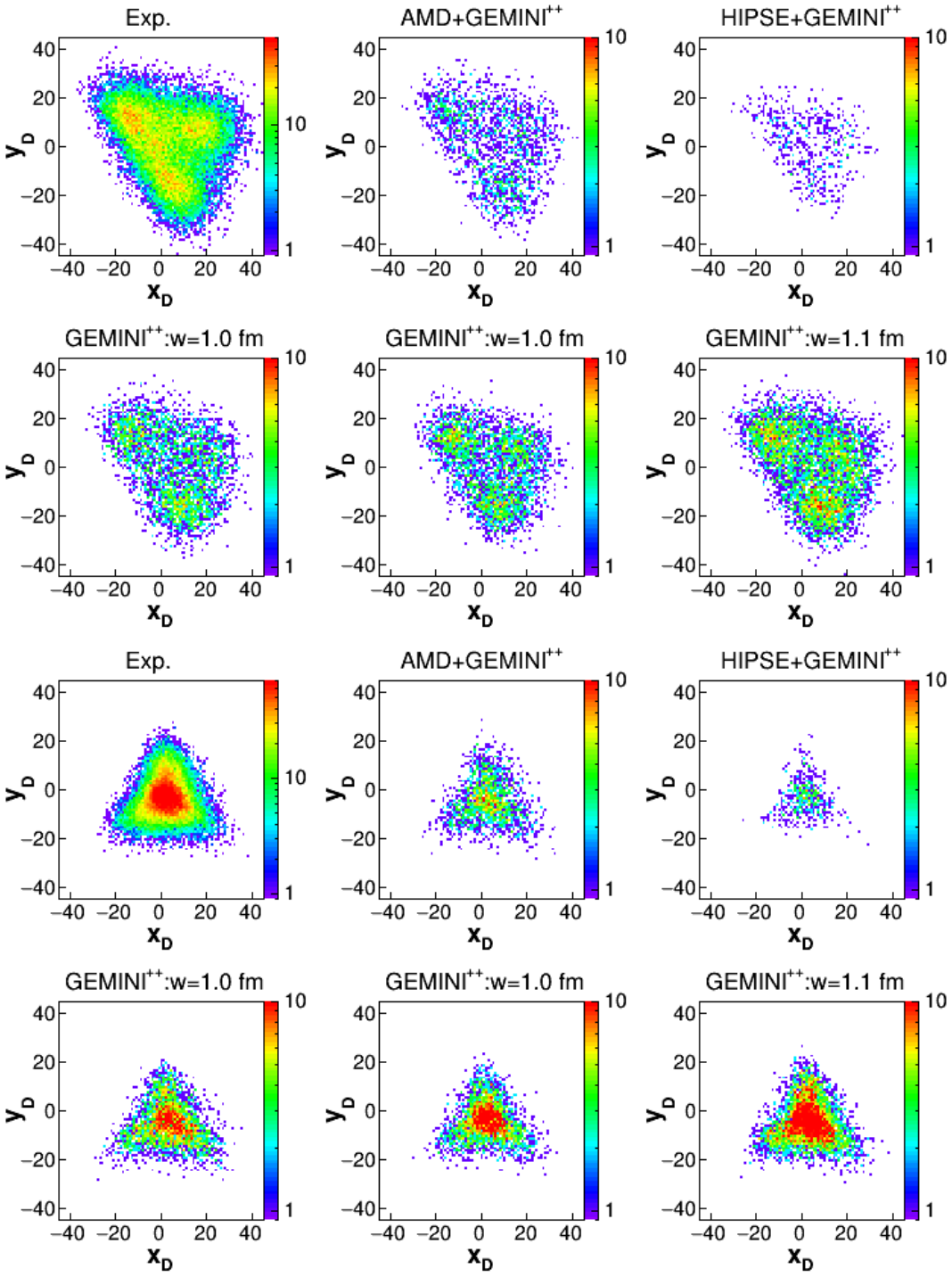

Figure 9.31: Dalitz plots for the reaction $^{18}O + ^{28}Si$ at 126 MeV. See text for more details.

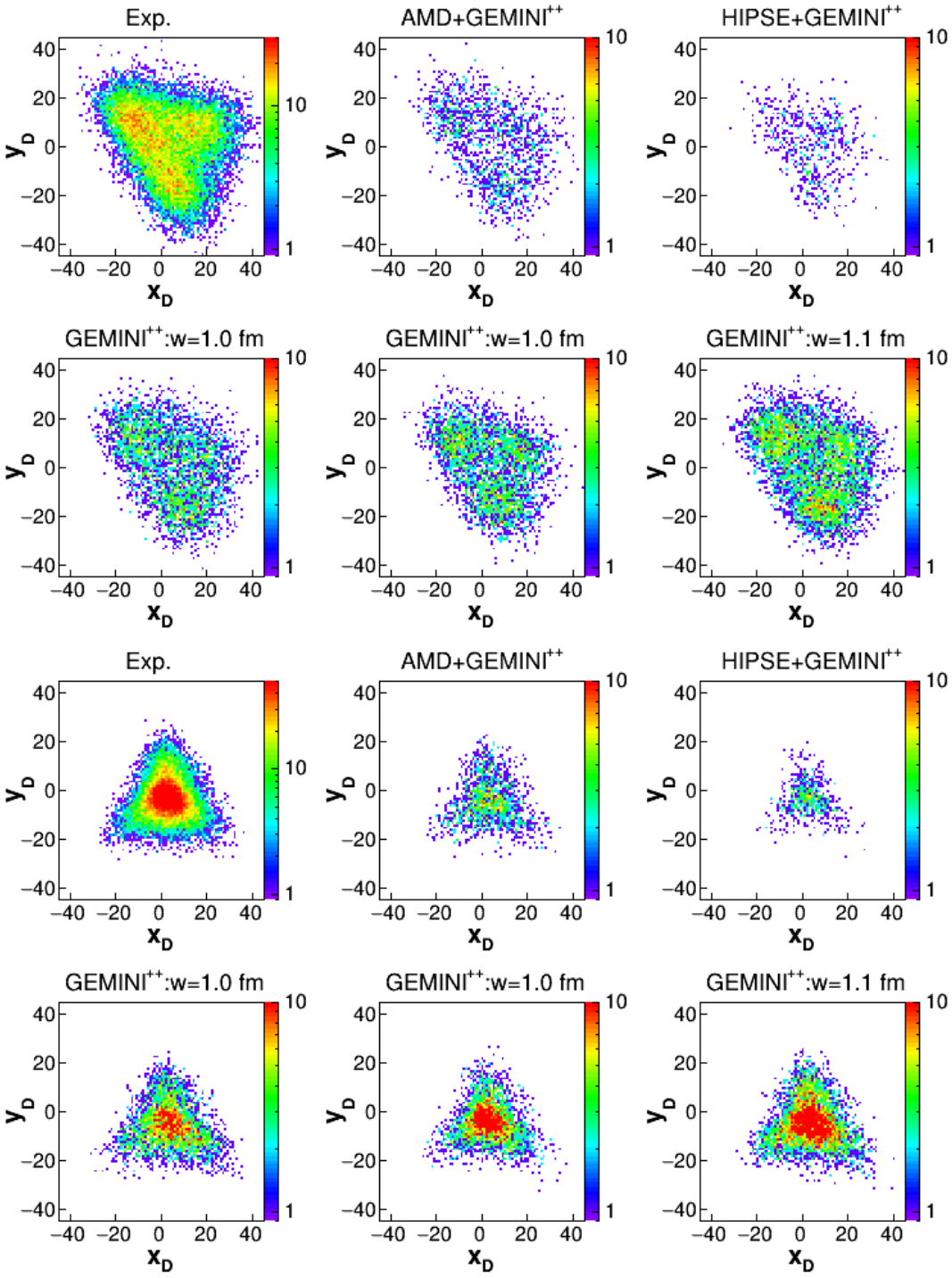

Figure 9.32: Dalitz plots for the reaction $^{19}F + ^{27}Al$ at 133 MeV. See text for more details.

induced reaction data are more similar to **G10**. Looking, however to "D1" Dalitz plot, we can see that the region close to $x = 0$ and $y = 0$ which is filled by experimental data and especially visible for the reactions $^{18}O +^{28} Si$ at 126 MeV and $^{19}F +^{27} Al$ at 133 MeV, is never reproduced by simulations that, on the contrary leave that region quite empty.

Moreover, in the data we have three specific regions of relative velocities, which are confirming the expected sequential emission of particles and which, as schematically reported in Fig. 9.33 correspond to a) left upper region α-particles with $E_{med} \cong E_{max}$, b) upper right region $E_{med} \cong E_{min}$ and c) lower bump $E_{med,min} \cong E_{med,max}$.

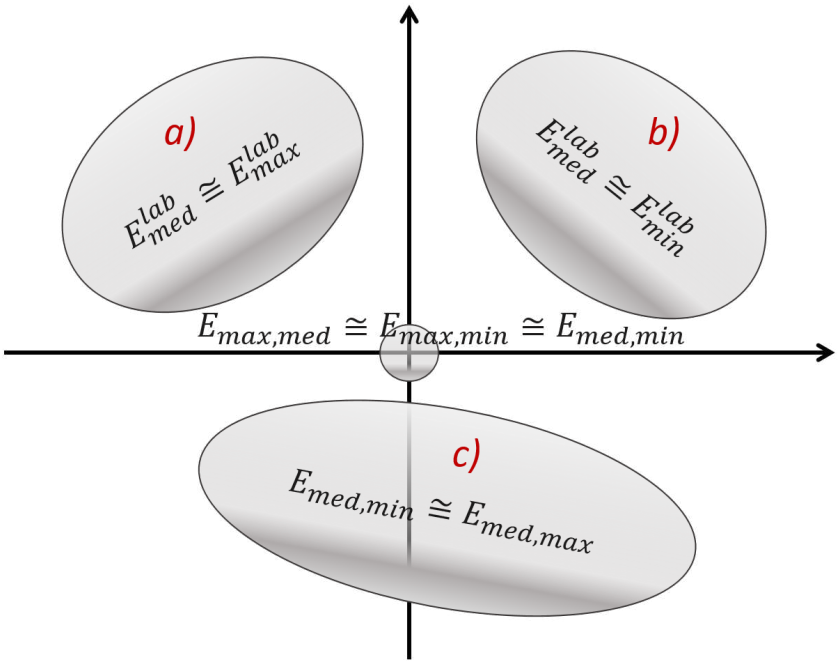

Figure 9.33: Schematic view of "D1" Dalitz plot.

In the experimental data, they are almost equally populated, with the growth of a fourth region around the (0,0) point as previously pointed out. In the simulations, the three regions are also visible but they are populated in a different way: in fact in the simulations either the three regions are well separated or the region b) and c) show a continuity (coordinates 0,20) while in the experimental data the continuity is between the

a) and c) region, passing by (0,0). So, in the data we have not only a majority of equal energy particles events, but also, some events in which the 3α-particles have the almost the same relative velocities.

9.3 Exclusive observables for multiple-α-channel

A further correlation we have observed is that one between the evaporation residue (ER) energy and either its correlated α-particle energy (in the case of 1α emission channel) or the relative energies between the α-particles in case of multiple α-particle emission. In particular we have analyzed the following decay channels: $^{42-xn}Ca + \alpha + xn$, $^{38-xn}Ar + 2\alpha + xn$ and $^{34-xn}S + 3\alpha + xn$

For the case of the exit channel $^{42-xn}Ca + \alpha + xn$, in the Fig. 9.34, the α-particle energy is displayed *versus* the energy of the evaporation residue detected in coincidence with the 1α-particles.

Looking at the correlation it is clearly visible a difference between experimental data and simulations, since a strong correlation can be observed for relatively low ER energy ($\sim$ 35 MeV), which is not so visible in simulations. In reality, for the $^{16}O+^{30}Si$ at 111 MeV reaction, **G00** and **G11** show a bump in that region, which is however less peaked, while **G10** shows a more continuous distribution. Even in experimental data this correlation seem to become less and less evident as a function of the excitation energy and of the asymmetry η (see the difference between ^{16}O at 128 MeV and ^{18}O at 126 MeV). To be more quantitative on this, further analysis is needed, for example correlating different slices in ER energy plot to the different regions in a Q-value *vs.* E_α plot. This will be the subject of a future dedicated work and it is out of the aim of this thesis work.

For the case of the exit channel: $^{38-xn}Ar + 2\alpha + xn$, the relative $\alpha - \alpha$ energies are shown with respect to the energy of the evaporation residue detected in coincidence with the 2α-particles in the Fig. 9.35 .

Even in this second decay channel a strong correlation at low ER energy ($E_{ER} < 35$ MeV) is observed. In this case it appears to be more pronounced for the two reaction at the intermediate excitation energy, which show a very similar trend. **G10** and **G11** show

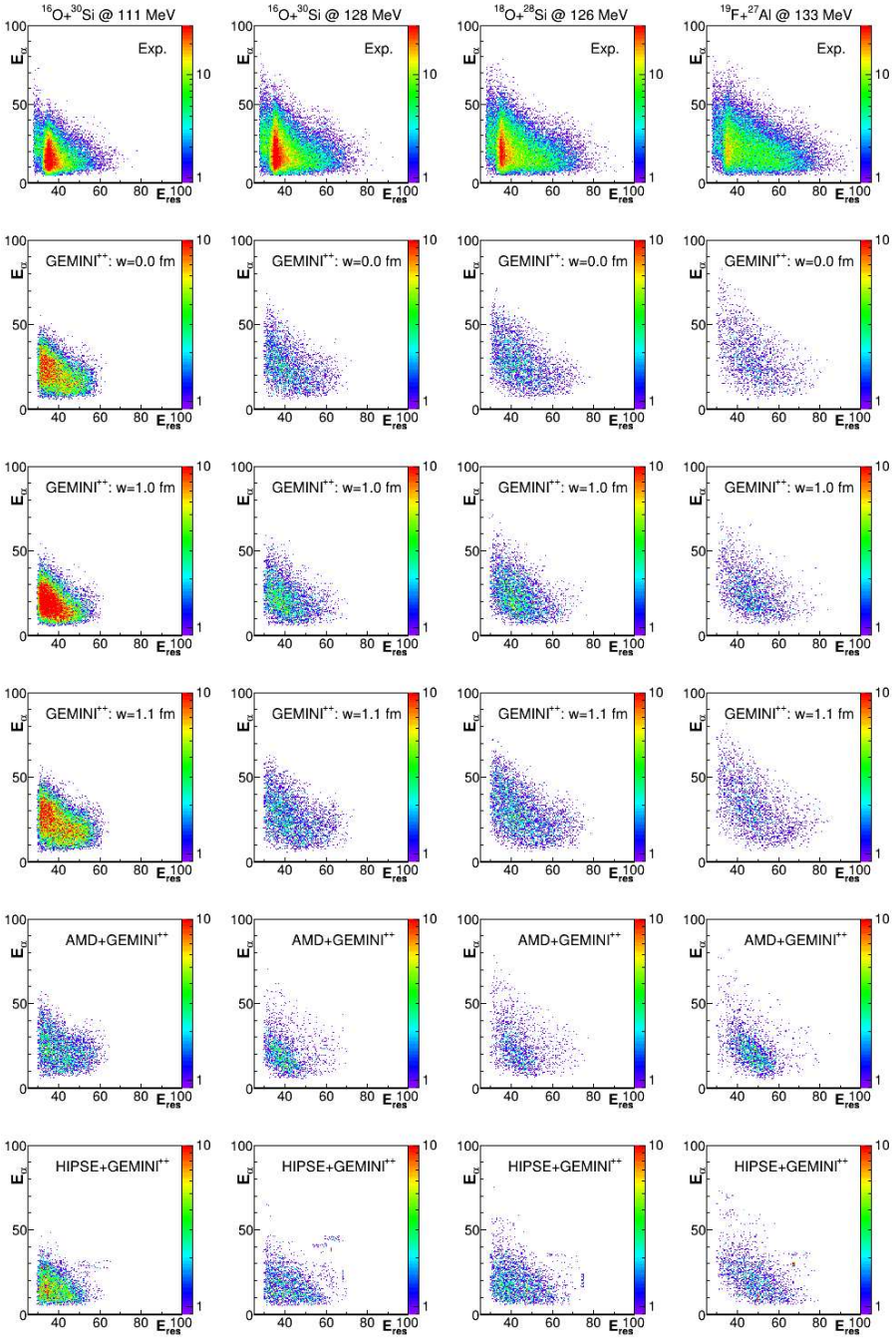

Figure 9.34: Plot of E_α *vs.* E_{res} for the exit channel $^{42-xn}Ca+\alpha+xn$ from the four studied reactions.

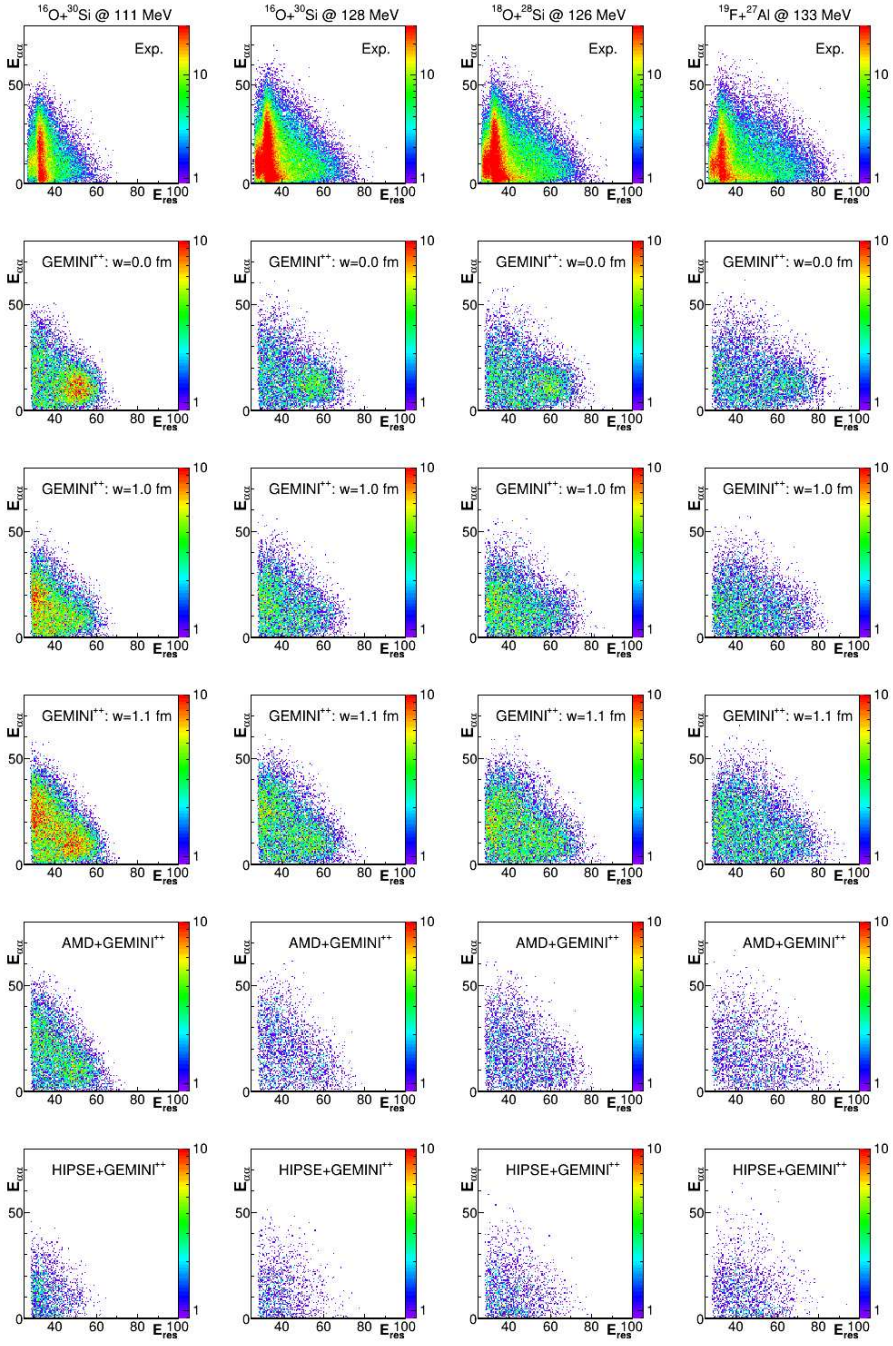

Figure 9.35: Plot of $E_{\alpha-\alpha}$ *vs.* E_{res} for the exit channel $^{38-xn}Ar + 2\alpha + xn$ from the four studied reactions.

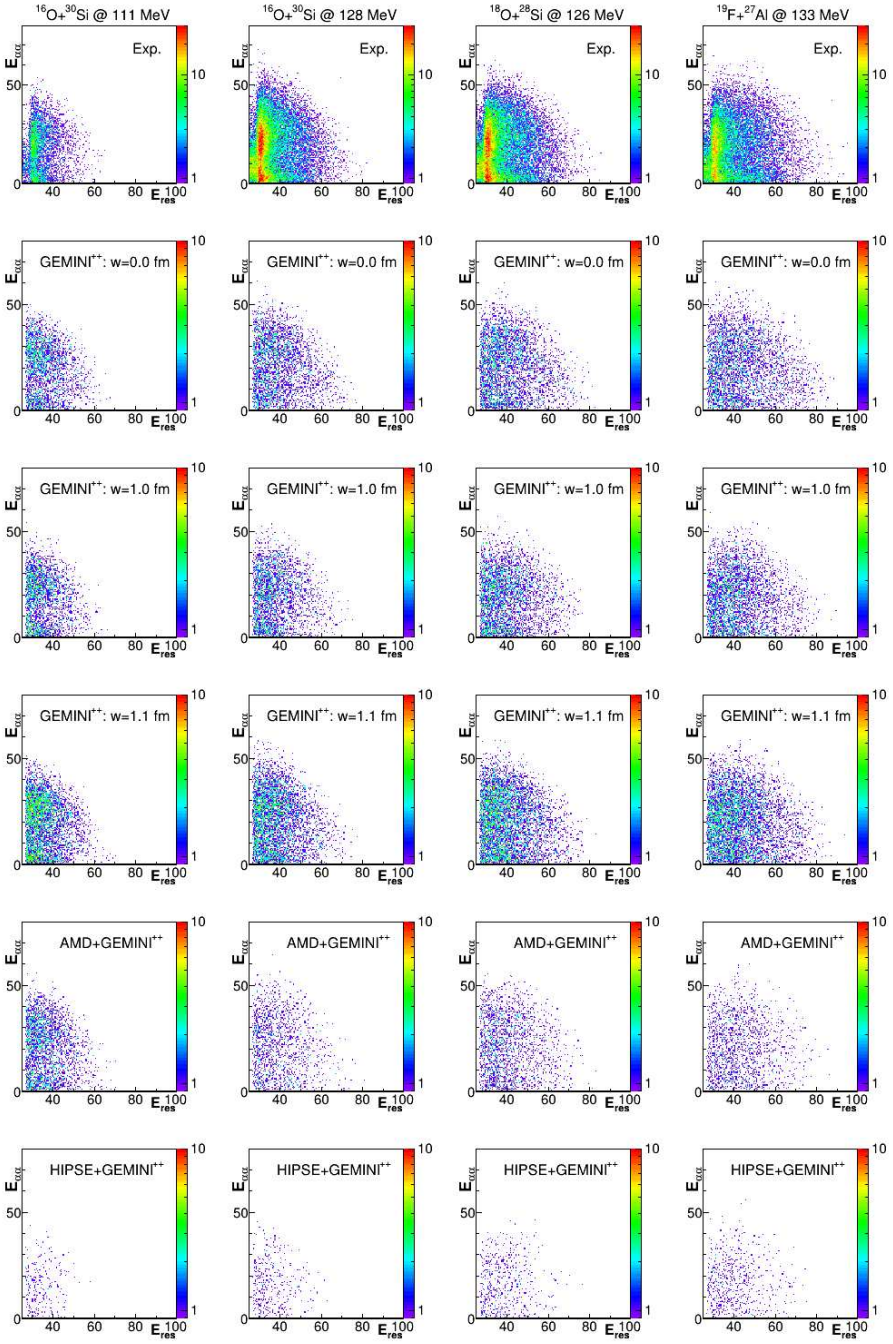

Figure 9.36: Plot of $E_{\alpha-\alpha}$ (faster-medium) *vs.* E_{res} for the exit channel $^{34-xn}S + 3\alpha + xn$ from the four studied reactions.

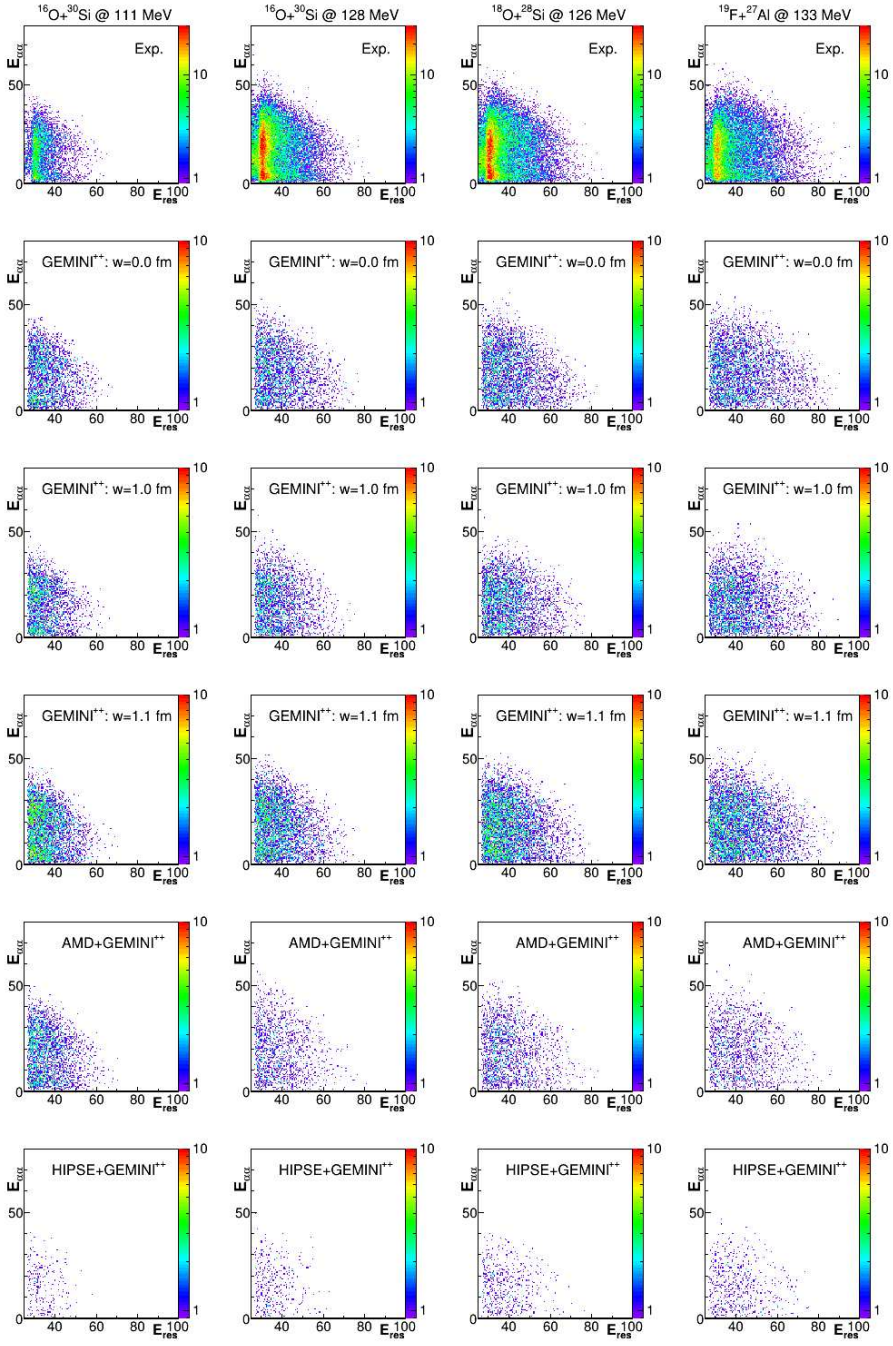

Figure 9.37: Plot of $E_{\alpha-\alpha}$ (faster-slower) *vs.* E_{res} for the exit channel $^{34-xn}S + 3\alpha + xn$ from the four studied reactions.

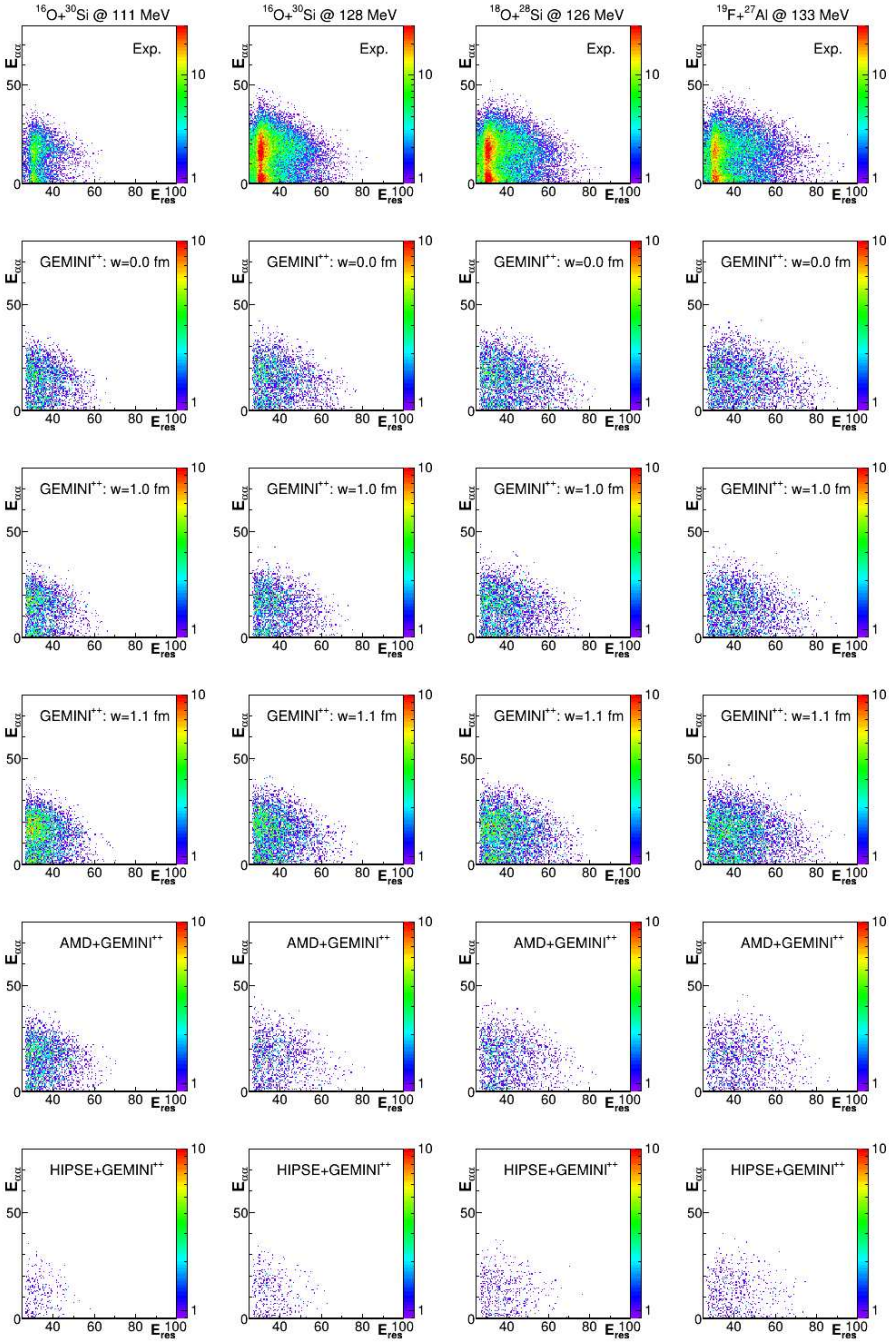

Figure 9.38: Plot of $E_{\alpha-\alpha}$ (medium-slower) *vs.* E_{res} for the exit channel $^{34-xn}S + 3\alpha + xn$ from the four studied reactions.

such a bump at low excitation energy, but it is surely less pronounced than in the experimental case. Moreover, going up with the excitation energy they do not show the observed increasing of this correlation. This can also be associated to what has been observed in the previously discussed $E_{\alpha-\alpha}$ *vs.* Q-value plots, that is a non-negligible difference in the dissipation between experiment and simulations, which favors experimentally higher neutron multiplicity connected to the studied exit channel and therefore a smaller energy remaining for the residual nucleus. This was somehow seen in the Chapter 10, where Q-value spectra were discussed in comparison to neutron emission channel threshold and probability (see Figs. 10.5, 10.12, 10.19 and 10.26).

For the case of the exit channel: $^{34-xn}S+3\alpha+xn$, the relative α-α-energy are compared with the energy of the evaporation residue detected in coincidence with the 3α-particles in the Fig. 9.36 $\div$ 9.38.

In this case the three relative energies ($E_{max,med}$, $E_{med,min}$ and $E_{max,min}$) have been displayed and show a very similar trend as a function of ER. Still a pronounced peak is observed at low E_{ER}: it is also clear a double bump in the $E_{\alpha-\alpha}$ axis, which refers to very small $E_{\alpha-\alpha}$ and to more distant α-particle emissions, already observed in the previous paragraph. From the simulations point of view, all the distributions are much more continuous, and only **G11** is somehow resembling a little bit to the experimental trend, even if with a much less pronounced low ER energy peak. Even in this case a quite larger dissipation of the experimental distribution was observed in the Q-value spectra (see Figs. 10.6, 10.13, 10.20 and 10.27 in Chapter 10) and, as it was previously underlined some particular configuration of the relative energies are present in the (0,0) region of the "D1" Dalitz plots, which were not observed with the same intensity in simulations.

As a conclusion, we may say that, studying in more detail specific decay channels, especially those in which α-particles are experimentally the predominant decay channel, we have observed interesting differences with respect to simulations for what concerns branching ratios, energy correlations, dissipation. These differences are evident in all studied reactions, but some peculiarities are found in each case, demonstrating that both excitation energy and entrance channel mass asymmetry may play a role. A summary of

the work will be discussed in the 10.4.

Chapter 10

Exclusive Channels Analysis

In order to give a more quantitative information on the studied reactions, the branching ratios for each detected evaporation residue have been calculated and compared to theoretical predictions. The BR is defined as the ratio between the yield of the selected decay channel and the total number of corresponding evaporation residues with $Z = Z_{ER}$. Each specific decay channel has been then analyzed in terms of Q-value and characteristics of the emitted particles (energy and angular distributions).

10.1 ^{16}O+^{30}Si at 111 MeV.

The branching ratios of the decay channels from the excited ^{46}Ti compound nucleus formed through the reaction $^{16}O + {}^{30}Si$ at 111 MeV are listed, comparing experimental data and simulations, in Tables 10.1 and 10.2. For an integrated visualization and for the sake of comparison, experimental and simulated BR for the most populated channels are reported in the graphics of Fig. 10.1 (odd Z residues) and Fig 10.2 (even Z residues).

We can observe, in general that for odd Z residues, the main decay channels are quite well reproduced by simulations. On the contrary, this is not the case for even Z residues: in fact, experimentally, the decay channels, in which the maximum number of α-particle can be emitted for that residue ($\#_{max,\alpha} = \frac{22 - Z_{ER}}{2}$), seem to be experimentally privileged with respect to the competing channels which are, at variance, highly predicted by

channels	EXP	$GEMINI^{++}$ $w = 0.0$ fm	$GEMINI^{++}$ $w = 1.0$ fm	$GEMINI^{++}$ $w = 1.1$ fm
$^{45-xn}Sc + p + xn$	92 ± 2	95	94	90
$^{44-xn}Sc + d + xn$	7.1 ± 0.4	4.3	5.3	8.2
$^{43-xn}Sc + t + xn$	1.15 ± 0.14	0.65	0.57	1.43
$^{44-xn}Ca + 2p + xn$	19.8 ± 0.3	72.1	65.0	60.9
$^{42-xn}Ca + \alpha + xn$	76.6 ± 0.9	20.8	28.1	29.6
$^{43-xn}Ca + ^3He + xn$	0.206 ± 0.025	0.285	0.207	0.393
$K + 3(z = 1) + xn$	2.83 ± 0.08	7.79	5.50	6.28
$K + 1(z = 1) + \alpha + xn$	95.2 ± 0.8	92.1	94.4	93.5
$^{41-xn}K + p + \alpha + xn$	91.8 ± 0.8	90.8	93.1	91.7
$^{38-xn}Ar + 2\alpha + xn$	63.7 ± 0.7	23.6	20.5	28.9
$Ar + 2(z = 1) + \alpha + xn$	32.6 ± 0.4	68.3	75.8	67.5
$^{40-xn}Ar + 2p + \alpha + xn$	30.6 ± 0.4	65.8	72.9	64.3
$Cl + 1(z = 1) + 2\alpha + xn$	88.7 ± 1.5	85.3	93.8	93.5
$^{37-xn}Cl + 1p + 2\alpha + xn$	86.4 ± 1.5	83.8	92.3	91.3
$Cl + 3(z = 1) + 1\alpha + xn$	1.97 ± 0.13	2.03	1.56	1.81
$^{34-xn}S + 3\alpha + xn$	83 ± 2	48	57	68
$S + 2(z = 1) + 2\alpha + xn$	8.7 ± 0.5	8.8	12.8	9.1
$S + 4(z = 1) + 1\alpha + xn$	0.03 ± 0.02	–	–	–
$P + 1(z = 1) + 3\alpha + xn$	50 ± 4	18	38	30
$^{33-xn}P + 1p + 3\alpha + xn$	49 ± 4	18	37	30
$P + 3(z = 1) + 2\alpha + xn$	0.4 ± 0.2	–	–	–
$P + 2\alpha + Li + xn$	13 ± 4	1	1	1
$P + 1p + 1\alpha + Be + xn$	4.0 ± 0.8	1.6	2.2	1.9
$P + 1\alpha + B + xn$	33 ± 3	79	59	67
$^{30-xn}Si + 4\alpha + xn$	81 ± 9	41	53	67
$Si + 2(z = 1) + 3\alpha + xn$	1.6 ± 0.8	0.8	–	1.6
$Si + 2\alpha + Be + xn$	9 ± 2	13	6	9
$Si + 1p + 1\alpha + B + xn$	6 ± 2	43	38	23
$Al + 1p + 4\alpha + xn$	27 ± 15	–	9	–
$Al + 2\alpha + B + xn$	50 ± 24	100	91	100

Table 10.1: Experimental and $GEMINI^{++}$ simulated branching ratios for the reaction $^{16}O + ^{30}Si$ at 111 MeV.

channels	EXP	*AMD+* *GEMINI*$^{++}$	*HIPSE+* *GEMINI*$^{++}$
$^{45-xn}Sc + p + xn$	92 ± 2	73	94
$^{44-xn}Sc + d + xn$	7.1 ± 0.4	23.5	5.3
$^{43-xn}Sc + t + xn$	1.15 ± 0.14	3.67	0.77
$^{44-xn}Ca + 2p + xn$	19.8 ± 0.3	82.6	75.9
$^{42-xn}Ca + \alpha + xn$	76.6 ± 0.9	8.5	14.5
$^{43-xn}Ca + ^3He + xn$	0.206 ± 0.025	0.282	1.337
$K + 3(z = 1) + xn$	2.83 ± 0.08	25.8	17.5
$K + 1(z = 1) + \alpha + xn$	95.2 ± 0.8	73.9	82.0
$^{41-xn}K + p + \alpha + xn$	91.8 ± 0.8	72.3	80.2
$^{38-xn}Ar + 2\alpha + xn$	63.7 ± 0.7	12.7	7.2
$Ar + 2(z = 1) + \alpha + xn$	32.6 ± 0.4	83.8	88.1
$^{40-xn}Ar + 2p + \alpha + xn$	30.6 ± 0.4	79.8	84.8
$Cl + 1(z = 1) + 2\alpha + xn$	88.7 ± 1.5	86.7	85.4
$^{37-xn}Cl + 1p + 2\alpha + xn$	86.4 ± 1.5	84.3	84.5
$Cl + 3(z = 1) + 1\alpha + xn$	1.97 ± 0.13	8.94	5.87
$^{34-xn}S + 3\alpha + xn$	83 ± 2	53	32
$S + 2(z = 1) + 2\alpha + xn$	8.7 ± 0.5	25.2	44.9
$S + 4(z = 1) + 1\alpha + xn$	0.03 ± 0.02	0.06	–
$P + 1(z = 1) + 3\alpha + xn$	50 ± 4	37	37
$^{33-xn}P + 1p + 3\alpha + xn$	49 ± 4	37	37
$P + 3(z = 1) + 2\alpha + xn$	0.4 ± 0.2	0.3	–
$P + 2\alpha + Li + xn$	13 ± 4	2	3
$P + 1p + 1\alpha + Be + xn$	4.0 ± 0.8	2.4	6.0
$P + 1\alpha + B + xn$	33 ± 3	59	52
$^{30-xn}Si + 4\alpha + xn$	81 ± 9	56	65
$Si + 2(z = 1) + 3\alpha + xn$	1.6 ± 0.8	1.6	2.9
$Si + 2\alpha + Be + xn$	9 ± 2	9	12
$Si + 1p + 1\alpha + B + xn$	6 ± 2	31	18
$Al + 1p + 4\alpha + xn$	27 ± 15	8	–
$Al + 2\alpha + B + xn$	50 ± 24	92	–

Table 10.2: Experimental and dynamical codes simulated branching ratios for the reaction $^{16}O + ^{30}Si$ at 111 MeV.

simulations.

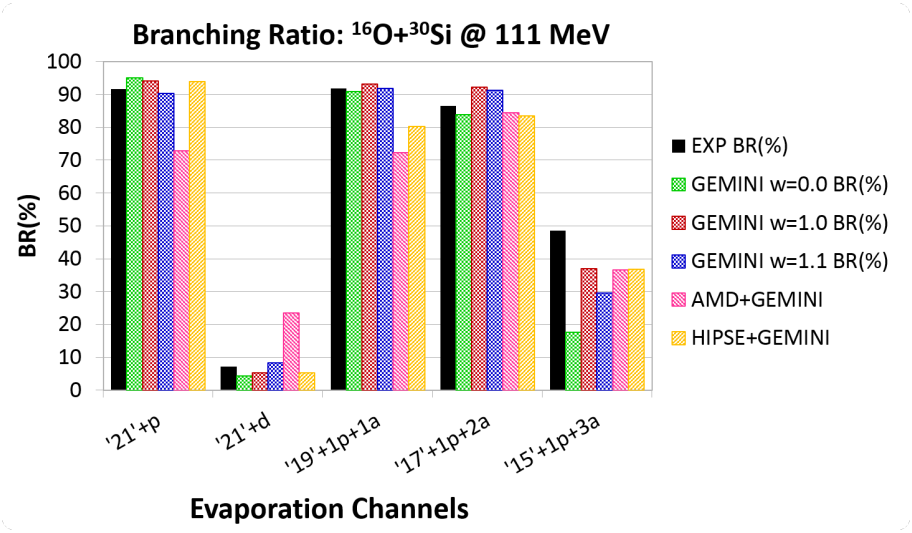

Figure 10.1: Experimental and simulated branching ratio for the reaction $^{16}O + ^{30}Si$ at 111 MeV: odd Z residues. Black bars are experimental data.

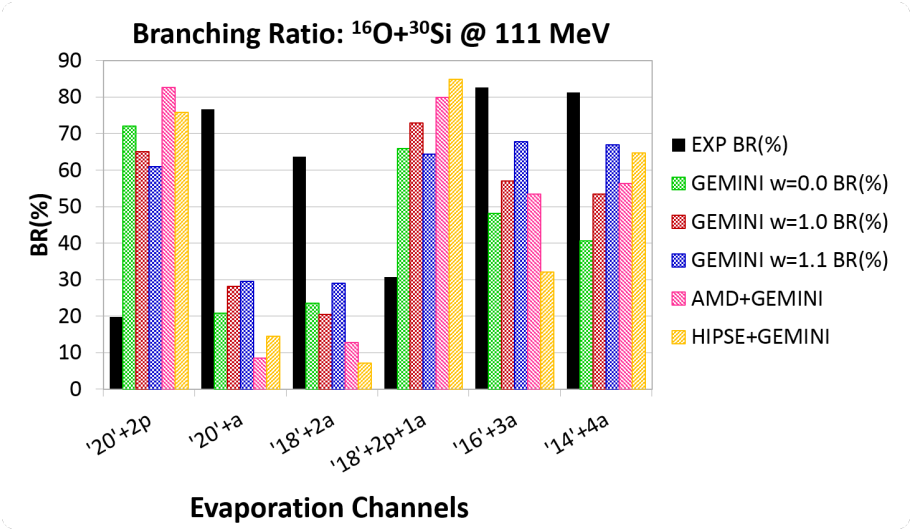

Figure 10.2: Experimental and simulated branching ratio for the reaction $^{16}O + ^{30}Si$ at 111 MeV: even Z residues. Black bars are experimental data.

In particular, there are always at least two main competing channels, which are often reversed in importance between experiment and simulations. In fact, apart from the BR

reported in the Figs. 10.1 and 10.2, it is worth mentioning the following cases:

- *S*-channel: experimentally the 80% of the cross section is going to the 3α decay channel, while from simulations this channel is populated from 30 to 70 %. Other channels are competing according to simulations like the 2α-2H channel (higher competitor in **HIPSE** and **AMD**), and the 1B+1p and the 1Be+1α, which takes from 20 to 30% of the cross section according to $GEMINI^{++}$. However, these channels are experimentally very poorly populated;

- *P*-channel: experimentally 50% in the 1p-3α channel and the rest mainly in 1α-1B (33%) and 2α-1Li (13%). From simulations the main decay channel is the 1α-1B (from 50% in the dynamical model up to 80% for **G00**);

- *Si* channel: experimentally 80% in the 4α decay channel, while in simulations also the 1p+1α+1B is predicted with a non-negligible cross section (from 20% up to 40% depending on model cases);

- *Al*-channel: experimentally 27% in the 1p-4α channel and 50% in the 2α+B channel, while from all simulations almost all cross section (from 90 to 100%) goes in the 2α+B decay channel.

To better show this effect the factor R is reported in Fig. 10.3 as a function of the Z_{ER}. The factor R is defined as the difference between the experimental BR and the BR derived by simulation:

$$R = R_{clus}(Z) = \frac{Y_{exp}(Z_{ER};\#_{max,\alpha})}{Y_{exp}} - \frac{Y_{sim}(Z_{ER};\#_{max,\alpha})}{Y_{sim}} \tag{10.1}$$

In general, one can observe more easily that R is quite large when the maximum number of α-particles, which can be emitted for that specific channel, is observed (up to 40% $\div$ 60% for $Z_{ER} = 20$ and 18), while for odd residues, the experimental BR is quite well accounted for by simulations ($R \sim 0$), apart in specific cases, that will be discussed specifically.

In the following, in Figs. 10.4, 10.5 and 10.6, the *missing energy Q-value* spectra of different multiple-α decay channels are presented for the reaction $^{16}O + ^{30}Si$ at 111 MeV.

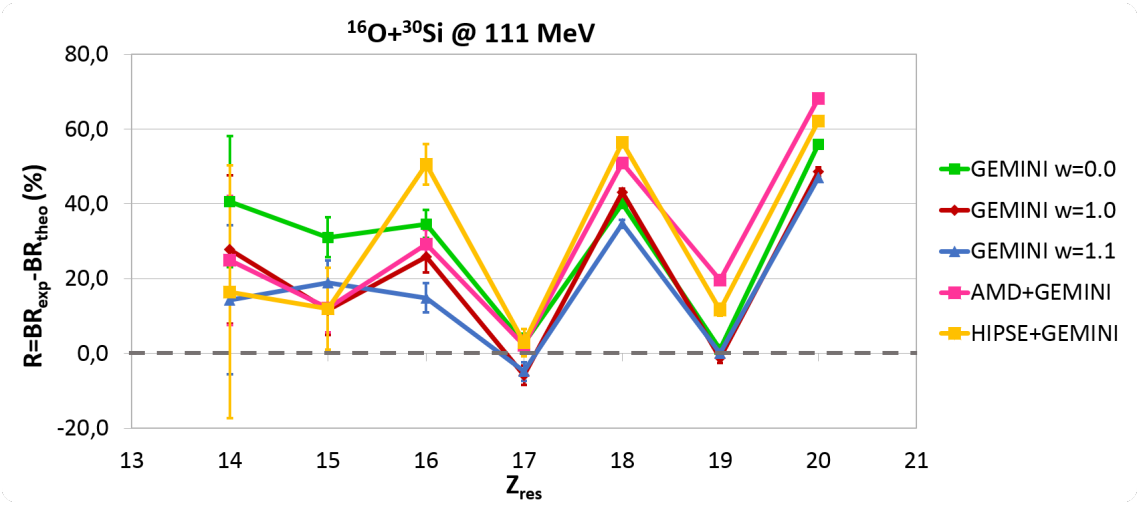

Figure 10.3: Difference R between simulated and experimental branching ratio as a function of Z_{ER}, for the reaction $^{16}O + ^{30}Si$ at 111 MeV.

The *missing energy Q-value* have been previosly defined as the reconstructed Q-value spectra in which the emitted neutron energies are missing, since neutrons are not detected in our experiment. In particular, in Fig. 10.4, the Q-value for the 1α-decay channel ($^{42-xn}Ca + \alpha + xn$) is presented together with its main competitor channel: $^{44-xn}Ca + 2p + xn$; looking at the shape the *missing energy Q-value* spectrum is well reproduced by all simulations in the case of $^{44-xn}Ca + 2p + xn$ channel, which may indicate that the *true Q-value* should be similar to that one simulated (light blue spectrum), where the $3n$ and $4n$ emission channels seem to be the most probable: therefore, either the $^{40}Ca + 2p + 4n$ or the $^{41}Ca + 2p + 3n$, followed by the $^{42}Ca + 2p + 2n$ are the final channels according both to all $GEMINI^{++}$ with barrier parameters: $w = 0.0$ fm (**G00**), $w = 1.0$ fm (**G10**) and $w = 1.1$ fm (**G11**) and to $AMD + GEMINI^{++}$ (**AMD**). $HIPSE + GEMINI^{++}$ (**HIPSE**) is predicting a more dissipative spectrum with a large production in the $4n$ and even $5n$ decay channel emission.

For the α-decay channel, on the contrary, no simulation is reproducing neither the shape nor the relative yield of the *missing energy Q-value*, strongly under-producing this decay channel, as already seen by the BR. The closer simulation is **G10**, which suggest, looking to the *true Q-value* (light blue in the picture) a dissipation through the $3n$ and $4n$

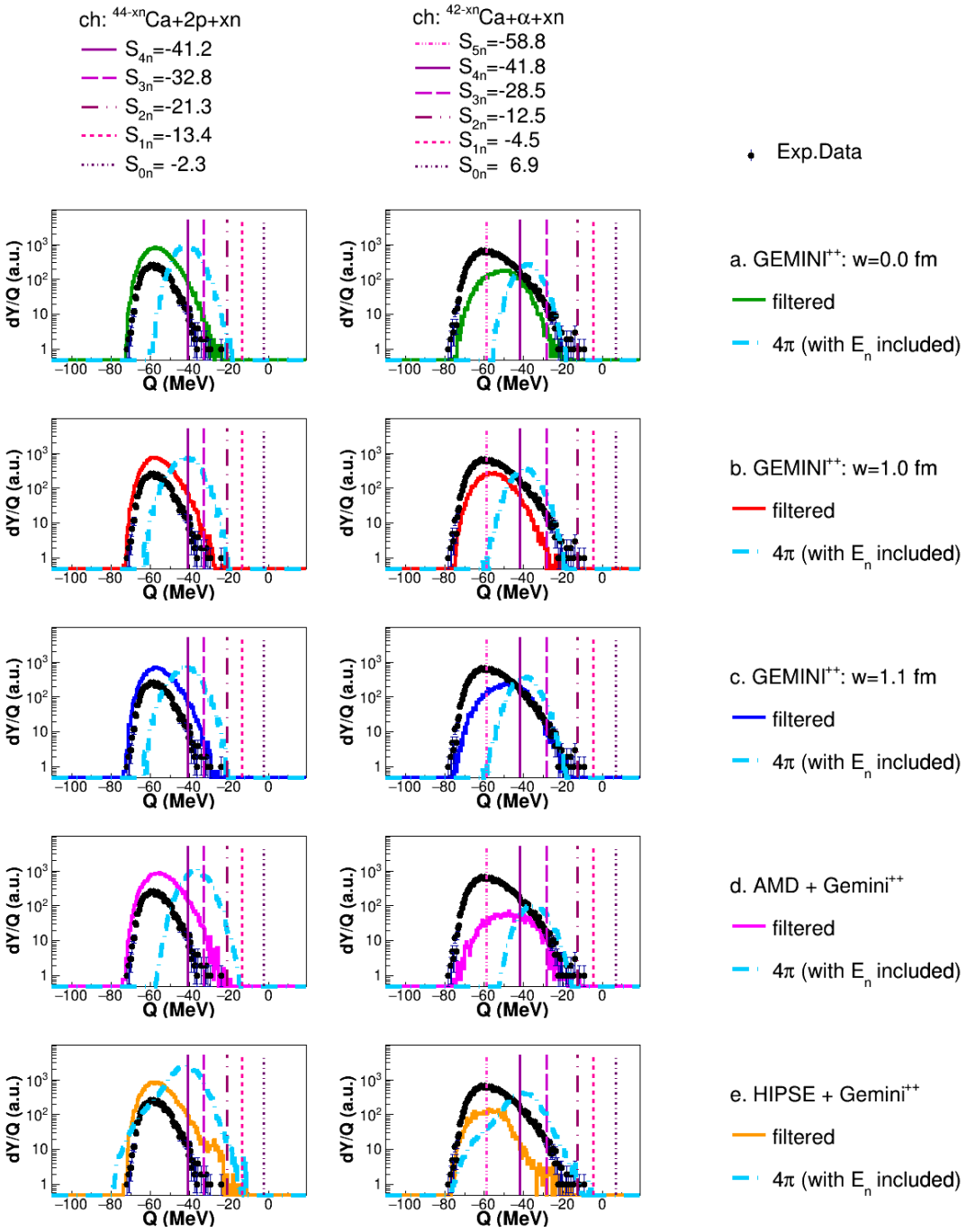

Figure 10.4: *Missing Energy* and *True Q-value* spectra for the two main decay channels where a Ca evaporation residue is left, for the reaction $^{16}O + ^{30}Si$ at 111 MeV.

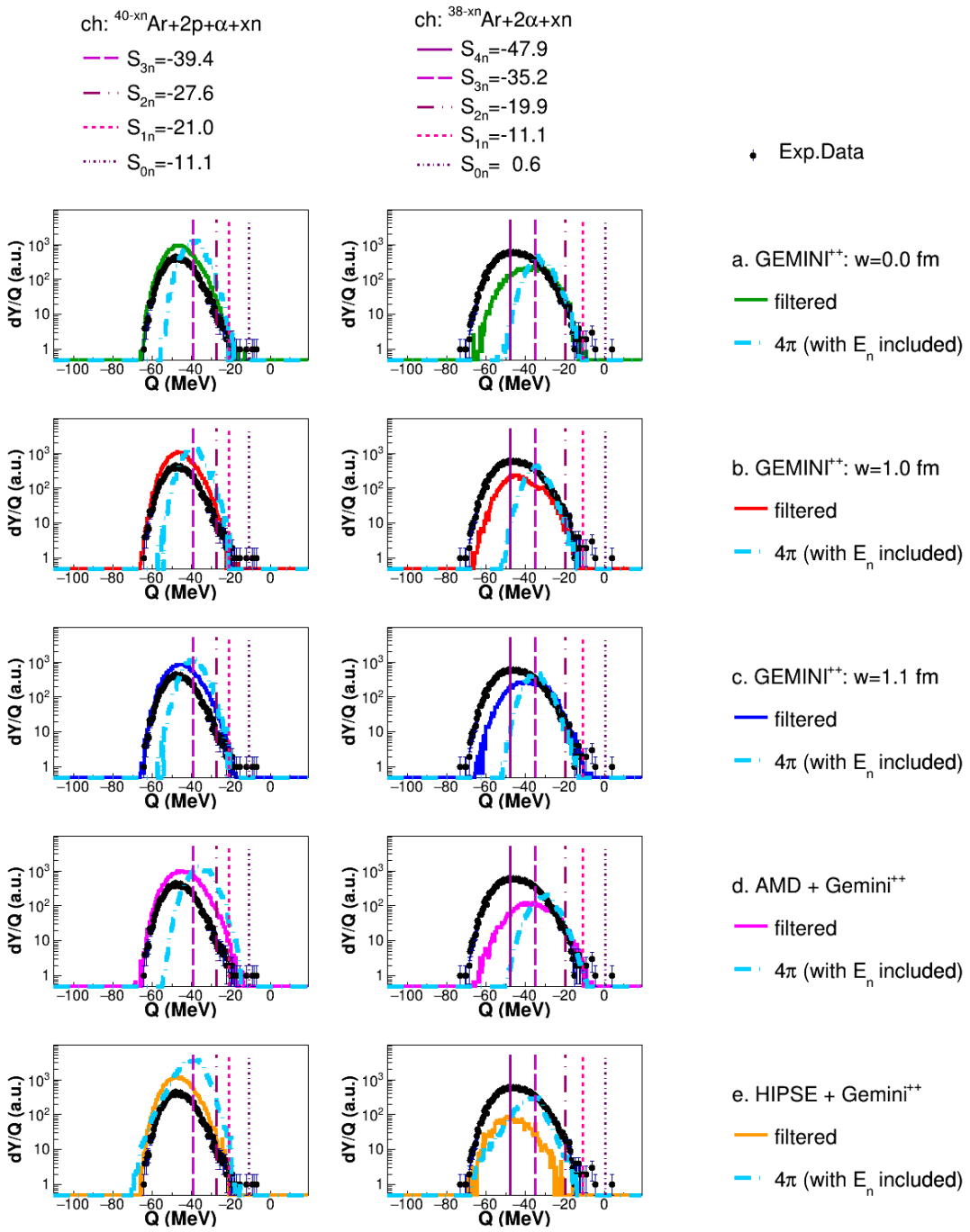

Figure 10.5: *Missing Energy* and *True Q-value* spectra for the two main decay channels where an *Ar* evaporation residue is left, for the reaction $^{16}O + ^{30}Si$ at 111 MeV.

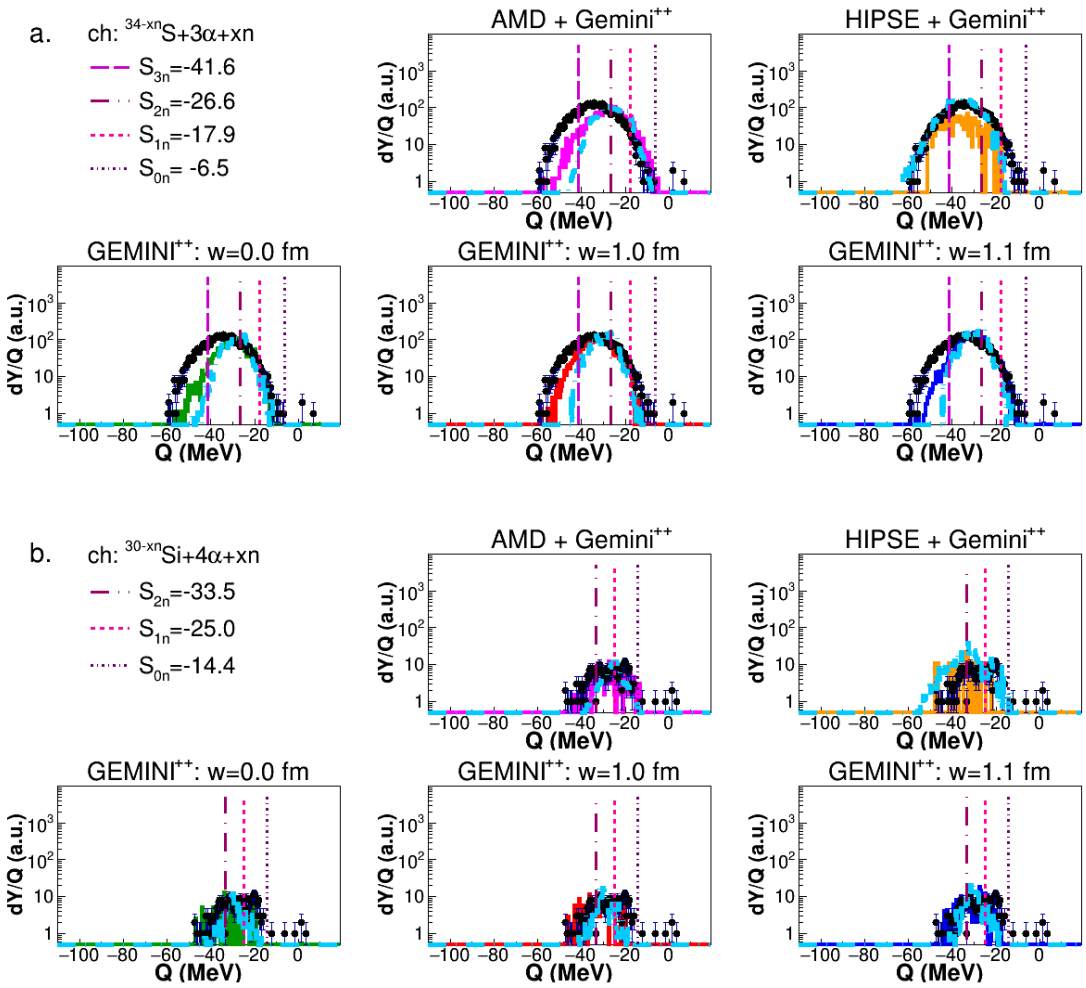

Figure 10.6: *Missing Energy* and *True Q-value* spectra for the two main decay channels where respectively a S (top panels) and a Si (lower panels) evaporation residue is left, for the reaction $^{16}O + ^{30}Si$ at 111 MeV.

channels: $^{39}Ca+\alpha+3n$, $^{38}Ca+\alpha+4n$. **HIPSE** is reproducing the peak position, but not really the shape and, again, it simulates a larger dissipation predicting also the opening of the $5n$ channel: $^{37}Ca+\alpha+5n$.

A similar representation is proposed in Fig. 10.5, where the Q-value for the 2α-decay channel ($^{38-xn}Ar + 2\alpha + xn$) is presented together with its main competitor channel: $^{40-xn}Ar+2p+1\alpha+xn$. Even in this case, on the left side ($^{40-xn}Ar+2p+\alpha+xn$ channel) of the Fig. 10.5, the *missing energy Q-value* is reproduced as a shape and only slightly

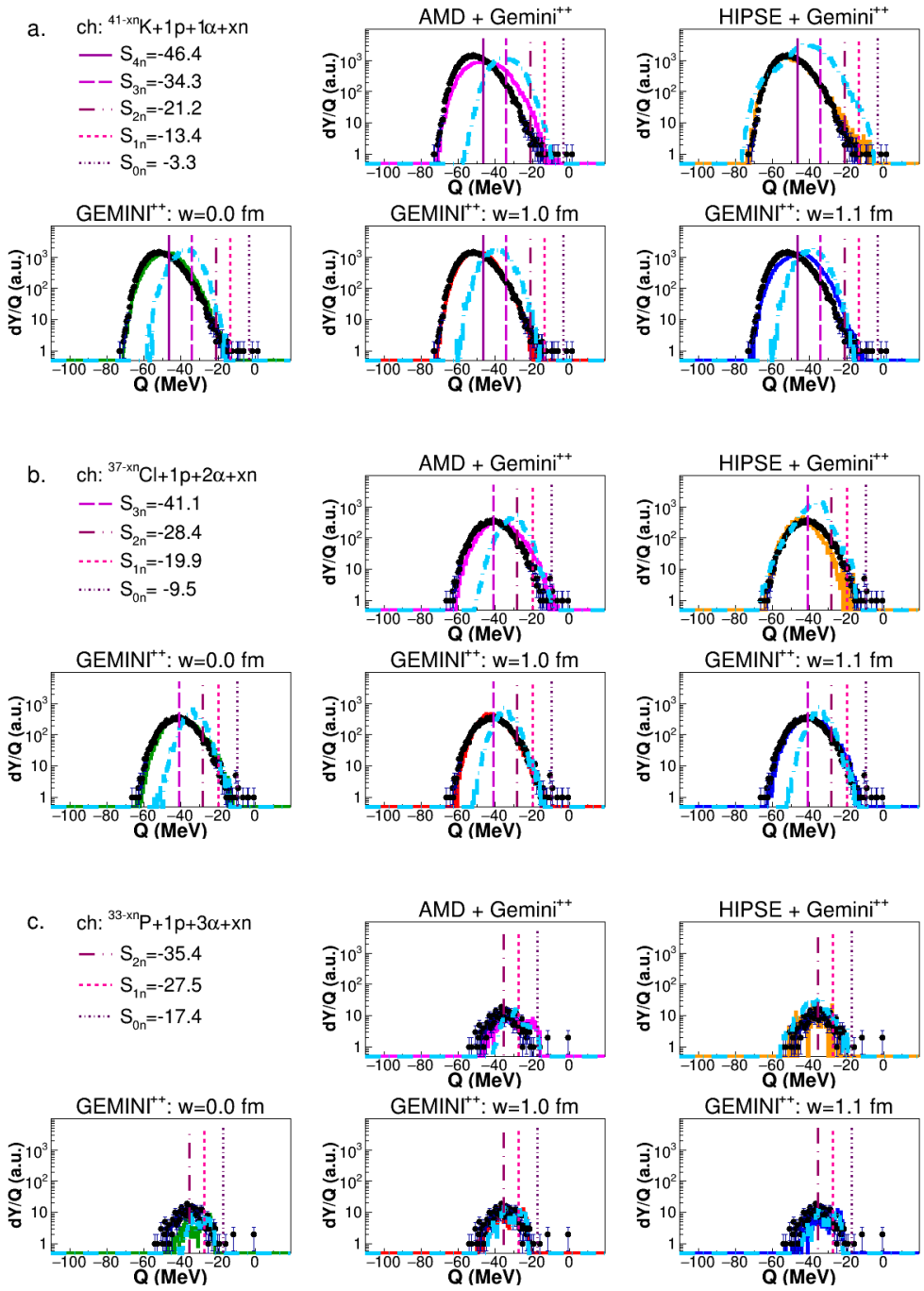

Figure 10.7: *Missing Energy* and *True Q-value* spectra for the three main decay channels where respectively a K (top panels) a Cl (middle panels) and a P (lower panels) evaporation residue is left, for the reaction $^{16}O + ^{30}Si$ at 111 MeV.

overestimated as yield: the expected major decay channels from the *true Q-value* taken, for example, by **G10**, are $^{38}Ar+2p+\alpha+2n$, $^{37}Ar+2p+\alpha+3n$ and following, with a smaller yield, the $^{36}Ar+2p+\alpha+4n$. On the other side, the $^{38-xn}Ar+2\alpha+xn$ is not represented by simulations and, therefore, it is, here, more difficult to draw an unambiguous result on the final n-emission channels. Again, all $GEMINI^{++}$ cases and **AMD** predict mainly the $^{36}Ar+2\alpha+2n$ and $^{35}Ar+2\alpha+3n$, while **HIPSE** is also predicting a non negligible cross section in the $^{34}Ar+2\alpha+4n$ decay channel.

Finally, in Fig. 10.6 the Q-value for the 3 and 4α-decay channels are illustrated. In particular, the *missing energy Q-value* for the 3α-decay channel, even if it is slightly more dissipative, is reasonably reproduced by **G10** while **HIPSE**, despite the too low cross section, is better reproducing the more dissipative part. In this case the most populated channels are: $^{33}S+3\alpha+n$ and $^{32}S+\alpha+2n$ according to all $GEMINI^{++}$ cases, while for **HIPSE** also the $^{31}S+\alpha+3n$ is predicted. The case of 4α, despite the very small statistics, is reasonably reproduced by **G11** and by **AMD**: from the reconstructed *true Q-value* (light blue spectrum) the most populated channels seem to be $^{30}Si+4\alpha$ and $^{29}Si+4\alpha+1n$, by **AMD**, while for **G10** alone the major channel is the $^{29}Si+4\alpha+1n$, with a small indication of the $^{28}Si+4\alpha+2n$ channel opening.

In Fig. 10.7 the Q-value for the 1p + multiple-α decay channels are reported; in particular, the Q-value for 1p + 1, 2 and 3α-decay channels, which correspond respectively to K, Cl and P evaporation residues, are illustrated. The *missing energy Q-value* spectra for the three decay channels are well reproduced by all simulations, even if **G10** seems to be the closest to the data in all cases. The reconstructed *true Q-value* spectra indicate respectively: $^{39}K+p+\alpha+2n$, $^{38}K+p+\alpha+3n$, $^{37}K+p+\alpha+4n$ in the K case; mainly $^{35}Cl+p+2\alpha+2n$, followed by a smaller probability of $^{34}Cl+p+2\alpha+3n$ and $^{36}Cl+p+2\alpha+n$ in the case of Cl; $^{32}P+p+3\alpha+n$ and $^{31}P+p+3\alpha+2n$ in the P case.

10.2 ^{16}O+^{30}Si at 128 MeV.

The decay from ^{46}Ti excited compound nucleus formed in the reaction $^{16}O+^{30}Si$ at 128 MeV is studied by looking at the experimental branching ratios of the different decay

channels	EXP	$GEMINI^{++}$ $w = 0.0$ fm	$GEMINI^{++}$ $w = 1.0$ fm	$GEMINI^{++}$ $w = 1.1$ fm
$^{45-xn}Sc + p + xn$	88 ± 2	94	93	88
$^{44-xn}Sc + d + xn$	10.2 ± 0.4	4.9	5.8	10.7
$^{43-xn}Sc + t + xn$	1.72 ± 0.14	0.92	1.14	1.52
$^{44-xn}Ca + 2p + xn$	30.6 ± 0.3	83.1	80.5	74.8
$^{42-xn}Ca + \alpha + xn$	60.8 ± 0.6	6.8	8.9	11.0
$^{43-xn}Ca + ^3He + xn$	0.37 ± 0.03	0.40	0.34	0.61
$K + 3(z = 1) + xn$	6.91 ± 0.09	22.72	17.95	18.20
$K + 1(z = 1) + \alpha + xn$	91.3 ± 0.5	76.9	81.7	81.3
$^{41-xn}K + p + \alpha + xn$	86.1 ± 0.5	75.3	80.0	78.8
$^{38-xn}Ar + 2\alpha + xn$	43.0 ± 0.3	9.56	7.77	11.68
$Ar + 2(z = 1) + \alpha + xn$	52.4 ± 0.3	83.4	88.4	84.3
$^{40-xn}Ar + 2p + \alpha + xn$	47.2 ± 0.3	78.8	83.3	78.1
$Cl + 1(z = 1) + 2\alpha + xn$	85.6 ± 0.6	80.4	87.1	87.7
$^{37-xn}Cl + 1p + 2\alpha + xn$	81.5 ± 0.6	78.6	85.2	84.8
$Cl + 3(z = 1) + 1\alpha + xn$	6.03 ± 0.10	7.32	7.06	6.87
$^{34-xn}S + 3\alpha + xn$	63.2 ± 0.7	30.9	30.5	42.7
$S + 2(z = 1) + 2\alpha + xn$	26.0 ± 0.4	24.0	37.0	31.0
$S + 4(z = 1) + 1\alpha + xn$	0.15 ± 0.02	0.05	0.07	0.04
$P + 1(z = 1) + 3\alpha + xn$	70.6 ± 1.4	40.0	59.6	53.9
$^{33-xn}P + 1p + 3\alpha + xn$	68.2 ± 1.4	39.0	58.1	52.5
$P + 3(z = 1) + 2\alpha + xn$	0.75 ± 0.09	0.23	0.32	0.46
$P + 2\alpha + Li + xn$	8.1 ± 0.3	1.5	1.7	1.5
$P + 1p + 1\alpha + Be + xn$	4.9 ± 0.2	7.1	5.7	5.7
$P + 1\alpha + B + xn$	12.9 ± 0.5	47.8	30.2	36.5
$^{30-xn}Si + 4\alpha + xn$	70 ± 2	31	40	46
$Si + 2(z = 1) + 3\alpha + xn$	5.2 ± 0.4	2.1	3.8	2.0
$Si + 2\alpha + Be + xn$	7.9 ± 0.5	6.7	5.1	7.0
$Si + 1p + 1\alpha + B + xn$	12.5 ± 0.7	56.5	48.0	42.3
$Al + 1p + 4\alpha + xn$	32 ± 4	8	20	18
$Al + 2\alpha + B + xn$	45 ± 5	88.8	76.8	81.9

Table 10.3: Experimental and $GEMINI^{++}$ simulated branching ratios for the reaction $^{16}O + ^{30}Si$ at 128 MeV.

channels	EXP	*AMD+* *GEMINI*$^{++}$	*HIPSE+* *GEMINI*$^{++}$
$^{45-xn}Sc + p + xn$	88 ± 2	22.7	93.9
$^{44-xn}Sc + d + xn$	10.2 ± 0.4	27.0	5.3
$^{43-xn}Sc + t + xn$	1.72 ± 0.14	50.2	0.8
$^{44-xn}Ca + 2p + xn$	30.6 ± 0.3	82.0	75.9
$^{42-xn}Ca + \alpha + xn$	60.8 ± 0.6	7.6	14.5
$^{43-xn}Ca + ^3He + xn$	0.37 ± 0.03	0.28	1.34
$K + 3(z = 1) + xn$	6.91 ± 0.09	54.62	17.52
$K + 1(z = 1) + \alpha + xn$	91.3 ± 0.5	44.8	82.0
$^{41-xn}K + p + \alpha + xn$	86.1 ± 0.5	43.4	80.2
$^{38-xn}Ar + 2\alpha + xn$	43.0 ± 0.3	4.12	7.21
$Ar + 2(z = 1) + \alpha + xn$	52.4 ± 0.3	90.7	88.1
$^{40-xn}Ar + 2p + \alpha + xn$	47.2 ± 0.3	84.6	84.8
$Cl + 1(z = 1) + 2\alpha + xn$	85.6 ± 0.6	66.9	85.4
$^{37-xn}Cl + 1p + 2\alpha + xn$	81.5 ± 0.6	64.8	83.5
$Cl + 3(z = 1) + 1\alpha + xn$	6.03 ± 0.10	26.97	5.87
$^{34-xn}S + 3\alpha + xn$	63.2 ± 0.7	22.0	32.1
$S + 2(z = 1) + 2\alpha + xn$	26.0 ± 0.4	59.0	44.9
$S + 4(z = 1) + 1\alpha + xn$	0.15 ± 0.02	0.96	-
$P + 1(z = 1) + 3\alpha + xn$	70.6 ± 1.4	64.5	37.2
$^{33-xn}P + 1p + 3\alpha + xn$	68.2 ± 1.4	62.6	36.7
$P + 3(z = 1) + 2\alpha + xn$	0.75 ± 0.09	2.2	-
$P + 2\alpha + Li + xn$	8.1 ± 0.3	1.7	1.9
$P + 1p + 1\alpha + Be + xn$	4.9 ± 0.2	7.0	5.2
$P + 1\alpha + B + xn$	12.9 ± 0.5	21.4	32.4
$^{30-xn}Si + 4\alpha + xn$	70 ± 2	43	65
$Si + 2(z = 1) + 3\alpha + xn$	5.2 ± 0.4	9.2	2.9
$Si + 2\alpha + Be + xn$	7.9 ± 0.5	5.6	3.3
$Si + 1p + 1\alpha + B + xn$	12.5 ± 0.7	36.1	34.2
$Al + 1p + 4\alpha + xn$	32 ± 4	34	64
$Al + 2\alpha + B + xn$	45 ± 5	56.0	40.0

Table 10.4: Experimental and dynamical codes simulated branching ratios for the reaction $^{16}O + ^{30}Si$ at 128 MeV.

channels, which are reported and compared to simulations in Table 10.3 (all $GEMINI^{++}$ cases) and Table 10.4 (**AMD** and **HIPSE**). Like in the previous case, experimental and simulated BR for the most populated channels are reported for an easier and faster com-

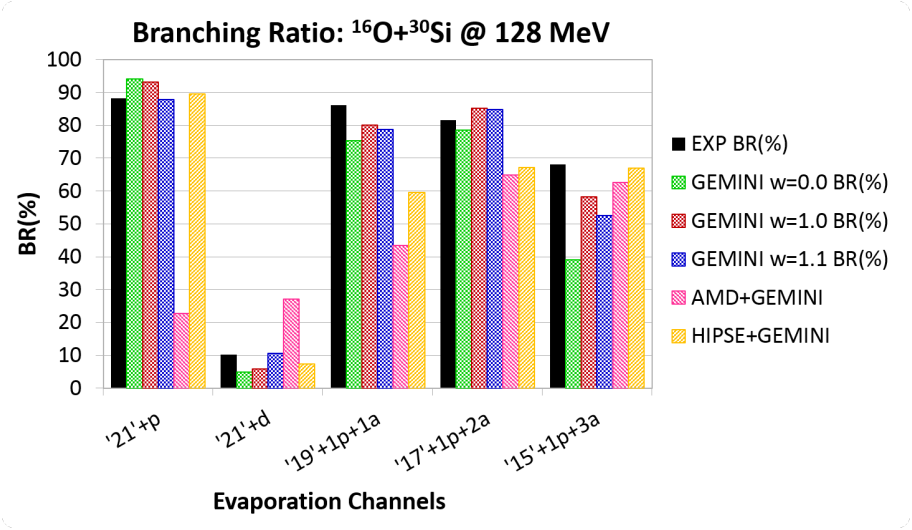

Figure 10.8: Experimental and simulated branching ratio for the reaction $^{16}O + ^{30}Si$ at 128 MeV: odd Z residues. Black bars are experimental data.

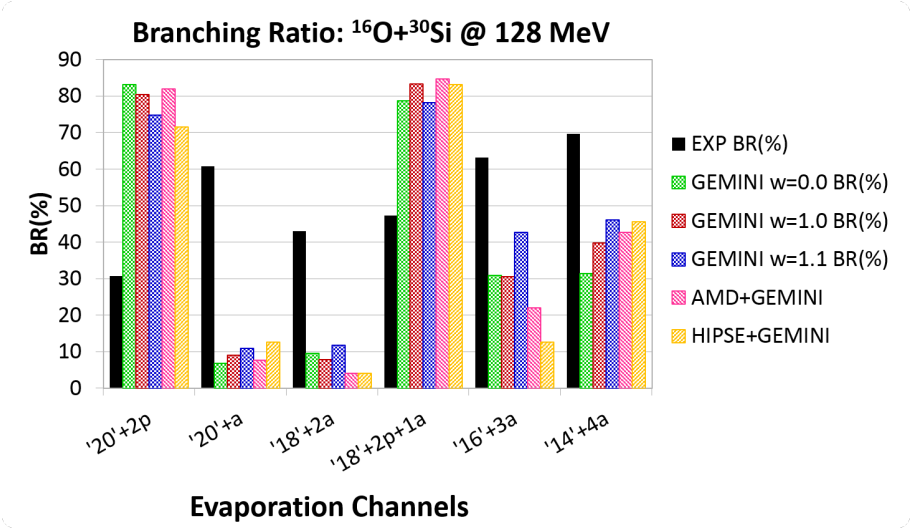

Figure 10.9: Experimental and simulated branching ratio for the reaction $^{16}O + ^{30}Si$ at 128 MeV: even Z residues. Black bars are experimental data.

parison in Fig. 10.8 (odd Z residues) and Fig 10.9 (even Z residues).

We can observe, in general, that a behavior similar to the previous case is observed: again, in fact, a good reproduction is observed for odd Z evaporation residues, while a huge overproduction is observed for the decay channels in which the maximum number of α-particles for a specific residue are emitted ($\#_{max,\alpha} = \frac{22 - Z_{ER}}{2}$). In this case, one can observe that **AMD** completely fails in describing the Sc decay channel, strongly over-predicting tritons and deuterons with respect to protons. All the other simulations are, on the contrary, well describing the relative BR, especially **G11**. For the other odd Z_{ER} the description is quite good even if differences can be observed between the different theoretical recipes. On the contrary, as it was underlined at low energy, the even Z_{ER} are, generally, not described at all by simulations, and, in particular, a much higher BR is observed for the $\#_{\alpha} = \frac{22 - Z_{ER}}{2}$ channel in experimental data, which grows at the expenses of their competing decay channels.

Apart from the BR shown in the figures the following cases worth to be discussed as in the previous reaction:

- S-channel: experimentally the 63% of the cross section is going to the 3α decay channel, while from simulations this channel is populated from 20 to 43 %. Other channels are competing according to simulations like the 2α-2H channel (again higher competitor in **HIPSE** and **AMD**), and the 1B+1p and the 1Be+1α, which takes from 25 to 45% of the cross section according to $GEMINI^{++}$. However, only the 2α+2H are highly experimentally populated (26%);

- P-channel: experimentally 68% in the 1p-3α channel and the rest mainly in 1α-1B (13%) and 2α-1Li (8%). From simulations two main decay channels are competing: the 1α-1B (from 21% in the dynamical model up to 50% for **G00**) and the 1p-3α channel (from 65% in the dynamical models to 60% in **G10**);

- Si-channel: experimentally 70% in the 4α decay channel, while in simulations also the 1p+1α+1B is predicted with a non negligible cross section (from 34% up to 57% depending on model cases);

- *Al*-channel: experimentally 32% in the 1p-4α channel and 45% in the 2α+B channel, while from all simulations a large amount of cross section (from 56 to 90%) goes in the 2α+B decay channel. Only **HIPSE** predicts a lower (40%) in this channel, but it estimates a BR of 64% in the 1p+4α decay channel.

Once again, we report the difference R as a function of the Z_{ER} in Fig. 10.10. Here, the shown BR are those for the branch of the maximum number of α. In this case, it can be underlined how a behavior similar to the low energy case of R is observed when compared to all $GEMINI^{++}$ cases, while for **AMD** and **HIPSE** even $Z_{ER} = 19$ and $Z_{ER} = 17$ yields are underestimated with respect to experimental data.

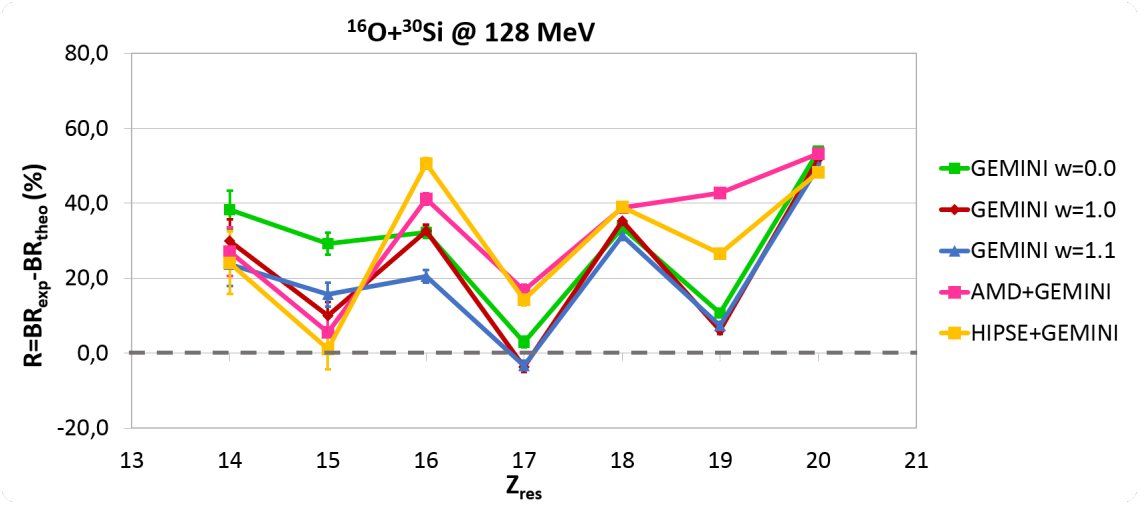

Figure 10.10: Difference R between simulated and experimental branching ratio as a function of Z_{ER}, for the reaction $^{16}O + ^{30}Si$ at 128 MeV.

In Figs. 10.11, 10.12 and 10.13 the Q-value spectra for the multiple-α decay channels are reported: black points are experimental data, colored full lines are simulated events filtered through the apparatus software replica, the light blue dots are, as in the previous case, related to *true Q-value* reconstructed by 4π simulations in which complete events are considered where also the neutron energies are taken into account. In particular, in Fig. 10.11 the *missing energy Q-value* spectrum for the 1α-decay channel ($^{42-xn}Ca+\alpha+xn$) is presented together with that one related to its main competitor channel: $^{44-xn}Ca+2p+xn$; as in the previous study at low energy, it is clear that the 2p channel is over-predicted,

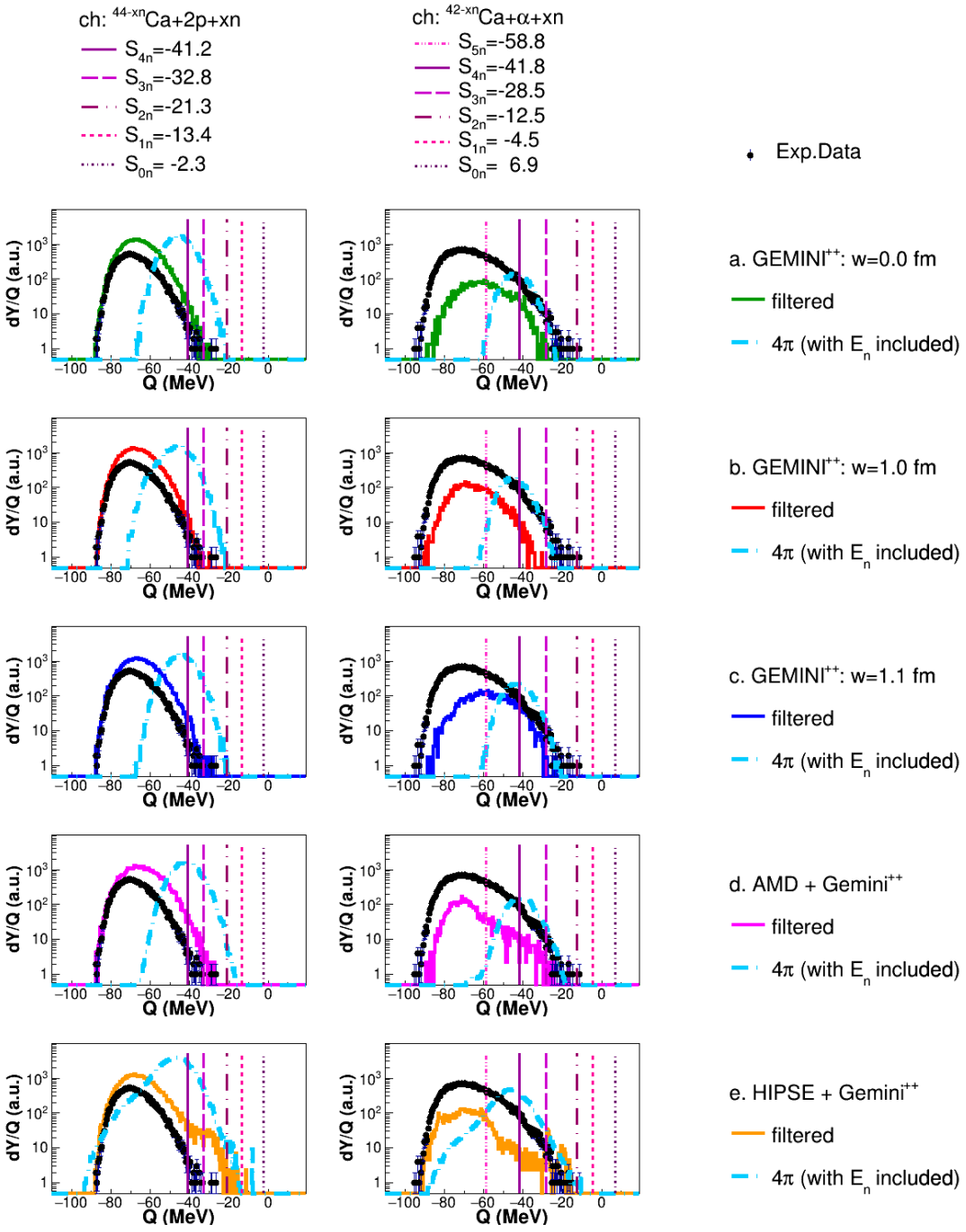

Figure 10.11: *Missing Energy* and *True Q-value* spectra for the two main decay channels where a Ca evaporation residue is left, for the reaction $^{16}O + ^{30}Si$ at 128 MeV.

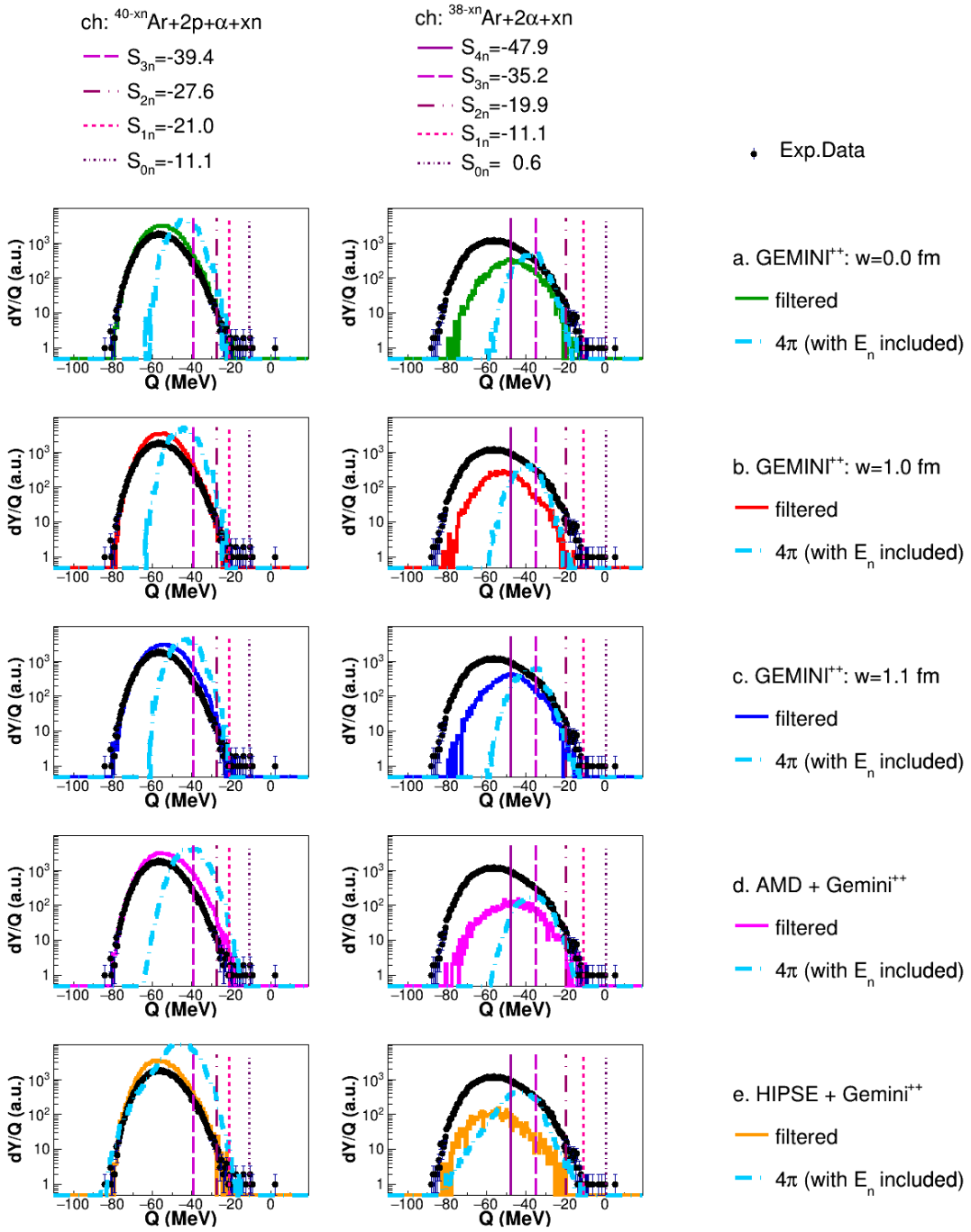

Figure 10.12: *Missing Energy* and *True Q-value* spectra for the two main decay channels where an *Ar* evaporation residue is left, for the reaction $^{16}O + ^{30}Si$ at 128 MeV.

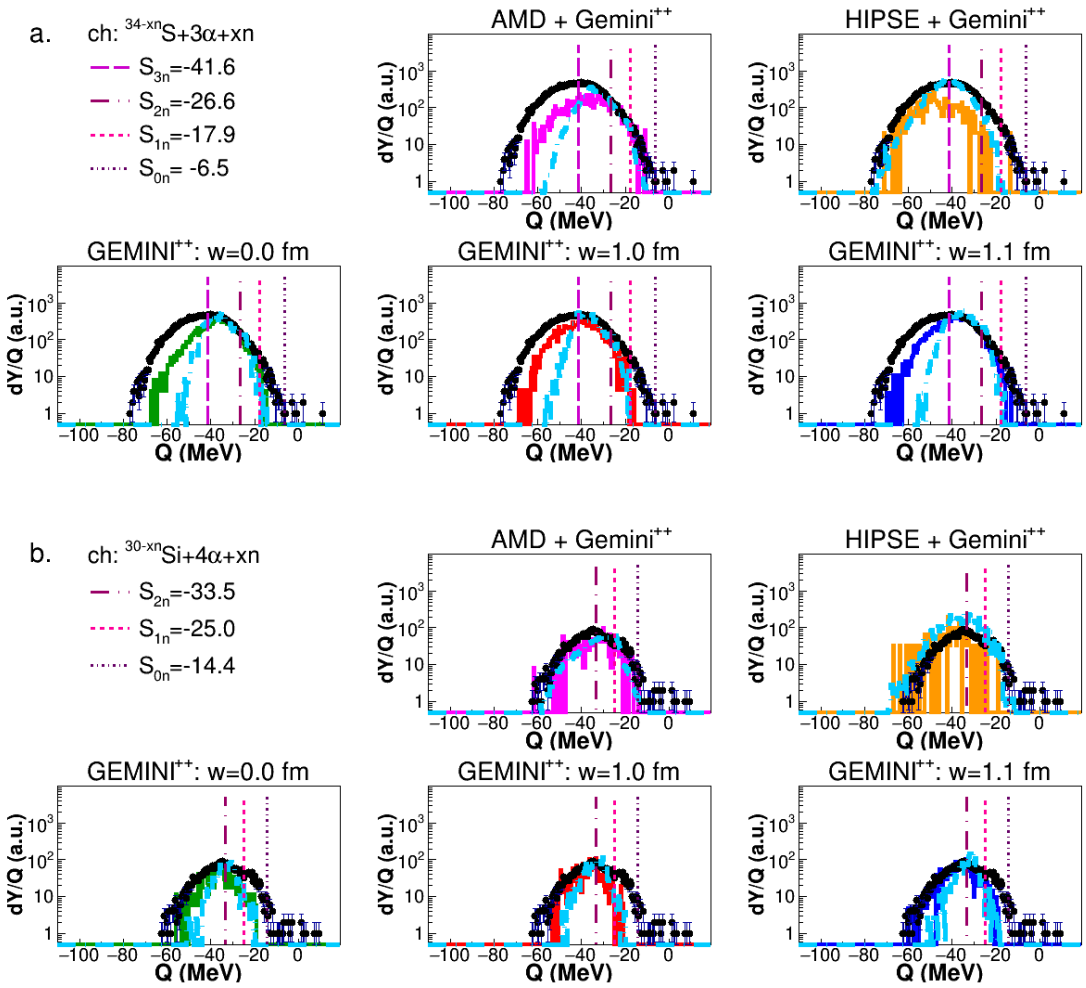

Figure 10.13: *Missing Energy* and *True Q-value* spectra for the two main decay channels where respectively a S (top panels) and a Si (lower panels) evaporation residue is left, for the reaction $^{16}O + ^{30}Si$ at 128 MeV.

but the general shape of the *missing energy Q-value* is reasonably reproduced, apart from the high tail of **HIPSE**. Decay channels from $2n$ to $5n$ can be observed by looking to the *true Q-value* reconstructed spectrum (light blue in the figure) in the $^{44-xn}Ca + 2p + xn$ decay channel, according to the different simulations. Only **HIPSE** is predicting much larger dissipation. For the $^{42-xn}Ca + \alpha + xn$ decay channels, on the contrary, the yield is strongly underestimated by all simulations and also the shape is quite different, with a larger dissipation, only partially reproduced by **HIPSE**. This may indicate that, in this

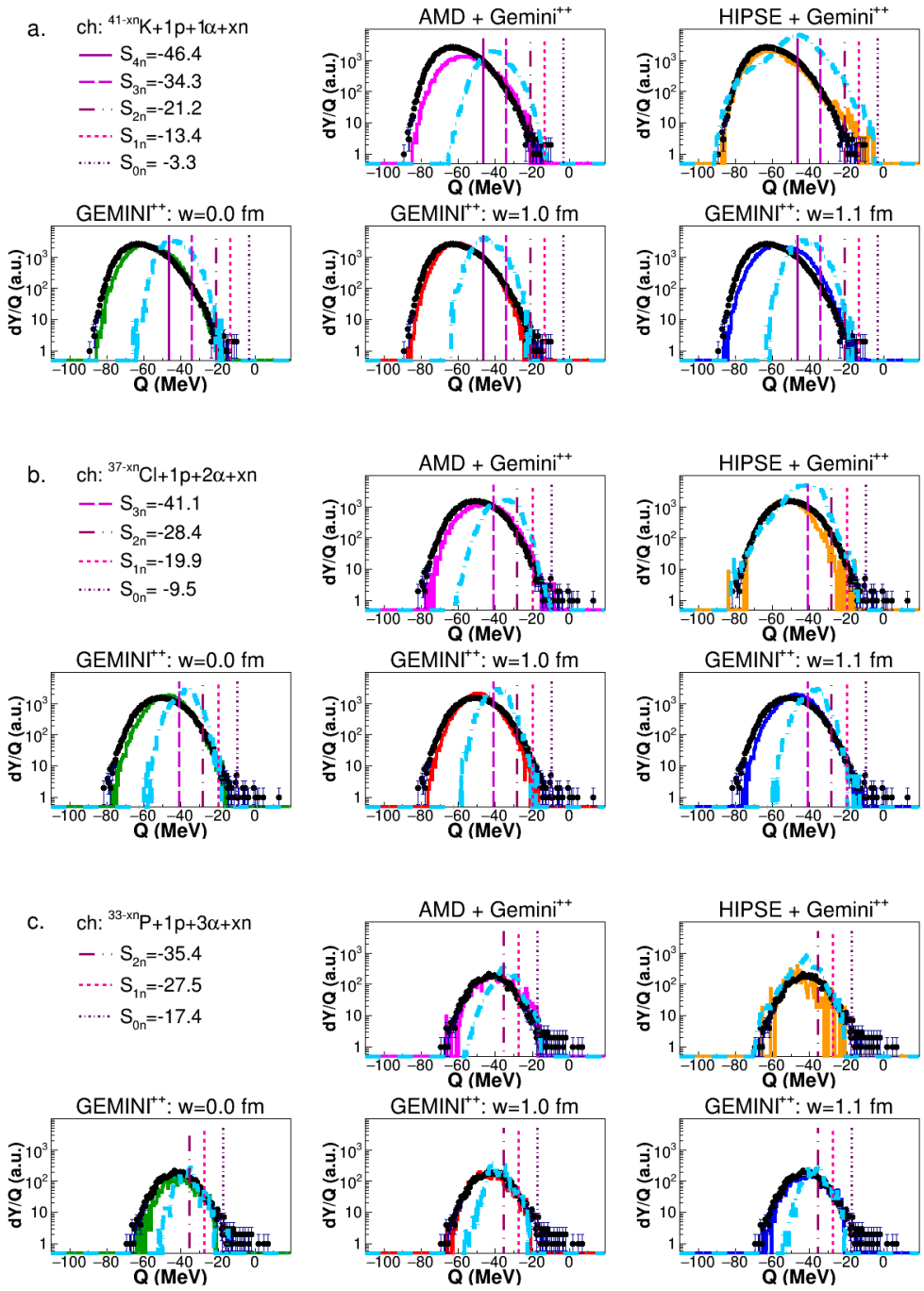

Figure 10.14: *Missing Energy* and *True Q-value* spectra for the three main decay channels where respectively a K (top panels) a Cl (middle panels) and a P (lower panels) evaporation residue is left, for the reaction $^{16}O + ^{30}Si$ at 128 MeV.

case, also important yield for decay channels with a number of emitted neutrons larger than 5 can be expected, at variance with the prediction of all $GEMINI^{++}$ cases and **AMD**.

A similar representation in proposed in Fig. 10.12, where the *missing energy Q-value* for the 2α-decay channel ($^{38-xn}Ar$+2α+xn) is presented together with its main competitor channel: $^{40-xn}Ar + 2p + 1\alpha + xn$. The $^{40-xn}Ar + 2p + 1\alpha + xn$ channels are reasonably reproduced by simulations, both for what concerns the yield and the shape. Only small differences can be observed and the best description is obtained by **G10** and by **HIPSE**. By looking to the *true Q-value* reconstructed by simulations (light blue in the spectrum), one can expect the $2n$, $3n$ and $4n$ opened channels. On the contrary, the $^{38-xn}Ar + 2\alpha + xn$ decay channels are strongly under-predicted by all models and also the shape is not reproduced. However, again **HIPSE** and **G10** are closer to the data: however as previously observed while almost all $GEMINI^{++}$ cases and **AMD** predict the $2n$, $3n$ and $4n$ decay channels, **HIPSE** is predicting a larger dissipation (looking at the *true Q-value*, where neutrons energies are reconstructed), predicting the opening of decay channels with a number of neutrons much larger than $4n$.

In Fig. 10.13 the Q-value for the 3 and 4α-decay channels are illustrated. The *missing energy Q-value* for the $^{34-xn}S + 3\alpha + xn$ channels is not reproduced by simulations: data are generally more dissipative, except for the **HIPSE** case, which is, however, unable to describe the less dissipative part, at variance with $GEMINI^{++}$ and **AMD** cases. Looking, therefore, to the reconstructed *true Q-value* spectra, in this case, one should probably take into account both the higher limit ($0n$) even if with small cross section and the most dissipative one (much larger than $3n$) observed respectively from **AMD** and from **HIPSE**. Observing, on the contrary, the $^{30-xn}Si + 4\alpha + xn$ *missing energy Q-value* spectra, one can observe that there is not a real difference between filtered calculations (no neutron energies) and the *true Q-value*, like if the neutron energies are in this case quite small and do not influence so much the final Q-value spectrum. In this case, the best reproduction is obtained by **AMD** showing a spectrum starting from the $0n$ emission channel ($^{30}Si + 4\alpha$) to that one where an emission of more than $2n$ is largely expected.

In Fig. 10.14 the Q-value spectra for $1p + 1, 2$ and 3α-decay channels, which correspond respectively to K, Cl and P evaporation residues, are illustrated. In the first case, the Q-value spectra related to the channels $^{41-xn}K+p+\alpha+xn$ are well reproduced by **HIPSE** and by **G10**. The reconstructed *true Q-value* show a privileged emission of 3 and $4n$ if one look to **G10**, while a **HIPSE** predicts with non negligible cross section also a larger number of exit neutrons. A similar situation is observed in the $^{37-xn}Cl + p + 2\alpha + xn$ and in the $^{33-xn}P + p + 3\alpha + xn$ cases, where an overall better agreement is observed with all simulations, but where only **HIPSE** predicts a larger *true Q-value* distribution.

10.3 $^{18}O+^{28}Si$ at 126 MeV.

In Tables 10.5 and 10.6, the branching ratio (BR) of the decay channels related to the reaction $^{18}O+^{28}Si$ at 126 MeV are listed, comparing experimental data and simulations. Again, experimental and simulated BR for the most populated channels are reported for a fast comparison in Fig. 10.15 (odd Z residues) and Fig 10.16 (even Z residues).

This reaction is behaving in a very similar way with respect to the previous one, as it is expected since they lead to the same excited compound nucleus ^{46}Ti at the same excitations energy $E^* = 98.5$ MeV. Again, we observe the same overproduction of the α-decaying channels, especially those related to the even Z_{ER}. As in the previous reactions, we discuss some of the BR which are not displayed:

- S-channel: experimentally the 60% of the cross section is going to the 3α decay channel, while from simulations this channel is populated from 18 to 40 %, similarly at the previous reaction. Again, the other competing decay channels are the 2α-2H channel (up to 60% in **HIPSE** and **AMD**), and the 1B+1p and the 1Be+1α, which takes about from 30% to 50% of the cross section according to GEMINI++. Experimentally only the 2α+2H is reasonably highly populated (29%);

- P-channel: experimentally 71% in the 1p-3α channel and the rest mainly in 1α-1B (11%) and 2α-1Li (8%). From simulations two main decay channels are competing: the 1α-1B (from 21% in the dynamical model up to 46% for **G00**) and the 1p-3α

channels	EXP	*GEMINI*$^{++}$ $w = 0.0$ fm	*GEMINI*$^{++}$ $w = 1.0$ fm	*GEMINI*$^{++}$ $w = 1.1$ fm
$^{45-xn}Sc + p + xn$	88 ± 2	92	91	87
$^{44-xn}Sc + d + xn$	10.4 ± 0.4	6.1	7.9	11.3
$^{43-xn}Sc + t + xn$	1.52 ± 0.14	1.60	1.36	2.12
$^{44-xn}Ca + 2p + xn$	30.7 ± 0.4	80.4	77.2	70.8
$^{42-xn}Ca + \alpha + xn$	60.4 ± 0.6	8.3	10.6	13.4
$^{43-xn}Ca + ^{3}He + xn$	0.41 ± 0.03	0.51	0.45	0.80
$K + 3(z = 1) + xn$	7.28 ± 0.09	19.39	15.48	15.70
$K + 1(z = 1) + \alpha + xn$	91.0 ± 0.5	80.1	84.1	83.7
$^{41-xn}K + p + \alpha + xn$	85.9 ± 0.5	78.2	82.1	80.8
$^{38-xn}Ar + 2\alpha + xn$	39.6 ± 0.3	9.93	8.48	12.37
$Ar + 2(z = 1) + \alpha + xn$	55.5 ± 0.3	81.4	86.8	82.8
$^{40-xn}Ar + 2p + \alpha + xn$	50.0 ± 0.3	76.1	81.0	75.8
$Cl + 1(z = 1) + 2\alpha + xn$	85.5 ± 0.6	79.6	87.2	87.4
$^{37-xn}Cl + 1p + 2\alpha + xn$	81.4 ± 0.6	77.5	85.1	84.5
$Cl + 3(z = 1) + 1\alpha + xn$	6.27 ± 0.10	6.38	6.26	6.44
$^{34-xn}S + 3\alpha + xn$	60.3 ± 0.7	27.7	28.3	39.8
$S + 2(z = 1) + 2\alpha + xn$	28.9 ± 0.4	23.7	35.7	31.2
$S + 4(z = 1) + 1\alpha + xn$	0.078 ± 0.014	0.050	0.107	0.087
$P + 1(z = 1) + 3\alpha + xn$	73.8 ± 1.4	41.9	60.5	54.2
$^{33-xn}P + 1p + 3\alpha + xn$	71.0 ± 1.4	40.5	58.3	51.9
$P + 3(z = 1) + 2\alpha + xn$	0.50 ± 0.07	0.27	0.42	0.19
$P + 2\alpha + Li + xn$	7.7 ± 0.3	1.5	1.5	1.5
$P + 1p + 1\alpha + Be + xn$	4.6 ± 0.2	6.6	5.6	5.7
$P + 1\alpha + B + xn$	11.0 ± 0.4	45.4	29.4	36.1
$^{30-xn}Si + 4\alpha + xn$	71 ± 2	31	38	49
$Si + 2(z = 1) + 3\alpha + xn$	4.8 ± 0.4	2.3	4.0	2.4
$Si + 2\alpha + Be + xn$	7.6 ± 0.5	8.0	6.7	6.1
$Si + 1p + 1\alpha + B + xn$	12.3 ± 0.6	55.2	47.5	40.1
$Al + 1p + 4\alpha + xn$	32 ± 3	11	18	13
$Al + 2\alpha + B + xn$	47 ± 5	86	75	84

Table 10.5: Experimental and *GEMINI*$^{++}$ simulated branching ratios for the reaction ^{18}O+^{28}Si at 126 MeV.

channels	EXP	$AMD+$ $GEMINI^{++}$	$HIPSE+$ $GEMINI^{++}$
$^{45-xn}Sc + p + xn$	88 ± 2	29	91
$^{44-xn}Sc + d + xn$	10.4 ± 0.4	26.3	6.8
$^{43-xn}Sc + t + xn$	1.52 ± 0.14	44.55	1.88
$^{44-xn}Ca + 2p + xn$	30.7 ± 0.4	83.6	74.8
$^{42-xn}Ca + \alpha + xn$	60.4 ± 0.6	5.7	12.2
$^{43-xn}Ca + ^{3}He + xn$	0.41 ± 0.03	0.30	1.54
$K + 3(z = 1) + xn$	7.28 ± 0.09	48.21	31.17
$K + 1(z = 1) + \alpha + xn$	91.0 ± 0.5	51.2	67.8
$^{41-xn}K + p + \alpha + xn$	85.9 ± 0.5	49.6	65.4
$^{38-xn}Ar + 2\alpha + xn$	39.6 ± 0.3	4.79	4.61
$Ar + 2(z = 1) + \alpha + xn$	55.5 ± 0.3	90.1	91.1
$^{40-xn}Ar + 2p + \alpha + xn$	50.0 ± 0.3	84.0	85.1
$Cl + 1(z = 1) + 2\alpha + xn$	85.5 ± 0.6	69.7	76.1
$^{37-xn}Cl + 1p + 2\alpha + xn$	81.4 ± 0.6	67.4	73.71
$Cl + 3(z = 1) + 1\alpha + xn$	6.27 ± 0.10	23.94	17.50
$^{34-xn}S + 3\alpha + xn$	60.3 ± 0.7	24.3	18.2
$S + 2(z = 1) + 2\alpha + xn$	28.9 ± 0.4	55.5	63.2
$S + 4(z = 1) + 1\alpha + xn$	0.078 ± 0.014	0.479	0.274
$P + 1(z = 1) + 3\alpha + xn$	73.8 ± 1.4	59.5	67.6
$^{33-xn}P + 1p + 3\alpha + xn$	71.0 ± 1.4	57.1	65.2
$P + 3(z = 1) + 2\alpha + xn$	0.50 ± 0.07	2.7	1.0
$P + 2\alpha + Li + xn$	7.7 ± 0.3	1.7	2.4
$P + 1p + 1\alpha + Be + xn$	4.6 ± 0.2	5.2	4.9
$P + 1\alpha + B + xn$	11.0 ± 0.4	27.6	20.6
$^{30-xn}Si + 4\alpha + xn$	71 ± 2	45	46
$Si + 2(z = 1) + 3\alpha + xn$	4.8 ± 0.4	9.2	6.5
$Si + 2\alpha + Be + xn$	7.6 ± 0.5	7.0	5.4
$Si + 1p + 1\alpha + B + xn$	12.3 ± 0.6	33.0	36.6
$Al + 1p + 4\alpha + xn$	32 ± 3	31	45
$Al + 2\alpha + B + xn$	47 ± 5	65	55

Table 10.6: Experimental and dynamical codes simulated branching ratios for the reaction $^{18}O + ^{28}Si$ at 126 MeV.

channel (from 65% in the dynamical models to 58% in **G10**);

- *Si*-channel: experimentally 71% in the 4α decay channel, while in simulations also the 1p+1α+1B is predicted with a non negligible cross section (from 33% up to 55% depending on model cases);

- *Al*-channel: experimentally 32% in the 1p-4α channel and 47% in the 2α+B channel, while from all simulations a large amount of cross section (from 55 to 86%) goes in the 2α+B decay channel.

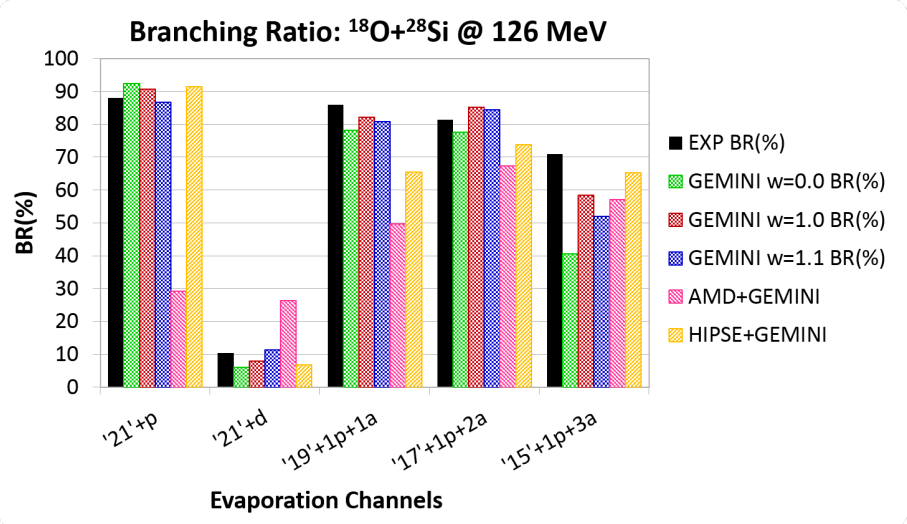

Figure 10.15: Experimental and simulated branching ratio for the reaction $^{18}O+^{28}Si$ at 126 MeV: odd Z residues. Black bars are experimental data.

The trend of the R difference, which is shown in Fig. 10.17 is also very similar to the previous case, since only very small differences can be observed. However, a direct comparison between the different reactions will be more quantitatively discussed in the following chapter. Moreover, even the Q-value spectra for all cases are repeating the same trend and behavior demonstrating that indeed the two reactions lead to a very similar excited source.

In Figs. 10.18, 10.19 and 10.20 the Q-value spectra for the multiple-α decay channels are reported: in particular, in Fig. 10.18 the Q-value spectra for the 1α-decay channel

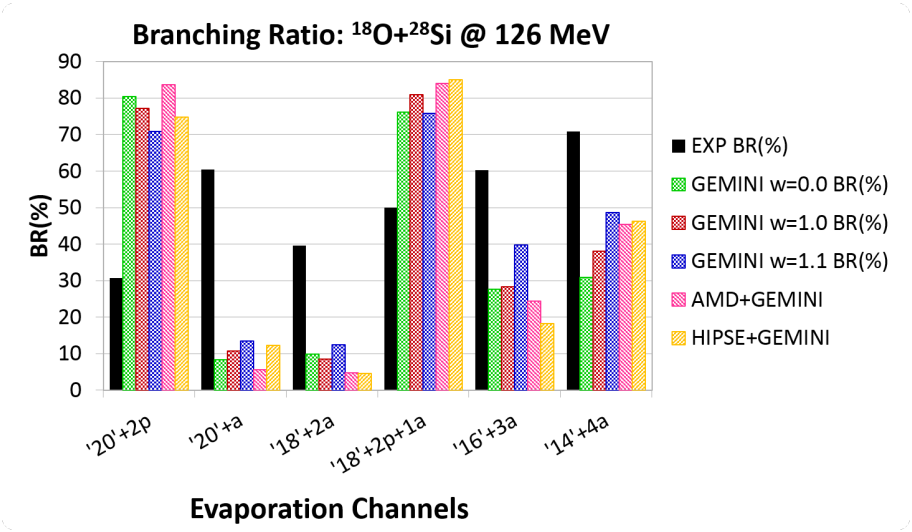

Figure 10.16: Experimental and simulated branching ratio for the reaction $^{18}O+^{28}Si$ at 126 MeV: even Z residues. Black bars are experimental data.

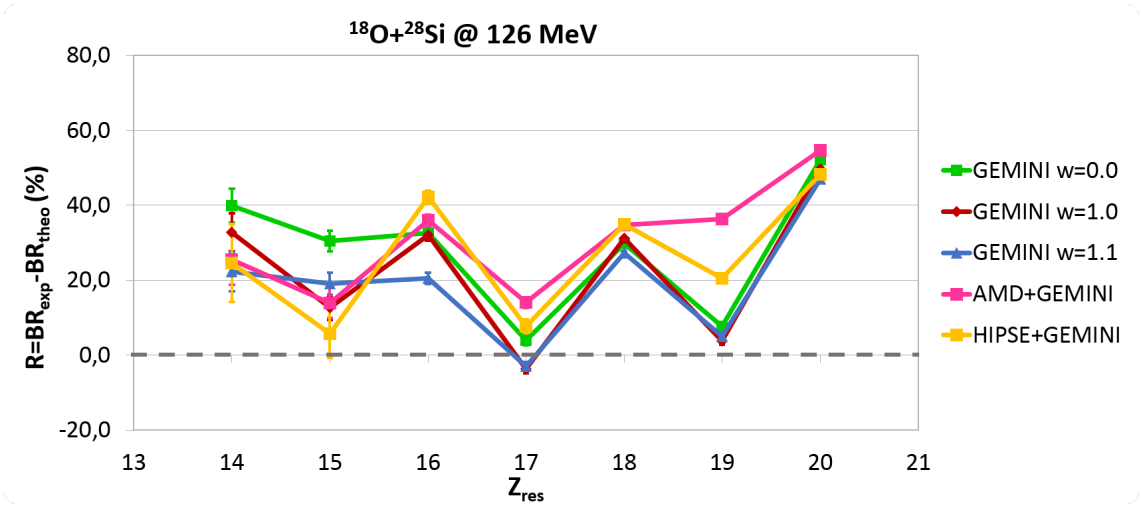

Figure 10.17: Difference R between simulated and experimental branching ratio as a function of Z_{ER}, for the reaction $^{18}O+^{28}Si$ at 126 MeV.

$(^{42-xn}Ca+\alpha+xn)$ are presented together with its main competitor channel: $^{44-xn}Ca+2p+xn$; while the Q-value spectra for the 2α-decay channel $(^{38-xn}Ar+2\alpha+xn)$ is presented, in Fig. 10.19, together with its main competitor channel: $^{40-xn}Ar+2p+1\alpha+xn$. Finally, the Q-value spectra for the 3 and 4α-decay channels are illustrated in Fig. 10.20. Moreover,

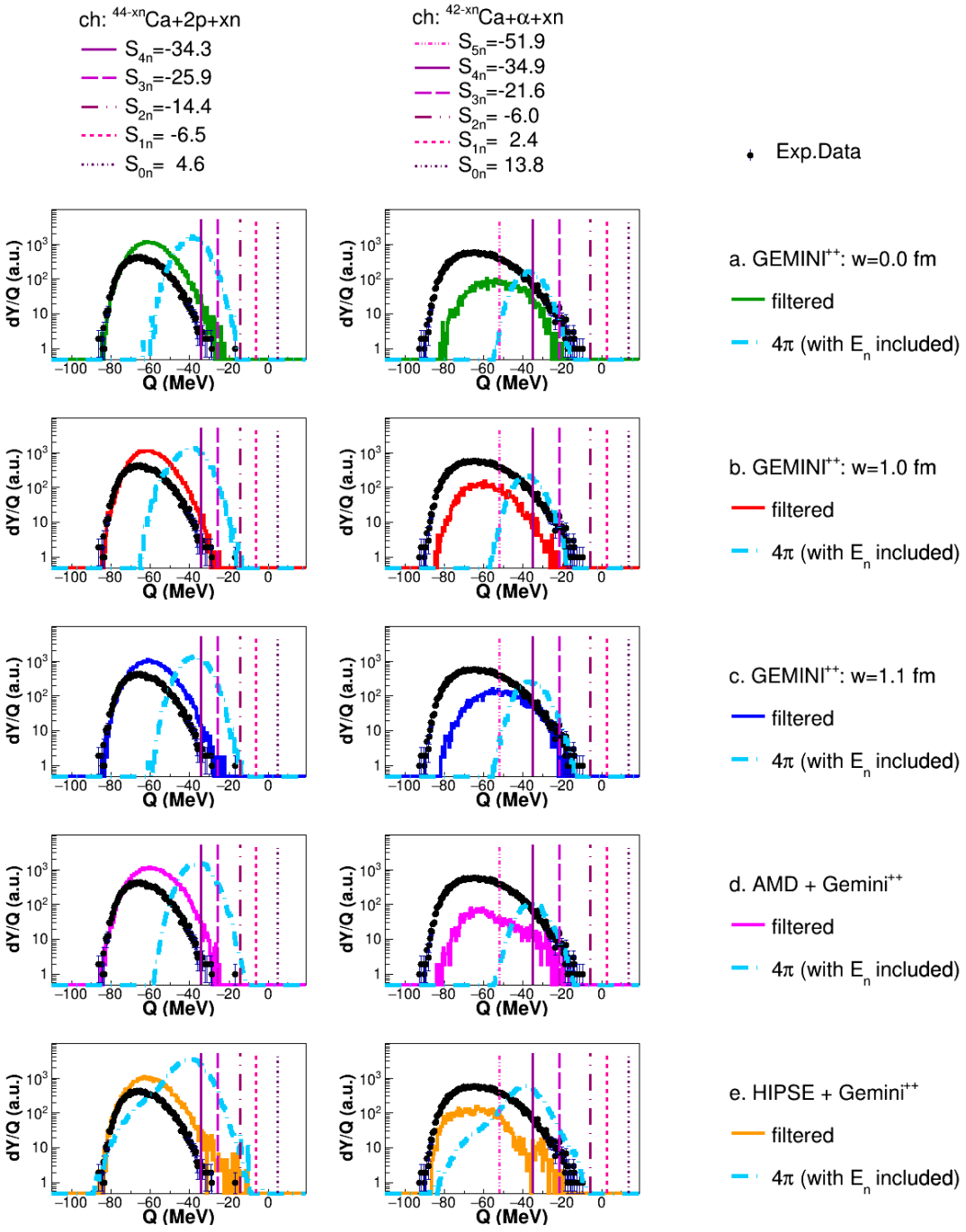

Figure 10.18: *Missing Energy* and *True Q-value* spectra for the two main decay channels where a Ca evaporation residue is left, for the reaction $^{18}O+^{28}Si$ at 126 MeV.

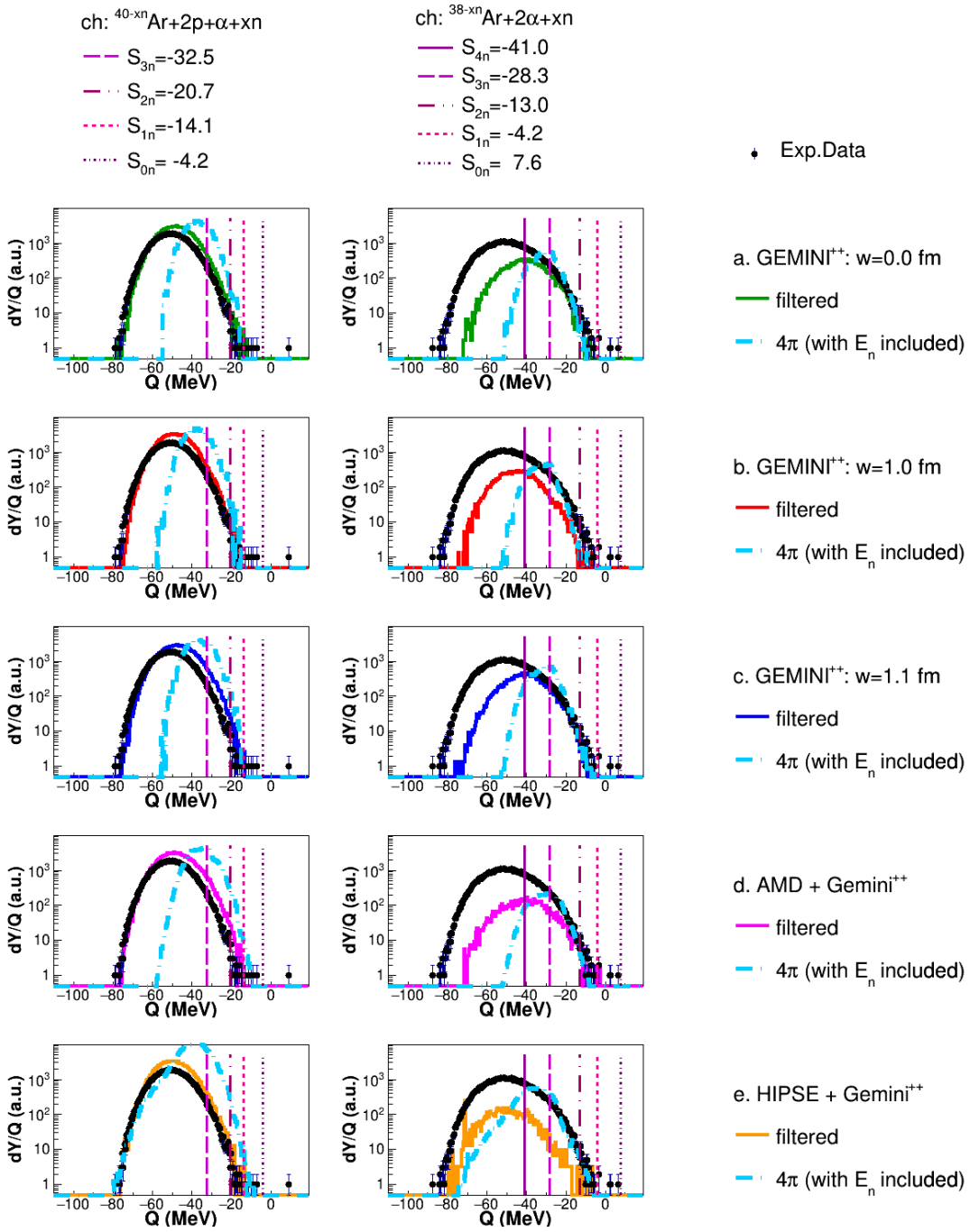

Figure 10.19: *Missing Energy* and *True Q-value* spectra for the two main decay channels where an *Ar* evaporation residue is left, for the reaction ^{18}O+^{28}Si at 126 MeV.

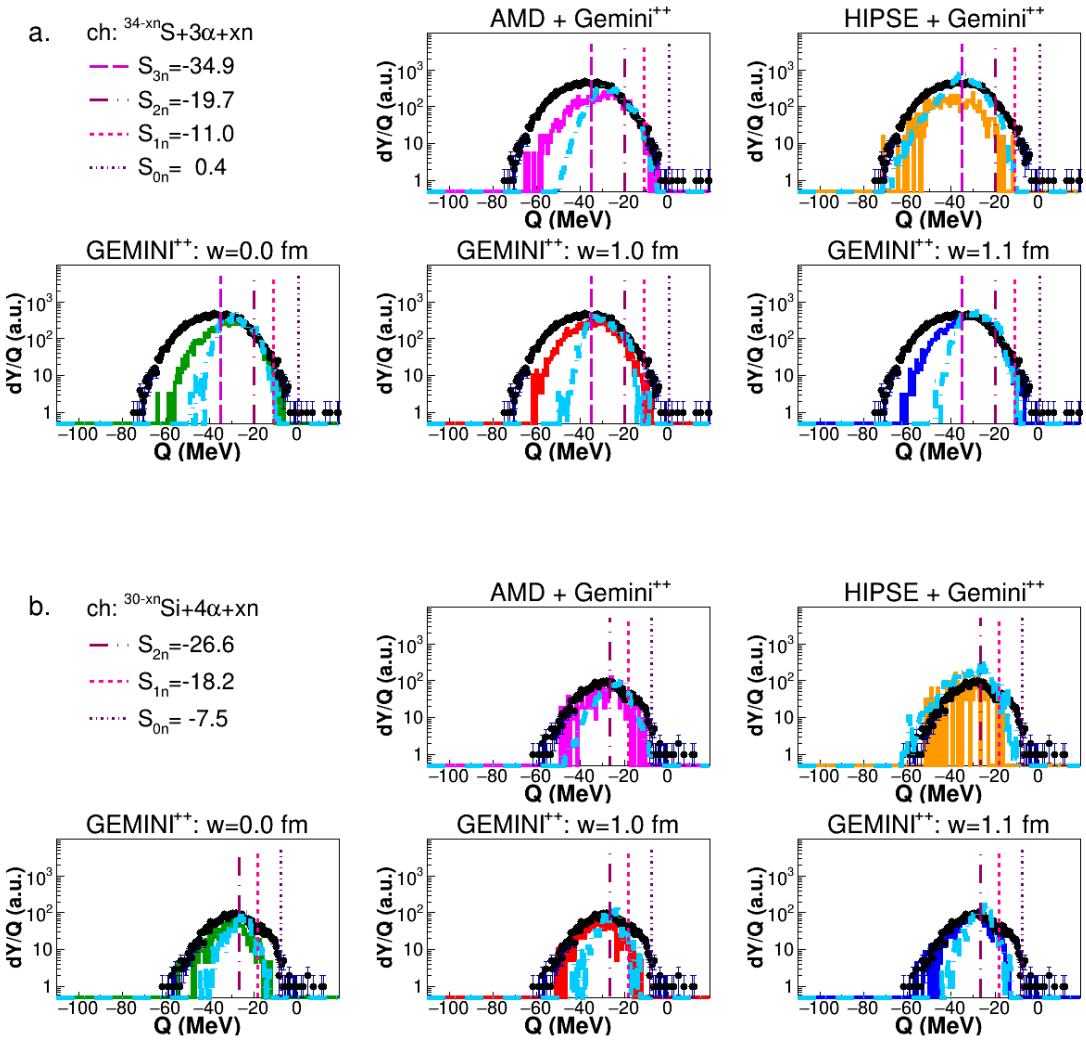

Figure 10.20: *Missing Energy* and *True Q-value* spectra for the two main decay channels where respectively a S (top panels) and a Si (lower panels) evaporation residue is left, for the reaction $^{18}O+^{28}Si$ at 126 MeV.

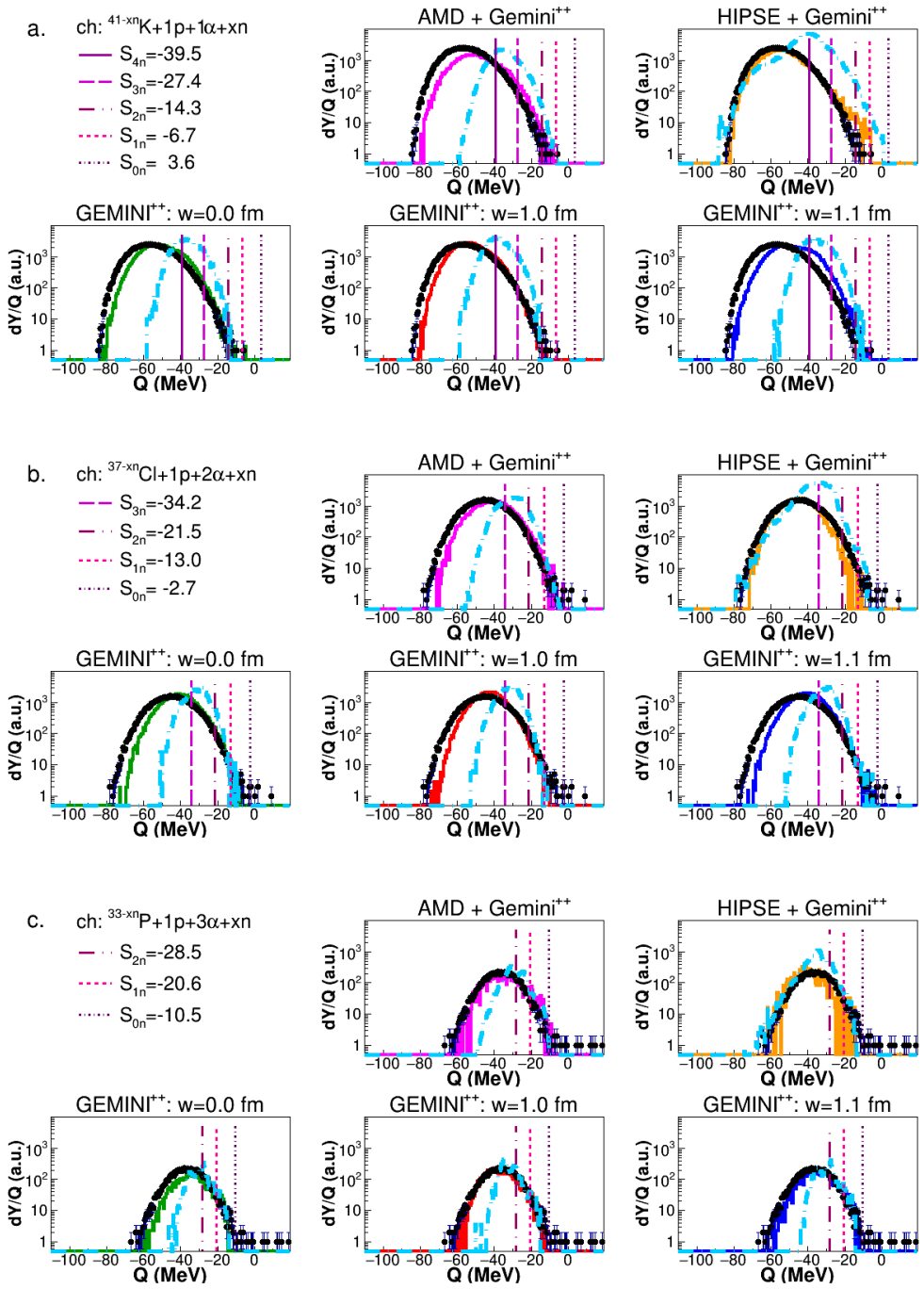

Figure 10.21: *Missing Energy* and *True Q-value* spectra for the three main decay channels where respectively a K (top panels) a Cl (middle panels) and a P (lower panels) evaporation residue is left, for the reaction ^{18}O+^{28}Si at 126 MeV.

the Q-value for the $1p$ + multiple-α decay channels are represented in the Q-value spectra displayed in Fig. 10.21; in particular, the Q-value for $1p$ + 1, 2 and 3α-decay channels, which correspond respectively to K, Cl and P evaporation residues, are illustrated: the shapes and the behavior with respect to simulations are very much similar to the previous reaction.

10.4 $^{19}F+^{27}Al$ at 133 MeV.

In Tables 10.7 and 10.8, the branching ratios of the decay channels related to the reaction $^{18}O+^{28}Si$ at 133 MeV are listed, comparing experimental data and simulations. Fig. 10.22 shows the experimental and simulated BR for the most populated channels for odd Z residues, while in Fig 10.23 the BR related to even Z residues are reported.

Similarly, to the previous reactions, even at this higher excitation energy, we observe a quite reproducible behavior by simulations for events in coincidence with odd-Z residues, while still a strong disagreement is observed with even Z_{ER}. However, it can be noticed that the BR are somehow reduced with respect to those found for the same channel at lower energies. The BR which are not displayed in the plots:

- S-channel: experimentally the 50% of the cross section is going to the 3α decay channel and another 37% goes into the 2α+2H, while from simulations the first channel is populated from 13 to 28%, while the other competing decay channel is populated up to 67% in **HIPSE** and **AMD** and around $30 \div 40$% in $GEMINI^{++}$. The other competing channels, the 1B+1p and the 1Be+1α, takes about from 30% to 48% of the cross section according to $GEMINI^{++}$. Experimentally they are poorly populated < 12%;

- P-channel: experimentally 77% in the 1p-3α channel and the rest mainly in 1α-1B (7%) and 2α-1Li (7%). From simulations two main decay channels are competing: the 1α-1B (from 11% in the dynamical model up to 31% for **G00**) and the 1p-3α channel (from 70% in the dynamical models to 65% in **G10**);

- Si-channel: experimentally 62% in the 4α decay channel, while in simulations also

channels	EXP	$GEMINI^{++}$ $w = 0.0$ fm	$GEMINI^{++}$ $w = 1.0$ fm	$GEMINI^{++}$ $w = 1.1$ fm
$^{45-xn}Sc + p + xn$	88 ± 2	91	89	84
$^{44-xn}Sc + d + xn$	10.6 ± 0.4	6.9	8.6	12.7
$^{43-xn}Sc + t + xn$	1.65 ± 0.15	1.82	2.10	2.99
$^{44-xn}Ca + 2p + xn$	35.6 ± 0.4	81.2	79.0	71.5
$^{42-xn}Ca + \alpha + xn$	53.4 ± 0.6	6.4	7.7	9.8
$^{43-xn}Ca + ^3He + xn$	0.46 ± 0.03	0.55	0.57	1.14
$K + 3(z = 1) + xn$	9.20 ± 0.11	26.21	22.05	21.48
$K + 1(z = 1) + \alpha + xn$	89.1 ± 0.5	73.1	77.3	77.6
$^{41-xn}K + p + \alpha + xn$	83.3 ± 0.5	71.1	75.1	74.5
$^{38-xn}Ar + 2\alpha + xn$	34.8 ± 0.3	7.33	5.89	8.56
$Ar + 2(z = 1) + \alpha + xn$	59.7 ± 0.4	83.5	89.0	86.0
$^{40-xn}Ar + 2p + \alpha + xn$	52.5 ± 0.3	77.3	81.8	77.4
$Cl + 1(z = 1) + 2\alpha + xn$	81.6 ± 0.6	74.9	81.6	82.8
$^{37-xn}Cl + 1p + 2\alpha + xn$	76.8 ± 0.6	72.8	79.3	79.6
$Cl + 3(z = 1) + 1\alpha + xn$	9.62 ± 0.14	9.56	10.02	9.80
$^{34-xn}S + 3\alpha + xn$	50.1 ± 0.6	19.8	19.6	28.3
$S + 2(z = 1) + 2\alpha + xn$	37.5 ± 0.6	32.6	45.6	43.0
$S + 4(z = 1) + 1\alpha + xn$	0.15 ± 0.02	0.18	0.13	0.19
$P + 1(z = 1) + 3\alpha + xn$	77.0 ± 1.4	49.9	66.3	63.2
$^{33-xn}P + 1p + 3\alpha + xn$	73.5 ± 1.3	47.4	64.9	60.1
$P + 3(z = 1) + 2\alpha + xn$	1.09 ± 0.10	0.81	0.94	0.84
$P + 2\alpha + Li + xn$	6.8 ± 0.3	1.8	1.4	1.4
$P + 1p + 1\alpha + Be + xn$	4.3 ± 0.2	9.4	7.2	7.2
$P + 1\alpha + B + xn$	7.5 ± 0.3	31.5	19.1	19.1
$^{30-xn}Si + 4\alpha + xn$	62 ± 2	28	32	43
$Si + 2(z = 1) + 3\alpha + xn$	9.5 ± 0.5	3.6	5.3	4.8
$Si + 2\alpha + Be + xn$	7.0 ± 0.4	7.0	6.8	6.8
$Si + 1p + 1\alpha + B + xn$	13.6 ± 0.6	57.3	51.3	51.3
$Al + 1p + 4\alpha + xn$	40 ± 3	13	25	25
$Al + 2\alpha + B + xn$	36 ± 3	79	70	70

Table 10.7: Experimental and $GEMINI^{++}$ simulated branching ratios for the reaction $^{19}F + ^{27}Al$ at 133 MeV.

channels	EXP	*AMD+* *GEMINI*$^{++}$	*HIPSE+* *GEMINI*$^{++}$
$^{45-xn}Sc + p + xn$	88 ± 2	20.4	89.5
$^{44-xn}Sc + d + xn$	10.6 ± 0.4	22.8	7.5
$^{43-xn}Sc + t + xn$	1.65 ± 0.15	56.82	3.03
$^{44-xn}Ca + 2p + xn$	35.6 ± 0.4	77.6	71.5
$^{42-xn}Ca + \alpha + xn$	53.4 ± 0.6	10.7	12.6
$^{43-xn}Ca + ^{3}He + xn$	0.46 ± 0.03	0.32	2.25
$K + 3(z=1) + xn$	9.20 ± 0.11	53.63	36.30
$K + 1(z=1) + \alpha + xn$	89.1 ± 0.5	45.6	62.0
$^{41-xn}K + p + \alpha + xn$	83.3 ± 0.5	44.1	59.5
$^{38-xn}Ar + 2\alpha + xn$	34.8 ± 0.3	3.7	4.0
$Ar + 2(z=1) + \alpha + xn$	59.7 ± 0.4	90.3	90.6
$^{40-xn}Ar + 2p + \alpha + xn$	52.5 ± 0.3	83.0	83.11
$Cl + 1(z=1) + 2\alpha + xn$	81.6 ± 0.6	63.7	69.6
$^{37-xn}Cl + 1p + 2\alpha + xn$	76.8 ± 0.6	61.3	67.2
$Cl + 3(z=1) + 1\alpha + xn$	9.62 ± 0.14	29.14	22.22
$^{34-xn}S + 3\alpha + xn$	50.1 ± 0.6	16.3	12.6
$S + 2(z=1) + 2\alpha + xn$	37.5 ± 0.6	63.8	67.0
$S + 4(z=1) + 1\alpha + xn$	0.15 ± 0.02	0.96	0.31
$P + 1(z=1) + 3\alpha + xn$	77.0 ± 1.4	66.0	69.8
$^{33-xn}P + 1p + 3\alpha + xn$	73.5 ± 1.3	63.1	67.0
$P + 3(z=1) + 2\alpha + xn$	1.09 ± 0.10	3.64	3.35
$P + 2\alpha + Li + xn$	6.8 ± 0.3	1.6	3.1
$P + 1p + 1\alpha + Be + xn$	4.3 ± 0.2	4.3	7.4
$P + 1\alpha + B + xn$	7.5 ± 0.3	19.6	11.5
$^{30-xn}Si + 4\alpha + xn$	62 ± 2	42	46
$Si + 2(z=1) + 3\alpha + xn$	9.5 ± 0.5	13.2	10.6
$Si + 2\alpha + Be + xn$	7.0 ± 0.4	4.0	8.6
$Si + 1p + 1\alpha + B + xn$	13.6 ± 0.6	33.8	29.6
$Al + 1p + 4\alpha + xn$	40 ± 3	43	64
$Al + 2\alpha + B + xn$	36 ± 3	46.3	28.6

Table 10.8: Experimental and dynamical codes simulated branching ratios for the reaction $^{19}F+^{27}Al$ at 133 MeV.

the 1p+1α+1B is predicted with a non negligible cross section (from 30% up to 57% depending on model cases);

- *Al*-channel: experimentally 40% in the 1p-4α channel and 36% in the 2α+B channel, while from all simulations a large part of the cross section (from 46 to 79%) goes in the 2α+B decay channel. Only in the **HIPSE** case the cross section is mainly in 1p-4α channel (64%) and the other main channel is the 2α+B with a BR of 29%.

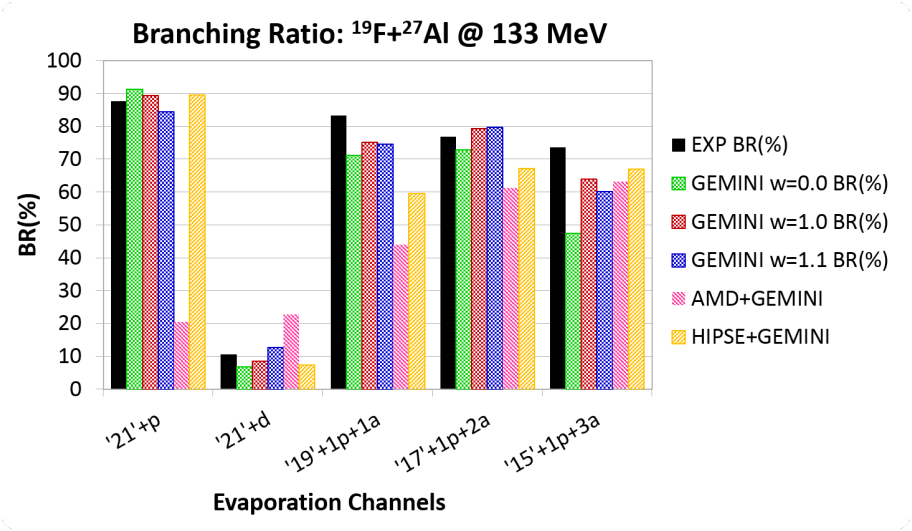

Figure 10.22: Experimental and simulated branching ratio for the reaction ^{19}F+^{27}Al at 133 MeV: odd Z residues. Black bars are experimental data.

In fact, in the graph shown in Fig. 10.24, reporting the difference R, previously defined, as a function of Z_{ER}, a somehow smaller staggering is observed, even if still present.

In Figs. 10.25, 10.26 and 10.27 the Q-value spectra for the multiple-α decay channels are reported: in particular, in Fig. 10.25 the Q-value spectra for the 1α-decay channel ($^{42-xn}Ca + \alpha + xn$) are presented together with its main competitor channel: $^{44-xn}Ca + 2p + xn$; the $2p + xn$ channel shows slightly more dissipated *missing energy Q-value*, which is again still slightly overestimated by all simulations as yield. The shape is, however, reasonably accounted for. It is much different the case of the $^{42-xn}Ca + \alpha + xn$, since the shape is very wide and never reproduced and the yield is largely underestimated by all simulations: indeed, even if models predict a larger *missing energy Q-value* distribution

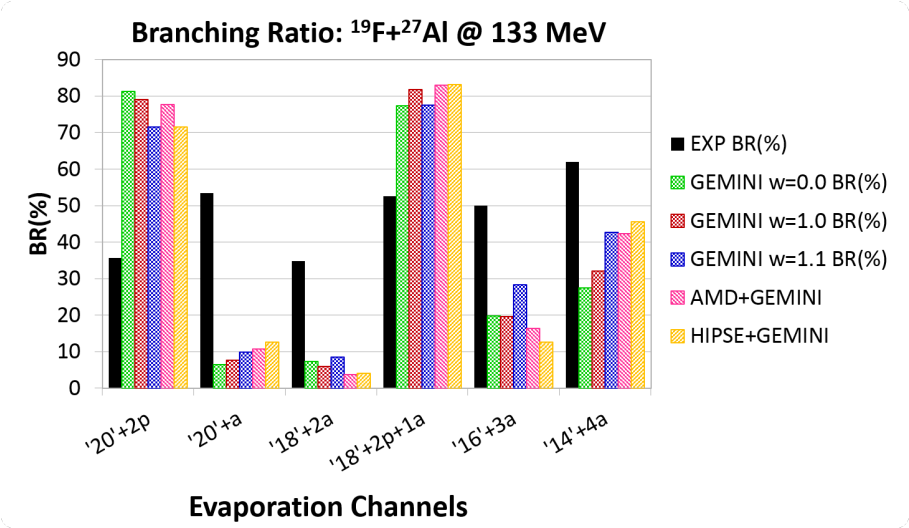

Figure 10.23: Experimental and simulated branching ratio for the reaction $^{19}F+^{27}Al$ at 133 MeV: even Z residues. Black bars are experimental data.

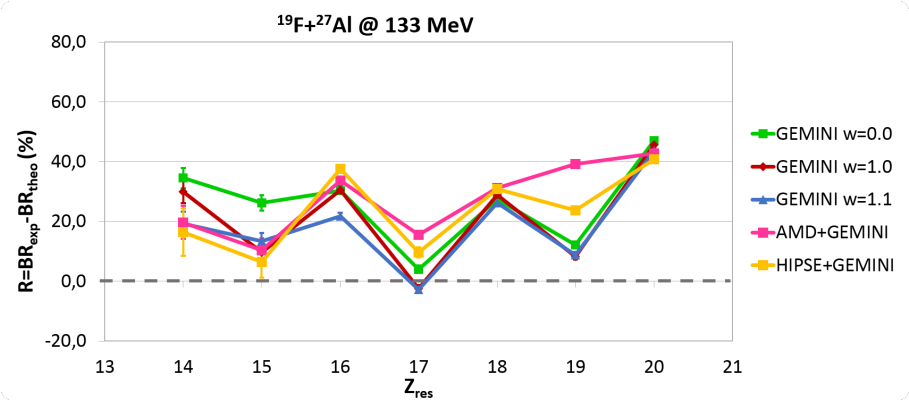

Figure 10.24: Difference R between simulated and experimental branching ratio as a function of Z_{ER}, for the reaction $^{19}F+^{27}Al$ at 133 MeV.

with respect to previous reactions, nevertheless this is not sufficient to reproduce the experimental distribution width.

A similar representation in proposed in Fig. 10.26, where the Q-value for the 2α-decay channel ($^{38-xn}Ar+2\alpha+xn$) is presented together with its main competitor channel: $^{40-xn}Ar+2p+1\alpha+xn$. These channels show a behavior very similar to that at lower energies: the $2p+\alpha+xn$ channels are almost well described by simulations, while the

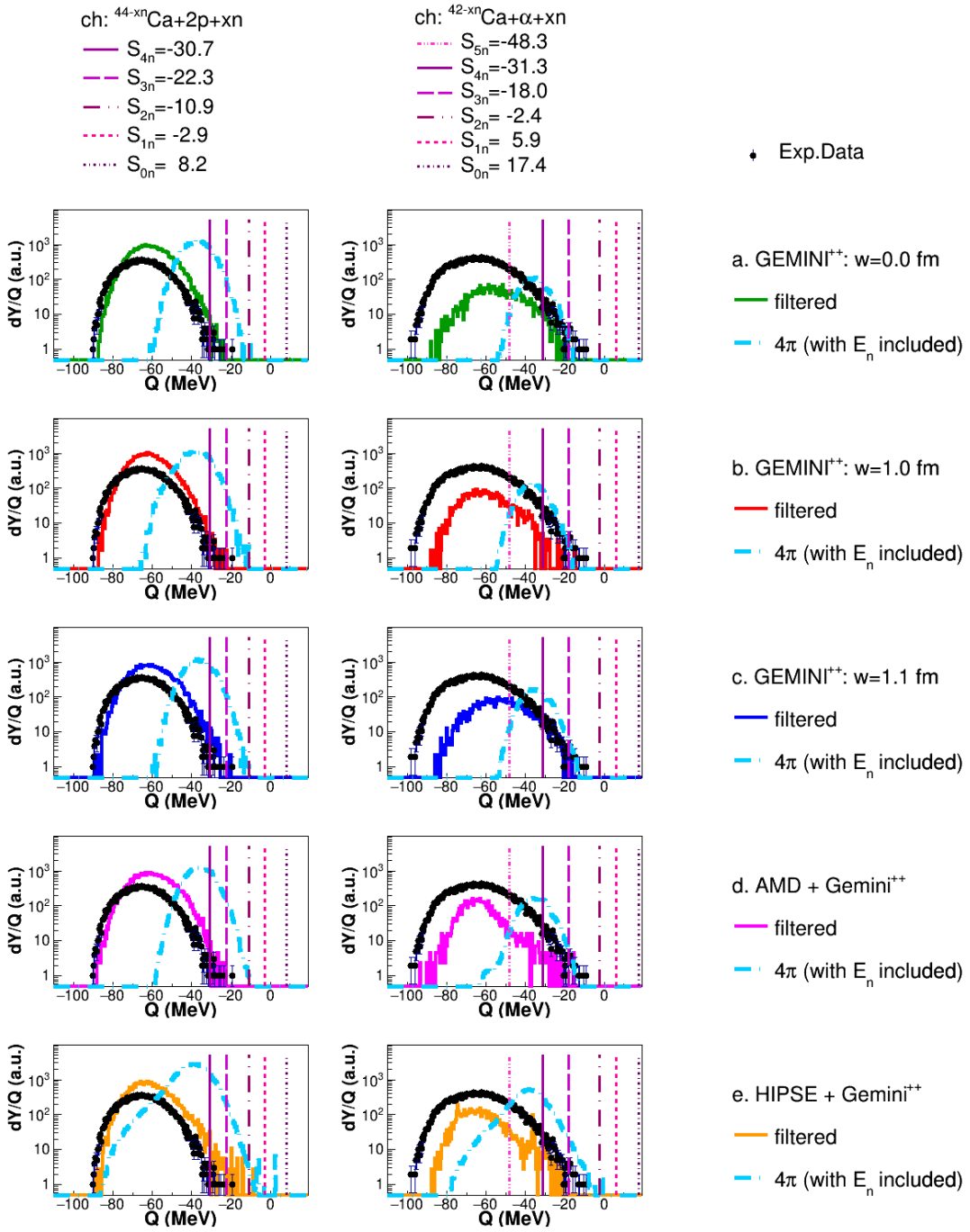

Figure 10.25: *Missing Energy* and *True Q-value* spectra for the two main decay channels where a *Ca* evaporation residue is left, for the reaction $^{19}F+^{27}Al$ at 133 MeV.

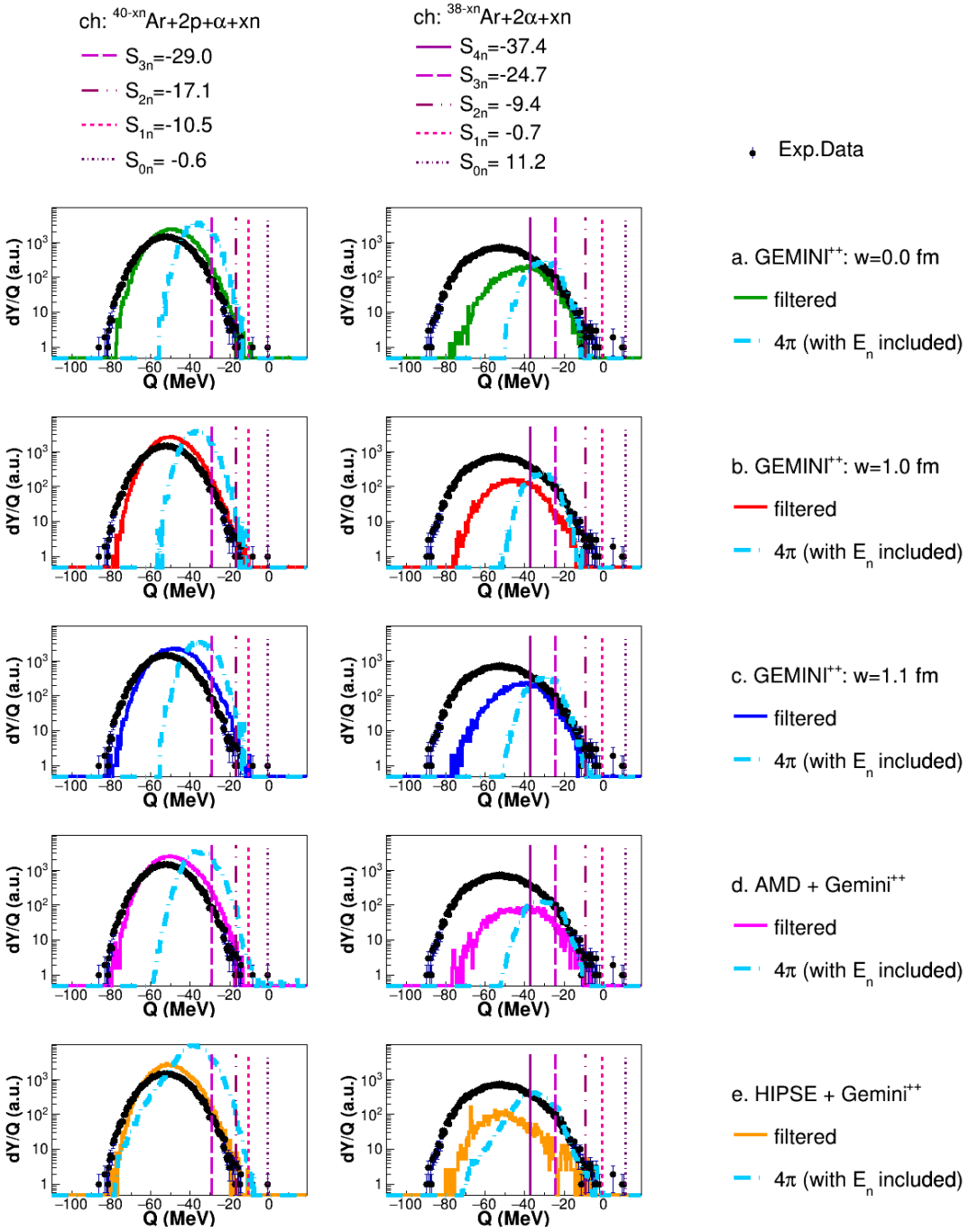

Figure 10.26: *Missing Energy* and *True Q-value* spectra for the two main decay channels where an *Ar* evaporation residue is left, for the reaction $^{19}F+^{27}Al$ at 133 MeV.

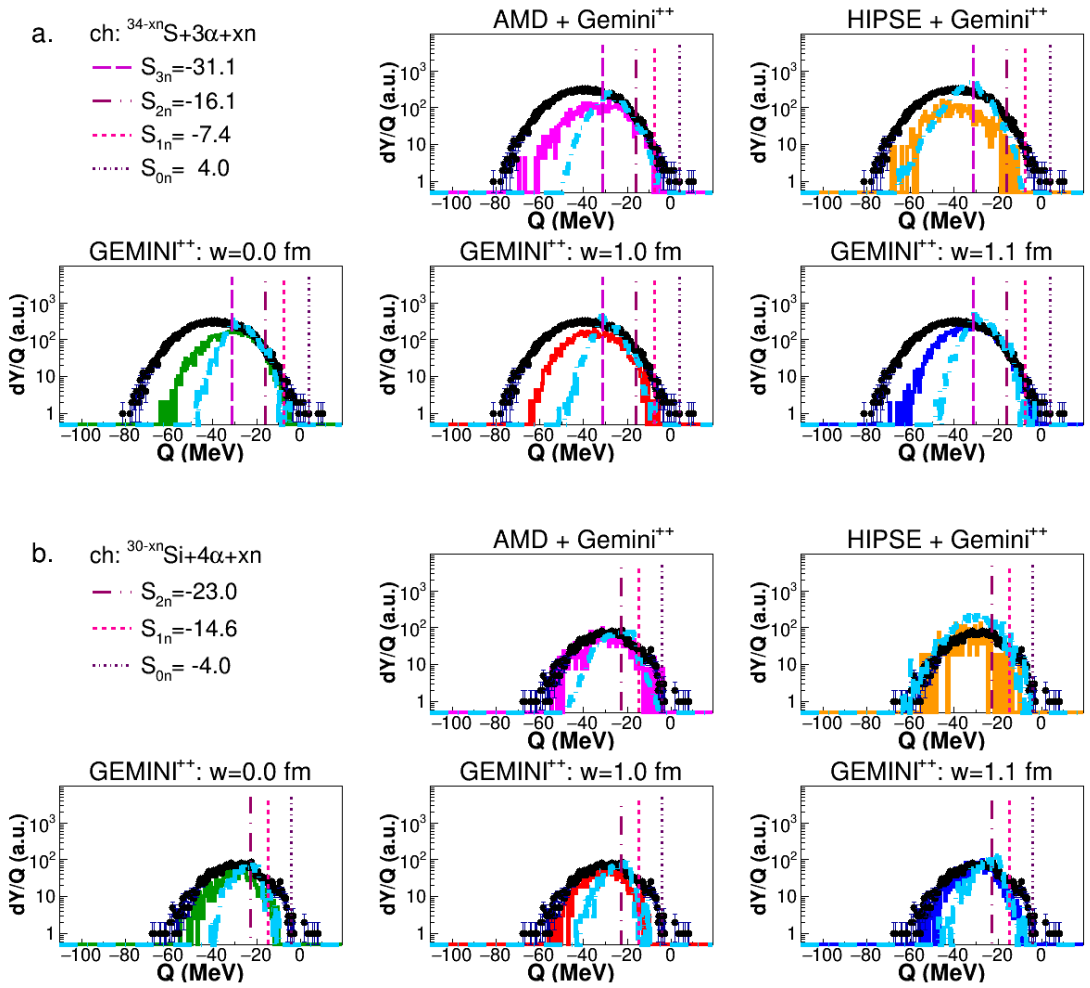

Figure 10.27: *Missing Energy* and *True Q-value* spectra for the two main decay channels where respectively a S (top panels) and a Si (lower panels) evaporation residue is left, for the reaction $^{19}F+^{27}Al$ at 133 MeV.

experimental *missing energy Q-value* for the $2\alpha+xn$ is strongly underestimated, in fact the yield and the width of the distribution are much larger (larger dissipation) than expected by all predictions. The closer simulation as shape is, in this case, **HIPSE**.

In Fig. 10.27 the Q-value for the 3 and 4α-decay channels are illustrated. The first part, regarding the $S+3\alpha+xn$, shows an experimental *missing energy Q-value* distribution much larger (more dissipative) than simulations with a larger discrepancy than the one observed at low energy. On the contrary, the 4α decay channel Q-value distribution is

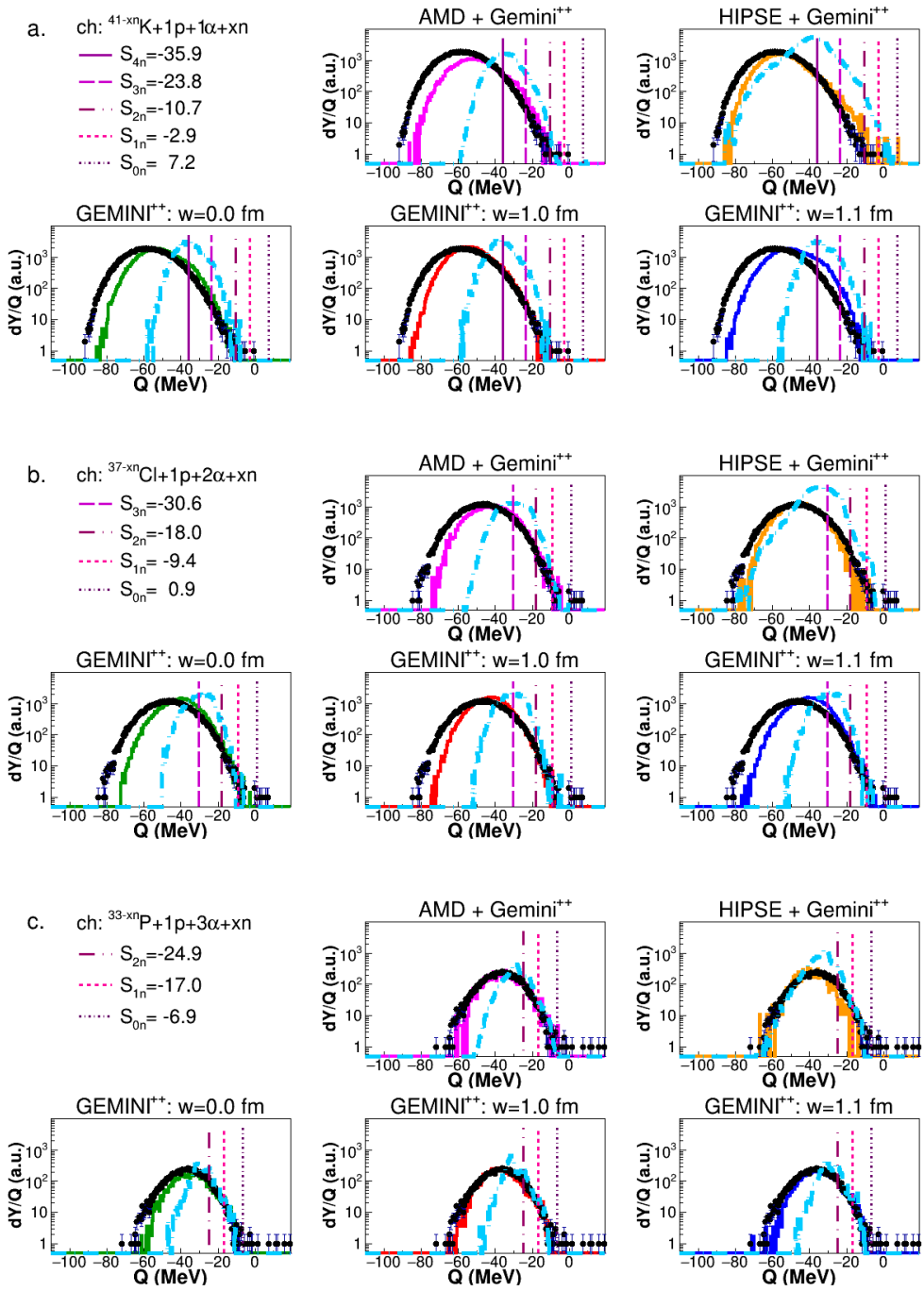

Figure 10.28: *Missing Energy* and *True Q-value* spectra for the three main decay channels where respectively a K (top panels) a Cl (middle panels) and a P (lower panels) evaporation residue is left, for the reaction $^{19}F+^{27}Al$ at 133 MeV.

better reproduced by all simulations.

In Fig. 10.28 the Q-value distribution for the $1p$ + multiple-α decay channels are reported; in particular, the Q-value for $1p$ + 1, 2 and 3α-decay channels, which correspond respectively to K, Cl and P evaporation residues, are illustrated. In the first case, the Q-value distributions related to the channels $^{41-xn}K+p+\alpha+xn$ are larger than simulations, showing a wider dissipation. A similar situation is observed in the $^{37-xn}Cl+p+2\alpha+xn$, however, the differences between experimental and simulated distributions are strongly reduced and, in the case of **HIPSE**, they are almost canceled. In the $^{33-xn}P+p+3\alpha+xn$ cases, an overall better agreement is observed with all simulations, but a larger *true Q-value* distribution is, as usual, predicted by **HIPSE**.

Main Results in Tables

The main results obtained in this thesis, reported in Chapters 6-10, are summarized in the following tables:

- Table 10.9: summary of results for quasi-complete events analysis (Chapter 6);
- Table 10.10: summary of results for complete events analysis (Chapter 7);
- Tables 10.11-10.14: summary of results for exclusive events analysis (Chapters 8-10).

LCP	BEST MODELS	NOTES
p	**G11**	For all the four reactions, the experimental angular distributions are overestimated by simulations in the $29.5^o \div 82.5^o$ angular region.
d	**G11**	Also **AMD** code reproduces the energy shape.
t	**G00** (^{16}O @ 7 MeV/u) **G10** (^{16}O @ 8 MeV/u & ^{19}F @ 7 MeV/u) **G00** (^{18}O @ 7 MeV/u)	For all the four reactions, the experimental angular distributions are reproduced only in the $97.5^o \div 150.4^o$ angular region.
^3He	**G10**	For all the four reactions, the experimental angular distributions are flatter than simulated ones in the $29.5^o \div 150.4^o$ angular region, while it is more peaked in the $8.8^o \div 17.4^o$ angular region.
α	**AMD** (^{16}O @ 7 MeV/u) **G11** & **AMD** (^{16}O @ 8 MeV/u & ^{18}O @ 7 MeV/u) **G00** (^{18}O @ 7 MeV/u)	For all the four reactions, the experimental angular distributions are underestimated by simulations in the $8.8^o \div 17.4^o$ angular region.

Table 10.9: Summary of the quasi-complete events analysis results for the four reactions. "BEST MODELS" are the simulation codes which better reproduce the three experimental observables: Angular Distribution, Multiplicity and Energy Spectra shape.

LCP	BEST MODELS	NOTES
p	**G11**	For all the four reactions, the experimental angular distributions are overestimated by simulations in the $29.5^o \div 82.5^o$ angular region. In the cases of ^{16}O-induced reactions also in the $97.5^o \div 150.4^o$ angular region. The multiplicities are overestimated for $M_p = 2 \div 3$.
d	**G10** ($29.5^o \div 82.5^o$) & **AMD** (^{16}O @ 7 and 8 MeV/u) **G11** (^{18}O @ 7 MeV/u & ^{19}F @ 7 MeV/u)	For both reactions, the experimental angular distribution are underestimated in the $8.8^o \div 17.4^o$ angular region. For both reactions, the experimental angular distributions are well reproduced only in the $97.5^o \div 150.4^o$ angular region.
t	**G11**	For all the four reactions, the experimental angular distributions are reproduced only in the $97.5^o \div 150.4^o$ angular region.
^3He	**AMD**	For all the four reactions, the experimental angular distributions are not reproduced at all.
α	**AMD** (^{16}O @ 7 MeV/u) **G11**(other reactions)	For all the four reactions, the experimental angular distributions are underestimated by simulations in the $8.8^o \div 17.4^o$ angular region. The multiplicities are underestimated for $M_\alpha \geq 2$.

Table 10.10: Summary of the complete events analysis results for the four reactions. "BEST MODELS" are the simulation codes which better reproduce the three experimental observables: Angular Distribution, Multiplicity and Energy Spectra shape.

ER	LCP	OBSERVABLES	BEST MODELS	NOTES
21	-	BR_{tot}	**HIPSE**	-
	1p	BR	**G10** (^{19}F @ 7 MeV/u)	This is the most populated channel with the Sc
			G11 (other reactions)	as evaporation residue ($\sim 90\%$).
	1d	"	**G10** (^{19}F @ 7 MeV/u)	$\sim 9\%$
			G11 (other reactions)	
	1t	"	**G11** (^{16}O-induced reactions)	$\sim 1.5\%$
			G00 (^{18}O & ^{19}F)	
	1p	Q-value	**G10** & **G11**	The better reproduced reaction is the ^{16}O @ 7 MeV/u.
	1d			Increasing the E^*_{CN}, the experimental LCP
	1t			Q-value became more dissipative than simulated one.
	p	Angular Distr.	**AMD** (^{16}O @ 7 MeV/u)	For all the four reactions, the experimental angular
		&	**G00** & **G10** & **G11**	distributions are underestimated by simulations
		E_{lab} shapes	(other reactions)	in the $8.8^o \div 17.4^o$ angular region.
	d	"	**G10**	For ^{16}O-induced reactions, the experimental angular
				distributions are underestimated by simulations
				in the $8.8^o \div 17.4^o$ angular region.
	t	"	-	No simulation reproduces well the experimental
				angular distribution.
20	-	BR_{tot}	**G00** (^{16}O @ 7 MeV/u)	**G11** (^{16}O @ 8 MeV/u) **G10** (^{18}O @ 7 MeV/u)
				AMD (^{19}F @ 7 MeV/u)
				EXP | SIM.
	1α	BR	-	$\sim 60 \div 80\%$ | $\sim 10 \div 30\%$
	2p	"	-	$\sim 20 \div 30\%$ | $\sim 60 \div 80\%$
	1α	Q-value	**G11**	Increasing the E^*_{CN}, the exp. LCP Q-value
	2p			became more dissipative than simulated one.
				p are overestimated & α are underestimated
	p	Angular Distr.	**G10**	For all the reactions, the exp. angular distribution
		&		are overestimated in the whole angular range.
	d	E_{lab} shapes	**G00** & **G10**	For ^{16}O @ 7 MeV/u, the experimental angular
				distribution are overestimated in $29.5^o \div 82.5^o$ region.
	t	"	"	For both ^{16}O-reactions, the angular distribution are
				reproduced only in $97.5^o \div 150.4^o$ angular region.
	^3He	"	-	No simulation reproduces well the experimental
				angular distribution.
	α	"	**G11**	For all the reactions, the exp. angular distribution
				are underestimated in the whole angular range.

Table 10.11: Summary of the exclusive events analysis results for the four reactions for the channels in coincidence with the residues: Sc and Ca.

ER	LCP	OBSERVABLES	BEST MODELS	NOTES
19	-	BR_{tot}	**AMD**	-
	1p+1α	BR	**G10**	This is the most populated channel with the K as evaporation residue ($\sim 80 \div 90\%$). The simulation underestimated it of $\sim 5\%$.
	1p+1α	Q-value	**G10**	The better reproduced reactions are those induced by ^{16}O. Increasing the E^*_{CN}, the experimental LCP Q-value became more dissipative than simulated one.
	p	Angular Distr. & E_{lab} shapes	**G10** & **G11**	The experimental angular distributions are slight overestimated by simulations in the $8.8^o \div 17.4^o$ angular region with the increase of E^*_{CN}.
	d	"	**G11**	-
	t	"	**G10**	-
	^3He	"		No simulation reproduces well the experimental. angular distribution.
	α	"	**G11**	The experimental angular distributions are slight underestimated by simulations in the $8.8^o \div 17.4^o$ angular region with the increase of E^*_{CN}.
18	-	BR_{tot}	**G00** (^{16}O @ 7 MeV/u) **AMD** (other reactions)	
				EXP | SIM.
	2α	BR	-	$\sim 40 \div 70\%$ | $\sim 10 \div 30\%$
	2p+1α	"	-	$\sim 30 \div 50\%$ | $\sim 70 \div 80\%$
	2α	$E_{\alpha-\alpha}$	**G10**	-
	2α	$cos(\theta_k)$	**G10** (^{18}O @ 7 MeV/u) **G00** (other reactions)	- -
	2α 2p+1α	Q-value	**G11**	Increasing the E^*_{CN}, the experimental LCP Q-value became more dissipative than simulated one. 2p+1α are overestimated & 2α are underestimated
	p	Angular Distr. &	**G11** & **G10**	For all the reactions, the exp. angular distribution are overestimated in the whole angular range.
	d	E_{lab} shapes	**G11**	"
	t	"	**G10**	For the three O-reactions, the angular distribution are reproduced only in $97.5^o \div 150.4^o$ angular region.
	^3He	"	**G11**	-
	α	"	**G11**	For all the reactions, the experimental angular distributions are only reproduced in $97.5^o \div 150.4^o$.

Table 10.12: Summary of the exclusive events analysis results for the four reactions for the channels in coincidence with the residues: K and Ar.

ER	LCP	OBSERVABLES	BEST MODELS	NOTES
17	-	BR_{tot}	**G10** (^{16}O @ 7 MeV/u)	**G11** (^{16}O @ 8 MeV/u & ^{18}O @ 7 MeV/u) **G00** (^{19}F @ 7 MeV/u)
	1p+2α	BR	**HIPSE** (^{16}O-reactions) **G11** (^{18}O @ 7 MeV/u) **G10** (^{19}F @ 7 MeV/u)	This is the most populated channel with the Cl as evaporation residue ($\sim 80\%$).
	1p+2α	Q-value	**G11**	The better reproduced reactions are those induced by ^{16}O. Increasing the E^*_{CN}, the experimental LCP Q-value became more dissipative than simulated one.
	p	Angular Distr.	**G10** & **G00** & **G11**	-
	d	&	**AMD**	-
	t	E_{lab} shapes	**G00** & **G10**	-
	^3He	"	**AMD**	The experimental angular distributions are reproduced only in the $8.8^o \div 17.4^o$.
	α	"	**AMD**	The experimental angular distributions are slight underestimated by simulations in the $8.8^o \div 17.4^o$.
16	-	BR_{tot}	-	All simulations slightly underestimate those BR_{tot}.
	3α	BR	-	$\sim 60\%$ (EXP) while $\sim 30\%$ (SIM.)
	3α	E_{rel}	**G10**	-
	3α	Dalitz Plots	**G11** & **G10**	No one model reproduces the exp. bump ($x \sim 20, y = 0$).
	3α	Q-value	**G11**	The better reproduced reactions are those induced by ^{16}O. Increasing the E^*_{CN}, the experimental LCP Q-value became more dissipative than simulated one.
	p	Angular Distr. &	**G11**	For all the reactions, the exp. angular distribution are overestimated in the whole angular range.
	d	E_{lab} shapes	**AMD**	-
	t	"	**G00**	For all the reactions, the exp. angular distribution are slightly overestimated in the whole angular region.
	^3He	"	-	too low statistics
	α	"	**G11** & **AMD**	For all the reactions, the experimental angular distributions are only reproduced in $97.5^o \div 150.4^o$.

Table 10.13: Summary of the exclusive events analysis results for the four reactions for the channels in coincidence with the residues: Cl and S.

ER	LCP	OBSERVABLES	BEST MODELS	NOTES
15	-	BR_{tot}	-	All simulations slightly underestimate those BR_{tot}.
				EXP | SIM.
	$1p+3\alpha$	BR		$\sim 50 \div 70\%$ | $\sim 20 \div 60\%$
	$2\alpha+Li$			$\sim 10\%$ | $\sim 1\%$.
	$1\alpha+B$			$\sim 10 \div 30\%$ | $\sim 20 \div 80\%$
	$1p+3\alpha$	Q-value	**G10** & **G11**	-
	p	Angular Distr.	**HIPSE** & **AMD**	-
	d	&	**AMD**	-
	t	E_{lab} shapes	-	too low statistics
	^3He	"	-	"
				reproduced only in the $8.8^o \div 17.4^o$.
	α	"	**AMD**	-
14	-	BR_{tot}	-	All simulations underestimate those BR_{tot}.
				EXP | SIM.
	4α	BR	**G11**	$\sim 70 \div 80\%$ | $\sim 30 \div 60\%$
	$2\alpha+Be$			$\lesssim 10\%$
	$1p+1\alpha+B$			$\sim 15 \div 25\%$ | $\sim 20 \div 50\%$
	3α	Q-value	**AMD**	-
	p	Angular Distr.	**G11**	For all the reactions, the exp. angular distribution
		&		are overestimated in the whole angular range.
	d	E_{lab} shapes	-	too low statistics
	t	"	-	"
	^3He	"	-	"
	α	"	**AMD**	For all the reactions, the experimental angular
				distributions are only reproduced in $97.5^o \div 150.4^o$.
13	-	BR_{tot}	-	All simulations underestimate those BR_{tot}.
				EXP | SIM.
	$1p+4\alpha$	BR	**G11**	$\sim 30 \div 40\%$ | $\sim 10 \div 60\%$
	$2\alpha+B$			$\sim 40 \div 50\%$ | $\sim 30 \div 90\%$
	p	Angular Distr.	**AMD**	low statistics
	α	& E_{lab} shapes	"	low statistics

Table 10.14: Summary of the exclusive events analysis results for the four reactions for the channels in coincidence with the residues: P, Si and Al.

Conclusions

In this thesis, the study of four heavy ion induced reactions have been reported; those reactions have been compared to each other in order to evaluate possible structural effects on the dynamics of the reactions. The studied systems are $^{16}O + ^{30}Si$ at 7 and 8 MeV/u, $^{18}O + ^{28}Si$ at 7 MeV/u and $^{19}F + ^{27}Al$ at 7 MeV/u. All systems lead to the same compound nucleus in case of central collision and complete fusion, that is $^{46}Ti^*$. The systems are studied in a low energy range, where the onset of pre-equilibrium emission is foreseen, but a region in which the statistical decay from compound nucleus is reasonably under control. The data, to be analyzed, have been severely selected, to avoid possible influence from contaminants and only central collisions, leading to fusion-evaporation, have been analyzed, by selecting the coincidence between light charged particles (LCP) or light fragments ($Z < 6$) and one big evaporation residue (ER).

The four studied reactions are different for mass entrance channel asymmetry $\eta = \frac{A_T - A_p}{A_T + A_p}$ and for excitation energy E^*_{CN}. In Table 10.15, these parameters and combinations of them are shown for each reaction, since they will be used to compare some of the obtained results.

The four systems have been chosen so to have three different mass entrance channel systems with the same projectile velocity (7 MeV/u) and the last system with a higher beam velocity (8 MeV/u) to have two different systems with the same E^* (^{16}O at 128 MeV and ^{18}O at 126 MeV). The aims were:

- to compare the thermalized emission between the different systems to look for possible structural effects in the statistical decay;

Systems	E_* (MeV)	$\eta = \frac{A_T - A_p}{A_T + A_p}$	$\frac{\eta}{E_*}$	$\eta * E_*$
$^{16}O +^{30} Si$ at 111 MeV	88,0	0,30	0,00346	26,8
$^{16}O +^{30} Si$ at 128 MeV	98,4	0,30	0,00309	29,9
$^{18}O +^{28} Si$ at 126 MeV	98,5	0,22	0,00221	21,4
$^{19}F +^{27} Al$ at 133 MeV	103,5	0,17	0,00168	18,0

Table 10.15: Mass entrance channel asymmetry η, excitation energy E^*_{CN} and two combination of them for the four studied reactions.

- to underline if any fast emission could be envisaged at these energies and if this component could be differently either enhanced or reduced, especially in the α-particle exit channel, depending on the diverse structures of the colliding partners;
- to compare experimental data with different simulations based on both statistical and on dynamical models: $GEMINI^{++}$ was used for the first part, with different parametrizations $w = 0.0$ fm (**G00**), $w = 1.0$ fm (**G10**) and $w = 1.1$ fm (**G11**), $AMD + GEMINI^{++}$ (**AMD**) and $HIPSE + GEMINI^{++}$ (**HIPSE**) were used for the comparison to dynamics.

Experimental data on different exclusive exit channels have been analyzed and compared between the different reactions and for each reaction to the different model predictions.

First of all the comparison between the charge (Z) distributions obtained for the four reaction after the strict selection on ER-LCP coincidences is displayed in Fig. 10.29. The Z-distributions show the expected trend as a function of the E^*, since the higher the E^* the longer the decay chains, which are shown by an enhancement of the yield of the lower Z residues. This is also well accounted for by all used models, as reported in Fig. 10.30, which slightly differ by each other on the relative yields of a specific residue, but which all show the expected and previously discussed trend as a function of E^*.

In Fig. 10.31 the experimental branching ratios (BR) for the major decay channels are reported comparing the four different reactions data; the decay channels are displayed

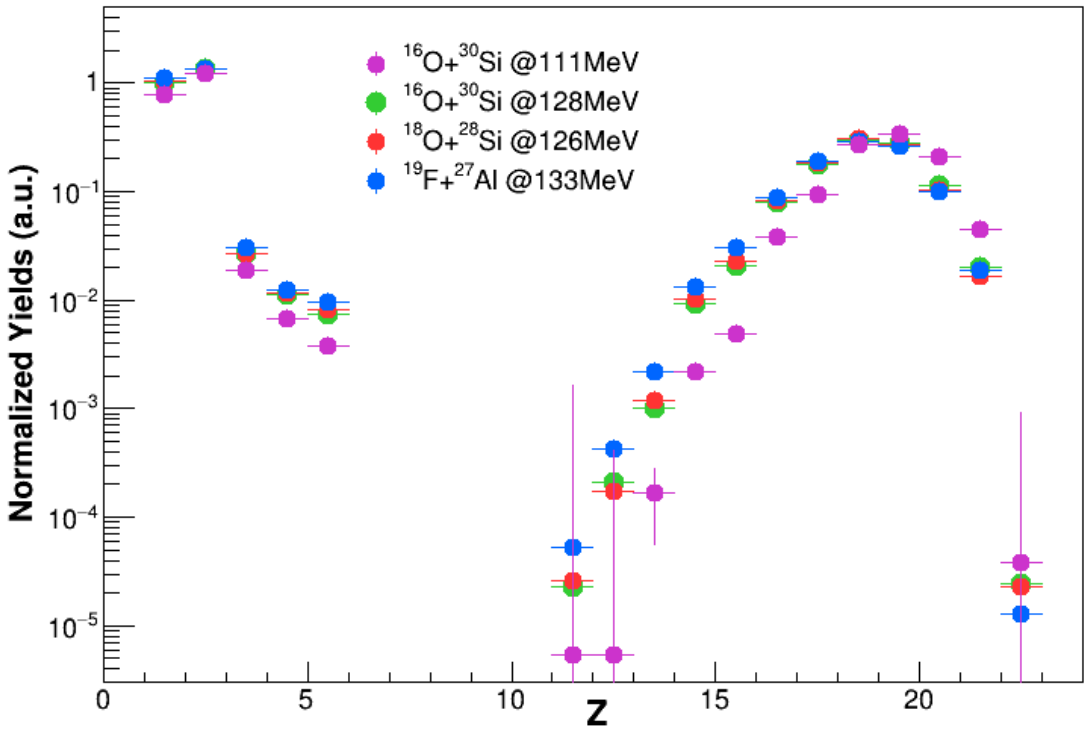

Figure 10.29: Comparison of experimental Z-distributions among the four reactions: $^{16}O+^{30}Si$ at 111 MeV, $^{16}O+^{30}Si$ at 128 MeV, $^{18}O+^{28}Si$ at 126 MeV and $^{19}F+^{27}Al$ at 133 MeV.

apart from the indication of neutron emission, which can only be deduced by comparison to model, as it was discussed in the thesis. It is quite clear that a trend as a function of the excitation energy can be observed, which goes in different direction depending on the decay channel. A better representation will be provided in the following and the result will be discussed for the decay channels in which the maximum number of α-particle can be emitted ($\#_{max,\alpha} = \frac{Z_{tot} - Z_{ER}}{2}$).

In Fig. 10.32, the difference on the BR between the experimental data derived for the four reactions and simulations performed with $GEMINI^{++}$ statistical code with the three different parametrization of the emission barrier (w = 0.0 fm, w = 1.0 fm and w = 1.1 fm) are displayed. As a general trend the difference in BR is quite similar for the four

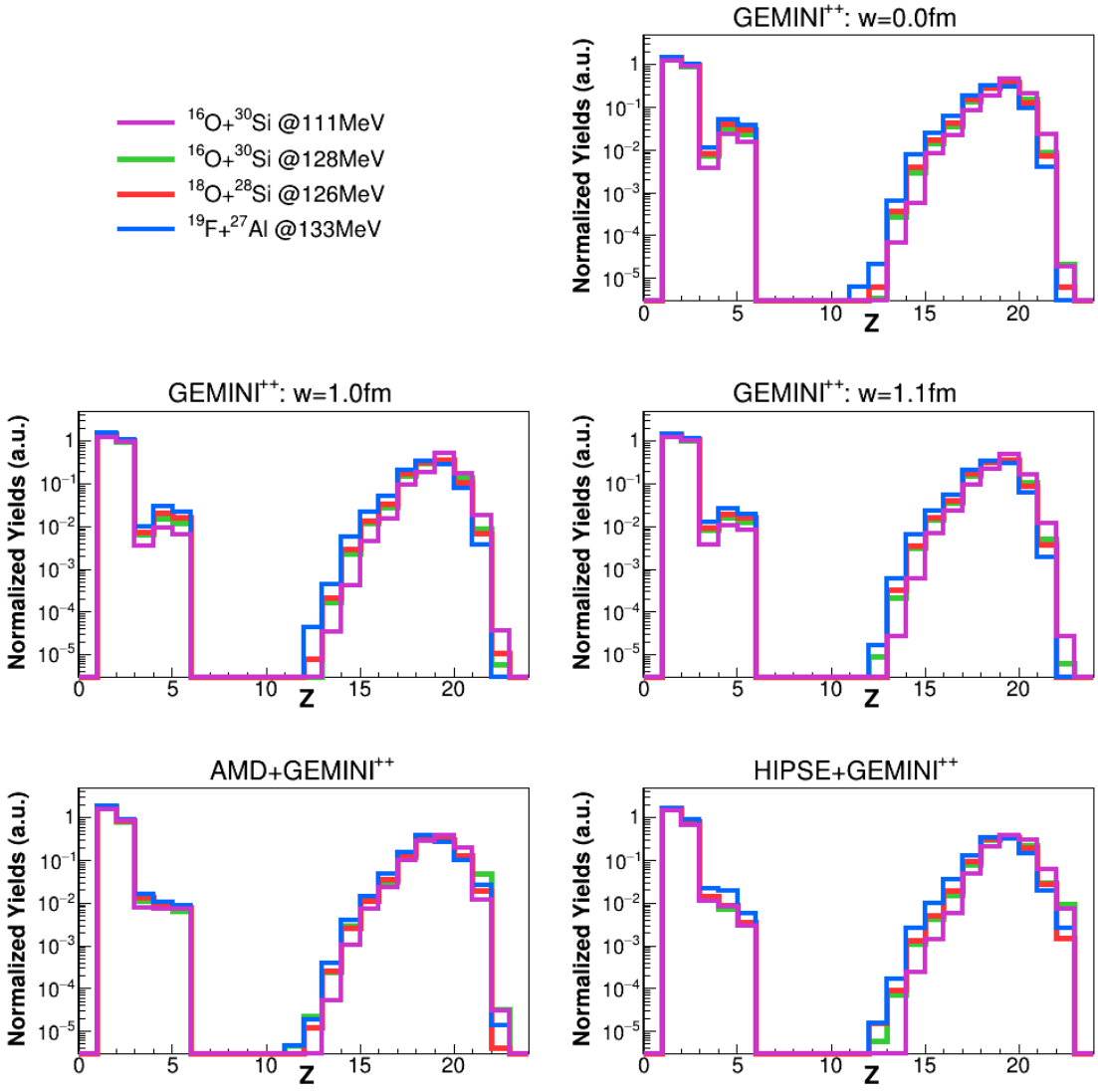

Figure 10.30: Comparison of simulated Z-distributions among the four studied reactions. The simulations are made with $GEMINI^{++}$ using the barrier parameters $w = 0.0$ fm, $w = 1.0$ fm and $w = 1.1$ fm, with $AMD + GEMINI^{++}$ and with $HIPSE + GEMINI^{++}$

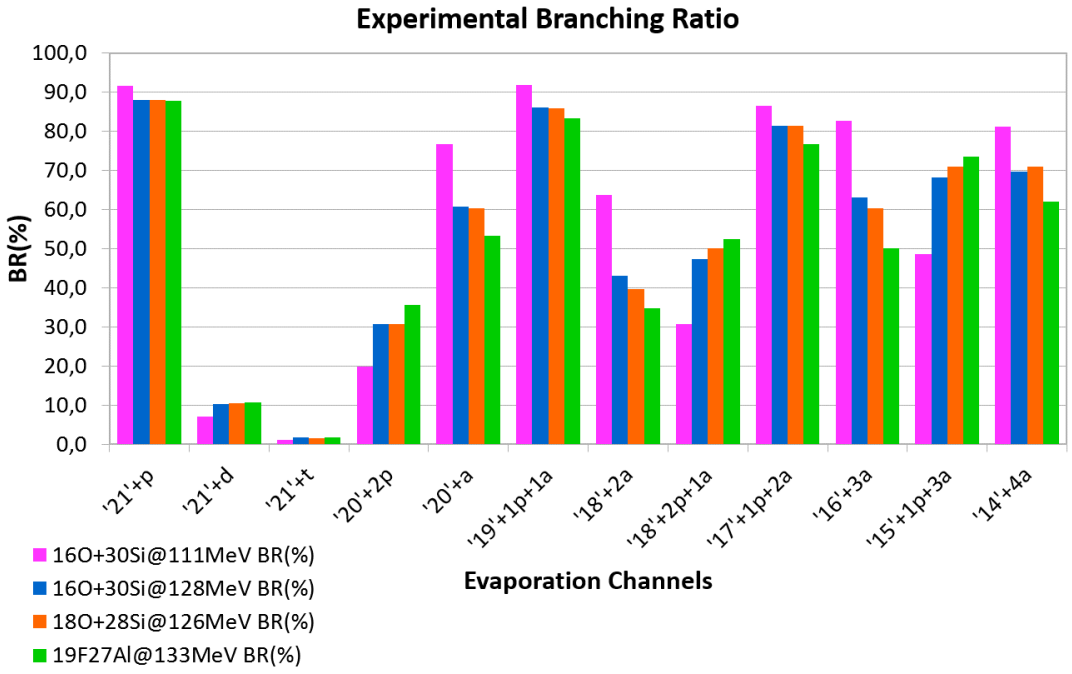

Figure 10.31: Comparison of experimental branching ratio among the four reactions.

reactions, even if in some specific channels like the 2α-channel ($Z_{ER} = 18$) a kind of larger difference is observed for the lower energy reaction almost independently by $GEMINI^{++}$ parametrization. Almost all reactions are quite in agreement with a standard statistical decay in the odd Z_{ER} channels, a part from the $Z_{ER} = 15$, which with all $GEMINI^{++}$ parametrization show a difference in BR similar to even Z_{ER} channels.

The difference at lower energy is even more enhanced when comparing the experimental data with **AMD** and with **HIPSE** (Fig. 10.33). However, in this case it appears that a more clear odd-even staggering effect is present at low energy and even $Z_{ER} = 15$ is better reproduced by **AMD** and **HIPSE**. However, in this case neither the BR difference of $Z_{ER} = 19$ nor that one of $Z_{ER} = 15$ are going to zero. For higher energies the staggering effect is softened and only $Z_{ER} = 15$ is close to zero, for the reaction $^{16}O +^{30} Si$ at 128 MeV. In other words, it seems that statistical model predictions are normally good for

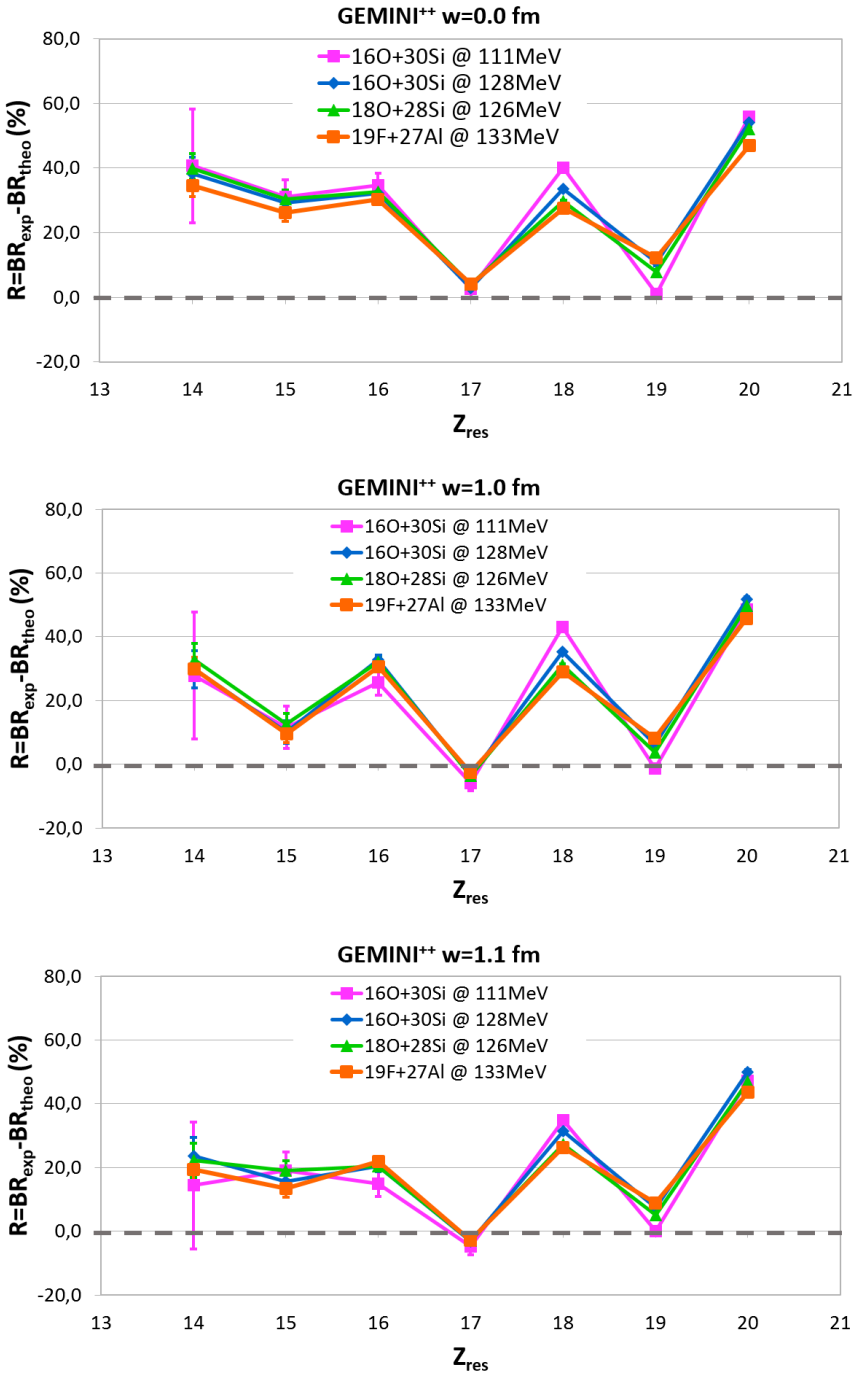

Figure 10.32: Comparison among the four studied reactions of the difference between the experimental and $GEMINI^{++}$ (**G00**, **G10** and **G11**) simulated BR.

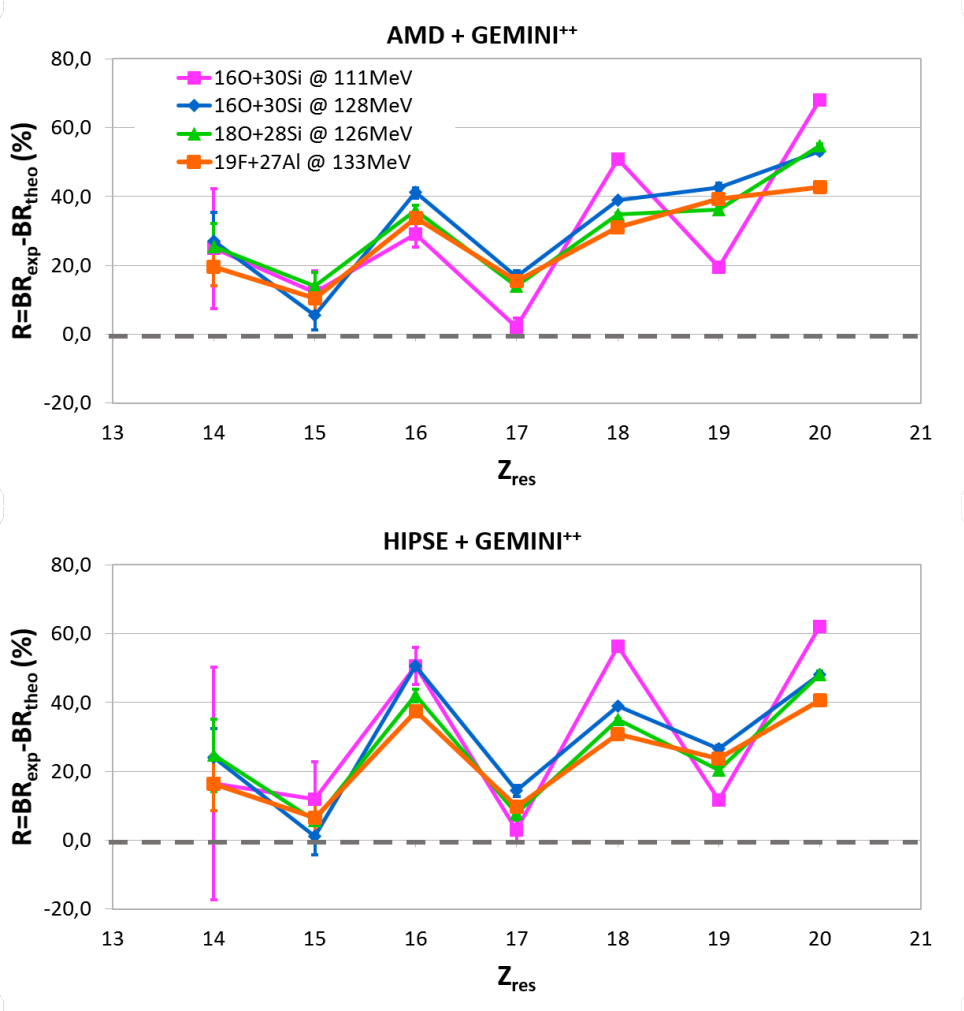

Figure 10.33: Same as Fig. 10.32 but for dynamical simulations: **AMD** and **HIPSE**.

$Z_{ER} = 19$ and $Z_{ER} = 17$, while other studied channels are strongly underestimated in the same way for all the studied reactions. The dynamical models, on the contrary, are able, generally only for some of the studied cases to reproduce $Z_{ER} = 17$ ($^{16}O + ^{30}Si$ at 111 MeV) and $Z_{ER} = 15$ ($^{16}O + ^{30}Si$ at 128 MeV). For all the other cases and decay channels the BR are underestimated, especially for the lower energy.

In order to see if any trend could be envisaged as a function of the CN excitation energy E^* and of the asymmetry parameter η, the trend of the BR obtained in the four cases has been studied and reported in Figs. 10.34 and 10.35 for the experimental data

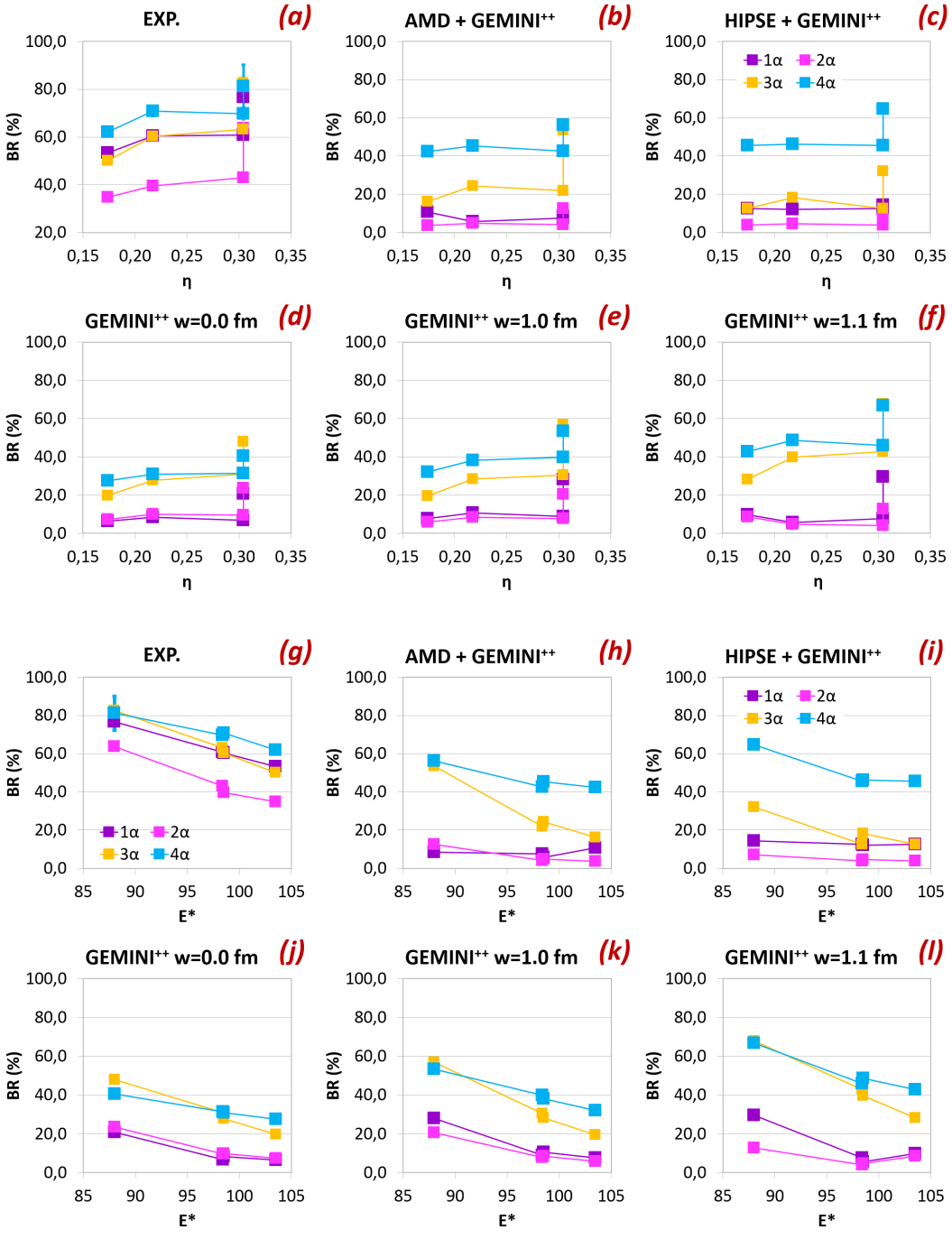

Figure 10.34: Branching ratio of multiple α channels as a function of the mass asymmetry parameter η ((a)-(f) panels) and of the excitation energy E_* ((g)-(l) panels).

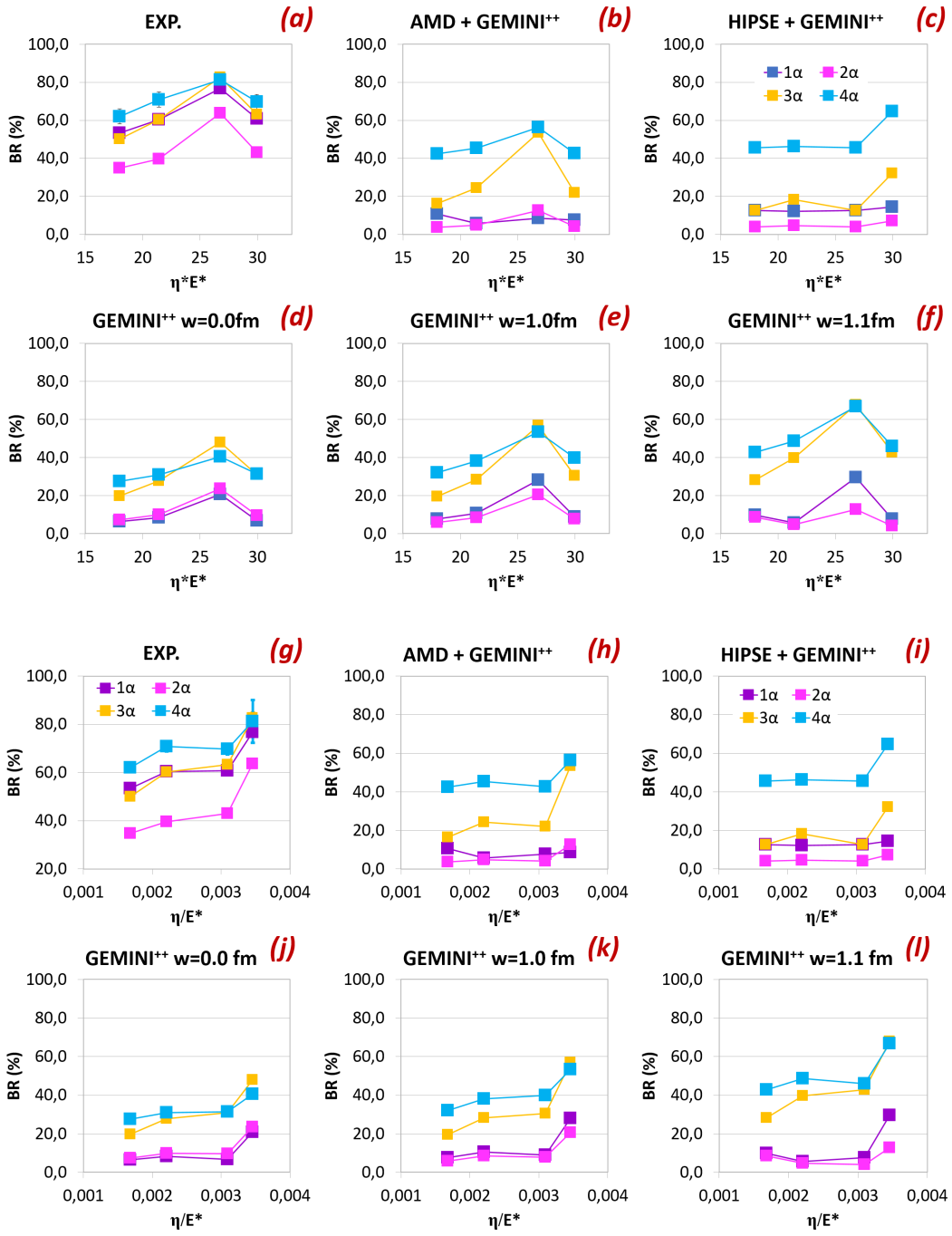

Figure 10.35: Branching ratio of multiple α channels as a function of the combination of η and E_*: $\eta * E^*$ ((a)-(f) panels) and $\frac{\eta}{E^*}$ ((g)-(l) panels).

and simulations (**G00**, **G10**, **G11**, **AMD** and **HIPSE**): in the six upper panels of Fig. 10.34, the BR as a function of η-parameter is shown, while in the six lower panels the BR is presented as a function of the E^*. Fig. 10.35 display the BR as a function of the combination of the two parameters: in six upper panels, BR *vs.* $\eta * E^*$ trends are illustrated and, in six lower panels, the BR *vs.* $\frac{\eta}{E^*}$ trends.

As demonstrated in the upper panels of Fig. 10.34, η alone seem not to be a good parameter, since for the same mass asymmetry ($\eta = 0,30$ - ^{16}O-induced reaction cases) very different BR are obtained for all the reported channels. On the contrary, the trend as a function of the E^* is somehow more effective, as it can be seen in the (g) panel. This trend was also expected for simulated data. However, apart from the different BR absolute number, which were already previously discussed, not even the trend is well reproduced for all studied channels apart from **G00** and **G10**, which can be considered close enough.

Looking therefore for a different parameter, we have chosen to look if a combination of the two parameters could be more effective: in fact, in this way one can disentangle the reactions which have the same η and, on the other hand, also those which are characterized by a very similar excitation energy. We choose the $\eta * E^*$ parameter (panels (a)-(f) of Fig. 10.35), which may indicate the amount of excitation energy weighted for the mass difference in the entrance channel. The trend of the BR is such that it grows up to a certain point for all decay channel studied and then it drops at the last point. This is reasonably reproduced, apart again from the absolute values, by $GEMINI^{++}$, even if with some differences in the trends of specific decay channels. **AMD** and **HIPSE** are, generally, less sensitive in the 1α and 2α cases and too sensitive in the 3α case.

The other combination is to look at the parameters ratio $\frac{\eta}{E^*}$ (panels (g)-(l) of Fig. 10.35): in this case, a quite continuous trend is observed for experimental data very similar for all the observed channels; again, it is reasonably reproduced by $GEMINI^{++}$, except for small local differences, while again **AMD** and **HIPSE** are very different for the 1α and 2α cases, but they also show a different trend for the 3α and 4α channels.

To conclude we have studied the four reactions, $^{16}O +^{30} Si$ at 111 MeV, $^{16}O +^{30} Si$ at 128 MeV, $^{18}O +^{28} Si$ at 126 MeV and $^{19}F +^{27} Al$ at 133 MeV, and compared them to

statistical model calculations and dynamical models.

After a very strict selection on experimental data, reproduced by a software replica of the apparatus and of the analysis constraints on the simulated data, we have observed a general reproduction of data when dealing with semi-inclusive data, for quasi-complete events ($Z_{tot} \geq 18$). However, when selecting only complete events ($Z_{tot} = 22$), where only neutral particles were missing both in experimental data and in simulations, several discrepancies have been found in the comparison to model predictions. Such discrepancies were visible on:

- the energy spectral shapes for the different particles: generally α-particles and other clusters were more sensitive to different model parametrization (like emission barrier);
- on specific branching ratios, especially those related to decay channels in which the maximum number of α-particles could be emitted ($\#_{max,\alpha} = \frac{22 - Z_{ER}}{2}$);
- on angular distributions, multiplicity plots, Q-value distributions; we have observed, for example, an anomalous high yield of cluster emitted at forward angles (especially α-particles), which could not be described by any of the used models;
- on correlation plots: either energy-energy, energy-angle or energy-Qvalues.

These differences changes according to the different reactions and some plots shown, in the Chapter 9 have tried to show the simplest comparison between the different reactions and a trend has been found depending both on the excitation energy and on the mass asymmetry parameter; such trend is in agreement with the trend of statistical model, even if strongly different absolute number of BR are found, which cannot be easily explained. Surely in some specific channels, particular categories of $\alpha - \alpha$ correlations are found which are not present in the simulations and may be linked to the different decay path, but this has to be studied in much more detail in a forthcoming study.

More complex differences have been outlined during the discussion in the different chapters, which may open new discussion on the proper description of de-excitations in medium light nuclei, formed through α-cluster structured partners. Further work can be

performed to analyze more specifically our findings, but this goes beyond the aim of the present thesis work.

Appendix A

LCP spectra of Chapter 6

A.1 $^{16}O+^{30}Si$ at 111 MeV.

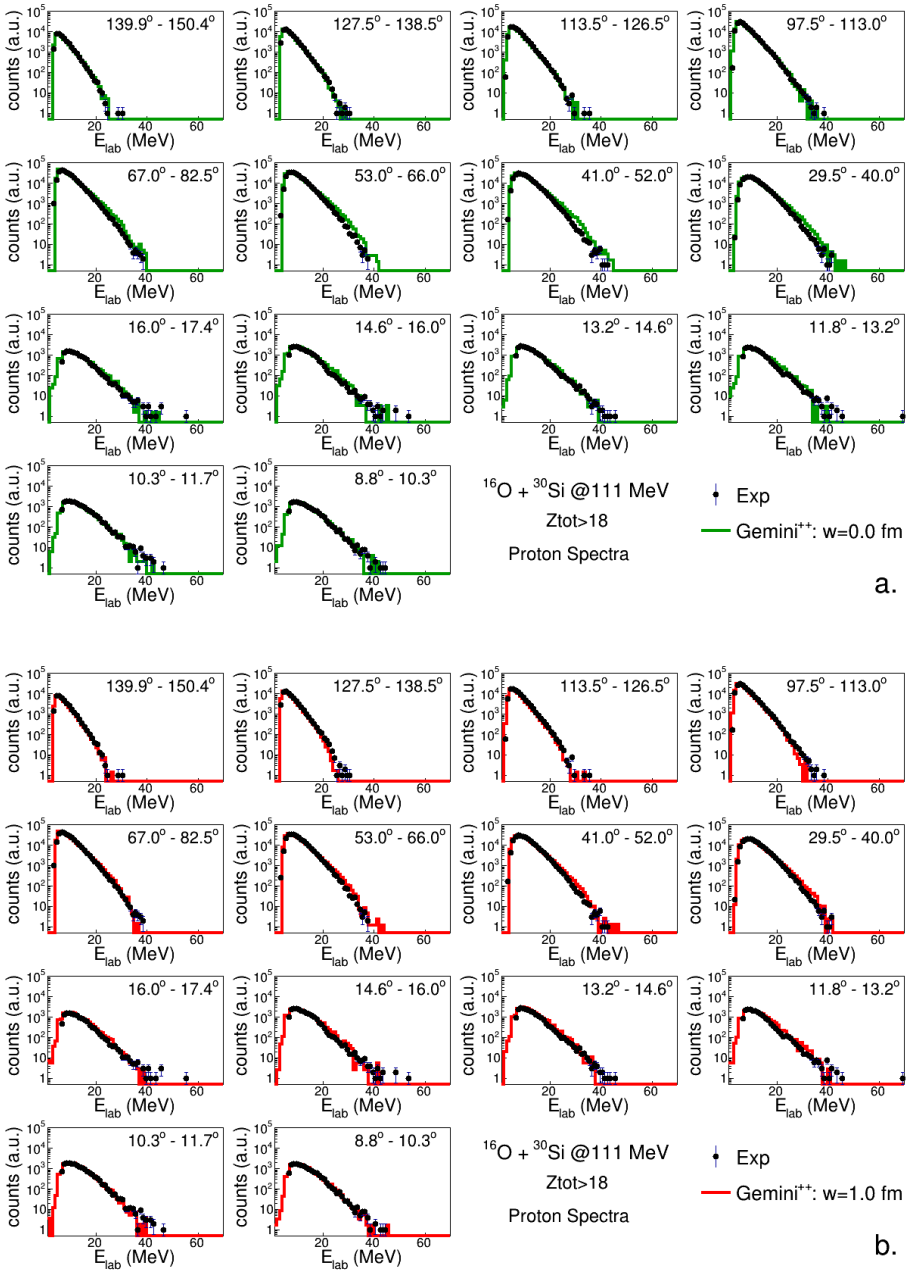

Figure A.1: Proton energy distributions for the reaction $^{16}O + ^{30}Si$ at 111 MeV: comparison between experimental data (black dots) and simulations performed with $GEMINI^{++}$, in which the $w = 0.0$ fm (green line in panel a.) and $w = 1.0$ fm (red line in panel b.) barrier parameter were set. Spectra are normalized to the maximum for shape comparison purposes. See text for more details on simulation parameters.

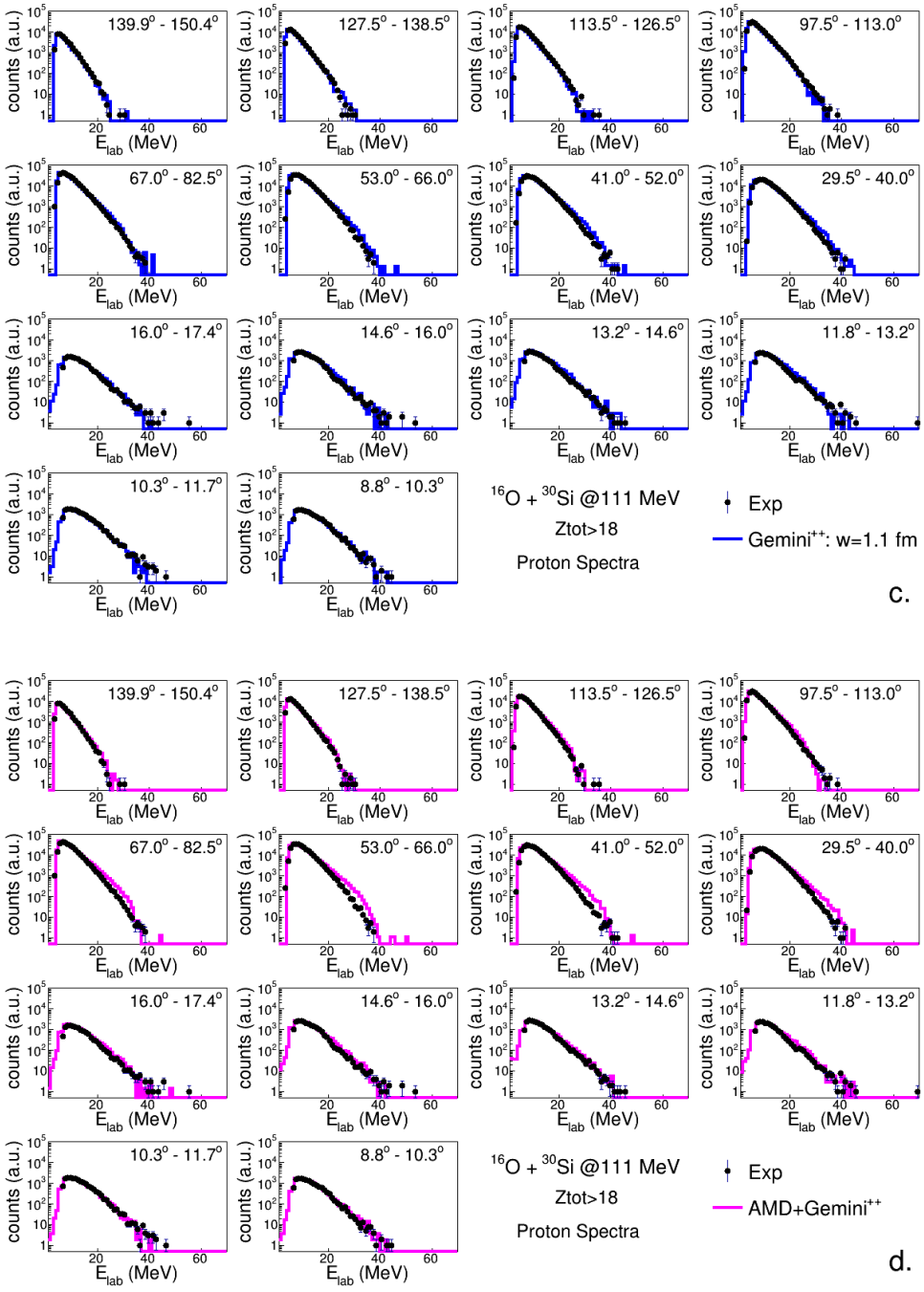

Figure A.2: Same as in the figure A.1 but comparison with $GEMINI^{++}$ (blue line in panel a.) and $AMD + GEMINI^{++}$ (pink line in panel b.); the parameter $w = 1.1$ fm was used for both $GEMINI^{++}$.

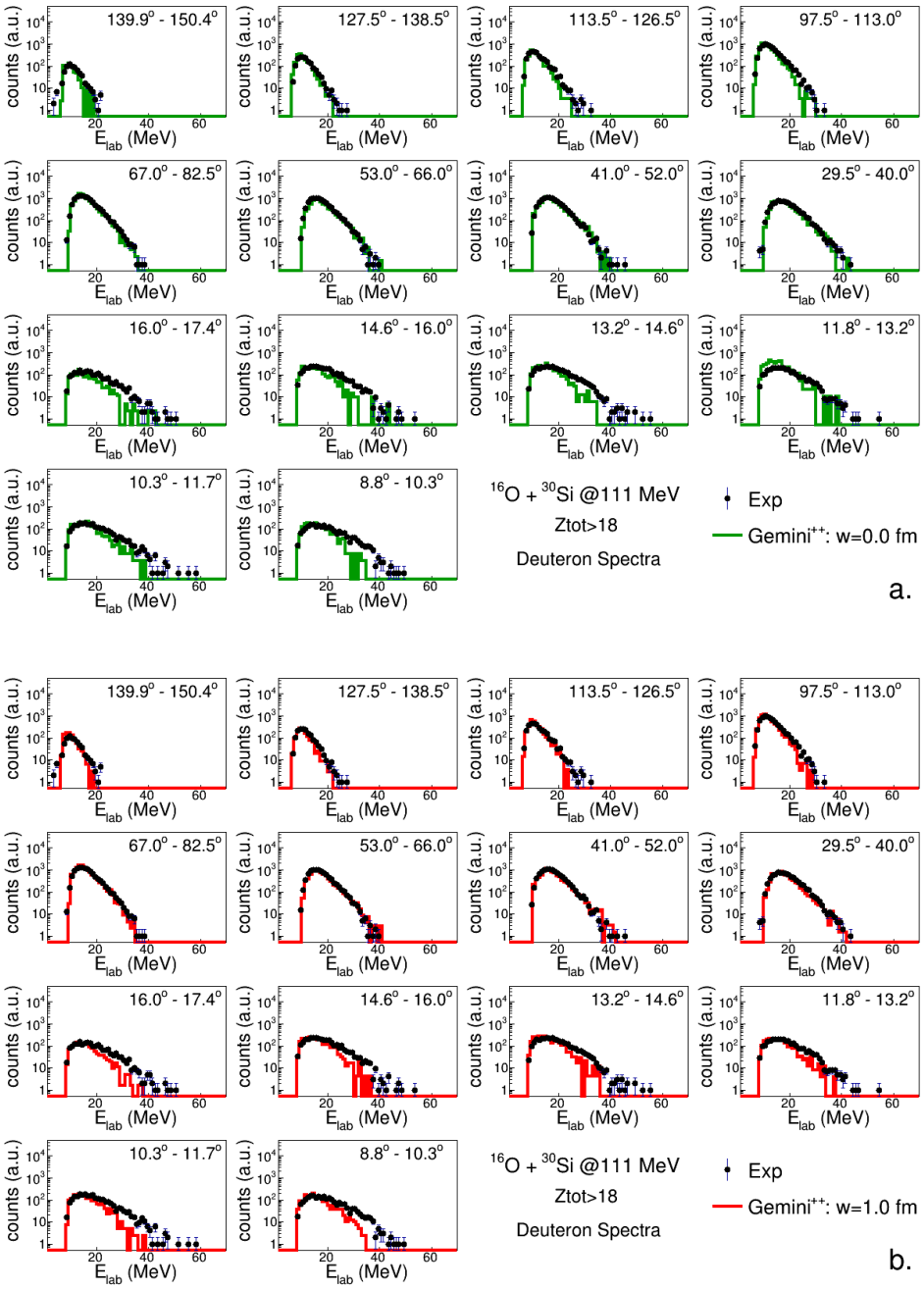

Figure A.3: Deuteron energy distributions for the reaction $^{16}O+^{30}Si$ at 111 MeV: comparison between experimental data (black dots) and simulations performed with $GEMINI^{++}$, in which the $w = 0.0$ fm (green line in panel a.) and $w = 1.0$ fm (red line in panel b.) barrier parameter were set. Spectra are normalized to the maximum for shape comparison purposes.

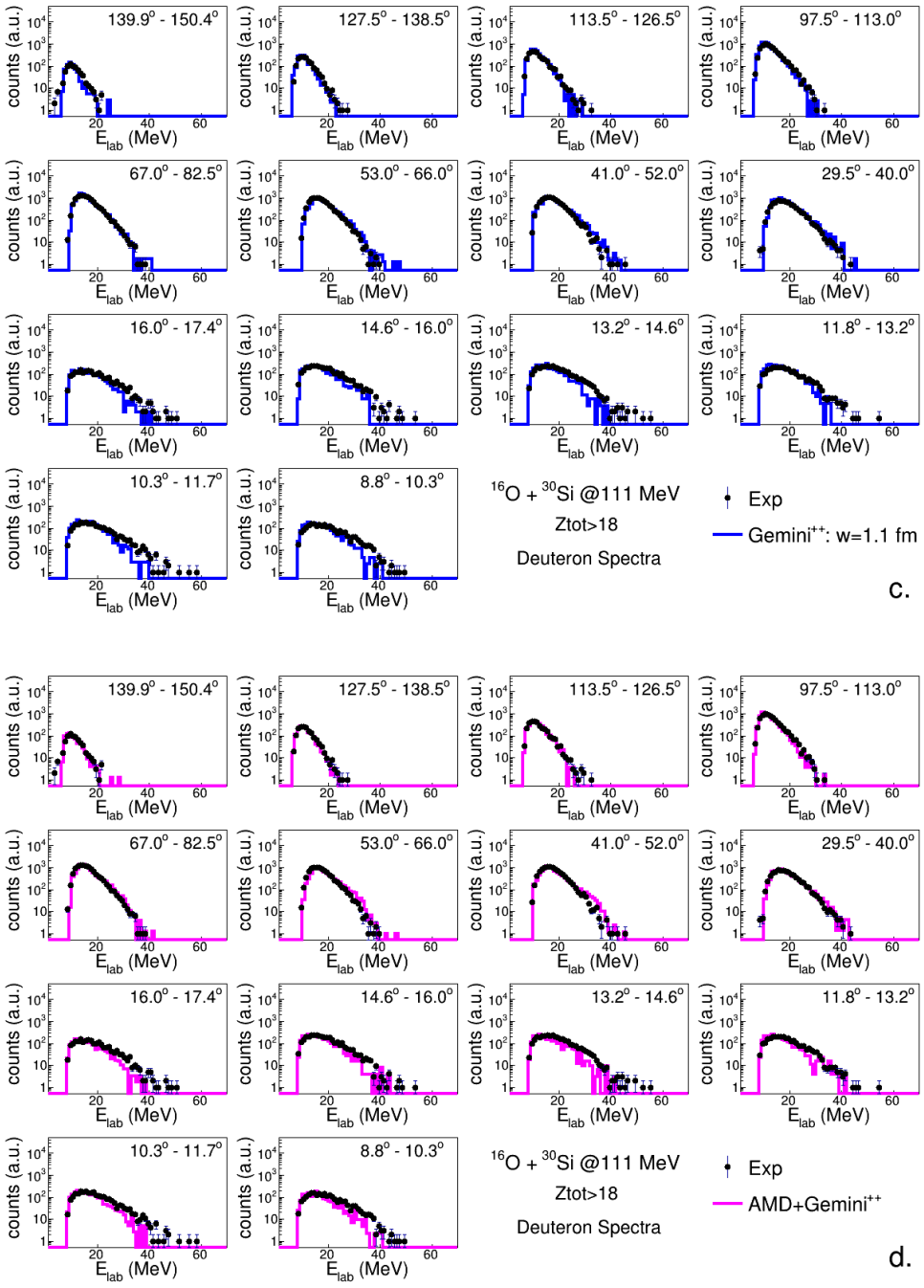

Figure A.4: Same as in the figure A.3 but comparison with $GEMINI^{++}$ (blue line in panel a.) and $AMD + GEMINI^{++}$ (pink line in panel b.); the parameter $w = 1.1$ fm was used for both $GEMINI^{++}$.

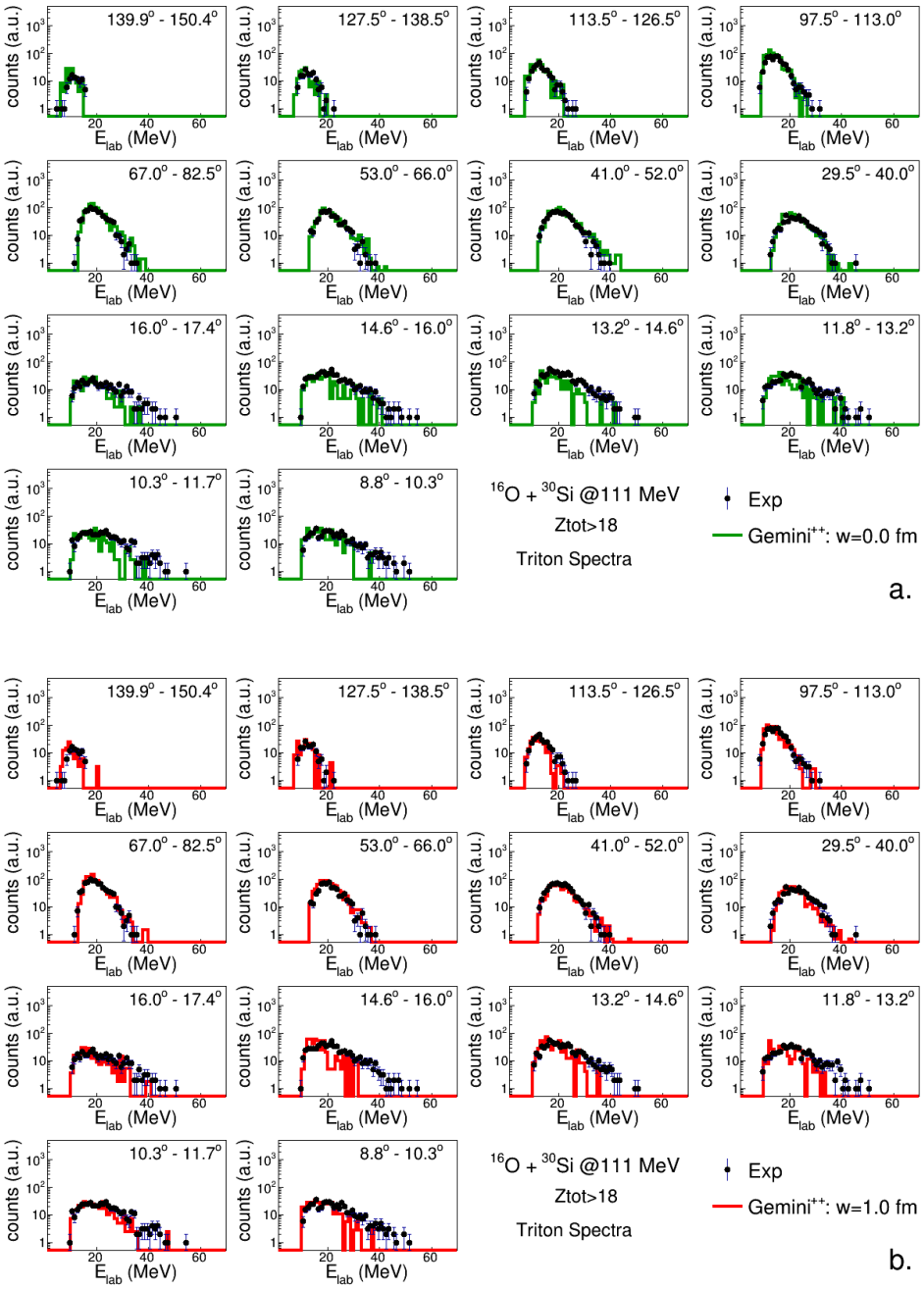

Figure A.5: Triton energy distributions for the reaction $^{16}O + ^{30}Si$ at 111 MeV: comparison between experimental data (black dots) and simulations performed with $GEMINI^{++}$, in which the $w = 0.0$ fm (green line in panel a.) and $w = 1.0$ fm (red line in panel b.) barrier parameter were set. Spectra are normalized to the maximum for shape comparison purposes.

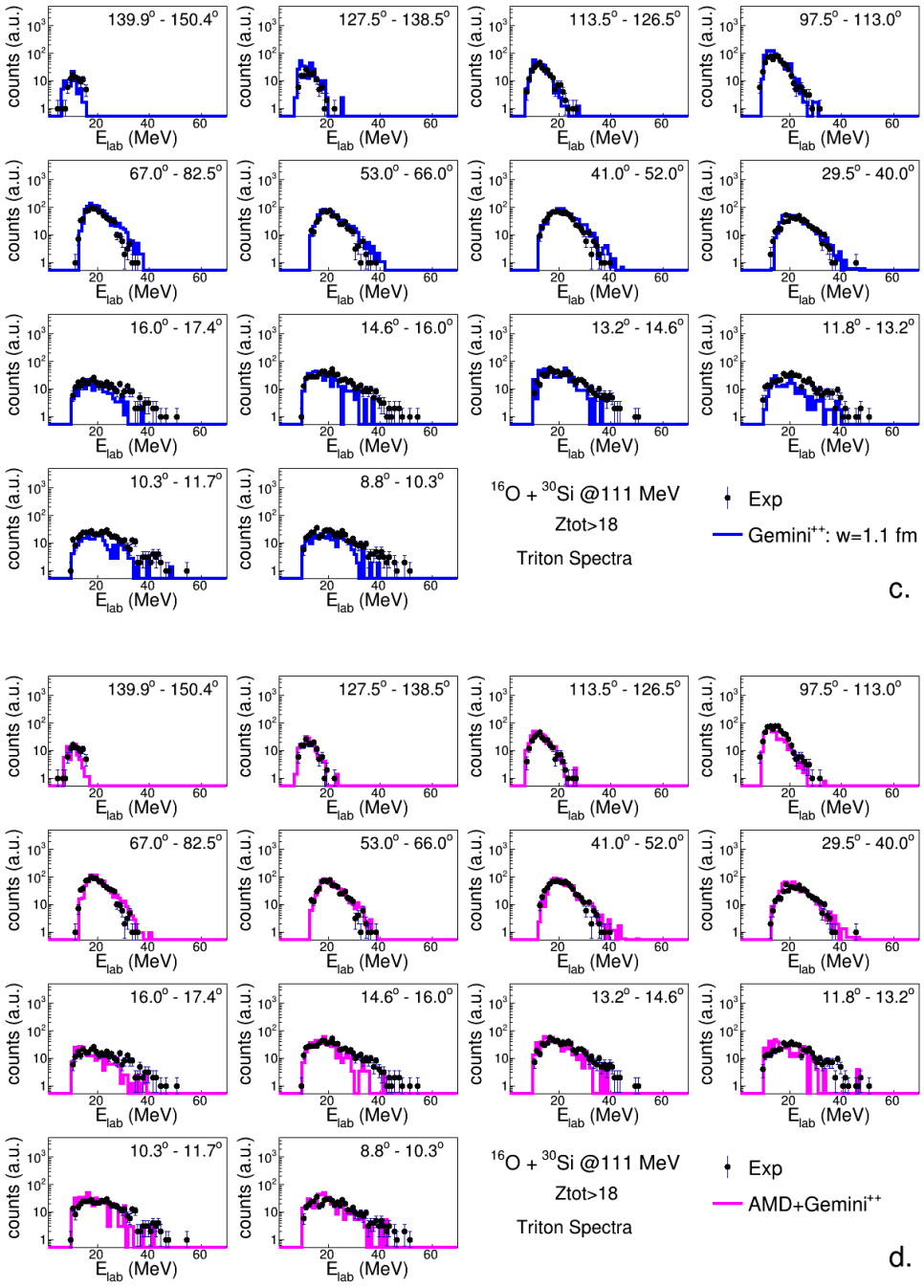

Figure A.6: Same as in the figure A.5 but comparison with $GEMINI^{++}$ (blue line in panel a.) and $AMD + GEMINI^{++}$ (pink line in panel b.); the parameter $w = 1.1$ fm was used for both $GEMINI^{++}$.

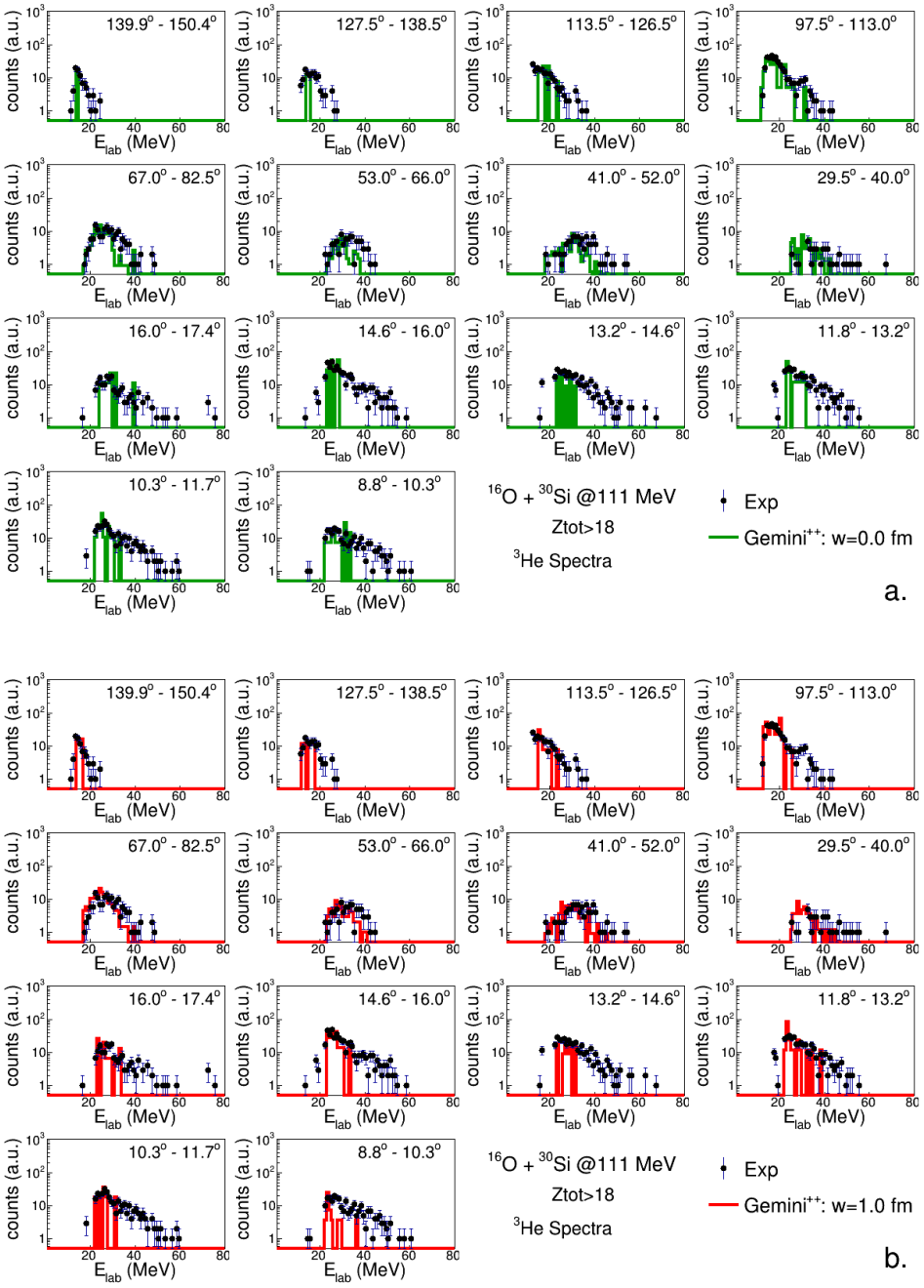

Figure A.7: ^3He energy distributions for the reaction $^{16}O + ^{30}Si$ at 111 MeV: comparison between experimental data (black dots) and simulations performed with $GEMINI^{++}$, in which the $w = 0.0$ fm (green line in panel a.) and $w = 1.0$ fm (red line in panel b.) barrier parameter were set. Spectra are normalized to the maximum for shape comparison purposes.

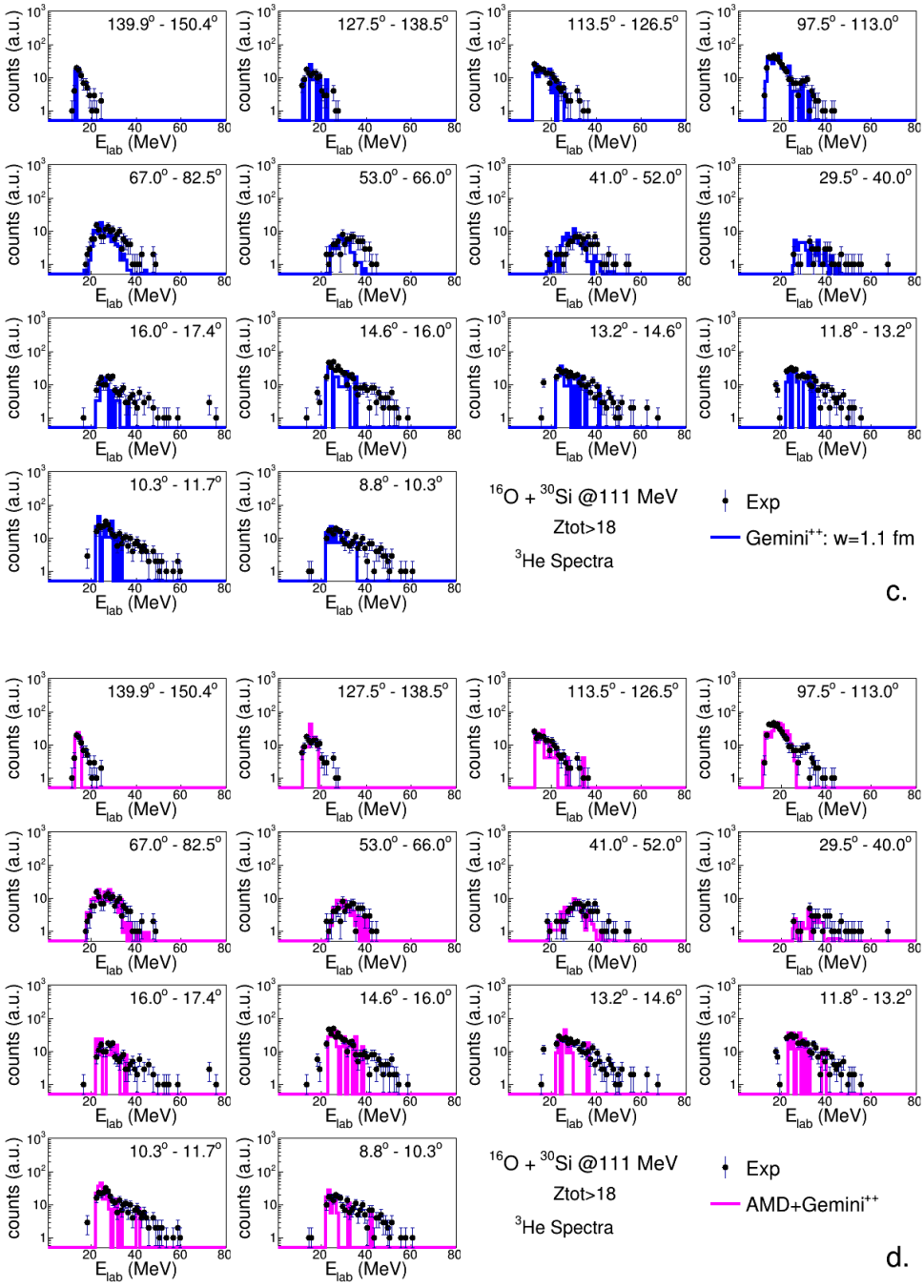

Figure A.8: Same as in the figure A.7 but comparison with $GEMINI^{++}$ (blue line in panel a.) and $AMD + GEMINI^{++}$ (pink line in panel b.); the parameter $w = 0.0$ fm was used for both $GEMINI^{++}$.

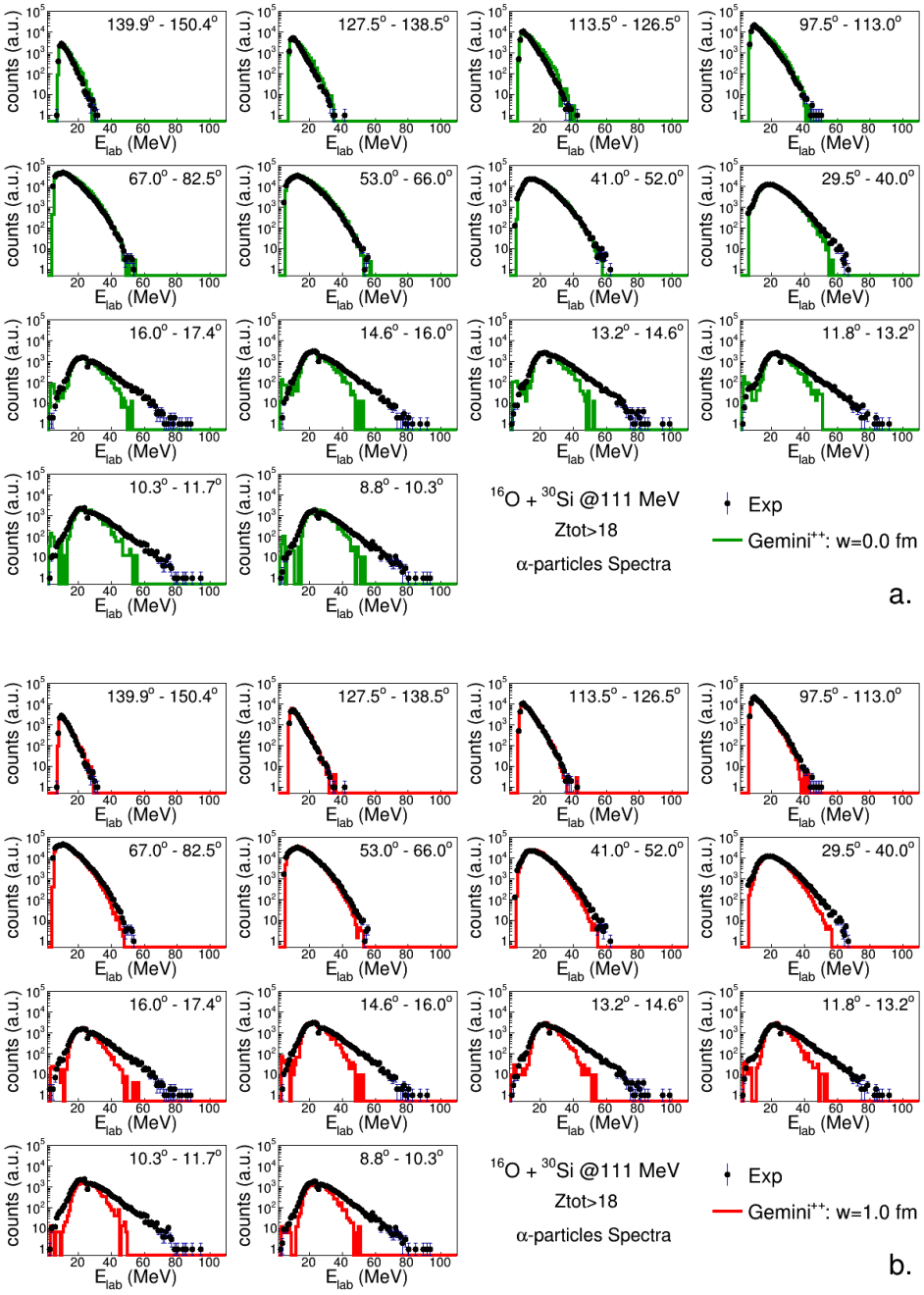

Figure A.9: α-particles energy distributions for the reaction $^{16}O + ^{30}Si$ at 111 MeV: comparison between experimental data (black dots) and simulations performed with $GEMINI^{++}$, in which the $w = 0.0$ fm (green line in panel a.) and $w = 1.0$ fm (red line in panel b.) barrier parameter were set. Spectra are normalized to the maximum for shape comparison purposes.

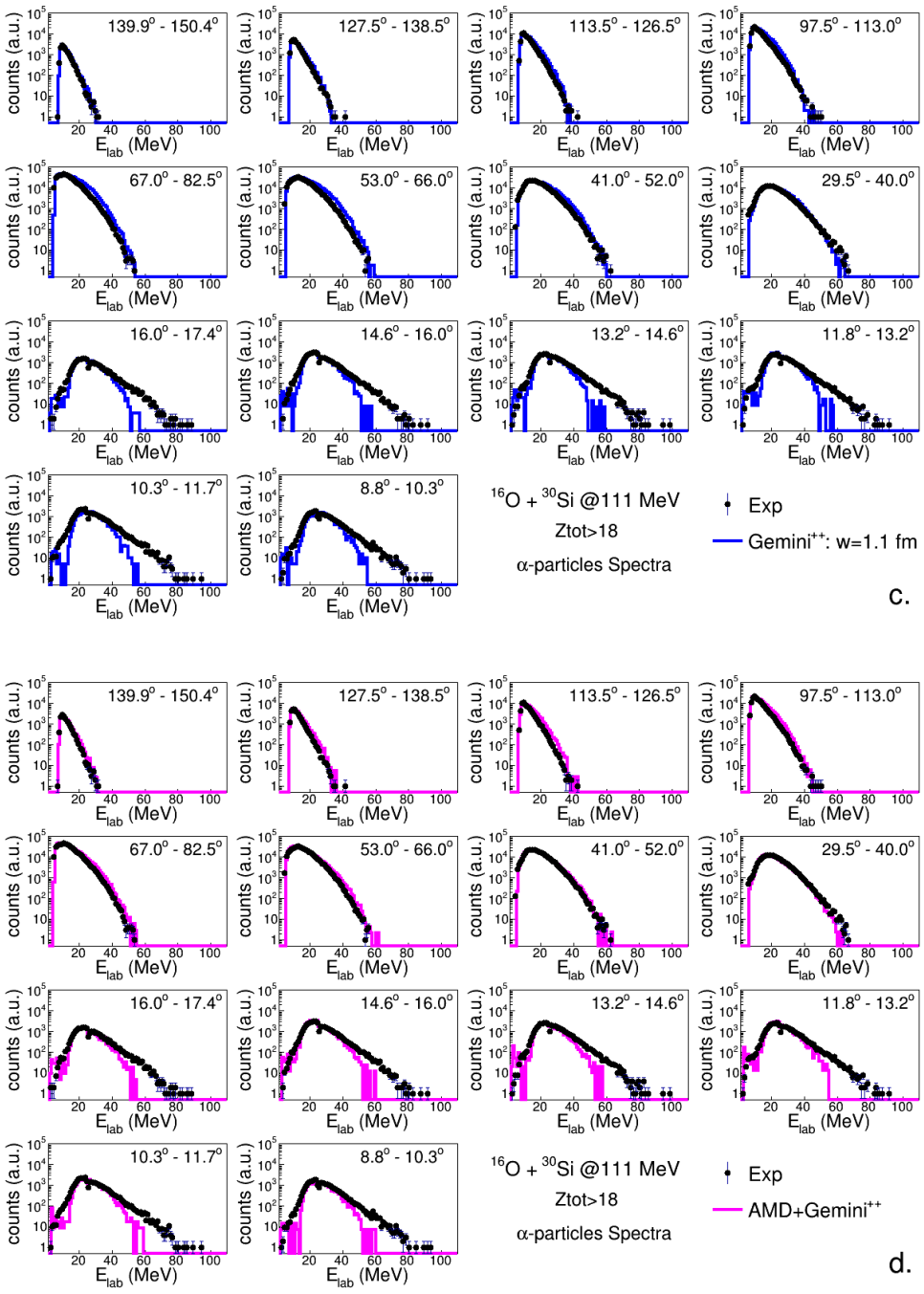

Figure A.10: Same as in the figure A.9 but comparison with $GEMINI^{++}$ (blue line in panel a.) and $AMD + GEMINI^{++}$ (pink line in panel b.); the parameter $w = 1.1$ fm was used for both $GEMINI^{++}$.

A.2 $^{16}O+^{30}Si$ at 128 MeV.

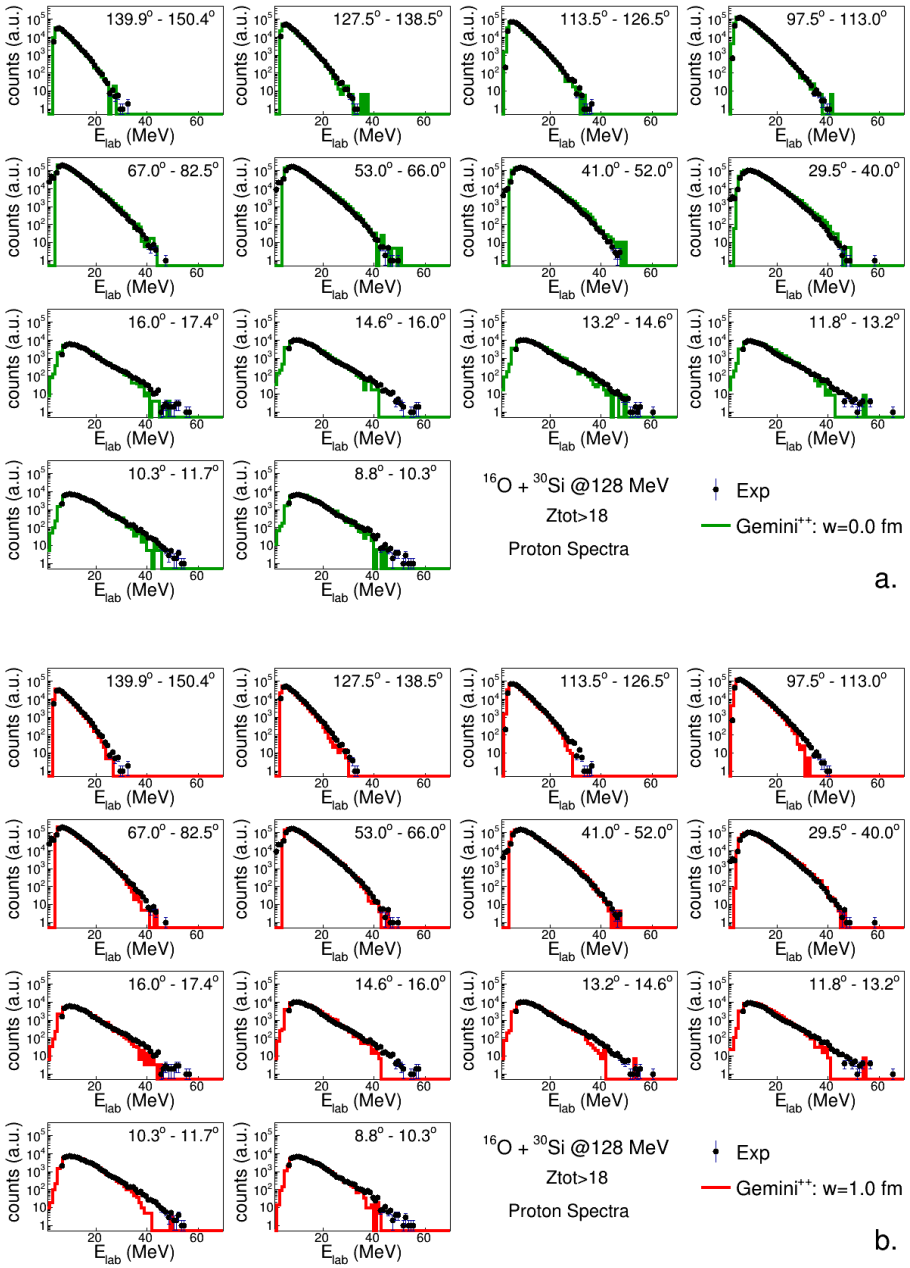

Figure A.11: Proton energy distributions for the reaction $^{16}O+^{30}Si$ at 128 MeV: comparison between experimental data (black dots) and simulations performed with $GEMINI^{++}$, in which the $w = 0.0$ fm (green line in panel a.) and $w = 1.0$ fm (red line in panel b.) barrier parameter were set. Spectra are normalized to the maximum for shape comparison purposes. See text for more details on simulation parameters.

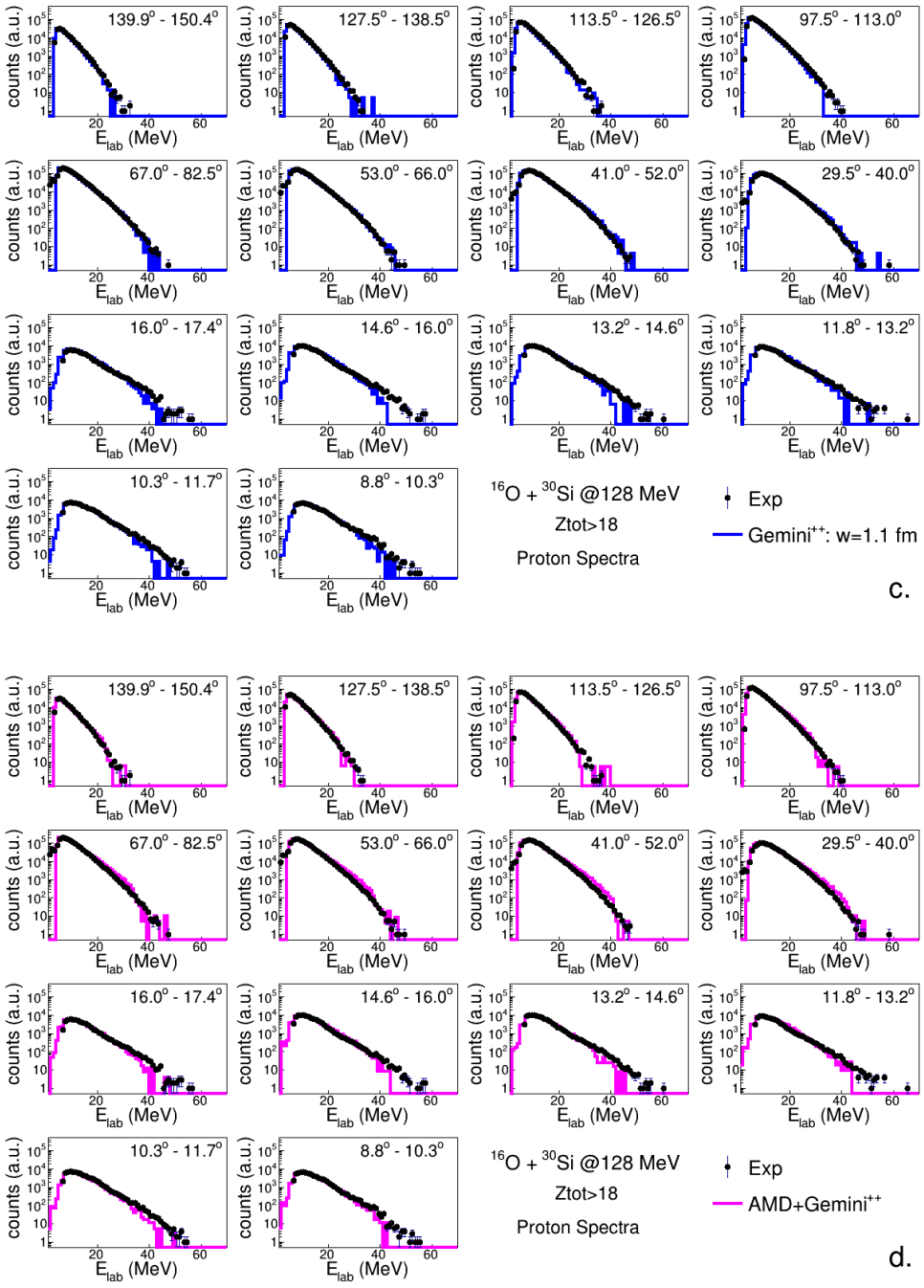

Figure A.12: Same as in the figure A.11 but comparison with $GEMINI^{++}$ (blue line in panel a.) and $AMD + GEMINI^{++}$ (pink line in panel b.); the parameter $w = 1.1$ fm was used for both $GEMINI^{++}$.

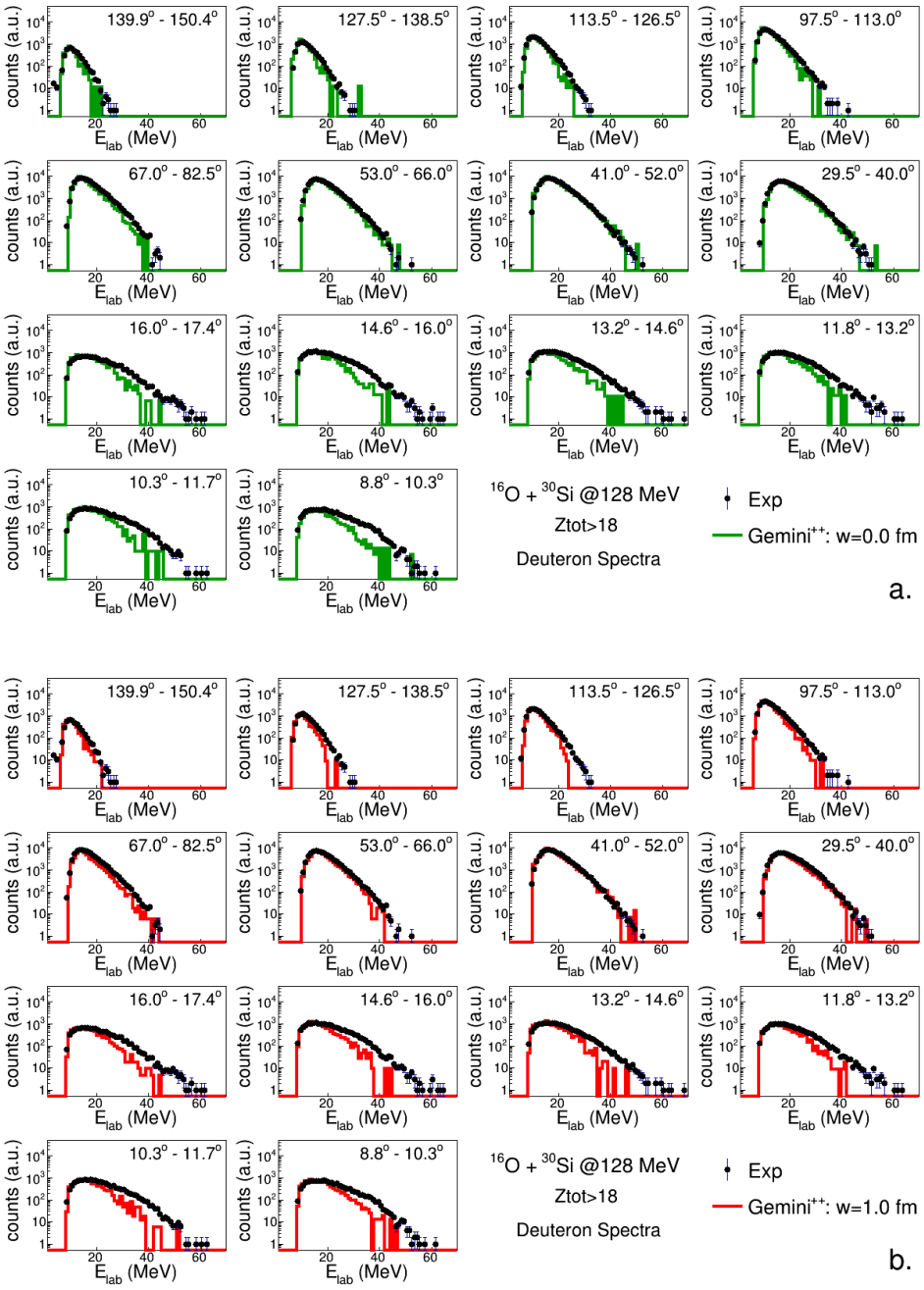

Figure A.13: Deuteron energy distributions for the reaction $^{16}O + ^{30}Si$ at 128 MeV: comparison between experimental data (black dots) and simulations performed with $GEMINI^{++}$, in which the $w = 0.0$ fm (green line in panel a.) and $w = 1.0$ fm (red line in panel b.) barrier parameter were set. Spectra are normalized to the maximum for shape comparison purposes.

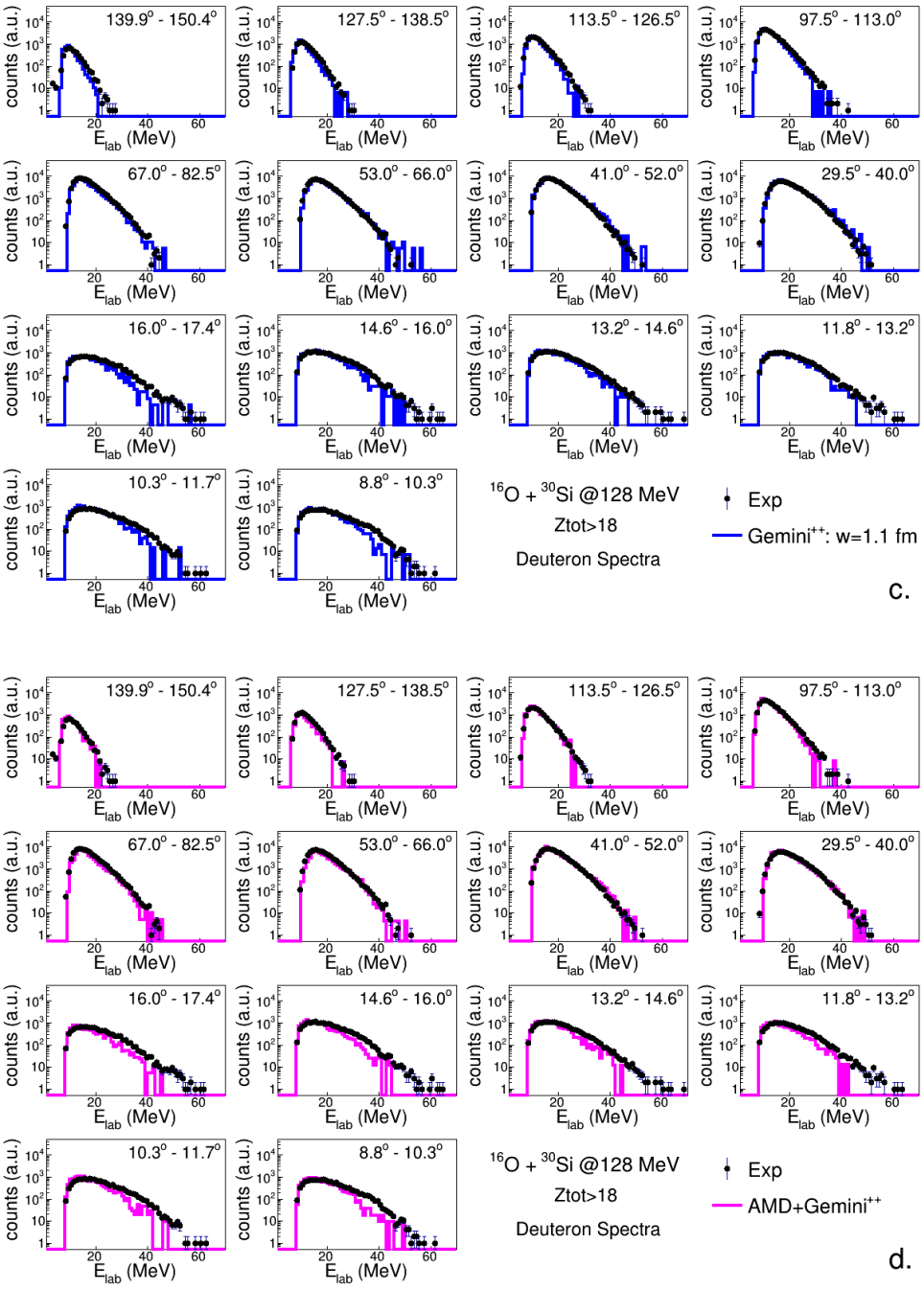

Figure A.14: Same as in the figure A.13 but comparison with $GEMINI^{++}$ (blue line in panel a.) and $AMD + GEMINI^{++}$ (pink line in panel b.); the parameter $w = 1.1$ fm was used for both $GEMINI^{++}$.

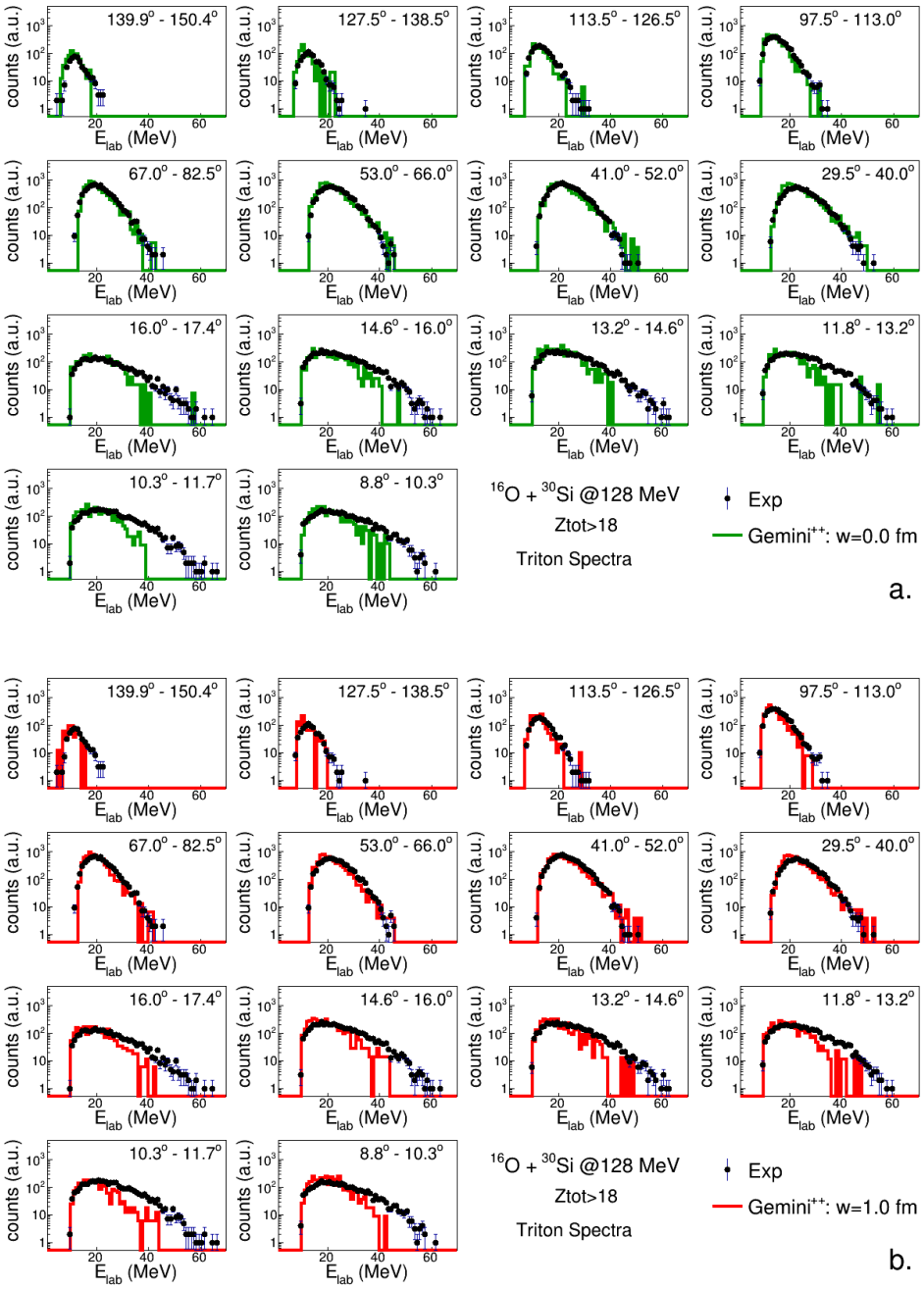

Figure A.15: Triton energy distributions for the reaction $^{16}O + ^{30}Si$ at 128 MeV: comparison between experimental data (black dots) and simulations performed with $GEMINI^{++}$, in which the $w = 0.0$ fm (green line in panel a.) and $w = 1.0$ fm (red line in panel b.) barrier parameter were set. Spectra are normalized to the maximum for shape comparison purposes.

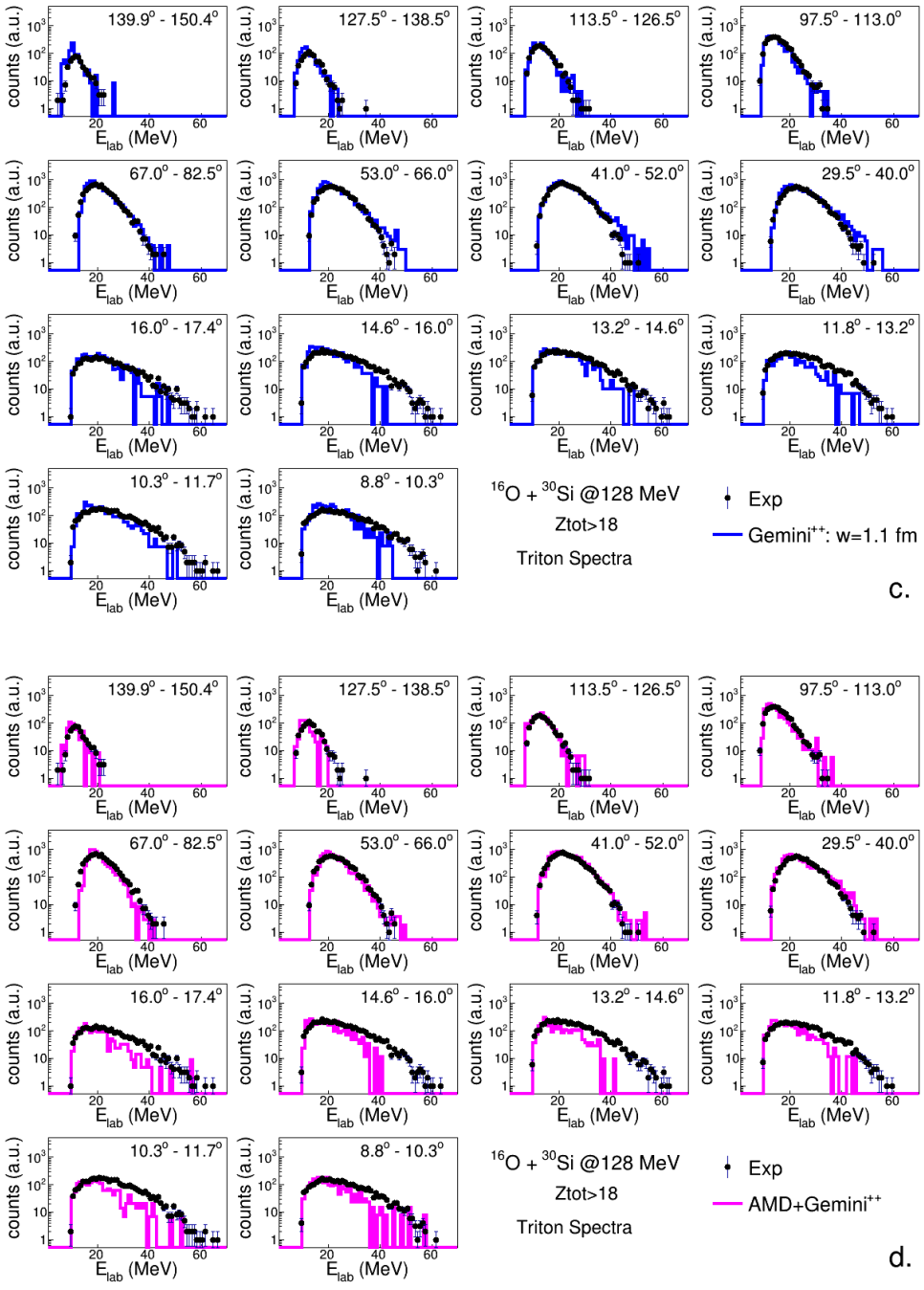

Figure A.16: Same as in the figure A.15 but comparison with $GEMINI^{++}$ (blue line in panel a.) and $AMD + GEMINI^{++}$ (pink line in panel b.); the parameter $w = 1.1$ fm was used for both $GEMINI^{++}$.

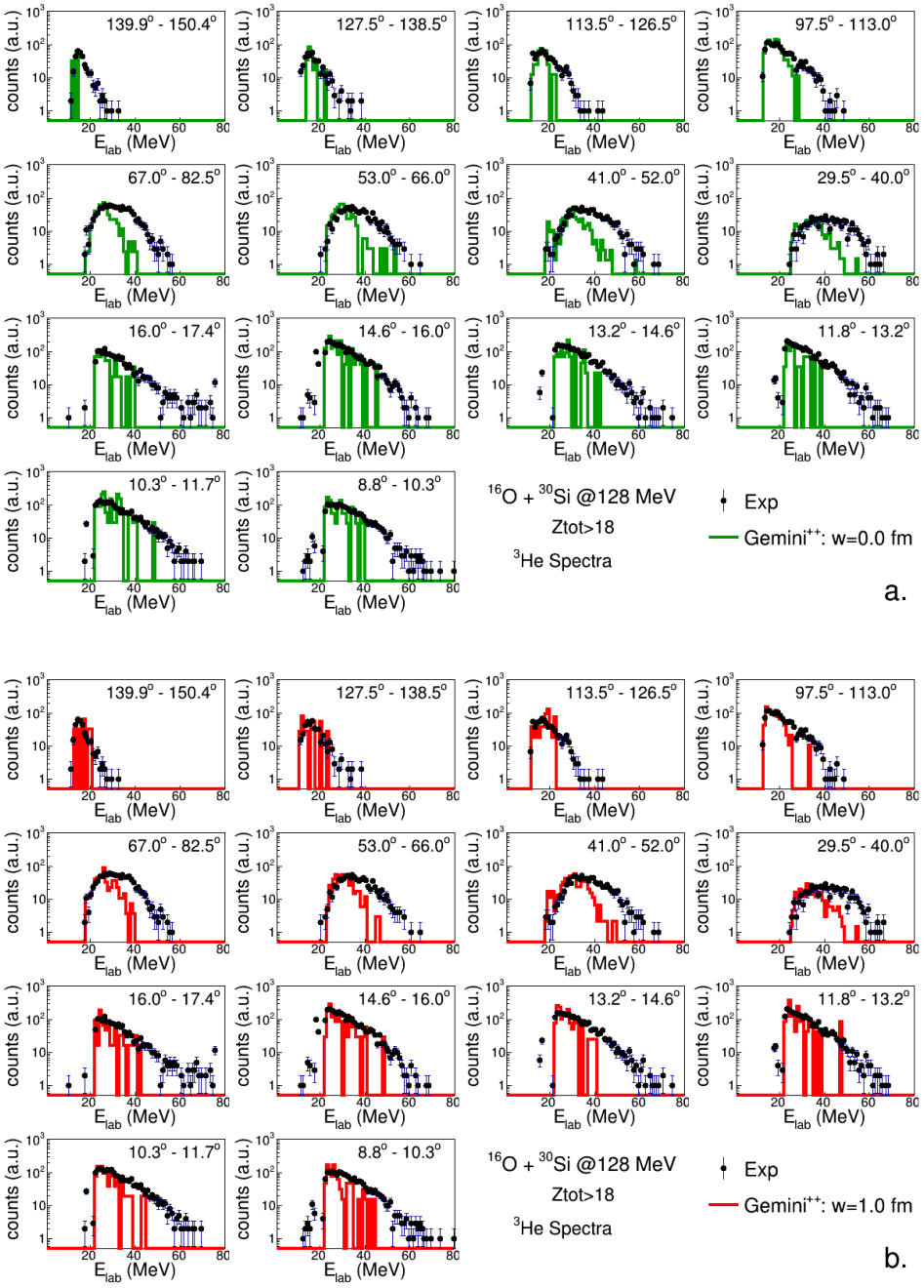

Figure A.17: ^3He energy distributions for the reaction $^{16}O + ^{30}Si$ at 128 MeV: comparison between experimental data (black dots) and simulations performed with $GEMINI^{++}$, in which the $w = 0.0$ fm (green line in panel a.) and $w = 1.0$ fm (red line in panel b.) barrier parameter were set. Spectra are normalized to the maximum for shape comparison purposes.

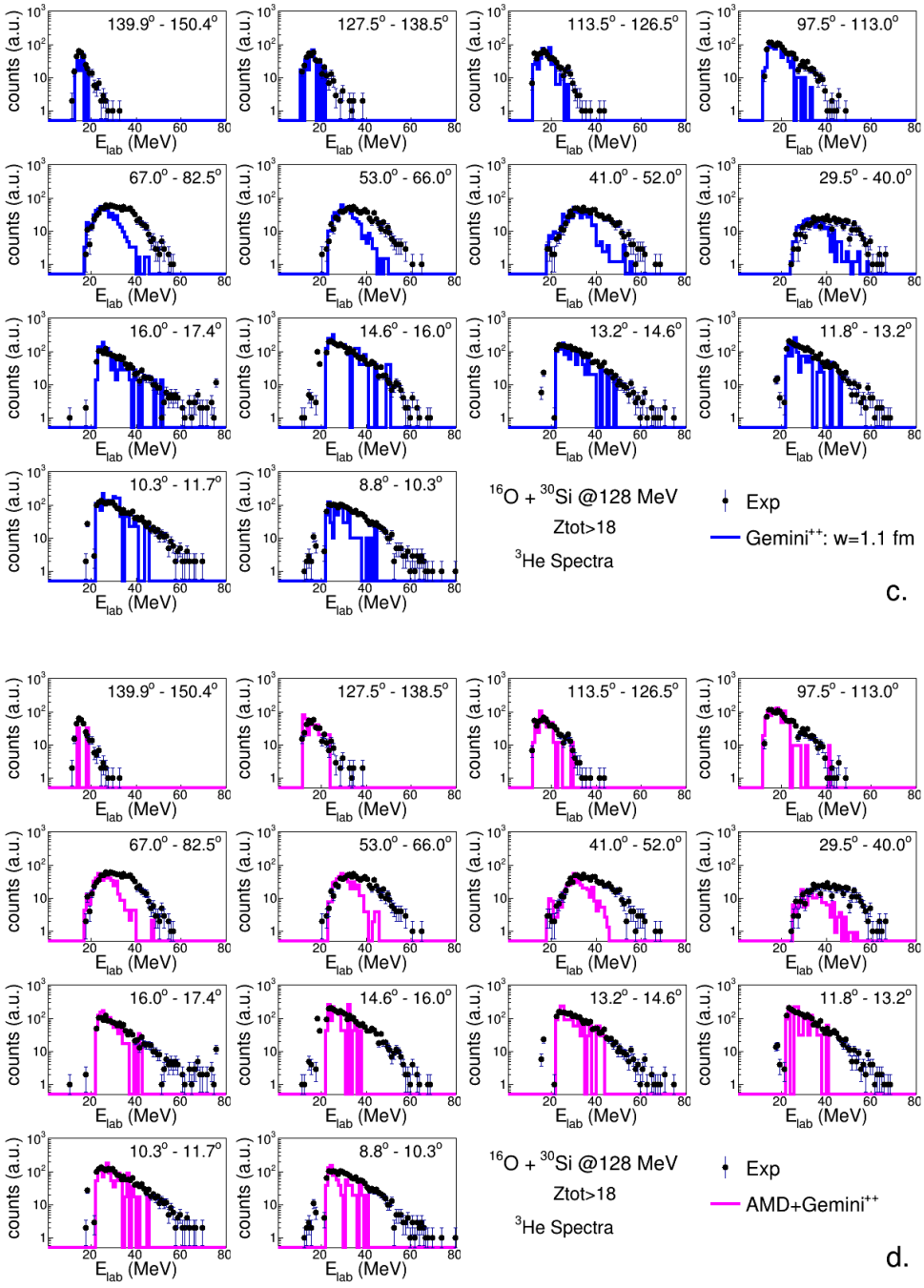

Figure A.18: Same as in the figure A.17 but comparison with $GEMINI^{++}$ (blue line in panel a.) and $AMD + GEMINI^{++}$ (pink line in panel b.); the parameter $w = 1.1$ fm was used for both $GEMINI^{++}$.

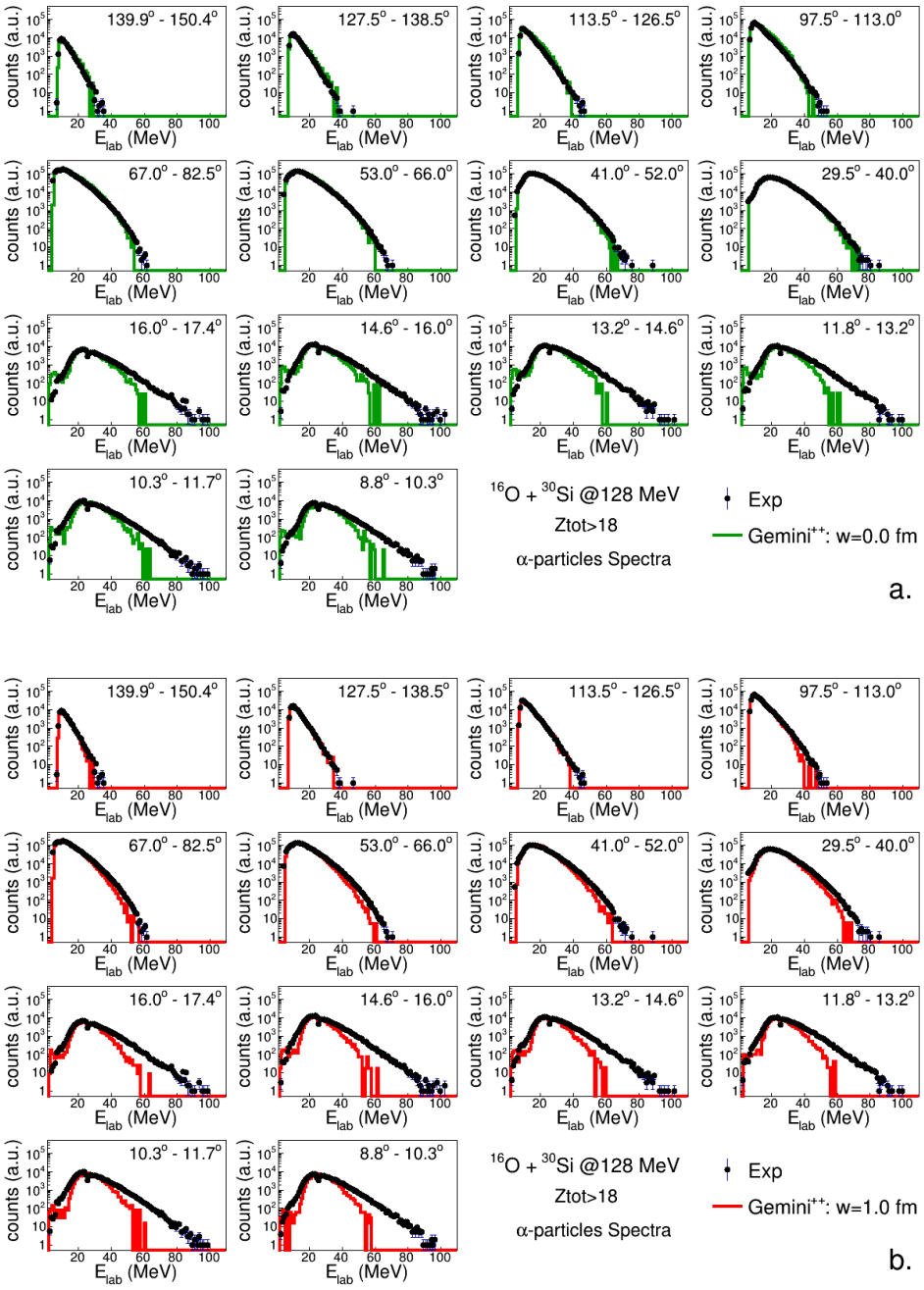

Figure A.19: α-particles energy distributions for the reaction $^{16}O + ^{30}Si$ at 128 MeV: comparison between experimental data (black dots) and simulations performed with $GEMINI^{++}$, in which the $w = 0.0$ fm (green line in panel a.) and $w = 1.0$ fm (red line in panel b.) barrier parameter were set. Spectra are normalized to the maximum for shape comparison purposes.

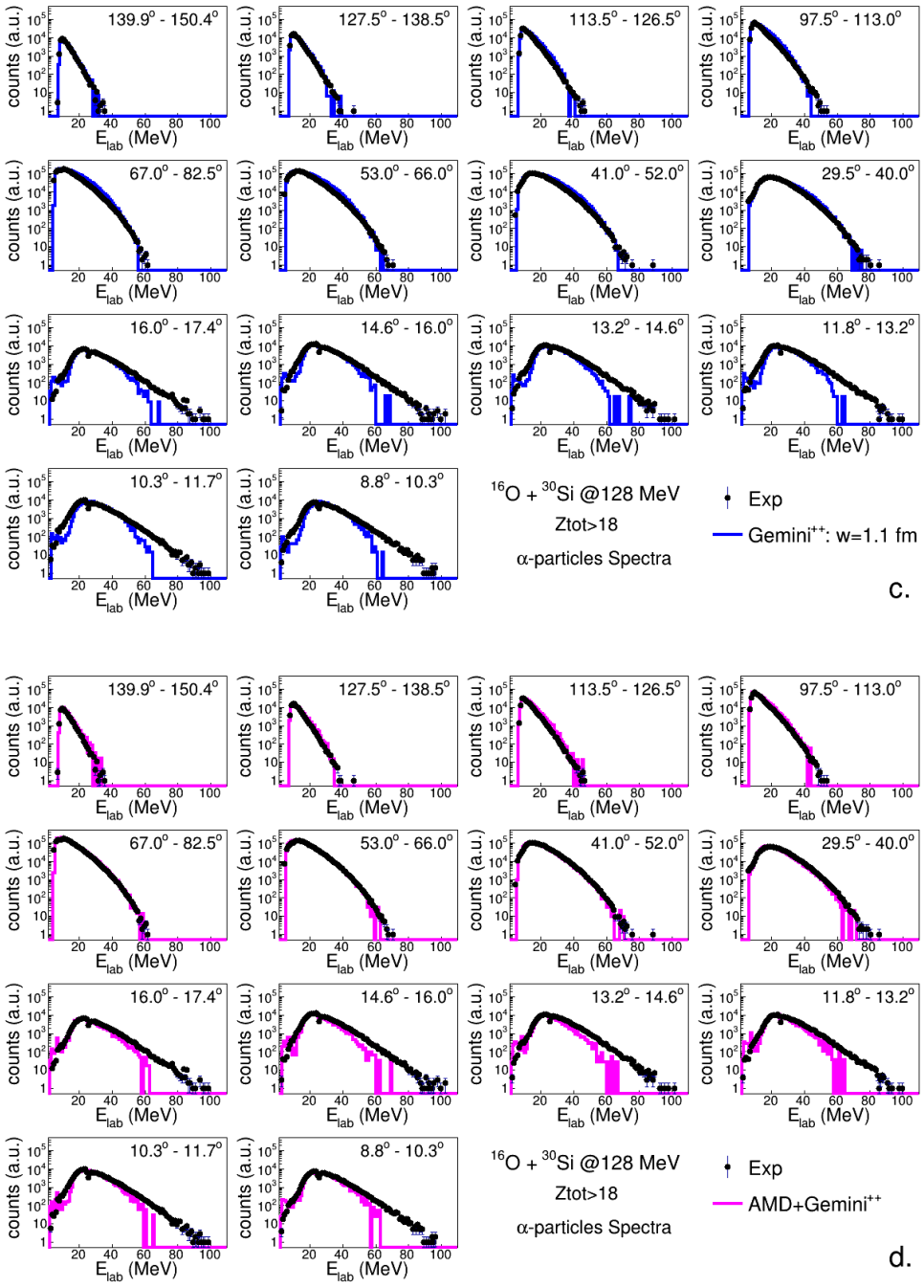

Figure A.20: Same as in the figure A.19 but comparison with $GEMINI^{++}$ (blue line in panel a.) and $AMD + GEMINI^{++}$ (pink line in panel b.); the parameter $w = 1.1$ fm was used for both $GEMINI^{++}$.

A.3 $^{18}O+^{28}Si$ at 126 MeV.

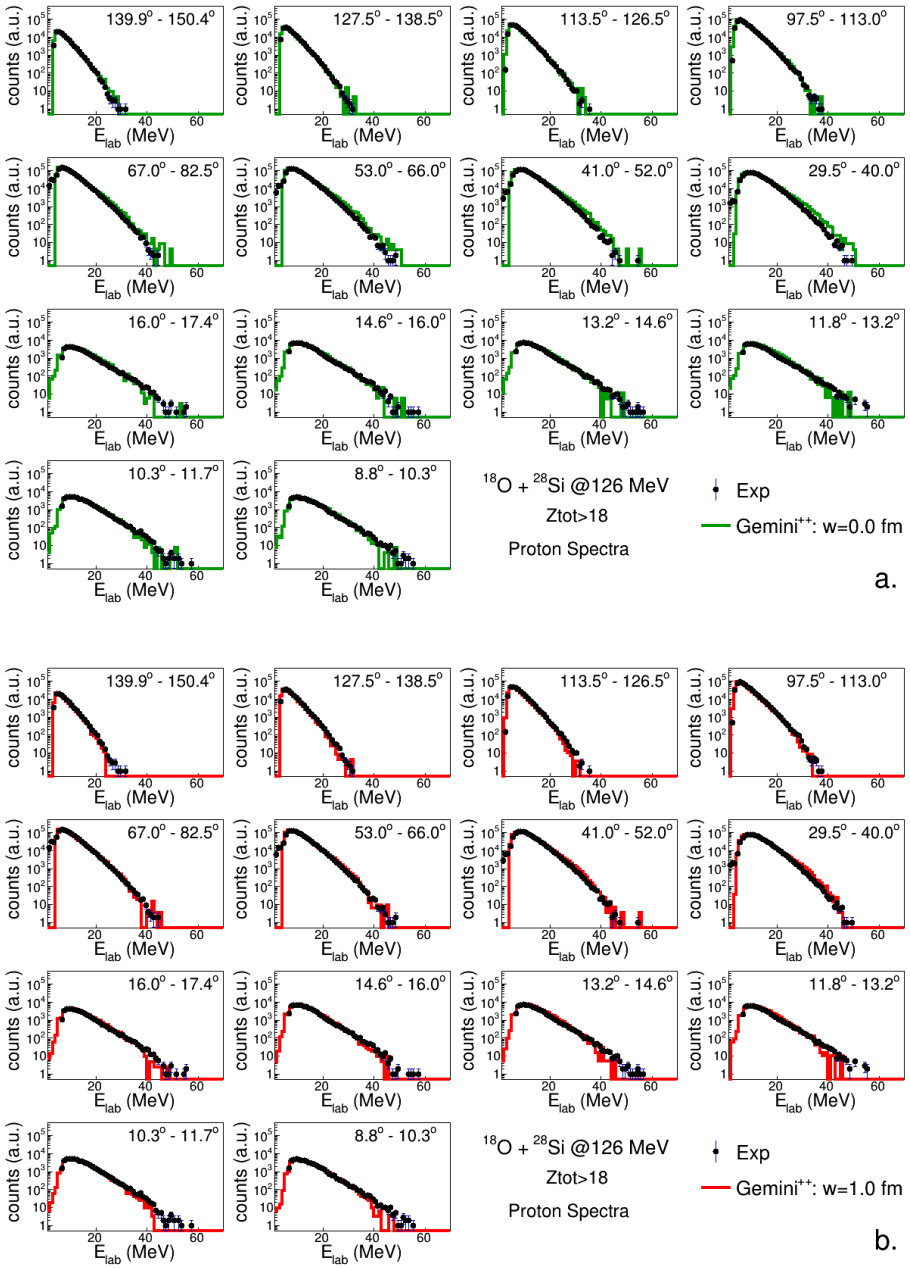

Figure A.21: Proton energy distributions for the reaction $^{18}O+^{28}Si$ at 126 MeV: comparison between experimental data (black dots) and simulations performed with $GEMINI^{++}$, in which the $w = 0.0$ fm (green line in panel a.) and $w = 1.0$ fm (red line in panel b.) barrier parameter were set. Spectra are normalized to the maximum for shape comparison purposes. See text for more details on simulation parameters.

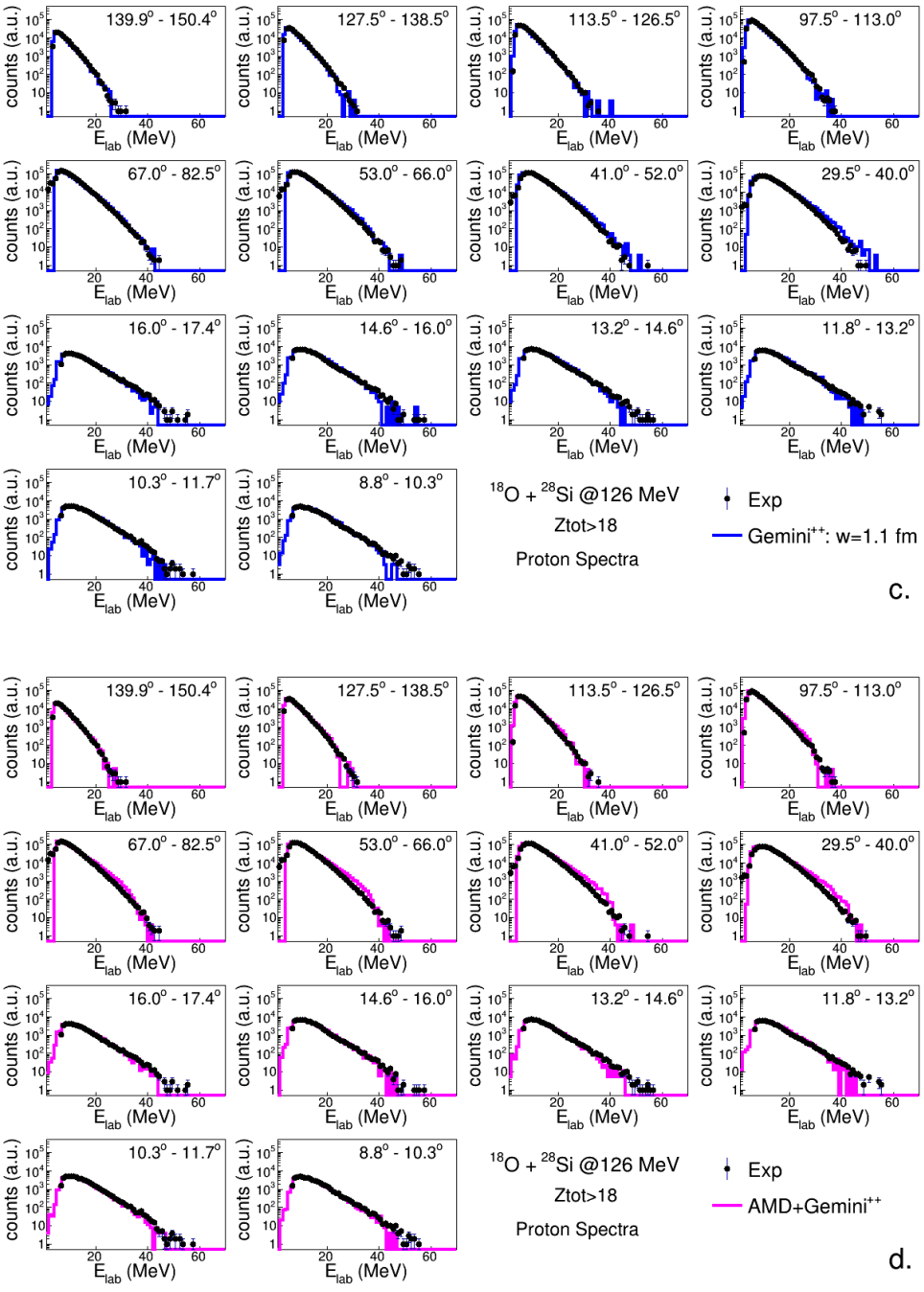

Figure A.22: Same as in the figure A.21 but comparison with $GEMINI^{++}$ (blue line in panel a.) and $AMD + GEMINI^{++}$ (pink line in panel b.); the parameter $w = 1.1$ fm was used for both $GEMINI^{++}$.

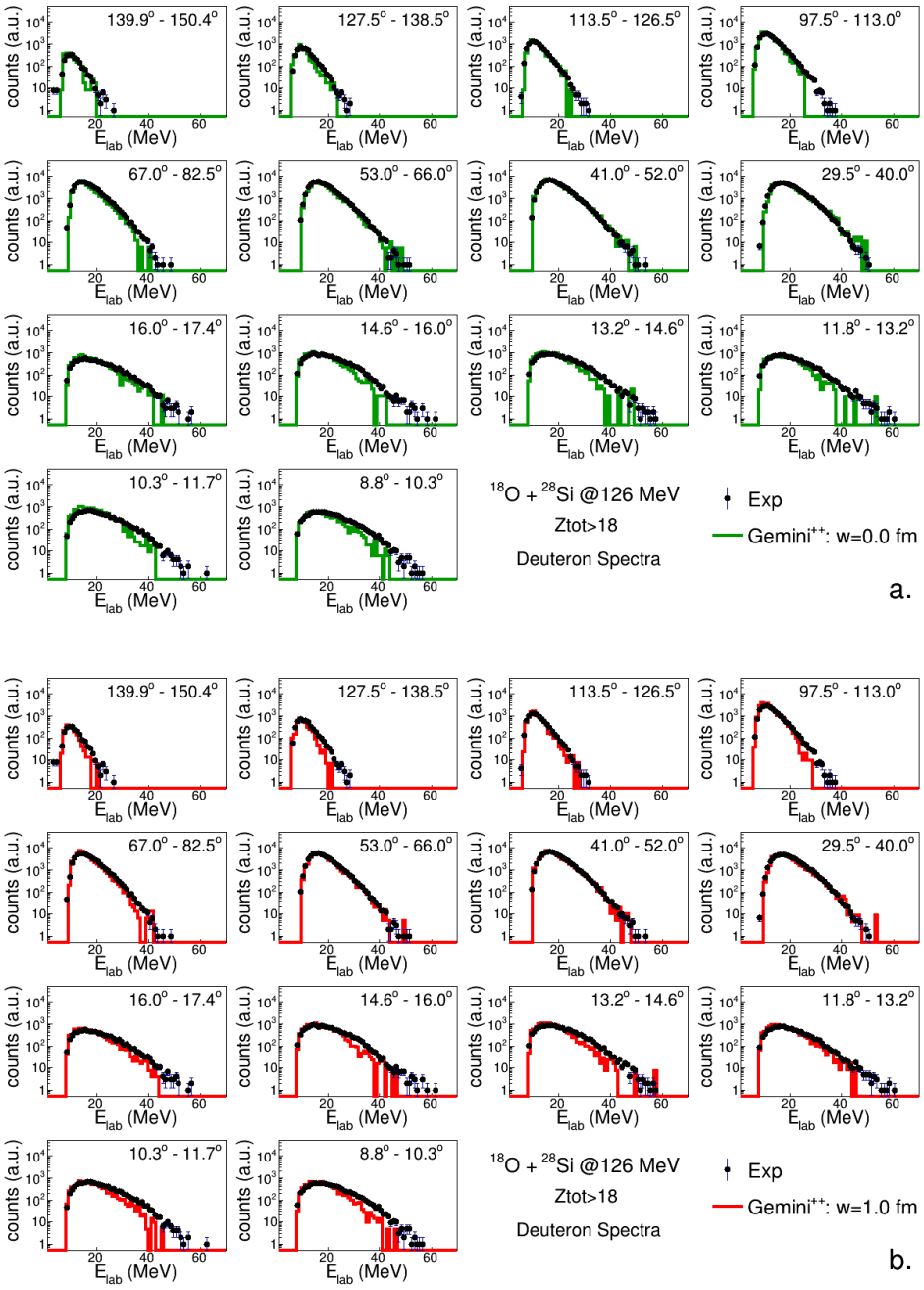

Figure A.23: Deuteron energy distributions for the reaction $^{18}O + ^{28}Si$ at 126 MeV: comparison between experimental data (black dots) and simulations performed with $GEMINI^{++}$, in which the $w = 0.0$ fm (green line in panel a.) and $w = 1.0$ fm (red line in panel b.) barrier parameter were set. Spectra are normalized to the maximum for shape comparison purposes.

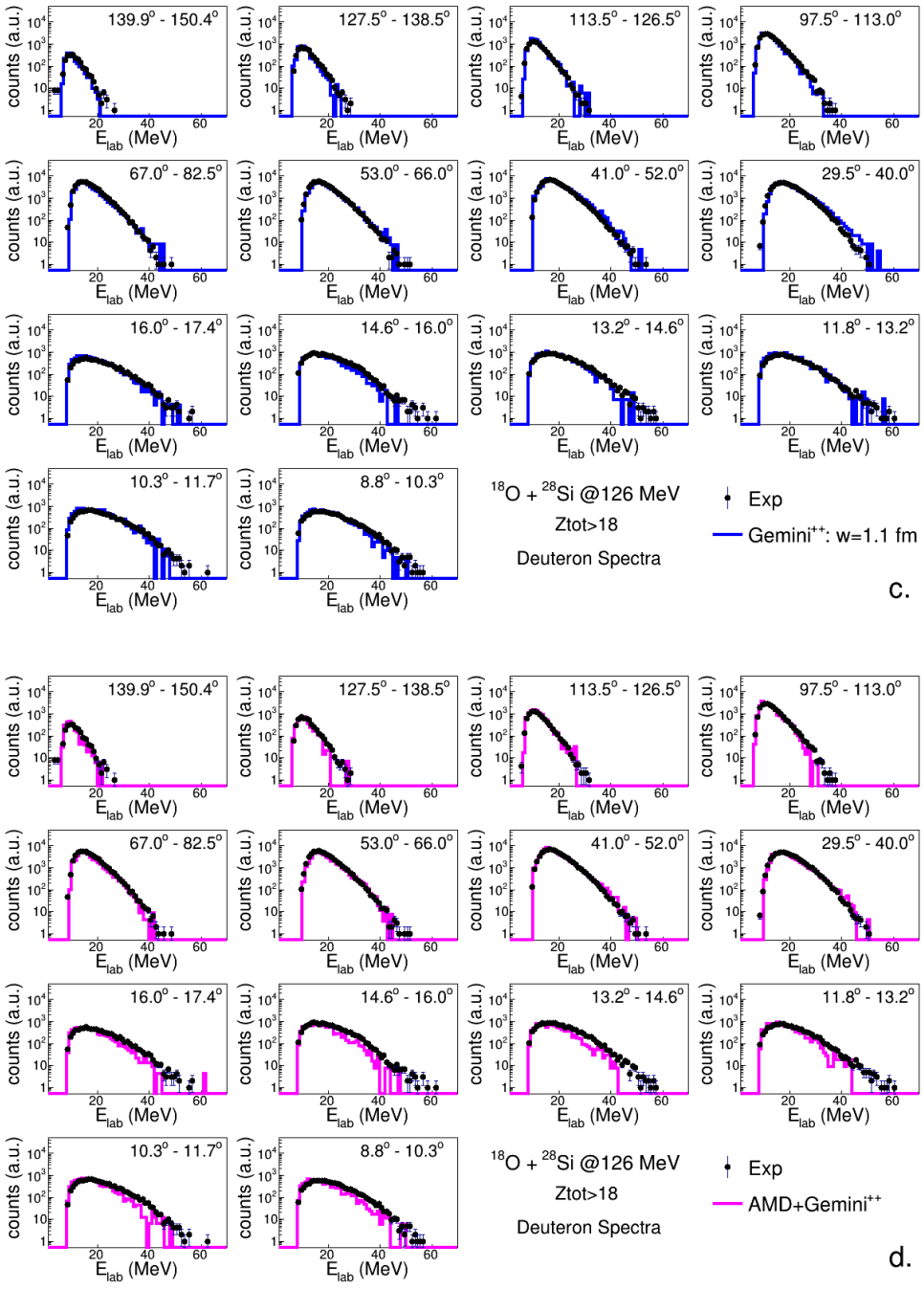

Figure A.24: Same as in the figure A.23 but comparison with $GEMINI^{++}$ (blue line in panel a.) and $AMD + GEMINI^{++}$ (pink line in panel b.); the parameter $w = 1.1$ fm was used for both $GEMINI^{++}$.

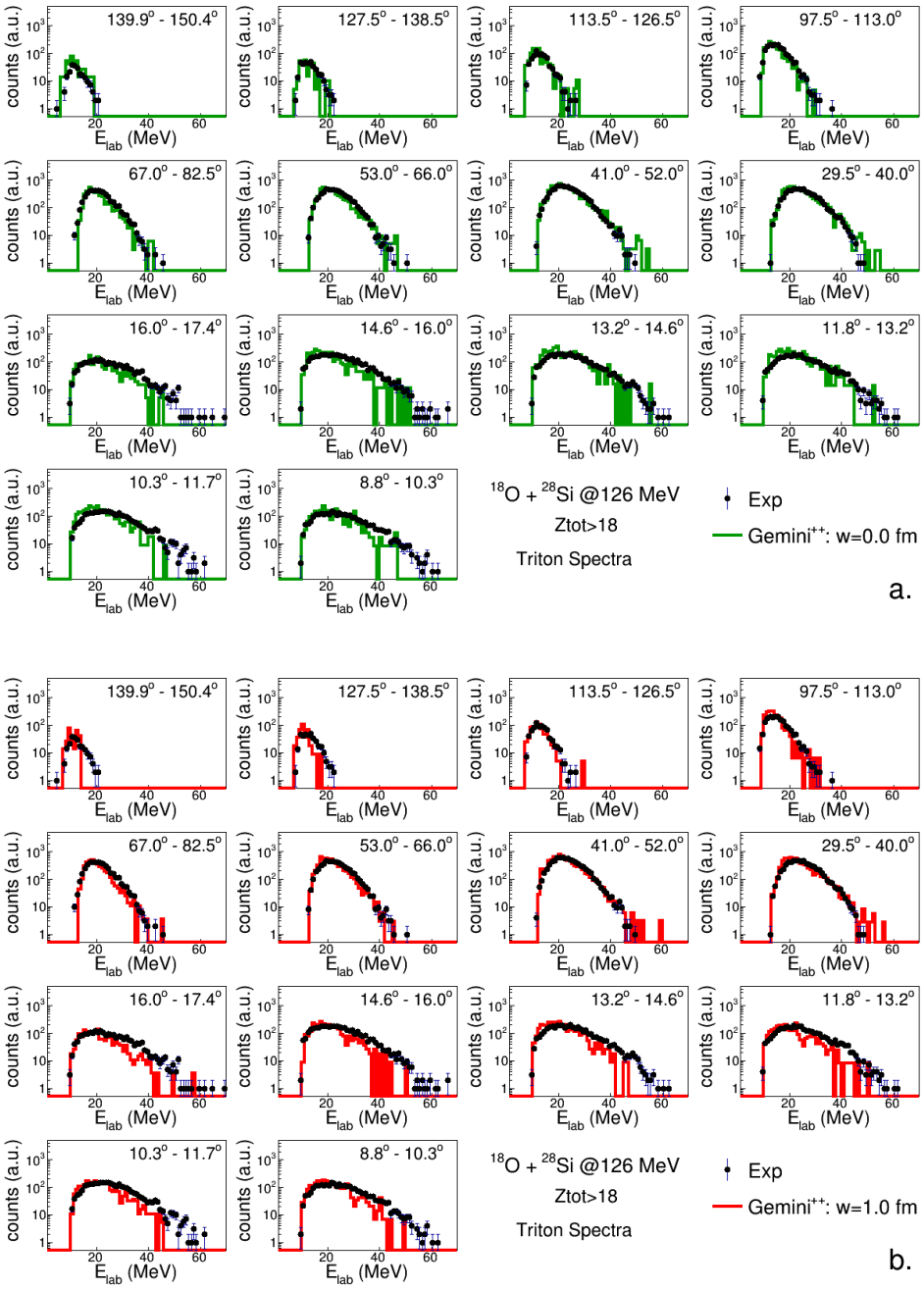

Figure A.25: Triton energy distributions for the reaction $^{18}O + ^{28}Si$ at 126 MeV: comparison between experimental data (black dots) and simulations performed with $GEMINI^{++}$, in which the $w = 0.0$ fm (green line in panel a.) and $w = 1.0$ fm (red line in panel b.) barrier parameter were set. Spectra are normalized to the maximum for shape comparison purposes.

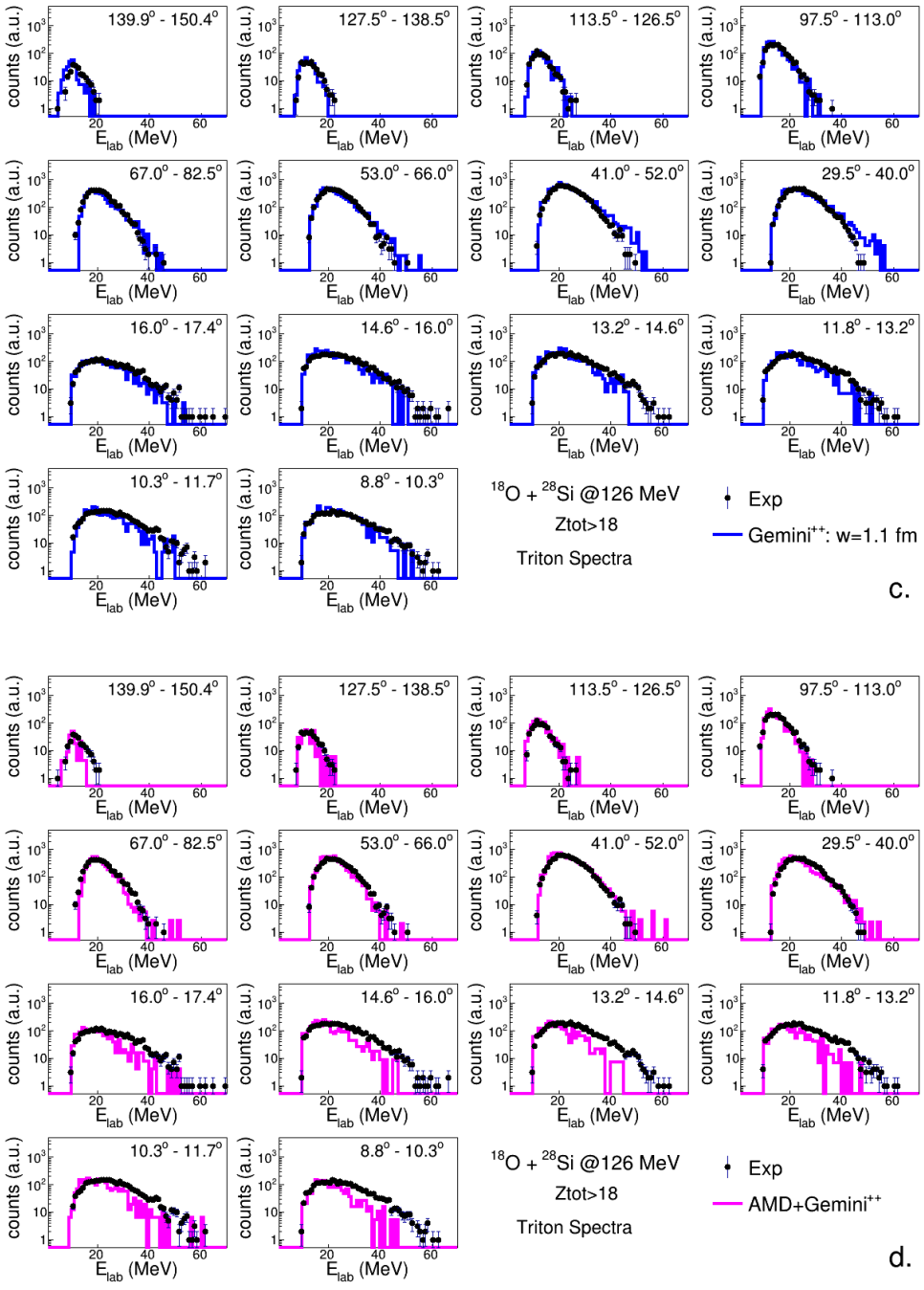

Figure A.26: Same as in the figure A.25 but comparison with $GEMINI^{++}$ (blue line in panel a.) and $AMD + GEMINI^{++}$ (pink line in panel b.); the parameter $w = 1.1$ fm was used for both $GEMINI^{++}$.

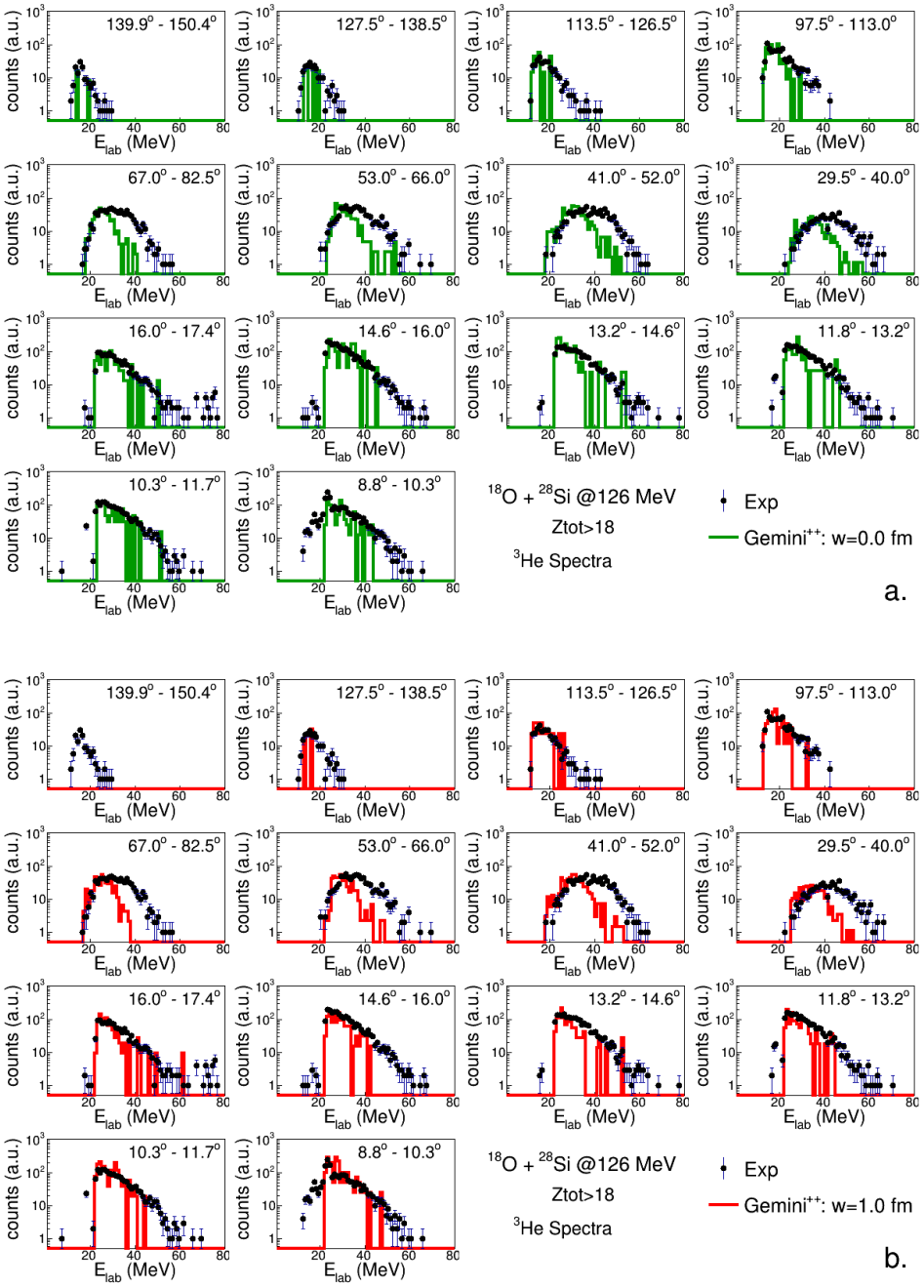

Figure A.27: ^3He energy distributions for the reaction $^{18}O + ^{28}Si$ at 126 MeV: comparison between experimental data (black dots) and simulations performed with $GEMINI^{++}$, in which the $w = 0.0$ fm (green line in panel a.) and $w = 1.0$ fm (red line in panel b.) barrier parameter were set. Spectra are normalized to the maximum for shape comparison purposes.

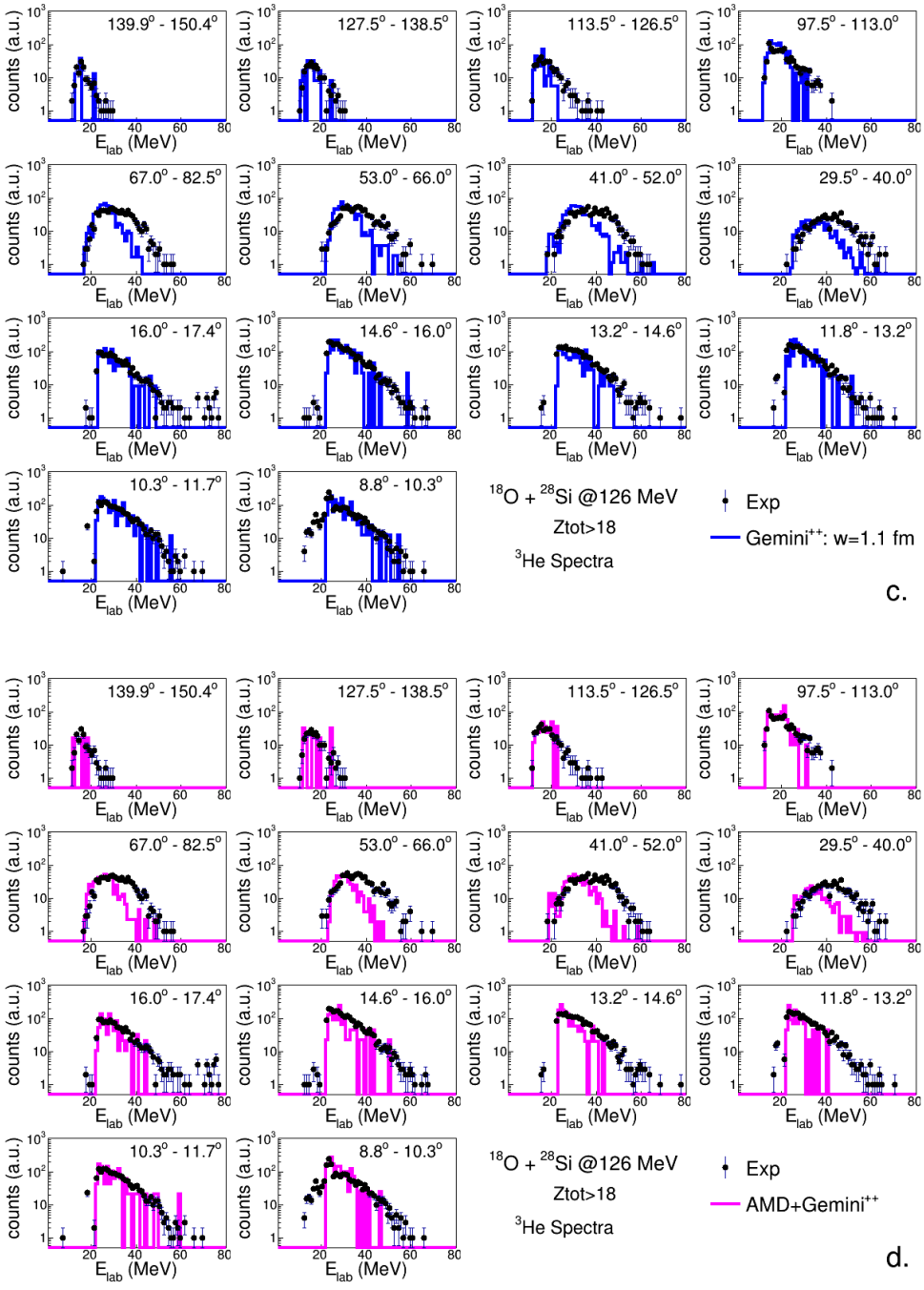

Figure A.28: Same as in the figure A.27 but comparison with $GEMINI^{++}$ (blue line in panel a.) and $AMD + GEMINI^{++}$ (pink line in panel b.); the parameter $w = 1.1$ fm was used for both $GEMINI^{++}$.

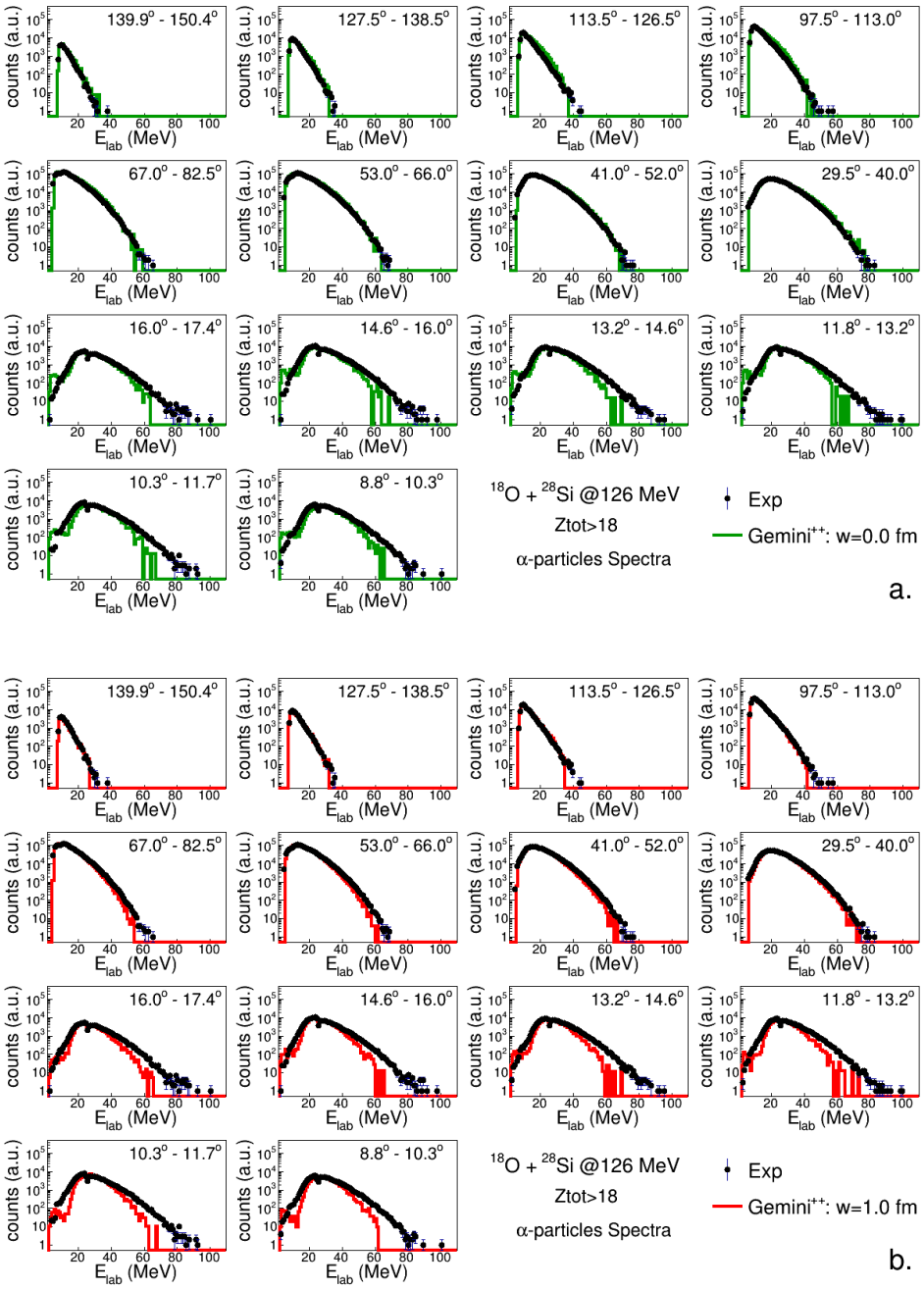

Figure A.29: α-particles energy distributions for the reaction $^{18}O + ^{28}Si$ at 126 MeV: comparison between experimental data (black dots) and simulations performed with $GEMINI^{++}$, in which the $w = 0.0$ fm (green line in panel a.) and $w = 1.0$ fm (red line in panel b.) barrier parameter were set. Spectra are normalized to the maximum for shape comparison purposes.

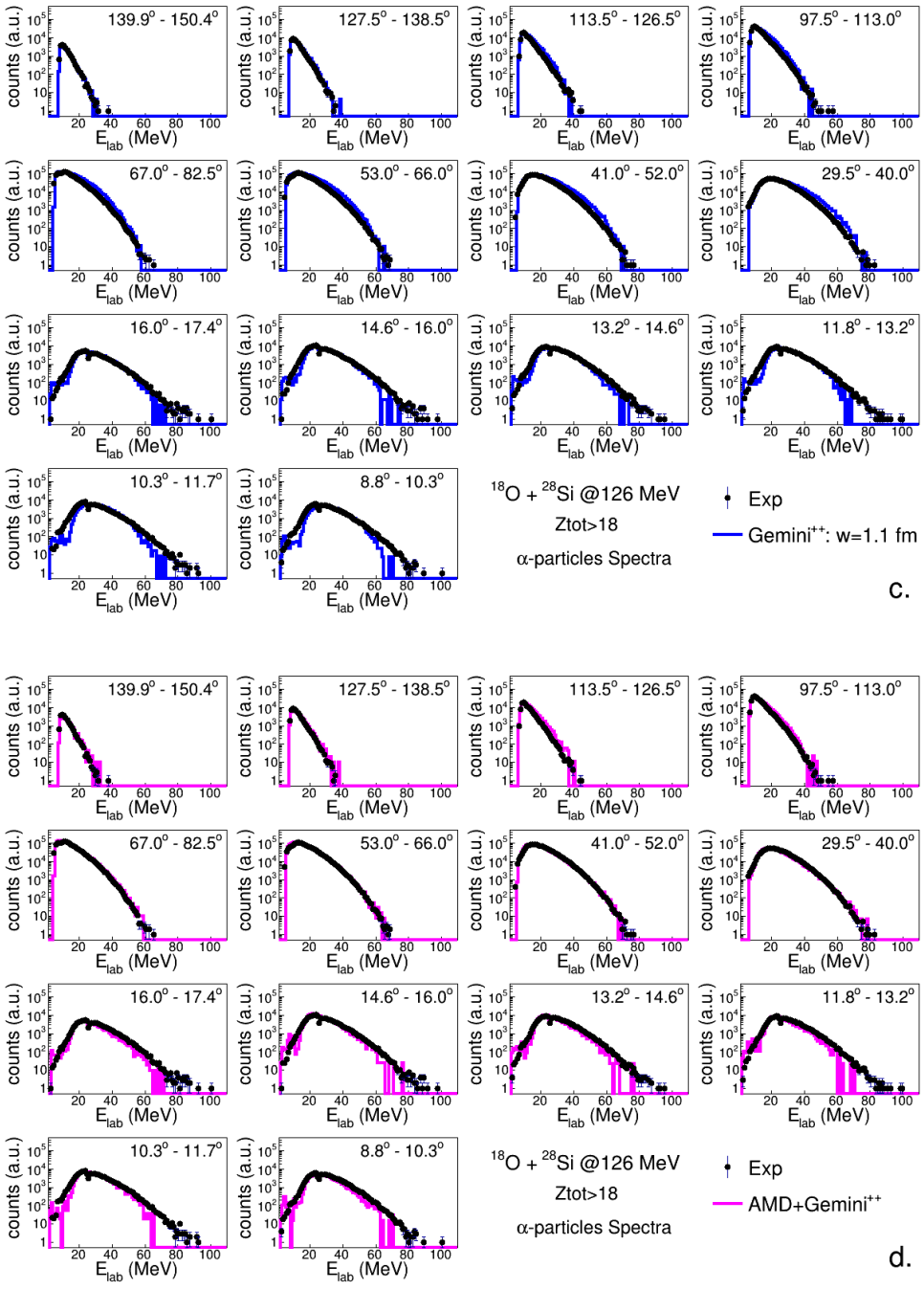

Figure A.30: Same as in the figure A.29 but comparison with $GEMINI^{++}$ (blue line in panel a.) and $AMD + GEMINI^{++}$ (pink line in panel b.); the parameter $w = 1.1$ fm was used for both $GEMINI^{++}$.

A.4 $^{19}F+^{27}Al$ at 133 MeV

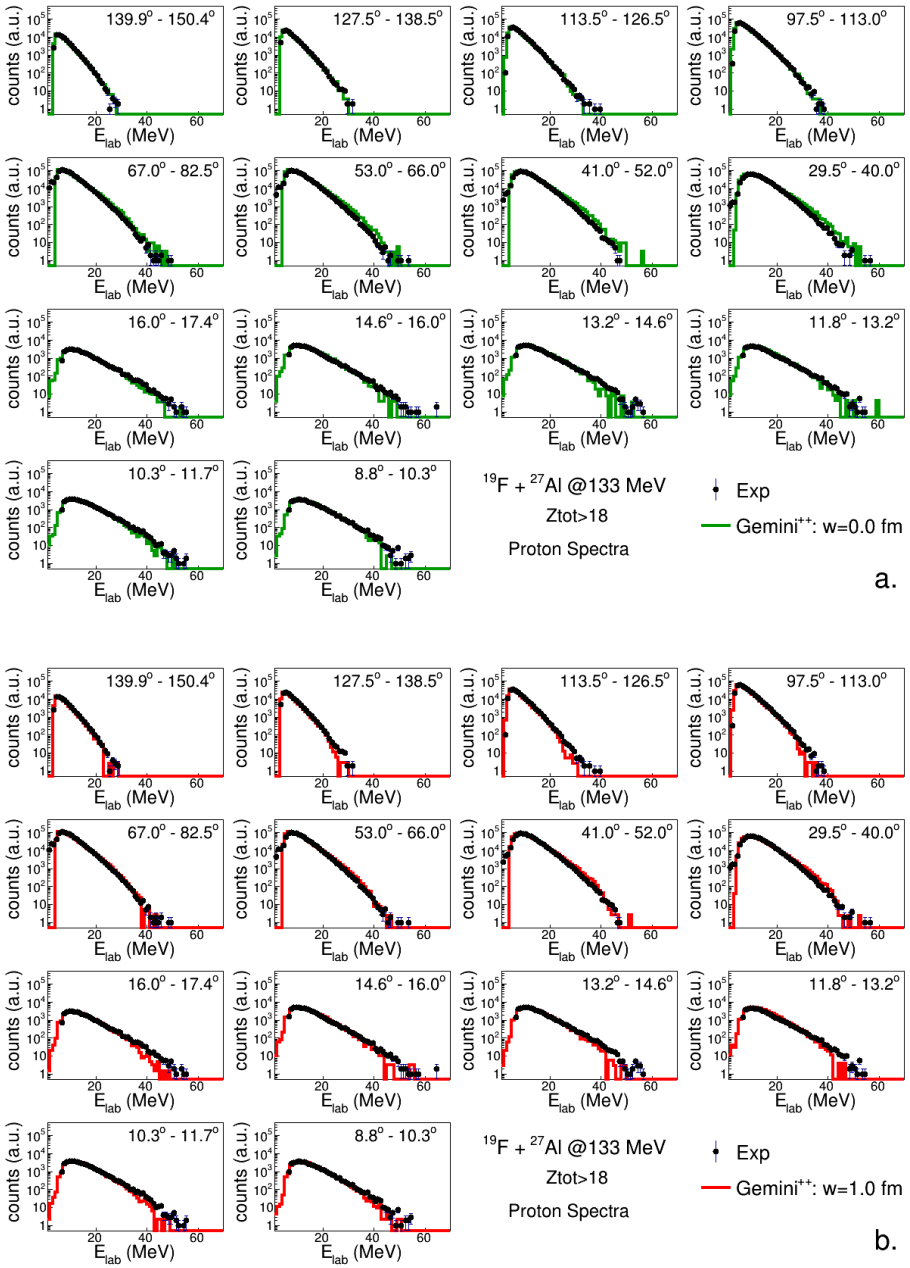

Figure A.31: Proton energy distributions for the reaction $^{19}F+^{27}Al$ at 133 MeV: comparison between experimental data (black dots) and simulations performed with $GEMINI^{++}$, in which the $w = 0.0$ fm (green line in panel a.) and $w = 1.0$ fm (red line in panel b.) barrier parameter were set. Spectra are normalized to the maximum for shape comparison purposes. See text for more details on simulation parameters.

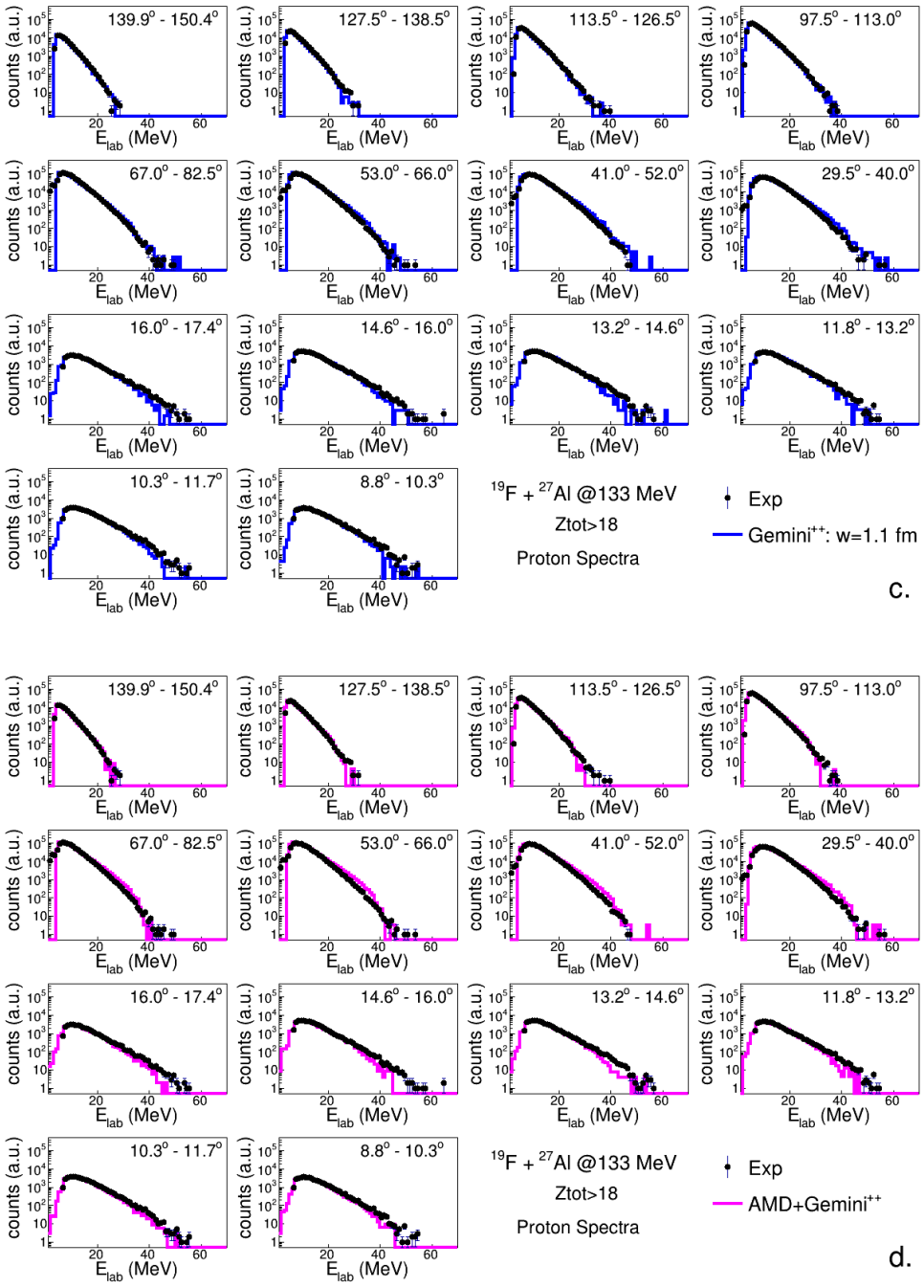

Figure A.32: Same as in the figure A.31 but comparison with $GEMINI^{++}$ (blue line in panel a.) and $AMD + GEMINI^{++}$ (pink line in panel b.); the parameter $w = 1.1$ fm was used for both $GEMINI^{++}$.

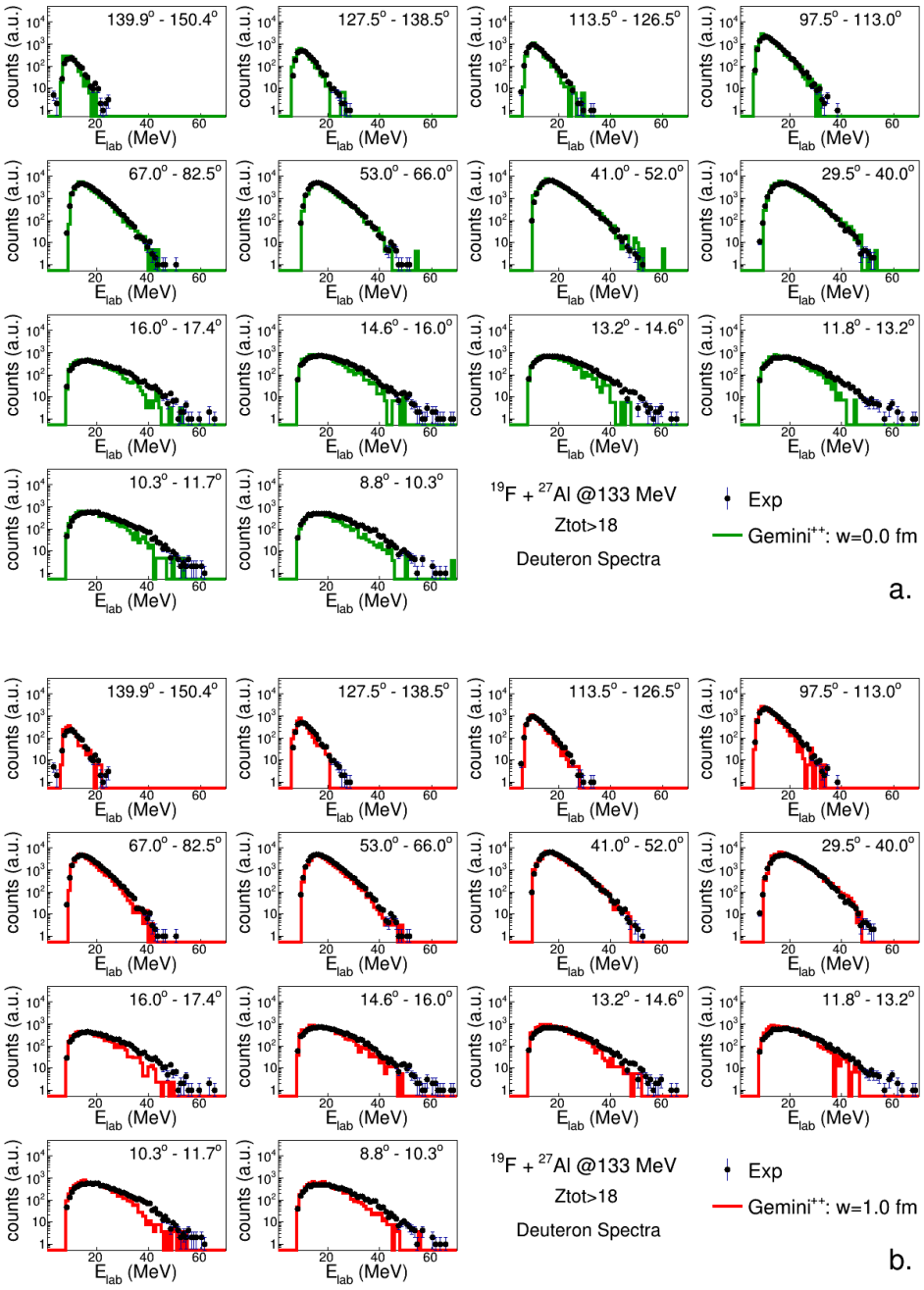

Figure A.33: Deuteron energy distributions for the reaction $^{19}F + ^{27}Al$ at 133 MeV: comparison between experimental data (black dots) and simulations performed with $GEMINI^{++}$, in which the $w = 0.0$ fm (green line in panel a.) and $w = 1.0$ fm (red line in panel b.) barrier parameter were set. Spectra are normalized to the maximum for shape comparison purposes.

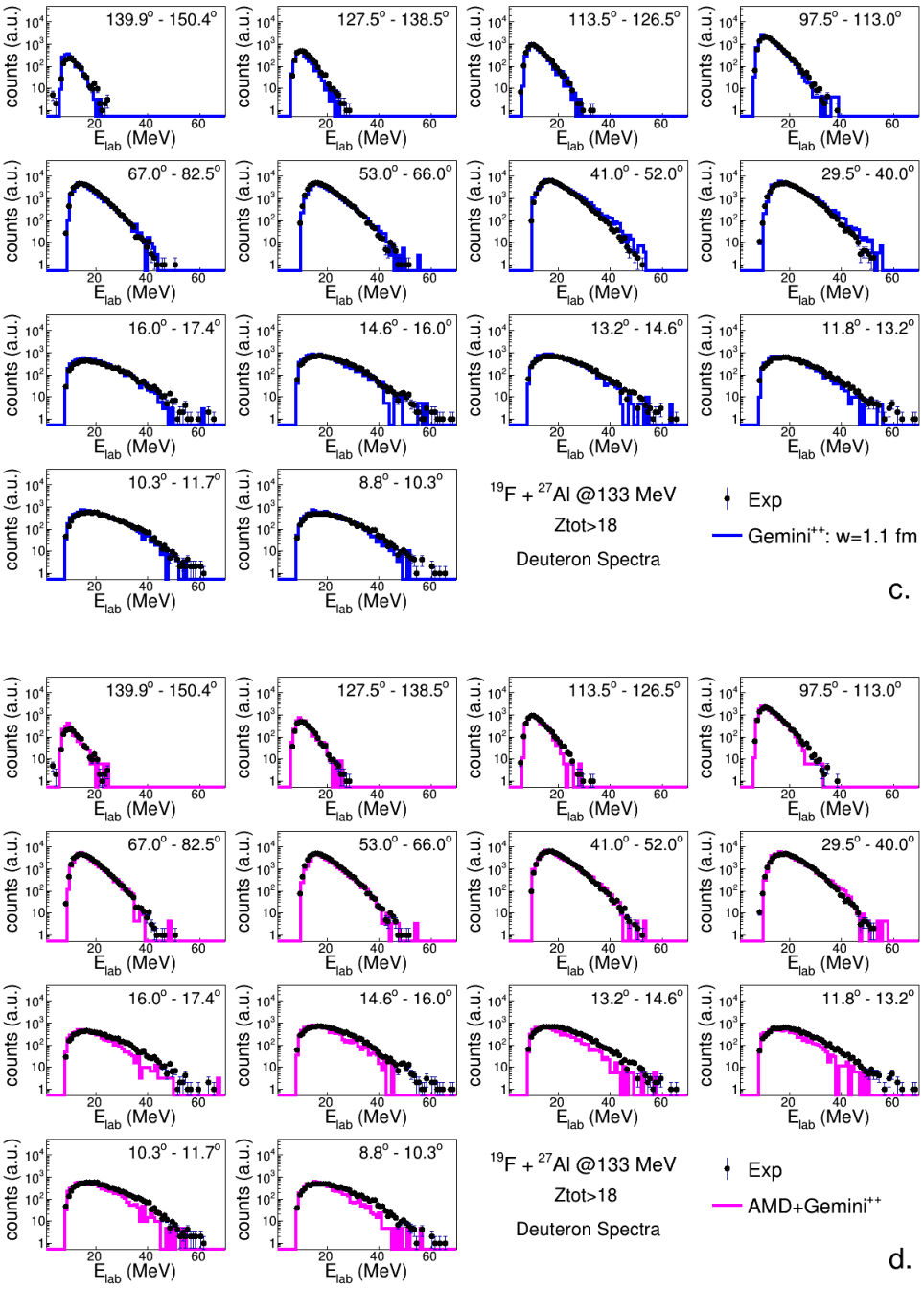

Figure A.34: Same as in the figure A.33 but comparison with $GEMINI^{++}$ (blue line in panel a.) and $AMD + GEMINI^{++}$ (pink line in panel b.); the parameter $w = 1.1$ fm was used for both $GEMINI^{++}$.

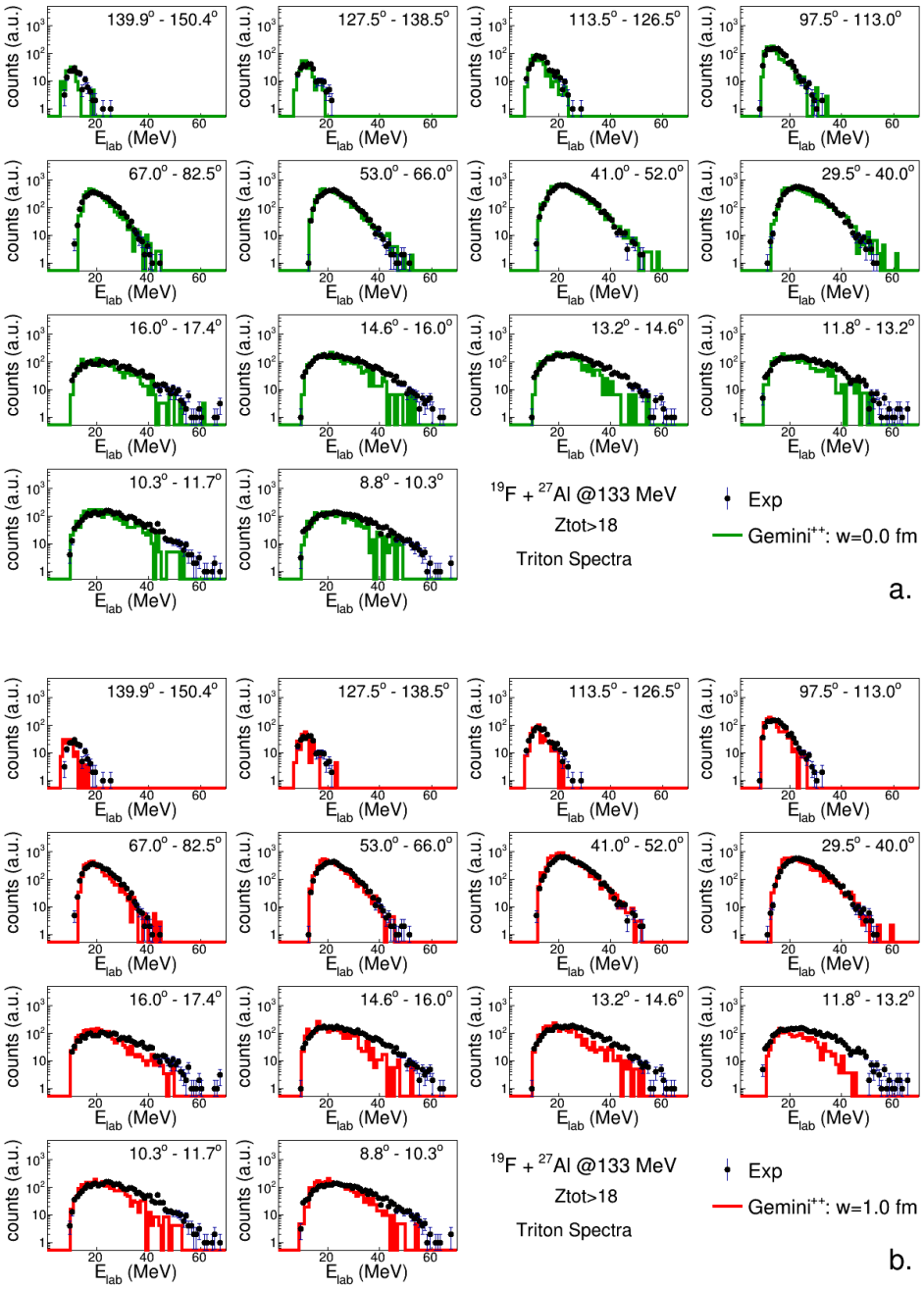

Figure A.35: Triton energy distributions for the reaction $^{19}F+^{27}Al$ at 133 MeV: comparison between experimental data (black dots) and simulations performed with $GEMINI^{++}$, in which the $w = 0.0$ fm (green line in panel a.) and $w = 1.0$ fm (red line in panel b.) barrier parameter were set. Spectra are normalized to the maximum for shape comparison purposes.

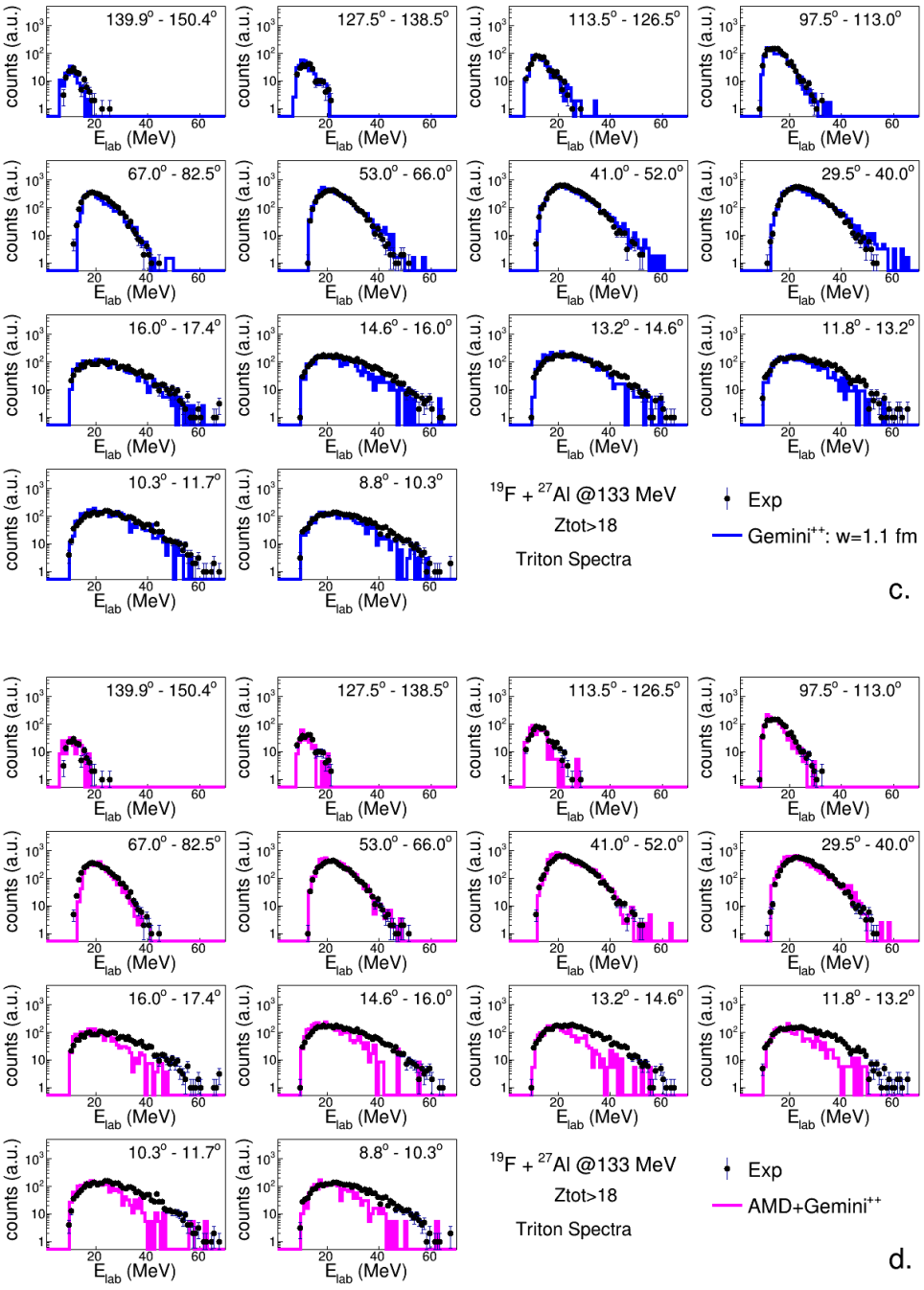

Figure A.36: Same as in the figure A.35 but comparison with $GEMINI^{++}$ (blue line in panel a.) and $AMD + GEMINI^{++}$ (pink line in panel b.); the parameter $w = 1.1$ fm was used for both $GEMINI^{++}$.

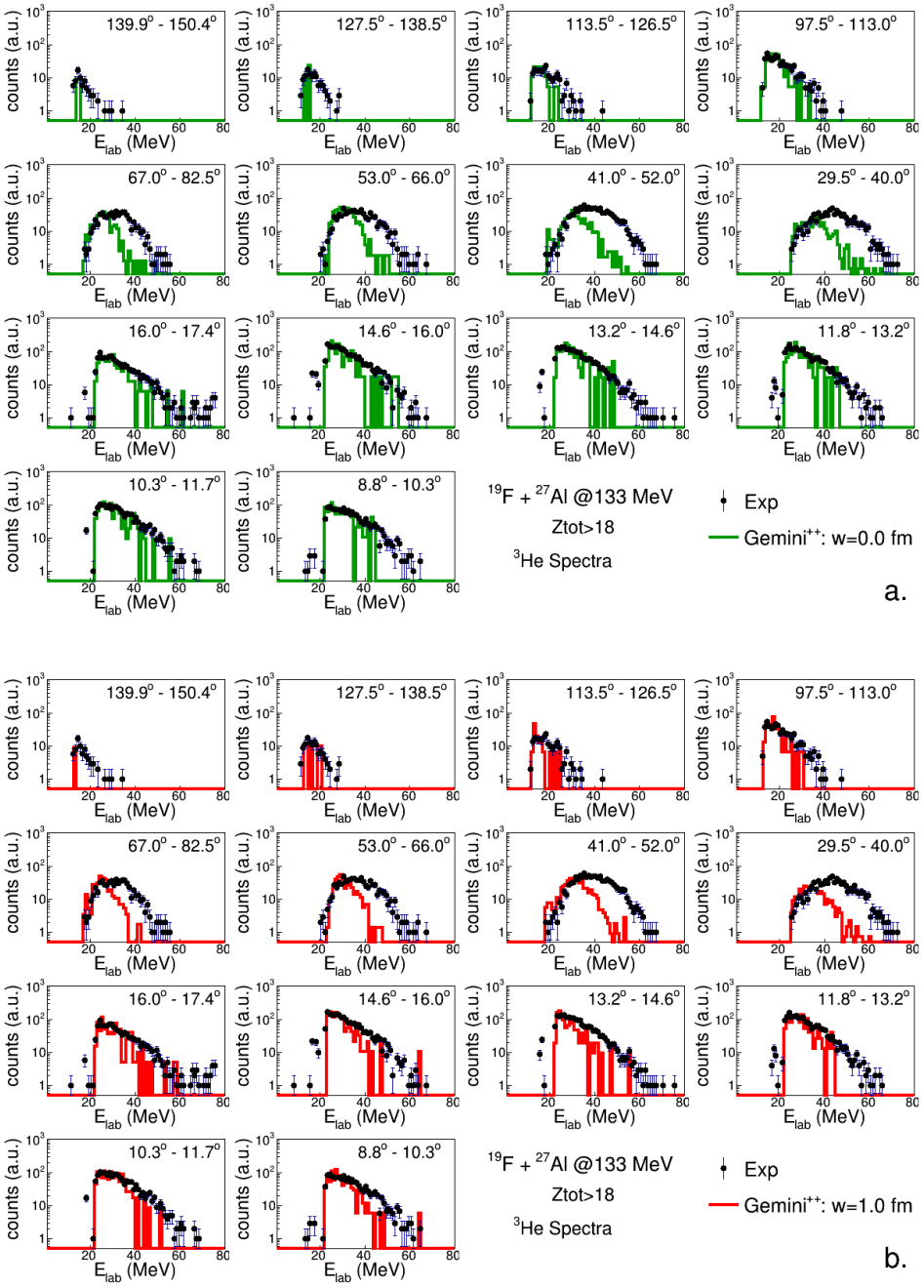

Figure A.37: ^{3}He energy distributions for the reaction $^{19}F + ^{27}Al$ at 133 MeV: comparison between experimental data (black dots) and simulations performed with $GEMINI^{++}$, in which the $w = 0.0$ fm (green line in panel a.) and $w = 1.0$ fm (red line in panel b.) barrier parameter were set. Spectra are normalized to the maximum for shape comparison purposes.

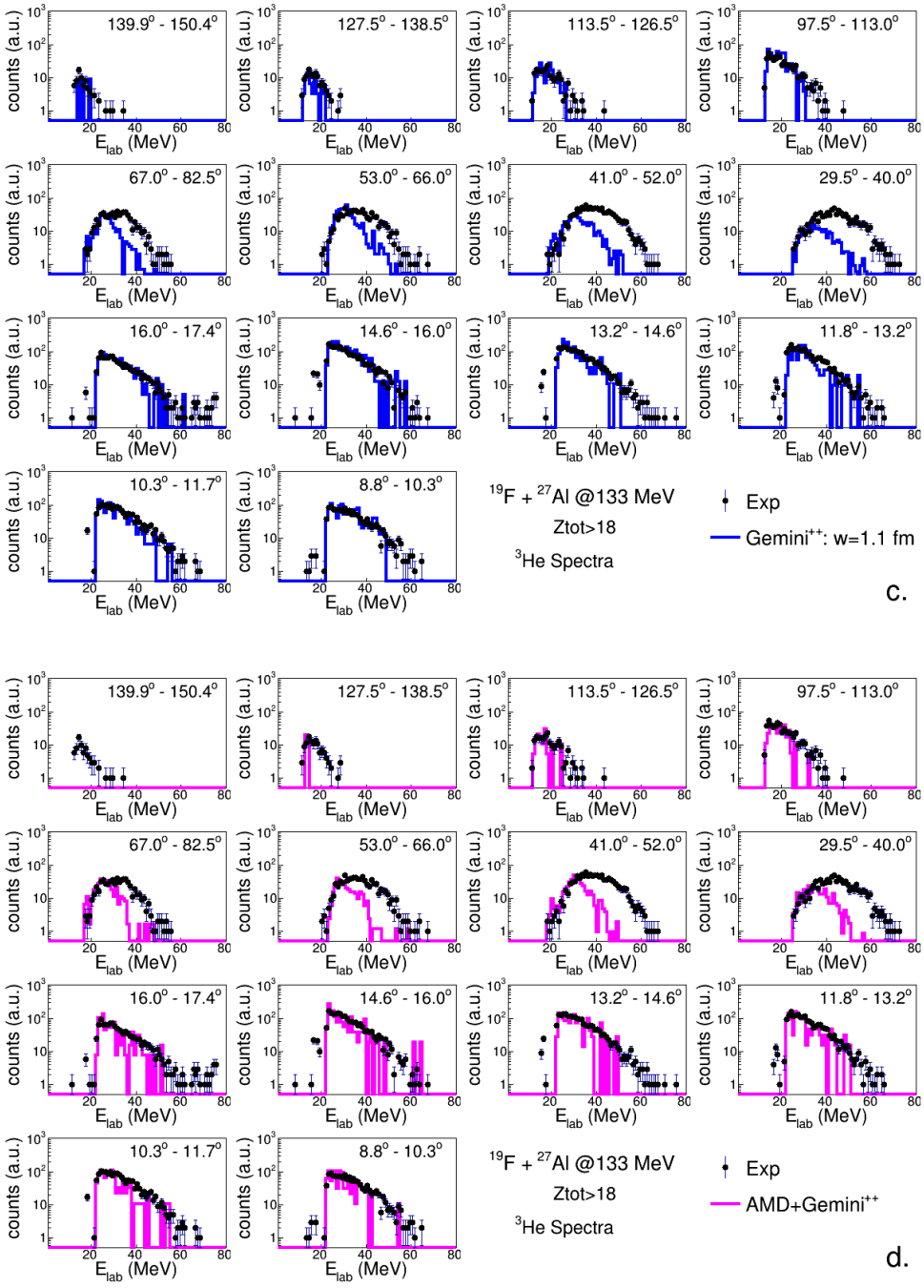

Figure A.38: Same as in the figure A.37 but comparison with $GEMINI^{++}$ (blue line in panel a.) and $AMD + GEMINI^{++}$ (pink line in panel b.); the parameter $w = 1.1$ fm was used for both $GEMINI^{++}$.

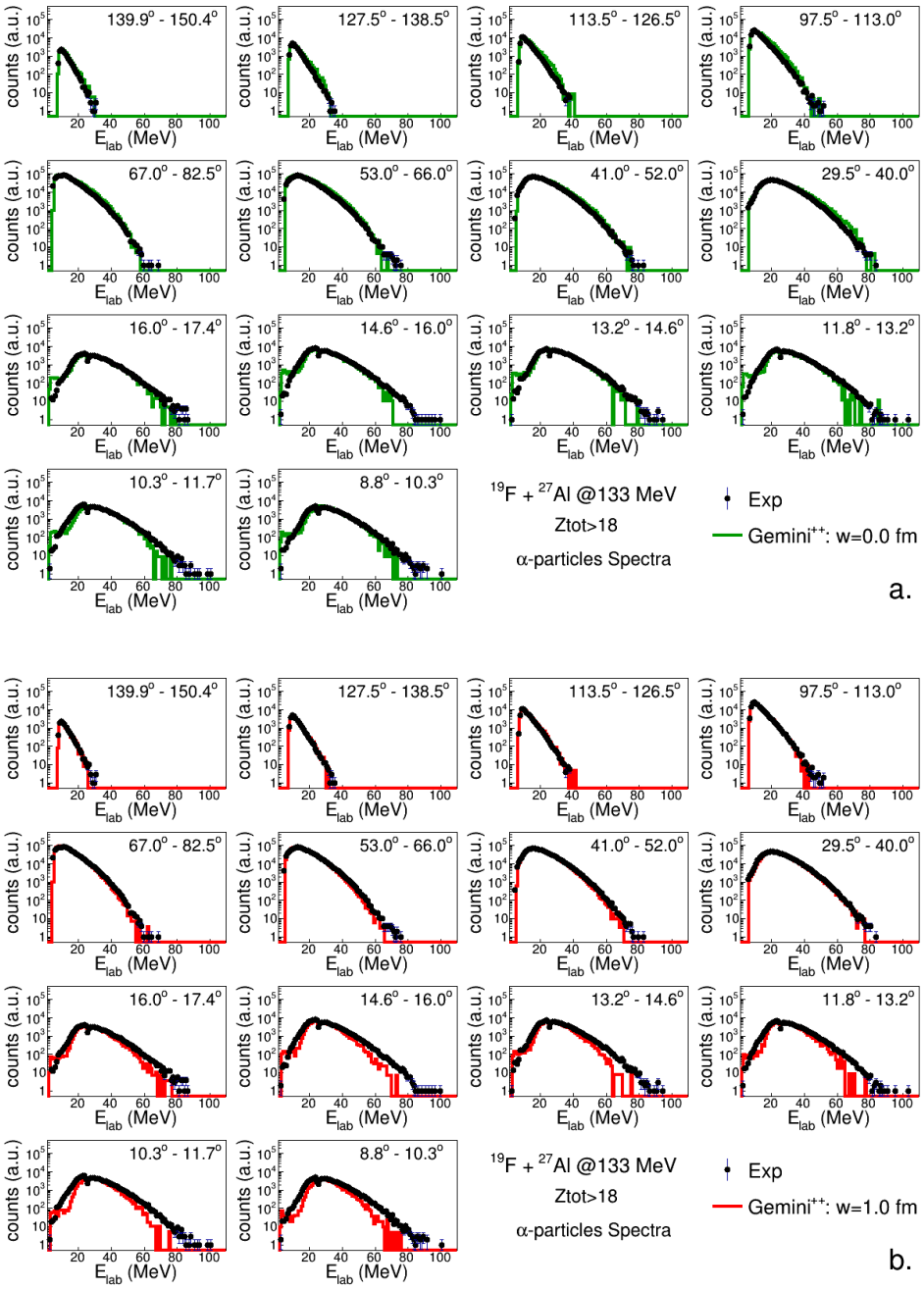

Figure A.39: α-particles energy distributions for the reaction $^{19}F + ^{27}Al$ at 133 MeV: comparison between experimental data (black dots) and simulations performed with $GEMINI^{++}$, in which the $w = 0.0$ fm (green line in panel a.) and $w = 1.0$ fm (red line in panel b.) barrier parameter were set. Spectra are normalized to the maximum for shape comparison purposes.

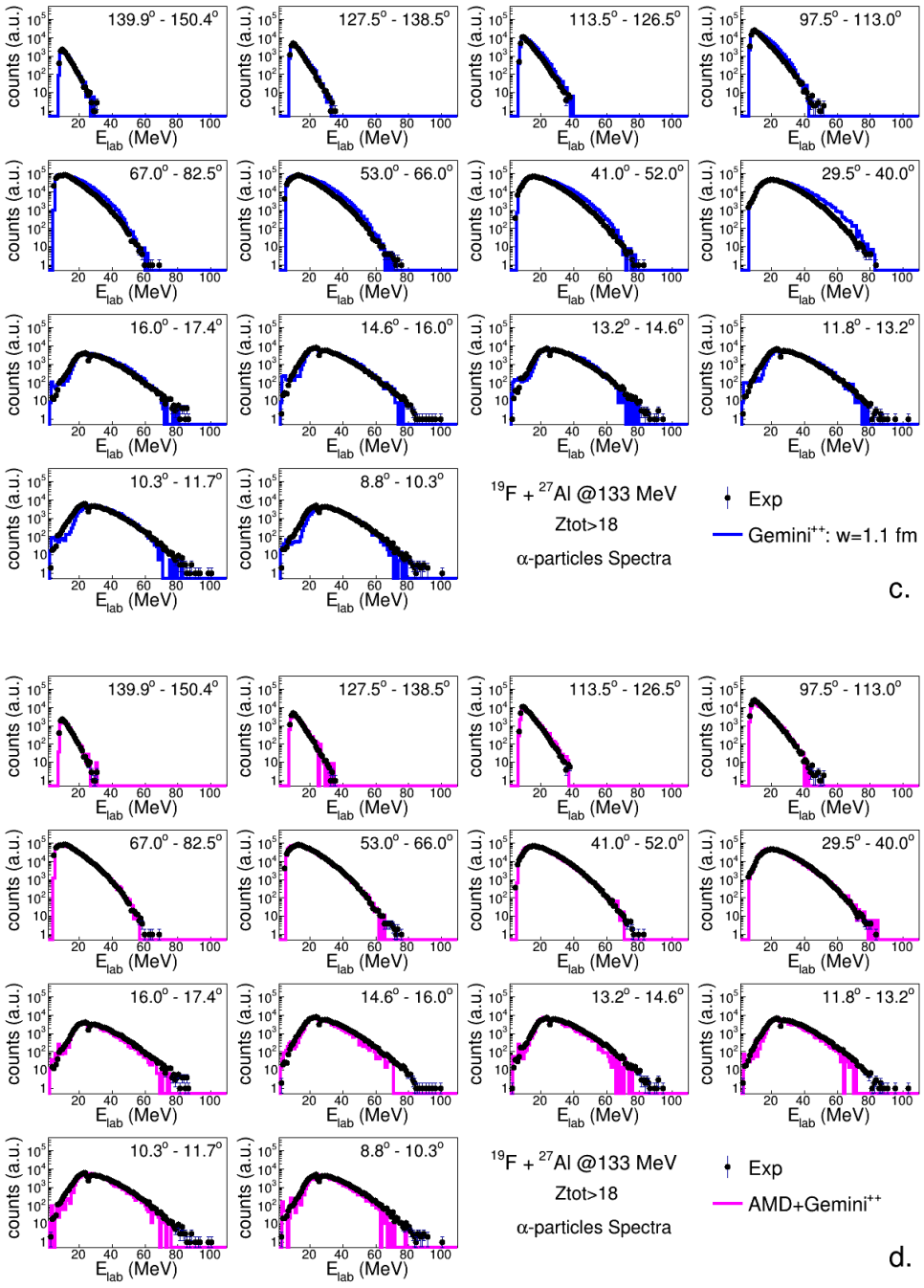

Figure A.40: Same as in the figure A.39 but comparison with $GEMINI^{++}$ (blue line in panel a.) and $AMD + GEMINI^{++}$ (pink line in panel b.); the parameter $w = 1.1$ fm was used for both $GEMINI^{++}$.

Appendix B

LCP spectra of Chapter 8

B.1 The Sc residue: $Z_{res} = 21$

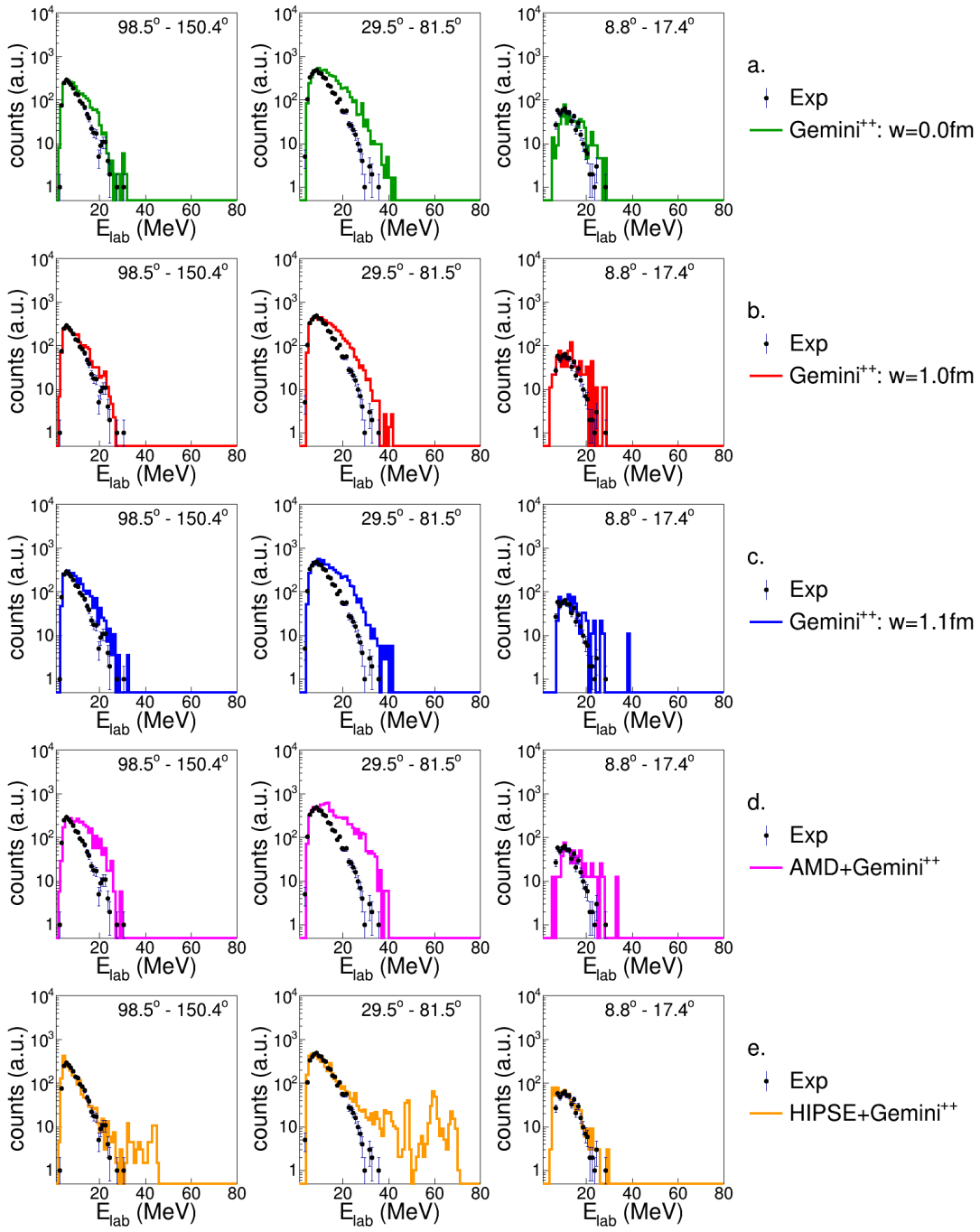

Figure B.1: Energy spectra of protons in coincidence with a *Sc*-residue for the reaction $^{16}O + ^{30}Si$ at 111 MeV.

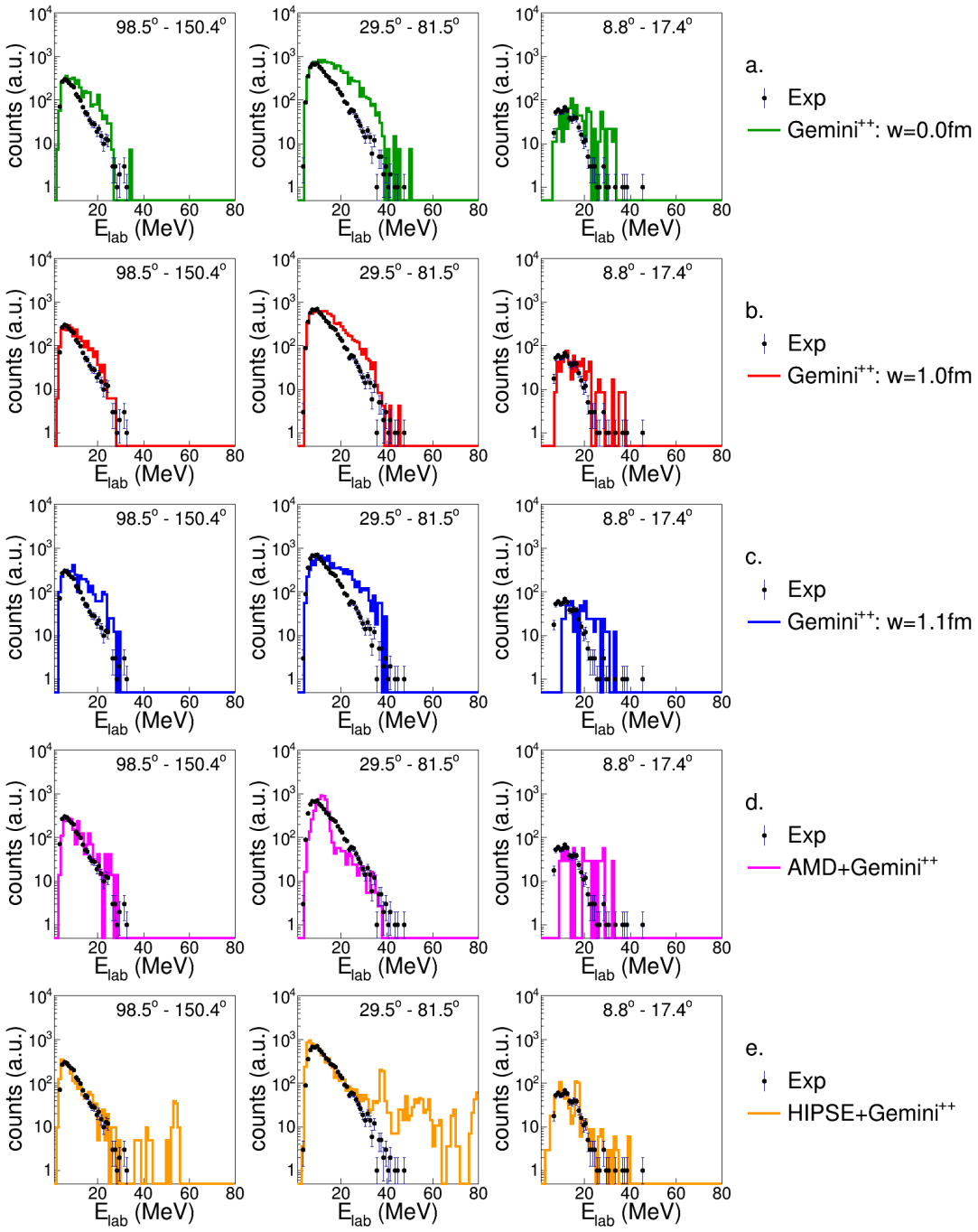

Figure B.2: Energy spectra of protons in coincidence with a *Sc*-residue for the reaction $^{16}O + ^{30}Si$ at 128 MeV

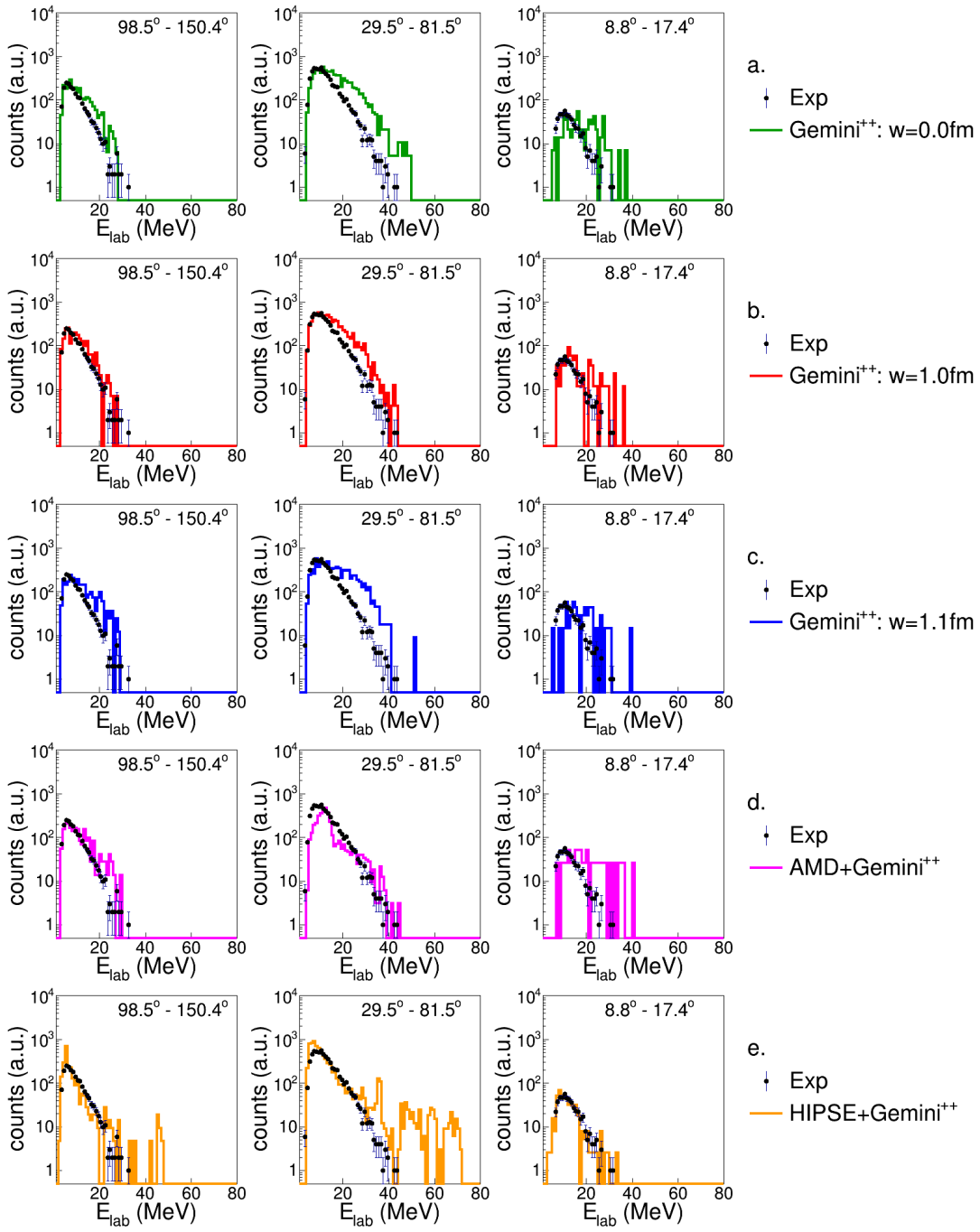

Figure B.3: Energy spectra of protons in coincidence with a *Sc*-residue for the reaction $^{18}O + ^{28}Si$ at 126 MeV

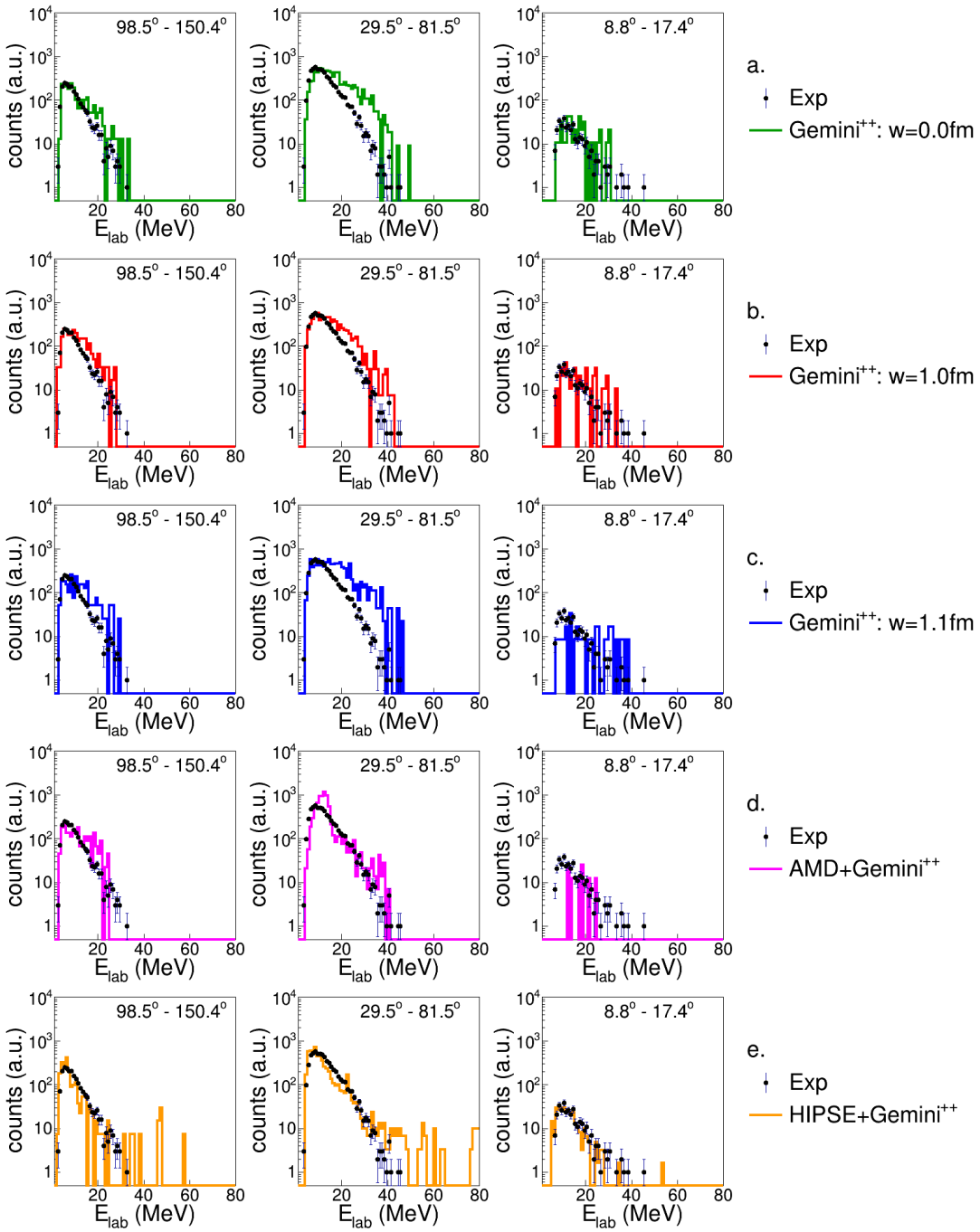

Figure B.4: Energy spectra of protons in coincidence with a *Sc*-residue for the reaction $^{19}F + ^{27}Al$ at 133 MeV

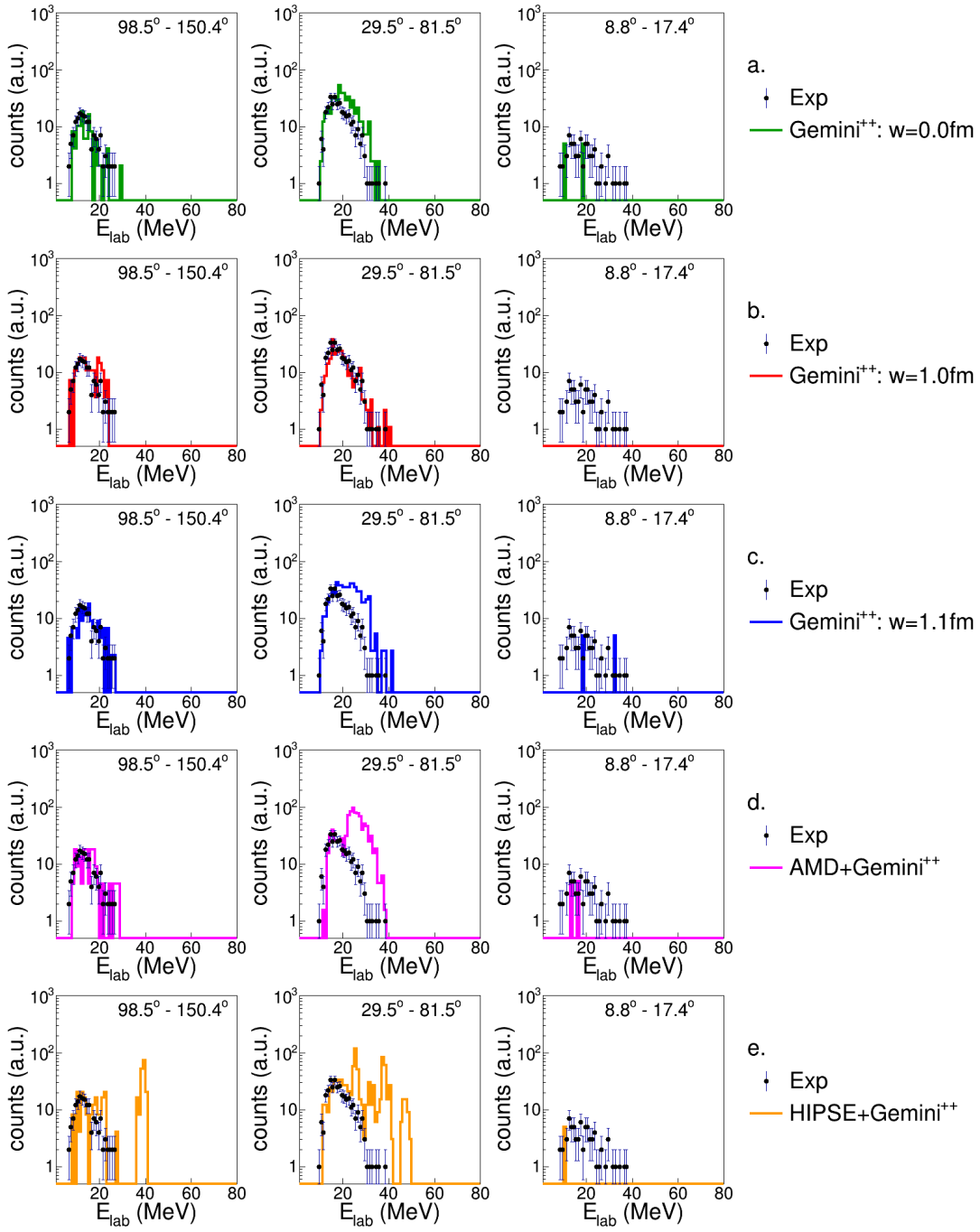

Figure B.5: Energy spectra of deuterons in coincidence with a *Sc*-residue for the reaction $^{16}O + ^{30}Si$ at 111 MeV.

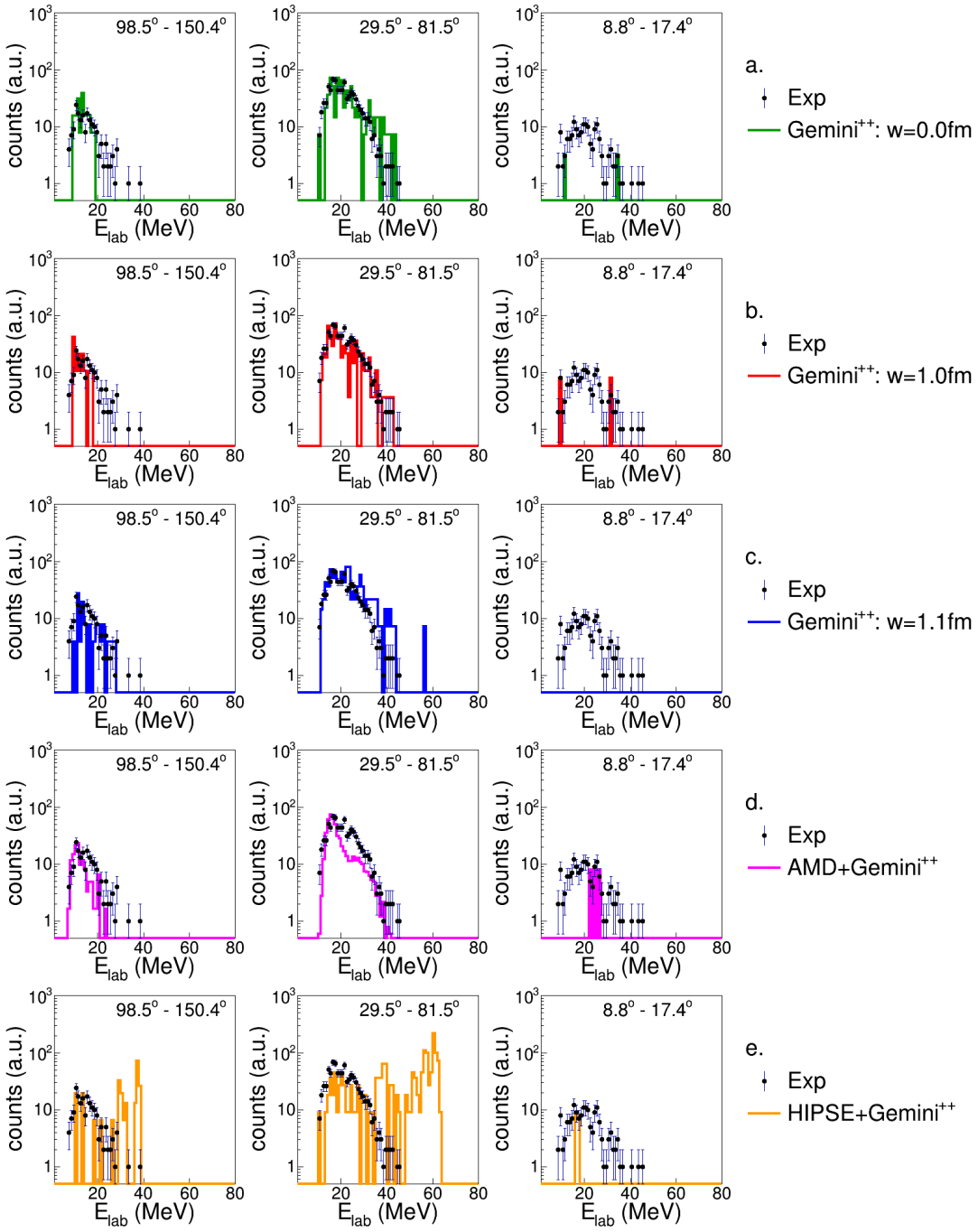

Figure B.6: Energy spectra of deuterons in coincidence with a *Sc*-residue for the reaction $^{16}O + ^{30}Si$ at 128 MeV

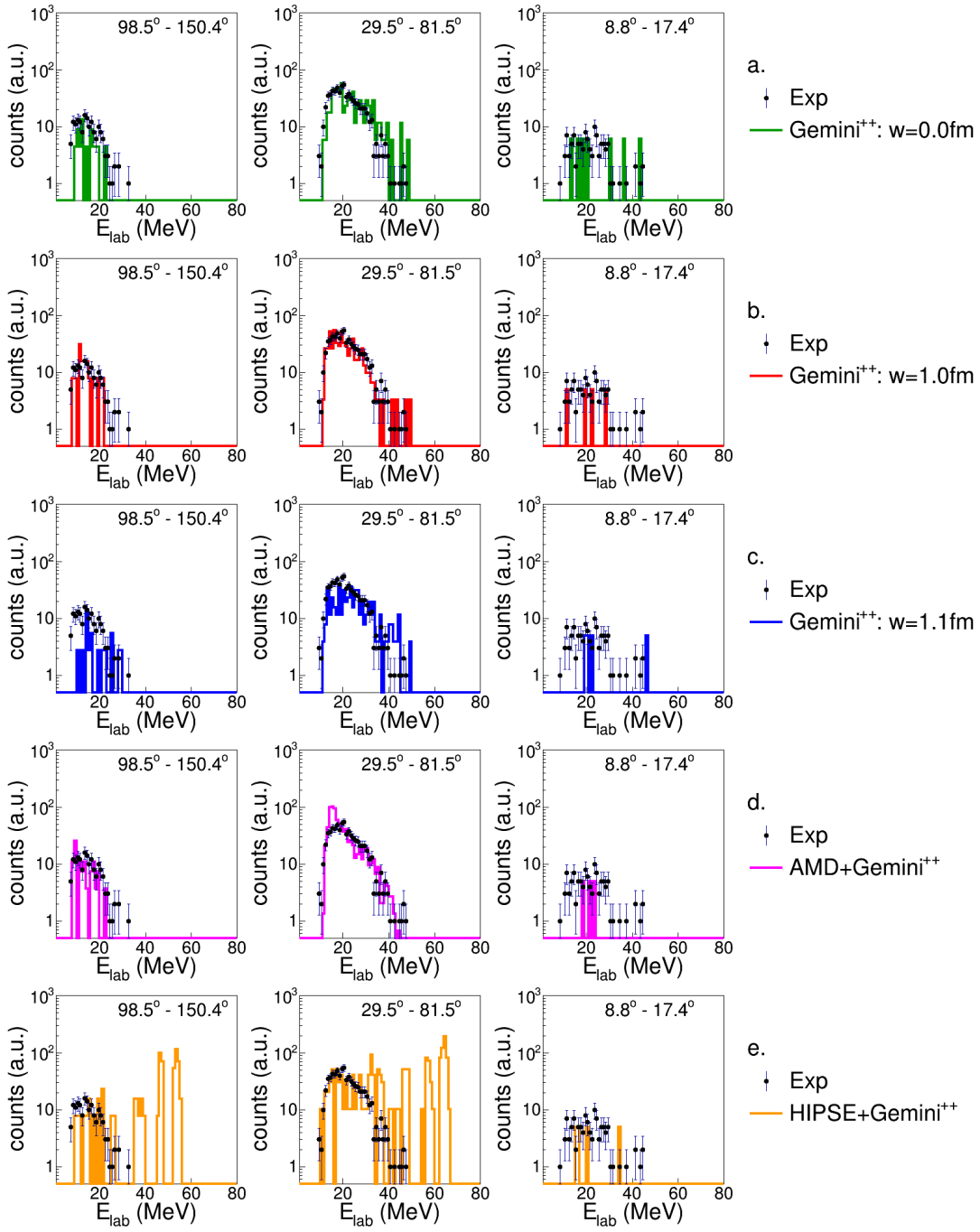

Figure B.7: Energy spectra of deuterons in coincidence with a *Sc*-residue for the reaction $^{18}O + ^{28}Si$ at 126 MeV

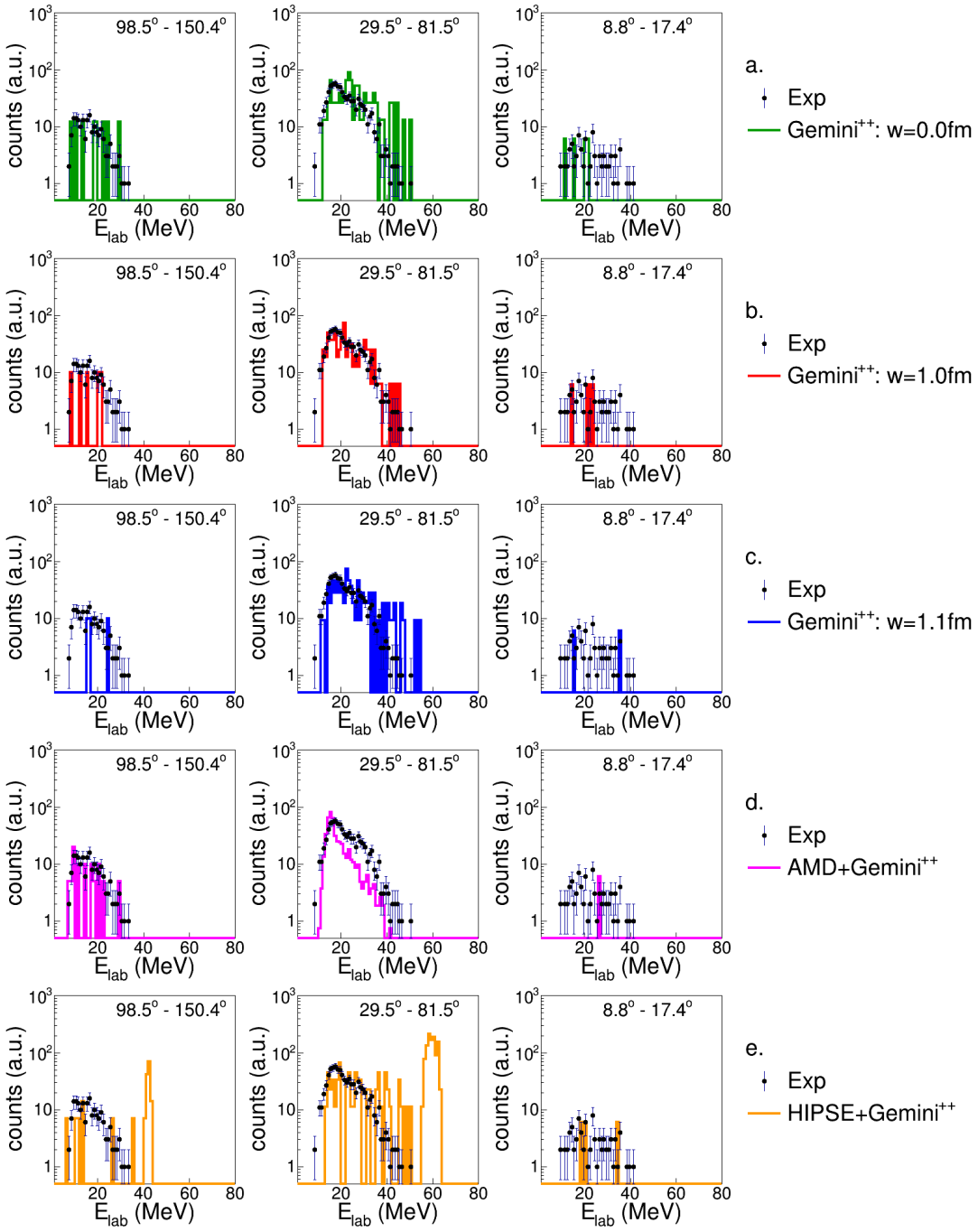

Figure B.8: Energy spectra of deuterons in coincidence with a *Sc*-residue for the reaction $^{19}F + ^{27}Al$ at 133 MeV

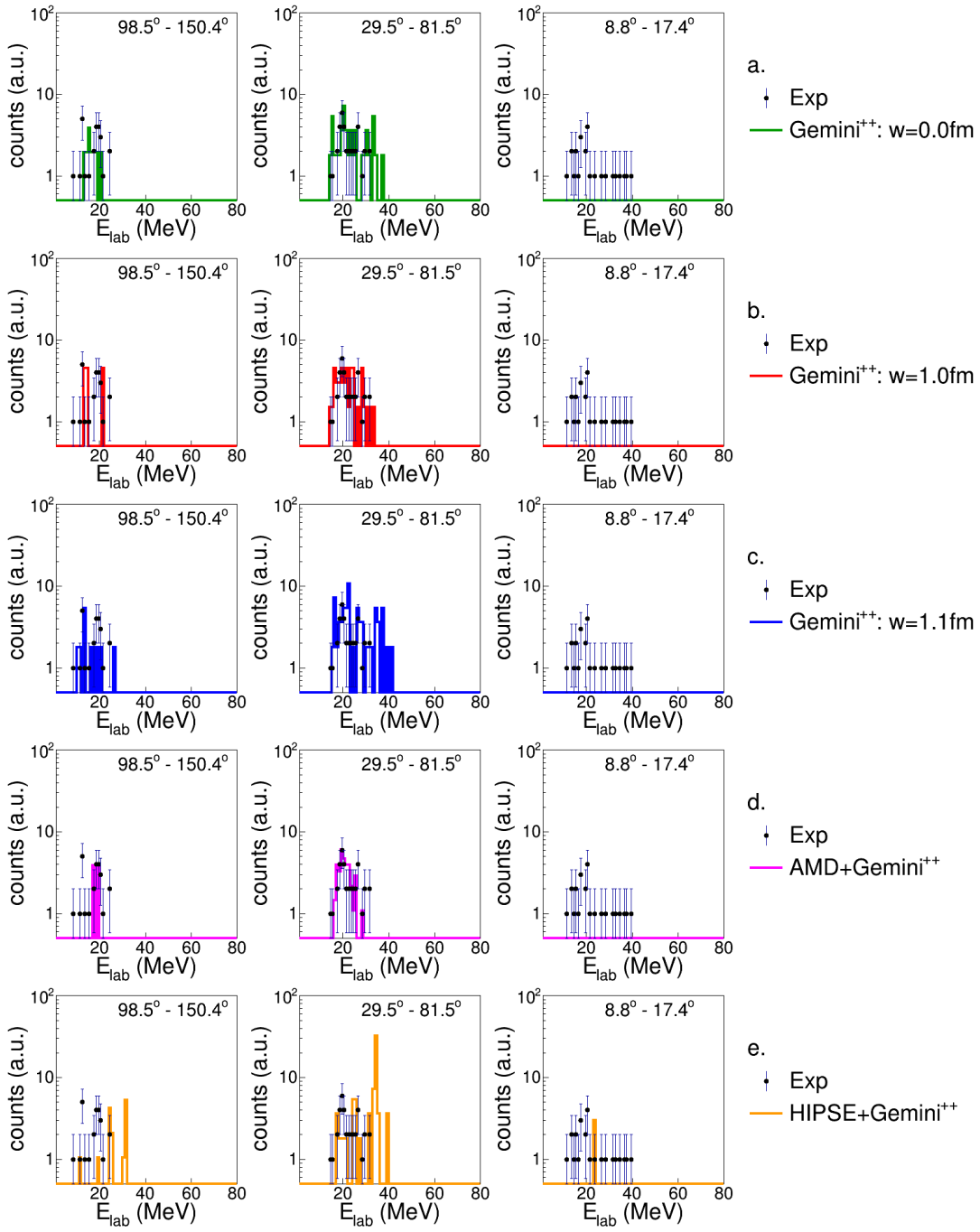

Figure B.9: Energy spectra of tritons in coincidence with a Sc-residue for the reaction $^{16}O+^{30}Si$ at 111 MeV.

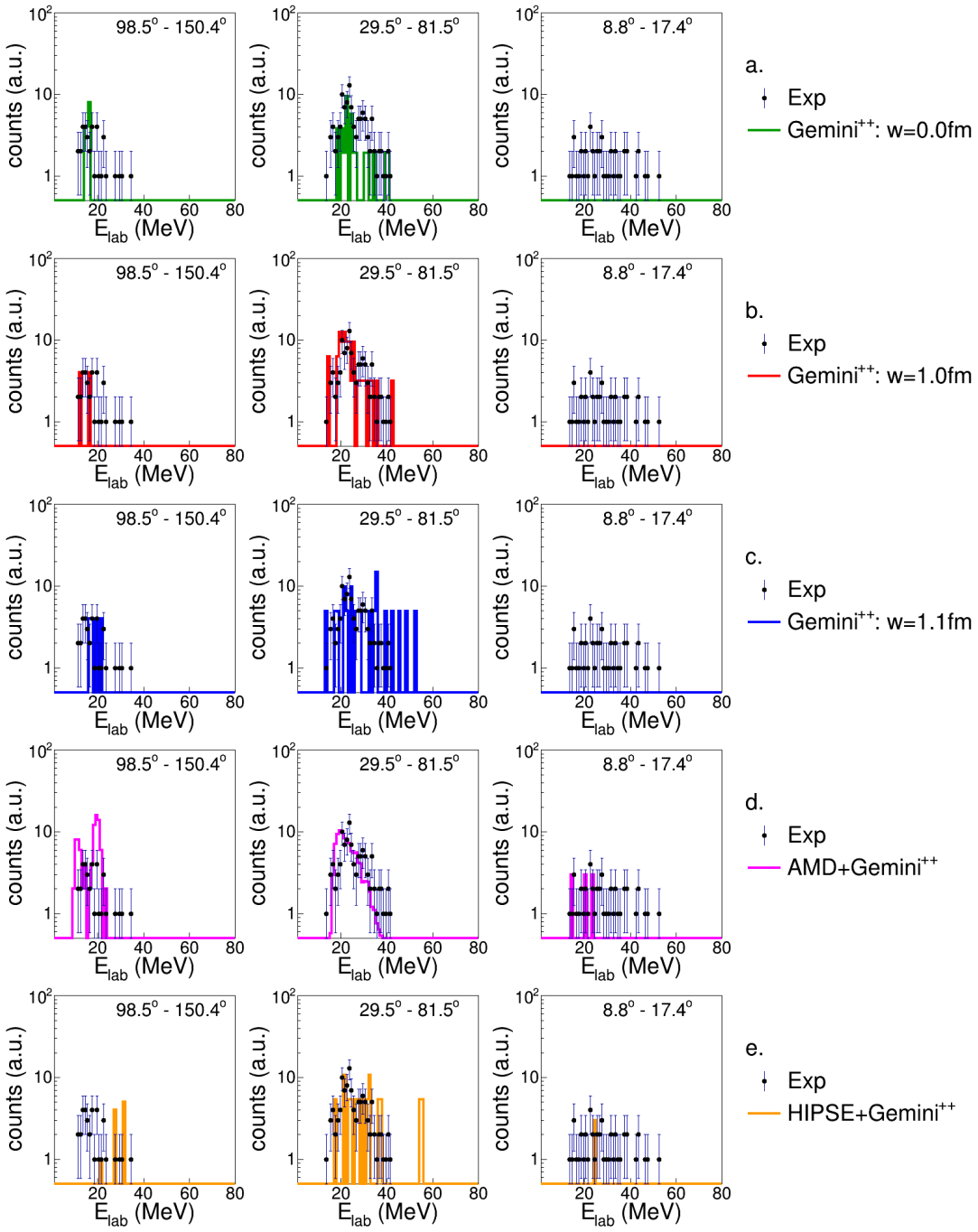

Figure B.10: Energy spectra of tritons in coincidence with a *Sc*-residue for the reaction $^{16}O + ^{30}Si$ at 128 MeV

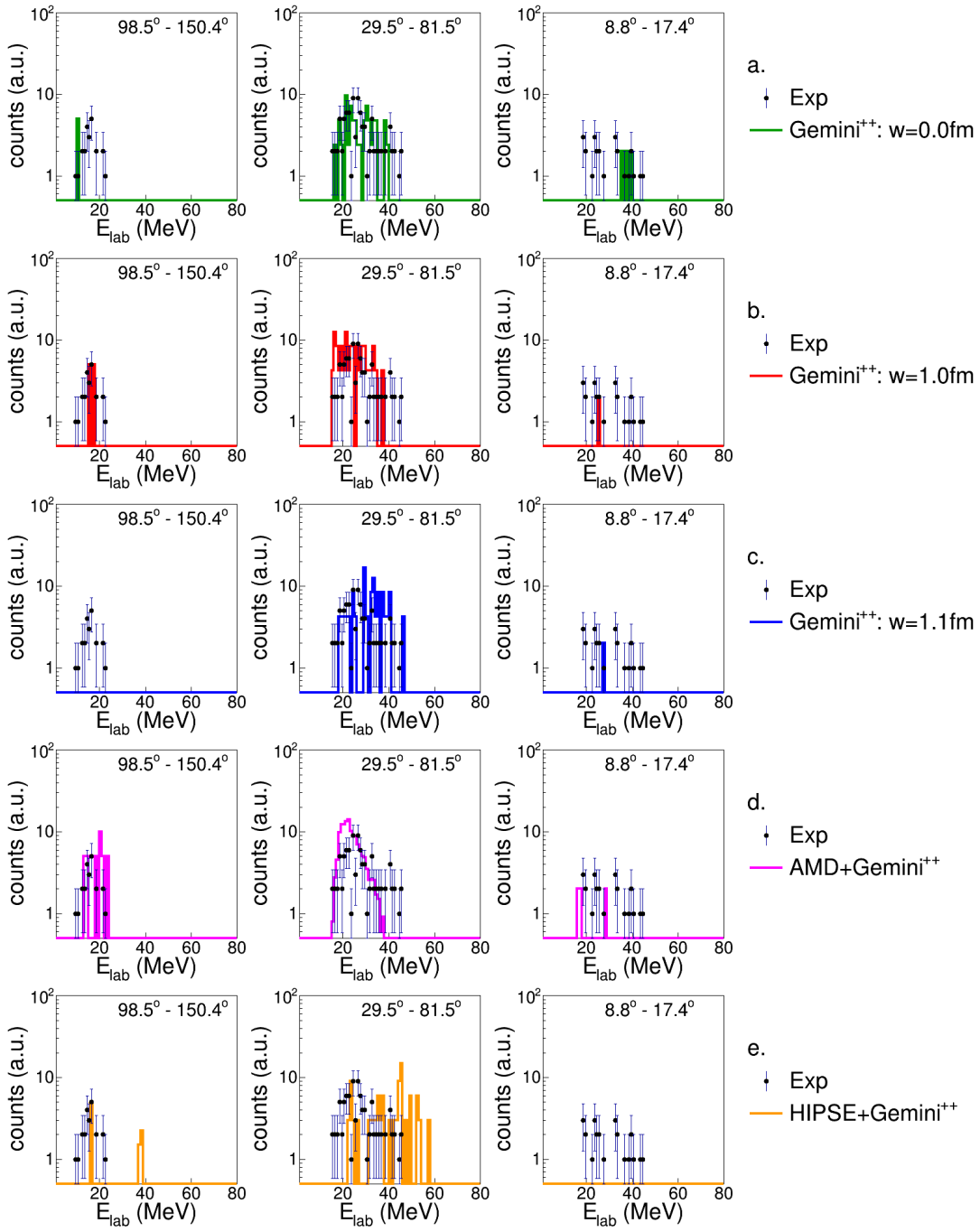

Figure B.11: Energy spectra of tritons in coincidence with a *Sc*-residue for the reaction $^{18}O + ^{28}Si$ at 126 MeV

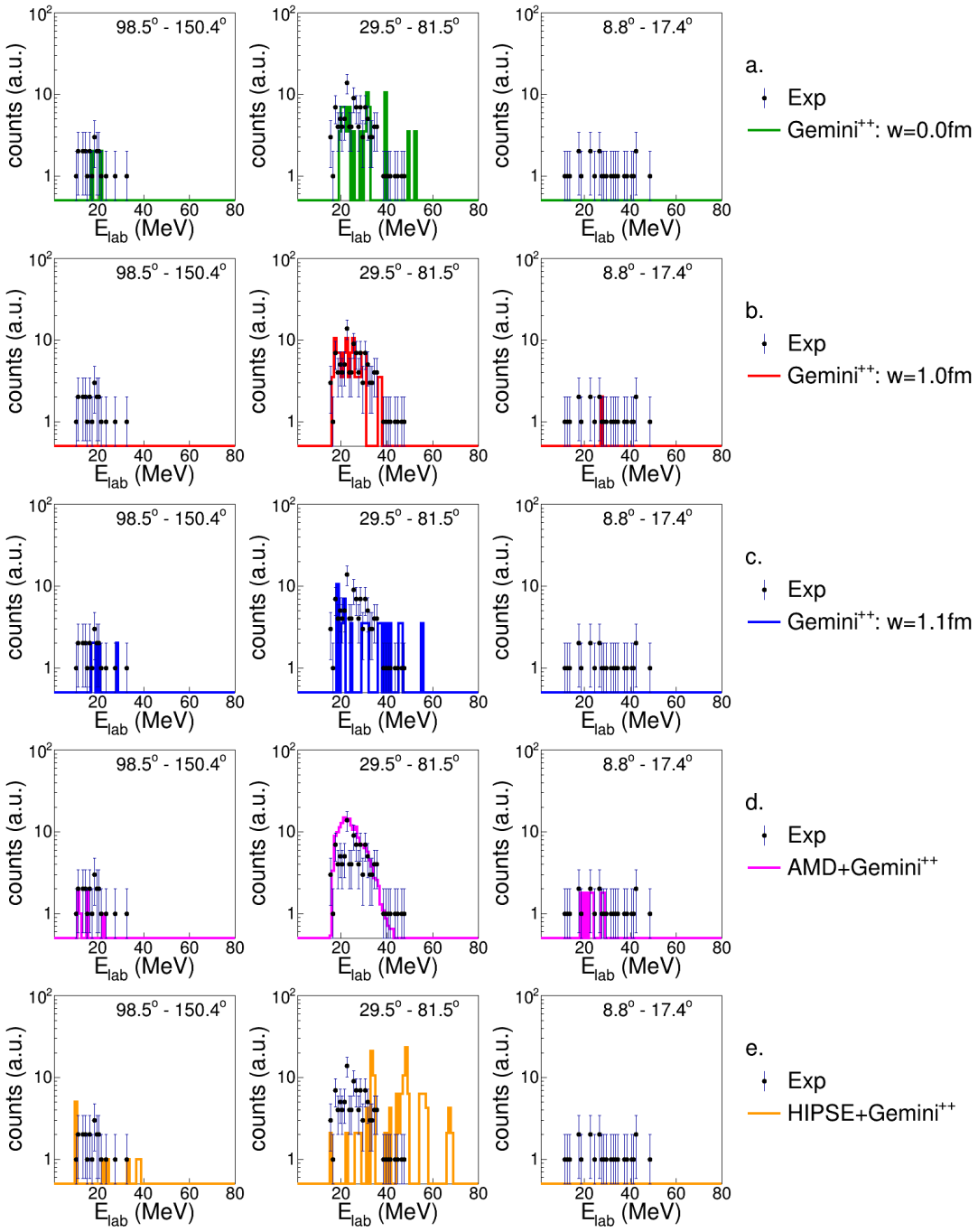

Figure B.12: Energy spectra of tritons in coincidence with a *Sc*-residue for the reaction $^{19}F + ^{27}Al$ at 133 MeV

B.2 The Ca residue: $Z_{res} = 20$

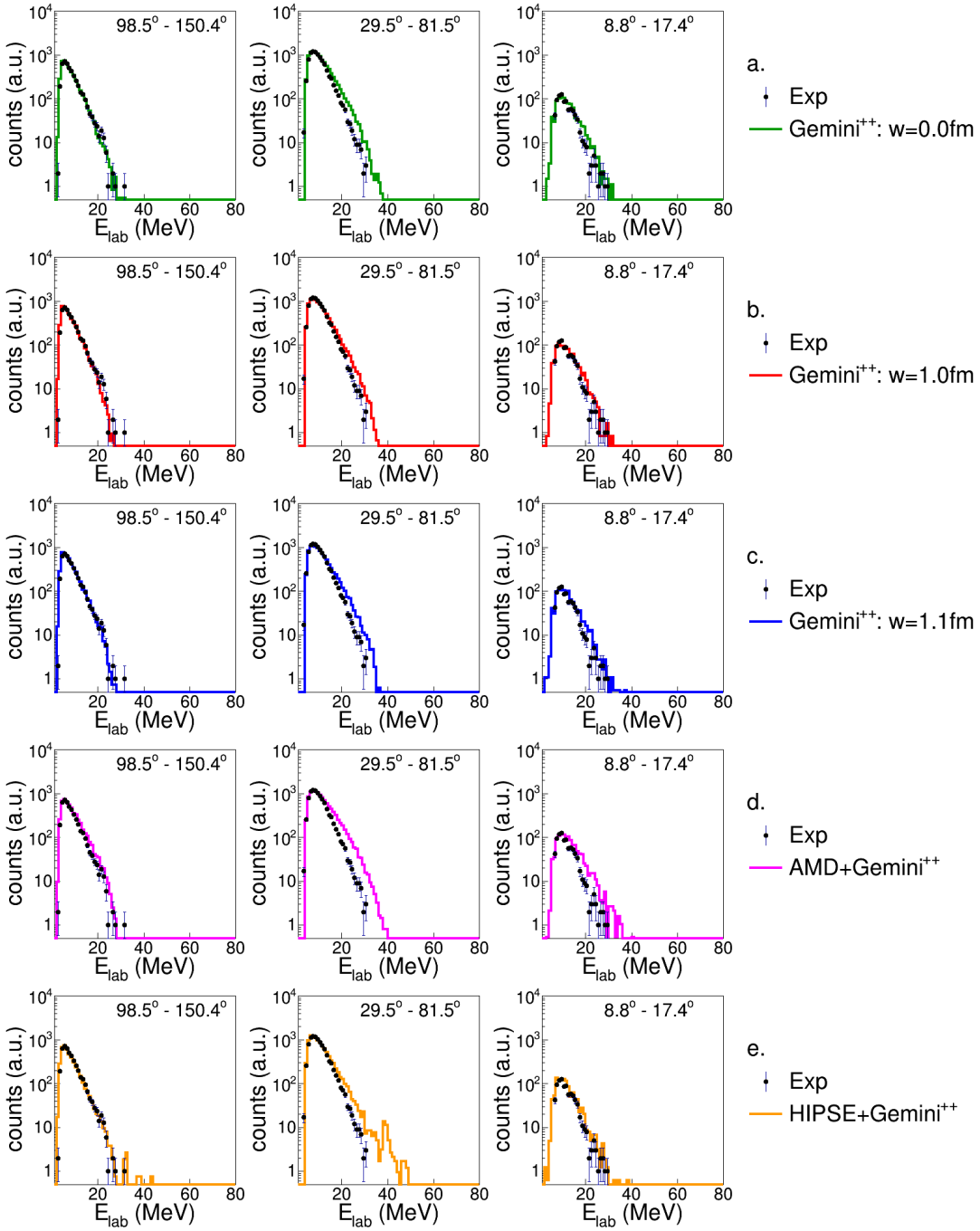

Figure B.13: Energy spectra of protons in coincidence with a Ca-residue for the reaction $^{16}O + ^{30}Si$ at 111 MeV.

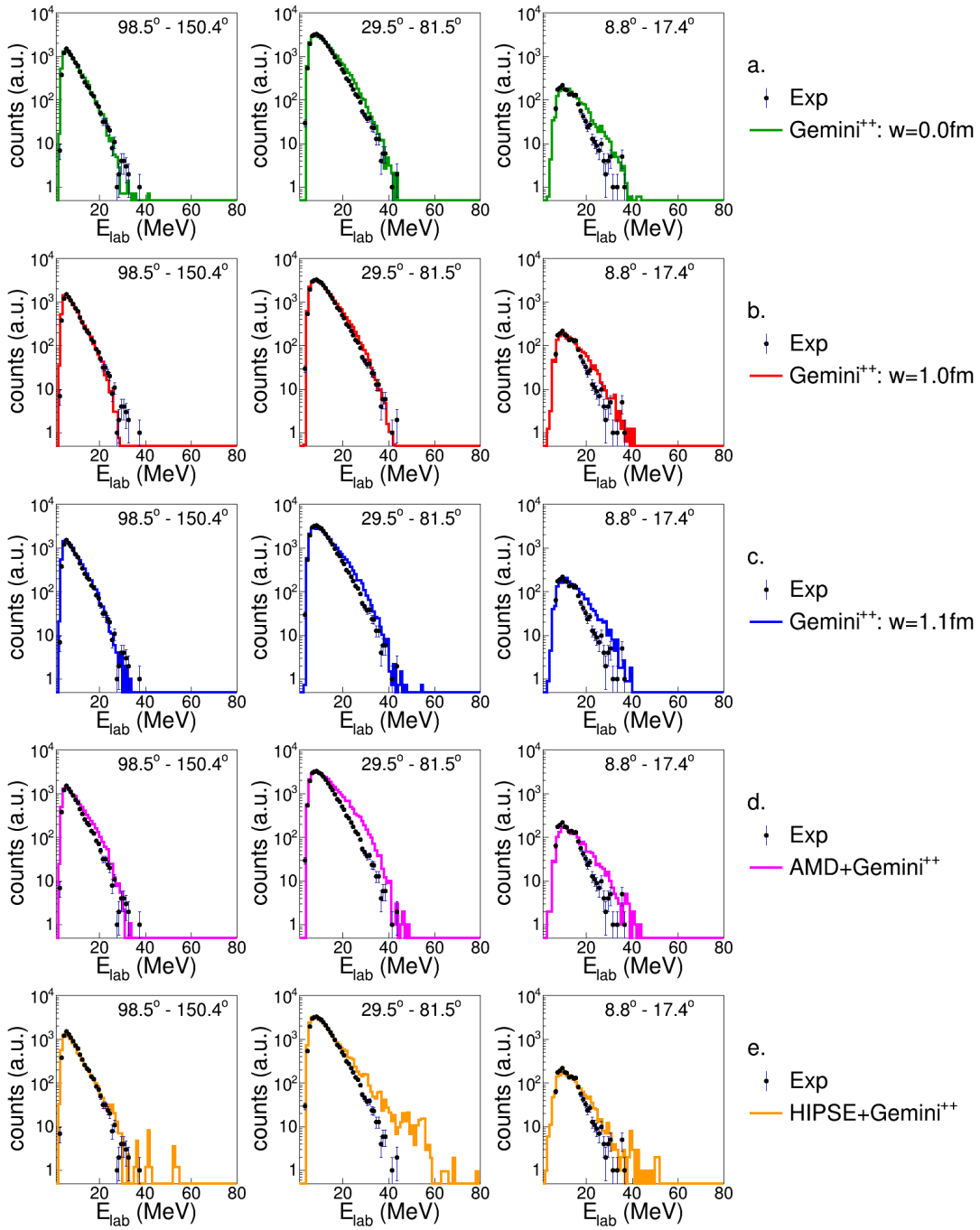

Figure B.14: Energy spectra of protons in coincidence with a Ca-residue for the reaction $^{16}O + ^{30}Si$ at 128 MeV

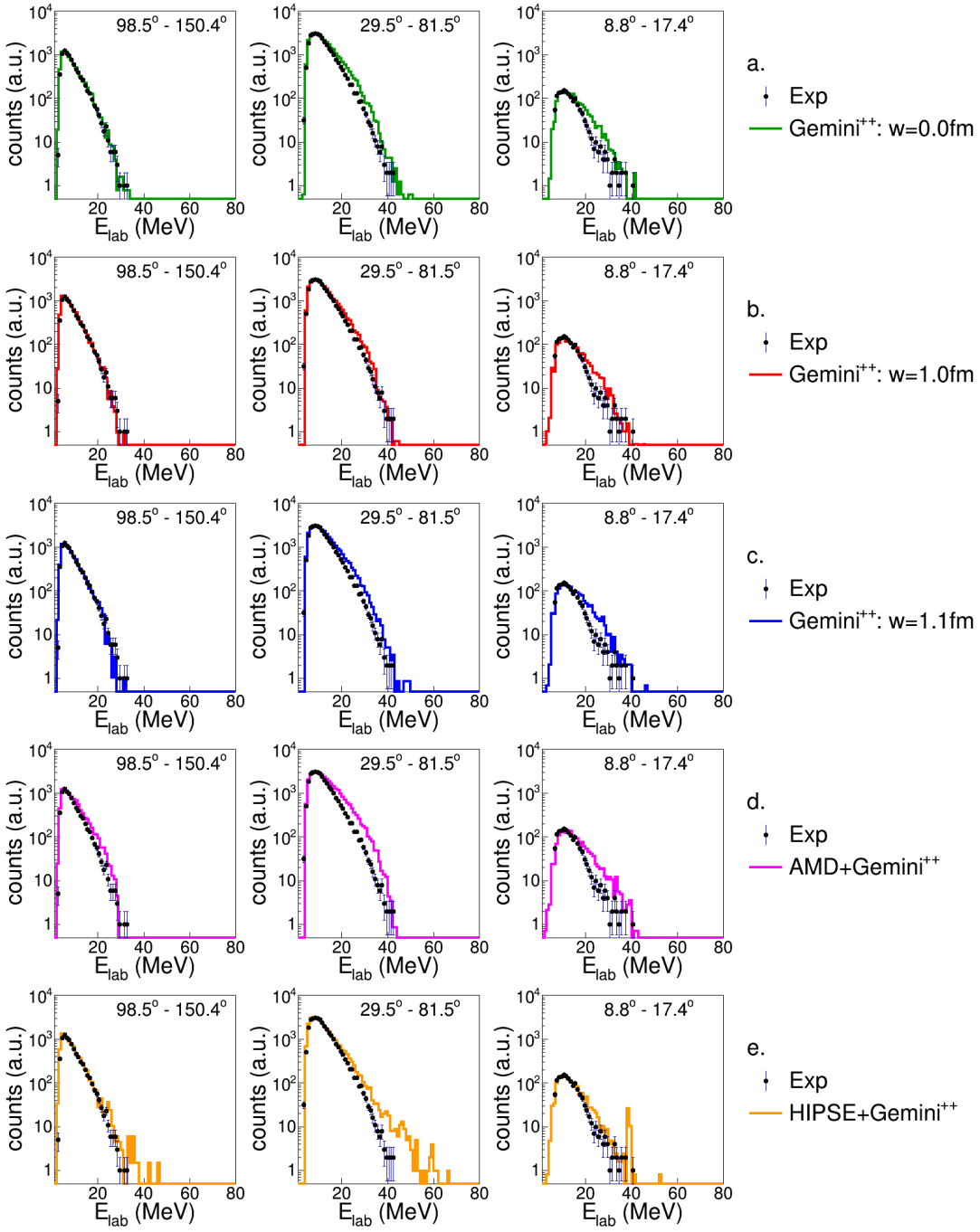

Figure B.15: Energy spectra of protons in coincidence with a Ca-residue for the reaction $^{18}O + ^{28}Si$ at 126 MeV

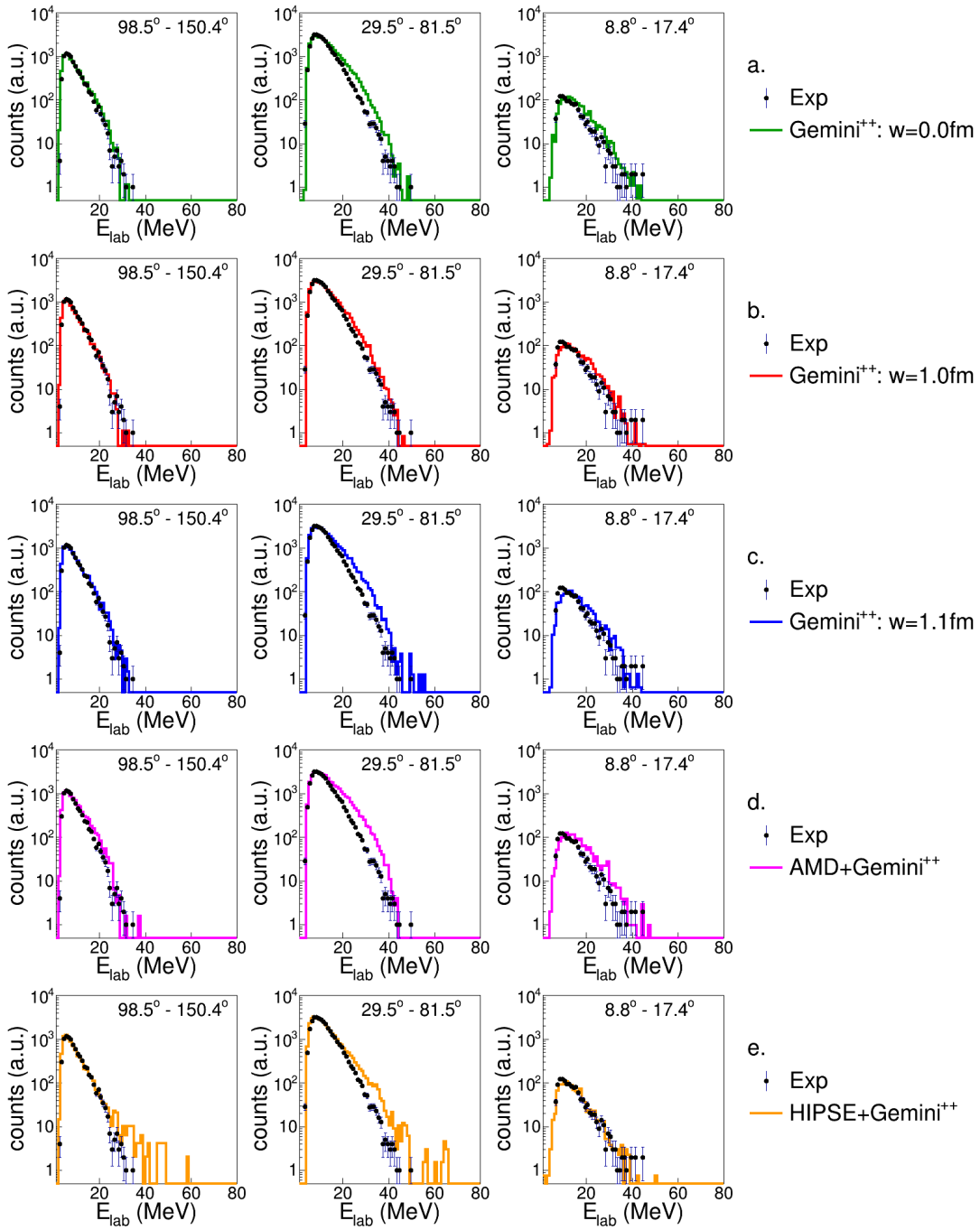

Figure B.16: Energy spectra of protons in coincidence with a Ca-residue for the reaction $^{19}F + ^{27}Al$ at 133 MeV

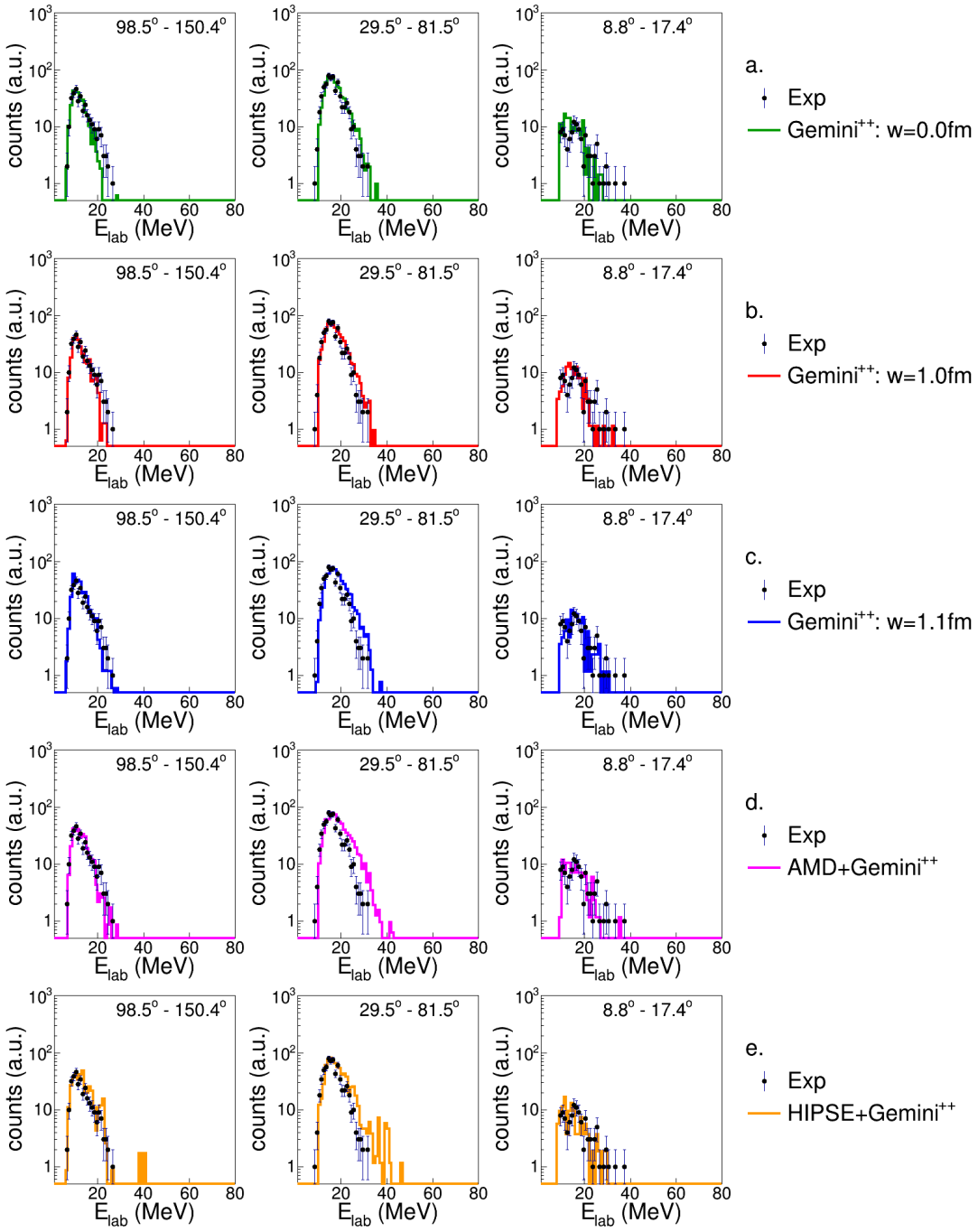

Figure B.17: Energy spectra of deuterons in coincidence with a Ca-residue for the reaction $^{16}O + ^{30}Si$ at 111 MeV.

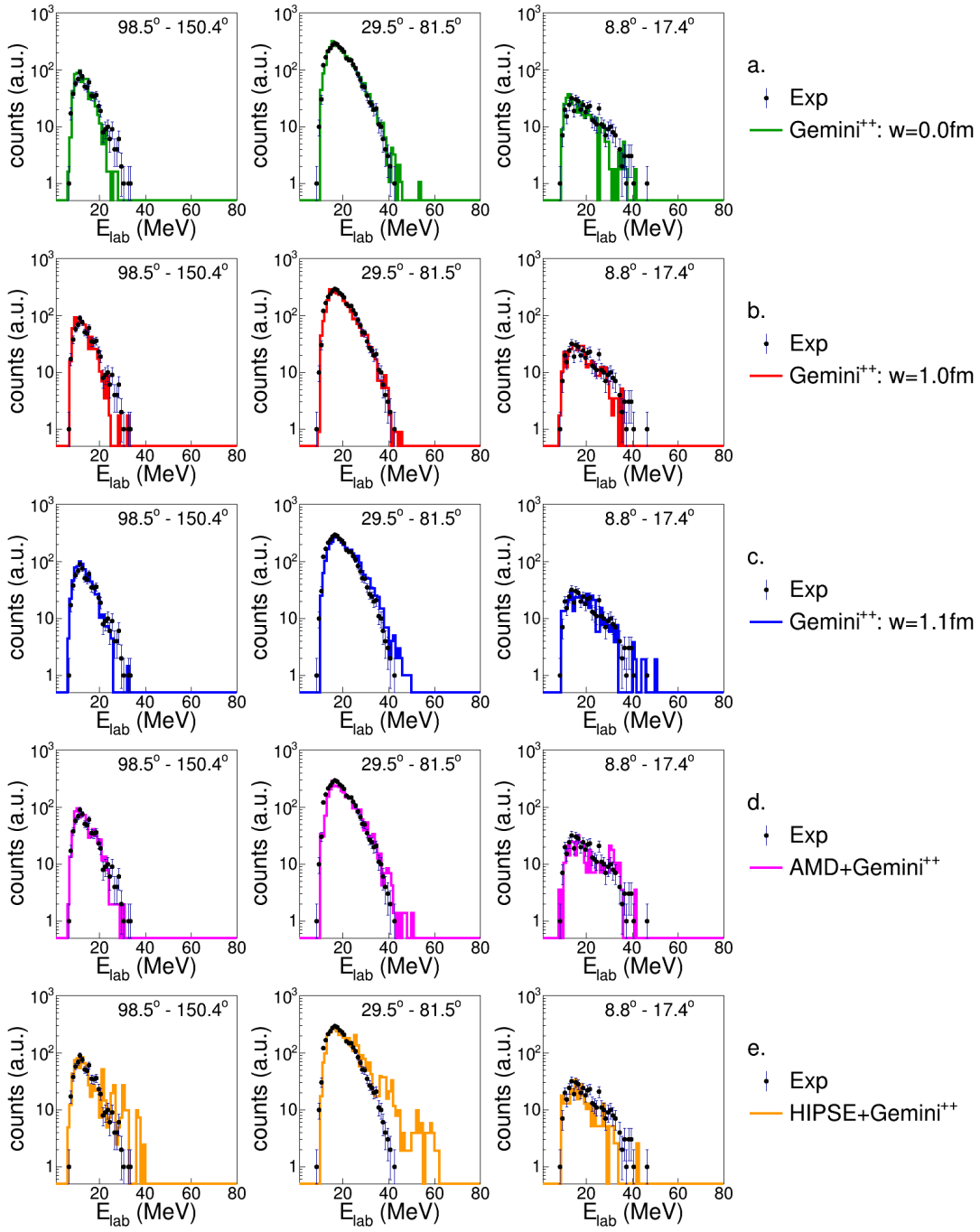

Figure B.18: Energy spectra of deuterons in coincidence with a Ca-residue for the reaction $^{16}O + ^{30}Si$ at 128 MeV

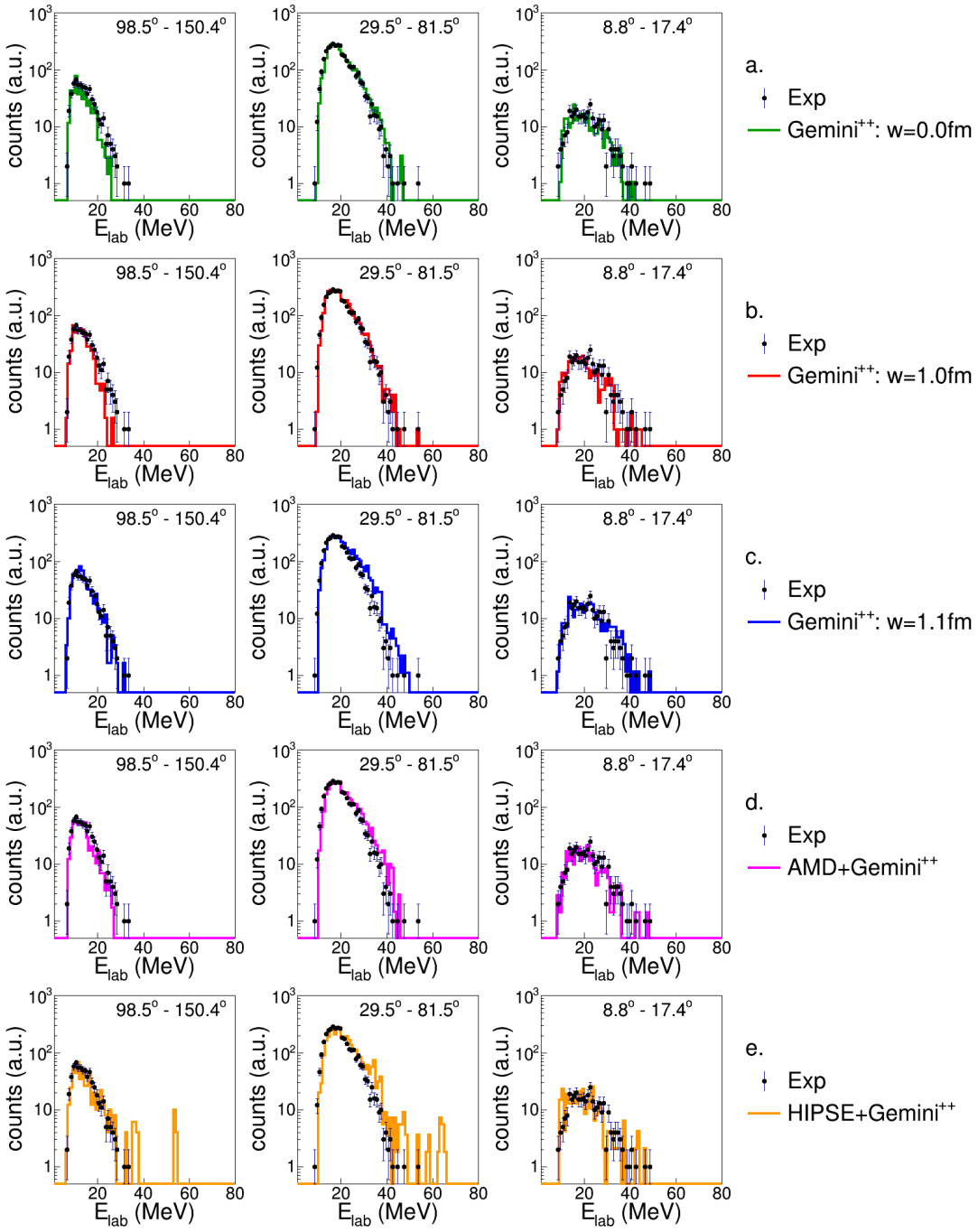

Figure B.19: Energy spectra of deuterons in coincidence with a *Ca*-residue for the reaction $^{18}O + ^{28}Si$ at 126 MeV

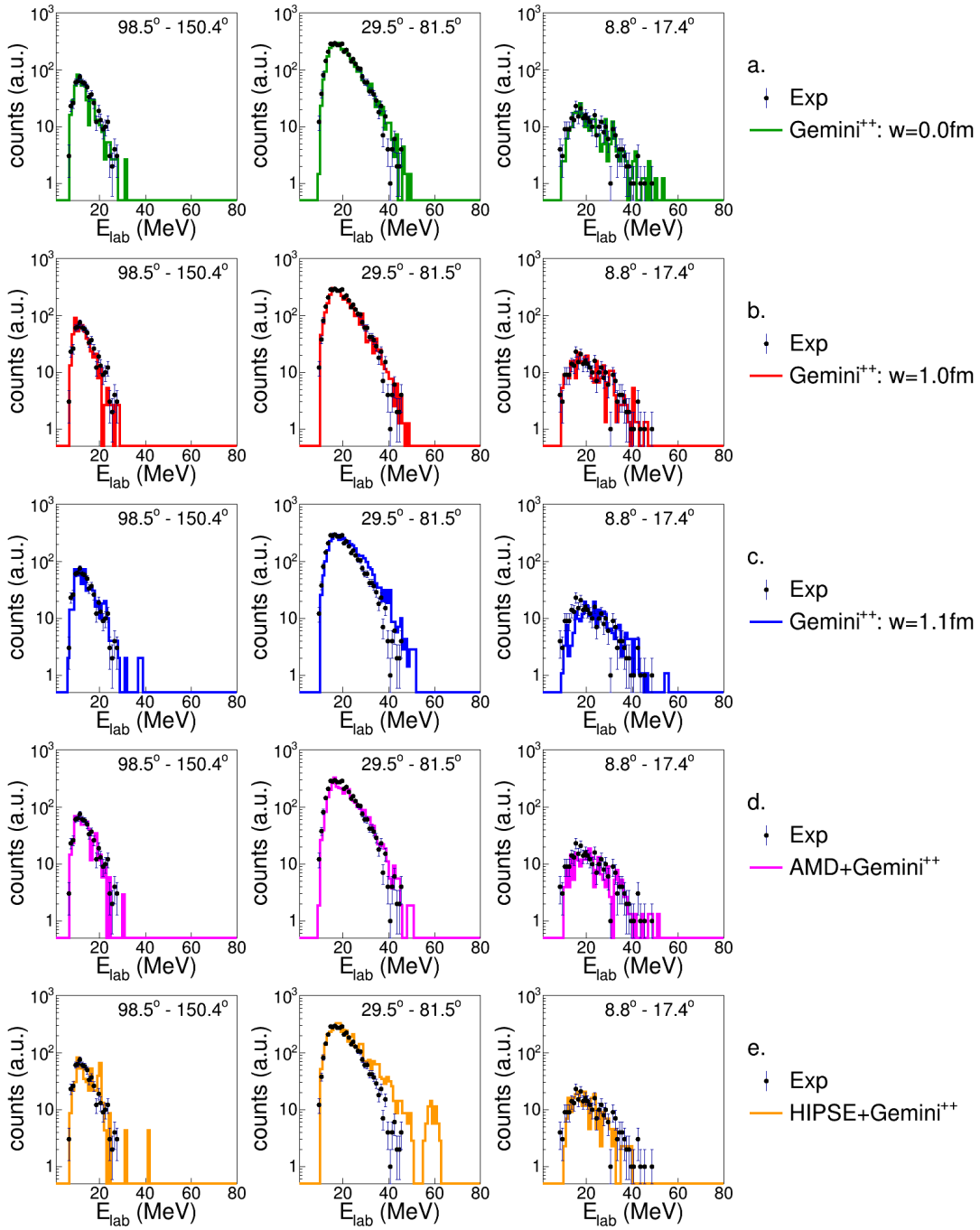

Figure B.20: Energy spectra of deuterons in coincidence with a Ca-residue for the reaction $^{19}F + ^{27}Al$ at 133 MeV

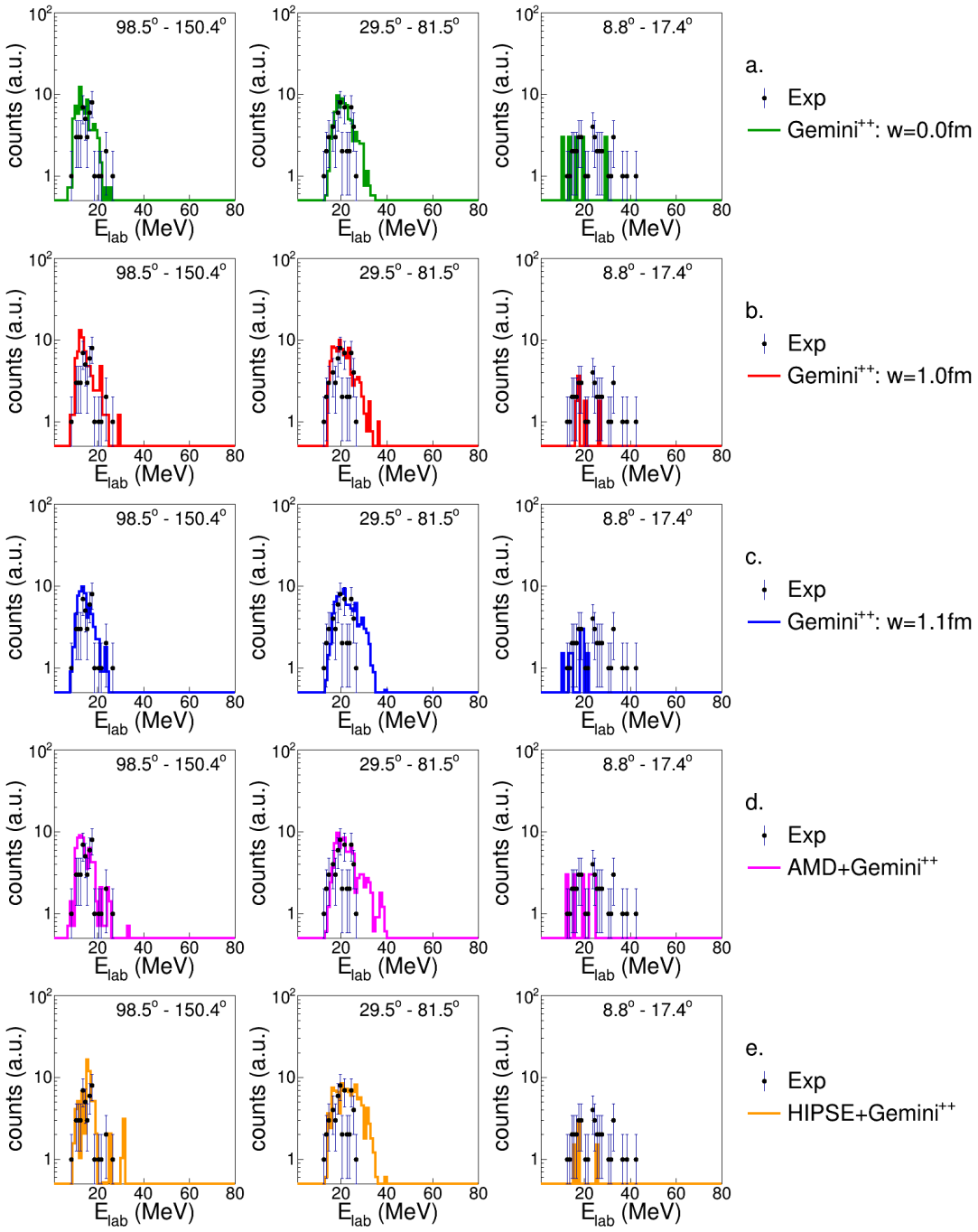

Figure B.21: Energy spectra of tritons in coincidence with a Ca-residue for the reaction $^{16}O + ^{30}Si$ at 111 MeV.

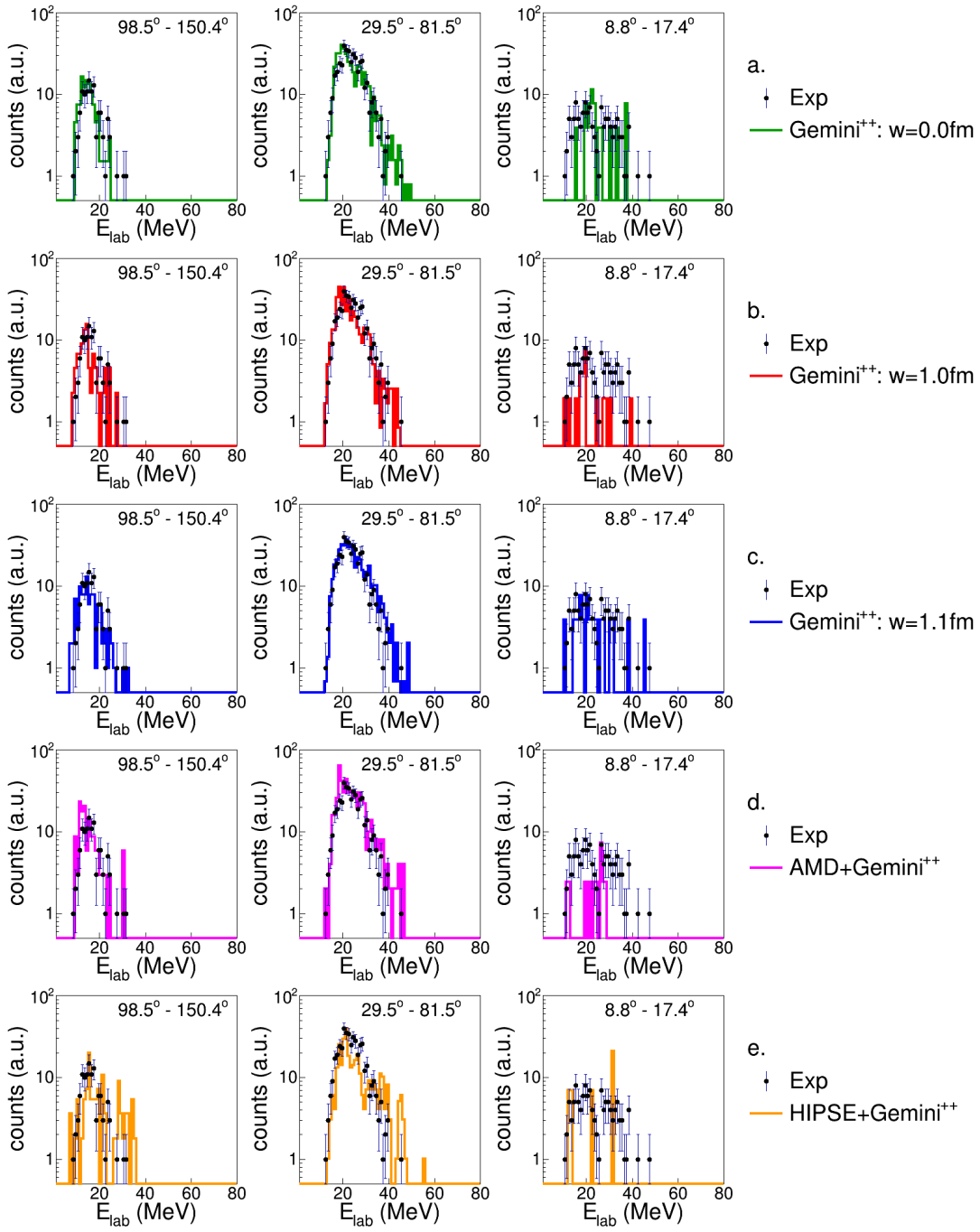

Figure B.22: Energy spectra of tritons in coincidence with a Ca-residue for the reaction $^{16}O + ^{30}Si$ at 128 MeV

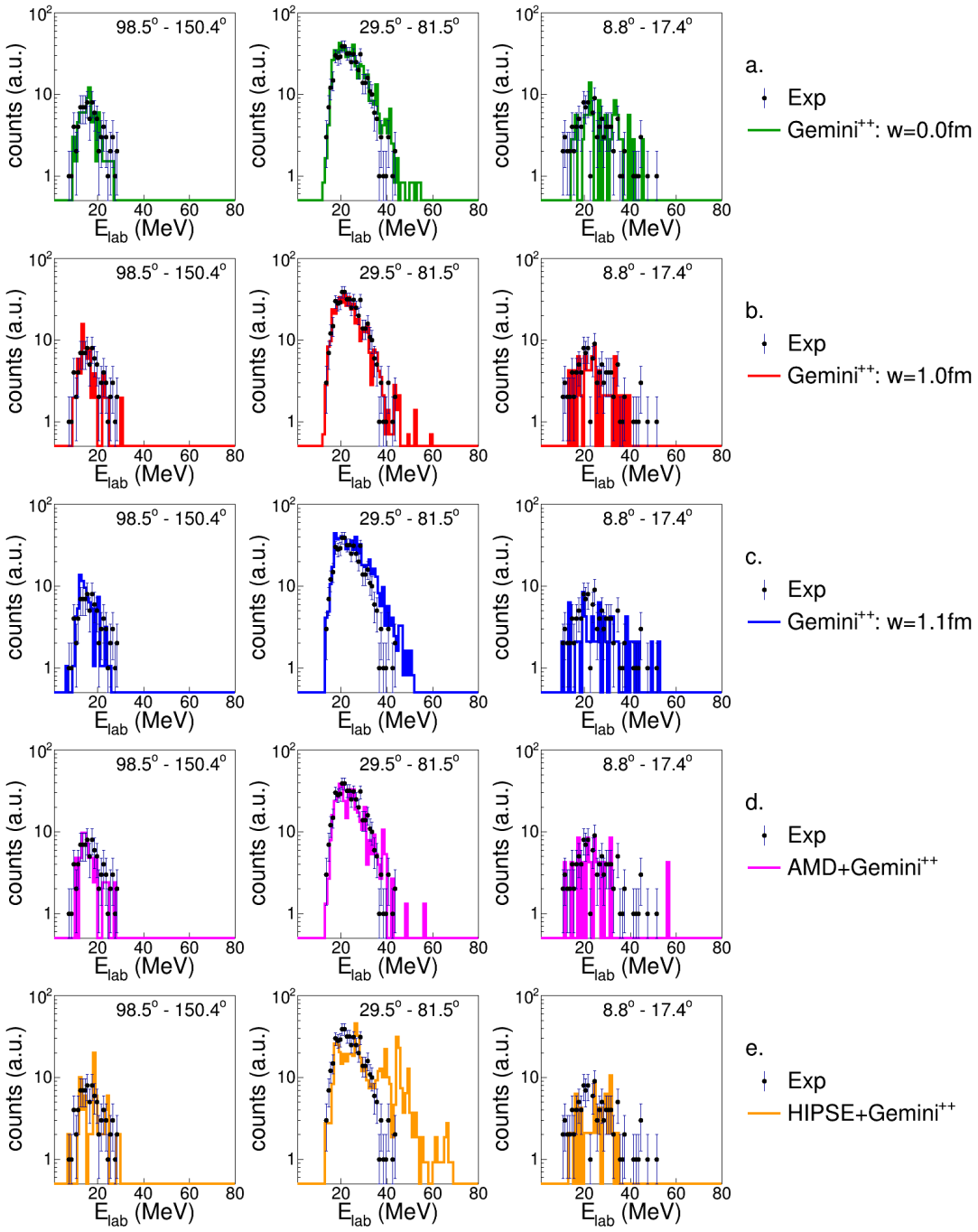

Figure B.23: Energy spectra of tritons in coincidence with a Ca-residue for the reaction $^{18}O + ^{28}Si$ at 126 MeV

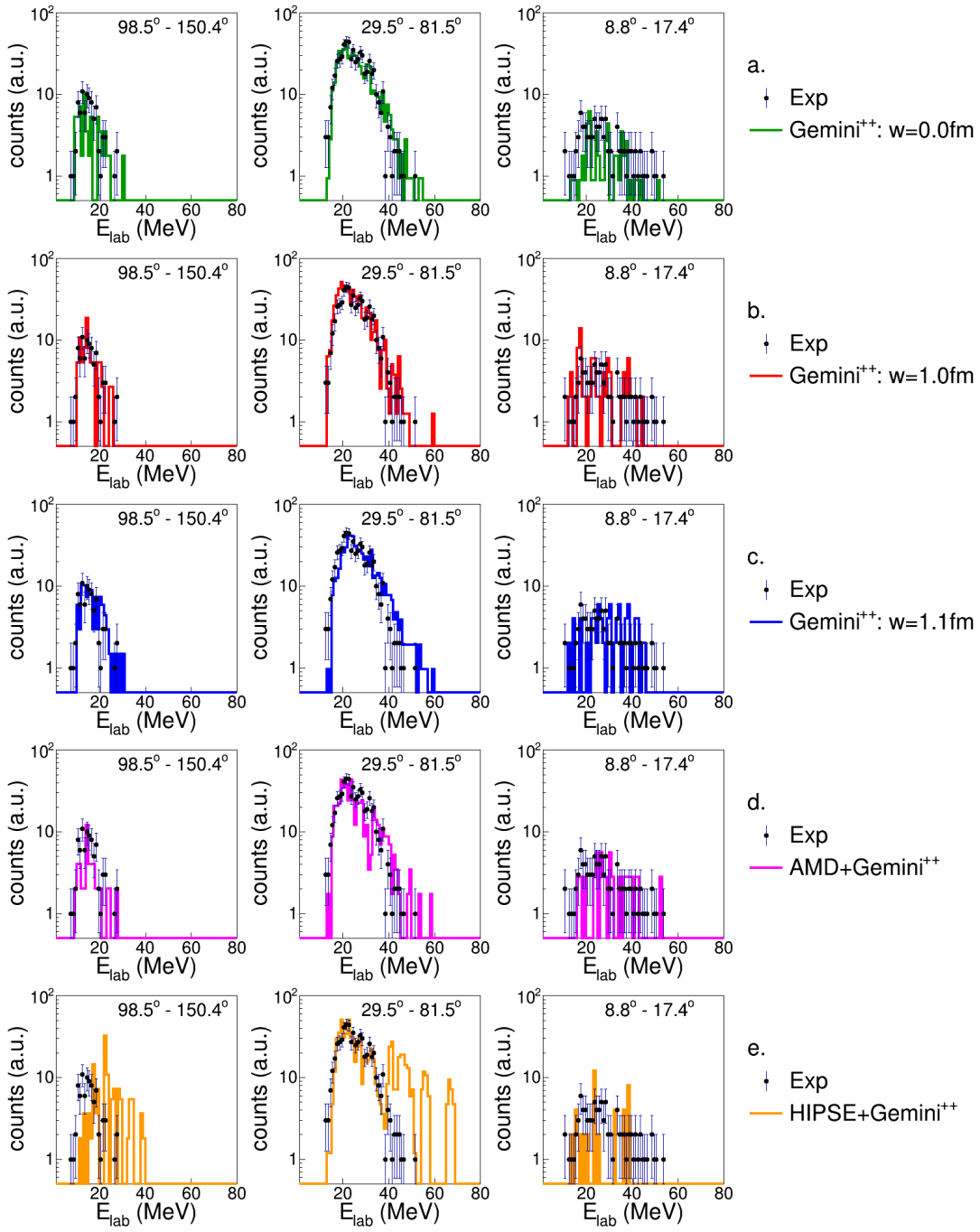

Figure B.24: Energy spectra of tritons in coincidence with a *Ca*-residue for the reaction $^{19}F + ^{27}Al$ at 133 MeV

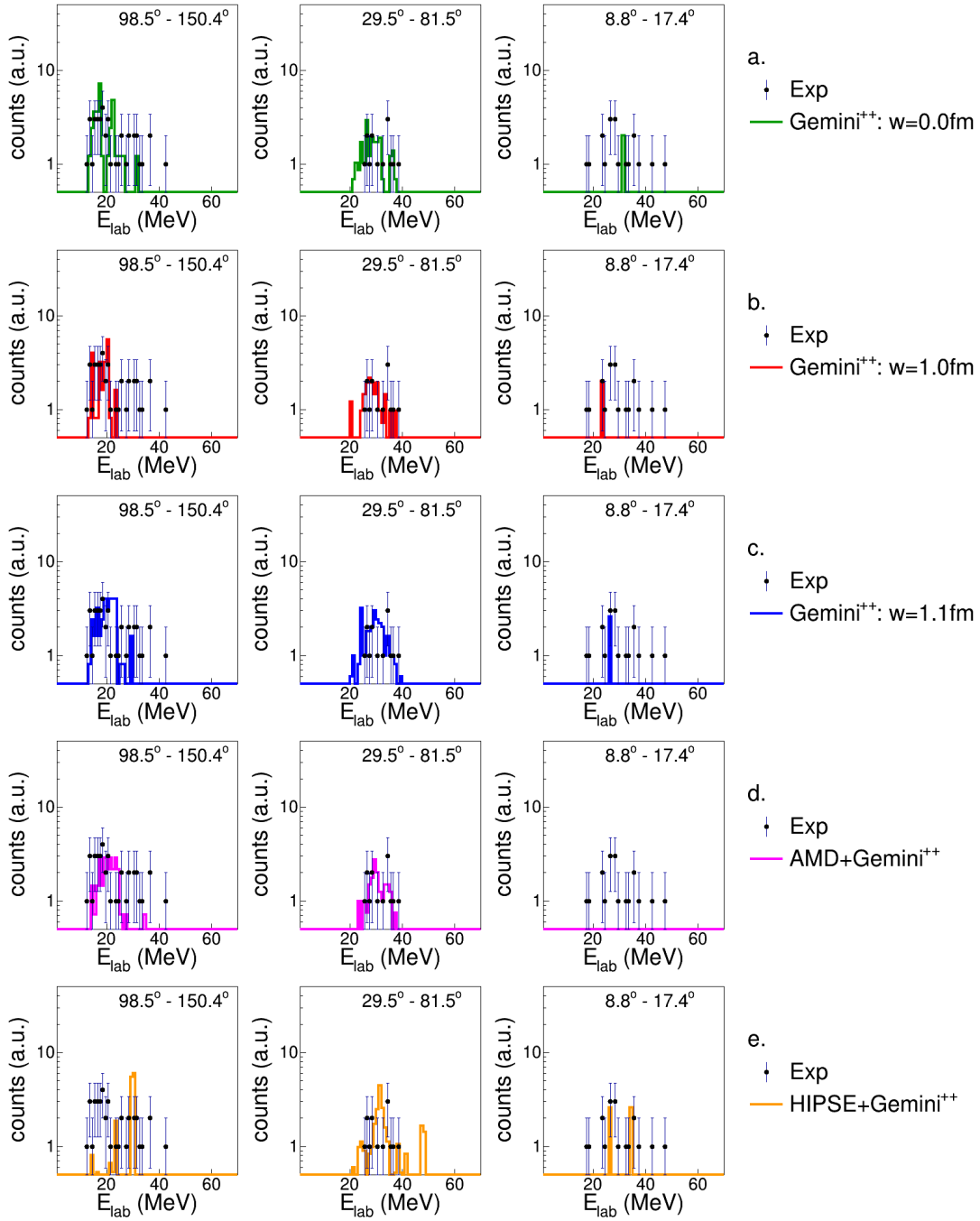

Figure B.25: Energy spectra of ^{3}He in coincidence with a Ca-residue for the reaction $^{16}O+^{30}Si$ at 111 MeV.

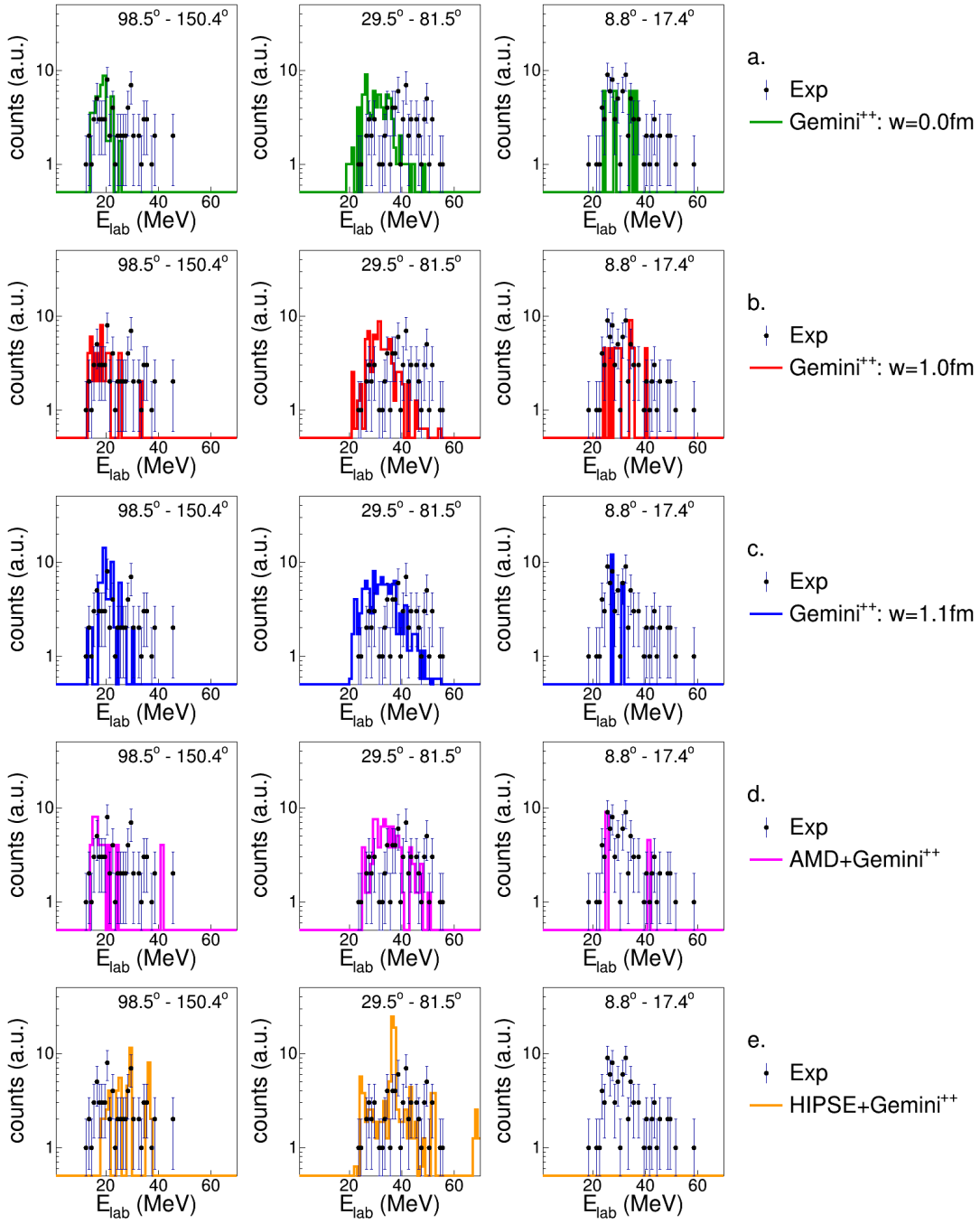

Figure B.26: Energy spectra of ^{3}He in coincidence with a Ca-residue for the reaction $^{16}O+^{30}Si$ at 128 MeV

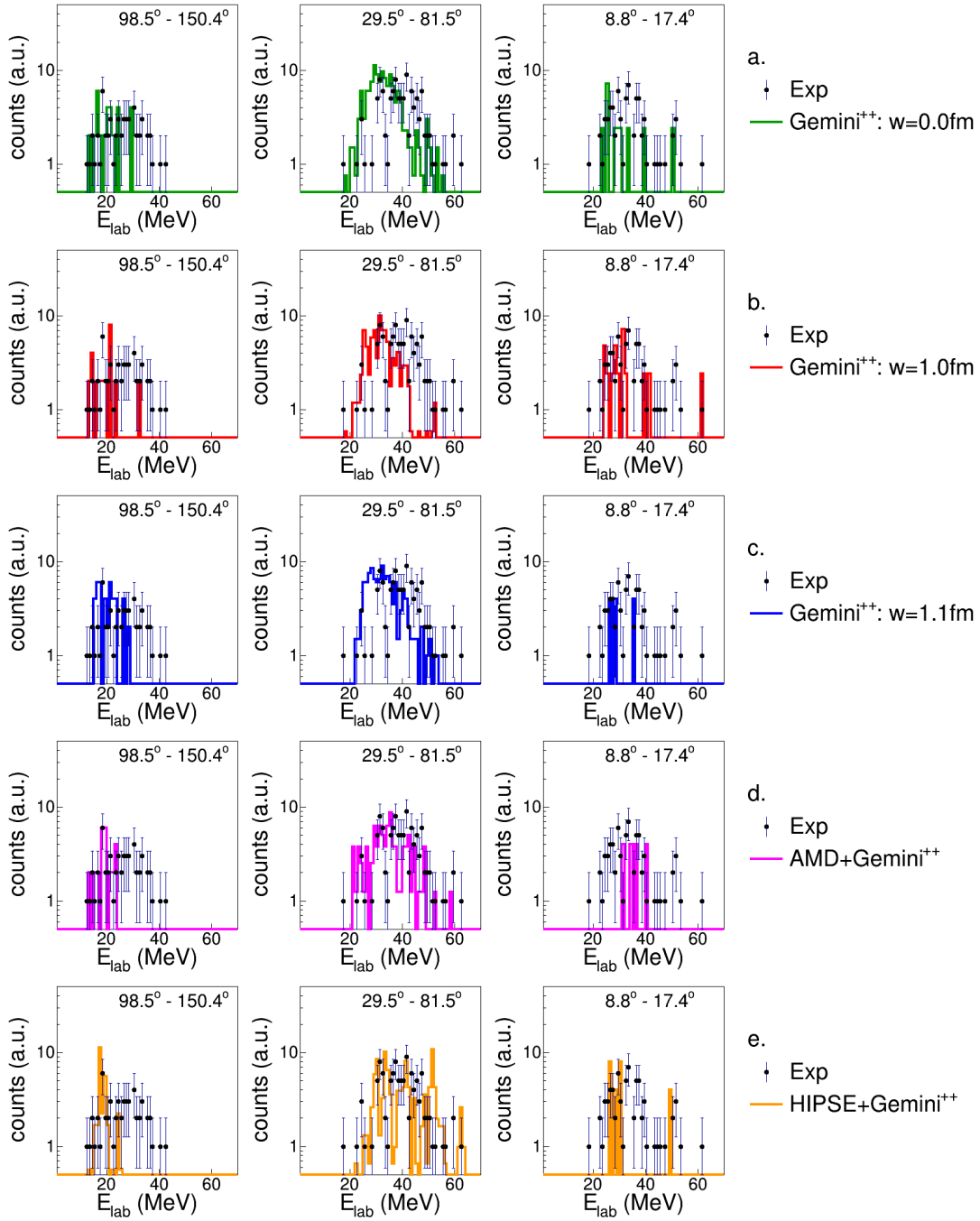

Figure B.27: Energy spectra of ^{3}He in coincidence with a Ca-residue for the reaction $^{18}O+^{28}Si$ at 126 MeV

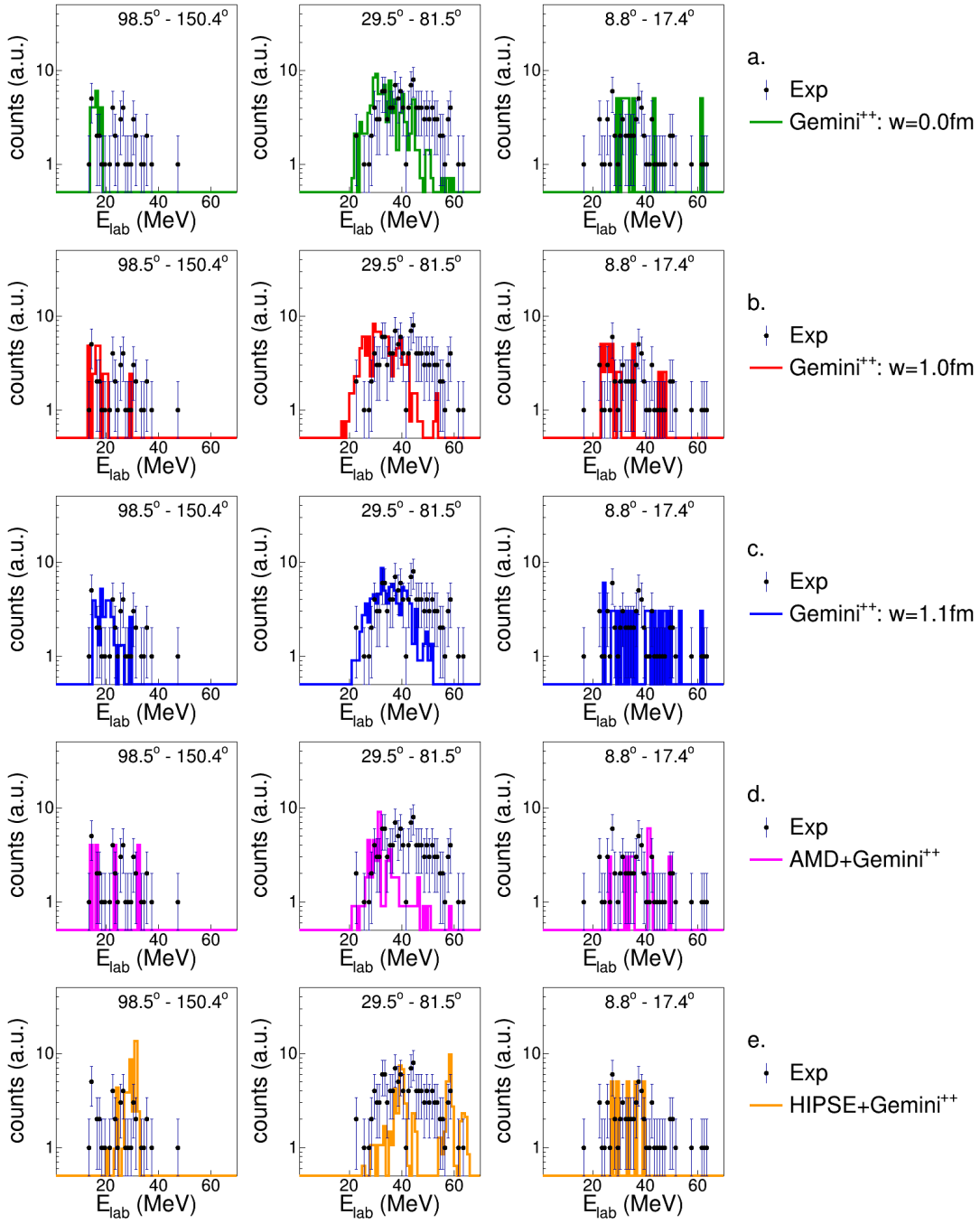

Figure B.28: Energy spectra of ^{3}He in coincidence with a Ca-residue for the reaction $^{19}F + ^{27}Al$ at 133 MeV

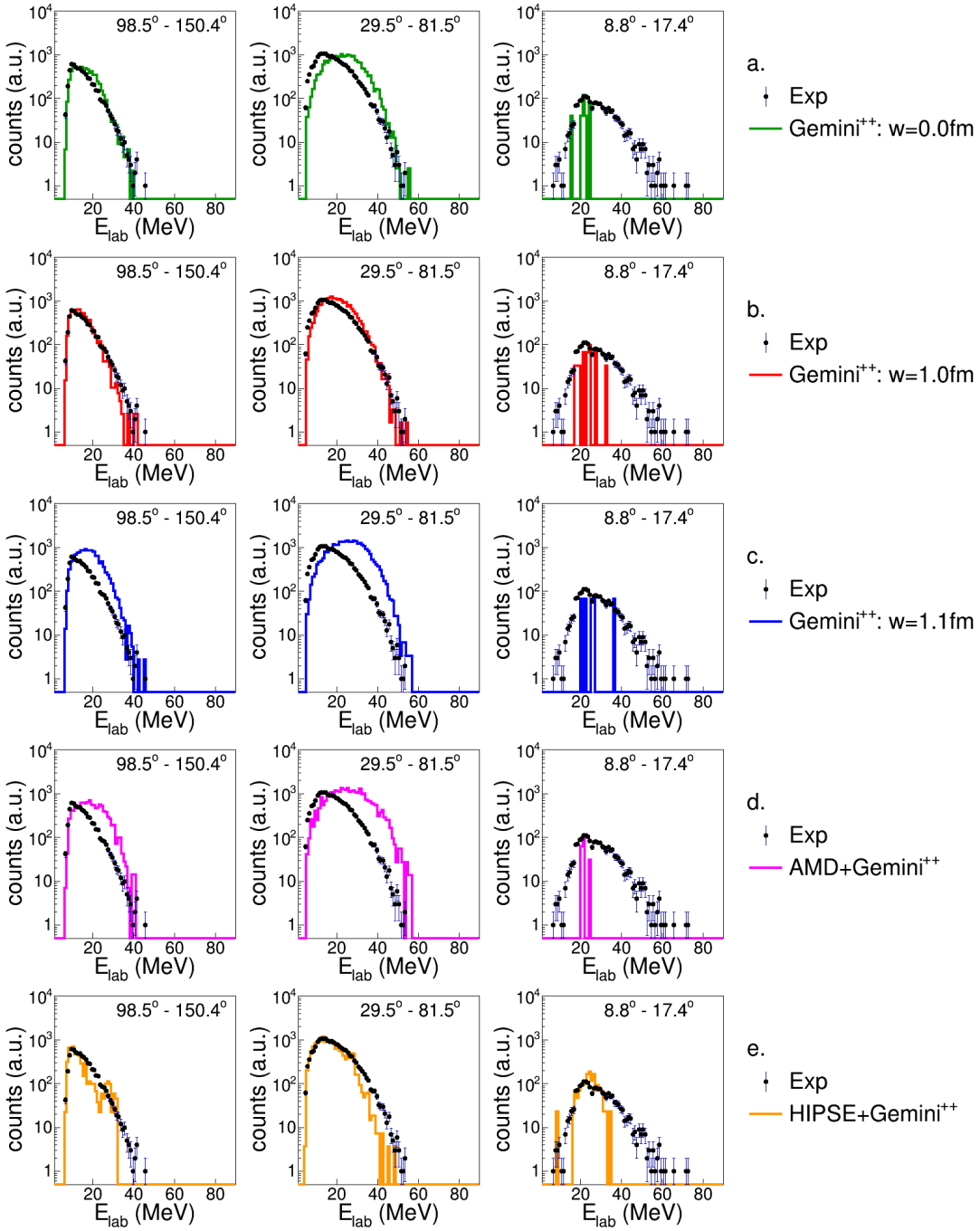

Figure B.29: Energy spectra of α-particles in coincidence with a Ca-residue for the reaction $^{16}O + ^{30}Si$ at 111 MeV.

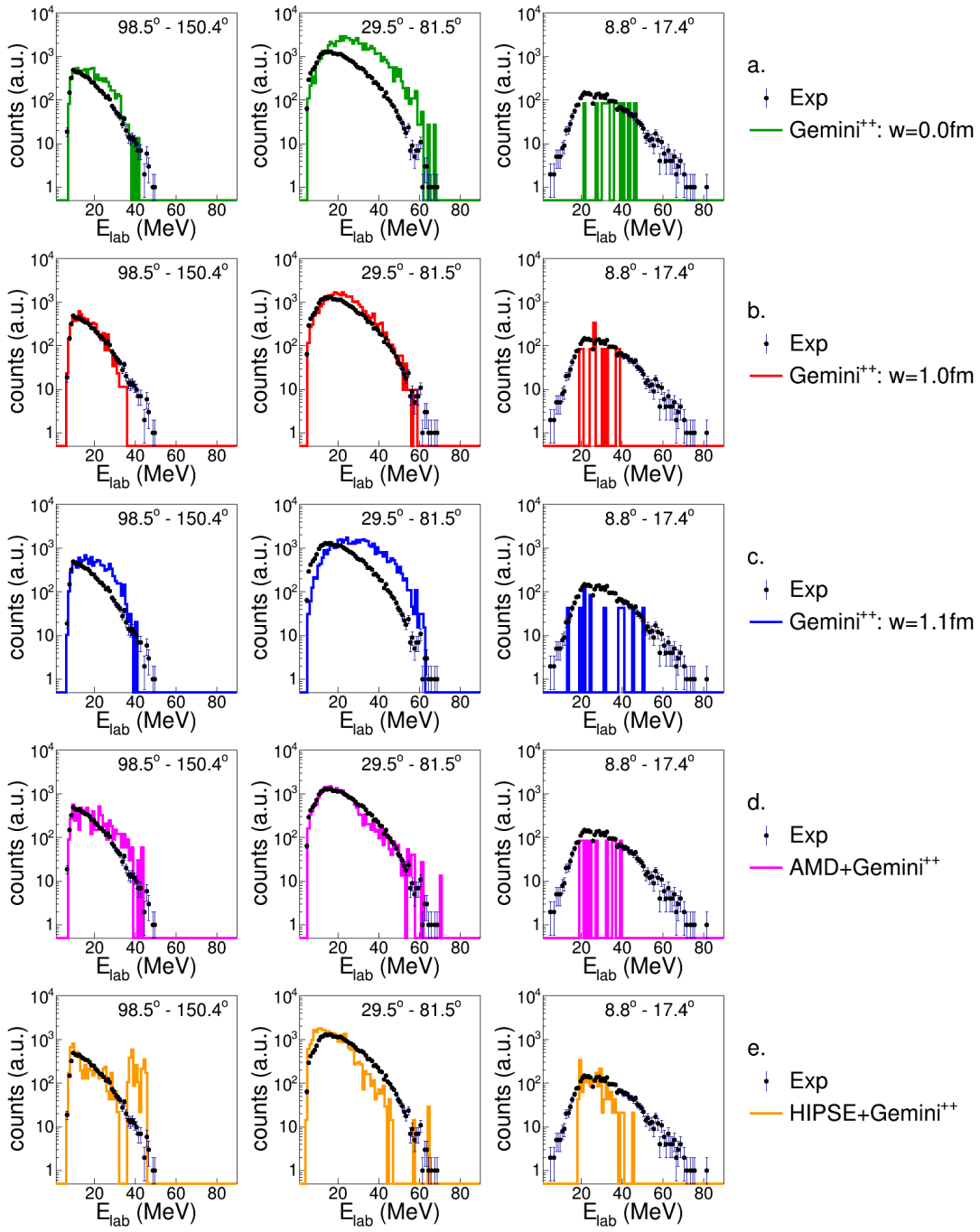

Figure B.30: Energy spectra of α-particles in coincidence with a Ca-residue for the reaction $^{16}O + ^{30}Si$ at 128 MeV

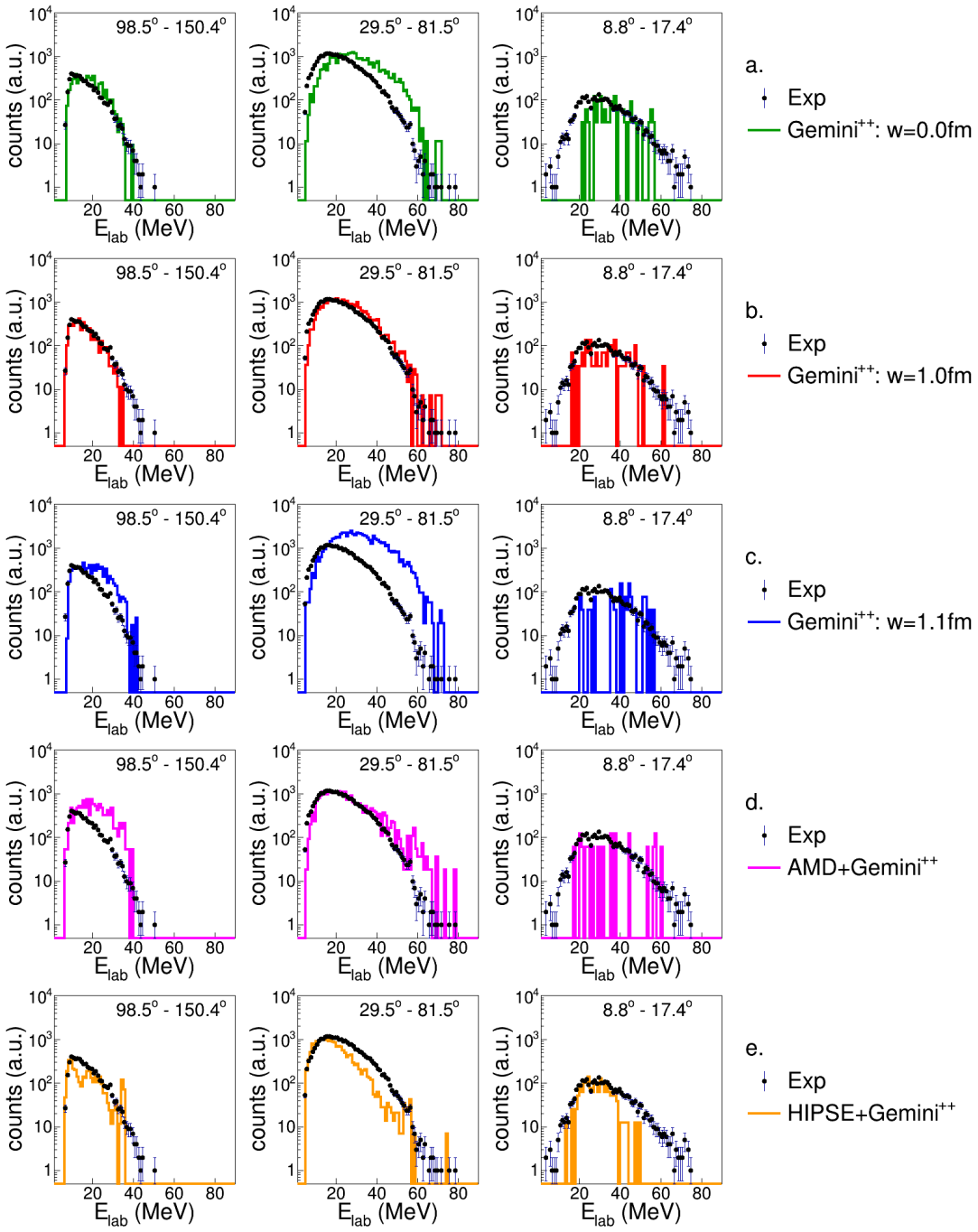

Figure B.31: Energy spectra of α-particles in coincidence with a Ca-residue for the reaction $^{18}O + ^{28}Si$ at 126 MeV

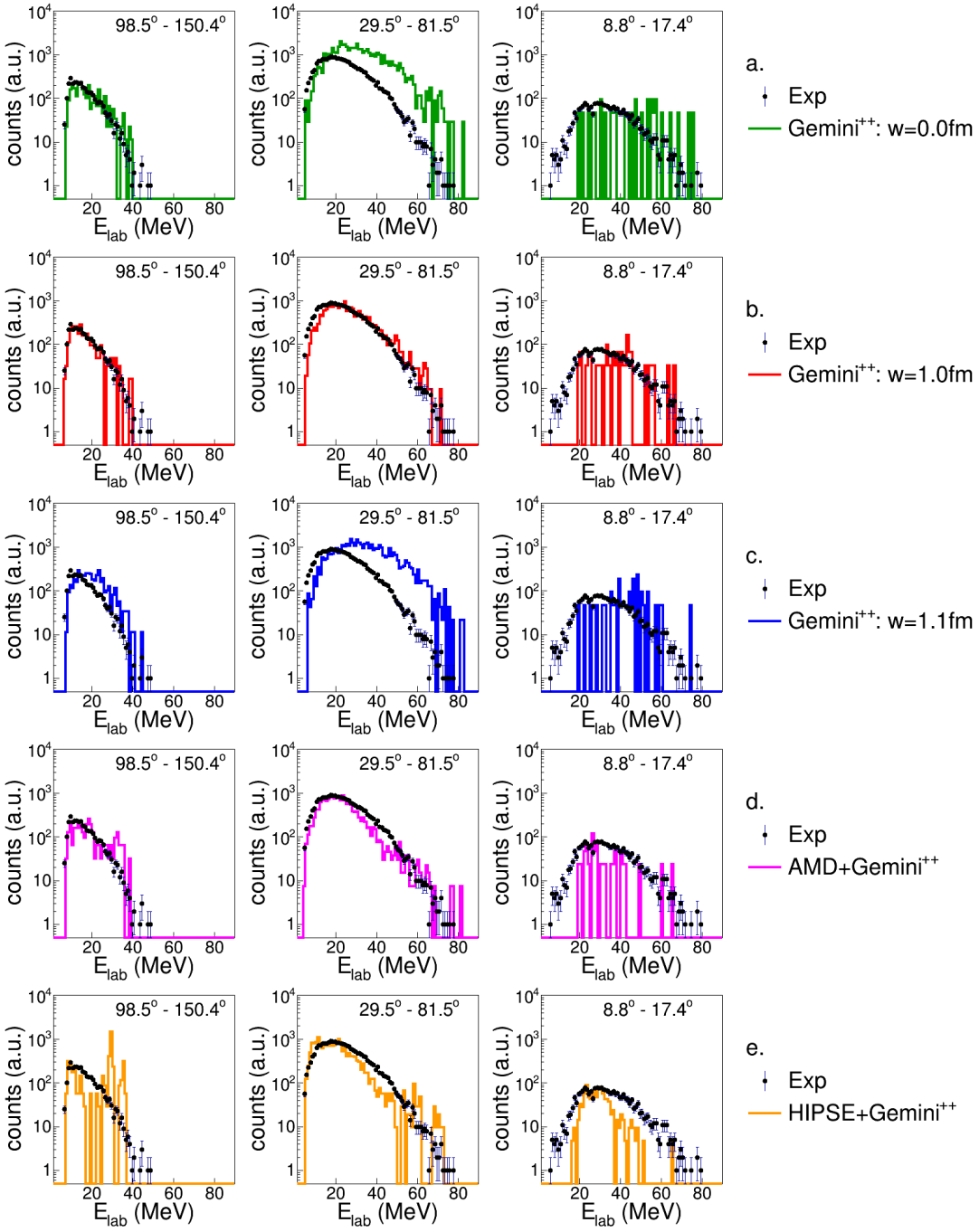

Figure B.32: Energy spectra of α-particles in coincidence with a Ca-residue for the reaction $^{19}F + ^{27}Al$ at 133 MeV

B.3 The K residue: $Z_{res} = 19$

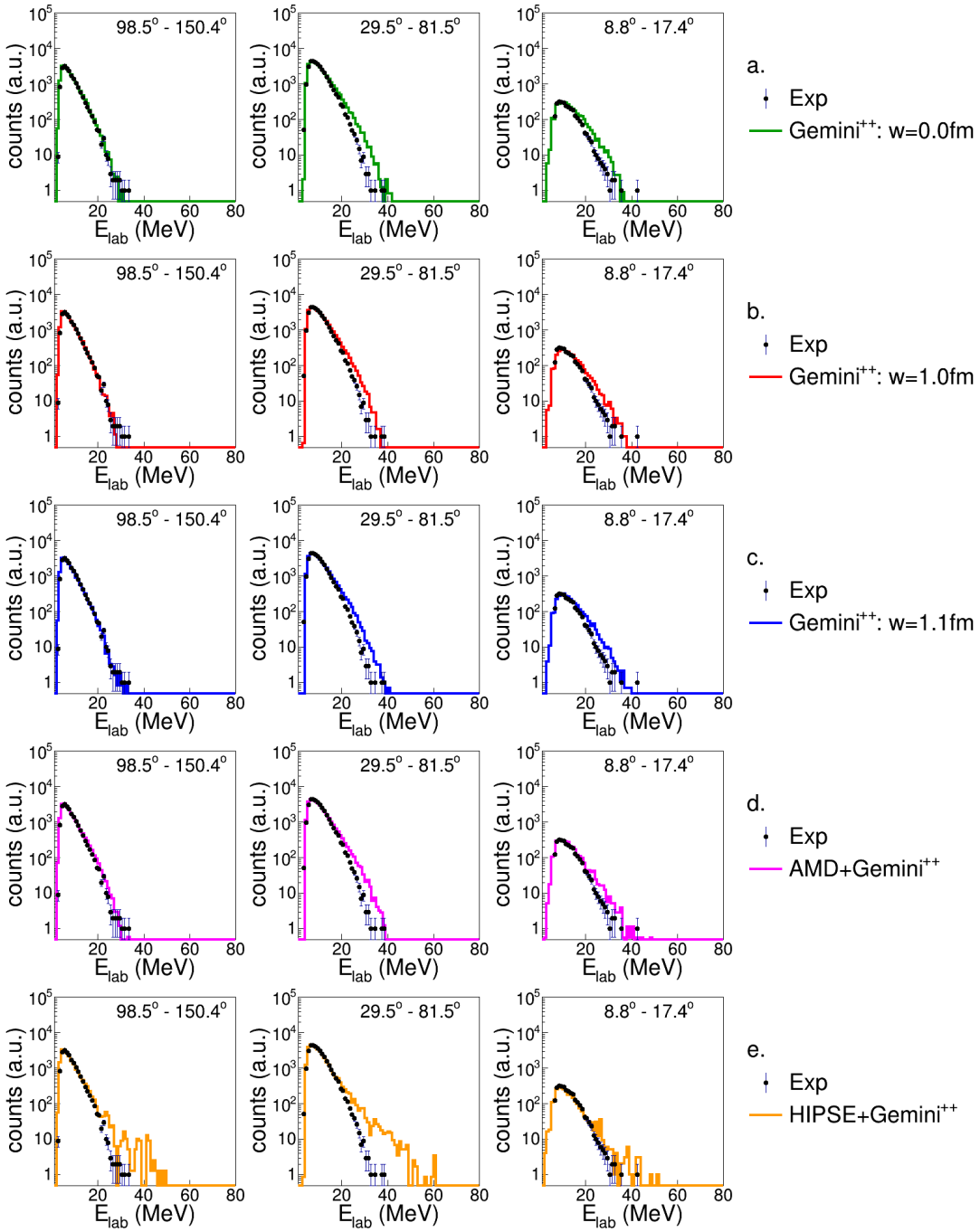

Figure B.33: Energy spectra of protons in coincidence with a K-residue for the reaction $^{16}O + ^{30}Si$ at 111 MeV.

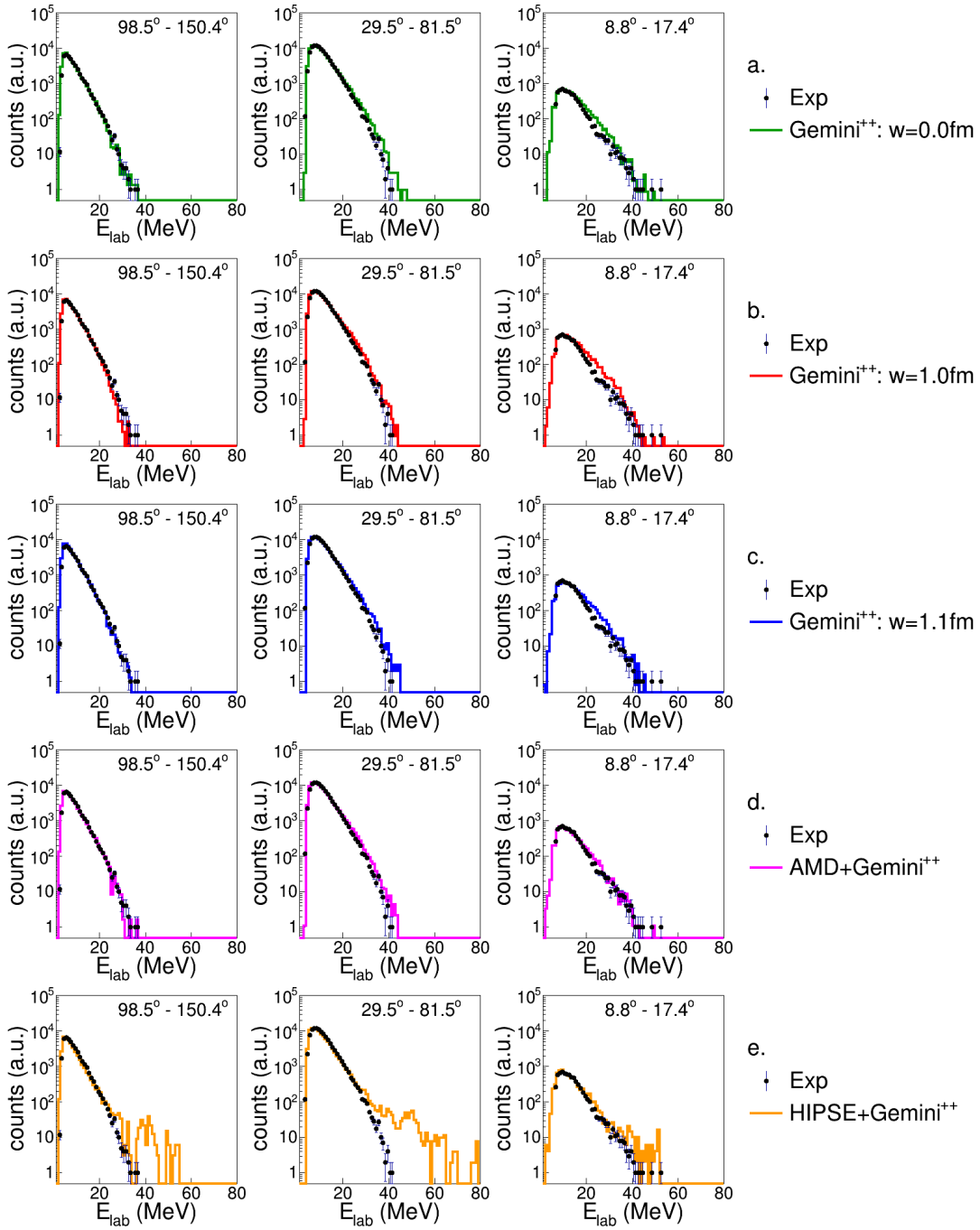

Figure B.34: Energy spectra of protons in coincidence with a K-residue for the reaction $^{16}O + ^{30}Si$ at 128 MeV

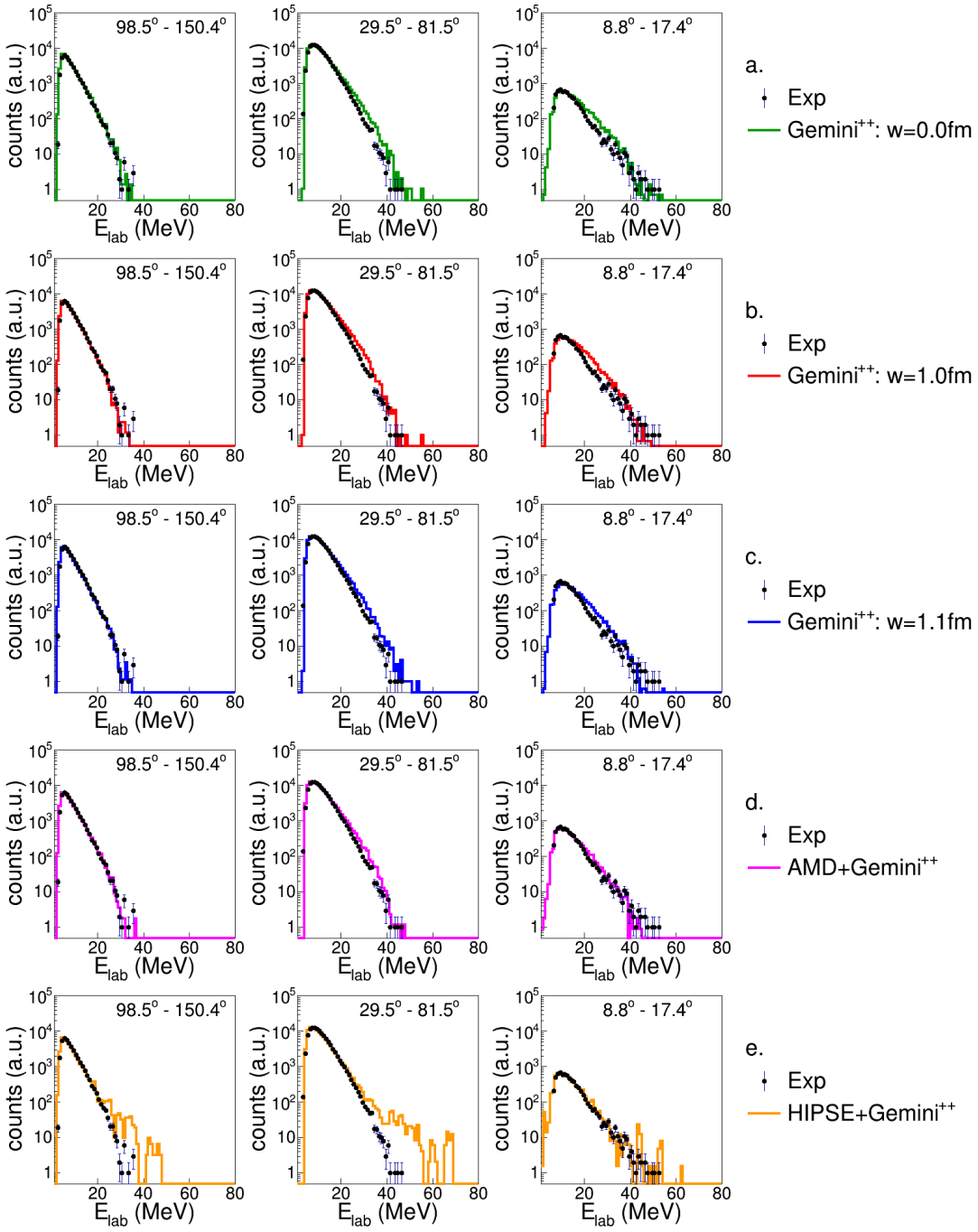

Figure B.35: Energy spectra of protons in coincidence with a K-residue for the reaction $^{18}O + ^{28}Si$ at 126 MeV

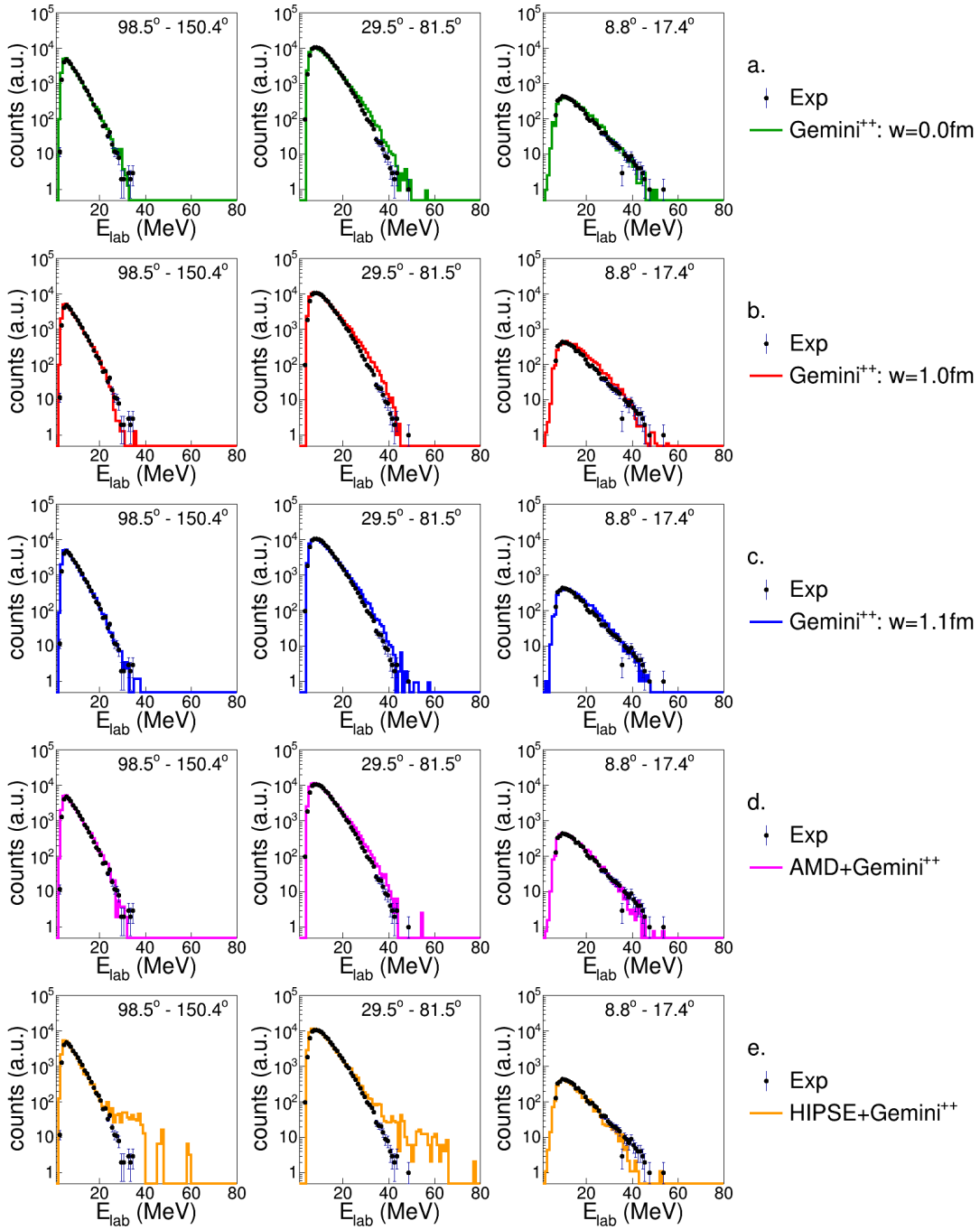

Figure B.36: Energy spectra of protons in coincidence with a K-residue for the reaction $^{19}F + ^{27}Al$ at 133 MeV

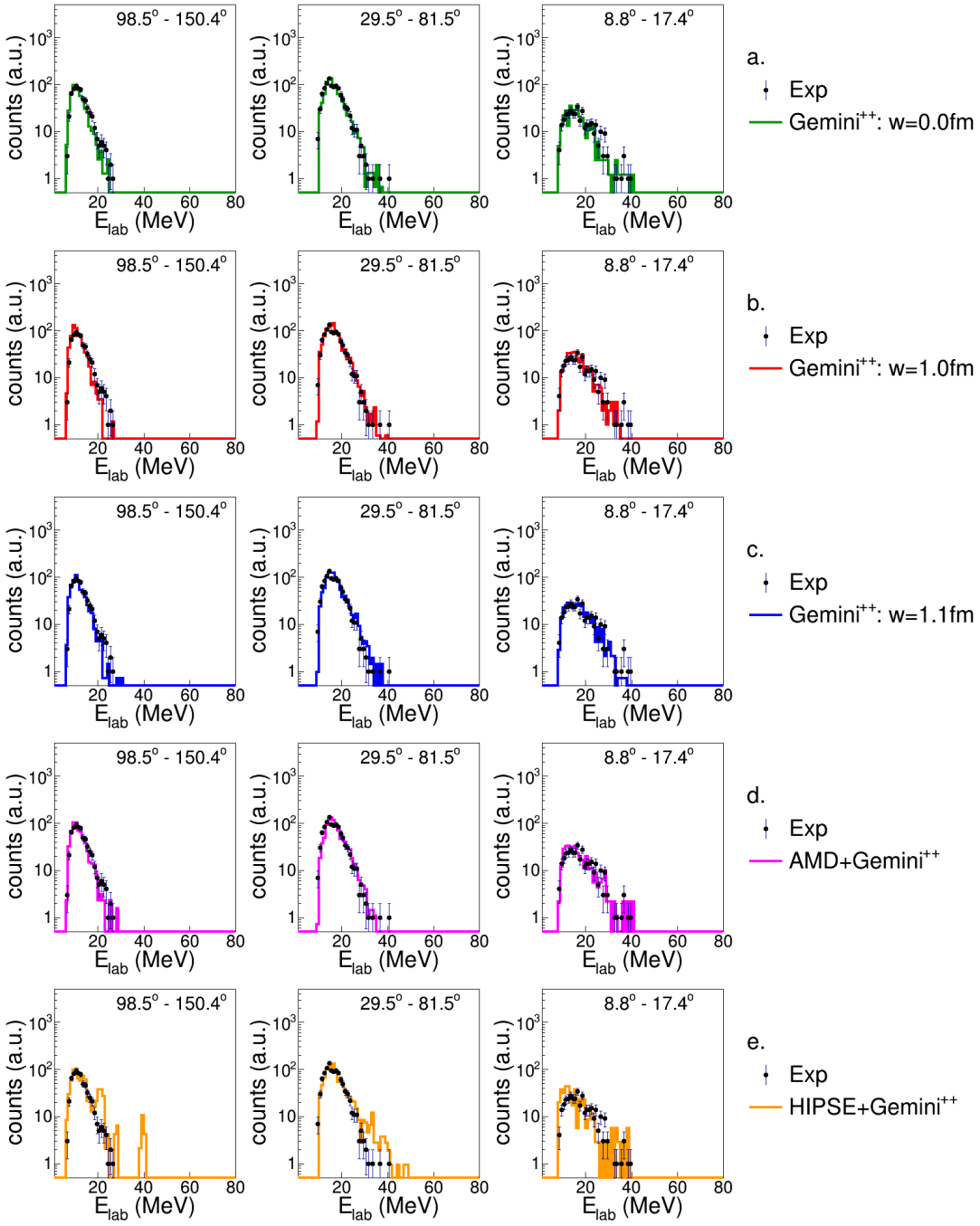

Figure B.37: Energy spectra of deuterons in coincidence with a K-residue for the reaction $^{16}O + ^{30}Si$ at 111 MeV.

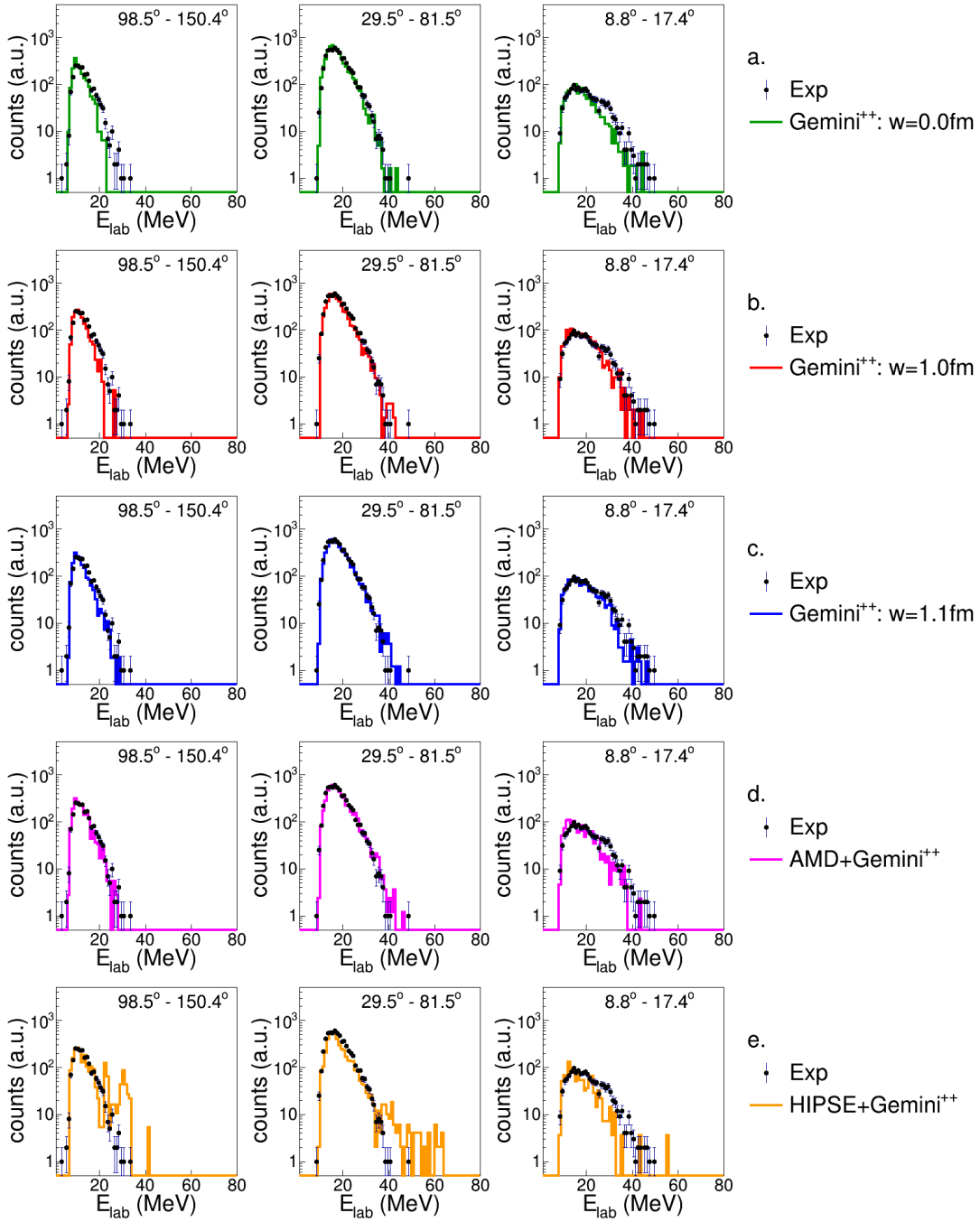

Figure B.38: Energy spectra of deuterons in coincidence with a K-residue for the reaction $^{16}O + ^{30}Si$ at 128 MeV

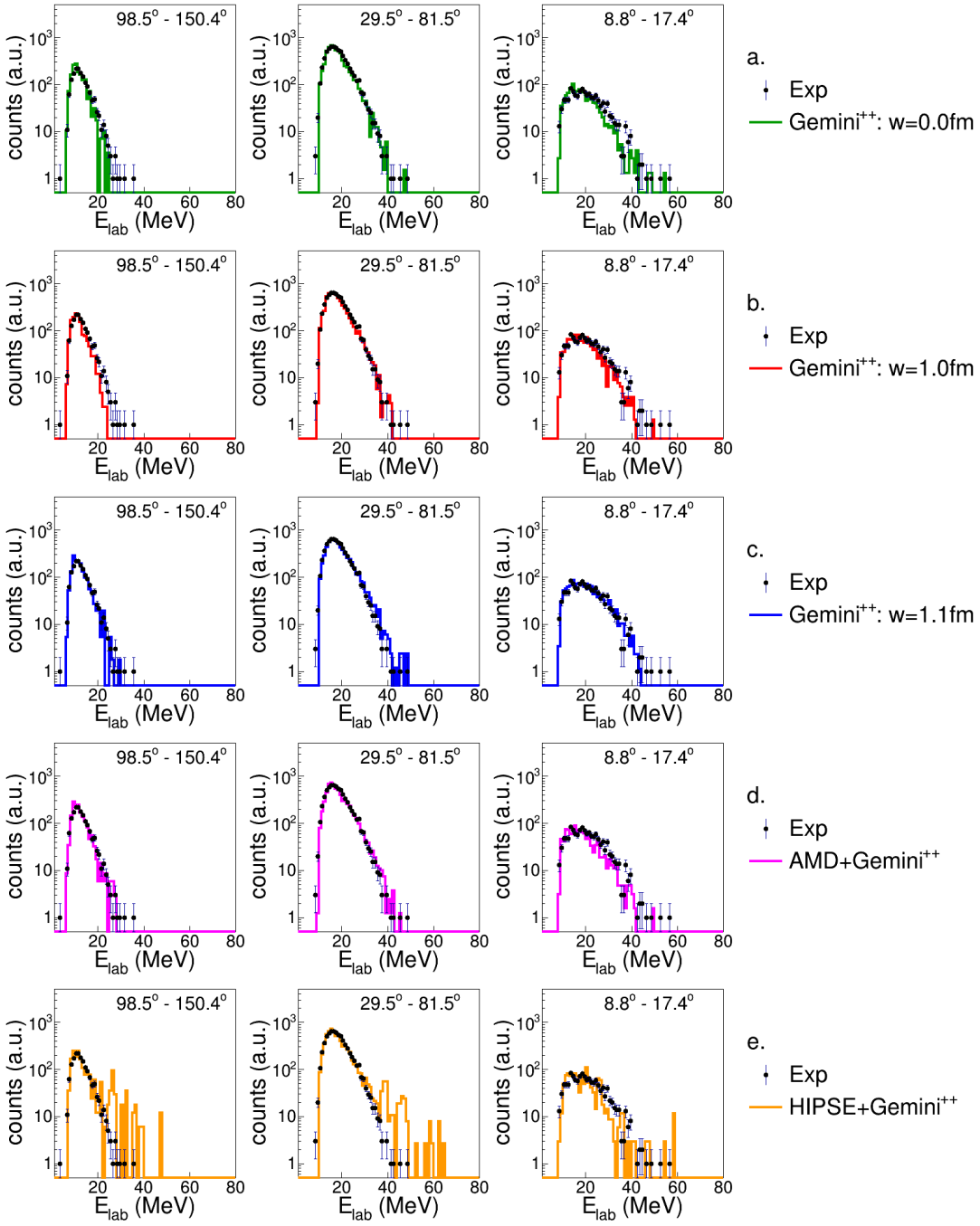

Figure B.39: Energy spectra of deuterons in coincidence with a K-residue for the reaction $^{18}O + ^{28}Si$ at 126 MeV

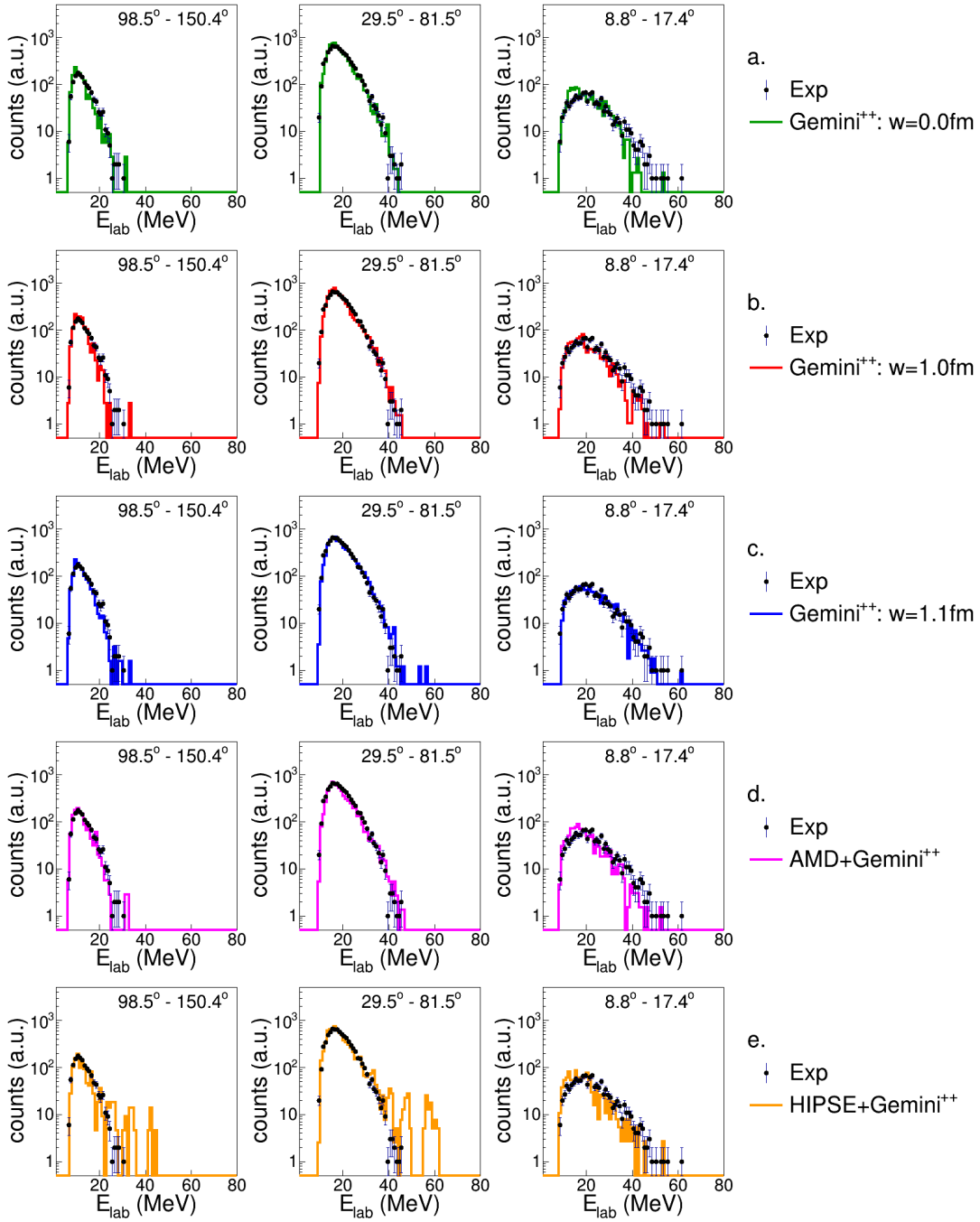

Figure B.40: Energy spectra of deuterons in coincidence with a K-residue for the reaction $^{19}F + ^{27}Al$ at 133 MeV

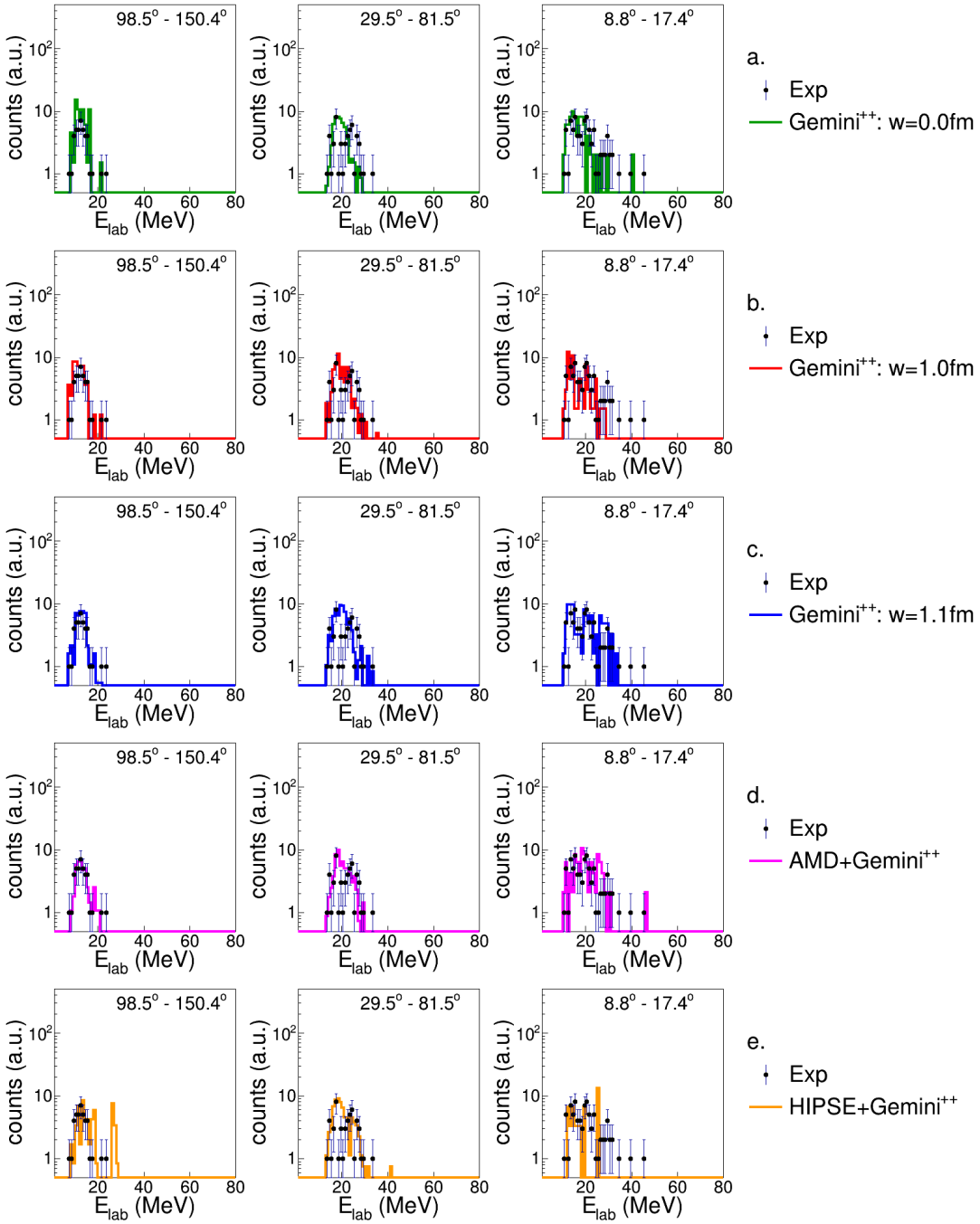

Figure B.41: Energy spectra of tritons in coincidence with a K-residue for the reaction $^{16}O + ^{30}Si$ at 111 MeV.

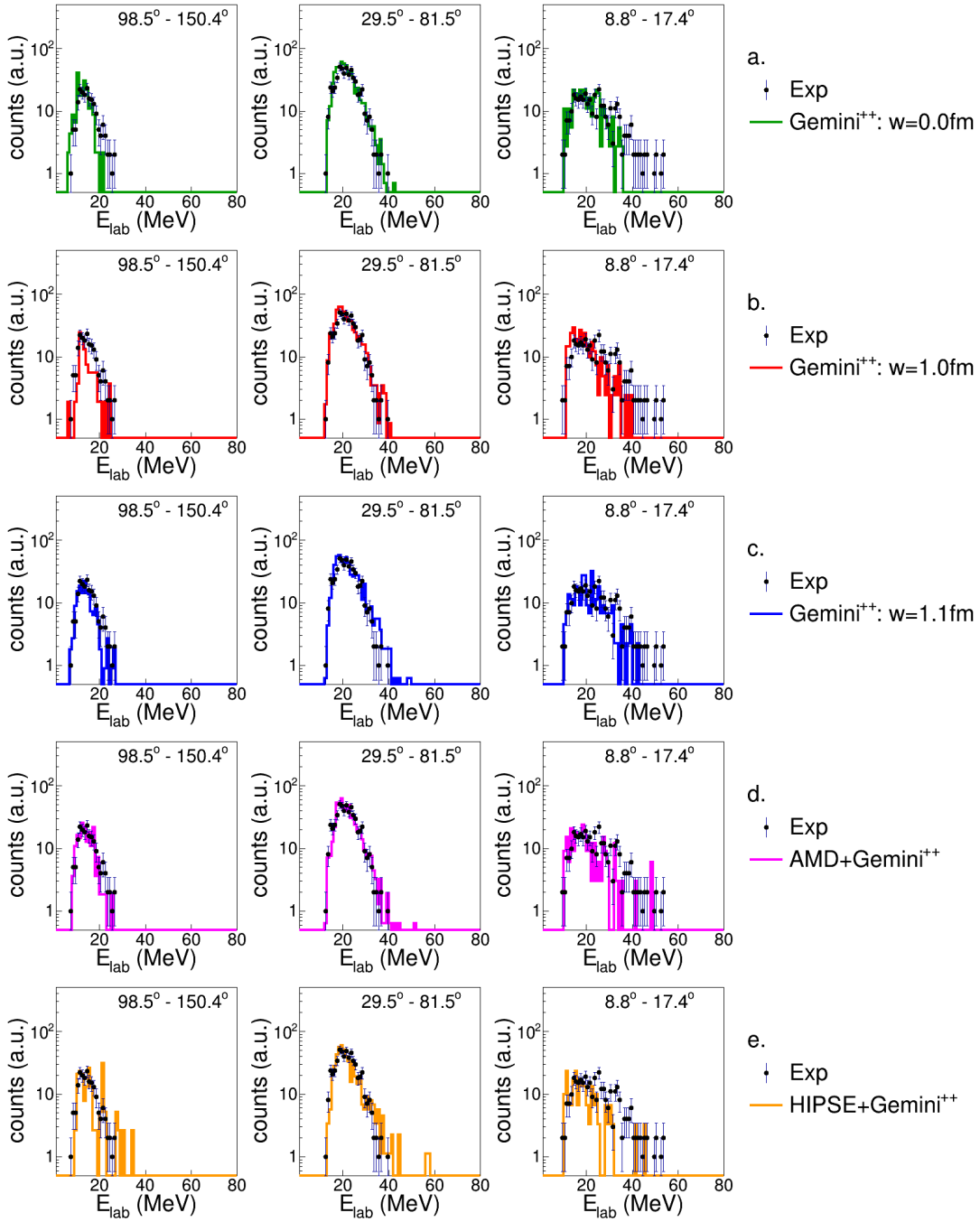

Figure B.42: Energy spectra of tritons in coincidence with a K-residue for the reaction $^{16}O + ^{30}Si$ at 128 MeV

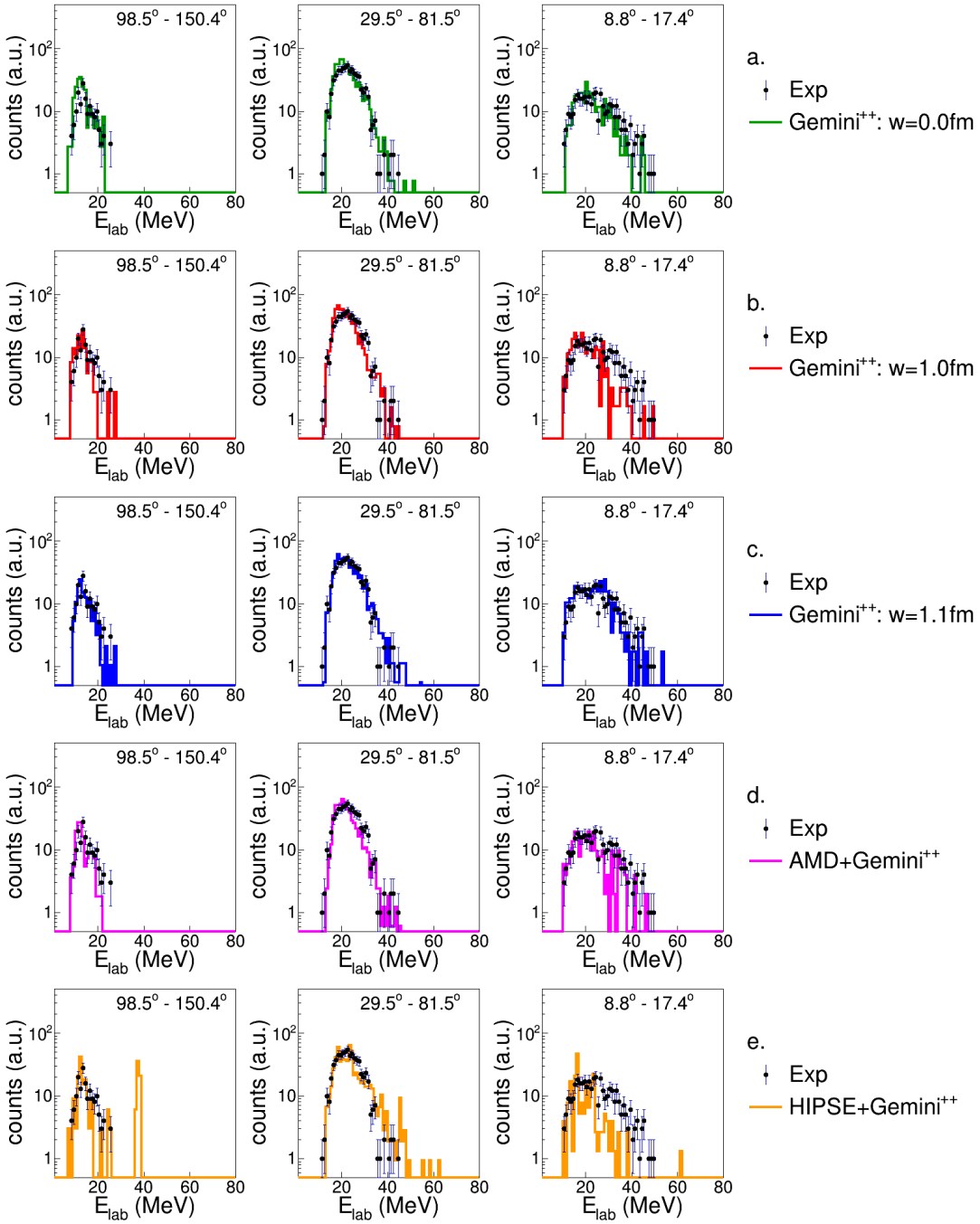

Figure B.43: Energy spectra of tritons in coincidence with a K-residue for the reaction $^{18}O + ^{28}Si$ at 126 MeV

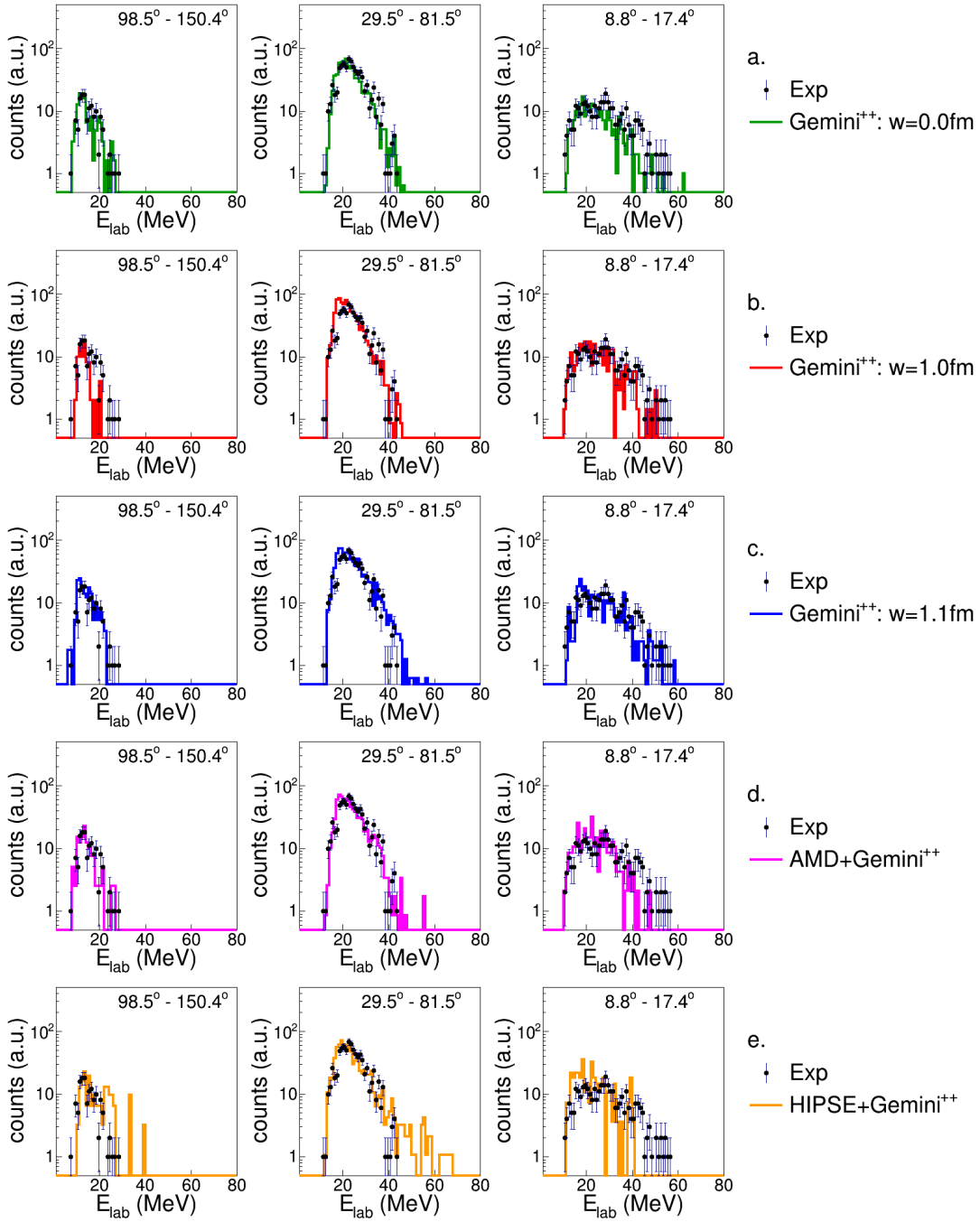

Figure B.44: Energy spectra of tritons in coincidence with a K-residue for the reaction $^{19}F + ^{27}Al$ at 133 MeV

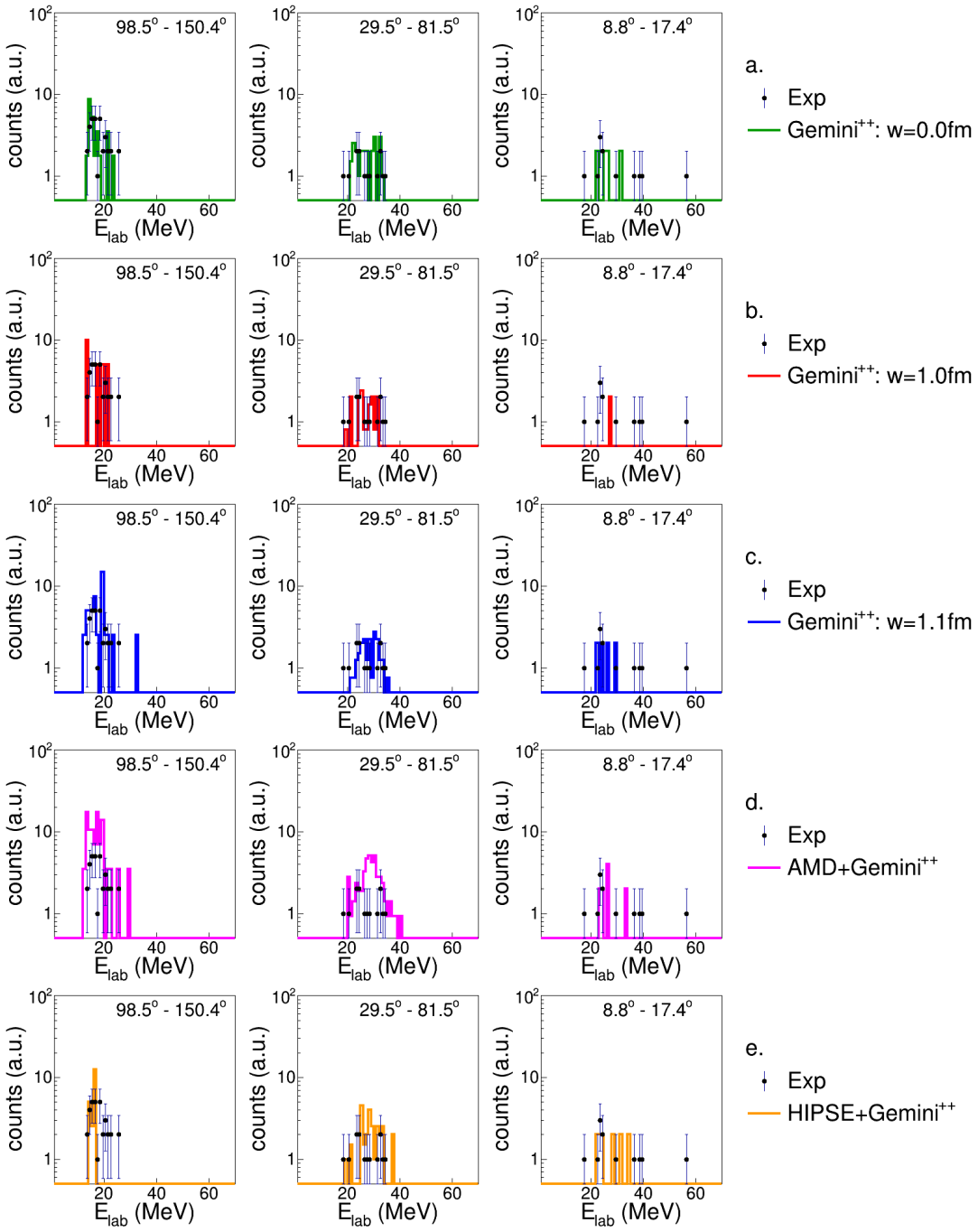

Figure B.45: Energy spectra of ^{3}He in coincidence with a K-residue for the reaction ^{16}O+^{30}Si at 111 MeV.

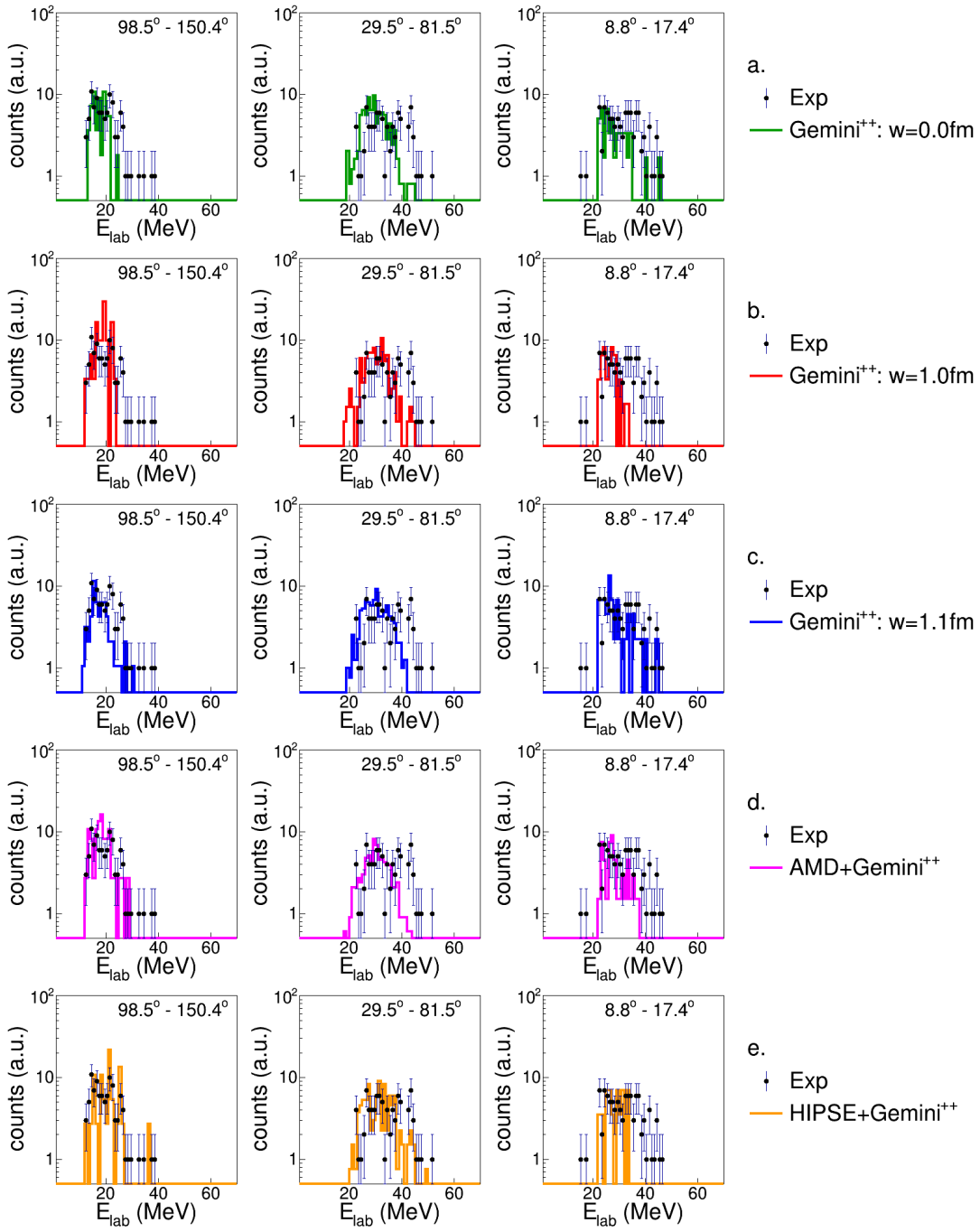

Figure B.46: Energy spectra of ^{3}He in coincidence with a K-residue for the reaction $^{16}O+^{30}Si$ at 128 MeV

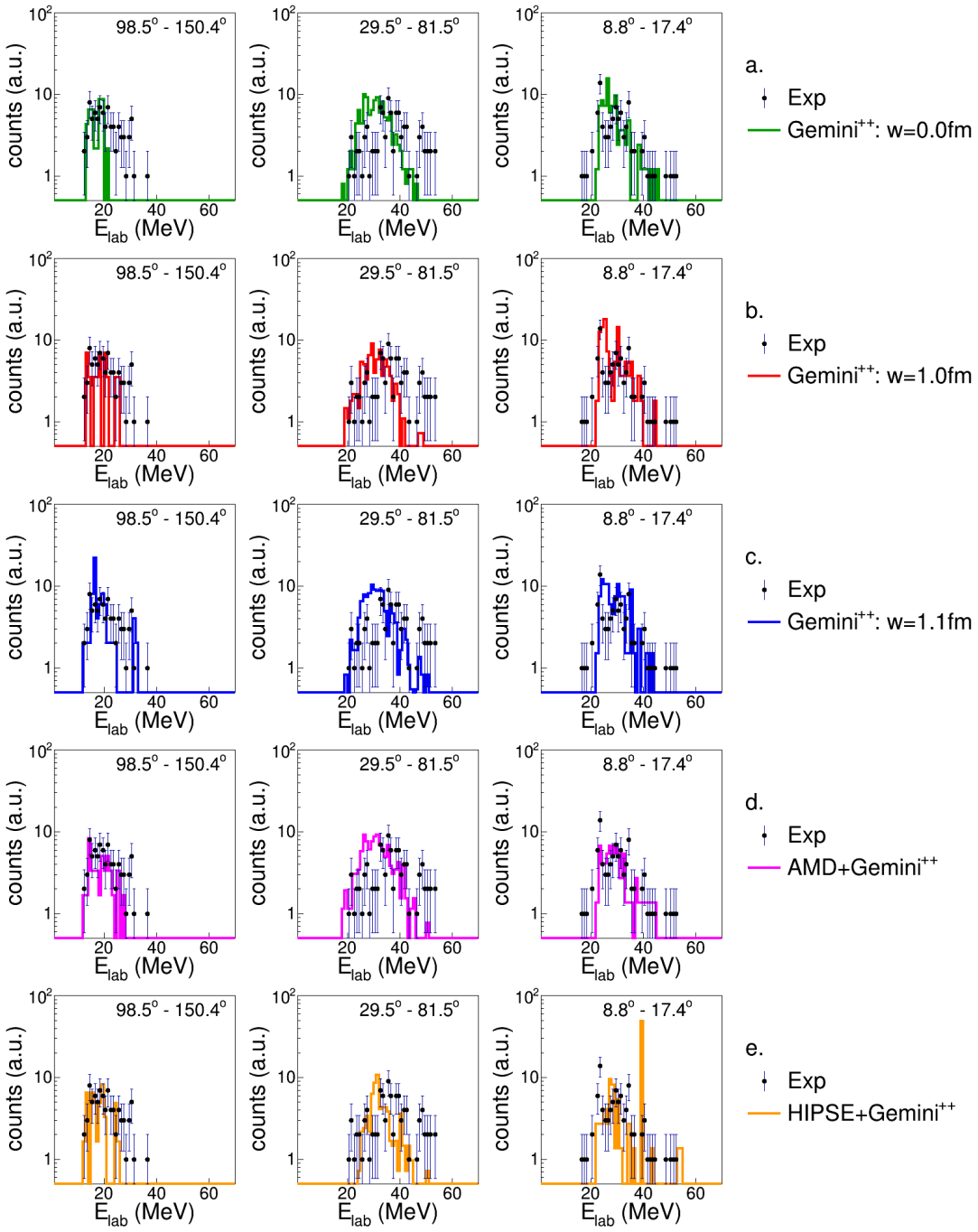

Figure B.47: Energy spectra of ^{3}He in coincidence with a K-residue for the reaction ^{18}O+^{28}Si at 126 MeV

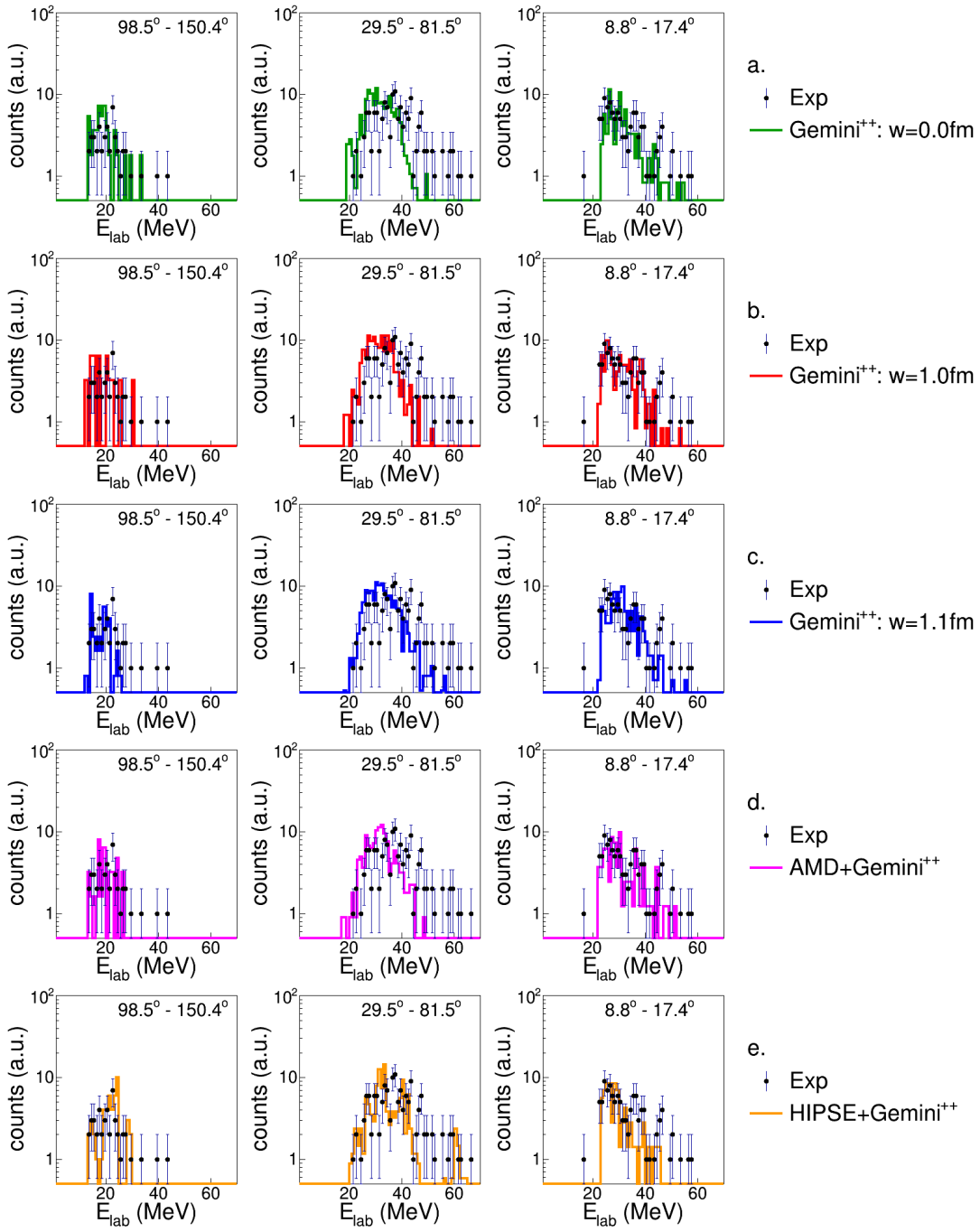

Figure B.48: Energy spectra of ^{3}He in coincidence with a K-residue for the reaction $^{19}F+^{27}Al$ at 133 MeV

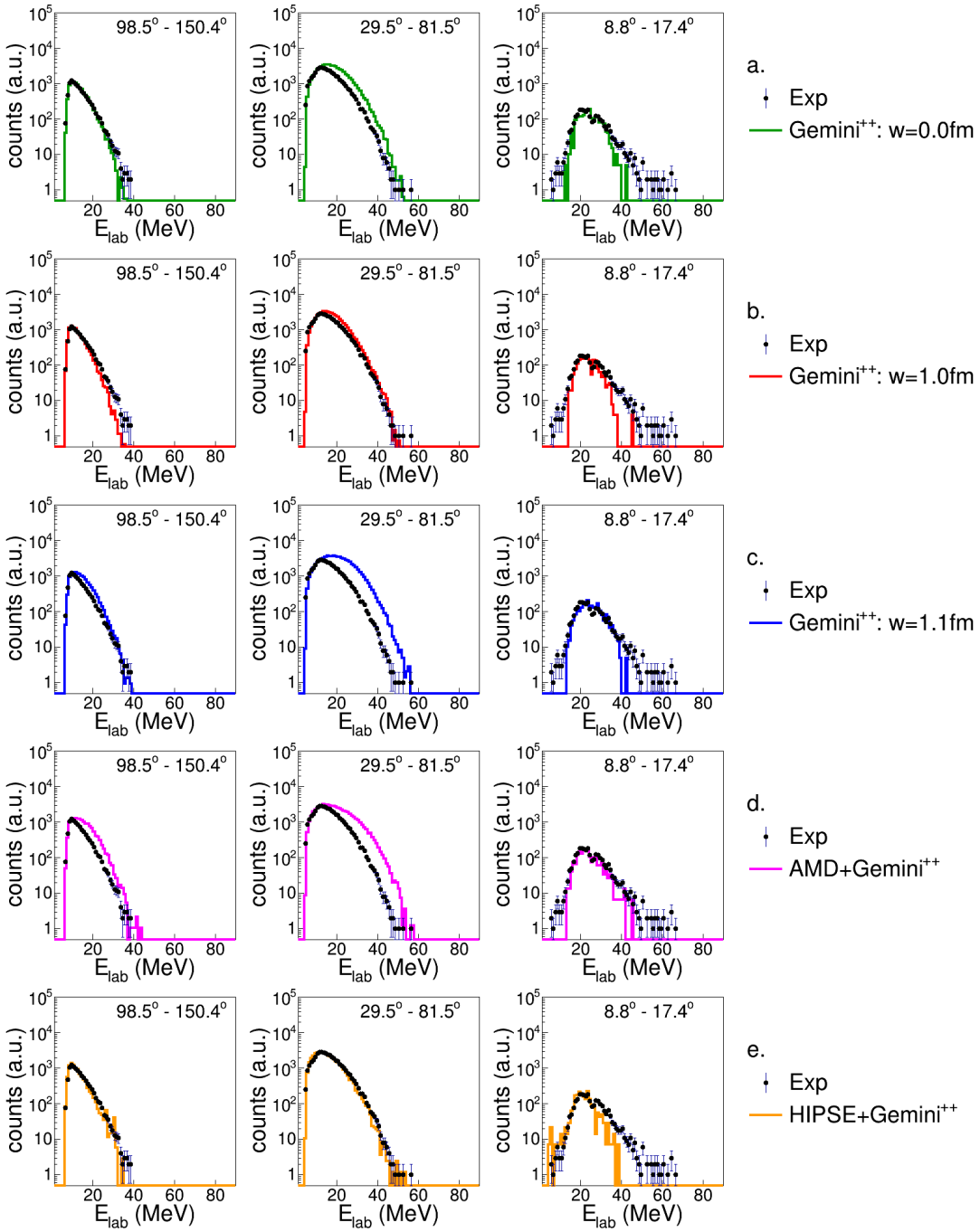

Figure B.49: Energy spectra of α-particles in coincidence with a K-residue for the reaction $^{16}O + ^{30}Si$ at 111 MeV.

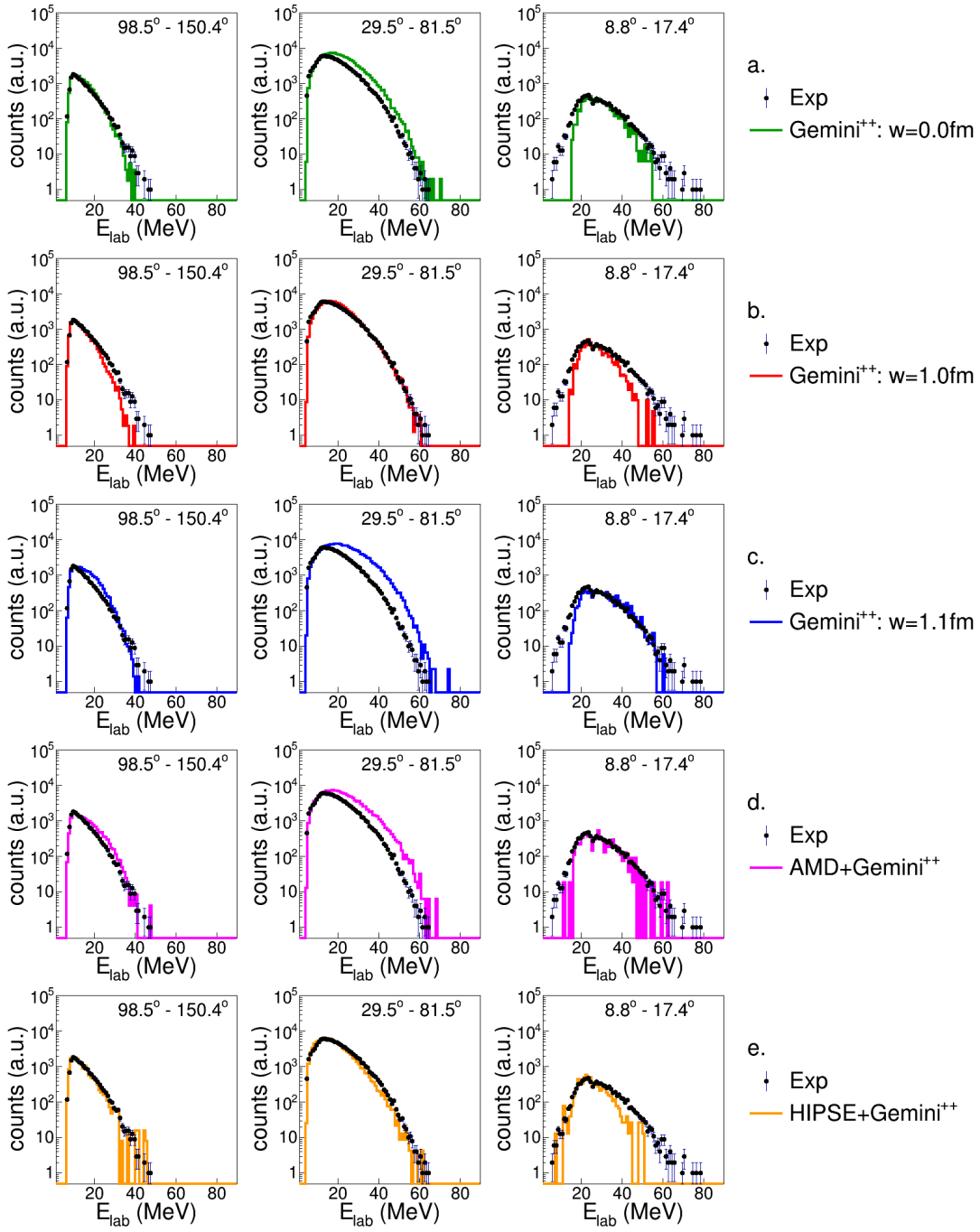

Figure B.50: Energy spectra of α-particles in coincidence with a K-residue for the reaction $^{16}O + ^{30}Si$ at 128 MeV

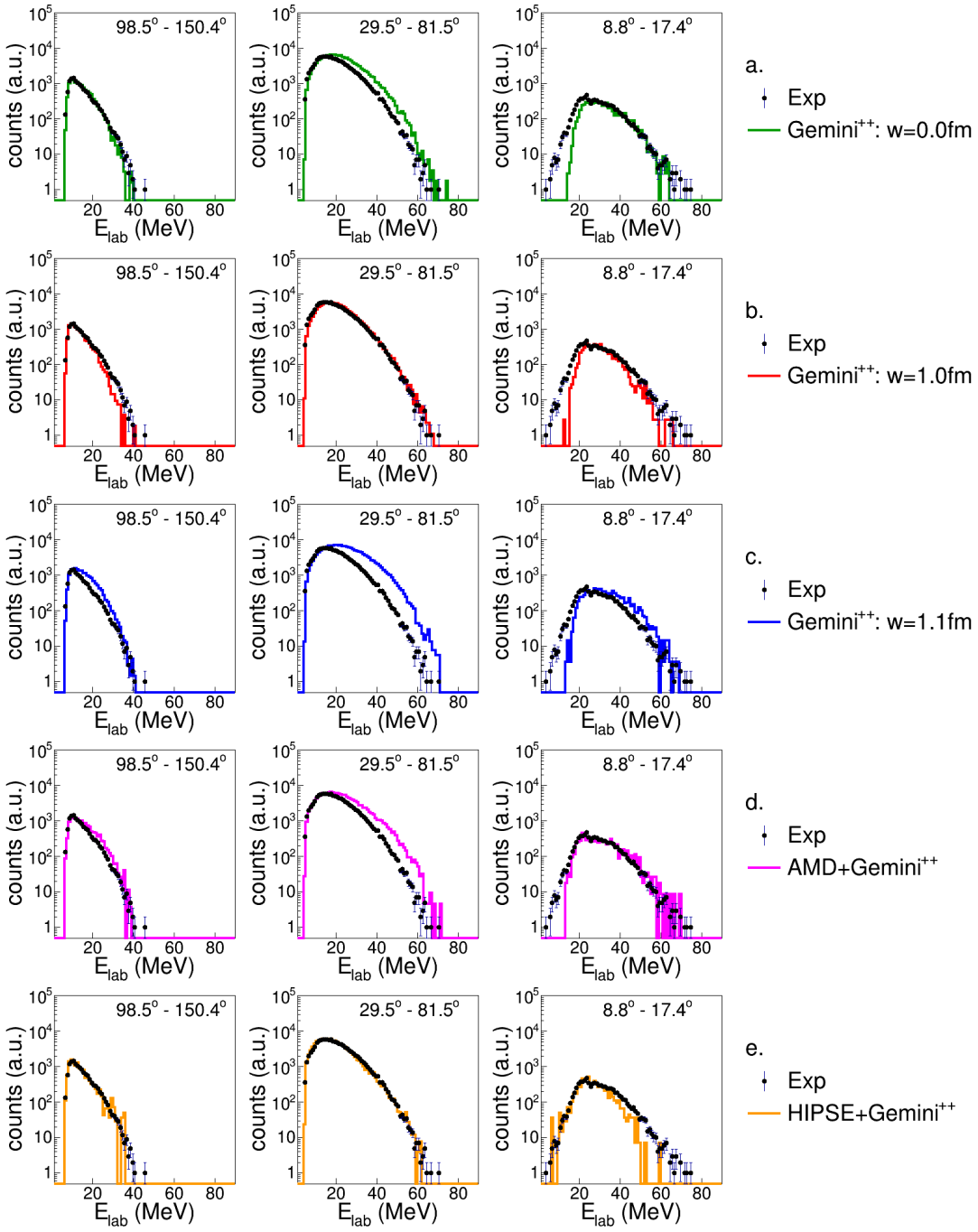

Figure B.51: Energy spectra of α-particles in coincidence with a K-residue for the reaction $^{18}O + ^{28}Si$ at 126 MeV

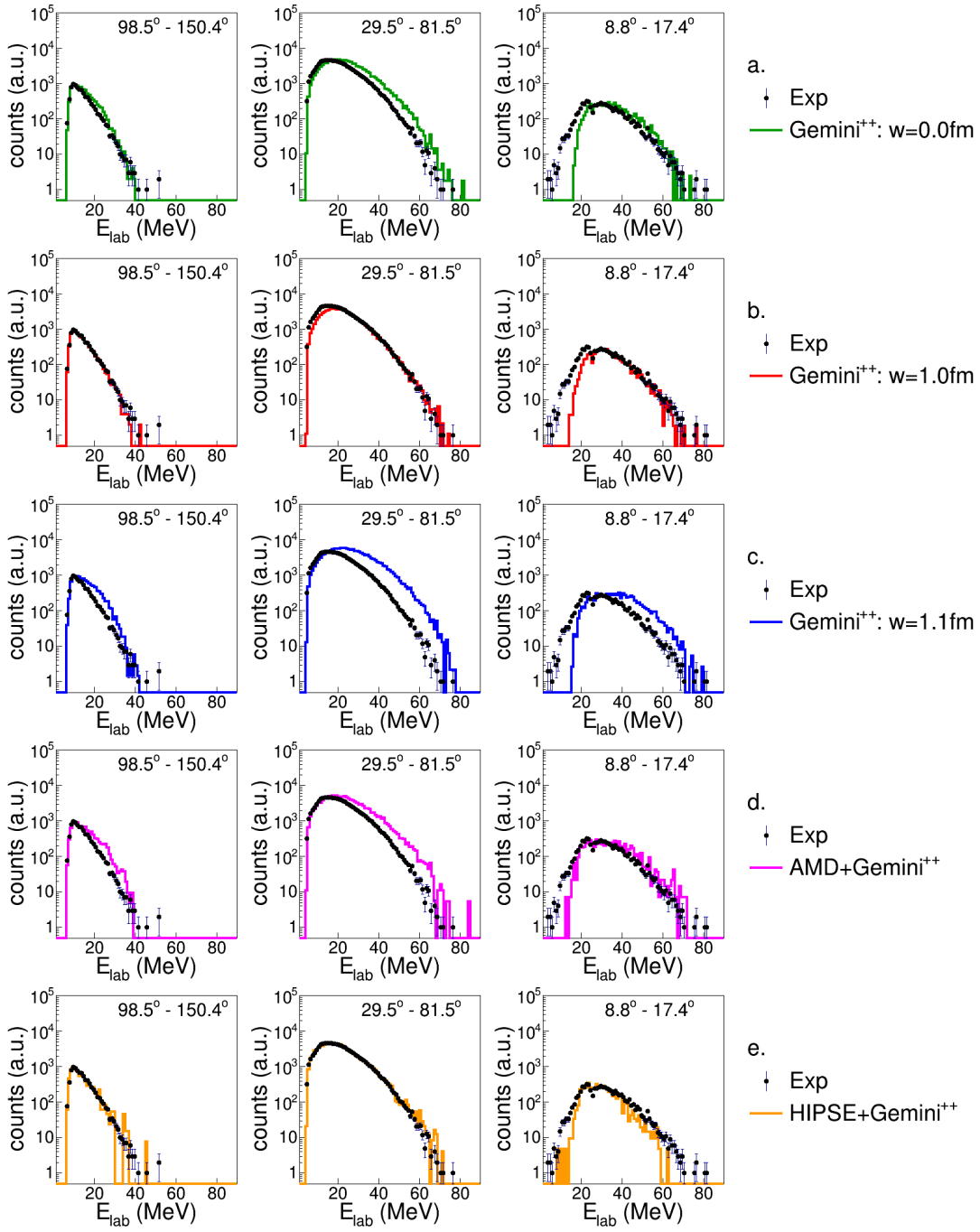

Figure B.52: Energy spectra of α-particles in coincidence with a K-residue for the reaction $^{19}F + ^{27}Al$ at 133 MeV

B.4 The Ar residue: $Z_{res} = 18$

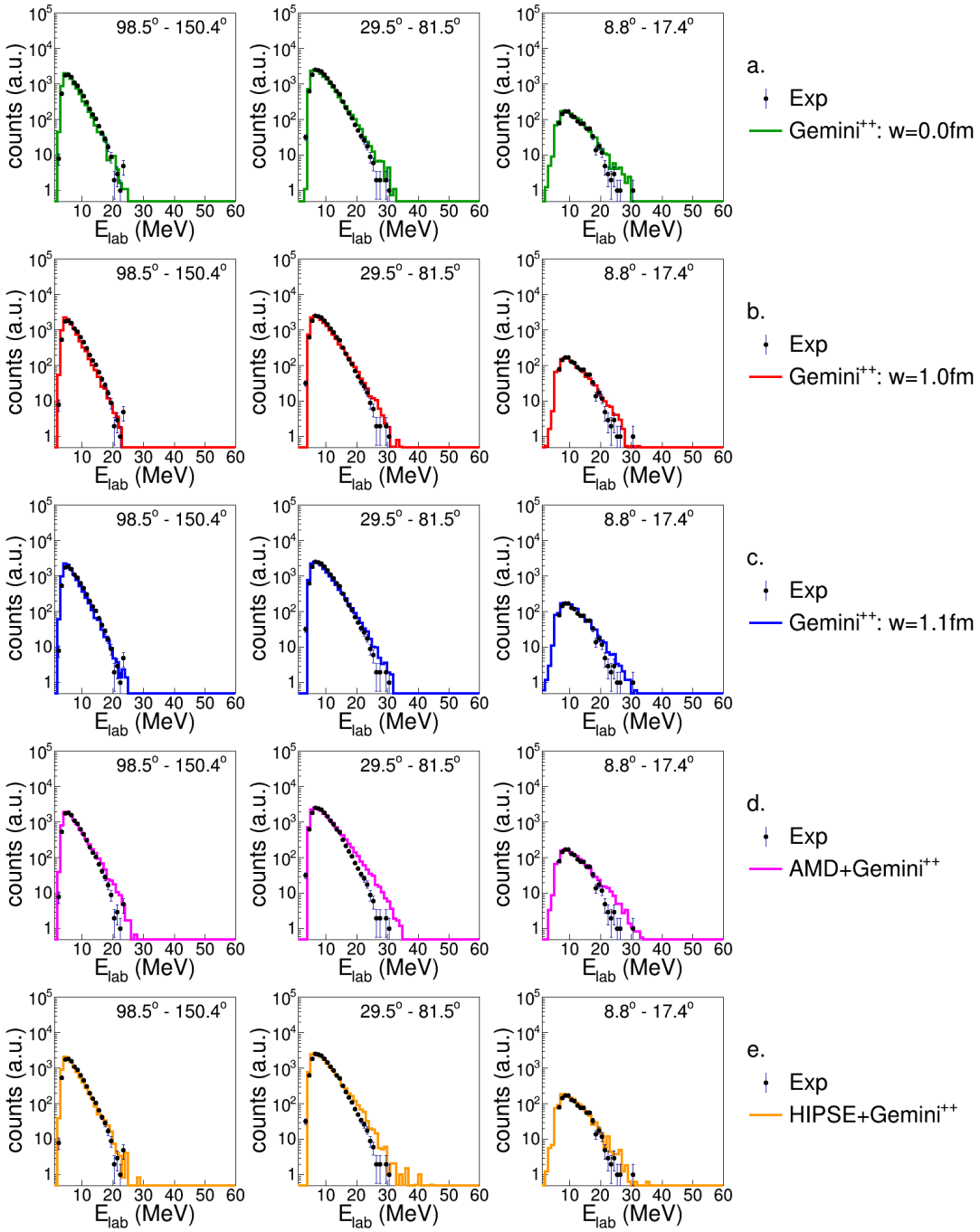

Figure B.53: Energy spectra of protons in coincidence with a *Ar*-residue for the reaction $^{16}O + ^{30}Si$ at 111 MeV.

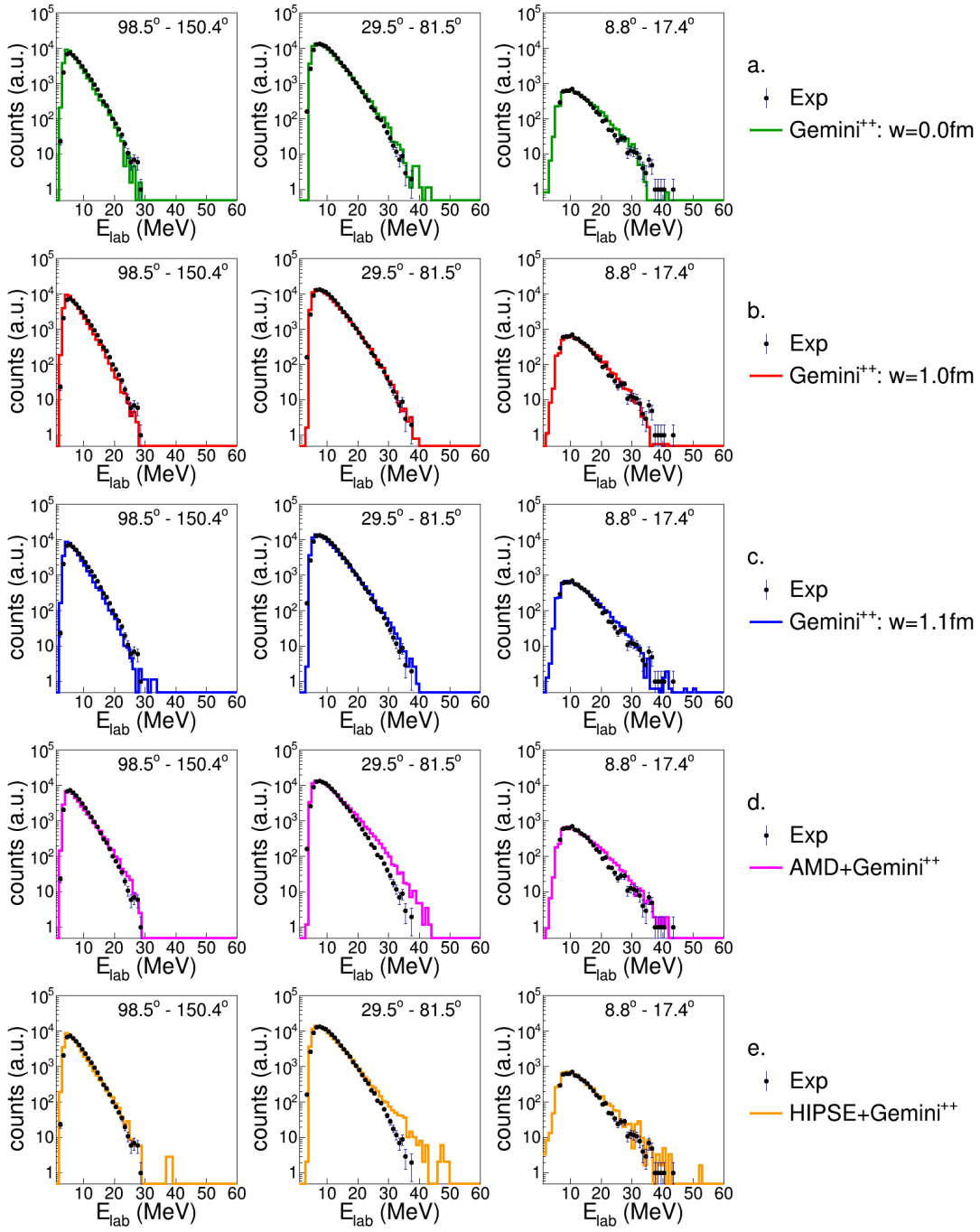

Figure B.54: Energy spectra of protons in coincidence with a Ar-residue for the reaction $^{16}O + ^{30}Si$ at 128 MeV

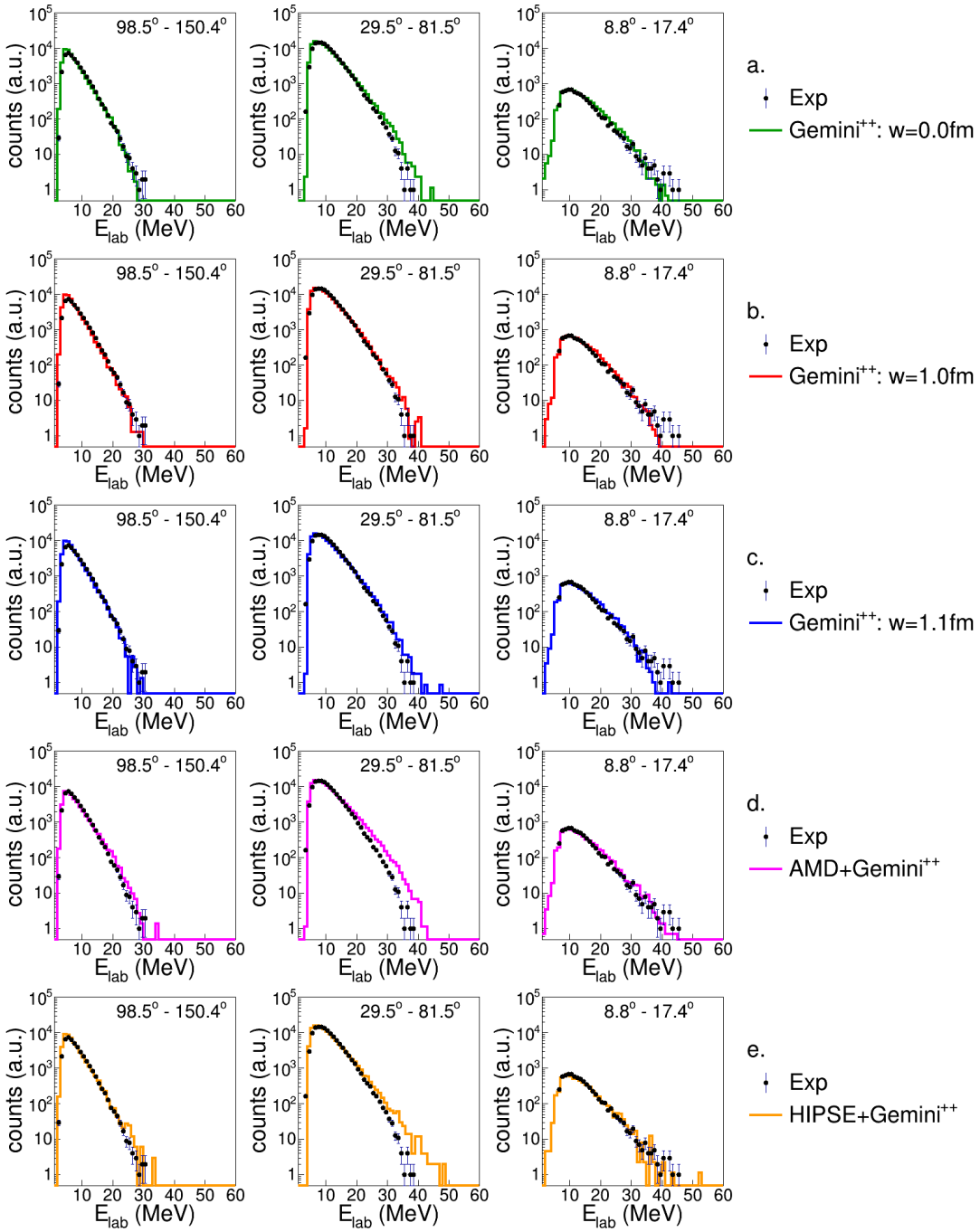

Figure B.55: Energy spectra of protons in coincidence with a *Ar*-residue for the reaction $^{18}O + ^{28}Si$ at 126 MeV

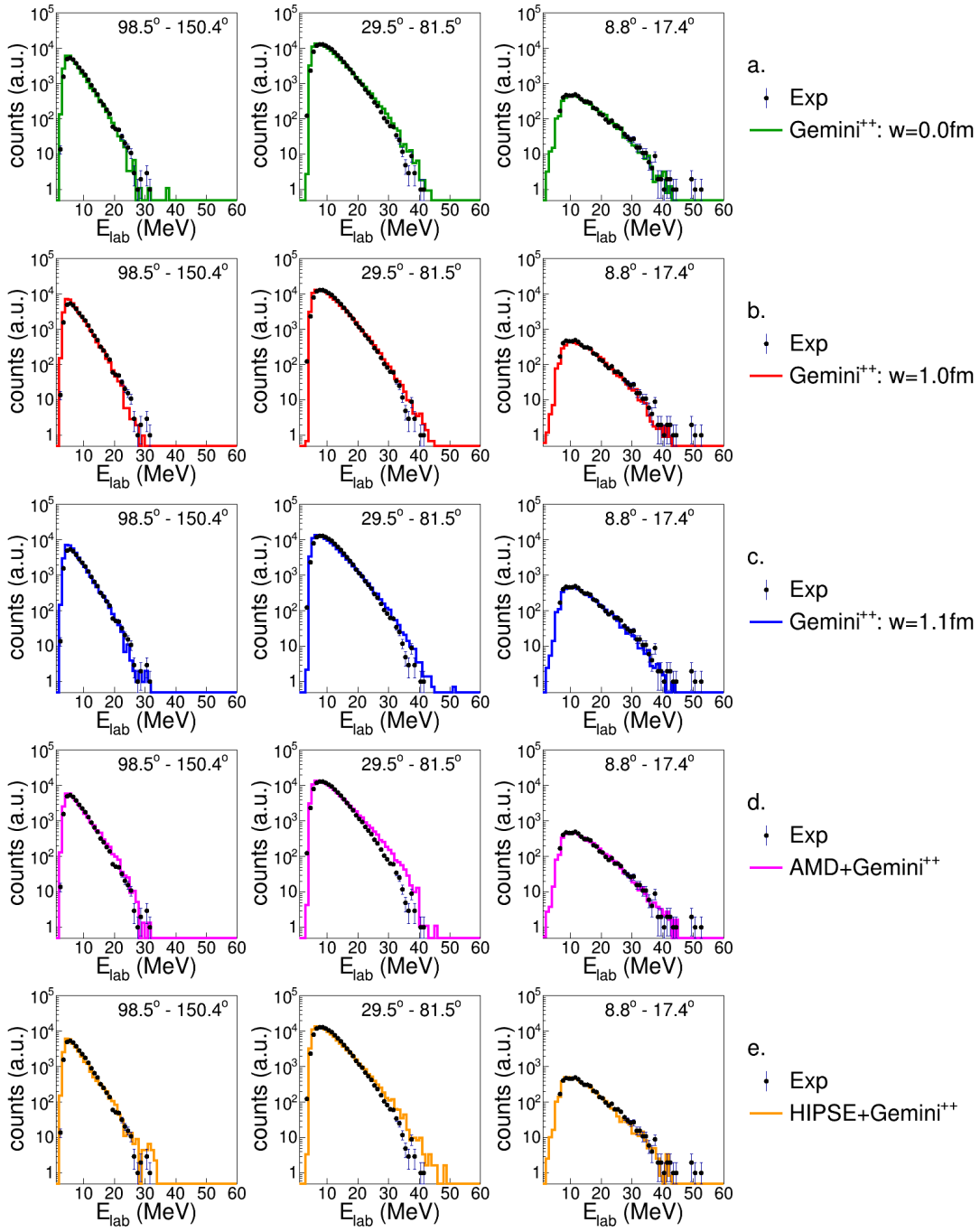

Figure B.56: Energy spectra of protons in coincidence with a Ar-residue for the reaction $^{19}F + ^{27}Al$ at 133 MeV

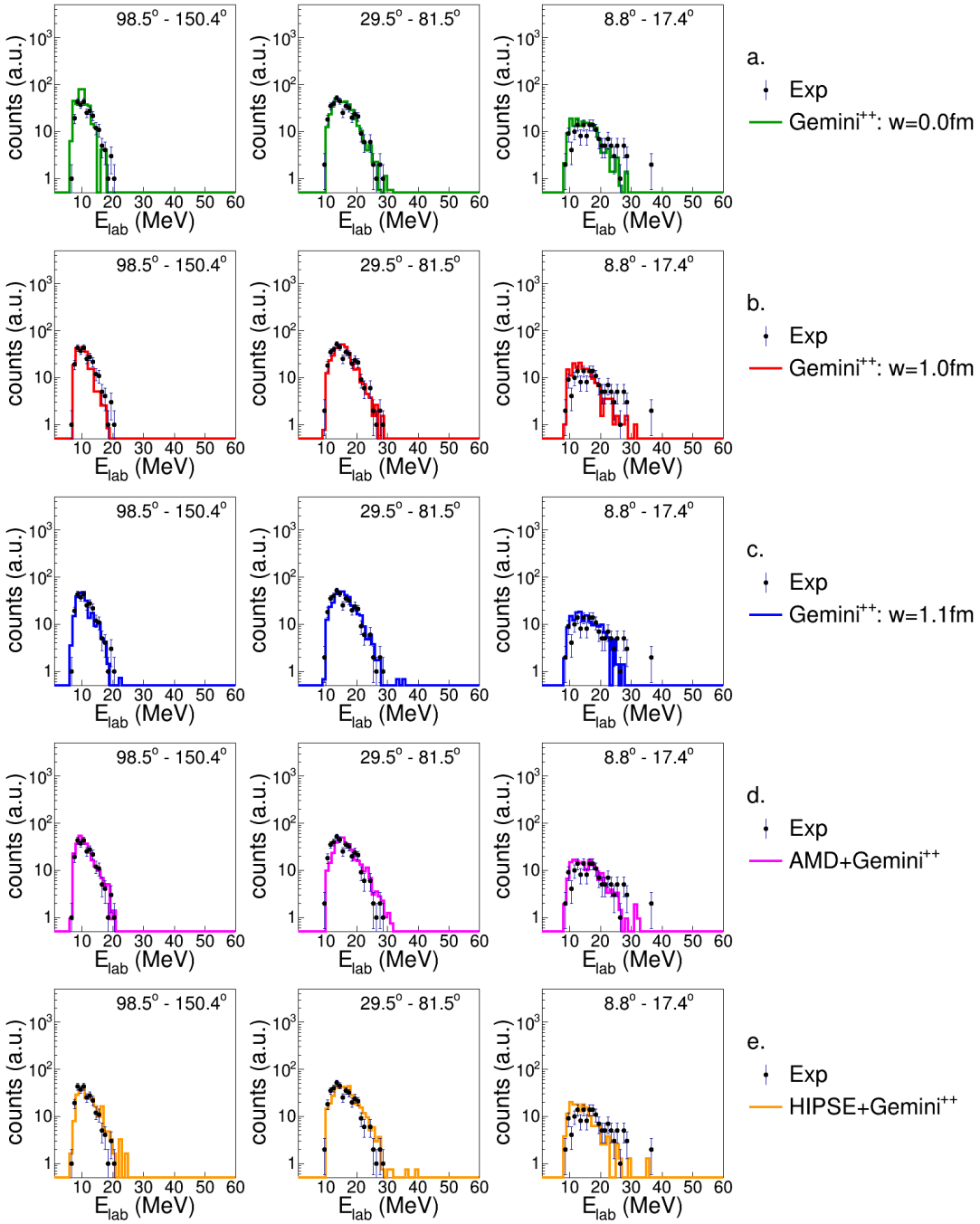

Figure B.57: Energy spectra of deuterons in coincidence with a *Ar*-residue for the reaction $^{16}O + ^{30}Si$ at 111 MeV.

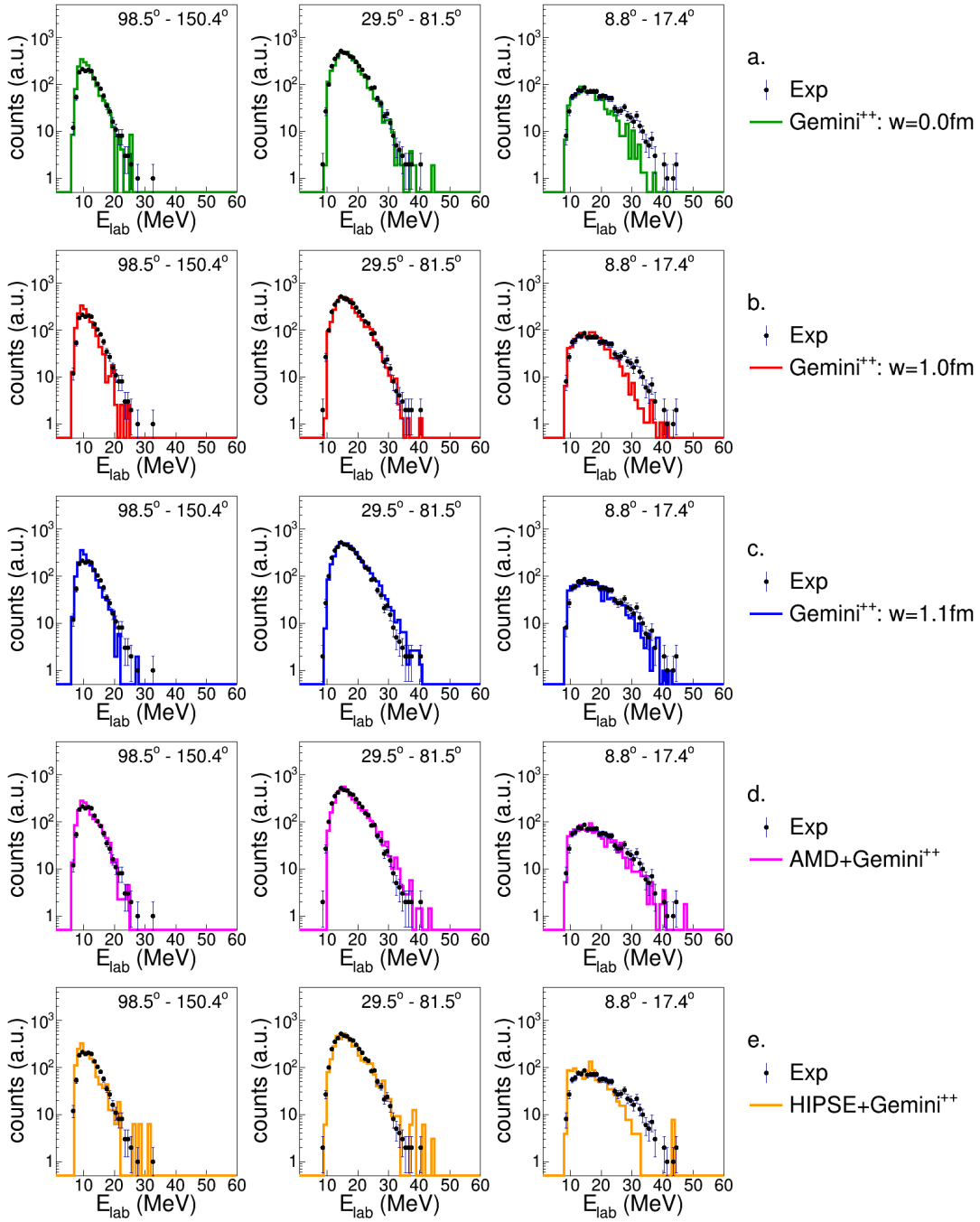

Figure B.58: Energy spectra of deuterons in coincidence with a *Ar*-residue for the reaction $^{16}O + ^{30}Si$ at 128 MeV

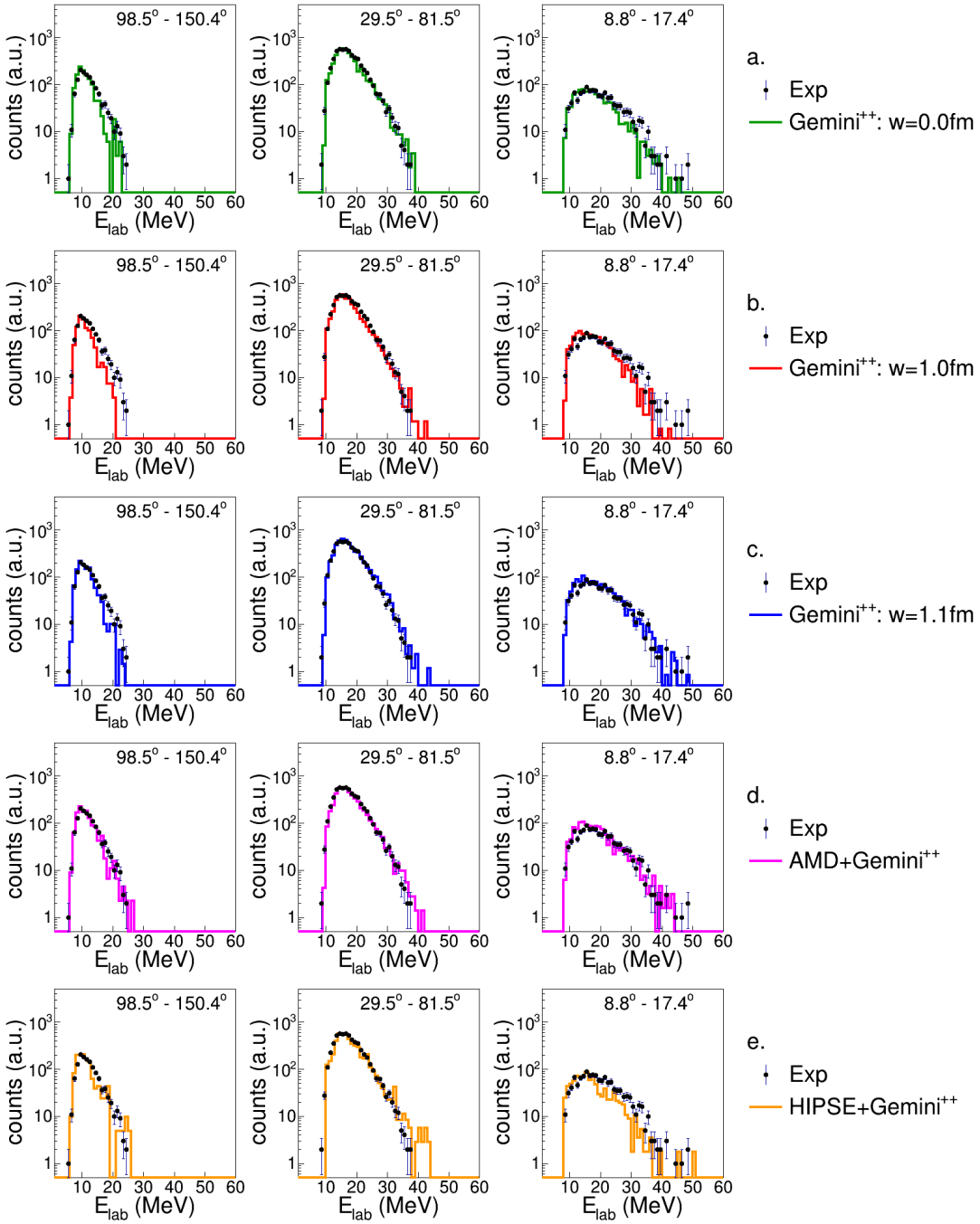

Figure B.59: Energy spectra of deuterons in coincidence with a *Ar*-residue for the reaction $^{18}O + ^{28}Si$ at 126 MeV

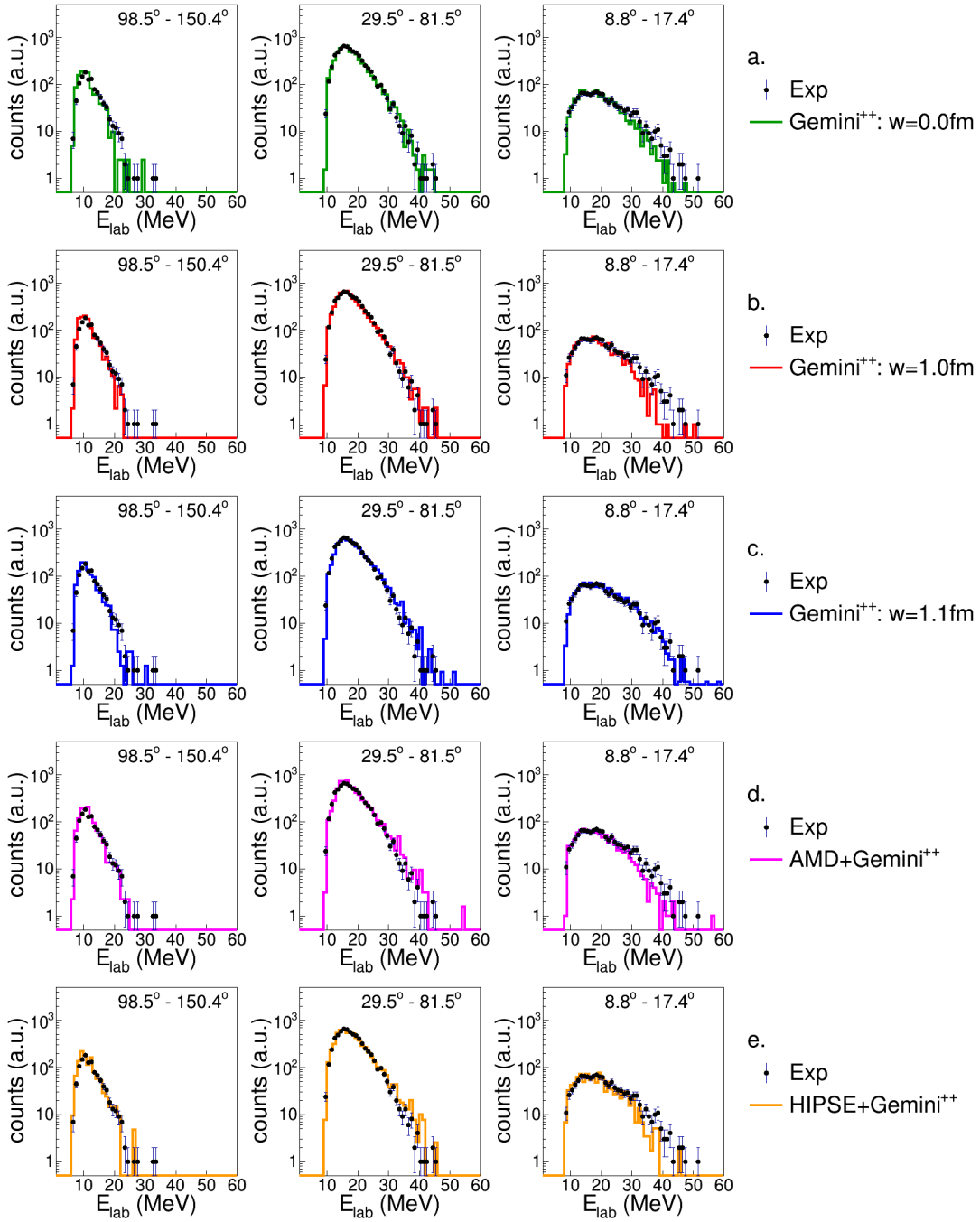

Figure B.60: Energy spectra of deuterons in coincidence with a *Ar*-residue for the reaction $^{19}F + ^{27}Al$ at 133 MeV

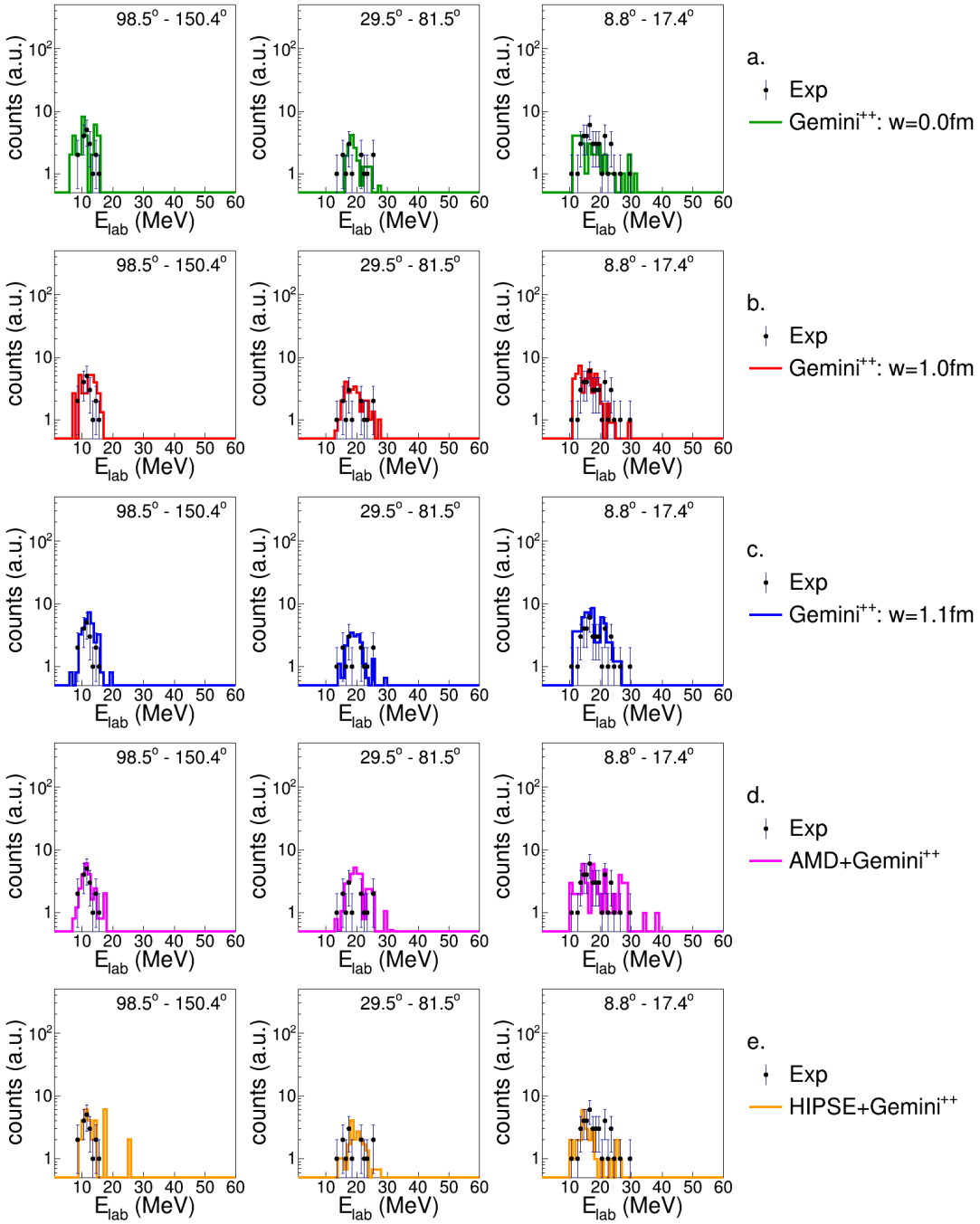

Figure B.61: Energy spectra of tritons in coincidence with a *Ar*-residue for the reaction $^{16}O + ^{30}Si$ at 111 MeV.

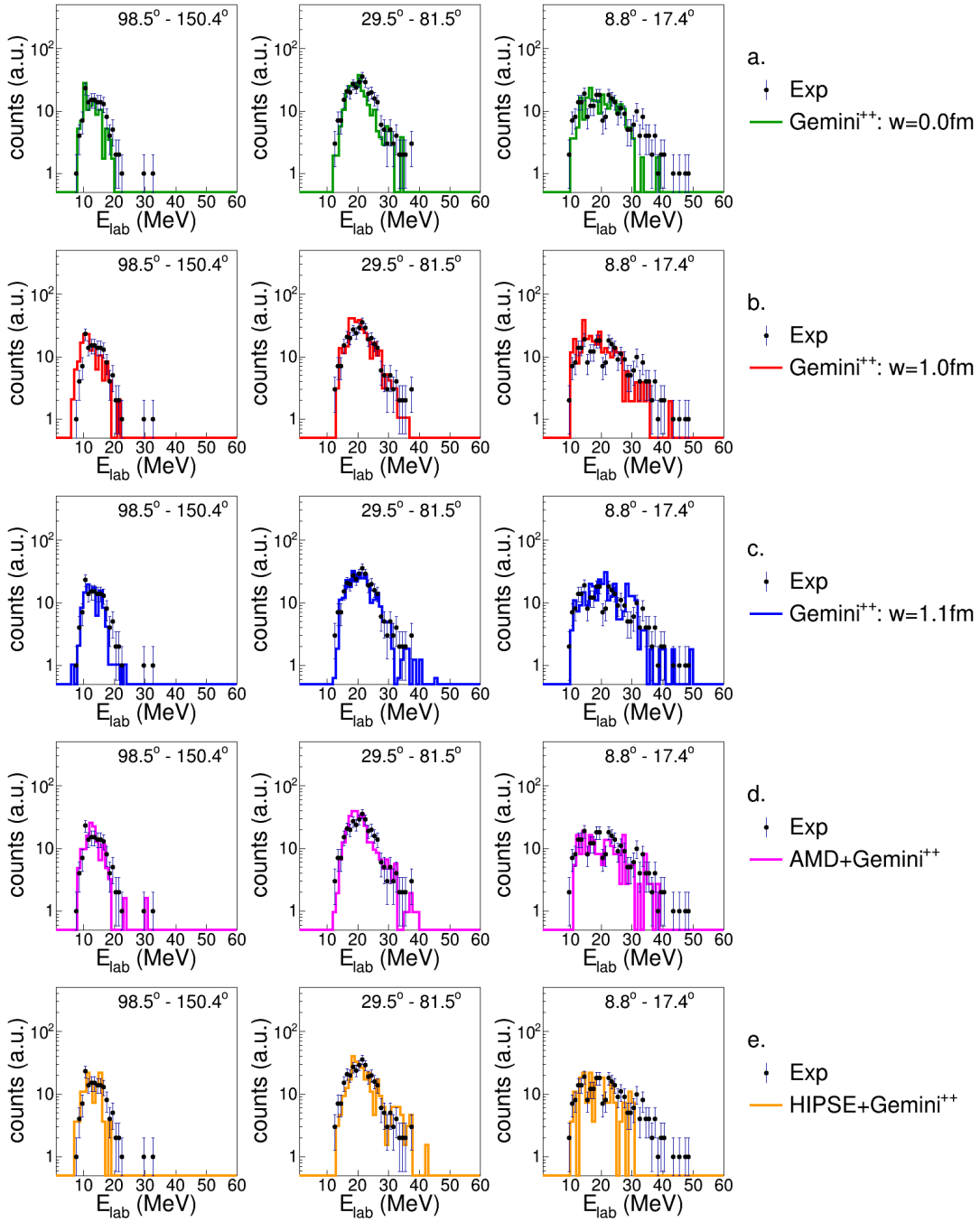

Figure B.62: Energy spectra of tritons in coincidence with a *Ar*-residue for the reaction $^{16}O + ^{30}Si$ at 128 MeV

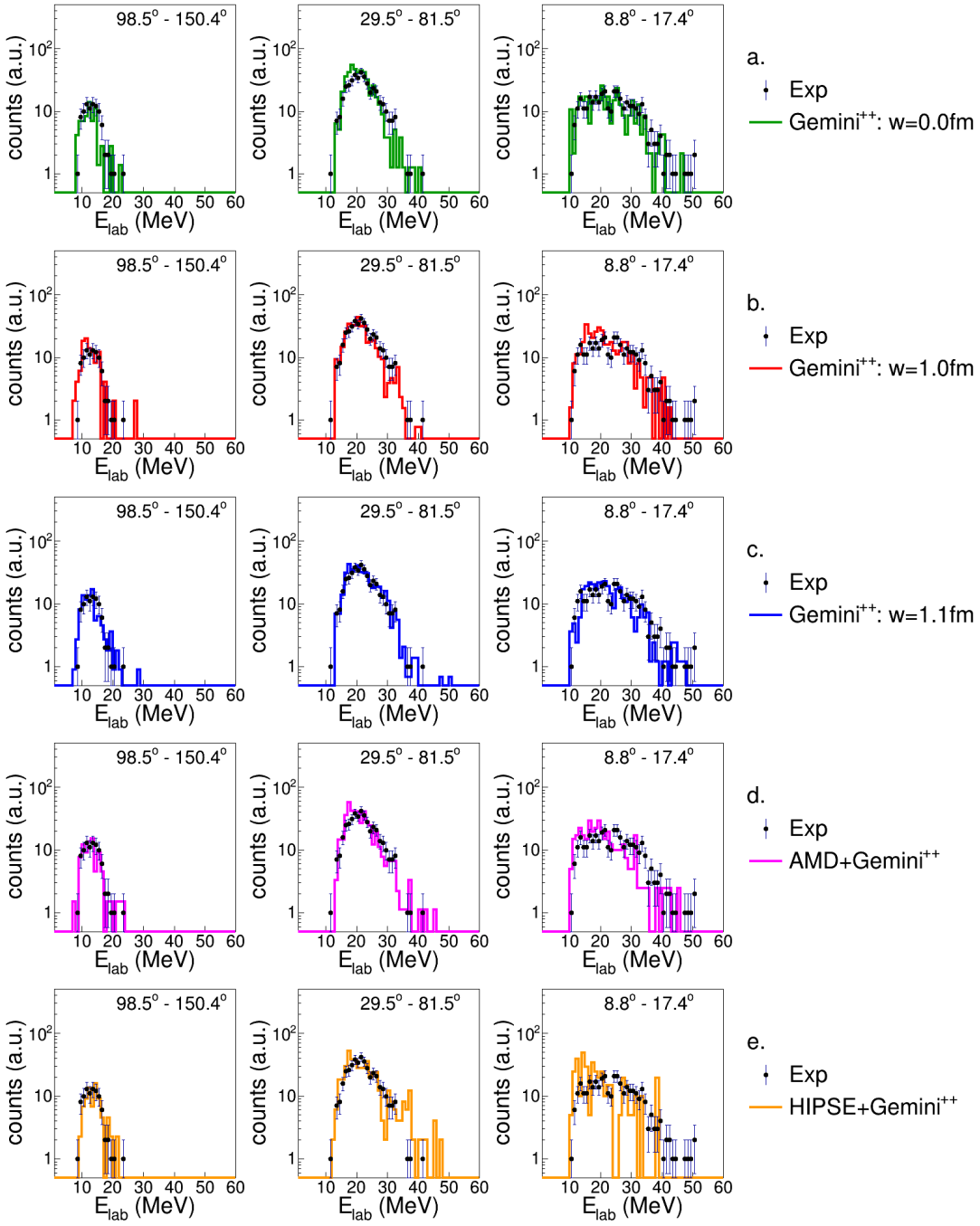

Figure B.63: Energy spectra of tritons in coincidence with a *Ar*-residue for the reaction $^{18}O + ^{28}Si$ at 126 MeV

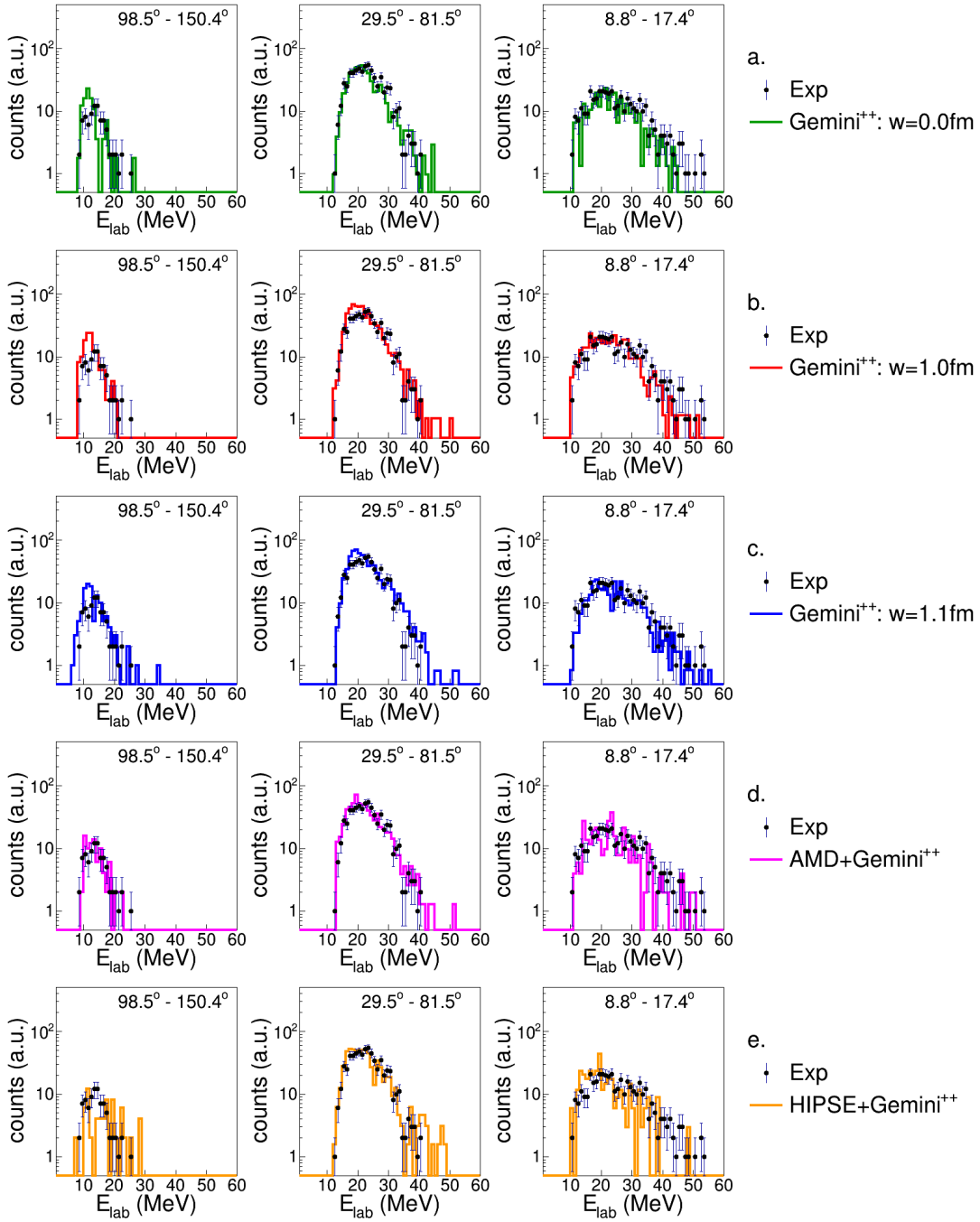

Figure B.64: Energy spectra of tritons in coincidence with a *Ar*-residue for the reaction $^{19}F + ^{27}Al$ at 133 MeV

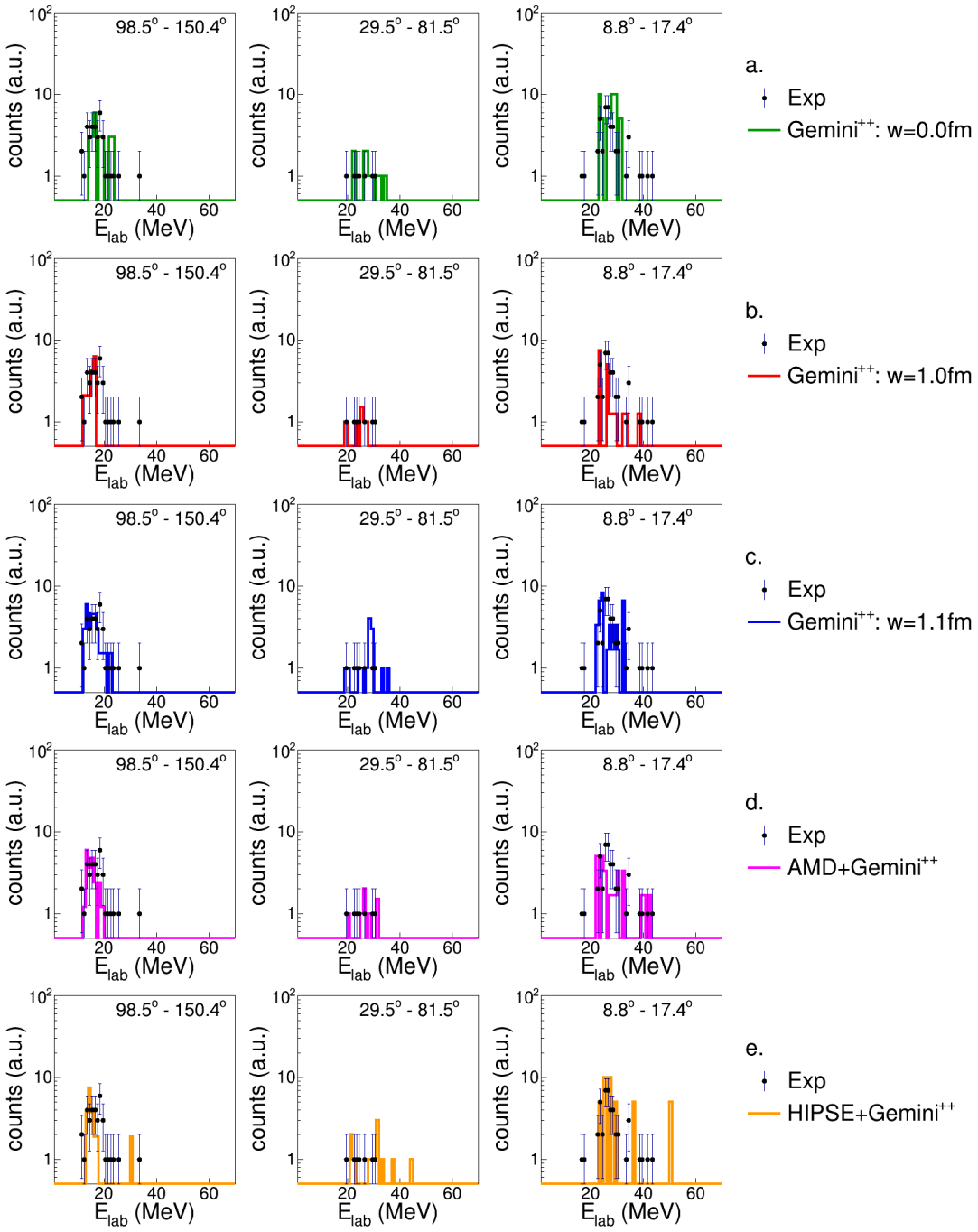

Figure B.65: Energy spectra of ^{3}He in coincidence with a Ar-residue for the reaction $^{16}O + ^{30}Si$ at 111 MeV.

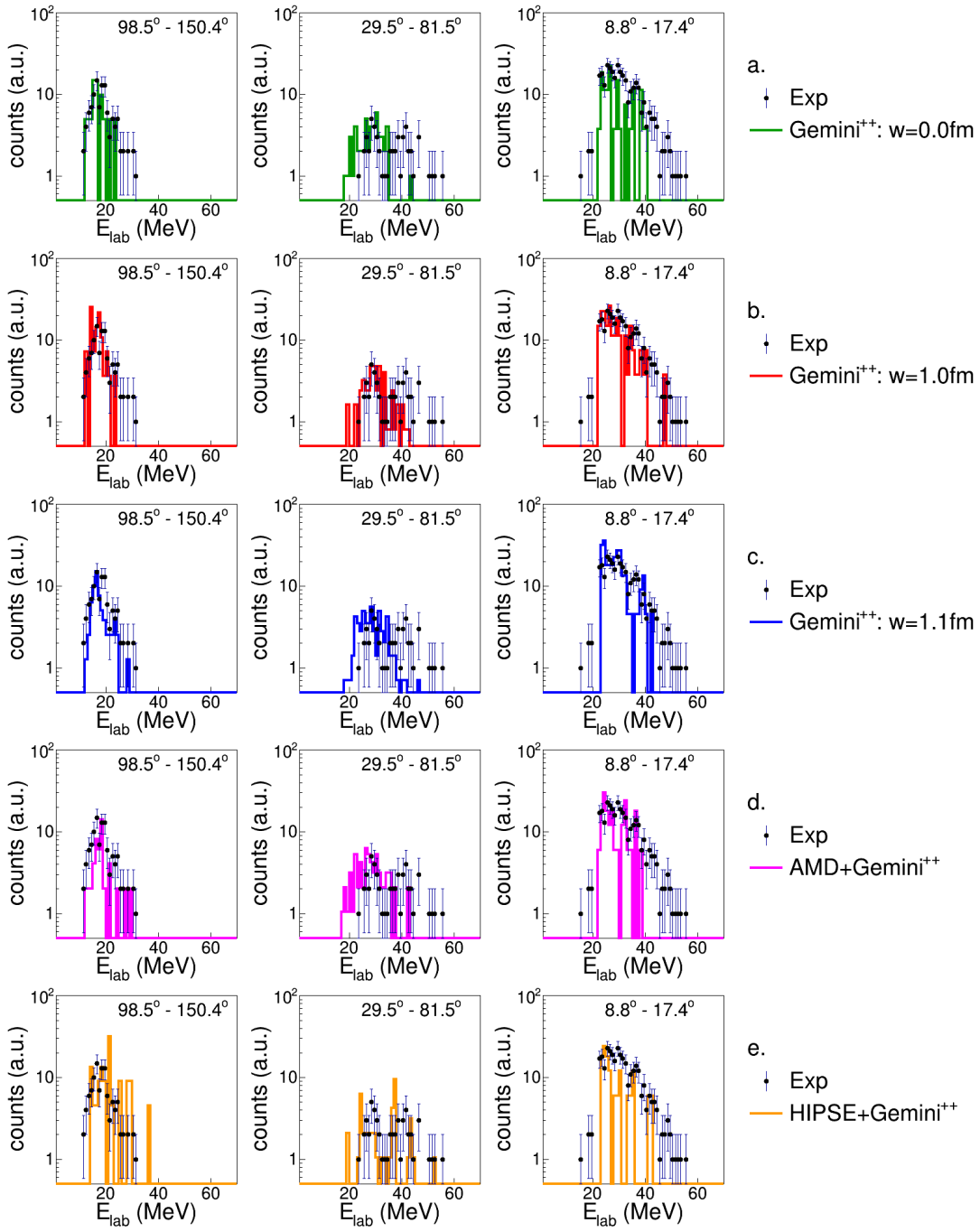

Figure B.66: Energy spectra of ^{3}He in coincidence with a Ar-residue for the reaction $^{16}O+^{30}Si$ at 128 MeV

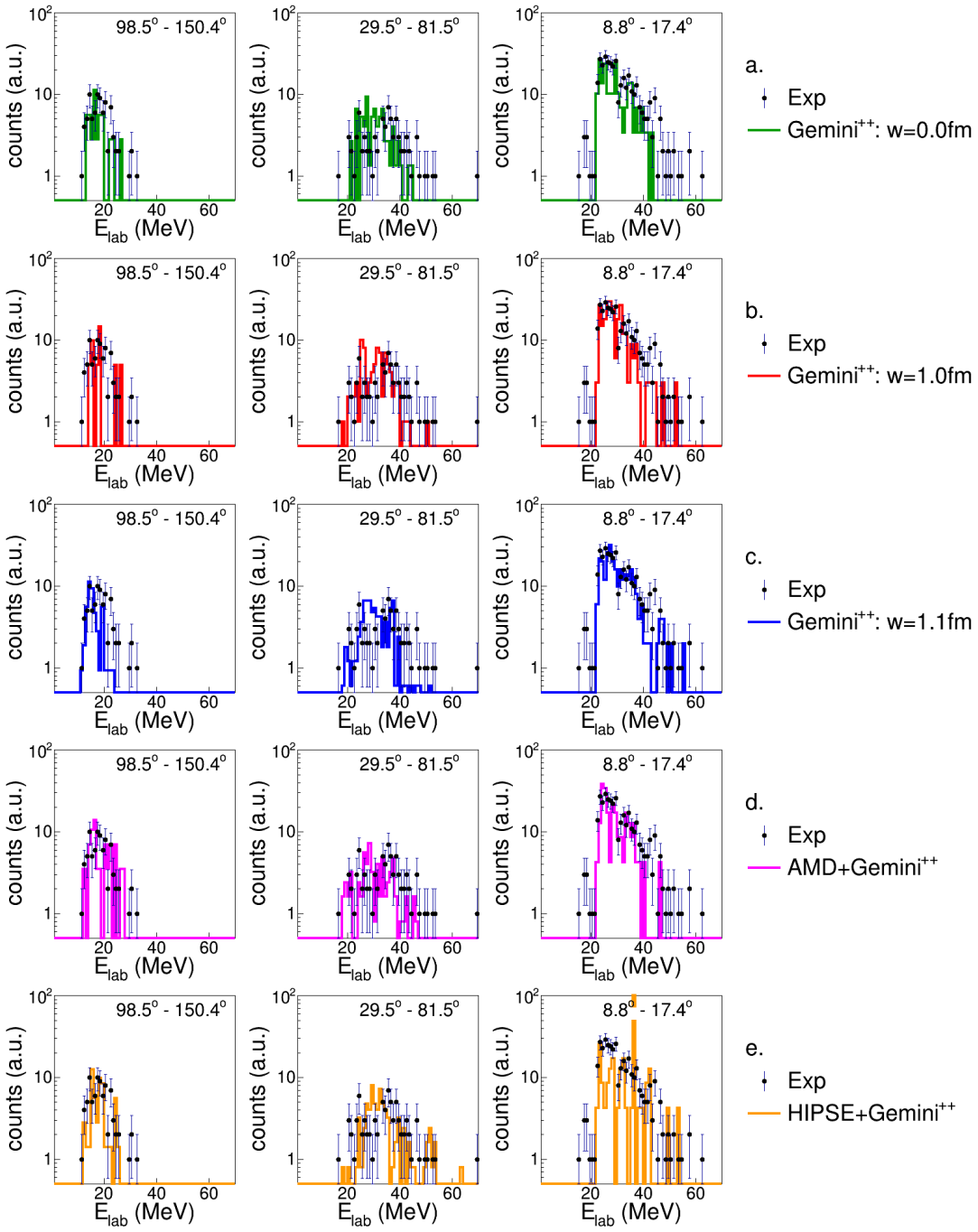

Figure B.67: Energy spectra of ^{3}He in coincidence with a Ar-residue for the reaction $^{18}O + ^{28}Si$ at 126 MeV

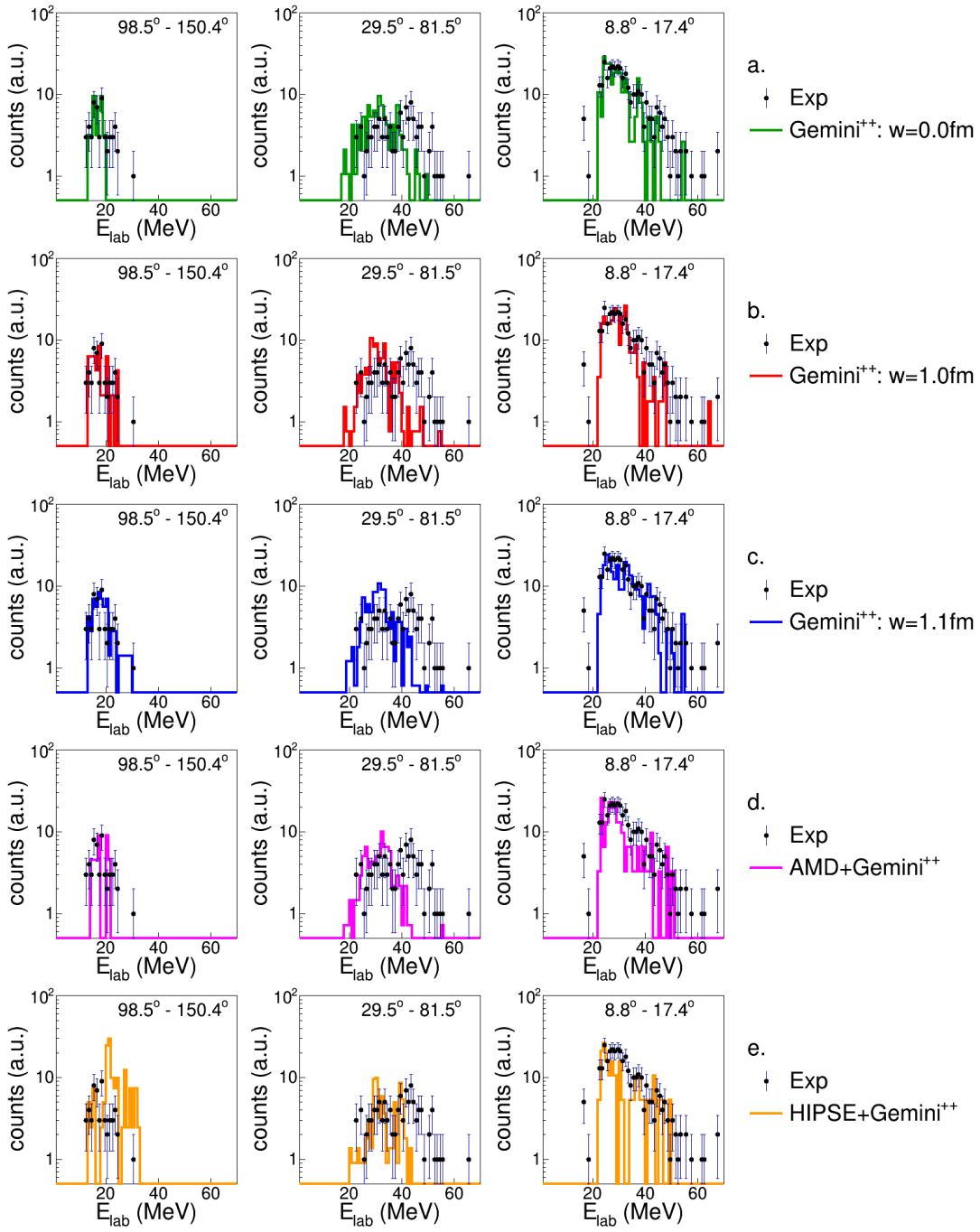

Figure B.68: Energy spectra of ^{3}He in coincidence with a Ar-residue for the reaction $^{19}F + ^{27}Al$ at 133 MeV

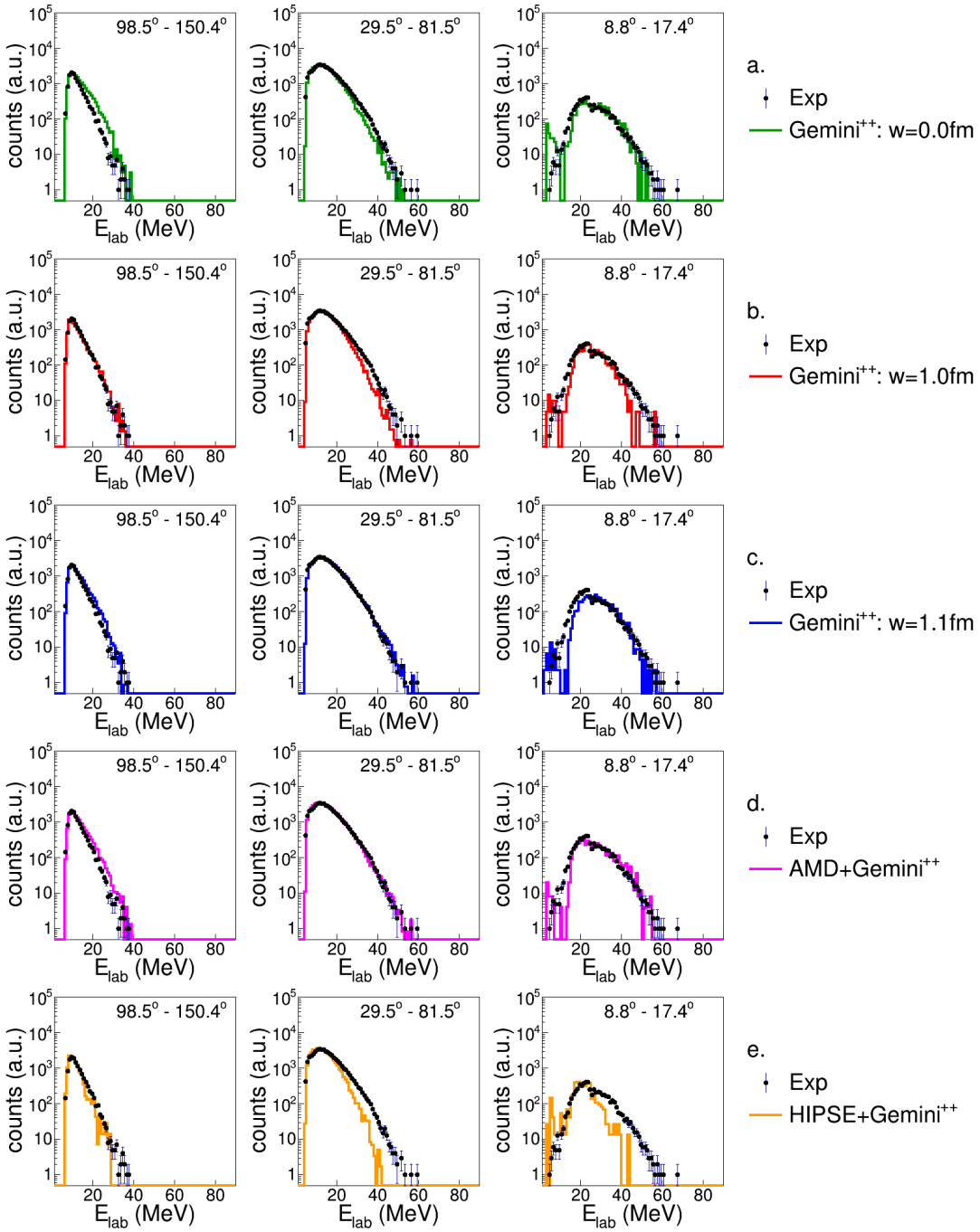

Figure B.69: Energy spectra of α-particles in coincidence with a Ar-residue for the reaction $^{16}O + ^{30}Si$ at 111 MeV.

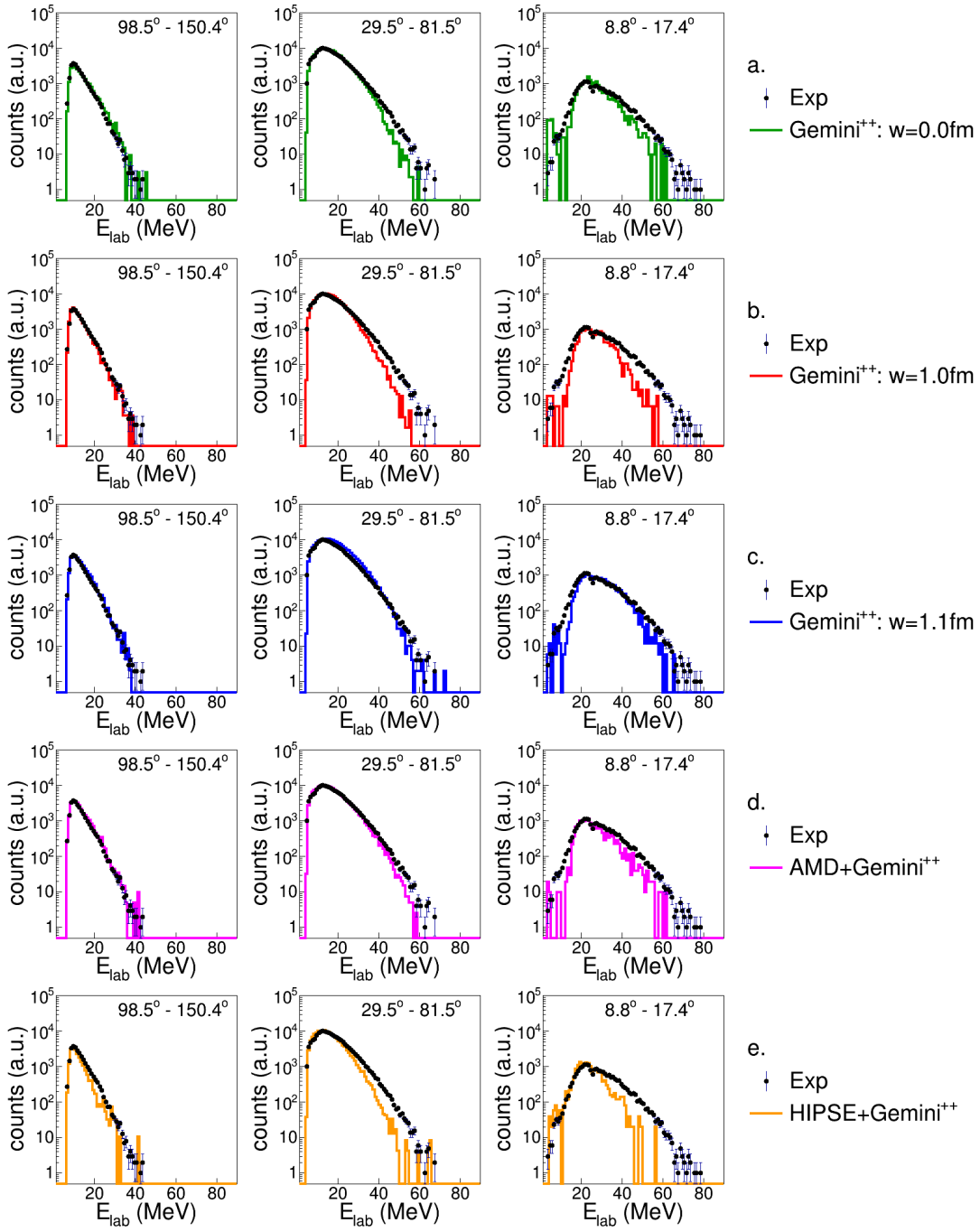

Figure B.70: Energy spectra of α-particles in coincidence with a Ar-residue for the reaction $^{16}O + ^{30}Si$ at 128 MeV

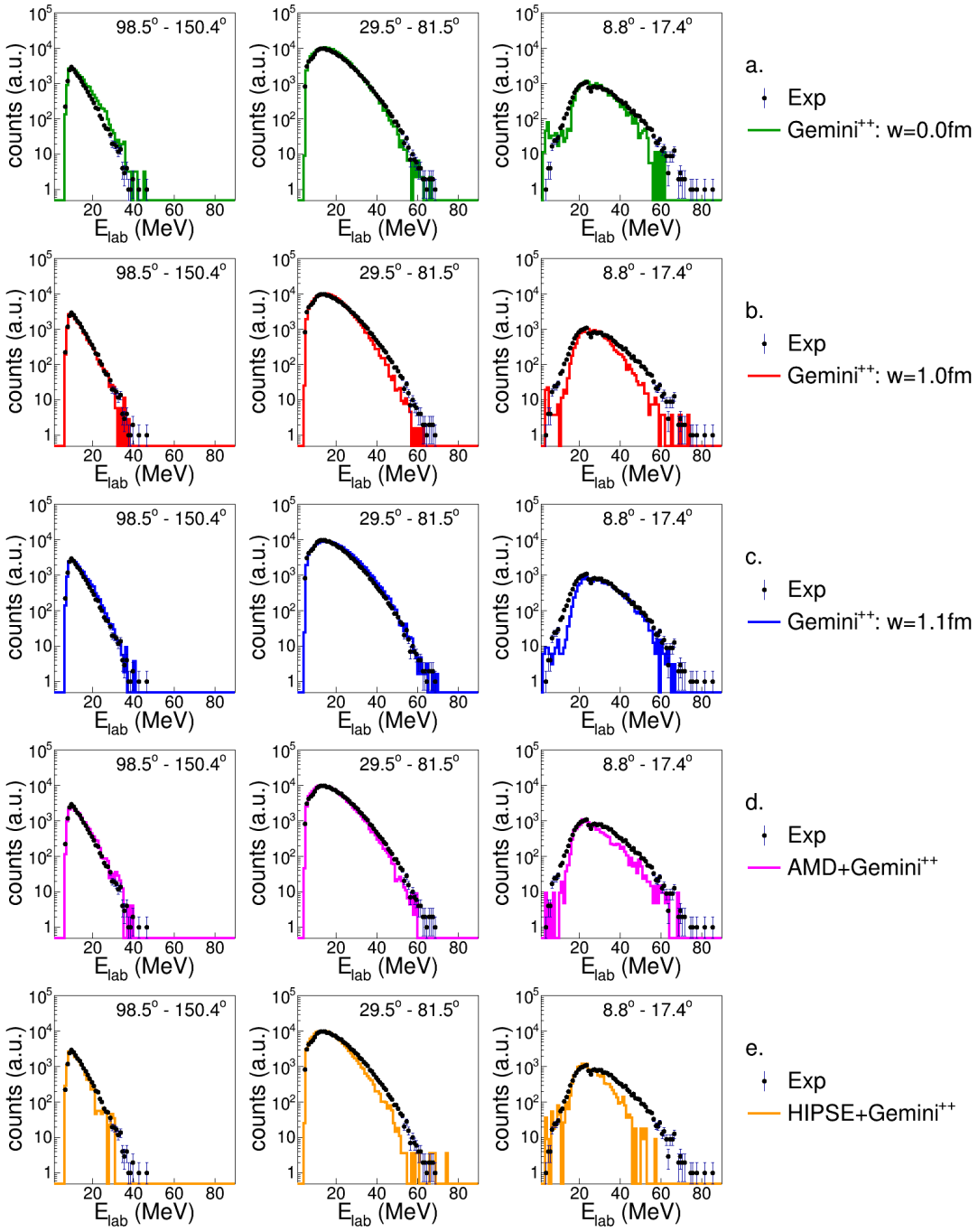

Figure B.71: Energy spectra of α-particles in coincidence with a Ar-residue for the reaction $^{18}O + ^{28}Si$ at 126 MeV

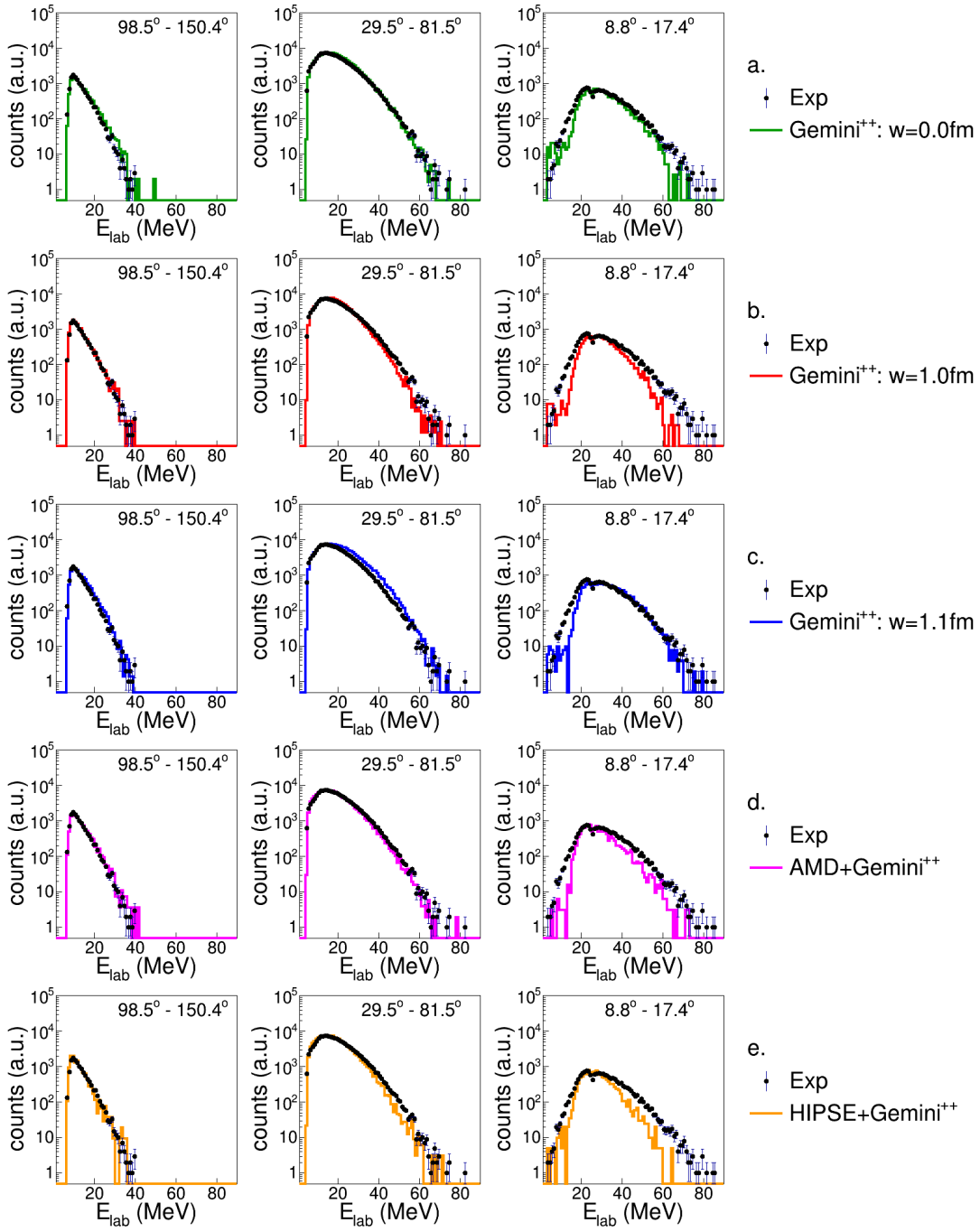

Figure B.72: Energy spectra of α-particles in coincidence with a Ar-residue for the reaction $^{19}F + ^{27}Al$ at 133 MeV

B.5 The Cl residue: $Z_{res} = 17$

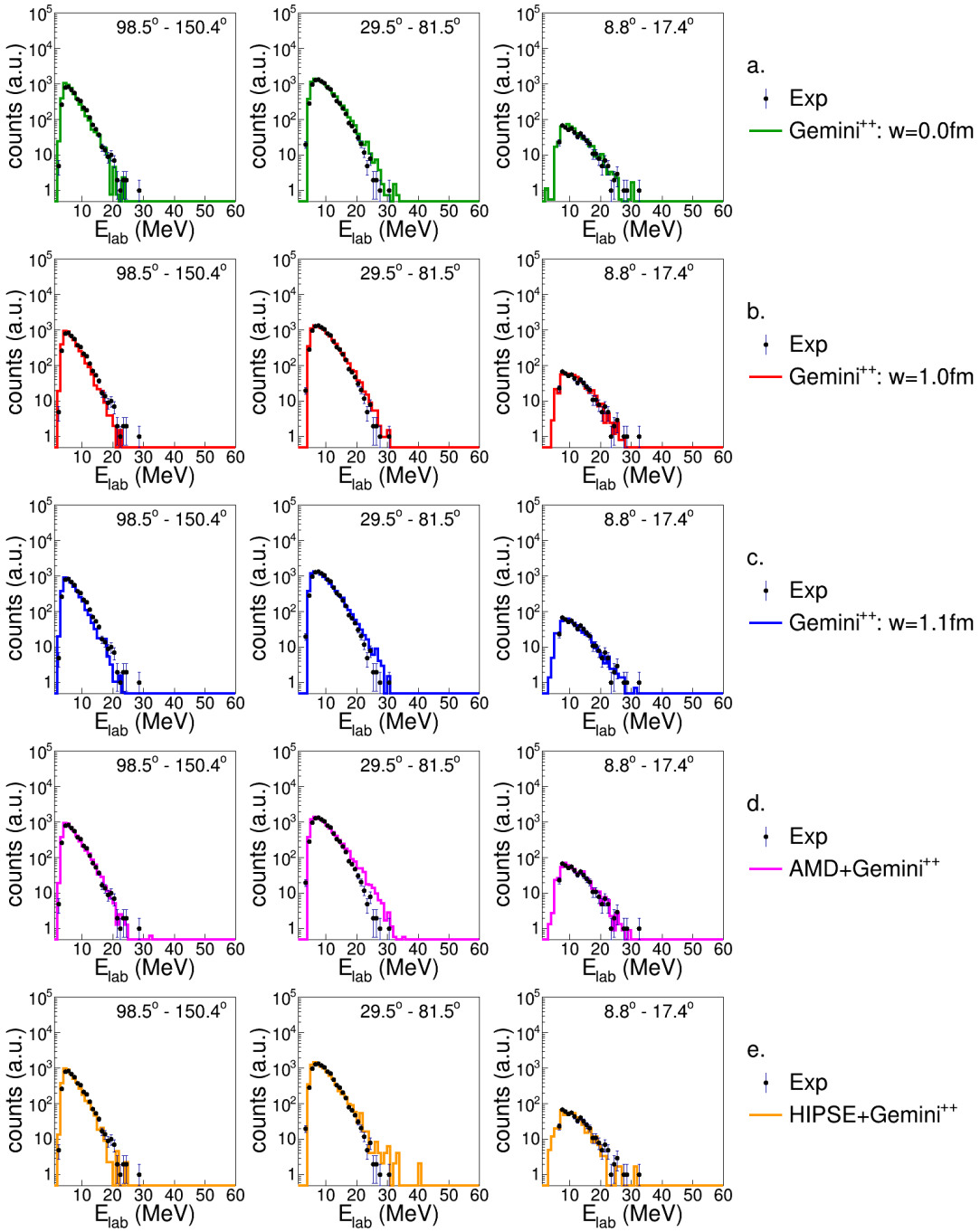

Figure B.73: Energy spectra of protons in coincidence with a *Cl*-residue for the reaction $^{16}O + ^{30}Si$ at 111 MeV.

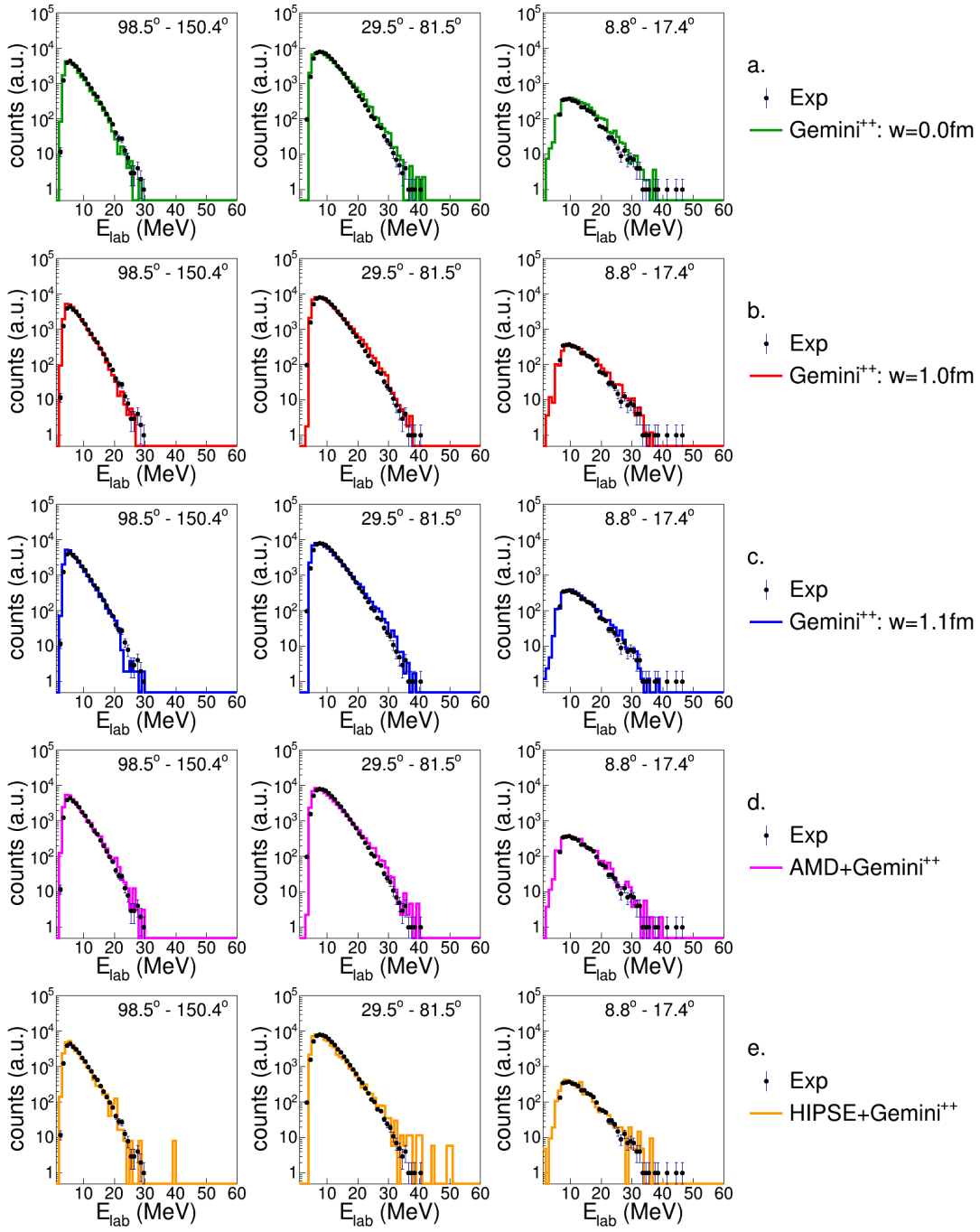

Figure B.74: Energy spectra of protons in coincidence with a *Cl*-residue for the reaction $^{16}O + ^{30}Si$ at 128 MeV

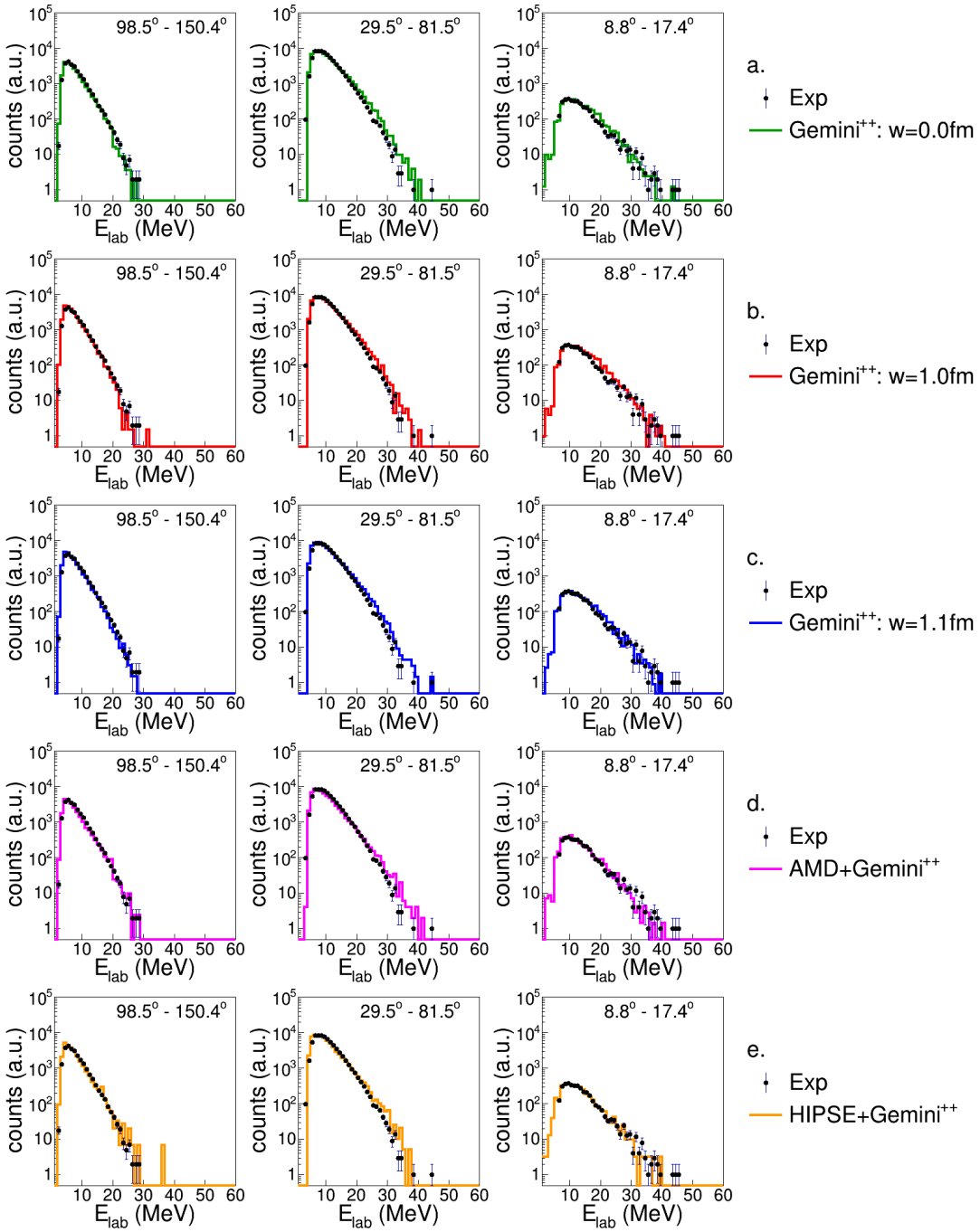

Figure B.75: Energy spectra of protons in coincidence with a *Cl*-residue for the reaction $^{18}O + ^{28}Si$ at 126 MeV

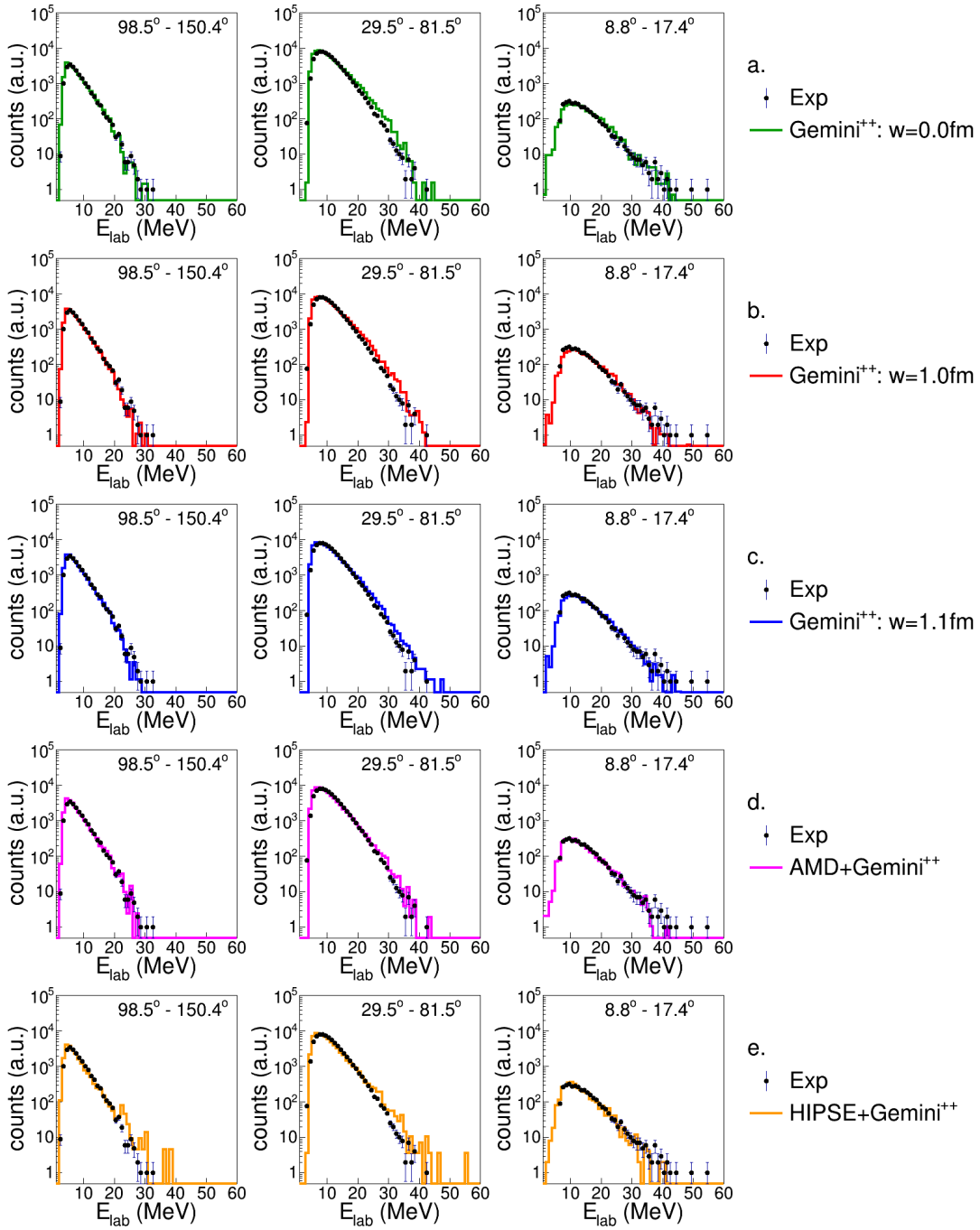

Figure B.76: Energy spectra of protons in coincidence with a *Cl*-residue for the reaction $^{19}F + ^{27}Al$ at 133 MeV

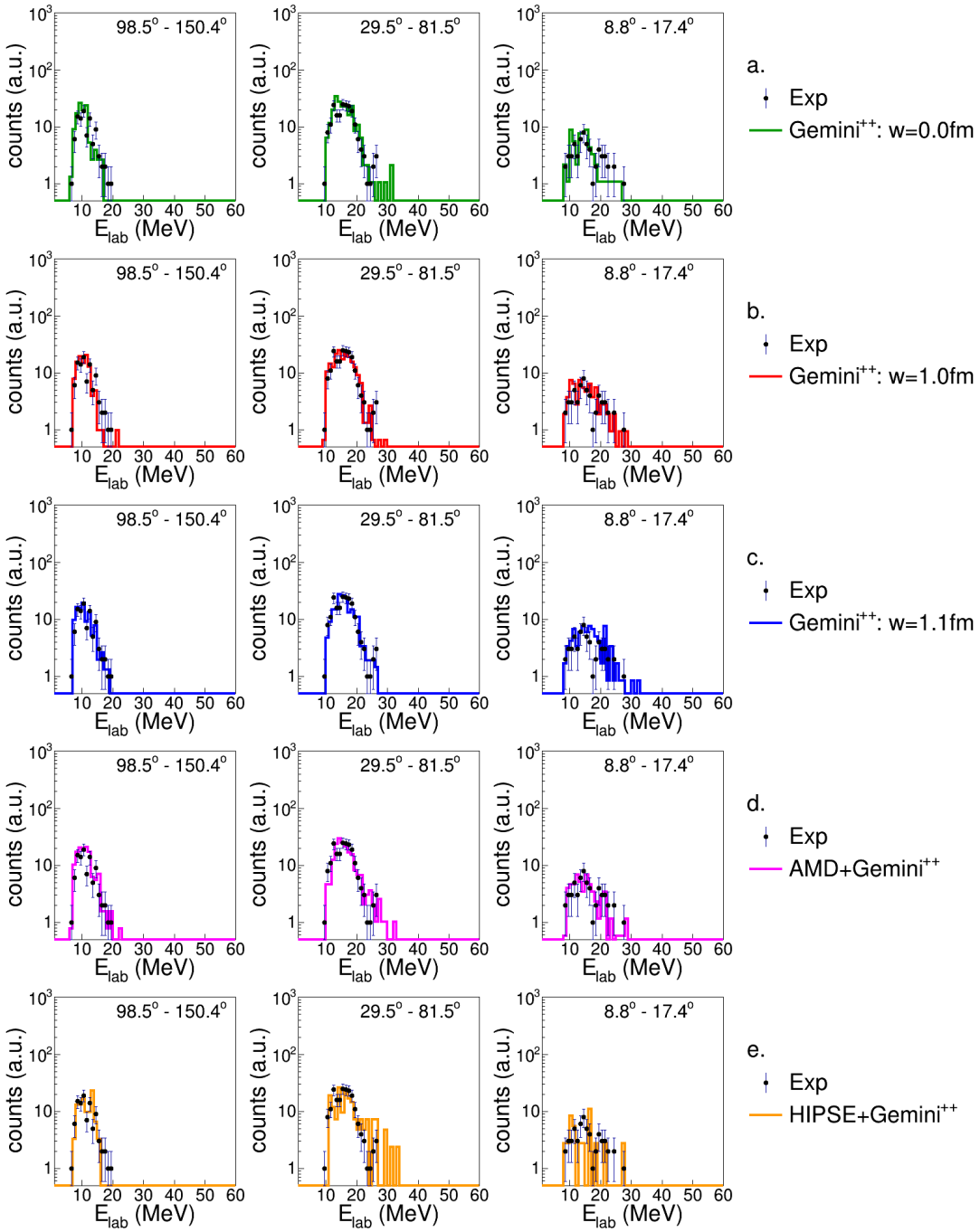

Figure B.77: Energy spectra of deuterons in coincidence with a *Cl*-residue for the reaction $^{16}O + ^{30}Si$ at 111 MeV.

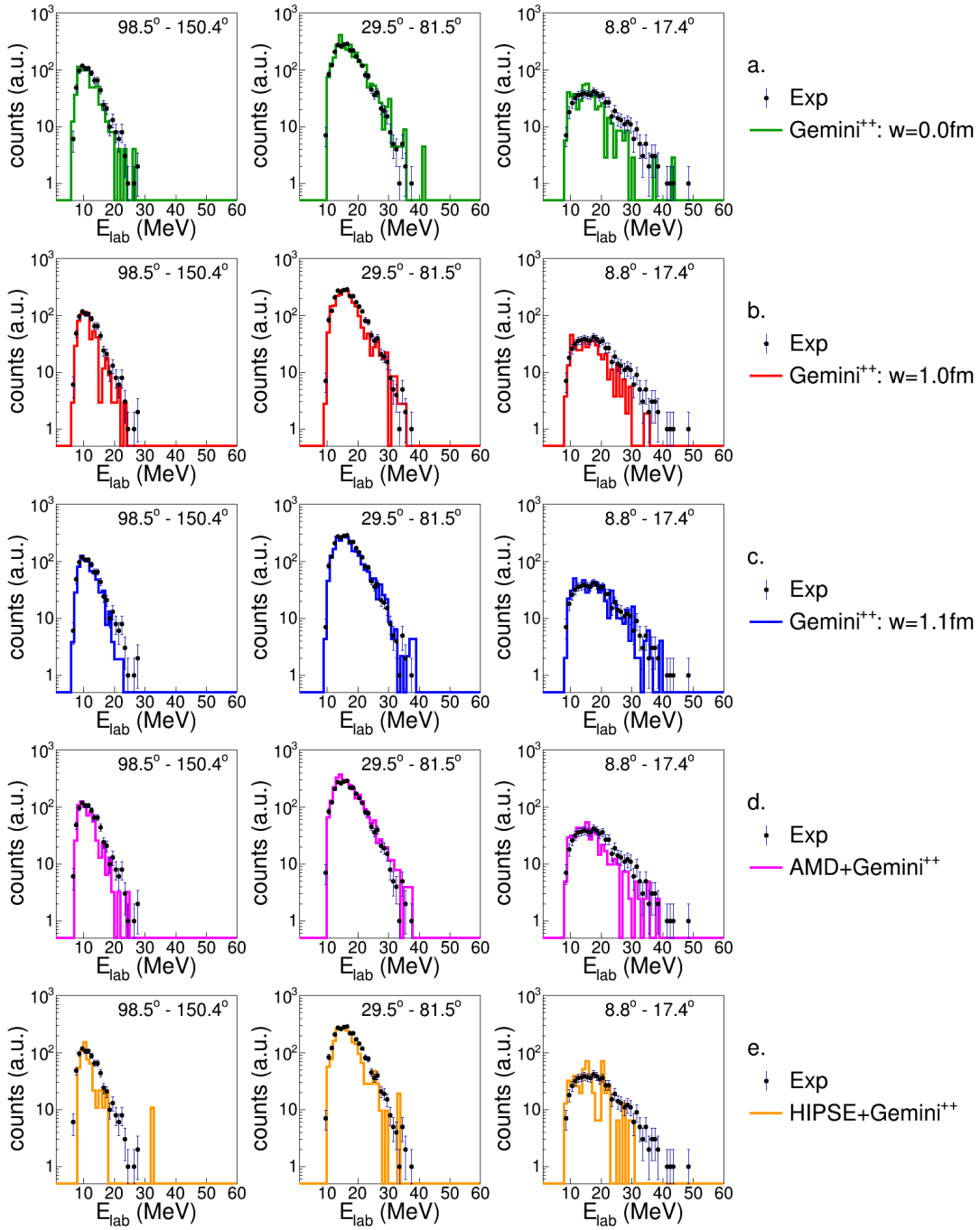

Figure B.78: Energy spectra of deuterons in coincidence with a Cl-residue for the reaction $^{16}O + ^{30}Si$ at 128 MeV

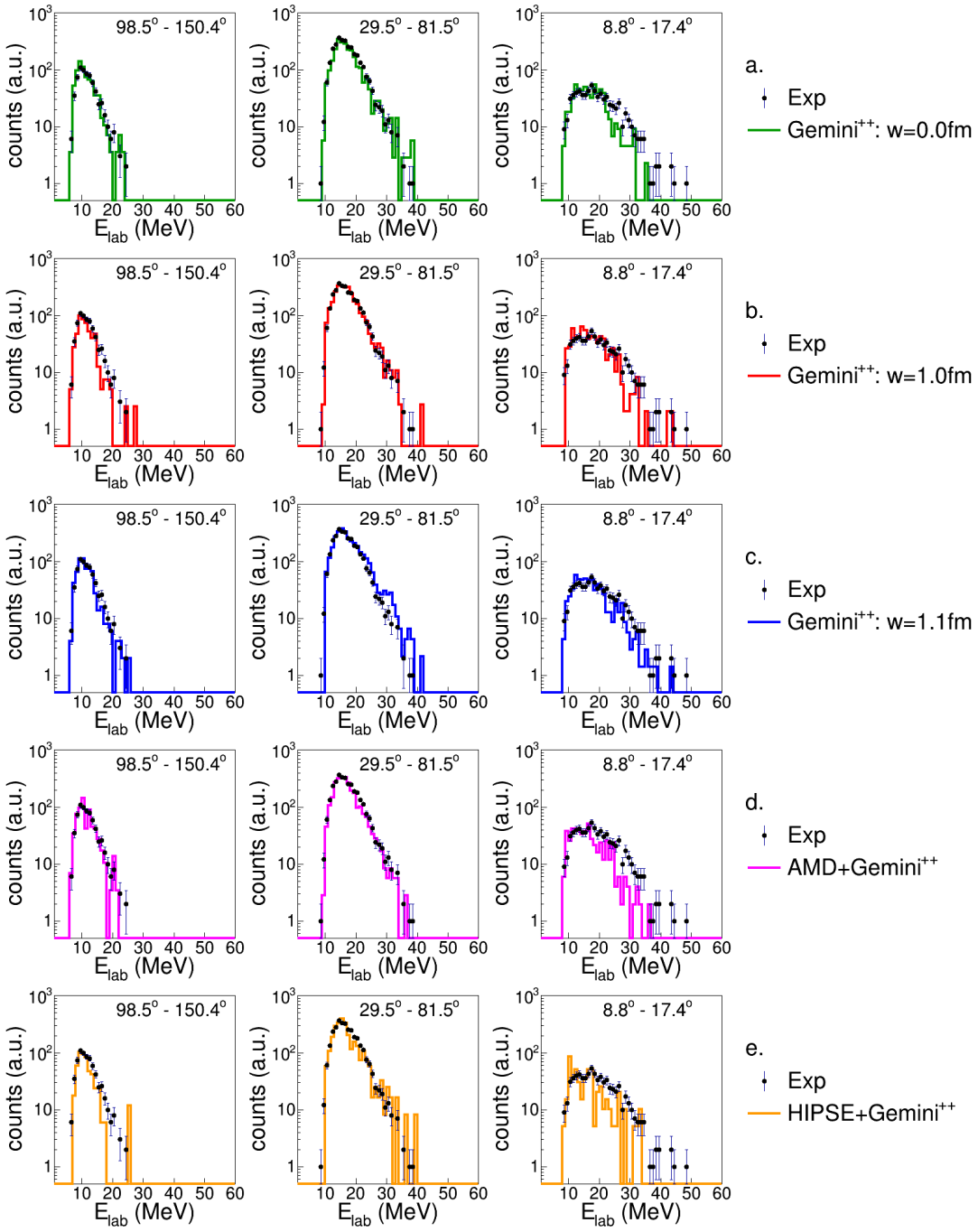

Figure B.79: Energy spectra of deuterons in coincidence with a *Cl*-residue for the reaction $^{18}O + ^{28}Si$ at 126 MeV

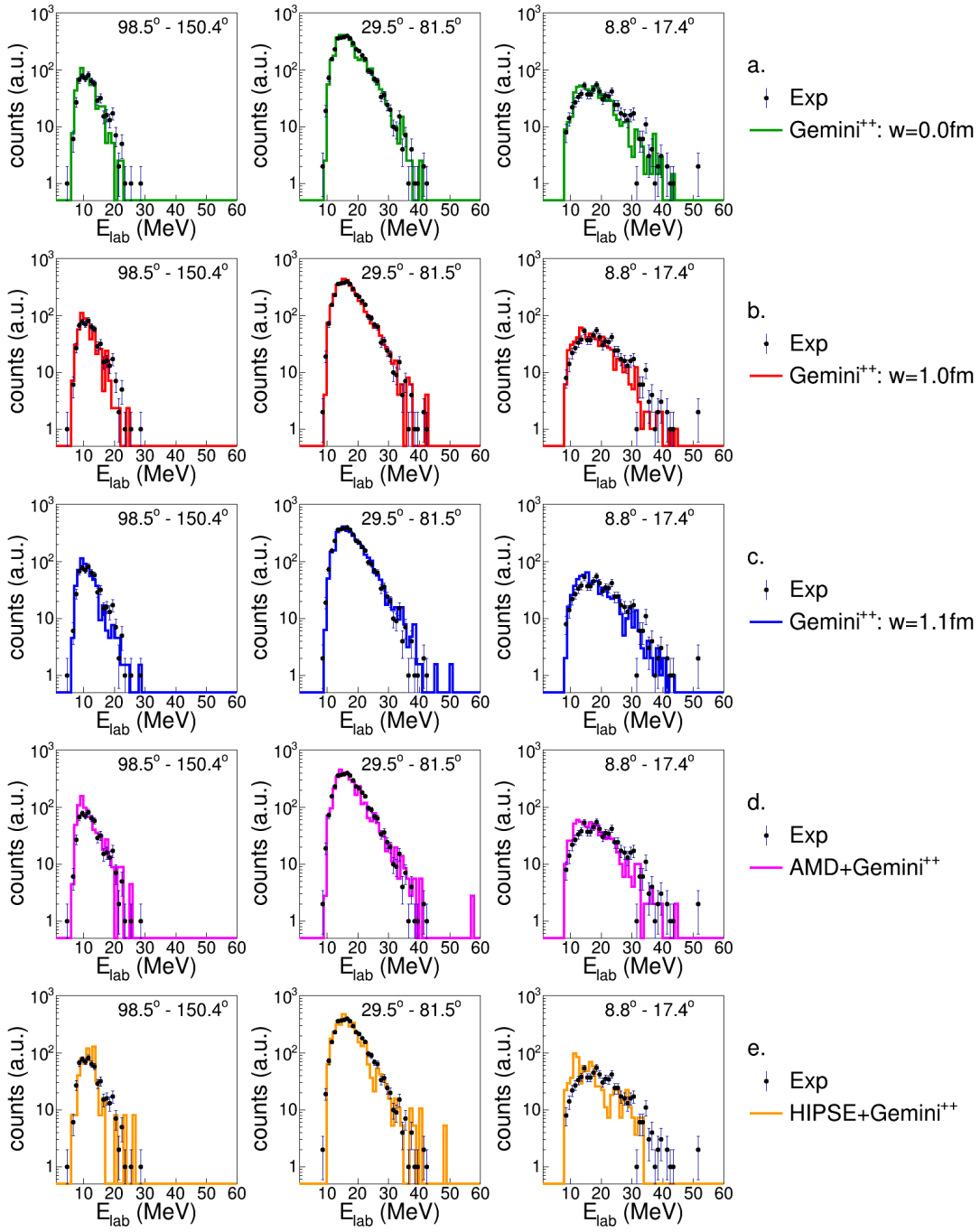

Figure B.80: Energy spectra of deuterons in coincidence with a Cl-residue for the reaction $^{19}F + ^{27}Al$ at 133 MeV

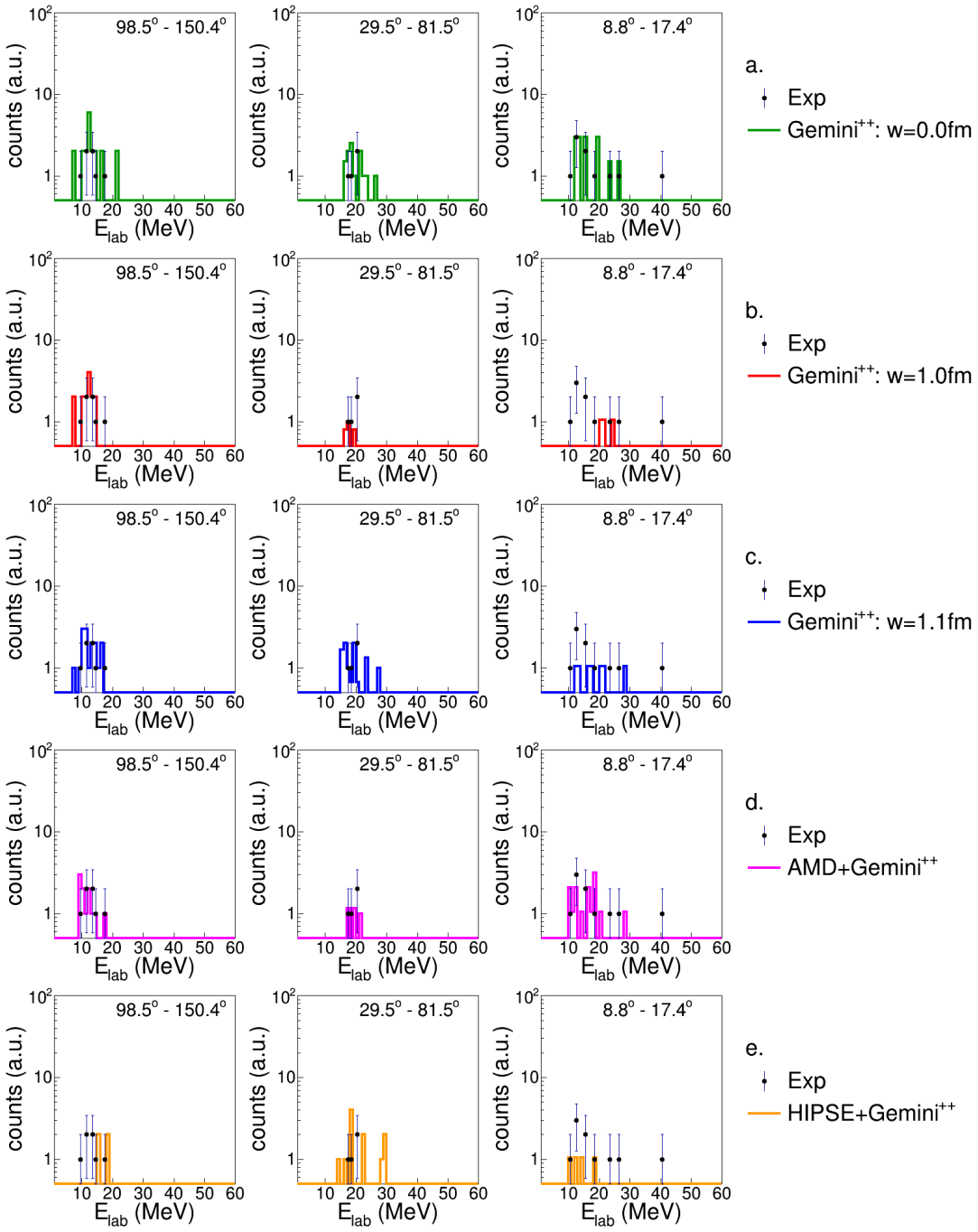

Figure B.81: Energy spectra of tritons in coincidence with a *Cl*-residue for the reaction $^{16}O + ^{30}Si$ at 111 MeV.

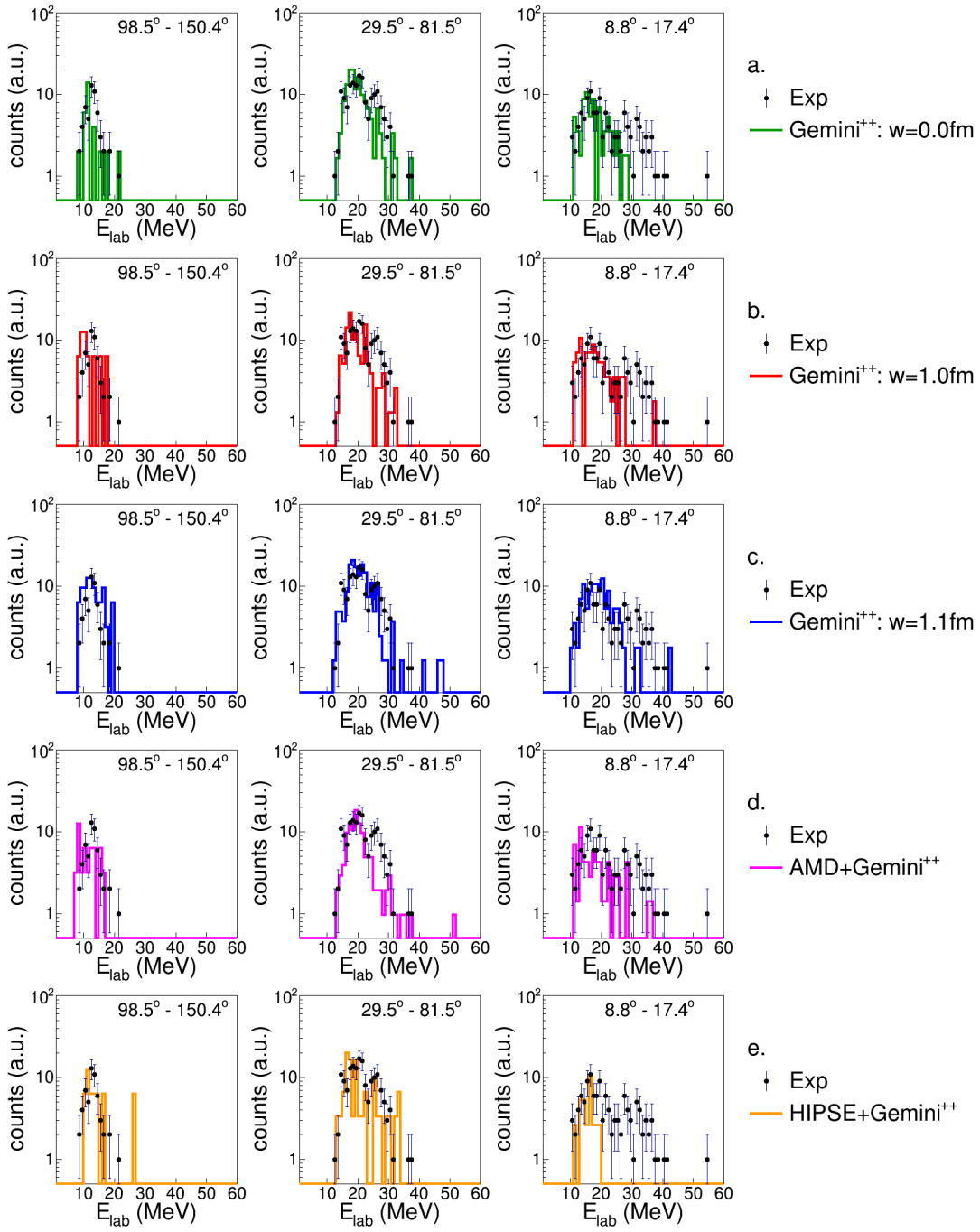

Figure B.82: Energy spectra of tritons in coincidence with a *Cl*-residue for the reaction $^{16}O + ^{30}Si$ at 128 MeV

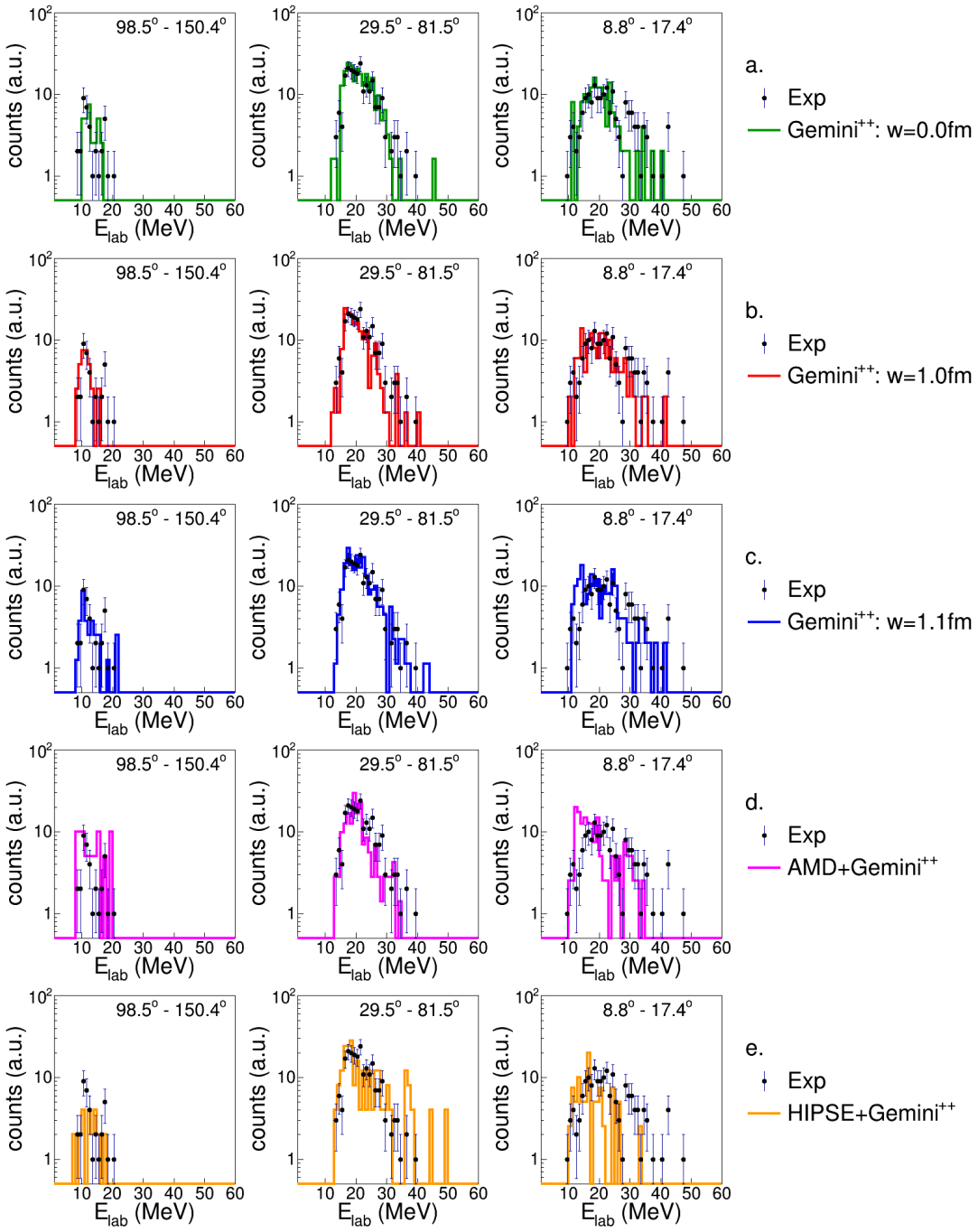

Figure B.83: Energy spectra of tritons in coincidence with a *Cl*-residue for the reaction $^{18}O + ^{28}Si$ at 126 MeV

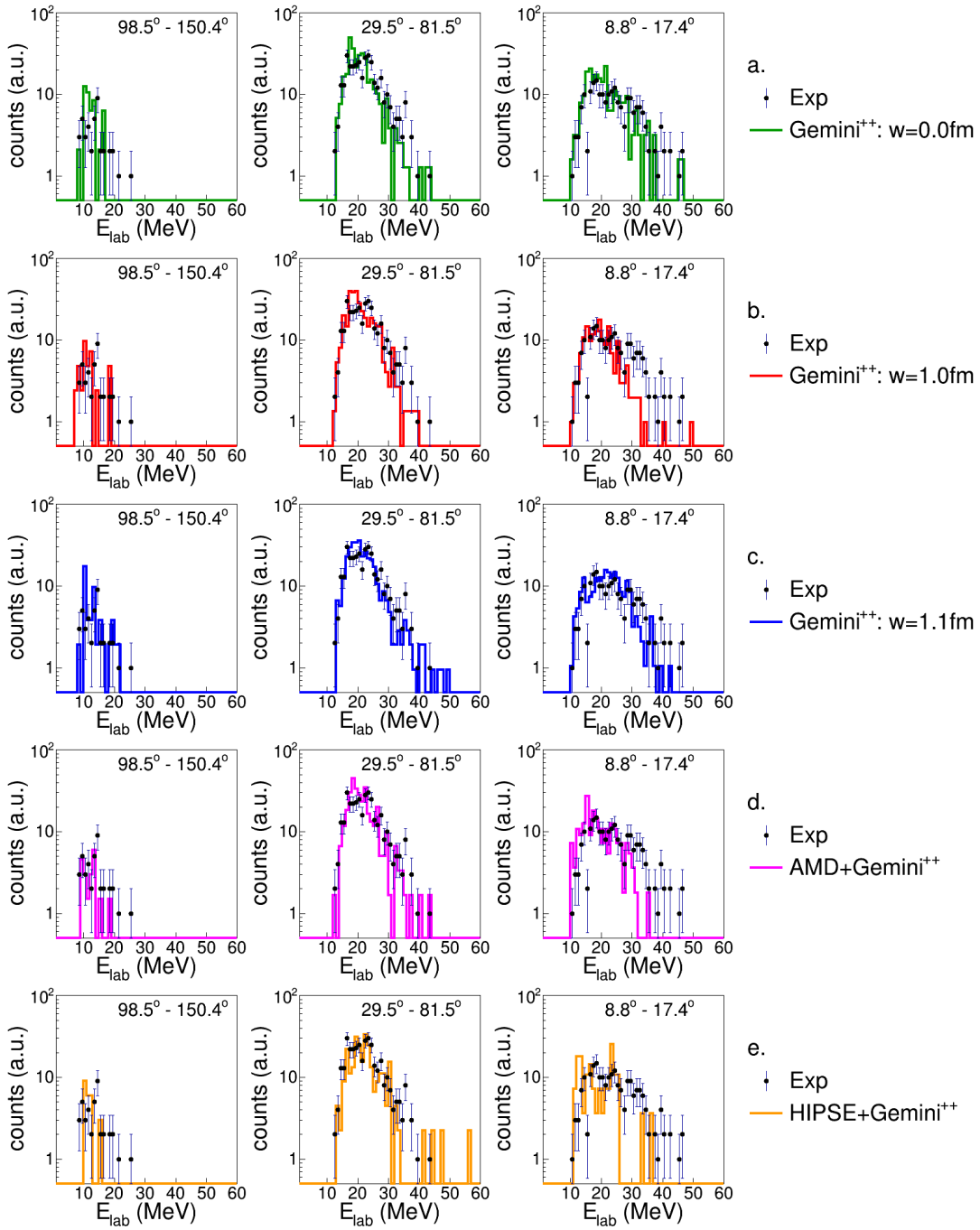

Figure B.84: Energy spectra of tritons in coincidence with a *Cl*-residue for the reaction $^{19}F + ^{27}Al$ at 133 MeV

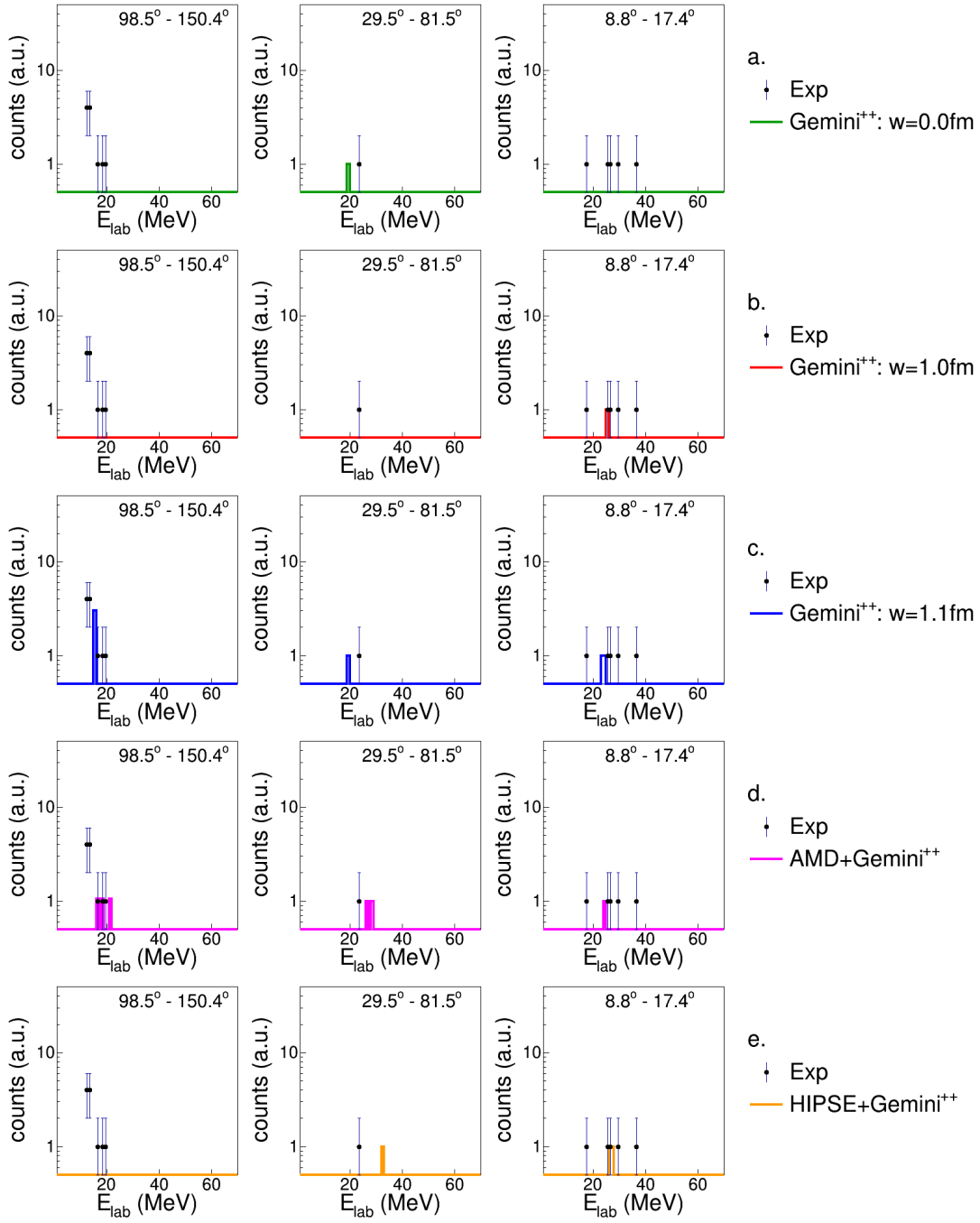

Figure B.85: Energy spectra of ^{3}He in coincidence with a Cl-residue for the reaction $^{16}O + ^{30}Si$ at 111 MeV.

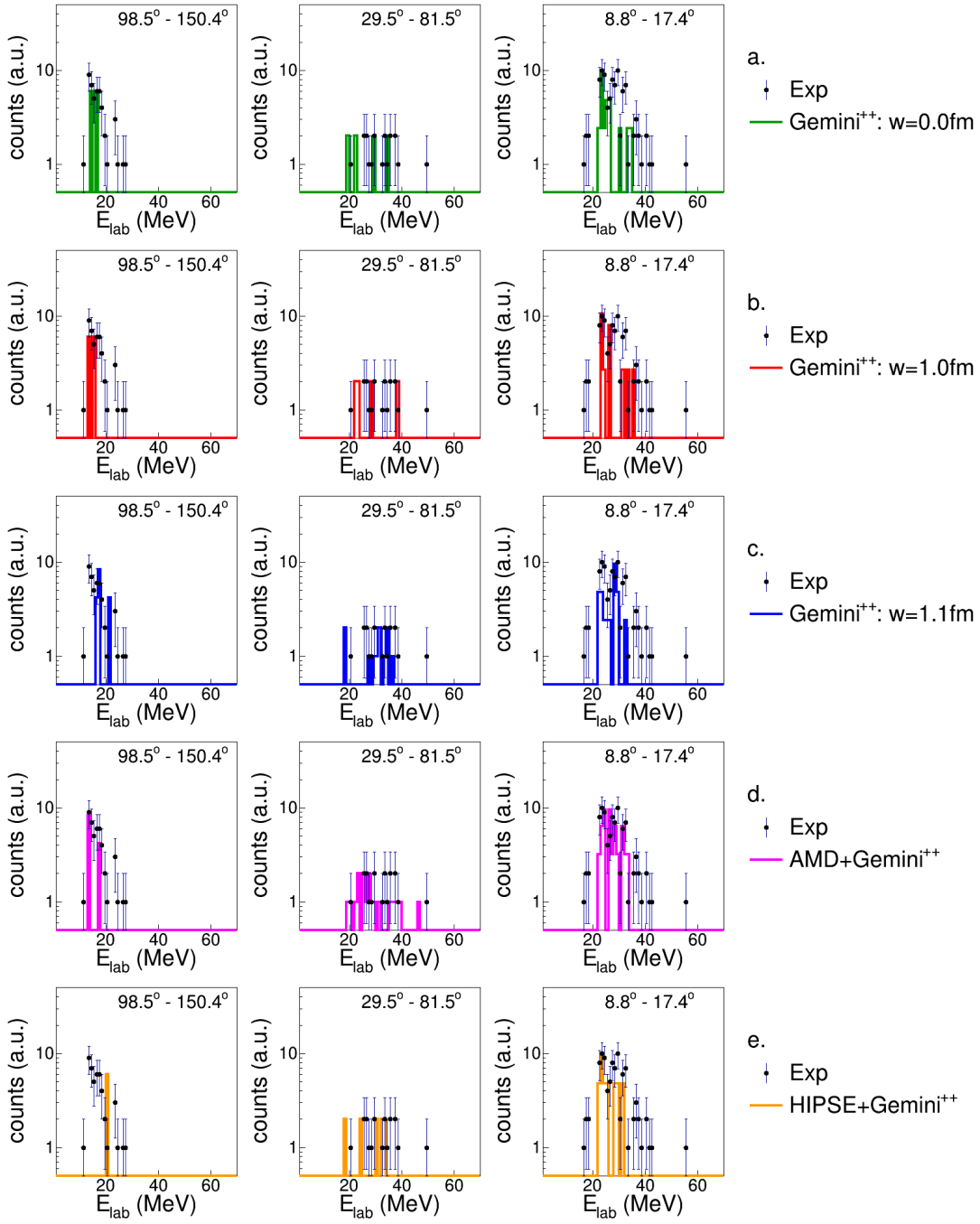

Figure B.86: Energy spectra of ^{3}He in coincidence with a Cl-residue for the reaction $^{16}O + ^{30}Si$ at 128 MeV

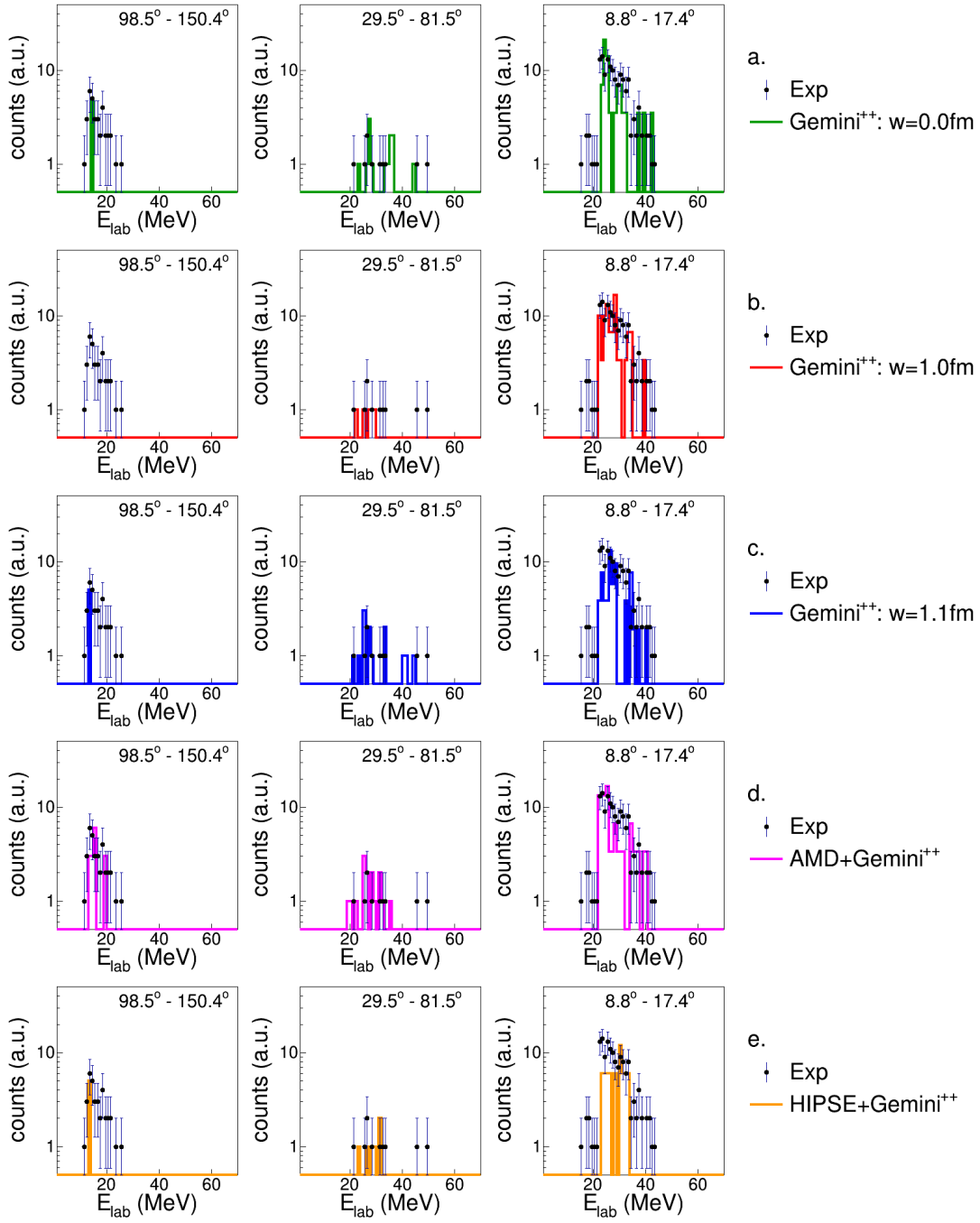

Figure B.87: Energy spectra of ^{3}He in coincidence with a Cl-residue for the reaction $^{18}O + ^{28}Si$ at 126 MeV

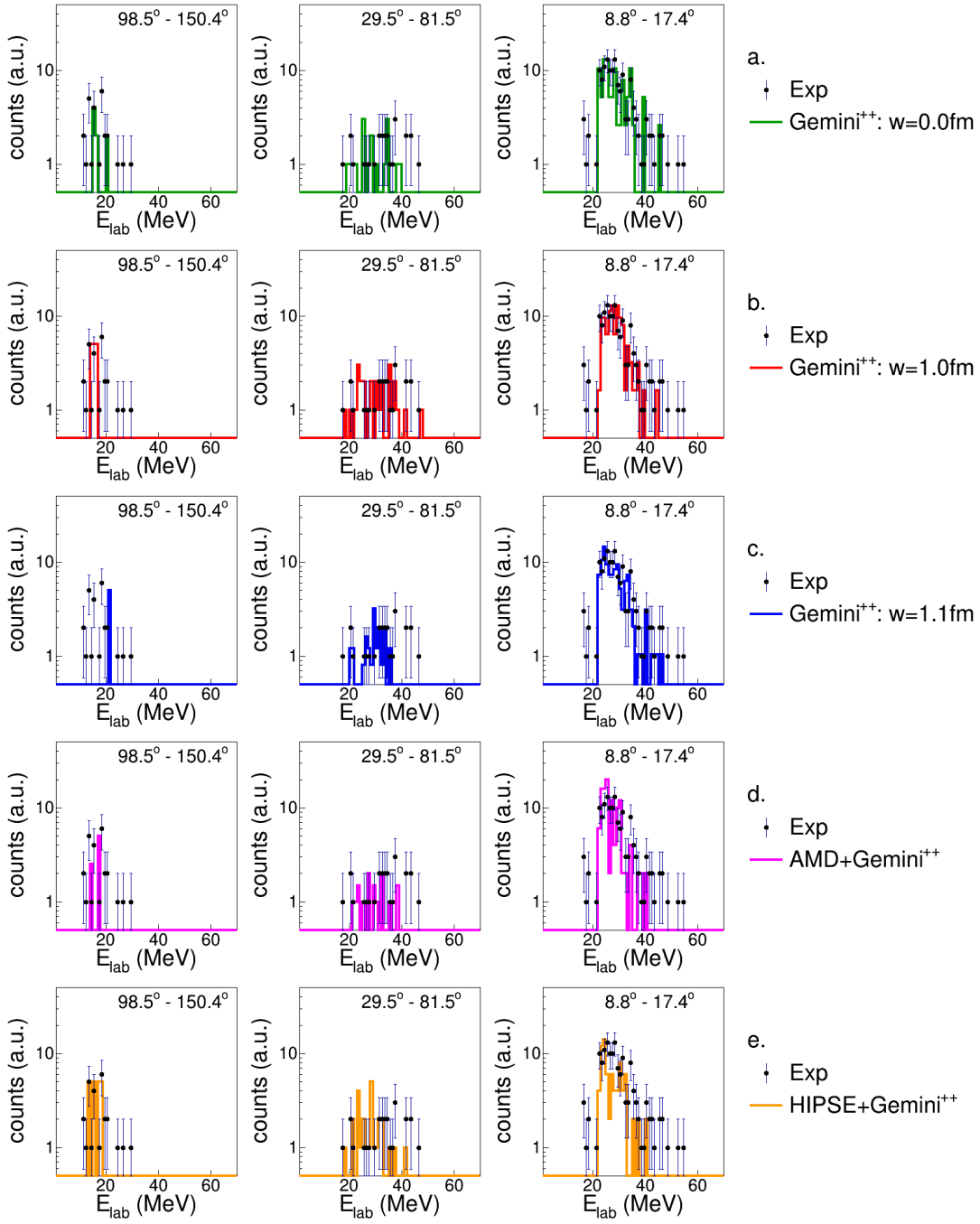

Figure B.88: Energy spectra of ^{3}He in coincidence with a Cl-residue for the reaction $^{19}F + ^{27}Al$ at 133 MeV

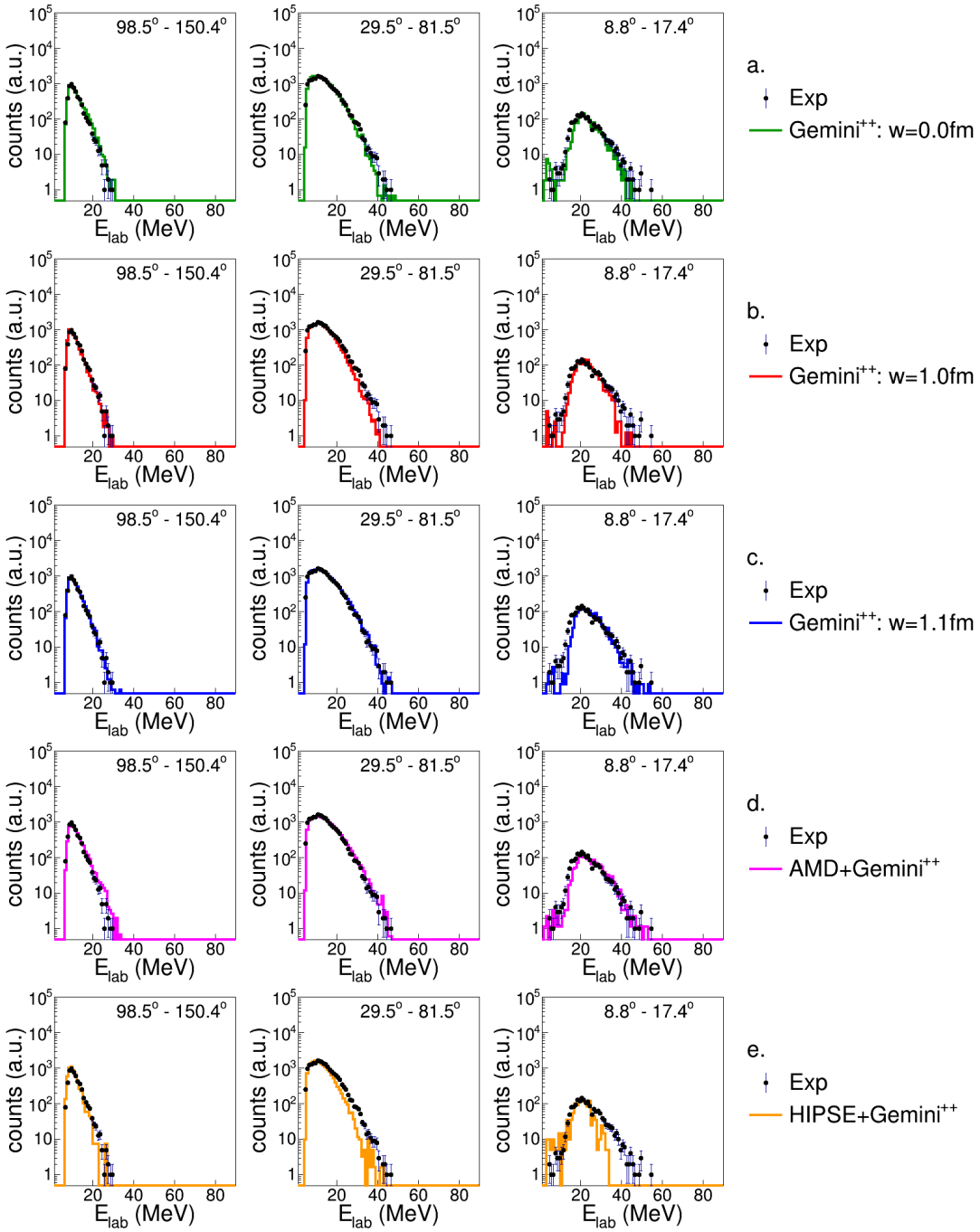

Figure B.89: Energy spectra of α-particles in coincidence with a Cl-residue for the reaction $^{16}O + ^{30}Si$ at 111 MeV.

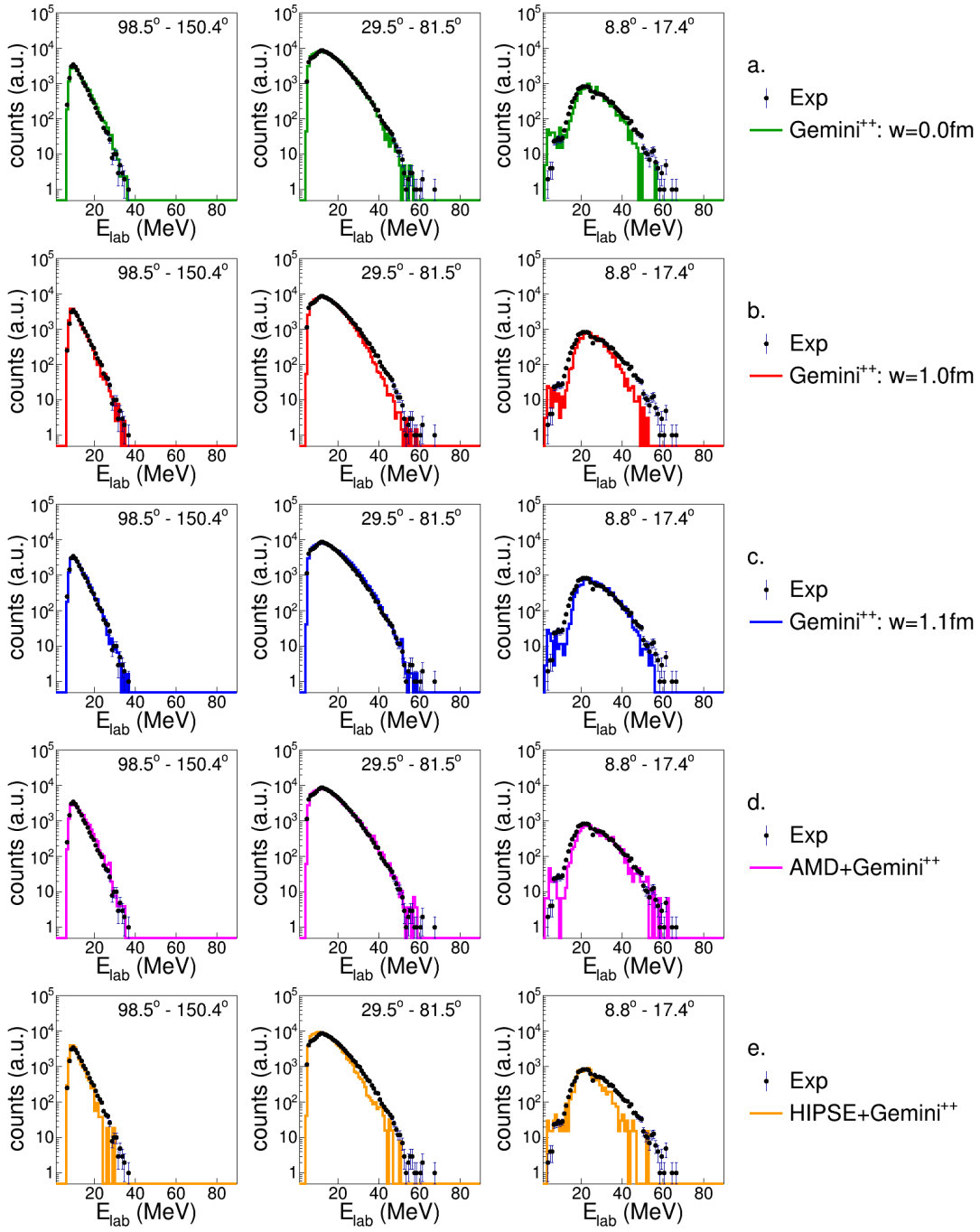

Figure B.90: Energy spectra of α-particles in coincidence with a Cl-residue for the reaction $^{16}O + ^{30}Si$ at 128 MeV

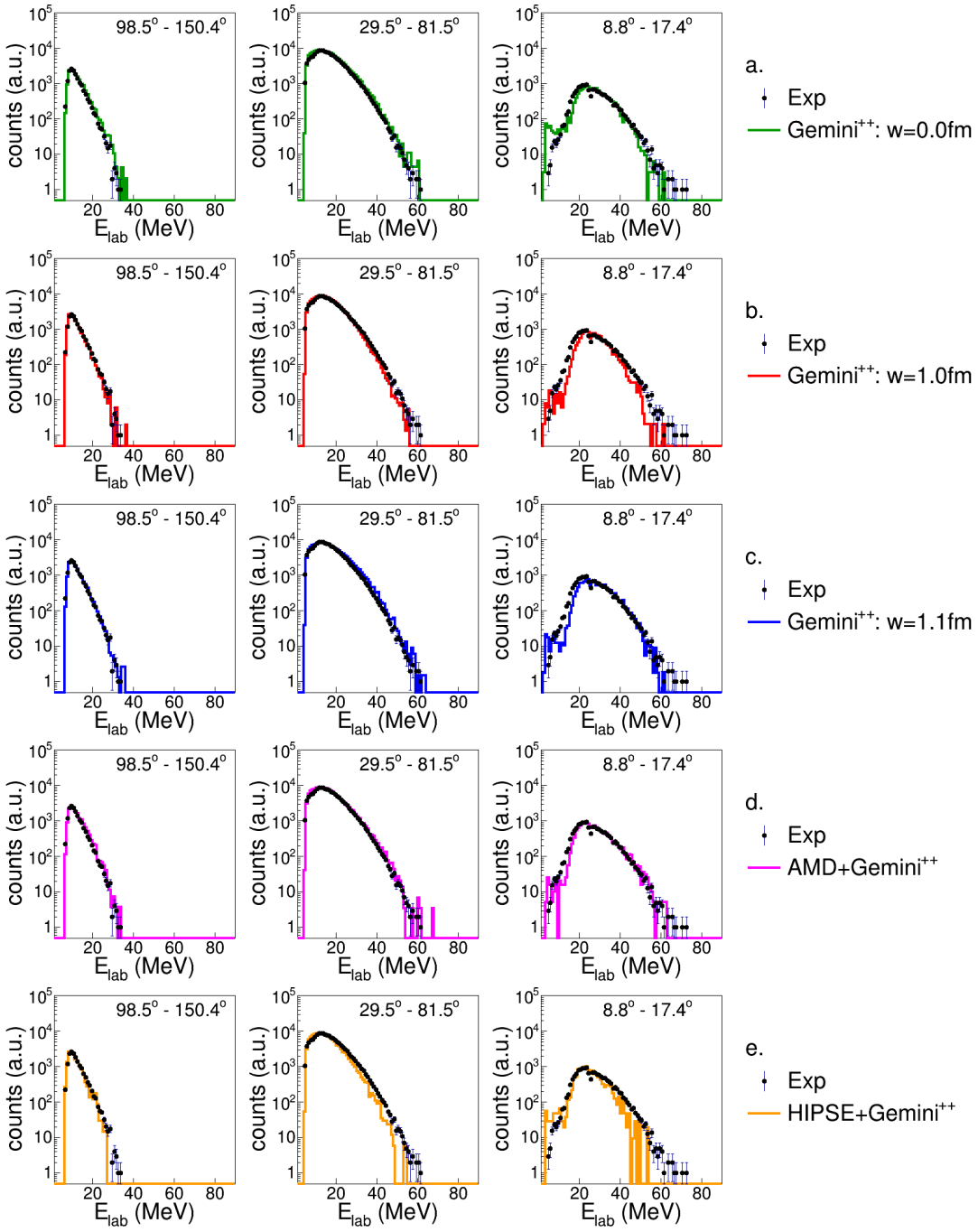

Figure B.91: Energy spectra of α-particles in coincidence with a Cl-residue for the reaction $^{18}O + ^{28}Si$ at 126 MeV

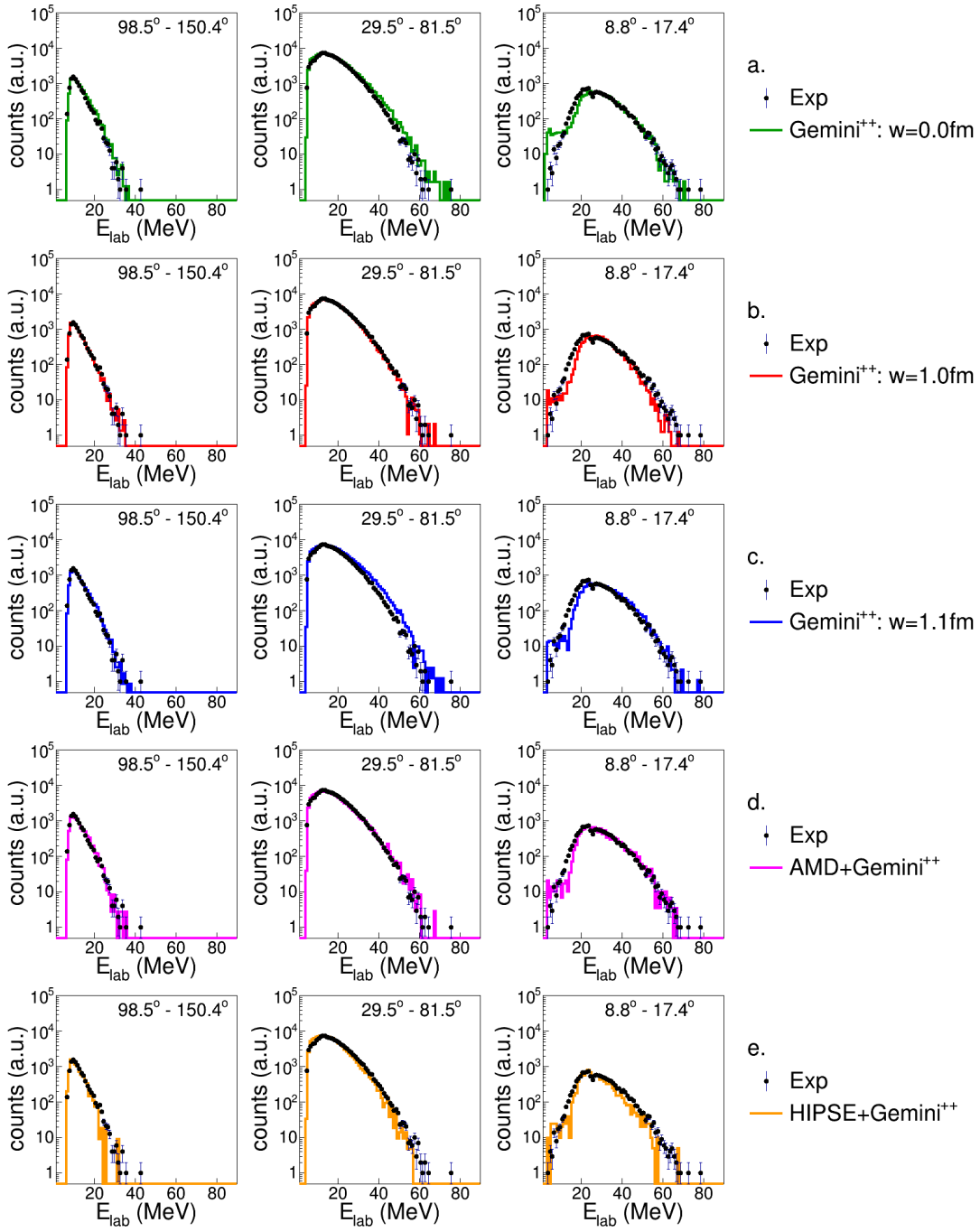

Figure B.92: Energy spectra of α-particles in coincidence with a Cl-residue for the reaction $^{19}F + ^{27}Al$ at 133 MeV

B.6 The S residue: $Z_{res} = 16$

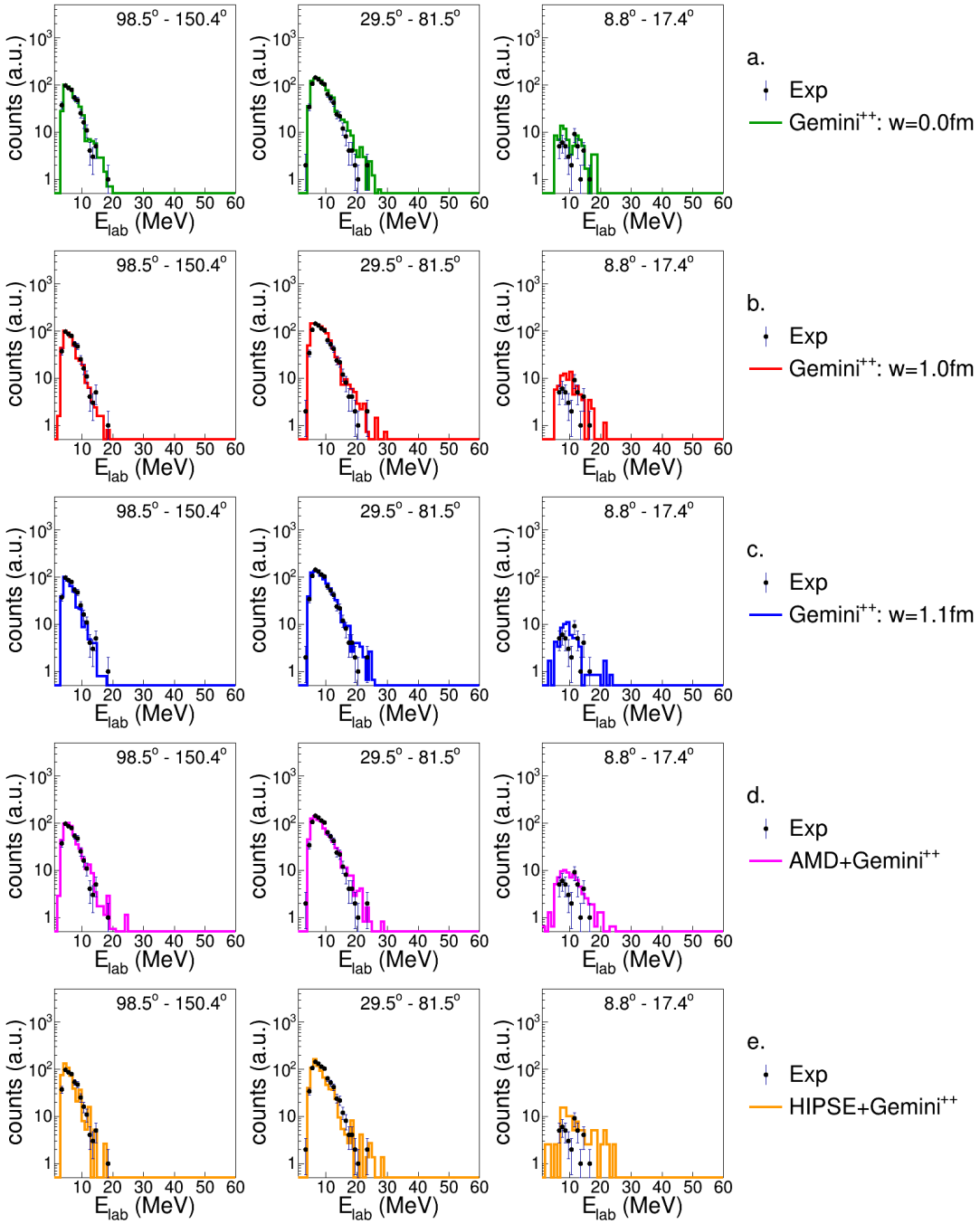

Figure B.93: Energy spectra of protons in coincidence with a S-residue for the reaction $^{16}O + ^{30}Si$ at 111 MeV.

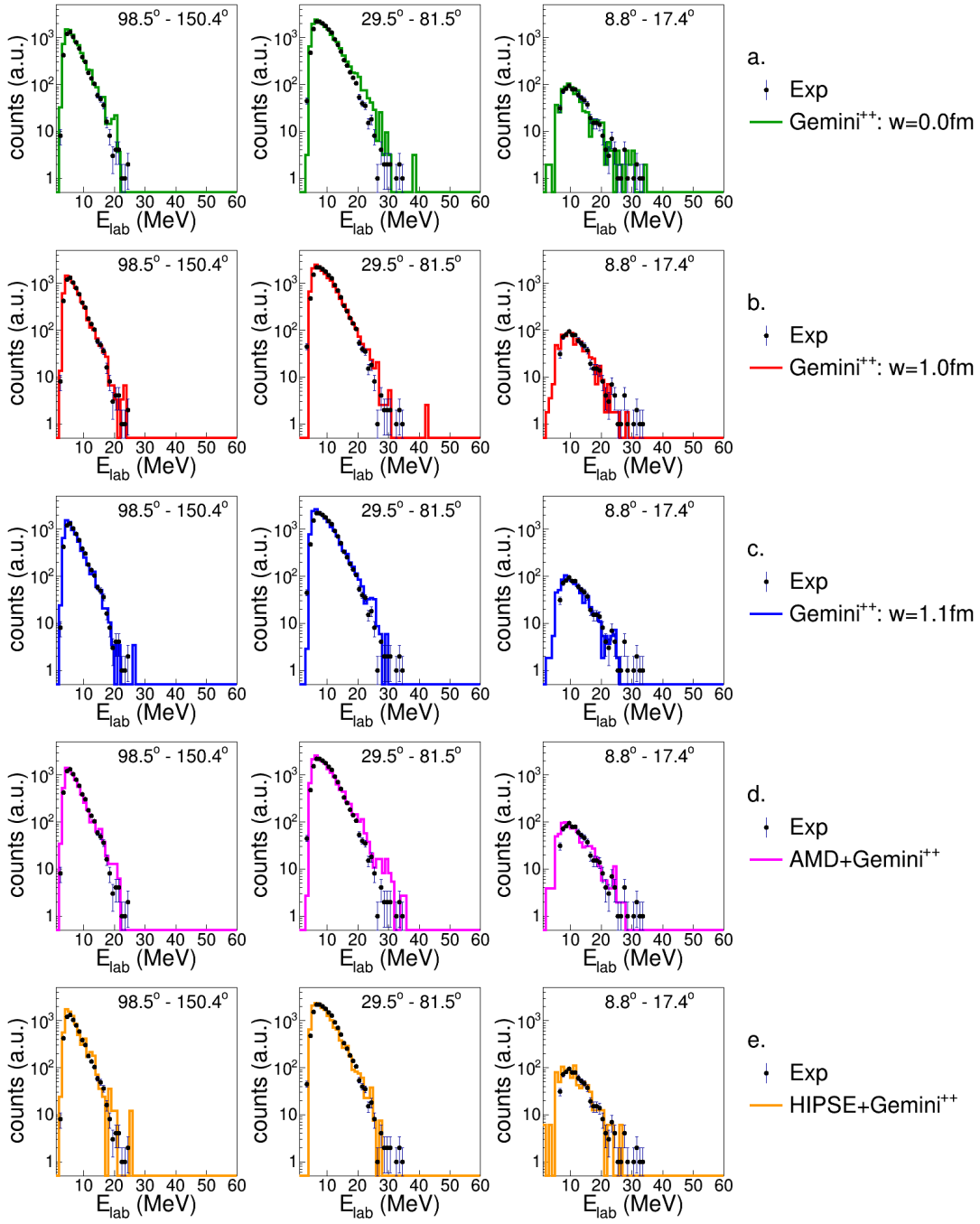

Figure B.94: Energy spectra of protons in coincidence with a S-residue for the reaction $^{16}O + ^{30}Si$ at 128 MeV

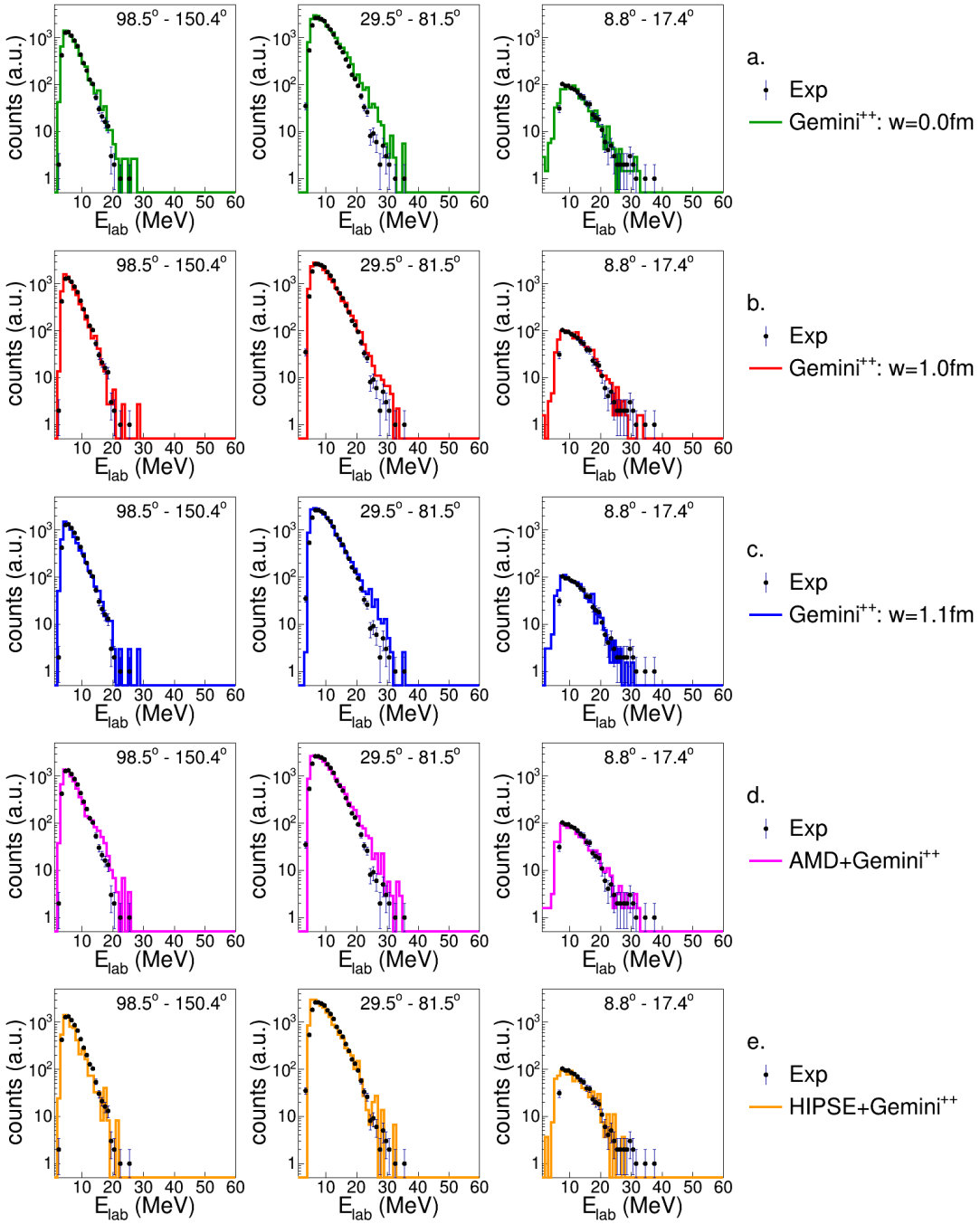

Figure B.95: Energy spectra of protons in coincidence with a S-residue for the reaction $^{18}O + ^{28}Si$ at 126 MeV

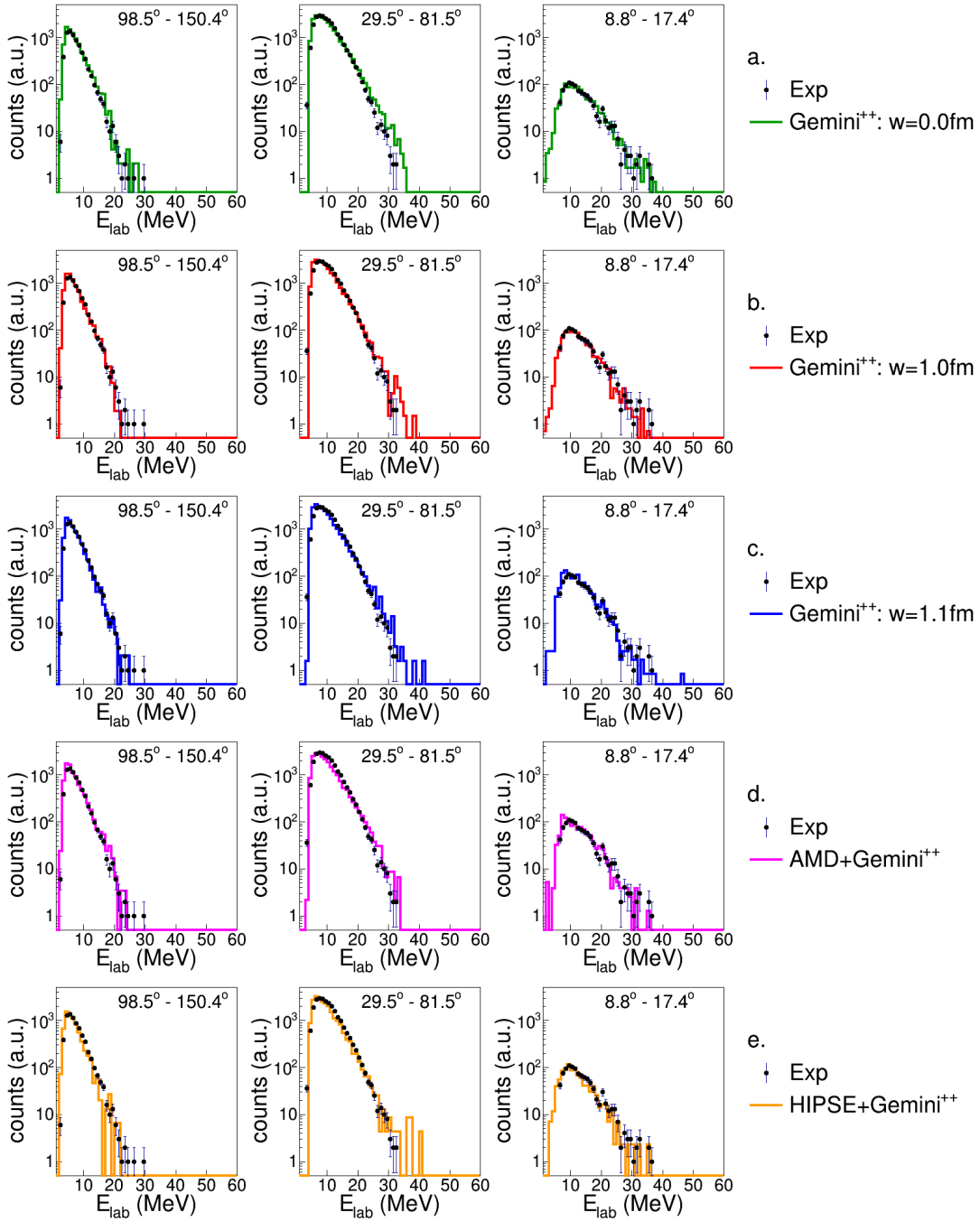

Figure B.96: Energy spectra of protons in coincidence with a S-residue for the reaction $^{19}F + ^{27}Al$ at 133 MeV

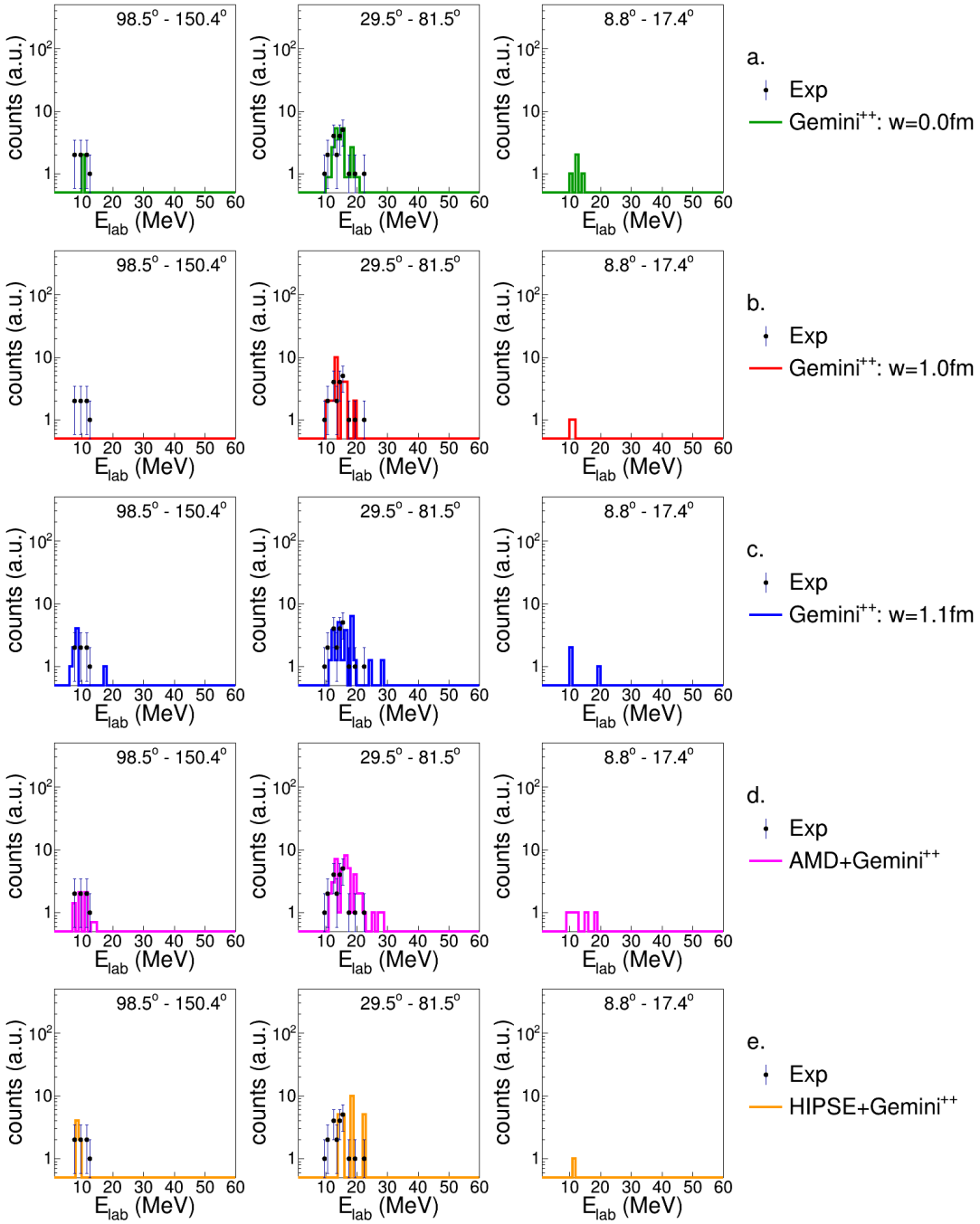

Figure B.97: Energy spectra of deuterons in coincidence with a S-residue for the reaction $^{16}O + ^{30}Si$ at 111 MeV.

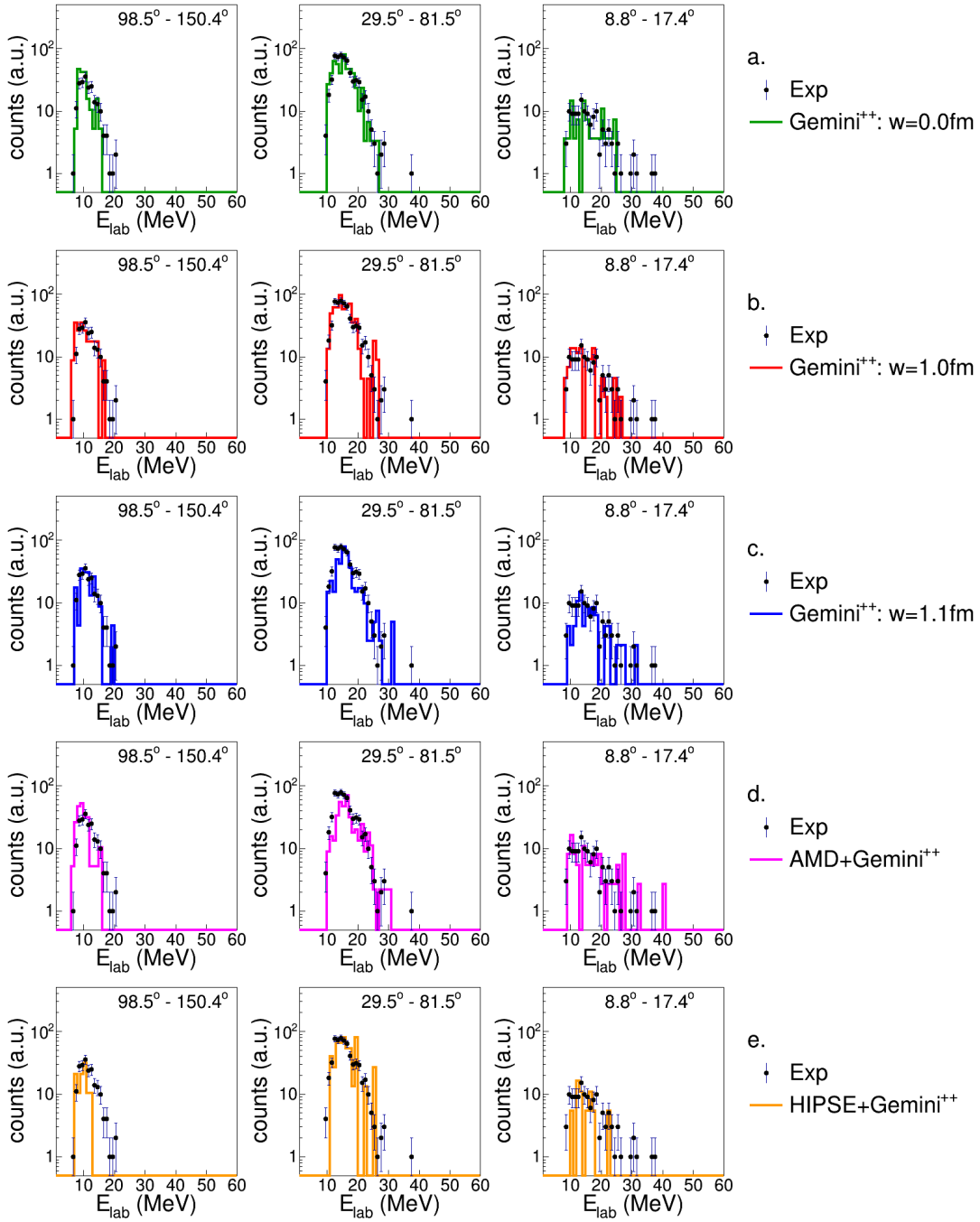

Figure B.98: Energy spectra of deuterons in coincidence with a S-residue for the reaction $^{16}O + ^{30}Si$ at 128 MeV

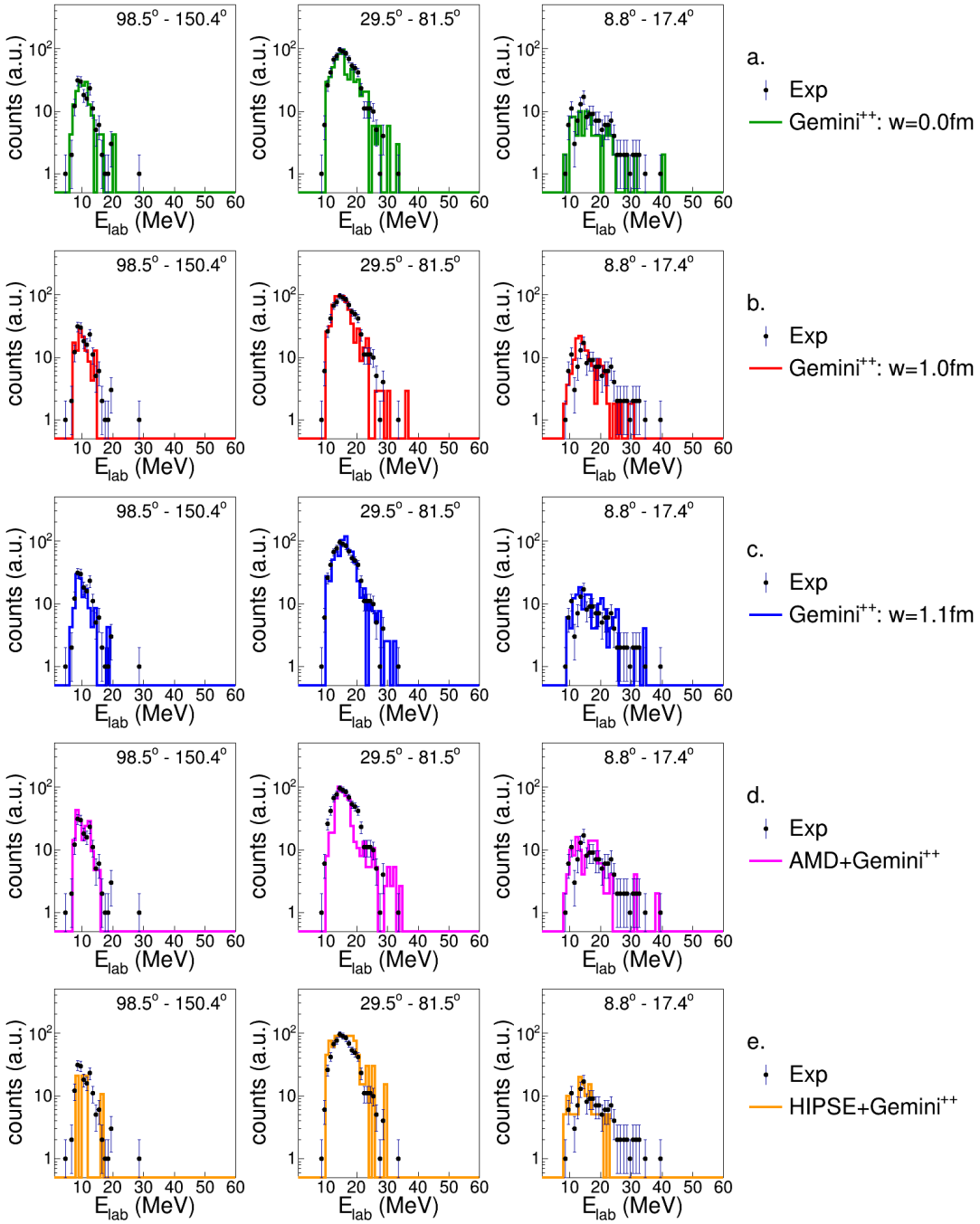

Figure B.99: Energy spectra of deuterons in coincidence with a S-residue for the reaction $^{18}O + ^{28}Si$ at 126 MeV

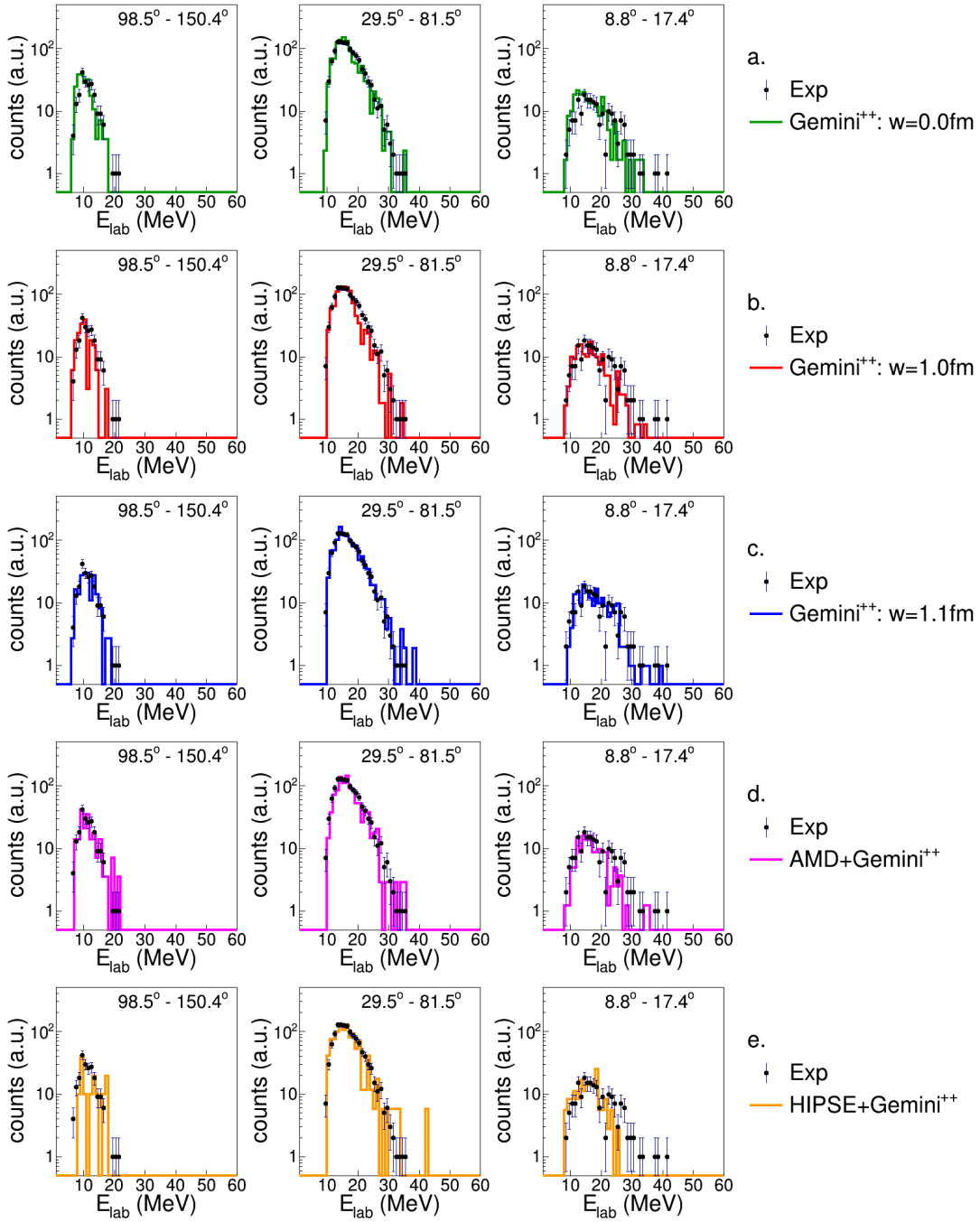

Figure B.100: Energy spectra of deuterons in coincidence with a S-residue for the reaction $^{19}F + ^{27}Al$ at 133 MeV

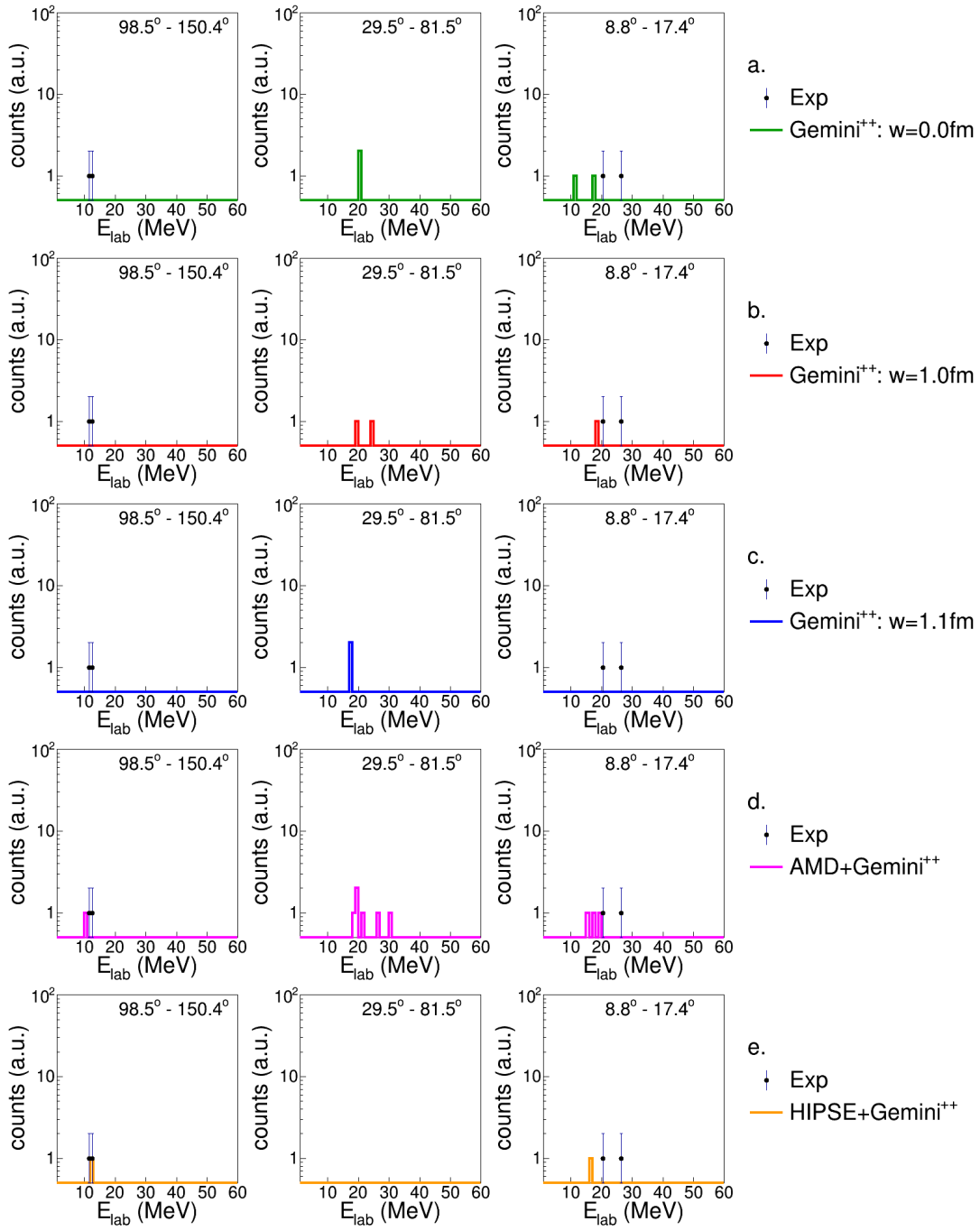

Figure B.101: Energy spectra of tritons in coincidence with a S-residue for the reaction $^{16}O + ^{30}Si$ at 111 MeV.

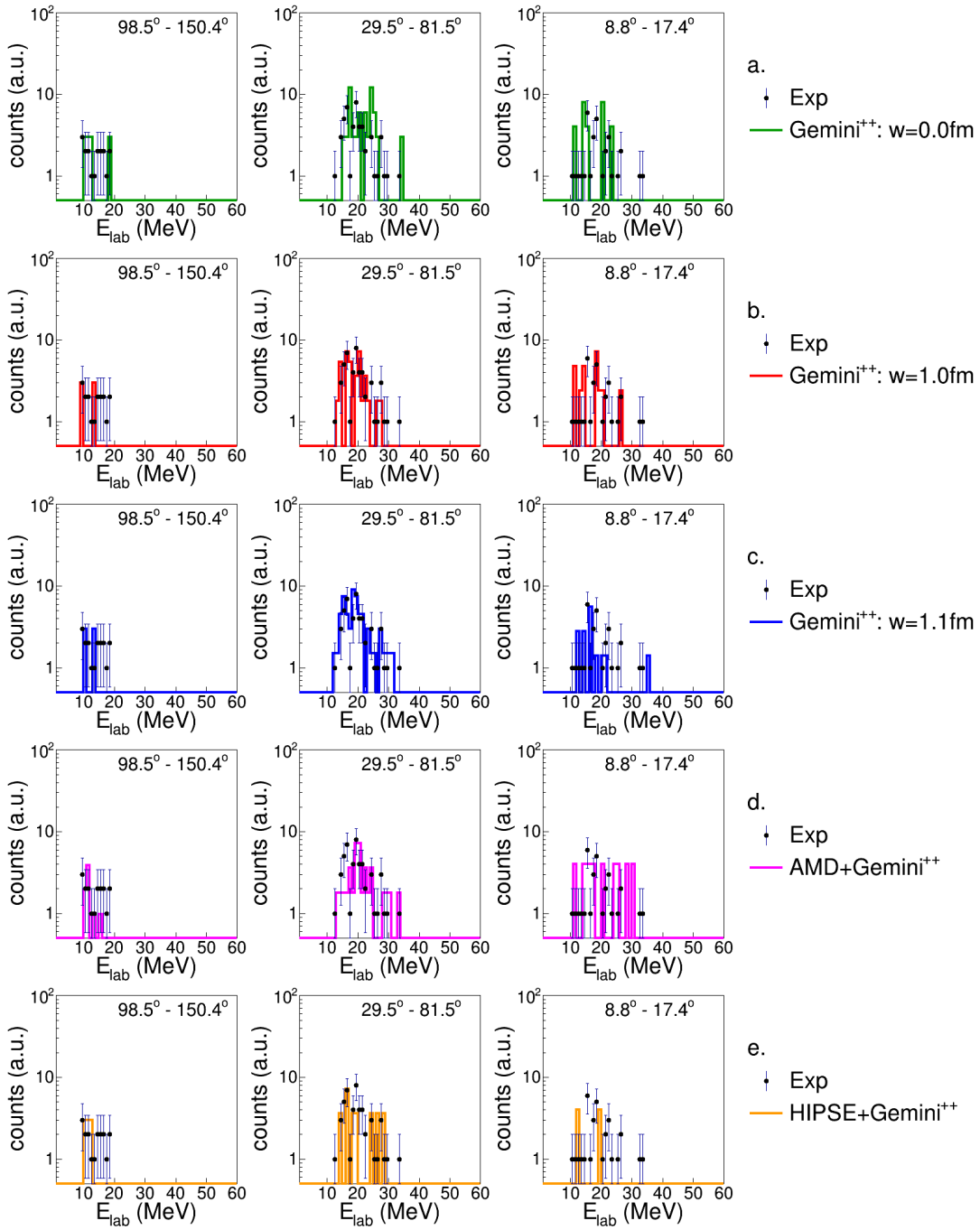

Figure B.102: Energy spectra of tritons in coincidence with a S-residue for the reaction $^{16}O + ^{30}Si$ at 128 MeV

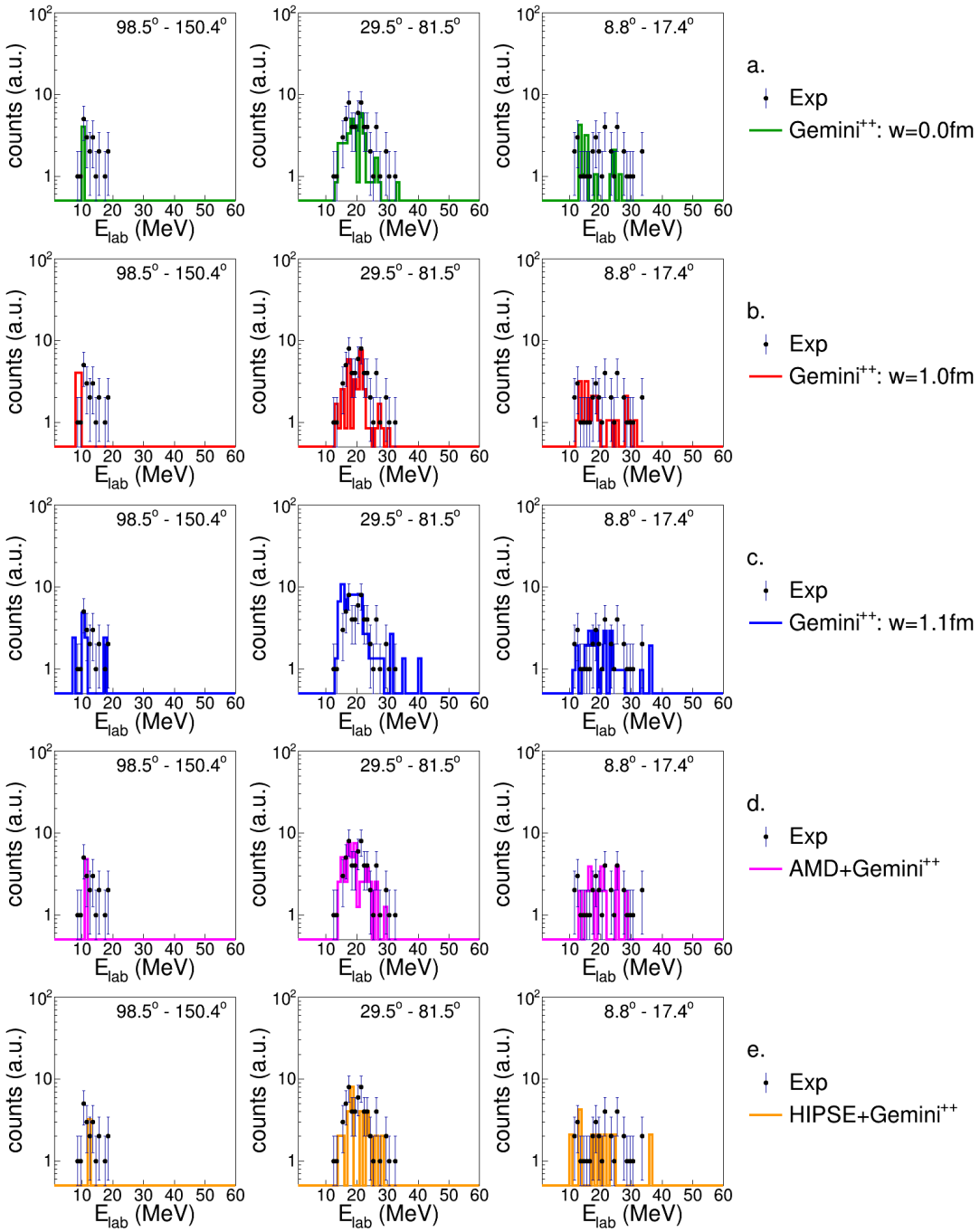

Figure B.103: Energy spectra of tritons in coincidence with a S-residue for the reaction $^{18}O + ^{28}Si$ at 126 MeV

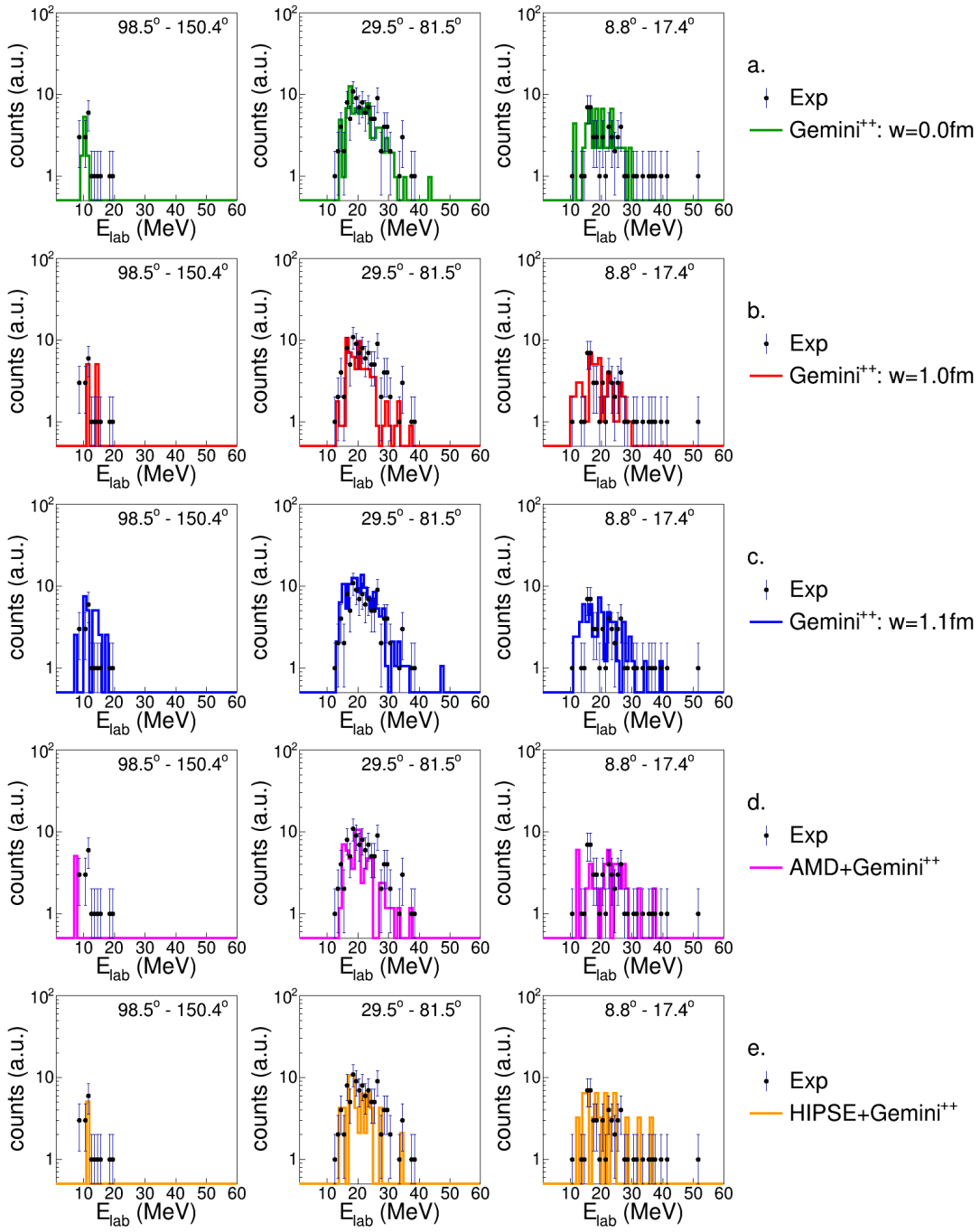

Figure B.104: Energy spectra of tritons in coincidence with a S-residue for the reaction $^{19}F + ^{27}Al$ at 133 MeV

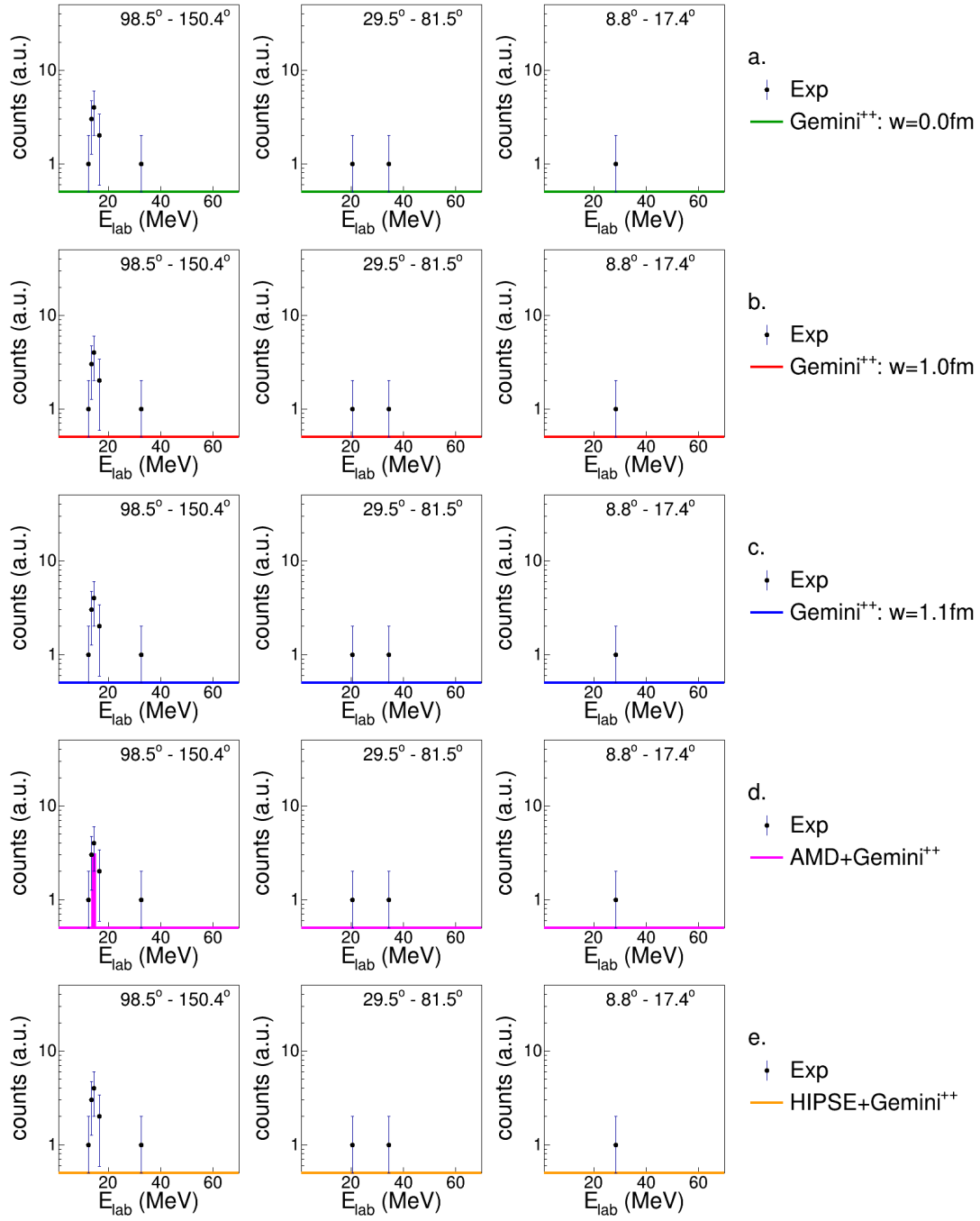

Figure B.105: Energy spectra of ^{3}He in coincidence with a S-residue for the reaction $^{16}O + ^{30}Si$ at 111 MeV.

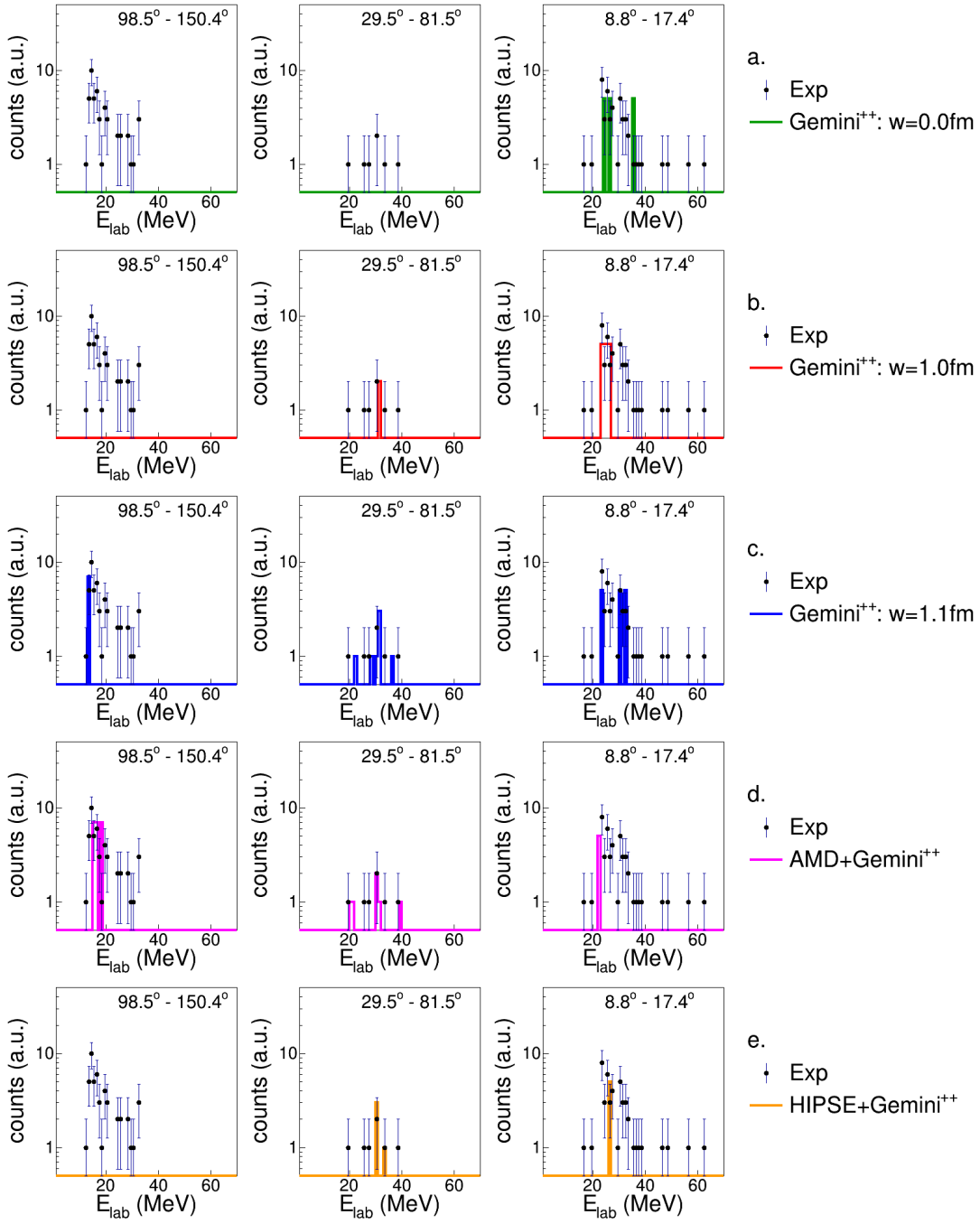

Figure B.106: Energy spectra of ^{3}He in coincidence with a S-residue for the reaction $^{16}O + ^{30}Si$ at 128 MeV

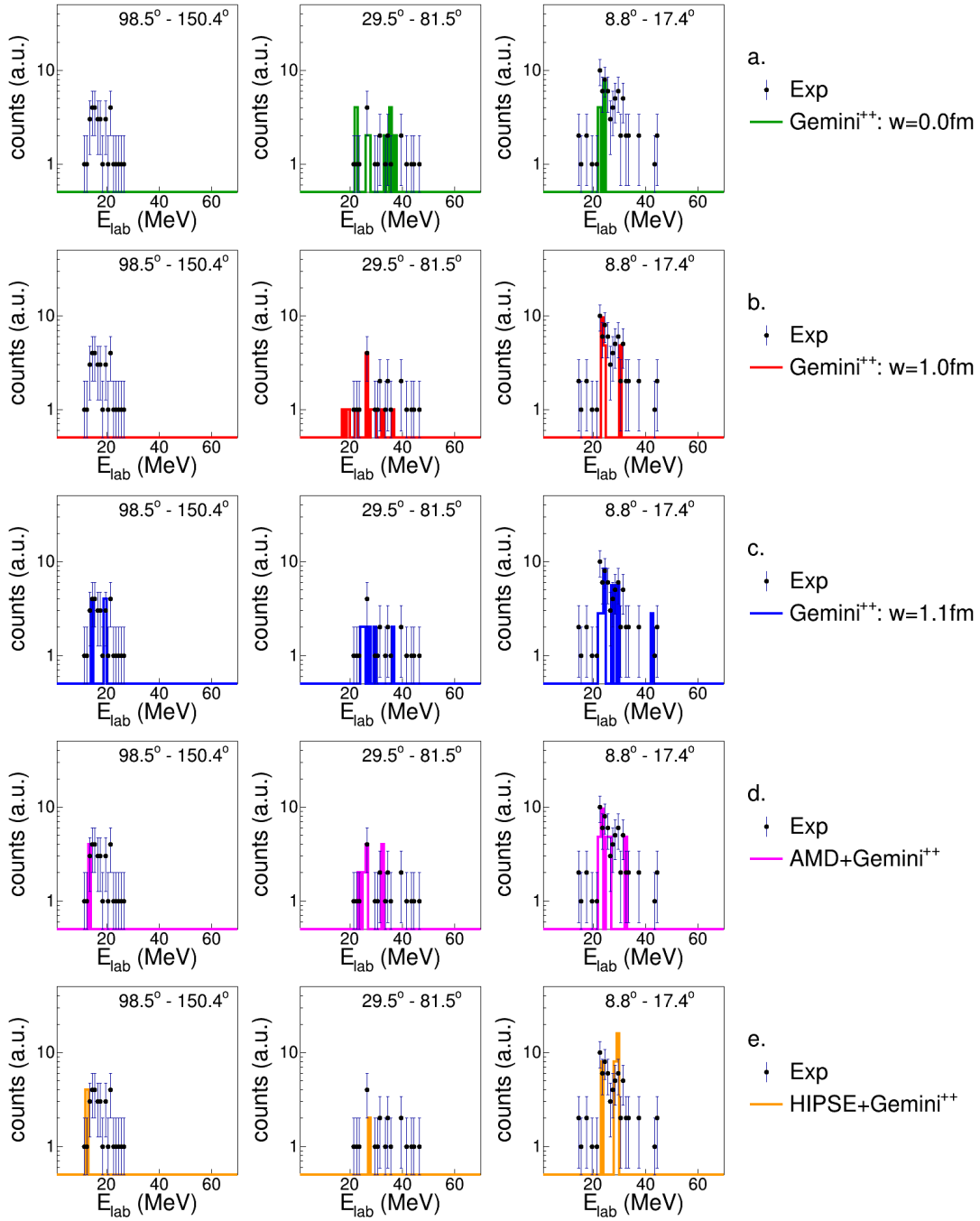

Figure B.107: Energy spectra of ^{3}He in coincidence with a S-residue for the reaction $^{18}O + ^{28}Si$ at 126 MeV

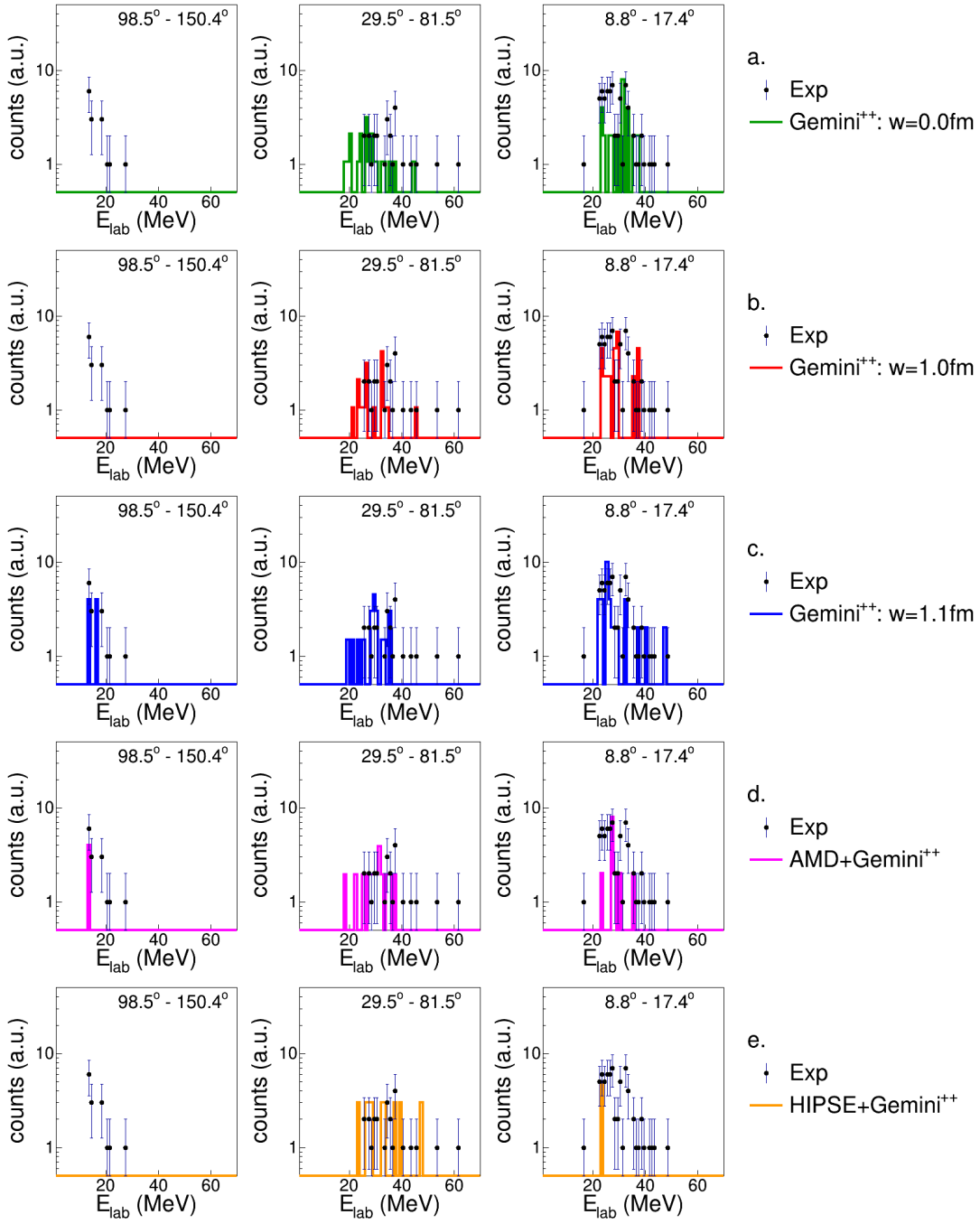

Figure B.108: Energy spectra of ^{3}He in coincidence with a S-residue for the reaction $^{19}F + ^{27}Al$ at 133 MeV

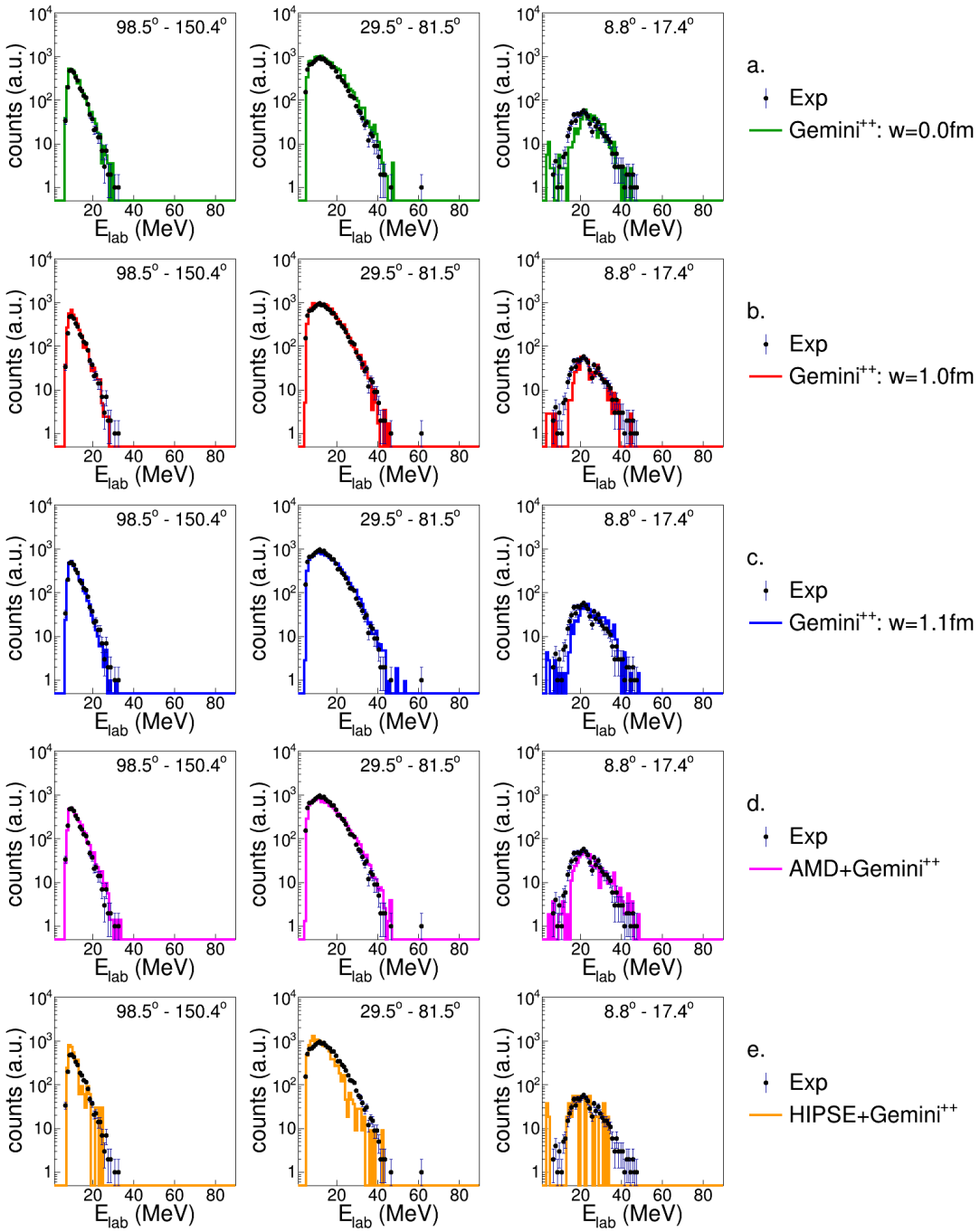

Figure B.109: Energy spectra of α-particles in coincidence with a S-residue for the reaction $^{16}O + ^{30}Si$ at 111 MeV.

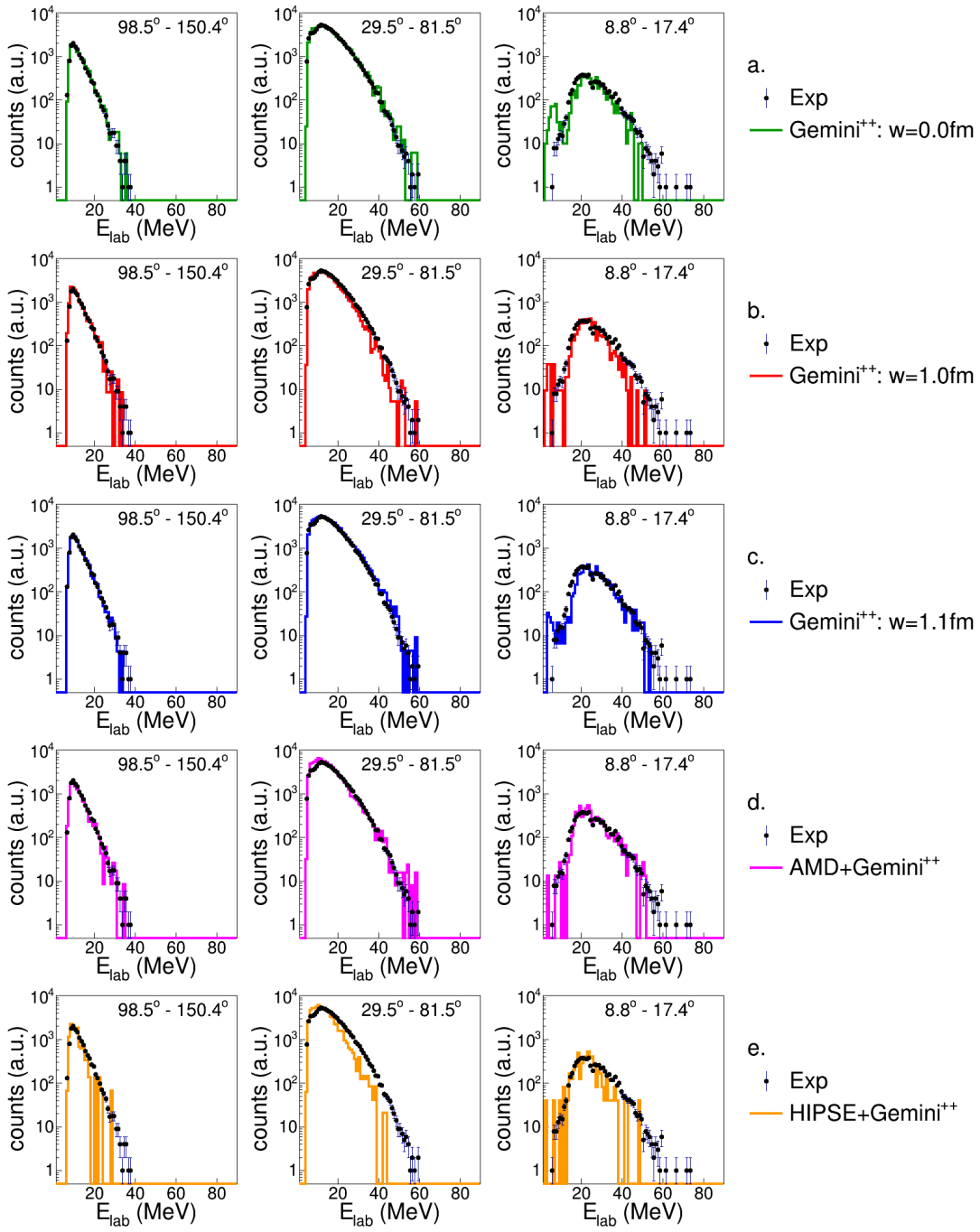

Figure B.110: Energy spectra of α-particles in coincidence with a S-residue for the reaction $^{16}O + ^{30}Si$ at 128 MeV

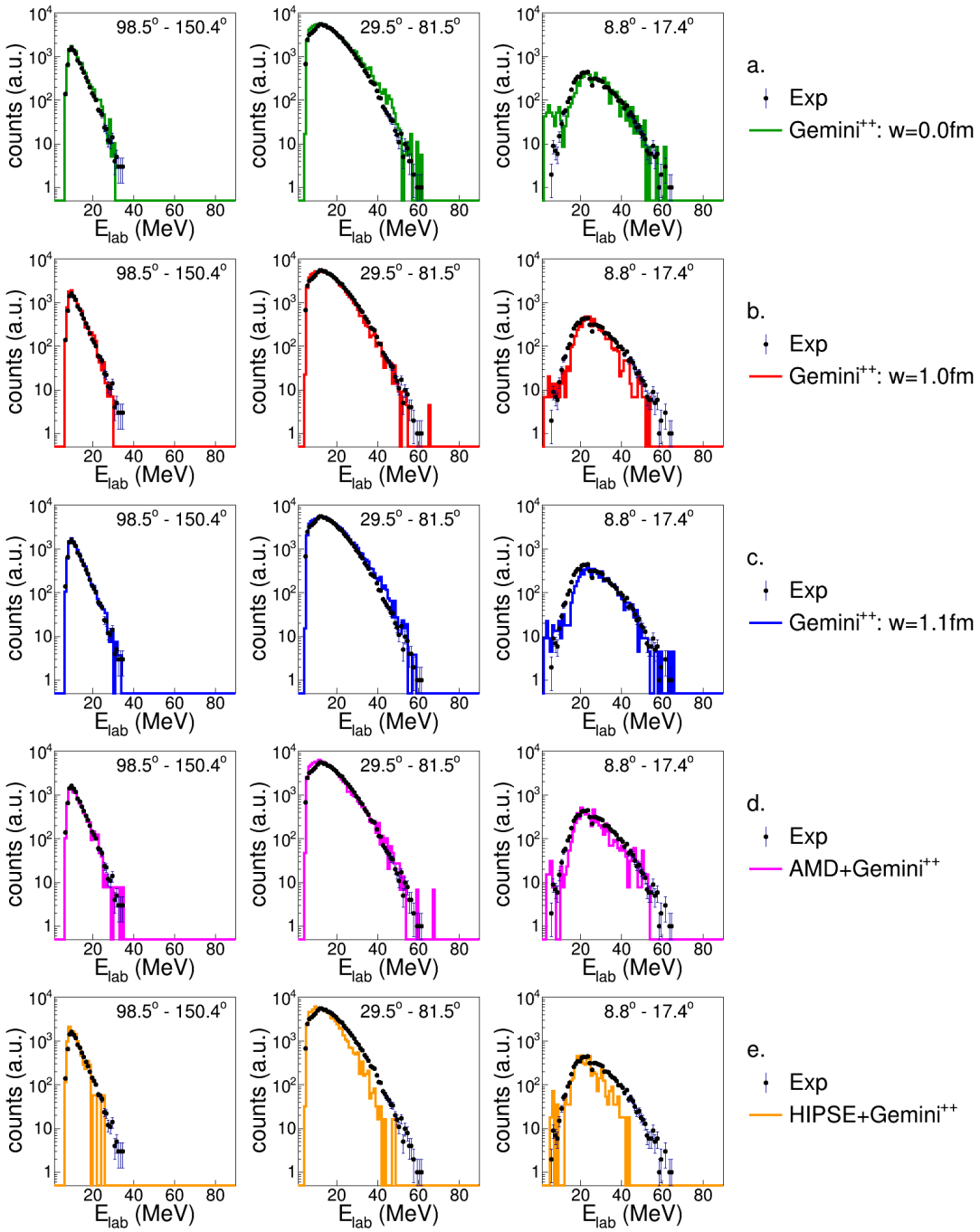

Figure B.111: Energy spectra of α-particles in coincidence with a S-residue for the reaction $^{18}O + ^{28}Si$ at 126 MeV

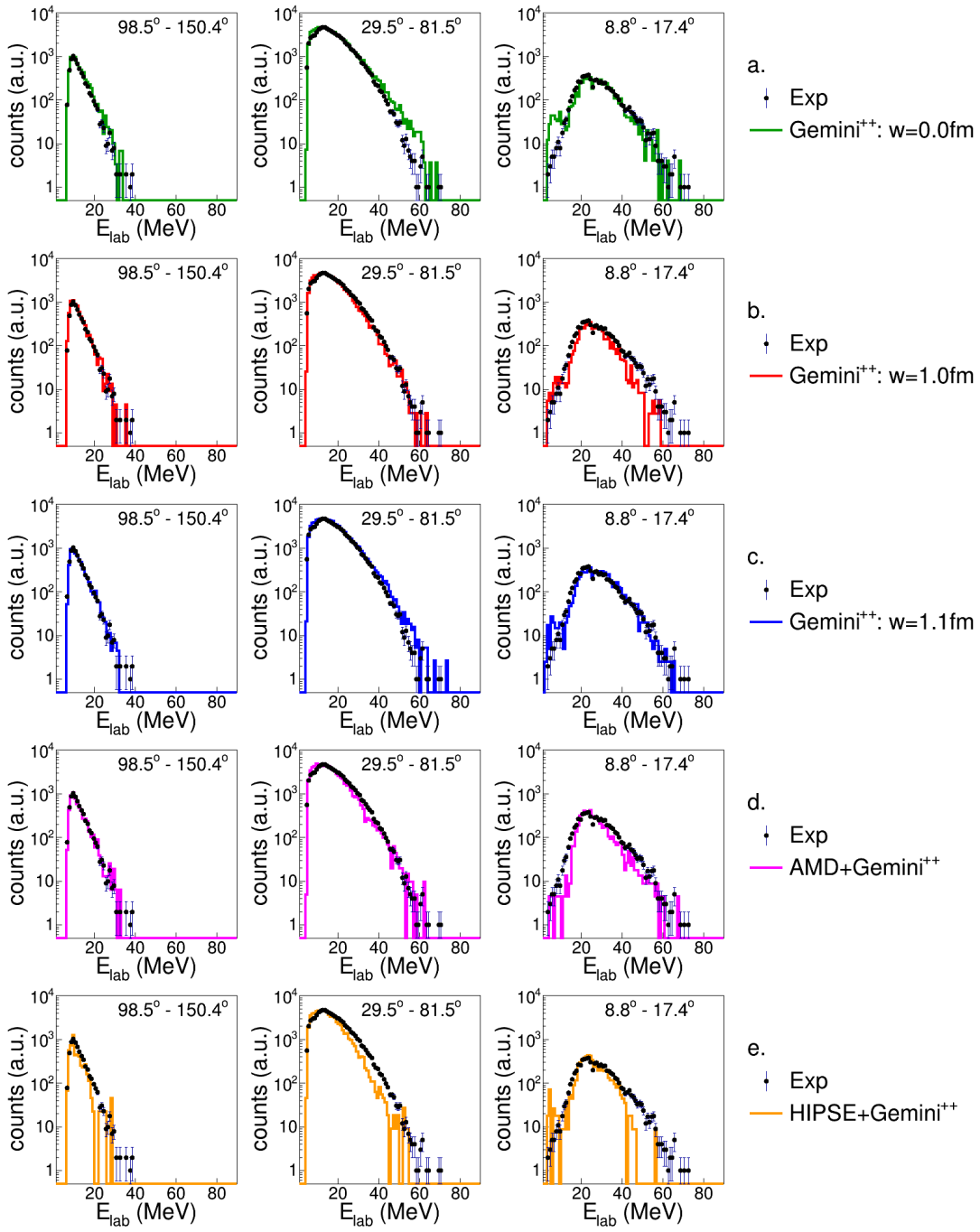

Figure B.112: Energy spectra of α-particles in coincidence with a S-residue for the reaction $^{19}F + ^{27}Al$ at 133 MeV

B.7 The P residue: $Z_{res} = 15$

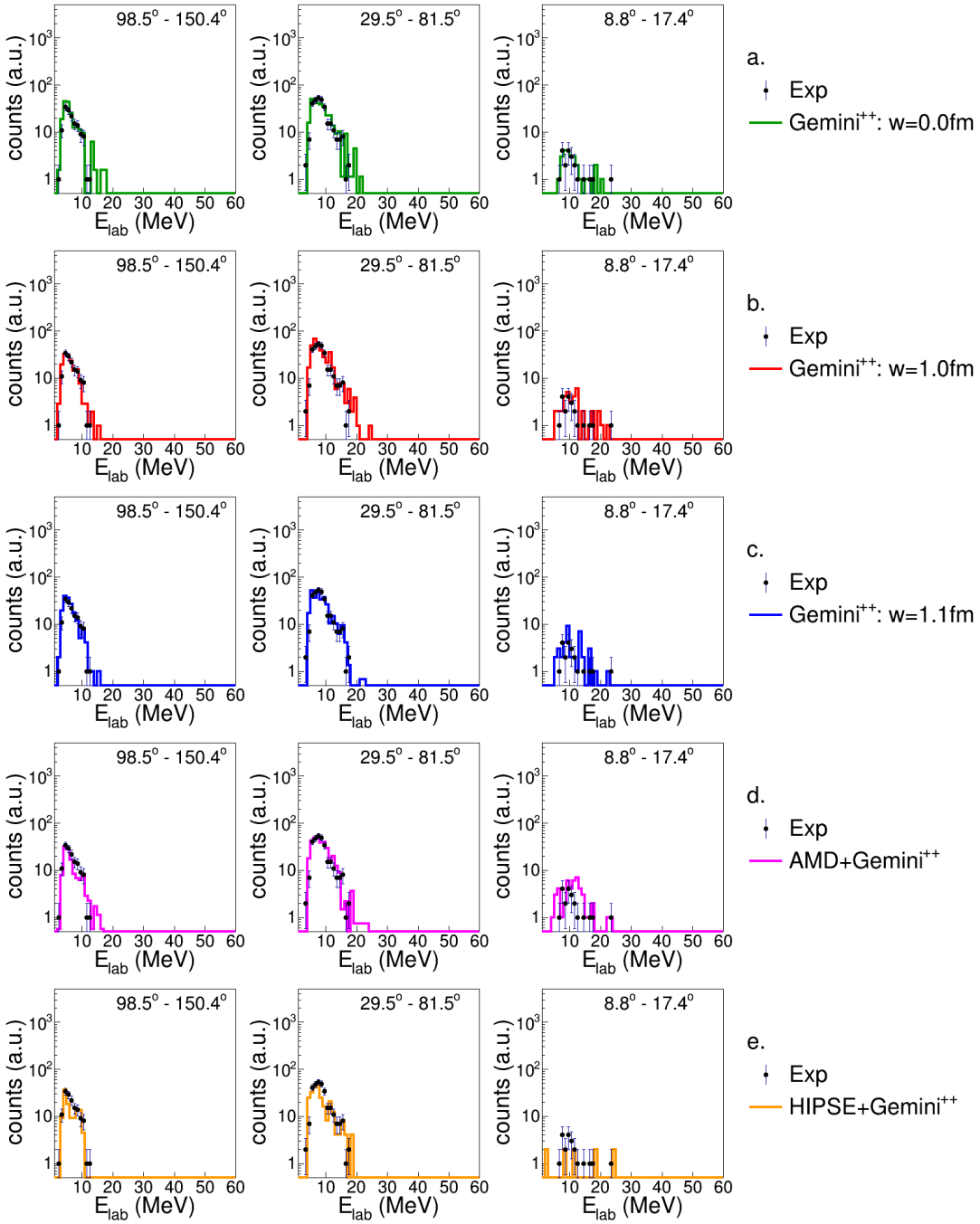

Figure B.113: Energy spectra of protons in coincidence with a P-residue for the reaction $^{16}O + ^{30}Si$ at 111 MeV.

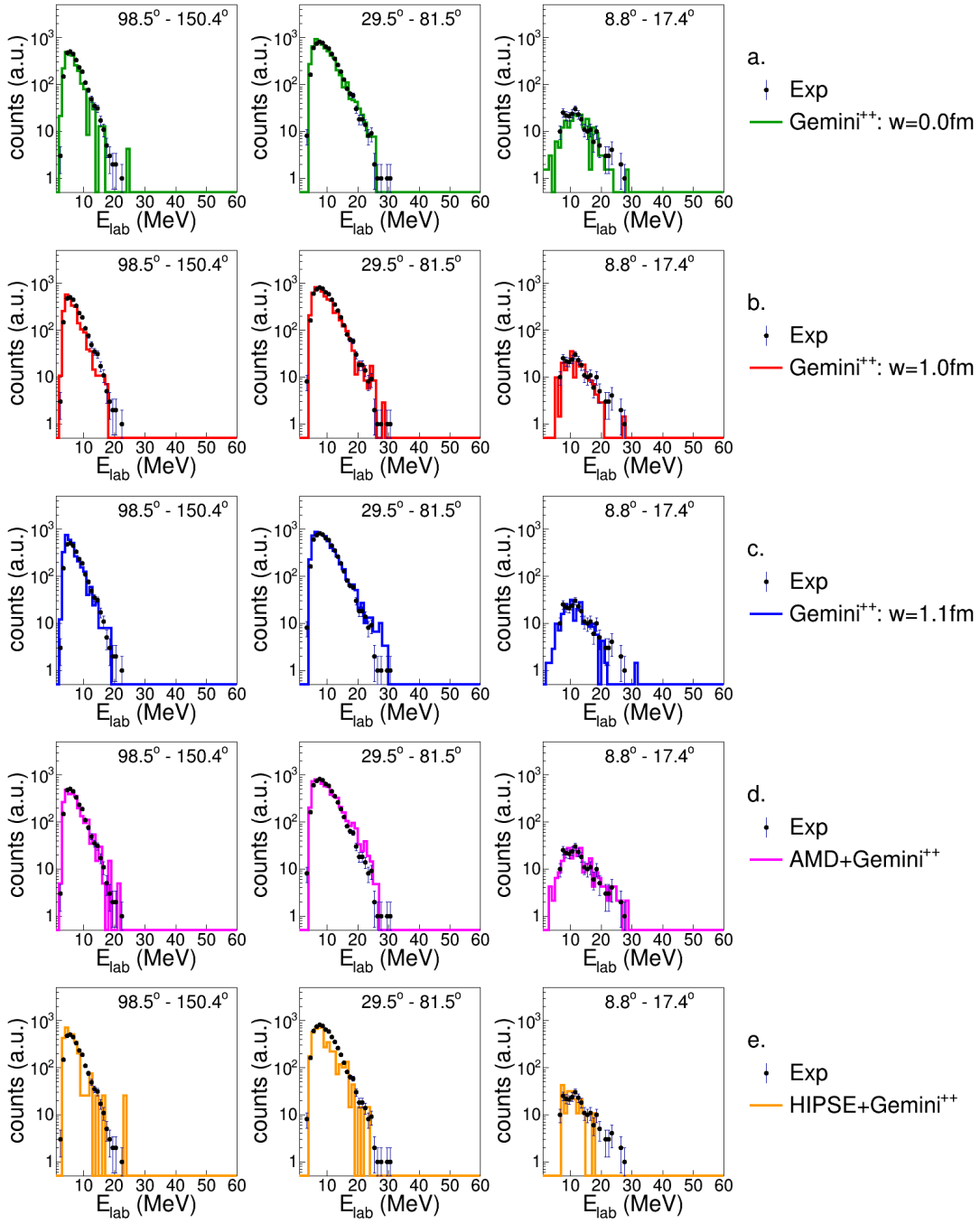

Figure B.114: Energy spectra of protons in coincidence with a P-residue for the reaction $^{16}O + ^{30}Si$ at 128 MeV

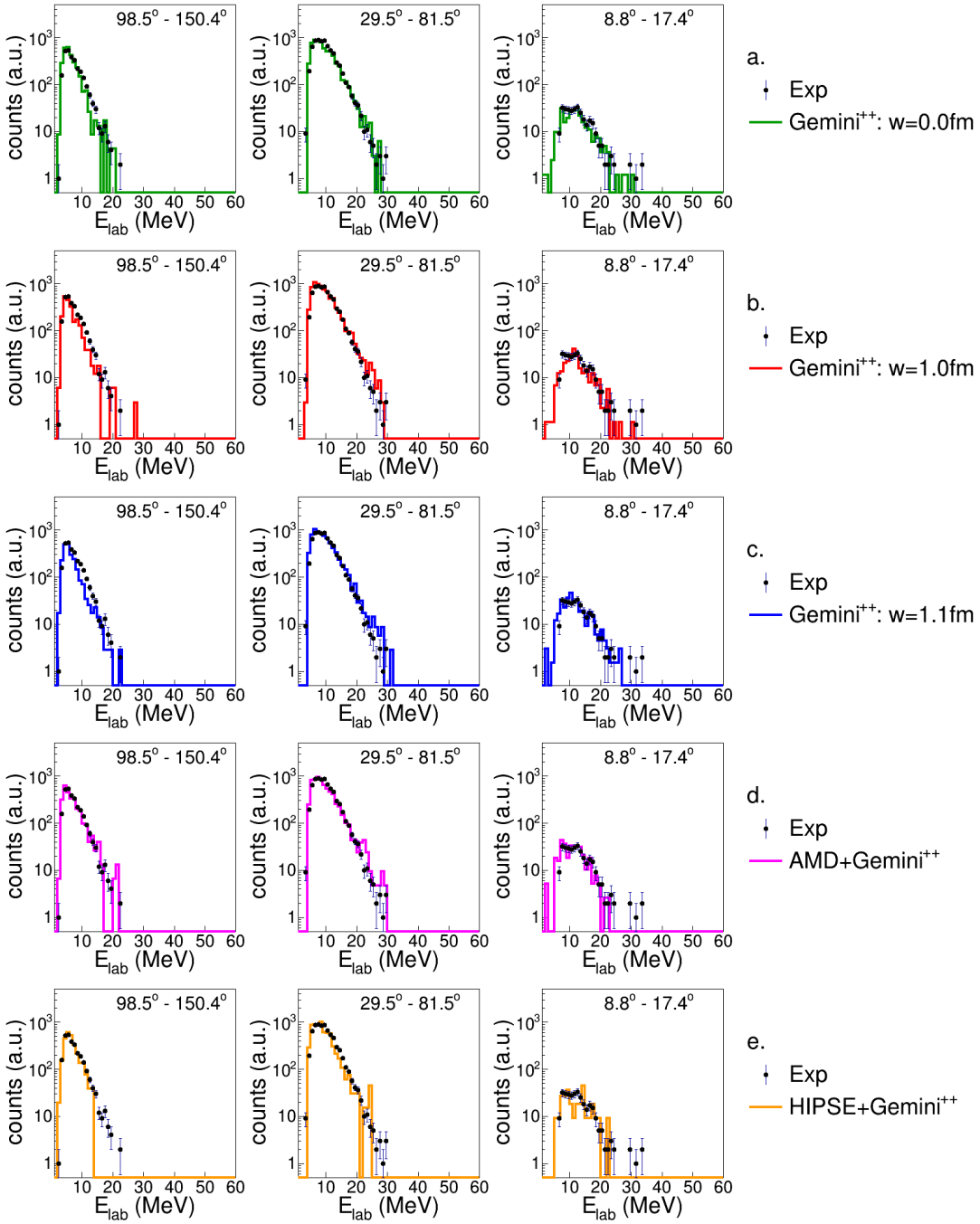

Figure B.115: Energy spectra of protons in coincidence with a P-residue for the reaction $^{18}O + ^{28}Si$ at 126 MeV

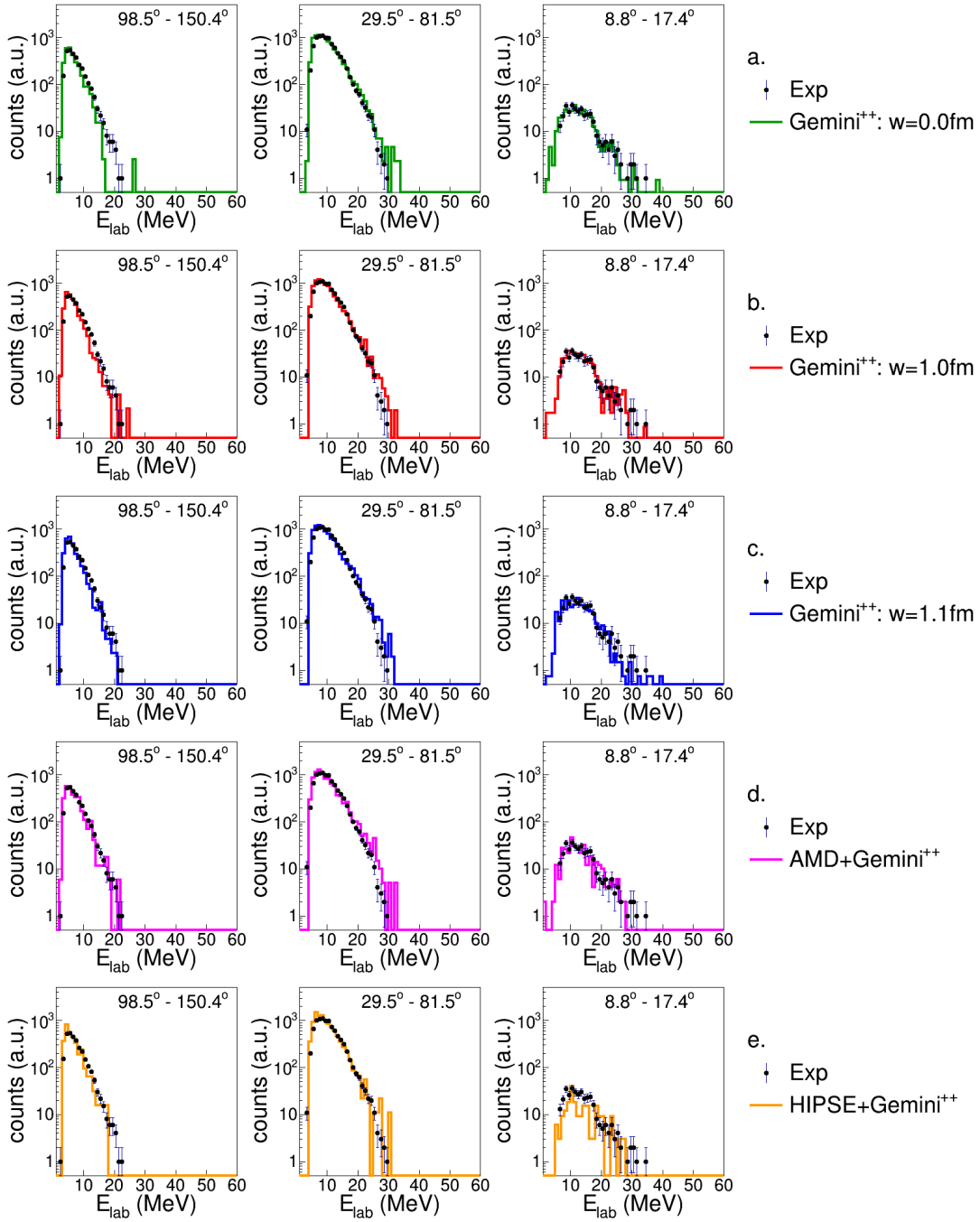

Figure B.116: Energy spectra of protons in coincidence with a P-residue for the reaction $^{19}F + ^{27}Al$ at 133 MeV

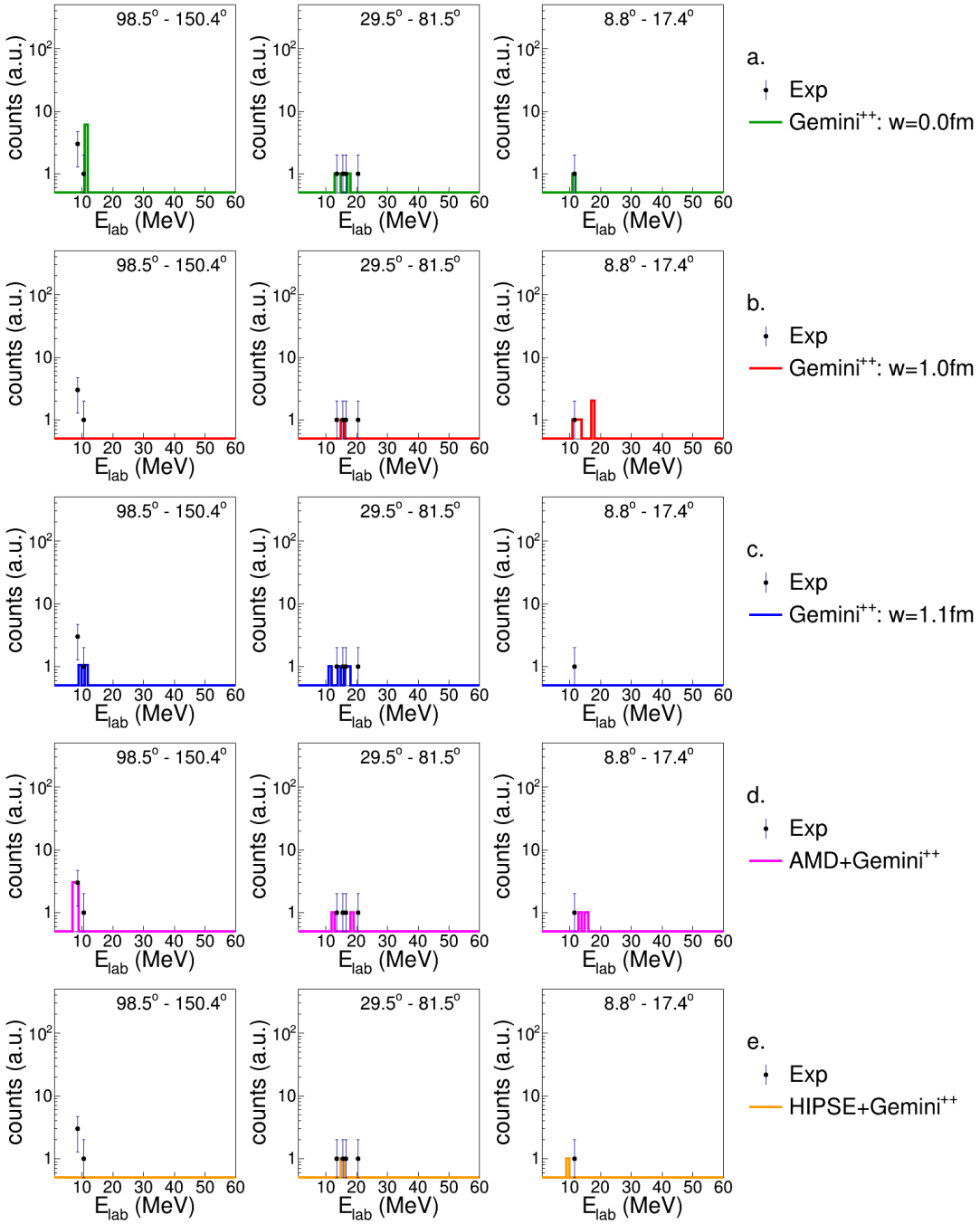

Figure B.117: Energy spectra of deuterons in coincidence with a P-residue for the reaction $^{16}O + ^{30}Si$ at 111 MeV.

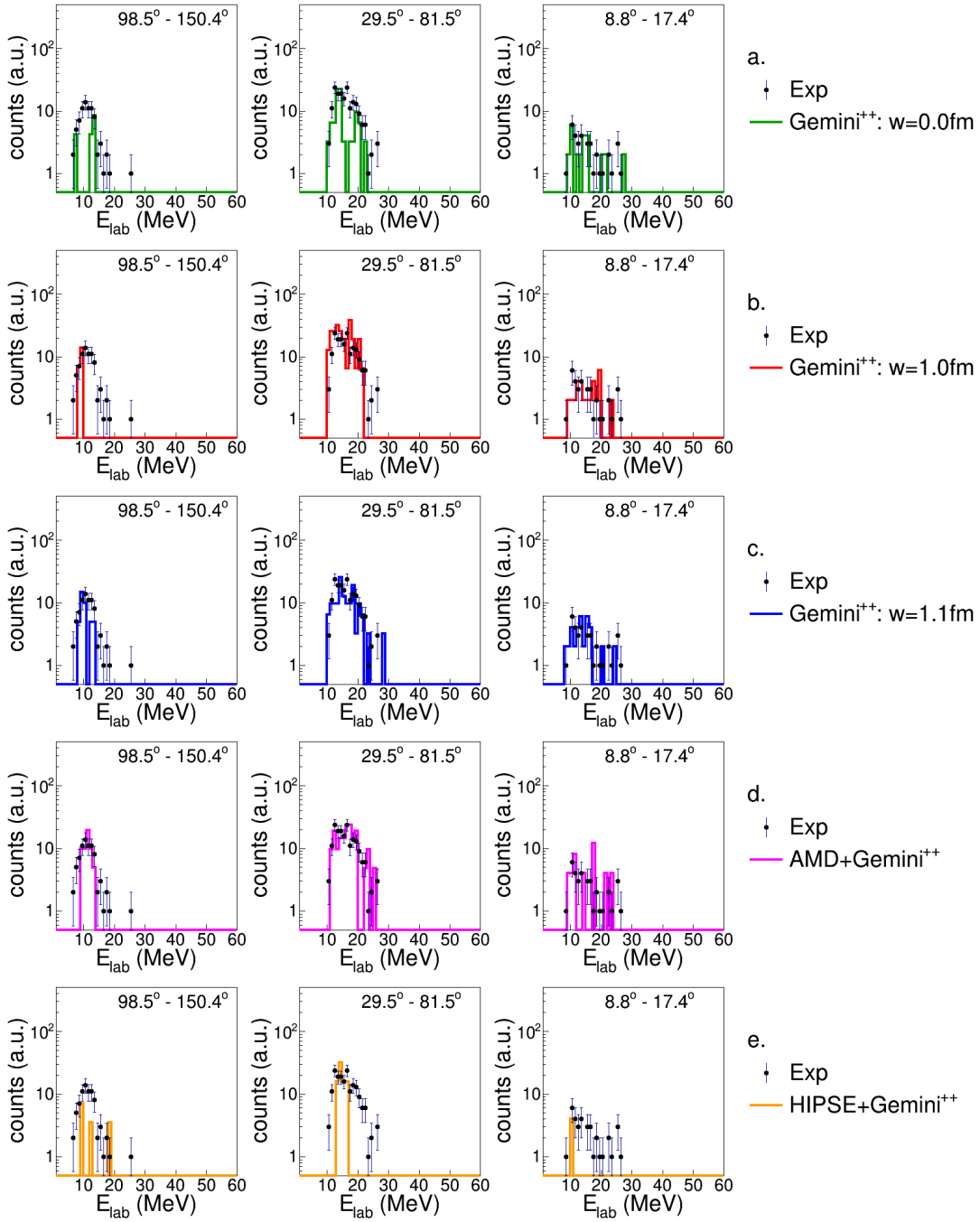

Figure B.118: Energy spectra of deuterons in coincidence with a P-residue for the reaction $^{16}O +^{30} Si$ at 128 MeV

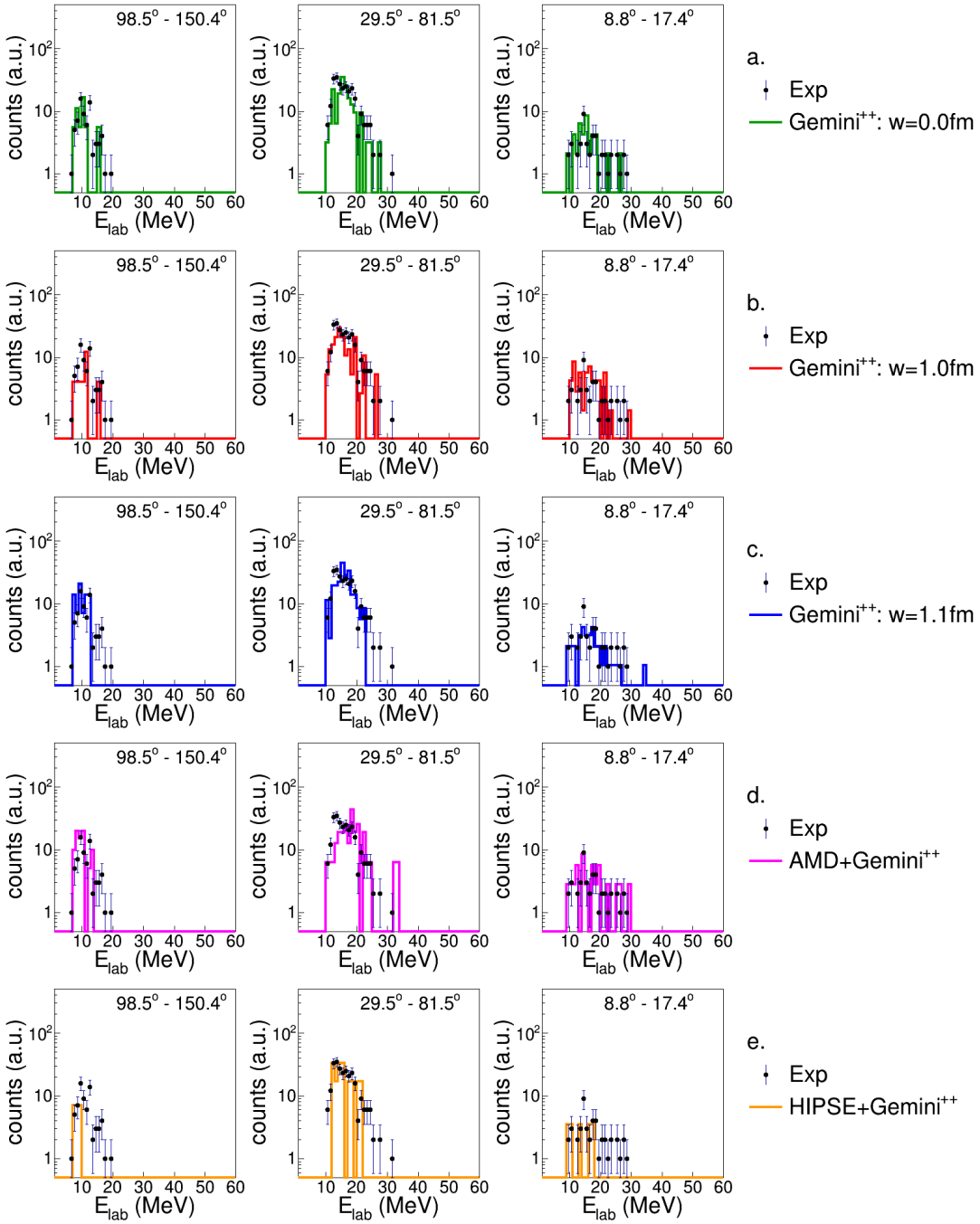

Figure B.119: Energy spectra of deuterons in coincidence with a P-residue for the reaction $^{18}O + ^{28}Si$ at 126 MeV

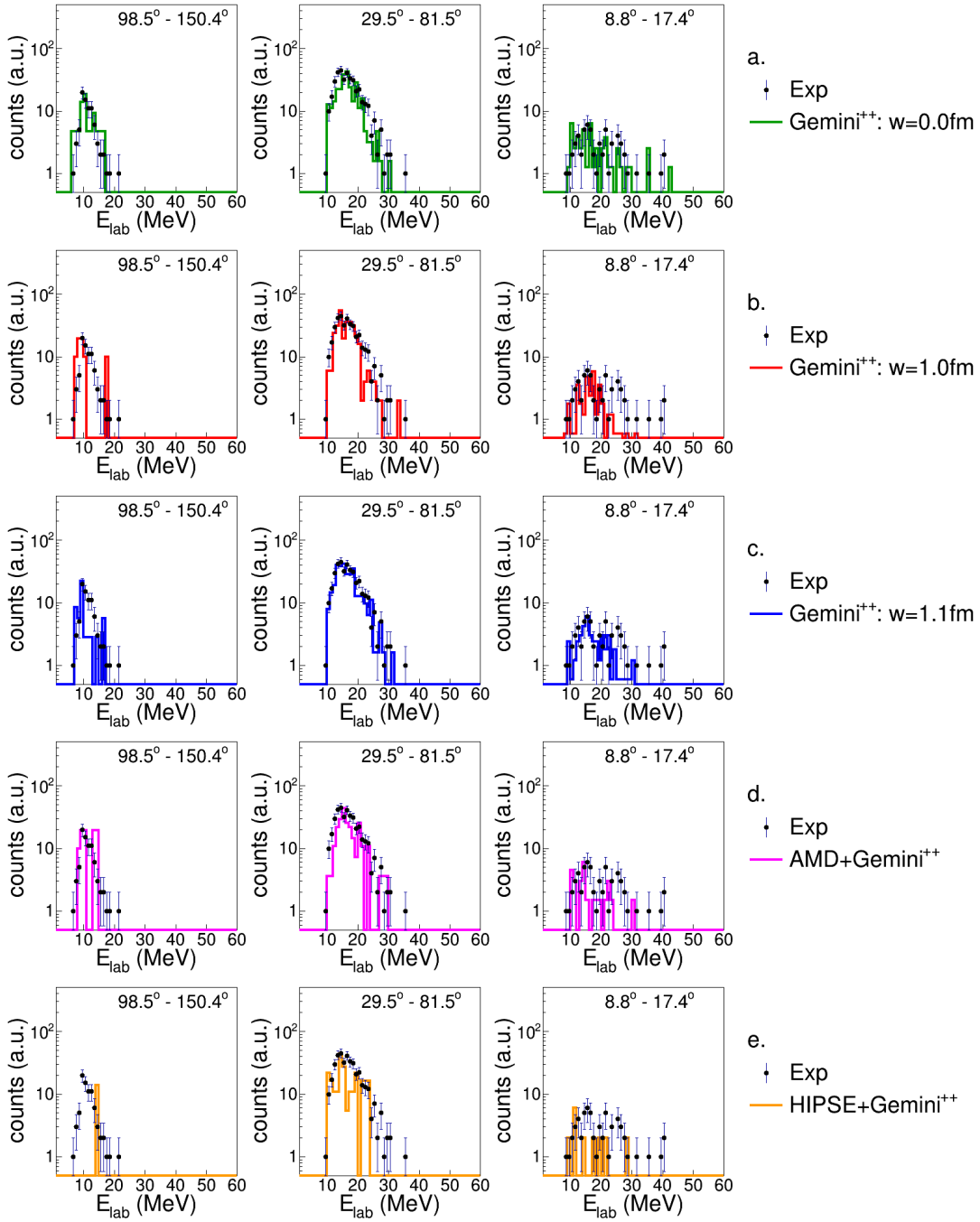

Figure B.120: Energy spectra of deuterons in coincidence with a P-residue for the reaction $^{19}F + ^{27}Al$ at 133 MeV

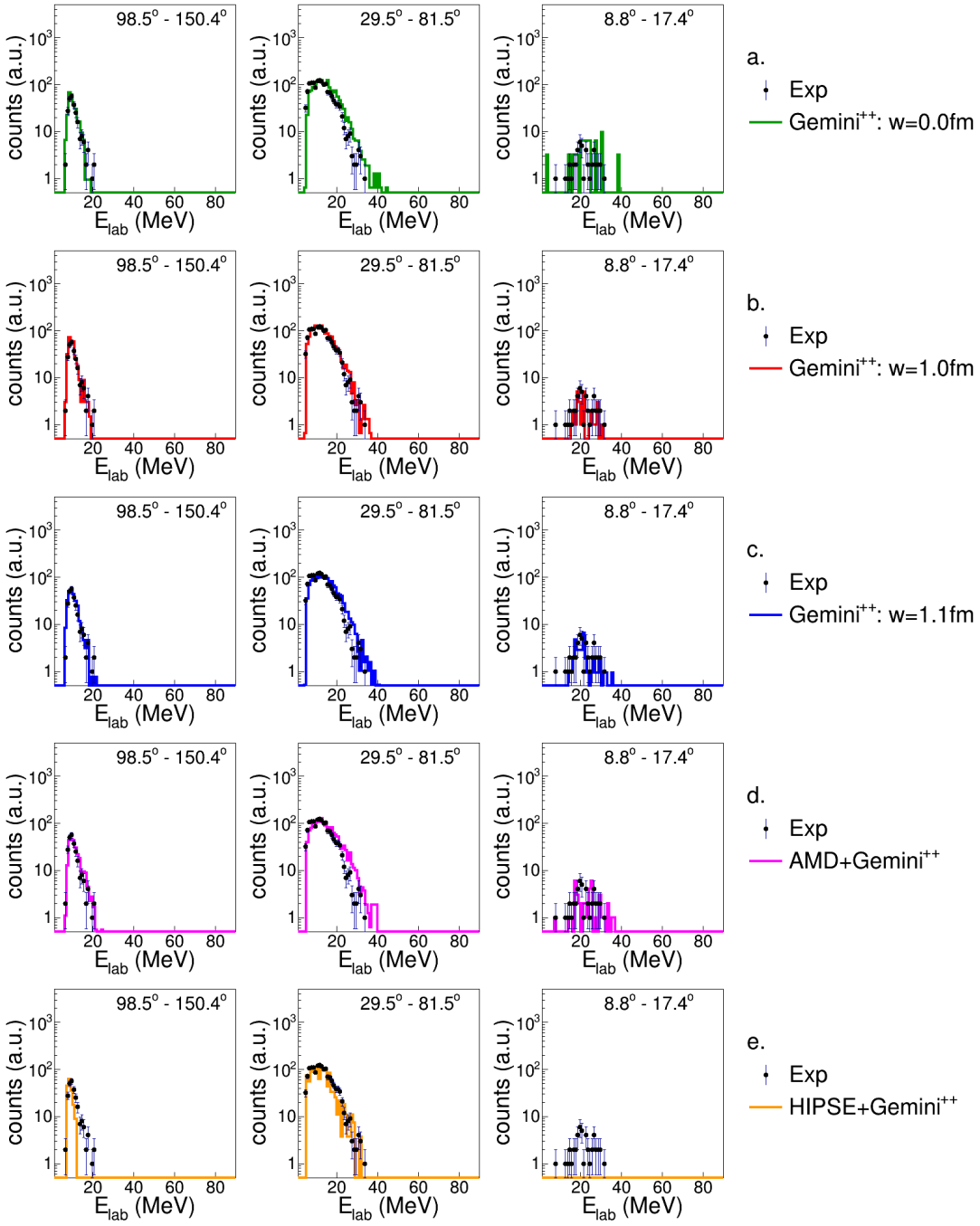

Figure B.121: Energy spectra of α-particles in coincidence with a P-residue for the reaction $^{16}O + ^{30}Si$ at 111 MeV.

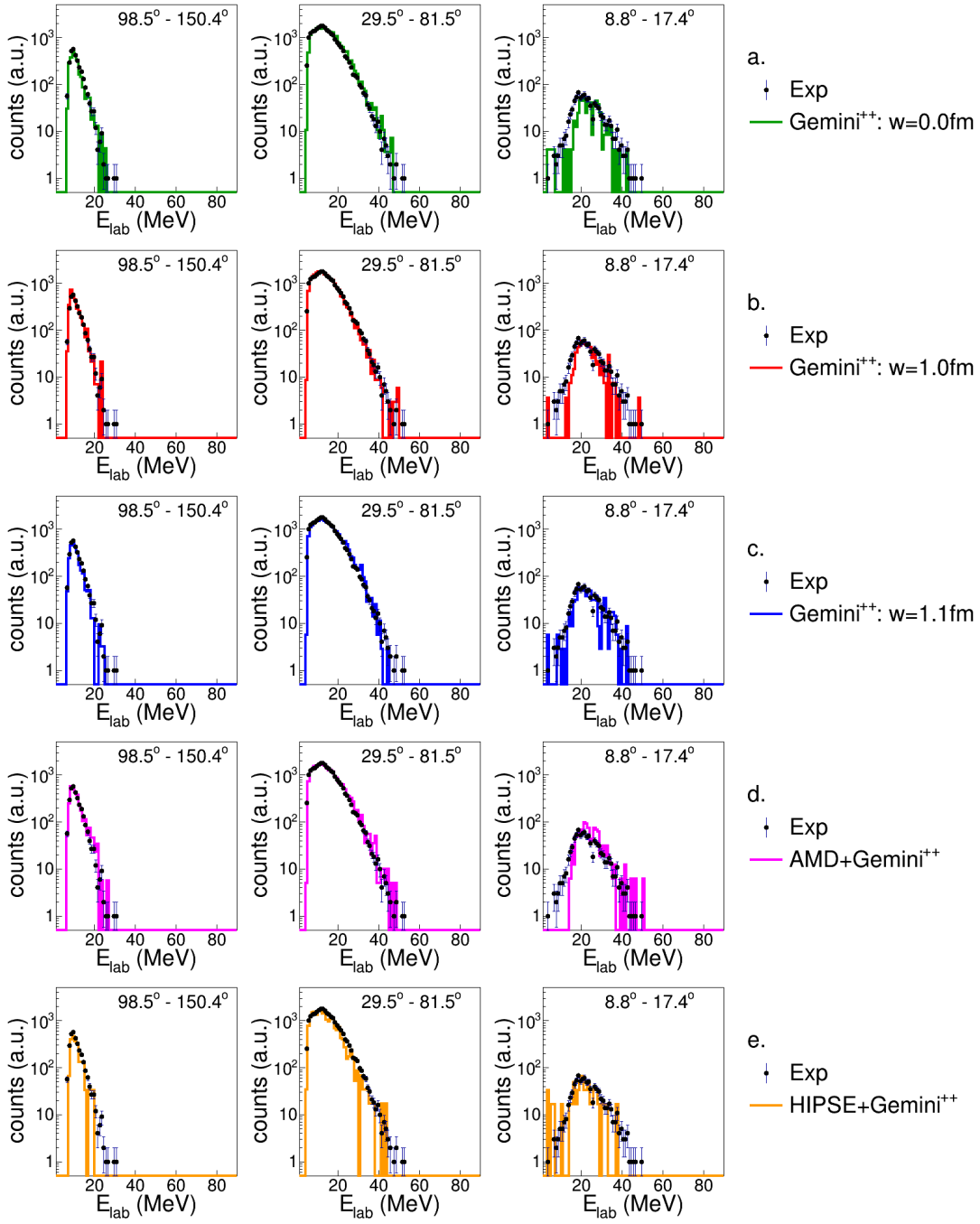

Figure B.122: Energy spectra of α-particles in coincidence with a P-residue for the reaction $^{16}O + ^{30}Si$ at 128 MeV

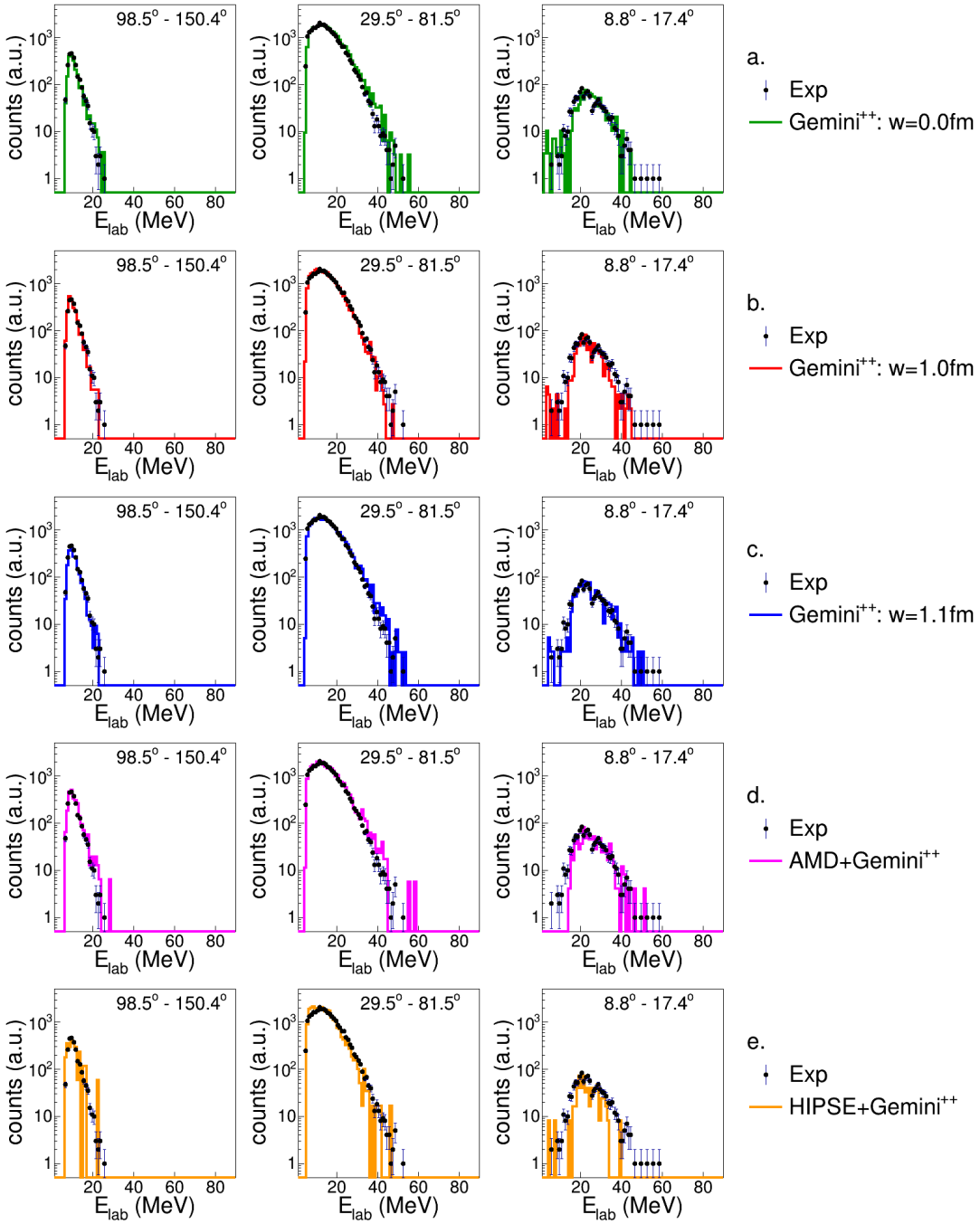

Figure B.123: Energy spectra of α-particles in coincidence with a P-residue for the reaction $^{18}O + ^{28}Si$ at 126 MeV

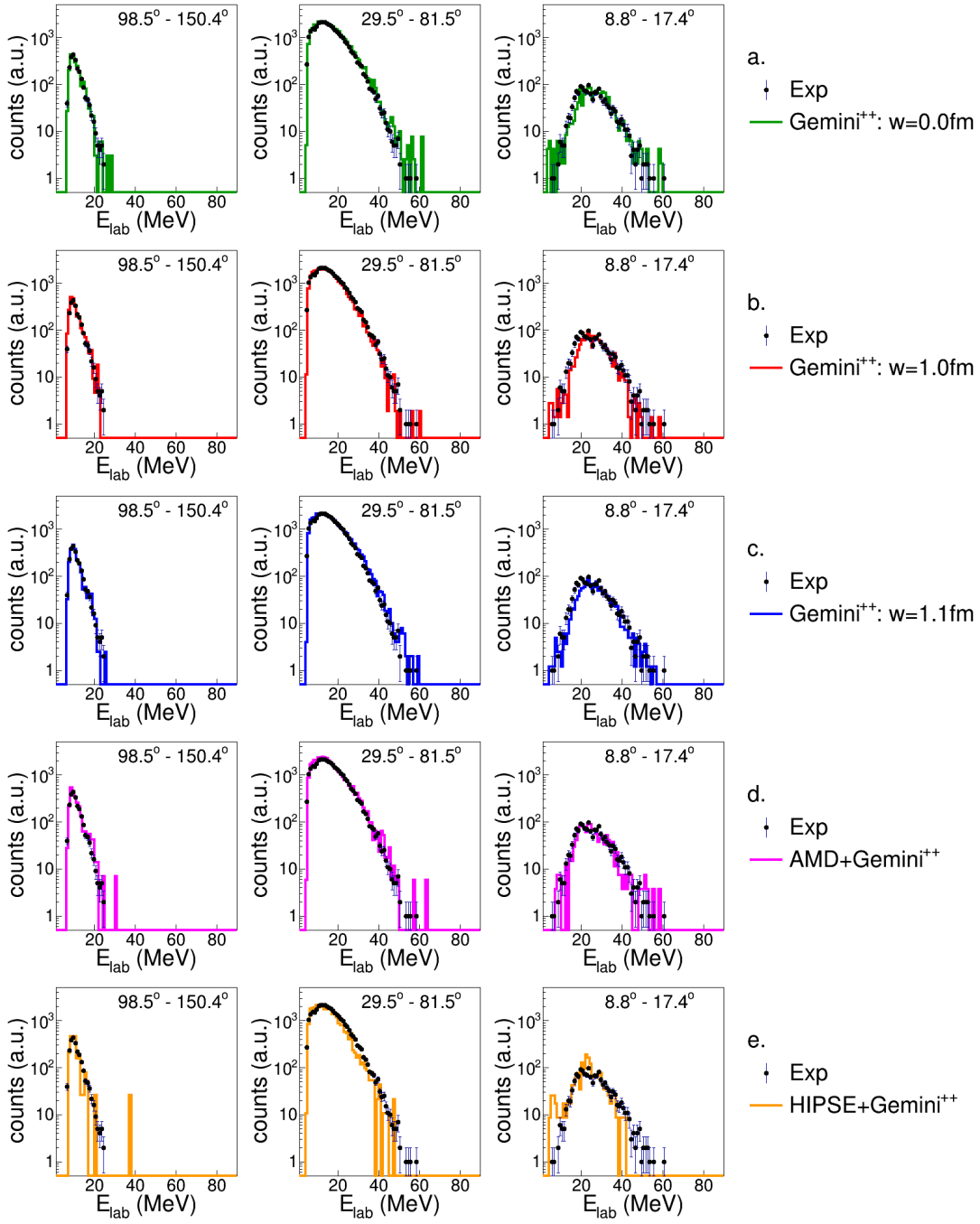

Figure B.124: Energy spectra of α-particles in coincidence with a P-residue for the reaction $^{19}F + ^{27}Al$ at 133 MeV

B.8 The Si residue: $Z_{res} = 14$

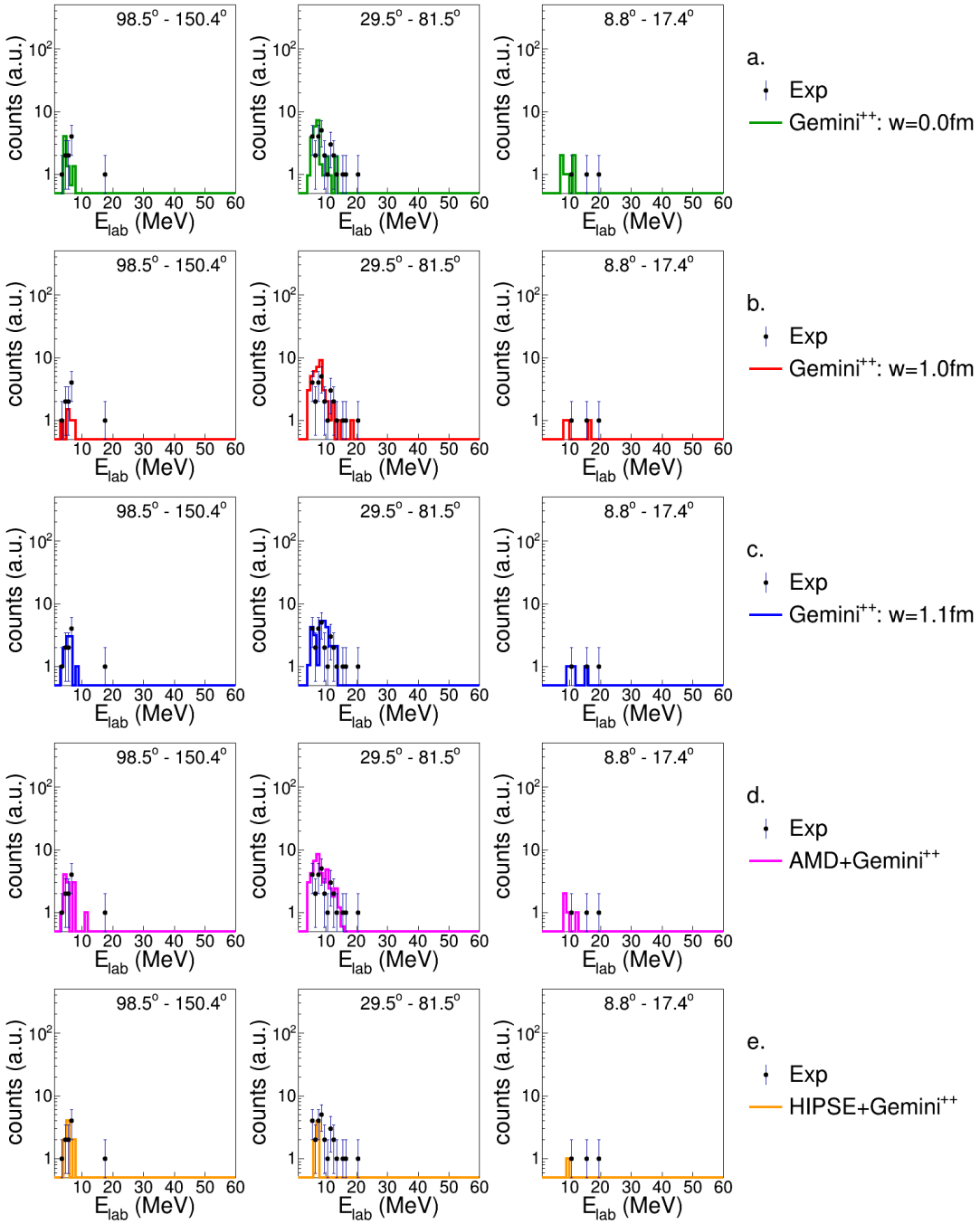

Figure B.125: Energy spectra of protons in coincidence with a *Si*-residue for the reaction $^{16}O + ^{30}Si$ at 111 MeV.

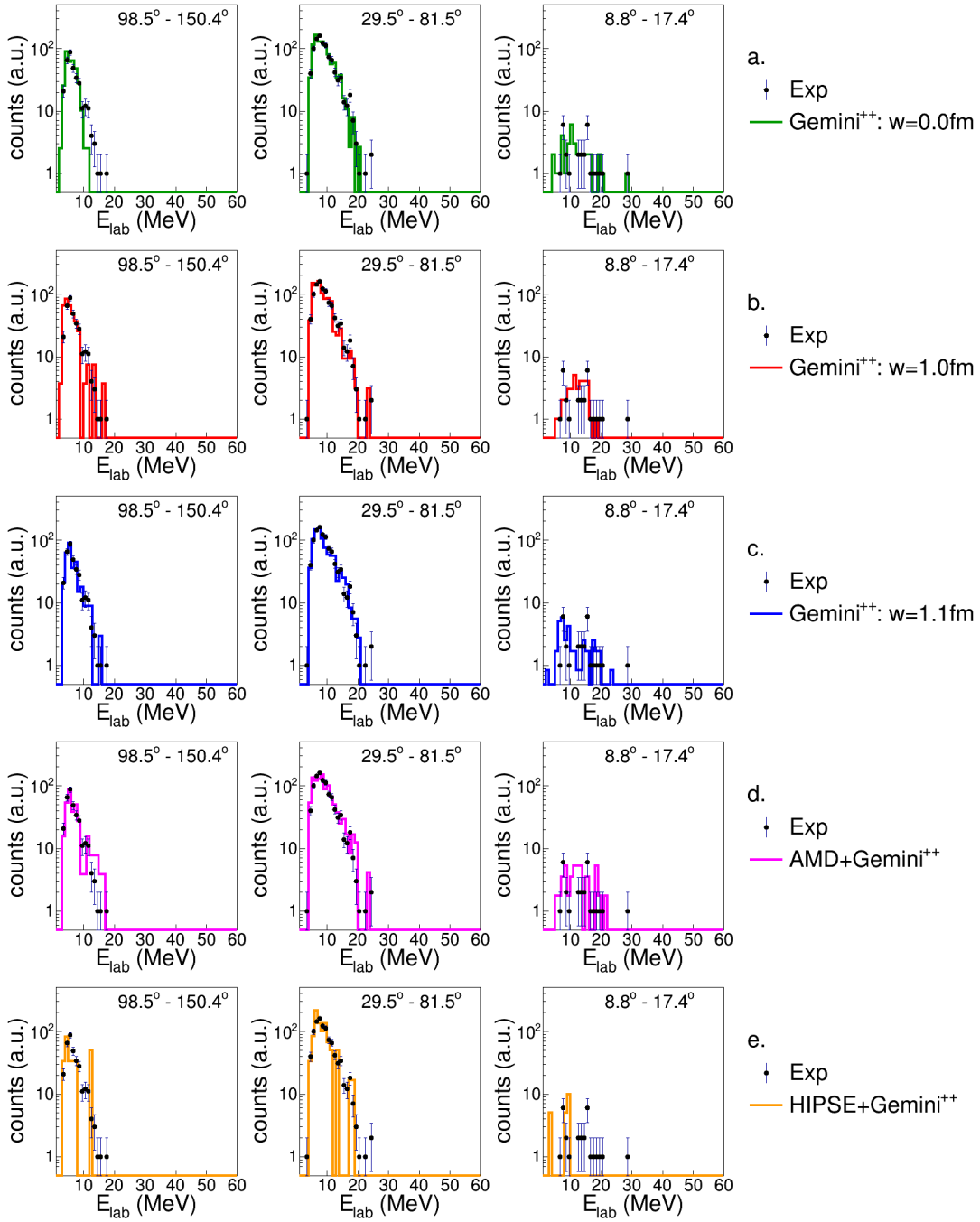

Figure B.126: Energy spectra of protons in coincidence with a Si-residue for the reaction $^{16}O + ^{30}Si$ at 128 MeV

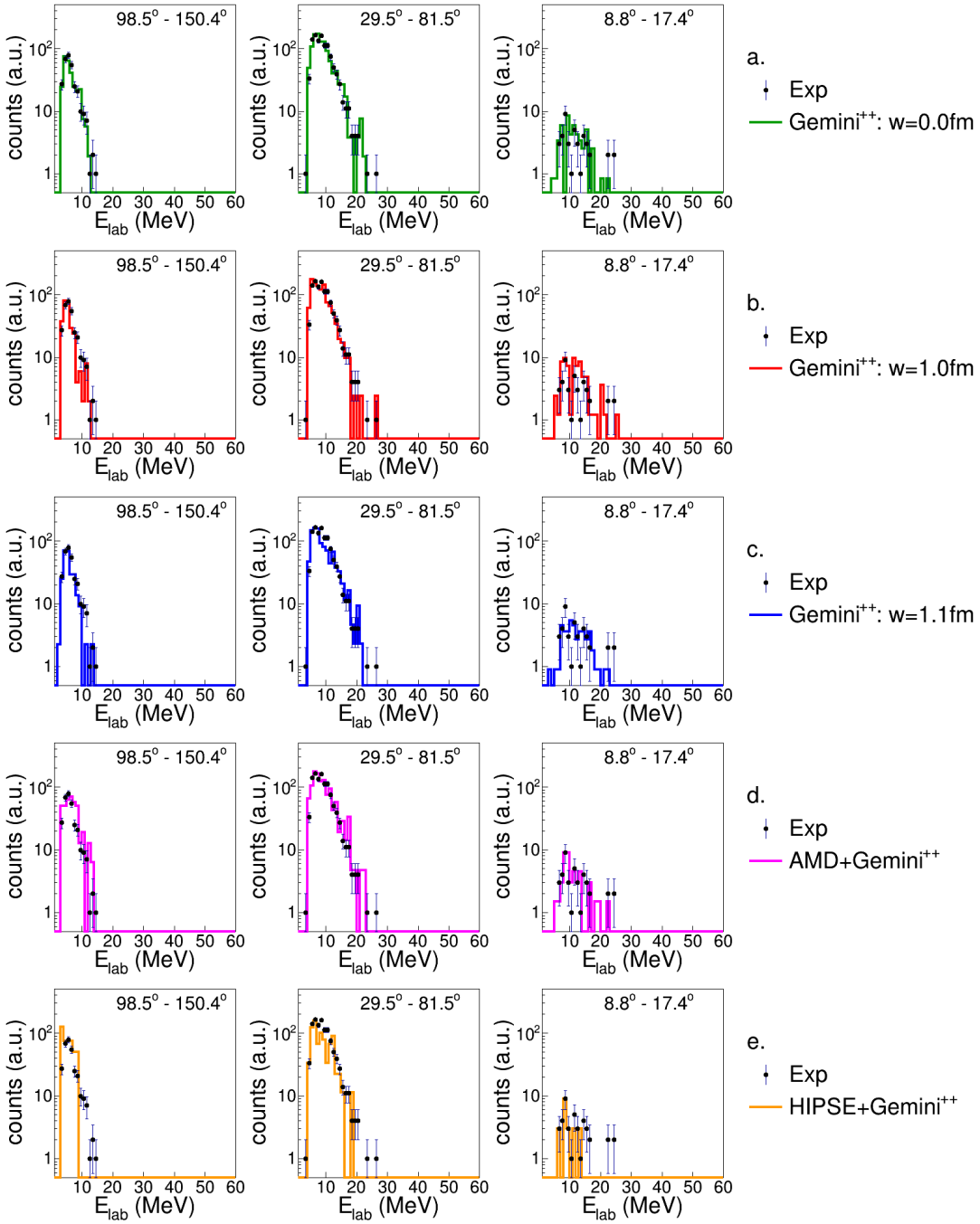

Figure B.127: Energy spectra of protons in coincidence with a *Si*-residue for the reaction $^{18}O + ^{28}Si$ at 126 MeV

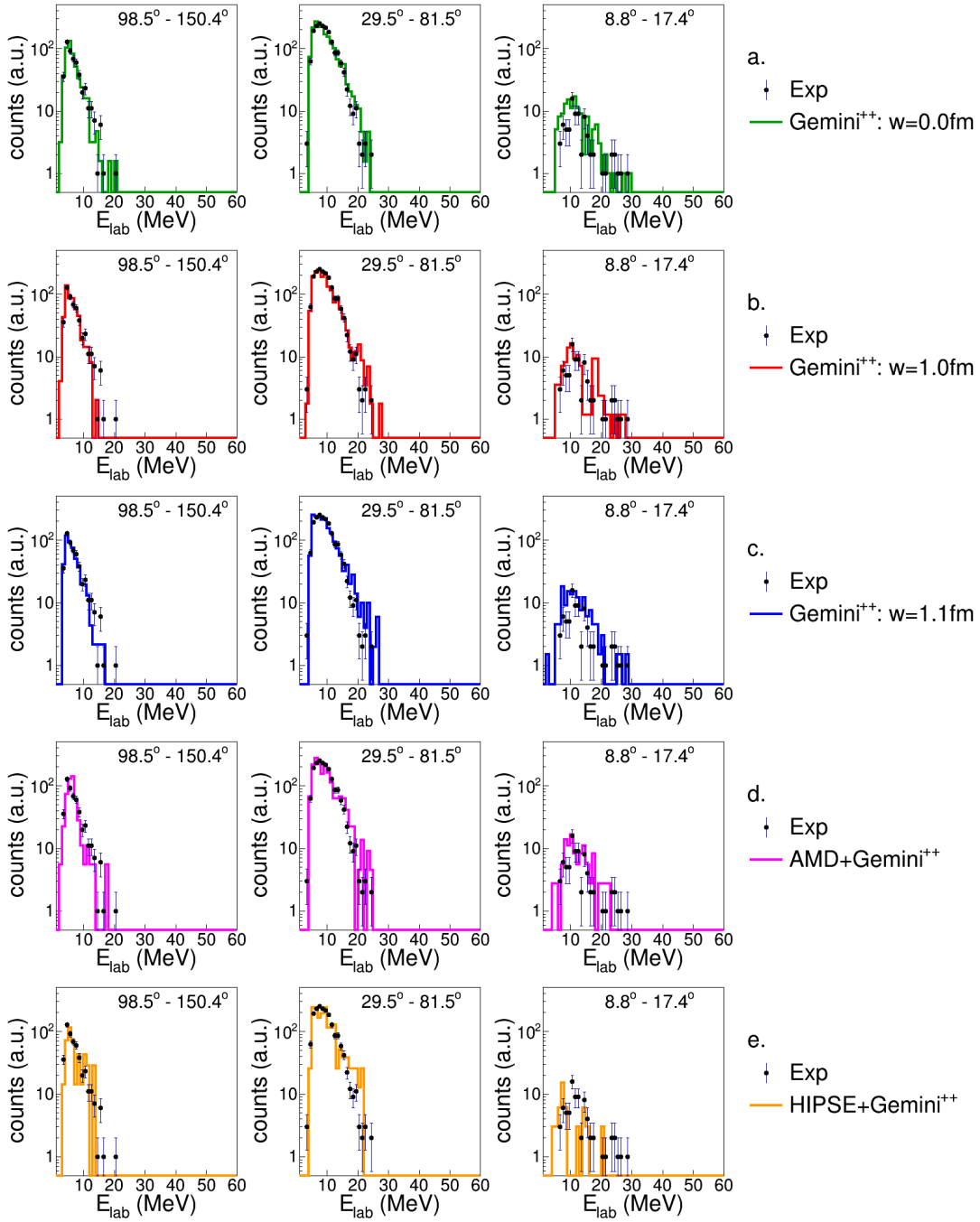

Figure B.128: Energy spectra of protons in coincidence with a *Si*-residue for the reaction $^{19}F + ^{27}Al$ at 133 MeV

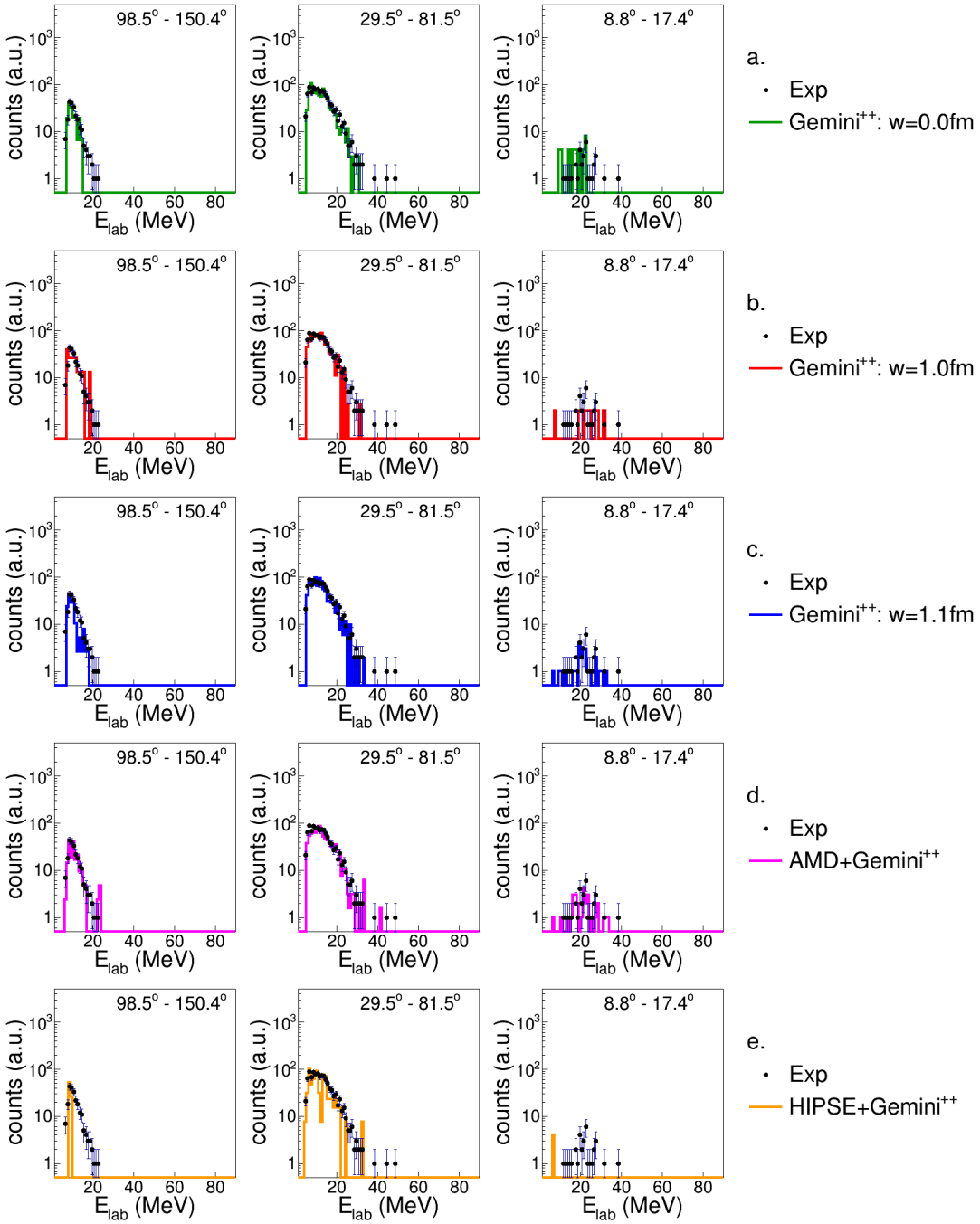

Figure B.129: Energy spectra of α-particles in coincidence with a Si-residue for the reaction $^{16}O + ^{30}Si$ at 111 MeV.

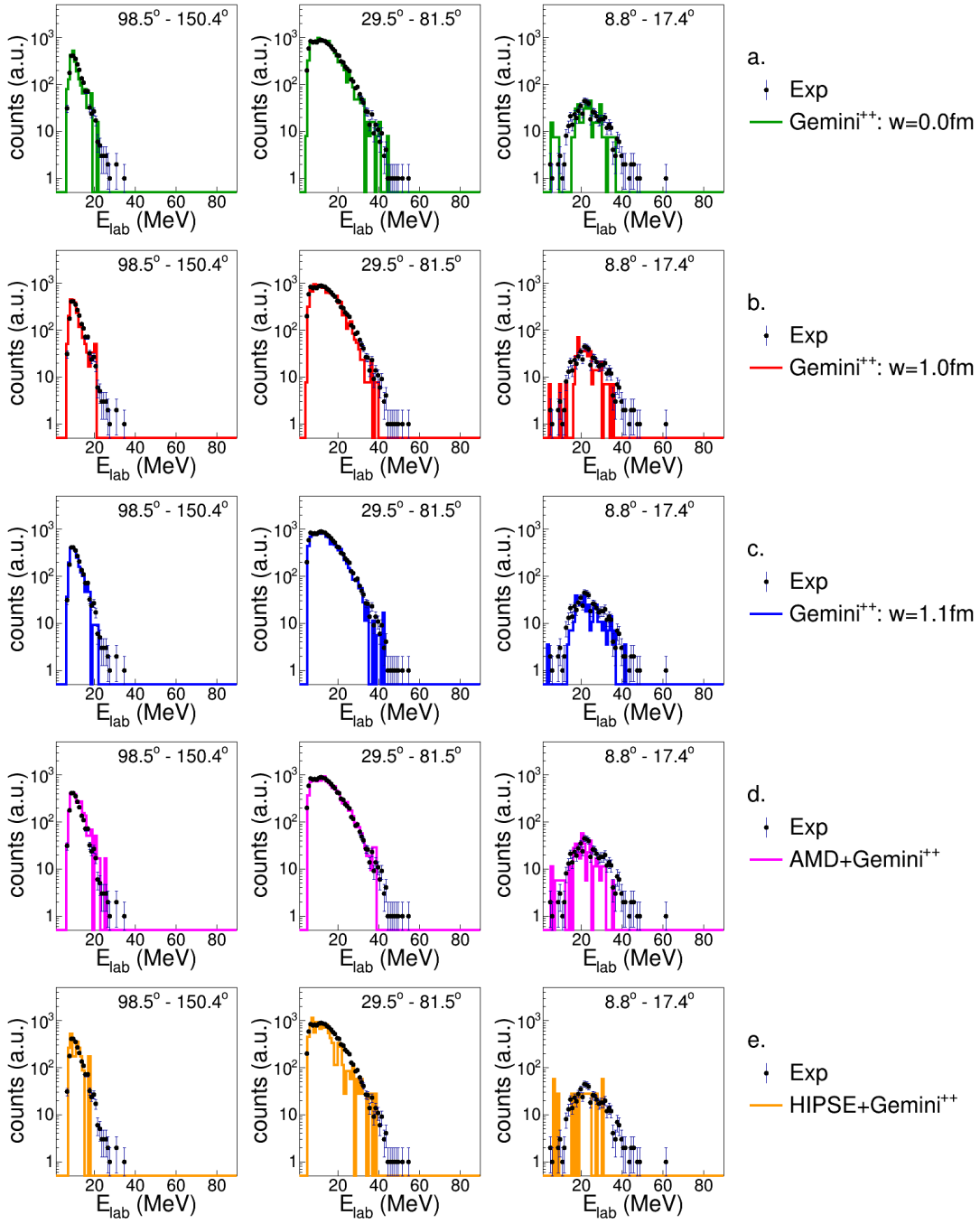

Figure B.130: Energy spectra of α-particles in coincidence with a Si-residue for the reaction $^{16}O + ^{30}Si$ at 128 MeV

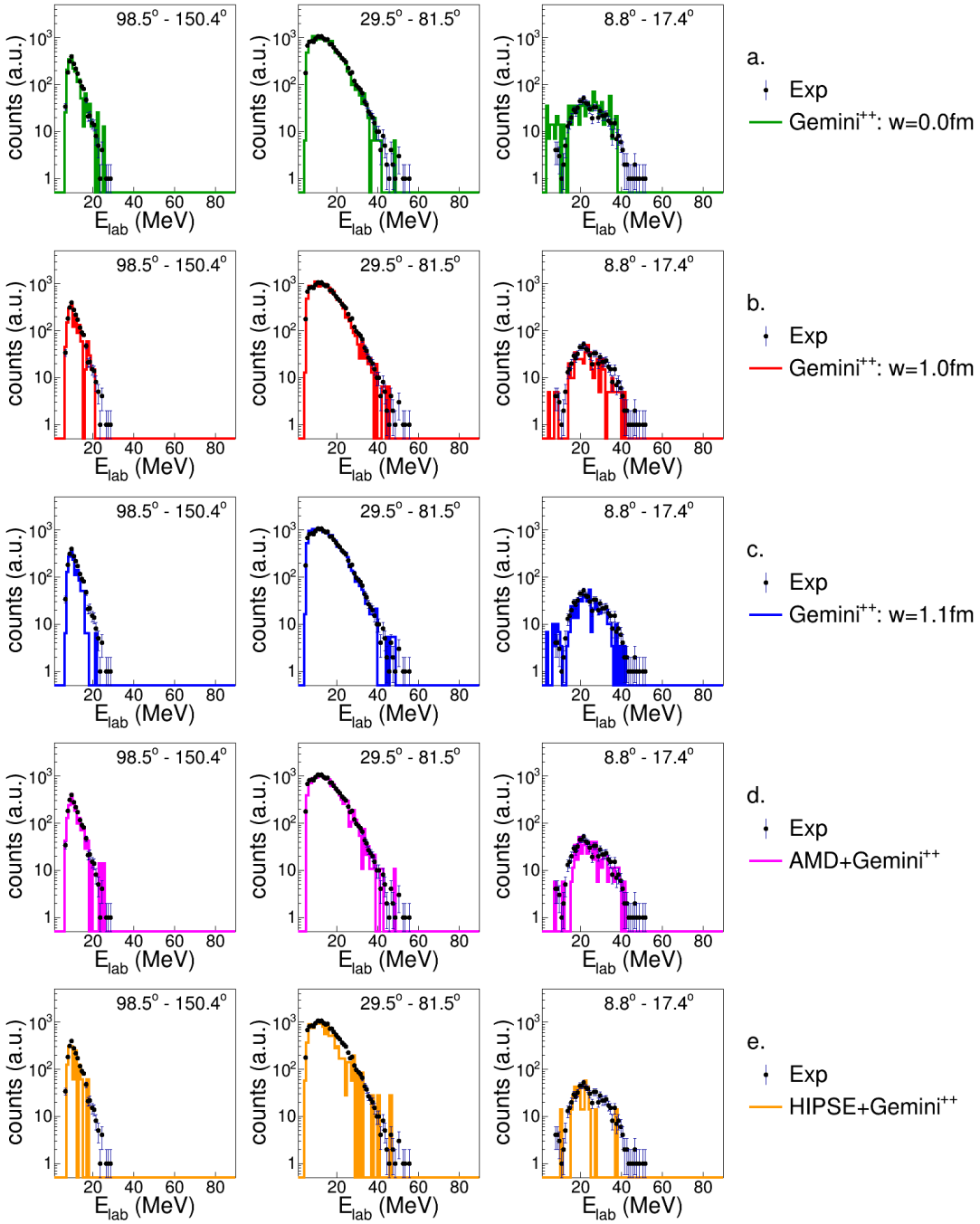

Figure B.131: Energy spectra of α-particles in coincidence with a Si-residue for the reaction $^{18}O + ^{28}Si$ at 126 MeV

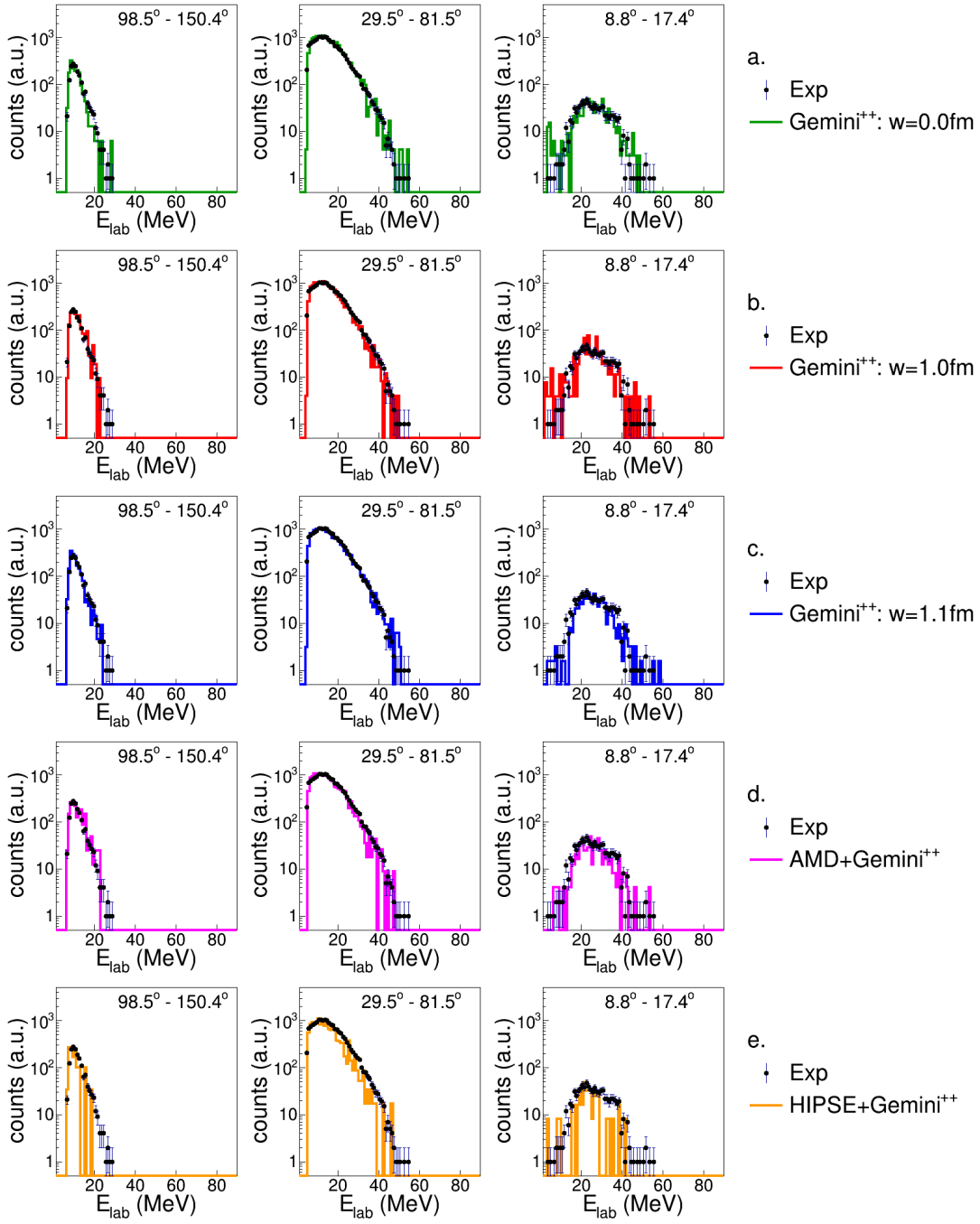

Figure B.132: Energy spectra of α-particles in coincidence with a Si-residue for the reaction $^{19}F + ^{27}Al$ at 133 MeV

B.9 The Al residue: $Z_{res} = 13$

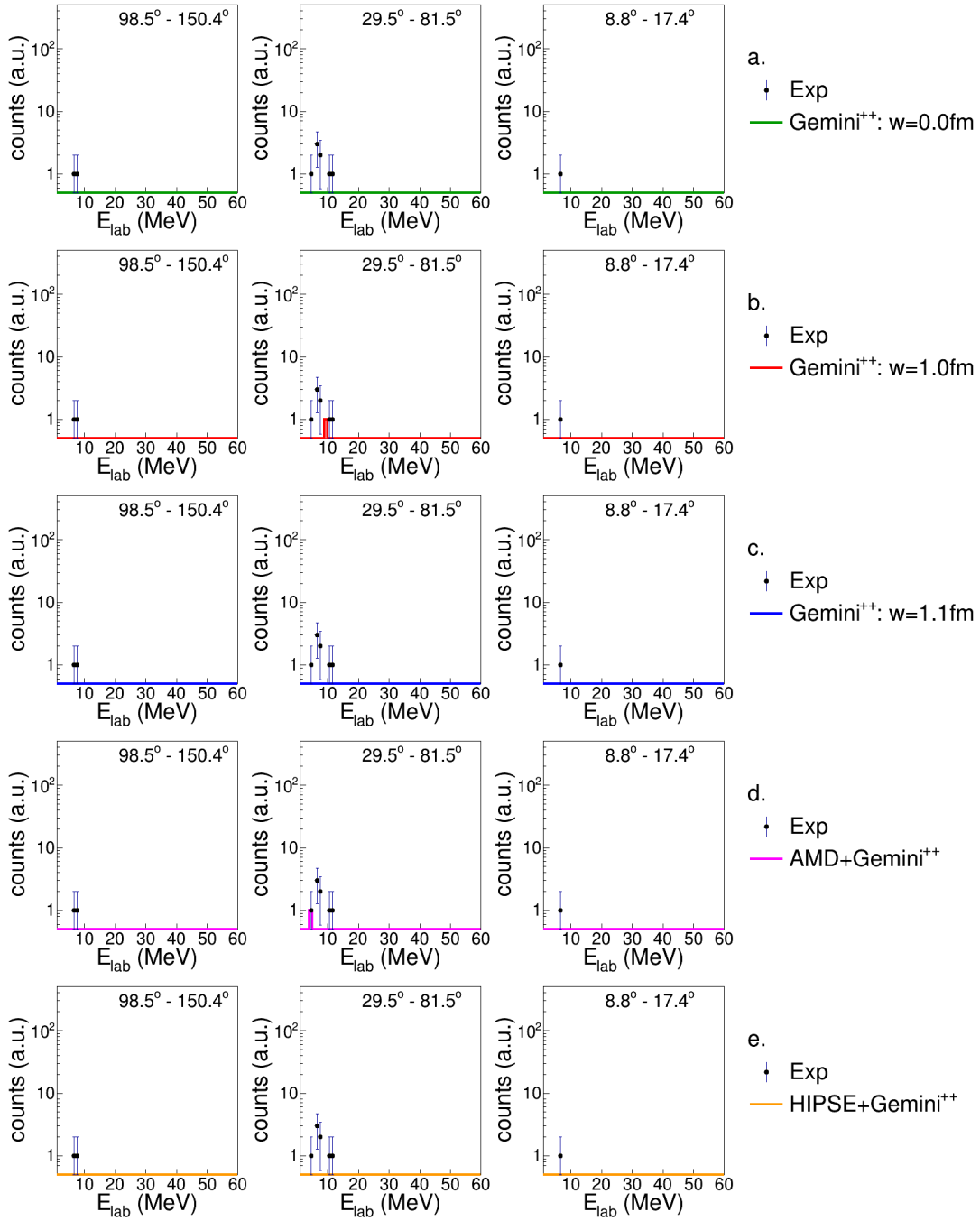

Figure B.133: Energy spectra of protons in coincidence with a *Al*-residue for the reaction $^{16}O + ^{30}Si$ at 111 MeV.

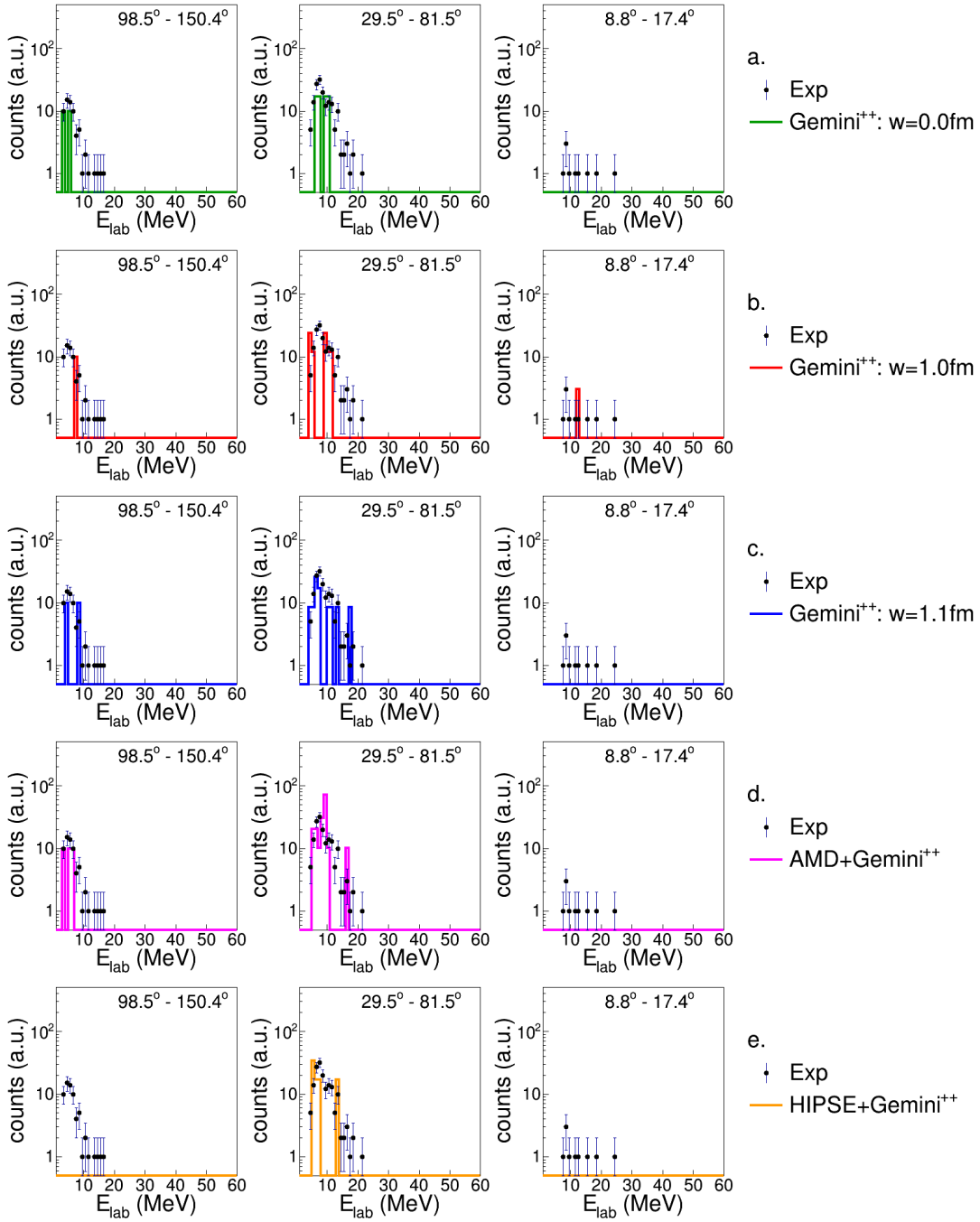

Figure B.134: Energy spectra of protons in coincidence with a *Al*-residue for the reaction $^{16}O + ^{30}Si$ at 128 MeV

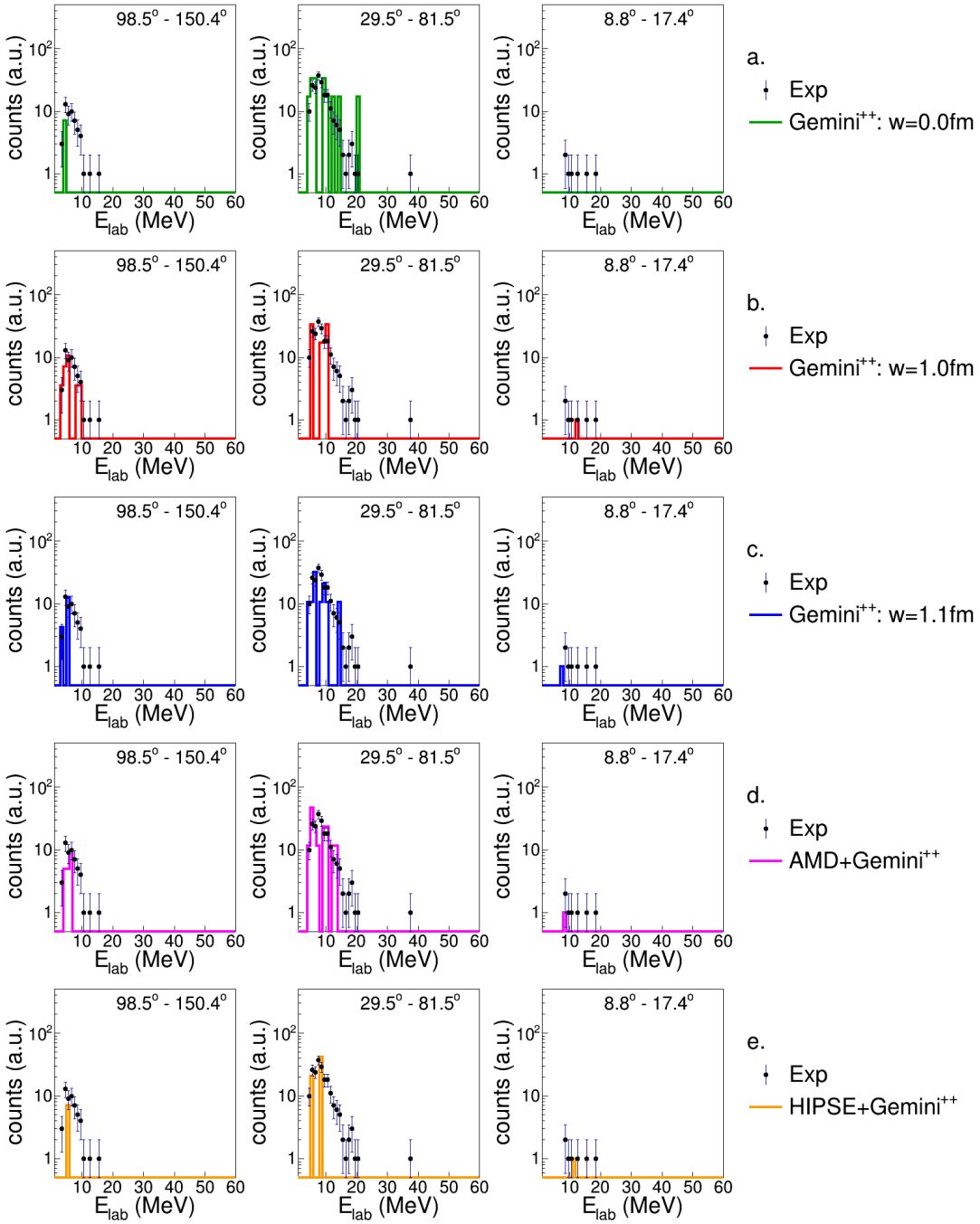

Figure B.135: Energy spectra of protons in coincidence with a *Al*-residue for the reaction $^{18}O + ^{28}Si$ at 126 MeV

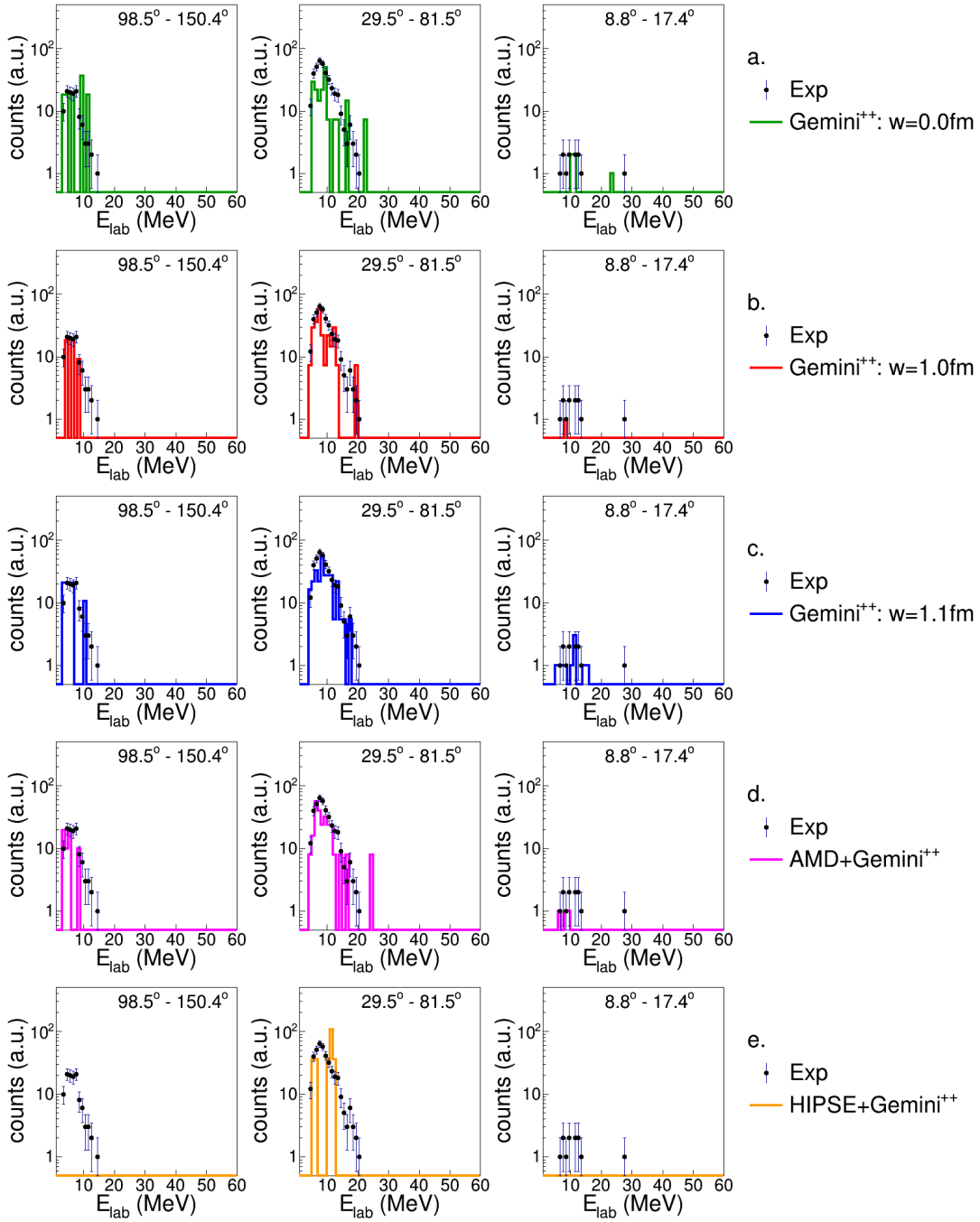

Figure B.136: Energy spectra of protons in coincidence with a *Al*-residue for the reaction $^{19}F + ^{27}Al$ at 133 MeV

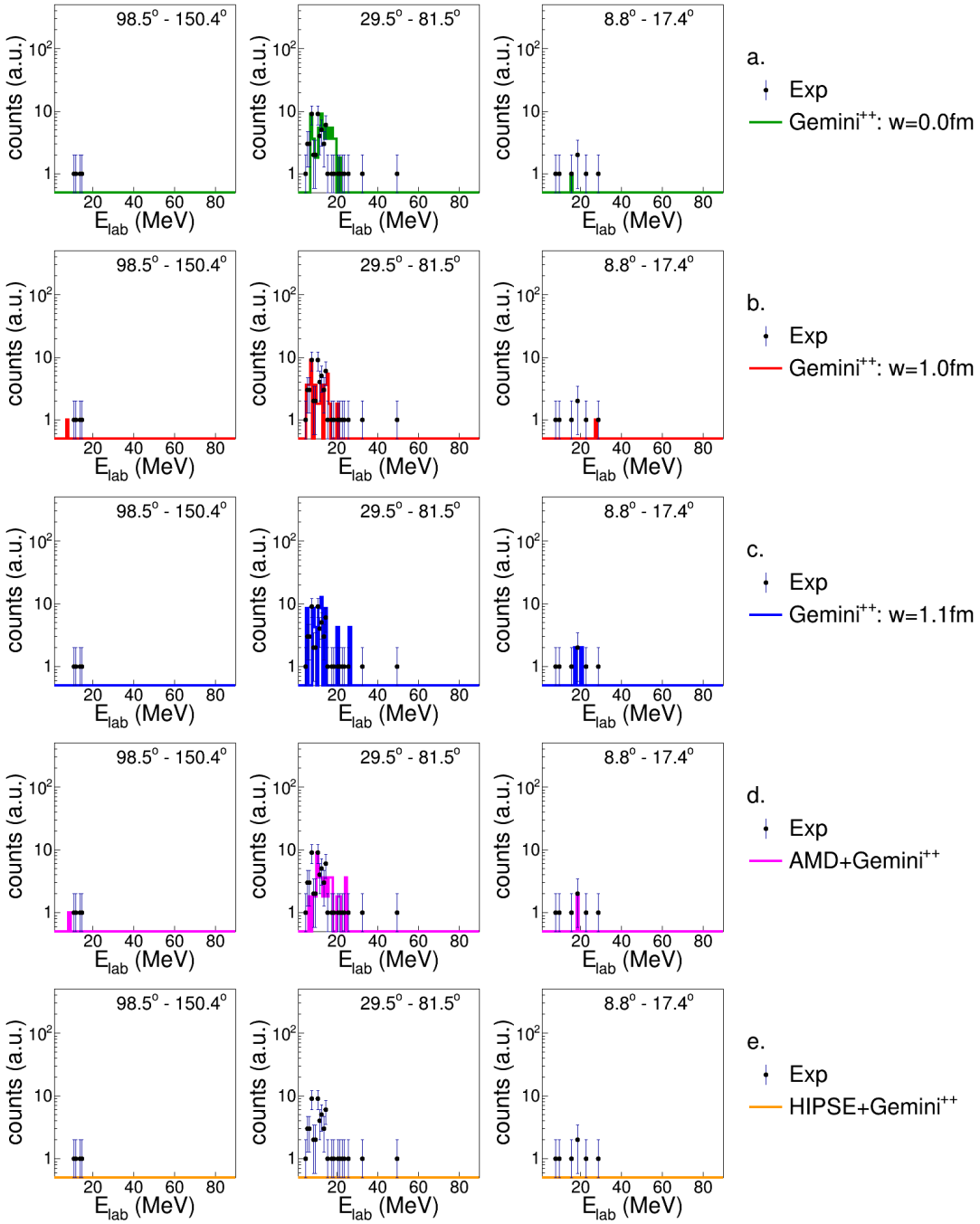

Figure B.137: Energy spectra of α-particles in coincidence with a *Al*-residue for the reaction $^{16}O + ^{30}Si$ at 111 MeV.

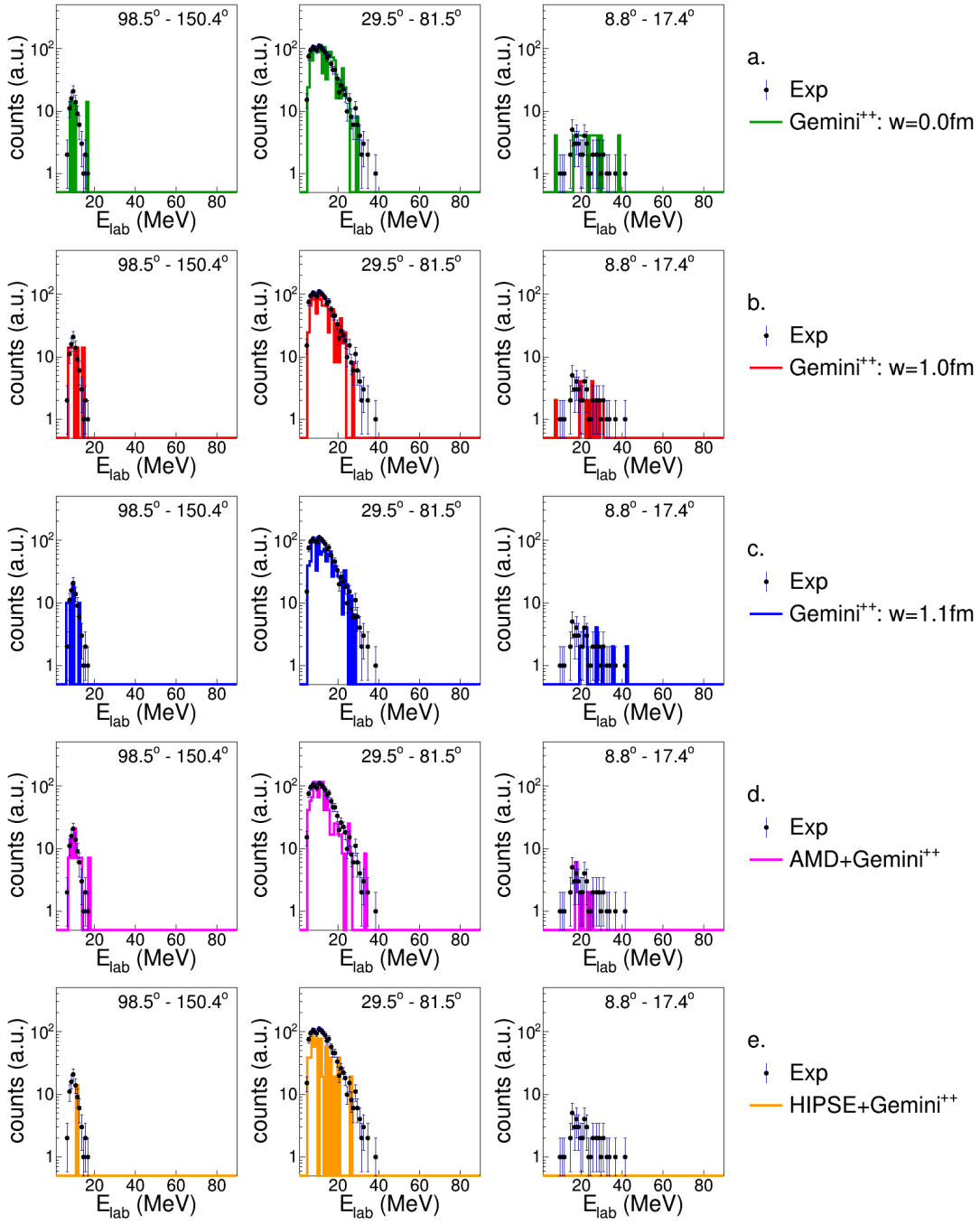

Figure B.138: Energy spectra of α-particles in coincidence with a *Al*-residue for the reaction $^{16}O + ^{30}Si$ at 128 MeV

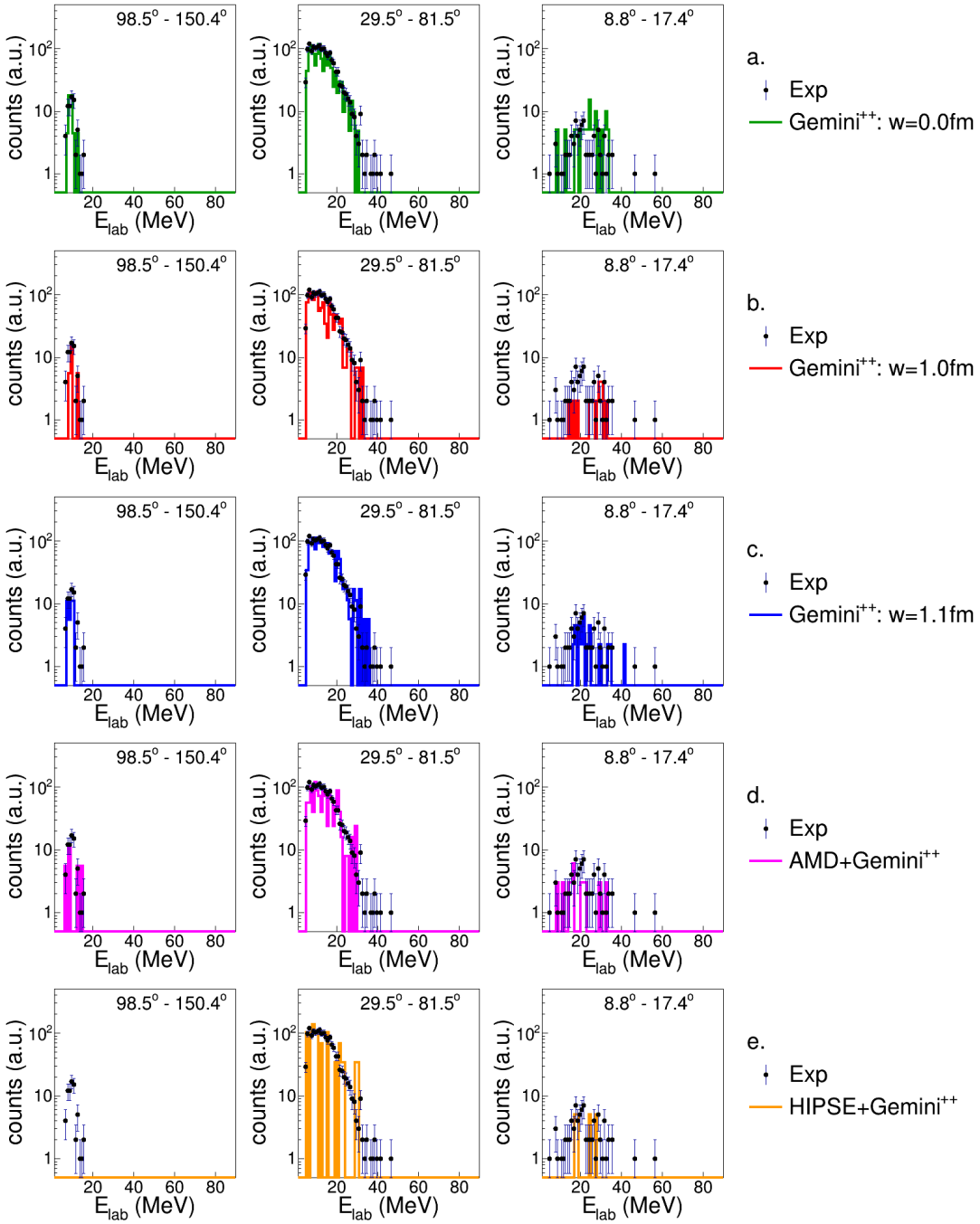

Figure B.139: Energy spectra of α-particles in coincidence with a *Al*-residue for the reaction $^{18}O + ^{28}Si$ at 126 MeV

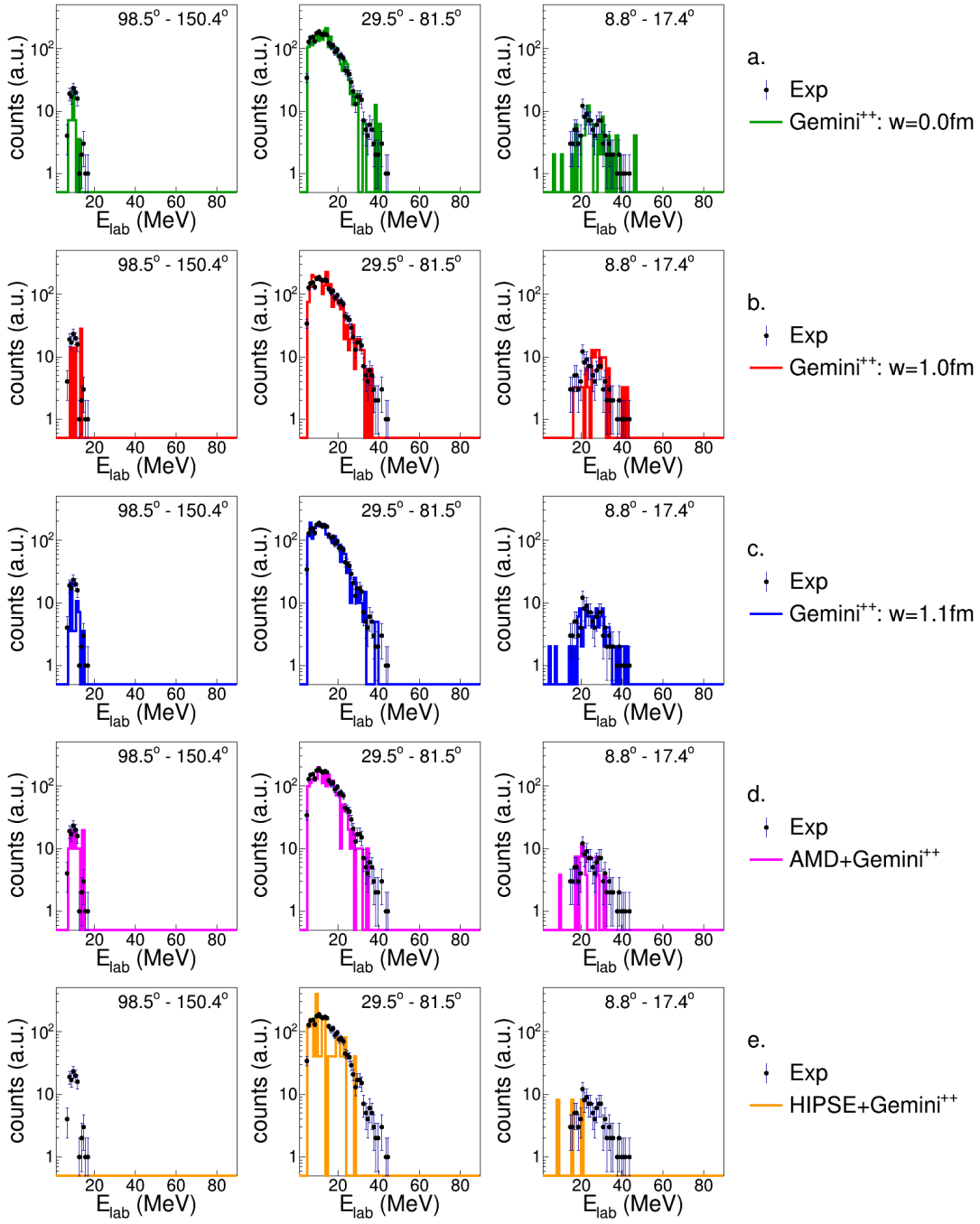

Figure B.140: Energy spectra of α-particles in coincidence with a Al-residue for the reaction $^{19}F + ^{27}Al$ at 133 MeV

Bibliography

[1] http:https://www.lnl.infn.it/index.php/it/.

[2] http:http://www.lnl.infn.it/~garfweb/garf/.

[3] http:http://www.bo.infn.it/nucl-ex/.

[4] R. A. Broglia and A. Winther, *Heavy Ion Reactions*, (1991) Addison-Wesley, Redford City.

[5] W. U. Schröder and J. R. Huizenga, *Treatise on Heavy-Ion Science* **Vol.2**, (1982) Plenum Press, New York-London.

[6] D. A. Bromley, *Treatise on Heavy-Ion Science* **Vol.1**, (1981) Plenum Press, New York-London.

[7] B. Borderie and M.F. Rivet, Progr. Part. Nucl. Phys. 61 (2008) 551-601. http://www.sciencedirect.com/science/article/pii/S0146641008000045.

[8] N. Bohr, Nature 137 (1936) 344-348. https://www.nature.com/articles/137344a0.

[9] T. Marchi *et al.*, *Nuclear Particle Correlations and Cluster Physics* (2017) 507-536. https://doi.org/10.1142/9789813209350_0020.

[10] E. Vogt, *Advanced in Nuclear Physics*, (1968) Plenum Press, New York-London.

[11] D. L. Hill and J. A: Wheeler, Phys. Rev. 89 (1953) 1102-1145. https://link.aps.org/doi/10.1103/PhysRev.89.1102.

[12] K. S. Krane, *Introductory Nuclear Physics*, (1987) Wiley, University of Michigan.

[13] A. J. Cole, *Statistical Models for Nuclear Decay* (2000) Fundamental and Applied Nucl. Phys. Institute of Physics publishing, Philadelphia

[14] V. Weisskopf, Phys. Rev. 52 (1937) 295-303. https://link.aps.org/doi/10.1103/PhysRev.52.295.

[15] V. F. Weisskopf and D. H. Ewing, Phys. Rev. 57 (1940) 472-485. https://link.aps.org/doi/10.1103/PhysRev.57.472.

[16] H. A. Bethe, Phys. Rev. 50 (1936) 332-341. https://link.aps.org/doi/10.1103/PhysRev.50.332.

[17] W. Hauser and H. Feshbach, Phys. Rev. 87 (1952) 366.373. https://link.aps.org/doi/10.1103/PhysRev.87.366.

[18] H. Feshbach, *Nuclear Spectroscopy* **part B** (1960) Accademic Press, New York.

[19] N. N. Ajitanand *et al.*, Phys. Rev. **C** 34 (1986) 877-889. https://link.aps.org/doi/10.1103/PhysRevC.34.877.

[20] L. Wolfenstein, Phys. Rev. 82 (1951) 690-696. https://link.aps.org/doi/10.1103/PhysRev.82.690.

[21] A. Bohr and B. Mottelson, *Nuclear Structure* **Vol. II**, (1975) Benjamin, New York.

[22] J. J. Griffin, Phys. Rev. Lett. 17 (1966) 478-481. http://link.aps.org/doi/10.1103/PhysRevLett.17.478.

[23] J. J. Griffin, Phys. Rev. Lett. 19 (1967) 57. http://link.aps.org/doi/10.1103/PhysRevLett.19.57.

[24] G. D. Harp, J. M. Miller, and B. J. Berne, Phys. Rev. 165 (1968) 1166-1169. http://link.aps.org/doi/10.1103/PhysRev.165.1166.

[25] M. Blann, Phys. Rev. Lett. 27 (1971) 337-340. http://link.aps.org/doi/10.1103/PhysRevLett.27.337.

[26] M. Blann, Phys. Rev. Lett. 28 (1972) 757-759. http://link.aps.org/doi/10.1103/PhysRevLett.28.757.

[27] L. Colli-Milazzo and G. Marcazzan-Braga, Phys. Rev. Lett. **B** 38 (1972) 150-158. http://www.sciencedirect.com/science/article/pii/0370269372900378.

[28] D. Brink and J. Castro, Nucl. Phys. **A** 216 (1973) 109-124. http://www.sciencedirect.com/science/article/pii/0375947473905216.

[29] L. Milazzo-Colli and G. Braga-Marcazzan, Nucl. Phys. **A** 210 (1973) 297-306. http://www.sciencedirect.com/science/article/pii/0375947473903035.

[30] E. Fabrici *et al.*, Phys. Rev. **C** 40 (1989) 2548-2557. http://link.aps.org/doi/10.1103/PhysRevC.40.2548.

[31] M. Cavinato *et al.*, Nucl. Phys. **A** 679 (2001) 753-764. http://www.sciencedirect.com/science/article/pii/S0375947400003572.

[32] N. Cindro *et al.*, Phys. Rev. Lett. 66 (1991) 868-871. http://link.aps.org/doi/10.1103/PhysRevLett.66.868.

[33] L.R. Hafstad and E. Teller, Phys. Rev. 54 (1938) 681-692. https://link.aps.org/doi/10.1103/PhysRev.54.681

[34] K. Ikeda *et al.*, Prog. Theor. Phys. Suppl. **E** 68 (1968) 464-475. https://doi.org/10.1143/PTPS.E68.464

[35] W. von Oertzen *et al.*, Phys. Rep. 432 (2006) 43-113. http://www.sciencedirect.com/science/article/pii/S0370157306002626

[36] H. Feldmeier *et al.* Nucl. Phys. **A** 586 (1995) 493-532. http://www.sciencedirect.com/science/article/pii/037594749400792L

[37] T. Neff *et al.* Nucl. Phys. **A** 752 (2005) 321-324. http://www.sciencedirect.com/science/article/pii/S0375947405001843

[38] H. Horiuchi and Y. Kanada- En'Yo, Nucl. Phys. **A** 616 (1997) 394-405. http://www.sciencedirect.com/science/article/pii/S0375947497001085

[39] Y. Kanada- En'Yo and H. Horiuchi, Prog. Theor. Phys. Suppl. 142 (2001) 205-263. http://dx.doi.org/10.1143/PTPS.142.205

[40] U. Brosa and S. Grossmann, JoP **G** 10 (1984) 933. http://stacks.iop.org/0305-4616/10/i=7/a=010.

[41] M. Colonna *et al.*, Nucl. Phys. **A** 583 (1995) 525-530. http://www.sciencedirect.com/science/article/pii/037594749400714X.

[42] C. Cline, Nucl. Phys. **A** 193 (1972) 417-437. http://www.sciencedirect.com/science/article/pii/0375947472903302.

[43] A. Iwamoto and K. Harada, Phys. Rev. **C** 26 (1982) 1821-1834. http://link.aps.org/doi/10.1103/PhysRevC.26.1821.

[44] J. Bisplinghoff and H. Keuser, Phys. Rev. **C** 35 (1987) 821-824. http://link.aps.org/doi/10.1103/PhysRevC.35.821.

[45] P.E. Hodgson and E. Běták, Physics Reports 374 (2003) 1-89. http://www.sciencedirect.com/science/article/pii/S0370157302002685.

[46] L. Morelli *et al.*, JoP **G** 41 (2014) 075107. http://stacks.iop.org/0954-3899/41/i=7/a=075107.

[47] L. Morelli *et al.*, JoP **G** 41 (2014) 075108. http://stacks.iop.org/0954-3899/41/i=7/a=075108.

[48] D. Fabris *et al.*, Acta Phys. Pol. **B** 46 (2015) 447-451. http://www.actaphys.uj.edu.pl/fulltext?series=Reg&vol=46&page=447

[49] L. Morelli *et al.*, JoP **G** 43 (2014) 075110. http://stacks.iop.org/0954-3899/43/i=4/a=045110.

[50] W. von Oertzen *et al.*, Phys. Rep. 432 (2006) 43-113. http://www.sciencedirect.com/science/article/pii/S0370157306002626.

[51] F. Gramegna *et al.*, NIM **A**, 389, (1997), 474-478, http://www.sciencedirect.com/science/article/pii/S0168900296012120.

[52] M. Bruno *et al.*, EPJ **A**, 49, (2013), 128, https://doi.org/10.1140/epja/i2013-13128-2.

[53] M. Chiari *et al.*, NIM **A** 484 (2002) 111-117, http://www.sciencedirect.com/science/article/pii/S0168900201019684.

[54] A. Moroni *et al.*, NIM **A** 556 (2006) 516-526, http://www.sciencedirect.com/science/article/pii/S0168900205020887.

[55] G. F. Knoll, *Radiaction detection and measurement*, John Wiley & Sons (2000).

[56] P. F. Mastinu *et al.*, NIM **A** 338 (1994) 419-424, http://www.sciencedirect.com/science/article/pii/0168900294913250; NIM **A** 343 (1994) 663, http://www.sciencedirect.com/science/article/pii/0168900294902518.

[57] W. R. Leo, *Techniques for Nuclear and Particle Physics Experiments*, Springer-Verlag Berlin Heidelberg (1994).

[58] F. Tonetto *et al.*, NIM **A** 420 (1999) 181-188, http://www.sciencedirect.com/science/article/pii/S016890029801136X.

[59] L. Morelli, PhD Thesis:*Competition between evaporation and fragmentation in nuclear reaction at 15-20MeV AMeV energy*,pag.36 (2011), http://www.bo.infn.it/rem/Morelli_Luca_tesi.pdf.

[60] G. Pasquali *et al.*, NIM **A** 570 (2007) 126-132, http://www.sciencedirect.com/science/article/pii/S0168900206017669.

[61] L. Bardelli *et al.*, Nuclear Physucs **A** 746 (2004) 272-276, http://www.sciencedirect.com/science/article/pii/S0375947404009820.

[62] L. Morelli *et al.*, NIM **A** 620 (2010) 305-313. http://www.sciencedirect.com/science/article/pii/S0168900210006637.

[63] L. Bardelli and G. Poggi, NIM **A** 560 (2016) 517-523. http://www.sciencedirect.com/science/article/pii/S0168900206000817.

[64] L. Bardelli and G. Poggi, NIM **A** 560 (2006) 524-538. http://www.sciencedirect.com/science/article/pii/S0168900206000829.

[65] M. P$\widehat{a}$rlog *et al.*, NIM **A** 482 (2002) 693.

[66] G. Casini *et al.*, Annual Report LNL (2004).

[67] R. Charity *et al.*, Phys. Rev. **C** 82 (2010) 014610. https://link.aps.org/doi/10.1103/PhysRevC.82.014610

[68] D. Mancusi *et al.*, Phys. Rev. **C** 82 (2010) 044610. https://link.aps.org/doi/10.1103/PhysRevC.82.044610

[69] R. Charity *et al.*, Nucl. Phys. **A** 483 (1988) 371-405. http://www.sciencedirect.com/science/article/pii/0375947488905428

[70] https://bitbucket.org/arekfu/gemini

[71] W. Hauser and H. Feshbac, Phys. Rev. 87 (1952) 366-373. https://link.aps.org/doi/10.1103/PhysRev.87.366

[72] N. Bohr and J. A. Wheeler, Phys. Rev. 56 (1939) 426-250. https://link.aps.org/doi/10.1103/PhysRev.56.426

[73] L. G. Moretto, Nucl. Phys. **A** 247 (1975) 211-230. http://www.sciencedirect.com/science/article/pii/0375947475906326

[74] A. J. Sierk, Phys. Rev. Lett. 55 (1985) 582-583. https://link.aps.org/doi/10.1103/PhysRevLett.55.582

[75] P. Moller *et al.*, Atom. Data Nucl. Data Tables 59 (1995) 185-381. http://www.sciencedirect.com/science/article/pii/S0092640X85710029

[76] J. B. Natowitz *et al.*, Phys. Rev. Lett. 89 (2002) 212701. https://link.aps.org/doi/10.1103/PhysRevLett.89.212701

[77] A. Ono, JoP conf. series 420 (2013) 012103. http://stacks.iop.org/1742-6596/420/i=1/a=012103

[78] N. Ikeno *et al.*, Phys. Rev. C 93 (2016) 044612. https://link.aps.org/doi/10.1103/PhysRevC.93.044612

[79] G. Tian *et al.*, Phys. Rev. C 97 (2018) 034610. https://link.aps.org/doi/10.1103/PhysRevC.97.034610

[80] E. Chabanat *et al.*, Nucl. Phys. A 635 (1998) 231-256. http://www.sciencedirect.com/science/article/pii/S0375947498001808

[81] E. Chabanat *et al.*, Nucl. Phys. A 643 (1998) 441. http://www.sciencedirect.com/science/article/pii/S0375947498005703

[82] A. Ono and H. Horiuchi, Prog. Part. Nucl. Phys. 53 (2004) 501-581. http://www.sciencedirect.com/science/article/pii/S0146641004000936

[83] A. Ono *et al.*, Phys. Rev. Lett. 68 (1992) 2898-2900. https://link.aps.org/doi/10.1103/PhysRevLett.68.2898

[84] A. Ono *et al.*, Prog. Theor. Phys. 87 (1992) 1185-1206. http://dx.doi.org/10.1143/ptp/87.5.1185

[85] A. Ono *et al.*, Phys. Rev. **C** 47 (1993) 2652-2660. https://link.aps.org/doi/10.1103/PhysRevC.47.2652

[86] A. Ono *et al.*, Phys. Rev. **C** 48 (1993) 2946-2955. https://link.aps.org/doi/10.1103/PhysRevC.48.2946

[87] A. Ono *et al.*, Phys. Rev. **C** 51 (1995) 299-309. https://link.aps.org/doi/10.1103/PhysRevC.51.299

[88] A. Ono *et al.*, Phys. Rev. **C** 53 (1996) 845-848. https://link.aps.org/doi/10.1103/PhysRevC.53.845

[89] L. Wilets *et al.*, Nucl. Phys. **A** 282 (1977) 341-350. http://www.sciencedirect.com/science/article/pii/0375947477902202

[90] G. F. Bertsch and S. Das Gupta, Phys. Rep. 160 (1988) 189-233. http://www.sciencedirect.com/science/article/pii/0370157388901706

[91] W. Cassing *et al.*, Phys. Rep. 188 (1990) 363-449. http://www.sciencedirect.com/science/article/pii/037015739090164W

[92] G. Q. Li and R. Machleidt, Phys. Rev. **C** 48 (1993) 1702-1712. https://link.aps.org/doi/10.1103/PhysRevC.48.1702

[93] G. Q. Li and R. Machleidt, Phys. Rev. **C** 49 (1994) 566-569. https://link.aps.org/doi/10.1103/PhysRevC.49.566

[94] D. D. S. Coupland *et al.*, Phys. Rev. **C** 84 (2011) 054603. https://link.aps.org/doi/10.1103/PhysRevC.84.054603

[95] J. Xu *et al.*, Phys. Rev. **C** 93 (2016) 044609. https://link.aps.org/doi/10.1103/PhysRevC.93.044609

[96] D. Lacroix *et al.*, Phys. Rev. **C** 69 (2004) 054604. https://link.aps.org/doi/10.1103/PhysRevC.69.054604

[97] D. Lacroix and D. Durand, AIP Conference Proceedings 791 (2005) 112. https://doi.org/10.1063/1.2114699

[98] D. Lacroix *et al.*, Phys. Rev. **C** 71 (2005) 024601. https://link.aps.org/doi/10.1103/PhysRevC.71.024601

[99] W. D. Myers and W. J. Swiatecki, Nucl. Phys. **A** 601 (1996) 141. http://www.sciencedirect.com/science/article/pii/0375947495005099

[100] W. K. Chu and J. M. Mayer and M.A. Nicolet, *Backscattering Spectroscopy*, (1978) Academiv Press, New York.

[101] L. C. Feldman and J. W. Mayer, *Fundamentals of Surface and Thin Film Analysis*, (1986) Elvier Science Publishing Co..

[102] F. Gramegna *et al.*, EPJ Web Conference 163 (2017) 00020. https://doi.org/10.1051/epjconf/201716300020.

[103] D. Durand, Nucl. Phys. **A** 541 (1992) 266-294. http://www.sciencedirect.com/science/article/pii/0375947492900974.

[104] W. D. Myers and W. J. Swiatecki, Acta. Phys. Pol. **B** 32 (2001) 1033. http://www.actaphys.uj.edu.pl/fulltext?series=Reg&vol=32&page=1033.

[105] K. Pomorski and J. Dudek, Phys. Rev. **C** 67 (2003) 044316. https://link.aps.org/doi/10.1103/PhysRevC.67.044316.

[106] A. Maj *et al.*, EPJ **A** 20 (2003) 165-166. https://doi.org/10.1140/epja/i2002-10345-8.

[107] K. Mazurek *et al.*, Phys. Rev. **C** 91 (2015) 31 https://link.aps.org/doi/10.1103/PhysRevC.91.034301

[108] M. Brekiesz *et al.*, Nucl. Phys. **A** 788 (2007) 224-230. http://www.sciencedirect.com/science/article/pii/S037594740700084X.

[109] M. Kmiecik *et al.*, Acta. Phys. Pol. **B** 38 (2007) 1437. http://www.actaphys.uj.edu.pl/fulltext?series=Reg&vol=38&page=1437.

[110] A. Maj *et al.*, Acta. Phys. Pol. **B** 32 (2001) 2433. http://adsabs.harvard.edu/abs/2001AcPPB..32.2433M.

[111] A. Maj *et al.*, Nucl. Phys. **A** 731 (2004) 319-326. http://www.sciencedirect.com/science/article/pii/S0375947403018815.

[112] A. Maj *et al.*, Nucl. Phys. **A** 687 (2001) 192-197. http://www.sciencedirect.com/science/article/pii/S0375947401006200.

[113] M. Brekiesz *et al.*, Acta. Phys. Pol. **B** 36 (2005) 1175. http://www.actaphys.uj.edu.pl/fulltext?series=Reg&vol=36&page=1175.

[114] I. Y. Lee *et al.*, Acta. Phys. Pol. **B** 32 (2001) 2499. http://www.actaphys.uj.edu.pl/fulltext?series=Reg&vol=32&page=2499.

[115] D. Ward *et al.*, PHys. Rev. **C** 66 (2002) 024317. https://link.aps.org/doi/10.1103/PhysRevC.66.024317.

[116] I. A. Egorova *et al.*, Phys. Rev. Lett. 109 (2012) 202502. https://link.aps.org/doi/10.1103/PhysRevLett.109.202502.

[117] L. V. Grigorenko *et al.*, Phys. Rev. **C** 80 (2009) 034602. https://link.aps.org/doi/10.1103/PhysRevC.80.034602.